



HAL
open science

Mode interactions in external flows

Javier Sierra Ausin

► **To cite this version:**

Javier Sierra Ausin. Mode interactions in external flows. Fluids mechanics [physics.class-ph]. Université Paul Sabatier - Toulouse III; Università degli studi (Salerno, Italie), 2023. English. NNT: 2023TOU30128 . tel-04299454

HAL Id: tel-04299454

<https://theses.hal.science/tel-04299454v1>

Submitted on 22 Nov 2023

HAL is a multi-disciplinary open access archive for the deposit and dissemination of scientific research documents, whether they are published or not. The documents may come from teaching and research institutions in France or abroad, or from public or private research centers.

L'archive ouverte pluridisciplinaire **HAL**, est destinée au dépôt et à la diffusion de documents scientifiques de niveau recherche, publiés ou non, émanant des établissements d'enseignement et de recherche français ou étrangers, des laboratoires publics ou privés.



Université
de Toulouse

THÈSE

En vue de l'obtention du

DOCTORAT DE L'UNIVERSITÉ DE TOULOUSE

Délivré par : *l'Université Toulouse 3 Paul Sabatier (UT3 Paul Sabatier)*
Cotutelle internationale *Università degli Studi di Salerno*

Présentée et soutenue le *26/04/2023* par :
Javier Sierra-Ausin

Mode interactions in external flows

JURY

DAVID FABRE	Maître de Conférences, UT3 Paul Sabatier	Directeur de thèse
FRANÇOIS GALLAIRE	Professeur, EPFL	Examineur
FLAVIO GIANNETTI	Professeur, Università degli Studi di Salerno	Directeur de thèse
PETER JORDAN	Directeur de recherche CNRS, PPRIME	Examineur
LUTZ LESSHAFFT	Directeur de recherche CNRS, LADHYX	Rapporteur
OLIVIER MARQUET	Maître de Recherche, ONERA	Examineur
AIMEE MORGANS	Professeure, Imperial College London	Examineur
LAURETTE TUCKERMAN	Directeur de recherche CNRS, PMMH	Rapporteur

École doctorale et spécialité :

MEGEP : Dynamique des fluides

Unité de Recherche :

Institut de Mécanique des Fluides de Toulouse (UMR 5502)

Directeur de Thèse :

David FABRE and Flavio GIANNETTI

Rapporteur :

Lutz LESSHAFFT and Laurette TUCKERMAN

Acknowledgements

First, I would like to thank the members of the jury for accepting to take part of this thesis. Thank you, François GALLAIRE, Peter JORDAN, Olivier MARQUET and Aimee MORGANS, I sincerely appreciate the time you have taken to examine my work. In addition, I am very grateful to Lutz LESSHAFFT and Laurette TUCKERMAN for accepting the arduous task of reading this manuscript. To all of you, I am honoured by your presence. Thank you!

Then, what to say, I am not very good in this kind of messages . . .

Thank you so much, David FABRE, first for believing in me, second for your scientific enthusiasm and third for your kindness. Thank you, Flavio GIANNETTI, I genuinely appreciate your guidance and your willingness to discuss whenever needed. Both of you always knew how to trigger my scientific curiosity, to give me freedom, and to provide assistance when needed. It has been a great pleasure to start my scientific career with you! During the first month of this journey, my father passed away, then in the second and third year of this scientific trip Sig. GIANNETTI and M. FABRE deceased. This thesis is dedicated to them.

Furthermore, I would like to thank all the co-authors that I have had the pleasure to work with, thank you for being part of this journey with me! Merci, Jacques MAGNAUDET, it has been a pleasure to collaborate with you. Among other things, the enriching discussions and the writing of the manuscript together, which it was quite instructive. Thank you, Edgar KNOBLOCH, for your availability, and for your willingness to always teach me something new. You are a source of inspiration to me. Grazie, Vincenzo CITRO, for all the discussion we had, your advices at the beginning of thesis, and your participation in many of the works of this thesis. Grazie Paolo LUCHINI for all the enriching discussions we have shared. Gracias, Manuel LORITE and Jose I. JIMENEZ for your contribution in this work. Gracias Adrian CORROCHANO, Soledad LE-CLAINCHE and Juan Angel MARTIN for your time and the work we have done together. Merci Pierre JOLIVET for your instant availability and your willingness to help. Grazie to Antonia TIRRI, Alessandro NITTI and Marco D. DE TULLIO for the many interesting discussions we have had and for the time we have spent together collaborating. Thank you to Lionel and Avraham HIRSCHBERG, Juan I. GUZMAN and Aimee MORGANS for the discussions and the work we have done together.

En plus, je voudrais remercier tous les membres de l'IMFT qui m'ont accompagné pendant ce séjour. Un labo superbe avec un cadre humain qui m'a permis m'épanouir pendant tout ce temps-là. Également, je voudrais remercier Océane

pour son support, sans elle tout cela aurait été impossible. Merci coeur!
Finalmente, me gustaría dar las gracias a mi familia, la cuál siempre ha estado a mi lado apoyandome. Gracias Julio, por ser como eres, siempre has sido como un segundo padre para mí. Un especial agradecimiento a mis hermanas, quienes siempre fueron un modelo a seguir y un apoyo si era necesario. Y un inmenso agradecimiento a mis padres, esta tesis no es nada más que el resultado de vuestro esfuerzo.
Esta tesis es para ti, *papá*.

Javier Sierra Ausin

Abstract

In this thesis, we study the formation of coherent structures in the early stages of transition from a laminar state towards a chaotic attractor. We aim to unveil the rich array of dynamical characteristics appearing in the laminar-chaos transition of external flows, and to determine some of the universal ingredients in the transition. In particular, we analyse the formation of large coherent structures under the competition among multiple global instabilities. These techniques are applied, to a different extent, to multiple physical problems: acoustics, wake and jet flows and problems with moving interfaces.

In acoustic problems, the instability of the jet flow past a hole is analysed in terms of its transfer function, the impedance, which allows us to consider the incompressible problem, as long as the flow is acoustically compact. The continuation of the emerging limit cycle from the self-sustained instability is carried out following a fixed-point method for limit cycles, which also provides information about the sensitivity of the cycle characteristics to localised variations in the flow-field. The flow problems with moving interfaces require the development of novel numerical techniques to analyse the issuing instabilities. Herein, we explore the techniques of a linearised diffusive Immerse Boundary Method in a case with Vortex-Induced-Vibrations (VIV), and the linearised Arbitrary Lagrangian Eulerian technique for the dynamics of a bubble in a straining flow.

In the case of multiple interacting flow instabilities, we analyse the organising centres: the steady-steady bifurcation with 1:2 resonance condition in the configuration of two concentric jets, a codimension-three Takens-Bogdanov bifurcation in the case of the wake flow behind a spinning cylinder, the steady-Hopf bifurcation in a case of an axisymmetric wake flow, and the triple Hopf in two cases, the wake flow dynamics behind a rotating particle (non-resonant) and the sound emissions of a rounded impinging jet (resonant). In addition to the qualitative description of the dynamics and the formation of spatio-temporal patterns in the flow, the analysis of these organising centres offers information about the connections between the underlying baseflow/perturbations and the nonlinear transitions. For instance, the existence of a (near-)resonance condition in the case of the rounded impinging jet suggests for the existence of a non-local feedback mechanism, which is herein analysed using a decomposed notion of the structural sensitivity tensor.

Keywords — Instabilities, acoustics, dynamical systems, mode interaction

Résumé

Dans cette thèse, nous étudions la formation de structures cohérentes dans les premiers stades de transition de l'état laminaire vers un attracteur chaotique. L'objectif vise à montrer la riche gamme des caractéristiques dynamiques apparaissant dans la transition laminaire-chaos pour les écoulements externes, déterminant ainsi certains ingrédients universels de la transition. L'analyse porte en particulier sur la formation des structures cohérentes issues de l'interaction entre plusieurs instabilités globales. Ces techniques s'appliquent, à degrés divers, à de multiples problèmes physiques : acoustique, écoulements de sillage et jet ou encore problèmes avec des interfaces mobiles.

Dans les problèmes acoustiques, l'instabilité de l'écoulement d'un jet à travers un trou est analysée à partir de sa fonction de transfert, l'impédance. Cela permet de considérer une modélisation incompressible tant que l'écoulement est acoustiquement compact. La continuation du cycle limite émergent à partir de l'instabilité autoentretenu est effectuée selon une méthode de point-fixe pour les cycles limites, une méthode qui fournit également des informations sur les grandeurs de sensibilité. Les problèmes d'écoulement à interfaces mobiles nécessitent le développement de nouvelles techniques numériques pour analyser les instabilités. Nous explorons, dans un cas, une technique Immersed Boundary Method linéarisée avec des Vibrations Induites par Vortex (VIV) et, dans un autre cas, la technique Lagrangienne Eulérienne Arbitraire linéarisée pour la dynamique d'une bulle dans un flux de déformation.

Dans le cas des écoulements avec des multiples instabilités qui interagissent, nous analysons les bifurcations à haute-codimension suivantes : une bifurcation stationnaire-stationnaire avec une condition de résonance 1:2 dans la configuration de jets concentriques, une bifurcation de Takens-Bogdanov de codimension trois dans le cas d'un écoulement de sillage derrière un cylindre en rotation, la bifurcation de Hopf-stationnaire dans le cas d'un écoulement de sillage axisymétrique et la bifurcation triple Hopf dans deux cas, celle de la dynamique de l'écoulement de sillage derrière une particule en rotation (non-résonnante) et celle des émissions sonores d'un jet incident (résonant). En plus de la description qualitative de la dynamique et de la formation de structures spatio-temporelles dans l'écoulement, l'analyse de ces bifurcations à haute-codimension offre de l'information par rapport aux mécanismes physiques de l'instabilité. À titre d'exemple, l'existence d'une condition de (quas)résonance, dans la configuration d'un jet incident arrondi, suggère l'existence d'un mécanisme de rétroaction non local qui est ici analysé en utilisant une notion décomposée du tenseur de la sensibilité structurelle.

Mots-Clés — Instabilités, Acoustique, Systèmes dynamiques, interactions des modes

Preface

In this thesis, we study the formation of exact coherent structures in the early stages of transition from a *laminar* state towards a *chaotic attractor*. Herein, we define exact coherent structures as invariant solutions of the Navier–Stokes equations. We aim to unveil the rich array of dynamical characteristics appearing in the laminar-chaos transition of fluid flows, and to determine the universal ingredients in the transition. In particular, we analyse the formation of large coherent structures under the competition among multiple *global instabilities*. These techniques are applied, to a different extent, to multiple physical problems: sound emissions of a jet past a hole or of a jet impinging on a wall; the wake flow (with or without mixed convection) behind bluff bodies and problems with moving interfaces such as Vortex-Induced-Vibrations (VIV) or the dynamics of a bubble in a straining flow.

The Thesis is divided into two parts. A brief introduction on the basic concepts and methods is presented in part A. In addition, it is provided a description of the main findings of the set of articles belonging to the category of mode interaction, which are listed just below. Part B contains the articles.

Mode interaction

Sierra-Ausin, Javier, David Fabre, Vincenzo Citro, and Flavio Giannetti (2020).

“Bifurcation scenario in the two-dimensional laminar flow past a rotating cylinder”. In: *Journal of Fluid Mechanics* 905.

Sierra-Ausin, J, M Lorite-Diez, et al. (2022). “Unveiling the competitive role of global modes in the pattern formation of rotating sphere flows”. In: *Journal of Fluid Mechanics* 942.

Corrochano, A. et al. (2023). “Mode selection in concentric jets with resonance 1:2”. In: *Journal of Fluid Mechanics (accepted)*.

Sierra-Ausin, J., D. Fabre, and E. Knobloch (2023). “Wake dynamics in buoyancy-driven flows: steady state–Hopf mode interaction with $O(2)$ symmetry revisited”. In: *Phys. Rev. E (submitted)*.

Sierra-Ausin, J. and F. Giannetti (2023). “On the linear and nonlinear mechanisms for the tonal and broadband noise of subsonic rounded impinging jets”. In: *Journal of Fluid Mechanics (to be submitted)*.

We have analysed five organising centres, which exemplify some of the most common laminar-chaotic transitions for self-sustained instabilities. These correspond to: a degenerate case of the Takens-Bogdanov bifurcation, the interaction between two non-oscillating modes in an axisymmetric configuration with 1:2

resonance, a steady-Hopf mode interaction, and the interaction between three oscillating modes (triple Hopf) with and without resonance.

The first case, a degenerate Takens–Bogdanov bifurcation, is actually a codimension-three bifurcation. Surprisingly, when varying two parameters, we (almost) find numerically a codimension-three bifurcation. The reason behind this anomaly might be the regularity of the Navier–Stokes equation when the Reynolds number tend to zero. The uniqueness of the steady-state solution at this limit constraints the number of steady solutions in the parameter space to be odd; at least when considering the laminar bifurcation problem. This suggests that this kind of degenerate Takens–Bogdanov bifurcation might be more general than it seems for the Navier–Stokes equations. This work that resulted in Sierra-Ausin, Javier, Fabre, Citro, and Giannetti (2020) was started during my master thesis, and it was finalized during the first months of the PhD. It provides a rationalisation for the existence of multiple steady states for the flow past a rotating cylinder, as it was already observed in previous studies. Two bistability regions are identified, the first with two stable fixed points and the second with a fixed point and a cycle. The presence of homoclinic and heteroclinic orbits, which are classical in the presence of Takens–Bogdanov bifurcations, was confirmed by direct numerical simulations.

The second scenario with two modes that interact corresponds to the steady-steady symmetry breaking with $1 : 2$ resonance of the azimuthal wave numbers. In Corrochano et al. (2023) we have analysed the dynamics near the primary bifurcation of two concentric jets. Under a set of conditions (Armbruster et al., 1988), one may identify near the bifurcating point several surprising non-trivial coherent structures of the jets: slowly drifting rotating waves, heteroclinic cycles and quasi-periodic solutions that approximate the dynamics of the heteroclinic cycle. Such an organising centre was also identified numerically (Nore, Tuckerman, et al., 2003) and experimentally (Nore, Moisy, et al., 2005) in the Von Karman swirling flow.

Third, we focus on a classical scenario with a *continuous* symmetry displaying mode interaction between slow and fast dynamics ($0 - i\omega$). The steady-Hopf bifurcation in axisymmetric ($O(2)$ symmetry) flows is analysed and applied to the Wake Flow of Axisymmetric bluff bodies (WFA) and the Wake Flow of Axisymmetric bluff bodies under Mixed-Convection (WFA-MC) in Sierra-Ausin, Fabre, and Knobloch (2023). This organising centre is also of relevance for the Taylor-Couette flow (Chossat et al., 2012), and for the trajectory instabilities in falling bodies (Tchoufag et al., 2015) and rising bubbles in a fluid (Bonnefis, 2019). We also analyse the existence of robust heteroclinic cycles, which are idealised Self-Sustained-Processes (SSP).

Finally, we study the interaction between three oscillating instabilities, a triple Hopf bifurcation ($i\omega_1 - i\omega_2 - i\omega_3$). This case is of relevance for fluid flows

interacting with rotating particles. In, Sierra-Ausin, Lorite-Diez, et al. (2022) we provide a bifurcation and a phase diagram of the wake flow behind a rotating sphere. This is an example of the non-resonant case, which arises naturally in fluid flows depending on several parameters and displaying multiple interacting self-sustained instabilities, where the core of the instability or *wavemaker* of the global modes is localised in space. The resonant case, instead, is relevant for the study of the non-linear interaction between a family of global modes associated to a non-local feedback-loop. In this case, the core of the instability is not localised in space, and the frequency of the global modes is nearly a multiple of a fundamental pulsation $\Delta\omega$. In Sierra-Ausin and Giannetti (2023) we analyse the dynamics of a laminar rounded impinging jet, which exemplifies the resonant-case. Therein, in addition to studying the resonant mode interaction, we propose an acoustic-hydrodynamic decomposition of the structural sensitivity map, which serves to identify the spatial localisation of the feedback-loop.

The continuation of limit-cycles with respect to parameters and the evaluation of their linear stability requires efficient numerical techniques. This was the objective during the first steps of this thesis. We developed a fixed-point method for the computation of periodic solutions of incompressible and compressible Navier–Stokes equations. Herein, we employ the *Harmonic Balance* or *Fourier–Galerkin* method for the reconstruction of the limit cycle; the resulting linear system is subsequently solved with a Newton-Krylov method. The evaluation of the linear stability of the periodic solution is evaluated with the Floquet–Hill method, the frequency domain counterpart of the classic Floquet analysis (Barkley et al., 1996). The sensitivity with respect to frequency variations of the limit cycle and its structural sensitivity is then evaluated in a fixed point manner following the works Giannetti and Luchini (2007), Giannetti, Camarri, and Luchini (2010), and Giannetti, Camarri, and Citro (2019). This novel numerical strategy greatly simplifies the numerical burden required for an efficient evaluation of the *wavemaker* of the instability with respect to time-stepping approaches. These techniques are discussed in two manuscripts

A fixed-point method for limit cycles

Sierra-Ausin, Javier, Pierre Jolivet, et al. (2021). “Adjoint-based sensitivity analysis of periodic orbits by the Fourier–Galerkin method”. In: *Journal of Computational Physics* 440, p. 110403.

Sierra-Ausin, Javier, Vincenzo Citro, Flavio Giannetti, et al. (2022). “Efficient computation of time-periodic compressible flows with spectral techniques”. In: *Computer Methods in Applied Mechanics and Engineering* 393, p. 114736.

In the following, we consider another acoustic problem: the whistling potentiality of the jet flow past a hole. Such a case is a canonical configuration to study the sound emission of humans. Sierra-Ausin, Fabre, Citro, et al. (2022) analyses the stability problem in terms of the zeros of the transfer function of the system: the *impedance*.

The study of the acoustic emissions of the jet flow past a hole has been continued, and we are preparing a manuscript comparing linear theory and experiments (Hirschberg et al., 2022; Hirschberg et al., 2023).

For the treatment of the boundary conditions in these problems, we have developed a non-reflecting boundary condition, the complex mapping technique (Sierra-Ausin, Javier, Fabre, and Citro, 2020), which allows us to efficiently tackle the numerical issues arising when dealing with compressible or convectively dominated flow configurations. The jet flow past a hole is here a canonical example where both problematics are present. The technique allows damping outgoing waves before reaching the numerical boundary, thus avoiding wave reflection from the numerical far-field boundaries.

The whistling of a jet past a hole

Sierra-Ausin, Javier, David Fabre, and Vincenzo Citro (2020). “Efficient stability analysis of fluid flows using complex mapping techniques”. In: *Computer Physics Communications* 251, p. 107100.

Hirschberg, Lionel et al. (2022). “Linear Theory and Experiments for Laminar Bias Flow Impedance: Orifice Shape Effect”. In: p. 2887.

Sierra-Ausin, J., D Fabre, V Citro, et al. (2022). “Acoustic instability prediction of the flow through a circular aperture in a thick plate via an impedance criterion”. In: *Journal of Fluid Mechanics* 943.

Hirschberg, Lionel et al. (2023). “Linear Theory and Experiments for Laminar Bias Flow Impedance”. In: *AIAA (to be submitted)*.

During the doctoral period, we have collaborated with the group of Politecnico di Bari on the linear stability properties of problems with moving interfaces. It includes the linear stability of a bubble suspended in an axisymmetric uniaxial straining flow (Sierra-Ausin, Bonnefis, et al., 2022). Thanks to a recently developed Linearized Arbitrary Lagrangian-Eulerian approach, we compute the steady equilibrium states and associated bubble shapes. In particular, we show a novel self-propelled instability of the bubble in this problem. Additionally, we have developed a framework to perform linear stability studies of fluid-structure-interaction (FSI) problems (Tirri et al., 2023). It consists on the linearisation of a diffusive immersed-boundary-method (IBM).

Linear stability with moving interfaces

- Sierra-Ausin, Javier, Paul Bonnefis, et al. (2022). “Dynamics of a gas bubble in a straining flow: Deformation, oscillations, self-propulsion”. In: *Physical Review Fluids* 7.11, p. 113603.
- Tirri, Antonia et al. (2023). “Linear stability analysis of fluid–structure interaction problems with an immersed boundary method”. In: *Journal of Fluids and Structures* 117, p. 103830.

Finally, I include here a set of manuscripts that were published during the time that I carried out this doctoral project, but that will not be covered in the thesis.

Miscellaneous

- Sierra-Ausin, Javier, Vincenzo Citro, and David Fabre (2019). “On boundary conditions for compressible flow simulations”. In: pp. 335–340.
- Citro, V, F Giannetti, and J. Sierra-Ausin (2020). “Optimal explicit Runge-Kutta methods for compressible Navier-Stokes equations”. In: *Applied Numerical Mathematics* 152, pp. 511–526.
- Sáez-Mischlich, Gonzalo, Sierra-Ausin, Javier, and Jérémie Gressier (2022). “The Spectral Difference Raviart–Thomas Method for Two and Three-Dimensional Elements and Its Connection with the Flux Reconstruction Formulation”. In: *Journal of Scientific Computing* 93.2, pp. 1–54.
- Sáez-Mischlich, Gonzalo, Sierra-Ausin, Javier, Gilles Grondin, et al. (2022). “On the properties of high-order least-squares finite-volume schemes”. In: *Journal of Computational Physics* 457, p. 111043.

Division of the work between the authors

For transparency, and with the aim of recognising the contributions of each author to the papers published during this PhD project, in the following it is outlined the individual contributions to the papers using the relevant CRediT (Contributor Roles Taxonomy) roles (Allen et al., 2019).

Paper 1 Sierra-Ausin, Javier, Fabre, Citro, and Giannetti (2020).

Javier Sierra-Ausin (JSA): Conceptualization, Methodology, Software, Formal analysis, Writing - Original Draft.

Vincenzo Citro (VC) and Flavio Giannetti (FG): Supervision, Writing –

review & editing.

David Fabre (DF): Software, Supervision, Writting – review & editing.

Paper 2 Sierra-Ausin, Lorite-Diez, et al. (2022)

JSA: Conceptualization, Methodology, Software, Formal analysis, Writting - Original Draft.

Manuel Lorite-Diez (MLD): Conceptualization, Software, Writting - Original Draft.

Jose Ignacio Jiménez-González (JIJG): Conceptualization, Supervision, Writting – review & editing.

DF & VC: Supervision, Writting – review & editing.

Paper 3 Corrochano et al. (2023)

Adrian Corrochano (AC): Conceptualization, Investigation, Writing - Original Draft.

JSA: Conceptualization, Formal analysis, Writting - Original Draft.

Juan Angel Martin (JAM), Soledad Le Clainche (SLC) and DF: Supervision & Writting – review & editing.

Paper 4 Sierra-Ausin, Fabre, and Knobloch (2023)

JSA: Methodology, Formal analysis, Software, Writting - Original Draft.

DF: Conceptualization, Methodology, Formal analysis, Supervision, Writting - Original Draft.

Edgar Knobloch (EK): Conceptualization, Writing - Original Draft, Writting - Review & Editing.

Paper 5 Sierra-Ausin and Giannetti (2023)

JSA: Conceptualization, Methodology, Formal analysis, Software, Writting - Original Draft.

FG: Conceptualization, Supervision, Software, Methodology, Writting - Review & Editing.

DF: Writting - Review & Editing.

Paper 6 Sierra-Ausin, Javier, Jolivet, et al. (2021)

JSA: Conceptualization, Methodology, Software, Writting - Original Draft.

Pierre Jolivet (PJ): Software, Writting - Review & Editing.

VC & FG: Supervision, Writting - Review & Editing.

Paper 7 Sierra-Ausin, Javier, Citro, Giannetti, et al. (2022)

JSA: Conceptualization, Software, Writting - Original Draft.

VC: Supervision, Writting - Original Draft.

DF & FG: Supervision, Writting - Review & Editing.

- Paper 8** Sierra-Ausin, Javier, Fabre, and Citro (2020) **JSA**: Conceptualization, Software, Writting - Original Draft.
DF: Conceptualization, Supervision, Writting - Original Draft.
VC: Supervision, Writting - Original Draft.
- Paper 9** Sierra-Ausin, Fabre, Citro, et al. (2022)
JSA: Conceptualization, Software, Writting - Original Draft.
DF: Conceptualization, Supervision, Writting - Original Draft.
VC: Supervision, Writting - Original Draft.
FG: Supervision, Review & Editing.
- Paper 10** Sierra-Ausin, Bonnefis, et al. (2022)
JSA: Conceptualization, Methodology, Writting - Original Draft. Paul Bonnefis: Software, Validation, Writting - Original Draft.
Antonia Tirri (AT): Investigation, Writting - Original Draft.
DF: Software, Supervision, Writting - Review & Editing. JM: Conceptualization, Methodology, Supervision, Writting - Original Draft.
- Paper 11** Tirri et al. (2023)
AT: Conceptualization, Methodology, Software, Validation, Writting - Original Draft.
Alessandro Nitti (AN): Software, Validation, Writting - Original Draft.
JSA: Software, Writing - Review & Editing
FG & Marco D. de Tullio (MDdT): Conceptualization, Methodology, Supervision, Writing - Review & Editing

Part A

Overview and summary

Contents

Acknowledgements	i
Abstract	iii
Résumé	v
Preface	vii
A Overview and summary	xv
I Introduction	1
1 Instabilities in external flows	4
1.1 Coherent structures and instabilities in jets. From ampli- fiers to oscillators.	4
1.2 Coherent structures in bluff bodies. A connection with pattern formation.	5
1.3 Coherent structures in FSI and bubbles. The treatment of the interface.	6
II Methodology	7
1 Generic dynamics	7
1.1 Computation of the laminar state – Newton iteration . . .	8
1.2 Evaluation of the linear dynamics of the baseflow	9
1.3 Computation of the limit cycle – Harmonic balance method	12
1.4 Linear stability of the limit cycle – Floquet–Hill method .	15
1.5 Non-linear dynamics – Mode interaction	19
III Flow physics	29
1 Governing equations	29
1.1 Incompressible Navier–Stokes equations	30
1.2 Mixed–convection Navier–Stokes equations	31
1.3 Compressible Navier–Stokes equations	32
1.4 Navier–Stokes equations for bubble dynamics	41
IV Mode interaction	47

1	Takens-Bogdanov – The organizing centre for the flow past spinning cylinders	47
2	Steady-Steady with 1:2 resonance	56
3	Steady-Hopf organizing centre	67
4	Triple Hopf organizing centre	74
4.1	Non-resonant – The flow past rotating particles	76
4.2	Resonant	82
V	Conclusions and outlook	87
1	Conclusions	87
1.1	Mode interaction	87
1.2	Compressible flows – Acoustics	89
1.3	Moving interfaces	89
2	Perspectives	90
B	Articles	91
VI	Articles – Mode interaction	92
1	Bifurcation scenario in the two-dimensional laminar flow past a rotating cylinder	93
2	Mode selection in concentric jets with resonance 1:2	118
3	A note on the steady-state mode and Hopf mode interaction in the presence of $O(2)$ -symmetry	151
4	Unveiling the competitive role of the global modes in the pattern formation of rotating sphere flows	188
5	On the linear and nonlinear mechanisms for the tonal and broadband noise of subsonic rounded impinging jets	230
VII	Articles – A fixed-point method for limit cycles	271
1	Adjoint-based sensitivity analysis of periodic orbits by the Fourier–Galerkin method	272
2	Efficient computation of time-periodic compressible flows with spectral techniques	293
VIII	Articles – The whistling of a jet past a hole	318
1	Acoustic instability prediction of the flow through a circular aperture in a thick plate via an impedance criterion	319
2	Linear Theory and Experiments for Laminar Bias Flow Impedance	352
3	Efficient stability analysis of fluid flows using complex mapping techniques	371
IX	Articles – Linear stability with moving interfaces	386

1	Linear stability analysis of fluid-structure interaction problems with an immersed boundary method	387
2	Dynamics of a gas bubble in a straining flow	408

CHAPTER I

Introduction

Fluids are ubiquitous in nature; they compose three of the four classical states of nature, liquids, gases and plasmas. They have been observed, analysed and studied since at least the classical period of ancient Greece. A legend says that the first philosophical, or, in our modern terms, mathematical theory dealing with fluid flows was the one that explains buoyancy, the Archimedes principle. Archimedes was charged to show that the crown made of gold for the king of Syracuse was not of pure gold, as the goldsmith had claimed. Archimedes thought long and hard but could not find a method for proving that the crown was not solid gold ¹. Not until, he filled a bathtub and then noticed some water spilled over the edge. At that moment, he noticed that the water displaced by his body was equal to the weight of the body. Then, forgetting that he was undressed,

¹The word *koronê*, the Greek translation of *crown*, was also used to denote the keel of a ship. If the story was that "Hieron commissioned an exceptionally heavy *koronê* and asked Archimedes to prove that it would not sink when placed on water", there is obvious scope for confusion with the notion of an exceptionally valuable, heavy, crown.

he went running naked down the streets from his home to the king, shouting *Eureka*. Archimedes' principle of buoyancy was the first theory of fluid mechanics. Since then, mathematicians, physicists, and engineers have worked together to unravel the enigmas behind the motion of fluids. The governing equations of fluid mechanics were mathematically formalized over several decades of progressively building the theories by Navier and Stokes during the XIXth century. They correspond to the conservation of momentum and mass for Newtonian fluids, the equivalent of Newton laws in classical physics. Despite the existence of the governing laws of fluid since far more than a century², the dynamics of flows still puzzle us. During the second half of the XIX century, a similar phenomenon was observed for the dynamics of N rigid spheres. The dynamics of the spheres is governed by the Newton equations, which are deterministic. That is, for a given initial condition of the position and velocity of the spheres at time t_0 we always obtain the same response at time t_1 . However, physicists and mathematicians soon realized about the difficulty or even unfeasibility of determining an exact solution for the equations of N rigid spheres when N becomes large (note that $N = 3$ is already large!). This problem led to two major discoveries. The dynamics of a large number of small spheres is used to model the motion of atoms or particles, in these cases $N > 10^{20}$. In those cases, the problem is no longer attacked from a deterministic point of view, but we aim to provide a *statistical* description of the system. *Equilibrium Statistical mechanics* has been founded during the XIXth century by the seminal work of Maxwell, Boltzmann and Gibbs (Penrose, 1979). The main aim was to explain the properties of macroscopic systems from the atomistic point of view. On the other hand, we have the discovery of deterministic chaos, which started with the pioneering work of Poincaré (Poincaré, 1890) and the advances of the second half of the XXth century by Chirikov, 1979, Hénon, 1976, Lorenz, 1963, Ruelle et al., 1971, and many others. It shows, in particular, that typical statistical features observed in systems with many degrees of freedom are also shared by systems with few degrees of freedom. These two developments come together with the developments of *Statistical mechanics far from equilibrium* and *ergodicity* theory (Coudene, 2009). The concept of the *Perron-Frobenius* operator, which is the time-evolution operator of the *physical measure* or SRB measure, links the classical concepts of Liouville operator for Hamiltonian mechanics and its invariant measure. An important property, believed to hold in some sense for most cases of chaotic attractors is *hyperbolicity*, that is that trajectories in the phase space expand or contract exponentially in time, and it has major consequences in the reconstruction of the statistical properties. First, one can construct *spectral determinants* or *zeta functions*, via *cycle expansions* (Cvitanovic et al., 2005), to recover a probabilistic description of the attractor, i.e. averaged observables,

²2023 is the bicentenary of Navier's work that led to the establishment of the master equations of fluid mechanics, known as the Navier-Stokes equations.

cumulants, etc. However, a major drawback for practical applications of these techniques is the dependency of cycle expansions in *a priori* knowledge of the topology of the phase space. In particular, this technique is highly efficient when one can encode dynamics with a *symbolic alphabet*. In this way, *symbolic dynamics* can be used to determine rules that forbid certain subsequences of dynamic symbols, which is known as *pruning*. In the absence of pruning rules, one may employ some physical insights of the problem to try to determine which are the most relevant regions of the phase space, e.g. solutions with large dissipation. Some recent works in the fluid mechanics community (Wedin et al., 2004; Gibson et al., 2008; Gibson et al., 2009; Olvera et al., 2017), just to mention a few, employ these methods to determine what is known as exact coherent structures.

The computation and the study of the instabilities and the formation of coherent structures is the subject of the *hydrodynamic stability theory* (Charru, 2011; Drazin et al., 2004; Huerre et al., 1990). The aim of classic hydrodynamic stability is to determine the *asymptotic stability*³ of the laminar steady state, which may be unique or multiple. Historically, hydrodynamic stability deals with the local stability analysis of the steady state, that is, the steady state depends non-trivially on a single coordinate (Briggs et al., 1964; Bers, 1975). In this setting, one distinguishes between two types of instabilities (Monkewitz, 1990). The exponential growth of a perturbation in a co-moving frame of reference, at the group velocity of the wave packet, corresponds to what is called a *convective instability*. Instead, the exponential growth of a perturbation in a fixed frame of reference, that is at a null group velocity, corresponds to an *absolute instability*. Free jets, shear, and boundary layers are the archetype flows displaying convective instabilities, while the wake flow behind bluff bodies is a classical flow configuration with an absolute instability. With the evolution of the computer processing speed and memory capabilities, the local restriction has been progressively reduced⁴ allowing us the determination of the asymptotic linear stability of two and three-dimensional steady states (Fabre, Citro, et al., 2018; Moulin et al., 2019). In this setting, we could draw a similar dichotomy as in the local framework. One may distinguish between modal (Taira et al., 2017) and non-modal (Schmid, 2007; Luchini et al., 2014) linear stability, owing to the properties of the linearized operator around the steady state. The asymptotic behaviour of the steady state is studied by modal linear stability, while, non-

³In the case the linearized operator around the steady state is hyperbolic, i.e. the spectrum does not contain the imaginary axis, linear stability implies asymptotic stability (Kapitula et al., 2013)

⁴A quote from Lutz Lesshaft HDR thesis (Lesshaft, 2018): "*Scientific development, even within one discipline as close-knit as open flow instability, does not usually advance in lockstep. When I took my position at LadHyX in 2009, global eigenmode analysis was the fashion of the time. This framework . . . had been introduced already in the late 1980s . . . The Ph.D. work of Nichols, Coenen and myself on jet instability was still entirely built on the local analysis of laminar steady base flows*

modal linear stability, introduced by Trefethen (1999), provides a rationalization about the transient growth in systems where the linearized operator is not *normal* (hermitian for complex operators). Assuming that transient growth is not large, and disturbances are small, modal stability, or as it is usually referred to, *global stability*, is sufficient to determine if the flow is stable and its threshold of instability. It is therefore sufficient to conduct a linear stability analysis, which is the central block of global stability approaches.

1

Instabilities in external flows

1.1

Coherent structures and instabilities in jets. From amplifiers to oscillators.

Here, we distinguish two types of instabilities: *amplifiers* and *oscillators*. In the first case, oscillations are driven by external perturbations and free jets are a canonical example, see fig. I.1 (b). In the second, oscillations are driven by intrinsic mechanisms. Some examples are impinging jets (Jaunet et al., 2019), the jet flow through an orifice (Fabre, Longobardi, Bonnefis, et al., 2019; Fabre, Longobardi, Citro, et al., 2020) or buoyant jets and plumes (Chakravarthy et al., 2018), an example of the latter is displayed in fig. I.1 (a).

The discrete spectrum of amplifiers around the baseflow is stable, that is

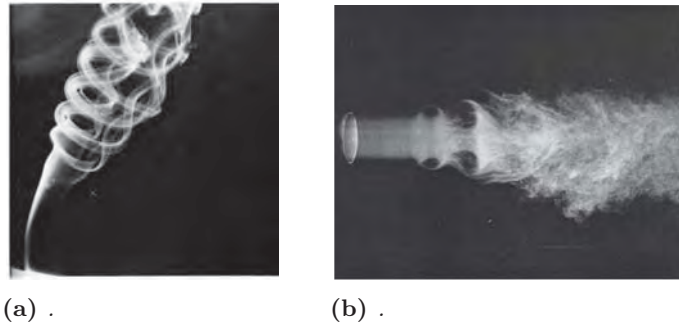


Figure I.1 – *Examples of the oscillator and amplifier type flow. (a) Photograph of the smoke rising from a cigarette (extracted from Van Dyke et al. (1983)) (b) response of an incompressible circular jet of Reynolds number $Re = 1.95 \times 10^4$ to an acoustic forcing of Strouhal number $St = 0.3$ (extracted from Crow et al. (1971)).*

amplifiers are *asymptotically stable* flows, but only linearly. These flows are characterised by large transient growth, which is determined in the *frequency domain* by means of the *resolvent operator* (Trefethen, 1999) or in the *time domain* as an optimal perturbation that maximises a given *gain* function (Shaabani-

Ardali et al., 2019; Garnaud et al., 2013).

In contrast, the baseflow of oscillators is *unstable* and they allow for self-sustained oscillations. The methodology in this case consists in the solution of the linear problem (eigenvalue problem), continuation of the periodic solution or arc-length continuation in the case of a saddle-node bifurcation. The identification of *physical mechanisms* is systematically determined in terms of *sensitivity* maps. Here, we may distinguish, the *structural sensitivity* (Giannetti and Luchini, 2007), the *sensitivity to the baseflow variations* (Marquet, Sipp, et al., 2008) or the *endogeneity* (Marquet and Lesshafft, 2015).

1.2

Coherent structures in bluff bodies. A connection with pattern formation.

The wake flow past bluff bodies, for instance a spherical particle, is a canonical model of numerous applications, such as particle-driven flows, sport aerodynamics and freely rising or falling bodies, where the changes in particles' paths are related to the destabilization of complex flow regimes and associated force distributions. In addition, the flow past bluff bodies serves as a canonical example of the oscillator class, where the study of instabilities is pursued by linear theory, see fig. I.2. However, the linear theory does not account for the successive formation of coherent structures with spatio-temporal broken symmetries, with respect to the laminar state. The systematic use of bifurcation theory helps



Figure I.2 – Left: von Kármán vortex street in a circular cylinder wake at Reynolds number $Re = 140$ (photograph taken from Van Dyke et al. (1983)). Right: quasi patterns in a Faraday wave experiment in a container in the shape of France. (photograph taken from Edwards et al. (1994)). .

to uncover the interplay between flow instabilities and the formation of flow patterns, thus drawing a connection between pattern formation in reaction–diffusion systems (Hoyle et al., 2006) and the formation of coherent structures in fluid flows. Bifurcation theory has been mostly employed to study wall bounded flow configurations such as Taylor–Couette flow (Chossat et al., 2012) or Rayleigh–Benard (Cross et al., 1993), among others. The study of unconfined flow configurations from a dynamical systems' perspective is more recent. The

primary instability leading to self-sustained oscillations, that is, the first Hopf bifurcation, has been studied for the flow past a cylinder flow (Gallaire et al., 2016; Sipp and Lebedev, 2007; Barkley et al., 1996), the flow past a rotating sphere (Citro, Tchoufag, et al., 2016), open cavity flows (Sipp, 2012) or for the fluttering and spiraling motion of buoyancy-driven bodies (Tchoufag et al., 2015). In addition, the mode interaction and pattern selection has been analysed for the wake flow past an axisymmetric disk Meliga, Chomaz, et al., 2009, in swirling jets Meliga, Gallaire, et al., 2012 or in falling objects (Tchoufag, 2013, Appendix C).

1.3

Coherent structures in FSI and bubbles. The treatment of the interface.

Bubbles, droplets, insect wings, flags, or heart valves share a common element: a deformable interface. They all possess a surface that is deformed or is displaced by the action of the fluid stresses around it. In addition, these surfaces also affect the dynamics of the flow, creating in this way a two-way coupling, which is in general nonlinear. Pfister (2019) provides a comprehensive introduction

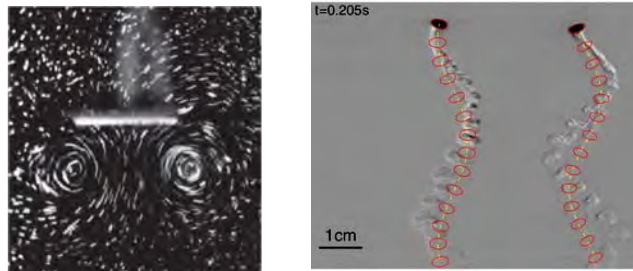


Figure I.3 – *Left: Flapping airfoil before the onset of instability (photograph extracted from Vandenberghe et al. (2004)). Right: Rising bubble in a quiescent flow, displaying a helicoidal trajectory and oscillations of the shape of the bubble (photograph extracted from (Veldhuis et al., 2008)).*

to the one-way and two-way coupling modelling techniques in Fluid-Structure-Interaction (FSI) problems. The authors employed a Lagrangian-based Arbitrary Lagrangian Eulerian (ALE) formalism, which was introduced by Hughes et al. (1981) and extended to time-dependent problems by Fernández et al. (2003a) and Fernández et al. (2003b), to model the deformation of elastic structures. Herein, we adopt a similar Lagrangian-based ALE method to analyse the instabilities of bubbles immersed in a fluid (Bonnesfis, 2019). The linear stability analysis of FSI problems is tackled with an Immersed Boundary Method (IBM) based on a moving-least-square (MLS) approach (Nitti et al., 2020).

CHAPTER II

Methodology

1

Generic dynamics

We introduce the governing equations of the fluid motion as an autonomous infinite dimensional dynamical system, which can be written using the following compact notation,

$$\begin{aligned} \mathbf{B} \frac{\partial \mathbf{q}}{\partial t} &= \mathbf{F}(\mathbf{q}, \boldsymbol{\eta}) && \text{in } \Omega, \\ 0 &= \mathbf{F}_{bc}(\mathbf{q}, \boldsymbol{\eta}) && \text{on } \partial\Omega, \end{aligned} \tag{II.1}$$

where the generic fluid domain of computation Ω with boundaries $\partial\Omega$ being sketched in fig. II.1. Here \mathbf{q} takes the role of the state variable of the system and $\boldsymbol{\eta}$ the parameter vector, that is, the dimensionless parameters of the problem. These parameters are classified by their significance: dynamical¹ (Reynolds,

¹Dimensionless numbers that are obtained as the ratio of two forces or diffusivities.

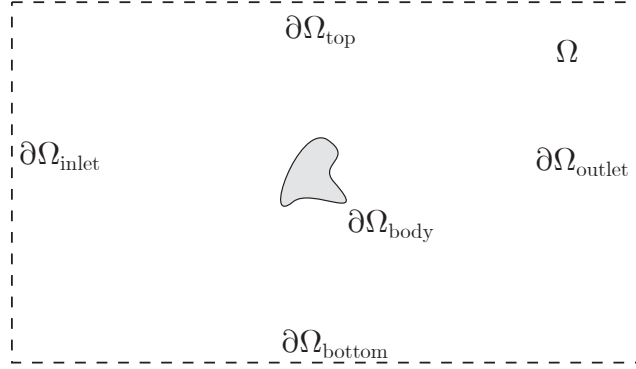


Figure II.1 – Sketch of a generic flow configuration with a solid body immersed within the fluid domain Ω , with boundaries $\partial\Omega$.

Prandtl numbers), kinematic (Mach number), geometrical (aspect ratio), etc. We use the generic notation for the boundary conditions operator \mathbf{F}_{bc} , which remains undefined, and it will be included into \mathbf{F} hereinafter. \mathbf{B} is a linear operator, \mathbf{F} is a nonlinear operator on a Hilbert space X with inner product $\langle \cdot, \cdot \rangle$. In this way, both differential algebraic problems (DAE) and evolutionary partial differential equations (PDE) are included. Natural Hilbert spaces for the infinite dimensional case are Sobolev spaces, see Kapitula et al. (2013), whereas in finite dimensions we will generally consider \mathbb{R}^n .

1.1

Computation of the laminar state – Newton iteration

The time-independent solution \mathbf{q}_0 , i.e., $\mathbf{F}(\mathbf{q}_0, \boldsymbol{\eta}) = \mathbf{0}$, of eq. (II.1) is efficiently solved by means of a Newton iteration. The steady-state is determined by substituting the ansatz $\mathbf{q}_0^{(n)} + \delta\mathbf{q}$ into eq. (II.1), where the *small correction* $\delta\mathbf{q}$ is computed from the linear expansion of eq. (II.1). In the following, the operator $D\mathbf{F}$ is defined to be the Jacobian operator of the vector field \mathbf{F} . Then we end up with the following classical Newton-scheme:

Initialize the steady-state guess $\mathbf{q}_0^{(0)}$ and solve the linear problem

$$D\mathbf{F}(\mathbf{q}_0^{(n)}, \boldsymbol{\eta})\delta\mathbf{q} = -\mathbf{F}(\mathbf{q}_0^{(n)}, \boldsymbol{\eta}) \quad \text{in } \Omega, \quad (\text{II.2})$$

while updating every iteration for the the steady-state guess

$$\mathbf{q}_0^{(n+1)} = \mathbf{q}_0^{(n)} + \delta\mathbf{q}.$$

1.2

Evaluation of the linear dynamics of the baseflow

The steady-state \mathbf{q}_0 is *asymptotically stable* if, for any *infinitesimally small* perturbation $\mathbf{q}'(t)$, the perturbed state $\mathbf{q}_0 + \mathbf{q}'(t)$ approaches \mathbf{q}_0 when $t \rightarrow \infty$

$$\mathbf{B} \frac{\partial \mathbf{q}'}{\partial t} = D\mathbf{F}(\mathbf{q}_0, \boldsymbol{\eta}) \mathbf{q}' \quad \text{in } \Omega. \quad (\text{II.3})$$

The Laplace transform of the time-variable of eq. (II.3), that is, we consider perturbations of the type $\mathbf{q}'(t) \mapsto \hat{\mathbf{q}} e^{\lambda t}$, leads to

$$\mathcal{L}_\lambda \hat{\mathbf{q}} = \left(\lambda \mathbf{B} - D\mathbf{F}(\mathbf{q}_0, \boldsymbol{\eta}) \right) \hat{\mathbf{q}} = 0 \quad \text{in } \Omega. \quad (\text{II.4})$$

For finite-dimensional vector fields \mathbf{F} , the spectrum of \mathcal{L}_λ is only composed of the eigenvalues of \mathcal{L}_λ , however, for infinite dimensional vector fields, the spectrum may contain a continuous spectrum. When the domain Ω is unbounded², the spectrum $\sigma(\mathcal{L}_\lambda)$ is decomposed into a discrete *point spectrum* $\sigma_{\text{pt}}(\mathcal{L}_\lambda)$ and a *continuous spectrum* $\sigma_{\text{cont}}(\mathcal{L}_\lambda)$. The continuous spectrum is associated with conditions at the far-field, and it is relevant for convective instabilities, whereas the modes of the discrete spectrum are energy bounded and with compact support in space. In the following, unless it is otherwise stated, we only consider the discrete spectrum.

Linear stability from a transfer function

In some cases, under additional assumptions (Sierra-Ausin, Fabre, Citro, et al., 2022; Sabino et al., 2020), one may evaluate the stability of the system by considering the zeros (respectively, poles) of a reduced input-output transfer function $Z(i\omega, \hat{\mathbf{q}}_\omega, \mathbf{s})$. Here $\mathbf{s} \in \mathbb{R}^p$ is an additional set of parameters, with $p \ll n$, where n is the size of $\hat{\mathbf{q}}_\omega \in \mathbb{R}^n$, once the problem has been discretised in space.

The first step consists in the evaluation of $\hat{\mathbf{q}}_\omega$ via a forced problem, that is, we determine the response of the linearised system to a harmonic forcing term $\hat{\mathbf{H}} e^{i\omega}$ with $\omega \in \mathbb{R}$,

$$\left(i\omega \mathbf{B} - D\mathbf{F}(\mathbf{q}_0, \boldsymbol{\eta}) \right) \hat{\mathbf{q}}_\omega = \hat{\mathbf{H}}. \quad (\text{II.5})$$

Then, one may define a scalar input-output transfer function as

$$Z(i\omega, \hat{\mathbf{q}}_\omega, \mathbf{s}) \equiv \mathbf{P}_Z \left(i\omega \mathbf{B} - D\mathbf{F}(\mathbf{q}_0, \boldsymbol{\eta}) \right)^{-1} \hat{\mathbf{H}}, \quad (\text{II.6})$$

where the operator \mathbf{P}_Z selects the (scalar) output of the system. Provided the transfer function is analytic, it can be analytically continued into the complex

²Actually, the *correct* notion behind the *pseudo-modes* or Weyl sequence composing the continuous spectrum is the closedness of the linear operator. However, herein we simply consider the unboundedness of the physical domain, which allows the existence of waves with a bounded amplitude but infinite energy, to avoid the introduction of additional definitions.

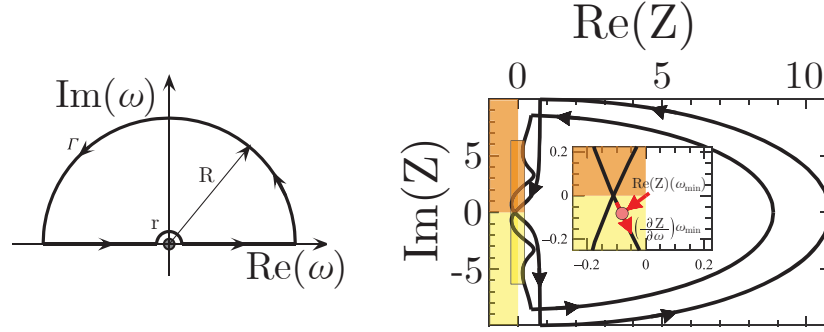


Figure II.2 – Nyquist diagram for the impedance Z along the complex contour Γ of integration enclosing the unstable complex plane, where Cauchy's argument principle is applied.

plane, and look for the values of $\lambda = \lambda_r + i\lambda_i \in \mathbb{C}$, that satisfy $Z(\lambda + i\omega, \hat{\mathbf{q}}_\omega, \mathbf{s}) = 0$. A first order expansion is as follows

$$0 = Z(\lambda + i\omega, \hat{\mathbf{q}}_\omega, \mathbf{s}) = Z(i\omega, \hat{\mathbf{q}}_\omega, \mathbf{s}) + \frac{\partial Z}{\partial \omega} \lambda + O(|\lambda|^2), \quad (\text{II.7})$$

which furnishes a criterion of instability, i.e., the system is then unstable if $\lambda_r > 0$, which happens if the Nyquist curve for impedance Z encircles the origin, while being oriented counter-clockwise (fig. II.2).

Non-normality and transient growth

Until this point, we have provided a necessary condition for the asymptotic stability of eq. (II.3). This condition turns out to be sufficient if the norm of the perturbation $\mathbf{q}'(t_0)$ is sufficiently small. On the other hand, if the norm of the perturbation is finite, transient effects may trigger a nonlinear response, which is the usual description of the instabilities in free jets that we have very briefly discussed in section 1.1. The general solution of eq. (II.3) can be written as

$$\mathbf{q}'(t) = S_{D\mathbf{F}(\mathbf{q}_0, \boldsymbol{\eta})}(t) \mathbf{q}'(t_0) \quad (\text{II.8})$$

where $S_{D\mathbf{F}(\mathbf{q}_0, \boldsymbol{\eta})}(t)$ is the semigroup³ generated by the linear operator $D\mathbf{F}(\mathbf{q}_0, \boldsymbol{\eta})$. From eq. (II.8), we define the maximal energy gain from an arbitrary initial perturbation as the norm of the semigroup at a time t ,

$$G(t) \equiv \|S_{D\mathbf{F}(\mathbf{q}_0, \boldsymbol{\eta})}(t)\| \equiv \sup_{\mathbf{q}'(t_0) \in X} \left\{ \frac{\|S_{D\mathbf{F}(\mathbf{q}_0, \boldsymbol{\eta})}(t) \mathbf{q}'(t_0)\|}{\|\mathbf{q}'(t_0)\|}, \quad \mathbf{q}'(t_0) \in X \right\} \quad (\text{II.9})$$

³Here, we assume the following: $D\mathbf{F}(\mathbf{q}_0, \boldsymbol{\eta})$ is a densely defined closed operator in the Hilbert space X that generates $S_{D\mathbf{F}(\mathbf{q}_0, \boldsymbol{\eta})}(t)$, which is a C_0 semigroup.

we can state the following about the gain.

In the large time limit ($t \rightarrow \infty$), if the linear operator $D\mathbf{F}(\mathbf{q}_0, \boldsymbol{\eta})$ is bounded (Kapitula et al., 2013), then

$$\lim_{t \rightarrow \infty} G(t) = e^{t\alpha(D\mathbf{F}(\mathbf{q}_0, \boldsymbol{\eta}))} \quad (\text{II.10})$$

where $\alpha(D\mathbf{F}(\mathbf{q}_0, \boldsymbol{\eta}))$ is the spectral abscissa (or spectral bound) of $D\mathbf{F}(\mathbf{q}_0, \boldsymbol{\eta})$, which is defined as the largest bound (real part) on the spectrum $\alpha(\mathbf{A}) = \sup_{z \in \sigma} \text{Re} z$. In the case of unbounded operators, that is, when we consider a continuous spectrum σ_{cont} , it turns out that eq. (II.10) is no longer true. Instead, one must replace the spectral abscissa by the numerical abscissa $\omega(\mathbf{A}) = \alpha(\frac{1}{2}(\mathbf{A} + \mathbf{A}^\dagger))$, \mathbf{A}^\dagger being the adjoint operator of \mathbf{A} . Then, in a Hilbert space X and for the kind of operators we have considered (they generate a C_0 semigroup), the following statement holds

$$\lim_{t \rightarrow \infty} G(t) = e^{t\omega(D\mathbf{F}(\mathbf{q}_0, \boldsymbol{\eta}))} \quad (\text{II.11})$$

which is equivalent to

$$\lim_{t \rightarrow \infty} \frac{\ln G(t)}{t} = \omega(D\mathbf{F}(\mathbf{q}_0, \boldsymbol{\eta})) \quad (\text{II.12})$$

The proof to eq. (II.12) can be found in Trefethen (1999, Ch. 19).

Additionally, it is of interest to relate the transient growth with the spectral properties of the linear operator. It turns out that there is a simple characterisation of the initial growth rate at time $t \rightarrow 0$, which is given by

$$\frac{d}{dt} G(t)|_{t=0} = \omega(D\mathbf{F}(\mathbf{q}_0, \boldsymbol{\eta})) \quad (\text{II.13})$$

A proof of this statement can be found in Trefethen (1999, Ch. 17). In addition, it is possible to bound at any time t the evolution of the gain by

$$e^{t\alpha(D\mathbf{F}(\mathbf{q}_0, \boldsymbol{\eta}))} \leq G(t) \leq e^{t\omega(D\mathbf{F}(\mathbf{q}_0, \boldsymbol{\eta}))}. \quad (\text{II.14})$$

These bounds are rather obscure; a direct physical interpretation is not immediately evident. In the finite dimensional case, when the operator $D\mathbf{F}(\mathbf{q}_0, \boldsymbol{\eta})$ is diagonalisable, we have the alternative upper bound,

$$e^{t\alpha(D\mathbf{F}(\mathbf{q}_0, \boldsymbol{\eta}))} \leq G(t) \leq \kappa(\mathbf{V}) e^{t\alpha(D\mathbf{F}(\mathbf{q}_0, \boldsymbol{\eta}))} = \|\mathbf{V}^{-1}\| \|\mathbf{V}\| e^{t\alpha(D\mathbf{F}(\mathbf{q}_0, \boldsymbol{\eta}))}. \quad (\text{II.15})$$

$\kappa(\mathbf{V})$ the condition number of the linear operator $D\mathbf{F}(\mathbf{q}_0, \boldsymbol{\eta})$. In this case, $\kappa(\mathbf{V}) = 1$ when the linear operator is a normal operator, that is,

$$D\mathbf{F}(\mathbf{q}_0, \boldsymbol{\eta})D\mathbf{F}^\dagger(\mathbf{q}_0, \boldsymbol{\eta}) = D\mathbf{F}^\dagger(\mathbf{q}_0, \boldsymbol{\eta})D\mathbf{F}(\mathbf{q}_0, \boldsymbol{\eta}),$$

then the condition number $\kappa(\mathbf{V}) = 1$, otherwise $\kappa(\mathbf{V}) > 1$ and transient growth is possible.

Transient effects and the receptivity process can be quantified by evaluating the resolvent operator norm

$$\mathcal{R}(i\omega) \equiv \sup_{\hat{\mathbf{H}} \neq 0} \frac{\|\hat{\mathbf{q}}_\omega\|}{\|\hat{\mathbf{H}}\|} = \sup_{\hat{\mathbf{H}} \neq 0} \frac{\|(\mathbf{i}\omega\mathbf{B} - D\mathbf{F}(\mathbf{q}_0, \boldsymbol{\eta}))^{-1}\hat{\mathbf{H}}\|}{\|\hat{\mathbf{H}}\|} \equiv \sup_{\hat{\mathbf{H}} \neq 0} \frac{\|(\mathcal{L}_{i\omega})^{-1}\hat{\mathbf{H}}\|}{\|\hat{\mathbf{H}}\|} \quad (\text{II.16})$$

which provides the frequency-response gain. More generally, we can define the resolvent operator norm for any $z \in \mathbb{C}$ as $\mathcal{R}(z)$, which promptly allows for the definition of the *pseudospectra* of the system as

$$\sigma_\epsilon = \{z \in \mathbb{C} : \mathcal{R}(z) = \epsilon^{-1}\}. \quad (\text{II.17})$$

A thorough analysis of $G(t)$ in terms of the pseudospectra may be found in the excellent book by Trefethen (1999, Ch. 14-19), in here we just state the following result without any further justification,

$$G(t) \leq \frac{L_\epsilon e^{t\alpha_\epsilon(D\mathbf{F}(\mathbf{q}_0, \boldsymbol{\eta}))}}{2\pi\epsilon}, \quad \forall \epsilon > 0, \forall t \leq 0, \quad (\text{II.18})$$

with L_ϵ the arc length boundary of σ_ϵ and the pseudo-spectral abscissa $\alpha_\epsilon(D\mathbf{F}(\mathbf{q}_0, \boldsymbol{\eta})) \equiv \sup_{z \in \sigma_\epsilon} \text{Re}z$. A summary of these results is depicted in fig. II.3 (b,c).

1.3

Computation of the limit cycle – Harmonic balance method

Here we propose a method to determine the periodic solution, with period T , of eq. (II.1). It is a natural choice to parameterise any T -periodic orbit \mathbf{q}^* in a $t \bmod T$ basis, i.e., a Fourier basis. For that purpose, let us consider the Fourier–Galerkin method, also denoted harmonic balance (HB) in literature (Urabe, 1965; Krack et al., 2019). We start our analysis by introducing the

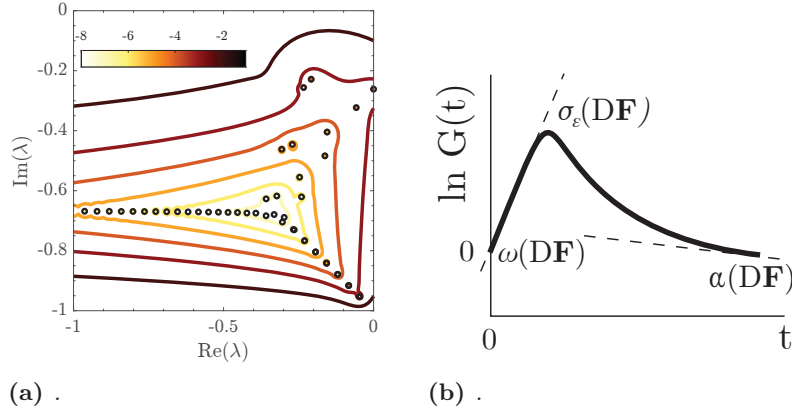


Figure II.3 – (a) An example of the (pesudo-)spectrum of a linear operator; the figure (a) illustrates pseudospectra of the Orr-Sommerfeld operator at neutrality ($\text{Re} = 5772$) for plane Poiseuille flow. Circle markers represent the eigenvalues, and the coloured isolines illustrate the pseudospectrum σ_ϵ in logarithmic scale. (b) A transient evolution of the gain $G(t)$ whose slope at $t \rightarrow 0$ is determined by the numerical abscissa, at $t \rightarrow \infty$ by the spectral radius and the maximum is approximated by the pseudospectrum.

Fourier–Galerkin projection operator π_N onto the Fourier basis as follows:

$$\begin{aligned}
 \pi_N : X \times \mathbb{R} &\rightarrow X \times (\mathbb{Z}/(2N+1)\mathbb{Z}) \\
 \pi_N(\mathbf{q}) &= \mathbf{q}_h(t) = \mathbf{q}_0 + \sum_{n=1}^N [\mathbf{q}_{c,n} \cos(n\omega t) + \mathbf{q}_{s,n} \sin(n\omega t)] \\
 &= \underbrace{[\mathbf{q}_0, \mathbf{q}_{1,c}, \mathbf{q}_{1,s}, \dots, \mathbf{q}_{N,c}, \mathbf{q}_{N,s}]}_{(\mathbf{Q}^{(\tau,N)})^T} \underbrace{[1, \cos(\omega t), \sin(\omega t), \dots, \cos(N\omega t), \sin(N\omega t)]}_{\mathcal{F}_N},
 \end{aligned} \tag{II.19}$$

where $\mathbf{Q}^{(\tau,N)}$ are the $2N+1$ Fourier coefficients of the approximated solution \mathbf{q}_h and \mathcal{F}_N is the Fourier basis in sine/cosine components. The ansatz $\mathbf{q}_h(t)$ and its derivative are smooth T -periodic functions. The T -residual is defined as the difference between the nonlinear and the time-derivative term, which is expressed as follows:

$$\begin{aligned}
 \mathbf{r} : X \times \mathbb{R} &\rightarrow X \times \mathbb{R} \\
 \mathbf{r}(\mathbf{q}, \frac{\partial \mathbf{q}}{\partial t}, t) &= \mathbf{B} \frac{\partial \mathbf{q}}{\partial t} - \mathbf{F}(\mathbf{q}).
 \end{aligned} \tag{II.20}$$

Following the Fourier–Galerkin or Bubnov–Galerkin method in the Fourier basis, the governing equations of HB are obtained by integrating the truncated residual equations weighted by the Fourier basis over a period $T = \frac{2\pi}{\omega}$. The obtained T -residual is called the *truncated T -residual*:

$$\begin{aligned}
 \hat{\mathbf{r}}_h : X \times (\mathbb{Z}/(2N+1)\mathbb{Z}) &\rightarrow X \times (\mathbb{Z}/(2N+1)\mathbb{Z}) \\
 \hat{\mathbf{r}}_h(\mathbf{Q}_N, \omega) &= \int_0^{\frac{2\pi}{\omega}} \mathbf{r}_h(\mathbf{q}_h, \frac{\partial \mathbf{q}_h}{\partial t}, t)^T \mathcal{F}_N dt = \mathbf{0},
 \end{aligned} \tag{II.21}$$

where

$$\mathbf{r}_h(\mathbf{q}_h, \frac{\partial \mathbf{q}_h}{\partial t}, t) = \mathbf{B} \frac{\partial \mathbf{q}_h}{\partial t} - \mathbf{F}(\mathbf{q}_h). \quad (\text{II.22})$$

Equation (II.22) provides $2N + 1$ equations for $2N + 2$ unknowns in the autonomous case. Autonomous systems present a continuous symmetry, i.e., $\mathbf{q}(t + \xi)$ is also a periodic solution with arbitrary ξ phase. The phase of the limit cycle remains to be fixed. This is usually done by imposing a condition at $t = 0$, i.e., $g(\mathbf{q}, \frac{\partial \mathbf{q}}{\partial t}, 0) = 0$ or an orthogonality condition $\int_0^T \mathbf{F}(\mathbf{q}_h)^T \mathbf{q}_h dt = 0$. Equation (II.22) corresponds to balancing each harmonic individually, that is, to have null Fourier coefficients of the truncated residual.

Fourier–Galerkin equations So far, the procedure to obtain a periodic orbit remains general. Now, without loss of generality, we shall consider the case where the nonlinear flow is of quadratic type, that is,

$$\mathbf{F}(\mathbf{q}, \eta) = \mathbf{L}\mathbf{q} + \mathbf{N}(\mathbf{q}, \mathbf{q}). \quad (\text{II.23})$$

The incompressible Navier–Stokes equations are of this type. Under these assumptions, eq. (II.22) takes the form:

$$\begin{aligned} 0 &= \mathbf{L}\mathbf{q}_0 + \mathbf{N}_0 \\ n\omega\mathbf{B}\mathbf{q}_{n,s} &= \mathbf{L}\mathbf{q}_{n,c} + \mathbf{N}_{n,c}, \quad n = 1, \dots, N \\ -n\omega\mathbf{B}\mathbf{q}_{n,c} &= \mathbf{L}\mathbf{q}_{n,s} + \mathbf{N}_{n,s}, \quad n = 1, \dots, N \\ g_h(\mathbf{q}_h) &= 0. \end{aligned} \quad (\text{II.24})$$

Here, a detailed description of the quadratic terms is given:

$$\begin{aligned} \mathbf{N}_0 &= \mathbf{N}(\mathbf{q}_0, \mathbf{q}_0) + \frac{1}{2} \sum_{i=1}^N \mathbf{N}(\mathbf{q}_{i,s}, \mathbf{q}_{i,s}) + \mathbf{N}(\mathbf{q}_{i,c}, \mathbf{q}_{i,c}) \\ \mathbf{N}_{i,c} &= [\mathbf{N}(\mathbf{q}_{i,c}, \mathbf{q}_0) + \mathbf{N}(\mathbf{q}_0, \mathbf{q}_{i,c})] \\ &\quad + \frac{1}{2} \sum_{j=1}^{i-1} [\mathbf{N}(\mathbf{q}_{j,c}, \mathbf{q}_{i-j,c}) - \mathbf{N}(\mathbf{q}_{j,s}, \mathbf{q}_{i-j,s})] \\ &\quad + \frac{1}{2} \sum_{j=i+1}^N [\mathbf{N}(\mathbf{q}_{j,c}, \mathbf{q}_{j-i,c}) + \mathbf{N}(\mathbf{q}_{j-i,s}, \mathbf{q}_{j,s})] \\ &\quad + \frac{1}{2} \sum_{j=i+1}^N [\mathbf{N}(\mathbf{q}_{j-i,c}, \mathbf{q}_{j,c}) + \mathbf{N}(\mathbf{q}_{j,s}, \mathbf{q}_{j-i,s})] \\ \mathbf{N}_{i,s} &= [\mathbf{N}(\mathbf{q}_{i,s}, \mathbf{q}_0) + \mathbf{N}(\mathbf{q}_0, \mathbf{q}_{i,s})] \\ &\quad + \frac{1}{2} \sum_{j=1}^{i-1} [\mathbf{N}(\mathbf{q}_{j,c}, \mathbf{q}_{i-j,s}) + \mathbf{N}(\mathbf{q}_{j,s}, \mathbf{q}_{i-j,c})] \\ &\quad - \frac{1}{2} \sum_{j=i+1}^N [\mathbf{N}(\mathbf{q}_{j,c}, \mathbf{q}_{j-i,s}) + \mathbf{N}(\mathbf{q}_{j-i,s}, \mathbf{q}_{j,c})] \\ &\quad + \frac{1}{2} \sum_{j=i+1}^N [\mathbf{N}(\mathbf{q}_{j-i,c}, \mathbf{q}_{j,s}) + \mathbf{N}(\mathbf{q}_{j,s}, \mathbf{q}_{j-i,c})]. \end{aligned}$$

Formally, eq. (II.24) will be denoted as:

$$\mathbf{0} = -\omega\tilde{\mathbf{B}}\mathbf{Q}^{(\tau,N)} + \tilde{\mathbf{L}}\mathbf{Q}^{(\tau,N)} + \tilde{\mathbf{N}}(\mathbf{Q}^{(\tau,N)}, \mathbf{Q}^{(\tau,N)}) = \tilde{\mathbf{r}}(\mathbf{Q}^{(\tau,N)}), \quad (\text{II.25})$$

where operators $\tilde{\mathbf{B}}$, $\tilde{\mathbf{L}}$, and $\tilde{\mathbf{N}}(\cdot, \cdot)$ are as follows,

$$\tilde{\mathbf{B}}\mathbf{Q}_N = \begin{bmatrix} \mathbf{0} & & & \\ & \mathbf{B}_1 & & \\ & & \ddots & \\ & & & \mathbf{B}_N \end{bmatrix} \begin{bmatrix} \mathbf{q}_0 \\ \mathbf{q}_1 \\ \vdots \\ \mathbf{q}_N \end{bmatrix} \quad \text{with } \mathbf{B}_n = \begin{bmatrix} \mathbf{0} & n\mathbf{B} \\ -n\mathbf{B} & \mathbf{0} \end{bmatrix} \text{ for } n = 1, \dots, N. \quad (\text{II.26})$$

$$\tilde{\mathbf{L}}\mathbf{Q}_N = \begin{bmatrix} \mathbf{L} & & & \\ & \mathbf{L} & & \\ & & \ddots & \\ & & & \mathbf{L} \end{bmatrix} \begin{bmatrix} \mathbf{q}_0 \\ \mathbf{q}_1 \\ \vdots \\ \mathbf{q}_N \end{bmatrix} \quad \text{with } \mathbf{q}_n = \begin{bmatrix} \mathbf{q}_{n,c} \\ \mathbf{q}_{n,s} \end{bmatrix} \text{ for } n = 1, \dots, N. \quad (\text{II.27})$$

$$\tilde{\mathbf{N}}(\mathbf{Q}_N, \mathbf{Q}_N) = \begin{bmatrix} \mathbf{N}_0 \\ \mathbf{N}_1 \\ \vdots \\ \mathbf{N}_N \end{bmatrix} \quad \text{with } \mathbf{N}_n = \begin{bmatrix} \mathbf{N}_{n,c} \\ \mathbf{N}_{n,s} \end{bmatrix} \text{ for } n = 1, \dots, N. \quad (\text{II.28})$$

Finally, we briefly recall that Stokes, 1972 studied the convergence of eq. (II.25). In particular, if the exact problem eq. (II.1) possesses a solution \mathbf{q}^* of period $T = \frac{2\pi}{\omega}$, then the solution $[\mathbf{Q}^{\tau, N}, \omega^{\tau, N}]$ of the system eq. (II.25), for sufficiently large N , converges to the exact solution \mathbf{q}^* if the monodromy matrix possesses a unique Floquet multiplier equal to one.

1.4

Linear stability of the limit cycle – Floquet–Hill method

In this section, the Floquet theory of finite dimensional systems in \mathbb{R}^N is addressed. Unfortunately, there does not exist a general theory for time-periodic PDEs, but some particular cases have been already tackled, see parabolic and hyperbolic evolution problems in Kuchment, 1993, Chapter 5 and references therein. For the sake of self-consistency, let us introduce a set of classical definitions in the study of dynamical systems.

Let $t \rightarrow \mathbf{q}^*(t)$ be a T -periodic solution of eq. (II.1) for a given set of parameters $\boldsymbol{\eta}^* \in \mathbb{R}^p$. The associated *flow* of eq. (II.1) is denoted by $\varphi(t; \mathbf{q}_0)$, which solves $\mathbf{B} \frac{\partial \mathbf{q}}{\partial t} = \mathbf{F}(\mathbf{q}, \boldsymbol{\eta})$ with $\mathbf{q}(0) = \mathbf{q}_0$.

Furthermore, we consider a codimension one hypersurface S , chosen in such a way that every trajectory that crosses S in a neighborhood of the intersection point $\mathbf{o} \in S$ of the periodic orbit with the surface S intersects transversally and in the same direction, see Kuznetsov, 2013. Such a section S is refer to as *Poincaré section*. Using the the Poincaré section, let us define the *Poincaré map*

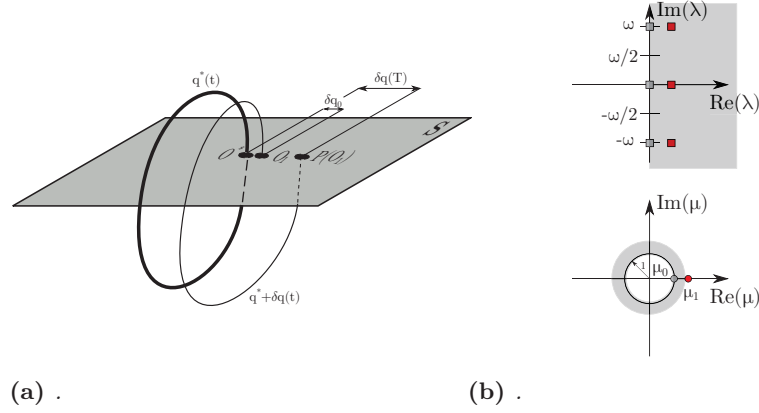


Figure II.4 – (a) An unstable periodic orbit \mathbf{q}^* crossing the Poincaré section at point \mathbf{o}^* , and the evolution perturbed orbit $\mathbf{q}^* + \delta\mathbf{q}(t)$ from the point \mathbf{o}_1 . (b) Floquet spectrum in terms of Floquet multipliers μ_n (resp. Floquet exponents λ_n on top figure) of an unstable periodic orbit \mathbf{q}^* . Red dots (square on the top figure) are associated to the unstable fundamental solution $\delta\mathbf{q}_1(t)$, whereas gray markers denote the neutral Floquet eigenvalue. .

or return map $\mathbf{P}(\mathbf{o})$:

$$\mathbf{P}(\mathbf{o}) := \mathbf{P}_S(\mathbf{o}) = \varphi(T_S(\mathbf{o}); \mathbf{o}), \quad (\text{II.29})$$

where $T_S(\mathbf{o})$ is the return time and it coincides with the period T of the periodic orbit when \mathbf{o}^* is a fixed point, i.e., $\mathbf{o}^* = \mathbf{P}(\mathbf{o}^*)$:

$$\mathbf{o} \xrightarrow[\mathbf{q} \rightarrow \mathbf{q}^*]{} \mathbf{o}^* \quad \text{implies} \quad T_S(\mathbf{o}) \rightarrow T.$$

The linear stability of the T -periodic orbit $\mathbf{q}^*(t)$ can be studied by checking the evolution of the perturbed distance $\delta\mathbf{q}(t)$ to the T -periodic orbit \mathbf{q}^* :

$$\delta\mathbf{q}(t) = \varphi(t; \mathbf{q}^* + \delta\mathbf{q}_0) - \varphi(t; \mathbf{q}^*), \quad \text{with} \quad \delta\mathbf{q}(0) = \delta\mathbf{q}_0. \quad (\text{II.30})$$

Measuring the distance after a period yields:

$$\delta\mathbf{q}(T) = \varphi(T; \mathbf{q}^* + \delta\mathbf{q}_0) - \varphi(T; \mathbf{q}^*) = \frac{\partial\varphi(T; \mathbf{q}^*)}{\partial\mathbf{q}} \delta\mathbf{q}_0 + O(\|\delta\mathbf{q}_0\|^2), \quad (\text{II.31})$$

where in the last expression appears the *monodromy matrix* $\frac{\partial\varphi(T; \mathbf{q}^*)}{\partial\mathbf{q}}$. To find another representation of the monodromy matrix, consider the following evolution equation:

$$\mathbf{B} \frac{\partial}{\partial t} \frac{\partial\varphi(t; \mathbf{q}^*)}{\partial\mathbf{q}} = \frac{\partial\mathbf{F}(\varphi, \boldsymbol{\eta}^*)}{\partial\varphi} \frac{\partial\varphi(t; \mathbf{q}^*)}{\partial\mathbf{q}}, \quad \frac{\partial\varphi(0; \mathbf{q}^*)}{\partial\mathbf{q}} = \mathbf{I}. \quad (\text{II.32})$$

Consequently, the monodromy matrix will be denoted by $\Phi(T) = \frac{\partial \varphi(T; \mathbf{q}^*)}{\partial \mathbf{q}}$, where the *fundamental solution matrix* $\Phi(t) \in \mathcal{M}(\mathbb{R})^{N \times N}$ satisfies the following matrix initial-value problem:

$$\mathbf{B} \frac{\partial \Phi}{\partial t} = \frac{\partial \mathbf{F}}{\partial \mathbf{q}}(\mathbf{q}^*, \boldsymbol{\eta}^*) \Phi, \quad \Phi(0) = \mathbf{I}. \quad (\text{II.33})$$

The spectrum of the monodromy matrix is composed of an eigenvalue $\mu = 1$, due to the translation invariance of the periodic orbit and another set of $N - 1$ eigenvalues. Due to the definition of the Poincaré map, it is not difficult to observe that the other $N - 1$ eigenvalues of the Jacobian operator coincide with those of the derivative of the Poincaré map $D\mathbf{P}(\boldsymbol{\sigma}^*)$, see the book of Seydel Seydel, 2009 and references therein for a proof.

Thanks to Floquet's theorem, the perturbation $\delta \mathbf{q}(t)$ is written as:

$$\delta \mathbf{q}(t) = \sum_{n=1}^N c_n \delta \mathbf{q}_n(t),$$

where *fundamental solutions* $\delta \mathbf{q}_n$ can be rewritten in the Floquet's normal form:

$$\delta \mathbf{q}_n(t) = e^{\lambda_n t} \mathbf{p}_n(t), \quad (\text{II.34})$$

where \mathbf{p}_n is a T -periodic vector and λ_n are called the *Floquet exponents*. They are related to the eigenvalues μ_n of the monodromy matrix, also called *Floquet multipliers*, by the following relation: $\lambda_n = \frac{\log(\mu_n)}{T} + ik\omega$ for $k \in \mathbb{Z}$. To see this relation, consider linear independence of fundamental solutions and let us substitute the Floquet's normal form into eq. (II.31). Then, we are left with the following expression:

$$\mu_n \mathbf{p}_n(0) = \frac{\partial \varphi(T; \mathbf{q}^*)}{\partial \mathbf{q}} \mathbf{p}_n(0) \iff \lambda_n \mathbf{B} \mathbf{p}_n = \left[-\mathbf{B} \frac{\partial}{\partial t} + \frac{\partial \mathbf{F}(\mathbf{q}^*, \boldsymbol{\eta}^*)}{\partial \mathbf{q}} \right] \mathbf{p}_n. \quad (\text{II.35})$$

In section 1.3, we have carried out a brief review of the stability of periodic orbits. The present section aims to determine an efficient algorithm for the solution of the Floquet stability eq. (II.35). Prior to the discussion of the algorithm, please note the following analogy between the HBM parametrization of the autonomous problem eq. (II.1) and the Poincaré map, introduced in eq. (II.29). Phase condition may be interpreted as the parametrization of a codimension one hypersurface. Then, the T -periodic solution \mathbf{q}_h^* taken at nT instants, $n \in \mathbb{N}$, is a fixed point of the Poincaré map. As discussed in section 1.3, eigenvalues of the derivative of the Poincaré map determine the stability of the periodic orbit, and these arise as a subproduct of the computation of the periodic orbit.

Nevertheless, this procedure to determine the Floquet stability would break the continuous symmetry, i.e., the phase is fixed, then the neutral Floquet multiplier,

i.e., $\mu = 1$, would not be in the spectrum set. Therefore, in practice, the phase condition is left in the stability study.

The Fourier–Galerkin form of Floquet stability eq. (II.35) consists in the projection onto the finite Fourier space $X \times (\mathbb{Z}/(2N + 1)\mathbb{Z})$, i.e., on a finite Fourier series.

The Floquet stability problem in the Fourier–Galerkin basis can be formally expressed with the following generalized eigenvalue problem:

$$\begin{aligned} \lambda^{(\tau,N)} \text{diag}(\mathbf{B})_{2N+1} \mathbf{P}^{(\tau,N)} &= D\tilde{\mathbf{r}}(\mathbf{Q}^{(\tau,N)}) \mathbf{P}^{(\tau,N)} \\ \text{where } D\tilde{\mathbf{r}}(\mathbf{Q}^{(\tau,N)}) \mathbf{P}^{(\tau,N)} &= \left[-\omega \tilde{\mathbf{B}} + \tilde{\mathbf{L}} + D\tilde{\mathbf{N}}(\mathbf{Q}^{(\tau,N)}) \right] \mathbf{P}^{(\tau,N)}, \end{aligned} \quad (\text{II.36})$$

where $\mathbf{P}^{(\tau,N)} = [\mathbf{p}_0, \mathbf{p}_{1,c}, \mathbf{p}_{1,s}, \dots, \mathbf{p}_{N,c}, \mathbf{p}_{N,s}]^T$ is the finite Fourier decomposition of the periodic eigenvector $\mathbf{p}(t)$ and $\lambda^{(\tau,N)}$ is the approximation of the Floquet exponent defined eq. (II.34). Please note that the explicit definition of the derivative of the residual operator $D\tilde{\mathbf{r}}(\mathbf{Q}^{(\tau,N)})$ is as follows,

where the derivative of the quadratic operator is a dense block-symmetric matrix as follows:

$$D\tilde{\mathbf{N}}(\mathbf{Q}^{(\tau,N)}) = \begin{bmatrix} DN^{(0)} & \dots & DN^{(0,i)} & \dots & DN^{(0,N)} \\ \vdots & \ddots & & & \vdots \\ DN^{(i,0)} & \dots & DN^{(i)} & \dots & DN^{(i,N)} \\ \vdots & & & \ddots & \vdots \\ DN^{(N,0)} & \dots & DN^{(N,i)} & \dots & DN^{(N)} \end{bmatrix}. \quad (\text{II.37})$$

Let us consider the detailed description of each block. In the following, let us denote $DN^{(\mathbf{q})} = \mathbf{N}(\cdot, \mathbf{q}) + \mathbf{N}(\mathbf{q}, \cdot)$, the linear operator of the derivative evaluated at \mathbf{q} .

Diagonal blocks $DN^{(i)}$

$$DN^{(0)} = DN^{(\mathbf{q}_0)} \quad (\text{II.38})$$

$$DN^{(i)} = \begin{bmatrix} DN^{(\mathbf{q}_0)} + \frac{1}{2} DN^{(\mathbf{q}_{2i,c})} & \frac{1}{2} DN^{(\mathbf{q}_{2i,s})} \\ \frac{1}{2} DN^{(\mathbf{q}_{2i,s})} & DN^{(\mathbf{q}_0)} - \frac{1}{2} DN^{(\mathbf{q}_{2i,c})} \end{bmatrix} \text{ if } 0 < i \leq \frac{N}{2} \quad (\text{II.39})$$

$$DN^{(i)} = \begin{bmatrix} DN^{(\mathbf{q}_0)} & \mathbf{0} \\ \mathbf{0} & DN^{(\mathbf{q}_0)} \end{bmatrix} \text{ if } i > \frac{N}{2}. \quad (\text{II.40})$$

Off diagonal-blocks $DN^{(i,j)}$

$$DN^{(0,j)} = \begin{bmatrix} \frac{1}{2} DN^{(\mathbf{q}_{j,c})} & \frac{1}{2} DN^{(\mathbf{q}_{j,s})} \end{bmatrix} \text{ if } j \neq 0, \quad (\text{II.41})$$

$$DN^{(i,0)} = \begin{bmatrix} \frac{1}{2}DN^{(\mathbf{q}_{i,c})} \\ \frac{1}{2}DN^{(\mathbf{q}_{i,s})} \end{bmatrix} \text{ if } i > 0. \quad (\text{II.42})$$

If $i \neq j, j \neq 0, j < i, j + i \leq N$:

$$DN^{(i,j)} = \begin{bmatrix} \frac{1}{2}DN^{(\mathbf{q}_{i-j,c})} + \frac{1}{2}DN^{(\mathbf{q}_{j+i,c})} & -\frac{1}{2}DN^{(\mathbf{q}_{i-j,s})} - \frac{1}{2}DN^{(\mathbf{q}_{j+i,s})} \\ \frac{1}{2}DN^{(\mathbf{q}_{i-j,s})} + \frac{1}{2}DN^{(\mathbf{q}_{j+i,s})} & \frac{1}{2}DN^{(\mathbf{q}_{i-j,c})} + \frac{1}{2}DN^{(\mathbf{q}_{j+i,c})} \end{bmatrix}. \quad (\text{II.43})$$

If $i \neq j, j \neq 0, j < i, j + i > N$:

$$DN^{(i,j)} = \begin{bmatrix} \frac{1}{2}DN^{(\mathbf{q}_{i-j,c})} & -\frac{1}{2}DN^{(\mathbf{q}_{i-j,s})} \\ \frac{1}{2}DN^{(\mathbf{q}_{i-j,s})} & \frac{1}{2}DN^{(\mathbf{q}_{i-j,c})} \end{bmatrix} \text{ if } i \neq j, j \neq 0, j < i, \quad (\text{II.44})$$

otherwise $DN^{(j,i)} = (DN^{(i,j)})^T$.

As depicted in fig. II.4, Floquet exponents are not unique in the complex field \mathbb{C} , nevertheless they are in $\mathbb{C}/i\omega\mathbb{R}$. Let us consider the finite dimensional case, i.e., $\mathbf{q}^* \in \mathbb{R}^n$. In such a case, the Floquet spectrum is of dimension n , i.e., there are n eigenvalues in $\mathbb{C}/i\omega\mathbb{R}$. Nonetheless, the dimension of the Floquet HBM problem is $(2N + 1)n$, there are $2N + 1$ in the same conjugacy class, i.e., $\lambda_k^r = \lambda_0^r + ik\omega, k \in \mathbb{Z}$, where λ_0^r is the eigenvalue closest to the real axis in the complex plane.

This remark motivates the definition of the *truncated spectra* Λ_N : this set of converged eigenvalues is a compact set in \mathbb{C} restricted to the strip $C_\omega \equiv \{z \in \mathbb{C} : \omega/2 \leq \text{Im}(z) \leq \omega/2\}$.

1.5

Non-linear dynamics – Mode interaction

So far, we have outlined some numerical and theoretical tools for the continuation of steady-states and limit cycles and the determination of their linear stability. In this subsection, we describe the *reduced dynamics* resulting from competing instability mechanisms of the steady-state, that is, from mode interaction. The study of mode interactions is, in a sense, a step-forward and a step-backward with respect to the study of a single limit cycle. It is a step-forward since it provides information about the existence of global bifurcations, such as, Saddle-Node to Infinite PERiod (SNIPER) bifurcation. And, it is a step-backward, because it is not exact since it is based on the dynamics of a reduced system which is determined from asymptotic matching methods, e.g., the multiple scales method or the homological equation. However, it is a valuable tool for the determination of the transition towards complex dynamics, including low dimensional chaos.

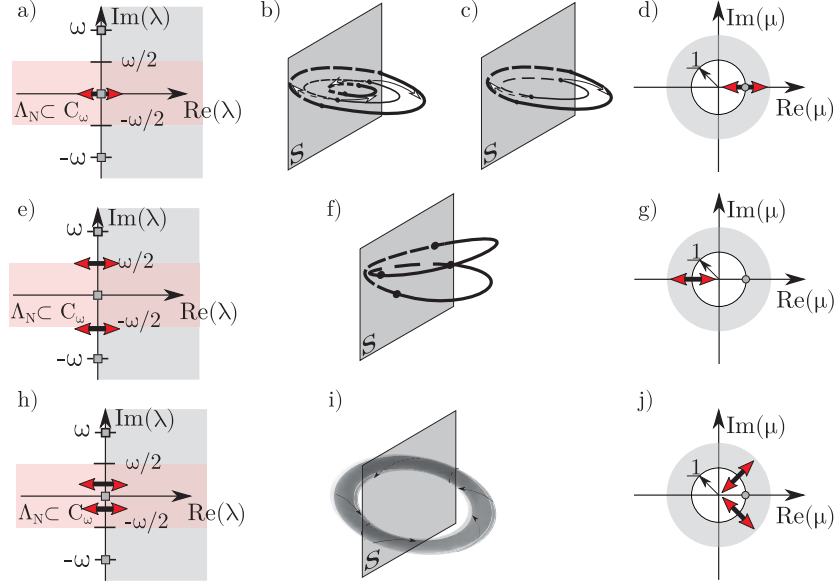


Figure II.5 – Local bifurcations of codimension one of periodic orbits. Spectrum in terms of Floquet exponents a), e), and h). Spectrum in terms of Floquet multipliers d), g), and j). Pitchfork bifurcation in a), b), and d). Fold bifurcation in a), c), and d). Period-doubling bifurcation in e), f), and g). Neimark–Sacker in h), i), and j) .

Reduction to the centre manifold

In the following, we proceed to the determination of the coefficients of a generic centre manifold, with the following linear expansion,

$$\mathbf{q}(t, \tau) = \mathbf{q}_0 + \sum_{k=1}^N z_\ell \hat{\mathbf{q}}_\ell e^{i(m_\ell \theta - \omega_\ell t)} + \text{c.c.} \quad (\text{II.45})$$

Note that the parameter N is the number of neutral modes that span the centre eigenspace. In addition, for the sake of simplicity, we consider a quadratic dependency on the state variable and parameters, that is, we replace eq. (II.1) by

$$\mathbf{B} \frac{\partial \mathbf{q}}{\partial t} = \mathbf{F}(\mathbf{q}, \boldsymbol{\eta}) \equiv \mathbf{L}\mathbf{q} + \mathbf{N}(\mathbf{q}, \mathbf{q}) + \mathbf{G}(\mathbf{q}, \boldsymbol{\eta}), \quad \mathbf{x} \in \Omega \quad (\text{II.46})$$

This form of the governing equations takes into account a linear dependence on the state variable \mathbf{q} through \mathbf{L} and a quadratic dependence on state variable and the parameters $\boldsymbol{\eta}$ through the operators $\mathbf{G}(\cdot, \cdot)$ and $\mathbf{N}(\cdot, \cdot)$.

Multiple-scales ansatz We expand the solution \mathbf{q} of eq. (II.46) in powers of a small parameter $\varepsilon \ll 1$:

$$\mathbf{q}(t, \tau) = \mathbf{q}_0 + \varepsilon \mathbf{q}_{(\varepsilon)}(t, \tau) + \varepsilon^2 \mathbf{q}_{(\varepsilon^2)}(t, \tau) + O(\varepsilon^3) \quad (\text{II.47})$$

The expansion encompasses a three-scale expansion of the original time that incorporates the fast timescale t of the self-sustained instability and two slow time scales $\tau \equiv \tau_1 + \varepsilon \tau_2$ of the evolution of the (complex) amplitudes $z_i(\tau)$, to be defined below. That is, we expand the time variable as

$$t \mapsto t + \varepsilon \tau_1 + \varepsilon^2 \tau_2 + O(\varepsilon^3) \quad (\text{II.48})$$

The resulting expansion of the left side of eq. (II.46) up to third order is as follows:

$$\varepsilon \mathbf{B} \frac{\partial \mathbf{q}_{(\varepsilon)}}{\partial t} + \varepsilon^2 \left[\mathbf{B} \frac{\partial \mathbf{q}_{(\varepsilon^2)}}{\partial t} + \mathbf{B} \frac{\partial \mathbf{q}_{(\varepsilon)}}{\partial \tau_1} \right] + \varepsilon^3 \left[\mathbf{B} \frac{\partial \mathbf{q}_{(\varepsilon^3)}}{\partial t} + \frac{\partial \mathbf{q}_{(\varepsilon^2)}}{\partial \tau_1} + \mathbf{B} \frac{\partial \mathbf{q}_{(\varepsilon)}}{\partial \tau_2} \right] \quad (\text{II.49})$$

while the right side is

$$\mathbf{F}(\mathbf{q}, \boldsymbol{\eta}) = \mathbf{F}_{(0)} + \varepsilon \mathbf{F}_{(\varepsilon)} + \varepsilon^2 \mathbf{F}_{(\varepsilon^2)} + \varepsilon^3 \mathbf{F}_{(\varepsilon^3)}. \quad (\text{II.50})$$

The expansion eq. (II.50) will be detailed at each order.

Order $O(\varepsilon^0)$ The leading order solution \mathbf{q}_0 of the multiple scales expansion eq. (II.47) is the steady state of the governing equations evaluated at the threshold of instability, i.e., $\boldsymbol{\eta} = \boldsymbol{\eta}_c$ or $\Delta \boldsymbol{\eta} \equiv \boldsymbol{\eta} - \boldsymbol{\eta}_c = 0$,

$$\mathbf{0} = \mathbf{F}(\mathbf{q}_0, \mathbf{0}), \quad \mathbf{x} \in \Omega. \quad (\text{II.51})$$

Order $O(\varepsilon^1)$ The first order correction $\mathbf{q}_{(\varepsilon)}(t, \tau)$ in the multiple scales expansion of eq. (II.47) is composed of the eigenmodes of the linearized system

$$\mathbf{q}_{(\varepsilon)}(t, \tau) \equiv \sum_{k=1}^N z_k(\tau) \hat{\mathbf{q}}_k e^{i(m_k \theta - \omega_k t)} + \text{c.c.} \quad (\text{II.52})$$

Each term $\hat{\mathbf{q}}_\ell$ in the first order expansion (II.52) solves the corresponding linear problem:

$$\mathbf{J}_{(\omega_\ell, m_\ell)} \hat{\mathbf{q}}_\ell = \left(i\omega_\ell \mathbf{B} - \frac{\partial \mathbf{F}}{\partial \mathbf{q}} \Big|_{\mathbf{q}=\mathbf{q}_0, \Delta \boldsymbol{\eta}=\mathbf{0}} \right) \hat{\mathbf{q}}_\ell, \quad \mathbf{x} \in \Omega, \quad (\text{II.53})$$

where $\frac{\partial \mathbf{F}}{\partial \mathbf{q}} \Big|_{\mathbf{q}=\mathbf{q}_0, \Delta \boldsymbol{\eta}=\mathbf{0}} = \mathbf{L}_{m_\ell} + \mathbf{N}_{m_\ell}(\mathbf{q}_0, \cdot) + \mathbf{N}_{m_\ell}(\cdot, \mathbf{q}_0)$. The subscript m_ℓ indicates the azimuthal wavenumber used for the evaluation of the operator.

Order $O(\varepsilon^2)$ The second order expansion term $\mathbf{q}_{(\varepsilon^2)}(t, \tau)$ is determined from the resolution of a set of forced linear systems, where the forcing terms are

evaluated from first and zeroth order terms. The expansion in terms of amplitudes $z_i(\tau)$ of $\mathbf{q}_{(\varepsilon^2)}(t, \tau)$ is assessed from term-by-term identification of the forcing terms at the second order. The nonlinear second order terms are

$$\begin{aligned} \mathbf{F}_{(\varepsilon^2)} &\equiv \sum_{j,k=1}^N \left(z_j z_k \mathbf{N}(\hat{\mathbf{q}}_j, \hat{\mathbf{q}}_k) e^{-i(m_j+m_k)\theta} e^{-i(\omega_j+\omega_k)t} + \text{c.c.} \right) \\ &+ \sum_{j,k=1}^N \left(z_j \bar{z}_k \mathbf{N}(\hat{\mathbf{q}}_j, \bar{\hat{\mathbf{q}}}_k) e^{-i(m_j-m_k)\theta} e^{-i(\omega_j-\omega_k)t} + \text{c.c.} \right) \\ &+ \sum_{\ell=1}^N \eta_\ell \mathbf{G}(\mathbf{q}_0, \mathbf{e}_\ell), \end{aligned} \quad (\text{II.54})$$

where \mathbf{e}_ℓ is an element of the orthonormal basis of \mathbb{R}^{N_p} , a vector composed of zeros except at the position ℓ where it is equal to unity. In the following we differentiate the resonant terms, whose amplitude are $z_j^{(\varepsilon^2)}$, and the non-resonant terms. The second order term can be expanded as

$$\mathbf{q}_{(\varepsilon^2)} \equiv \sum_{j=1}^N (z_j^{(\varepsilon^2)} \hat{\mathbf{q}}_j^{(\varepsilon^2)} + \text{c.c.}) + \sum_{\substack{j,k=1 \\ k \leq j}}^N (z_j z_k \hat{\mathbf{q}}_{j,k} + z_j \bar{z}_k \hat{\mathbf{q}}_{j,-k} + \text{c.c.}) + \sum_{\ell=1}^N \Delta \eta_\ell \mathbf{q}_0^{(\eta_\ell)}, \quad (\text{II.55})$$

with the rules $\hat{\mathbf{q}}_{j,k} = \hat{\mathbf{q}}_{k,j}$ and $\hat{\mathbf{q}}_{-j,-k} = \bar{\hat{\mathbf{q}}}_{j,k}$. Terms $\hat{\mathbf{q}}_{j,j}$ are harmonics of the flow, $\hat{\mathbf{q}}_{j,k}$ with $j \neq k$ are coupling terms, $\hat{\mathbf{q}}_{j,-j}$ are harmonic base flow modification terms and $\mathbf{q}_0^{(\eta_\ell)}$ are base flow corrections due to the assumed departure of the parameter η_ℓ from the critical point measured by ε .

Finally, for the non-resonant forcing terms, the second-order terms are computed by solving the following nonresonant system of equations,

$$\mathbf{J}_{(\omega_j+\omega_k, m_j+m_k)} \hat{\mathbf{q}}_{j,k} = \hat{\mathbf{F}}_{(\varepsilon^2)}^{(j,k)}, \quad (\text{II.56})$$

where $\hat{\mathbf{F}}_{(\varepsilon^2)}^{(j,k)} \equiv \mathbf{N}(\hat{\mathbf{q}}_j, \hat{\mathbf{q}}_k) + \mathbf{N}(\hat{\mathbf{q}}_k, \hat{\mathbf{q}}_j)$ and

$$\mathbf{J}_{(0,0)} \mathbf{Q}_0^{(\eta_\ell)} = \mathbf{G}(\mathbf{Q}_0, \mathbf{e}_\ell). \quad (\text{II.57})$$

In the case of a resonant pair, $\omega_j \pm \omega_k = \omega_\ell$ and $m_j \pm m_k = m_\ell$, for $j \neq k$ and $\ell, j, k = 1, \dots, N$, we shall solve for the following bordered system,

$$\begin{pmatrix} \mathbf{J}_{(\omega_\ell, m_\ell)} & \hat{\mathbf{q}}_\ell \\ \hat{\mathbf{q}}_\ell^\dagger & 0 \end{pmatrix} \begin{pmatrix} \hat{\mathbf{q}}_\ell^{(\varepsilon^2)} \\ e_{(j,k)}^{(\ell)} \end{pmatrix} = \begin{pmatrix} \hat{\mathbf{F}}_{(\varepsilon^2)}^{(j,k)} \\ 0 \end{pmatrix} \quad (\text{II.58})$$

with $e_{(j,k)}^{(\ell)}$ a coefficient of the normal form issued of the resonant interaction. If there is not a resonant interaction between the modes j and k , the coefficient $e_{(j,k)} = 0$. If the Jacobian $\mathbf{J}_{(0,0)}$ in eq. (II.57) is singular, we substitute $\hat{\mathbf{F}}_{(\varepsilon^2)}^{(j,k)}$ by

$\mathbf{G}(\mathbf{Q}_0, \mathbf{e}_\ell)$ in eq. (II.58), which gives us the following system

$$\begin{pmatrix} \mathbf{J}_{(0,0)} & \hat{\mathbf{q}}_\ell \\ \hat{\mathbf{q}}_\ell^\dagger & 0 \end{pmatrix} \begin{pmatrix} \hat{\mathbf{q}}_0^{(\eta_\ell, \varepsilon^2)} \\ e_0^{(\ell)} \end{pmatrix} = \begin{pmatrix} \mathbf{G}(\mathbf{Q}_0, \mathbf{e}_\ell) \\ 0 \end{pmatrix} \quad (\text{II.59})$$

Order $\mathcal{O}(\varepsilon^3)$ At third order, there are secular terms. The linear λ_ℓ and cubic terms $a_{(i,j)}$ for $i = 1, 2$ are determined by imposing the solvability condition,

$$\lambda_\ell = \frac{\langle \hat{\mathbf{q}}_\ell^\dagger, \hat{\mathbf{F}}_{(\varepsilon^3)}^{(z_\ell)} \rangle}{\langle \hat{\mathbf{q}}_\ell^\dagger, \mathbf{B}\hat{\mathbf{q}}_\ell \rangle}, \quad a_{(\ell,j)} = \frac{\langle \hat{\mathbf{q}}_\ell^\dagger, \hat{\mathbf{F}}_{(\varepsilon^3)}^{(z_\ell|z_j|^2)} \rangle}{\langle \hat{\mathbf{q}}_\ell^\dagger, \mathbf{B}\hat{\mathbf{q}}_\ell \rangle}. \quad (\text{II.60})$$

The forcing terms for the linear coefficients are

$$\hat{\mathbf{F}}_{(\varepsilon^3)}^{(z_j)} \equiv \sum_{\ell=1}^N \eta_\ell \left([\mathbf{N}(\hat{\mathbf{q}}_j, \mathbf{q}_0^{(\eta_\ell)}) + \mathbf{N}(\mathbf{q}_0^{(\eta_\ell)}, \hat{\mathbf{q}}_j)] + \mathbf{G}(\hat{\mathbf{q}}_j, \mathbf{e}_\ell) \right). \quad (\text{II.61})$$

The forcing terms for the cubic coefficients are

$$\begin{aligned} \hat{\mathbf{F}}_{(\varepsilon^3)}^{(z_j|z_k|^2)} \equiv & [\mathbf{N}(\hat{\mathbf{q}}_j, \hat{\mathbf{q}}_{|z_k|^2}) + \mathbf{N}(\hat{\mathbf{q}}_{|z_k|^2}, \hat{\mathbf{q}}_j)] \\ & + [\mathbf{N}(\hat{\mathbf{q}}_{-k}, \hat{\mathbf{q}}_{z_j z_k}) + \mathbf{N}(\hat{\mathbf{q}}_{j,k}, \hat{\mathbf{q}}_{-k})] \\ & + [\mathbf{N}(\hat{\mathbf{q}}_k, \hat{\mathbf{q}}_{z_j \bar{z}_k}) + \mathbf{N}(\hat{\mathbf{q}}_{z_j \bar{z}_k}, \hat{\mathbf{q}}_k)]. \end{aligned} \quad (\text{II.62})$$

if $j \neq k$ and

$$\begin{aligned} \hat{\mathbf{F}}_{(\varepsilon^3)}^{(z_j|z_j|^2)} \equiv & [\mathbf{N}(\hat{\mathbf{q}}_j, \hat{\mathbf{q}}_{|z_j|^2}) + \mathbf{N}(\hat{\mathbf{q}}_{|z_j|^2}, \hat{\mathbf{q}}_j)] \\ & + [\mathbf{N}(\hat{\mathbf{q}}_{-j}, \hat{\mathbf{q}}_{z_j^2}) + \mathbf{N}(\hat{\mathbf{q}}_{z_j^2}, \hat{\mathbf{q}}_{-j})], \end{aligned} \quad (\text{II.63})$$

for the diagonal forcing terms.

If there is a resonant forcing term to the ℓ^{th} mode, which we would name $\hat{\mathbf{F}}_{(\varepsilon^3)}^{\mathbf{z}_\ell^R}$, we can determine the coefficient associated with this term as before,

$$\chi_{\mathbf{z}_\ell^R} = \frac{\langle \hat{\mathbf{q}}_\ell^\dagger, \hat{\mathbf{F}}_{(\varepsilon^3)}^{\mathbf{z}_\ell^R} \rangle}{\langle \hat{\mathbf{q}}_\ell^\dagger, \mathbf{B}\hat{\mathbf{q}}_\ell \rangle}. \quad (\text{II.64})$$

Finally, we would obtain the following expression of the centre manifold,

$$\frac{dz_\ell}{d\tau} = e_0^{(\ell)} + z_\ell (\lambda_\ell + \sum_{j=1}^N a_{(\ell,j)} |z_j|^2) + \sum_{j,k=1}^N e_{(j,k)}^{(\ell)} z_j z_k + \sum_{\mathbf{z}_\ell^R} \chi_{\mathbf{z}_\ell^R} \mathbf{z}_\ell^R \quad (\text{II.65})$$

For the sake of simplicity if we have only a resonant third order term to the ℓ^{th} mode, we shall name it χ_ℓ , as it is the case in eq. (II.75) of the next subsection. The reduction of the complete dynamics to the centre manifold is performed in more detail in the part B. Unfortunately, bear in mind that the notation

employed in the articles and in chapter IV may slightly change with respect to the one employed in here. The reduction of the incompressible Navier–Stokes equations to the normal form of a saddle-node bifurcation is detailed in Sierra-Ausin, Javier, Fabre, Citro, and Giannetti (2020, App. B). The determination of the coefficients of the degenerate Hopf bifurcation, the Bautin bifurcation, is detailed in Sierra-Ausin, Javier, Fabre, Citro, and Giannetti (2020, App. C). The non-resonant triple Hopf organising centre is discussed in Sierra-Ausin, Lorite-Diez, et al. (2022, App. A), and the resonant case in Sierra-Ausin and Giannetti (2023, App. B). The steady-Hopf bifurcation is covered in Sierra-Ausin, Fabre, and Knobloch (2023, App.). Finally, the steady-steady with 1:2 resonance is analysed in Corrochano et al. (2023, App. A).

Classification of codimension two bifurcations

In fig. II.5 we have seen that the bifurcations of the limit-cycle are characterised by their frequency-content. The same is true for the bifurcations of the steady-state. In that sense, if the instability is oscillatory we say that is a *Hopf bifurcation*, instead, if the instability is non-oscillating, can be of three sub-kinds: *saddle-node* (SN), *pitchfork or symmetry-breaking* (SB), *transcritical bifurcation* (Tr). These are all the possibilities for bifurcations of codimension-one. These singularities take place at a given codimension-one manifold in the parameter space. Thus, they are generic in systems depending on a parameter. Similarly, a *bifurcation of codimension- N* takes place at certain manifold of codimension- N in the parameter space, and it occurs generically in systems depending on N parameters. In addition, the unfolding of the bifurcation, that is, the exploration of the neighbourhood of the bifurcation point in the parameter space, turns out to be relevant for the dynamics of systems depending on less than N parameters. In this sense, the codimension- N manifold in the parameter space aids to classify the dynamics of systems near the bifurcation point. That is why, hereinafter, we use interchangeably the concepts of bifurcation of higher codimension (codimension- N , $N \leq 2$), mode interaction, and organising centre. Let us now turn our attention of instabilities, in the presence of two competing modes, we can distinguish:⁴

- (a) $0 - 0$ Zero-zero or Taken-Bogdanov bifurcation (TB).
- (b) $0 - i\omega$ Zero-Hopf bifurcation (ZH).
- (c) $i\omega_1 - i\omega_2$ Double Hopf bifurcation (HH).

⁴Herein, we do not consider the degenerated case of the Hopf bifurcation: *Bautin* or *Generalised Hopf* bifurcation, nor the degenerated pitchfork bifurcation, nor the degenerated case of the saddle node bifurcation: the *cusp* bifurcation, .

The TB bifurcation corresponds to the resonant interaction⁵ between two non-oscillating modes, giving rise to unsteadiness. The ZH bifurcation is a canonical case of slow-fast dynamics in systems displaying a symmetry breaking (0 mode) and a self-sustaining instability ($i\omega$ mode). Finally, The HH bifurcation corresponds to the competition of two self-sustained instabilities, leading to periodic or quasi-periodic dynamics.

In addition to the frequency-content, in order to fully describe the reduced dynamics of the system, one must also consider the spatial wavelength. That is, the wave number of a three-dimensional symmetry breaking instability. For a helical instability from an axisymmetric steady-state the relevant ansatz is $e^{im(\theta - \frac{\omega}{m}t)}$, with a phase velocity $\frac{\omega}{m}$. Similarly, for travelling/standing pulses from a two-dimensional steady-state is $e^{ik_z(z - \frac{\omega}{k_z}t)}$ with a phase velocity $\frac{\omega}{k_z}$. For the sake of simplicity, we consider herein only the helical case. Based on the space-time frequency content, we may distinguish:

- (a) $\omega_1 = 0, \omega_2 = 0$ Zero-zero bifurcation.
 - (i) (m_1, m_2) with $m_1 = m_2 = 0$ Takens-Bogdanov (TB) with a normal form of dimension two. We take $z_1 = x_1 + iy_1$ and $z_2 = x_2 + iy_2$, so the centre manifold is as follows,

$$\begin{aligned} \dot{x}_1 &= x_2 + e_0^{(1)} + \lambda_1 x_1 + e_{(1,1)}^{(1)} x_1^2 + e_{(1,2)}^{(1)} x_1 x_2 + e_{(2,2)}^{(1)} x_2^2 \\ \dot{x}_2 &= e_0^{(2)} + \chi_2 x_1 + \lambda_2 x_2 + e_{(1,1)}^{(2)} x_1^2 + e_{(1,2)}^{(2)} x_1 x_2 + e_{(2,2)}^{(2)} x_2^2 \end{aligned} \quad (\text{II.66})$$

which under the following non-degeneracy conditions $e_{(1,1)}^{(2)} \neq 0$ and $e_{(1,1)}^{(1)} + e_{(1,2)}^{(2)} \neq 0$ we can perform a nonlinear change of coordinates, $u_1 = P_1(y_1, y_2)$ and $u_2 = P_2(y_1, y_2)$ can be recast to its topological normal form (Kuznetsov, 2013),

$$\begin{aligned} \dot{u}_1 &= u_2 \\ \dot{u}_2 &= \beta_1 + \beta_2 u_1 + u_1^2 + s u_1 u_2 \end{aligned} \quad (\text{II.67})$$

with β_1 and β_2 playing the role of the unfolding parameters and $s = \pm 1$.

In Sierra-Ausin, Javier, Fabre, Citro, and Giannetti (2020) we study a degenerate codimension three TB bifurcation, which arises in the wake flow behind a spinning cylinder. In particular, the degenerate TB bifurcation is the organizing centre of this problem, and it justifies the existence of a saddle-node homoclinic bifurcation and the hysteresis observed in previous numerical simulations (Pralits et al., 2010; Thompson et al., 2014).

⁵The linear part of the centre manifold is a dimension two, zero-eigenvalue Jordan block

- (ii) (m_1, m_2) with $m_1 = 0$ and $m_2 \neq 0$ the same normal form as the ZH whose dimension is three. Its centre manifold is as follows,

$$\begin{aligned}\dot{x}_1 &= e_0^{(1)} + \lambda_1 x_1 + e_{(1,1)}^{(1)} x_1^2 + e_{(1,2)}^{(1)} x_1 x_2 + e_{(2,2)}^{(1)} x_2^2 \\ \dot{z}_2 &= z_2 \left(\lambda_2 + a_{(2,2)} |z_2|^2 + e_{(1,2)}^{(2)} x_1 + a_{(2,1)} x_1^2 \right)\end{aligned}\quad (\text{II.68})$$

- (iii) (m_1, m_2) with $m_1 \neq 0$ and $m_2 \neq 0$ with the same normal form as the HH whose dimension is four, and it as follows,

$$\begin{aligned}\dot{z}_1 &= z_1 \left(\lambda_1 + a_{(1,1)} |z_1|^2 + a_{(1,2)} |z_2|^2 \right) \\ \dot{z}_2 &= z_2 \left(\lambda_2 + a_{(2,2)} |z_2|^2 + a_{(2,1)} |z_1|^2 \right)\end{aligned}\quad (\text{II.69})$$

Equation (II.69) corresponds to the non-resonant case. In addition, we may find resonant cases, such as, the 1 : 2 resonance (Porter et al., 2000) or 1 : 3 (Porter et al., 2001). The resonant cases are particularly rich, in Corrochano et al. (2023) we study the transition from an axisymmetric state towards a symmetry-broken state with a 1 : 2 azimuthal resonance in a configuration of two concentric jets, its polar normal form is as follows,

$$\dot{r}_1 = e_{(-1,2)}^{(1)} r_1 r_2 \cos(\chi) + r_1 \left(\lambda_1 + a_{(1,1)} r_1^2 + a_{(1,2)} r_2^2 \right), \quad (\text{II.70a})$$

$$\dot{r}_2 = e_{(1,1)}^{(2)} r_1^2 \cos(\chi) + r_2 \left(\lambda_2 + a_{(2,1)} r_1^2 + a_{(2,2)} r_2^2 \right), \quad (\text{II.70b})$$

$$\dot{\chi} = - \left(2e_{(-1,2)}^{(1)} r_2 + e_{(1,1)}^{(2)} \frac{r_1^2}{r_2} \right) \sin(\chi), \quad (\text{II.70c})$$

with the polar coordinates related to the complex amplitudes by $z_1 = r_1 e^{i\phi_1}$ and $z_2 = r_2 e^{i\phi_2}$ where r_j and ϕ_j for $j = 1, 2$ are the amplitude and phase of the symmetry-breaking modes $m_1 = 1$ and $m_2 = 2$, respectively. Note that the resonance makes that the phase $\chi = \phi_2 - 2\phi_1$ is coupled with the amplitudes r_1 and r_2 .

- (b) $(0 - i\omega)$ Zero-Hopf bifurcation (ZH).

- (i) (m_1, m_2) with $m_1 = m_2 = 0$ it is the generic ZH bifurcation and it is the same as eq. (II.68).
(ii) (m_1, m_2) with $m_1 \neq 0$ and $m_2 \neq 0$ has a normal form of dimension six,

$$\begin{aligned}\dot{z}_1 &= \lambda_1 z_1 + \chi_1 \bar{z}_2 z_2 (\bar{z}_1)^{2m_2/m_1 - 1} \\ &\quad + (a_{(1,1)} |z_1|^2 + a_{(1,2)} |z_2|^2 + \bar{a}_{(1,2)} |z_3|^2) z_1\end{aligned}\quad (\text{II.71})$$

$$\begin{aligned}\dot{z}_2 &= (\lambda_2 + i\omega_h) z_2 + \chi_2 z_1^{2m_2/m_1} z_{-2} \\ &\quad + (a_{(2,1)} |z_1|^2 + a_{(2,2)} |z_2|^2 + a_{(2,3)} |z_3|^2) z_2\end{aligned}\quad (\text{II.72})$$

$$\begin{aligned} \dot{z}_3 = & (\lambda_2 + i\omega_h)z_3 + \chi_2 \bar{z}_1^{2m_2/m_1} z_2 \\ & + (a_{(2,1)}|z_1|^2 + a_{(2,2)}|z_3|^2 + a_{(2,3)}|z_2|^2)z_3, \end{aligned} \quad (\text{II.73})$$

with $m_2/m_1 \in \mathbb{N}$, otherwise $\chi_1 = \chi_2 = 0$. In Sierra-Ausin, Fabre, and Knobloch (2023) we have performed a detailed analysis of this normal form with a particular emphasis on applications to axisymmetric wake flows (WFA) and axisymmetric wake flows with mixed convection (WFA-MC).

(c) $(i\omega_1 - i\omega_2)$ Double Hopf bifurcation (HH).

- (i) (m_1, m_2) with $m_1 = m_2 = 0$ it is the generic HH bifurcation, whose normal form is eq. (II.69).
- (ii) (m_1, m_2) with $m_1 = 0$ and $m_2 \neq 0$ it has a normal form of dimension six, with the normal form eq. (II.70) with $\chi_1 = \chi_2 = 0$ in the non-resonant case.
- (iii) (m_1, m_2) with $m_1 \neq 0$ and $m_2 \neq 0$ has a normal form of dimension eight, see (Golubitsky et al., 2012).

In the presence of three competing instabilities, the number of possibilities is much larger, and it is beyond the scope of this manuscript to enumerate all of them. In this thesis, we study the $\text{SO}(2)$ -equivariant triple Hopf with and without resonance condition. The state variable for $N = 3$ is expanded as,

$$\mathbf{q}(t) = \sum_{k=1}^N (z_k(\tau) \hat{\mathbf{q}}_{(z_k)}(r, z) e^{i(m_k \theta - \omega_k t)} + \text{c.c.}). \quad (\text{II.74})$$

The resonance condition that we use is $2\omega_2 - \omega_1 = \omega_3$ and $2m_2 - m_1 = m_3$. Its normal form is as follows,

$$\begin{aligned} \dot{z}_1 &= z_1 (\lambda_1 + a_{(1,1)}|z_1|^2 + a_{(1,2)}|z_2|^2 + a_{(1,3)}|z_3|^2) + \chi_1 z_2^2 \bar{z}_3 \\ \dot{z}_2 &= z_2 (\lambda_2 + a_{(2,1)}|z_1|^2 + a_{(2,2)}|z_2|^2 + a_{(2,3)}|z_3|^2) + \chi_2 z_1 \bar{z}_2 z_3 \\ \dot{z}_3 &= z_3 (\lambda_3 + a_{(3,1)}|z_1|^2 + a_{(3,2)}|z_2|^2 + a_{(3,3)}|z_3|^2) + \chi_3 z_2^2 \bar{z}_1 \end{aligned} \quad (\text{II.75})$$

In the case that the resonance condition is not satisfied $\chi_j = 0$ for $j = 1, 2, 3$. In the asymptotic expansion, the resonance condition does not need to be *exactly* satisfied, but the terms $2\omega_2 - (\omega_1 + \omega_3)$ and $2m_2 - (m_1 + m_3)$ have to be small. In this way, they can be considered of a higher order in the multiple scale expansion. This normal form arises in applications of wake flows behind rotating bodies (Sierra-Ausin, Lorite-Diez, et al., 2022) and in the strong tonal sound emissions of rounded impinging jets (Sierra-Ausin and Giannetti, 2023). The former one is an example of the non-resonant case, and the latter is an example of the resonant case.

CHAPTER III

Flow physics

1

Governing equations

In the following, we introduce the governing equations of four different problems, the incompressible Navier–Stokes equations, the Boussinesq approximation to model the problem of mixed convection, the compressible Navier–Stokes equations and the Navier–Stokes equations for moving interfaces.

1.1

Incompressible Navier–Stokes equations

We consider the evolution of an incompressible fluid within a domain Ω . The operators of the dynamical system eq. (II.1) are

$$\mathbf{B} = \begin{pmatrix} \mathbf{I} & \mathbf{0} \\ 0 & 0 \end{pmatrix}, \quad \mathbf{F}(\mathbf{q}, \boldsymbol{\eta}) = \begin{pmatrix} -\mathbf{u} \cdot \nabla \mathbf{u} - \nabla p + \frac{2}{\text{Re}} \nabla \cdot (\mathbf{D}(\mathbf{u})) \\ \nabla \cdot \mathbf{u} \end{pmatrix}, \quad (\text{III.1})$$

here the state variable $\mathbf{q} = [\mathbf{u}, p]^T$ is composed of the velocity field and the hydrodynamic pressure; the strain tensor is defined as $\mathbf{D}(\mathbf{u}) \equiv \frac{1}{2}(\nabla \mathbf{u} + \nabla \mathbf{u}^T)$. The problem depends on a single dimensionless number, the Reynolds number – defined as follows:

$$\text{Re} = \frac{U_\infty L}{\nu} \quad (\text{III.2})$$

where U_∞ is the characteristic velocity, L is the characteristic length of the problem, and ν is the kinematic viscosity. Herein, we express the vector of parameters as $\boldsymbol{\eta} = \text{Re}$.

Finite-element formulation

The finite element formulation is based on the variational form of the governing equations. The variational form is subjected to the definition of the inner product, which for a scalar or vectorial quantity is defined as $\langle \phi_1, \phi_2 \rangle$:

$$\langle \phi_1, \phi_2 \rangle = \int_{\Omega} \bar{\phi}_1 \cdot \phi_2 \, d\Omega,$$

The weak form of the Navier-Stokes equations is obtained by introducing test functions $[\mathbf{v}, q]$ associated with the momentum and continuity equations, and integrating over the domain

$$\forall [\mathbf{v}, q]^T, \quad \langle \mathbf{v}, \partial_t \mathbf{u} \rangle = \left\langle \mathbf{v}, -\mathbf{u} \cdot \nabla \mathbf{u} - \nabla p + \frac{2}{\text{Re}} \nabla \cdot (\mathbf{D}(\mathbf{u})) \right\rangle + \langle q, \nabla \cdot \mathbf{u} \rangle. \quad (\text{III.3})$$

It is customary to integrate by parts the stress-tensor and to reduce the derivation of the state variable to first order,

$$\forall [\mathbf{v}, q]^T, \quad \langle \mathbf{v}, \partial_t \mathbf{u} \rangle = - \langle \mathbf{v}, \mathbf{u} \cdot \nabla \mathbf{u} \rangle - \left\langle \mathbf{D}(\mathbf{v}), \frac{2}{\text{Re}} \mathbf{D}(\mathbf{u}) \right\rangle + \langle \nabla \mathbf{v}, p \rangle + \langle q, \nabla \cdot \mathbf{u} \rangle. \quad (\text{III.4})$$

So far, we have not specified the functional space of the unknowns $[\mathbf{u}, p]$ and the test functions $[\mathbf{v}, q]^T$. The most common choice is $\mathbf{u}, \mathbf{v} \in H_{\text{div}}(\Omega)$, where

$$H_{\text{div}}(\Omega) = \{ \mathbf{v} : \mathbf{v} \in (L^2(\Omega))^N \text{ and } \nabla \cdot \mathbf{v} \in L^2(\Omega) \}$$

and $p, q \in L^2(\Omega)$. A discretization of $[H_{\text{div}}(\Omega), L^2(\Omega)]^T$ is the Taylor-Hood

basis $[P_2, P_2, P_1]^T$, where P_n are Lagrange elements of order n .

1.2

Mixed-convection Navier–Stokes equations

We adopt the Boussinesq approximation to model the problem of mixed convection. In this case, the two operators of the dynamical system eq. (II.1) are as follows,

$$\mathbf{B} = \begin{pmatrix} \mathbf{I} & \mathbf{0} & \mathbf{0} \\ 0 & 0 & 0 \\ 0 & 0 & 1 \end{pmatrix}, \quad \mathbf{F}(\mathbf{q}, \boldsymbol{\eta}) = \begin{pmatrix} -\mathbf{u} \cdot \nabla \mathbf{u} - \nabla p + \frac{2}{\text{Re}} \nabla \cdot (\mathbf{D}(\mathbf{u})) + \text{Ri} T \mathbf{e}_z \\ \nabla \cdot \mathbf{u} \\ -\mathbf{u} \cdot \nabla T + \frac{1}{\text{Pr Re}} \nabla^2 T \end{pmatrix}, \quad (\text{III.5})$$

where the state variable $\mathbf{q} = [\mathbf{u}, p, T]^T$ is composed of the velocity field, the hydrodynamic pressure and the temperature. The parameters are the Reynolds number, the Prandtl number and the Richardson number – defined as follows:

$$\text{Re} = \frac{U_\infty L}{\nu}, \quad \text{Ri} = -\frac{\beta \mathbf{e}_z \cdot \mathbf{g} (T_S - T_\infty) L}{U_\infty^2}, \quad \text{Pr} = \frac{\nu}{\kappa}. \quad (\text{III.6})$$

In the definition of the dimensionless number: U_∞ is the characteristic velocity, L is the characteristic length, ν is the kinematic viscosity, β is the coefficient of thermal expansion, T_S is the temperature of a solid boundary, T_∞ is the characteristic temperature and κ is the thermal diffusivity. Herein, we express the vector of parameters as $\boldsymbol{\eta} = [\text{Re}, \text{Ri}, \text{Pr}]^T$.

Finite element formulation

The weak form of the mixed convection Navier-Stokes equations is promptly defined by introducing test functions $[\mathbf{v}, q, s]$ associated with the momentum, continuity and convection equations, integrating by parts and integrating over the domain

$$\begin{aligned} \forall [\mathbf{v}, q, s], \quad \partial_t \langle \mathbf{v}, \mathbf{u} \rangle + \partial_t \langle s, T \rangle = & - \langle \mathbf{v}, \mathbf{u} \cdot \nabla \mathbf{u} \rangle - \langle \mathbf{D}(\mathbf{v}), \frac{2}{\text{Re}} \mathbf{D}(\mathbf{u}) \rangle + \langle \nabla \mathbf{v}, p \rangle \\ & + \langle \mathbf{v}, \text{Ri} T \mathbf{e}_z \rangle + \langle q, \nabla \cdot \mathbf{u} \rangle - \langle s, \mathbf{u} \cdot \nabla T \rangle \\ & - \left\langle \nabla s, \frac{1}{\text{Pr Re}} \nabla T \right\rangle \end{aligned} \quad (\text{III.7})$$

The unknowns $[\mathbf{u}, p, T]^T \in [H_{\text{div}}(\Omega), L^2(\Omega), L^2(\Omega)]^T$ and the test functions $[\mathbf{v}, q, s]^T \in [H_{\text{div}}(\Omega), L^2(\Omega), L^2(\Omega)]^T$. The solution is determined in the discrete $[P_2, P_2, P_1, P_1]^T$ space.

1.3

Compressible Navier–Stokes equations

Let us introduce the compressible Navier–Stokes equations as the governing equations of motion of a perfect gas described in primitive variables $\mathbf{q} = [\rho, u_r, u_\theta, u_z, p, T]^T$, and the set of control parameters $\boldsymbol{\eta} = [Re, M_\infty, Pr]^T$. These are formally expressed as

$$\mathbf{F}(\mathbf{q}, \boldsymbol{\eta}) = - \begin{pmatrix} \mathbf{u} \cdot \nabla \rho + \rho \nabla \cdot \mathbf{u} \\ \rho \mathbf{u} \cdot \nabla \mathbf{u} - \nabla p + \nabla \cdot \boldsymbol{\tau}(\mathbf{u}) \\ (\gamma - 1) \left[\rho T \nabla \cdot \mathbf{u} - \gamma M_\infty^2 \boldsymbol{\tau}(\mathbf{u}) : \mathbf{D}(\mathbf{u}) \right] + \rho \mathbf{u} \cdot \nabla T + \frac{\gamma}{Pr Re} \nabla^2 T \\ -\rho T + 1 + \gamma M_\infty^2 p \end{pmatrix}, \quad \mathbf{B} = \begin{pmatrix} 1 & 0 & 0 & 0 \\ 0 & \rho \mathbf{I} & 0 & 0 \\ 0 & 0 & \rho & 0 \\ 0 & 0 & 0 & 0 \end{pmatrix}, \quad (\text{III.8})$$

where the state variable $\mathbf{q} = [\rho, \mathbf{u}, T, p]^T$ is composed of the density, velocity field, temperature, and pressure. Below in an example, we shall indicate how we proceed to render the state variable dimensionless, see eq. (III.29). The parameters are the Reynolds number, the Prandtl number and the Mach number – defined as follows:

$$Re = \frac{U_\infty L}{\nu}, \quad M_\infty = \frac{U_\infty}{\sqrt{\gamma R_g T_\infty}}, \quad Pr = \frac{\nu}{\kappa}. \quad (\text{III.9})$$

In the definition of the dimensionless number: U_∞ is the characteristic velocity, L is the characteristic length, ν is the kinematic viscosity, $\gamma = \frac{c_p}{c_v}$ is the isentropic coefficient, R_g is the constant of the gas, T_∞ is the characteristic temperature and κ is the thermal diffusivity. Herein, we express the vector of parameters as $\boldsymbol{\eta} = [Re, M_\infty, Pr]^T$.

Finite element formulation

The weak form of the compressible Navier–Stokes equations is promptly defined by introducing test functions $[\mathbf{v}, q, r, j]$ associated with the momentum, continuity and convection equations, integrating by parts and integrating over the domain, we obtain the following set of equations,

$$\begin{aligned} \forall [\mathbf{v}, q, r, j], \quad & \langle r, \partial_t \rho \rangle + \langle r, \mathbf{u} \cdot \nabla \rho + \rho \nabla \cdot \mathbf{u} \rangle \\ & + \langle \mathbf{v}, \rho_0 \partial_t \mathbf{u} \rangle + \langle \mathbf{v}, \rho \mathbf{u} \cdot \nabla \mathbf{u} \rangle - \langle \nabla \cdot \mathbf{v}, p \rangle + \langle \nabla \mathbf{v} : \boldsymbol{\tau}(\mathbf{u}) \rangle \\ & + \langle j, \rho \mathbf{u} \cdot \nabla T \rangle + \langle j, \rho \partial_t T \rangle \\ & - \langle j, \gamma(\gamma - 1) M_\infty^2 \boldsymbol{\tau}(\mathbf{u}) : \mathbf{D}(\mathbf{u}) \rangle + \frac{\gamma}{Pr Re} \langle \nabla j, \nabla T \rangle \\ & + \langle q, 1 + \gamma M_\infty^2 p \rangle - \langle q, \rho T \rangle. \end{aligned} \quad (\text{III.10})$$

The unknowns $[\mathbf{u}, p, \rho, T]^T \in [(H^1)^N, L^2(\Omega), L^2(\Omega), L^2(\Omega)]^T$ and the test functions $[\mathbf{v}, q, r, j]^T \in [(H^1)^N, L^2(\Omega), L^2(\Omega), L^2(\Omega)]^T$. The solution is determined in the discrete $[P_2, P_2, P_1, P_1, P_1]^T$ space.

Artificial Boundary Conditions – Complex mapping

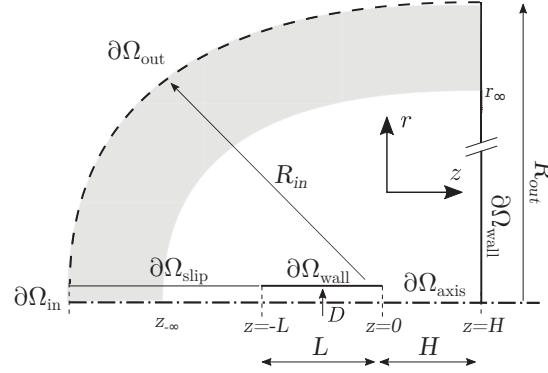


Figure III.1 – Diagram of a rounded impinging jet. The physical domain, represented as a white area, is complemented with a radial buffer layer, shown as a light grey shaded zone..

The far-field boundaries should be transparent or at least absorbing in order to avoid the reflection of the outgoing waves. For the evaluation of the linear stability of the compressible Navier–Stokes equations, we introduce a buffer region, see fig. III.1, which damps the outgoing waves before reaching the boundary, and thus avoids possible reflections.

Herein, we shall denote $\Psi(x, t)$ a given wave propagating in the direction x . The difficulty we want to solve is associated to the existence of solutions behaving as $\Psi(x, t) \approx e^{ikx - i\omega t}$ as $x \rightarrow \infty$, which, according to the argument of k , may be oscillating, or even worse, exponentially growing. The idea is to consider an analytical continuation of the solution for *complex* x , and solve in a region of the complex plane where all physically relevant solutions are nicely decaying. To this aim, we will define a mapping from a (real) numerical coordinate X defined in a truncated domain $X \in [0, X_{max}]$ to the physical coordinate x .

Definition of a smooth mapping The application of the proposed method to a given problem leads to two separate regions: (i) an unmodified domain for $X < X_0$ and (ii) a mapped region for $X > X_0$, characterized by a parameter γ_c defining the direction in the complex plane. The simplest choice is as follows:

$$x = \mathcal{G}_x(X) = \begin{cases} X & \text{for } X < X_0, \\ [1 + i\gamma_c]X & \text{for } X > X_0, \end{cases} \quad (\text{III.11})$$

which transforms the x -derivatives as follows:

$$\frac{\partial}{\partial x} = \begin{cases} \frac{\partial}{\partial X_1} & \text{for } X < X_0, \\ \frac{\partial}{1 + i\gamma_c \partial X} & \text{for } X > X_0, \end{cases} \quad (\text{III.12})$$

In practice, it is desirable to design a mapping function which gradually enters into the complex plane with a transition region of characteristic length L_c , in order to avoid possible reflections caused by an abrupt change at $X = X_0$. This can be achieved using a mapping function with the form:

$$\mathcal{G}_x : \mathbb{R} \rightarrow \mathbb{C} \quad \text{such that} \quad x = \mathcal{G}_x(X) = [1 + i\gamma_c g(X)]X \quad (\text{III.13})$$

where $g(X)$ has to be chosen as a smooth function such as $g(X) = 0$ for $X < X_0$ and $g(X) \approx 1$ for $X > X_0 + L_c$ up to X_{max} for a length $L_{CM} = X_{max} - (X_0 + L_c)$ where complex mapping is activated. We found good performance using $g(X) = \tanh\left(\left[\frac{X - X_0}{L_c}\right]^2\right)$. To apply the method to a linear PDE of the form eq. (III.10), one has simply to modify the spatial derivatives as follows:

$$\frac{\partial}{\partial x} \equiv \mathcal{H}_x \frac{\partial}{\partial X} \quad \text{with} \quad \mathcal{H}_x(X) = \left(\frac{\partial \mathcal{G}_x}{\partial X}\right)^{-1}. \quad (\text{III.14})$$

For a given PDE problem, the regularity of the complex mapping function $g \in \mathcal{C}^r(\Omega)$ is determined by the highest derivative order of the considered PDE problem. This requirement is due to the fact that the derivative should be continuous between the physical and the complex mapping domain to avoid any numerical reflection.

Decomposition of the linear perturbation

When considering an eigenmode ($\hat{\mathbf{q}}$) arising from the compressible Navier–Stokes equations, it is useful to attempt to decompose it into three components: *acoustic*, *hydrodynamic* and *entropic*. There is a large literature on the decomposition of acoustic sources (Ewert et al., 2003; Spieser, 2020) to compute acoustic propagation effects. In our case, we follow the reciprocal reasoning, we adopt a monolithic computation of the compressible flow, i.e. we do not decompose the flow into acoustic sources and acoustic propagation, and we would like to unveil the feedback loop responsible for the instability mechanism and the frequency selection. We adopt the definition that the acoustic component of the velocity field is derived from a potential function.

For this purpose, we adopt a Helmholtz-Hodge decomposition (Schoder et al., 2020) of the perturbation velocity field into *acoustic* (potential) and *hydrodynamic* (solenoidal)

$$\hat{\mathbf{u}} = \hat{\mathbf{u}}_{ac} + \hat{\mathbf{u}}_{hyd} = \nabla \phi_c + \nabla \times \Psi \quad (\text{III.15})$$

applying divergence to eq. (III.15), the potential ϕ_c is determined from the following Poisson equation

$$\begin{aligned} \Delta\phi_c &= \nabla \cdot \hat{\mathbf{u}} & \text{in } \Omega \\ \nabla\phi_c \cdot \mathbf{n} &= \hat{\mathbf{u}} \cdot \mathbf{n} & \text{on } \partial\Omega. \end{aligned} \quad (\text{III.16})$$

The hydrodynamic component of the velocity is subsequently determined by subtracting $\hat{\mathbf{u}}_{\text{hyd}} = \hat{\mathbf{u}} - \hat{\mathbf{u}}_{\text{ac}} = \hat{\mathbf{u}} - \nabla\phi_c$. The uniqueness of the Helmholtz decomposition is subjected to the L^2 -orthogonality condition, in our case satisfied by the suitable boundary condition of eq. (III.16), and the decay of the velocity field at the far-field (Schoder et al., 2020).

The pressure component of the mode $\hat{\mathbf{q}}$ is determined from the momentum equation

$$-\frac{1}{\rho_0}\nabla\hat{p} = i\omega\hat{\mathbf{u}} + \hat{\mathbf{u}} \cdot \nabla\mathbf{u}_0 + \mathbf{u}_0 \cdot \nabla\hat{\mathbf{u}} + \frac{\hat{\rho}}{\rho_0}\mathbf{u}_0 \cdot \nabla\mathbf{u}_0 - \frac{1}{\text{Re}}\nabla \cdot \tau(\hat{\mathbf{u}}), \quad (\text{III.17})$$

from the decomposition $\hat{p} = \hat{p}_{\text{ac}} + \hat{p}_{\text{hyd}} + \hat{p}_{\text{s}}$ and applying the divergence operator to the momentum equation, we obtain the following equations

$$-\frac{1}{\rho_0}\Delta\hat{p}_{\text{ac}} + \frac{\nabla\rho_0 \cdot \nabla\hat{p}_{\text{ac}}}{\rho_0^2} - \nabla \cdot \left(\frac{M_\infty^2}{T_0}(\mathbf{u}_0 \cdot \nabla\mathbf{u}_0) \frac{\hat{p}_{\text{ac}}}{\rho_0} \right) = \quad (\text{III.18a})$$

$$i\omega\nabla \cdot \hat{\mathbf{u}}_{\text{ac}} + \nabla \cdot (\mathbf{u}_0 \cdot \nabla\hat{\mathbf{u}}_{\text{ac}}) + \nabla \cdot (\hat{\mathbf{u}}_{\text{ac}} \cdot \nabla\mathbf{u}_0) \quad (\text{III.18b})$$

$$-\frac{1}{\rho_0}\Delta\hat{p}_{\text{hyd}} + \frac{\nabla\rho_0 \cdot \nabla\hat{p}_{\text{hyd}}}{\rho_0^2} - \nabla \cdot \left(\frac{M_\infty^2}{T_0}(\mathbf{u}_0 \cdot \nabla\mathbf{u}_0) \frac{\hat{p}_{\text{hyd}}}{\rho_0} \right) = \quad (\text{III.18c})$$

$$\nabla \cdot (\mathbf{u}_0 \cdot \nabla\hat{\mathbf{u}}_{\text{hyd}}) + \nabla \cdot (\hat{\mathbf{u}}_{\text{hyd}} \cdot \nabla\mathbf{u}_0) \quad (\text{III.18d})$$

with decay at the far-field $r \rightarrow \infty$. Details of the derivation are given in Sierra-Ausin and Giannetti (2023, App. A). Finally, the entropic part of the pressure is recovered by subtracting the two other components to the pressure of the mode $\hat{p}_{\text{s}} = \hat{p} - \hat{p}_{\text{ac}} - \hat{p}_{\text{hyd}}$, which accounts for the dissipation effects of the viscous stress-tensor.

The other two components, temperature and density, are determined as follows. The acoustic and hydrodynamic components are considered to evolve isentropically and are directly determined from the pressure,

$$\hat{T}_{\text{ac}} = (\gamma - 1)M_\infty^2\hat{p}_{\text{ac}}, \quad \hat{T}_{\text{hyd}} = (\gamma - 1)M_\infty^2\hat{p}_{\text{hyd}}, \quad \hat{T}_{\text{s}} = \hat{T} - \hat{T}_{\text{ac}} - \hat{T}_{\text{hyd}}, \quad (\text{III.19})$$

$$\hat{\rho}_{\text{ac}} = M_\infty^2 \frac{\rho_0}{T_0} \hat{p}_{\text{ac}}, \quad \hat{\rho}_{\text{hyd}} = M_\infty^2 \frac{\rho_0}{T_0} \hat{p}_{\text{hyd}}, \quad \hat{\rho}_{\text{s}} = \hat{\rho} - \hat{\rho}_{\text{ac}} - \hat{\rho}_{\text{hyd}}. \quad (\text{III.20})$$

Non-local structural sensitivity decomposition

We consider the case of a global instability caused by a feedback process between two travelling waves. In this case one cannot provide a direct *local*

definition of the *wavemaker* or *structural sensitivity*. That is, we can still formulate the concept of structural sensitivity, but it is no longer localised in space, i.e., it displays a support all along the interacting path between the two travelling waves. We briefly recall the concept of structural sensitivity, before introducing an adequate decomposition of the wavemaker for global instabilities generated by non-local feedback process. The adjoint equations are herein used to evaluate the effect of a linear harmonic forcing $\mathbf{H}(\hat{\mathbf{q}}) \equiv \delta(\mathbf{x} - \mathbf{x}_0)\mathbf{P}_\mathbf{H}\mathbf{C}_0\mathbf{P}_{\hat{\mathbf{q}}}\hat{\mathbf{q}}$,

$$\left(-i\omega\mathbf{B}|_{\mathbf{q}_0} + \mathbf{D}\mathbf{F}|_{\mathbf{q}_0}\right)\hat{\mathbf{q}} = \mathbf{H}(\hat{\mathbf{q}}), \quad (\text{III.21})$$

where \mathbf{C}_0 is a generic linear operator acting on $\hat{\mathbf{q}}$, and $\mathbf{P}_\mathbf{H}$ a diagonal matrix that selects the type of forcing. In the following, we neglect mass injection to the system, and we simply consider momentum forcing and a source of heat release, that is, $\mathbf{P}_\mathbf{H} = \text{diag}(0, \mathbf{I}, 1, 0, 0)$. The projection operator $\mathbf{P}_{\hat{\mathbf{q}}}$ is also a diagonal matrix that selects the dependency of the forcing on the perturbation. The structural sensitivity tensor is therefore defined as

$$\begin{aligned} i\delta\omega &= \langle \mathbf{P}_\mathbf{H}\hat{\mathbf{q}}^\dagger, \delta(\mathbf{x} - \mathbf{x}_0)\mathbf{C}_0\mathbf{P}_{\hat{\mathbf{q}}}\hat{\mathbf{q}} \rangle \\ &\leq \|\mathbf{C}_0\| \|\mathbf{P}_\mathbf{H}\hat{\mathbf{q}}^\dagger\|_{L^2} \|\mathbf{P}_{\hat{\mathbf{q}}}\hat{\mathbf{q}}\|_{L^2} = \|\mathbf{C}_0\| \mathbf{S}_s(\mathbf{x}_0), \end{aligned} \quad (\text{III.22})$$

that is, the structural sensitivity map is defined as $\mathbf{S}_s(\mathbf{x}_0) \equiv \|\mathbf{P}_\mathbf{H}\hat{\mathbf{q}}^\dagger\|_{L^2} \|\mathbf{P}_{\hat{\mathbf{q}}}\hat{\mathbf{q}}\|_{L^2}$. The scalar field \mathbf{S}_s is then an upper bound function for the eigenvalue variation, and it can be employed to determine locations where the feedback is stronger. Therefore, allowing an identification of the regions where the instability mechanism acts. However, when it is not localized within a small physical region, it does not clearly identify the *wavemaker*, but a possible interacting region between the components of the global mode.

Decomposing the mode $\hat{\mathbf{q}}$ we can rewrite the harmonic forcing as $\mathbf{H}(\hat{\mathbf{q}}) = \mathbf{H}(\hat{\mathbf{q}}_{\text{ac}} + \hat{\mathbf{q}}_{\text{hyd}} + \hat{\mathbf{q}}_{\text{s}})$, which due to linearity of the forcing term on the eigenmode is simply expressed as

$$\mathbf{H}(\hat{\mathbf{q}}) = \mathbf{H}(\hat{\mathbf{q}}_{\text{ac}}) + \mathbf{H}(\hat{\mathbf{q}}_{\text{hyd}}) + \mathbf{H}(\hat{\mathbf{q}}_{\text{s}}). \quad (\text{III.23})$$

Thus, we have a first decomposition of the harmonic forcing $\mathbf{H}(\hat{\mathbf{q}})$ from the splitting of the state variable. However, the term $\mathbf{H}(\hat{\mathbf{q}}_{\text{ac}})$ is not necessarily a forcing term that uniquely induces acoustic perturbations. Assume, for simplicity, that the previous forcing term depends uniquely on the acoustic velocity, $\mathbf{H}(\mathbf{u}_{\text{ac}})$, and it only acts on the momentum equation, that is, we neglect mass or heat injection. The forcing term must be rotational-free, i.e., $\nabla \times \mathbf{H}(\mathbf{u}_{\text{ac}}) = 0$, otherwise it will induce vortical perturbations into the flow. Therefore, $\mathbf{H}(\hat{\mathbf{q}}_{\text{ac}})$ should be interpreted as a generic forcing or feedback term that depends on the acoustic perturbation. To determine the effect of the forcing, that is, which kind

of response induces, we decompose the forcing operator into $\mathbf{H} = \mathbf{H}_{ac} + \mathbf{H}_{hyd} + \mathbf{H}_s$. Following, this reasoning, we may decompose eq. (III.21),

$$\begin{aligned} \langle \hat{\mathbf{q}}_{ac}^\dagger, \left(-i\omega\mathbf{B}|_{\mathbf{q}_0} + \mathbf{DF}|_{\mathbf{q}_0} \right) \hat{\mathbf{q}}_{ac} \rangle \hat{\mathbf{q}}_{ac} &= \mathbf{H}_{ac}(\hat{\mathbf{q}}_{ac}) + \mathbf{H}_{ac}(\hat{\mathbf{q}}_{hyd}) + \mathbf{H}_{ac}(\hat{\mathbf{q}}_s), \\ \langle \hat{\mathbf{q}}_{hyd}^\dagger, \left(-i\omega\mathbf{B}|_{\mathbf{q}_0} + \mathbf{DF}|_{\mathbf{q}_0} \right) \hat{\mathbf{q}}_{hyd} \rangle \hat{\mathbf{q}}_{hyd} &= \mathbf{H}_{hyd}(\hat{\mathbf{q}}_{ac}) + \mathbf{H}_{hyd}(\hat{\mathbf{q}}_{hyd}) + \mathbf{H}_{hyd}(\hat{\mathbf{q}}_s), \\ \langle \hat{\mathbf{q}}_s^\dagger, \left(-i\omega\mathbf{B}|_{\mathbf{q}_0} + \mathbf{DF}|_{\mathbf{q}_0} \right) \hat{\mathbf{q}}_s \rangle \hat{\mathbf{q}}_s &= \mathbf{H}_s(\hat{\mathbf{q}}_{ac}) + \mathbf{H}_s(\hat{\mathbf{q}}_{hyd}) + \mathbf{H}_s(\hat{\mathbf{q}}_s), \end{aligned} \quad (\text{III.24})$$

The interpretation of the adjoint $\hat{\mathbf{q}}^\dagger$ as a measure of the receptivity with respect to a harmonic forcing allows us to decompose the adjoint. In this manner, the adjoint variable serves to project the forcing term onto each of the subspaces with the decomposed adjoint $\hat{\mathbf{q}}^\dagger = \hat{\mathbf{q}}_{ac}^\dagger + \hat{\mathbf{q}}_{hyd}^\dagger + \hat{\mathbf{q}}_s^\dagger$. That is, $\mathbf{H}_{ac}(\hat{\mathbf{q}}) = \langle \hat{\mathbf{q}}_{ac}^\dagger, \mathbf{H}(\hat{\mathbf{q}}) \rangle \hat{\mathbf{q}}_{ac}$, $\mathbf{H}_{hyd}(\hat{\mathbf{q}}) = \langle \hat{\mathbf{q}}_{hyd}^\dagger, \mathbf{H}(\hat{\mathbf{q}}) \rangle \hat{\mathbf{q}}_{hyd}$ and $\mathbf{H}_s(\hat{\mathbf{q}}) = \langle \hat{\mathbf{q}}_s^\dagger, \mathbf{H}(\hat{\mathbf{q}}) \rangle \hat{\mathbf{q}}_s$. Then, we can rewrite eq. (III.24),

$$\begin{aligned} &\left(\langle \hat{\mathbf{q}}_{ac}^\dagger, \left(-i\omega\mathbf{B}|_{\mathbf{q}_0} + \mathbf{DF}|_{\mathbf{q}_0} \right) \hat{\mathbf{q}}_{ac} \rangle + \langle \hat{\mathbf{q}}_{ac}^\dagger, \mathbf{H}(\hat{\mathbf{q}}_{ac}) \rangle + \langle \hat{\mathbf{q}}_{ac}^\dagger, \mathbf{H}(\hat{\mathbf{q}}_{hyd}) \rangle + \langle \hat{\mathbf{q}}_{ac}^\dagger, \mathbf{H}(\hat{\mathbf{q}}_s) \rangle \right) \hat{\mathbf{q}}_{ac} = 0 \\ &\left(\langle \hat{\mathbf{q}}_{hyd}^\dagger, \left(-i\omega\mathbf{B}|_{\mathbf{q}_0} + \mathbf{DF}|_{\mathbf{q}_0} \right) \hat{\mathbf{q}}_{hyd} \rangle + \langle \hat{\mathbf{q}}_{hyd}^\dagger, \mathbf{H}(\hat{\mathbf{q}}_{ac}) \rangle + \langle \hat{\mathbf{q}}_{hyd}^\dagger, \mathbf{H}(\hat{\mathbf{q}}_{hyd}) \rangle + \langle \hat{\mathbf{q}}_{hyd}^\dagger, \mathbf{H}(\hat{\mathbf{q}}_s) \rangle \right) \hat{\mathbf{q}}_{hyd} = 0 \\ &\left(\langle \hat{\mathbf{q}}_s^\dagger, \left(-i\omega\mathbf{B}|_{\mathbf{q}_0} + \mathbf{DF}|_{\mathbf{q}_0} \right) \hat{\mathbf{q}}_s \rangle + \langle \hat{\mathbf{q}}_s^\dagger, \mathbf{H}(\hat{\mathbf{q}}_{ac}) \rangle + \langle \hat{\mathbf{q}}_s^\dagger, \mathbf{H}(\hat{\mathbf{q}}_{hyd}) \rangle + \langle \hat{\mathbf{q}}_s^\dagger, \mathbf{H}(\hat{\mathbf{q}}_s) \rangle \right) \hat{\mathbf{q}}_s = 0, \end{aligned} \quad (\text{III.25})$$

which exemplifies the role of the decomposed adjoint variable to project the structural forcing perturbation onto the corresponding subspace.

An inspection of ?? suggests the definition of a *non-local structural sensitivity* matrix as

$$\begin{aligned} i\delta\omega_j^k &= \langle \hat{\mathbf{q}}_k^\dagger, \delta(\mathbf{x} - \mathbf{x}_0)\mathbf{C}_0\hat{\mathbf{q}}_j \rangle \\ &\leq \|\mathbf{C}_0\| \|\hat{\mathbf{q}}_k^\dagger(\mathbf{x}_0)\| \|\hat{\mathbf{q}}_j(\mathbf{x}_0)\| = \|\mathbf{C}_0\| \mathbf{S}^{(j,k)}_s(\mathbf{x}_0), \\ \mathbf{S}^{(j,k)}_s(\mathbf{x}_0) &= \|\hat{\mathbf{q}}_k^\dagger(\mathbf{x}_0)\| \|\hat{\mathbf{q}}_j(\mathbf{x}_0)\| \text{ with } j, k = ac, hyd, s. \end{aligned} \quad (\text{III.26})$$

The new *structural sensitivity* provides information about the cross-interaction between vortical and acoustic components of the flow. It is usually the case that the feedback loop is initiated by the hydrodynamic instability of the shear layer, which induces an acoustic response. In turn, when an acoustic wave impinges on the region where the shear layer is most sensitive, it promotes back the hydrodynamic instability, continuing the loop. With this novel definition, $\mathbf{S}_s^{(hyd,ac)}$ identifies the most sensitive region of the flow to vortical perturbations, inducing an acoustic response. This first region can be named the wavemaker of the hydrodynamic perturbations exciting an acoustic response. The second (and third) wavemaker of interest corresponds to the excitation of a hydrodynamic response from hydrodynamic ($\mathbf{S}_s^{(hyd,hyd)}$) or acoustic perturbations ($\mathbf{S}_s^{(ac,hyd)}$). Physically, $\mathbf{S}_s^{(hyd,hyd)}$ determines the hydrodynamic wavemaker, which in a causal reasoning, could be argued to be the region initiating the feedback process. And $\mathbf{S}_s^{(ac,hyd)}$ determines the most sensitive region of the flow to an acoustic

perturbation inducing a hydrodynamic excitation, that is, the retro-action of the acoustic wave into the hydrodynamic instability. Additionally, we introduce a further decomposition of the non-local structural sensitivity map to account only for the forcing of the momentum equation for a forcing term that depends uniquely on the velocity field, that is,

$$\begin{aligned} i\delta\omega_j^k &= \langle \hat{\mathbf{u}}_k^\dagger, \delta(\mathbf{x} - \mathbf{x}_0) \mathbf{C}_0 \hat{\mathbf{u}}_j \rangle \\ &\leq \| \mathbf{C}_0 \| \| \hat{\mathbf{u}}_k^\dagger(\mathbf{x}_0) \| \| \hat{\mathbf{u}}_j(\mathbf{x}_0) \| = \| \mathbf{C}_0 \| \mathbf{S}_{\mathbf{u},s}^{(j,k)}(\mathbf{x}_0), \\ \mathbf{S}_{\mathbf{u},s}^{(j,k)}(\mathbf{x}_0) &= \| \hat{\mathbf{u}}_k^\dagger(\mathbf{x}_0) \| \| \hat{\mathbf{u}}_j(\mathbf{x}_0) \| \text{ with } j, k = \text{ac, hyd, s.} \end{aligned} \quad (\text{III.27})$$

Overall, the adjoint is decomposed as follows,

$$\begin{aligned} \hat{\mathbf{u}}^\dagger &= \hat{\mathbf{u}}_{\text{hyd}}^\dagger + \hat{\mathbf{u}}_{\text{ac}}^\dagger = \nabla \phi_c^\dagger + \nabla \times \boldsymbol{\Psi}^\dagger, \\ \hat{s}^\dagger &= \hat{s}_s^\dagger \\ \hat{\rho}^\dagger &= \hat{\rho}_{\text{ac}}^\dagger + \hat{\rho}_{\text{hyd}}^\dagger + \hat{\rho}_s^\dagger, \text{ (Sierra-Ausin and Giannetti, 2023, App. A)} \\ \hat{p}^\dagger &= \hat{p}_{\text{ac}}^\dagger = \frac{\nabla \cdot \hat{\mathbf{u}}^\dagger}{\gamma M_\infty^2} \\ \hat{T}^\dagger &= \hat{T}_{\text{ac}}^\dagger + \hat{T}_s^\dagger = -\frac{\nabla \cdot \hat{\mathbf{u}}^\dagger}{\gamma M_\infty^2} + (\hat{s}^\dagger \mathbf{u}_0 \cdot \nabla s_0 - \frac{\gamma}{\text{Pr Re } \rho_0} \Delta s_0) \end{aligned} \quad (\text{III.28})$$

An important property of the adjoint-direct mode bases is the bi-orthogonality. The pairs of primitive variables $\{0, \hat{\mathbf{u}}, \hat{s}\}; (0, \hat{\mathbf{u}}^\dagger, \hat{s})\}$ are bi-orthogonal, but that is no longer true when considering the complete primitive variable $\{(\hat{\rho}, \hat{\mathbf{u}}, \hat{s}); (\hat{\rho}^\dagger, \hat{\mathbf{u}}^\dagger, \hat{s})\}$, that is, when considering the continuity equation or the density variable. The set of bases lacks the bi-orthogonality property when mass is injected to the system, which implies the existence of an intrinsic coupling mechanism between the three components of the mode via the continuity equation, which in turn, impedes the decomposition of the sources of mass as acoustic, hydrodynamic or entropic. In the following, we will restrict ourselves to sources in the momentum equation, that is, we use eq. (III.27) to analyse the response of the system to body forces.

Example: Rounded laminar impinging jet

Let us consider the flow configuration of a rounded subsonic impinging jet. The computational domain was depicted in fig. III.1. For this problem we consider that the primitive variables have been made dimensionless to

$$\begin{aligned} \mathbf{x} &= \frac{\tilde{\mathbf{x}}}{D}, \quad t = \frac{\tilde{t} \tilde{u}_z|_{z=0}}{D}, \quad \rho = \frac{\tilde{\rho}}{\tilde{\rho}|_{fs}}, \quad \mathbf{u} = \frac{\tilde{\mathbf{u}}}{\tilde{u}_z|_{z=0}}, \quad T = \frac{\tilde{T}}{\tilde{T}|_{fs}}, \\ p &= \frac{\tilde{p} - \tilde{p}|_{fs}}{\tilde{\rho}|_{fs} \tilde{u}_z|_{z=0}^2}, \quad M_\infty = \frac{\tilde{u}_z|_{z=0}}{(\gamma R_g \tilde{T}|_{fs})^{1/2}}, \quad \text{Re} = \frac{\tilde{\rho}|_{fs} \tilde{u}_z|_{z=0} D}{\mu(\tilde{T}|_{fs})} \end{aligned} \quad (\text{III.29})$$

where R_g is the ideal gas constant, $\tilde{u}_z|_{z=0}$ denote the average value of the axial velocity at the cross-section $z = 0$, and $\tilde{\rho}|_{fs}$, $\tilde{p}|_{fs}$, $\tilde{T}|_{fs}$ denote the values on the far-field or free-stream. And the Navier–Stokes equations eq. (III.8) are complemented with the following boundary conditions,

$$\begin{aligned}
 u_z = 1, & & u_r = 0, & & T = (1 - \frac{\gamma-1}{2}M_\infty^2) & \text{on } \partial\Omega_{in} \\
 u_z = 0, & & u_r = 0, & & \nabla T \cdot \mathbf{n} = 0 & \text{on } \partial\Omega_{wall} \\
 u_r = 0, & & \nabla T \cdot \mathbf{n} = 0 & & & \text{on } \partial\Omega_{slip} \\
 \rho = 1, & & p = 0, & & T = 1 & \text{on } \partial\Omega_{out}.
 \end{aligned} \tag{III.30}$$

The inlet boundary condition models the inflow from a reservoir with a constant total temperature equal to unity. In such a way, the energy of the system is kept constant for every Mach number M_∞ . The length of the pipe is a constant of the problem that determines the height of the boundary layer, here we have chosen $L = 2.5D$. The flow in the slip region is nearly constant, thus the length of this region is not an important parameter of the problem. The location of the start of the absorbing layer is chosen to be $z_{-\infty} = r_\infty = 15D$. Finally, the distance between the nozzle end location ($z = 0$) and the impinging wall is H , which is kept constant $H = 5D$. Then the linear Navier–Stokes equations eq. (II.4) are complemented with the following homogeneous boundary conditions,

$$\begin{aligned}
 \hat{u}_z = 0, & & \hat{u}_r = 0, & & \hat{T} = 0 & \text{on } \partial\Omega_{in} \\
 \hat{u}_z = 0, & & \hat{u}_r = 0, & & \nabla \hat{T} \cdot \mathbf{n} = 0 & \text{on } \partial\Omega_{wall} \\
 \hat{u}_r = 0, & & \nabla \hat{T} \cdot \mathbf{n} = 0 & & & \text{on } \partial\Omega_{slip} \\
 \hat{\rho} = 0, & & \hat{p} = 0, & & \hat{T} = 0 & \text{on } \partial\Omega_{out}.
 \end{aligned} \tag{III.31}$$

Let us illustrate the application of this decomposition to a particular example. Figure III.2 depicts the components of the density fluctuations $\hat{\rho}$ of a global mode with frequency $\omega_i \approx 3.1$ for a baseflow of the impinging jet at $M_J \approx 0.9$ and $Re = 800$. The decomposition allows us to identify the hydrodynamic component of the density $\hat{\rho}_{hyd}$, displayed in (a). Similarly, the entropic component of the density $\hat{\rho}_s$, which is illustrated in (c), is localised within the shear layer. The fluctuations of these two fields are mainly underpinned by the instability of the shear layer; as one may appreciate from the number of nodes along the axial direction. Instead, the acoustic component of the density field $\hat{\rho}_{ac}$, displayed in (b), corresponds to a guided jet wave, which results from the propagation of the local production of divergence of the velocity field within the jet.

Figure III.3 displays two pairs of structural sensitivity pairs. The first, $\mathbf{S}_{\mathbf{u},s}^{(hyd,ac)}$, is the map measuring the eigenvalue drift due to an acoustic response induced by a hydrodynamic structural perturbation. At large Mach numbers ($M_J \approx 0.9$), fig. III.3 (a) shows that $\mathbf{S}_{\mathbf{u},s}^{(hyd,ac)}$ is localised near the nozzle lip and within the jet at an axial location around $z \approx H - D$. The region within the

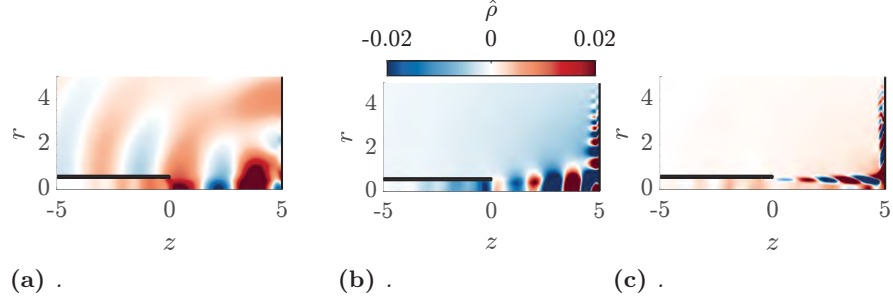


Figure III.2 – Density decomposition of the global mode with $St \approx 0.5$ at criticality ($Re = 900$) at $M_\infty = 0.6$. (a) Acoustic component of density $\hat{\rho}_{ac}$. (b) Hydrodynamic component of density $\hat{\rho}_{hyd}$. (c) Entropic component of density $\hat{\rho}_s$.

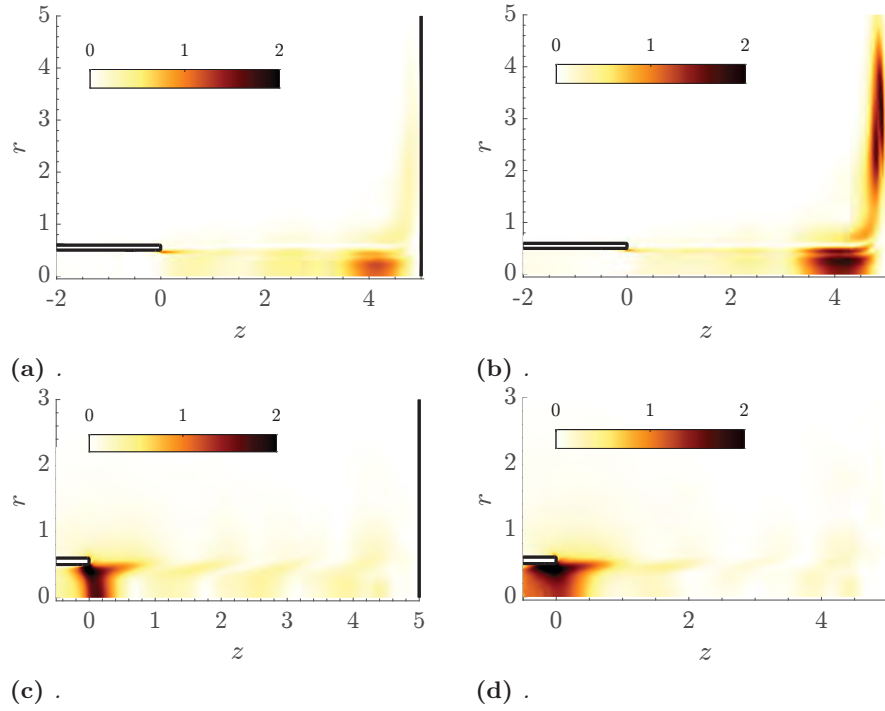


Figure III.3 – (a-b) An example of the map $\mathbf{S}_{u,s}^{(hyd,ac)}$ for a mode at a large Mach ($M_J \approx 0.9$) number and another at an intermediate Mach number ($M_J \approx 0.5$). (c-d) Map $\mathbf{S}_{u,s}^{(ac,hyd)}$ for the global mode ($M_J \approx 0.9$) and ($M_J \approx 0.5$). More details can be found in Sierra-Ausin and Giannetti (2023, Sec. 4).

jet is found at the spatial location with the largest production of divergence of the velocity field. An acoustic guided jet mode (cf fig. III.2) is then responsible for the closure of the feedback-loop. When the Mach number is decreased, the production of divergence of velocity is less effective and the most effective mechanism to close the feedback loop turns out to be a vortex-sound mechanism, that is, the sensitivity map $\mathbf{S}_{\mathbf{u},s}^{(hyd,ac)}$ highlights the region where the linearised Lamb vector is large (not shown). Figure III.3 (c-d) displays the complementary sensitivity map $\mathbf{S}_{\mathbf{u},s}^{(ac,hyd)}$, which measures eigenvalue drift due to a hydrodynamic response induced by an acoustic perturbation. Not surprisingly, the impingement of acoustic perturbations onto the nozzle lip is the most effect mechanism to trigger the instability of the shear layer, which is mostly of vortical nature. Such a mechanism is largely insensitive to Mach number variations.

1.4

Navier–Stokes equations for bubble dynamics

Herein, we overview the modelling and numerical approach for the computation of problems with a free interface. This section is based on Sierra-Ausin, Bonnefis, et al. (2022, App. A), and it illustrates the (Linearised) Arbitrary Lagrangian Eulerian (L-ALE) method. In this case, since the governing equations include the kinematic and dynamic boundary conditions, we do not write the governing equations in their operator form eq. (II.1). In addition, a detailed description of the finite element formulation may be found in Bonnefis (2019). Free-boundary problems involving a Newtonian fluid contained in a time-dependent fluid domain $\Omega(t)$ bounded by a fixed boundary Γ_s and a free boundary $\Gamma_b(t)$ subjected to capillary effects are governed by (III.32)-(III.35) supplemented with appropriate boundary conditions on Γ_s .

$$\partial_{t_\Omega} \mathbf{u} + \mathbf{u} \cdot \nabla_\Omega \mathbf{u} = \rho^{-1} \nabla_\Omega \cdot \boldsymbol{\Sigma}_\Omega \quad \text{in } \Omega(t), \quad (\text{III.32})$$

$$\nabla_\Omega \cdot \mathbf{u} = 0 \quad \text{in } \Omega(t), \quad (\text{III.33})$$

$$\partial_{t_\Omega} \eta = \mathbf{u} \cdot \mathbf{n} \quad \text{on } \Gamma_b(t), \quad (\text{III.34})$$

$$\boldsymbol{\Sigma}_\Omega \cdot \mathbf{n} = (-p_b + \gamma \kappa) \mathbf{n} \quad \text{on } \Gamma_b(t). \quad (\text{III.35})$$

In the L-ALE approach, we first consider a *reference* domain Ω_0 , which is fixed and allows unknowns to be evaluated in an Eulerian manner, and the *physical* domain $\Omega(t)$, which depends upon time and where Lagrangian quantities are evaluated. Let \mathbf{x}_0 and \mathbf{x} denote the local position (with respect to some fixed origin) of a given geometrical point in Ω_0 and Ω , respectively. Then, the two domains are connected through the diffeomorphism $\Phi : \Omega_0 \mapsto \Omega$, with $\Phi(\mathbf{x}_0, t) = \mathbf{x}$. In the L-ALE approach, this diffeomorphism is linearized in the form $\Phi(\mathbf{x}_0, t) = \mathbf{x}_0 + \boldsymbol{\xi}(\mathbf{x}_0)$, where $\boldsymbol{\xi}(\mathbf{x}_0)$ is a displacement field such that $\|\boldsymbol{\xi}(\mathbf{x}_0)\| = \|\mathbf{x} - \mathbf{x}_0\| \sim O(\varepsilon_0 \|\mathbf{x}_0\|)$

with $\varepsilon_0 \ll 1$. The field $\boldsymbol{\xi}(\mathbf{x}_0)$ propagates the Lagrangian displacement of the interface η into the fluid domain. This displacement field is arbitrary since it is not determined by the governing equations (III.32)-(III.35), i.e. it is not dictated by the actual motion of the fluid elements, except at the free boundary. It only needs to obey the no-penetration condition (III.34), plus some mild smoothness properties. Usually, the smoothness of $\boldsymbol{\xi}$ is ensured by assuming that its distribution within the fluid domain is governed by an elliptic equation, such as the Laplace equation or the Cauchy equation for an elastic material. An illustration of the L-ALE methodology is depicted in fig. III.4. The sketch shows how the free boundary, labelled Γ_b in the physical domain Ω and $\Gamma_{b,0}$ in the reference domain Ω_0 , transforms from one domain to the other. Although the geometric properties of this boundary, especially its unit normal \mathbf{n} and tangent \mathbf{t} , may be evaluated in both domains, we always evaluate them in Ω_0 , after which they may be mapped forward onto the physical domain via Φ if needed. The L-ALE formalism leads to an approach in which the

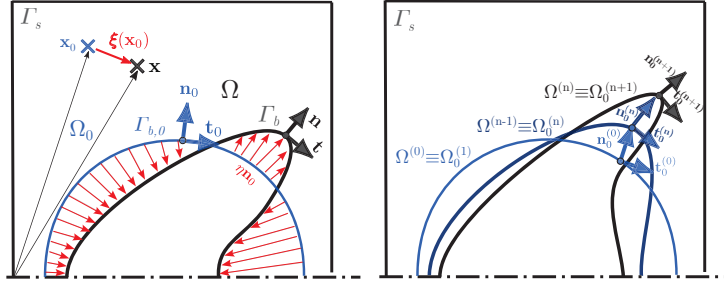


Figure III.4 – Sketch of the geometrical transformations involved in the L-ALE approach. (a): general framework, showing in particular the physical domain Ω and the reference domain Ω_0 (the corresponding free boundary is Γ_b and $\Gamma_{b,0}$, respectively); (b): successive updates of the reference domain during the iterations of the Newton method. .

governing equations and the deformation of the physical domain are solved simultaneously and consistently, which ensures the stability of the algorithm involved. Such an approach, in which the unknown to be determined is the state vector $\mathbf{q} = [\mathbf{u}, p, p_b, \boldsymbol{\xi}, \eta]^T$ (T denoting the transpose), is sometimes referred to as ‘monolithic’. To obtain the steady-state solution of (III.32)-(III.35), we solve the corresponding *steady* nonlinear problem using a Newton method, following the methodology introduced in Bonnefis, 2019. For the numerical resolution, the volume fields $[\mathbf{u}, p]^T$ are discretized following a Taylor–Hood scheme, i.e. the mixed-finite-element Lagrange basis (P_2, P_2, P_1) and the mesh deformation $\boldsymbol{\xi}$ is discretized within the (P_2, P_2) finite element space. The free-surface field η is discretized within Galerkin-Fourier spaces. The displacement of the free-surface η is orthogonally projected onto a Fourier basis $\eta(s_0) = \sum_{k=0}^{N_b} \phi_k(s_0) X_\eta(k)$,

where ϕ_k is a Fourier basis, $X_\eta(k)$ the coefficients of η within that basis, N_b the number of Fourier elements and s_0 the arc-length coordinate. The steady-state solution, $\mathbf{q}_0 = [\mathbf{u}_0, p_0, p_{b,0}, \mathbf{0}, 0]^T$, is determined iteratively by solving the system of equations governing the increment $\mathbf{q}' = [\mathbf{u}', p', p'_b, \boldsymbol{\xi}, \eta]^T$, namely,

$$\begin{aligned}
 \mathbf{L}_{NS}[\mathbf{q}'] &\equiv \mathbf{u}' \cdot \nabla_{\Omega_0} \mathbf{u}_0 + \mathbf{u}_0 \cdot \nabla_{\Omega_0} \mathbf{u}' &= -\mathbf{u}_0 \cdot \nabla_{\Omega_0} \mathbf{u}_0 && \text{in } \Omega_0, \\
 &\quad -\rho^{-1} \nabla_{\Omega_0} \cdot \boldsymbol{\Sigma}_{\Omega_0}(\mathbf{u}', p') &\quad + \rho^{-1} \nabla_{\Omega_0} \cdot \boldsymbol{\Sigma}_{\Omega_0} && \\
 &\quad + \mathbf{Q}_{\Omega_0}(\boldsymbol{\xi}) &&& \\
 \mathbf{L}_{div}[\mathbf{q}'] &\equiv \nabla_{\Omega_0} \cdot \mathbf{u}' - \nabla_{\Omega_0} \mathbf{u}_0 : \nabla_{\Omega_0}^T \boldsymbol{\xi} &= -\nabla_{\Omega_0} \cdot \mathbf{u}_0 && \text{in } \Omega_0, \\
 \mathbf{L}_{kin}[\mathbf{q}'] &\equiv \mathbf{u}' \cdot \mathbf{n}_0 + \mathbf{u}_0 \cdot \mathbf{n}' &= -\mathbf{u}_0 \cdot \mathbf{n}_0 && \text{on } \Gamma_{b,0}, \\
 \mathbf{L}_{dyn}[\mathbf{q}'] &\equiv (p'_b - p' - \gamma \kappa') \mathbf{n}_0 &= (p_0 - p_{b,0} + \gamma \kappa_0) \mathbf{n}_0 && \text{on } \Gamma_{b,0}, \\
 &\quad + (p_{b,0} - p_0 - \gamma \kappa_0) \mathbf{n}' &\quad - 2\mu \mathbf{D}_{\Omega_0}(\mathbf{u}_0) \cdot \mathbf{n}_0 && \\
 &\quad + 2\mu \mathbf{D}_{\Omega_0}(\mathbf{u}') \cdot \mathbf{n}_0 &&& \\
 &\quad + 2\mu \mathbf{D}_{\Omega_0}(\mathbf{u}_0) \cdot \mathbf{n}' &&& \\
 \mathbf{L}_{com}[\mathbf{q}'] &\equiv \boldsymbol{\xi} - \eta \mathbf{n}_0 &= \mathbf{0} && \text{on } \Gamma_{b,0}, \\
 \mathbf{L}_E[\boldsymbol{\xi}] &\equiv \nabla_{\Omega_0} \cdot \mathbf{E}(\boldsymbol{\xi}) &= \mathbf{0} && \text{in } \Omega_0,
 \end{aligned} \tag{III.36}$$

where the Ω_0 subscript indicates that the corresponding spatial derivative is evaluated in the reference domain Ω_0 bounded (partly) by the free boundary $\Gamma_{b,0}$. In (III.36), the first four equations correspond to the linearized form of the governing equations (III.32)-(III.35). The deformation of the domain induces several extra terms in these linearized equations, especially an extra momentum source term $\mathbf{Q}_{\Omega_0}(\boldsymbol{\xi}) = -\mathbf{u}_0 \cdot \nabla_{\Omega_0} \mathbf{u}_0 \cdot \nabla_{\Omega_0} \boldsymbol{\xi} + \rho^{-1} (\nabla_{\Omega_0} \cdot \boldsymbol{\Sigma}_{\Omega_0}) \cdot \nabla_{\Omega_0}^T \boldsymbol{\xi} + \rho^{-1} \mu \nabla_{\Omega_0} \cdot \{ \nabla_{\Omega_0} \mathbf{u}_0 \cdot \nabla_{\Omega_0} \boldsymbol{\xi} + (\nabla_{\Omega_0} \mathbf{u}_0 \cdot \nabla_{\Omega_0} \boldsymbol{\xi})^T \}$ in the momentum equation. The last two equations determine the displacement field $\boldsymbol{\xi}$ throughout the domain. The elliptic operator \mathbf{E} controls the spatial distribution of this arbitrary displacement within Ω_0 , subject to the compatibility condition $\boldsymbol{\xi} = \eta' \mathbf{n}_0$ on $\Gamma_{b,0}$. Here, following Pfister, 2019, we assume that this distribution obeys a linear elastic response, i.e. we set $\mathbf{E}(\boldsymbol{\xi}) = 2\mu_e \mathbf{D}_{\Omega_0}(\boldsymbol{\xi}) + \lambda_e (\nabla_{\Omega_0} \cdot \boldsymbol{\xi}) \mathbf{I}$. With this choice, the last equation in (III.36) may be interpreted as the Cauchy equation of elasticity, the coefficients λ_e and μ_e being Lamé pseudo-coefficients which we both set to unity.

At each iteration n , the pseudo-steady state solution is updated in the form $\mathbf{q}_0^{(n)} = \mathbf{q}_0^{(n-1)} + \mathbf{q}' = [\mathbf{u}_0 + \mathbf{u}', p_0 + p', p_{b,0} + p'_b, \boldsymbol{\xi}, \eta]^T$. The reference domain Ω_0 is also updated, based on conditions $\mathbf{x}_{\Omega_0^{(n)}} = \mathbf{x}_{\Omega_0^{(n-1)}} + \boldsymbol{\xi}$ and $\mathbf{x}_{\Gamma_0^{(n)}} = \mathbf{x}_{\Gamma_0^{(n-1)}} + \eta$ linking the position of a given point standing in the fluid domain or on the free boundary in two successive reference configurations, as sketched in fig. III.4(b). In cases where the free boundary is a closed surface, the enclosed volume must stay equal to its initial value, \mathcal{V}_b , provided effects of compressibility are negligible in the corresponding medium. This implies

$$\mathbf{L}_{vol}[\mathbf{q}'] \equiv \int_{\Gamma_{b,0}} \eta d\mathcal{S}_0 = \int_{\Omega_{b,0}} (1 + \nabla_{\Omega_0} \cdot \boldsymbol{\xi}) d\mathcal{V}_0 - \mathcal{V}_b \quad \text{on } \Gamma_{b,0}. \tag{III.37}$$

In the vicinity of a saddle-node bifurcation, the jacobian matrix is ill-conditioned, in particular it is singular at the bifurcation point. In these cases, instead of the natural continuation on parameters, for instance on the Weber number We , we continue the solution on the arc-length coordinate s with a pseudo-arc-length continuation method. It consists in replacing the jacobian matrix by a bordered matrix, i.e. a matrix with an additional column and an additional line. The application of this technique is problem dependent, because it depends on the parameters of the problem. Thus, here we consider continuation with steps Δs on the couple of parameters (p_b, S) , the pressure within the bubble p_b and the strain rate S . If we denote eq. (III.36) plus any additional constraint such as by $\mathbf{L}|_{\mathbf{q}_0} \mathbf{q}' = -\mathbf{F}(\mathbf{q}_0)$, then the bordered system is as follows,

$$\begin{pmatrix} \mathbf{L}|_{\mathbf{q}_0^{(n-1)}} & D_{bc} \\ \frac{dp_b}{ds} & \frac{dS}{ds} \end{pmatrix} \begin{pmatrix} \mathbf{q}' \\ S' \end{pmatrix} = \begin{pmatrix} -\mathbf{F}(\mathbf{q}_0^{(n-1)}) - D_{bc}(S_0^{(n-1)}) \\ -\frac{dp_b}{ds}(p_{b,0}^{(n-1)} - p_{b,0}^{(0)}) - \frac{dS}{ds}(S_0^{(n-1)} - S_0^{(0)}) + \Delta s \end{pmatrix} \quad (\text{III.38})$$

where the vector of unknowns \mathbf{q}' is increased with the Newton update of the strain rate S' . The operator D_{bc} , which is a column vector in the bordered matrix, serves to impose the boundary conditions on the velocity field, and it only depends on the strain rate S . The derivative $\frac{dp_b}{ds}$ acts on the pressure of the bubble only, and $\frac{dS}{ds}$ on the strain rate. They are determined at the initial step of the Newton method from the resolution of $\mathbf{L}|_{\mathbf{q}_0^{(0)}} \frac{d\mathbf{q}}{dS}|_{\mathbf{q}_0^{(0)}} = -\frac{\mathbf{F}(\mathbf{q}_0^{(0)})}{dS}$. From the field $\frac{d\mathbf{q}}{dS}|_{\mathbf{q}_0^{(0)}}$, we select the rate of variation of the pressure of the bubble with the strain rate $\frac{dp_b}{dS}|_{\mathbf{q}_0^{(0)}}$ and, since $\frac{dS}{dS} = 1$, the vector $[\frac{dp_b}{ds}, \frac{dS}{ds}]^T = [\frac{dp_b}{dS}|_{\mathbf{q}_0^{(0)}}, 1]^T / ((\frac{dp_b}{dS}|_{\mathbf{q}_0^{(0)}})^2 + 1)^{1/2}$.

Once the steady state is reached, the linear stability of the corresponding solution is determined by examining the fate of disturbances with the eigenmode form $\mathbf{q}' = [\hat{\mathbf{u}}, \hat{p}, \hat{p}_b, \hat{\boldsymbol{\xi}}, \hat{\eta}]^T e^{-i\omega t}$, the hatted complex amplitudes depending on \mathbf{x}_0 . In cases where the base configuration is axisymmetric, as in the physical problem considered in this paper, we rather consider disturbances of the form $\mathbf{q}' = [\hat{\mathbf{u}}, \hat{p}, \hat{p}_b, \hat{\boldsymbol{\xi}}, \hat{\eta}]^T e^{im\theta - i\omega t}$, with θ the polar angle of the (r, θ, z) cylindrical coordinate system and m the corresponding wavenumber, the hatted amplitudes depending now only on r and z . Such solutions are obtained by solving the eigenvalue problem

$$\begin{aligned} -i\omega(\hat{\mathbf{u}} - \hat{\boldsymbol{\xi}} \cdot \nabla_{\Omega_0} \mathbf{u}_0) + \mathbf{L}_{NS}[\hat{\mathbf{q}}] &= \mathbf{0} && \text{in } \Omega_0, \\ \mathbf{L}_{div}[\hat{\mathbf{q}}] &= 0 && \text{in } \Omega_0, \\ -i\omega\hat{\eta} + \mathbf{L}_{kin}[\hat{\mathbf{q}}] &= 0 && \text{on } \Gamma_{b,0}, \\ \mathbf{L}_{dym}[\hat{\mathbf{q}}] &= \mathbf{0} && \text{on } \Gamma_{b,0}, \\ \mathbf{L}_{com}[\hat{\mathbf{q}}] &= \mathbf{0} && \text{on } \Gamma_{b,0}, \\ \mathbf{L}_E[\hat{\boldsymbol{\xi}}] &= \mathbf{0} && \text{in } \Omega_0, \end{aligned} \quad (\text{III.39})$$

supplemented with

$$\mathbf{L}_{vol}[\hat{\mathbf{q}}] = 0 \quad \text{on } \Gamma_{b,0} \quad (\text{III.40})$$

if the constraint (III.37) holds. In (III.39), the term $i\omega\hat{\boldsymbol{\xi}} \cdot \nabla_{\Omega_0} \mathbf{u}_0$ arising in the linearized momentum equation is the acceleration of the moving domain, which must be subtracted to obtain the actual fluid acceleration in Ω_0 . Here, the reference domain is that corresponding to the steady-state solution of (III.36), i.e. $\Omega_0 \equiv \Omega_0^{(N)}$, where N is the number of iterations carried out to reach the steady solution through the Newton method, as depicted in fig. III.4(c). Problems (III.36) and (III.39) are solved thanks to the open finite element software FreeFem++ (see Bonnefis, 2019 for details).

CHAPTER IV

Mode interaction

This chapter serves a summary of chapter VI, and it is entirely based on those articles.

1

Takens-Bogdanov – The organizing centre for the flow past spinning cylinders

In this section, we analyse a physical case, whose dynamics are organized by a degenerate case of the Takens-Bogdanov bifurcation, which has been defined in section 1.5. The Takens-Bogdanov bifurcation is of codimension-two when the two non-degeneracy conditions on the coefficients of the centre manifold eq. (II.66) are met, that is, $e_{(1,1)}^{(2)} \neq 0$ and $e_{(1,1)}^{(1)} + e_{(1,2)}^{(2)} \neq 0$. Otherwise, when $e_{(1,1)}^{(2)} \neq 0$ and $e_{(1,1)}^{(1)} + e_{(1,2)}^{(2)} = 0$ or $e_{(1,1)}^{(2)} = 0$ and $e_{(1,1)}^{(1)} + e_{(1,2)}^{(2)} \neq 0$, the

bifurcation is of codimension-three. The former ($e_{(1,1)}^{(2)} \neq 0$ and $e_{(1,1)}^{(1)} + e_{(1,2)}^{(2)} = 0$) is referred to as the *cusplike case*, and it has been extensively analysed by Dumortier, Roussarie, and Sotomayor (1987). It has the following normal form,

$$\begin{aligned}\dot{u}_1 &= u_2 \\ \dot{u}_2 &= \beta_1 + \beta_2 u_2 + \beta_3 u_1 u_2 + u_1^2 \pm u_1^3 u_2.\end{aligned}\tag{IV.1}$$

The unfolding of the cusplike case is rather similar to the codimension-two Takens-Bogdanov, but with the two saddle-node curves intersecting tangentially in a cusplike point.

The second case, $e_{(1,1)}^{(2)} = 0$ and $e_{(1,1)}^{(1)} + e_{(1,2)}^{(2)} \neq 0$ has been analysed by Dumortier, Roussarie, Sotomayor, and Zoladek (2006). The authors have shown that the centre manifold eq. (II.66) can be reduced to the following normal form,

$$\begin{aligned}\dot{u}_1 &= u_2 \\ \dot{u}_2 &= \beta_1 + \beta_2 u_1 + \beta_3 u_2 + b u_1 u_2 + s_1 u_1^2 u_2 + s_2 u_1^3,\end{aligned}\tag{IV.2}$$

for $s_1, s_2 = \pm 1$ and $b > 0$. The authors distinguish three subcases: *saddle*, *focus* and *elliptic* cases. When the coefficient $s_1 = 1$, the subsequent bifurcation scenario is referred to as the *saddle case*. The scenario with $s_1 = -1$ and $0 < b < 2\sqrt{2}$ is named the *focus case*. The *elliptic* subcase occurs when $s_1 = -1$ and $b > 2\sqrt{2}$.

In the following, we restrict ourselves to the discussion of the dynamics of the *focus case*, which is relevant for the dynamics of the flow past a spinning cylinder. The two-dimensional flow past a rotating circular cylinder is controlled by two parameters: the Reynolds number $Re = \frac{U_\infty D}{\nu}$ and the rotation rate $\alpha = \frac{\Omega D}{2U_\infty}$. Ω is the dimensional cylinder angular velocity, U_∞ is the free stream velocity, D the diameter of the cylinder and ν the dynamic viscosity of the fluid.

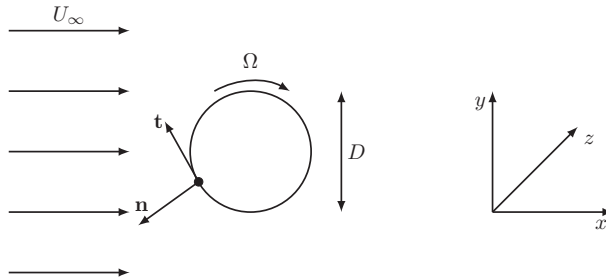


Figure IV.1 – Sketch of a rotating cylinder immersed in a uniform flow..

The incompressible Navier-Stokes equations eq. (III.1) are complemented with the following boundary conditions: on the cylinder surface, no-slip boundary conditions are set by $\mathbf{U} \cdot \mathbf{t} = \Omega D/2$ and $\mathbf{U} \cdot \mathbf{n} = 0$, where (\mathbf{t}, \mathbf{n}) are the director vectors of the surface in the plane (x-y); in the far field, uniform boundary

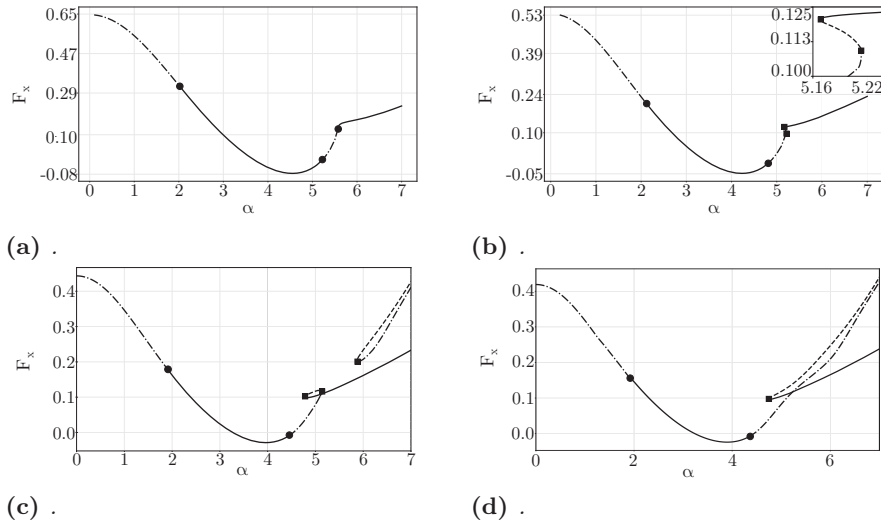


Figure IV.2 – Evolution of the horizontal force F_x as a function of the rotation rate α for four Reynolds numbers, (a) $Re = 60$, (b) $Re = 100$, (c) $Re = 170$ and (d) $Re = 200$. Solid lines — denote stable steady states, dashed-dotted lines $\text{-}\cdot\cdot\cdot\text{-}$ denote unstable steady states of focus type or nodes, dashed lines $\text{-}\cdot\cdot\text{-}$ are used for steady states of saddle type. Solid circles \bullet denote Hopf bifurcations and solid squares \square denote saddle node bifurcations. .

conditions are set $U \rightarrow (U_\infty, 0)$ when $r \rightarrow \infty$, where r is the distance to the cylinder centre (see fig. IV.1). In the discussion, we consider clockwise rotation of the cylinder surface ($\alpha > 0$).

Characterisation of multiple steady state solutions

To introduce the existence of multiple steady states, we first characterize them by plotting in fig. IV.2 the associated lift as a function of the rotation rate α , for four different values of α . In these plots, stable solution are indicated by continuous lines and unstable ones by dashed lines. For $Re = 60$, as illustrated in fig. IV.2(a), only one steady state exists for all values of α . This state is stable except in the ranges $\alpha \lesssim 2$ (corresponding to the existence of mode I), and $5.2 \lesssim \alpha \lesssim 5.5$ (corresponding to the existence of mode II). For higher Reynolds numbers, a small region of multiple solutions arise in a small-scale interval around $\alpha \approx 5$. This phenomenon is illustrated in fig. IV.2 (b) for $Re = 100$ and is associated to a "s" shape of the curve, featuring two successive folds. Note that before the first fold, the steady solution is 2-unstable (focus type); at the first fold it turns into 1-unstable (saddle type) and at the second fold it turns into stable.

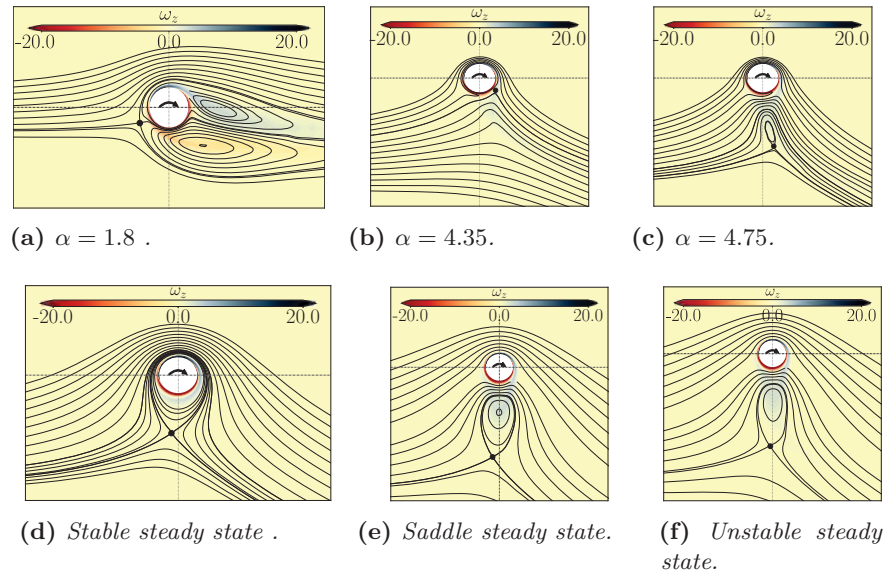


Figure IV.3 – Steady flow around a rotating cylinder (vorticity levels and streamlines) for selected parameters. (a) : $\alpha = 1.8, Re = 200$ (at the supercritical Hopf bifurcation threshold) ; (b) : $\alpha = 4.35, Re = 200$ (at the Hopf bifurcation); (c) : ($\alpha = 4.75, Re = 200$ (at the fold bifurcation). (d – f) correspond to three base-flow solutions existing in the range of multiple solutions, namely for $\alpha = 5.25$ and $Re = 200$. The circled dot shows the position of the hyperbolic stagnation point..

Topological description of steady state solutions

We now illustrate the spatial structure of some steady state solutions, with emphasis on the topological structure of the corresponding flows. We restrict to the case $Re = 200$ as previously considered in fig. IV.2(d). Figure IV.3(a) corresponds to $\alpha = 1.8$, the value at which mode I is re-stabilised. The corresponding flow is characterised by a stagnation point located beneath the cylinder axis, on the left side of the y -cylinder axis. Compared to the steady flow in the non-rotating case, which is characterized by a symmetrical recirculation region, the upper recirculating bubble is reduced whereas the lower one is moved downwards. Further increasing the rotation speed, both recirculation bubbles shrink and eventually vanish. At $\alpha = 4.35$ (fig. IV.3(b)) corresponding to the lower threshold for the existence of mode II, recirculating bubbles have already disappeared, and the vorticity wraps the cylinder. Stagnation point is located on the opposite side but downstream the cylinder vertical axis.

Figure IV.3(c) corresponds to the steady state flow at the fold bifurcation observed for $\alpha = 4.75$ and giving rise to the disconnected states observed in fig. IV.2 (d). Compared to the previous state, the flow is topologically different, as no stagnation point is observed along the wall of the cylinder. On the other hand,

two stagnation points are observed within the flow. One of them is elliptic and located at the centre of the detached recirculation bubble. The other is hyperbolic and located along the streamline bounding the recirculation bubble. Figure IV.3(*d – f*) displays the three coexisting steady states at $\alpha = 5.25$ and $Re = 200$. Topology of streamlines of unstable and stable steady states differs. In the stable case (plot *d*) there is a single recirculation region encircling the cylinder and bounded by a hyperbolic stagnation point, as in the classical potential solution existing in this range of rotation rates. On the other hand, for both unstable states, the topology is similar, as in the case of fig. IV.3(*c*). The recirculation region is detached from the cylinder and contains an elliptic stagnation point located approximately in the midpoint between the hyperbolic point and the bottom point of the cylinder surface. In the unstable steady state, the recirculating region is more stretched, as it can be seen in fig. IV.3 (*d-f*).

We highlight that even though topological changes in the streamlines of the steady states and bifurcations of the velocity field are in general independent events (see Brøns (2007)), in some cases these two events occur in a small neighbourhood of the space of parameters (see Heil et al. (2017)). In the current situation, it has been confirmed that there is not a one-to-one relation between both phenomena. For instance, the transition between detached recirculation bubble (as in plot *c*) and recirculation bubble encircling the cylinder (as in plot *d*) along the stable branch occurs at some value of α in the range $[4.75 - 5.25]$ where no dynamical bifurcation occurs. Yet for larger Reynolds numbers, i.e. $Re \gtrsim 190$, successive creation and destruction of vortices seems to be relevant in the preservation of the disconnected branch of steady states.

Bifurcation diagram in the parameter plane (Re, α)

The bifurcation curves detected in the $\alpha < 10, Re < 200$ range by linear stability analysis of all steady state solutions are depicted in fig. IV.4. Three Hopf bifurcation curves are detected and plotted with full lines. The first one encircles the range of existence of unsteady mode I. The second one delimits the range of existence of unsteady mode II in its lower and left parts, but not on its upper part. The third one (in grey) occurs along a steady state which is already unstable, and hence is not likely to be related to a bifurcation observable in DNS or experiments.

In addition, we have identified two bifurcation curves associated to saddle-nodes or "folds", here denoted F_+ and F_- . These curves delimit the range of existence of multiple two-dimensional steady states, displayed as a grey region in fig. IV.4. Note that the extension of this region explains the difference between the cases $Re = 170$ and $Re = 200$ discussed in the previous paragraph; according to the figure, for a sufficiently large rotation rate ($\alpha > 5$) we should always expect multiple steady state solutions for $Re \gtrsim 190$.

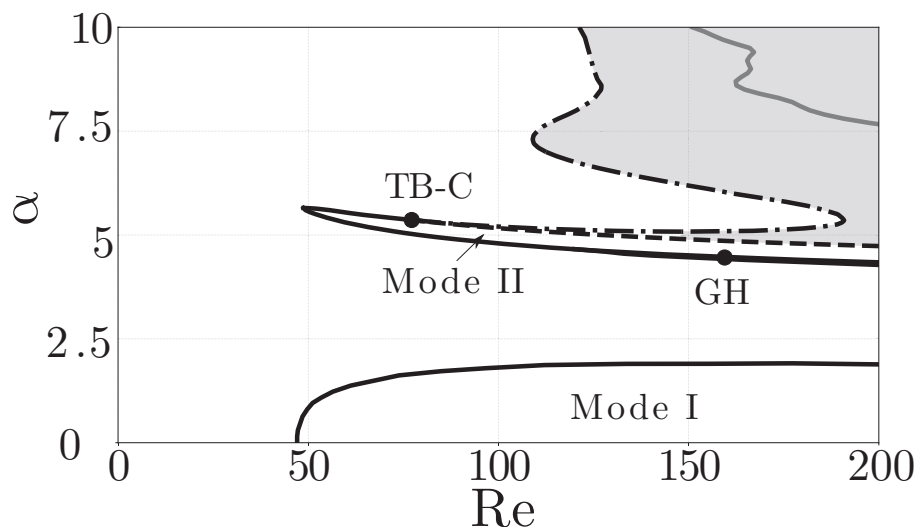


Figure IV.4 – Bifurcation curves in the range $Re \in [0, 200]$ and $\alpha \in [0, 10]$. Black and gray lines are used to denote local bifurcations. Solid lines — indicate the presence of a Hopf bifurcation, dashed line --- designate the first fold bifurcation curve, F_- and dashed dotted line $\text{-}\cdot\cdot\cdot\text{-}$ denote the second fold bifurcation, F_+ . The grey region indicates the coexistence of three steady states. The solid grey curve inside the grey region denotes a secondary Hopf bifurcation occurring on one of the unstable steady states. Mode I is the classical vortex shedding mode, whereas Mode II was described by Pralits et al. (2010). A generalized Hopf (GH) bifurcation separates the supercritical Hopf bifurcation left to the GH point to the subcritical Hopf bifurcation right to the GH point .

In fig. IV.4, the two saddle-node curves seem to merge, with the Hopf curve existing for lower Re at a point with coordinates $Re \approx 75$, $\alpha \approx 5.4$. Inspection shows that there are actually both a 0^2 or Takens-Bogdanov (TB) bifurcation and a cusp (C) bifurcation in very close vicinity in this range of parameters.

Qualitative study of the normal form

The transition occurring for $Re \approx 75$ and $\alpha \approx 5.4$ is characterized by the end of the Hopf curve (H_-) at a fold curve (F_+) (characteristic of a Takens-Bogdanov bifurcation), and a transition between one and three steady states (characteristic of a cusp). This suggests that the present situation is actually very close to a codimension-3 bifurcation, which turn out to be of the saddle subtype. The dynamical behaviour of the system can thus be expected to be well predicted using the normal form describing the universal unfolding of eq. (IV.2). We should think of the unfolding parameters (β_1, β_2 and β_3) to be mapped from the physical parameters (Re, α) . fig. IV.5 illustrates all the possible behaviours of the dynamical system, sketched by sample phase portraits, along with their

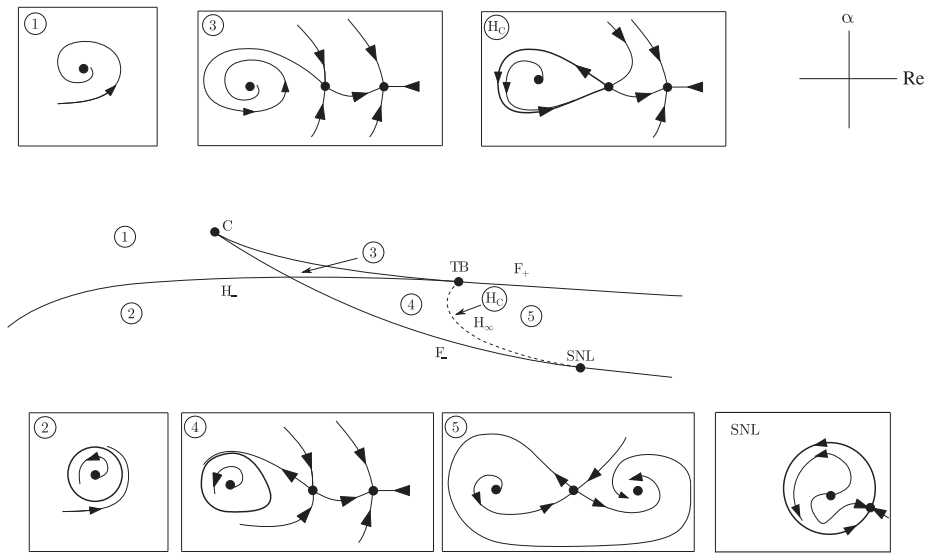
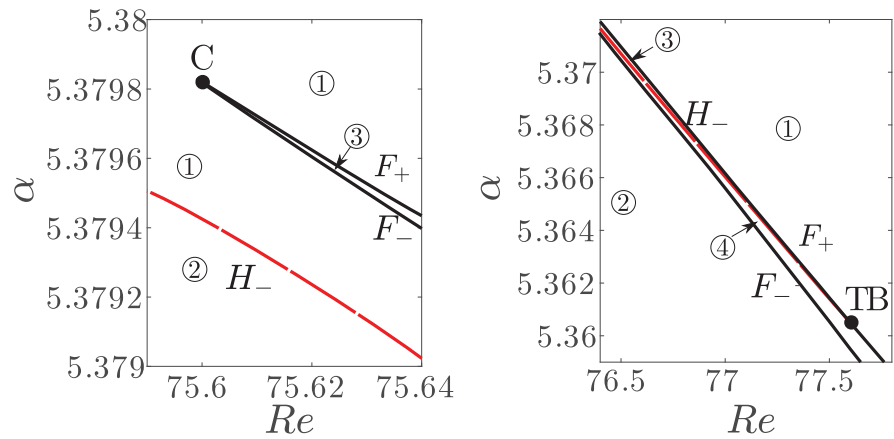


Figure IV.5 – Bifurcation diagram predicted using the normal form eq. (IV.2) in the stable focus case (adapted from Dumortier, Roussarie, Sotomayor, and Zoladek (2006)), and qualitative phase portrait in regions (1), (2), (3), (4), (5) and along curve H_∞ . Note that in the qualitative phase portraits, focus and node points are not distinguished. .

range of existence in the (β_1, β_2) plane. This figure corresponds to a subset of the complete diagram displayed in Dumortier, Roussarie, Sotomayor, and Zoladek (2006, Ch. 1, pages 6-8), restricted to a range of parameters which is sufficient to explain all the dynamical features of the present problem. The bifurcation diagram displays two codimension-two points, a cusp C and a Takens Bogdanov TB . These codimension-two points result from the tangential intersection of two codimension-one curves: the cusp point C occurs when the two fold curves F_+ and F_- collide, while the TB point arises from the intersection of the supercritical H_- Hopf curve and the F_+ fold. In addition, the bifurcation diagram predicts a homoclinic global bifurcation along a curve H_∞ originating from the TB point and terminating along the F_- fold on a point denoted SNL (for saddle-node-loop). Left from this point, the F_- curve corresponds to a local saddle-node while right from this point it corresponds to a homoclinic saddle-node bifurcation (appearance of two fixed points along a previously existing cycle). Note that the SNL point and the intersection of H_- and F_- are formally not codimension-2 points (see Dumortier, Roussarie, Sotomayor, and Zoladek (2006)).

Phase portraits obtained in the various regions delimited by bifurcation boundaries are displayed in the subplots offig. IV.5. One of the most interesting predictions is the existence of two regions characterized by the existence of *two stable states* (bistability). The first region (3), in the vicinity of the cusp, is



(a) Zoom in the region of cusp bifurcation.. (b) Zoom in the region of Takens Bogdanov bifurcation..

Figure IV.6 – Zooms of figure IV.4 in the vicinity of the C and TB codimension-2 points. Black solid lines denote fold bifurcations F_{\pm} , the long dashed (red online) line is used for the Hopf bifurcation line H_{-} and the short dashed (red online) curve denotes the local change from stable focus to stable node. Numbers correspond to each phase portrait of fig. IV.5 (a).

characterized by two stable steady states. The third region (4) is characterized by both a stable steady state and a stable cycle. In all other regions, there is a single stable solution, which is either a steady state (in regions 1 and 5) or a cycle (in region 2). Note that in these phase portraits, nodes, and foci points are not distinguished. Distinguishing between these cases (Dumortier, Roussarie, Sotomayor, and Zoladek, 2006) leads to consider a larger number of subcases (for instance region 1 could be split in two subregions corresponding to a stable node and a stable focus ...) but the transition between these subcases are not associated to bifurcations.

In order to check the predictions of the normal form approach, we have conducted an accurate exploration of the range of parameters corresponding to the C-TB region. The exploration allowed us to confirm the existence of both a cusp and a Takens-Bogdanov point. fig. IV.6 displays an enlargement of the full bifurcation diagram (fig. IV.4) in two narrow ranges centred on the C and TB codimension-2 points. The bifurcation curves and the regions are numbered with the same convention as in figure IV.5. Although it is not possible to present all results in a single figure because the curves are very steep and close to each others, the numerical results fully confirm the predictions of the normal form. In particular, the numerical results allow confirming the coexistence of two stable states (in regions 3) and of a stable cycle and a stable state (in region 4). However, a precise mapping of the curve H_{∞} bounding the region 4 could not

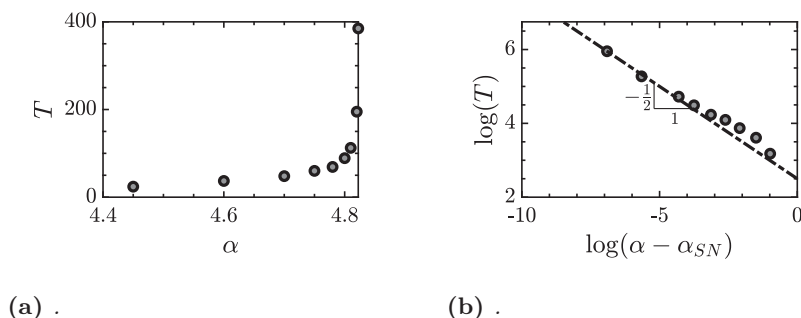


Figure IV.7 – Evolution of the period of the limit cycle as it approaches the homoclinic connection. a) Linear plot of the period T as a function of the rotation rate α where α_{SN} is the rotation rate at the saddle node. b) Logarithm of the period and the distance to the bifurcation point. .

be achieved, but the occurrence of a global homoclinic bifurcation was confirmed (see below).

The normal form predicts a homoclinic curve H_∞ and a homoclinic saddle-node bifurcation along the F_- curve, right from the SNL point, corresponding to the appearance of two steady solutions along a previously existing cycle.

A generic feature of the imminent presence of a homoclinic saddle-node bifurcation is the divergence of the period of the limit cycle on which the saddle node appears. More precisely, the period is expected to scale as $\propto \frac{1}{\sqrt{\alpha_{SN} - \alpha}}$ as $\alpha \rightarrow \alpha_{SN}$ (see Gasull et al. (2005)). To check this prediction, time-stepping simulations were conducted for $Re = 170$ and values of α just below the F_- curve. As shown in fig. IV.7 the period of the limit cycle effectively diverges as one approaches the bifurcation following the theoretical behaviour.

Dynamics near the threshold can be perfectly understood in a two-dimensional manifold. Phase portraits of the bifurcation are displayed in fig. IV.8. These phase portraits were computed with an initial guess generated by a small linear perturbation to a steady state in the direction of its corresponding eigenmode. The initial guess is then integrated in time until it reaches its limit set, i.e. a periodic, homoclinic orbit or another steady state. Below the bifurcation threshold (fig. IV.8(a)) a stable limit cycle exists, represented by a thick solid line. At the bifurcation threshold, a saddle-node arises along this cycle, which ceases to exist, giving rise to a homoclinic connection (an approximation of this orbit is delineated by a thick solid line in fig. IV.8(b)). Beyond the saddle-node bifurcation, the saddle-node splits into two fixed points. Hence, three steady states exist, including a stable one (see fig. IV.8(c)). There exist four stable heteroclinic connections, two between *unstable-stable* steady states represented by a dashed line in fig. IV.8(c) and other two between *saddle-stable* steady states denoted by a solid line. This sequence of events is fully consistent to the sequence

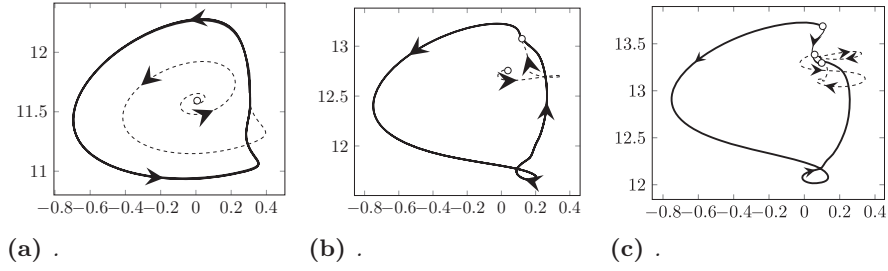


Figure IV.8 – Phase portrait of the dynamics of the rotating cylinder at $Re = 170$ for three values of the rotation rate α . Vertical (horizontal) axis is the lift force F_y (drag force F_x) on the cylinder surface, empty dots denote steady state solutions. (a-b) Limit sets (resp. transients) are depicted by a thick solid line (resp. thin dashed). c) Heteroclinic connections between unstable-stable (resp. saddle-stable) are depicted by thin solid lines (resp. dashed dotted).

connecting phase portraits (2), (SNL) and (4) in fig. IV.5.

2

Steady-Steady with 1:2 resonance – Robust heteroclinic cycles in the flow of concentric jets

We now turn our attention to a second organizing centre, the steady-steady bifurcation with $O(2)$ symmetry and with strong azimuthal resonance 1 : 2. Such an organizing centre is observed in the coaxial flow between two concentric jets. In the past, such a scenario had been observed in numerical simulations of the counter-rotating von Kármán swirling flow by Nore, Tuckerman, et al. (2003) and subsequently observed in experiments by the same authors (Nore, Moisy, et al., 2005). The mathematical aspects of the bifurcation scenario have been extensively studied in the past by (Dangelmayr, 1986; Jones et al., 1987; Porter et al., 2001; Armbruster et al., 1988) and the reflection symmetry breaking case ($SO(2)$) by Porter et al. (2005).

Problem definition

The governing equations of the flow within the domain are the incompressible Navier–Stokes equations (eq. (III.1)). These are written in cylindrical coordinates (r, θ, z) , which are made dimensionless by considering D as the reference length scale and $W_{o,max}$ as the reference velocity scale, which is the maximum velocity in the outer pipe at $z = z_{min}$. The incompressible Navier–Stokes equations eq. (III.1) are complemented with the following boundary conditions

$$\mathbf{U} = (0, 0, W_i) \text{ on } \Gamma_{in,i} \text{ and } \mathbf{U} = (0, 0, W_o) \text{ on } \Gamma_{in,o}, \quad (\text{IV.3})$$

which occurs between point (c) and (d) in fig. IV.10. The final segment, that ranges between $\delta_u > \delta_u^2$, is characterized by two quasi-planar jets that rapidly mix to form a larger one at around $z \approx 5$.

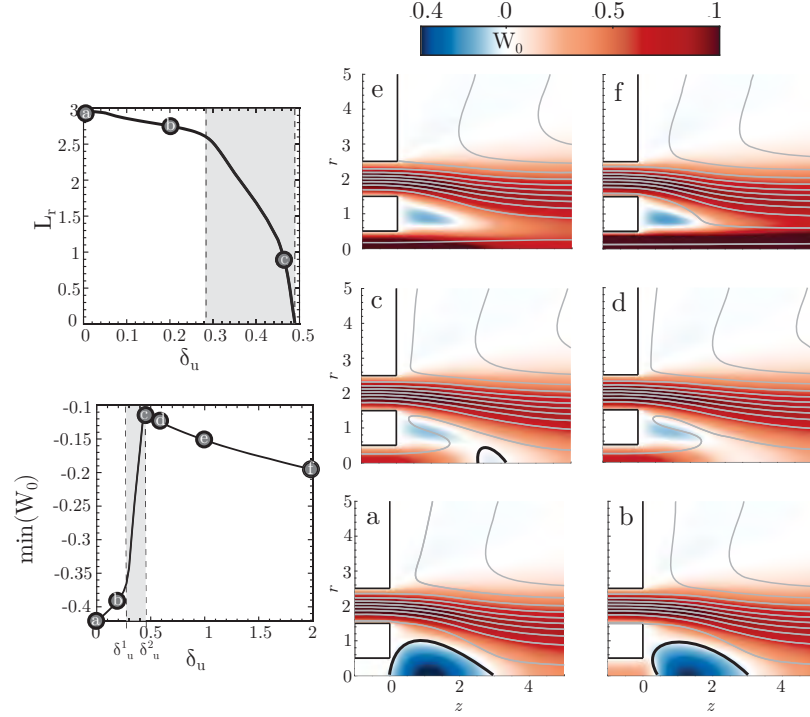


Figure IV.10 – Evolution of the recirculation length (L_r) of the recirculating bubble with respect to the velocity ratio δ_u between the inner and outer jet. The diagram of the second row on the left displays the minimum value within the domain of the axial velocity. It is spatially localized within the recirculating region for $\delta_u < 0.5$ and near the middle wall for larger values of the velocity ratio. Meridional projections of the axisymmetric stream-function isolines and the axial velocity contour in a range of $(z, r) \in [-1, 5] \times [0, 5]$.

Linear stability analysis

We briefly discuss the main findings of the linear stability study at fixed velocity ratio $\delta_u = 1$ and $\delta_u = 2$. We have tracked the evolution of the critical Reynolds number with respect to the distance for four branches of global modes. Two steady modes with azimuthal wavenumber $m = 1$ and $m = 2$, hereinafter referred to as modes S_1 and S_2 , respectively. A cross-section view at $z = 1$ is displayed in fig. IV.11 (a-b). The other two unsteady modes, named F_1 and F_2 have respectively azimuthal wavenumbers $m = 1$ and $m = 2$. A cross-section

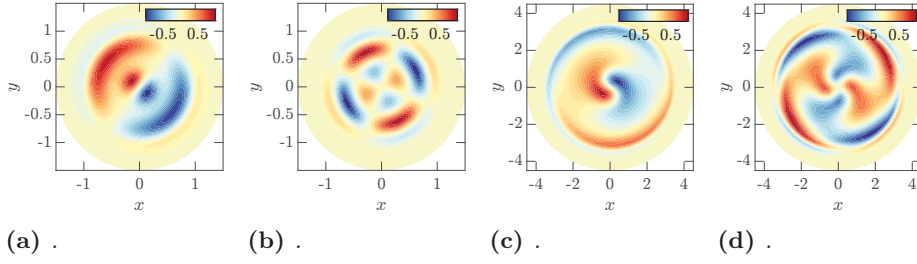


Figure IV.11 – Cross-section view at $z = 1$ of the four unstable modes at criticality for the annular jet case ($\delta_u = 0$). The streamwise vorticity ϖ_z is visualised by colours. (a) Mode S_1 for $L = 0.5$, (b) Mode S_2 for $L = 0.5$, (c) Mode F_1 for $L = 3$ and (d) Mode F_2 for $L = 3$.

view of these two modes is displayed in fig. IV.11 (c-d). Please note that for the chosen set of parameters, the onset of instability for axisymmetric unsteady mode F_0 is always located at larger Reynolds numbers than the aforementioned modes. This is one of the major differences with the case studied by Canton et al. (2017), who found that for small values of the jet distance $L \approx 0.1$, the dominant instability is an unsteady axisymmetric one, which would be named F_0 with our nomenclature. Thus, in the following, we only include the results for the S_1 , S_2 , F_1 and F_2 modes. The primary instability of the annular jet is then a steady symmetry-breaking bifurcation that leads to a jet flow with a single symmetry plane, displayed in fig. IV.11 (a). In contrast, bifurcations that lead to the mode S_2 possess two orthogonal symmetry planes, see fig. IV.11 (b).

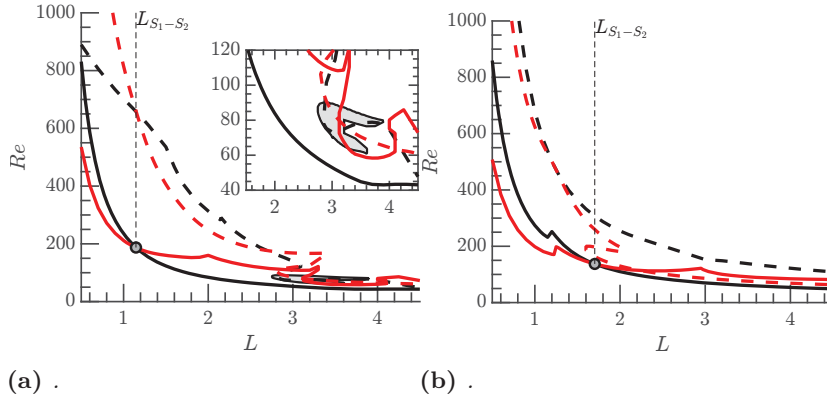


Figure IV.12 – Neutral lines of the four modes found studying the configuration of two concentric jets, fixing the velocity ratio. (a) $\delta_u = 1$, (b) $\delta_u = 2$. Black lines: modes with $m = 1$, red lines: modes with $m = 2$. Solid lines: steady modes, dashed lines: unsteady modes..

Figure IV.12 compares the results obtained for a constant velocity ratio when varying the distance between jets. The increase of the distance between the

jets has a de-stabilising effect. The largest critical Reynolds number is found at the smallest explored distance between the jets, that is, $L = 0.5$. The points where mode switching occurs are highlighted in fig. IV.12. We can appreciate that the interaction between the branch S_1 (non-oscillating $m = 1$ mode) and S_2 (non-oscillating $m = 2$ mode) happens in both considered velocity ratio δ_u . Another feature of the neutral curves is the existence of turning points, which are not shown here, see the associated article for more information.

Normal form, basic solutions and their properties

Herein, we perform a normal form reduction, which allows us to predict non-axisymmetric steady, periodic, quasiperiodic and heteroclinic cycles between non-axisymmetric states.

In order to unravel the existence and the stability of the nonlinear states near the codimension two point, let us write the flow field as

$$\mathbf{q} = \mathbf{q}_0 + \text{Re}[r_1(\tau)e^{i\phi_1(\tau)}e^{-i\theta}\hat{\mathbf{q}}_{s,1}] + \text{Re}[r_2(\tau)e^{i\phi_2(\tau)}e^{-2i\theta}\hat{\mathbf{q}}_{s,2}] \quad (\text{IV.4})$$

in polar coordinates for the complex amplitudes $z_1 = r_1e^{i\phi_1}$ and $z_2 = r_2e^{i\phi_2}$ where r_j and ϕ_j for $j = 1, 2$ are the amplitude and phase of the symmetry-breaking modes $m = 1$ and $m = 2$, respectively. The normal form is expressed in reduced polar notation as follows,

$$\dot{r}_1 = e_3r_1r_2 \cos(\chi) + r_1\left(\lambda_{(s,1)} + c_{(1,1)}r_1^2 + c_{(1,2)}r_2^2\right), \quad (\text{IV.5a})$$

$$\dot{r}_2 = e_4r_1^2 \cos(\chi) + r_2\left(\lambda_{(s,2)} + c_{(2,1)}r_1^2 + c_{(2,2)}r_2^2\right), \quad (\text{IV.5b})$$

$$\dot{\chi} = -\left(2e_3r_2 + e_4\frac{r_1^2}{r_2}\right) \sin(\chi), \quad (\text{IV.5c})$$

where the phase $\chi = \phi_2 - 2\phi_1$ is coupled with the amplitudes r_1 and r_2 because of the existence of the 1 : 2 resonance. Before proceeding to the analysis of the basic solutions of eq. (IV.5), we can simplify these equations by the rescaling $\left(\frac{r_1}{|e_3e_4|^{1/2}}, \frac{r_2}{e_3}\right) \rightarrow (r_1, r_2)$, which yields the following equivalent system,

$$\dot{r}_1 = r_1r_2 \cos(\chi) + r_1\left(\lambda_{(s,1)} + c_{11}r_1^2 + c_{12}r_2^2\right), \quad (\text{IV.6a})$$

$$\dot{r}_2 = sr_1^2 \cos(\chi) + r_2\left(\lambda_{(s,2)} + c_{21}r_1^2 + c_{22}r_2^2\right), \quad (\text{IV.6b})$$

$$\dot{\chi} = -\frac{1}{r_2}\left(2r_2^2 + sr_1^2\right) \sin(\chi), \quad (\text{IV.6c})$$

with the coefficients

$$s = \text{sign}(e_3e_4), \quad c_{11} = \frac{c_{(1,1)}}{|e_3e_4|}, \quad c_{12} = \frac{c_{(1,2)}}{e_3^2}, \quad c_{21} = \frac{c_{(2,1)}}{|e_3e_4|}, \quad c_{22} = \frac{c_{(2,2)}}{e_3^2}.$$

Finally, we consider a third normal form equivalent to the previous ones but which removes the singularity of eqs. (IV.5) and (IV.6) when $r_2 = 0$ (Corrochano et al., 2023). The third normal form, which we shall refer to as reduced Cartesian normal form, takes advantage of the simple transformation $x = r_2 \cos(\chi)$, $y = r_2 \sin(\chi)$ (Porter et al., 2005):

$$\dot{r}_1 = r_1 \left(\lambda_{(s,1)} + c_{11}r_1^2 + c_{12}(x^2 + y^2) + x \right), \quad (\text{IV.7a})$$

$$\dot{x} = sr_1^2 + 2y^2 + x \left(\lambda_{(s,2)} + c_{21}r_1^2 + c_{22}(x^2 + y^2) \right), \quad (\text{IV.7b})$$

$$\dot{y} = -2xy + y \left(\lambda_{(s,2)} + c_{21}r_1^2 + c_{22}(x^2 + y^2) \right), \quad (\text{IV.7c})$$

In this final representation standing wave solutions are contained within the invariant plane $y = 0$, and due to the invariance of eq. (IV.7) under the reflection $y \mapsto -y$, one can restrict attention, without loss of generality, to solutions with $y \geq 0$, cf (Porter et al., 2001). The system eq. (IV.6) possess four types of fixed points, which are listed in table IV.1.

Name	Definition	Bifurcations	Comments
O	$r_{1,O} = r_{2,O} = 0$	–	Steady axisymmetric state
P	$r_{2,P}^2 = \frac{-\lambda_{(s,2)}}{c_{22}}, r_{1,P} = 0$	$\lambda_{(s,2)} = 0$	Bifurcation from O
MM	$r_{1,MM} = -\frac{\lambda_{(s,1)} \pm r_{2,MM} + c_{12}r_{2,MM}^2}{c_{11}}$ $P_{MM}(r_{2,MM} \cos(\chi_{MM})) = 0$ $\cos(\chi_{MM}) = \pm 1$	$\lambda_{(s,1)} = 0$ $\sigma_{\pm} = 0$	Bifurcation from O Bifurcation from P
TW	$\cos(\chi_{TW}) = \frac{(2c_{11} + c_{12})\lambda_{(s,2)} - (2c_{21} + c_{22})\lambda_{(s,1)}}{\Sigma_{TW}(2\lambda_{(s,1)} + \lambda_{(s,2)})}$ $r_{2,TW}^2 = \frac{-(2\lambda_{(s,1)} + \lambda_{(s,2)})}{\Sigma_{TW}}$ $r_{1,TW}^2 = 2r_{2,TW}^2$	$\cos(\chi_{TW}) = \pm 1$	Bifurcation from MM

Table IV.1 – Definition of the fixed points of the reduced polar normal form eq. (IV.6). σ_{\pm} is defined in eq. (IV.8), the polynomial P_{MM} is defined in eq. (IV.9) and $\Sigma_{TW} \equiv 4c_{11} + 2(c_{12} + c_{21}) + c_{22}$.

First, the axisymmetric steady state (O) is represented by $(r_1, r_2) = (0, 0)$, so it is the trivial steady state of the normal form. The second steady state is what it is denoted as pure mode (P). In the original coordinates, it corresponds to the symmetry breaking structure associated to the mode S_2 . This state bifurcates from the axisymmetric steady state (O) when $\lambda_{(s,2)} = 0$. The third fixed point is the mixed mode state (MM), which is listed in table IV.1. It corresponds to the reflection-symmetry-preserving-state associated to the mode S_1 . It may bifurcate directly from the trivial steady state O, when $\lambda_{(s,1)} = 0$ or from P whenever $\sigma_+ = 0$ or $\sigma_- = 0$, where σ_{\pm} is defined as

$$\sigma_{\pm} \equiv \lambda_{(s,1)} - \frac{-\lambda_{(s,2)}c_{12}}{c_{22}} \pm \sqrt{\frac{-\lambda_{(s,2)}}{c_{22}}}. \quad (\text{IV.8})$$

The representation in the reduced polar form is

$$r_{1,MM} = -\frac{\lambda_{(s,1)} \pm r_{2,MM} + c_{12}r_{2,MM}^2}{c_{11}}, \quad \cos(\chi_{MM}) = \pm 1,$$

and the condition $P_{MM}(r_{2,MM} \cos(\chi_{MM})) = 0$, where P_{MM} is defined as

$$P_{MM}(x) \equiv s\mu_1 + (s + c_{21}\lambda_{(s,1)} - c_{(1,1)}\lambda_{(s,2)})x + (c_{21} + sc_{12})x^2 + (c_{12}c_{21} - c_{11}c_{22})x^3. \quad (\text{IV.9})$$

Finally, the fourth fixed point of the system are travelling waves (TW). It is surprising that the interaction between two steady states causes a time-periodic solution. The travelling wave emerges from MM in a parity-breaking pitchfork bifurcation that breaks the reflection symmetry when $\cos(\chi_{TW}) = \pm 1$. The TW drifts at a steady rotation rate ω_{TW} along the group orbit, i.e., the phases $\dot{\phi}_1 = r_{2,TW} \sin(\chi_{TW})$ and $\dot{\phi}_2 = -s \frac{r_{1,TW}^2}{r_{2,TW}} \sin(\chi_{TW})$ are non-null.

Name	Bifurcation condition	Comments
SW	$sr_1^2 - 2c_{11}r_1^2r_{2,MM} \cos(\chi_{MM}) - 2c_{22}r_{2,MM}^3 \cos(\chi_{MM})^3 = 0$	Bif. from MM
MTW	$D_{TW} - T_{TW}I_{TW} = 0, I_{TW} > 0$	Bif. from TW

Table IV.2 – Definition of the limit cycles of the reduced polar normal form eq. (IV.6).

Mixed modes and travelling waves may further bifurcate into standing waves (SW) and modulated travelling waves (MTW), respectively. These are generic features of the 1 : 2 resonance for small values of $\lambda_{(s,1)}$ and $\lambda_{(s,2)}$, when $s = -1$. In the original coordinates, SW are periodic solutions, whereas MTW are quasiperiodic. Standing waves emerge via a Hopf bifurcation from MM when the conditions $P_{SW}(r_{2,MM} \cos(\chi_{MM})) > 0$ for

$$P_{SW}(x) \equiv (2c_{22}x^3 - sr_1^2)c_{11} - (2c_{12}x + 1)(c_{21}x + s)x,$$

and the one listed in table IV.2 are satisfied. MTW are created when a torus bifurcation happens on the travelling wave branch, which occurs when the conditions listed in table IV.2 are satisfied.

Another remarkable feature of eq. (IV.5) is the existence of robust heteroclinic

Name	Condition	Comments
Ht AGH	$\lambda_{(s,1)} > 0, \lambda_{(s,2)} > 0, c_{22} < 0$ $\sigma_+ > 0, \sigma_- < 0$	Existence Asymptotic stability

Table IV.3 – Definition of the conditions for the existence of the Ht AGH (robust heteroclinic cycles connecting pure modes) of the reduced polar normal form eq. (IV.6).

cycles that are asymptotically stable. When $s = -1$, there are open sets of parameters (see table IV.3) where the reduced polar normal form exhibits structurally stable connections between π -translations on the circle of pure modes, cf (Armbruster et al., 1988). These structures are robust and have been observed in a large variety of systems, (Nore, Tuckerman, et al., 2003; Nore, Moisy, et al., 2005; Mercader et al., 2002; Palacios et al., 1997; Mariano et al., 2005). In addition to these robust heteroclinic cycles connecting pure modes, there exist more complex limit cycles connecting O, P, MM and SW, cf (Porter et al., 2001). These cycles are located for larger values of $\lambda_{(s,1)}$ and $\lambda_{(s,2)}$, with possibly chaotic dynamics (Shilnikov type). In this study, we have not identified any of these.

Results of the steady-steady 1 : 2 mode interaction

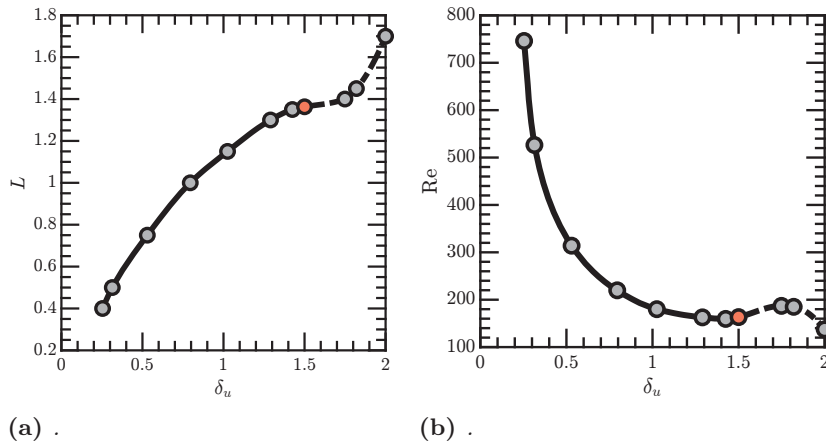


Figure IV.13 – Evolution of the codimension two interaction $S_1 - S_2$ in the space of parameters (Re, L, δ_u) . Grey points denote the points that were computed, and the red point denotes the transition from steady to unsteady with low frequency .

The location of the mode interaction between S_1 and S_2 in the (Re, δ_u) plane is depicted in fig. IV.13. It shows that the mode switching between the modes S_1 and S_2 is indeed stationary only for $\delta_u < 1.5$ and $L < 1.3$. For larger values of the velocity ratio and the jet distance, the interaction is not purely stationary; the linear modes oscillates with a slow frequency. It implies that the mode selection for large velocity ratios near the codimension two points is similar to that reported by Meliga, Gallaire, et al. (2012) for swirling jets. However, even when the two primary bifurcations are non-oscillating (S_1 and S_2), the 1 : 2 resonance of the azimuthal wavenumbers induces a slow frequency, which we denote as travelling wave solutions (TW).

We consider the bifurcation sequence for $\delta_u = 1.0$ and $L = 1.15$, which

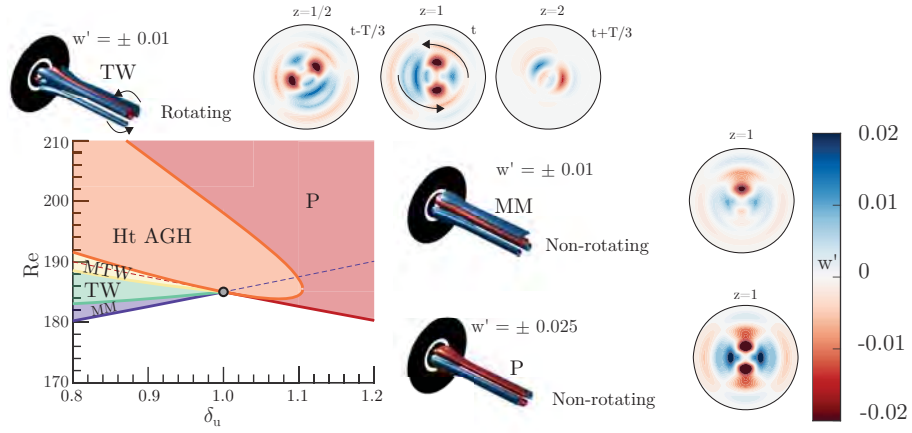


Figure IV.14 – Parametric portrait at the codimension two point $S_1 : S_2$ for parameter values $(L, \delta_u) = (1.15, 1.0)$. Visualizations of blue and red surfaces in the isometric views represent the respective positive and negative isocontour values of the perturbative axial velocity indicated in the figure .

is qualitatively similar to transitions in the range $0.5 < \delta_u < 1.5$, near the codimension two points, which are depicted in fig. IV.13. At the codimension two points for $\delta_u < 0.5$, at least one of the two bifurcations is sub-critical and a normal form reduction up to fifth order is necessary. Subcritical transition was also noticed for a distance between jets $L = 0.1$ by Canton et al. (2017), who reported high levels of the linear gain associated to transient growth mechanisms. This last case is not considered in here. Figure IV.14 displays the phase portrait of the stable attractors near the $S_1 : S_2$ interaction. For values of $\delta_u > 1.0$, the axisymmetric steady state loses its axisymmetry leading to a new steady state with symmetry $m = 2$, herein denoted as pure mode (P). A reconstruction of the flow field of such a state is performed at the bottom right of fig. IV.14, which shows that the state P possesses two orthogonal planes of symmetry. Near the codimension two point, for values of the velocity ratio $\delta_u < 1.1$, the state P is only observable, that is non-linearly stable, within a small interval with respect to the Reynolds number. For larger values of the velocity ratio, the state P remains stable within the analysed interval of Reynolds numbers. For values of the velocity ratio $\delta_u < 1.0$, the bifurcation diagram is more complex. Figure IV.15 displays the bifurcation diagram of the fixed-point solutions of eq. (IV.7) on the left diagram and the full set of solutions of the normal form in the right diagram. The axisymmetric steady state first bifurcates towards a Mixed-Mode solution, which is the solution in the $y = 0$ plane for the right diagram of fig. IV.15. A solution with a non-symmetric wake has been reconstructed in

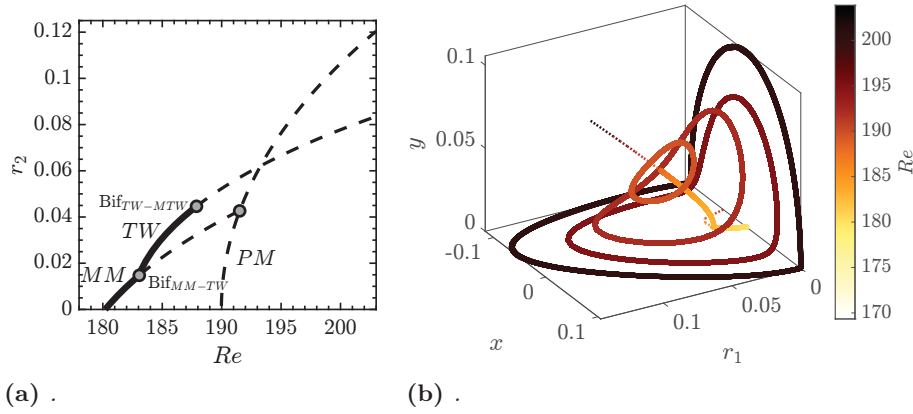


Figure IV.15 – Bifurcation diagram with respect to the Reynolds number for $L = 1.15$ and $\delta_u = 0.8$. The left diagram reports the evolution of r_2 for the fixed point solutions of the normal form. The right diagram displays the bifurcation diagram in the Cartesian coordinates. Solid lines and dashed lines denote stable attractors and unstable attractors, respectively.

fig. IV.14. The Mixed-Mode solution is only stable within a small interval of the Reynolds number. A secondary bifurcation, denoted Bif_{MM-TW} , gives rise to a slowly rotating wave of the wake. The TW and the MM solutions are identical at the bifurcation point. The phase speed is zero at the bifurcation, thus this is not a Hopf bifurcation. It corresponds to a *drift instability* that breaks the azimuthal symmetry, i.e. it starts to slowly drift. This unusual feature, that travelling waves bifurcate from a steady solution at a steady bifurcation, is a generic feature of the 1 : 2 resonance. A reconstruction of the travelling wave solution is depicted on the top of fig. IV.14. It corresponds to the line with non-zero y component in the right diagram of fig. IV.15. The TW solution loses its stability in a tertiary bifurcation, denoted as Bif_{TW-MTW} . It conforms to a Hopf bifurcation of the TW solution, which gives birth to a quasi-periodic solution named Modulated Travelling Wave (MTW). A representation of this kind of solution in the Cartesian coordinates (r_1, x, y) is depicted on the right image of fig. IV.15.

Eventually, the Modulated Travelling Wave experiences a global bifurcation. That occurs when the periodic MTW solution, in the (r_1, x, y) coordinates, nearly intersects the invariant $r_1 = 0$ and $y = 0$ planes. The transition sequence is represented in the right image of fig. IV.15 in the Cartesian coordinates (r_1, x, y) . The amplitude of the MTW limit cycle increases until the MTW arising at the tertiary bifurcation Bif_{TW-MTW} are destroyed by meeting a heteroclinic cycle at Bif_{MTW-Ht} . The locus of Bif_{MTW-Ht} is reported in fig. IV.14. The conditions for the existence of the heteroclinic cycles are listed in table IV.3. When σ_- becomes negative, the cycle is attracting and robust heteroclinic cycles are

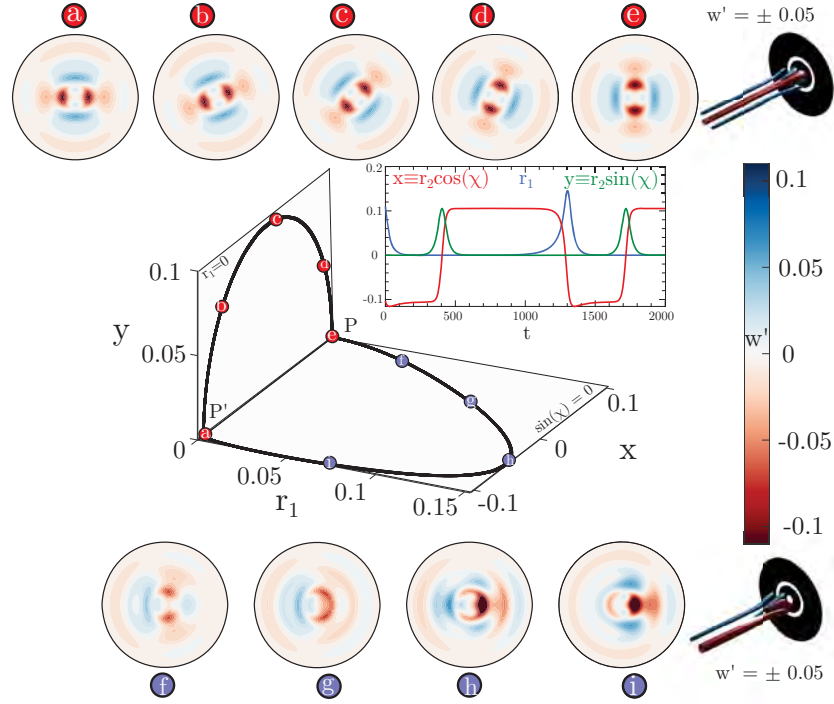


Figure IV.16 – Heteroclinic cycle solution for parameter values $Re = 200$, $\delta_u = 0.8$. The top and bottom image sequences along the heteroclinic cycle show (from left to right) an axial slice plane at $z = 1$ of the instantaneous fluctuations of the axial velocity of the flow field as viewed from downstream, along with a three-dimensional isometric view (d on the top and g on the bottom). The middle diagram displays the heteroclinic cycle in the coordinates (r_1, x, y) .

observed. It is destroyed when σ_+ becomes negative, in that case the pure modes are no longer saddles which breaks the heteroclinic connection. Figure IV.16 displays the instantaneous fluctuation field from a heteroclinic orbit connecting P and its conjugate solution P' , which is obtained by a rotation of $\pi/2$, for parameter values $Re = 200$ and $\delta_u = 0.8$. The dynamics of the cycle takes place in two phases. Figure IV.16 depicts the motion of the coherent structure associated to the heteroclinic cycle. Starting from the conjugated pure mode P' , the cycle leaves the point (a), located in the vicinity of P' , along the unstable eigenvector y , which is the stable direction of P . The first phase consists in a rapid rotation by $\pi/2$ of the wake, it corresponds to the sequence a-b-c-d-e displayed in fig. IV.16. Then it is followed by a slow approach following the direction y and departure from the pure mode state P along the direction r_1 . The second phase consists in a rapid horizontal motion of the wake, which is

an evolution from P to P' that takes place by the breaking of the reflectional symmetry with respect to the vertical axis; it constitutes the sequence e-f-g-h-i-a. Please note that equivalent motions are also possible. The first phase of rapid counter-clockwise rotation by $\pi/2$ can be performed in the opposite sense. It corresponds to a motion in the Cartesian coordinates along the plane r_1 along negative values of y . The sequence e-f-g-h-i-a can be replaced by a horizontal movement in the opposite sense, which adjusts to connect the plane $y = 0$ corresponding to negative values of r_1 .

3

Steady-Hopf – A common organizing centre for the wake flow past axisymmetric bluff bodies

This section presents a mathematical study of a truncated normal form relevant to the bifurcations observed in axisymmetric wakes, in particular, a disk and a sphere. We consider the interaction between a steady state bifurcation and Hopf bifurcation in a system with $O(2)$ symmetry when both modes have the same wavenumber. This situation arises naturally in numerous flow configurations, for example, *Taylor–Couette flow* (TCF), the *wake flow of axisymmetric* objects (WFA) and the *wake of axisymmetric objects in mixed convection* (WFA-MC). The bifurcation diagrams are interpreted in terms of symmetry considerations. The normal form coefficients are computed for several examples of wake flows and the resulting predictions compared with the results of direct numerical flow simulations. In general, satisfactory agreement is obtained.

The flow state $\mathbf{q} = [\mathbf{u}, p]$ is specified by the velocity field \mathbf{u} and the hydrodynamic pressure p (the WFA-MC also includes the temperature field T). Near the mode interaction (a codimension-two bifurcation) the flow state takes the form

$$\begin{aligned} \mathbf{q} = & \mathbf{q}_0 + \operatorname{Re}[z_0(t)e^{-i\theta}\hat{\mathbf{q}}_s] \\ & + \operatorname{Re}[z_1(t)e^{-i\theta}\hat{\mathbf{q}}_{h,-1} + z_2(t)e^{i\theta}\hat{\mathbf{q}}_{h,1}] + \text{h.o.t.} \end{aligned} \quad (\text{IV.10})$$

Here \mathbf{q}_0 is the steady flow that is invariant under the action of the whole $O(2)$ group, $\hat{\mathbf{q}}_s$ is the steady mode and $\hat{\mathbf{q}}_h$ is the Hopf (unsteady) mode. The Ansatz in eq. (IV.10) takes into account the continuous (translation or rotation) symmetry via the terms $e^{\pm i\theta}$, where $\theta \in S^1$ is an angle-like variable in the periodicity direction; for axisymmetric problems it corresponds to the azimuthal angle, while in the TCF it corresponds to the axial direction: $\theta \equiv -2\pi x/\Lambda$, where Λ is the mode wavelength. Here without loss of generality the azimuthal wavenumber m is taken to be $m = 1$.

We will not deal with the general case, instead we consider a truncated form retaining only nonlinearities of third order. Such a truncated system can be

expressed in the following explicit form:

$$\begin{aligned} \dot{z}_0 = & \lambda_s z_0 + l_0 z_0 |z_0|^2 + l_1 (|z_1|^2 + |z_2|^2) z_0 \\ & + i l_2 (|z_2|^2 - |z_1|^2) z_0 + l_3 \bar{a}_0 \bar{a}_2 z_1 \end{aligned} \quad (\text{IV.11a})$$

$$\begin{aligned} \dot{z}_1 = & (\lambda_h + i\omega_h) z_1 + (B|z_1|^2 + (A+B)|z_2|^2) z_1 \\ & + C z_1 |z_0|^2 + D z_0^2 z_2 \end{aligned} \quad (\text{IV.11b})$$

$$\begin{aligned} \dot{z}_2 = & (\lambda_h + i\omega_h) z_2 + (B|z_2|^2 + (A+B)|z_1|^2) z_2 \\ & + C z_2 |z_0|^2 + D \bar{a}_0^2 z_1, \end{aligned} \quad (\text{IV.11c})$$

where l_0, l_1, l_2, l_3 are real coefficients and A, B, C, D are complex coefficients. Using the polar representation of the complex amplitudes $z_j = r_j e^{i\phi_j}$ for $j = 0, 1, 2$, eq. (IV.11) can be reduced to a system of four coupled equations governing the amplitudes r_0, r_1, r_2 and the phase $\Psi \equiv \phi_1 - \phi_2 - 2\phi_0$:

$$\begin{aligned} \dot{r}_0 = & [\lambda_s + l_0 r_0^2 + l_1 (r_1^2 + r_2^2)] r_0 \\ & + l_3 r_0 r_1 r_2 \cos \Psi \end{aligned} \quad (\text{IV.12a})$$

$$\begin{aligned} \dot{r}_1 = & [\lambda_h + B_r r_1^2 + (A_r + B_r) r_2^2 + C_r r_0^2] r_1 \\ & + r_0^2 r_2 (D_r \cos \Psi + D_i \sin \Psi) \end{aligned} \quad (\text{IV.12b})$$

$$\begin{aligned} \dot{r}_2 = & [\lambda_h + B_r r_2^2 + (A_r + B_r) r_1^2 + C_r r_0^2] r_2 \\ & + r_0^2 r_1 (D_r \cos \Psi - D_i \sin \Psi) \end{aligned} \quad (\text{IV.12c})$$

$$\begin{aligned} \dot{\Psi} = & (A_i - 2l_2)(r_2^2 - r_1^2) - 2l_3 r_1 r_2 \sin \Psi \\ & + r_0^2 D_i \cos \Psi \left[\frac{r_2}{r_1} - \frac{r_1}{r_2} \right] - r_0^2 D_r \sin \Psi \left[\frac{r_2}{r_1} + \frac{r_1}{r_2} \right], \end{aligned} \quad (\text{IV.12d})$$

Interestingly, the polar system only involves 9 of the 13 original coefficients, namely: $l_0, l_1, l_3, A_r, B_r, C_r, D_r, D_i$ and $A_i - 2l_2$. The system eq. (IV.12) is decoupled from the evolution of the phase ϕ_0 and the "mean phase" of the Hopf component $\phi_m = (\phi_1 + \phi_2)/2$, which evolve according to

$$\dot{\phi}_0 = l_2 (r_2^2 - r_1^2) + l_3 r_1 r_2 \sin \Psi, \quad (\text{IV.13a})$$

$$\begin{aligned} \dot{\phi}_m = & \omega_h + (B_i + \frac{1}{2} A_i)(r_1^2 + r_2^2) + C_i r_0^2 \\ & + \frac{1}{2} r_0^2 D_i \cos \Psi \left[\frac{r_2}{r_1} + \frac{r_1}{r_2} \right] \\ & + \frac{1}{2} r_0^2 D_i \sin \Psi \left[\frac{r_1}{r_2} - \frac{r_2}{r_1} \right]. \end{aligned} \quad (\text{IV.13b})$$

Types of solutions

The solutions that are stationary in the polar representation are summarized in the table IV.4. The simplest solution is the trivial solution (TS) $(z_0, z_1, z_2) =$

Table IV.4 – Nomenclature and symmetry groups of the steady state solutions of the system (IV.12).

Name	Representative	Isotropy group (complex)	Isotropy group (polar)	Frequencies
Pure modes:				
TS	$(0, 0, 0, nd)$	$O(2) \times S^1$	$D_4 \rtimes \mathbb{Z}_2(\kappa)$	0
SS	$(r_a, 0, 0, nd)$	$\mathbb{Z}_2(\kappa) \times S^1$	$\mathbb{Z}_2(\kappa) \times \mathbb{Z}_2(\Phi_\pi)$	0
RW	$(0, r_a, 0, nd)$	$SO(2)$	$\mathbb{Z}_4(R_{\pi/2}\Phi_{\pi/2})$	1
SW	$(0, r_a, r_a, nd)$	$\mathbb{Z}_2(\kappa) \times \mathbb{Z}_2(R_\pi\Phi_\pi)$	$\mathbb{Z}_2(\kappa) \times \mathbb{Z}_2(R_\pi\Phi_\pi)$	1
Mixed modes:				
MM ₀	$(r_a, r_b, r_b, 0)$	$\mathbb{Z}_2(\kappa)$	$\mathbb{Z}_2(\kappa)$	1
MM _π	(r_a, r_b, r_b, π)	$\mathbb{Z}_2(\kappa \cdot R_\pi\Phi_\pi)$	$\mathbb{Z}_2(\kappa \cdot R_\pi\Phi_\pi)$	1
MW	$(0, r_a, r_b, \Psi)$	$\mathbb{Z}_2(R_\pi\Phi_\pi)$	$\mathbb{Z}_2(R_\pi\Phi_\pi)$	1
Precessing waves:				
General	(r_a, r_b, r_c, Ψ)	$\mathbb{1}$	$\mathbb{1}$	2
Type A	(r_a, r_b, r_b, Ψ)	$\mathbb{1}$	$\mathbb{1}$	2
Type B	$(r_a, r_b, r_c, 0 \text{ or } \pi)$	$\mathbb{1}$	$\mathbb{1}$	2
Type C	$(r_a, r_b, 0, \Psi)$	$\mathbb{1}$	$\mathbb{1}$	2

$(0, 0, 0)$. This solution corresponds to Couette flow in the TCF problem, and to the axisymmetric solution in the WFA and WFA-MC problems. There are three primary solutions: steady state modes (SS), rotating waves (RW) and standing waves (SW). The steady state mode (SS) takes the form $(z_0, 0, 0)$, $z_0 \neq 0$. This state corresponds to the Taylor Vortex state in the TCF problem and the Steady Shedding mode in the wake problems.

The RW and SW solutions arise in a primary Hopf bifurcation of the trivial state. Because of $O(2)$ symmetry, the eigenvalues at the Hopf bifurcation are doubled, and the Hopf bifurcation produces simultaneously a branch of rotating waves (RW, $(z_0, z_1, z_2) = (0, z_1, 0)$) and standing waves (SW, $(z_0, z_1, z_2) = (0, z_1, z_1)$). The RW break reflection symmetry; consequently, there are two RW, rotating in opposite directions and related by reflection. In contrast, the SW are reflection-symmetric oscillations with zero mean. In the TCF problem the RW corresponds to the Spiral Vortex state, while in the wake problem they correspond to the Spiral Shedding state, observed, for example, in the wake of a rising bubble (Mougin et al., 2001). While the SW state corresponds, respectively, to the Ribbon state in the TCF problem and the Symmetric Periodic Shedding state observed, for example, in the wake of a disk when $R \approx 150$. Each of these solutions corresponds to a one-dimensional fixed point subspace spanned either by z_0 or z_1 , and their presence is therefore guaranteed by the equivariant branching lemma (Golubitsky et al., 2012).

Secondary bifurcations may lead to states with a higher-dimensional fixed point subspace. An example is provided by mixed mode states that correspond to a (nonlinear) superposition of the SS and SW modes. There are two possible states of this type. The first is denoted by MM₀, and corresponds, respectively, to a pattern called Twisted Vortices in the TCF problem and to the reflection symmetry-preserving mode (RSP) in the wake problem. The second mixed mode, MM_π, corresponds, respectively, to Wavy Vortices in the TCF problem and to

Table IV.5 – Nomenclature and symmetry group of limit cycle solutions of the system (IV.12).

Name of solution	Representative in polar coordinates	Isotropy group	Frequencies in primitive coordinates
$\overline{\text{MM}}_{0,\pi}$	$(r_a(t), r_b(t), r_c(t), 0 \text{ or } \pi)$	$\mathbb{1}$	2
$\overline{\text{IMM}}$	$(0, r_b, r_c, \Psi(t))$	$\mathbb{1}$	2
$\overline{\text{PuW}}$	$(r_a(t), r_b(t), r_c(t), \Psi(t))$ with $\bar{r}_b = \bar{r}_c$ and $\overline{\sin \Psi} = 0$	$\mathbb{1}$	2
3-frequency waves: (3FW)			
General	$(r_a(t), r_b(t), r_c(t), \Psi(t))$	$\mathbb{1}$	3
Type A	$(r_a(t), r_b(t), r_b(t), \Psi(t))$ with $\overline{\sin \Psi} \neq 0$	$\mathbb{1}$	3
Type B	$(r_a(t), r_b(t), r_c(t), 0 \text{ or } \pi)$ with $\bar{r}_b \neq \bar{r}_c$	$\mathbb{1}$	3
Type C	$(0, r_b(t), r_c(t), \text{nd})$ with $\bar{r}_b \neq \bar{r}_c$	$\mathbb{1}$	3
Type D	$(r_a(t), r_b(t), 0, \Psi(t))$ with $\overline{\sin \Psi} \neq 0$	$\mathbb{1}$	3

the reflection symmetry-breaking mode (RSB) in the wake problem. Finally, one can also find a mixed mode state involving the Hopf modes, referred to as a modulated wave state (MW), consisting of a (nonlinear) superposition of two rotating wave modes. This state is referred to as the Modulated Spiral mode (MSP) in the TCF problem and the Modulated Wave mode (MW) in the wake problem. It is a mode with two temporal frequencies, which are in general incommensurate, and so corresponds to a 2-torus. This type of solution does not occur generically in the third-order system, although it arises in higher order normal forms or in the degenerate case corresponding to $A_r = 0$ (Knobloch, 1986).

The last solution type, that is, a state arising in a tertiary bifurcation, corresponds to a fixed point in the (r_0, r_1, r_2, Ψ) coordinates with no further symmetry. According to eq. (IV.13), in such states the phase ϕ_0 of the steady mode generically precesses at a constant rate given by $\dot{\phi}_0$. Consequently, states of this type display two frequencies, one of which is close to the critical Hopf frequency while the other is a low frequency given by eq. (IV.13a). These solutions will be referred to as Precessing Waves (PrW) or *drifting waves*.

The solutions that are periodic in the polar representation are summarized in table IV.5. We distinguish three types of solutions. The first type is referred to as a Modulated Mixed Mode, since it displays the same spatial symmetries as the mixed modes already described. We also find periodic states, which are called Pulsating Waves (PuW). In such states, the polar coordinates (r_0, r_1, r_2, Ψ) all oscillate periodically in time, but the pulsation retains a certain symmetry. Specifically, $\bar{r}_1 = \bar{r}_2$ and $\overline{\sin \Psi} = 0$, where the overbar indicates an average over the pulsation period. The last type of periodic solution corresponds to the case where the (r_0, r_1, r_2, Ψ) coordinates are once again all periodic, but the conditions $\bar{r}_1 = \bar{r}_2$ and $\overline{\sin \Psi} = 0$ are violated. We call these states Three-

Frequency Waves (3FW), since they are characterized by a frequency near the critical Hopf frequency, the pulsation frequency, and finally the precession frequency.

Mixed convection in the flow past a disk

Let us revisit the problem of pattern formation behind a disk falling through a stratified fluid. In our formulation the disk is held fixed, with flow past it (the WFA-MC problem). This problem has many practical applications in engineering such as cooling, heating (Kotouč et al., 2009), sedimentation (Gan et al., 2003), melting (Mcleod et al., 1996), combustion (Sadhal et al., 2012), vaporization (Chiang et al., 1993). A heated disk represents a heat source embedded within the physical domain, where the solid body is subjected to forces of hydrodynamic and thermal origin. There are two main cases of interest, the case of a hot falling sphere where the fluid within the wake is accelerated with respect to the spherical body. Such a configuration is called *assisting flow*. The opposite case, where the wake of a hot ascending spherical particle is decelerated by buoyancy effects, is referred to as *opposing flow*. We focus on the *opposing flow* case under mixed convection conditions. This problem depends on three control parameters, the Reynolds number Re , the Richardson number Ri , and the aspect ratio of the disk χ , where $1/\chi$ is the dimensionless thickness. The WFA problem for $Ri = 0$ and $1/\chi \approx 0$ has already been studied by Fabre, Auguste, et al. (2008). They used numerical simulations to determine the normal form coefficients fitted from the simulations. The case $\chi = 3$ was studied in detail by Auguste et al. (2010). A more rigorous study via multiple-scale analysis was performed by Meliga, Chomaz, et al. (2009). Later, Chrust et al. (2010) explored the flow dependence on the parameters (Re, χ) using numerical simulations and proposed a classification of the patterns observed. These studies demonstrated the importance of the disk thickness on the transition scenario. Chrust et al. observed that, when the thickness $1/\chi$ is large, for instance $\chi = 1$, the symmetry plane is preserved for large values of the Reynolds number, i.e., only SS and MM_0 (possibly with modulated mixed modes or precessing waves) are observed before spatio-temporal chaos appears. In the limit of zero thickness, when $1/\chi \approx 0$, the transition scenario starts with the formation of a SS pattern followed by the breaking of the symmetry plane, leading to a MM_π mode and eventually to standing waves SW . At intermediate values of the thickness, a large variety of spatio-temporal patterns may be observed, as highlighted by the study of Auguste et al. In the present study, we shall look for the connections between the *opposing flow* case in mixed convection and the situation at $Ri = 0$, in terms of the spatio-temporal patterns observed in the flow. Figure IV.17 displays the location of the codimension-two point corresponding to the Hopf-Steady State bifurcation, obtained by varying $1/\chi \in [0, 1]$. The top panels show the

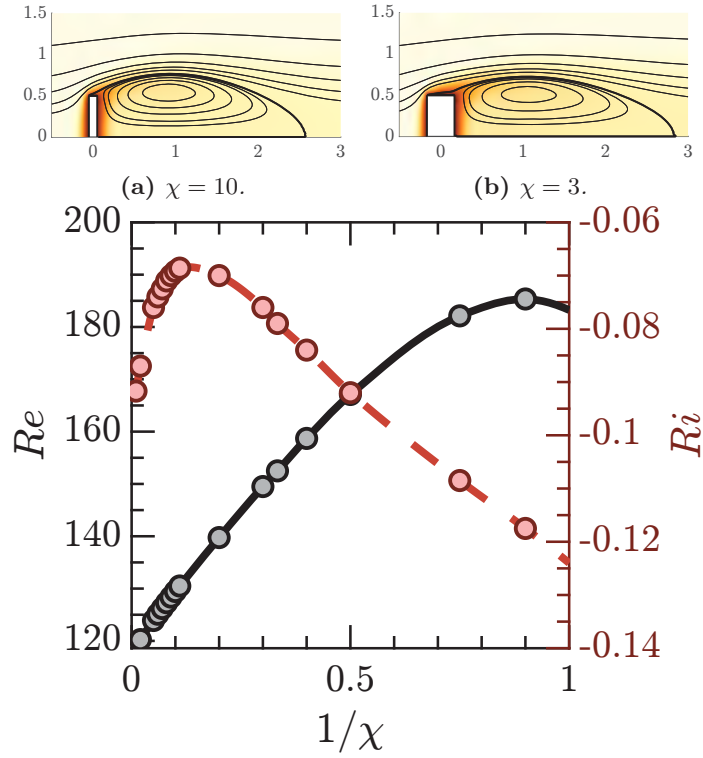


Figure IV.17 – The location of the codimension-two Hopf-Steady State bifurcation in the (Re, Ri) plane as a function of the aspect ratio χ of the disk (Re : black line; Ri : red line). The colour-coded symbols refer to the points obtained in numerical computations. Top: temperature distribution of the basic state at (a) $1/\chi = 0.1$ ($Re \approx 130$, $Ri \approx -0.068$), (b) $1/\chi \approx 0.33$ ($Re \approx 150$, $Ri \approx -0.078$).

corresponding temperature distribution in space and the growing extent of the recirculation bubble in the steady states associated with two distinct values of the aspect ratio χ of the disk. In the range of aspect ratios considered here, the critical Reynolds number grows linearly with the thickness $1/\chi$ of the disk, as previously observed by Fernandes et al. (2007). In addition, the critical Richardson number displays a maximum around $1/\chi \approx 0.1$ followed by a linear decrease in the critical Richardson number. Here, we briefly cover the case of thickness $\chi = 3$. This case displays a large number of spatio-temporal structures. To the left of the organizing center, the transition scenario is based on the initial formation of standing waves, followed by modulated waves and an eventual tertiary bifurcation, not taken into account in the normal form, leading to temporal chaos. Figure IV.19 displays the reconstruction of the lift coefficient from the normal form at $Ri = 0$, in comparison to the results obtained numerically by Auguste et al. (2010). It distinguishes five regions, with

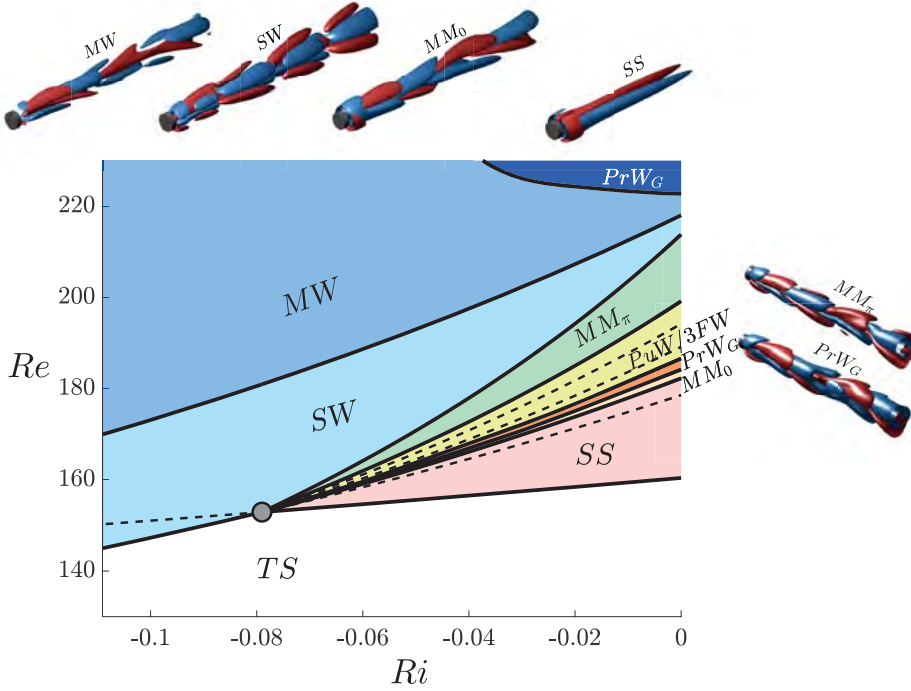


Figure IV.18 – The predicted patterns in the flow past a disk with $\chi = 3$ under mixed convection (opposing flow) conditions in parameter space. Snapshots of the reconstructed states are included..

the *Knit-Knot* (KK) region among them. The transition begins at $Re \approx 159.4$ ($Re \approx 159.8$ in Auguste et al. (2010)) via the formation of a steady state pattern (SS), which eventually bifurcates into a mixed mode (MM_0) at around $Re \approx 182.5$ ($Re \approx 179.9$ in Auguste et al. (2010)). The MM_0 state loses stability at around $Re \approx 184.5$. Quantitatively, up to this point, the sequence of bifurcations is reasonably well predicted with regard to the data reported by Auguste et al. (2010). The *Knit-Knot* region in our analysis covers a large variety of states with similar characteristics in terms of the frequency components (at least two), and the lift coefficient C_L . The authors identified this motion as temporally quasiperiodic motion resulting from the spontaneously broken reflection symmetry. The temporal dynamics of the KK state may be described as the composition of a state with frequency ω_h and a low frequency state, whose pulsation experiences large variation within its region of existence (from $T_p \approx 96 \frac{2\pi}{\omega_h}$ at $Re = 185$ to $T_p \approx 48 \frac{2\pi}{\omega_h}$ at $Re = 187$ and then to $T_p \approx 54 \frac{2\pi}{\omega_h}$ at $Re = 190$). This bifurcation sequence is followed by the appearance of the MM_π state, estimated to be around $Re \approx 198.5$ ($Re \approx 190.4$ in Auguste et al. (2010)) which connects to the standing wave branch at around $Re \approx 214$ ($Re \approx 215.2$ in Auguste et al. (2010)). According to theory, this sequence of bifurcations should

be followed by the formation of a modulated wave branch and precessing waves. However, we do not discuss these patterns here due to the lack of simulation data to compare with and because these patterns can only be described using the fifth order normal form whose coefficients were not computed. For more information, see fig. IV.18.

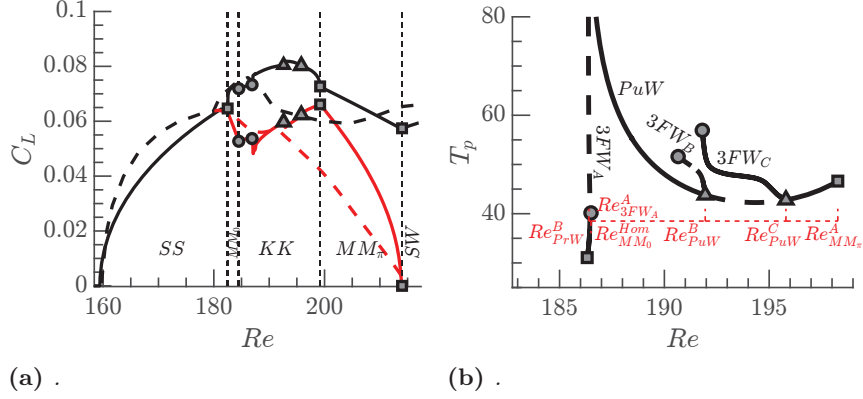


Figure IV.19 – (a) Bifurcation diagram in terms of the lift coefficient C_L for the WFA problem ($Ri = 0$) with $\chi = 3$. Solid lines were computed from the normal form, dashed lines were extracted from Auguste et al. (2010). Black lines denote $C_{L,max}$ and red lines denote the average of C_L . (b) Bifurcation diagram in the Knit-Knot region of fig. IV.19 in terms of the period T_P of the low frequency modulation. Square markers: Hopf bifurcation. Circles: saddle-node bifurcation. Triangles: Neimark-Sacker bifurcation. .

4

Triple Hopf organizing centre – From the flow past rotating particles to the acoustic emission of impinging jets

Here we analyse the triple Hopf organizing centre with and without a resonance condition. The non-resonant case arises naturally in fluid flows depending on several parameters and displaying multiple interacting self-sustained instabilities, where the core of the instability or *wavemaker* of each global mode is localised. This is exemplified in the case of the wake flow behind rotating spherical particles (Sierra-Ausin, Lorite-Diez, et al., 2022). The resonant case, instead, is relevant when the core of the instability is not localised in space, and it may even occur when the flow configuration depends on a single parameter. In this case, the frequency of the global modes is expected to be nearly a multiple of a fundamental pulsation $\Delta\omega$. The intense tonal sound emissions of rounded impinging jets at large subsonic Mach numbers (Sierra-Ausin and Giannetti, 2023) are a good example of this kind of resonant non-local feedback.

We expand the flow field into a baseflow component (in our case the steady state) and self-sustained coherent structures,

$$\mathbf{q}(t) = \mathbf{q}_0 + \sum_{k=1}^N (z_k(\tau) \hat{\mathbf{q}}_{(z_k)}(r, z) e^{i(m_k \theta - \omega_k t)} + \text{c.c.}), \quad (\text{IV.14})$$

The resonance condition is $2\omega_2 - \omega_1 = \omega_3$ and $2m_2 - m_1 = m_3$, that is, triads of nearby interacting modes. Its normal form is as follows,

$$\begin{aligned} \dot{z}_1 &= z_1 (\lambda_1 + \nu_{11}|z_1|^2 + \nu_{12}|z_2|^2 + \nu_{13}|z_3|^2) + \chi_1 z_2^2 \bar{z}_3 \\ \dot{z}_2 &= z_2 (\lambda_2 + \nu_{21}|z_1|^2 + \nu_{22}|z_2|^2 + \nu_{23}|z_3|^2) + \chi_2 z_1 \bar{z}_2 z_3 \\ \dot{z}_3 &= z_3 (\lambda_3 + \nu_{31}|z_1|^2 + \nu_{32}|z_2|^2 + \nu_{33}|z_3|^2) + \chi_3 z_2^2 \bar{z}_1 \end{aligned} \quad (\text{IV.15})$$

where $\nu_{k\ell}, \lambda_k, \chi_k \in \mathbb{C}$ for $k, \ell = 1, 2, 3$. If the resonance condition is not satisfied, then $\chi_j = 0$ for $j = 1, 2, 3$. The real part of the linear terms, named λ_k , correspond to the growth rate of the k^{th} mode. Respectively, the imaginary part of λ_k is associated to the frequency variation of the k^{th} mode with respect to the frequency of the neutral mode, i.e., with respect to the frequency ω_k determined from linear stability analysis. The terms $\nu_{k\ell}$ are the third order self ($k = \ell$) and cross interaction ($k \neq \ell$) coefficients. The resonant coefficients χ_k arise because of the quantization of the eigenvalues in the spectrum at a nearly constant distance $\Delta\omega$, i.e. frequency gaps $\Delta\omega_k = (\omega_{k+1} - \omega_k)$ are nearly constant. Figure IV.20 (a) displays a spectrum with these characteristics (we assume $m_k = 0$). In the analysis, we consider that the imperfections in the frequency difference between two modes is small, that is, $(\Delta\omega_{k+1} - \Delta\omega_k) \sim \varepsilon^2$. In this way, the term $z_2^2 \bar{z}_3$ is nearly resonant with z_1 , or in other terms $\omega_2 - \Delta\omega_2 \approx \omega_1$. The resonance

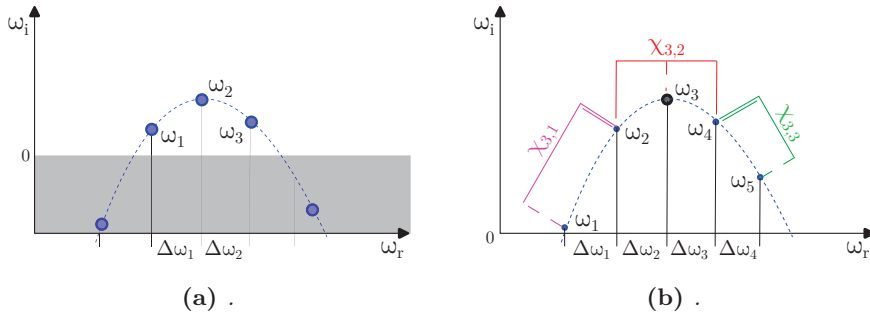


Figure IV.20 – (a) An example of an arc-discrete spectrum centred around ω_2 . (b) Dependency of the coupling coefficient on $\chi_{3,i}$ on the modes (solid line denotes dependency on amplitude z_j , dashed line on the conjugate amplitude \bar{z}_j). .

condition can be extended to a larger number of modes, that is, a N -Hopf

interaction. The general case with arbitrary N limit cycles may be expressed as

$$\dot{z}_j = z_j(\lambda_j + \sum_{k=1}^N \nu_{jk}|z_k|^2) + \text{NL}_{j,\text{res}} \quad \text{for } j = 1, \dots, N \quad (\text{IV.16})$$

where $\text{NL}_{j,\text{res}}$ are the resonant terms at the third order. Figure IV.20 (b) illustrates the resonant interactions for $N = 5$. It admits three resonant terms for the equation of z_3 , i.e. $\text{NL}_{3,\text{res}} = \chi_{3,1}z_2^2\bar{z}_1 + \chi_{3,2}z_2\bar{z}_3z_4 + \chi_{3,3}z_4^2\bar{z}_5$.

4.1

Non-resonant – The flow past rotating particles

The flow past an axisymmetric rotating body is controlled by two parameters: the Reynolds number (Re) and the rotation rate (Ω) which is defined as the ratio of the tangential velocity $\Omega^*D^*/2$ on the sphere surface to the inflow velocity W_∞^* , that is, $Re = \frac{W_\infty^*D^*}{\nu^*}$, $\Omega = \frac{\Omega^*D^*}{2W_\infty^*}$.

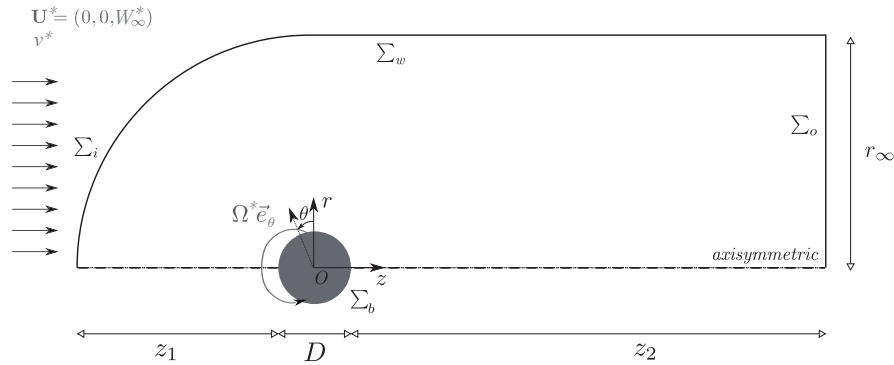


Figure IV.21 – Sketch of the problem and geometric configuration.

The incompressible Navier–Stokes equations (eq. (III.1)) are complemented with the following boundary conditions

$$\mathbf{U} = (0, \Omega, 0) \text{ on } \Sigma_b \quad \mathbf{U} = (0, 0, 1) \text{ on } \Sigma_i. \quad (\text{IV.17})$$

A no-slip boundary condition is set on the rotating sphere and a uniform boundary condition is set in the inlet, as shown in fig. IV.21.

Classification of solutions

In the following, the RHS of eq. (IV.15) is designated $\mathbf{f}(\mathbf{z})$ where $\mathbf{z} = (z_1, z_2, z_3)$. The reduced vector \mathbf{f} is equivariant under the action of the group

Name	Representative	Isotropy group (complex)	Frequencies
TS (Trivial state)	$(0, 0, 0)$	$SO(2) \times \mathbb{T}^3$	0
RW (Rotating wave)	$(r_a, 0, 0)$	$S(1, r, 0, 0) \times \mathbb{T}^2$	1
MM (Mixed mode)	$(r_a, r_b, 0)$	$S(1, r, l, 0) \times S^1$	2
IMM (Interacting mixed mode)	(r_a, r_b, r_c)	$\mathbf{1}$	3

Table IV.6 – Nomenclature and symmetry group (cf Sierra-Ausin, Lorite-Diez, et al., 2022) of fixed point solutions of the system eq. (IV.19).

$\Gamma \equiv SO(2) \times \mathbb{T}^3$, with the following action representation

$$\begin{aligned} \theta \cdot \mathbf{z} &\equiv (z_1 e^{i\theta}, z_2 e^{ir\theta}, z_3 e^{is\theta}) \\ (\psi_1, \psi_2, \psi_3) \cdot \mathbf{z} &\equiv (z_1 e^{i\psi_1}, z_2 e^{i\psi_2}, z_3 e^{i\psi_3}), \end{aligned} \quad (\text{IV.18})$$

where $l, r, s \in \mathbb{Z}$, $\theta \in [0, 2\pi)$ and $\psi_i \in [0, 2\pi)$ for $i = 1, 2, 3$. Here, (ψ_1, ψ_2, ψ_3) and θ are the representations in \mathbb{C}^3 of the actions of the group Γ , which correspond to the time-shift and rotational invariance, respectively. The substitution of the polar decomposition of $\mathbf{z} = \mathbf{r}e^{i\Phi}$, with $\mathbf{r} = (r_1, r_2, r_3)$ and $\Phi = (\phi_1, \phi_2, \phi_3)$, into eq. (IV.15) yields the following decoupled phase-amplitude system

$$\begin{aligned} \dot{r}_\ell &= r_\ell \left[\Lambda_\ell^R + \mathcal{V}_{\ell k}^R r_k^2 \right], \quad k, \ell = 1, 2, 3, \\ \dot{\phi}_\ell &= \Lambda_\ell^I + \mathcal{V}_{\ell k}^I r_k^2, \quad k, \ell = 1, 2, 3, \end{aligned} \quad (\text{IV.19})$$

where $\Lambda = \Lambda^R + \Lambda^I \equiv (\lambda_1, \lambda_2, \lambda_3)^T$ and the matrix $\mathcal{V} = \mathcal{V}^R + i\mathcal{V}^I$ is

$$\mathcal{V} \equiv \begin{pmatrix} \nu_{11} & \nu_{12} & \nu_{13} \\ \nu_{21} & \nu_{22} & \nu_{23} \\ \nu_{31} & \nu_{32} & \nu_{33} \end{pmatrix} \quad (\text{IV.20})$$

To ease the presentation of the fixed point solutions of eq. (IV.19), let us introduce the inverse of the linear operator \mathcal{V} , which can be written as

$$\mathcal{V}^{-1} = \frac{1}{\det \mathcal{V}} \begin{pmatrix} \det \mathcal{V}_{11} & \det \mathcal{V}_{21} & \det \mathcal{V}_{31} \\ \det \mathcal{V}_{12} & \det \mathcal{V}_{22} & \det \mathcal{V}_{32} \\ \det \mathcal{V}_{13} & \det \mathcal{V}_{23} & \det \mathcal{V}_{33} \end{pmatrix}, \quad (\text{IV.21})$$

where $\det \mathcal{V}_{k\ell}$ denotes the minor of the matrix \mathcal{V} , obtained by eliminating the line k and the column ℓ . In the following, the notation $\dot{\mathbf{r}} = \mathbf{f}^R(\mathbf{r})$ will be adopted to denote the amplitude equation of the nonlinear system eq. (IV.19). The remainder of this subsection will be devoted to the study of the three fixed-point solutions of eq. (IV.19).

Rotating waves correspond to the simplest non-trivial fixed point of eq. (IV.19), which in the original set of equations is a periodic solution. They arise as the result of a supercritical Hopf bifurcation of the steady state (named Trivial

Name of solutions	Definition	Eigenvalues
RW_i (for $i = 1, 2, 3$)	$r_i^{(RW)} = \sqrt{-\frac{\lambda_i^R}{\nu_{ii}^R}}$	$-\lambda_i^R,$ $\lambda_j^R - \nu_{ji}^R \frac{\lambda_i^R}{\nu_{ii}^R},$ for $j \neq i$
$MM_{ij}, (i, j = 1, 2, 3)$ $(j \neq i, k \neq i, k \neq j)$	$r_i^{(MM_{ij})} = \sqrt{\frac{\lambda_j^R \nu_{ij}^R - \lambda_i^R \nu_{ij}^R}{\det(\mathcal{V}_{kk})}}$ $r_j^{(MM_{ij})} = \sqrt{\frac{\lambda_i^R \nu_{ji}^R - \lambda_j^R \nu_{ii}^R}{\det(\mathcal{V}_{kk})}}$	$\frac{\nu_{ii}^R r_i^2 + \nu_{jj}^R r_j^2}{2} \pm \sqrt{(\nu_{ii}^R r_i^2 - \nu_{jj}^R r_j^2)^2 / 4 + \nu_{ij}^R \nu_{ji}^R r_i^2 r_j^2}$ $\frac{1}{\det(\mathcal{V}_{kk}^R)} [\lambda_k^R \det(\mathcal{V}_{kk}^R) + \lambda_i^R \det(\mathcal{V}_{ik}^R) + \lambda_j^R \det(\mathcal{V}_{jk}^R)]$
IMM_{123}	$(r_1^2, r_2^2, r_3^2)^T = -(\mathcal{V}^R)^{-1} \Lambda^R$	Eigs of $D\mathbf{f}^R$

Table IV.7 – Defining equations and eigenvalues of the solutions of the polar third order normal form eq. (IV.19).

State in table IV.6) and they may eventually bifurcate into mixed modes; the eigenvalues of rotating waves may be found in the first row of table IV.7. Mixed modes, defined in table IV.7, are the result of the interaction between two rotating waves, as the Modulated Waves (MW) of section 3. A mixed-mode has a representative in the normal form with two non-zero amplitude terms, thus they correspond to a T^2 -quasiperiodic state in the original system of equations. These states may experience two kinds of bifurcations. They may lose stability in the transversal direction or within their own subspace, these two conditions are listed in table IV.7. Eventually, a bifurcation in the transversal direction of a mixed-mode may be associated with the appearance of an interacting mixed mode (IMM_{123}) attractor. An interacting mixed mode corresponds to a T^3 -quasiperiodic state in the original system of equations, and it is represented by three non-zero amplitude terms. However, T^3 -quasiperiodic states are hardly observed in numerical simulations of dissipative systems, as it is the case of Navier-Stokes equations (eq. (III.1)), instead a chaotic attractor is usually observed (Newhouse et al., 1978).

Linear stability

The breaking of the reflection symmetry regarding the azimuthal angle induces the prevalence of rotating waves along the rotation of the sphere. Consequently, bifurcations that lead to standing waves or to a symmetry breaking steady state do not occur generically. The existence of standing waves or a steady state mode requires the matching between the phase speed of the helical pattern and the rotation of the body, which is another condition to be met. In our findings, within the parameter space $Re < 300$ and $\Omega < 4$, we have found the existence of three distinct types of rotating waves, named RW_1 , RW_2 and RW_3 , which are depicted in fig. IV.22. Linear stability results (fig. IV.23a) reveal that the axisymmetric steady state, referred in the following as Trivial State (TS), is stable in the white shaded region and unstable in the grey shaded region. The neutral curve of stability displays two regions in the parameter space (Re, Ω)

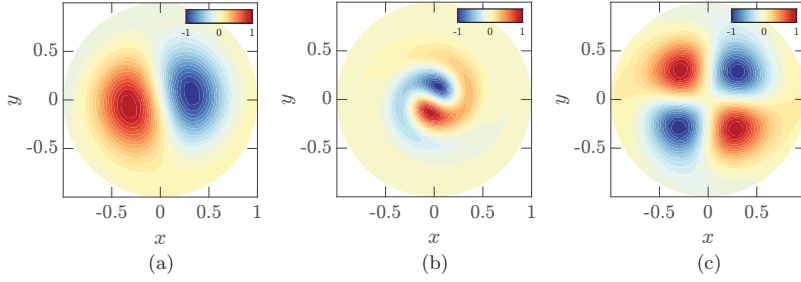


Figure IV.22 – Cross-section view at $z = 3.5$ of the three unstable modes. The streamwise component of the vorticity vector ϖ_z is visualised by colours. (a) RW_1 at point $(Re_A, \Omega_A) = (77, 2.24)$. (b) RW_2 at point $(Re_B, \Omega_B) = (188, 1.01)$. RW_3 at point (Re_A, Ω_A) .

for which the first primary bifurcations are rotating waves of low frequency (LF) where the wake past the sphere displays a single helix (RW_1), depicted in fig. IV.22 (a). In the second region, the flow pattern of the wake displays a double helix (RW_3) with a high frequency (HF), depicted in fig. IV.22 (c). The onset of instability of the third branch (RW_2) displaying a flow pattern of the wake with a single helix with a medium frequency (MF), depicted in fig. IV.22 (b), turns out to be linearly unstable for $\Omega \leq 4$. Each pair of neutral curves intersects once, leading to three codimension-2 points (A, B, C). Another aspect of importance is the evolution of frequencies of the instability. Frequencies at critical parameters are reported in fig. IV.23 (b) as a function of Ω . The frequency evolution is divided into two regions, a first of a rapid evolution for low rotation rates $\Omega < 1$ and a second one where the frequency of the three modes hardly depends on the rotation rate.

Bifurcation diagram at a constant rotation rate

Herein, we fix the rotation rate to a constant $\Omega = 1.75$. Let us assume that we have determined the normal form, following the procedure detailed in Sierra-Ausin, Lorite-Diez, et al. (2022). Bifurcation events are designated by their corresponding value of the Reynolds number, $Re_{state_a}^{state_b}$ where $state_a$ stands for the simplest state that exists before the bifurcation and $state_b$ stands for the resulting state after the bifurcation. In addition, the notation $Re_{state_a}^{\sigma_k, s}$ indicates a bifurcation of the $state_a$ where the eigenvalue σ_k ($k = 1, 2, 3$) has changed sign: s indicates stabilization and u indicates the change from stable to unstable of the referring eigenvalue/eigenmode pair. In the following, there is only a bifurcation of this kind, the one associated to the mixed mode MM_{12} that is stabilized/destabilized because of a change of sign of the eigenvalue in the transversal direction (r_3). Thus, we simplify the notation to $Re_{state_a}^s$ or $Re_{state_a}^u$.

Figure IV.24 displays the bifurcation diagram, with Reynolds number as

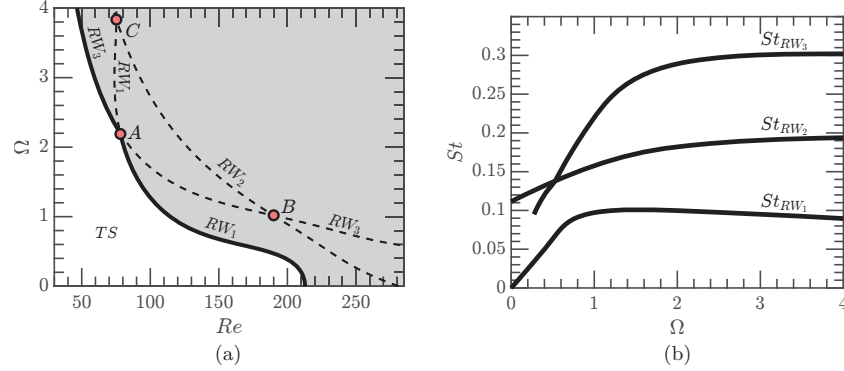


Figure IV.23 – Linear stability properties of the rotating sphere configuration. (a) Neutral curve of stability: the onset of the primary instability is portrayed with a solid black line (—), whereas the continuation of the neutral curves is depicted with dashed black lines (---). (b) Frequency evolution with respect to Ω of linear modes at the critical Reynolds number ($Re_c(\Omega)$).

the control parameter for $\Omega = 1.75$. There exist three primary bifurcations, i.e., bifurcations from the axisymmetric steady state, located at $Re_{TS}^{RW_1}$, $Re_{TS}^{RW_2}$ and $Re_{TS}^{RW_3}$, respectively. However, the RW_2 branch remains unstable all along the analysed interval. The first transition to occur is a supercritical Hopf bifurcation leading to the RW_1 solution, which is then followed by another supercritical Hopf bifurcation leading to RW_3 . For the range of Reynolds numbers $Re_{RW_1} < Re < Re_{RW_3}^{MM_{13}}$ there exists a single stable attractor, which corresponds to the limit cycle associated with the solution RW_1 . At $Re_{RW_3}^{MM_{13}}$ the RW_3 branch experiences a Neimark-Sacker bifurcation that results in the appearance of the mixed mode solution MM_{13} . In the interval $Re_{RW_3}^{MM_{13}} < Re < Re_{RW_1}^{MM_{13}}$ both primary solutions (RW_1 and RW_3) are stable under any arbitrary perturbation and in addition they are connected by the unstable mixed-mode MM_{13} , which is located on the separatrix of the basin of attraction of the two primary solutions (the phase portrait of this scenario is sketched in fig. IV.24 (b.1)). Eventually, the solution branch MM_{13} terminates at $Re = Re_{RW_1}^{MM_{13}}$, which makes RW_3 the single attractor of the system for the interval $Re_{RW_1}^{MM_{13}} < Re < Re_{RW_3}^{MM_{23}}$. The RW_3 branch eventually bifurcates into the mixed mode branch MM_{23} , which is a stable attractor within the interval $Re_{RW_3}^{MM_{23}} < Re < Re_{MM_{23}}^{MM_{123}}$. The other primary branch, the unstable RW_1 undergoes another Neimark-Sacker bifurcation at $Re_{RW_1}^{MM_{12}}$ which results into the existence of the MM_{12} branch, yet unstable for perturbations in the transversal direction of the mixed mode (in the r_3 direction). The MM_{12} mixed mode branch appears to be stable only within a small interval $Re_{MM_{12}}^s < Re < Re_{MM_{12}}^u$, where two bifurcations, which are associated to an instability in the transversal direction r_3 , occur at the two limit

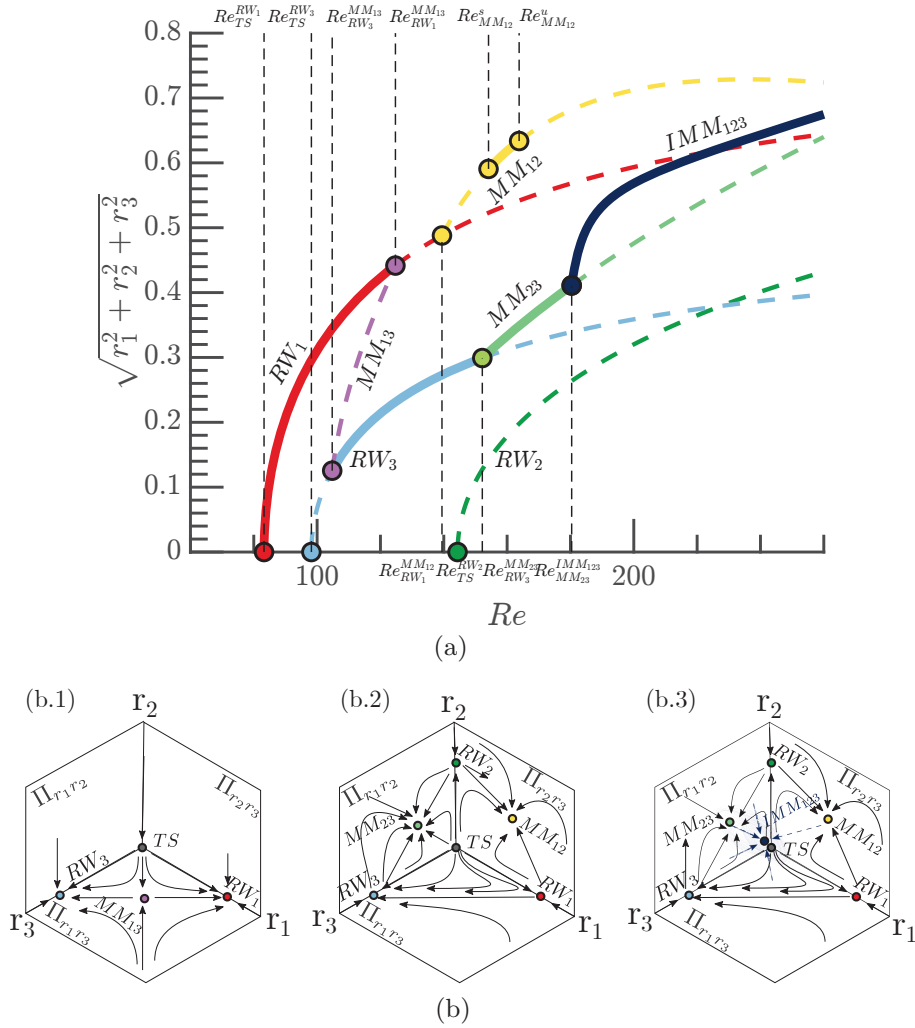


Figure IV.24 – (a) Transition scenario at $\Omega = 1.75$. Attractors are depicted with solid lines, whereas unstable invariant states are represented with dashed lines. (b) Schematic representation of phase portraits. (b.1.) Two stable rotating waves separated by a mixed mode solution. (b.2.) Two stable mixed modes. (b.3.) An interacting mixed mode attractor, the chaotic attractor that shadows the IMM_{123} is sketched in a lighter blue color..

values. We have employed s and u to denote the stable or unstable nature of MM_{12} regime. Thus, for $Re_{MM_{12}}^s < Re < Re_{MM_{12}}^u$ there is a second region with multiple stable attractors, which is schematically displayed in fig. IV.24 (b.2). The last bifurcation accounted by the normal form is the destabilisation of the MM_{23} branch at $Re = Re_{MM_{23}}^{IMM_{123}}$ that leads to the appearance of the IMM_{123} branch, whose phase portrait is sketched in fig. IV.24 (b.3). Please note that despite the fact that IMM_{123} is a fixed point solution of the normal form, the Newhouse-Takens-Ruelle theorem indicates that the original system of equations may exhibit a chaotic attractors shadowing the IMM_{123} solution. A systematic comparison of flow observables, such as the longitudinal and transversal forces, between normal form estimations and direct numerical simulations is discussed in Sierra-Ausin, Lorite-Diez, et al. (2022).

4.2

Resonant

This section is based on Sierra-Ausin and Giannetti (2023, Section 5). We consider the following normal form

$$\begin{aligned}
 \dot{r}_1 &= r_1 [\lambda_1^R + \nu_{11}^R r_1^2 + \nu_{12}^R r_2^2 + \nu_{13}^R r_3^2] + r_2^2 r_3 [\cos(\psi)\chi_1^R + \sin(\psi)\chi_1^I] \\
 \dot{r}_2 &= r_2 [\lambda_2^R + \nu_{21}^R r_1^2 + \nu_{22}^R r_2^2 + \nu_{23}^R r_3^2] + r_1 r_2 r_3 [\cos(\psi)\chi_2^R - \sin(\psi)\chi_2^I] \\
 \dot{r}_3 &= r_3 [\lambda_3^R + \nu_{31}^R r_1^2 + \nu_{32}^R r_2^2 + \nu_{33}^R r_3^2] + r_2^2 r_1 [\cos(\psi)\chi_3^R + \sin(\psi)\chi_3^I] \\
 \dot{\psi} &= \delta\omega + \cos(\psi) [-\chi_3^I r_1 r_2^2 / r_3 + 2\chi_2^I r_1 r_3 - \chi_1^I r_3 r_2^2 / r_1] \\
 &\quad - \sin(\psi) [\chi_3^R r_1 r_2^2 / r_3 + 2\chi_2^R r_1 r_3 + \chi_1^R r_2^2 r_3 / r_1].
 \end{aligned}
 \tag{IV.22}$$

Here, we use the notation $\psi = (\phi_3 - \phi_2) - (\phi_2 - \phi_1)$ for the resonant phase, $\delta\omega \equiv \delta\omega^L + \delta\omega^{NL}$ with $\delta\omega^L \equiv [\omega_1 + \omega_3 - 2\omega_2]$ for the linear frequency mismatch at neutrality, and the nonlinear frequency mismatch $\delta\omega^{NL} \equiv \Delta\omega_2^{NL} - \Delta\omega_1^{NL} = [\omega_1^{NL} + \omega_3^{NL} - 2\omega_2^{NL}]$, where $\omega_k^{NL} = \lambda_k^I + \nu_{k1}^I r_1^2 + \nu_{k2}^I r_2^2 + \nu_{k3}^I r_3^2$ for $k = 1, 2, 3$. The upper scripts R and I are used to denote the real and imaginary part of the coefficient. The details about the computation of the coefficients of the normal form, and the numerical modelling may be found in Sierra-Ausin and Giannetti (2023, Section 2, Appendix B)

We analyse the solutions of eq. (IV.22) in the presence of resonant coupling, the phase-locked transition from a resonant quasiperiodic state to a modulated three frequency state with a small frequency modulation. The new modulating frequency, being proportional to the imperfections in the frequency quantization ($\delta\omega^{NL}$), is expected to induce a transition to a chaotic attractor, following the route to chaos suggested by Ruelle–Takens–Newhouse, when this new frequency is of the order of the frequency difference between two modes, e.g., $\Delta\omega_1^{NL}$.

Stochastic modelling

Ruelle–Takens–Newhouse (Newhouse et al., 1978) state that one may obtain a chaotic Axiom A attractor by perturbing a three-tori solution, with a given arbitrarily small perturbation. However, it fails to provide the precise route to chaos, which may occur following a torus breakdown (Tanaka, 2005), which occurs because of the loss of smoothness of the two or three tori attractors (Marques et al., 2001). In order to account for the loss of smoothness of the system, we replace

$$\delta\omega^{NL} \mapsto \delta\omega^{NL}(1 + dW_t),$$

with dW_t a differential Wiener process and a constant $\delta\omega^{NL}$ determined by integrating eq. (IV.22). That is, we replace the equation for the resonant phase by

$$\begin{aligned} d\psi &= \delta\omega^L dt + \delta\omega^{NL}(dt + dW_t) \\ &+ \left(\cos(\psi) \left[-\chi_3^I r_1 r_2^2 / r_3 + 2\chi_2^I r_1 r_3 - \chi_1^I r_3 r_2^2 / r_1 \right] \right) dt \\ &- \left(\sin(\psi) \left[\chi_3^R r_1 r_2^2 / r_3 + 2\chi_2^R r_1 r_3 + \chi_1^R r_2^2 r_3 / r_1 \right] \right) dt. \end{aligned} \quad (\text{IV.23})$$

The model is essentially similar to the following case of multiplicative noise with respect to the polar amplitudes on the resonant phase. Consider the mapping

$$\nu_{ij}^I \mapsto \nu_{ij}^I (1 + dW_t^{ij}) \text{ and } \lambda_i^I \mapsto \lambda_i^I (1 + dW_t^i),$$

which leads to

$$\begin{aligned} \delta\omega^{NL} \mapsto & \delta\omega^{NL} + (dW_t^1 + dW_t^3 - 2dW_t^2) \\ & + \left(\sum_{j=1}^3 \nu_{1j}^I r_j^2 dW_t^{1j} \right) + \left(\sum_{j=1}^3 \nu_{3j}^I r_j^2 dW_t^{3j} \right) \\ & - 2 \left(\sum_{j=1}^3 \nu_{2j}^I r_j^2 dW_t^{2j} \right). \end{aligned} \quad (\text{IV.24})$$

The substitution of eq. (IV.24) into eq. (IV.22) leads to eq. (IV.23) when the value of the polar amplitudes is fixed, leading to a one-way coupling. Herein, we choose such a model for simplicity; the proposed model fixes the value of $\delta\omega^{NL}$ and accounts for the uncertainty with an additive noise term.

This phenomenological modelling is based on the fact that the sources of sound responsible for the closure of the feedback become less coherent with decreasing Mach number, which is described in Sierra-Ausin and Giannetti (2023, Section 3 and 4). Such a modelling is faithful with the deterministic normal form eq. (IV.22) in the mean sense, that is, $\mathbb{E}(\delta\omega^{NL}(1 + dW)) = \delta\omega^{NL}$. At low subsonic Mach number, the increase of $\delta\omega^{NL}$ is caused by the elongated nature of the wavemaker, which enables the existence of sources of vortex sound at distinct spatial locations. Each of these sources it is associated with a distinct fundamental frequency $\Delta\omega$, which is inversely proportional to the convective

time it takes for the hydrodynamic perturbations to reach the source of vortex sound at the wavemaker and to the acoustic time it takes for the perturbation to reach back to the lip of the nozzle. Therefore, providing a phenomenological interpretation to the increase of the modulation frequency with a decreasing Mach number. Thus, the transition to a broadband spectrum can be interpreted as the consequence of the loss of coherence of the feedback process and the fact that the levels of the acoustic pressure decrease with decreasing Mach number. The latter effect is attributed to the fact that with decreasing Mach number, the production of the divergence of velocity field is reduced, which occurs mostly within the jet and near the wall. Additionally, the propagation of the guided jet wave becomes less effective with decreasing Mach number, because of the increase of its wavelength.

Resonant – An example of broadband and tonal noise

At low Mach numbers, a broadband spectrum characterises the dynamical attractor. Figure IV.25 (a) displays the spectrum obtained from axisymmetric numerical simulations, which is displayed with red, blue and black solid lines for pressure probes at an axial location $z = 0$ and a radial position $r = 1D$, $r = 2D$ and $r = 4D$, respectively. This type of dynamics is *modelled* by a periodic solution (MMdM) of the normal form eq. (IV.22), which is a three-tori solution in the original coordinates of the ansatz eq. (IV.14). The Modulated Mixed drift Wave possesses a modulation frequency $\omega' \approx \Delta\omega$, i.e., the modulation frequency has a similar magnitude to the frequency difference between the other two dominant frequencies. In that scenario, the original dynamics of the Navier–Stokes equations¹ are expected to be chaotic with a broadband spectrum. However, fig. IV.25 (a) shows a tonal spectrum (yellow line), which has been obtained from the deterministic normal form. Such a feature is characteristic of this particular type of normal form, and it is a pathological property of the truncation. Instead, when considering the stochastic model with $\delta\omega \approx 0.1$, one obtains a spectrum (green line) which offers a considerably better comparison with respect to the data of the axisymmetric simulation. In this case, the spectrum displays a wide peak of small magnitude around f_1 and f_2 , and a broadband spectrum with a similar slope to the numerical results (red line). Though the matching is not perfect, the ratio between the peak and the broadband levels is slightly larger in the deterministic model, which suggests a higher degree of stochasticity of the axisymmetric numerical simulation. The difference may be explained from the fact that the axisymmetric numerical simulations allow for a vortical feedback. Vortices emitted by the roll-up of the radial shear layer near the wall and outside the jet are propagated towards the lip. These vortices are

¹Herein, we have simulated the axisymmetric Navier–Stokes equations, which provide a similar qualitative picture (broadband or tonal spectrum) to the three-dimensional high Reynolds number flows.

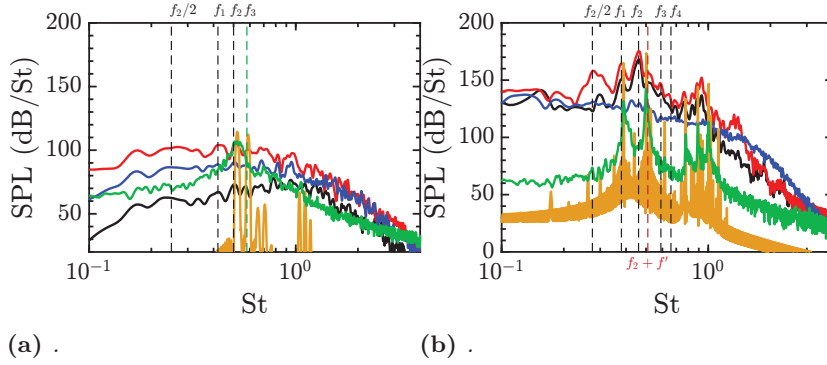


Figure IV.25 – (a) Sound pressure levels at $M_\infty = 0.3$, $Re = 2000$. Probes of instantaneous pressure fluctuations at the axial location $z = 0$ and radial positions $r = 1D$ (red - axisymmetric time-stepping, yellow - deterministic normal form, green stochastic normal form with $\delta\omega = 0.1$), $r = 2D$ (black - axisymmetric time-stepping) and $r = 4D$ (dark blue - axisymmetric time-stepping). The vertical dashed lines highlight the frequencies of the peaks obtained with the axisymmetric time-stepping simulation. (b) Sound pressure levels at $M_\infty = 0.3$, $Re = 2000$. Same legend as (a).

produced aperiodically in a chaotic region of the flow, and they reach the lip of the nozzle, triggering the shear layer instability. Such a feature is strongly nonlinear, and it is not accounted by the normal form. A possible correction to the stochastic model would consist in the inclusion of a diffusion coefficient $\sqrt{D_{\text{eff}}}$ in $\delta\omega(1 + \sqrt{D_{\text{eff}}}dW)$, and thus determine the effective diffusion from the fitting of numerical or experimental data (Callaham et al., 2021).

At large Mach numbers, the dynamical attractor is characterized by a tonal spectrum with large peaks at discrete frequencies. This type of dynamics is modelled by a fixed-point (MrW) or a periodic solution (MMdW) of the normal form eq. (IV.22). In this case, the modulation frequency of the Modulated Mixed resonant Wave is smaller than the frequency difference between the modes ($\omega' \ll \Delta\omega$). In that scenario, the spectrum of the Navier–Stokes equations is expected to be weakly tonal with wide and large magnitude peaks. In this case, the deterministic normal form offers a good qualitative description of the spectrum, it is able to identify the main frequency peaks and the frequency modulation f' . The frequency modulation obtained from numerical simulations is $f'_{DNS} \approx 0.05$, while the frequency modulation from the normal form is $f' \approx 0.04$. Additionally, as in the broadband case, we compare in fig. IV.25 (b) the results of the axisymmetric numerical simulation (red line) with those of the deterministic normal form (yellow line) and the stochastic model (green line). It shows a reasonable comparison, though the sound pressure levels are underestimated. Additionally, since the model is weakly nonlinear, it fails to predict the existence

of a peak at $f_2/2$, which occurs because of a secondary instability of the radial shear layer. Inspection of the numerical results suggests that such a frequency peak occurs because of a vortex-pairing instability of the radial shear layer (Shaabani-Ardali et al., 2019).

Conclusions and outlook

1

Conclusions

1.1

Mode interaction

In this thesis, we have systematically studied cases of fluid instabilities displaying mode interaction. One of the objectives of this dissertation has been to establish a connection between the fluid instabilities and the patterns or coherent structures of the flow. In that sense, one may consider the organising centre of the bifurcation problem to be a kind of weakly non-linear class, that is universal for some types of instabilities.

Under that consideration, in the absence of an equivariance condition, that is, a symmetry property, of the governing equations the Hopf-Hopf or triple Hopf

organising centre (section 4) is the most common type of weakly-non linear class of flows that one may encounter. Thus, it is expected to be of relevance for flow configurations without any continuous nor discrete symmetry. This kind of organising centre corresponds to the Ruelle-Takens-Newhouse route to chaos. However, even in this (simple) case, this is not the whole story. As it has been evidenced in section 4, the core of the instability may be localised in space, or it may lie along an extended region of the flow. The oscillating instabilities of the flow past bluff bodies are usually of the first type, whereas many flow configurations with a convective unstable shear layer, for example: cavity flows, some cases of flow past an airfoil, impinging jets or screeching jets, are found to be of the second type. The instability of the second type is said to be due to a non-local feedback loop. The fact that the core of the instability is not localised in space may have important consequences for the spectrum of the baseflow. The spectrum may display a family of discrete modes with nearly equidistant frequencies, suggesting a frequency selection criterion based on the properties of the feedback loop. Thus, any reduced equation describing the dynamics of these flows shall account for the (weakly-)¹resonant conditions arising from the linear frequencies of the modes in the spectrum.

The flow instability behind a spinning cylinder exemplifies another type organising centre: a focus Takens-Bogdanov bifurcation. It corresponds to a degenerate case of the Takens-Bogdanov bifurcation. This organising centre is the simplest scenario accounting for an intersection of Hopf and saddle-node lines, and the existence of an odd number of steady-states. In the classical Takens-Bogdanov bifurcation, there are only regions in the parameter space with an even number of steady-states. The existence of three co-existing steady-states due to two successive saddle-node bifurcations, provides a clear evidence of a near-cusp bifurcation. Such a dynamical scenario might be more general than it seems. When considering a laminar configuration, if there is a fold bifurcation, one would expect at least another fold. Why? The governing equations simplify to the Stokes equations when the Reynolds number tends to zero, these equations are linear and with unique solution. Therefore, a fold bifurcation at a low Reynolds number necessarily implies the existence of a second fold, otherwise we would have two steady-state solutions when the Reynolds number tends to zero, which is impossible. This reasoning suggests that the focus Takens-Bogdanov is almost a codimension-three bifurcation, and that the third condition is nearly satisfied by some mild regularity properties of the equations. Vaguely, such a flow displays a Takens-Bogdanov instability due to the competition between the instability of the shear layer inducing the von Kármán street and the spin of the cylinder, which tends to reduce the frequency of the instability.

In the presence of continuous symmetries, we have analysed two axisymmetric

¹We use here the word *weakly* to include situations where the resonant condition is nearly satisfied, but not in a strict sense.

configurations: the steady-Hopf (section 3) and steady-steady (1:2) (section 2) organising centres. The first arises in many flow configurations, such as the wake flow past an axisymmetric bluff body or the flow/path instabilities of rising/-falling objects or bubbles. The second has been experimentally and numerically Nore, Tuckerman, et al., 2003; Nore, Moisy, et al., 2005 in a Von Kármán flow, and leads to robust heteroclinic cycles, which can be assumed to be the simplest example of a Self-Sustaining-Process (SSP).

1.2

Compressible flows – Acoustics

In the thesis, we have considered two canonical flow configurations. First, we have considered the whistling potentiality of a jet flow through a hole in Sierra-Ausin, Fabre, Citro, et al. (2022), which is a canonical configuration to study the sound emitted by humans. Second in Sierra-Ausin and Giannetti (2023) we analyse the properties of the hydrodynamic-acoustic feedback-loop underpinning the tonal and broadband sound emissions of a rounded subsonic impinging jet. In this second work, we propose a novel decomposition of the structural sensitivity map for instabilities supported by an acoustic-hydrodynamic feedback.

For both compressible problems, the design of non-reflecting boundary conditions is delicate, and we introduced a novel complex-mapping technique (Sierra-Ausin, Javier, Fabre, and Citro, 2020) for this purpose. The instability of the jet flow through an orifice has been analysed in terms of the zeros of the transfer function of the system, the impedance. The numerical continuation of the emerging limit cycles has been carried out via a fixed-point method (Sierra-Ausin, Javier, Jolivet, et al., 2021; Sierra-Ausin, Javier, Citro, Giannetti, et al., 2022), which is preferred over a time-integration scheme due to the time-step constraints at low Mach number.

1.3

Moving interfaces

We have analysed two flow configurations having a moving interface. First the vortex-induced vibration by a single and a pair of spring-mounted, damped, rigid circular cylinder, immersed in a Newtonian viscous flow and capable of moving in the direction orthogonal to the unperturbed flow is analysed with a linearised diffusive immersed boundary method in Tirri et al. (2023). Second, in Sierra-Ausin, Bonnefis, et al. (2022) we study linear stability of a bubble suspended in an axisymmetric uniaxial straining flow with a linearised ALE approach.

Perspectives

In each of the manuscripts, we discuss perspectives of possible future works. Herein, we suggest some directions of research that are of interest in the author's view.

The systematic analysis of the organising centres discussed in the dissertation could be extended also to analyse the qualitative properties of the phase space with data assimilation and optimisation techniques. A promising perspective for future works could be the extension of the work carried out by Cenedese et al. (2022) to account for *outer-resonance* conditions, which in our nomenclature are resonance conditions. In this direction, it would be also of great interest to derive a stochastic centre-like manifold for systems far from equilibrium. Such a description would directly connect with ideas of spontaneous stochasticity and the diffusion of information by performing a coarse graining in systems with a large number of chaotic degrees of freedom (Wouters et al., 2017; Schmuck et al., 2013).

Another interesting perspective is the combination of the methodology of mode-interaction in the study of problems with a moving interface. For instance, the bifurcation analysis of the steady-Hopf bifurcation can be applied directly to the case of a rising bubble in an unbounded domain. The extension, however, is not trivial since it involves the linearisation of the ALE procedure at each order of the multiple-scales expansion. Similarly, the mode interaction between two oscillating instabilities can be directly applied to the VIV instability of several cylinders in tandem or aligned.

Finally, the identification of the active regions of the flow when the instability core is not localised in space may be extended to study instabilities issued of a non-local hydrodynamic feedback-loop, that is, due to the instant effect of the pressure to impose the incompressibility condition, to thermo-acoustic instabilities in combustion applications and to instabilities underpinned by a mechanism due to the coupling between deformation of the interface and the flow.

Part B

Articles

CHAPTER VI

Articles – Mode interaction

Bifurcation scenario in the two-dimensional laminar flow past a rotating cylinder

J. Sierra^{1,2}, D. Fabre¹, V. Citro² and F. Giannetti^{2,†}

¹Institut de Mécanique des Fluides de Toulouse (IMFT), Toulouse 31400, France

²Dipartimento di Ingegneria Industriale (DIIN), Università degli Studi di Salerno, Fisciano 84084, Italy

(Received 14 January 2020; revised 19 June 2020; accepted 12 August 2020)

The aim of this paper is to provide a complete description of the bifurcation scenario of a uniform flow past a rotating circular cylinder up to $Re = 200$. Linear stability theory is used to depict the neutral curves and analyse the arising unstable global modes. Three codimension-two bifurcation points are identified, namely a Takens–Bogdanov, a cusp and generalised Hopf, which are closely related to qualitative changes in orbit dynamics. The occurrence of the cusp and Takens–Bogdanov bifurcations for very close parameters (corresponding to an imperfect codimension-three bifurcation) is shown to be responsible for the existence of multiple steady states, as already observed in previous studies. Two bistability regions are identified, the first with two stable fixed points and the second with a fixed point and a cycle. The presence of homoclinic and heteroclinic orbits, which are classical in the presence of Takens–Bogdanov bifurcations, is confirmed by direct numerical simulations. Finally, a weakly nonlinear analysis is performed in the neighbourhood of the generalised Hopf, showing that above this point the Hopf bifurcation is subcritical, leading to a third range of bistability characterised by both a stable fixed point and a stable cycle.

Key words: bifurcation

1. Introduction

The flow past a circular cylinder is a classical configuration which has been widely adopted in the fluid dynamics community as a canonical model to investigate vortex shedding behind bluff bodies. In the case of a fixed cylinder, i.e. without rotation, the dynamics and the corresponding bifurcations are well known (Williamson 1996). The case of a rotating cylinder, which has implications for flow control using wall motion (Modi 1997; el Hak 2000), has recently received attention. A number of numerical studies in a two-dimensional framework have been conducted (Kang, Choi & Lee 1999; Stojković, Breuer & Durst 2002, 2003; Mittal 2004) and have revealed the existence of several steady and unsteady regimes. Linear stability approaches (Pralits, Brandt & Giannetti 2010; Pralits, Giannetti & Brandt 2013) have shown the existence of two separated regions

† Email address for correspondence: fgiannetti@unisa.it

of instability in the (Re, α) plane, where α is the dimensionless rotation rate and Re is the Reynolds number. The so called Mode I becomes unstable via a supercritical Hopf bifurcation and it is present for $0 \leq \alpha \leq 2$. This mode is the one associated with the classical Bénard–von-Kármán vortex street, and characterised by the alternate shedding of vortices of opposite sign. At higher rotation rates, around $4.5 \leq \alpha < 6$ another unsteady mode exists, denoted as Mode II. The physical mechanism driving this mode is rather different, as it corresponds to a slow-frequency shedding of vortices with the same vorticity sign. Its onset is less well characterised than Mode I from the point of view of bifurcation theory: the fact that the frequency is very low suggests a more complex bifurcation scenario and its supercritical or subcritical nature is still unclear. The full characterisation of Mode II is complicated by the fact that, in approximately the same range of (Re, α) parameter space, a region where three steady-state solutions coexist has been evidenced (Pralits *et al.* 2010; Rao *et al.* 2013a). A more thorough characterisation of this phenomenon has been carried out by Thompson *et al.* (2014) who observed that the region of existence of multiple steady-state solutions grows with the Reynolds number. Note also that the picture is further complicated by the existence of three-dimensional (3-D) instabilities in this range. This point is outside of the range of the present paper which restricts to 2-D dynamics, but a brief review on 3-D stability properties of this flow can be found in [appendix E](#).

To explain the existence of multiple steady states, Rao *et al.* (2013a) conjectured that they emerge from a cusp bifurcation point. Indeed, a cusp correctly explains the change in the number of steady states from one to three. However, a cusp is not generally associated with the existence of a Hopf bifurcation in the same range of parameters, so it cannot explain, alone, all the features discussed above. The fact that the frequency of Mode II is very small is an indicator of a second kind of codimension-two bifurcation, namely a O^2 or Takens–Bogdanov bifurcation (Kuznetsov 2013, chapter 8, p. 314) This bifurcation typically occurs when the frequency of a limit cycle vanishes. However, in the vicinity of a standard Takens–Bogdanov bifurcation, only two steady states generally exist, not three. This combination of features suggests that the picture could hide a codimension-three bifurcation point, also known as a generalised Hopf bifurcation. The unfolding of this generalised Takens–Bogdanov bifurcation has been studied by Dumortier *et al.* (2006) and Kuznetsov (2005) from a mathematical point of view, but to our knowledge such a feature has not yet been evidenced in a fluid dynamics system such as the one considered here.

The main purpose of the present work is to review the classification of the possible 2-D states in the $(Re, \alpha) \in [0, 200] \times [0, 10]$ parameter plane with the point of view of dynamical system theory. Firstly, we will characterise the nature of the codimension-one bifurcation curves (Hopf or saddle nodes). We give a cartography of the regions where multiple steady states exist and give a detailed description of these multiple states as well as their stability properties. We further identify three codimension-two points, namely a Takens–Bogdanov (TB) bifurcation, a cusp and a generalised Hopf (GH) bifurcation. We show that the two first are effectively located very close to each other and that the whole dynamics in this range of parameters is effectively described by the unfolding of a codimension-three bifurcation point.

The article is organised as follows: in § 2 the formulation of the problem is discussed together with the methodology adopted in the present analysis. Section 3 begins with a characterisation of the multiple steady states. A complete bifurcation diagram covering the range $(Re, \alpha) \in [0, 200] \times [0, 10]$ is then presented. The next subsections aim at clarifying the picture in the vicinity of the identified codimension-two points.

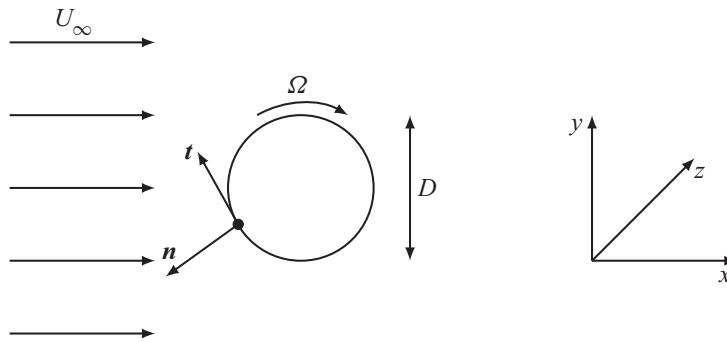


FIGURE 1. Sketch of a rotating cylinder immersed in a uniform flow.

2. Problem formulation and investigation methods

2.1. Geometrical configuration and general equations

The two-dimensional flow past a rotating circular cylinder is controlled by two parameters: the Reynolds number $Re = U_\infty D/\nu$ and the rotation rate $\alpha = \Omega D/2U_\infty$. Here, Ω is the dimensional cylinder angular velocity, U_∞ is the free stream velocity, D the diameter of the cylinder and ν the dynamic viscosity of the fluid. The fluid motion inside the domain is governed by the two-dimensional incompressible Navier–Stokes equations,

$$\frac{\partial \mathbf{U}}{\partial t} + \mathbf{U} \cdot \nabla \mathbf{U} = -\nabla P + \nabla \cdot \boldsymbol{\tau}(\mathbf{U}), \tag{2.1a}$$

$$\nabla \cdot \mathbf{U} = 0, \tag{2.1b}$$

where \mathbf{U} is the velocity vector whose components are (U, V) , P is the reduced pressure and the viscous stress tensor $\boldsymbol{\tau}(\mathbf{U})$ can be expressed as $\nu(\nabla \mathbf{U} + \nabla \mathbf{U}^T)$. The incompressible Navier–Stokes equations (2.1) are complemented with the following boundary conditions: on the cylinder surface, no-slip boundary conditions are set by $\mathbf{U} \cdot \mathbf{t} = \Omega D/2$ and $\mathbf{U} \cdot \mathbf{n} = 0$, where (\mathbf{t}, \mathbf{n}) are the director vectors of the surface in the plane (x, y) ; in the far field, uniform boundary conditions are set $\mathbf{U} \rightarrow (U_\infty, 0)$ when $r \rightarrow \infty$, where r is the distance to the cylinder centre (see figure 1). In the discussion we consider clockwise rotation of the cylinder surface ($\alpha > 0$).

In the following, Navier–Stokes equations (2.1) and the associated boundary conditions will be written symbolically under the form $\mathcal{B}(\partial \mathbf{Q}/\partial t) = \mathcal{N}\mathcal{S}(\mathbf{Q})$, where $\mathbf{Q} = (\mathbf{U}, P)$ is the state vector and \mathcal{B} is a linear projection operator, meaning that the time derivatives apply only on the velocity components.

2.2. Linear stability analysis

Under the framework of linear stability analysis, we first need to identify base-flow solutions defined as the steady solutions \mathbf{Q}_b of the (two-dimensional) Navier–Stokes equations, namely the solutions of $\mathcal{N}\mathcal{S}(\mathbf{Q}_b) = 0$. We then characterise the dynamics of small-amplitude perturbations around this base flow by expanding them over the basis of linear eigenmodes, i.e.

$$\mathbf{Q}(x, y, t) = \mathbf{Q}_b(x, y) + \epsilon \sum_j \hat{\mathbf{q}}_j(x, y) \exp(\lambda_j t). \tag{2.2}$$

Here, ϵ is a small parameter, λ_j the eigenvalues and \hat{q}_j the eigenmodes. The eigenpairs $[\lambda_j, \hat{q}_j]$ have to be determined as the solutions of the following eigenvalue problem:

$$\lambda \hat{u} + \mathbf{u}_b \cdot \nabla \hat{u} + \hat{u} \cdot \nabla \mathbf{u}_b = -\nabla \hat{p} + \nabla \cdot \boldsymbol{\tau}(\hat{u}) \quad (2.3a)$$

$$\nabla \cdot \hat{u} = 0. \quad (2.3b)$$

Which will be written in the following under the symbolic form $\lambda_j \mathcal{B} \hat{q}_j + \mathcal{LNS} \hat{q}_j = 0$. In the following we consider that eigenmodes $\hat{q}(x, y)$ have been normalised, see [appendix C](#) for further details. Note that in (2.2), to fully represent the dynamics, the summation over eigenmodes may involve a continuous sum over the spectrum, i.e. the discrete and the continuous or essential spectra of the operator (see Kapitula & Promislow (2013) for a rigorous discussion). However, to determine global stability we only need to consider a limited number of eigenmodes, so we keep the summation as a discrete sum indexed by j .

Owing to the eigenvalues, two cases can be distinguished:

- (i) If all eigenvalues λ_j have negative real part the considered base flow is a stable solution.
- (ii) If n eigenvalues have positive real part, the considered base flow will be referred to as a n -unstable solution. Note that 1-unstable solutions are commonly referred to as saddle points because a projection of their dynamics in a 2-D plane (phase portrait) has an attractive direction and another repulsing one, while 2-unstable solutions are either unstable nodes or unstable foci depending if the leading eigenvalues are both real or complex conjugates.

The transition from stable to unstable (or from n -unstable to $n + 1$ -unstable) is called a local bifurcation. The simplest bifurcations (such as saddle nodes and Hopf) are said to be codimension-one and occur along given curves in the parameter plane (Re, α). The intersection of two such curves tangentially is called a codimension-two bifurcation and generally leads to a rich dynamics in the vicinity of the intersection point.

2.3. Notions of bifurcation theory

From the viewpoint of dynamical system theory, the expression (2.2) can be generalised as a decomposition of the perturbations over the leading modes of the system

$$\mathcal{Q}(x, y, t) = \mathcal{Q}_b(x, y) + \sum_j A_j(t) \hat{q}_j(x, y). \quad (2.4)$$

Then, the problem can be reduced to a low-dimensional system governing the amplitudes $A_j(t)$

$$\frac{d}{dt} A_j = \lambda_j A_j + (NL), \quad (2.5)$$

where (NL) represent the nonlinear interactions between modes. Investigation of these nonlinear terms allows us to predict the dynamics in the vicinity of bifurcation points. Systematic methods exist to compute these nonlinear terms (such as weakly nonlinear expansions, centre manifold reduction or Lyapunov–Schmidt reduction). However, restricting ourselves to a qualitative point of view (up to a continuous change of coordinates with continuous inverse), it is also possible to predict a number of features by examining the generic normal form of the bifurcation, namely, a standard form to which the dynamical system can be reduced by a series of elementary manipulations

(see Wiggins (2003) for details). Particular forms of codimension-two bifurcations encountered in the rotating cylinder are discussed in §§ 3.5 and 3.6.

2.4. Numerical methodology

In the present manuscript, we adopt the same numerical methodology used in Fabre *et al.* (2020) and described in Fabre *et al.* (2019). The computation of the steady-state solutions, the resolution of the linear problems and the time stepping techniques are implemented using the open-source finite element software FreeFem++. Parametric studies and generation of figures are performed using Octave/Matlab thanks to the generic drivers of the StabFem project (see a presentation of these functionalities in Fabre *et al.* 2019). According to the philosophy of this project, codes reproducing parts of the results of the present paper are available from the StabFem website (<https://gitlab.com/stabfem/StabFem>). On a standard laptop, all the computations discussed below can be obtained in a few hours, except time stepping simulations which take longer. Results presented in § 3 are obtained with a computational domain $L_x = 120$ and $L_y = 80$ in the streamwise and cross-stream directions, respectively. The cylinder centre is located 40 diameters downstream of the inlet, symmetrically between the top and bottom boundaries. Numerical convergence issues are discussed in appendix D by a meticulous comparison between results obtained with different meshes, where domain dimension and grid density were varied.

Steady nonlinear Navier–Stokes equations are solved by a Newton method. In the degenerated cases, pseudo-arc length continuation is performed to be able to compute multiple steady-state solutions, as described in appendix A. The generalised eigenvalue problem (2.3) is solved by the Arnoldi method or by a simple inverse iteration algorithm. Finally, nonlinear unsteady Navier–Stokes equations are integrated forward in time with a second-order time scheme (Jallas, Marquet & Fabre 2017).

3. Results

3.1. Characterisation of multiple steady-state solutions

To introduce the existence of multiple steady states, we first characterise them by plotting in figure 2 the associated lift as function of the rotation rate α , for four different values of α . In these plots, stable solutions are indicated by continuous lines and unstable ones by dashed lines, following the usual convention in dynamical systems theory.

For $Re = 60$, as illustrated in figure 2(a), only one steady state exists for all values of α , for $Re = 60$. This state is stable except in the ranges $\alpha \lesssim 2$ (corresponding to the existence of Mode I), and $5.2 \lesssim \alpha \lesssim 5.5$ (corresponding to the existence of Mode II).

For higher Reynolds numbers, a small region of multiple solutions arises in a small-scale interval around $\alpha \approx 5$. This phenomenon is illustrated in figure 2(b) for $Re = 100$ and is associated with an ‘s’ shape of the curve, featuring two successive folds. Note that, before the first fold, the steady solution is 2-unstable (focus type); at the first fold it turns into 1-unstable (saddle type) and at the second fold it turns into stable. To detect these folds, pseudo-arc length continuation is carried out with α as a parameter and the horizontal force exerted on the cylinder surface F_x as a monitor to track and distinguish multiple steady states (see appendix A for a more detailed discussion).

For larger values of the Reynolds number, as illustrated in figure 2(c) for $Re = 170$, the interval of existence of multiple states for $\alpha \approx 5$ expands to $\alpha \in [4.75, 5.12]$. In addition, we observe a second range displaying multiple states for $\alpha > 5.87$. This second interval is associated with a fold bifurcation at $\alpha = 5.87$, giving rise to two additional and

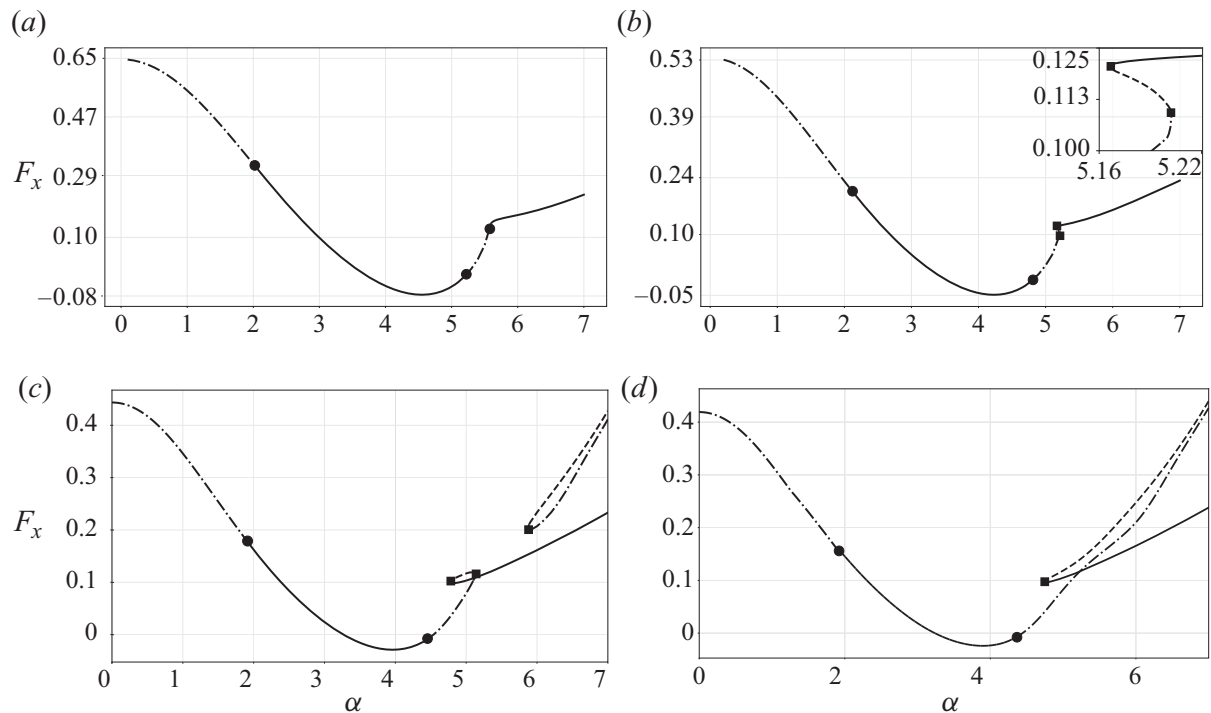


FIGURE 2. Evolution of the horizontal force F_x as a function of the rotation rate α for four Reynolds numbers, (a) $Re = 60$, (b) $Re = 100$, (c) $Re = 170$ and (d) $Re = 200$. Solid lines — denote stable steady states, dashed-dotted lines -.-.- denote unstable steady states of focus type or nodes, dashed lines --- are used for steady states of saddle type. Solid circles • denote Hopf bifurcations and solid squares ■ denote saddle-node bifurcations.

disconnected steady solutions. Note that both these solutions are unstable, respectively of node and saddle types.

Finally, for $Re = 200$, as illustrated in figure 2(d), we observe that the two ranges of multiple steady states are merged into a single one. In this case there is a single saddle-node bifurcation around $\alpha = 4.75$ leading to two branches of steady states which are disconnected from the branch existing for lower values of α . Here, one of these branches is stable and the second is unstable (saddle type).

3.2. Topological description of steady-state solutions

We now illustrate the spatial structure of some steady-state solutions, with emphasis on the topological structure of the corresponding flows. We restrict ourselves to the case $Re = 200$, as previously considered in figure 2(d).

Figure 3(a) corresponds to $\alpha = 1.8$, the value at which Mode I is re-stabilised. The corresponding flow is characterised by a stagnation point located beneath the cylinder axis, on the left side of the y -cylinder axis. Compared to the steady flow in the non-rotating case, which is characterised by a symmetrical recirculation region, the upper recirculating bubble is reduced whereas the lower one is moved downwards.

Further increasing the rotation speed, both recirculation bubbles shrink and eventually vanish. At $\alpha = 4.35$ (figure 3b) corresponding to the lower threshold for the existence of Mode II, recirculating bubbles have already disappeared and the vorticity wraps the cylinder. Stagnation point is located on the opposite side but downstream the cylinder vertical axis.

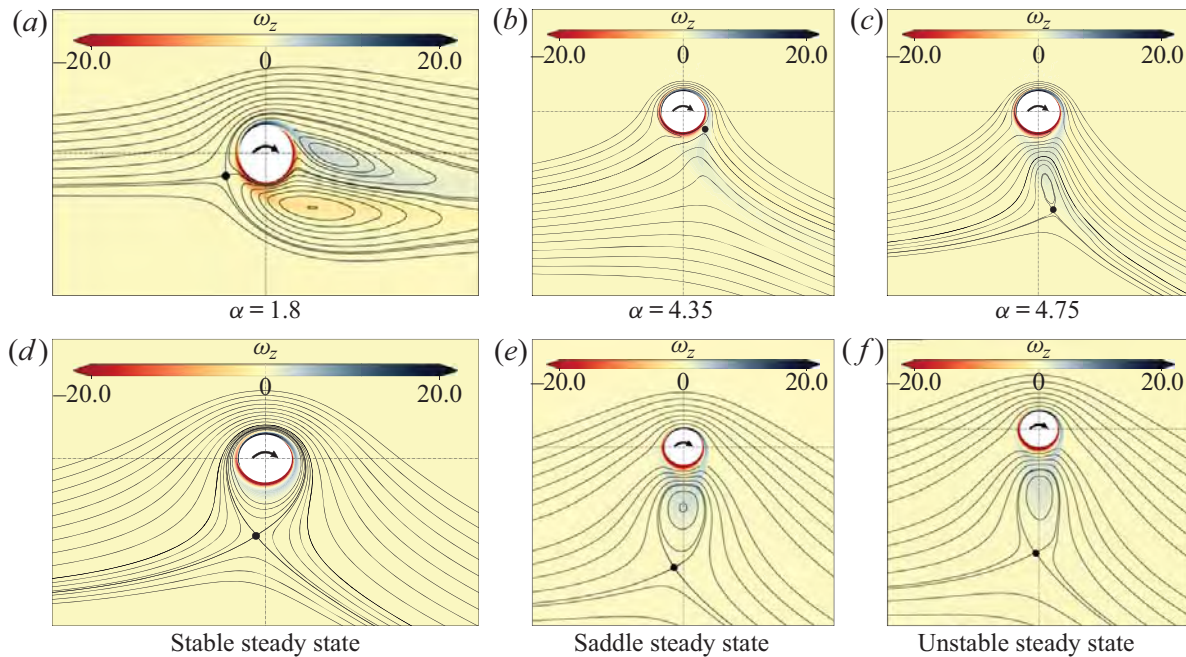


FIGURE 3. Steady flow around a rotating cylinder (vorticity levels and streamlines) for selected parameters. (a) $\alpha = 1.8$, $Re = 200$ (at the supercritical Hopf bifurcation threshold); (b) $\alpha = 4.35$, $Re = 200$ (at the Hopf bifurcation); (c) $\alpha = 4.75$, $Re = 200$ (at the fold bifurcation). (d–f) Correspond to three base-flow solutions existing in the range of multiple solutions, namely for $\alpha = 5.25$ and $Re = 200$. The circled dot shows the position of the hyperbolic stagnation point.

Figure 3(c) corresponds to the steady-state flow at the fold bifurcation observed for $\alpha = 4.75$ and giving rise to the disconnected states observed in figure 2(d). Compared to the previous state, the flow is topologically different as no stagnation point is observed along the wall of the cylinder. On the other hand, two stagnation points are observed within the flow. One of them is elliptic and located at the centre of the detached recirculation bubble. The other is hyperbolic and located along the streamline bounding the recirculation bubble.

Figure 3(d–f) displays the three coexisting steady states at $\alpha = 5.25$ and $Re = 200$. The topology of the streamlines of unstable and stable steady states differs. In the stable case (panel d) there is a single recirculation region encircling the cylinder and bounded by a hyperbolic stagnation point, as in the classical potential solution existing in this range of rotation rates. On the other hand, for both unstable states, the topology is similar to the case of figure 3(c). The recirculation region is detached from the cylinder and contains an elliptic stagnation point located approximately in the midpoint between the hyperbolic point and the bottom point of the cylinder surface. In the unstable steady state, the recirculating region is more stretched, as it can be seen in figure 3(d–f).

We highlight that even though topological changes in the streamlines of the steady states and bifurcations of the velocity field are in general independent events (see Brøns 2007), in some cases these two events occur in a small neighbourhood of the space of parameters (see Heil *et al.* 2017). In the current situation it has been confirmed that there is not a one-to-one relation between both phenomena. For instance, the transition between detached recirculation bubble (as in panel c) and recirculation bubble encircling the cylinder (as in panel d) along the stable branch occurs at some value of α in the range [4.75–5.25] where no dynamical bifurcation occurs. Yet, for larger Reynolds numbers,

i.e. $Re \gtrsim 190$, successive creation and destruction of vortices seems to be relevant in the preservation of the disconnected branch of steady states.

3.3. Analysis of the spatial structure of direct and adjoint eigenmodes

To explain why the steady state displayed in figure 3(f) is unstable, the two corresponding unstable modes (both associated with real eigenvalues) are displayed in figure 4 for $Re = 200$ and $\alpha = 5.25$. Direct modes are characterised by two recirculating regions of opposite vorticity. Vorticity is stronger and more localised in Mode IIa while Mode IIb displays a larger region with non-zero vorticity. Adjoint eigenvectors \hat{q}^\dagger for Mode IIa and Mode IIb are also displayed in figure 4. Adjoint fields (Luchini & Bottaro 2014) can be interpreted as a kind of Green's function for the receptivity of the global mode. Scalar product of the adjoint field with a forcing function or an initial condition provides the amplitude of the instability mode (see Giannetti & Luchini 2007). Therefore, Mode IIa is highly receptive in the upper right side of the near wake of the cylinder. The region of maximum receptivity extends from the close upper right region of the cylinder to a larger region at the bottom right of the cylinder and it is weaker than Mode IIa. Both modes present weak sensitivity to forcing upstream of the cylinder.

3.4. Bifurcation diagram in the parameter plane (Re, α)

The bifurcation curves detected in the $\alpha < 10, Re < 200$ range by linear stability analysis of all steady-state solutions are depicted in figure 5.

Three Hopf bifurcation curves are detected and plotted with full lines. The first one encircles the range of existence of unsteady Mode I. The second one delimits the range of existence of unsteady Mode II in its lower and left parts, but not on its upper part. The third one (in grey) occurs along a steady state which is already unstable, and hence is not likely to be related to a bifurcation observable in DNS or experiments.

In addition, we have identified two bifurcation curves associated with saddle nodes or 'folds', here denoted F_+ and F_- . These curves delimit the range of existence of multiple two-dimensional steady states, displayed as a grey region in figure 5. Note that the extension of this region explains the difference between the cases $Re = 170$ and $Re = 200$ discussed in the previous paragraph; according to the figure a single interval of α is found for $Re \gtrsim 190$.

In figure 5, the two fold curves seem to merge with the Hopf curve existing for lower Re at a point with coordinates $Re \approx 75, \alpha \approx 5.4$. Inspection shows that there are actually both a 0^2 or TB bifurcation and a cusp (C) bifurcation in very close vicinity in this range of parameters. This region will be studied in § 3.5. Additionally, in another range of parameters located at the lower threshold of existence of the Mode II, we have identified the existence of a Bautin or GH bifurcation which splits the Hopf curve into supercritical ($Re < Re_{GH}$) and subcritical ($Re > Re_{GH}$). This region will be studied in § 3.6.

3.5. Cusp–Takens–Bogdanov region

3.5.1. Qualitative study of the normal form

The transition occurring for $Re \approx 75$ and $\alpha \approx 5.4$ is characterised by the end of the Hopf curve (H_-) at a fold curve (F_+) (characteristic of a Takens–Bogdanov bifurcation), and a transition between one and three steady states (characteristic of a cusp). This suggests that the present situation is actually very close to a codimension-three bifurcation. The dynamical behaviour of the system can thus be expected to be well predicted using

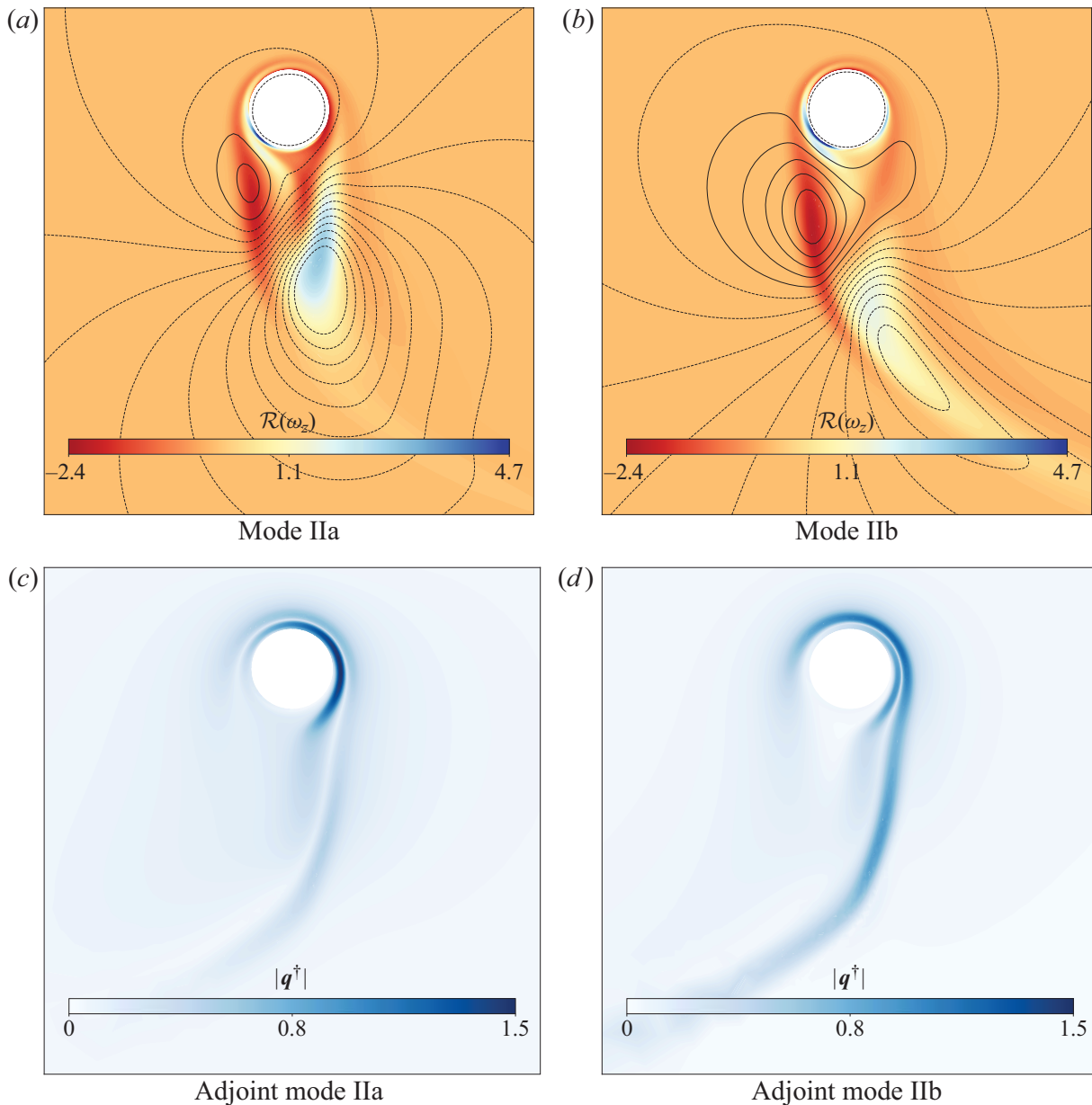


FIGURE 4. Contour plot of vorticity ω_z of Mode IIa and Mode IIb at $\alpha = 5.25$ and $Re = 200$ of the unstable steady state (a,b). The magnitude of adjoint modes (c,d).

the normal form describing the universal unfolding of the codimension-three planar bifurcation, also called a generalised TB bifurcation. This normal form has been studied by both Dumortier *et al.* (2006) and Kuznetsov (2013, chapter 8.3). The normal form can be written as follows:

$$\frac{dy_1}{dt} = y_2, \tag{3.1a}$$

$$\frac{dy_2}{dt} = \beta_1 + \beta_2 y_1 + \beta_3 y_2 + \epsilon y_1^3 + c_1 y_1 y_2 - y_1^2 y_2, \tag{3.1b}$$

where β_1, β_2 and β_3 are unfolding parameters (mapped from the physical parameters (Re, α)), c_1, ϵ (which can be rescaled to ± 1) are fixed coefficients which depend on the nonlinear terms of the underlying system. Note that this normal form generalises both the normal form of the standard TB bifurcation (which is recovered for $\beta_1(Re, \alpha) = 0$)

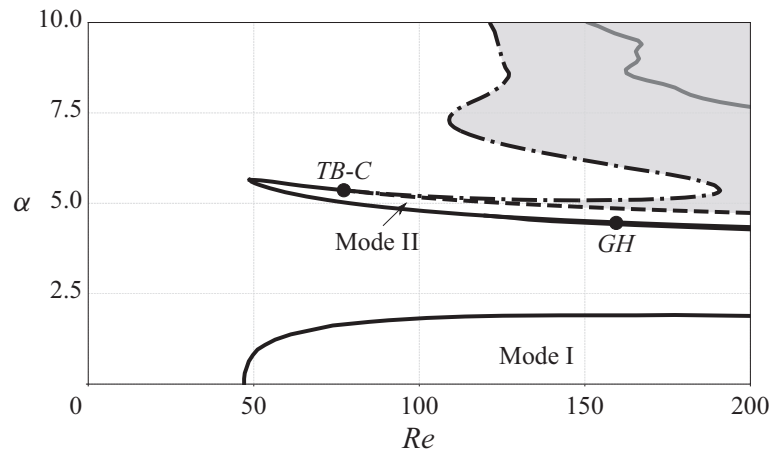


FIGURE 5. Bifurcation curves in the range $Re \in [0, 200]$ and $\alpha \in [0, 10]$. Black and grey lines are used to denote local bifurcations. Solid lines — indicate the presence of a Hopf bifurcation, dashed line - - - designates the first fold bifurcation curve, F_- , and dashed dotted line - . - denotes the second fold bifurcation, F_+ . Grey region indicates the coexistence of three steady states. Solid grey line inside the grey region denotes a secondary Hopf bifurcation occurring on one of the unstable steady states.

and the one of the fold bifurcations (which is recovered for $\beta_3(Re, \alpha) = 0$). The occurrence of both these codimension-two conditions for very close values of the parameters is characteristic of an imperfect codimension-three bifurcation and justifies the relevance of the associated normal form.

The dynamics of the normal form (3.1) has been explored by Dumortier *et al.* (2006) who classified the possible phase portraits and the associated bifurcation diagrams as functions of the unfolding parameters $(\beta_1, \beta_2, \beta_3)$ along a spherical surface. They showed that all possible bifurcation diagrams fall into three possible categories, called focus, saddle and node according to the values of the coefficients c_1 and ϵ . The situation $0 < c_1 < 2\sqrt{2}$ and $\epsilon = -1$ corresponds to the stable focus case and is found to lead to a bifurcation diagram consistent with the present situation, so we concentrate on this case.

Figure 6 illustrates all the possible behaviours of the dynamical system, sketched by sample phase portraits, along with their range of existence in the (β_1, β_2) plane. This figure corresponds to a subset of the complete diagram displayed in Dumortier *et al.* (2006, chapter 1, pp. 6–8), restricted to a range of parameters which is sufficient to explain all the dynamical features of the present problem. The bifurcation diagram displays two codimension-two points, a cusp C and a TB. These codimension-two points result from the tangential intersection of two codimension-one curves: the cusp point C occurs when the two fold curves F_+ and F_- collide, while the TB point arises from the intersection of the supercritical H_- Hopf curve and the F_+ fold. In addition, the bifurcation diagram predicts a homoclinic global bifurcation along a curve H_∞ originating from the TB point and terminating along the F_- fold on a point denoted SNL (for saddle-node loop). Left from this point, the F_- curve corresponds to a local saddle node while right from this point it corresponds to a homoclinic saddle-node bifurcation (appearance of two fixed points along a previously existing cycle). Note that the SNL point and the intersection of H_- and F_- are formally not codimension-two points (see Dumortier *et al.* 2006).

Phase portraits obtained in the various regions delimited by bifurcation boundaries are displayed in the panels of figure 6. One of the most interesting predictions is the existence of two regions characterised by the existence of two stable states, a bistability phenomenon. The first region (3), in the vicinity of the cusp, is characterised by two stable

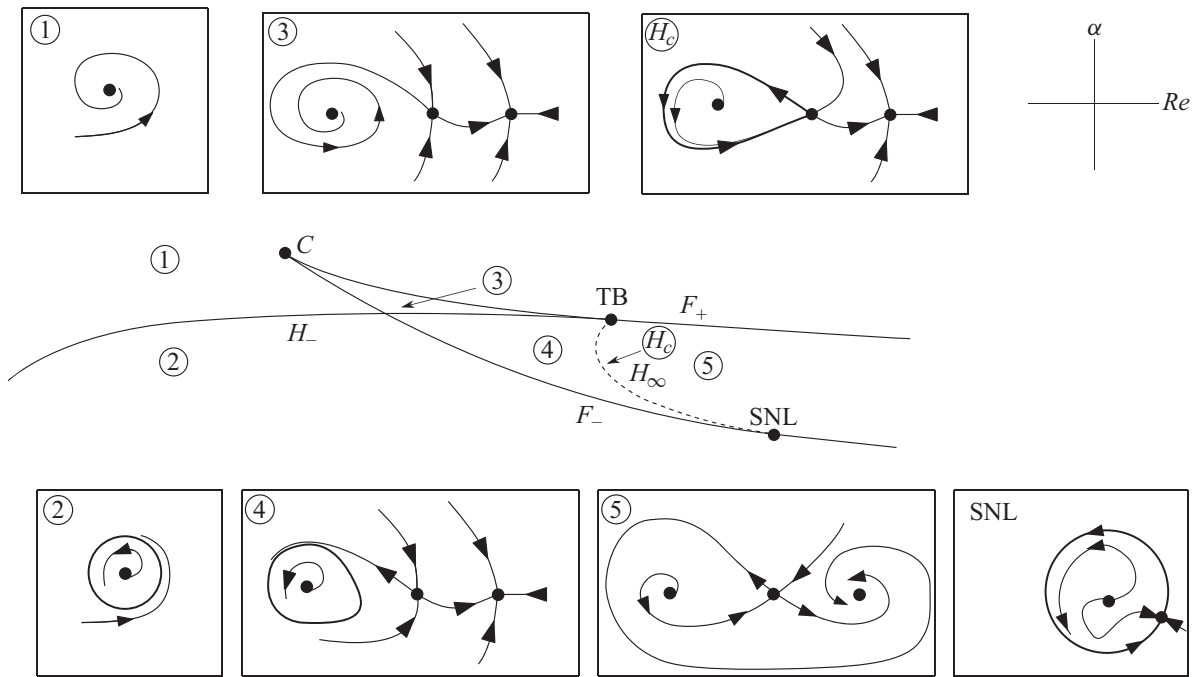


FIGURE 6. Bifurcation diagram predicted using the normal form 3.1 in the stable focus case (adapted from Dumortier *et al.* 2006), and qualitative phase portrait in regions (1), (2), (3), (4), (5) and along curve H_∞ . Note that in the qualitative phase portraits, focus and node points are not distinguished.

Type	Re	α
TB	77.6	5.36
C	75.6	5.38
GH	160	4.46

TABLE 1. Position of codimension-two bifurcation points.

steady states. The third region (4) is characterised by both a stable steady state and a stable cycle. In all other regions, there is a single stable solution which is either a steady state (in regions 1 and 5) or a cycle (in region 2).

Note that in these phase portraits nodes and foci are not distinguished. Distinguishing between these cases (Dumortier *et al.* 2006) leads to consideration of a larger number of subcases (for instance region 1 could be split in two subregions corresponding to a stable node and a stable focus ...) but the transitions between these subcases are not associated with bifurcations.

3.5.2. Numerical results in the C–TB region

In order to check the predictions of the normal form approach, we have conducted an accurate exploration of the range of parameters corresponding to the C–TB region. The exploration allowed us to confirm the existence of both a cusp and a Takens–Bogdanov point. The locations in the (α, Re) plane are given in table 1.

Figure 7 displays ‘zooms’ of the full bifurcation diagram (figure 5) in two narrow ranges centred on the C and TB codimension-two points. The bifurcation curves and the regions

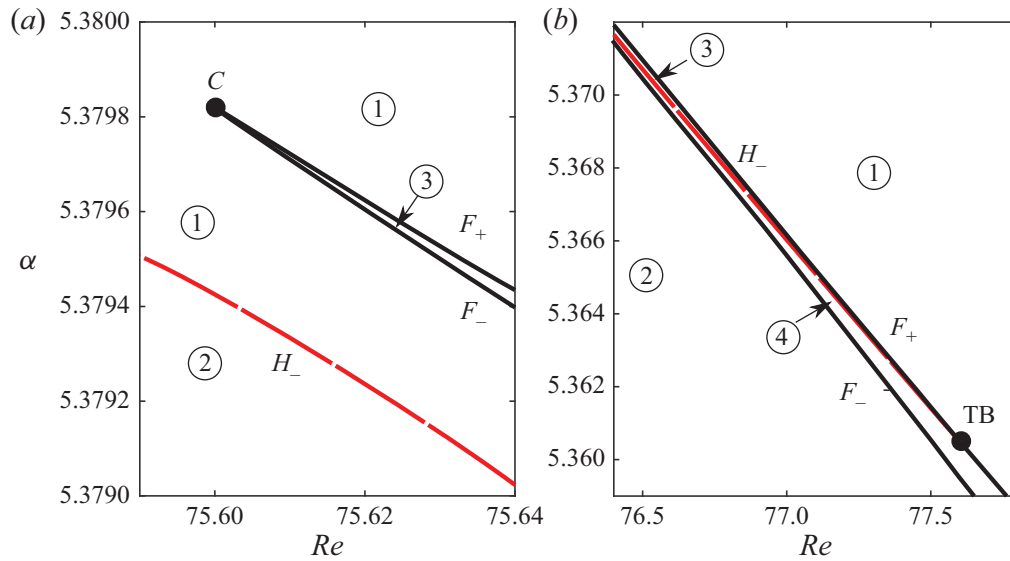


FIGURE 7. Zooms of figure 5 in the vicinity of the C and TB codimension-two points. Black solid lines denote fold bifurcations F_{\pm} , long dashed (red) line is used for the Hopf bifurcation line H_- and short dashed (red) curve denotes the local change from stable focus to stable node. Numbers correspond to each phase portrait of figure 6(a). (a) Zoom in the region of cusp bifurcation. (b) Zoom in the region of Takens–Bogdanov bifurcation.

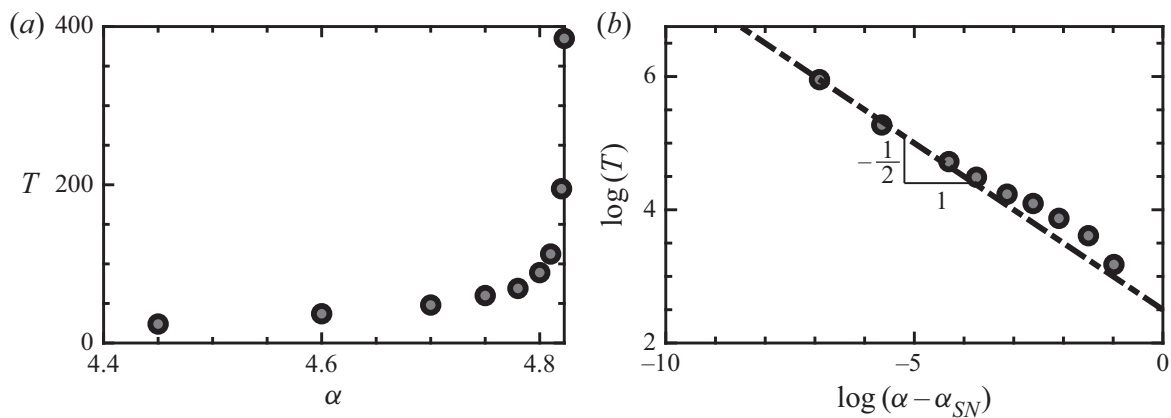


FIGURE 8. Evolution of the period of the limit cycle as it approaches the homoclinic connection. (a) Linear plot of the period T as a function of the rotation rate α where α_{SN} is the rotation rate at the saddle node. (b) Logarithm of the period and the distance to the bifurcation point.

are numbered with the same convention as in figure 6. Although it is not possible to present all results in a single figure because the curves are very steep and close to each other, the numerical results fully confirm the predictions of the normal form. In particular, the numerical results allow us to confirm the coexistence of two stable states (in regions 3) and of a stable cycle and a stable state (in region 4). However, a precise mapping of the curve H_{∞} bounding the region 4 could not be achieved, but the occurrence of a global homoclinic bifurcation was confirmed (see § 3.5.3).

3.5.3. Homoclinic bifurcation

As explained in § 3.5, the normal form predicts a homoclinic curve H_{∞} and a homoclinic saddle-node bifurcation along the F_- curve, right from the SNL point, corresponding to the appearance of two steady solutions along a previously existing cycle.

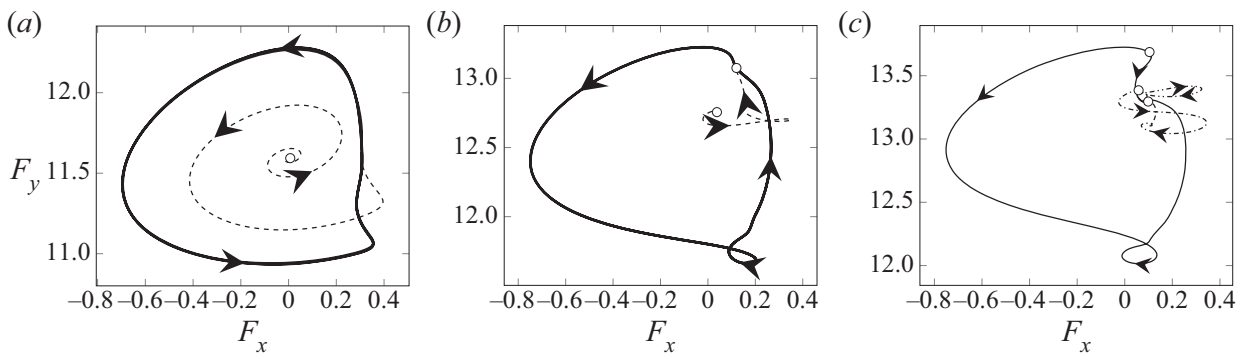


FIGURE 9. Phase portrait of the dynamics of the rotating cylinder at $Re = 170$ for three values of the rotation rate α . Vertical (horizontal) axis is the lift force F_y (drag force F_x) on the cylinder surface, empty dots denote steady-state solutions. (a,b) Limit sets (respectively transients) are depicted by a thick solid line (respectively thin dashed). (c) Heteroclinic connections between unstable–stable (respectively saddle–stable) are depicted by thin solid lines (respectively dashed dotted).

A generic feature of the imminent presence of a homoclinic saddle-node bifurcation is the divergence of the period of the limit cycle on which the saddle node appears. More precisely, the period is expected to scale as $\propto 1/\sqrt{\alpha_{SN} - \alpha}$ as $\alpha \rightarrow \alpha_{SN}$ (see Gasull, Mañosa & Villadelprat 2005). To check this prediction, time stepping simulations were conducted for $Re = 170$ and values of α just below the F_- curve. As shown in figure 8 the period of the limit cycle effectively diverges as one approaches the bifurcation following the theoretical behaviour.

Dynamics near the threshold can be perfectly understood in a two-dimensional manifold. Phase portraits of the bifurcation are displayed in figure 9. These phase portraits were computed with an initial guess generated by a small linear perturbation to a steady state in the direction of its corresponding eigenmode. The initial guess is then integrated in time until it reaches its limit set, i.e. a periodic, homoclinic orbit or another steady state. Below the bifurcation threshold (figure 9a) a stable limit cycle exists, represented by a thick solid line. At the bifurcation threshold, a saddle node arises along this cycle, which ceases to exist, giving rise to a homoclinic connection (an approximation of this orbit is delineated by a thick solid line in figure 9b). Beyond the saddle-node bifurcation, the saddle node splits into two fixed points. Hence, three steady states exist, including a stable one (see figure 9c). There exist four stable heteroclinic connections, two between unstable–stable steady states represented by a dashed line in figure 9(c) and other two between saddle–stable steady states denoted by a solid line. This sequence of events is fully consistent to the sequence connecting phase portraits (2), (SNL) and (4) in figure 6.

3.6. Generalised Hopf

3.6.1. Normal form analysis

Bautin bifurcation or GH is a codimension-two bifurcation where the equilibrium has purely imaginary eigenvalues $\lambda_{1,2} = \pm i\omega_0$ with $\omega_0 > 0$, and the third-order coefficient of the normal form vanishes. Generalised Hopf bifurcation is thus a degenerate case of the generic Hopf bifurcation, where the cubic normal form is not sufficient to determine the nonlinear stability of the system. To unravel the dynamics near the Bautin bifurcation point

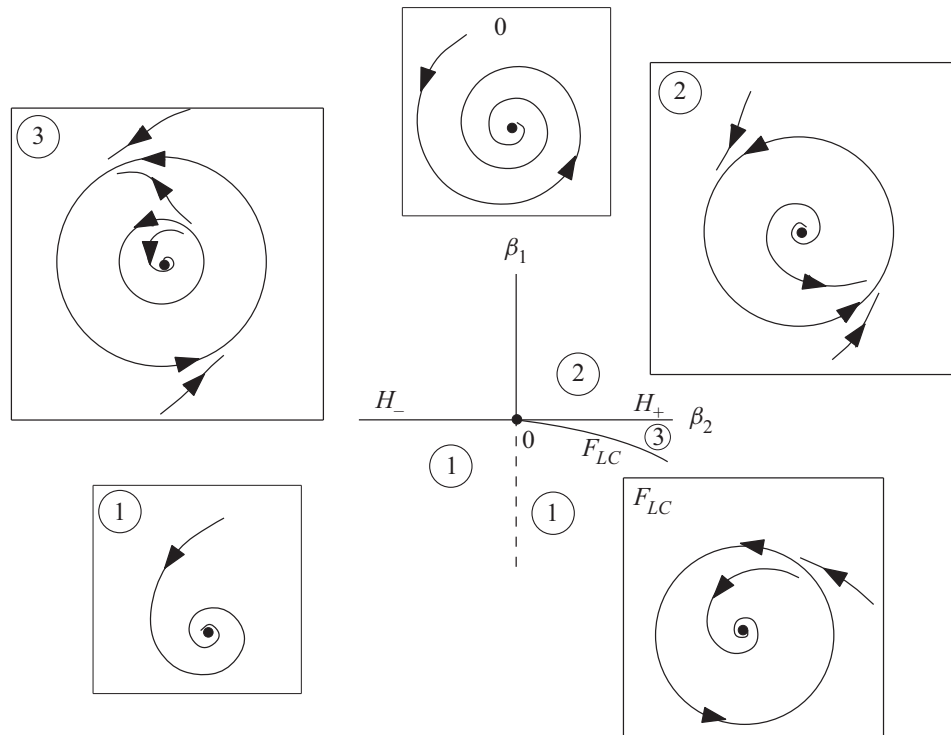


FIGURE 10. Qualitative bifurcation scenario in the vicinity of the GH bifurcation.

consider the normal form

$$\begin{cases} \frac{dx_1}{dt} = \beta_2 x_1 - x_2 + \beta_1 x_1 (x_1^2 + x_2^2) \pm x_1 (x_1^2 + x_2^2)^2. \\ \frac{dx_2}{dt} = \beta_2 x_2 + x_1 + \beta_1 x_2 (x_1^2 + x_2^2) \pm x_2 (x_1^2 + x_2^2)^2. \end{cases} \quad (3.2)$$

Three curves are of special interest:

- (i) System (3.2) undergoes a supercritical Hopf bifurcation in the half-line $H_+ = \{(\beta_1, \beta_2) | \beta_2 > 0, \beta_1 = 0\}$. This curve separates a region containing a stable focus to a region containing an unstable focus plus a stable limit cycle.
- (ii) System (3.2) undergoes a subcritical Hopf bifurcation in the half-line $H_- = \{(\beta_1, \beta_2) | \beta_2 < 0, \beta_1 = 0\}$. This curve separates a region containing an unstable focus, from one containing a stable focus and two limit cycles (one being stable and the other one being unstable).
- (iii) System (3.2) undergoes a fold cycle bifurcation on the curve $F_{LC} = \{(\beta_1, \beta_2) | \beta_1^2 + 4\beta_2 = 0, \beta_1 < 0\}$. This curve separates a region containing two limit cycles from one which does not contain any limit cycle (a stable fixed point also exists in both regions).

The most notable feature of this bifurcation is the existence of a bistability region characterised by two stable states (a fixed point and a cycle). Therefore, hysteretic behaviour is expected as one successively crosses curves H_- and F_{LC} . The bistability range is also characterised by the existence of an unstable limit cycle constituting the ‘edge state’ bounding the basins of attraction of the two stable states (figure 10).

3.6.2. Weakly nonlinear analysis

Unstable limit cycles are not easy to track, since they require stabilisation techniques, such as BoostConv (Citro *et al.* 2017) or edge-state tracking (Bengana *et al.* 2019), or the use of continuation techniques, such as harmonic balance (Fabre *et al.* 2019). Alternatively, we have performed a multiple-scale analysis up to fifth order (see appendix C). This method was previously used to study thermoacoustic bifurcations in the Rijke tube (Orchini, Rigas & Juniper 2016), displaying a good match with time stepping simulations with a much lower computational cost. By performing a weakly nonlinear analysis up to fifth order it is possible to determine a complex amplitude equation for the amplitude A of the critical linear mode \hat{q} . Here, the critical linear mode is normalised so that its $L^2\mathcal{B}$ -norm (see appendix C), i.e. its kinetic energy, is unity, which corresponds to the same normalisation as in Mantič-Lugo, Arratia & Gallaire (2014). The governing equation is a Stuart Landau equation, depending on a small parameter $\epsilon^2 = Re_c(\alpha)^{-1} - Re^{-1}$

$$\frac{dA}{dt} = (i\omega_0 + \epsilon^2\lambda_0 + \epsilon^4\lambda_1)A + (v_{1,0} + \epsilon^2v_{1,1})|A|^2A + v_{2,0}|A|^4A. \tag{3.3}$$

We remark that (3.3) is equivalent to (3.2) if separating real and imaginary parts. Searching for a solution under the form $A = |A| e^{i\omega t}$, and injecting into (3.3) leads to

$$\left. \begin{aligned} |A| &= \sqrt{-\frac{v_{1,r}}{2v_{2,r}} \pm \sqrt{\frac{v_{1,r}^2}{4v_{2,r}^2} - \frac{\lambda_r}{v_{2,r}}}} \\ \omega &= \omega_0 + v_{1,i}|A| + v_{2,i}|A|^2 \end{aligned} \right\}, \tag{3.4}$$

where $v_1 = v_{1,0} + \epsilon^2v_{1,1}$, $\lambda = \epsilon^2\lambda_0 + \epsilon^4\lambda_1$, $v_2 = v_{2,0}$ and subscripts r, i denote real and imaginary parts respectively. It turns out that $v_{2,r}$ is always negative while $v_{1,r}$ changes sign at $(Re, \alpha) = (Re_{GH}, \alpha_{GH})$. One can deduce the following consequences:

- (i) If $Re < Re_{GH}$ (i.e. $v_{2r} < 0$), (3.4) has a single solution $|A|$ for $\lambda_r > 0$ (i.e. $Re > Re_c$) and none for $\lambda_r < 0$ (i.e. $Re < Re_c$). In this case, the Hopf bifurcation is supercritical.
- (ii) If $Re > Re_{GH}$, (i.e. $v_{2r} > 0$), (3.4) has a single solution $|A|$ for $\lambda_r > 0$ (i.e. $Re > Re_c$), two solutions if $\lambda_c < \lambda_r < 0$ with $\lambda_c = v_{1,r}^2/4v_{2,r}$ and no solution if $\lambda_r < \lambda_c$. In this case, the Hopf bifurcation is subcritical. The condition $\lambda_r = \lambda_c$ defines a curve in the (Re, α) plane which corresponds to the fold cycle bifurcation associated with the emergence of the two limit cycles.

Figure 11 represents the amplitude and frequency of the limit cycles predicted by (3.4) for three values of Re . According to these results, the fold curve is predicted to be very close to the Hopf curve, i.e. within a few tenths of Re up to $Re = 250$. This behaviour allows us to clarify the transition occurring at the GH point in figure 6. For $Re < Re_{GH}$, when increasing Re for fixed α (or increasing α with fixed Re), the transition occurs via a supercritical Hopf bifurcation. On the other hand, for $Re > Re_{GH}$, the transition is predicted to be subcritical, involving the existence of a band where both steady state and Mode II coexist. Note that the width of the bistability band predicted by the weakly nonlinear analysis is very narrow, and could thus be difficult to evidence using direct numerical simulations.

4. Conclusion and discussion

The present study allowed us to clarify the bifurcation scenario in the two-dimensional flow past a rotating cylinder, especially concerning the range of parameters corresponding

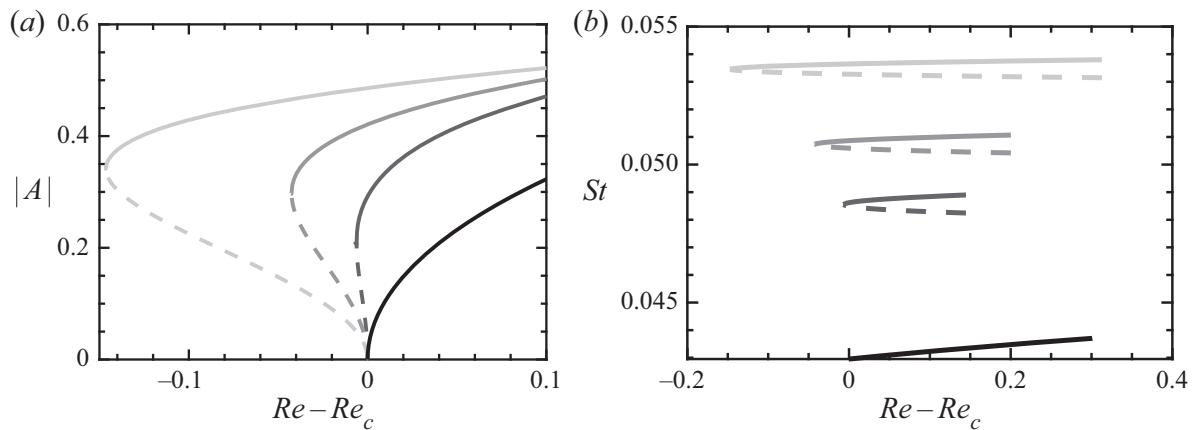


FIGURE 11. (a) Amplitudes of stable (solid line) and unstable (dashed line) limit cycles for four $Re_c = 100; 170; 200; 250$, where Re_c denotes the Reynolds number at the Hopf bifurcation. Grey scale: darker curves designate quantities associated with a lower Re , i.e. black curve $Re = 100$ and light grey $Re = 250$. (b) Strouhal number of limit cycles.

to the onset of the ‘Mode II’ unsteady vortex shedding mode. Using steady-state calculation involving arclength continuation and linear stability analysis, we have been able to draw all bifurcation curves existing in the range of parameters corresponding to $Re < 200$ and $\alpha < 5$. Three codimension-two bifurcations have been identified along the border of the range of existence of this mode, namely a Takens–Bogdanov, a cusp and a generalised Hopf. The first two are located in close vicinity, in such a way that the whole dynamics can be understood using the normal form of the codimension-three bifurcation (for a generalised Takens–Bogdanov bifurcation). The analysis also allowed us to identify three ranges of parameters characterised by bistability, two of them located in the vicinity of the Takens–Bogdanov and cusp points, the third one emanating from the generalised Hopf point. Time stepping simulations and a weakly nonlinear analysis have confirmed these findings, and have also allowed us to characterise the homoclinic and heteroclinic orbits connecting the fixed points, in full accordance with the predictions of the normal form theory.

The most surprising result of the study is the existence of an almost perfect codimension-three bifurcation in a problem characterised by only two control parameters. Such a feature suggests that the problem could be quite sensible to any small perturbations in a way such that small perturbations could completely change the scenario. We have checked that the scenario is robust with respect to numerical discretisation issues (see [appendix D](#)). The dependency with respect to additional physical parameters is more interesting. The effect of compressibility is an interesting question which we expect to investigate in future studies. Preliminary results have shown that for a Mach number of order 0.1, the dynamics in the region of the near-codimension-three point is effectively greatly modified. Other additional parameters, such as for instance shear or confinement, could be added. Finally, one may question the relevance of the present findings for three-dimensional flows. A short review of three-dimensional stability properties of the rotating cylinder flow is given in [appendix E](#). The discussion confirms that the most important results of the present study occur in range of parameters where no three-dimensional instabilities are present.

Declaration of interests

The authors report no conflict of interest.

Appendix A. Pseudo arc-length continuation

Arc-length continuation is a standard technique in dynamical systems theory. It allows for the continuation of a given solution branch through a turning or fold point. At the turning point the Jacobian of the system is singular; therefore, any iterative method based on the Jacobian is doomed to failure. To prevent the stall in the convergence of the Newton’s method, an extra condition needs to be added to the system of equations. In the current study we have chosen a pseudo arc-length methodology, which is based in a predictor–corrector strategy. The extended system adds an extra equation which ensures the tangency to the branch of the solution. For that purpose, a parameter is chosen, here either Re or α , and a monitor of the variation, either the horizontal force acting on the cylinder surface F_x or the vertical force F_y . The parameter and the monitor are parametrised by the length of the branch, here indicated by the parameter s . The current solution is varied by a given step Δs tangent to the solution branch and later corrected by a orthogonal correction. Let us denote by the subscript j the arc-length iteration and by the superscript n the Newton iteration of the corrector step, where N is used to denote the last step. In the description below, let us consider without loss of generality we have fixed the parameter α and the monitor F_x .

A.1. Predictor

The predictor step consists in the determination of a initial guess α_j^0 for the iteration j of the arc length. The initial guess is determined from a tangent extrapolation of the solution branch.

$$\alpha_j^0 = \alpha_{j-1}^N + \frac{d\alpha_{j-1}^N}{ds} \Delta s, \tag{A 1a}$$

$$\mathbf{q}_j^0 = \mathbf{q}_{j-1}^N + \frac{d\mathbf{q}_{j-1}^N}{ds} \Delta s \implies F_x(\mathbf{q}_j^0) = F_x(\mathbf{q}_{j-1}^N) + \frac{dF_x(\mathbf{q}_{j-1}^N)}{ds} \Delta s. \tag{A 1b}$$

In (A 1), $d\alpha_{j-1}^N/ds$ is the slope of the tangent in the α direction and $d\mathbf{q}_{j-1}^N/ds$ in the direction of the vector field. The tangent is computed from the differentiation of the stationary Navier–Stokes equations (2.1)

$$\frac{d\mathbf{q}_{j-1}^N}{ds} = - \left[\frac{\partial NS_{\mathbf{q}_{j-1}^N}}{\partial \mathbf{q}} \right]^{-1} \frac{\partial NS_{\mathbf{q}_{j-1}^N}}{\partial \alpha}, \tag{A 2}$$

where we have used the notation $NS_{\mathbf{q}_{j-1}^N} = 0$ to denote the steady incompressible Navier–Stokes equation whose solution is \mathbf{q}_{j-1}^N . The tangent is completed with a normalisation condition in the arc length

$$\left\| \frac{dF_x(\mathbf{q}_{j-1}^N)}{ds} \right\|_2^2 + \left\| \frac{d\alpha_{j-1}^N}{ds} \right\|_2^2 = 1. \tag{A 3}$$

A.2. Corrector

This step consists in an orthogonal correction of the tangent guess. To do so one needs to solve the following system of equations

$$\begin{bmatrix} \frac{\partial NS_{q_j^n}}{\partial \mathbf{q}} & \frac{\partial NS_{q_j^n}}{\partial \alpha} \\ \frac{dF_x(q_{j1}^n)}{ds} F_x(\cdot) & \frac{d\alpha_j^n}{ds} \end{bmatrix} \begin{bmatrix} \Delta \mathbf{q}_j^{n+1} \\ \Delta \alpha_j^{n+1} \end{bmatrix} = \begin{bmatrix} -NS(\mathbf{u}) \\ \Delta s - \frac{dF_x}{ds} F_x(\mathbf{q}_j^n - \mathbf{q}_{j-1}^N) - \frac{d\alpha}{ds} (\alpha_j^n - \alpha_{j-1}^N) \end{bmatrix}, \quad (\text{A } 4)$$

where the last equation of (A 4) comes from the differentiation of the normalisation condition (A 3) and considering that $\Delta \alpha_j = \Delta \alpha_j^{n+1} + \alpha_j^n - \alpha_{j-1}^N = \alpha_j^N - \alpha_{j-1}^N$ (similarly on \mathbf{q}).

Appendix B. Weakly nonlinear analysis to determine the normal form of the saddle-node bifurcation

Saddle-node bifurcation and homoclinic saddle-node bifurcation are locally characterised by the normal form of the saddle-node bifurcation (see Kuznetsov 2013). In the generic case, when $a_2(Re, \alpha) \neq 0$ and $a_0(Re, \alpha) \neq 0$ the central manifold is unravelled by its second-order normal form

$$\frac{dx_1}{dt} = a_0(Re, \alpha) + a_2(Re, \alpha)x_1^2 + O(x_1^3). \quad (\text{B } 1)$$

Coefficients $a_2(Re, \alpha) \neq 0$ and $a_0(Re, \alpha) \neq 0$ can be obtained with aid of weakly nonlinear analysis. Let us consider the following transformations:

$$t = \tau_0 + \epsilon^2 \tau_1, \quad (\text{B } 2a)$$

$$\frac{d}{dt} = \frac{d}{d\tau_0} + \epsilon^2 \frac{d}{d\tau_1}, \quad (\text{B } 2b)$$

$$\mathbf{Q} = \mathbf{Q}_b + \epsilon \hat{\mathbf{q}} + \epsilon^2 \mathbf{q}_2, \quad (\text{B } 2c)$$

where $\epsilon^2 = (1/Re_c) - (1/Re)$. The system at order ϵ^0 is the incompressible Navier–Stokes system that provides the base flow. The system at order ϵ^1 is identical to the linearised Navier–Stokes problem (2.3). At order ϵ^2 secular term appears and solvability condition must be imposed

$$a_0 = \frac{\langle \hat{\mathbf{u}}^\dagger, -\tau(\mathbf{U}_b) \rangle}{\langle \hat{\mathbf{u}}^\dagger, \hat{\mathbf{u}} \rangle}, \quad (\text{B } 3)$$

$$a_2 = \frac{\langle \hat{\mathbf{u}}^\dagger, -\hat{\mathbf{u}} \nabla \hat{\mathbf{u}} \rangle}{\langle \hat{\mathbf{u}}^\dagger, \hat{\mathbf{u}} \rangle}. \quad (\text{B } 4)$$

Here, $\hat{\mathbf{u}}^\dagger$ denotes the adjoint or left eigenvector of linearised Navier–Stokes equations associated with the null eigenvalue.

Appendix C. WNL to determine the normal form of the Hopf bifurcation degeneracy

Weakly nonlinear analysis has been used extensively in the case of Hopf bifurcations to unravel the frequency of the limit cycle near the bifurcation threshold

(see Gallaire *et al.* 2016) and to determine the validity of stability analysis on the mean flow (see Sipp & Lebedev 2007). In this article WNL analysis is used to determine the existence of a generalised Hopf bifurcation (see § 3.6). The starting point of the weakly nonlinear method is the decomposition of the flow field into multiple scales

$$\begin{aligned}
 \mathcal{Q} = & \mathcal{Q}_b + \epsilon [A_{wnl} \hat{\mathbf{q}} e^{i\omega_0 t} + \text{c.c.}] \\
 & + \epsilon^2 \left[\mathbf{q}_{2,0} + |A_{wnl}| \mathbf{q}_{2,0}^{|A_{wnl}|} + (A_{wnl}^2 \mathbf{q}_{2,2} e^{2i\omega_0 t} + \text{c.c.}) \right] \\
 & + \epsilon^3 \left[A_{wnl} e^{i\omega_0 t} \left(\mathbf{q}_{3,1} + |A_{wnl}|^2 \mathbf{q}_{3,1}^{|A_{wnl}|^2} + |A_{wnl}|^2 \mathbf{q}_{3,1}^{A_{wnl} \bar{A}_{wnl}} \right) + A_{wnl}^3 e^{3i\omega_0 t} \mathbf{q}_{3,3} + \text{c.c.} \right] \\
 & + \epsilon^4 \left[\mathbf{q}_{4,0} + |A_{wnl}|^2 \mathbf{q}_{4,0}^{|A_{wnl}|^2} + |A_{wnl}|^4 \mathbf{q}_{4,0}^{|A_{wnl}|^4} \right. \\
 & \left. + A_{wnl}^2 e^{2i\omega_0 t} \left(\mathbf{q}_{4,2} + |A_{wnl}|^2 \mathbf{q}_{4,2}^{|A_{wnl}|^2} \right) + A_{wnl}^4 e^{4i\omega_0 t} \mathbf{q}_{4,4} + \text{c.c.} \right] + O(\epsilon^5), \tag{C 1a}
 \end{aligned}$$

where the complex amplitude A_{wnl} depends upon a slow time scale $\tau = \epsilon^2 t$. The choice of the parameter ϵ is the same as in Fabre *et al.* (2019), $\epsilon^2 = 1/Re_c(\alpha) - 1/Re$, where the critical Reynolds $Re_c(\alpha)$ is a function of the rotation rate α . When the ansatz (C 1) is substituted into the Navier–Stokes equations, at orders $O(\epsilon^3)$ and $O(\epsilon^5)$ solvability conditions need to be imposed due to the presence of secular terms which lead to a Stuart–Landau equation depending upon the slow time scale τ

$$\frac{\partial A_{wnl}}{\partial \tau} = (\lambda_0 + \epsilon^2 \lambda_1) A_{wnl} + (\nu_{1,0} + \epsilon^2 \nu_{1,1}) |A_{wnl}|^2 A_{wnl} + \epsilon^2 \nu_{2,0} |A_{wnl}|^4 A_{wnl}. \tag{C 2}$$

If we take into account the definition of the slow time scale $\tau = \epsilon^2 t$, the fact that up to leading order $O(\epsilon)$ we have $dA_{wnl}/dt = i\omega_0 \epsilon A_{wnl}$ and we define a new amplitude which depends on ϵ as $A = \epsilon A_{wnl}$ we can rewrite (C 2) as

$$\frac{dA}{dt} = (i\omega_0 + \epsilon^2 \lambda_0 + \epsilon^4 \lambda_1) A + (\nu_{1,0} + \epsilon^2 \nu_{1,1}) |A|^2 A + \nu_{2,0} |A|^4 A. \tag{C 3}$$

In the following we consider that the eigenmode $\hat{\mathbf{q}}$ and its adjoint $\hat{\mathbf{q}}^\dagger$ have been normalised so that $\|\hat{\mathbf{q}}\|_{\mathcal{B}}^2 = \langle \hat{\mathbf{q}}, \mathcal{B} \hat{\mathbf{q}} \rangle = \langle \hat{\mathbf{u}}, \hat{\mathbf{u}} \rangle = 1$ and $\langle \hat{\mathbf{q}}^\dagger, \mathcal{B} \hat{\mathbf{q}} \rangle = \langle \hat{\mathbf{u}}^\dagger, \hat{\mathbf{u}} \rangle = 1$. This normalisation is the same as that one used in the self-consistent methodology (see Mantič-Lugo *et al.* 2014): with this choice, A is a real constant representing the amplitude of the linear mode with respect to its L^2 norm. In the following we will use the notation $\mathcal{LN}S_{i\omega} \mathbf{q} = i\omega \mathcal{B} \mathbf{q} - \mathcal{LN}S \mathbf{q}$ to denote the application of the linearised operator at a specific frequency ω .

The ansatz (C 1) is substituted into the incompressible Navier–Stokes equations (2.1):

- (i) Order $O(\epsilon^0)$ leads to the steady-state Navier–Stokes equations (2.1).
- (ii) Order $O(\epsilon^1)$ leads to the linearised Navier–Stokes equations (2.3).
- (iii) Order $O(\epsilon^2)$ contains three terms, which are computed as the solution of three linear systems:

$$\mathcal{LN}S_0 \mathbf{q}_{2,0} = -2 \nabla \cdot (d(\mathbf{U}_b)), \tag{C 4a}$$

$$\mathcal{LN}S_0 \mathbf{u}_{2,0}^{|A_{wnl}|} = -\hat{\mathbf{q}} \cdot \nabla \bar{\hat{\mathbf{u}}} + \bar{\hat{\mathbf{u}}} \cdot \nabla \hat{\mathbf{q}}, \tag{C 4b}$$

$$\mathcal{LN}S_{2i\omega_0} \mathbf{u}_{2,2} = -\hat{\mathbf{u}} \cdot \nabla \hat{\mathbf{u}}. \tag{C 4c}$$

(iv) At order $O(\epsilon^3)$ there are degenerate terms, i.e. terms corresponding to the frequency $i\omega_0$. The operator $\mathcal{LN}\mathcal{S}_{i\omega_0}$ is not injective (\hat{q} belongs to its kernel) and it is not surjective because \hat{q}^\dagger belongs to the kernel of its adjoint and the operator is Fredholm in L^2 . Therefore we need to impose solvability conditions in order to obtain terms $q_{3,1}$, $q_{3,1}^{|A_{wnl}|^2}$ and $q_{3,1}^{A_{wnl}\bar{A}_{wnl}}$. Solvability conditions at $O(\epsilon^3)$ correspond to

$$\mu_1 = -\frac{\langle \hat{u}^\dagger, \hat{u} \cdot \nabla u_{2,0}^{|A_{wnl}|} + u_{2,0}^{|A_{wnl}|} \cdot \nabla \hat{u} \rangle}{\langle \hat{u}^\dagger, \hat{u} \rangle}, \tag{C5}$$

$$\mu_2 = -\frac{\langle \hat{u}^\dagger, \bar{\hat{u}} \cdot \nabla u_{2,2} + u_{2,2} \cdot \nabla \bar{\hat{u}} \rangle}{\langle \hat{u}^\dagger, \hat{u} \rangle}, \tag{C6}$$

$$\lambda_0 = -\frac{\langle \hat{u}^\dagger, \hat{u} \cdot \nabla u_{2,0} + u_{2,0} \cdot \nabla \hat{u} + 2\nabla \cdot (d(\hat{u})) \rangle}{\langle \hat{u}^\dagger, \hat{u} \rangle}, \tag{C7}$$

where $\mu_1 + \mu_2 = \nu_{1,0}$. Additionally, given the fact that L^2 is a Hilbert space and the operator is Fredholm, the space can be decomposed into a direct sum of the range of the operator $\mathcal{LN}\mathcal{S}_{i\omega_0}$ and the kernel of its adjoint. This implies that secular terms are determined up to a constant in the direction of the eigenmode \hat{q} , i.e. $q_{3,1} \rightarrow q_{3,1} + \delta_0 \hat{q}$, $\delta_0 \in \mathbb{R}$. This degree of freedom is fixed by considering $\delta_0 = 0$, i.e. each secular term is orthogonal to the linear adjoint mode \hat{q}^\dagger in the norm \mathcal{B} , i.e. $\langle \hat{q}^\dagger, \mathcal{B}q_{3,1} \rangle = 0$. This choice for the extra degree of freedom has been also used in Carini, Auteri & Giannetti (2015). This leads to

$$\begin{pmatrix} \mathcal{LN}\mathcal{S}_{i\omega_0} & -\mathcal{B}\hat{q} \\ \hat{q}^{\dagger H}\mathcal{B} & 0 \end{pmatrix} \begin{pmatrix} q_{3,1} \\ \lambda_0 \end{pmatrix} = \begin{pmatrix} F_{3,1} \\ 0 \end{pmatrix} \tag{C8}$$

and similarly for pairs $(q_{3,1}^{|A_{wnl}|^2}, \mu_1)$ and $(q_{3,1}^{A_{wnl}\bar{A}_{wnl}}, \mu_2)$ replacing $F_{3,1}$ by $F_{3,1}^{|A_{wnl}|^2}$ and $F_{3,1}^{A_{wnl}\bar{A}_{wnl}}$ respectively. Please note that

$$\left. \begin{aligned} F_{3,1} &= -\hat{u} \cdot \nabla u_{2,0} - u_{2,0} \cdot \nabla \hat{u} - 2\nabla \cdot (d(\hat{u})) \\ F_{3,1}^{|A_{wnl}|^2} &= -\hat{u} \cdot \nabla u_{2,0}^{|A_{wnl}|} - u_{2,0}^{|A_{wnl}|} \cdot \nabla \hat{u} \\ F_{3,1}^{A_{wnl}\bar{A}_{wnl}} &= -\bar{\hat{u}} \cdot \nabla u_{2,2} - u_{2,2} \cdot \nabla \bar{\hat{u}} \end{aligned} \right\}. \tag{C9}$$

The other non-resonant term is solved as usually,

$$\mathcal{LN}\mathcal{S}_{3i\omega_0}q_{3,3} = F_{3,3} = -\hat{u} \cdot \nabla u_{2,2} - u_{2,2} \cdot \nabla \hat{u}. \tag{C10}$$

(v) At order $O(\epsilon^4)$ we find six terms which are solved by the resolution of the following linear systems

$$\left. \begin{aligned} \mathcal{LNS}_0 \mathbf{q}_{4,0} &= \mathbf{F}_{4,0} \\ \mathcal{LNS}_0 \mathbf{q}_{4,0}^{|A_{wnl}|^2} &= \mathbf{F}_{4,0}^{|A_{wnl}|^2} \\ \mathcal{LNS}_0 \mathbf{q}_{4,0}^{|A_{wnl}|^4} &= \mathbf{F}_{4,0}^{|A_{wnl}|^4} \\ \mathcal{LNS}_{2i\omega_0} \mathbf{q}_{4,2} &= \mathbf{F}_{4,2} \\ \mathcal{LNS}_{2i\omega_0} \mathbf{q}_{4,2}^{|A_{wnl}|^2} &= \mathbf{F}_{4,2}^{|A_{wnl}|^2} \\ \mathcal{LNS}_{4i\omega_0} \mathbf{q}_{4,4} &= \mathbf{F}_{4,4} \end{aligned} \right\}, \tag{C 11}$$

where the right-hand side terms are

$$\mathbf{F}_{4,0} = -\mathbf{u}_{2,0} \cdot \nabla \mathbf{u}_{2,0} - 2\nabla \cdot d(\mathbf{u}_{2,0}), \tag{C 12}$$

$$\begin{aligned} \mathbf{F}_{4,0}^{|A_{wnl}|^2} &= -\mathbf{u}_{3,1} \cdot \nabla \bar{\hat{\mathbf{u}}} - \bar{\hat{\mathbf{u}}} \cdot \nabla \mathbf{u}_{3,1} - \bar{\mathbf{u}}_{3,1} \cdot \nabla \hat{\mathbf{u}} - \hat{\mathbf{u}} \cdot \nabla \bar{\mathbf{u}}_{3,1} \\ &\quad - \mathbf{u}_{2,0} \cdot \nabla \mathbf{u}_{2,0}^{|A_{wnl}|^2} - \mathbf{u}_{2,0}^{|A_{wnl}|^2} \cdot \nabla \mathbf{u}_{2,0}, \end{aligned} \tag{C 13}$$

$$\begin{aligned} \mathbf{F}_{4,0}^{|A_{wnl}|^4} &= -\mathbf{u}_{2,2} \cdot \nabla \bar{\mathbf{u}}_{2,2} - \bar{\mathbf{u}}_{2,2} \cdot \nabla \mathbf{u}_{2,2} - \mathbf{u}_{2,0}^{|A_{wnl}|^2} \cdot \nabla - \mathbf{u}_{2,0}^{|A_{wnl}|^2} \\ &\quad - \mathbf{u}_{3,1}^{|A_{wnl}|^2} \cdot \nabla \bar{\hat{\mathbf{u}}} - \bar{\hat{\mathbf{u}}} \cdot \nabla \mathbf{u}_{3,1}^{|A_{wnl}|^2} - \bar{\mathbf{u}}_{3,1}^{|A_{wnl}|^2} \cdot \nabla \hat{\mathbf{u}} - \hat{\mathbf{u}} \cdot \nabla \bar{\mathbf{u}}_{3,1}^{|A_{wnl}|^2} \\ &\quad - \mathbf{u}_{3,1}^{A_{wnl}\bar{A}_{wnl}} \cdot \nabla \bar{\hat{\mathbf{u}}} - \bar{\hat{\mathbf{u}}} \cdot \nabla \mathbf{u}_{3,1}^{A_{wnl}\bar{A}_{wnl}} - \bar{\mathbf{u}}_{3,1}^{A_{wnl}\bar{A}_{wnl}} \cdot \nabla \hat{\mathbf{u}} - \hat{\mathbf{u}} \cdot \nabla \bar{\mathbf{u}}_{3,1}^{A_{wnl}\bar{A}_{wnl}}, \end{aligned} \tag{C 14}$$

$$\begin{aligned} \mathbf{F}_{4,2} &= -\mathbf{u}_{2,0}^{|A_{wnl}|^2} \cdot \nabla \mathbf{u}_{2,0} - \mathbf{u}_{2,0} \cdot \nabla \mathbf{u}_{2,0}^{|A_{wnl}|^2} - \mathbf{u}_{3,1} \cdot \nabla \hat{\mathbf{u}} - \hat{\mathbf{u}} \cdot \nabla \mathbf{u}_{3,1} \\ &\quad - 2\nabla \cdot d(\mathbf{u}_{2,2}), \end{aligned} \tag{C 15}$$

$$\begin{aligned} \mathbf{F}_{4,2}^{|A_{wnl}|^2} &= -\mathbf{u}_{2,0} \cdot \nabla \mathbf{u}_{2,2} - \mathbf{u}_{2,2} \cdot \nabla \mathbf{u}_{2,0} - \mathbf{u}_{3,1}^{|A_{wnl}|^2} \cdot \nabla \hat{\mathbf{u}} - \hat{\mathbf{u}} \cdot \nabla \mathbf{u}_{3,1}^{|A_{wnl}|^2} \\ &\quad - \mathbf{u}_{3,1}^{A_{wnl}\bar{A}_{wnl}} \cdot \nabla \hat{\mathbf{u}} - \hat{\mathbf{u}} \cdot \nabla \mathbf{u}_{3,1}^{A_{wnl}\bar{A}_{wnl}} - \mathbf{u}_{3,3} \cdot \nabla \bar{\hat{\mathbf{u}}} - \bar{\hat{\mathbf{u}}} \cdot \nabla \mathbf{u}_{3,3}, \end{aligned} \tag{C 16}$$

$$\mathbf{F}_{4,4} = -\mathbf{u}_{2,2} \cdot \nabla \mathbf{u}_{2,2} - \mathbf{u}_{3,3} \cdot \nabla \hat{\mathbf{u}} - \hat{\mathbf{u}} \cdot \nabla \mathbf{u}_{3,3}. \tag{C 17}$$

(vi) At order $O(\epsilon^5)$ we find three degenerate terms proportional to A_{wnl} , $A_{wnl}|A_{wnl}|^2$ and $A_{wnl}|A_{wnl}|^4$. As for the case of the third-order solvability conditions, they lead to the computation of coefficients λ_1 , $\nu_{1,1}$ and $\nu_{2,0}$

$$\left. \begin{aligned} \lambda_1 &= \langle \hat{\mathbf{u}}^\dagger, \mathbf{F}_{5,1} \rangle \\ \nu_{1,1} &= \langle \hat{\mathbf{u}}^\dagger, \mathbf{F}_{5,1}^{A_{wnl}|A_{wnl}|^2} \rangle \\ \nu_{2,0} &= \langle \hat{\mathbf{u}}^\dagger, \mathbf{F}_{5,1}^{A_{wnl}|A_{wnl}|^4} \rangle \end{aligned} \right\}, \tag{C 18}$$

where $F_{5,1}$, $F_{5,1}^{|A_{wnl}|^2}$ and $F_{5,1}^{|A_{wnl}|^4}$ are defined as follows:

$$F_{5,1} = -\mathbf{u}_{2,0} \cdot \nabla \mathbf{u}_{3,1} - \mathbf{u}_{2,0} \cdot \nabla \mathbf{u}_{3,1} - \mathbf{u}_{4,0} \cdot \nabla \hat{\mathbf{u}} - \hat{\mathbf{u}} \cdot \nabla \mathbf{u}_{4,0} - 2\nabla \cdot d(\mathbf{u}_{3,1}), \quad (\text{C } 19)$$

$$\begin{aligned} F_{5,1}^{A_{wnl}|A_{wnl}|^2} &= -\mathbf{u}_{2,0} \cdot \nabla \mathbf{u}_{3,0}^{|A_{wnl}|^2} - \mathbf{u}_{3,0}^{|A_{wnl}|^2} \cdot \nabla \mathbf{u}_{2,0} \\ &\quad - \mathbf{u}_{2,0} \cdot \nabla \mathbf{u}_{3,0}^{A_{wnl}\bar{A}_{wnl}} - \mathbf{u}_{3,0}^{A_{wnl}\bar{A}_{wnl}} \cdot \nabla \mathbf{u}_{2,0} \\ &\quad - \mathbf{u}_{2,0}^{|A_{wnl}|^2} \cdot \nabla \mathbf{u}_{3,1} - \mathbf{u}_{3,1} \cdot \nabla \mathbf{u}_{2,0}^{|A_{wnl}|^2} \\ &\quad - \mathbf{u}_{2,2} \cdot \nabla \bar{\mathbf{u}}_{3,1} - \bar{\mathbf{u}}_{3,1} \cdot \nabla \mathbf{u}_{2,2} \\ &\quad - \hat{\mathbf{u}} \cdot \nabla \mathbf{u}_{4,0}^{|A_{wnl}|^2} - \mathbf{u}_{4,0}^{|A_{wnl}|^2} \cdot \nabla \hat{\mathbf{u}} \\ &\quad - \bar{\hat{\mathbf{u}}} \cdot \nabla \mathbf{u}_{4,0}^{A_{wnl}^2} - \mathbf{u}_{4,0}^{A_{wnl}^2} \cdot \nabla \bar{\hat{\mathbf{u}}} \\ &\quad - 2\nabla \cdot d(\mathbf{u}_{3,0}^{|A_{wnl}|^2}) - 2\nabla \cdot d(\mathbf{u}_{3,0}^{A_{wnl}\bar{A}_{wnl}}), \end{aligned} \quad (\text{C } 20)$$

$$\begin{aligned} F_{5,1}^{A_{wnl}|A_{wnl}|^4} &= -\mathbf{u}_{2,0}^{|A_{wnl}|^2} \cdot \nabla \mathbf{u}_{3,0}^{|A_{wnl}|^2} - \mathbf{u}_{3,0}^{|A_{wnl}|^2} \cdot \nabla \mathbf{u}_{2,0}^{|A_{wnl}|^2} \\ &\quad - \mathbf{u}_{2,0}^{|A_{wnl}|^2} \cdot \nabla \mathbf{u}_{3,0}^{A_{wnl}\bar{A}_{wnl}} - \mathbf{u}_{3,0}^{A_{wnl}\bar{A}_{wnl}} \cdot \nabla \mathbf{u}_{2,0}^{|A_{wnl}|^2} \\ &\quad - \mathbf{u}_{2,2} \cdot \nabla \bar{\mathbf{u}}_{3,0}^{|A_{wnl}|^2} - \bar{\mathbf{u}}_{3,0}^{|A_{wnl}|^2} \cdot \nabla \mathbf{u}_{2,2} \\ &\quad - \mathbf{u}_{2,2} \cdot \nabla \bar{\mathbf{u}}_{3,0}^{A_{wnl}\bar{A}_{wnl}} - \bar{\mathbf{u}}_{3,0}^{A_{wnl}\bar{A}_{wnl}} \cdot \nabla \mathbf{u}_{2,0} \\ &\quad - \mathbf{u}_{4,0}^{|A_{wnl}|^4} \cdot \nabla \bar{\hat{\mathbf{u}}} - \bar{\hat{\mathbf{u}}} \cdot \nabla \mathbf{u}_{4,0}^{|A_{wnl}|^4} \\ &\quad - \mathbf{u}_{4,0}^{A_{wnl}^2|A_{wnl}|^2} \cdot \nabla \bar{\hat{\mathbf{u}}} - \bar{\hat{\mathbf{u}}} \cdot \nabla \mathbf{u}_{4,0}^{A_{wnl}^2|A_{wnl}|^2} \\ &\quad - \bar{\mathbf{u}}_{2,2} \cdot \nabla \mathbf{u}_{3,3} - \mathbf{u}_{3,3} \cdot \nabla \bar{\mathbf{u}}_{2,2}. \end{aligned} \quad (\text{C } 21)$$

Appendix D. Mesh convergence

Mesh independence of the solutions has been verified systematically. First, we have considered a given mesh refinement and varied the physical size of the domain, see [table 2](#). We have observed that for a domain length of 80 diameters downstream the cylinder centre, 40 diameters upstream the cylinder centre and 40 in the cross-stream direction the solution is not affected by the imposition of boundary conditions. Secondly, we have looked at the effect of the mesh refinement on the properties of the solution. For that purpose a parametric study of eigenvalues, Hopf WNL coefficients and global monitors of a given steady-state solution have been carried out, see ([table 3](#)). The sensitivity to mesh convergence of cusp and Takens–Bogdanov bifurcation points has been also tested. Results show that each of them is found within $\Delta Re_c < 0.2$. Every mesh is computed by Delaunay triangulation. Mesh M_1 has been generated by blocks, as it is generally done with structured meshes; M_2 and M_3 have been computed following the mesh adaption procedure described in Fabre *et al.* (2019, appendix A), with respect to base flow only and with respect to base flow and direct mode structure; M_4 and M_5 are the consequence of successive division of each triangle edge by two and four respectively, with respect to mesh M_3 . The mesh selected for this study is M_1 which provides results within the one per cent of relative error with respect to the finest mesh. One of the reasons that led us not to use mesh adaptation is the fact that the structure of the mode greatly changes within

Mesh	X_{min}	X_{max}	Y_{max}	Method
M_1	-40	80	40	Meshed by blocks
M_2	-40	80	40	Adapted BF
M_3	-40	80	40	Adapted BF + EM
M_4	-40	80	40	Adapted BF + EM + (split 2)
M_5	-40	80	40	Adapted BF + EM + (split 4)
M_6	-20	40	20	Meshed by blocks

TABLE 2. Geometrical parameters of the physical domain of meshes M_i and the method adopted for their generation.

Mesh	ω_c	α_c	F_x	F_y	μ_1	μ_2	N_p
M_1	0.3057	4.433	-0.0107	10.712	-0.0348 + 0.0669i	0.0334 - 0.0231i	32 291
M_2	0.3035	4.447	-0.0028	10.791	-0.0442 + 0.0548i	0.0469 - 0.0553i	1966
M_3	0.3067	4.429	-0.0146	10.700	-0.0351 + 0.0663i	0.0330 - 0.0232i	7682
M_4	0.3075	4.424	-0.0160	10.675	-0.0349 + 0.0655i	0.03290 - 0.0227i	30 364
M_5	0.3027	4.444	-0.0142	10.772	-0.0349 + 0.0691i	0.0342 - 0.0240i	120 728
M_6	0.3078	4.4486	-0.0575	10.7844	-0.0343 + 0.0695i	0.0324 - 0.0219i	8089
M_7	0.3053	4.4308	-0.0226	10.7018	-0.0354 + 0.0669i	0.0336 - 0.0231i	72 088

TABLE 3. Comparison of the performance of several meshes at $Re_c = 170$.

the parameter range (Re , α) investigated: this would have required many successive mesh adaptations.

Appendix E: Three-dimensional stability of steady-state solutions

In this section, we review three-dimensional stability studies carried out by Pralits *et al.* (2013), Rao *et al.* (2013a,b), Radi *et al.* (2013) and Rao *et al.* (2015).

It is now well known the secondary three-dimensional transition from a two-dimensional unsteady flow towards a three-dimensional flow at $Re \approx 190$ and $\alpha = 0$, see Williamson (1996). Vortices in the wake of the fixed cylinder, i.e. $\alpha = 0$, develop spanwise waviness whose wavelength is approximately four cylinder diameters. The rotation of the cylinder surface on this linear steady mode, denoted as Mode A in Rao *et al.* (2015), has a stabilising effect for rotation rates $\alpha < 1$, see figure 12.

Instead, if we consider the stability of an infinitesimal spanwise perturbation on a steady-state solution, the flow displays spanwise waviness at a much lower Reynolds number $Re \approx 100$ and $\alpha = 0$. The onset of instability of this stationary mode, denoted as Mode E in Rao *et al.* (2015), is shown in figure 12 as a function of (Re , α).

In the same region of existence of the unsteady two-dimensional Mode II, experimental evidence has shown the presence of a three-dimensional mode, see Linh (2011). A steady three-dimensional mode, here denoted as Mode II-3D, extends to lower Reynolds values than the two-dimensional threshold of the non-rotating cylinder, and for a larger interval in α than the two-dimensional Mode II. The instability mechanism of Mode II-3D is of hyperbolic nature, see Pralits *et al.* (2013).

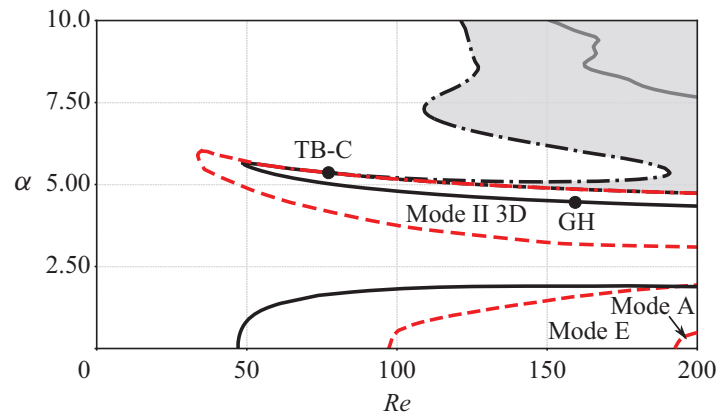


FIGURE 12. Neutral stability curves in the range $Re \in [0, 200]$ and $\alpha \in [0, 10]$. Black and grey lines are used to denote two-dimensional local bifurcations whereas red lines are used to designate the boundaries of three-dimensional local bifurcations. Dashed and point-dashed lines indicate the presence of a stationary bifurcation boundary, solid lines are used to designate unsteady bifurcation boundaries.

Finally, note that the occurrence of two unstable modes has also been documented in the flow past rotating spheres (Citro *et al.* 2016; Fabre *et al.* 2017). However, the spatial structure of the direct and adjoint modes for our geometrical configuration is very different with respect to the case of the rotating sphere flow.

REFERENCES

- BENGANA, Y., LOISEAU, J. CH., ROBINET, J. CH. & TUCKERMAN, L. S. 2019 Bifurcation analysis and frequency prediction in shear-driven cavity flow. *J. Fluid Mech.* **875**, 725–757.
- BRØNS, M. 2007 Streamline topology: patterns in fluid flows and their bifurcations. *Adv. Appl. Mech.* **41**, 1–42.
- CARINI, M., AUTERI, F. & GIANNETTI, F. 2015 Centre-manifold reduction of bifurcating flows. *J. Fluid Mech.* **767**, 109–145.
- CITRO, V., LUCHINI, P., GIANNETTI, F. & AUTERI, F. 2017 Efficient stabilization and acceleration of numerical simulation of fluid flows by residual recombination. *J. Comput. Phys.* **344**, 234–246.
- CITRO, V., TCHOUFAG, J., FABRE, D., GIANNETTI, F. & LUCHINI, P. 2016 Linear stability and weakly nonlinear analysis of the flow past rotating spheres. *J. Fluid Mech.* **807**, 62–86.
- DUMORTIER, F., ROUSSARIE, R., SOTOMAYOR, J. & ZOLADEK, H. 2006 *Bifurcations of Planar Vector Fields: Nilpotent Singularities and Abelian Integrals*. Springer.
- FABRE, D., CITRO, V., SABINO, D., FERREIRA, B. P., SIERRA, J., GIANNETTI, F. & PIGOU, M. 2019 A practical review to linear and nonlinear approaches to flow instabilities. *Appl. Mech. Rev.* **70** (6), 060802.
- FABRE, D., LONGOBARDI, R., CITRO, V. & LUCHINI, P. 2020 Acoustic impedance and hydrodynamic instability of the flow through a circular aperture in a thick plate. *J. Fluid Mech.* **885**, A11.
- FABRE, D., TCHOUFAG, J., CITRO, V., GIANNETTI, F. & LUCHINI, P. 2017 The flow past a freely rotating sphere. *Theor. Comput. Fluid Dyn.* **31**, 475–482.
- GALLAIRE, F., BOUJO, E., MANTIC-LUGO, V., ARRATIA, C., THIRIA, B. & MELIGA, P. 2016 Pushing amplitude equations far from threshold: application to the supercritical Hopf bifurcation in the cylinder wake. *Fluid Dyn. Res.* **48** (6), 061401.
- GASULL, A., MAÑOSA, V. & VILADELPRAT, J. 2005 On the period of the limit cycles appearing in one-parameter bifurcations. *J. Differ. Equ.* **213** (2), 255–288.
- GIANNETTI, F. & LUCHINI, P. 2007 Structural sensitivity of the first instability of the cylinder wake. *J. Fluid Mech.* **581**, 167–197.

- EL HAK, M. G. 2000 *Flow Control: Passive, Active, and Reactive Flow Management*. Cambridge University Press.
- HEIL, M., ROSSO, J., HAZEL, A. L. & BRØNS, M. 2017 Topological fluid mechanics of the formation of the Kármán-vortex street. *J. Fluid Mech.* **812**, 199–221.
- JALLAS, D., MARQUET, O. & FABRE, D. 2017 Linear and nonlinear perturbation analysis of the symmetry breaking in time-periodic propulsive wakes. *Phys. Rev. E* **95** (6), 063111.
- KANG, S., CHOI, H. & LEE, S. 1999 Laminar flow past a rotating circular cylinder. *Phys. Fluids* **11** (11), 3312–3321.
- KAPITULA, T. & PROMISLOW, K. 2013 *Spectral and Dynamical Stability of Nonlinear Waves*, vol. 47. Springer.
- KUZNETSOV, Y. A. 2005 Practical computation of normal forms on center manifolds at degenerate Bogdanov–Takens bifurcations. *Intl J. Bifurcation Chaos* **15** (11), 3535–3546.
- KUZNETSOV, Y. A. 2013 *Elements of Applied Bifurcation Theory*, vol. 112. Springer Science & Business Media.
- LINH, D. T. T. 2011 Flow past a rotating circular cylinder. PhD thesis, Department of Mechanical Engineering, National University of Singapore.
- LUCHINI, P. & BOTTARO, A. 2014 Adjoint equations in stability analysis. *Annu. Rev. Fluid Mech.* **46**, 493–517.
- MANTIČ-LUGO, V., ARRATIA, C. & GALLAIRE, F. 2014 Self-consistent mean flow description of the nonlinear saturation of the vortex shedding in the cylinder wake. *Phys. Rev. Lett.* **113** (8), 084501.
- MITTAL, S. 2004 Three-dimensional instabilities in flow past a rotating cylinder. *Trans. ASME: J. Appl. Mech.* **71** (1), 89–95.
- MODI, V. J. 1997 Moving surface boundary-layer control: a review. *J. Fluids Struct.* **11** (6), 627–663.
- ORCHINI, A., RIGAS, G. & JUNIPER, M. P. 2016 Weakly nonlinear analysis of thermoacoustic bifurcations in the Rijke tube. *J. Fluid Mech.* **805**, 523–550.
- PRALITS, J. O., BRANDT, L. & GIANNETTI, F. 2010 Instability and sensitivity of the flow around a rotating circular cylinder. *J. Fluid Mech.* **650**, 513–536.
- PRALITS, J. O., GIANNETTI, F. & BRANDT, L. 2013 Three-dimensional instability of the flow around a rotating circular cylinder. *J. Fluid Mech.* **730**, 5–18.
- RADI, A., THOMPSON, M. C., RAO, A., HOURIGAN, K. & SHERIDAN, J. 2013 Experimental evidence of new three-dimensional modes in the wake of a rotating cylinder. *J. Fluid Mech.* **734**, 567–594.
- RAO, A., LEONTINI, J. S., THOMPSON, M. C. & HOURIGAN, K. 2013a Three-dimensionality in the wake of a rapidly rotating cylinder in uniform flow. *J. Fluid Mech.* **717**, 1–29.
- RAO, A., LEONTINI, J. S., THOMPSON, M. C. & HOURIGAN, K. 2013b Three-dimensionality in the wake of a rapidly rotating cylinder in uniform flow. *J. Fluid Mech.* **730**, 379–391.
- RAO, A., RADI, A., LEONTINI, J. S., THOMPSON, M. C., SHERIDAN, J. & HOURIGAN, K. 2015 A review of rotating cylinder wake transitions. *J. Fluids Struct.* **53**, 2–14.
- SIPP, D. & LEBEDEV, A. 2007 Global stability of base and mean flows: a general approach and its applications to cylinder and open cavity flows. *J. Fluid Mech.* **593**, 333–358.
- STOJKOVIĆ, D., BREUER, M. & DURST, F. 2002 Effect of high rotation rates on the laminar flow around a circular cylinder. *Phys. Fluids* **14** (9), 3160–3178.
- STOJKOVIĆ, D., BREUER, M. & DURST, F. 2003 On the new vortex shedding mode past a rotating circular cylinder. *Phys. Fluids* **15** (5), 1257–1260.
- THOMPSON, M. C., RAO, A., LEONTINI, J. S. & HOURIGAN, K. 2014 The existence of multiple solutions for rotating cylinder flows. In *19th Australasian Fluid Mechanics Conference, Melbourne, Australia December 8-11*. RMIT University.
- WIGGINS, S. 2003 *Introduction to Applied Nonlinear Dynamical Systems and Chaos*, vol. 2. Springer Science & Business Media.
- WILLIAMSON, C. H. K. 1996 Vortex dynamics in the cylinder wake. *Annu. Rev. Fluid Mech.* **28** (1), 477–539.

Banner appropriate to article type will appear here in typeset article

1 **Mode selection in concentric jets: the steady-steady** 2 **1:2 resonant mode interaction with O(2) symmetry**

3 **A. Corrochano**¹, **J. Sierra-Ausín**^{2,3}, **J. A. Martín**¹,
4 **D. Fabre**², **S. Le Clainche**¹ †

5 ¹School of Aerospace Engineering, Universidad Politécnica de Madrid, Madrid 28040, Spain

6 ²Institut de Mécanique des Fluides de Toulouse (IMFT), Toulouse 31400, France

7 ³DIIN, Università degli Studi di Salerno, Via Giovanni Paolo II, 84084 Fisciano (SA), Italy

8 (Received xx; revised xx; accepted xx)

9 The linear and non-linear stability of two concentric jets separated by a duct wall is analysed by
10 means of global linear stability and weakly non-linear analysis. Three governing parameters
11 are considered, the Reynolds number based on the inner jet, the inner-to-outer jet velocity
12 ratio (δ_u), and the length of the duct wall (L) separating the jet streams. Global linear stability
13 analysis demonstrates the existence of unsteady modes of inherent convective nature, and
14 symmetry-breaking modes that lead to a new non-axisymmetric steady-state with a single or
15 double helix. Additionally, we highlight the existence of multiple steady-states, as a result
16 of a series of saddle-node bifurcations and its connection to the changes in the topology of
17 the flow. The neutral lines of stability have been computed for inner-to-outer velocity ratios
18 within the range $0 < \delta_u < 2$ and duct wall distances in the interval $0.5 < L < 4$. They reveal
19 the existence of hysteresis, and mode switching between two symmetry breaking modes with
20 azimuthal wavenumbers $1 : 2$. Finally, the mode interaction is analysed, highlighting the
21 presence of travelling waves emerging from the resonant interaction of the two steady states,
22 and the existence of robust heteroclinic cycles that are asymptotically stable.

23 **Key words:** Concentric jets, linear stability analysis, dynamical systems, wakes/jets

24 **1. Introduction**

25 Double concentric jets is a configuration enhancing the turbulent mixing of two jets, which
26 is used in several industrial applications where the breakup of the jet into droplets due to
27 flow instabilities is presented as the key technology. Combustion (i.e., combustion chamber
28 of rocket engines, gas turbine combustion, internal combustion engines, etc.) and noise
29 reduction (e.g., in turbofan engines) are the two main applications of this geometry, although
30 the annular jets can also be found in some other relevant applications such as ink-jet printers
31 or spray coating.

32 The qualitative picture emerging from this type of flow divides the inner field of concentric
33 jets in three different regions: (i) initial merging zone, (ii) transitional zone and (iii) merged

† Email address for correspondence: soledad.leclainche@upm.es

Abstract must not spill onto p.2

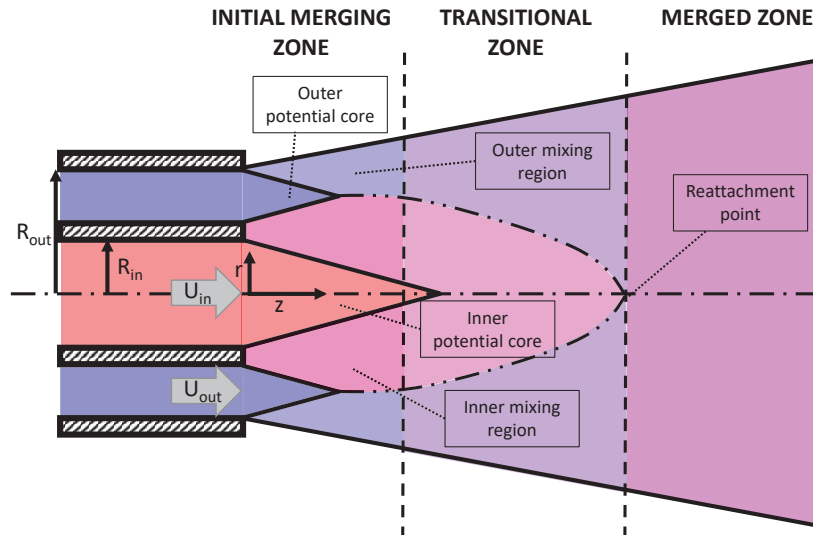


Figure 1: Sketch representing the three flow regimes in the near field of double concentric jets. Figure based on the sketch presented in (Ko & Kwan 1976; Talamelli & Gavarini 2006).

34 zone, as presented in fig. 1, that follows the initial sketch presented by Ko & Kwan (1976).
 35 In the initial merging zone (i), just at the exit of the two jets, two axisymmetric shear layers
 36 (inner and outer boundary layer) develop and start to merge. In this region, we distinguish
 37 the inner and outer shear layers, related with the inner and outer jet stream. Then, most of the
 38 mixing occurs in the transitional zone (ii), that extends until the external shear layer reaches
 39 the centreline. Finally, in the merged zone (iii), the two jets are totally merged, modelling a
 40 single jet flow.

41 Several parameters define the characteristic of this flow: the inner and outer jet velocities,
 42 the jet diameters, the shape and thickness of the wall separating both jets, the Reynolds
 43 number, the boundary layer state and thickness at the jet exit and the free stream turbulence.
 44 Based on these parameters, it is possible to identify several types of flow behaviour, which
 45 can be related with the presence of flow instabilities.

46 Numerous studies have investigated the interaction between the inner and outer shear
 47 layers of the jet and their effect on the flow instability. Starting with Ko & Kwan (1976), they
 48 postulated that the double concentric jet configuration could be considered as a combination
 49 of single jets. Nevertheless, Dahm *et al.* (1992) revealed by means of flow visualisations,
 50 diverse topology patterns as function of the outer/inner jet velocity ratio, reflecting that the
 51 dynamics of the inner and outer jet shear layers were different from that in a single jet.
 52 Moreover, this study exhibited a complex interaction between vortices identified in both
 53 shear layers, affecting the instability mechanism of the flow. Subsequently, different flow
 54 regimes are recognised as a function of the outer/inner velocity ratio. For cases in which
 55 the outer velocity is much larger than the inner velocity, the outer shear layer dominates the
 56 flow dynamics (Buresti *et al.* 1994), and a low frequency recirculation bubble can be spotted
 57 at the jet outlet (Rehab *et al.* 1997). For still high outer/inner velocity ratios, the outer jet
 58 drives the flow dynamics, exciting the inner jet which ends oscillating at the same frequency
 59 as the external jet. This trend is known as the lock-in phenomenon, identified by several
 60 authors (Dahm *et al.* 1992; Rehab *et al.* 1997; da Silva *et al.* 2003; Segalini & Talamelli
 61 2011). Moreover, the oscillation frequency detected was similar to the one defined by a
 62 Kelvin-Helmholtz flow instability, generally encountered in single jets. When the outer/inner

63 velocity ratio is similar, a Von Kármán vortex street is detected near the separating wall,
64 depicted in various investigations (Olsen & Karchmer 1976; Dahm *et al.* 1992; Buresti *et al.*
65 1994; Segalini & Talamelli 2011). A wake instability affected the inner and outer shear
66 layers, reversing the lock-in phenomenon. Finally, for small outer/inner velocity ratios, the
67 inner jet presents its own flow instability in the shear layer, while a different flow instability
68 was identified in the outer jet, as shown by Segalini & Talamelli (2011).

69 The velocity ratio between jets has also an influence on noise attenuation, which was
70 analysed experimentally by Williams *et al.* (1969). It was observed that for some given
71 configurations, more noise attenuation was present than for the others, with a maximum
72 between 12 and 15dB.

73 Regarding the geometric configuration of the concentric jets, Buresti *et al.* (1994) detected
74 the presence of an alternate vortex shedding when the separation wall thickness between the
75 two jets was sufficiently large, also recognised by Dahm *et al.* (1992); Olsen & Karchmer
76 (1976). This finding was as well presented by Wallace & Redekopp (1992), including the
77 influence of the wall thickness and sharpness on the characteristics of the jet.

78 This vortex shedding has been theoretically analysed (Talamelli & Gavarini 2006) by means
79 of linear stability analysis, and experimentally tested (Örlü *et al.* 2008). These investigations
80 agree on the vortex shedding driving the evolution of both outer and inner shear layer.
81 Consequently, a global absolute instability can be triggered by this mechanism with no
82 external energy input. The vortex shedding can be therefore considered as a potential tool for
83 passive flow control, delaying the transition to turbulence by means of controlling the near
84 field of the jet.

85 The study performed in Talamelli & Gavarini (2006) constituted an entry point for
86 subsequent researches (although ignoring the effect of the duct wall separating the two
87 streams). A similar procedure was employed to investigate the local linear spatial stability of
88 compressible, inviscid coaxial jets (Perrault-Joncas & Maslowe 2008) and lately accounting
89 for the effects of heat conduction and viscosity (Gloor *et al.* 2013). Both investigations
90 found two modes of instability, one being associated with the primary and the other with
91 the secondary stream, showing an independence between modes, the effect of velocity ratio
92 mainly affects the first mode, while the second mode was primarily influenced by the diameter
93 ratio between jets. Gloor *et al.* (2013) also identified parameter regimes in which the stability
94 of the two layers is not independent anymore, and pointed that viscous effects are essential
95 only below a specific Reynolds number. Subsequently, this work was expanded in Balestra
96 *et al.* (2015) to investigate the local inviscid spatio-temporal instability characteristics of
97 heated coaxial jet flows, where the presence of an absolutely unstable outer mode was
98 identified.

99 Recently, Canton *et al.* (2017) performed a global linear stability analysis to study more
100 in detail this vortex shedding mechanism behind the wall. They examined a concentric jet
101 configuration with a very small wall thickness ($0.1D$, with D the inner jet diameter), but
102 the authors selected an outer/inner velocity ratios where it was known that the alternate
103 vortex shedding behind the wall was driving the flow. A global unstable mode (absolute
104 instability) with azimuthal wavenumber $m = 0$ was found, confirming that the primary
105 instability was axisymmetric (the modes with $m = 1, 2$ were stable at the flow conditions
106 at which the study was carried out). The highest intensity of the global mode was located
107 in the wake of the jet, composed by an array of counter-rotating vortex rings. The shape
108 of the mode changes when moving along its neutral curve, revealing through the numerical
109 simulations a Kelvin-Helmholtz instability over the shear-layer between the two jets and in
110 the outer jet at high Reynolds numbers. Nevertheless, the authors showed that the wavemaker
111 was located in the bubble formed upstream the separating wall, in good agreement with

112 the results presented by Tammisola (2012), who performed a similar stability analysis in a
113 two-dimensional configuration (wakes with co-flow).

114 The stability of annular jets, a limit case where the inner jets have zero velocity, has
115 also been investigated. In different analyses of annular jets (Bogulawski & Wawrzak 2020;
116 Michalke 1999), it has been illustrated that this type of axisymmetric configuration does not
117 behave as it appears. The $m = 0$ modes studied have been shown to be stable, and the dominant
118 mode found by both studies is helical ($m = 1$). In addition, to characterise the annular jet,
119 these investigations analyse the behaviour of the case by adding an azimuthal component
120 to the inflow velocity, making the discharge of the annular jet eddy-like, comparing the
121 evolution of the frequency and growth rate of this $m = 1$ mode.

122 The convective stability of weakly swirling coaxial jets has also been studied, as done in
123 Montagnani & Auteri (2019), where the optimal response modes are determined from an
124 external forcing. The impact of velocity ratio between jets, effect of swirl, and influence
125 of Reynolds number is presented by means of non-modal analysis. They showed that
126 small transient perturbations rapidly grow, experiencing a considerable spatial amplification,
127 where nonlinear interactions come into play being capable of triggering turbulence and
128 large oscillations. For non-swirling coaxial jets, the stability characteristics are found to be
129 dominated by the axisymmetric and sinuous optimal modes.

130 The current study aims to expand the investigations of Canton *et al.* (2017), who used
131 a specific geometry and varied the outer-to-inner velocity ratio. Herein, we aim to provide
132 a complete characterisation of the leading global modes, and to demonstrate the effect of
133 three parameters on the linear stability properties. These three parameters are: the duct wall
134 thickness separating the two jets, which is explored in the interval $L \in [0.5, 4]$, the inner-
135 to-outer velocity δ_u , within the range $\delta_u \in [0, 2]$, and the Reynolds numbers based on the
136 inner jet. We find unstable global modes with azimuthal wavenumbers $m = 0$ (axisymmetric
137 modes), $m = 1$ and $m = 2$.

138 This work also performs a study of the mode interaction between two steady modes with
139 azimuthal wavenumbers $m = 1$ and $m = 2$. Different analyses have been done to determine
140 the attracting coherent structures when there is an interaction between modes. Some of these
141 flow structures are non-axisymmetric steady states, travelling waves or most remarkably
142 robust heteroclinic cycles.

143 The article is organised as follows. Section 2 defines the problem and the governing
144 equations for the coaxial jet configuration, as well as the linear stability equations and the
145 methodology for mode selection. A characterisation of the axisymmetric steady-state is done
146 in Section 3. In particular, we show the existence of multiple steady-states, as a result of
147 a series of saddle-node bifurcations. Section 4 is devoted to the discussion of the global
148 linear stability results. Section 4.1 is intended to illustrate the basic features of the most
149 unstable global modes, such as their spatial distribution and frequency content, as well as, a
150 brief discussion about the instability physical mechanism. In the following subsections, we
151 perform a parametric exploration in terms of the inner-to-outer velocity ratio, and the duct
152 wall length between the jet streams in order to determine the neutral curves of global stability.
153 Section 5 undertakes a detailed study of the unfolding of the codimension-two bifurcation
154 between two steady-modes with azimuthal wavenumbers $m = 1$ and $m = 2$. Therein, we
155 discuss the consequences of 1 : 2 resonance, which leads to the emergence of unsteady
156 flow structures, such as travelling waves or robust heteroclinic cycles, among others. Finally,
157 Section 6 summarises the main conclusions of the current study.

Focus on Fluids articles must not exceed this page length

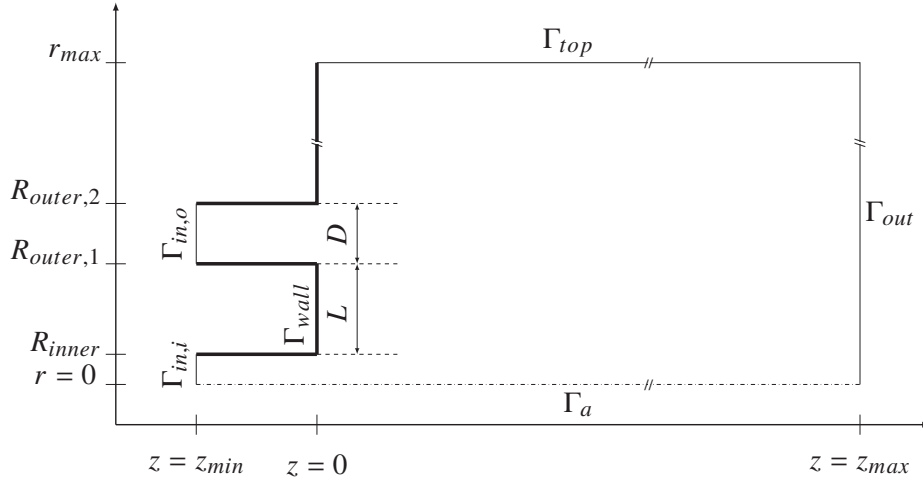


Figure 2: Computational domain of the configuration of two concentric jets, used in StabFem.

158 2. Problem formulation

159

2.1. Computational domain and general equations

160

The computational domain, represented in fig. 2, models a coaxial flow configuration, which is composed of two inlet regions, an inner and outer pipe, both having a distance D between walls and length $5D$, i.e. $z_{min} = -5D$. The computational domain has an extension of $z_{max} = 50D$ and $r_{max} = 25D$. The distance between the pipes is equal to L , measured from the inner face of the outer tube to the face of the inner jet.

165

The governing equations of the flow within the domain are the incompressible Navier–Stokes equations. These are written in cylindrical coordinates (r, θ, z) , which are made dimensionless by considering D as the reference length scale and $W_{o,max}$ as the reference velocity scale, which is the maximum velocity in the outer pipe at $z = z_{min}$.

169

$$\frac{\partial \mathbf{U}}{\partial t} + \mathbf{U} \cdot \nabla \mathbf{U} = -\nabla P + \nabla \cdot \tau(\mathbf{U}), \quad \nabla \cdot \mathbf{U} = 0, \quad (2.1a)$$

170

171

$$\text{with } \tau(\mathbf{U}) = \frac{1}{Re} (\nabla \mathbf{U} + \nabla \mathbf{U}^T), \quad Re = \frac{W_{o,max} D}{\nu}. \quad (2.1b)$$

172

The dimensionless velocity vector $\mathbf{U} = (U, V, W)$ is composed of the radial, azimuthal and axial components, P is the dimensionless-reduced pressure, the dynamic viscosity ν and the viscous stress tensor $\tau(\mathbf{U})$.

175

The incompressible Navier–Stokes equations eq. (2.1) are complemented with the following boundary conditions

177

$$\mathbf{U} = (0, 0, W_i) \text{ on } \Gamma_{in,i} \text{ and } \mathbf{U} = (0, 0, W_o) \text{ on } \Gamma_{in,o}, \quad (2.2)$$

where

$$W_i = \delta_u \tanh(b_i(1 - 2r)) \text{ and } W_o = \tanh \left[b_o \left(1 - \left| \frac{2r - (R_{outer,1} + R_{outer,2})}{D} \right| \right) \right].$$

178

179

180

181

The parameter δ_u corresponds to the velocity ratio between the two jets, defined as $\delta_u = W_{i,max}/W_{o,max}$, the volumetric flow rate of the inner and outer jet are defined as $\dot{V}_i = 2\pi \int_0^{R_{inner}} r W_i dr$ and $\dot{V}_o = 2\pi \int_{R_{outer,1}}^{R_{outer,2}} r W_o dr$, respectively. The parameters b_o and b_i represent the boundary layer thickness within the nozzle, which are fixed equal to 5 (as in

182 Canton *et al.* (2017)). With this choice of parameters the volumetric flow rate of the inner
 183 jet is a function of the inner-to-outer velocity $\dot{V}_i = 3.73\delta_u$, whereas the flow rate of the outer
 184 jet is a function of the duct wall length separating the two jets $\dot{V}_o = 5.41L$. There is a weak
 185 influence of the boundary layer thickness on the stability properties of the jet, and it is related
 186 to the vortex shedding regime developed upstream the separation wall (more details may be
 187 found in Talamelli & Gavarini (2006)). Finally, no-slip boundary condition is set on Γ_{wall}
 188 and stress-free ($(\frac{1}{Re}\tau(\mathbf{U}) - P) \cdot \mathbf{n} = \mathbf{0}$) boundary condition is set on Γ_{top} and Γ_{out} , as shown
 189 in fig. 2.

190 In the sequel, Navier–Stokes equations eq. (2.1) and the associated boundary conditions
 191 will be written symbolically under the form

$$192 \quad \mathbf{B} \frac{\partial \mathbf{Q}}{\partial t} = \mathbf{F}(\mathbf{Q}, \boldsymbol{\eta}) \equiv \mathbf{L}\mathbf{Q} + \mathbf{N}(\mathbf{Q}, \mathbf{Q}) + \mathbf{G}(\mathbf{Q}, \boldsymbol{\eta}), \quad (2.3)$$

193 with the flow state vector $\mathbf{Q} = [\mathbf{U}, P]^T$, $\boldsymbol{\eta} = [Re, \delta_u]^T$, and the entries of the matrix \mathbf{B}
 194 arises from rearranging eq. (2.1). Such a form of the governing equations takes into account
 195 a linear dependency on the state variable \mathbf{Q} through \mathbf{L} . And a quadratic dependency on the
 196 parameters and the state variable through operators $\mathbf{G}(\cdot, \cdot)$ and $\mathbf{N}(\cdot, \cdot)$.

197 2.2. Asymptotic stability

198 2.2.1. Linear stability analysis

199 In this study, the authors attempt to characterise the stable asymptotic state from the spectral
 200 properties of the Navier–Stokes equations eq. (2.1). First, let us consider the stability of
 201 an axisymmetric steady-state solution named \mathbf{Q}_0 , which will be also referred to as *trivial*
 202 *steady-state*. For that purpose, let us evaluate a solution of eq. (2.1) in the neighbourhood of
 203 the trivial steady state, i.e., a perturbed state as follows,

$$204 \quad \mathbf{Q}(\mathbf{x}, t) = \mathbf{Q}_0(\mathbf{x}, t) + \varepsilon \hat{\mathbf{q}}(r, z) e^{-i(\omega t - m\theta)}, \quad (2.4)$$

205 where $\varepsilon \ll 1$, $\hat{\mathbf{q}} = [\hat{\mathbf{u}}, \hat{p}]^T$ is the perturbed state, ω is the complex frequency and m is the
 206 azimuthal wavenumber. The next step consists in the characterisation of the dynamics of
 207 small-amplitude perturbations around this base flow by expanding them over the basis of
 208 linear eigenmodes (2.4). If there is a pair $[i\omega_\ell, \hat{\mathbf{q}}_\ell]$ with $\text{Im}(\omega_\ell) > 0$ (resp. the spectrum
 209 is contained in the half of the complex plane with negative real part) there exists a basin
 210 of attraction in the phase space where the trivial steady-state \mathbf{Q}_0 is unstable (resp. stable)
 211 (Kapitula & Promislow 2013). The eigenpair $[i\omega_\ell, \hat{\mathbf{q}}_\ell]$ is determined as a solution of the
 212 following eigenvalue problem,

$$213 \quad \mathbf{J}_{(\omega_\ell, m_\ell)} \hat{\mathbf{q}}_{(z_\ell)} \equiv \left(i\omega_\ell \mathbf{B} - \frac{\partial \mathbf{F}}{\partial \mathbf{q}} \Big|_{\mathbf{q}=\mathbf{Q}_0, \boldsymbol{\eta}=\mathbf{0}} \right) \hat{\mathbf{q}}_{(z_\ell)} = 0, \quad (2.5)$$

214 where the linear operator \mathbf{J} is the Jacobian of eq. (2.1), and $\left(\frac{\partial \mathbf{F}}{\partial \mathbf{q}} \Big|_{\mathbf{q}=\mathbf{Q}_0, \boldsymbol{\eta}=\mathbf{0}} \right) \hat{\mathbf{q}}_{(z_\ell)} = \mathbf{L}_{m_\ell} \hat{\mathbf{q}}_{(z_\ell)} +$
 215 $\mathbf{N}_{m_\ell}(\mathbf{Q}_0, \hat{\mathbf{q}}_{(z_\ell)}) + \mathbf{N}_{m_\ell}(\hat{\mathbf{q}}_{(z_\ell)}, \mathbf{Q}_0)$. The subscript m_ℓ indicates the azimuthal wavenumber used
 216 for the evaluation of the operator. In the following, we account for eigenmodes $\hat{\mathbf{q}}_{(z_\ell)}(r, z)$
 217 that have been normalised in such a way $\langle \hat{\mathbf{u}}_{(z_\ell)}, \hat{\mathbf{u}}_{(z_\ell)} \rangle_{L^2} = 1$.

218 The identification of the *core* region of the self-excited instability mechanism (Gianneti &
 219 Luchini 2007) is evaluated by means of the structural sensitivity tensor

$$220 \quad \mathbf{S}_s = (\hat{\mathbf{u}}^\dagger)^* \otimes \hat{\mathbf{u}}. \quad (2.6)$$

221 2.2.2. Methodology for the study of mode selection

In the following, we briefly outline the main aspects of the methodology employed in the study
 of *mode interaction* or unfolding of a bifurcation with codimension-two, a comprehensive

explanation is left to appendix A. Herein, we use the concept of mode interaction as a synonym of the analysis of a bifurcation with codimension-two, that is, a bifurcation satisfying two conditions, e.g., a bifurcation where two modes become at the same time unstable. The determination of the attractor or coherent structure is explored within the framework of equivariant bifurcation theory. The trivial steady-state is axisymmetric, i.e. the symmetry group is the orthogonal group $O(2)$. Near the onset of the instability, dynamics can be reduced to those of the centre manifold. Particularly, due to the non-uniqueness of the manifold one can always look for its simplest polynomial expression, which is known as the *normal form* of the bifurcation. The reduction to the normal form is carried out via a multiple scales expansion of the solution \mathbf{Q} of eq. (2.3). The expansion considers a two scale development of the original time $t \mapsto t + \varepsilon^2 \tau$, here ε is the order of magnitude of the flow disturbances, assumed to be small $\varepsilon \ll 1$. In this study we carry out a normal form reduction via a weakly non-linear expansion, where the small parameters are

$$\varepsilon_{\delta_u}^2 = \delta_{u,c} - \delta_u \sim \varepsilon^2 \text{ and } \varepsilon_v^2 = (\nu_c - \nu) = (Re_c^{-1} - Re^{-1}) \sim \varepsilon^2.$$

222 A fast timescale t of the self-sustained instability and a slow timescale of the evolution of the
 223 amplitudes $z_i(\tau)$ are also considered in eq. (2.11), for $i = 1, 2, 3$. The ansatz of the expansion
 224 is as follows

$$225 \quad \mathbf{Q}(t, \tau) = \mathbf{Q}_0 + \varepsilon \mathbf{q}_{(\varepsilon)}(t, \tau) + \varepsilon^2 \mathbf{q}_{(\varepsilon^2)}(t, \tau) + O(\varepsilon^3). \quad (2.7)$$

226 Herein, we evaluate the mode interaction between two steady symmetry breaking states with
 227 azimuthal wave number $m_1 = 1$ and $m_2 = 2$, that is,

$$228 \quad \mathbf{q}_{(\varepsilon)}(t, \tau) = (z_1(\tau) \hat{\mathbf{q}}_{(z_1)}(r, z) e^{-im_1 \theta} + \text{c.c.}) \\ + (z_2(\tau) \hat{\mathbf{q}}_{(z_2)}(r, z) e^{-im_2 \theta} + \text{c.c.}), \quad (2.8)$$

229 where z_1 and z_2 are the complex amplitudes of the two symmetric modes $\hat{\mathbf{q}}_{(z_1)}$ and $\hat{\mathbf{q}}_{(z_2)}$.
 230 Note that the expansion of the LHS of eq. (2.3) up to third order is as follows

$$231 \quad \varepsilon \mathbf{B} \frac{\partial \mathbf{q}_{(\varepsilon)}}{\partial t} + \varepsilon^2 \mathbf{B} \frac{\partial \mathbf{q}_{(\varepsilon^2)}}{\partial t} + \varepsilon^3 \left[\mathbf{B} \frac{\partial \mathbf{q}_{(\varepsilon^3)}}{\partial t} \right] + O(\varepsilon^4), \quad (2.9)$$

232 and the RHS respectively,

$$233 \quad \mathbf{F}(\mathbf{q}, \eta) = \mathbf{F}_{(0)} + \varepsilon \mathbf{F}_{(\varepsilon)} + \varepsilon^2 \mathbf{F}_{(\varepsilon^2)} + \varepsilon^3 \mathbf{F}_{(\varepsilon^3)} + O(\varepsilon^4). \quad (2.10)$$

234 Then, the problem up to third order in z_1 and z_2 can be reduced to (Armbruster *et al.* 1988)

$$235 \quad \dot{z}_1 = \lambda_1 z_1 + e_3 \bar{z}_1 z_2 + z_1 (c_{(1,1)} |z_1|^2 + c_{(1,2)} |z_2|^2), \\ \dot{z}_2 = \lambda_2 z_2 + e_4 z_1^2 + z_2 (c_{(2,1)} |z_1|^2 + c_{(2,2)} |z_2|^2). \quad (2.11)$$

236 where λ_1 and λ_2 are the unfolding parameters of the normal form. The procedure followed for
 237 the determination of the coefficients $c_{(i,j)}$ for $i, j = 1, 2$ and e_3 and e_4 is left to Appendix A.
 238 An exhaustive analysis of the nonlinear implications of this normal form on dynamics is left
 239 to section 5.

240 2.2.3. Numerical methodology for stability tools

241 Results presented herein follow the same numerical approach adopted by Fabre *et al.* (2019);
 242 Sierra *et al.* (2020a,b, 2021); Sierra-Ausin *et al.* (2022a,b), where a comparison with DNS
 243 can be found. The calculation of the steady-state, the eigenvalue problem and the normal
 244 form expansion are implemented in the open-source software FreeFem++. Parametric studies
 245 and generation of figures are collected by StabFem drivers, an open-source project available
 246 in <https://gitlab.com/stabfem/StabFem>. For steady-state, stability and normal form
 247 computations, we set the *stress-free* boundary condition at the outlet, which is the natural
 248 boundary condition in the variational formulation.

249 The resolution of the steady nonlinear Navier-Stokes equations is tackled by means of the
 250 Newton method. While, the generalised eigenvalue problem (eq. (2.5)) is solved following
 251 the Arnoldi method with spectral transformations. The normal form reduction procedure of
 252 section 2.2.2 only requires to solve a set of linear systems, which is also carried out within
 253 StabFem. On a standard laptop, every computation considered below can be attained within
 254 a few hours.

255 3. Characterisation of the axisymmetric steady-state

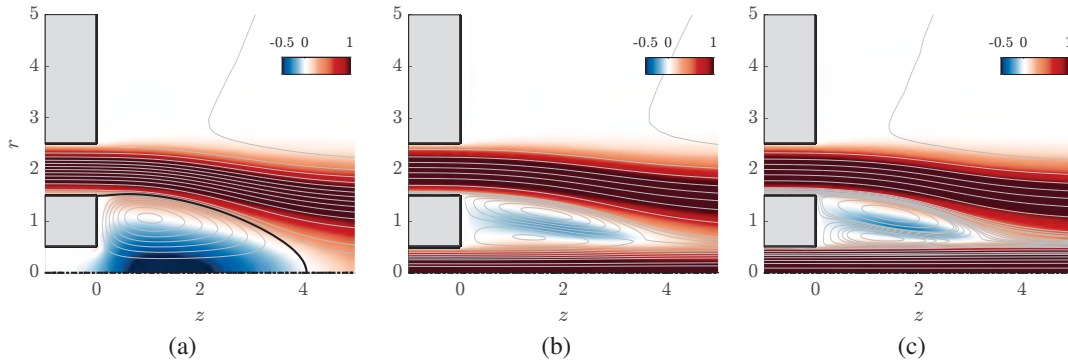


Figure 3: ($Re = 400, L = 1$) Meridional projections of the axisymmetric streamfunction isolines and the axial velocity contour in a range of $(z, r) \in [-1, 5] \times [0, 5]$. The large recirculation bubble is depicted with a thick black line. (a) $\delta_u = 0$. (b) $\delta_u = 1$. (c) $\delta_u = 2$.

256 The base flow is briefly described as a function of the inner-to-outer velocity ratio δ_u ,
 257 the Reynolds number and the length L of the duct wall separating the two jet streams. We
 258 begin by characterising the development of the axisymmetric steady-state with varying δ_u at
 259 a constant Reynolds number fixed to $Re = 400$ and distance between the jets $L = 1$. The axial
 260 velocity component of the steady-state is illustrated in fig. 3 for three values of the velocity
 261 ratio. The most remarkable difference between them is the modification of the topology of
 262 the flow near the duct separating the two coaxial jet streams. The annular jet case ($\delta_u = 0$),
 263 represented in fig. 3 (a), displays a large recirculation bubble. On the other hand, for the
 264 velocity ratios $\delta_u = 1$ and $\delta_u = 2$ there is no longer a large recirculation bubble, but two
 265 closed regions of recirculating fluid near the duct separating the two coaxial jets. These last
 266 two cases are illustrated in fig. 3 (b-c).

267 Figure 4 displays the evolution of the recirculation length (L_r) associated with the large
 268 recirculating bubble, which characterises the configurations of coaxial jets with a low value
 269 of the velocity ratio δ_u . Figure 4(a) shows that the recirculation length is nearly constant
 270 for values of the velocity ratio δ_u smaller than the magnitude of the velocity vector in the
 271 recirculation region. The value of the plateau, for a constant duct wall length L , increases
 272 with the Reynolds number. Reciprocally, at constant Reynolds number, the recirculation
 273 length increases with the duct wall length L separating the jet streams. For configurations
 274 of coaxial jets operated within this interval of the velocity ratio δ_u , we can say that the
 275 inner jet is trapped by the large recirculation region. Instead, when the velocity ratio δ_u
 276 is of similar magnitude to the axial velocity in the recirculating region, the inner jet is
 277 sufficiently energetic to break the recirculating region. For those values of the velocity
 278 ratio, the recirculation length is a rapidly decreasing function of δ_u . From fig. 4(a) we may
 279 conclude that larger distances between the jets respectively, a smaller value of the Reynolds

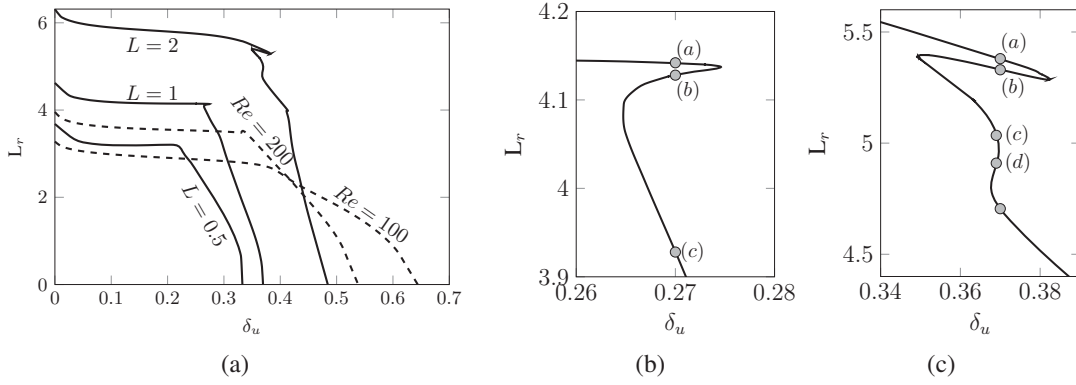


Figure 4: Evolution of the recirculation length (L_r) of the recirculating bubble with respect to the velocity ratio δ_u between the inner and outer jet. Solid lines are computed for a fixed Reynolds number $Re = 400$, while dashed lines are computed for a fixed distance $L = 1$. The figure (b) magnifies the region near the saddle-node bifurcation for $L = 1$, while figure (c) corresponds to an enlargement of the region near the saddle-node for $L = 2$.

280 number, lead to the existence of the recirculation region for larger velocity ratios. In addition,
 281 fig. 4 demonstrates the existence of multiple steady-states for the same velocity ratio. An
 282 enlargement of the region with multiple steady-states is displayed in Figure 4 (b) for the case
 283 of $L = 1$. It shows the existence of three steady-states in the interval of $0.265 \lesssim \delta_u \lesssim 0.275$,
 284 where the extreme points correspond to the location of the saddle-nodes. Figure 5 depicts
 285 the base flows associated with the circle markers in fig. 4 (b). Particularly, it demonstrates
 286 that the saddle-node bifurcations are, in some cases, associated with changes in the topology
 287 of the flow. From fig. 5 (a) to (b), one may appreciate the formation of a recirculating region
 288 along the duct wall separating the jet streams. While, from (b) to (c) we observe the formation
 289 of an additional region of recirculating flow near the upper corner of the duct wall. The large
 290 recirculation bubble is displaced downstream due to the formation of the two additional
 recirculation regions.

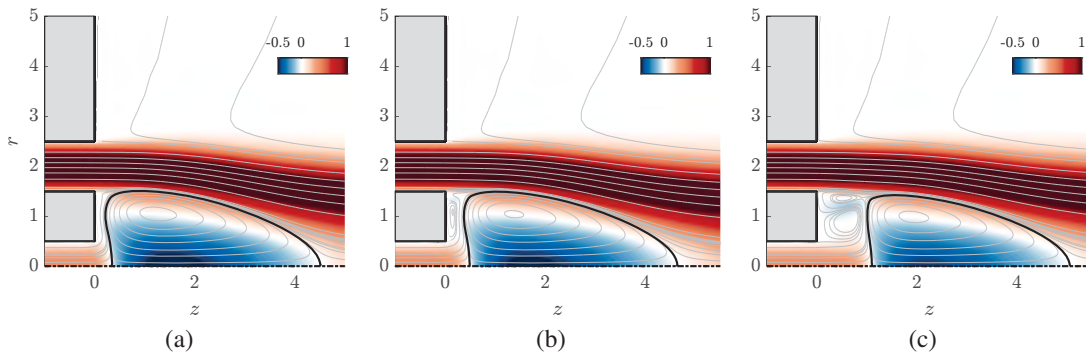


Figure 5: ($Re = 400, L = 1$) Meridional projections of the axisymmetric streamfunction isolines and the axial velocity contour in a range of $(z, r) \in [-1, 5] \times [0, 5]$. Each subfigure is associated to a marker of fig. 4 (b).

291
 292 Figure 4 (c) corresponds to an enlargement of the region with multiple steady-states for a
 293 distance $L = 2$ between the jet streams. The base flows associated to the circle markers are
 294 illustrated in fig. 6. It demonstrates that changes in the flow topology do not always occur

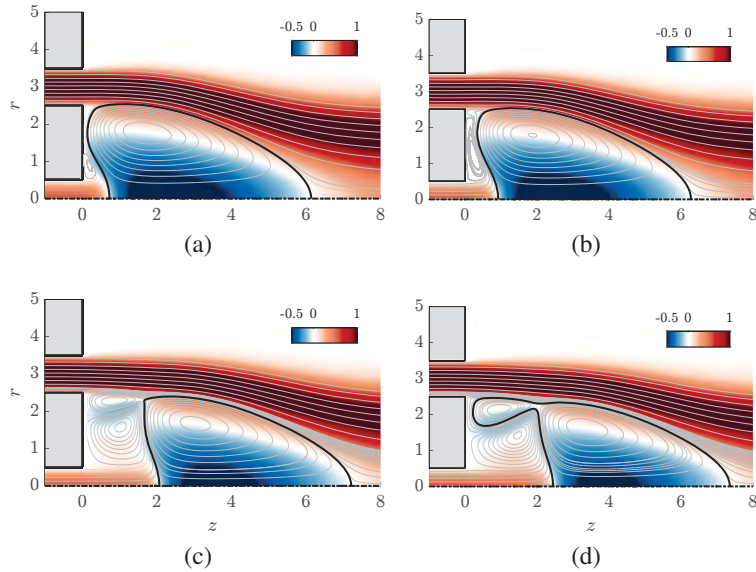


Figure 6: ($Re = 400, L = 2$) Meridional projections of the axisymmetric streamfunction isolines and the axial velocity contour in a range of $(z, r) \in [-1, 8] \times [0, 5]$. Each subfigure is associated to a marker of fig. 4 (c).

295 through saddle-node bifurcations. The base flow depicted in fig. 6 (a) already features a small
 296 region of a recirculating flow near the lower corner of the thick wall duct. Furthermore, from
 297 (a) to (b) we observe a stretching of the recirculation region attached to the duct wall, but
 298 without any change in the topology of the flow. On the contrary, the transitions from (b) to
 299 (c) and (c) to (d) are associated to changes in the topology of the flow. The passage from
 300 (b) to (c) is characterised by the formation of a vortex ring near the upper corner of the duct
 301 wall. Likewise, from (c) to (d) we appreciate a reconnection between the large recirculation
 302 bubble and the new vortex ring. Finally, the flow topology of the fifth steady-state, the circle
 303 marker without any text annotation, is identical to (d). In addition, it is worth noting that in
 304 the interval $0 < \delta_\mu < 2$ no further fold bifurcations are observed. Leading to the conclusion,
 305 that the saddle-node bifurcations are tightly connected to changes in the topology of the flow,
 306 leading to the disappearance of the large recirculation bubble and the formation of the two
 307 regions of recirculating fluid. Nonetheless, they are not neither the cause nor the effect of the
 308 modifications in the flow topology.

309 Lastly, the influence on the flow rate has been analysed, as the change of the distance
 310 between jets L , maintaining the same velocity profile on the outer jet, affects the value of
 311 the outer flow rate $\dot{V}_o \approx 5.4L$. On the other hand, the flow rate of the inner jet only depends
 312 on the inner-to-outer velocity ratio $\dot{V}_i \approx 3.7\delta_u$. As seen on figure 7, there are no significant
 313 changes on the recirculation bubble when the flow rate is changed. Figures 7 (b) and (c) show
 314 that similar cases with different flow rates but same ratio $(\frac{\dot{V}_o}{\dot{V}_i})$ between the inner and outer
 315 jet, present similar recirculation bubble.

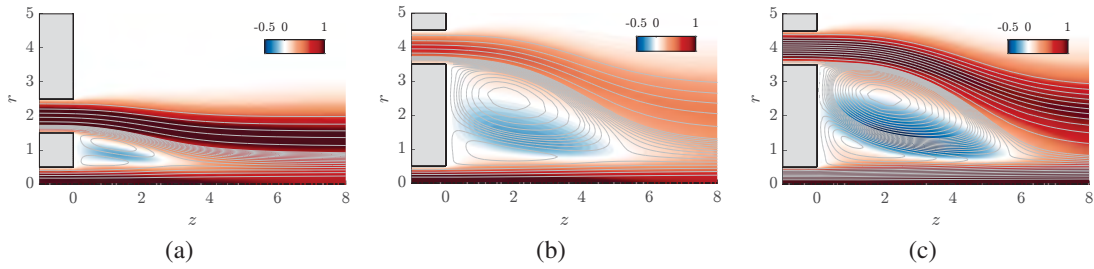


Figure 7: ($Re = 200$) Meridional projections of the axisymmetric streamfunction isolines and the axial velocity contour in a range of $(z, r) \in [-1, 5] \times [0, 8]$. (a) ($L = 1, \delta_u = 1$). (b) Duct wall length $L = 3$ and with the same flow rate of the outer jet (\dot{V}_o) of case (a). (c) ($L = 3, \delta_u = 2$) with the same ratio of the flow rate ($\frac{\dot{V}_o}{\dot{V}_i}$) between the inner and outer jet of cases (a) and (b)).

316 **4. Linear stability analysis**

317

4.1. Spectrum

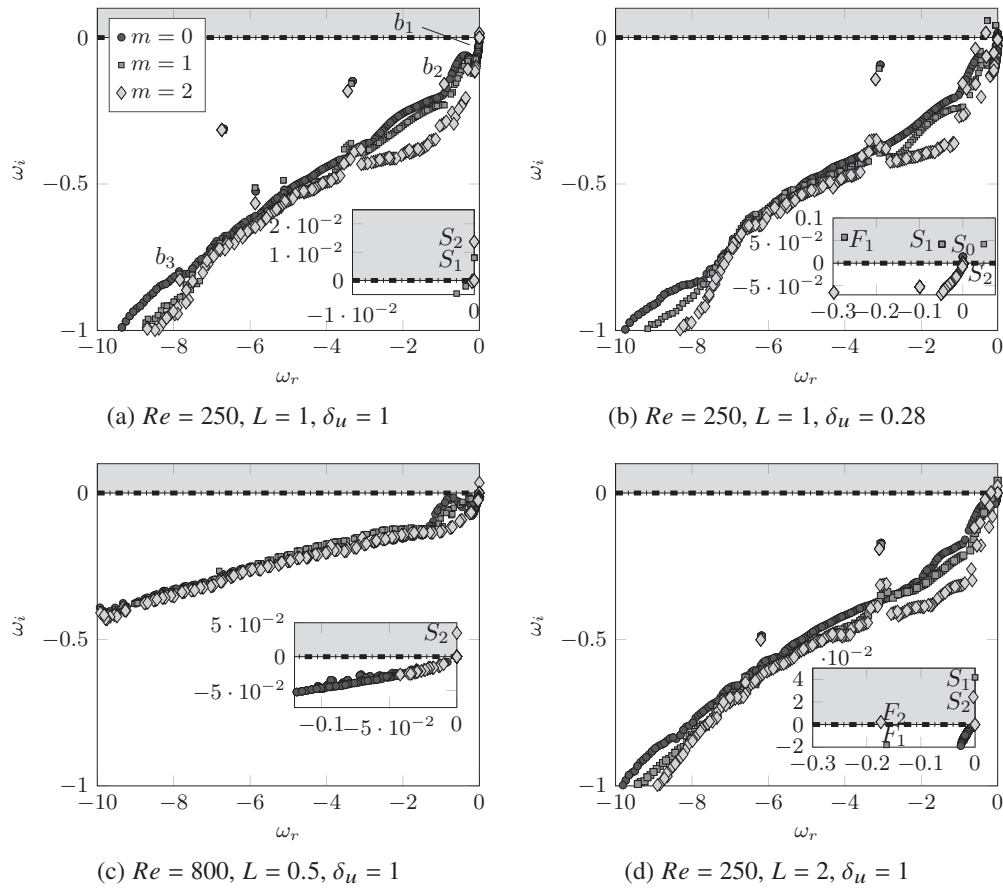


Figure 8: Spectrum computed at four different configurations of (Re, L, δ_u) for $m = 0, 1, 2$. The inset inside each subfigure magnifies the region near the origin. Stationary or low frequency modes are designated S, while oscillating/flapping modes are designated F, with the azimuthal wavenumber as the subscript.

318 Herein, we analyse the asymptotic linear stability of the steady-state in four distinct
 319 configurations. The first spectrum, depicted in fig. 8 (a), has been computed for a velocity
 320 ratio $\delta_u = 1$. Similarly, the second spectrum corresponds to a velocity ratio $\delta_u = 0.28$, which
 321 represents the middle branch after the saddle-node, that is, the equivalent of the marker (b) in
 322 fig. 4 (b) for $Re = 250$. These two configurations have been determined for a duct wall length
 323 $L = 1$. The remaining two spectrums have been computed for duct wall distances of $L = 0.5$
 324 and $L = 2$, which are illustrated in fig. 8 (c) and fig. 8 (d), respectively. The computation
 325 of the spectrum reveals the existence of eigenmodes, with azimuthal wavenumbers $m = 0$,
 326 $m = 1$ and $m = 2$, that become unstable.

First, the four spectrums display three types of continuous branches, referred to as b_i

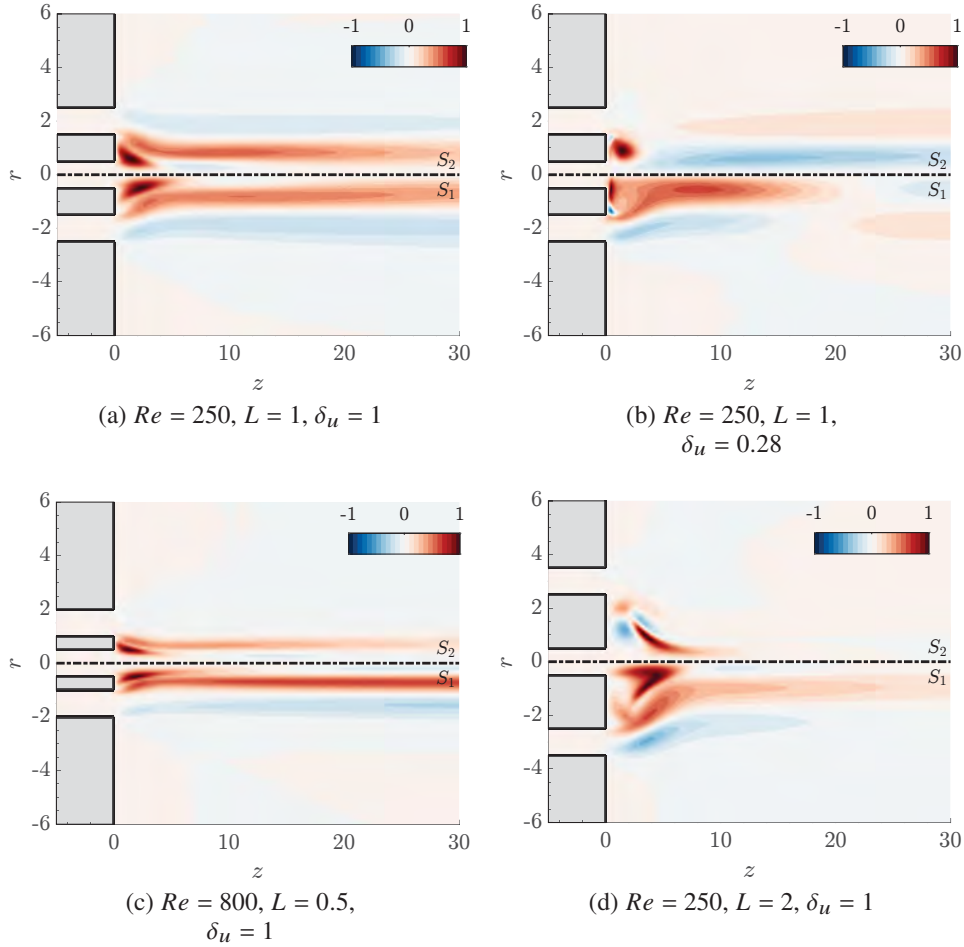


Figure 9: Axial velocity component of the non-oscillating global modes S_1 (bottom panel of the subfigure) and S_2 (top panel of the subfigure). The label of the subfigures coincide with the label of fig. 8.

327
 328 ($i = 1, 2, 3$), as it was the case in the configuration of coaxial jets described by Canton *et al.*
 329 (2017). The branch b_3 is composed of spurious modes. The branch b_2 is constituted of modes
 330 localised within the jet shear layers. While the branch b_1 is composed by nearly steady modes
 331 with support in the fluid region surrounding the jets.
 332 Second, in the four configurations we find two *non-oscillating* unstable modes (or nearly
 333 neutral as it is the case in fig. 8 (c)) with azimuthal wavenumber $m = 1$ and $m = 2$,

334 hereinafter referred to as modes S_1 and S_2 , respectively. These two modes are depicted in
 335 fig. 9, which illustrates their axial velocity component for the four configurations. Their
 336 spatial distribution is mostly localised inside the recirculating region of the flow, but they
 337 are also supported along the shear layer of the jets. Evaluating both the direct and adjoint
 338 modes, we can identify the *core* of the global instability from the maximum values of the
 function $\|\mathbf{S}_s(r, z)\|_F$, which has been defined in eq. (2.6).

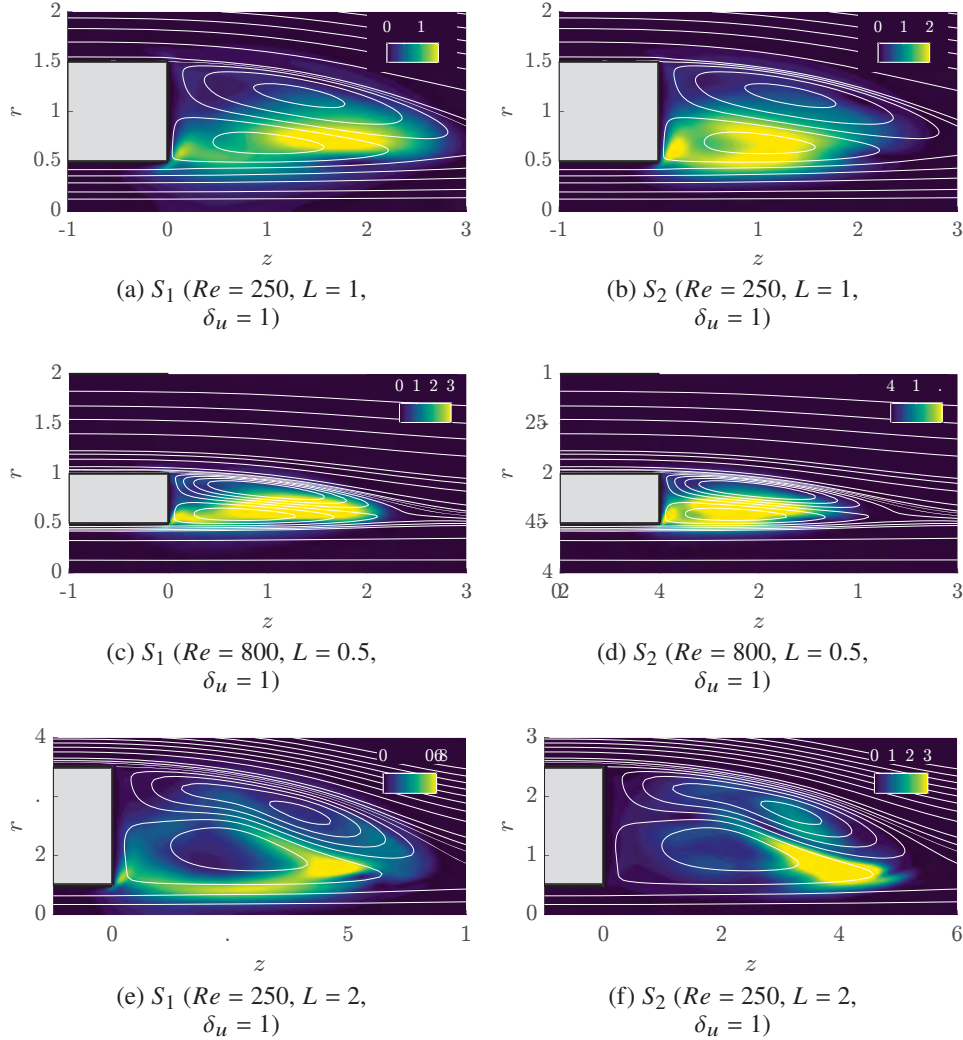


Figure 10: Structural sensitivity map $\|\mathbf{S}_s(r, z)\|_F$. White lines are employed to represent the steady-state streamlines.

339

340 Figure 10 illustrates the sensitivity maps for the modes displayed in fig. 9 (a,c,d). The
 341 sensitivity maps $\|\mathbf{S}_s(r, z)\|_F$ are compact supported within the region of recirculating fluid,
 342 featuring negligible values elsewhere. The maximum values of the sensitivity maps, displayed
 343 in fig. 10 (a,c,e) for the mode S_1 , are found within the inner vortex ring, in particular near
 344 the downstream part of the inner vortical region, and on the interface between the two
 345 vortical rings. By increasing the wall length separating the jet streams, the wavemaker moves
 346 downstream towards the right end of the inner vortical region. A similar observation is drawn
 347 from fig. 10 (b,d,f), where the core of the instability is also found within the inner vortex ring.

348 Similar observations were drawn in the case of the wake behind rotating spheres (Sierra-
 349 Ausín *et al.* 2022), where the core of the instability was also found near the downstream part
 350 of the recirculating flow region. Therein, it was concluded that the instability is supported by
 351 the recirculating flow region.

Figure 8 (d) illustrates the existence of two *oscillating/flapping* modes with azimuthal

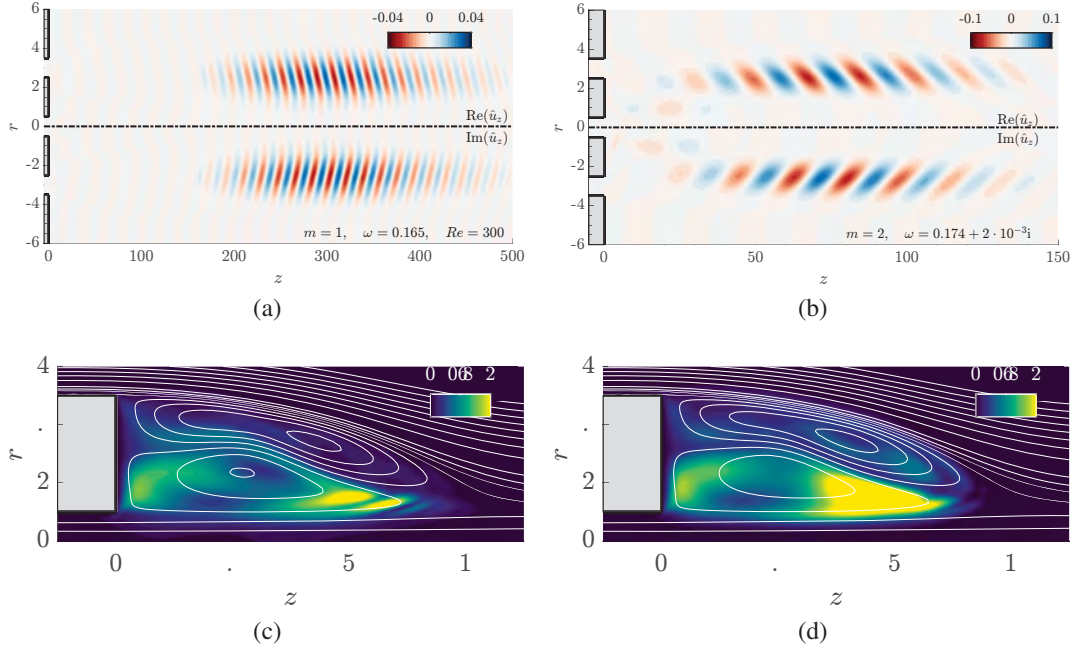


Figure 11: Axial velocity component of the oscillating global modes F_1 (a) and F_2 (b).
 Structural sensitivity map $\|\mathbf{S}_s(r, z)\|_F$ of mode F_1 (c) and F_2 (d). White lines are
 employed to represent the steady-state streamlines.

352
 353 wavenumber $m = 1$ and $m = 2$, hereinafter referred to as F_1 and F_2 , respectively. The
 354 axial velocity component of these two modes is displayed in fig. 11, together with their
 355 associated structural sensitivity map. The unsteady modes F_1 and F_2 possess a much larger
 356 spatial support than S_1 and S_2 . They are formed by an array of counter-rotating vortex spirals
 357 sustained along the shear layer of the base flow. For the mode F_2 the amplitude of these
 358 structures grows downstream of the nozzle, in the axial direction, with a maximum around $z \approx$
 359 70, after which they slowly decay. The mode F_1 grows further downstream, with a maximum
 360 around $z \approx 300$. The spatial structure of these eigenmodes resembles the axisymmetric
 361 mode of Figure 9 in Canton *et al.* (2017) or the optimal response modes determined by
 362 Montagnani & Auteri (2019). As it was the case for the non-oscillating modes, the core of
 363 the instability is found near the downstream part of the inner vortex ring. Tentatively, one
 364 may conclude that vortical perturbations are produced within the recirculating flow region
 365 and convected downstream while experiencing a considerable spatial amplification, which in
 366 turn justifies the resemblance with the optimal response modes determined by Montagnani
 367 & Auteri (2019).

368 There is an unstable $m = 0$ mode, hereinafter referred to as S_0 , in the spectrum displayed
 369 in Figure 8 (b). Such a mode, which is illustrated fig. 12 (a), is the result of a saddle-node
 370 bifurcation leading to the existence of multiple steady-states, a feature that has been discussed
 371 in section 3. It is a mode that promotes the formation of a recirculating flow region attached
 372 to the duct wall. In section 3 we have remarked that the S_0 modes can be related to changes

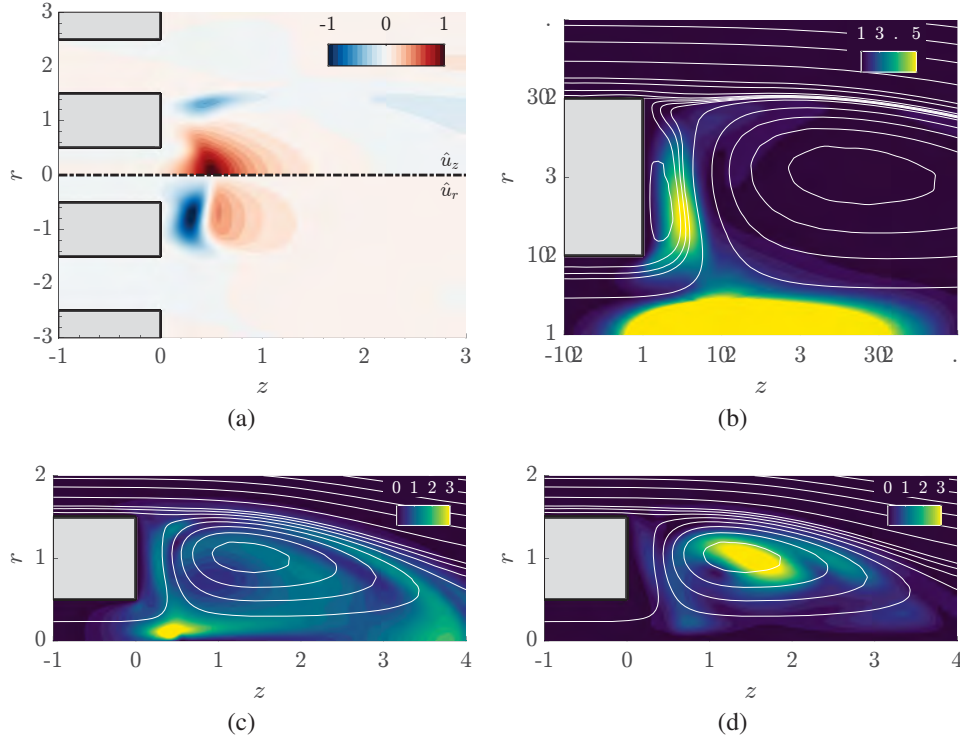


Figure 12: (a) Global mode S_0 for the configuration ($Re = 250$, $L = 1$, $\delta_u = 0.28$). The top panel of (a) represents the axial velocity, while the bottom panel depicts the radial velocity component. Structural sensitivity map $\|S_s(r, z)\|_F$ of the mode S_0 (b), S_1 (c) and S_2 (d). White lines are employed to represent the steady-state streamlines.

373 in the topology of the flow, and to a downstream shift of the recirculation bubble. Thus, it is
 374 not surprising that the core of the instability, shown in fig. 12 (b), is found on the interface
 375 between the recirculating region attached to the wall and the large recirculation bubble, and
 376 mostly in a region close to the axis found near the leftmost end of the recirculation bubble.
 377 The changes in the base flow due to the S_0 mode have an impact on the instability core of
 378 the S_1 and S_2 modes, which are depicted in fig. 12 (c) and (d), respectively. The maximum
 379 values of the structural sensitivity are found on the leftmost end of the recirculation bubble
 380 near the axis of revolution, while it is found in the centre of the recirculation bubble for the
 381 mode S_2 .

382 4.2. Annular jet configuration $\delta_u = 0$

383 Herein, we investigate the effect of the duct wall length ($0.5 < L < 4$) on the linear stability
 384 of the annular jet ($\delta_u = 0$).

385 The linear stability findings are summarised in fig. 13, which displays the evolution of
 386 the critical Reynolds number with respect to the duct wall distance (L) for the four most
 387 unstable modes: two non-oscillating S_1 and S_2 , and two oscillating F_1 and F_2 . A cross-
 388 section view at $z = 1$ is displayed in fig. 14. Please note that for the chosen set of parameters
 389 the axisymmetric unsteady mode F_0 , is always found at larger Reynolds numbers than the
 390 aforementioned modes, that is why in the following, we only include the results for the S_1 ,
 391 S_2 , F_1 and F_2 modes. This is one of the major differences with the case studied by Canton
 392 *et al.* (2017). For small values of the duct wall length ($L \approx 0.1$) separating the jet streams,
 393 the dominant instability is a vortex-shedding mode, which in our nomenclature is referred

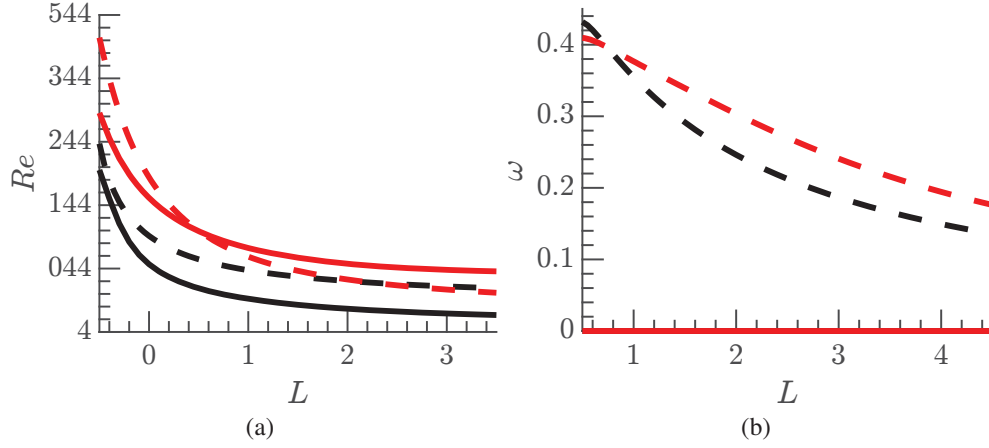


Figure 13: Linear stability boundaries for the annular jet ($\delta_u = 0$). (b) Frequency evolution of the unsteady modes. Legend: S_1 mode is displayed with a solid black line, S_2 with a solid red line and F_1 and F_2 modes are depicted with dashed black and red lines, respectively.

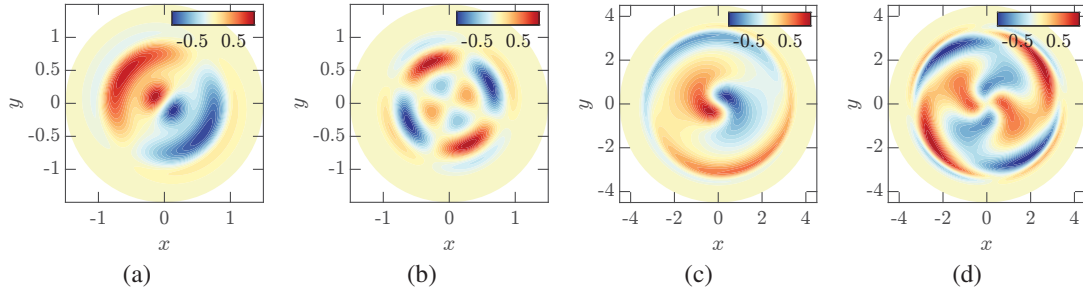


Figure 14: Cross-section view at $z = 1$ of the four unstable modes at criticality for the annular jet case ($\delta_u = 0$). The streamwise component of the vorticity vector ϖ_z is visualised by colours. (a) Mode S_1 for $L = 0.5$, (b) Mode S_2 for $L = 0.5$, (c) Mode F_1 for $L = 3$ and (d) Mode F_2 for $L = 3$.

394 to as F_0 . On the contrary, for duct wall lengths in the interval $0.5 < L < 4$, the primary
 395 instability of the annular jet is a steady symmetry-breaking bifurcation that leads to a jet
 396 flow with a single symmetry plane, displayed in fig. 14 (a). In contrast, bifurcations that
 397 lead to the mode S_2 possess two orthogonal symmetry planes, see fig. 14 (b). In section 4.1
 398 it has been established that non-oscillating modes S_1 and S_2 for $\delta_u = 1$ display most of
 399 its compact support within the region of recirculating fluid. Likewise, in the annular jet
 400 configuration, fig. 15 demonstrates that the spatial distribution of these two stationary modes
 401 S_1 and S_2 is found inside the recirculation bubble. For jet distances $L < 2$, the second mode
 402 that bifurcates is F_1 mode, depicted in fig. 16 (a). This situation corresponds to a bifurcation
 403 scenario similar to other axisymmetric flow configurations, such as the flow past a sphere or a
 404 disk (Auguste *et al.* 2010; Meliga *et al.* 2009). For larger distances between jets, the scenario
 405 changes. The second bifurcation from the axisymmetric steady-state is the F_2 , displayed in
 406 fig. 16 (b). Other configurations where the primary or secondary instability involves modes
 407 with azimuthal component $m = 2$ are swirling jets (Meliga *et al.* 2012) and the wake flow
 408 past a rotating sphere (Sierra-Ausín *et al.* 2022). The unsteady modes F_1 and F_2 display
 409 a similar structure to the unsteady modes discussed in section 4.1. They are formed by an

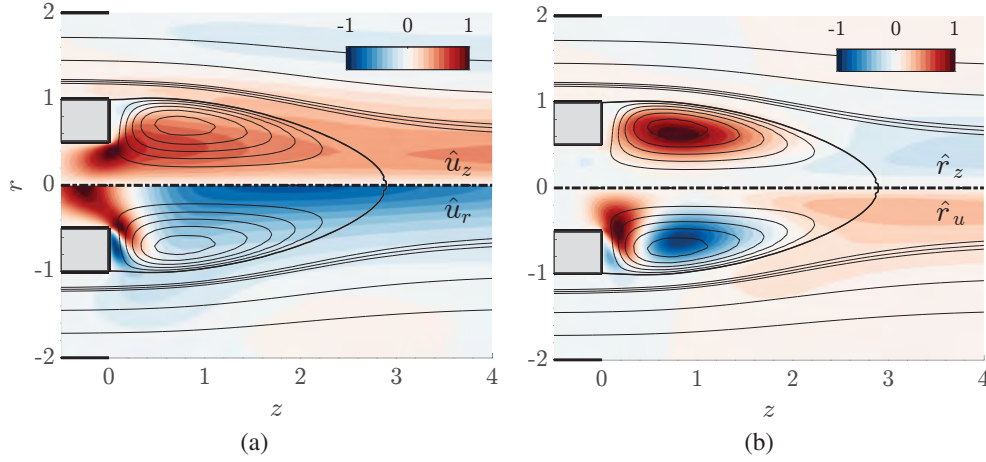


Figure 15: Global modes S_1 (a) and S_2 (b) at criticality for $L = 0.5$ and $\delta_u = 0$. The top panel of (a) represents the axial velocity, while the bottom panel depicts the radial velocity component. Black lines represent the streamlines of the base flow.

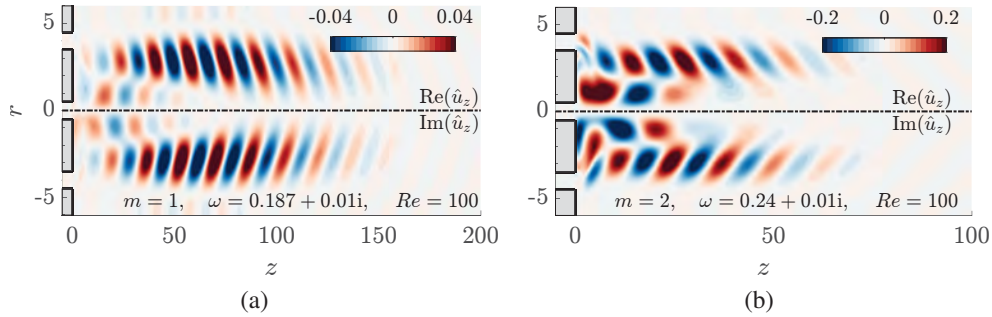


Figure 16: Axial velocity component of the neutral modes for $L = 3$ and $\delta_u = 0$ (a) F_1 , (b) F_2 .

410 array of counter-rotating vortex spirals developing in the wake of the separating duct wall
 411 and convected downstream, while experiencing an important spatial amplification until they
 412 eventually decay after reaching a maximum amplitude.

413 4.3. Fixed distance between jets and variable velocity ratio δ_u

414 In the following, we focus on the influence of the velocity ratio δ_u between jets for fixed jet
 415 distances L . Figure 17 displays the neutral curve of stability for jet distances (a) $L = 0.5$
 416 and (b) $L = 1$. One may observe that the primary bifurcation is not always associated to
 417 the mode S_1 as it is the case for $\delta_u = 0$. For sufficiently large velocity ratios, the primary
 418 instability leads to a non-axisymmetric steady-state with a double helix, corresponding to
 419 the unstable mode S_2 . As can be appreciated in fig. 9 (b), for small values of δ_u , the mode
 420 S_1 expands downstream over a relatively large area, having a higher activity than mode S_2 ,
 421 which is confined to the recirculation region. As the ratio between velocities is increased, as
 422 observed in fig. 9 (a), mode S_2 enlarges and resembles to mode S_1 , controlling the instability
 423 mechanism for large values of δ_u . Another interesting feature, which could motivate a control
 424 strategy, is the occurrence of vertical asymptotes. This sudden change in the critical Reynolds
 425 number is due to the retraction, disappearance of the recirculation bubble and the formation
 426 of a new recirculating flow region, aspects that have been covered in section 3. For $L = 0.5$,

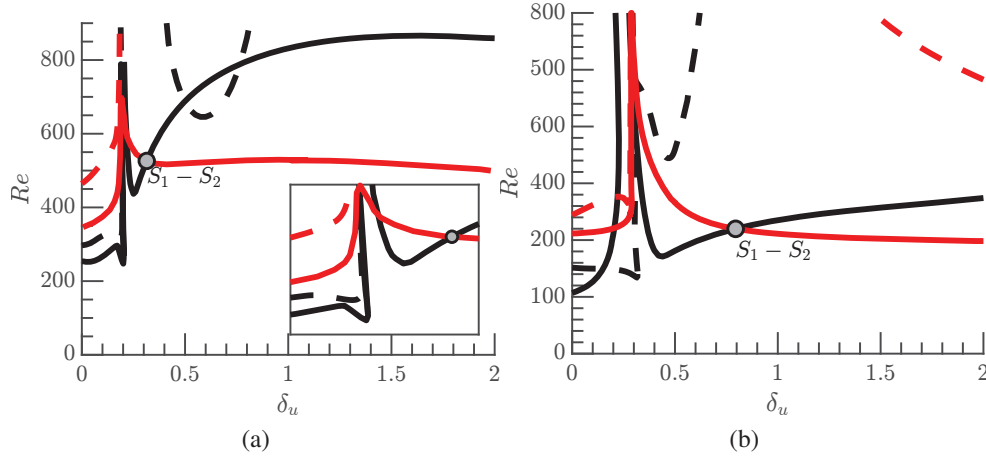


Figure 17: Linear stability boundaries for the concentric jets (a) $L = 0.5$ and (b) $L = 1$. Same legend as fig. 13.

427 this sudden change occurs for $\delta_u \approx 0.25$, and for higher values of δ_u the critical Reynolds
 428 number is around twice larger than the one of the annular jet ($\delta_u = 0$). The case of jet distance
 429 $L = 1$ was discussed in section 3. The sudden change in the stability of the branch S_1 occurs
 430 between $\delta_u \in [0.25, 0.5]$. Within this narrow interval, the primary branch of instability is
 431 the F_1 . At around $\delta_u = 0.4$, the primary bifurcation is again the branch S_1 , which becomes
 432 secondary at around $\delta_u \approx 0.8$ in favour of the branch S_2 . In fig. 17 we have highlighted the
 433 codimension two point interaction between the $S_1 - S_2$ modes, which will be analysed in
 434 detail in section 5. Around this point, we can observe the largest ratio $(\frac{Re_c|_{\delta_u \neq 0}}{Re_c|_{\delta_u = 0}})$ between
 435 the value of the critical Reynolds number of the primary instability for a concentric jet
 436 configuration ($\delta_u \neq 0$) and the annular jet problem ($\delta_u = 0$).

437 4.4. Fixed velocity ratio δ_u and variable distance between jets

438 Figure 18 compares the results obtained for a constant velocity ratio when varying the
 439 distance between jets. As observed before, the increase of the distance between the jets has
 440 a de-stabilising effect. The largest critical Reynolds number is found at $\delta_u = 0$, and the
 441 critical Reynolds number decreases with the duct wall length L between the jet streams. The
 442 points of codimension two are highlighted in fig. 18. We can appreciate that the interaction
 443 between the branch S_1 and S_2 happens for every velocity ratio δ_u explored, and it is the mode
 444 interaction associated to the smallest distance between jets. Additionally, for a velocity ratio
 445 $\delta_u = 0.5$ there exist two points where the branches of the linear modes S_1 and F_1 intersect.
 446 Another feature of the neutral curves is the existence of turning points, which are associated
 447 to the existence of saddle node bifurcations of the axisymmetric steady-state, addressed in
 448 section 3. The saddle-node bifurcations of the steady-state induce the existence of regions in
 449 the neutral curves with a *tongue* shape. These saddle node bifurcations are also responsible
 450 for the formation of the vertical asymptotes observed in fig. 17. Finally, it is of interest the
 451 transition of the modes S_1 and S_2 , which induce the symmetry breaking of the axisymmetric
 452 steady state to slow low frequency spiralling structures. These modes have been identified
 453 for $\delta_u = 0.5$ for $m = 1$, $\delta_u = 1$ for $m = 2$, and $\delta_u = 2$ for both $m = 1$ and $m = 2$. As it will be
 454 clarified in section 5, these oscillations are issued from the non-linear interaction of modes,
 455 emerging simultaneously for a specific Reynolds number, and changing their position as the
 456 most unstable global mode of the flow.

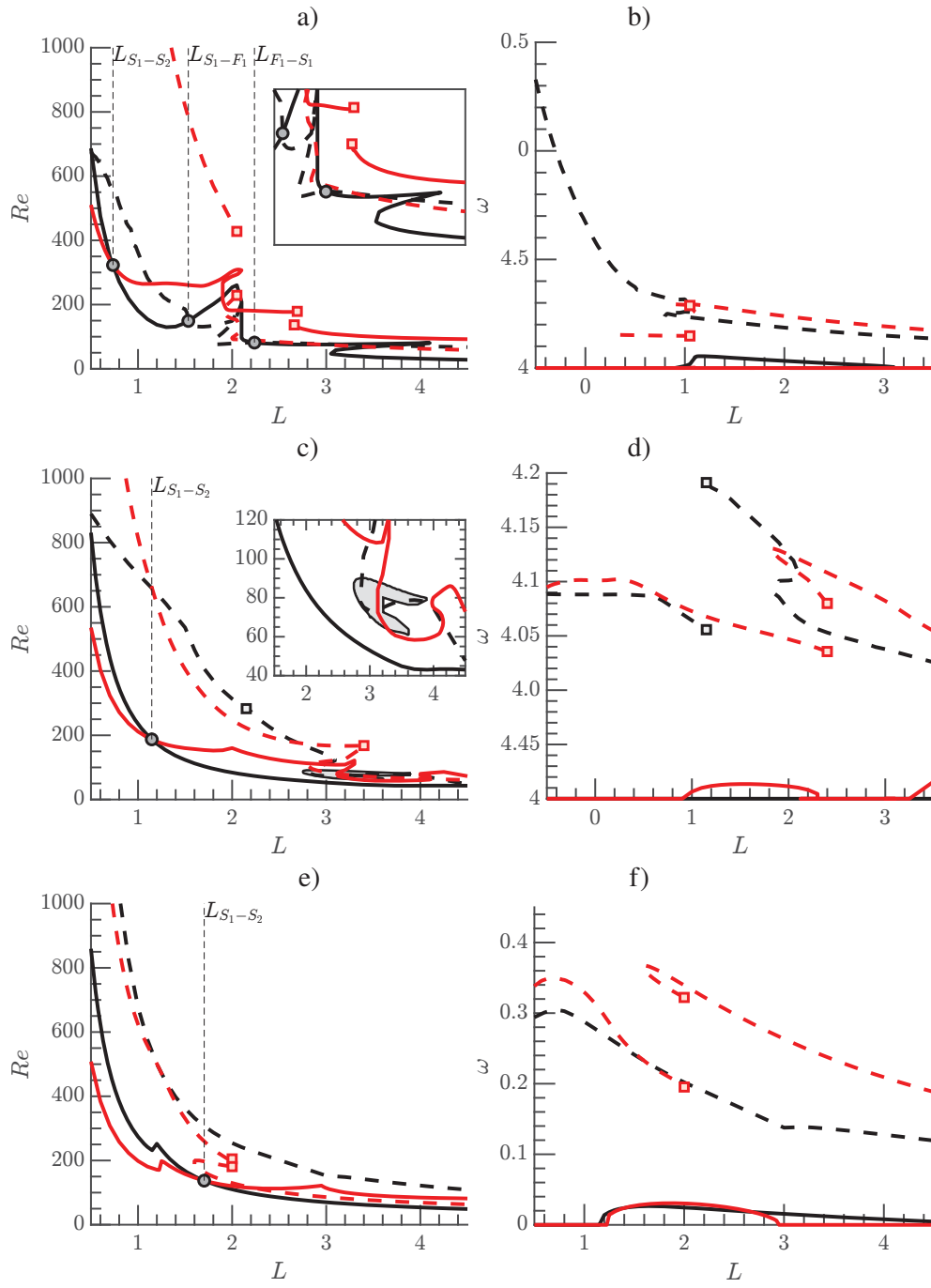


Figure 18: Neutral lines of the four modes found studying the configuration of two concentric jets fixing the velocity ratio. (a-b) $\delta_u = 0.5$, (c-d) $\delta_u = 1$, (e-f) $\delta_u = 2$. Black lines: modes with $m = 1$, red lines: modes with $m = 2$. Straight lines: steady modes, dashed lines: unsteady modes. The discontinuity points, i.e., the points where the second most unstable mode (of a given type) becomes the most unstable are highlighted with square markers.

457 **5. Mode interaction between two steady states. Resonance 1 : 2**

458 **5.1. Normal form, basic solutions and their properties**

459 The linear diagrams of section 4 have shown the existence of the mode interaction between
 460 the modes S_1 and S_2 . It corresponds roughly to the mode interaction that occurs at the largest
 461 critical Reynolds number for any value of L herein explored. In this section, we analyse the
 462 dynamics near the $S_1 : S_2$ organising centre. We perform a normal form reduction, which
 463 allows us to predict non-axisymmetric steady, periodic, quasiperiodic and heteroclinic cycles
 464 between non-axisymmetric states.

465 The mode interaction that is herein analysed corresponds to a steady-steady bifurcation
 466 with $O(2)$ symmetry and with strong resonance 1 : 2. Such a bifurcation scenario has
 467 been extensively studied in the past by (Dangelmayr 1986; Jones & Proctor 1987; Porter &
 468 Knobloch 2001; Armbruster *et al.* 1988) and the reflection symmetry breaking case (SO(2))
 469 by Porter & Knobloch (2005). In order to unravel the existence and the stability of the
 470 nonlinear states near the codimension two point, let us write the flow field as

471
$$\mathbf{q} = \mathbf{Q}_0 + \text{Re} \left[r_1(\tau) e^{i\phi_1(\tau)} e^{-i\theta} \hat{\mathbf{q}}_{s,1} \right] + \text{Re} \left[r_2(\tau) e^{i\phi_2(\tau)} e^{-2i\theta} \hat{\mathbf{q}}_{s,2} \right] \quad (5.1)$$

472 in polar coordinates for the complex amplitudes $z_1 = r_1 e^{i\phi_1}$ and $z_2 = r_2 e^{i\phi_2}$ where r_j and ϕ_j
 473 for $j = 1, 2$ are the amplitude and phase of the symmetry-breaking modes $m = 1$ and $m = 2$,
 474 respectively. The complex-amplitude normal form eq. (2.11) is expressed in this reduced
 475 polar notation as follows,

479
$$\dot{r}_1 = e_3 r_1 r_2 \cos(\chi) + r_1 \left(\lambda_{(s,1)} + c_{(1,1)} r_1^2 + c_{(1,2)} r_2^2 \right), \quad (5.2a)$$

480
$$\dot{r}_2 = e_4 r_1^2 \cos(\chi) + r_2 \left(\lambda_{(s,2)} + c_{(2,1)} r_1^2 + c_{(2,2)} r_2^2 \right), \quad (5.2b)$$

481
$$\dot{\chi} = - \left(2e_3 r_2 + e_4 \frac{r_1^2}{r_2} \right) \sin(\chi), \quad (5.2c)$$

 482

483 where the phase $\chi = \phi_2 - 2\phi_1$ is coupled with the amplitudes r_1 and r_2 because of the
 484 existence of the 1 : 2 resonance. The individual phases evolve as

485
$$\begin{aligned} \dot{\phi}_1 &= e_3 r_2 \sin(\chi), \\ \dot{\phi}_2 &= -e_4 \frac{r_1^2}{r_2} \sin(\chi). \end{aligned} \quad (5.3)$$

Before proceeding to the analysis of the basic solutions of eq. (5.2), we can simplify these
 equations by the rescaling

$$\left(\frac{r_1}{|e_3 e_4|^{1/2}}, \frac{r_2}{e_3} \right) \rightarrow (r_1, r_2),$$

489 which yields the following equivalent system

490
$$\dot{r}_1 = r_1 r_2 \cos(\chi) + r_1 \left(\lambda_{(s,1)} + c_{11} r_1^2 + c_{12} r_2^2 \right), \quad (5.4a)$$

491
$$\dot{r}_2 = s r_1^2 \cos(\chi) + r_2 \left(\lambda_{(s,2)} + c_{21} r_1^2 + c_{22} r_2^2 \right), \quad (5.4b)$$

492
$$\dot{\chi} = - \frac{1}{r_2} \left(2r_2^2 + s r_1^2 \right) \sin(\chi), \quad (5.4c)$$

 493

where the coefficients

$$s = \text{sign}(e_3 e_4), \quad c_{11} = \frac{c_{(1,1)}}{|e_3 e_4|}, \quad c_{12} = \frac{c_{(1,2)}}{e_3^2}, \quad c_{21} = \frac{c_{(2,1)}}{|e_3 e_4|}, \quad c_{22} = \frac{c_{(2,2)}}{e_3^2}.$$

Name	Definition	Bifurcations	Comments
O	$r_{1,O} = r_{2,O} = 0$	–	Steady axisymmetric state
P	$r_{2,P}^2 = \frac{-\lambda_{(s,2)}}{c_{22}}, r_{1,P} = 0$	$\lambda_{(s,2)} = 0$	Bifurcation from O
MM	$r_{1,MM} = -\frac{\lambda_{(s,1)} \pm r_{2,MM} + c_{12} r_{2,MM}^2}{c_{11}}$ $P_{MM}(r_{2,MM} \cos(\chi_{MM})) = 0$ $\cos(\chi_{MM}) = \pm 1$	$\lambda_{(s,1)} = 0$ $\sigma_{\pm} = 0$	Bifurcation from O Bifurcation from P
TW	$\cos(\chi_{TW}) = \frac{(2c_{11} + c_{12})\lambda_{(s,2)} - (2c_{21} + c_{22})\lambda_{(s,1)}}{\Sigma_{TW}(2\lambda_{(s,1)} + \lambda_{(s,2)})}$ $r_{2,TW}^2 = \frac{-(2\lambda_{(s,1)} + \lambda_{(s,2)})}{\Sigma_{TW}}$ $r_{1,TW}^2 = 2r_{2,TW}^2$	$\cos(\chi_{TW}) = \pm 1$	Bifurcation from MM

Table 1: Definition of the fixed points of the reduced polar normal form eq. (5.4). σ_{\pm} is defined in eq. (5.6), the polynomial P_{MM} is defined in eq. (5.7) and $\Sigma_{TW} \equiv 4c_{11} + 2(c_{12} + c_{21}) + c_{22}$.

494 Finally, we consider a third normal form equivalent to the previous ones but which removes the
495 singularity of eqs. (5.2) and (5.4) when $r_2 = 0$. Standing waves ($\sin \chi = 0$) naturally encounter
496 this type of artificial singularity, which manifests as in eq. (5.4) as an instantaneous jump
497 from one standing subspace to the other by a π -translation. This is the case of the heteroclinic
498 cycles, previously studied by Armbruster *et al.* (1988); Porter & Knobloch (2001). The third
499 normal form, which we shall refer to as reduced Cartesian normal form, takes advantage of
503 the simple transformation $x = r_2 \cos(\chi)$, $y = r_2 \sin(\chi)$ (Porter & Knobloch 2005):

$$504 \quad \dot{r}_1 = r_1 \left(\lambda_{(s,1)} + c_{11} r_1^2 + c_{12} (x^2 + y^2) + x \right), \quad (5.5a)$$

$$505 \quad \dot{x} = s r_1^2 + 2y^2 + x \left(\lambda_{(s,2)} + c_{21} r_1^2 + c_{22} (x^2 + y^2) \right), \quad (5.5b)$$

$$506 \quad \dot{y} = -2xy + y \left(\lambda_{(s,2)} + c_{21} r_1^2 + c_{22} (x^2 + y^2) \right), \quad (5.5c)$$

508 In this final representation standing wave solutions are contained within the invariant plane
509 $y = 0$, and due to the invariance of eq. (5.5) under the reflection $y \mapsto -y$, one can restrict
510 attention, without loss of generality, to solutions with $y \geq 0$, cf Porter & Knobloch (2001).

511 The system eq. (5.4) possess four types of fixed points, which are listed in table 1.

512 First, the axisymmetric steady state (O) is represented by $(r_1, r_2) = (0, 0)$, so it is the
513 trivial steady-state of the normal form. The second steady-state is what it is denoted as pure
514 mode (P). In the original coordinates, it corresponds to the symmetry breaking structure
515 associated to the mode S_2 . This state bifurcates from the axisymmetric steady state (O) when
516 $\lambda_{(s,2)} = 0$. The third fixed point is the mixed mode state (MM), which is listed in table 1. It
517 corresponds to the reflection symmetry preserving state associated to the mode S_1 . It may
518 bifurcate directly from the trivial steady state O, when $\lambda_{(s,1)} = 0$ or from P whenever $\sigma_+ = 0$
519 or $\sigma_- = 0$, where σ_{\pm} is defined as

$$520 \quad \sigma_{\pm} \equiv \lambda_{(s,1)} - \frac{-\lambda_{(s,2)} c_{12}}{c_{22}} \pm \sqrt{\frac{-\lambda_{(s,2)}}{c_{22}}}. \quad (5.6)$$

Name	Bifurcation condition	Comments
SW	$sr_1^2 - 2c_{11}r_1^2r_{2,MM} \cos(\chi_{MM}) - 2c_{22}r_{2,MM}^3 \cos(\chi_{MM})^3 = 0$	Bif. from MM
MTW	$D_{TW} - T_{TW}I_{TW} = 0, I_{TW} > 0$	Bif. from TW

Table 2: Definition of the limit cycles of the reduced polar normal form eq. (5.4).

The representation in the reduced polar form is

$$r_{1,MM} = -\frac{\lambda_{(s,1)} \pm r_{2,MM} + c_{12}r_{2,MM}^2}{c_{11}}, \quad \cos(\chi_{MM}) = \pm 1,$$

521 and the condition $P_{MM}(r_{2,MM} \cos(\chi_{MM})) = 0$, where P_{MM} is defined as

$$522 \quad P_{MM}(x) \equiv s\mu_1 + (s + c_{21}\lambda_{(s,1)} - c_{(1,1)}\lambda_{(s,2)})x + (c_{21} + sc_{12})x^2 + (c_{12}c_{21} - c_{11}c_{22})x^3. \quad (5.7)$$

523 Finally, the fourth fixed point of the system are travelling waves (TW). It is surprising that
 524 the interaction between two steady-states causes a time-periodic solution. The travelling
 525 wave emerges from MM in parity-breaking pitchfork bifurcation that breaks the reflection
 526 symmetry when $\cos(\chi_{TW}) = \pm 1$. The TW drifts at a steady rotation rate ω_{TW} along the
 527 group orbit, i.e., the phases $\dot{\phi}_1 = r_{2,TW} \sin(\chi_{TW})$ and $\dot{\phi}_2 = -s \frac{r_{1,TW}^2}{r_{2,TW}} \sin(\chi_{TW})$ are non-null.

Mixed modes and travelling waves may further bifurcate into standing waves (SW) and modulated travelling waves (MTW), respectively. These are generic features of the 1 : 2 resonance for small values of $\lambda_{(s,1)}$ and $\lambda_{(s,2)}$, when $s = -1$. In the original coordinates, SW are periodic solutions, whereas MTW are quasiperiodic. Standing waves emerge via a Hopf bifurcation from MM when the conditions $P_{SW}(r_{2,MM} \cos(\chi_{MM})) > 0$ for

$$P_{SW}(x) \equiv (2c_{22}x^3 - sr_1^2)c_{11} - (2c_{12}x + 1)(c_{21}x + s)x,$$

528 and the one listed in table 2 are satisfied. MTW are created when a torus bifurcation happens
 529 on the travelling wave branch when the conditions listed in table 2 are satisfied.

530 Another remarkable feature of eq. (5.2) is the existence of robust heteroclinic cycles that
 531 are asymptotically stable. When $s = -1$, there are open sets of parameters where the reduced
 532 polar normal form exhibits structurally stable connections between π -translations on the
 533 circle of pure modes, cf Armbruster *et al.* (1988). These structures are robust and have been
 534 observed in a large variety of systems, (Nore *et al.* 2003, 2005; Mercader *et al.* 2002; Palacios
 535 *et al.* 1997; Mariano & Stazi 2005). In addition to these robust heteroclinic cycles connecting
 536 pure modes, there exist more complex limit cycles connecting O, P, MM and SW, cf Porter &
 537 Knobloch (2001). These cycles are located for larger values of $\lambda_{(s,1)}$ and $\lambda_{(s,2)}$, with possibly
 538 chaotic dynamics (Shilnikov type). In this study, we have not identified any of these. Finally,
 539 a summary of the basic solutions and the bifurcation path is sketched in fig. 19.

540 5.2. Results of the steady-steady 1 : 2 mode interaction

541 Section 4.4 reported the location of mode interaction points for discrete values of the velocity
 542 ratio δ_u . The location of the mode interaction between S_1 and S_2 is depicted in fig. 20. It shows
 543 that the mode switching between the modes S_1 and S_2 is indeed stationary only for $\delta_u < 1.5$
 544 and $L < 1.3$. For larger values of the velocity ratio and the jet distance, the interaction is not
 545 purely stationary; at least one of the linear modes oscillates with a slow frequency. It implies

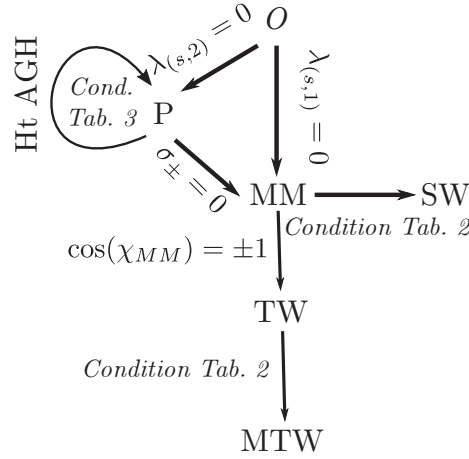


Figure 19: Schematic representation of the basic solutions of eq. (5.2) and their bifurcation path.

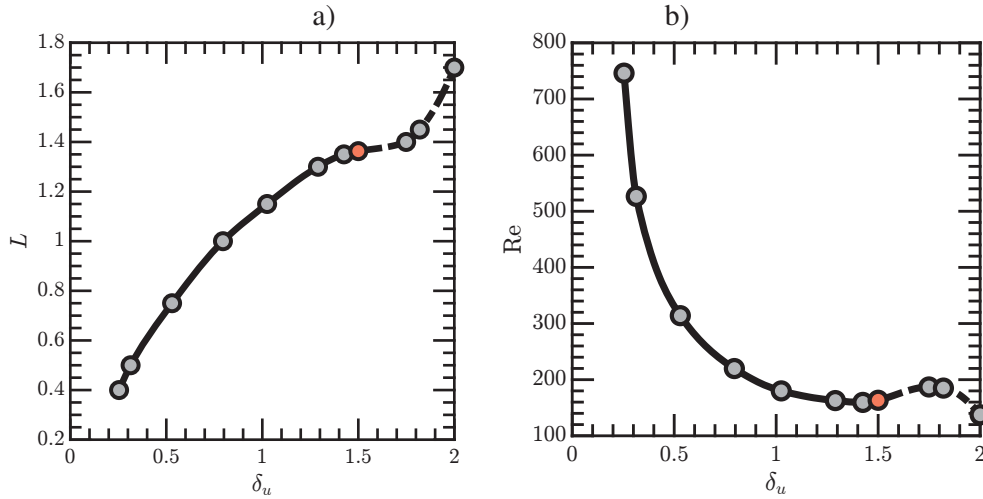


Figure 20: Evolution of the codimension two interaction $S_1 - S_2$ in the space of parameters (Re, L, δ_u) . Grey points denote the points that were computed and the red point denotes the transition from steady to unsteady with low frequency as reported in section 4.4.

546 that the mode selection for large velocity ratios near the codimension two points is similar
 547 to the one reported by Meliga *et al.* (2012) for swirling jets. However, even when the two
 548 primary bifurcations are non-oscillating (S_1 and S_2), the 1 : 2 resonance of the azimuthal
 549 wavenumbers induces a slow frequency, what we denote as travelling wave solutions (TW).

550 We consider the bifurcation sequence for $\delta_u = 1.0$ and $L = 1.15$, which is qualitatively
 551 similar to transitions in the range $0.5 < \delta_u < 1.5$, near the codimension two points, which
 552 are depicted in fig. 20. At the codimension two points for $\delta_u < 0.5$, at least one of the
 553 two bifurcations is sub-critical and a normal form reduction up to fifth order is necessary.
 554 Subcritical transition was also noticed for a distance between jets $L = 0.1$ by Canton *et al.*
 555 (2017), who reported high levels of the linear gain associated to transient growth mechanisms.
 556 This last case is out of the scope of the present manuscript. Figure 21 displays the phase
 557 portrait of the stable attractors near the $S_1 : S_2$ interaction. For values of $\delta_u > 1.0$, the
 558 axisymmetric steady-state loses its axisymmetry leading to a new steady-state with symmetry

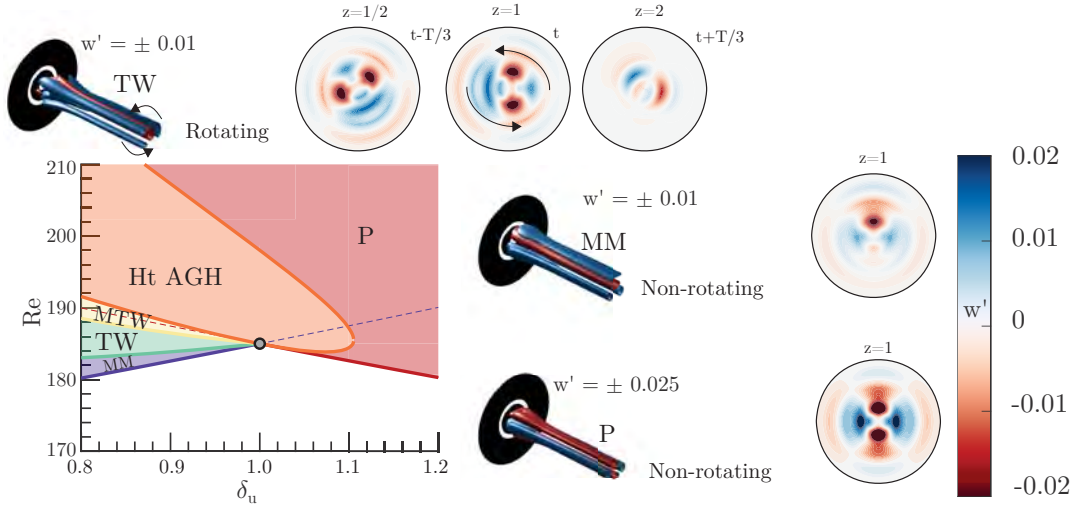


Figure 21: Parametric portrait at the codimension two point $S_1 : S_2$ for parameter values $(L, \delta_u) = (1.15, 1.0)$. The colour-shaded areas corresponds to the regions in the parameter space where a given solution is attracting, e.g., the green-shaded area is the region where TW is the attracting solution. Solid lines indicate codimension-one bifurcations, dashed-lines indicate when $\lambda_{(s,2)} = 0$ (P) and $\lambda_{(s,1)} = 0$ (MM), a grey marker denotes the codimension-two point. The visualisations of blue and red surfaces in the isometric views represent the respective positive and negative isocontour values of the perturbative axial velocity indicated in the figure.

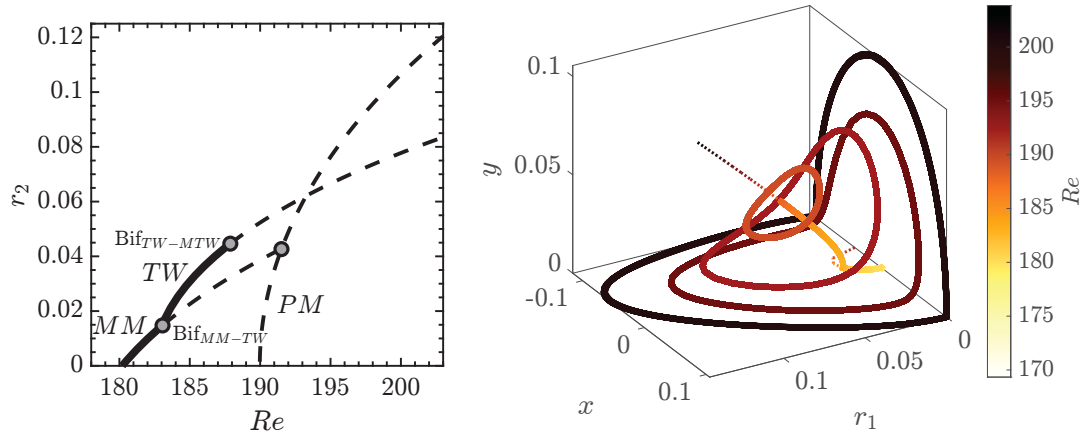


Figure 22: Bifurcation diagram with respect to the Reynolds number for $L = 1.15$ and $\delta_u = 0.8$. The left diagram reports the evolution of r_2 for the fixed point solutions of the normal form. The right diagram displays the bifurcation diagram in the Cartesian coordinates. Solid lines and dashed lines denote stable attractors and unstable attractors, respectively.

559 $m = 2$, herein denoted as pure mode (P). A reconstruction of the perturbative component of
 560 the flow field of such a state is performed at the bottom right of fig. 21, which shows that the
 561 state P possesses two orthogonal planes of symmetry. Near the codimension two point, for
 562 values of the velocity ratio $\delta_u < 1.1$, the state P is only observable, that is non-linearly stable,
 563 within a small interval with respect to the Reynolds number. For larger values of the velocity
 564 ratio, the state P remains stable within the analysed interval of Reynolds numbers. For values

565 of the velocity ratio $\delta_u < 1.0$, the bifurcation diagram is more complex. Figure 22 displays
 566 the bifurcation diagram of the fixed-point solutions of eq. (5.5) on the left diagram and the
 567 full set of solutions of the normal form in the right diagram. The axisymmetric steady-state
 568 first bifurcates towards a Mixed-Mode solution, which is the solution in the $y = 0$ plane for
 569 the right diagram of fig. 22. A solution with a non-symmetric wake has been reconstructed
 570 in fig. 21. The Mixed-Mode solution is only stable within a small interval of the Reynolds
 571 number. A secondary bifurcation, denoted Bif_{MM-TW} , gives rise to a slowly rotating wave
 572 of the wake. The TW and the MM solutions are identical at the bifurcation point. The phase
 573 speed is zero at the bifurcation, thus this is not a Hopf bifurcation. It corresponds to a *drift*
 574 *instability* that breaks the azimuthal symmetry, i.e. it starts to slowly drift. This unusual
 575 feature, that travelling waves bifurcate from a steady solution at a steady bifurcation, is a
 576 generic feature of the 1 : 2 resonance. A reconstruction of the travelling wave solution is
 577 depicted on the top of fig. 21. It corresponds to the line with non-zero y component in the
 578 right diagram of fig. 22. The TW solution loses its stability in a tertiary bifurcation, denoted
 579 as Bif_{TW-MTW} . It conforms to a Hopf bifurcation of the TW solution, which gives birth
 580 to a quasi-periodic solution name Modulated Travelling Wave (MTW). A representation of
 581 this kind of solution in the Cartesian coordinates (r_1, x, y) is depicted on the right image of
 582 fig. 22.

583 Eventually, the Modulated Travelling Wave experiences a global bifurcation. That occurs
 584 when the periodic MTW solution, in the (r_1, x, y) coordinates, nearly intersects the invariant
 585 $r_1 = 0$ and $y = 0$ planes. The transition sequence is represented in the right image of fig. 22 in
 586 the Cartesian coordinates (r_1, x, y) . The amplitude of the MTW limit cycle increases until the
 587 MTW arising at the tertiary bifurcation Bif_{TW-MTW} are destroyed by meeting a heteroclinic
 588 cycle at Bif_{MTW-Ht} . The locus of Bif_{MTW-Ht} is reported in fig. 21 and in good agreement
 589 with Armbruster *et al.* (1988). The conditions for the existence of the heteroclinic cycles
 590 are: $\lambda_{(s,1)} > 0$, $\lambda_{(s,2)} > 0$, $c_{22} < 0$. When σ_- becomes negative, the cycle is attracting
 591 and robust heteroclinic cycles are observed. It is destroyed when σ_+ becomes negative, in
 592 that case the pure modes are no longer saddles which breaks the heteroclinic connection.
 593 Figure 23 displays the instantaneous fluctuation field from a heteroclinic orbit connecting P
 594 and its conjugate solution P', which is obtained by a rotation of $\pi/2$, for parameter values
 595 $\text{Re} = 200$ and $\delta_u = 0.8$. The dynamics of the cycle takes place in two phases. Figure 23
 596 depicts the motion of the coherent structure associated to the heteroclinic cycle. Starting
 597 from the conjugated pure mode P', the cycle leaves the point (a), located in the vicinity of P',
 598 along the unstable eigenvector y , which is the stable direction of P. The first phase consists
 599 in a rapid rotation by $\pi/2$ of the wake, it corresponds to the sequence a-b-c-d-e displayed in
 600 fig. 23. Then it is followed by a slow approach following the direction y and departure from
 601 the pure mode state P along the direction r_1 . The second phase consists in a rapid horizontal
 602 motion of the wake, which is an evolution from P to P' that takes place by the breaking
 603 of the reflectional symmetry with respect to the vertical axis; it constitutes the sequence
 604 e-f-g-h-i-a. Please note that equivalent motions are also possible. The first phase of rapid
 605 counter-clockwise rotation by $\pi/2$ can be performed in the opposite sense. It corresponds
 606 to a motion in the Cartesian coordinates along the plane r_1 along negative values of y . The
 607 sequence e-f-g-h-i-a can be replaced by a horizontal movement in the opposite sense, which
 608 adjusts to connect the plane $y = 0$ corresponding to negative values of r_1 .

609 6. Discussion & Conclusions

610 The current study provides a complete description of the configuration consisting of two
 611 coaxial jets, broadly found in industrial processes, covering a wide range of applications such
 612 as noise reduction, mixing enhancement, or combustion control. The numerical procedure

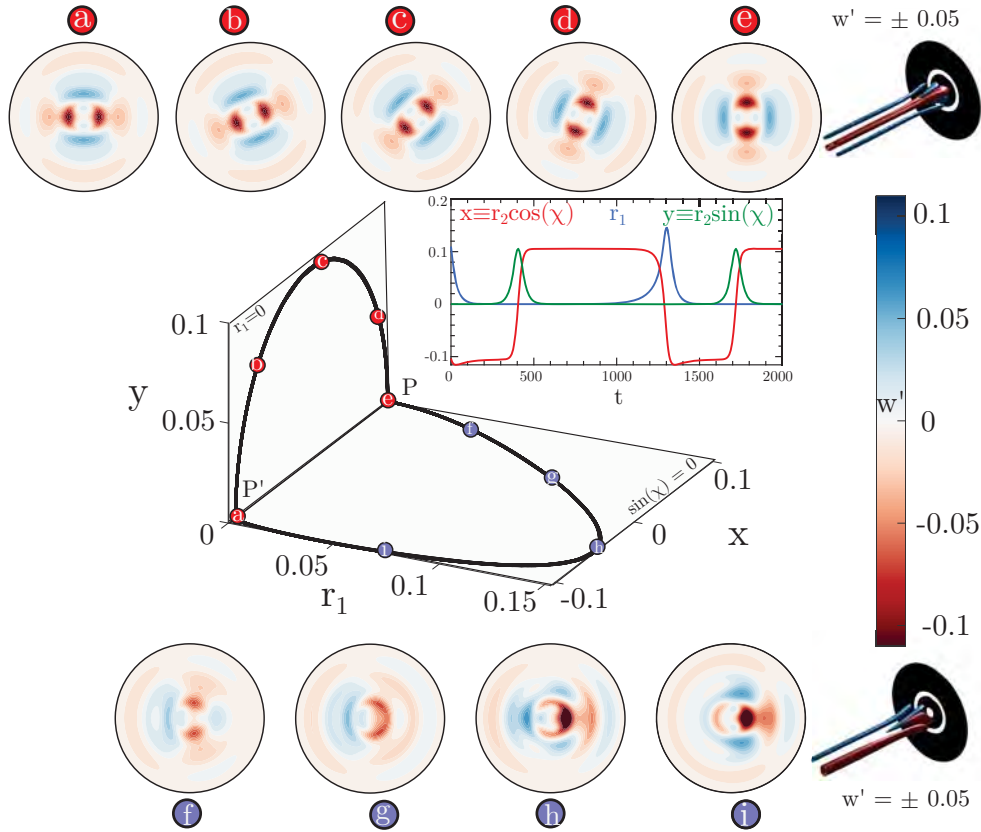


Figure 23: Heteroclinic cycle solution for parameter values $Re = 200$, $\delta_u = 0.8$. The top and bottom image sequences along the heteroclinic cycle show (from left to right) an axial slice plane at $z = 1$ of the instantaneous fluctuations of the axial velocity of the flow field as viewed from downstream, along with a three-dimensional isometric view (d on the top and g on the bottom). The middle diagram displays the heteroclinic cycle in the coordinates (r_1, x, y) .

613 herein employed has been validated with the existing literature in the case of the stability
 614 analysis (see **B** for a detailed overview). A large region of the parameter space is explored
 615 $(\delta_u, L) \in ([0, 2], [0.5, 4.5])$, substantially expanding the work of Canton *et al.* (2017).

616 Section 3 provides an analysis of the basic properties of the steady-state, such as the
 617 topology of the flow and its variations in terms of the three parameters (Re, L, δ_u) . It also
 618 highlights the existence of multiple steady-states, as a result of a series of saddle-node
 619 bifurcations, and its connection to the changes in the topology of the flow. Highlighting,
 620 nonetheless, that changes in the topology are not a direct consequence of a saddle-node
 621 bifurcation. The linear stability analysis performed in Section 4 reveals the existence of two
 622 unstable steady modes: S_1 and S_2 , which are mostly located within the recirculation bubble,
 623 and two unsteady ones: F_1 and F_2 , which are also produced within the recirculating region of
 624 the flow, but they are convected downstream, while experiencing substantial amplification.
 625 In addition, in section 4, we briefly discuss the consequences of the retraction and eventual
 626 disappearance of the recirculation bubble and the formation of a new recirculating flow
 627 region, aspects that have been covered in section 3, in terms of the sudden changes in the
 628 critical Reynolds number. Subsequently, the critical Reynolds number is determined for a

629 wide range of inner-to-outer velocity ratios and duct wall lengths. An increase of the velocity
630 ratio has an overall stabilising effect, and it leads to the swap from mode S_1 , characterised
631 with one symmetry plane, to mode S_2 that possesses two symmetry planes. Afterwards,
632 the effect of the distance L between jets is analysed. The primary effect of increasing this
633 distance is a decrease in the critical Reynolds number for all values of δ_u investigated.

634 Section 5 analyses the mode interaction between two symmetry breaking modes with
635 azimuthal wavenumbers $m = 1$ and $m = 2$. The unfolding of the codimension-two bifurcation
636 reveals the presence of unsteadiness as a result of the resonant 1 : 2 interaction between the
637 two steady-modes. The codimension-two point is located at a velocity ratio $\delta_u = 1.0$ and
638 distance between jets of $L = 1.15$, a situation that it is qualitatively equivalent to transitions
639 found in the range $0.5 < \delta_u < 1.5$. For values lower than $\delta_u = 1.0$, the bifurcation diagram
640 exhibits an intricate path. First, a Mixed-Mode (MM) solution emerges, which displays a non-
641 symmetric wake. The Mixed-Mode solution is only stable for a small range of the Reynolds
642 number. Subsequently, a slowly rotating wake is triggered in the form of a Travelling Wave
643 (TW). This unusual feature, an unsteady state emerging from a steady state, corresponds to a
644 drift instability commonly found at 1 : 2 resonance. Then, the TW solution encounters a Hopf
645 bifurcation, developing a quasi-periodic solution in the form of a Modulated Travelling Wave
646 (MTW). Finally, the MTW solution undergoes a global bifurcation meeting a heteroclinic
647 cycle (Ht). This heteroclinic orbit links the solution P with its conjugate solution P', spinning
648 the wake from P' to P, and moving it horizontally from P to P'. On the other hand, for values
649 higher than $\delta_u = 1.0$, a non-axisymmetric steady state emerges as a pure mode P with two
650 orthogonal planes of symmetry. If the transition happens for values of the velocity ratio close
651 to unity, a further increase in the velocity ratio rapidly leads to the heteroclinic cycle.

652 Physical realizations of the 1 : 2 mode interaction have been observed by Mercader *et al.*
653 (2002) and Nore *et al.* (2003, 2005) for confined flow configurations. However, to the author's
654 knowledge, this is the first time that a robust heteroclinic cycle resulting from this type of
655 1 : 2 interaction is reported in the literature for an external flow configuration, as it is the
656 coaxial jet configuration.

657 **Funding** A.C., J.A.M. and S.L.C. acknowledge the grant PID2020-114173RB-I00 funded
 658 by MCIN/AEI/ 10.13039/501100011033. S.L.C., J.A.M. and A.C. acknowledge the support
 659 of Comunidad de Madrid through the call Research Grants for Young Investigators from
 660 Universidad Politécnic de Madrid. AC also acknowledges the support of Universidad
 661 Politécnic de Madrid, under the programme ‘Programa Propio’.

662

663 **Declaration of interests** The authors declare no conflict of interest.

664 Appendix A. Normal form reduction

665 In this section we provide a detailed explanation of the normal form reduction to obtain
 666 the coefficients of eq. (2.11), we define the terms of the compact notation of the governing
 667 equations eq. (2.3), which is reminded here, for the sake of conciseness,

$$668 \quad \mathbf{B} \frac{\partial \mathbf{Q}}{\partial t} = \mathbf{F}(\mathbf{Q}, \boldsymbol{\eta}) \equiv \mathbf{LQ} + \mathbf{N}(\mathbf{Q}, \mathbf{Q}) + \mathbf{G}(\mathbf{Q}, \boldsymbol{\eta}). \quad (\text{A } 1)$$

669 The nonlinear convective operator $\mathbf{N}(\mathbf{Q}_1, \mathbf{Q}_2) = \mathbf{U}_1 \cdot \nabla \mathbf{U}_2$ accounts for the quadratic
 670 interaction on the state variable. The linear operator on the state variable is $\mathbf{LQ} = [\nabla P, \nabla \cdot \mathbf{U}]^T$.
 671 The remaining term accounts for the linear variations in the state variable and the parameter
 672 vector. It is defined as $\mathbf{G}(\mathbf{Q}, \boldsymbol{\eta}) = \mathbf{G}(\mathbf{Q}, [\eta_1, 0]^T) + \mathbf{G}(\mathbf{Q}, [0, \eta_2]^T)$ where $\mathbf{G}(\mathbf{Q}, [\eta_1, 0]^T) =$
 673 $\eta_1 \nabla \cdot (\nabla \mathbf{U} + \nabla \mathbf{U}^T)$ and $\mathbf{G}(\mathbf{Q}, [0, \eta_2]^T)$. The former operator shows the dependency on the
 674 parameter η_1 , which accounts for the viscous effects. The latter operator depends on the
 675 parameter η_2 , which accounts for the velocity ratio between jets and it is used to impose the
 676 boundary condition $\mathbf{U} = (0, \eta_2 \tanh(b_i(1 - 2r)), 0)$ on $\Gamma_{in,i}$. In addition, we consider the
 677 following splitting of the parameters $\boldsymbol{\eta} = \boldsymbol{\eta}_c + \Delta \boldsymbol{\eta}$. Here $\boldsymbol{\eta}_c$ denotes the critical parameters
 678 $\boldsymbol{\eta}_c \equiv [Re_c^{-1}, \delta_{u,c}]^T$ attained when the spectra of the Jacobian operator possess at least an
 679 eigenvalue whose real part is zero. The distance in the parameter space to the threshold is
 680 represented by $\Delta \boldsymbol{\eta} = [Re_c^{-1} - Re^{-1}, \delta_{u,c} - \delta_u]^T$.

681

A.1. Multiple scales ansatz

682 The multiple scales expansion of the solution \mathbf{q} of eq. (2.3) is

$$683 \quad \mathbf{q}(t, \tau) = \mathbf{Q}_0 + \varepsilon \mathbf{q}_{(\varepsilon)}(t, \tau) + \varepsilon^2 \mathbf{q}_{(\varepsilon^2)}(t, \tau) + O(\varepsilon^3), \quad (\text{A } 2)$$

684 where $\varepsilon \ll 1$ is a small parameter. The distance in the parameter space to the critical point
 685 $\Delta \boldsymbol{\eta} = [Re_c^{-1} - Re^{-1}, \delta_{u,c} - \delta_u]^T$ is assumed to be of second order, i.e. $\Delta \eta_i = O(\varepsilon^2)$ for $i = 1, 2$.
 686 The expansion eq. (A 2) considers a two scale expansion of the original time $t \mapsto t + \varepsilon^2 \tau$. A
 687 fast timescale t and a slow timescale of the evolution of the amplitudes $z_i(\tau)$ in eq. (A 2), for
 688 $i = 1, 2$. Note that the expansion of the LHS eq. (2.3) up to third order is as follows

$$689 \quad \varepsilon \mathbf{B} \frac{\partial \mathbf{q}_{(\varepsilon)}}{\partial t} + \varepsilon^2 \mathbf{B} \frac{\partial \mathbf{q}_{(\varepsilon^2)}}{\partial t} + \varepsilon^3 \left[\mathbf{B} \frac{\partial \mathbf{q}_{(\varepsilon^3)}}{\partial t} + \mathbf{B} \frac{\partial \mathbf{q}_{(\varepsilon)}}{\partial \tau} \right], \quad (\text{A } 3)$$

690 and the RHS respectively,

$$691 \quad \mathbf{F}(\mathbf{q}, \boldsymbol{\eta}) = \mathbf{F}_{(0)} + \varepsilon \mathbf{F}_{(\varepsilon)} + \varepsilon^2 \mathbf{F}_{(\varepsilon^2)} + \varepsilon^3 \mathbf{F}_{(\varepsilon^3)}. \quad (\text{A } 4)$$

692 The expansion eq. (A 4) will be detailed at each order.

693 A.1.1. Order ε^0

694 The zeroth order \mathbf{Q}_0 of the multiple scales expansion eq. (A 2) is the steady state of the
 695 governing equations evaluated at the threshold of instability, i.e. $\boldsymbol{\eta} = \boldsymbol{\eta}_c$,

696
$$\mathbf{0} = \mathbf{F}(\mathbf{Q}_0, \eta_c). \quad (\text{A } 5)$$

697 A.1.2. Order ε^1

698 The first order $\mathbf{q}_{(\varepsilon)}(t, \tau)$ of the multiple scales expansion of eq. (A 2) is composed of the
699 eigenmodes of the linearised system

700
$$\mathbf{q}_{(\varepsilon)}(t, \tau) \equiv (z_1(\tau)e^{-im_1\theta}\hat{\mathbf{q}}_1 + z_2(\tau)e^{i-m_2\theta}\hat{\mathbf{q}}_2 + \text{c. c.}). \quad (\text{A } 6)$$

701 in our case, $m_1 = 1$ and $m_2 = 2$. Each term $\hat{\mathbf{q}}_\ell$ of the first order expansion eq. (A 6) is a
702 solution of the following linear equation

703
$$\mathbf{J}_{(\omega_\ell, m_\ell)}\hat{\mathbf{q}}_\ell \equiv \left(i\omega_\ell \mathbf{B} - \frac{\partial \mathbf{F}}{\partial \mathbf{q}}|_{\mathbf{q}=\mathbf{Q}_0, \eta=\eta_c} \right) \hat{\mathbf{q}}_\ell = 0, \quad (\text{A } 7)$$

704 where $\frac{\partial \mathbf{F}}{\partial \mathbf{q}}|_{\mathbf{q}=\mathbf{Q}_0, \eta=\eta_c} \hat{\mathbf{q}}_\ell = \mathbf{L}_{m_\ell} \hat{\mathbf{q}}_\ell + \mathbf{N}_{m_\ell}(\mathbf{Q}_0, \hat{\mathbf{q}}_\ell) + \mathbf{N}_{m_\ell}(\hat{\mathbf{q}}_\ell, \mathbf{Q}_0)$. The subscript m_ℓ indicates
705 the azimuthal wavenumber used for the evaluation of the operator.

706 A.1.3. Order ε^2

707 The second order expansion term $\mathbf{q}_{(\varepsilon^2)}(t, \tau)$ is determined from the resolution of a set of
708 forced linear systems, where the forcing terms are evaluated from first and zeroth order
709 terms. The expansion in terms of amplitudes $z_i(\tau)$ ($i = 1, 2$) of $\mathbf{q}_{(\varepsilon^2)}(t, \tau)$ is assessed from
710 term-by-term identification of the forcing terms at the second order. Non-linear second order
711 terms in ε are

712
$$\begin{aligned} \mathbf{F}_{(\varepsilon^2)} &\equiv \sum_{j,k=1}^2 \left(z_j z_k \mathbf{N}(\hat{\mathbf{q}}_j, \hat{\mathbf{q}}_k) e^{-i(m_j+m_k)\theta} + \text{c.c.} \right) \\ &+ \sum_{j,k=1}^2 \left(z_j \bar{z}_k \mathbf{N}(\hat{\mathbf{q}}_j, \bar{\hat{\mathbf{q}}}_k) e^{-i(m_j-m_k)\theta} + \text{c.c.} \right) \\ &+ \sum_{\ell=0}^2 \eta_\ell \mathbf{G}(\mathbf{Q}_0, \mathbf{e}_\ell), \end{aligned} \quad (\text{A } 8)$$

713 where the terms proportional to $z_j z_k$ are named $\hat{\mathbf{F}}_{(\varepsilon^2)}^{(z_j z_k)}$ and \mathbf{e}_ℓ is an element of the
714 orthonormal basis of \mathbb{R}^2 .

715 Then, we look for a second order term expanded as follows

716
$$\mathbf{q}_{(\varepsilon^2)} \equiv \sum_{\substack{j,k=1 \\ k \leq j}}^2 (z_j z_k \hat{\mathbf{q}}_{z_j z_k} + z_j \bar{z}_k \hat{\mathbf{q}}_{z_j \bar{z}_k} + \text{c.c.}) + \sum_{\ell=1}^2 \eta_\ell \mathbf{Q}_0^{(\eta_\ell)}. \quad (\text{A } 9)$$

717 Terms $\hat{\mathbf{q}}_{z_j^2}$ are azimuthal harmonics of the flow. The terms $\hat{\mathbf{q}}_{z_j z_k}$ with $j \neq k$ are coupling
718 terms, and $\hat{\mathbf{q}}_{|z_j|^2}$ are harmonic base flow modification terms. Finally, $\mathbf{Q}_0^{(\eta_\ell)}$ are base flow
719 corrections due to a variation of the parameter η_ℓ from the critical point.

720 At this order, there exist two resonant terms, the terms proportional to $\bar{z}_1 z_2$ and z_1^2 , which
721 are associated with the singular Jacobian $\mathbf{J}_{(0, m_k)}$ for $k = 1, 2$. To ensure the solvability of
722 these terms, we must enforce compatibility conditions, i.e. the *Fredholm alternative*. The
723 resonant terms are then determined from the resolution of the following set of *bordered*
724 *systems*

725
$$\begin{pmatrix} \mathbf{J}_{(0, m_k)} & \hat{\mathbf{q}}_k \\ \hat{\mathbf{q}}_k^\dagger & 0 \end{pmatrix} \begin{pmatrix} \hat{\mathbf{q}}_{(\mathbf{z}^{(R)})} \\ e \end{pmatrix} = \begin{pmatrix} \hat{\mathbf{F}}_{(\varepsilon^2)}^{(\mathbf{z}^{(R)})} \\ 0 \end{pmatrix}, \quad \mathbf{z}^{(R)} \in [\bar{z}_1 z_2, z_1^2]^T, \quad (\text{A } 10)$$

726 where $e = e_3$ for $\mathbf{z}^{(R)} = \bar{z}_1 z_2$ and $e = e_4$ for $\mathbf{z}^{(R)} = z_1^2$. The non-resonant terms are computed
727 by solving the following non-degenerated forced linear systems

$$728 \quad \mathbf{J}_{(0,m_j+m_k)} \hat{\mathbf{q}}_{z_j z_k} = \hat{\mathbf{F}}_{(\epsilon^2)}^{(z_j z_k)}, \quad (\text{A } 11)$$

729 and

$$730 \quad \mathbf{J}_{(0,0)} \mathbf{Q}_0^{(\eta_\ell)} = \mathbf{G}(\mathbf{Q}_0, \mathbf{e}_\ell). \quad (\text{A } 12)$$

731 A.1.4. Order ϵ^3

732 At third order, there exist six degenerate terms. In our case, we are not interested in solving
733 for terms of third-order, instead, we will determine the linear and cubic coefficients of the
734 third order normal form eq. (2.11) from a set of compatibility conditions.

735 The linear terms $\lambda_{(s,1)}$ and $\lambda_{(s,2)}$ and cubic terms $c_{(i,j)}$ for $i = 1, 2$ are determined as follows

$$736 \quad \lambda_{(s,1)} = \frac{\langle \hat{\mathbf{q}}_1^\dagger, \hat{\mathbf{F}}_{(\epsilon^3)}^{(z_1)} \rangle}{\langle \hat{\mathbf{q}}_1^\dagger, \mathbf{B} \hat{\mathbf{q}}_1 \rangle}, \quad \lambda_{(s,2)} = \frac{\langle \hat{\mathbf{q}}_2^\dagger, \hat{\mathbf{F}}_{(\epsilon^3)}^{(z_2)} \rangle}{\langle \hat{\mathbf{q}}_2^\dagger, \mathbf{B} \hat{\mathbf{q}}_2 \rangle}, \quad c_{(i,j)} = \frac{\langle \hat{\mathbf{q}}_i^\dagger, \hat{\mathbf{F}}_{(\epsilon^3)}^{(z_i |z_j|^2)} \rangle}{\langle \hat{\mathbf{q}}_i^\dagger, \mathbf{B} \hat{\mathbf{q}}_i \rangle}. \quad (\text{A } 13)$$

737 The forcing terms for the linear coefficient are

$$738 \quad \hat{\mathbf{F}}_{(\epsilon^3)}^{(z_j)} \equiv \sum_{\ell=1}^2 \eta_\ell \left([\mathbf{N}(\hat{\mathbf{q}}_j, \mathbf{Q}_0^{(\eta_\ell)}) + \mathbf{N}(\mathbf{Q}_0^{(\eta_\ell)}, \hat{\mathbf{q}}_j)] + \mathbf{G}(\hat{\mathbf{q}}_j, \mathbf{e}_\ell) \right). \quad (\text{A } 14)$$

739 which allows the decomposition of $\lambda_{(s,\ell)} = \lambda_{(s,\ell),\text{Re}}(\text{Re}_c^{-1} \text{Re}^{-1}) + \lambda_{(s,\ell),\delta_u}(\delta_{u,c} - \delta_u)$ for
740 $\ell = 1, 2$.

741 The forcing terms for the cubic coefficients are

$$742 \quad \hat{\mathbf{F}}_{(\epsilon^3)}^{(z_j |z_k|^2)} \equiv \left[\mathbf{N}(\hat{\mathbf{q}}_j, \hat{\mathbf{q}}_{|z_k|^2}) + \mathbf{N}(\hat{\mathbf{q}}_{|z_k|^2}, \hat{\mathbf{q}}_j) \right] \\ + \left[\mathbf{N}(\hat{\mathbf{q}}_{-k}, \hat{\mathbf{q}}_{z_j z_k}) + \mathbf{N}(\hat{\mathbf{q}}_{j,k}, \hat{\mathbf{q}}_{-k}) \right] \\ + \left[\mathbf{N}(\hat{\mathbf{q}}_k, \hat{\mathbf{q}}_{z_j \bar{z}_k}) + \mathbf{N}(\hat{\mathbf{q}}_{z_j \bar{z}_k}, \hat{\mathbf{q}}_k) \right]. \quad (\text{A } 15)$$

743 if $j \neq k$ and

$$744 \quad \hat{\mathbf{F}}_{(\epsilon^3)}^{(z_j |z_j|^2)} \equiv \left[\mathbf{N}(\hat{\mathbf{q}}_j, \hat{\mathbf{q}}_{|z_j|^2}) + \mathbf{N}(\hat{\mathbf{q}}_{|z_j|^2}, \hat{\mathbf{q}}_j) \right] \\ + \left[\mathbf{N}(\hat{\mathbf{q}}_{-j}, \hat{\mathbf{q}}_{z_j^2}) + \mathbf{N}(\hat{\mathbf{q}}_{z_j^2}, \hat{\mathbf{q}}_{-j}) \right], \quad (\text{A } 16)$$

745 for the diagonal forcing terms.

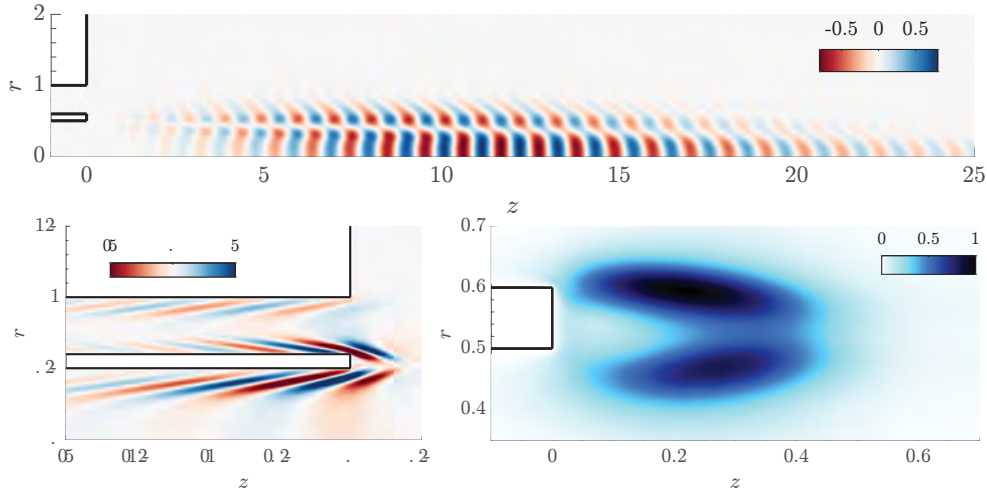
746 Appendix B. Validation of the code - Comparison with the literature

747 The calculations made in StabFem in the sections at the main manuscript are validated
748 comparing the leading global mode in the geometry proposed by Canton *et al.* (2017).
749 Moreover, the critical Reynolds number and associated frequency are also analysed. In the
750 cited work, the authors use an analogous geometry with the following parameters:

- 751 • Radius of the inner jet $R_{inner} = 0.5$
- 752 • Diameter of the outer jet $D = 0.4$
- 753 • Distance between jets $L = 0.1$
- 754 • Ratio between velocities $\delta_u = 1$

755 The linear stability analysis has been carried out imposing $m = 0$, as done by Canton
756 *et al.* (2017), so the leading global mode will be axisymmetric. The critical Reynolds number
757 Re_c and the frequency ω of the leading global mode are compared in Tab. 3. As seen, few

	Canton <i>et al.</i> (2017)	Present work
Re_c	1420	1405
ω	5.73	5.72

Table 3: Comparison of Re_c and ω between previous work and the present one.Figure 24: Direct mode, adjoint mode and sensitivity of the leading global mode studied by Canton *et al.* (2017) calculated using StabFem.

758 differences can be found on the critical Reynolds number and the frequency. The relative
 759 error in the Re_c calculation is 1.06% and the one of the frequency is 0.17%.

760 The global mode is now calculated using StabFem and compared with the one calculated
 761 by Canton *et al.* (2017). This mode can be found in figures 9, 10 and 11 on the cited paper.
 762 As it can be seen, there are not substantial differences between the direct modes, being both
 763 of them a vortex street with their biggest amplitude situated 10 units downstream the exit
 764 of the jets. The adjoint mode is concentrated within the nozzle, with its biggest amplitude
 765 situated on the sharp corners. There is no difference between the adjoint mode calculated
 766 with StabFem and the one in Canton *et al.* (2017). Finally, the structural sensitivity is similar
 767 to the one computed by Canton *et al.* (2017). It is composed by two lobes in the space between
 768 the exit of the two jets.

REFERENCES

- 769 ARMBRUSTER, DIETER, GUCKENHEIMER, JOHN & HOLMES, PHILIP 1988 Heteroclinic cycles and modulated
 770 travelling waves in systems with $o(2)$ symmetry. *Physica D: Nonlinear Phenomena* **29** (3), 257–282.
 771 AUGUSTE, F., FABRE, D. & MAGNAUDET, J. 2010 Bifurcations in the wake of a thick circular disk. *Theoretical
 772 and Computational Fluid Dynamics* **24**, 305–313.
 773 BALESTRA, GIOELE, GLOOR, MICHAEL & KLEISER, LEONHARD 2015 Absolute and convective instabilities of
 774 heated coaxial jet flow. *Physics of Fluids* **27** (5).
 775 BOGULAWSKI, A. & WAWRZAK, K. 2020 Absolute instability of an annular jet: local stability analysis.
 776 *Meccanica* **55**, 2179–2198.
 777 BURESTI, G., TALAMELLI, G. A. & PETAGNA, P. 1994 Experimental characterization of the velocity field of
 778 a coaxial jet configuration. *Exp. Therm. Fluid Sci.* **9**, 135.
 779 CANTON, J., AUTERI, F. & CARINI, M. 2017 Linear global stability of two incompressible coaxial jets. *J.
 780 Fluid Mech.* **824**, 886–911.

- 781 DAHM, W. J. A., FRIELER, C. E. & TRYGGVASON, G. 1992 Vortex structure and dynamics in the near field of
782 a coaxial jet. *J. Fluid Mech.* **241**, 371.
- 783 DANGELMAYR, GERHARD 1986 Steady-state mode interactions in the presence of 0 (2)-symmetry. *Dynamics*
784 *and Stability of Systems* **1** (2), 159–185.
- 785 FABRE, D., CITRO, V., FERREIRA SABINO, D., BONNEFIS, P., SIERRA, J., GIANNETTI,
786 F. & PIGOU, M. 2019 A Practical Review on Linear and Nonlinear
787 Global Approaches to Flow Instabilities. *Applied Mechanics Reviews* **70** (6),
788 060802, arXiv: [https://asmedigitalcollection.asme.org/appliedmechanicsreviews/article-](https://asmedigitalcollection.asme.org/appliedmechanicsreviews/article-pdf/70/6/060802/6075557/amr_070_06_060802.pdf)
789 [pdf/70/6/060802/6075557/amr_070_06_060802.pdf](https://asmedigitalcollection.asme.org/appliedmechanicsreviews/article-pdf/70/6/060802/6075557/amr_070_06_060802.pdf).
- 790 GIANNETTI, F. & LUCHINI, P. 2007 Structural sensitivity of the first instability of the cylinder wake. *J. Fluid*
791 *Mech.* **581**, 167–197.
- 792 GLOOR, MICHAEL, OBRIST, DOMINIK & KLEISER, LEONHARD 2013 Linear stability and acoustic characteristics
793 of compressible, viscous, subsonic coaxial jet flow. *Physics of Fluids* **25** (8).
- 794 JONES, CA & PROCTOR, MRE 1987 Strong spatial resonance and travelling waves in Bénard convection.
795 *Physics Letters A* **121** (5), 224–228.
- 796 KAPITULA, TODD & PROMISLOW, KEITH 2013 *Spectral and dynamical stability of nonlinear waves*, vol.
797 457. Springer.
- 798 KO, N.W.M. & KWAN, A.S.H. 1976 The initial region of subsonic coaxial jets. *J. Fluid Mech.* **73**, 305.
- 799 MARIANO, PAOLO MARIA & STAZI, FURIO LORENZO 2005 Computational aspects of the mechanics of complex
800 materials. *Archives of Computational Methods in Engineering* **12** (4), 391–478.
- 801 MELIGA, PHILIPPE, CHOMAZ, JEAN-MARC & SIPP, DENIS 2009 Global mode interaction and pattern selection
802 in the wake of a disk: a weakly nonlinear expansion. *Journal of Fluid Mechanics* **633**, 159–189.
- 803 MELIGA, PHILIPPE, GALLAIRE, FRANÇOIS & CHOMAZ, JEAN-MARC 2012 A weakly nonlinear mechanism for
804 mode selection in swirling jets. *Journal of Fluid Mechanics* **699**, 216–262.
- 805 MERCADER, ISABEL, PRAT, JOANA & KNOBLOCH, EDGAR 2002 Robust heteroclinic cycles in two-dimensional
806 rayleigh–Bénard convection without Boussinesq symmetry. *International Journal of Bifurcation and*
807 *Chaos* **12** (11), 2501–2522.
- 808 MICHALKE, A. 1999 Absolute inviscid instability of a ring jet with back-flow and swirl. *Eur. J. Mech.*
809 *B/Fluids* **18**, 3–12.
- 810 MONTAGNANI, DAVIDE & AUTERI, FRANCO 2019 Non-modal analysis of coaxial jets. *Journal of Fluid*
811 *Mechanics* **872**, 665–696.
- 812 NORE, C, MOISY, F & QUARTIER, L 2005 Experimental observation of near-heteroclinic cycles in the von
813 Kármán swirling flow. *Physics of Fluids* **17** (6), 064103.
- 814 NORE, CAROLINE, TUCKERMAN, LAURETTE S, DAUBE, OLIVIER & XIN, SHIHE 2003 The 1 [ratio] 2 mode
815 interaction in exactly counter-rotating von Kármán swirling flow. *Journal of Fluid Mechanics* **477**,
816 51–88.
- 817 OLSEN, W. & KARCHMER, A. 1976 Lip noise generated by flow separation from nozzle surfaces. *AIAA J.* **76**,
818 3.
- 819 ÖRLÜ, R., SEGALINI, A., ALFREDSSON, P. H. & TALAMELLI, A. 2008 On the passive control of the near-field
820 of coaxial jets by means of vortex shedding. *Proceedings of the International Conference on Jets,*
821 *Wakes and Separated Flows, ICJWSF-2008, Technical University of Berlin, Berlin, Germany, Sept.*
822 *16–19*.
- 823 PALACIOS, ANTONIO, GUNARATNE, GEMUNU H, GORMAN, MICHAEL & ROBBINS, KAY A 1997 Cellular
824 pattern formation in circular domains. *Chaos: An Interdisciplinary Journal of Nonlinear Science*
825 **7** (3), 463–475.
- 826 PERRAULT-JONCAS, DOMINIQUE & MASLOWE, SHERWIN A. 2008 Linear stability of a compressible coaxial
827 jet with continuous velocity and temperature profiles. *Physics of Fluids* **20** (7).
- 828 PORTER, J & KNOBLOCH, E 2001 New type of complex dynamics in the 1: 2 spatial resonance. *Physica D:*
829 *Nonlinear Phenomena* **159** (3-4), 125–154.
- 830 PORTER, J & KNOBLOCH, E 2005 Dynamics in the 1: 2 spatial resonance with broken reflection symmetry.
831 *Physica D: Nonlinear Phenomena* **201** (3-4), 318–344.
- 832 REHAB, H., VILLERMAUX, E. & HOPFINGER, E. J. 1997 Flow regimes of large-velocity-ratio coaxial jets. *J.*
833 *Fluid Mech.* **345**, 357.
- 834 SEGALINI, A. & TALAMELLI, A. 2011 Experimental analysis of dominant instabilities in coaxial jets. *Phys.*
835 *Fluids* **23**, 024103.
- 836 SIERRA, JAVIER, FABRE, DAVID & CITRO, VINCENZO 2020a Efficient stability analysis of fluid flows using
837 complex mapping techniques. *Computer Physics Communications* **251**, 107100.

- 838 SIERRA, J., FABRE, D., CITRO, V. & GIANNETTI, F. 2020*b* Bifurcation scenario in the two-dimensional laminar
839 flow past a rotating cylinder. *Journal of Fluid Mechanics* **905**, A2.
- 840 SIERRA, J., JOLIVET, P., GIANNETTI, F. & CITRO, V. 2021 Adjoint-based sensitivity analysis of periodic orbits
841 by the fourier–galerkin method. *Journal of Computational Physics* **440**, 110403.
- 842 SIERRA-AUSIN, JAVIER, CITRO, VINCENZO, GIANNETTI, FLAVIO & FABRE, DAVID 2022*a* Efficient computation
843 of time-periodic compressible flows with spectral techniques. *Computer Methods in Applied
844 Mechanics and Engineering* **393**, 114736.
- 845 SIERRA-AUSIN, J., FABRE, D., CITRO, V. & GIANNETTI, F. 2022*b* Acoustic instability prediction of the flow
846 through a circular aperture in a thick plate via an impedance criterion. *Journal of Fluid Mechanics*
847 **943**, A48.
- 848 SIERRA-AUSÍN, J., LORITE-DÍEZ, M., JIMÉNEZ-GONZÁLEZ, J.I., CITRO, V. & FABRE, D. 2022 Unveiling the
849 competitive role of global modes in the pattern formation of rotating sphere flows. *Journal of Fluid
850 Mechanics* **942**, A54.
- 851 DA SILVA, C. B., BALARAC, G. & MÉTAIS, O. 2003 Transition in high velocity ratio coaxial jets analysed
852 from direct numerical simulations. *J. Turbul.* **24**, 1.
- 853 TALAMELLI, A. & GAVARINI, I. 2006 Linear instability characteristics of incompressible coaxial jets. *Flow
854 Turbulence Combust.* **76**, 221–240.
- 855 TAMMISOLA, O. 2012 Oscillatory sensitivity patterns for global modes in wakes. *J. Fluid Mech.* **701**, 251–
856 277.
- 857 WALLACE, D. & REDEKOPP, L.G. 1992 Linear instability characteristics of wake-shear layers. *Phys. Fluids*
858 **4**, 189—191.
- 859 WILLIAMS, T.J., ALI, M.R.M.H. & ANDERSON, J.S. 1969 Noise and flow characteristics of coaxial jets. *J.
860 Mech. Eng. Sci.* **1**, 2.

Wake dynamics in buoyancy-driven flows: steady state–Hopf mode interaction with $O(2)$ symmetry revisited

Javier Sierra-Ausin^{1,2}, David Fabre¹ and Edgar Knobloch³

¹*UPS-IMFT, Allée du Professeur Camille Soula, 31000 Toulouse, France*

²*Università degli Studi di Salerno, 132 Via Giovanni Paolo II, 84084 Fisciano, Salerno, Italy and*

³*Department of Physics, University of California at Berkeley, Berkeley, California 94720, USA*

(Dated: July 23, 2023)

We present a detailed mathematical study of a truncated normal form relevant to the bifurcations observed in wake flow past axisymmetric bodies, with and without thermal stratification. We employ abstract normal form analysis to identify possible bifurcations and the corresponding bifurcation diagrams in parameter space. The bifurcations and the bifurcation diagrams are interpreted in terms of symmetry considerations. Particular emphasis is placed on the presence of attracting robust heteroclinic cycles in certain parameter regimes. The normal form coefficients are computed for several examples of wake flows behind buoyant disks and spheres, and the resulting predictions compared with the results of direct numerical flow simulations. In general, satisfactory agreement is obtained.

I. INTRODUCTION

Bifurcation, defined here as a transition between two states with different symmetry, is a key concept in many fields of modern physics. Generally speaking, the larger the symmetry of a problem, the greater is the number of ways the symmetry may be broken, leading to the richest collections of bifurcation scenarios. *Equivariant bifurcation theory* [1] constitutes a mathematical framework for studying such problems, and predicts the possible states that may arise and the bifurcation routes between them. A key idea for the parameter space exploration of physical problems is the identification of points of *codimension two* (or greater), namely sets of parameters at which two (or more) bifurcations arise simultaneously. The richest range of possible behavior is usually encountered in the vicinity of such points. The theory also provides a systematic procedure for constructing truncated dynamical systems called *normal forms* that enable a classification of all admissible states near such codimension-two points and their stability properties. This classification depends only on the symmetry properties of the problem and is thus common to all problems involving the same symmetry.

Fluid mechanics has proved to be a particularly rich playground for the investigation of bifurcations [2]. The classical problems for which bifurcation theory has proved both relevant and helpful include, among others, Taylor–Couette flow (TCF, [3, 4]) and Rayleigh–Bénard convection (RBC, [5]). Bifurcation theory is also relevant to wake flows, with the wake of a fixed two-dimensional (2D) cylinder transverse to the flow providing the classic example. Here the wake experiences a Hopf bifurcation leading to the von Kármán vortex street beyond $Re \approx 47$, where Re is a suitably defined Reynolds number. The case where the cylinder rotates was recently shown to give rise to a much richer range of behavior that was also successfully explained using bifurcation theory [6].

The present work is primarily devoted to transitions in *wake flows past axisymmetric objects* (WFA) within

a homogeneous fluid. The geometry which attracted the largest number of studies is that of a sphere. Here, experiments [7, 8] and numerical investigations [9–11] reveal a primary steady state bifurcation resulting in the loss of axisymmetry, followed by a secondary bifurcation leading to reflection-symmetric periodic states. The case of a rotating sphere, recently analysed in [12], reveals a primary bifurcation leading to a rotating wave pattern. Secondary and tertiary bifurcations are therein interpreted as the result of an interaction between three rotating wave patterns. The cases of disks [13–15] and ellipsoids [15] have also been investigated, revealing a collection of new states and bifurcation scenarios involving the loss and recovery of planar symmetry.

Two other related classes of problems will also be considered here. The first is the path taken by objects in free motion, such as rising bubbles or falling solid disks (WFA-FO problem, see [16]). For falling or rising disks, experiments [16–19]) and simulations [20, 21] reveal a rich range of possible behavior. As shown in [22], linear stability analysis predicts correctly the primary bifurcations for these flows, while weakly nonlinear analysis [23] reproduces the zigzag path observed in experiments. The case of a rising bubble proved to be more challenging. For bubbles of a fixed ellipsoidal shape, linear stability analysis predicts correctly the destabilization of the path observed in experiments [24], while [25] conducted a linear stability analysis for a deformable bubble, leading to the conclusion that shape deformation plays little role in the resulting dynamics.

The last class of problems considered here is closely related to the two previous ones and corresponds to wake flows past fixed objects in a thermally stratified background involving mixed convection due to Prandtl number effects (WFA-MC). Motivated by interest in the transition to a turbulent wake in this system, the authors of Ref. [26] conducted a parameter study using numerical simulations at two different Prandtl numbers, $Pr = 0.72$ and $Pr = 7$. For both ellipsoids and disks [15], a large collection of states with various symmetry properties was

revealed, closely related to the states found in the two previous sets of problems.

Fabre et al. [13] were the first to recognize that equivariant bifurcation theory is relevant to these sets of problems, and to note that the relevant spatial symmetry (corresponding to the mathematical group $O(2)$) is the same as that in Taylor-Couette flow, thus highlighting an unexpected analogy between both systems. Fabre et al. thus reconsidered the normal form initially introduced in [3, 4] for the TCF problem, and showed that with an appropriate choice of the coefficients, the dynamics of the flow past a sphere and a thin disk are correctly reproduced. Auguste et al. [14] successfully applied the same approach to a thick disk. Subsequently, Meliga et al. [27] reconsidered the case of the sphere and the thick disk using a multiple scale analysis to determine the coefficients in the normal form. Their results are in agreement with the numerical simulations of [13], thereby confirming the relevance of the approach. However, their derivation method is not fully rigorous, as the problem is not strictly of codimension two. However, exact codimension-two points were detected in both the WFA-MC [26] and the WFA-FO [22] problems, indicating that in these problems a rigorous normal form derivation may be undertaken.

As previously mentioned, Golubitsky and collaborators [3, 28] investigated solutions of the normal form corresponding to the steady/Hopf interaction in the presence of $O(2)$ symmetry, with application to the TCF problem, exploring the dynamics up to secondary bifurcations. However, they do not provide a systematic study of the problem and many details are left to the reader. Their study also overlooks possible ternary bifurcation to states which are not observed in the TCF problem but are nonetheless relevant to the problems considered here. The purpose of this work is thus to revisit and extend these results and to explain how they can be applied to the TFC, WFA, and WFA-MC problems. Our method differs from that of Golubitsky et al. [3, 28] in several aspects:

- The study is restricted to a truncated problem where only third-order nonlinearities are considered.
- Two systems are introduced: a polar coordinate representation that eliminates the two continuous symmetries of the system and a second system written in its natural Hilbert basis which reduces the dynamics to its fundamental domain. These techniques, when systematically employed, reduce the six-dimensional system to four dimensions and the fixed-point solutions to a single representative of each group orbit and enable us to establish the presence of robust heteroclinic cycles in this system.
- The amplification rates λ_s and λ_h of the two primary modes are included explicitly in the unfolding of the problem. Golubitsky et al. considered the

amplification rates as unspecified functions of a single control parameter only.

Our approach is thus much more in line with that used by Hirschberg and Knobloch [29, 30] for the related problem of interaction of two steady-state modes with $O(2)$ symmetry. There are strong similarities between these two situations, as emphasized in what follows.

The paper is organized as follows. Section II presents the normal form and introduces a reduction to polar coordinates that is used in what follows. Section III proposes a general nomenclature for the various solutions of the problem. Section IV reviews the fixed-point solutions of the normal form: pure modes, mixed modes, and possible bifurcations of higher order. Section V considers a degenerate case in which a number of details can be investigated analytically. Section VI presents a numerical exploration of various solutions of the truncated problem. Next, section VII explains how the various results can be used to construct consistent stability diagrams, while section VIII applies these results to the flow past a fixed axisymmetric object, in particular, a disk and a sphere. The paper concludes with a brief discussion in Section IX. Some technical details are relegated to a pair of Appendices. Background to the techniques we use and their application to problems arising in fluid mechanics may be found in [2].

II. NORMAL FORM AND REDUCTION TO AMPLITUDE EQUATIONS

A. Problem parametrization

The flow state $\mathbf{q} = [\mathbf{u}, p]$ is specified by the velocity field \mathbf{u} and the hydrodynamic pressure p (the WFA-MC also includes the temperature field T). Near the mode interaction (a codimension-two bifurcation) the flow state takes the form

$$\mathbf{q} = \mathbf{Q}_0 + \text{Re}[a_0(t)e^{-i\theta}\hat{\mathbf{q}}_s] + \text{Re}[a_1(t)e^{-i\theta}\hat{\mathbf{q}}_{h,-1} + a_2(t)e^{i\theta}\hat{\mathbf{q}}_{h,1}] + \text{h.o.t.} \quad (1)$$

Here \mathbf{Q}_0 is the steady-state flow state that is invariant under the action of the whole $O(2)$ group, $\hat{\mathbf{q}}_s$ is the steady mode and $\hat{\mathbf{q}}_h$ is the Hopf (unsteady) mode. The Ansatz in eq. (1) takes into account the continuous (translation or rotation) symmetry via the terms $e^{\pm i\theta}$, where $\theta \in S^1$ is an angle-like variable in the periodicity direction; for axisymmetric problems it corresponds to the azimuthal angle, while in the TCF it corresponds to the axial direction: $\theta \equiv -2\pi x/\Lambda$, where Λ is the mode wavelength. Here without loss of generality the azimuthal wavenumber m is taken to be $m = 1$. Both the steady-state flow and the eigenmodes are functions of other spatial variables (radial distance and azimuthal angle for the TFC; radial and axial distances for axisymmetric wake problems), but this dependence is not of importance here.

In the following we shall be interested in the dynamics arising from the interaction between the amplitude a_0 of the steady mode and the amplitudes a_1 , a_2 of the left and right-rotating waves associated with the Hopf mode. All three amplitudes are in general complex functions of the time t and their behavior near the mode interaction is described by normal form theory.

B. Universal normal form

The normal form is obtained in a standard way: provided the original system of equations is Γ -equivariant under the group $\Gamma \equiv O(2) \times S^1$, the normal form must also be Γ -equivariant. The Hilbert–Weyl and Poénaru theorems, stated in [28, Ch 1], ensure the existence of a finite set of Γ -equivariant polynomials generating the Γ -equivariant Taylor expansion (at the origin) of any smooth mapping. The group Γ acts on \mathbb{C}^3 which decomposes into irreducibles $\mathbb{C} \oplus \mathbb{C}^2$ corresponding to the steady and Hopf modes. The action of the group Γ is generated by rotations R_α , reflection κ , and the temporal phase shift Φ of the Hopf mode. The canonical representation of these actions is as follows:

$$\begin{aligned} R_\alpha &: (a_0, a_1, a_2) \rightarrow (a_0 e^{i\alpha}, a_1 e^{i\alpha}, a_2 e^{-i\alpha}) \\ \Phi &: (a_0, a_1, a_2) \rightarrow (a_0, a_1 e^{i\phi}, a_2 e^{i\phi}) \\ \kappa &: (a_0, a_1, a_2) \rightarrow (\bar{a}_0, a_2, a_1). \end{aligned} \quad (2)$$

Based on these considerations, Golubitsky *et al.* [3, 28] show that the resulting normal form can be written as follows:

$$\begin{aligned} \begin{pmatrix} \dot{a}_0 \\ \dot{a}_1 \\ \dot{a}_2 \end{pmatrix} &= (c^1 + i\delta c^2) \begin{pmatrix} a_0 \\ 0 \\ 0 \end{pmatrix} + (c^3 + i\delta c^4) \begin{pmatrix} \bar{a}_0 a_1 \bar{a}_2 \\ 0 \\ 0 \end{pmatrix} \\ &+ (p^1 + iq^1) \begin{pmatrix} 0 \\ a_1 \\ a_2 \end{pmatrix} + (p^2 + iq^2) \delta \begin{pmatrix} 0 \\ a_1 \\ -a_2 \end{pmatrix} \\ &+ (p^3 + iq^3) \begin{pmatrix} 0 \\ a_0^2 a_2 \\ \bar{a}_0^2 a_1 \end{pmatrix} + (p^4 + iq^4) \delta \begin{pmatrix} 0 \\ a_0^2 a_2 \\ -\bar{a}_0^2 a_1 \end{pmatrix}, \end{aligned} \quad (3)$$

where $\delta \equiv |a_2|^2 - |a_1|^2$, and the 12 real quantities c^i , p^i and q^i , $i = 1, 2, 3, 4$, are functions of the control parameters and of the five generators of the ring of invariant polynomials under the action of the group Γ :

$$\begin{aligned} \rho &\equiv |a_0|^2, \quad N \equiv |a_1|^2 + |a_2|^2, \quad \Delta \equiv (|a_2|^2 - |a_1|^2)^2, \\ \eta &\equiv \text{Re}(a_0^2 \bar{a}_1 a_2), \quad \xi \equiv (|a_2|^2 - |a_1|^2) \text{Im}(a_0^2 \bar{a}_1 a_2). \end{aligned} \quad (4)$$

C. Normal form in polar coordinates

Using the polar representation of the complex amplitudes $a_j = r_j e^{i\phi_j}$ for $j = 0, 1, 2$, eq. (3) can be reduced to a system of four coupled equations governing the amplitudes r_0 , r_1 , r_2 and the phase $\Psi \equiv \phi_1 - \phi_2 - 2\phi_0$:

$$\begin{aligned} \dot{r}_0 &= [c^1 + c^3 r_1 r_2 \cos \Psi - c^4 \delta \sin \Psi] r_0 \\ \dot{r}_1 &= [p^1 + \delta p^2] r_1 \\ &+ [(p^3 + \delta p^4) \cos \Psi + (q^3 + \delta q^4) \sin \Psi] r_0^2 r_2 \\ \dot{r}_2 &= [p^1 - \delta p^2] r_2 \\ &+ [(p^3 - \delta p^4) \cos \Psi - (q^3 - \delta q^4) \sin \Psi] r_0^2 r_1 \\ \dot{\Psi} &= 2(q^2 \delta - c^2 \delta - c^3 \sin \Psi - c^4 \delta \cos \Psi) \\ &+ \frac{r_0^2}{r_1 r_2} [(q^3 + N q^4) \cos \Psi - (N p^3 + \Delta p^4) \sin \Psi]. \end{aligned} \quad (5)$$

Note that this system is four-dimensional due to the two continuous symmetries of the system (3). Invariance under the action of the phase shift Φ reduces the three angle-like variables (ϕ_0, ϕ_1, ϕ_2) to two $(\phi_0, \phi_1 - \phi_2)$; invariance under the rotations R_α then leads to the single phase Ψ .

The polar system is equivariant under the action of the group Γ_ρ which is isomorphic to the Pauli group $\Gamma_\rho \simeq D_4 \rtimes \mathbb{Z}_2$, where the symbol \rtimes indicates the semi-direct product between groups. The generators of the group are the reflection κ and $R_{\pi/2} \Phi_{\pi/2}$, the discrete rotation through $\pi/2$ with an equal time shift. For the sake of conciseness, let us introduce the action of the following group elements on the polar vector field:

$$\begin{aligned} \kappa &: (r_0, r_1, r_2, \Psi) \rightarrow (r_0, r_2, r_1, -\Psi) \\ R_{\pi/2} \Phi_{\pi/2} &: (r_0, r_1, r_2, \Psi) \rightarrow (r_0, -r_1, r_2, \Psi + \pi) \\ R_\pi \Phi_\pi &: (r_0, r_1, r_2, \Psi) \rightarrow (-r_0, r_1, r_2, \Psi) \\ R_{\pi/2} \Phi_{-\pi/2} &: (r_0, r_1, r_2, \Psi) \rightarrow (r_0, r_1, -r_2, \Psi + \pi), \end{aligned} \quad (6)$$

where $R_{\pi/2} \Phi_{-\pi/2} = \kappa \cdot (R_{\pi/2} \Phi_{\pi/2})^3 \cdot \kappa$ and $R_\pi \Phi_\pi = (R_{\pi/2} \Phi_{\pi/2})^2$. In the next section we present a classification of the various solutions based on the polar representation.

D. Group-theoretic considerations

Branching of solutions is determined by the structure of the isotropy lattice acting on fixed points of the normal form (3). The isotropy subgroups of solutions that arise at primary bifurcations correspond to maximal isotropy subgroups of Γ , that is, isotropy subgroups that are not included in any other isotropy subgroup other than Γ itself. In a similar manner, solutions arising at secondary bifurcations have isotropy subgroups that are maximal in a subgroup strictly smaller than Γ . This process continues until the trivial group is reached, corresponding to the most general fixed point subspace of the normal form.

Prior to the introduction of the isotropy lattice of the normal form (3), let us introduce the following notation to denote some of the isotropy subgroups of Γ : the group of rotations $\widetilde{SO(2)}$,

$$\widetilde{SO(2)} \equiv \{R_\phi \Phi_{-\phi} \mid \phi \in [0, 2\pi)\}, \quad (7a)$$

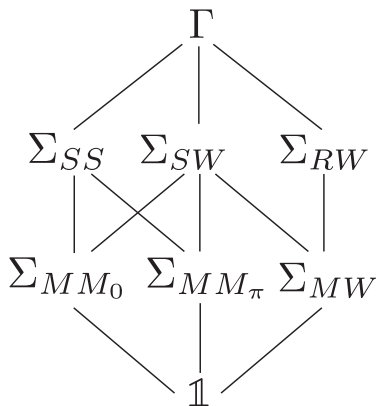


FIG. 1: Lattice of isotropy subgroups of the symmetry group Γ (resp. Γ_ρ).

and the group $\mathbb{Z}_n(g)$, a cyclic subgroup generated by the element g , satisfying $g^n = \text{Id}$. The isotropy lattice of the normal form (3) is represented in fig. 1. In section III we use the information extracted from this lattice to determine the types of invariant solutions admitted by the normal form. In addition to the isotropy subgroups of the complex normal form, table III lists the isotropy subgroups of the solutions of the polar system (5).

E. Third order normal form

Here we will not deal with the general case, instead we consider a truncated form retaining only nonlinearities of third order. Such a truncated system can be expressed in the following explicit form:

$$\dot{a}_0 = \lambda_s a_0 + l_0 a_0 |a_0|^2 + l_1 (|a_1|^2 + |a_2|^2) a_0 + i l_2 (|a_2|^2 - |a_1|^2) a_0 + l_3 \bar{a}_0 \bar{a}_2 a_1 \quad (8a)$$

$$\dot{a}_1 = (\lambda_h + i\omega_h) a_1 + (B|a_1|^2 + (A+B)|a_2|^2) a_1 + C a_1 |a_0|^2 + D a_0^2 a_2 \quad (8b)$$

$$\dot{a}_2 = (\lambda_h + i\omega_h) a_2 + (B|a_2|^2 + (A+B)|a_1|^2) a_2 + C a_2 |a_0|^2 + D \bar{a}_0^2 a_1, \quad (8c)$$

where l_0, l_1, l_2, l_3 are real coefficients and A, B, C, D are complex coefficients. The correspondence with the notation of Golubitsky *et al.* [3, 28] is reported in tables I and II.

The system (8) then corresponds to the polar equations

$$\dot{r}_0 = [\lambda_s + l_0 r_0^2 + l_1 (r_1^2 + r_2^2)] r_0 + l_3 r_0 r_1 r_2 \cos \Psi \quad (9a)$$

$$\dot{r}_1 = [\lambda_h + B_r r_1^2 + (A_r + B_r) r_2^2 + C_r r_0^2] r_1 + r_0^2 r_2 (D_r \cos \Psi + D_i \sin \Psi) \quad (9b)$$

$$\dot{r}_2 = [\lambda_h + B_r r_2^2 + (A_r + B_r) r_1^2 + C_r r_0^2] r_2 + r_0^2 r_1 (D_r \cos \Psi - D_i \sin \Psi) \quad (9c)$$

$$\dot{\Psi} = (A_i - 2l_2)(r_2^2 - r_1^2) - 2l_3 r_1 r_2 \sin \Psi + r_0^2 D_i \cos \Psi \left[\frac{r_2}{r_1} - \frac{r_1}{r_2} \right] - r_0^2 D_r \sin \Psi \left[\frac{r_2}{r_1} + \frac{r_1}{r_2} \right]. \quad (9d)$$

Interestingly, the polar system only involves 9 of the 13 original coefficients, namely: $l_0, l_1, l_3, A_r, B_r, C_r, D_r, D_i$ and $A_i - 2l_2$. The system (9) is decoupled from the evolution of the phase ϕ_0 and the "mean phase" of the Hopf component $\phi_m = (\phi_1 + \phi_2)/2$, which evolve according to

$$\dot{\phi}_0 = l_2 (r_2^2 - r_1^2) + l_3 r_1 r_2 \sin \Psi, \quad (10a)$$

$$\dot{\phi}_m = \omega_h + (B_i + \frac{1}{2} A_i)(r_1^2 + r_2^2) + C_i r_0^2 + \frac{1}{2} r_0^2 D_i \cos \Psi \left[\frac{r_2}{r_1} + \frac{r_1}{r_2} \right] + \frac{1}{2} r_0^2 D_i \sin \Psi \left[\frac{r_1}{r_2} - \frac{r_2}{r_1} \right]. \quad (10b)$$

In addition we introduce a system whose coordinates are invariant under the group action, except for the reflection symmetry in Ψ . We do this primarily because we would like to use the resulting system to study a particular degenerate case in section V. The advantage of such a system is that dynamics occur in the "fundamental domain", that is, there is only one representative of each group orbit. The system is defined in terms of the invariants

$$R = r_0^2, \quad S = r_1^2 + r_2^2, \quad P = r_1 r_2, \quad Q = \cos \Psi. \quad (11)$$

In term of these coordinates the evolution equations become

$$\dot{R} = 2[\lambda_s + l_0 R + l_1 S + l_3 P] R \quad (12a)$$

$$\dot{S} = 2[\lambda_h + B_r S + C_r R] S + 4[A_r P + D_r Q R] P \quad (12b)$$

$$\dot{P} = [\lambda_h + B_r S + C_r R] P + 4[A_r P + D_r Q R] S - D_i R \sqrt{(1 - Q^2)(S^2 - 4P^2)} \quad (12c)$$

TABLE I: Correspondence of the real coefficients of the normal form (8) with the literature.

	λ_s	λ_h	ω_h	l_0	l_1	l_2	l_3
[3, 28]	$c_\mu^1 \cdot \mu$	$p_\mu^1 \cdot \mu$	q_0^1	c_ρ^1	c_N^1	c_0^2	c_0^3
[4]	$\alpha_0 \mu + \beta_0 \nu$	$\alpha_1 \mu + \beta_1 \nu$	ω_0	c_0	$\text{Re}(d_0)$	$-\text{Im}(d_0)$	f_0

$$\dot{Q} = [2l_3 + \frac{D_r RS}{P}](1 - Q^2) + [(A_i - 2l_2) - \frac{D_i R Q}{P}] \sqrt{(1 - Q^2)(S^2 - 4P^2)}. \quad (12d)$$

In the study that follows, we take the nonlinear coefficients l_j for $j = 1, 2, 3, 4$, A, B, C, D as well as the frequency ω_h of the Hopf mode as constant. The amplification rates λ_s and λ_h will be used as unfolding parameters. Our study provides predictions for the existence and stability of the possible solutions in the (λ_s, λ_h) plane. To apply these results to the flows we are interested in, we have to specify the dependence of the amplification rates on the control parameters of the problem. The WFA problem employs a single control parameter R while the WFA-MC problem is specified by two control parameters R_1 and R_2 related to the magnitude of the incoming velocity and the temperature difference between the object and the background, respectively. In this case the amplification rates can be assumed to have the following dependence:

$$\begin{aligned} \lambda_s &= \alpha_s(R_1 - R_1^*) + \beta_s(R_2 - R_2^*), \\ \lambda_h &= \alpha_h(R_1 - R_1^*) + \beta_h(R_2 - R_2^*), \end{aligned} \quad (13)$$

where R_1^* and R_2^* are the threshold values given by the linear stability analysis of the axisymmetric steady state; for the WFA problem $\beta_s = \beta_h = 0$.

In the TCF problem R_1, R_2 are related to the angular velocities of the inner and outer cylinders; in the vicinity of the bicritical (codimension-two) point (R_1^*, R_2^*) the amplification rates can be assumed to depend linearly on the distance to this point:

$$\begin{aligned} \lambda_s &= c_{R_1}^1(R_1 - R_1^*) + c_{R_2}^1(R_2 - R_2^*), \\ \lambda_h &= p_{R_1}^1(R_1 - R_1^*) + p_{R_2}^1(R_2 - R_2^*). \end{aligned} \quad (14)$$

Numerical values for (R_1^*, R_2^*) and for the parameters $c_{R_1}^1, c_{R_2}^1, p_{R_1}^1, p_{R_2}^1$ are tabulated in [3] for several values of the radius ratio $\eta < 1$ (i.e. the ratio of the radii of the inner and outer cylinders).

III. CLASSIFICATION OF THE SOLUTIONS

The nomenclature used to classify the various solutions is given in tables III and IV. We describe every possible solution, although the emphasis will be put on the solutions that arise generically in the third-order problem and in the degenerate case considered in section V.

TABLE II: Correspondence of the complex coefficients of the normal form (8) with the literature.

	A	B	C	D
[3, 28]	$2(p_0^2 + iq_0^2)$	$(p_N^1 - p_0^2) + i(q_N^1 - q_0^2)$	$p_\rho^1 + iq_\rho^1$	$p_0^3 + iq_0^3$
[4]	$e_1 - d_1$	d_1	c_1	f_1

To illustrate the various solutions graphically, we project the four-dimensional phase space into a plane spanned either by the complex amplitude $A(t)$ or by $A_j'(t)$ for $j = 0, 1$, where

$$\begin{aligned} A(t) &\equiv a_0(t) + a_1(t) + \bar{a}_2(t), \\ A_j'(t) &\equiv A(t)e^{-i\phi_j(t)}, \text{ for } j = 0, 1, \end{aligned} \quad (15)$$

hereafter referred to as the A -projection and the A' -projection, respectively.

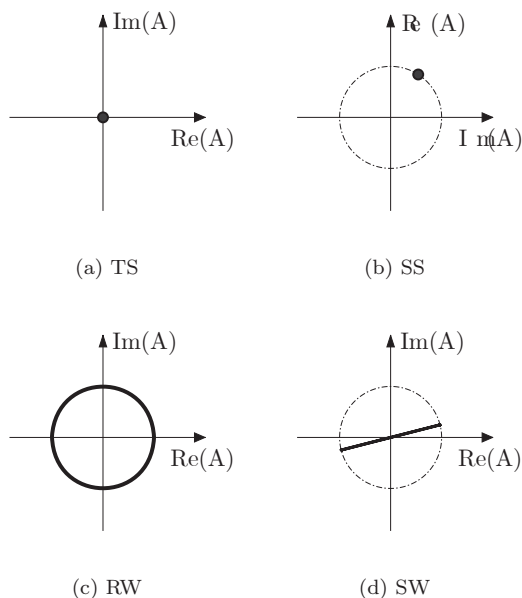
The function A provides a global measure of the dynamics of the system and combines contributions from both the steady and unsteady components. In the wake problem, the real and imaginary parts of A can be identified with the leading order contribution to the lift forces in the y and z directions, respectively. In the TCF problem they represent, for example, the vorticity levels at two points located a quarter of a wavelength apart in the periodicity direction.

The solutions that are stationary in the polar representation are summarized in the table III. The simplest solution is the trivial solution (TS) $(a_0, a_1, a_2) = (0, 0, 0)$. This solution corresponds to Couette flow in the TCF problem, and to the axisymmetric solution in the WFA and WFA-MC problems. In the A -projection this solution corresponds to the origin (Figure 2a). There are three primary solutions: steady-state modes (SS), rotating waves (RW) and standing waves (SW). The steady state mode (SS) takes the form $(a_0, 0, 0)$, $a_0 \neq 0$. This state corresponds to the Taylor Vortex state in the TCF problem and the Steady Shedding mode in the wake problems. In the A -projection this state is represented by an off-center point (Figure 2b). As shown in table V and in fig. 2b using a thin dashed-dotted line there is a circle of such states related by rotations R_{ϕ_0} ; each state is in addition reflection-symmetric.

The RW and SW solutions arise in a primary Hopf bifurcation of the trivial state. Because of $O(2)$ symmetry, the eigenvalues at the Hopf bifurcation are doubled, and the Hopf bifurcation produces simultaneously a branch of rotating waves (RW, $(a_0, a_1, a_2) = (0, a_1, 0)$) and standing waves (SW, $(a_0, a_1, a_2) = (0, a_1, a_1)$). The RW break reflection symmetry; consequently, there are two RW, rotating in opposite directions and related by reflection. In contrast, the SW are reflection-symmetric oscillations with zero mean. In the TCF problem the RWs correspond to the Spiral Vortex state, while in the wake problem they correspond to the Spiral Shedding state, observed, for example, in the wake of a rising bubble [31]. In the A -projection the RW state corresponds to a limit cycle centered at the origin (Figure 2c), while the SW state is represented by a radial oscillation through the origin (Figure 2d). In the TCF problem, the SWs correspond to the Ribbon state while in the wake problem they correspond to the Symmetric Periodic Shedding state observed, for example, in the wake of a disk when $R \approx 150$. As for SS, there is a circle of SW states related by rotations, see fig. 2d. Each of these solutions corresponds to a one-dimensional fixed point subspace

TABLE III: Nomenclature and symmetry groups of the steady-state solutions of the system (5).

Name	Representative	Isotropy group (complex)	Isotropy group (polar)	Frequencies
Pure modes:				
TS	$(0, 0, 0, nd)$	$O(2) \times S^1$	$D_4 \times \mathbb{Z}_2(\kappa)$	0
SS	$(r_a, 0, 0, nd)$	$\mathbb{Z}_2(\kappa) \times S^1$	$\mathbb{Z}_2(\kappa) \times \mathbb{Z}_2(\Phi_\pi)$	0
RW	$(0, r_a, 0, nd)$	$SO(2)$	$\mathbb{Z}_4(R_{\pi/2}\Phi_{\pi/2})$	1
SW	$(0, r_a, r_a, nd)$	$\mathbb{Z}_2(\kappa) \times \mathbb{Z}_2(R_\pi\Phi_\pi)$	$\mathbb{Z}_2(\kappa) \times \mathbb{Z}_2(R_\pi\Phi_\pi)$	1
Mixed modes:				
MM ₀	$(r_a, r_b, r_b, 0)$	$\mathbb{Z}_2(\kappa)$	$\mathbb{Z}_2(\kappa)$	1
MM _π	(r_a, r_b, r_b, π)	$\mathbb{Z}_2(\kappa \cdot R_\pi\Phi_\pi)$	$\mathbb{Z}_2(\kappa \cdot R_\pi\Phi_\pi)$	1
MW	$(0, r_a, r_b, \Psi)$	$\mathbb{Z}_2(R_\pi\Phi_\pi)$	$\mathbb{Z}_2(R_\pi\Phi_\pi)$	1
Precessing waves:				
General	(r_a, r_b, r_c, Ψ)	$\mathbf{1}$	$\mathbf{1}$	2
Type A	(r_a, r_b, r_b, Ψ)	$\mathbf{1}$	$\mathbf{1}$	2
Type B	$(r_a, r_b, r_c, 0 \text{ or } \pi)$	$\mathbf{1}$	$\mathbf{1}$	2
Type C	$(r_a, r_b, 0, \Psi)$	$\mathbf{1}$	$\mathbf{1}$	2

FIG. 2: The trivial state (TS) and the primary branching solutions SS, RW and SW in the complex A plane.

spanned either by a_0 or a_1 , and their presence is therefore guaranteed by the equivariant branching lemma.

Secondary bifurcations may lead to states with a higher-dimensional fixed point subspace. These states correspond to the next rung of the lattice of isotropy subgroups. An example is provided by mixed mode states that correspond to a (nonlinear) superposition of the SS and SW modes. There are two possible states of this type. The first is denoted by MM₀, and corresponds, respectively, to a pattern called Twisted Vortices in the TCF problem and to the reflection symmetry-preserving mode (RSP) in the wake problem. In the A -projection

the solution oscillates back and forth in the radial direction but now with non-zero mean (Figure 3a). The second mixed mode, MM_π, corresponds, respectively, to Wavy Vortices in the TCF problem and to the reflection symmetry-breaking mode (RSB) in the wake problem. In the A -projection this solution corresponds to a back-and-forth along a line segment perpendicular to the radial direction (Figure 3b). The phase ϕ_0 of both these states is arbitrary. In other words, there is a circle of solutions of each type, as indicated in fig. 3a) and fig. 3b). Finally, one can also find a mixed mode state involving the Hopf modes, referred to as a modulated wave state (MW), consisting of a (nonlinear) superposition of two rotating wave modes. This state is referred to as the Modulated Spiral mode (MSP) in the TCF problem and the Modulated Wave mode (MW) in the wake problem. It is a mode with two temporal frequencies, which are in general incommensurate, and so corresponds to a 2-torus as sketched in fig. 3c. This type of solution does not occur generically in the third-order system, although it arises in higher order normal forms or in the degenerate case corresponding to $A_r = 0$ [32].

The last solution type, that is, a state arising in a tertiary bifurcation, corresponds to a fixed point in the (r_0, r_1, r_2, Ψ) coordinates with no further symmetry. According to eq. (10), in such states the phase ϕ_0 of the steady mode generically precesses at a constant rate given by $\dot{\phi}_0$. Consequently, states of this type display two frequencies, one of which is close to the critical Hopf frequency while the other is a low frequency given by eq. (10a). Such modes have been called "modulated rotating waves" in [3], but here we prefer to avoid the ambiguous word "modulated" which has been used to describe a large variety of very different states in the past. Instead, these solutions will be referred to as Precessing Waves (PrW) or "drifting waves".

The precession of these states is best appreciated in the A' -projection, showing the state in a frame of reference precessing with the steady-state component a_0 . In

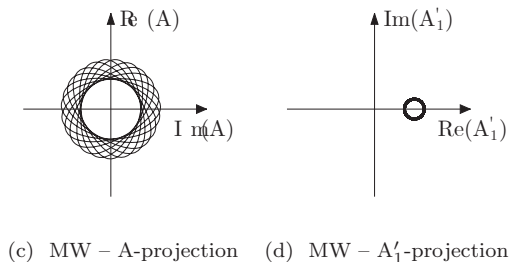
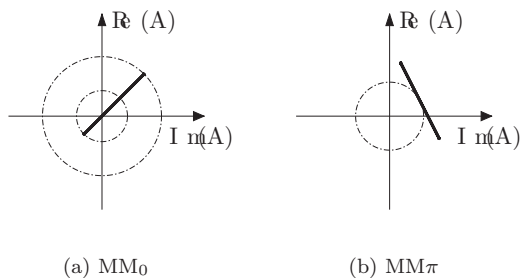


FIG. 3: The secondary states (a) MM_0 , (b) MM_π and (c) MW in the complex A plane. (d) The A'_1 -projection of the MW state.

this frame of reference, the PrW is periodic and takes the form of an ellipse (Figure 4b). Note that in this representation the polar coordinates (r_0, r_1, r_2, Ψ) can be interpreted graphically: r_0 is the distance of the center of the ellipse to the origin, $(r_1 + r_2)/2$ and $(r_1 - r_2)/2$ are the major and minor axes, and Ψ is twice the angle between the major axis of the ellipse and the direction of the steady-state component.

There are in fact four types of PrW as explained in Table III. The general solution, PrW General, occurs generically in the third order normal form and corresponds to the most general fixed-point solution of eq. (9). In addition, there are special PrW states. The first two, called PrW Type A and Type B, do not occur generically in the third order problem, but they are found in normal forms of higher order or in the degenerate case considered in section V. The third solution, PrW Type C is another degenerate solution that arises in the third order normal form but only when the three conditions $A_i - 2l_2 = D_r = D_i = 0$ are satisfied.

The solutions that are periodic in the polar representation are summarized in table IV. We distinguish three types of solutions. The first type is referred to as a Modulated Mixed Mode since it displays the same spatial symmetries as the mixed modes already described. For example, in the A -projection the Modulated Mixed Mode state \widetilde{MM}_π evolves on a 2-torus, whose shape resembles that of MM_π (Figure 5a). The A'_0 -projection (Figure 5b) yields an identical but rotated picture, indicating that the phase of the steady-state component remains constant. The related state \widetilde{MM}_0 is not displayed, since its

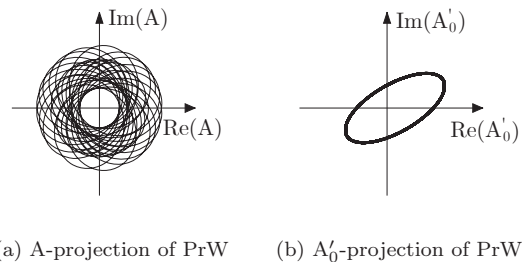


FIG. 4: The tertiary state PrW.

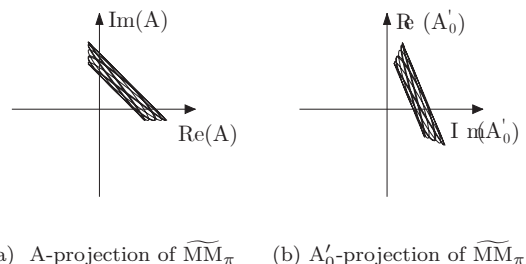


FIG. 5: The Modulated Mixed Mode \widetilde{MM}_π in the complex A plane.

A -projection is identical to that of the MM_0 state. Its modulus $|A|$, however, pulsates with two independent frequencies.

We also find periodic states we call Pulsating Waves (PuW). In such states, the polar coordinates (r_0, r_1, r_2, Ψ) all oscillate periodically in time, but the pulsation retains a certain symmetry. Specifically, $\bar{r}_1 = \bar{r}_2$ and $\overline{\sin \Psi} = 0$, where the overbar indicates an average over the pulsation period. According to eq. (10) the phase ϕ_0 of the steady-state component also pulsates periodically, but the average value of its derivative over one pulsation period vanishes. Consequently, the pattern does not precess. In the A -projection the solution evolves on a 2-torus that remains confined within a given angular sector (Figure 6a), indicating the absence of net precession. The A'_0 -projection (Figure 6b) also reveals a 2-torus, albeit of different form.

The last type of periodic solution corresponds to the case where the (r_0, r_1, r_2, Ψ) coordinates are once again all periodic, but the conditions $\bar{r}_1 = \bar{r}_2$ and $\overline{\sin \Psi} = 0$ are violated. In the A -projection, this state appears irregular (Figure 7a), while the A'_0 -projection (Figure 7b) reveals a 2-torus. In fact, this solution actually evolves on a 3-torus, owing to net drift in the phase ϕ_0 . We call these states Three-Frequency Waves (3FW), since they are characterized by a frequency near the critical Hopf frequency, the pulsation frequency, and finally the precession frequency.

The classification of the solutions of the generic steady-Hopf interaction with $O(2)$ symmetry presented by Gol-

TABLE IV: Nomenclature and symmetry group of limit cycle solutions of the system (5).

Name of solution	Representative in polar coordinates	Isotropy group	Frequencies in primitive coordinates
$\widetilde{MM}_{0,\pi}$	$(r_a(t), r_b(t), r_c(t), 0 \text{ or } \pi)$	$\mathbf{1}$	2
\widetilde{IMM}	$(0, r_b, r_c, \Psi(t))$	$\mathbf{1}$	2
PuW	$(r_a(t), r_b(t), r_c(t), \Psi(t))$ with $\bar{r}_b = \bar{r}_c$ and $\sin \Psi = 0$	$\mathbf{1}$	2
3-frequency waves: (3FW)			
General	$(r_a(t), r_b(t), r_c(t), \Psi(t))$	$\mathbf{1}$	3
Type A	$(r_a(t), r_b(t), r_b(t), \Psi(t))$ with $\sin \Psi \neq 0$	$\mathbf{1}$	3
Type B	$(r_a(t), r_b(t), r_c(t), 0 \text{ or } \pi)$ with $\bar{r}_b \neq \bar{r}_c$	$\mathbf{1}$	3
Type C	$(0, r_b(t), r_c(t), \text{nd})$ with $\bar{r}_b \neq \bar{r}_c$	$\mathbf{1}$	3
Type D	$(r_a(t), r_b(t), 0, \Psi(t))$ with $\sin \Psi \neq 0$	$\mathbf{1}$	3

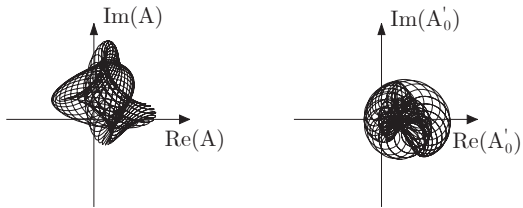
(a) A-projection of PuW (b) A'_0 -projection of PuW

FIG. 6: The Pulsating Wave PuW in the complex A plane.

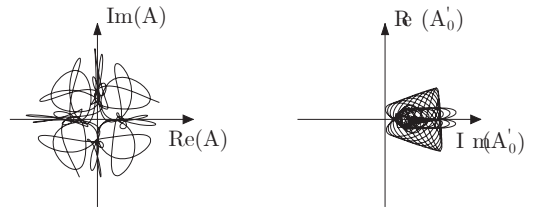
(a) A-projection of 3FW (b) A'_0 -projection of 3FW

FIG. 7: The Three-Frequency Wave 3FW in the complex A plane.

ubitsky *et al.* [3, 28] and covered in section IID is based on maximal isotropy subgroups of the symmetry group $O(2) \times S^1$ of the normal form. This technique predicts the existence up to tertiary bifurcations of fixed points of the complex normal form 3. These isotropy subgroups correspond to the symmetries of the solutions within the fixed point subspace of each isotropy group (cf. table III). However, several of the states identified here have trivial symmetry (denoted by $\mathbf{1}$), and their existence cannot be established by group-theoretic arguments alone. Thus, the polar representation introduced here is helpful for the explicit computations required to establish the presence of these more complex states.

IV. DYNAMICS OF THE SOLUTIONS

In this section, we describe the various solutions of the truncated third-order system (8). We summarize not only the solutions but also their stability properties, assuming that all necessary non-degeneracy conditions hold.

A. Pure modes

Table V contains the definition and eigenvalues of the trivial state and of the pure modes. Since the polar angle Ψ is undefined for these states, the results are obtained from the primitive amplitude equations (8). Therefore, six eigenvalues are listed for each branch. The condition for supercriticality of the primary branch is also given. This can be deduced from elementary considerations. For example, the SS branch is supercritical if $l_0 < 0$, as can be seen in both the equation for the branch (which is then defined for $\lambda_s > 0$) and the first non-zero eigenvalue (which is then negative, implying that stability has been transferred to the SS branch). The conditions for supercriticality also provide the conditions for the subcriticality (if the corresponding parameter has the opposite sign) and non-degeneracy (if the corresponding quantity is non-zero).

The bifurcation at $\lambda_h = 0$ is the standard Hopf bifurcation with $O(2)$ symmetry, and so gives rise simultaneously to branches of RW and SW. The RW rotate counterclockwise (clockwise) when $\omega_h > 0$ ($\omega_h < 0$). Reflection symmetry implies that for each RW $(r_1, r_2) = (r_1, 0)$

TABLE V: Defining equations and eigenvalues of primary branches in the third order normal form (8).

Name of solutions (condition for supercriticality)	Definition	Eigenvalues	Notes
Pure modes:			
TS	$r_0 = r_1 = r_2 = 0$	λ_s (twice) $\lambda_h \pm i\omega_h$ (twice each)	Bif. to SS Bif. to SW and RW
SS $l_0 < 0$	$r_0 = \sqrt{-\frac{\lambda_s}{l_0}} \equiv r_P$ ϕ_0 arbitrary $r_1 = r_2 = 0$	0 $2l_0 r_P^2$ $\lambda_h + i\omega_h + (C + D)r_P^2$ and c.c. $\lambda_h + i\omega_h + (C - D)r_P^2$ and c.c.	Inv. under rotation Bif. from TS Bif. to MM_0 Bif. to MM_π
SW $2B_r + A_r < 0$	$r_1 = r_2 = \sqrt{-\frac{\lambda_h}{(2B_r + A_r)}} \equiv r_S$ $r_0 = 0$ $\phi_1 - \phi_2$ arbitrary $\dot{\phi}_1 = \dot{\phi}_2 = \omega_h + (2B_i + A_i)r_S^2$	0 0 $(4B_r + 2A_r)r_S^2$ $-2A_r r_S^2$ $\lambda_s + (2l_1 + l_3)r_S^2$ $\lambda_s + (2l_1 - l_3)r_S^2$	Inv. under time shift Inv. under rotation Bif. from TS Bif. to RW Bif. to MM_0 Bif. to MM_π
RW $B_r < 0$	$r_1 = \sqrt{-\frac{\lambda_h}{B_r}} \equiv r_R$ $r_0 = r_2 = 0$ $\dot{\phi}_1 = \omega_h + B_i r_R^2$	0 $2B_r r_R^2$ $A_r r_R^2$ and c.c. $\lambda_s + (l_1 + il_2)r_R^2$ and c.c.	Inv. under time shift + rotation Bif. from TS Bif. to SW Bif. to PrW

there is also a RW $(r_1, r_2) = (0, r_1)$ rotating in the opposite direction. The condition $A_r = 0$ represents a degeneracy that is analysed theoretically in [1, 2, 32, 33]. In the vicinity of this degeneracy two-frequency states are present, and these are analyzed in appendix B.

B. Mixed modes

The defining equations for the mixed modes are given in table VI. We differentiate between nondegenerate solutions of the third-order truncated normal form, which are the Mixed Modes of type $MM_{0,\pi}$, and degenerate solutions, which are the Modulated Wave modes MW briefly discussed in appendix B. The nondegeneracy conditions for the existence of MM branches are $\Delta_\pm = (2B_r + A_r)l_0 - (2l_1 \pm l_3)(C_r \pm D_r) \neq 0$, with the positive sign for MM_0 and the negative sign for MM_π . Inspection shows that these states bifurcate supercritically from the SS branch if $\Delta_\pm l_0 < 0$ and from the SW branch if $\Delta_\pm(2B_r + A_r) < 0$. Modulated Wave modes MW are degenerate solutions of the third order normal form (9) and exist when $A_r = 0$ and $\Delta_b = l_3 \sin \Psi \neq 0$.

At this point, it is interesting to point out the similarities between the present problem and the related problem of the interaction between two steady-state modes with opposite parity analysed by Hirschberg & Knobloch [29, 30]. The latter problem has two pure modes and two mixed modes, which are defined by equations similar to those defining our SS and SW pure modes and mixed modes. So, if we restrict to the subspace generated by the SS and SW pure modes, all the results of Hirschberg & Knobloch [29, 30] can be directly applied to the present case. This is not so, however, within the

system (8), which reveals the presence of additional secondary bifurcations (see below).

C. Stability of mixed modes and tertiary bifurcations

Higher order bifurcations can be detected by linearizing the normal form (8) around the mixed modes in table VI. Working with the primitive equations, as done in Golubitsky et al. [28], leads to the same results, but the procedure is more involved. Within the polar representation four eigenvalues need to be computed; the remaining eigenvalues are both zero owing to the two continuous symmetries, the invariance of the mixed modes under rotation and time translation.

1. Mixed modes

To obtain the results listed in table VI, consider the following expansion: $r_0 = r_a + x_0$, $r_1 = r_b + x_1$, $r_2 = r_b + x_2$ and $\Psi = \Psi_0 + \psi$, with either $\Psi_0 = 0$ for MM_0 or $\Psi = \pi$ for MM_π ; in either case we suppose the perturbation is infinitesimal, $|x_0|, |x_1|, |x_2|, |\psi| \ll 1$. In terms of the quantities $\rho = x_1 - x_2$ and $x_M = (x_1 + x_2)/2$ the resulting linear stability problem is block-diagonal:

TABLE VI: Defining equations and eigenvalues of mixed modes in the third order normal form (8).

Name of solutions (condition for supercriticality)	Definition	Eigenvalues	Notes
MM ₀ Δ ₊ ≠ 0	$r_a^2 = \frac{(2l_1+l_3)\lambda_h - (2B_r+A_r)\lambda_s}{\Delta_+}$ $r_b^2 = \frac{(C_r+D_r)\lambda_s - l_0\lambda_h}{\Delta_+}$ $\Delta_+ = (2B_r + A_r)l_0 - (2l_1 + l_3)(C_r + D_r)$	eigs of M_a^+ eigs of M_b^+	Bif. to $\overline{\text{MM}}_0$ Bif. to PrW and/or PuW
MM _π Δ ₋ ≠ 0	$r_a^2 = \frac{(2l_1-l_3)\lambda_h - (2B_r+A_r)\lambda_s}{\Delta_-}$ $r_b^2 = \frac{(C_r-D_r)\lambda_s - l_0\lambda_h}{\Delta_-}$ $\Delta_- = (B_r + A_r)l_0 - (2l_1 - l_3)(C_r - D_r)$	eigs of M_a^- eigs of M_b^-	Bif. to $\overline{\text{MM}}_\pi$ Bif. to PrW and/or PuW
MW 2B _r + A _r < 0, A _r > 0 p _N ² < 0, p _Δ ¹ < 0 Existence I: A _r /p _N ² < 0	$r_a^2 = \frac{1}{2} \left[-\frac{A_r}{2p_N^2} - \sqrt{\frac{\chi}{4p_\Delta^1 p_N^2}} \right]$ $r_b^2 = \frac{1}{2} \left[-\frac{A_r}{2p_N^2} + \sqrt{\frac{\chi}{4p_\Delta^1 p_N^2}} \right]$	$-2r_{SW}^2 (A_r + 4r_{SW}^2 p_N^2)$ $-r_{RW}^2 (A_r - 2r_{RW}^2 p_N^2)$ $\lambda_s - l_1 \frac{A_r}{p_N^2}$	Bif. from/to SW Bif. from/to RW Bif. to PrW or 3FW
Existence II: $0 < \frac{\chi}{p_\Delta^2 p_N^2} < \frac{A_r^2}{(p_N^2)^2}$	$\chi = A_r(A_r + 2B_r) - 4p_N^2 - A_r \frac{p_N^2}{p_N^2} \lambda_h$		

$$\begin{pmatrix} \dot{x}_0 \\ \dot{x}_M \end{pmatrix} = M_a^\pm \begin{pmatrix} x_0 \\ x_M \end{pmatrix} \text{ with}$$

$$M_a^\pm = 2 \begin{pmatrix} l_0 r_a^2 & (2l_1 \pm l_3) r_a r_b \\ (C_r \pm D_r) r_a r_b & (2B_r + A_r) r_b^2 \end{pmatrix},$$

$$\begin{pmatrix} \dot{\rho} \\ \dot{\psi} \end{pmatrix} = M_b^\pm \begin{pmatrix} \rho \\ \psi \end{pmatrix} \text{ with}$$

$$M_b^\pm = 2 \begin{pmatrix} -A_r r_b^2 \mp D_r r_a^2 & \pm D_i r_a^2 r_b \\ (2l_2 - A_i) r_b \mp D_i r_a^2 / r_b & \mp (D_r r_a^2 + l_3 r_b^2) \end{pmatrix}, \quad (16)$$

with the upper sign applying to MM₀ and the lower one to MM_π. The matrices M_a^+ , M_b^+ , M_a^- , M_b^- correspond, respectively, to the matrices denoted M_0 , M_1 , N_0 and N_1 in Golubitsky et al. [28], but are obtained here in a much more straightforward way. The expressions are identical, except for the prefactor 2 which is missing in Golubitsky et al. and an overall change of sign in their matrix M_1 .

Let us first discuss the situation in the subspace (x_0, x_M) , which is governed by the system (16a). This system is completely analogous to that studied by Hirschberg & Knobloch [29], since it involves perturbations within the SS/SW invariant subspace of the problem. In particular, the determinant of the matrix M_a^\pm (i.e. the product of the eigenvalues) is $4r_a r_b \Delta_\pm$. It follows that a steady state bifurcation cannot occur along either mixed mode within the SS/SW subspace. This fact could have been anticipated by noting that this subspace does not admit symmetry-breaking bifurcations of these states. As a result only Hopf bifurcations are possible. It follows that the eigenvalues of the matrix M_a^\pm are either real with constant sign, or complex conjugate with a possible Hopf bifurcation. Inspection shows that the situation depends upon the signs of the quantities l_0 , $2B_r + A_r$, and Δ_\pm . If $\Delta_\pm < 0$, both eigenvalues

are real and their product is negative. Therefore, one of the eigenvalues is stable and the other unstable. This means that the corresponding branch MM_{0,π} is always less stable than the primary SS and SW branches. In the case $\Delta_\pm > 0$, the product of the eigenvalues is positive, and their sum is given by the trace of the matrix, i.e. $2(l_0 r_a^2 + (2B_r + A_r) r_b^2)$. When $l_0 < 0$ and $2B_r + A_r < 0$, i.e., when both primary bifurcations are supercritical, the trace remains negative, indicating that both eigenvalues are stable along the whole mixed mode branch. Similarly, when $l_0 > 0$, and $2B_r + A_r > 0$, i.e. when both primary bifurcations are subcritical, the trace remains positive, indicating that both eigenvalues are unstable along the whole branch. The last possibility, $l_0(2B_r + A_r) < 0$, arises when one of the primary bifurcations is subcritical while the other is supercritical. In this case, the real part of the eigenvalues changes sign somewhere along the branch, signaling the occurrence of a Hopf bifurcation. The solution born at such a Hopf bifurcation is referred to here as a Modulated Mixed Kode ($\overline{\text{MM}}_{\Psi_0}$, see table IV). The frequency of oscillation of the Modulated Mixed Mode at the Hopf bifurcation is given by the determinant of the matrix M_a^\pm and may be expressed in terms of r_a^2 as follows:

$$\omega_a^2 = -\frac{l_0 \Delta_\pm}{2B_r + A_r} r_a^4. \quad (17)$$

According to Hirschberg & Knobloch [29], the corresponding bifurcation is degenerate within the third order truncation, and higher order terms are required to determine whether it is subcritical or supercritical.

Consider now the situation in the (ρ, ψ) subspace, governed by the system (16b). Inspection shows that the matrix M_b^\pm may have complex or real eigenvalues. So, in this subspace, each of the mixed modes can experience steady bifurcations (associated with the vanishing of a single eigenvalue of M_b^\pm) and/or Hopf bifurcations

(associated with the vanishing of the real part of a pair of complex eigenvalues of M_b^\pm). To discuss the nature of the solutions born at these tertiary bifurcations it is useful to note that the phase drift $\dot{\phi}_0$ of the steady mode component is related to these quantities by the equation

$$\dot{\phi}_0 = -2l_2r_b\rho \pm l_3r_b^2\psi + \mathcal{O}(\rho^3, \rho^2\psi, \psi^2\rho, \psi^3), \quad (18)$$

obtained from eq. (10a).

A steady state bifurcation will generically give rise to a branch with constant, nonzero (ρ, ψ) , and according to eq. (18) such a state will therefore precess at a constant angular velocity. The corresponding bifurcation will be referred to as a parity-breaking bifurcation, and the states produced as Precessing Waves (PrW, see table III). On the other hand, a Hopf bifurcation will generically give rise to a limit cycle in the (ρ, ψ) plane. Since this cycle is symmetric about $(\rho, \psi) = (0, 0)$, eq. (18) implies that the resulting state will drift back and forth with zero net drift. The result is a direction-reversing wave [34] and we refer here to states of this type as Pulsating Waves (PuW, see table IV).

These predictions are in agreement with those of Golubitsky et al. except for their expectation that the symmetry-breaking Hopf bifurcation (i.e. the Hopf bifurcation in the (ρ, ψ) subspace) gives rise to a 3-frequency state. We see that while the bifurcation is indeed associated with translations of the pattern and hence motion along a three-torus, this motion is in fact a two-frequency motion (in the original variables).

The eigenvalues of the matrix M_b^\pm solve a quadratic equation which cannot be simplified easily, and generally has to be investigated on a case-by-case basis. However, it is instructive to consider the situation in the vicinity of the bifurcation points of the mixed modes from the pure modes. In the vicinity of the bifurcation from the SS mode one has $r_b \ll r_a$, and the eigenvalues of M_b^\pm are, at leading order, $(\mp 2Dr_a^2, \mp \bar{D}r_a^2)$. Thus, if $D_r > 0$ (resp. $D_r < 0$), the MM_0 is more (resp. less) stable than the MM_π mode in the vicinity of the bifurcation from the SS mode. Similarly, near the bifurcation from the SW mode, the requirement $r_a \ll r_b$ shows that the eigenvalues of M_b^\pm are, at leading order, $(-2A_r r_b^2, \mp 2l_3 r_b^2)$. The first eigenvalue indicates stability for both MM_0 and MM_π modes provided $A_r > 0$. Recall that the parameter A_r also determines if the SW branch is more or less stable than the RW branch. Thus, the mixed modes inherit this property from the SW branch in the vicinity of the bifurcation point. The second eigenvalue likewise implies that if $l_3 > 0$ (resp. $l_3 < 0$), the MM_0 is more (resp. less) stable than the MM_π in the vicinity of the bifurcation from the SW mode.

D. Bifurcation from Rotating Waves to Precessing Waves

As indicated in table III, the RW branch has a couple of complex eigenvalues which may lead to a bifurcation to a Precessing Wave (PrW). This situation was investigated by Crawford et al. [35] using the primitive sixth-order system. The derivation was lengthy and required the demonstration of an extension of the Hopf theorem to complex equations. The use of the polar representation introduced here leads to substantial simplifications because, within this representation, this bifurcation is in fact a steady-state one, and the resulting Precessing Wave is a stationary solution of the polar equations.

We consider here the clockwise ($\omega_h > 0$) RW with $(r_1, r_2) \equiv (r_R, 0)$, where r_R is given in table III. According to the table, a bifurcation occurs along this branch when the bifurcation parameter, defined by

$$\sigma_R \equiv \lambda_s + l_1 r_R^2, \quad (19)$$

vanishes. Inspection shows that the corresponding eigenvector breaks the symmetry of the mixed mode (i.e., it points in the a_0 direction). We expect, therefore, that the branch originating in this bifurcation will be characterized by $r_0 = \mathcal{O}(\sigma_R^{1/2})$. We further anticipate that $r_2 = \mathcal{O}(\sigma_R)$ and $r_1 = r_R + x_1$ with $x_1 = \mathcal{O}(\sigma_R)$. We also assume that Ψ has a finite limit in the vicinity of the bifurcation point. With these assumptions, the stationary solutions of the polar system (12) obey the following equations at leading order:

$$\sigma_R + l_0 r_0^2 + 2l_1 r_R x_1 + l_3 r_R r_2 \cos \Psi = 0 \quad (20a)$$

$$2B_r r_R x_1 + C_r r_0^2 = 0 \quad (20b)$$

$$A_r r_R r_2 = -r_0^2 (D_r \cos \Psi - D_i \sin \Psi) \quad (20c)$$

$$(A_i - 2l_2) r_R r_2 = -r_0^2 (D_i \cos \Psi + D_r \sin \Psi). \quad (20d)$$

To solve these equations, we add the squares of equations eqs. (20c) and (20d) to obtain

$$\left[A_r^2 + (A_i - 2l_2)^2 r_R^2 r_2^2 \right] = |D|^2 r_0^4. \quad (21)$$

This equation allows us to express r_2 in terms of r_0 . Eliminating $\sin \Psi$ from eqs. (20c) and (20d) leads to

$$\cos \Psi = -\frac{D_r A_r + D_i (A_i - 2l_2)}{|D| \sqrt{A_r^2 + (A_i - 2l_2)^2}}. \quad (22)$$

Finally, x_1 is easily expressed as a function of r_0 from eq. (20b). Introducing these expressions into eq. (20a) yields a classical branching equation which can be cast in the form

$$\begin{aligned} \sigma_R + H^r r_0^2 &= 0, \\ \text{with } H^r &= l_0 - l_1 \frac{C_r}{B_r} - l_3 \frac{D_r A_r + D_i (A_i - 2l_2)}{A_r^2 + (A_i - 2l_2)^2}. \end{aligned} \quad (23)$$

It follows that in the vicinity of the bifurcation point, the Precessing Waves are given by the branching equation $r_0 \approx (-\sigma_R/H^r)^{1/2}$, and the bifurcation is then supercritical if $H_r < 0$.

The precession rate corresponding to this solution is given by eq. (10a) and reads

$$\dot{\phi}_0 = -l_2 r_R^2 + H^i r_0^2 \quad (24)$$

with $H^i = l_2 \frac{C_r}{B_r} + l_3 \frac{D_i A_r - D_r (A_i - 2l_2)}{A_i^2 + (A_i - 2l_2)^2}$.

Note that the branching parameter H^r and the term H^i correspond, respectively, to the real and imaginary parts of the complex Hopf coefficient H computed in [35], at the end of a much lengthier analysis.

E. Robust heteroclinic cycles

As already mentioned one may expect the presence of structurally stable or robust heteroclinic cycles in our system in view of its similarity to the mode interaction problem studied in [29, 30] when written in polar coordinates. More generally, a heteroclinic cycle is a set of trajectories $\{(\bar{r}_0^{(j)}(t), \bar{r}_1^{(j)}(t), \bar{r}_2^{(j)}(t), \bar{\Psi}^{(j)}(t))\}_{j=1,2,\dots,m}$ that connect equilibrium solutions $\{(r_0^{(j)}, r_1^{(j)}, r_2^{(j)}, \Psi^{(j)})\}_{j=1,2,\dots,m}$ with the property that $(\bar{r}_0^{(j)}(t), \bar{r}_1^{(j)}(t), \bar{r}_2^{(j)}(t), \bar{\Psi}^{(j)}(t))$ is backward asymptotic to $(r_0^{(j)}, r_1^{(j)}, r_2^{(j)}, \Psi^{(j)})$ and forward asymptotic to $(r_0^{(j+1)}, r_1^{(j+1)}, r_2^{(j+1)}, \Psi^{(j+1)})$ with the convention $(r_0^{(m+1)}, r_1^{(m+1)}, r_2^{(m+1)}, \Psi^{(m+1)}) = (r_0^{(1)}, r_1^{(1)}, r_2^{(1)}, \Psi^{(1)})$. Such cycles are *robust* if each connection is robust, i.e. cannot be destroyed by changing parameters. Robust heteroclinic cycles typically do not exist in general nonsymmetric vector fields. However, they may exist in symmetric systems such as ours. First examples of robust heteroclinic cycles connecting saddle points were found in [36, 37]. Afterwards, Melbourne, Krupa and collaborators [38, 39] established a general approach to the existence and stability of structurally stable heteroclinic cycles in Γ -equivariant systems. The existence of a robust heteroclinic cycle requires the following conditions:

- Each saddle solution sits on a flow-invariant line l_j , say, and each such line is the fixed-point subspace for the isotropy subgroup of the saddle solution, i.e. $l_j = \text{Fix}(\Sigma_{j-1}) \cap \text{Fix}(\Sigma_j)$.
- The isotropy subgroups of the invariant lines are maximal isotropy subgroups.
- The invariant plane containing the invariant line is the fixed point subspace of a maximal isotropy subgroup.

The proof of this result is based on the existence of cycles in the isotropy lattice, such as fig. 8 for the present

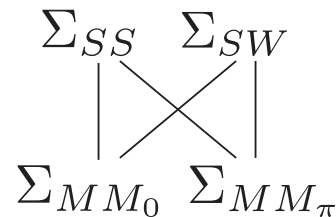


FIG. 8: Structure within in the isotropy lattice suggesting that there may exist of a robust heteroclinic cycle.

case, and suggests that the present system may possess robust heteroclinic cycles.

Indeed, the isotropy lattice in fig. 8 suggests the existence of a robust heteroclinic cycle between the steady-state mode SS and the standing wave mode SW. Such a heteroclinic cycle possesses two connections that lie within the $\text{Fix}(\mathbb{Z}(\kappa))$ and $\text{Fix}(\mathbb{Z}(\kappa \cdot (\pi, \pi)))$ subspaces. In our notation the heteroclinic connections lie in the invariant subspaces of the two MM solutions. Melbourne et al. [40] found that in the supercritical case such a cycle exists whenever the steady-state mode SS is a saddle (resp. sink) in the fixed-point subspace $\text{Fix}(\mathbb{Z}(\kappa))$ of the isotropy subgroup of the MM_0 mode and a sink (resp. saddle) in the fixed-point subspace $\text{Fix}(\mathbb{Z}(\kappa \cdot (\pi, \pi)))$ of the isotropy subgroup of the MM_π mode. Similarly, the SW mode must be a sink (resp. saddle) in $\text{Fix}(\mathbb{Z}(\kappa))$ and a saddle (resp. sink) in $\text{Fix}(\mathbb{Z}(\kappa \cdot (\pi, \pi)))$. These conditions are satisfied if the first three existence conditions in table VII are satisfied. In addition, no other fixed point solutions can be present in either of the fixed point subspaces and solutions starting in the neighborhood of the trivial mode are required to remain bounded, a condition that is satisfied if the last two existence conditions in table VII hold.

The necessary and sufficient conditions for the asymptotic stability of a particular type of robust heteroclinic cycle referred to as *Type A* are derived in [39]. This type of heteroclinic cycle is constructed in such a way that each trajectory connecting two fixed-point solutions lies within the fixed point subspace of an isotropy group isomorphic to \mathbb{Z}_2 . Because of this the necessary and sufficient condition for asymptotic stability is

$$\prod_{j=1}^m \min(-\nu_j^c, \nu_j^e - \nu_j^t) > \prod_{j=1}^m \nu_j^e, \quad (25)$$

where ν_j^c , ν_j^e , ν_j^t , ν_j^r denote the contracting, expanding, transversal and radial eigenvalues of the solution j . The *contracting* eigenvalue of the solution j corresponds to the minimum eigenvalue (maximum $-\nu_j$) in the fixed point subspace of solution j ; the *expanding* eigenvalue corresponds to the eigenvalue with the largest real part among the eigenvalues restricted to the fixed point subspace of the backward asymptotic heteroclinic connection; the *radial* eigenvalue is the eigenvalue with the

TABLE VII: Defining conditions for structurally and asymptotically stable heteroclinic cycles connecting SS and SW. Here $\nu_{SS}^{\pm} \equiv \lambda_h + (C_r \pm D_r)r_P^2$ and $\nu_{SW}^{\pm} \equiv \lambda_s + (2l_1 \pm l_3)r_S^2$.

Name of solution (condition for supercriticality)	Existence	Asymptotic stability (Asymp. stable if ii) and either i-a) or i-b))
Hets _{SS-SW} $l_0 > 0$ $A_r + 2B_r > 0$	$\nu_{SS}^+ \nu_{SS}^- < 0$ $\nu_{SW}^+ \nu_{SW}^- < 0$ $\nu_{SS}^+ \nu_{SW}^- > 0$ $\frac{\lambda_s}{\lambda_h} \frac{(C_r + D_r)}{l_0} + \frac{\lambda_h}{\lambda_s} \frac{(2l_1 + l_0)}{(2B_r + A_r)} > -2$ $\frac{\lambda_s}{\lambda_h} \frac{(C_r - D_r)}{l_0} + \frac{\lambda_h}{\lambda_s} \frac{(2l_1 - l_0)}{(2B_r + A_r)} > -2$	i-a) $\nu_{SS}^+ \nu_{SW}^- < -\nu_{SS}^- \min(-\nu_{SW}^+, \nu_{SW}^- + 2A_r r_s^2)$ i-b) $\nu_{SS}^- \nu_{SW}^+ < -\nu_{SS}^+ \min(-\nu_{SW}^+, \nu_{SW}^+ + 2A_r r_s^2)$ ii) $A_r > 0$

smallest real part (largest $-\nu_j^r$) within the intersection between the two previous fixed point subspaces and the *transverse* eigenvalue correspond to the eigenvalue with the largest real part among the eigenvalues restricted to the orthogonal complement. The proof of the identity eq. (25) is based on the use of a set of Poincaré return maps to obtain global estimates of stability from local ones. For more details the reader is referred to [38, 39]. The application of eq. (25) shows that in our case the heteroclinic cycle Het_{SS-SW} is asymptotically stable provided condition ii) and either condition i-a) or i-b) in table VII hold. This possibility was not considered in [28].

V. THE DEGENERATE CASE $D_i = 0$, $A_i - 2l_2 = 0$

In this section we consider a codimension-two degenerate case where the parameters D_i and $A_i - 2l_2$ both vanish. This situation arises when all the nonlinear coefficients in eq. (8) are real. This case is of basic theoretical interest since it actually corresponds to the case where an additional \mathbb{Z}_2 symmetry is present in the primitive amplitude equations. In this case eq. (8) also reduces to a special case of the equations studied in generality by Silber & Knobloch [41] provided we also take $l_0 = A_r + 2B_r$, $\lambda_s = \lambda_h$.

In this case the equations in polar coordinates take the following form:

$$\dot{r}_0 = [\lambda_s + l_0 r_0^2 + l_1(r_1^2 + r_2^2) + l_3 r_1 r_2 \cos \Psi] r_0 \quad (26a)$$

$$\dot{r}_2 + \dot{r}_1 = \left[\lambda_h + B_r(r_1^2 + r_2^2) + A_r r_1 r_2 + r_0^2 (C_r + D_r \cos \Psi) \right] (r_1 + r_2) \quad (26b)$$

$$\dot{r}_2 - \dot{r}_1 = \left[\lambda_h + B_r(r_1^2 + r_2^2) - A_r r_1 r_2 + r_0^2 (C_r - D_r \cos \Psi) \right] (r_2 - r_1) \quad (26c)$$

$$\dot{\Psi} = - \left[2l_3 r_1 r_2 + D_r r_0^2 \frac{r_1^2 + r_2^2}{r_1 r_2} \right] \sin \Psi. \quad (26d)$$

In this case the $PQRS$ coordinates are particularly useful. The equations in these coordinates take the following form:

$$\dot{R} = 2[\lambda_s + l_0 R + l_1 S + l_3 PQ]R, \quad (27a)$$

$$\dot{S} = 2[\lambda_h + B_r S + C_r R]S + 4[A_r P + D_r RQ]P, \quad (27b)$$

$$\dot{P} = 2[\lambda_h + B_r S + C_r R]P + [A_r P + D_r RQ]S, \quad (27c)$$

$$\dot{Q} = [2l_3 P^2 + D_r RS] \frac{1-Q^2}{P}. \quad (27d)$$

These equations possess an additional reflection symmetry

$$\kappa_r : (r_0, r_1, r_2, \Psi) \rightarrow (r_0, r_2, r_1, \Psi) \quad (28)$$

responsible for a reflection symmetry in Ψ :

$$(\kappa_r \cdot \kappa) \cdot (r_0, r_1, r_2, \Psi) = (r_0, r_1, r_2, -\Psi).$$

This symmetry has several consequences. First, the isotropy group of the polar normal form is now $\Gamma_\rho^{(d)} \simeq \mathbb{Z}_2^2 \times D_4 \simeq \mathbb{Z}_2^4 \times \mathbb{Z}_2$. Its isotropy lattice, depicted in fig. 9, displays new isotropy groups whose fixed point subspaces are of dimension three, viz. Σ_{PrW_A} , Σ_{PrW_B} , $\Sigma_{\widetilde{IMM}}$. The fixed point subspaces $\text{Fix}(\Sigma_{PrW_A})$ and $\text{Fix}(\Sigma_{PrW_B})$ are characterized by $r_1 = r_2$ and $\sin \Psi = 0$, respectively, and are of dimension four in the space of complex amplitudes, i.e. they display two-frequency behavior, see table VIII. In contrast, the fixed point subspace $\text{Fix}(\Sigma_{\widetilde{IMM}})$ is characterized by $r_0 = 0$. Strictly speaking this is not an invariant subspace of the cubic truncation (since $A_r \neq 0$) but it does become so when the truncation is extended to fifth order, cf. appendix B. This subspace is also of dimension four, and is spanned by solutions of the form $(0, a_1, a_2)$, i.e., by $r_1 \neq r_2$ and the corresponding phases (ϕ_1, ϕ_2) .

In addition, it turns out that the isotropy subgroups associated to the Interacting Mixed Modes Σ_{IMM_0} and

TABLE VIII: Nomenclature and isotropy group of steady-state solutions of the system (26).

Name	Representative	Isotropy group (polar)	Frequencies
Primary bifurcations:			
SS	$(r_a, 0, 0, nd)$	$\mathbb{Z}_2(\kappa_r) \times \mathbb{Z}_2(\kappa) \times \mathbb{Z}_2(\Phi_\pi)$	0
RW ₀	$(0, r_a, 0, nd)$	$D_4(R_{\pi/2}\Phi_{\pi/2}, \kappa \cdot \kappa_r)$	1
RW _π	$(0, r_a, 0, nd)$	$D_4(R_{\pi/2}\Phi_{\pi/2}, \kappa \cdot \kappa_r \cdot \Phi_\pi)$	1
SW ₀	$(0, r_a, r_a, nd)$	$\mathbb{Z}_2(\kappa_r) \times \mathbb{Z}_2(\kappa) \times \mathbb{Z}_2(R_\pi\Phi_\pi)$	1
SW _π	$(0, r_a, r_a, nd)$	$\mathbb{Z}_2(\kappa_r\Phi_\pi) \times \mathbb{Z}_2(\kappa) \times \mathbb{Z}_2(R_\pi\Phi_\pi)$	1
Secondary bifurcations:			
MM ₀	$(r_a, r_b, r_b, 0)$	$\mathbb{Z}_2(\kappa_r) \times \mathbb{Z}_2(\kappa)$	1
MM _π	(r_a, r_b, r_b, π)	$\mathbb{Z}_2(\kappa_r\Phi_\pi) \times \mathbb{Z}_2(\kappa \cdot R_\pi\Phi_\pi)$	1
IMM ₀	$(0, r_a, r_b, 0)$	$\mathbb{Z}_2(\kappa_r \cdot \kappa) \times \mathbb{Z}_2(R_\pi\Phi_\pi)$	1
IMM _π	$(0, r_a, r_b, \pi)$	$\mathbb{Z}_2(\kappa_r \cdot \kappa \cdot \Phi_\pi) \times \mathbb{Z}_2(R_\pi\Phi_\pi)$	1
Tertiary bifurcations:			
PrW _A	(r_a, r_b, r_b, Ψ)	$\mathbb{Z}_2(\kappa_r)$	2
PrW _B	$(r_a, r_b, r_c, 0 \text{ or } \pi)$	$\mathbb{Z}_2(\kappa_r \cdot \kappa)$	2
$\widetilde{\text{IMM}}$	$(0, r_a, r_b, \Psi(t)), \Psi(t) = \phi_1(t) - \phi_2(t)$	$\mathbb{Z}_2(R_\pi\Phi_\pi)$	2

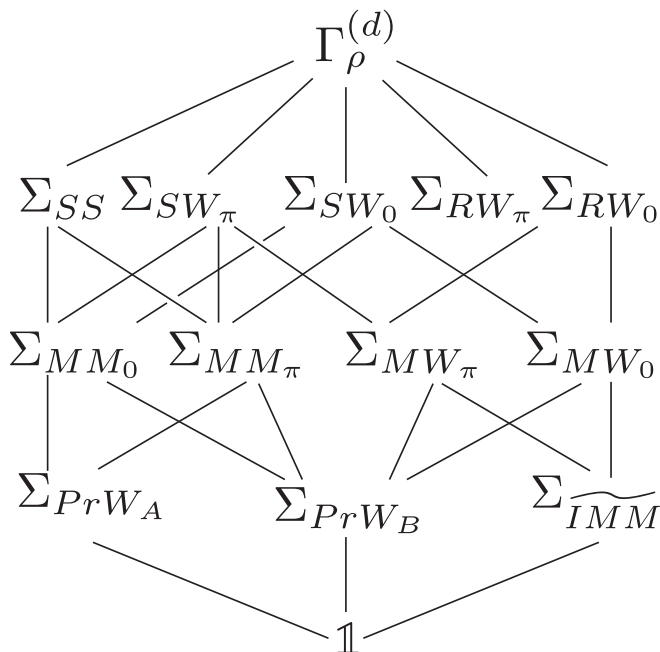


FIG. 9: Lattice of isotropy groups of the degenerate normal form.

Σ_{IMM_π} are not conjugates of each other, i.e. these solutions are distinct as in the case of the Mixed modes MM_0 and MM_π . The reason behind the distinction between the subgroups Σ_{SW_0} , Σ_{SW_π} (resp. Σ_{RW_0} , Σ_{RW_π}) is algebraic: these isotropy groups are not conjugate of each other, although their fixed point representative are of the same type. This is because the phase Ψ is undefined for either rotating waves and standing waves - a consequence of the fact that for these states $a_0 = 0$. However, we find it convenient to distinguish between SW_0 and SW_π (resp. RW_0 and RW_π) based on the limiting

behavior of the Mixed Modes (resp. Mixed Waves) as $r_0 \rightarrow 0$, as indicated in the isotropy lattice fig. 9.

In this degenerate case the conditions for higher order bifurcations, as well as the complete definition of all possible branches of precessing waves, can be obtained explicitly. The corresponding results are tabulated in table IX. It will be found that there are at most three branches of precessing waves. The first two are denoted PrW_A and PrW_B , while the third kind is generic with no additional symmetry and hence trivial isotropy, and is denoted PrW_G .

A. Bifurcations from Mixed Modes and Rotating Waves

Bifurcations from Mixed Modes are governed by the eigenvalues of the matrices M_b^\pm defined in section IVC (apart from the possible bifurcation to a modulated mixed mode if $l_0(2B_r + A_r) < 0$). In the present case, the matrix is diagonal with real eigenvalues. Therefore symmetry-breaking bifurcations from MM can only lead to PrW (Precessing Waves), excluding the possibility of PuW (Pulsating Waves). The number of such bifurcations follows from the eigenvalues of M_b^\pm . The first of these is $2(-A_r r_b^2 \mp D_r r_a^2)$, and this quantity changes sign along the MM_0 (MM_π) branch. The second eigenvalue of M_b^\pm is $\mp 2(l_3 r_b^2 + D_r r_a^2)$. Thus if $l_3 D_r > 0$, this eigenvalue remains of one sign for both mixed modes. On the other hand, if $l_3 D_r < 0$, it changes sign somewhere along both branches. So, the number of branching points to Precessing Waves along the MM branches is either one (if $l_3 D_r > 0$) or three (if $l_3 D_r < 0$). These results are restated in the top part of table IX, where the conditions for a zero eigenvalue are stated in terms of λ_s and λ_h instead of r_a and r_b using table VI.

We also report in the table the branching point from the RW branch, investigated in section IVD. This point

exists generically and the corresponding branch has $\Psi = 0$ (resp. $\Psi = \pi$) if $A_r D_r < 0$ (resp. $A_r D_r > 0$). We end up with a total number of either 2 or 4 bifurcation points to Precessing Waves.

The $\widetilde{\text{IMM}}$ solution is degenerate as was the case already for the generic third order normal form. The addition of higher order terms, as done in appendix B, leads to the existence of the solution $\widetilde{\text{IMM}}$, which in this degenerate case is a heteroclinic connection between the Interacting Modes IMM_0 and IMM_π . This last statement follows from the integration of eq. (26d) with $r_0 = 0$, which leads to $\Psi \rightarrow 0$ as $t \rightarrow \infty$ and $\Psi \rightarrow \pi$ as $t \rightarrow -\infty$ if $l_3 r_a r_b > 0$ and to $\Psi \rightarrow \pi$ as $t \rightarrow \infty$ and $\Psi \rightarrow 0$ as $t \rightarrow -\infty$ if $l_3 r_a r_b < 0$.

B. The subspace $r_1 = r_2$

The dynamics within the invariant subspace $\text{Fix}(\Sigma_{PrW_A})$, defined in polar coordinates as

$$\text{Fix}(\Sigma_{PrW_A}) = \{(r_0, r_1, r_2, \Psi) : r_1 = r_2\}, \quad (29)$$

take the form

$$\dot{r}_0 = [\lambda_s + l_0 r_0^2 + 2l_1 r_1^2 + l_3 r_1^2 \cos \Psi] r_0 \quad (30a)$$

$$\dot{r}_1 = [\lambda_h + (A_r + 2B_r)r_1^2 + (C_r + D_r \cos \Psi)r_0^2] r_1 \quad (30b)$$

$$\dot{\Psi} = -2[l_3 r_1^2 + D_r r_0^2] \sin \Psi. \quad (30c)$$

The PRQ coordinates can also be used in this subspace (which corresponds to $S = 2P$):

$$\dot{R} = 2[\lambda_s + l_0 R + (2l_1 + l_3 Q)P]R, \quad (31a)$$

$$\dot{P} = 2[\lambda_h + (2B_r + A_r)P + (C_r + D_r Q)R]P, \quad (31b)$$

$$\dot{Q} = 2[l_3 P + D_r R](1 - Q^2). \quad (31c)$$

The resulting systems are formally identical to those governing the interaction of two steady-state modes with opposite parity studied by Hirschberg & Knobloch, eq. (10) of [29], given by the correspondence

$$\begin{aligned} r_0 &\equiv r, r_1 \equiv \rho, \Psi \equiv 2\Psi, \lambda_s \equiv \lambda, \lambda_h \equiv \mu, l_0 \equiv a, \\ 2l_1 &\equiv b, l_3 \equiv e, 2B_r + A_r \equiv d, C_r \equiv c, D_r \equiv f. \end{aligned} \quad (32)$$

The results of [29, 30] can therefore be applied to the system eq. (30). We use these results to conclude that when $D_r l_3 < 0$ the two branches of mixed modes are connected by a tertiary branch of the form $r_0 \neq 0$, $r_1 =$

$r_2 \neq 0$, $\sin \Psi \neq 0$. In the nomenclature of the present manuscript this branch corresponds to a Precessing Wave of type A (see table III). The defining equations for this solution are

$$R = r_0^2 = \frac{\sigma_{0A} - \sigma_{\pi A}}{2D_r \Sigma_A}, \quad (33a)$$

$$P = r_1^2 = r_2^2 = -\frac{\sigma_{0A} - \sigma_{\pi A}}{2l_3 \Sigma_A}, \quad (33b)$$

$$Q = \cos \Psi = \frac{\sigma_{\pi A} + \sigma_{0A}}{\sigma_{\pi A} - \sigma_{0A}}, \quad (33c)$$

where

$$\begin{aligned} \Sigma_A &\equiv (2B_r + A_r + 2l_1)D_r - l_3(C_r + l_0) \neq 0, \\ \Sigma_A^a &\equiv D_r(A_r + 2B_r) - l_0 l_3, \\ H_A^{0,\pi} &\equiv (\Delta_+ + \Delta_-) - 4D_r l_3(1 - \Sigma_A/\Sigma_A^a) \\ \frac{1}{2}(\sigma_{0A} + \sigma_{\pi A}) &\equiv ((2B_r + A_r)D_r - C_r l_3)\lambda_s \\ &\quad + (2D_r l_1 - l_0 l_3)\lambda_h, \\ \frac{1}{2}(\sigma_{0A} - \sigma_{\pi A}) &\equiv D_r l_3(\lambda_s + \lambda_h), \end{aligned} \quad (33d)$$

as in eq. (17) of [29]. The range of existence of this connecting branch in the (λ_s, λ_h) plane is obtained by imposing the condition $\cos \Psi \in [-1, 1]$ on eq. (33c); the conditions obtained from $\cos \Psi = \pm 1$ are identical to the conditions obtained from the vanishing of the second eigenvalue of M_b^\pm and displayed in table IX, confirming that the PrW_A branch connects the two Mixed Mode branches.

The stability of all the solutions within the invariant subspace $\text{Fix}(\Sigma_{PrW_A})$ is determined as in Ref. [29]. The linearized dynamics within this subspace are governed by a 3×3 matrix with determinant D_A , trace T_A and second invariant I_A given below:

$$D_A = -\frac{4}{D_r \Sigma_A^2 l_3} \sigma_{\pi A} \sigma_{0A} (\sigma_{\pi A} - \sigma_{0A}), \quad (34a)$$

$$T_A = \frac{\Sigma_A^a (\sigma_{\pi A} - \sigma_{0A})}{D_r l_3 \Sigma_A}, \quad (34b)$$

$$\begin{aligned} I_A &= -\frac{\Delta_+ \sigma_{\pi A}^2 + \Delta_- \sigma_{0A}^2}{D_r l_3 \Sigma_A^2} \\ &\quad + \frac{(-4D_r l_3 + \Delta_+ + \Delta_-)}{D_r l_3 \Sigma_A^2} \sigma_{\pi A} \sigma_{0A}. \end{aligned} \quad (34c)$$

Since $-1 < Q < 1$ along the PrW_A branch the quantity $\sigma_{\pi A} - \sigma_{0A} \equiv -2D_r l_3(\lambda_s + \lambda_h)$ cannot vanish along it. As a consequence, D_A only vanishes at the bifurcations to Mixed Modes (defined by $Q = \pm 1$), and no steady state bifurcations occurs within the invariant subspace Σ_{PrW_A} along the branch. The necessary and sufficient conditions for the stability of the branch within its fixed point subspace are $D_A < 0$, $T_A < 0$, $I_A > 0$ and $H_A \equiv$

TABLE IX: Higher order bifurcations in the degenerate case $D_i = 0$, $A_i - 2l_2 = 0$. Note: ⁽¹⁾Results for bifurcations to modulated mixed modes hold in the generic case. ⁽²⁾Results relevant to the PrW of type A also hold in the less degenerate case to $D_i = 0$, $A_i - 2l_2 \neq 0$. ⁽³⁾The bifurcation from rotating waves leads to a PrW_B in the present case, and to a general PrW in the generic case. ⁽⁴⁾The conditions listed for the existence of Hopf bifurcations ensure an odd number of Hopf lines (1 or 3). The condition for an odd number of Hopf lines in the case of a termination at the MM_π fixed point is $\Delta_+ \Lambda_B^+ > 0$.

Branch	New solution	Bifurcation point	Condition for existence
MM ₀	PrW _A ⁽²⁾	$\sigma_{0A} \equiv [l_3(C_r + D_r) - D_r(2B_r + A_r)]\lambda_s + [(2l_1 + l_3)D_r - l_0l_3]\lambda_h = 0$	$l_3D_r < 0$
	PrW _B	$\sigma_{0B} \equiv -[A_rC_r - 2B_rD_r]\lambda_s + [A_rl_0 - D_r(2l_1 + l_3)]\lambda_h = 0$	$A_rD_r < 0$
	$\widetilde{MM}_0^{(1)}$	$2(B_r + A_r)(C_r + D_r - l_0)\lambda_s + l_0(2l_1 + l_3 - 2B_r - A_r)\lambda_h = 0$	$(2B_r + A_r)l_0 < 0$
MM _π	PrW _A ⁽²⁾	$\sigma_{\pi A} \equiv [l_3(C_r - D_r) - D_r(2B_r + A_r)]\lambda_s + [(2l_1 - l_3)D_r - l_0l_3]\lambda_h$	$l_3D_r < 0$
	PrW _B	$\sigma_{\pi B} \equiv -[A_rC_r + 2B_rD_r]\lambda_s + [A_rl_0 + D_r(2l_1 - l_3)]\lambda_h = 0$	$A_rD_r > 0$
	$\widetilde{MM}_\pi^{(1)}$	$(2B_r + A_r)(C_r + D_r - l_0)\lambda_s + l_0(2l_1 + l_3 - 2B_r - A_r)\lambda_h = 0$	$(2B_r + A_r)l_0 < 0$
RW	PrW _B ^(1,3)	$\sigma_R \equiv \lambda_s - l_1\lambda_h/B_r = 0$	Generic
PrW _A	PrW _G	$\equiv (l_3(\sigma_{0A} + \sigma_{\pi A}) - A_r(\sigma_{\pi A} - \sigma_{0A})) / (\Sigma_A l_3) = 0$	$l_3D_r < 0$, $A_r^2 < l_3^2$
	3FW(A)	$H_A = 0$	eq. (38).
PrW _B	PrW _G	$\sigma_{BG} \equiv [2l_3B_rD_r - A_r^2C_r]\lambda_s + [A_r^2l_0 - 2l_1l_3D_r - l_3A_rD_r]\lambda_h = 0$	If $A_rD_r < 0$, $A_r^2 - A_rl_3 < 0$, If $A_rD_r > 0$, $A_r^2 + A_rl_3 < 0$
	3FW(B) ⁽⁴⁾	$H_B = 0$	eq. (49)
PrW _G	3FW	$\Omega^4 - II_G\Omega^2 + D_G = 0$, $T_G\Omega^2 - I_G = 0$	–

$I_A - D_A/T_A > 0$. Inspection of eq. (34a) shows that the determinant is negative (resp. positive) whenever $\sigma_{\pi A} - \sigma_{0A} > 0$, which occurs when $l_3 > 0$, $D_r < 0$ (resp. $l_3 < 0$, $D_r > 0$) corresponding to the bifurcation of PrW_A from the MM_π mode (resp. MM₀). Provided that the determinant is negative, then the trace is negative if and only if $\frac{\Sigma_A}{\Sigma_A^a} > 0$. If these two conditions are satisfied, the necessary and sufficient condition of the positivity of the second invariant I_A all along the branch is that $\Delta_+ \geq 0$ and $\Delta_- \geq 0$ (defined in table VI), since $\sigma_{0A}\sigma_{\pi A} \leq 0$ all along the branch. The fourth condition is as follows,

$$0 < H_A \equiv \frac{1}{D_rl_3\Sigma_A^2} \left[-\Delta_+\sigma_{\pi A}^2 - \Delta_-\sigma_{0A}^2 + \sigma_{\pi A}\sigma_{0A}(\Delta_+ + \Delta_- - 4D_rl_3(1 - \Sigma_A/\Sigma_A^a)) \right]. \quad (35)$$

Thus, if the previous three conditions are satisfied, the necessary and sufficient condition for $H_A > 0$ all along the branch is

$$\left| \left(1 - \frac{\Sigma_A}{\Sigma_A^a}\right) - \frac{\Delta_+ + \Delta_-}{4D_rl_3} \right| \geq -\frac{\sqrt{\Delta_+\Delta_-}}{2D_rl_3}, \quad (36)$$

which is immediately satisfied if $0 < \Sigma_A/\Sigma_A^a < 1$. Summarizing, the necessary and sufficient condition for the stability of the branch within the invariant subspace Σ_{PrW_A} all along its existence is

$$\Delta_+ > 0, \quad \Delta_- > 0, \quad 0 < \frac{\Sigma_A^a}{\Sigma_A} < 1, \quad l_3 > 0. \quad (37)$$

The condition $\frac{\Sigma_A^a}{\Sigma_A} < 1$ can be replaced by eq. (36).

The quantity $H_A(\sigma_{0,A}, \sigma_{\pi,A})$ can be interpreted as the distance to a Hopf bifurcation of the PrW_A branch, which

is located at $H_A(\sigma_{0,A}, \sigma_{\pi,A}) = 0$. In particular, because the trace T_A divides D_A , we have at most two Hopf bifurcations. There is a supercritical Hopf from the PrW_A branch leading to a stable 3FW if the following conditions are satisfied:

$$\Delta_+ > 0, \quad \Delta_- > 0, \quad l_3D_r < 0, \quad \frac{\sqrt{\Delta_+\Delta_-}}{2D_rl_3} \leq \left(1 - \frac{\Sigma_A}{\Sigma_A^a}\right) - \frac{\Delta_+ + \Delta_-}{4D_rl_3} \leq -\frac{\sqrt{\Delta_+\Delta_-}}{2D_rl_3}. \quad (38)$$

The case of a single Hopf bifurcation arises when the following two degeneracy conditions hold, $\Delta_- \Delta_+ = 0$ and $\Sigma_A = \Sigma_A^a$. Therefore, whenever eq. (38) is satisfied and $\Delta_+\Delta_- \neq 0$ we have two Hopf bifurcations in the $(\sigma_{0,A}, \sigma_{\pi,A})$ plane, located at

$$\sigma_{\pi A} = K_{A,H}^\pm \sigma_{0A}, \quad K^\pm \equiv \frac{H_A^{0,\pi}}{2\Delta_+} \pm \frac{1}{\Delta_+} \left((H_A^{0,\pi})^2 - 4\Delta_+\Delta_- \right)^{\frac{1}{2}}, \quad (39)$$

with $H_A^{0,\pi}$ defined in eq. (33d).

In the present situation we also need to determine one additional eigenvalue that describes the stability in the $r_2 - r_1$ direction. This eigenvalue, hereafter σ_{AG} , is given by

$$\sigma_{AG} \equiv \frac{2P(l_3Q - A_r)}{l_3(\sigma_{0A} + \sigma_{\pi A}) - A_r(\sigma_{\pi A} - \sigma_{0A})} = \frac{2P(l_3Q - A_r)}{\Sigma_A l_3}. \quad (40)$$

A necessary and sufficient condition ensuring the existence of a steady state bifurcation associated with the vanishing of σ_{AG} is that the signs of σ_{AG} at either end of the branch are opposite. This leads to the condition reported in the last column of table IX.

C. The subspace $\sin \Psi = 0$

The second fixed point subspace corresponds to $\sin \Psi = 0$. At first glance, this subspace corresponds to two distinct cases, $\Psi = 0$ and $\Psi = \pi$. However, because of the symmetry of the polar equations, a jump in Ψ by π is equivalent to a change of sign of either r_1 or r_2 . As a consequence, to investigate this subspace, we may set $\Psi = 0$ but allow arbitrary signs r_1 and r_2 . Both Mixed Mode solutions belong to this subspace (MM $_{\pi}$ corresponds to $\Psi = 0$, $r_2 = -r_1$). The pure modes can also be considered as part of this subspace, even though Ψ is not defined for these branches. Within this subspace, the equations take the form:

$$\dot{r}_0 = [\lambda_s + l_0 r_0^2 + l_1 (r_1^2 + r_2^2) + l_3 r_1 r_2] r_0 \quad (41a)$$

$$\dot{r}_1 = \left[\lambda_h + B_r r_1^2 + (A_r + B_r) r_2^2 + C_r r_0^2 \right] r_1 + D_r r_0^2 r_2 \quad (41b)$$

$$\dot{r}_2 = \left[\lambda_h + B_r r_2^2 + (A_r + B_r) r_1^2 + C_r r_0^2 \right] r_2 + D_r r_0^2 r_1 \quad (41c)$$

$$\dot{R} = 2[\lambda_s + l_0 R + l_1 S + l_3 P] R \quad (42a)$$

$$\dot{S} = \frac{2[\lambda_h + B_r S + C_r R] S}{+4[A_r P + D_r R] P} \quad (42b)$$

$$\dot{P} = \frac{2[\lambda_h + B_r S + C_r R] P}{+[A_r P + D_r R] S}. \quad (42c)$$

To detect the existence of Precessing Waves in the present subspace, we look for steady solutions of the above equations. From eqs. (42b) and (42c) we obtain the conditions

$$\lambda_h + B_r S + C_r R = 0, \quad A_r P + D_r R = 0. \quad (43)$$

The Precessing Waves in question belong to this subspace, leading to

$$R = r_0^2 = -\frac{A_r}{D_r} \frac{\sigma_{0B} - \sigma_{\pi B}}{4\Sigma_B}, \quad (44a)$$

$$P = r_1 r_2 = \frac{\sigma_{0B} - \sigma_{\pi B}}{4\Sigma_B}, \quad (44b)$$

$$S = r_1^2 + r_2^2 = -\frac{\sigma_{0B} + \sigma_{\pi B}}{2\Sigma_B}, \quad (44c)$$

where $\Sigma_B \equiv B_r(A_r l_0 - D_r l_3) - l_1(A_r C_r) \neq 0$,

$$\sigma_R \equiv \lambda_s - \frac{l_1}{B_r} \lambda_h,$$

$$\sigma_{0B} + \sigma_{\pi B} \equiv 2 \left[(A_r C_r) \lambda_s + (l_3 D_r - A_r l_0) \lambda_h \right],$$

$$\sigma_{0B} - \sigma_{\pi B} \equiv 4B_r D_r \sigma_R. \quad (44d)$$

These expressions define a single branch of Precessing Waves referred to as the PrW $_B$ branch. One may check that the conditions obtained on imposing $P = 0$ and $S = 2|P|$ yield, respectively, the conditions listed in table IX for the bifurcation from Rotating Waves and the relevant Mixed Mode, confirming that the PrW $_B$ branch connects these two branches. Note that the sign of P is given by $A_r D_r$. So, had we adopted the convention that both r_1 and r_2 are positive and Ψ is either 0 or π we would have arrived at the conclusion that PrW $_B$ is associated with $\Psi = 0$ if $A_r D_r < 0$ and $\Psi = \pi$ if $A_r D_r > 0$. Note that the precession frequency given by eq. (10a) vanishes when $l_2 = 0$. In this case, the resulting mode will actually be singly periodic in the primitive variables, instead of a two-frequency wave. However, this property is not visible when working with the polar variables.

The stability of the PrW $_B$ branch within its invariant subspace Fix(Σ_{PrW_B}) can be determined by studying its characteristic polynomial in a similar manner as done for PrW $_A$ in section V B. The invariants of the 3×3 stability matrix are the determinant D_B , trace T_B and I_B given below:

$$\begin{aligned} D_B &= -4\Sigma_B R(2P - S)(2P + S) \\ &= \frac{A_r}{D_r \Sigma_B^2} \sigma_{\pi B} \sigma_{0B} (\sigma_{\pi B} - \sigma_{0B}) \end{aligned} \quad (45a)$$

$$\begin{aligned} T_B &= 2l_0 R + (A_r + 2B_r) S \\ &= \frac{A_r l_0 (\sigma_{\pi B} - \sigma_{0B}) - D_r (A_r + 2B_r) (\sigma_{0B} + \sigma_{\pi B})}{2D_r \Sigma_B} \end{aligned} \quad (45b)$$

$$\begin{aligned} I_B &= R(\Delta_+ (2P + S) + \Delta_- (-2P + S)) \\ &\quad + 2A_r B_r (S^2 - 4P^2) \\ &= \frac{A_r}{4D_r \Sigma_B^2} (\Delta_- \sigma_{\pi B}^2 - \Delta_+ \sigma_{0B}^2) \\ &\quad + \frac{A_r}{4D_r \Sigma_B^2} (8B_r D_r + \Delta_+ - \Delta_-) \sigma_{0B} \sigma_{\pi B}. \end{aligned} \quad (45c)$$

The vanishing of σ_R coincides with the origin of the PrW $_B$ branch along the RW branch. Note that the vanishing of σ_R implies $\sigma_{0B} = \sigma_{\pi B}$. Similarly, one of the quantities σ_{0B} or $\sigma_{\pi B}$ vanishes on the termination of the PrW $_B$ branch on one of the mixed modes. One may verify that the third point where D_B vanishes is located outside the existence interval of the branch, confirming that no parity-breaking bifurcation occurs along the branch. In addition, one may confirm that $\sigma_{0B} \sigma_{\pi B} > 0$, except at the termination point.

The necessary conditions for stability within the $\text{Fix}(\text{PrW}_B)$ subspace are $D_B < 0$, $T_B < 0$, $I_B > 0$ and $H_B \equiv I_B - D_B/T_B > 0$. From eq. (45a) one may easily verify that the determinant is negative if and only if $\Sigma_B < 0$. Similarly, the trace has constant negative sign if $A_r + 2B_r < 0$ and $l_0 < 0$, which are the conditions for the supercriticality of Standing Waves and the Steady-State mode, respectively. If instead $l_0(A_r + 2B_r) < 0$, then the trace changes sign within the region of existence of the PrW_B solution. Analogously, the necessary conditions for a constant positive sign of the second invariant I_B everywhere along the branch are

$$A_r B_r > 0 \quad \text{and} \quad \Delta_+ > 0 \text{ if } A_r D_r < 0 \\ \text{or } \Delta_- > 0 \text{ if } A_r D_r > 0. \quad (46)$$

The first condition ensures that the second invariant is positive at its birth from the RW branch, while the second condition ensures that I_B is positive at its termination on the corresponding MM branch. To ensure that $I_B > 0$ along the whole PrW_B branch it suffices to have $\Delta_- > -C_+$ if $A_r D_r < 0$, a condition that depends only on Δ_+ and $B_r D_r$, or $\Delta_+ > -C_-$ if $A_r D_r > 0$ for $C_- > 0$, a condition that depends only on Δ_- and $B_r D_r$.

The PrW_B branch is stable when $H_B > 0$. If H_B changes sign along the PrW_B branch a Hopf bifurcation with frequency Ω takes place ($H_B = 0$), characterized by the following set of conditions

$$T_B \Omega^2 - D_B = 0, \quad \Omega^2 - I_B = 0. \quad (47)$$

These equations yield the conditions for the presence of a Hopf bifurcation along the PrW_B branch stated above. In terms of the eigenvalues $\sigma_{0B}(\lambda_s, \lambda_h)$ and $\sigma_{\pi B}(\lambda_s, \lambda_h)$ of the Mixed Modes the Hopf distance H_B is given by

$$H_B \equiv -\frac{A_r}{8D_r^2\Sigma_B^3} \left(\Delta_- \Lambda_B^- \sigma_{\pi B}^3 - \Delta_+ \Lambda_B^+ \sigma_{0B}^3 \right) \\ + \left[\Lambda_B^+ (8B_r D_r - \Delta_-) + 2A_r l_0 \Delta_+ - 8D_r \Sigma_B \right] \sigma_{\pi B} \sigma_{0B}^2 \\ + \left[\Lambda_B^- (8B_r D_r + \Delta_+) + 2A_r l_0 \Delta_- + 8D_r \Sigma_B \right] \sigma_{\pi B}^2 \sigma_{0B} \\ \Lambda_B^\pm \equiv D_r (A_r + 2B_r) \pm A_r l_0. \quad (48)$$

The condition $H_B = 0$ describes a planar cubic algebraic curve in $(\sigma_{0B}, \sigma_{\pi B})$. A possible procedure is to determine the type of the planar curve isomorphic to one of the five canonical forms [42], and then determine the number of solutions from it. Instead of following this procedure we prefer to provide a sufficient condition for the appearance of a Hopf bifurcation along this branch. Provided eq. (46) holds, the frequency Ω is real, and there exists an odd number (one or three) of Hopf bifurcations whenever H_B has opposite signs at the two endpoints of the branch. This occurs when

$$\Delta_- \Lambda_B^- < 0 \quad (\text{MM}_0), \quad \Delta_+ \Lambda_B^+ > 0 \quad (\text{MM}_\pi). \quad (49)$$

When eq. (49) does not hold the number of Hopf bifurcations is even (none or two). In such a case one can

distinguish between the different scenarios using, for instance, the Descartes sign rule for positive roots.

In addition to the three eigenvalues governing the stability of the PrW_B branch within the $\sin \Psi = 0$ subspace discussed above, there is a fourth eigenvalue governing the stability in the orthogonal direction given by

$$\sigma_{BG} = -(2l_3 P - A_r S). \quad (50)$$

The vanishing of this eigenvalue leads to the birth of a branch of General Precessing Waves. The resulting condition in terms of λ_s and λ_h is listed in table IX. A condition ensuring that such a bifurcation occurs somewhere along the branch is that σ_{BG} has opposite signs at its termination points on RW and the relevant MM. This leads to the condition reported in the last column of table IX. This condition is the same as for the bifurcation from PrW_A .

D. The third branch of precessing waves

As demonstrated in the previous sections, two bifurcations can occur along the precessing waves of type A and B giving rise to a precessing wave with no symmetry called PrW_G . Here we investigate this branch as well as its stability. We look for a steady solution of the polar equations with $r_0 \neq 0$, $r_1 \neq r_2$ and $\sin \Psi \neq 0$, cf. Table VIII. The same manipulations as before lead to the following conditions:

$$\begin{aligned} 0 &= P Q l_3 + R l_0 + S l_1 + \lambda_s, \\ 0 &= B_r S + C_r R + \lambda_h, \\ 0 &= A_r P + D_r Q R, \\ 0 &= D_r R S + 2P^2 l_3. \end{aligned} \quad (51)$$

The solution of this system yields the conditions for the presence of the PrW_G branch:

$$\begin{aligned} R &= \frac{2B_r \lambda_s - (2l_1 + A_r) \lambda_h}{\Sigma_G}, \\ S &= 2 \frac{C_r \lambda_s - l_0 \lambda_h}{\Sigma_G}, \\ P &= \frac{-1}{l_3 \Sigma_G} \left(D_r l_3 (B_r \lambda_s - (2l_1 + A_r) \lambda_h) (C_r \lambda_s - l_0 \lambda_h) \right)^{\frac{1}{2}}, \\ Q &= A_r \left(\frac{C_r \lambda_s - l_0 \lambda_h}{D_r l_3 [2B_r \lambda_s - (2l_1 + A_r) \lambda_h]} \right)^{\frac{1}{2}}, \\ &\text{where } \Sigma_G = C_r (A_r + 2l_1) - 2B_r l_0 \neq 0. \end{aligned} \quad (52)$$

These expressions define a single solution branch. One may check that imposing $Q^2 = 1$ and $S = 2|P|$ yields, respectively, the same conditions as found for the steady bifurcations from the PrW_A and PrW_B branches listed in table IX, confirming that the PrW_G solution indeed links these two branches.

The invariants of the stability matrix are

$$\begin{aligned}
T_G &= 2Rl_0 + S(A_r + 2B_r) \\
&= \frac{2(\sigma_S(A_r + 2B_r) + l_0\sigma_R)}{\Sigma_G}, \\
D_G &= 8\Sigma_G D_r l_3 R^2 (4P^2 - S^2)(Q^2 - 1), \\
&= \frac{32}{\Sigma_G^3 l_3} \sigma_S \sigma_R (A_r^2 \sigma_S + D_r l_3 \sigma_R) (D_r \sigma_R + \sigma_S l_3) \\
I_G &= \frac{4A_r}{\Sigma_G^2} (2(B_r - A_r)\sigma_S^2 - D_r^2 \sigma_R^2) \\
&+ \frac{\sigma_S \sigma_R}{\Sigma_G^2 l_3} (4D_r(2A_r B_r - 3l_3^2) + 4l_0 l_3 (A_r + 2B_r)) \\
&- 4 \frac{\sigma_S \sigma_R}{\Sigma_G^2 l_3} ((A_r + 2l_1)(A_r D_r + C_r l_3)) \\
II_G &= -\frac{8}{\Sigma_G^3} (D_r^2 l_0 \sigma_R^3 + 4A_r^2 B_r \sigma_S^3) \\
&+ \frac{8D_r \sigma_S \sigma_R^2}{\Sigma_G^3 l_3} (2\Sigma_B + l_3(\Sigma_A - 4B_r D_r) - l_0(A_r^2 + l_3^2)) \\
&+ \frac{8\sigma_S^2 \sigma_R}{\Sigma_G^3 l_3} (A_r l_3 \Sigma_G - 6B_r D_r l_3^2) \\
&+ \frac{8\sigma_S^2 \sigma_R}{\Sigma_G^3 l_3} A_r^2 (D_r A_r + 2D_r(l_1 - B_r) - 2l_3 l_0). \tag{53}
\end{aligned}$$

The determinant D_G only vanishes at the termination points, that is, whenever $Q^2 = 1$ or $S = 2|P|$, which rules out the possibility of a steady state bifurcation. Thus there can only be Hopf bifurcations along the PrW_G branch. The frequency Ω solves the following equations obtained from the characteristic polynomial

$$\Omega^4 - II_G \Omega^2 + D_G = 0, \quad T_G \Omega^2 - I_G = 0, \tag{54}$$

leading to the following sixth order equation in terms of λ_s and λ_h :

$$II_G^2 - II_G I_G T_G + T_G^2 D_G = 0. \tag{55}$$

E. A robust heteroclinic cycle

The isotropy lattice (see fig. 9) of the degenerate case under discussion suggests the possibility that new heteroclinic cycles may exit. One of the most intriguing possibilities is a connection between the isotropy subspace of Mixed Modes and the subspaces of Precessing Waves A and B, corresponding to a cycle of type C in the classification of Krupa and Melbourne [39]. The conditions for the existence of a robust heteroclinic cycle connecting Mixed Modes consists in demanding that MM_0 is a saddle whose unstable manifold is of dimension one (resp. sink) within Σ_{PrW_B} and a sink (resp. saddle) within Σ_{PrW_A} . Then MM_π would need to be a sink (resp. saddle) within Σ_{PrW_B} and a saddle (resp. sink) within Σ_{PrW_A} . However, for the mixed mode MM_π to be a saddle within Σ_{PrW_A} and the mixed mode MM_0 to be a sink it is necessary that $\sigma_{\pi_A} - \sigma_{0_A} < 0$ with $D_r l_3 < 0$, conditions

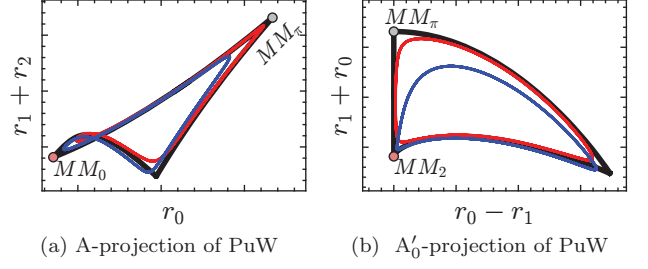


FIG. 10: Heteroclinic cycle between MM_π and MM_0 in the polar normal form (9) with $A_i - 2l_2 = D_i = \sin \Psi = 0$ (black line) and corresponding results when $A_i - 2l_2 \neq 0$ and $D_i = 0$ (red line) or $D_i \neq 0$ and $A_i - 2l_2 = 0$ (blue line).

that indicate that there is a fixed point within the invariant subspace Σ_{PrW_A} , i.e. PrW_A (resp. PrW_B). Despite the existence of a fixed point within the invariant subspace Σ_{PrW_A} (resp. Σ_{PrW_B}), a robust heteroclinic cycle may still exist, cf. [43]. In the case of an invariant fixed point subspace of dimension two the existence of heteroclinic cycles relies on the use of the Poincaré-Bendixson theorem, see for instance [40]. In this case the fixed-point subspace is required to be free of any other fixed point other than those connected by the heteroclinic cycle. Instead when the dimension is three, one may use the invariant sphere theorem, or more generally a Lyapunov functional to establish attraction. In our case the presence of a robust heteroclinic cycle requires that the coefficients $C_r \pm D_r$ and $2l_1 \pm l_3$ should both be positive, since otherwise the Precessing Waves A and B are globally attractive except possibly within a ball of size $\mathcal{O}(\lambda_s, \lambda_h)$ in the subspace R, S, P . These conditions are listed in table X. Note that our reasoning does not exclude the existence of a small heteroclinic cycle within the $\mathcal{O}(\lambda_s, \lambda_h)$ ball near PrW , although such a state (if it exists) would require a larger set of defining conditions and would be restricted to a small region of phase space.

If the conditions listed in table X are satisfied then there exists a robust heteroclinic cycle between mixed modes, which bifurcates to a 3FW in the case $A_i - 2l_2 \neq 0$ and $D_i = 0$, and to a PuW or 3FW in the case with $A_i - 2l_2 \neq 0$ and $D_i \neq 0$, see fig. 10. Finally, the application of the theory of Krupa and Melbourne [39] also allows one to establish the existence of heteroclinic cycles between standing waves and mixed modes, whose existence and stability conditions are listed in table X. As for the heteroclinic cycles between mixed modes, these heteroclinic cycles persist in the form of limit cycles of the polar normal form when the degeneracy conditions are not satisfied, see fig. 11.

TABLE X: Defining conditions for structurally and asymptotically stable heteroclinic cycles connecting mixed modes or standing waves and a mixed mode.

Name of solutions (comments)	Cond. of existence	Asymptotic stability (Asymp. stable if either i-a) or i-b)
Het _{MM₀-MM_π} Stable radial dir. Sink-saddle conditions Non-attractivity of PrW	$\Delta_+ > 0, \Delta_- > 0, l_0 < 0, A_r + 2B_r < 0$ $\sigma_{0A}\sigma_{0B} > 0, \sigma_{\pi A}\sigma_{\pi B} < 0, l_3 D_r < 0, A_r D_r > 0,$ $2l_1 \pm l_3 > 0, C_r \pm D_r > 0$	i-a) $\sigma_{\pi A} + \sigma_{\pi B} < 0,$ i-b) $\sigma_{0A} - \sigma_{0B} > 0$
Het _{SW-MM_π} Stable radial dir. SW saddle in Fix($\Sigma_{MM\pi}$) MM _π saddle in Fix(Σ_{PrWB})	$\Delta_- > 0, l_0 < 0, A_r + 2B_r < 0, A_r > 0$ $\sigma_{SW}^- > 0, \sigma_{SW}^+ < 0$ $\sigma_{\pi A}\sigma_{\pi B} < 0, A_r D_r > 0$	i-a) $2(2B_r + A_r)\lambda_s - (2l_1 - A_r)\lambda_h > 0$ i-b) $\sigma_{\pi A} + \sigma_{\pi B} < 0$
Het _{SW-MM₀} Stable radial dir. SW saddle in Fix(Σ_{MM_0}) MM ₀ saddle in Fix(Σ_{PrWB})	$\Delta_+ > 0, l_0 < 0, A_r + 2B_r < 0, A_r > 0$ $\sigma_{SW}^- < 0, \sigma_{SW}^+ > 0$ $\sigma_{0A}\sigma_{0B} > 0, A_r D_r < 0$	i-a) $2(2B_r + A_r)\lambda_s - (2l_1 - A_r)\lambda_h > 0$ i-b) $\sigma_{\pi A} - \sigma_{\pi B} > 0$

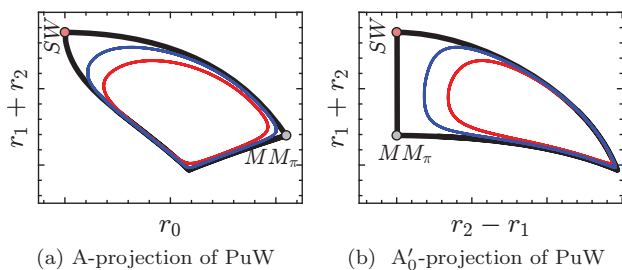


FIG. 11: Heteroclinic cycle (black) between MM_π and SW in the polar normal form (9) with $A_i - 2l_2 = D_i = \sin \Psi = 0$ (black line) and corresponding results with $A_i - 2l_2 \neq 0$ (red line) or $D_i \neq 0$ (blue line).

VI. NUMERICAL EXPLORATION OF THE THIRD-ORDER NORMAL FORM (9)

The section V has shown the existence of multiple fixed points with additional symmetries, e.g. PrW_A and PrW_B , in the degenerate case (equivariant under the group $O(2) \times \mathbb{Z}_2 \times S^1$). The additional \mathbb{Z}_2 symmetry is characteristic of mode interactions in $O(2)$ symmetric systems with strong resonance conditions (1:2 [43], 1:3 [44]). Departure from the degeneracy condition ($A_i - 2l_2 = D_i = 0$) breaks this additional \mathbb{Z}_2 symmetry and may be responsible for destroying the Het_{SS-SW} heteroclinic cycle, leading to more complex dynamics. This section is devoted to the numerical exploration of the degenerate case $A_i - 2l_2 = D_i = 0$ and the implications of the departure from this condition ($A_i - 2l_2 \neq 0$ and/or $D_i \neq 0$). For this purpose, we choose generic values for the normal form coefficients, listed in table XI. These coefficients are chosen in such a way that primary bifurcations, i.e., bifurcations leading to SS, SW and RW are supercritical, and the flow is globally stable, that is, there is no finite-time blow-up.

As the bifurcation parameter, we have selected the polar angle θ such that the unfolding parameters are $\lambda_S = \rho \cos \theta$ and $\lambda_H = \rho \sin \theta$, with $\rho = (0, \infty)$ and $\theta \in [0, 2\pi)$. In contrast to [43] the bifurcation diagram barely depends on ρ , and we have fixed the value of ρ at $\rho = 0.5$. The numerical continuation of the polar normal form is carried out with the numerical continuation software MATCONT [45]. In the following, we will show the bifurcation diagrams associated to the degenerate and non-degenerate cases. There are two major differences. First, the two connected branches of symmetric Precessing Waves (PrW_A and PrW_B) are a characteristic feature of the degenerate case (symmetry $O(2) \times \mathbb{Z}_2 \times S^1$). In the non-degenerate case, these two branches split into two disconnected branches of general Precessing Waves PrW_G . Secondly, in the degenerate case we observe Het_{SS-SW} cycles, which break apart as the orbit intersects the invariant subspace $r_1 = r_2$. Instead, in the non-degenerate case we have identified complex heteroclinic cycles around Het_{PrWA} . Such a feature was also observed by Porter and Knobloch [43], who concluded that the transition from Het_{SS-SW} cycles to this second set is a characteristic of systems with $O(2) \times \mathbb{Z}_2$ symmetry where the \mathbb{Z}_2 symmetry is weakly broken.

A. The degenerate case $A_i - 2l_2 = D_i = 0$

Figure 12 shows the bifurcations of the fixed point branches of the polar normal form with the parameters listed in table XI and the degeneracy conditions $A_i - 2l_2 = D_i = 0$. Along this particular path, the

TABLE XI: Cubic coefficients of the normal form.

l_0	l_1	l_3	A_r	B_r	C_r	D_r
-6.19	-1.4	-1.7	0.96	-1.08	4	10

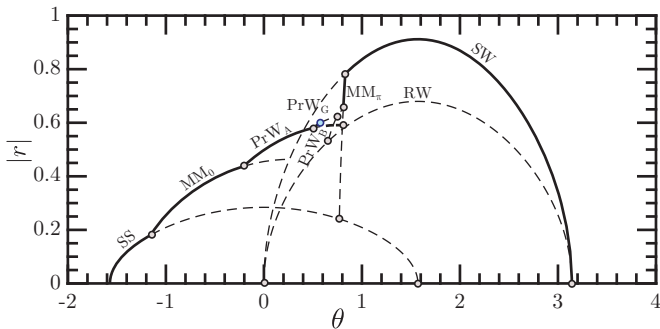


FIG. 12: Bifurcation diagram in the degenerate case when $\rho = 0.5$, showing $|r| = \sqrt{r_0^2 + r_1^2 + r_2^2}$ as a function of the angle θ .

trivial state first loses stability at $\theta = -\pi/2$ in a primary pitchfork bifurcation to the SS mode, which terminates at $\theta = \pi/2$. The SS mode gives birth to the MM_0 branch when $\theta = \arctan(C_r + D_r)/l_0 \approx -1.15$ and to the MM_π branch when $\theta = \arctan(C_r - D_r)/l_0 \approx 0.77$ (table V). The mixed mode MM_0 subsequently produces the PrW_A branch in a symmetry-breaking bifurcation when $\sigma_{0A} = 0$ (table IX) and then terminates on the SW branch. A magnified visualization is displayed in fig. 13(a), where we can observe the PrW_A which terminates on the MM_π branch and eventually gives birth to a general precessing wave PrW_G via a symmetry-breaking bifurcation when $\sigma_{AG} = 0$. The PrW_G mode experiences a Hopf bifurcation that leads to a 3FW (blue point in fig. 12). fig. 14 illustrates a stable periodic orbit (3FW) with a thick black line and the stable manifold of PrW_A with a thin gray line. The existence of a global attractor (PrW_A) in the invariant subspace $r_1 = r_2$ prevents the existence of a true heteroclinic cycle Het_{SS-SW} , but allows the existence of shadowing stable periodic orbits that approximate it, see fig. 14. These orbits exist in $0.52 < \theta < 0.592$ and collapse in a global bifurcation when the limit cycle intersects the invariant subspace $r_1 = r_2$ at $\theta \approx 0.592$. Once a trajectory intersects the $r_1 = r_2$ subspace, it is trapped within it and so is attracted to the only attractor in this subspace, i.e., the PrW_A state. The same phenomenon occurs in the small region of coexistence of MM_π and the heteroclinic cycle, $0.78 < \theta < 0.82$. The PrW_G branch terminates on the PrW_B branch, which connects RW and MM_π . Finally, the MM_π branch is stable between its endpoint on the SW branch and its symmetry-breaking bifurcation that leads to the PrW_B branch. For $0.82 < \theta \leq \pi$ the only stable state is the SW branch.

B. Non-degenerate case $A_i - 2l_2 = -1$, $D_i = 0.35$

The general picture of the bifurcation scenario, depicted in fig. 12, remains qualitatively unchanged. However, the Precessing Wave branches are modified. We

first examine the case when one of the two degeneracy conditions is still satisfied. The case $A_i - 2l_2 = 0$ but $D_i \neq 0$ is illustrated in fig. 13(b) and reveals the existence of two distinct PrW_G branches. This case corresponds to an imperfect bifurcation, where the two symmetry-breaking pitchfork bifurcations leading to the PrW_G branch in the degenerate case are replaced by a saddle-node bifurcation on each branch. The second case, $D_i = 0$ but $A_i - 2l_2 \neq 0$, illustrated in fig. 13(c), shows the presence of PrW_A and PrW_G branches, the latter replacing the symmetric PrW_B branch. These branches connect via a transcritical bifurcation, which is responsible, in this case, for the stability of the whole upper section of the PrW_G branch since no Hopf bifurcation takes place.

We next turn our attention to the non-degenerate case $A_i - 2l_2 \neq 0$, $D_i \neq 0$. The bifurcation diagram of the fixed points of the polar normal form is depicted in fig. 15. The figure displays two disconnected branches of general Precessing Waves PrW_G . The first of these, referred to as $PrW_{G,1}$ in the figure, becomes unstable through a Hopf bifurcation, leading to a 3FW branch (not shown). The second PrW_G branch, labeled $PrW_{G,2}$, bifurcates from and terminates on the MM_π branch with a saddle-node bifurcation in between: the upper section is stable, whereas the lower is unstable. Because of the symmetry under reflection κ , there is in fact a pair of such saddle-node bifurcations, $PrW_{G,2}^\pm$, both occurring at $\theta = \theta_{SN} \approx 0.663445$. Moreover, each is of Saddle-Node-in-a-Periodic-Orbit (SNIPER) type but with complex leading eigenvalues at the fold points $PrW_{G,2}^\pm$: $(0, -0.6795, -0.0182 \pm 0.4418i)$. For a study of this situation in the absence of κ symmetry, see [46]. In the presence of this symmetry, this case can either lead to a pair of symmetry-related homoclinics to $PrW_{G,2}^\pm$ or, as in this case, to a heteroclinic cycle connecting $PrW_{G,2}^+$ to $PrW_{G,2}^-$ and vice versa, a consequence of intertwined nature of the stable and unstable manifolds of $PrW_{G,2}^\pm$. In the former case the near-homoclinic orbit to the left of $PrW_{G,2}^\pm$ contains a certain number of decreasing oscillations as it approaches and leaves $PrW_{G,2}^\pm$, the number of these oscillations depending on the speed with which the trajectory passes through the $PrW_{G,2}^\pm$ neighborhood, and hence on the distance of θ from θ_{SN} . In the latter case the unstable manifold associated with the degenerate eigenvalue injects the trajectory into the image fold point and the same local behavior there leads to reinjection back into the original fold, generating a κ -symmetric heteroclinic cycle, cf. [47]. Figure 16 shows such an orbit in two projections, computed for θ just below $\theta_{SN} \approx 0.663445$. At this θ the $PrW_{G,2}^\pm$ points are absent and the orbit shown is actually a long period periodic orbit. Figure 17a shows the period of such orbits as a function of $\theta_{SN} - \theta$, confirming the expected relation $T \sim (\theta_{SN} - \theta)^{-1/2}$. This divergence is a consequence of a slowdown of the trajectory in the vicinity of the phase space location where the $PrW_{G,2}$ appear when θ increases through θ_{SN} , resulting

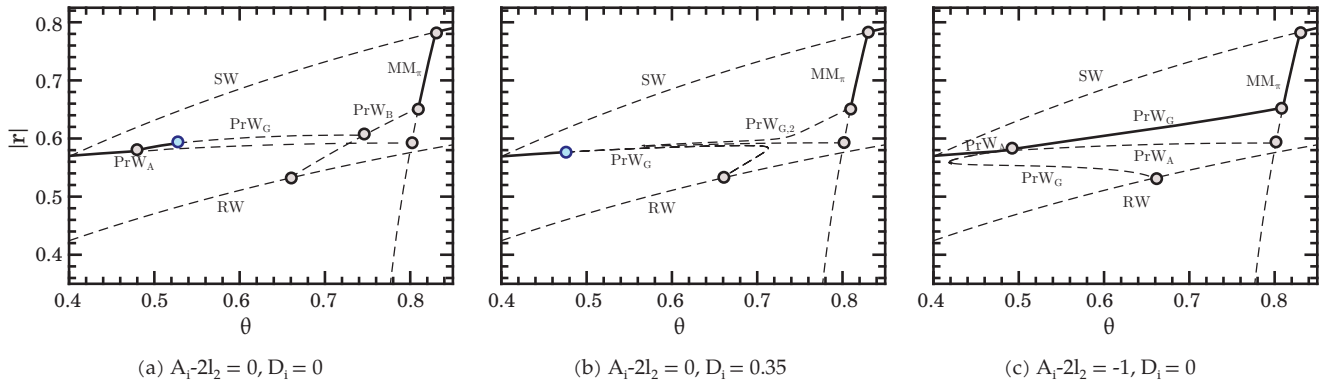


FIG. 13: Bifurcation diagram in the degenerate case when $\rho = 0.5$, showing $|r| = \sqrt{r_0^2 + r_1^2 + r_2^2}$ as a function of the angle θ . Legend: Solid (dashed) lines are stable (unstable) fixed points. Symmetry-breaking bifurcations are illustrated with gray points and Hopf bifurcations with blue points. Note: in (a) as well as in fig. 12 the PrW_G branch has been artificially displaced upwards to visually differentiate it from the PrW_A branch.

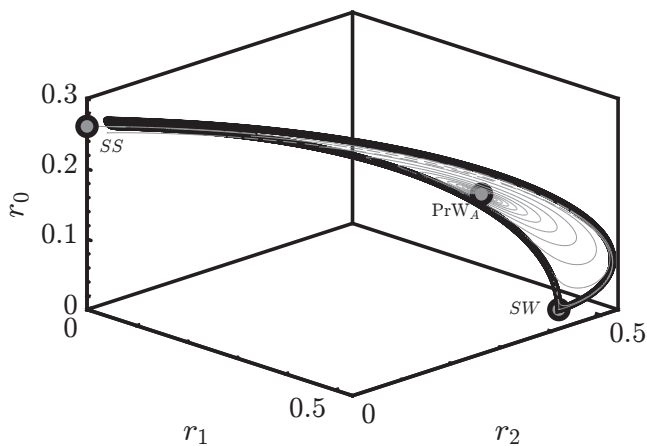


FIG. 14: Example of a heteroclinic cycle $SS-SW$ (thick line). The gray line corresponds to the stable manifold of PrW_A .

in increased accumulation of turns as this point is approached. Note that these orbits inherit the stability of the (upper) $PrW_{G,2}$ branch (cf. fig. 15) and hence represent attractors of the system.

Figure 18 shows sample attractors found on decreasing θ further. Figure 18a shows a stable symmetric orbit at $\theta = 0.663$, followed by asymmetric chaotic attractors (with a positive Lyapunov exponent) generated with increasing distance from θ_{SN} . The absence of chaotic states near θ_{SN} is a consequence of the fact the flow in this region is locally contracting.

To understand the origin of these states, we examine the behavior of a typical periodic orbit associated with the SNIPER bifurcation. As already explained this orbit depends sensitively on the value of $\theta < \theta_{SN}$. In fig. 19a we show the period T of this orbit as a function of θ

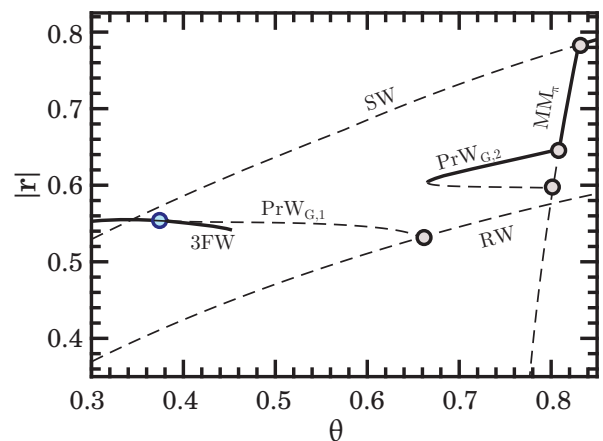


FIG. 15: Bifurcation scenario in the non-degenerate case showing $|r| = \sqrt{r_0^2 + r_1^2 + r_2^2}$ as a function of the angle θ with the same legend as in fig. 13. The end point of $PrW_{G,1}$ is located at $\theta \approx 0.6581$, i.e., below θ_{SN} but above the global bifurcation at $\theta \approx 0.6454$. Note: The blue point and subsequently the 3FW branch have been artificially displaced, so the crossing point between the SW and $PrW_{G,1}$ and the blue point do not coincide.

obtained using numerical continuation. This period diverges as $\theta \rightarrow \theta_{SN}$ from below and the orbit approaches the heteroclinic cycle shown in fig. 16. As θ decreases the period T decreases, although this decrease is interrupted by a series of back-to-back folds. Each such pair is responsible for the elimination of one small amplitude turn of the trajectory (not shown), resulting in a gradual unwinding of the trajectory. As θ decreases towards the leftmost fold and beyond, the trajectory develops small loops in the vicinity of $PrW_{G,1}$ (fig. 20) and its period begins to diverge again, this time logarithmically (fig. 17b), indicating approach to a heteroclinic connection involving $PrW_{G,1}$ and located at $\theta = \theta_{het} \approx 0.6454$. Since

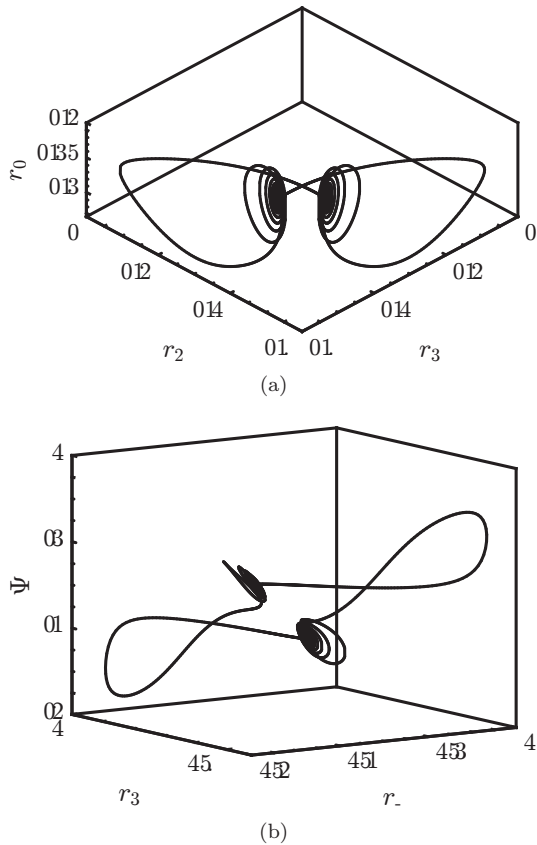


FIG. 16: Heteroclinic cycle at $\theta_{SN} \approx 0.663445$.

the leading unstable eigenvalues of $\text{PrW}_{G,1}$ at this parameter values are complex, $0.2446 \pm 0.3661i$, while the leading stable eigenvalue is real, -0.0251 , these points are both saddle-foci. The complex unstable eigenvalues account for the oscillatory approach to the global bifurcation at $\theta \approx 0.6454$ while the fact that the flow near $\text{PrW}_{G,1}$ is locally expanding implies that we should expect stable chaotic dynamics near this parameter value, as in the classical example of Shil'nikov where the signs of the eigenvalues are reversed [48–50].

In fig. 19a the solid line tracks the period of the κ -symmetric orbit. As $\theta \rightarrow 0.6454$ from above, this orbit collides with $\text{PrW}_{G,1}$, forming a heteroclinic connection from $\text{PrW}_{G,1}$ to its image under κ and back again. Near θ_{het} this orbit is accompanied by back-to-back symmetry-breaking bifurcations, generating asymmetric periodic orbits (fig. 19b). These asymmetric orbits are free to period-double into chaos, resulting in 'bubbles' of chaotic behavior, as described in [51] and references therein. Close to the primary heteroclinic bifurcation these bubbles 'burst' via the formation of pairs of subsidiary homoclinic orbits. The red dashed and thin solid lines in fig. 19b show examples of this generic behavior in our problem; fig. 19c compares the homoclinic orbit at the green dashed asymptote with the corresponding period-doubled orbit on the red dashed branch at the

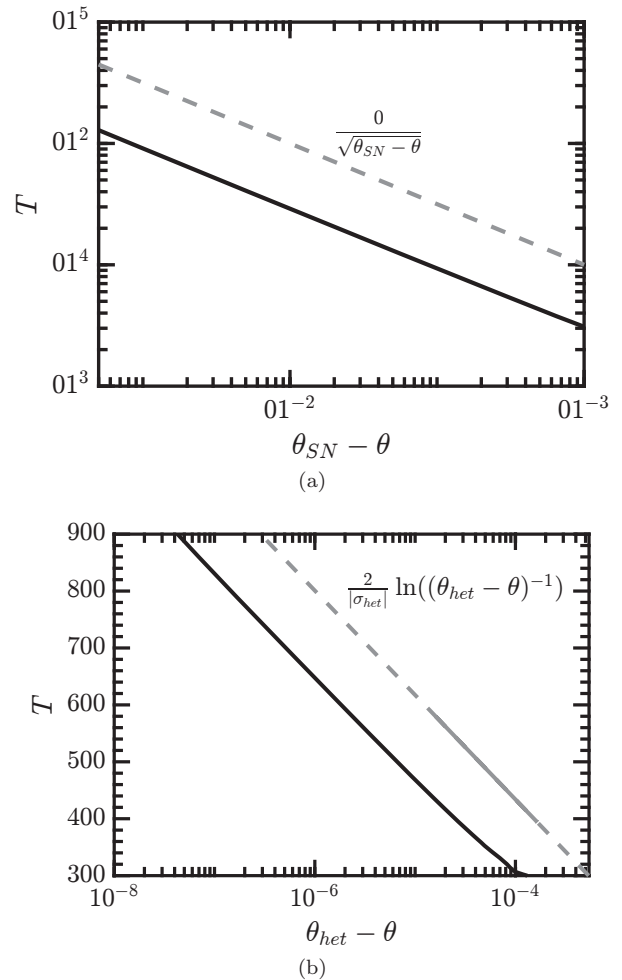


FIG. 17: (a) Evolution of the period of the stable limit cycles shadowing the heteroclinic cycle as a function of the distance $\theta_{SN} - \theta$ to the saddle-node bifurcation. (b) Evolution of the period near the heteroclinic bifurcation at θ_{het} , where $\sigma_{het} = -0.0251$ is the leading stable eigenvalue of the $\text{PrW}_{G,1}$ fixed point.

same θ value. Further details are omitted. Thus, the primary symmetric periodic orbit is associated with a number of chaotic intervals located around subsidiary homoclinic orbits originating in global bifurcations of asymmetric orbits associated with it, cf. fig. 18. In particular, stable chaotic motion is also observed for θ below the primary heteroclinic bifurcation at $\theta_{het} \approx 0.6454$.

We mention that the periodic orbit originating from the Hopf point on the $\text{PrW}_{G,1}$ branch ($\theta \approx 0.3841$, blue point in Fig 15) is stable from the Hopf point to $\theta \approx 0.4518$, where the first of several Neimark-Sacker bifurcations takes place. These are interspersed with additional global bifurcations and intervals of chaos as θ increases towards $\theta_{het} \approx 0.6454$. Some sample solutions are shown in fig. 21 to whet appetite. The details depend on the parameters used and are omitted.

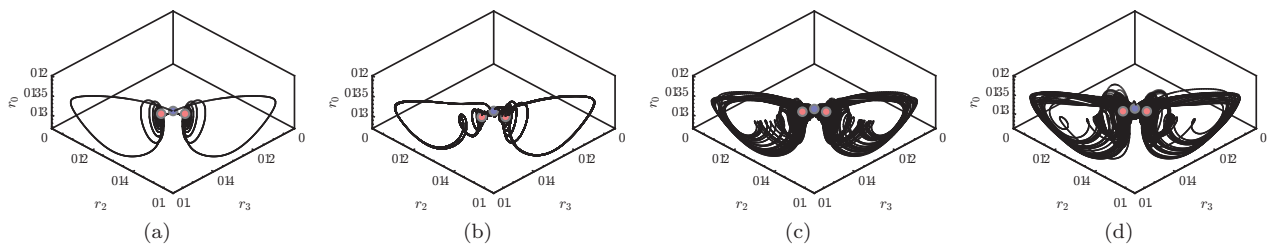


FIG. 18: Stable attractors in a (r_0, r_1, r_2) projection for (a) $\theta = 0.663$ (symmetric periodic orbit); (b) $\theta = 0.647$ (asymmetric orbit); (c) $\theta = 0.645$ (asymmetric orbit); (d) $\theta = 0.643$ (asymmetric orbit). The symmetry-related $\text{PrW}_{G,2}$ fixed points corresponding to the saddle-node at $\theta \approx 0.663445$ are indicated by red points, with the PrW_A point (present in the degenerate case only) depicted as a blue point; these are shown for orientation only.

VII. NORMAL FORM REDUCTION

The process of reducing the governing equations to normal form near a multiple bifurcation is based on center manifold reduction followed by a series of near-identity variable changes to simplify the dynamical equations on the center manifold. The resulting equations are then *unfolded* by introducing parameters that break apart the multiple bifurcation in a generic way. In infinite-dimensional problems, such as those arising in fluid mechanics, it is preferable to employ multiple scales techniques to compute both the normal form and the coefficients within it as part of the same calculation. We employ here this technique to determine all the coefficients in the third-order normal form (8).

First, let us introduce the following formal expression for the governing equations on a domain Ω :

$$\begin{aligned} \mathbf{B} \frac{\partial \mathbf{q}}{\partial t} &= \mathbf{F}(\mathbf{q}, \boldsymbol{\eta}) \equiv \mathbf{L}\mathbf{q} + \mathbf{N}(\mathbf{q}, \mathbf{q}) + \mathbf{G}(\mathbf{q}, \boldsymbol{\eta}), \quad \mathbf{x} \in \Omega, \\ \mathbf{D}_{bc}\mathbf{q}(\mathbf{x}) &= \mathbf{q}_{\partial\Omega}, \quad \mathbf{x} \in \partial\Omega. \end{aligned} \quad (56)$$

Here $\partial\Omega$ represents the domain boundary. This form of the governing equations takes into account a linear dependence on the state variable \mathbf{q} through \mathbf{L} and a quadratic dependence on state variable and the parameters $\boldsymbol{\eta}$ through the operators $\mathbf{G}(\cdot, \cdot)$ and $\mathbf{N}(\cdot, \cdot)$. Equation (56) formally includes the incompressible Navier–Stokes equations written in cylindrical coordinates for the TFC and WFA problems, whereas for WFA-MC one must consider the Boussinesq approximation of the incompressible Navier–Stokes equations written in cylindrical coordinates as well. For this set of equations, the

operators in eq. (56) take the following form,

$$\begin{aligned} \mathbf{L}\mathbf{q} &= \begin{pmatrix} -\nabla P \\ \nabla \cdot \mathbf{U} \\ 0 \end{pmatrix}, \\ \mathbf{N}(\mathbf{q}_1, \mathbf{q}_2) &= - \begin{pmatrix} \mathbf{U}_1 \cdot \nabla \mathbf{U}_2 \\ 0 \\ \mathbf{U}_1 \cdot \nabla T \end{pmatrix}, \\ \mathbf{G}(\mathbf{q}, \boldsymbol{\eta}) &= \begin{pmatrix} \frac{1}{\text{Re}} \nabla \cdot (\nabla \mathbf{U} + (\nabla \mathbf{U})^T) + \text{Ri} T \mathbf{e}_z \\ 0 \\ \frac{1}{\text{RePr}} \nabla^2 T \end{pmatrix}. \end{aligned} \quad (57)$$

In red color we have included the modification for the WFA-MC problem with respect to the WFA problem. The set of parameters $\boldsymbol{\eta} \in \mathbb{R}^{N_p}$, where N_p is the number of parameters, is composed of the two dimensionless angular velocities of the cylindrical annulus for TFC, the inverse of the Reynolds number for WFA, and the inverse of the Reynolds, Richardson and Prandtl numbers for WFA-MC. In the following, we will consider the most general case, that is, the WFA-MC case where the vector of parameters takes the form $\boldsymbol{\eta} \equiv [\eta_0, \eta_1, \eta_2] = [\text{Re}^{-1}, \text{Ri}, \text{Pr}]^T$. The Reynolds number is defined as the ratio of inertial and viscous forces, i.e., $\text{Re} = \frac{U_\infty D}{\nu}$, with U_∞ the uniform velocity at the far field, D the diameter of the bluff body and ν the kinematic viscosity; while the Prandtl number, $\text{Pr} = \frac{\nu}{\kappa}$, stands for the ratio of viscous and thermal diffusivity (κ). The Richardson number is defined as $\text{Ri} = -\frac{\beta(\mathbf{e}_{U_\infty} \cdot \mathbf{g})(T_b - T_\infty)D}{U_\infty^2}$, with β the thermal expansion coefficient, $\mathbf{e}_{U_\infty} = \mathbf{U}_\infty / U_\infty$ the unit vector in the direction of the far field velocity, \mathbf{g} the gravity vector, and T_b and T_∞ the temperature of the bluff body and at the far field, respectively. Finally, without loss of generality, we suppose that the dependence of the solution on the trace (solution restricted to the boundary of the domain) is linear, i.e. we take \mathbf{D}_{bc} to be a linear boundary condition operator. One can also consider the dependence of the boundary conditions on parameters, that is either $\mathbf{D}_{bc}(\boldsymbol{\eta})$ or $\mathbf{q}_{\partial\Omega}(\boldsymbol{\eta})$, which may be used, for instance, for modeling of a moving wall. For the sake of simplicity and without loss of generality, this case is not considered.

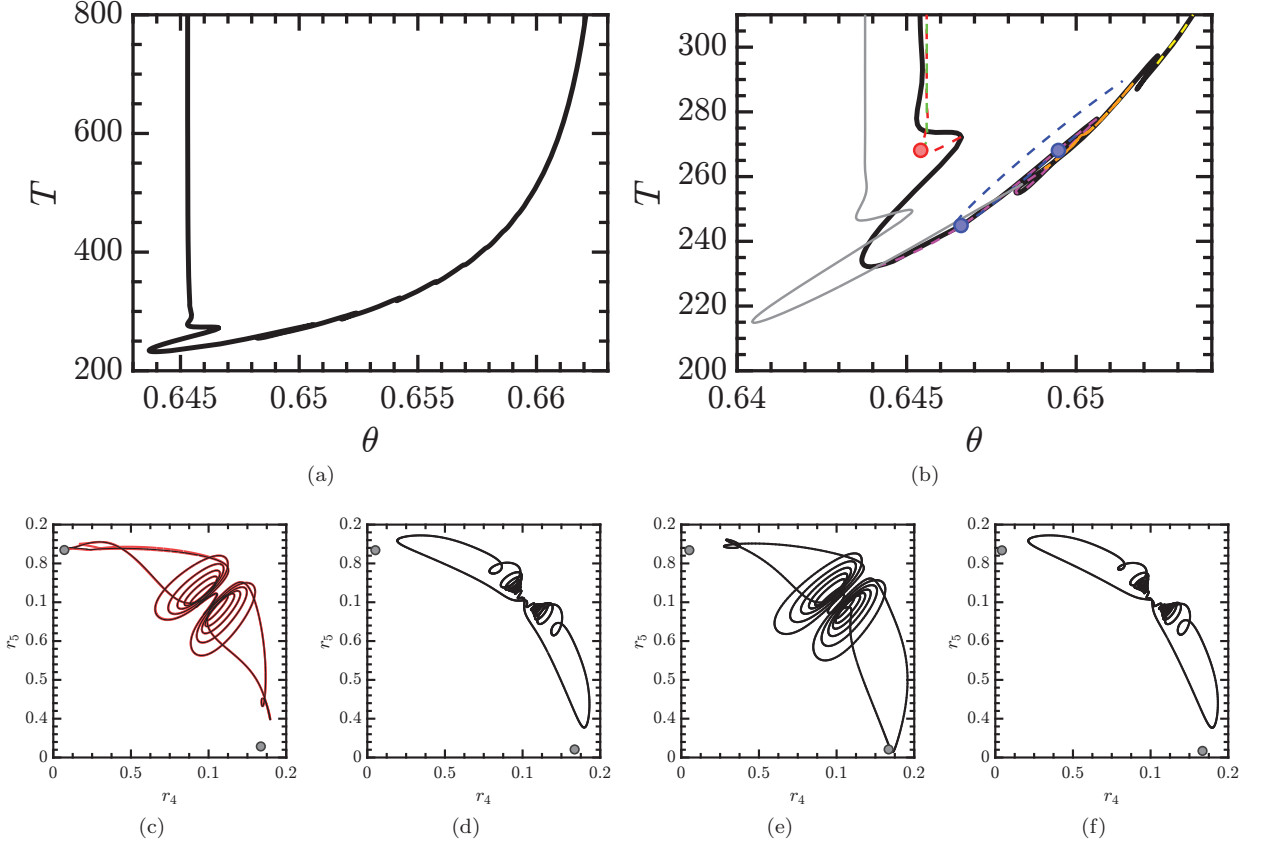


FIG. 19: (a) Evolution of the period T of a symmetric periodic orbit born in the SNIPER bifurcation $\theta \approx 0.663445$ and terminating in a heteroclinic bifurcation at $\theta \approx 0.6454$ (thick solid line). Secondary branches of asymmetric states are displayed in thin lines: solid line for the branch whose period diverges at $\theta \approx 0.64377$ and dashed lines for the other branches, see panel (b) for more detail. The secondary branches are accompanied by back-to-back period-doubling cascades (three period-doubling points are indicated with solid circles of the same color as the branch) which open up via the formation of subsidiary homoclinic orbits as in panel (c), black line; the superposed red curve shows an accompanying period-doubled solution. Portraits (d-f) display the (r_1, r_2) projection at $\theta = 0.65$ for the dashed magenta, blue, and orange branches showing a symmetric and two asymmetric periodic orbits, respectively. The location of $\text{Pr}W_{G,1}$ is indicated with small circle in (c-f). Only (c) is close to homoclinic; the proximity of orbit (e) to the lower fixed point is a projection effect.

A. Multiple scales Ansatz

The multiple scales expansion of the solution \mathbf{q} of eq. (56) consists of an expansion of eq. (1) in powers of a small parameter $\varepsilon \ll 1$:

$$\mathbf{q}(t, \tau) = \mathbf{Q}_0 + \varepsilon \mathbf{q}_{(\varepsilon)}(t, \tau) + \varepsilon^2 \mathbf{q}_{(\varepsilon^2)}(t, \tau) + O(\varepsilon^3) \quad (58)$$

Parameters $\boldsymbol{\eta}$ are assumed to be of second order, i.e. $\eta_i = O(\varepsilon^2)$ for $i = 0, 1, 2$. The expansion (58) encompasses a two-scale expansion of the original time, $t \mapsto t + \varepsilon^2 \tau$, that incorporates the fast time scale t of the self-sustained instability and the slow time scale τ of the evolution of the amplitudes $a_i(\tau)$ in eq. (1), for $i = 0, 1, 2$. The resulting expansion of the left side of

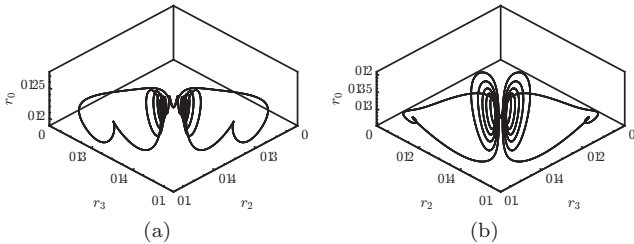


FIG. 20: The periodic orbit at the seventh and eighth folds from the right, with a period-doubling bubble in between (not shown). (a) $\theta = 0.6437$. (b) $\theta = 0.6466$.

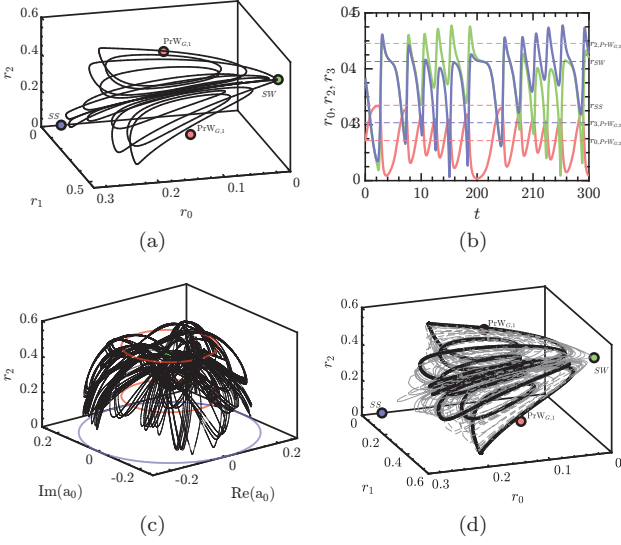


FIG. 21: (a) Phase portrait of a near-homoclinic orbit to the SW state in the (r_0, r_1, r_2) space at $\theta = 0.452$, and (b) the corresponding time series showing $r_0(t)$ (red), $r_1(t)$ (green) and $r_2(t)$ (blue). Near the homoclinic connection r_1 approaches r_2 and r_0 falls to zero. (c) A trajectory at $\theta = 0.457$ in the $(\text{Re}(a_0), \text{Im}(a_0), r_2)$ space showing that the trajectory intermittently visits SW states with different phases ϕ , each visit resulting in a switch between an oscillation about one $\text{Pr}W_{G,1}$ state to an oscillation about the other; red circles represent the group orbit of the two $\text{Pr}W_{G,1}$ states while the blue circle represents the group orbit of the SS states [52]. (d) Chaotic attractor at $\theta = 0.49$ (thin dashed grey line) together with an (unstable) κ -symmetric periodic orbit computed at $\theta \approx 0.4896$.

eq. (56) up to third order is as follows:

$$\varepsilon \mathbf{B} \frac{\partial \mathbf{q}(\varepsilon)}{\partial t} + \varepsilon^2 \mathbf{B} \frac{\partial \mathbf{q}(\varepsilon^2)}{\partial t} + \varepsilon^3 \left[\mathbf{B} \frac{\partial \mathbf{q}(\varepsilon^3)}{\partial t} + \mathbf{B} \frac{\partial \mathbf{q}(\varepsilon)}{\partial \tau} \right] \quad (59)$$

while the right side is

$$\mathbf{F}(\mathbf{q}, \boldsymbol{\eta}) = \mathbf{F}_{(0)} + \varepsilon \mathbf{F}_{(\varepsilon)} + \varepsilon^2 \mathbf{F}_{(\varepsilon^2)} + \varepsilon^3 \mathbf{F}_{(\varepsilon^3)}. \quad (60)$$

The expansion eq. (60) will be detailed at each order.

1. Order ε^0

The leading order solution \mathbf{Q}_0 of the multiple scales expansion eq. (58) is the steady state of the governing equations evaluated at the threshold of instability, i.e. $\boldsymbol{\eta} = \boldsymbol{\eta}_c$,

$$\begin{aligned} \mathbf{0} &= \mathbf{F}(\mathbf{Q}_0, \mathbf{0}), \quad \mathbf{x} \in \Omega, \\ \mathbf{D}_{bc} \mathbf{Q}_0(\mathbf{x}) &= \mathbf{Q}_{0, \partial \Omega}, \quad \mathbf{x} \in \partial \Omega. \end{aligned} \quad (61)$$

2. Order ε^1

The first order correction $\mathbf{q}_{(\varepsilon)}(t, \tau)$ in the multiple scales expansion of eq. (58) is composed of the eigenmodes of the linearized system

$$\begin{aligned} \mathbf{q}_{(\varepsilon)}(t, \tau) \equiv & \text{Re}(a_0(\tau) e^{-im_0 \theta} \hat{\mathbf{q}}_0) \\ & + \text{Re}(a_1(\tau) e^{-i\omega t} e^{-im_1 \theta} \hat{\mathbf{q}}_1) \\ & + \text{Re}(a_2(\tau) e^{-i\omega t} e^{-im_2 \theta} \hat{\mathbf{q}}_2), \end{aligned} \quad (62)$$

where the reflection symmetry in $O(2)$ imposes the requirement $m_2 = -m_1$.

Each term $\hat{\mathbf{q}}_\ell$ in the first order expansion (62) solves the corresponding linear problem:

$$\begin{aligned} \mathbf{J}_{(\omega_\ell, m_\ell)} \hat{\mathbf{q}}_\ell &= \left(i\omega_\ell \mathbf{B} - \frac{\partial \mathbf{F}}{\partial \mathbf{q}} \Big|_{\mathbf{q}=\mathbf{Q}_0, \boldsymbol{\eta}=\boldsymbol{\eta}_c} \right) \hat{\mathbf{q}}_\ell, \quad \mathbf{x} \in \Omega, \\ \mathbf{D}_{bc} \hat{\mathbf{q}}_\ell(\mathbf{x}) &= 0, \quad \mathbf{x} \in \partial \Omega, \end{aligned} \quad (63)$$

where $\frac{\partial \mathbf{F}}{\partial \mathbf{q}} \Big|_{\mathbf{q}=\mathbf{Q}_0, \boldsymbol{\eta}=\boldsymbol{\eta}_c} \hat{\mathbf{q}}_\ell = \mathbf{L}_{m_\ell} \hat{\mathbf{q}}_\ell + \mathbf{N}_{m_\ell}(\mathbf{Q}_0, \hat{\mathbf{q}}_\ell) + \mathbf{N}_{m_\ell}(\hat{\mathbf{q}}_\ell, \mathbf{Q}_0)$. The subscript m_ℓ indicates the azimuthal wavenumber used for the evaluation of the operator.

3. Order ε^2

The second order expansion term $\mathbf{q}_{(\varepsilon^2)}(t, \tau)$ is determined from the resolution of a set of forced linear systems, where the forcing terms are evaluated from first and zeroth order terms. The expansion in terms of amplitudes $a_i(\tau)$ of $\mathbf{q}_{(\varepsilon^2)}(t, \tau)$ is assessed from term-by-term identification of the forcing terms at the second order. The nonlinear second order terms are

$$\begin{aligned} \mathbf{F}_{(\varepsilon^2)} \equiv & \sum_{j,k=0}^2 \left(a_j a_k \mathbf{N}(\hat{\mathbf{q}}_j, \hat{\mathbf{q}}_k) e^{-i(m_j+m_k)\theta} e^{-i(\omega_j+\omega_k)t} + \text{c.c.} \right) \\ & + \sum_{j,k=0}^2 \left(a_j \bar{a}_k \mathbf{N}(\hat{\mathbf{q}}_j, \bar{\hat{\mathbf{q}}}_k) e^{-i(m_j-m_k)\theta} e^{-i(\omega_j-\omega_k)t} + \text{c.c.} \right) \\ & + \sum_{\ell=0}^2 \Delta \eta_\ell \mathbf{G}(\mathbf{Q}_0, \mathbf{e}_\ell), \end{aligned} \quad (64)$$

where \mathbf{e}_ℓ is an element of the orthonormal basis of \mathbb{R}^{N_p} , a vector composed of zeros except at the position ℓ where it is equal to unity.

Since no quadratic combination of elements in eq. (62) results in resonant terms, the second order term can be expanded as

$$\mathbf{q}_{(\varepsilon^2)} \equiv \sum_{\substack{j,k=0 \\ k \leq j}}^2 (a_j a_k \hat{\mathbf{q}}_{j,k} + a_j \bar{a}_k \hat{\mathbf{q}}_{j,-k} + \text{c.c.}) + \sum_{\ell=0}^2 \Delta \eta_\ell \mathbf{Q}_0^{(\eta_\ell)}, \quad (65)$$

with the rules $\hat{\mathbf{q}}_{j,k} = \hat{\mathbf{q}}_{k,j}$ and $\hat{\mathbf{q}}_{-j,-k} = \bar{\hat{\mathbf{q}}}_{j,k}$. Note the slight abuse of notation with $\hat{\mathbf{q}}_{-0} = \bar{\hat{\mathbf{q}}}_0$. Terms $\hat{\mathbf{q}}_{j,j}$ are harmonics of the flow, $\hat{\mathbf{q}}_{j,k}$ with $j \neq k$ are coupling terms, $\hat{\mathbf{q}}_{j,-j}$ are harmonic base flow modification terms

and $\mathbf{Q}_0^{(\eta_\ell)}$ are base flow corrections due to the assumed departure of the parameter $\Delta\eta_\ell = \eta_{\ell_c} - \eta_\ell$ from the critical point measured by ε .

Finally, the second-order terms are computed by solving the following nonresonant system of equations,

$$\mathbf{J}_{(\omega_j + \omega_k, m_j + m_k)} \hat{\mathbf{q}}_{j,k} = \hat{\mathbf{F}}_{(\varepsilon^2)}^{(j,k)}, \quad (66)$$

where $\hat{\mathbf{F}}_{(\varepsilon^2)}^{(j,k)} \equiv \mathbf{N}(\hat{\mathbf{q}}_j, \hat{\mathbf{q}}_k) + \mathbf{N}(\hat{\mathbf{q}}_k, \hat{\mathbf{q}}_j)$ and

$$\mathbf{J}_{(0,0)} \mathbf{Q}_0^{(\eta_\ell)} = \mathbf{G}(\mathbf{Q}_0, \mathbf{e}_\ell). \quad (67)$$

4. Order ε^3

At third order resonant terms are generated and these lead to secular (nonperiodic) terms in the expansion. We eliminate these terms by imposing a solvability condition on the system via the Fredholm alternative. This condition determines the required normal form at third order in ε . Specifically, the linear terms λ_s and λ_h are determined as follows

$$\lambda_s = \frac{\langle \hat{\mathbf{q}}_0^\dagger, \hat{\mathbf{F}}_{(\varepsilon^3)}^{(a_0)} \rangle}{\langle \hat{\mathbf{q}}_0^\dagger, \mathbf{B}\hat{\mathbf{q}}_0 \rangle}, \quad \lambda_h = \frac{\langle \hat{\mathbf{q}}_1^\dagger, \hat{\mathbf{F}}_{(\varepsilon^3)}^{(a_1)} \rangle}{\langle \hat{\mathbf{q}}_1^\dagger, \mathbf{B}\hat{\mathbf{q}}_1 \rangle} = \frac{\langle \hat{\mathbf{q}}_2^\dagger, \hat{\mathbf{F}}_{(\varepsilon^3)}^{(a_2)} \rangle}{\langle \hat{\mathbf{q}}_2^\dagger, \mathbf{B}\hat{\mathbf{q}}_2 \rangle}, \quad (68)$$

while the (real) cubic coefficients l_i for $i = 0, 1, 2, 3$ are given by

$$l_0 = \frac{\langle \hat{\mathbf{q}}_0^\dagger, \hat{\mathbf{F}}_{(\varepsilon^3)}^{(a_0|a_0|^2)} \rangle}{\langle \hat{\mathbf{q}}_0^\dagger, \mathbf{B}\hat{\mathbf{q}}_0 \rangle}, \quad l_3 = \frac{\langle \hat{\mathbf{q}}_0^\dagger, \hat{\mathbf{F}}_{(\varepsilon^3)}^{(\bar{a}_0 a_1 \bar{a}_2)} \rangle}{\langle \hat{\mathbf{q}}_0^\dagger, \mathbf{B}\hat{\mathbf{q}}_0 \rangle}$$

$$l_1 - il_2 = \frac{\langle \hat{\mathbf{q}}_0^\dagger, \hat{\mathbf{F}}_{(\varepsilon^3)}^{(a_0|a_1|^2)} \rangle}{\langle \hat{\mathbf{q}}_0^\dagger, \mathbf{B}\hat{\mathbf{q}}_0 \rangle}, \quad l_1 + il_2 = \frac{\langle \hat{\mathbf{q}}_0^\dagger, \hat{\mathbf{F}}_{(\varepsilon^3)}^{(a_0|a_2|^2)} \rangle}{\langle \hat{\mathbf{q}}_0^\dagger, \mathbf{B}\hat{\mathbf{q}}_0 \rangle}. \quad (69)$$

Finally, the complex coefficients A, B, C and D are given by

$$B = \frac{\langle \hat{\mathbf{q}}_1^\dagger, \hat{\mathbf{F}}_{(\varepsilon^3)}^{(a_1|a_1|^2)} \rangle}{\langle \hat{\mathbf{q}}_1^\dagger, \mathbf{B}\hat{\mathbf{q}}_1 \rangle}, \quad A + B = \frac{\langle \hat{\mathbf{q}}_1^\dagger, \hat{\mathbf{F}}_{(\varepsilon^3)}^{(a_1|a_2|^2)} \rangle}{\langle \hat{\mathbf{q}}_1^\dagger, \mathbf{B}\hat{\mathbf{q}}_1 \rangle},$$

$$C = \frac{\langle \hat{\mathbf{q}}_1^\dagger, \hat{\mathbf{F}}_{(\varepsilon^3)}^{(a_1|a_0|^2)} \rangle}{\langle \hat{\mathbf{q}}_1^\dagger, \mathbf{B}\hat{\mathbf{q}}_1 \rangle}, \quad D = \frac{\langle \hat{\mathbf{q}}_1^\dagger, \hat{\mathbf{F}}_{(\varepsilon^3)}^{(a_2^2)} \rangle}{\langle \hat{\mathbf{q}}_1^\dagger, \mathbf{B}\hat{\mathbf{q}}_1 \rangle}. \quad (70)$$

The forcing terms associated with the solvability conditions in eqs. (68) to (70) are detailed in appendix A 1.

VIII. CONSTRUCTION OF BIFURCATION DIAGRAMS

We now explain how the results derived in the previous section can be used to construct consistent bifurcation diagrams. The method is similar to that used in Hirschberg & Knobloch [29] and is explained in fig. 22. As illustrated in this figure, the conditions for the occurrence of the various bifurcations can be interpreted as lines in

the (λ_s, λ_h) plane. For example, the primary steady-state bifurcation occurs along the line $\lambda_s = 0$, which is the horizontal axis in this representation. Similarly, the primary Hopf bifurcation occurs along the line $\lambda_h = 0$, which is the vertical axis. The conditions relevant to the birth of mixed modes also correspond to straight lines, as displayed in the figure. For both the wake problem (WFA or WFA-MC) and the TCF problem, variation of the base-flow parameters defines a path in the (λ_s, λ_h) plane. The bifurcation diagram can then be constructed by considering the successive crossings of this path with the lines defining the bifurcations.

Let us consider first the bifurcation scenario of the WFA-MC case as a function of Reynolds numbers η_{Re} and η_{Ri} , at a constant distance in terms of the second parameter from the organizing centre. We denote by $\eta_{Re}|_{Ri=Ri_c}$ the path followed at a constant Richardson number equal to that at which the unsteady and steady modes become simultaneously unstable, i.e., at the same critical Reynolds number. Similarly, we denote by $\eta_{Re}|_{Ri=0}$ the straight line path from quadrant III (defined by $\lambda_s < 0, \lambda_h < 0$), traversing quadrant IV ($\lambda_s > 0, \lambda_h < 0$), and then crossing into quadrant I ($\lambda_s > 0, \lambda_h > 0$). This path is relevant to the wake problem (WFA) for increasing the Reynolds number if we assume a linear dependence of the form eq. (13). When following this path, the first bifurcation is the primary bifurcation leading to the SS mode. There are two possible secondary bifurcations on this branch, leading to MM_0 and MM_π and these occur along the lines $-l_0\lambda_h + (C_r \pm D_r)\lambda_s = 0$ with positive sign for MM_0 and negative sign for MM_π . The sign of D_r indicates which of these bifurcations occurs first along the given path. For example, if $D_r < 0$, as displayed on the figure, the bifurcation to MM_π occurs first. Moreover, if $\Delta_- > 0$ (as assumed in the figure), this bifurcation is supercritical and gives rise to a stable branch. The bifurcation from SS to MM_π may occur subsequently, as found in the figure, but the branch born at this bifurcation is necessarily unstable, according to the considerations in section IV C.

Similarly, the lines $-(2B_r + A_r)\lambda_s + (l_1 \pm l_3)\lambda_h = 0$ indicate secondary bifurcations from SW to MM_0 (positive sign) and MM_π (negative sign). Starting from the pure SW mode and following the prescribed path backward, the sign of l_3 lets us distinguish which of these lines will be crossed first. For example, if $l_3 < 0$, as displayed on the figure, the bifurcation to MM_π occurs first, leading to a stable branch if $\Delta > 0$.

Figure 22b exhibits the case corresponding to $l_3 < 0$, $D_r < 0$, $\Delta_+ > 0$, $\Delta_- > 0$, the situation relevant to wake flow past a fixed disk. The figure displays the bifurcation diagram for a disk of aspect ratio $\chi = 10$. For more details, see section VIII B.

In the following, we analyze the predicted transition behavior of the flow past a fixed sphere and a fixed disk. In some figures, we use the lift coefficient to illustrate the bifurcation diagram; this is defined as $C_L = \frac{L}{\frac{1}{2}\rho_\infty U_\infty^2 D}$, with L the lift force, ρ_∞ , and U_∞ the density

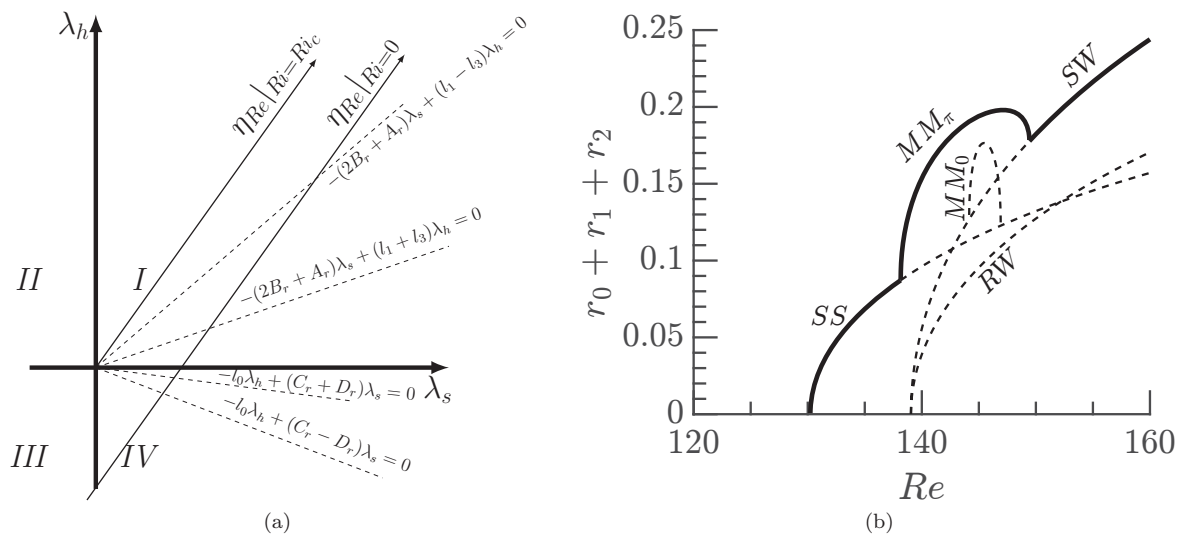


FIG. 22: Illustration of the construction of the stability diagram for the WFA problem with a fixed disk of aspect ratio $\chi = 10$. (a) The unfolding plane (λ_s, λ_h) . Dashed lines indicate the loci of bifurcations from SS and SW to $MM_{0,\pi}$. The paths labeled $\eta_{Re}|_{Ri=Ri_c}$ and $\eta_{Re}|_{Ri=0}$ are the paths followed in this plane for $Ri = Ri_c$ and $Ri = 0$, respectively. (b) Bifurcation diagram corresponding to the $\eta_{Re}|_{Ri=0}$ path. See section VIII B for details.

and velocity at the far field (assumed equal to unity) and D the diameter of the object.

A. Mixed convection in the flow past a sphere

Let us revisit the problem of pattern formation behind a sphere falling through a thermally stratified fluid. In our formulation the sphere is held fixed, with flow past it (the WFA-MC problem). This problem has many practical applications in engineering such as cooling, heating [26], sedimentation [53], melting [54], combustion [55], and vaporization [56]. A heated sphere represents a heat source embedded within the physical domain, where the solid body is subjected to forces of hydrodynamic and thermal origin. There are two main cases of interest. The case of a hot falling sphere where the fluid within the wake is accelerated with respect to the spherical body is called *assisting* case and is characterized by a positive Richardson number ($Ri > 0$). The opposite case, where the wake of a hot ascending spherical particle is decelerated by buoyancy effects, is referred to as the *opposing* case and corresponds to a negative Richardson number ($Ri < 0$). Kotouc et al. [26] studied numerically both configurations for two Prandtl numbers, $Pr = 0.72$ and $Pr = 7$. The assisting flow case displays an organising center of Hopf-Hopf type with azimuthal wavenumbers $m = 1$ and $m = 2$. The opposing flow configuration exhibits instead a point in the (Re, Ri) parameter space where a steady-state mode and a pair of unsteady modes with azimuthal wavenumber $m = \pm 1$ are simultaneously unstable.

The opposing flow case at $Pr = 0.72$ displays a

large variety of patterns. The codimension-two point at (Re_c, Ri_c) point, see tables XII and XIII, splits the parameter space in the following sense: for $Ri_c < Ri < 0$ the primary bifurcation breaks the axisymmetry of the steady-state solution, i.e., it corresponds to a steady-state mode (state I in Kotouc et al. [26]); for $Ri < Ri_c$ the primary branch is a standing wave (state XIV in Kotouc et al. [26]), i.e., a solution with mean-zero lift force preserving the symmetry plane. For Richardson numbers $Ri < Ri_c$ the observed transition to more complex spatio-temporal patterns is explained by the interaction between the unsteady pair of modes. In this regime the cubic truncation is degenerate, as already explained, and in order to lift the degeneracy between the modulated wave states MW and \widehat{IMM} (these states are labelled XX in Kotouc et al. and not distinguished) one must either include higher order terms in the normal form or introduce terms that break the $O(2)$ symmetry, see appendix B. These modulated wave states then bifurcate further, generating general Precessing Waves. In the study of Kotouc et al. [26], the authors did not observe PrW_G , and instead identified aperiodic states, i.e., states that did not display any particular spatiotemporal symmetry. This finding could be explained by a subsequent bifurcation towards a 3FW, although this is not taken into account in the normal form.

When $Ri > Ri_c$ a large variety of states exist. The axisymmetric steady state loses stability with respect to a nonaxisymmetric steady-state mode, thereby losing axisymmetry. The resulting SS state then transitions into a mixed mode MM_0 that preserves reflection symmetry and is associated with a nonzero mean lift. The MM_0 state further transitions into a general Precessing

TABLE XII: Location of the codimension-two point and the corresponding Strouhal number at unsteady onset, together with the linear coefficients in the normal form for the WFA-MC flow past a sphere or a disk.

Case	Re_c	Ri_c	St_c	λ_s	λ_h
Sphere	172	-0.13	$8.5 \cdot 10^{-2}$	$86.7 \cdot \eta_{Re} + 0.82 \cdot \eta_{Ri}$	$(84.7 - 67.9i) \cdot \eta_{Re} + (2.19 - 3.31i) \cdot \eta_{Ri}$
Disk $\chi = 10$	129.4	-0.069	$1.07 \cdot 10^{-1}$	$76.8 \cdot \eta_{Re} + 0.057 \cdot \eta_{Ri}$	$(66.0 - 25.2i) \cdot \eta_{Re} + (0.52 - 1.10i) \cdot \eta_{Ri}$
Disk $\chi = 3$	152.9	-0.079	$9.5 \cdot 10^{-2}$	$95.3 \cdot \eta_{Re} + 0.37 \cdot \eta_{Ri}$	$(92.5 - 40.0i) \cdot \eta_{Re} + (1.10 - 1.48i) \cdot \eta_{Ri}$

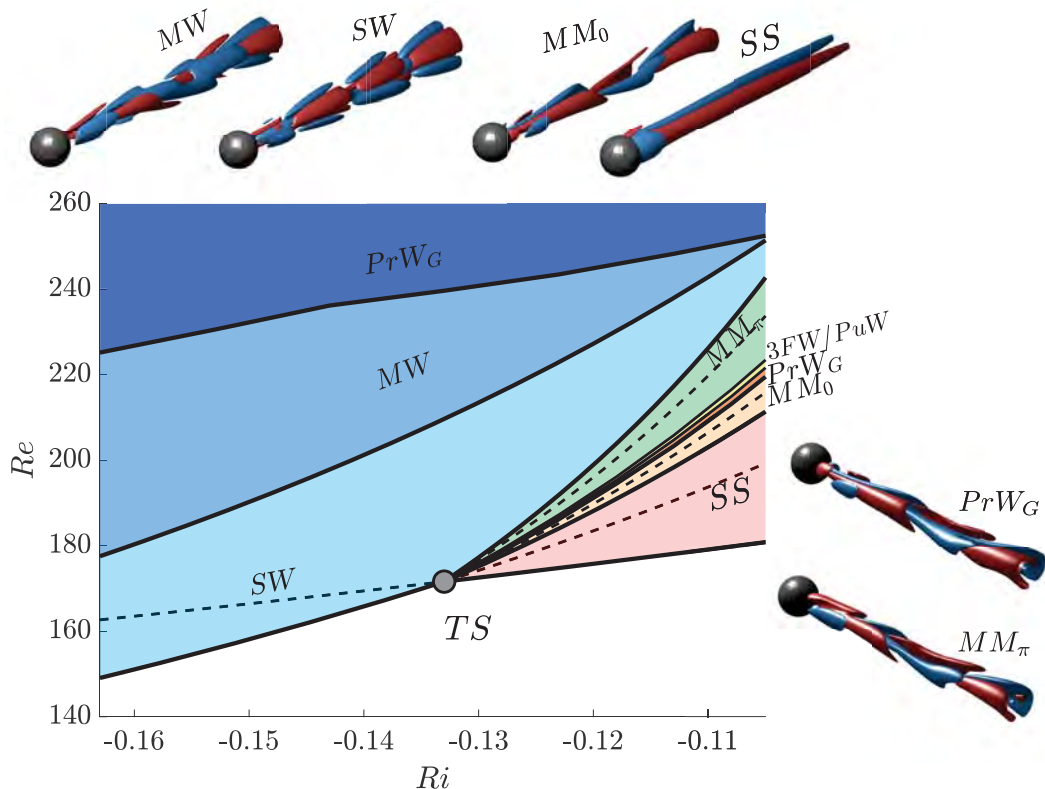


FIG. 23: The predicted patterns in the flow past a sphere under mixed convection (opposing flow) conditions in parameter space. Snapshots of the reconstructed states are included.

Wave (PrW_G), i.e., a state without a symmetry plane and slowly rotating mean lift, which in turn bifurcates into a 3FW and finally to a Pulsating Wave state. These three states are located within small regions of the parameter space. However, they have been numerically determined: PrW_G was numerically observed by Kotouc et al. [26] for $Ri > -0.1$ (state XIII) and the 3FW or PuW state were

identified for $Ri \approx -0.1$ (state XIX), which is a state that displays a temporary symmetry plane and at least two frequency components. The Pulsating Wave state eventually transitions into MM_π , i.e., a mixed mode without a symmetry plane (also state XIII in [26]). This series of bifurcations is followed either by a standing wave, or modulated wave modes or a Precessing Wave, which is in qualitative accordance with the study of Kotouc et al.

TABLE XIII: Cubic and quintic coefficients of the normal form for the WFA-MC flow past a sphere.

l_0	l_1	l_2	l_3	p_Δ^1
-10.57	-4.57	-0.078	0.27	-201.1
A	B	C	D	p_N^2
$1.07 + 0.75i$	$-2.8 + 3.54i$	$-3.78 + 3.02i$	$0.79 - 1.0i$	-18.10

B. Mixed convection in the flow past a disk

Let us now examine the transition scenario for axisymmetric wake flow past a disk, focusing on the *opposing flow* case under mixed convection conditions. This problem depends on three control parameters, the Reynolds number Re , the Richardson number Ri , and the aspect

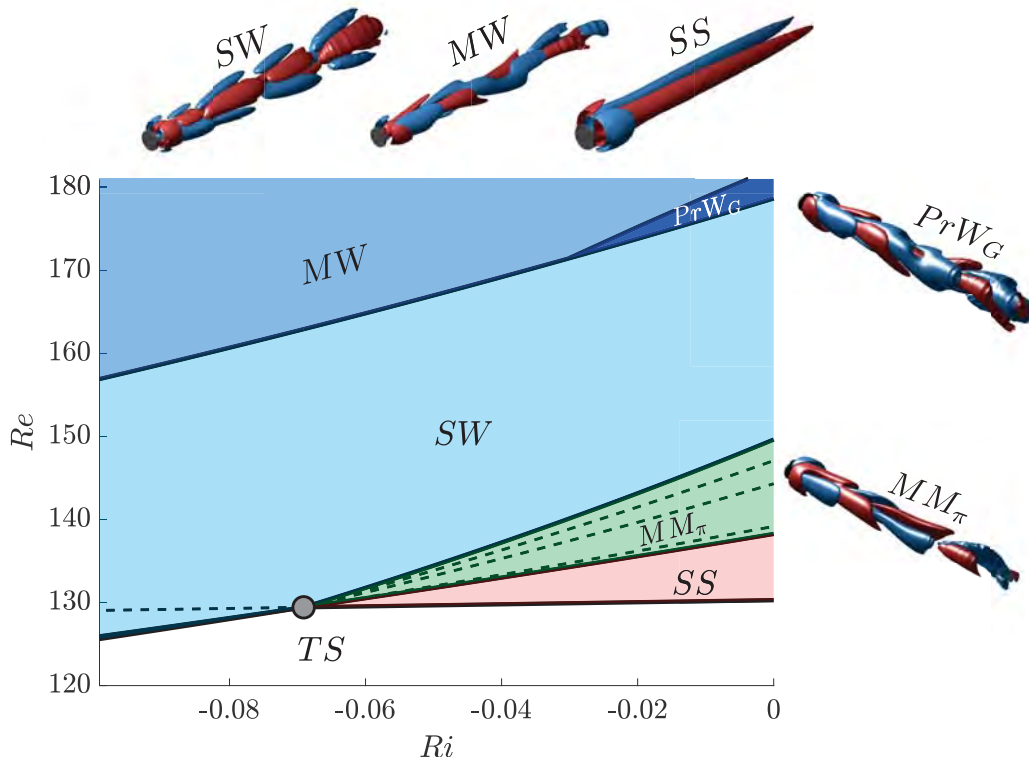


FIG. 24: The predicted patterns in the flow past a disk with $\chi = 10$ under mixed convection (opposing flow) conditions in parameter space. Snapshots of the reconstructed states are included.

ratio of the disk χ , where $1/\chi$ is the dimensionless thickness.

The WFA problem for $Ri = 0$ and $1/\chi \approx 0$ has already been studied by Fabre et al. [13] using numerical simulations and normal form coefficients fitted from the simulations. The case $\chi = 3$ was studied in detail by Auguste et al. [14]. A more rigorous study via multiple-scale analysis was performed by Meliga et al. [27]. Later, Chrust et al. [15] explored the flow dependence on the parameters (Re, χ) using numerical simulations and proposed a classification of the patterns observed. These studies demonstrated the importance of the disk thickness on the transition scenario. Chrust et al. observed that, when the thickness $1/\chi$ is large, for instance $\chi = 1$, the symmetry plane is preserved for large values of the Reynolds

number, i.e., only SS and MM_0 (possibly with modulated mixed modes or precessing waves) are observed before spatio-temporal chaos appears. In the limit of zero thickness, when $1/\chi \approx 0$, we will see that the transition scenario starts with the formation of a SS pattern followed by the breaking of the symmetry plane, leading to a MM_π mode and eventually to standing waves SW . At intermediate values of the thickness, a large variety of spatio-temporal patterns may be observed, as highlighted by the study of Auguste et al. In the present study, we shall look for the connections between the *opposing flow* case in mixed convection and the situation at $Ri = 0$, in terms of the spatio-temporal patterns observed in the flow.

Figure 25 displays the location of the codimension-two point corresponding to the Hopf-Steady State bifurcation obtained by varying $1/\chi \in [0, 1]$. The top panels show the corresponding temperature distribution in space and the growing extent of the recirculation bubble in the steady states associated with two distinct values of the aspect ratio χ of the disk. In the range of aspect ratios considered here, the critical Reynolds number grows linearly with the thickness $1/\chi$ of the disk, as previously observed by Fernandes et al. [18]. In addition, the critical Richardson number displays a maximum around $1/\chi \approx 0.1$ followed by a linear decrease in the critical Richardson number.

TABLE XIV: Cubic and quintic coefficients of the normal form for the WFA-MC flow past a disk with $\chi = 10$.

l_0	l_1	l_2	l_3	p_Δ^1
-4.45	-5.94	0.92	-2.28	-50
A	B	C	D	p_N^2
$0.1 - 1.29i$	$-2.14 + 1.69i$	$-0.64 - 2.35i$	$-1.05 + 1.10i$	-1

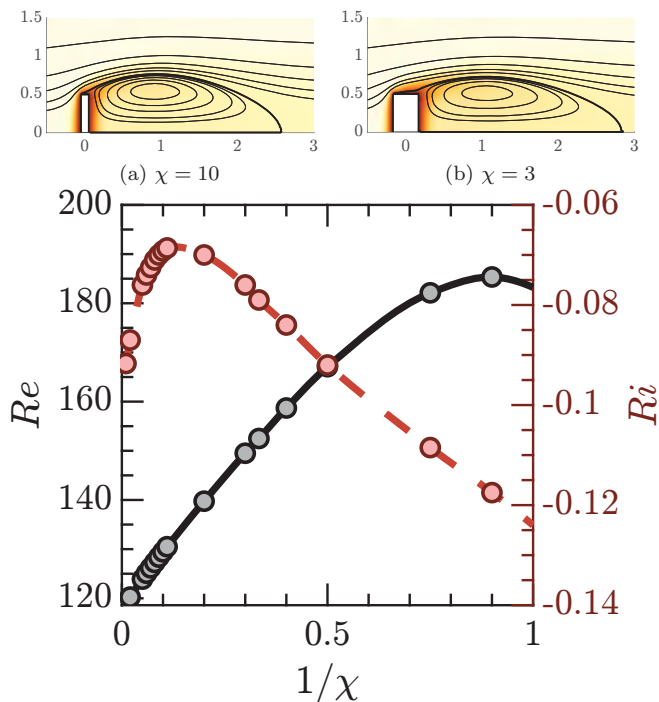


FIG. 25: The location of the codimension-two Hopf-Steady State bifurcation in the (Re, Ri) plane as a function of the aspect ratio χ of the disk (Re : black line; Ri : red line). The color-coded symbols refer to the points obtained in numerical computations. Top: temperature distribution of the trivial steady-state at (a) $1/\chi = 0.1$ ($Re \approx 130$, $Ri \approx -0.068$), (b) $1/\chi \approx 0.33$ ($Re \approx 150$, $Ri \approx -0.078$).

In the following we shall discuss in detail the two cases $\chi = 10$ and $\chi = 3$. The case $\chi = 10$ corresponds to a case with a relatively simple transition scenario, similar to that explained by Meliga et al. [27]. On the other hand, the case $\chi = 3$ displays a larger number of spatio-temporal structures, and is qualitatively similar to the case of the sphere discussed in section VIII A.

The parameter space summarizing the normal form predictions for $\chi = 10$ is displayed in fig. 24. In this case, to the left of the codimension-two point (grey point in the diagram), the trivial steady state transitions to standing waves and the subsequent bifurcations are uniquely explained by the unsteady modes. To the right of the codimension-two point the primary bifurcation breaks the axisymmetry of the steady state, i.e., it generates the SS state, followed by a periodic state with no reflection symmetry and non-zero mean lift, i.e., the MM_π state. The mixed mode MM_π state eventually bifurcates into a standing wave solution, which finally bifurcates to MW via the effect of higher order terms.

The dynamics near the organizing center for the flow past a disk with thickness $1/\chi = 1/3$ is richer. As in the previous cases, to the left of the organizing center

the transition scenario is based on the initial formation of standing waves, followed by modulated waves and an eventual tertiary bifurcation, not taken into account in the normal form, leading to temporal chaos. To the right of the organizing center the transition scenario is qualitatively similar to that of the sphere (compare section VIII A and fig. 26), although in the present case the codimension-two point is sufficiently close for the theory to provide quantitative predictions of the transition scenario. In other words, the transition scenario in the simple WFA problem of the disk with aspect ratio $\chi = 3$ is constrained by the dynamical structures emanating from the organizing center at $Ri \neq 0$, something that is not the case for the sphere, see Kotouc et al. [26, Fig 4.]. Figure 27 displays the reconstruction of the lift coefficient from the normal form at $Ri = 0$, in comparison to the results obtained numerically by Auguste et al. in [14]. It distinguishes five regions, with the *Knit-Knot* (KK) region among them. The transition begins at $Re \approx 159.4$ ($Re \approx 159.8$ [14]) via the formation of a steady-state pattern (SS), which eventually bifurcates into a mixed mode (MM_0) at around $Re \approx 182.5$ ($Re \approx 179.9$ in [14]). The MM_0 state loses stability at around $Re \approx 184.5$. Quantitatively, up to this point, the sequence of bifurcations is reasonably well predicted with regard to the data reported by [14]. The Knit-Knot region in our analysis covers a large variety of states with similar characteristics in terms of the frequency components (at least two), and the lift coefficient C_L . Auguste et al. [14] identified this motion as temporally quasiperiodic motion resulting from spontaneously broken reflection symmetry. The temporal dynamics of the KK state may be described as the composition of a state with frequency ω_h and a low frequency state, whose frequency experiences large variation within its region of existence (from $T_p \approx 96 \frac{2\pi}{\omega_h}$ at $Re = 185$ to $T_p \approx 48 \frac{2\pi}{\omega_h}$ at $Re = 187$ and then to $T_p \approx 54 \frac{2\pi}{\omega_h}$ at $Re = 190$, cf. fig. 29). This bifurcation sequence is followed by the appearance of the MM_π state, estimated to be around $Re \approx 198.5$ ($Re \approx 190.4$ in [14]) which connects to the standing wave branch at around $Re \approx 214$ ($Re \approx 215.2$ in [14]). According to theory, this sequence of bifurcations should be followed by the formation of a modulated wave branch and precessing waves. However, we do not discuss these patterns here due to the lack of simulation data to compare with and because these patterns can only be described using the fifth order normal form whose coefficients we have not computed.

TABLE XV: Cubic and quintic coefficients of the normal form for the WFA-MC flow past a disk with $\chi = 3$.

l_0	l_1	l_2	l_3	p_Δ^1
-6.19	-4.86	0.47	-2.76	-50
A	B	C	D	p_N^2
$0.56 - 0.38i$	$-2.3 + 2.3i$	$-1.7 + 0.32i$	$0.79 + 0.52i$	-6

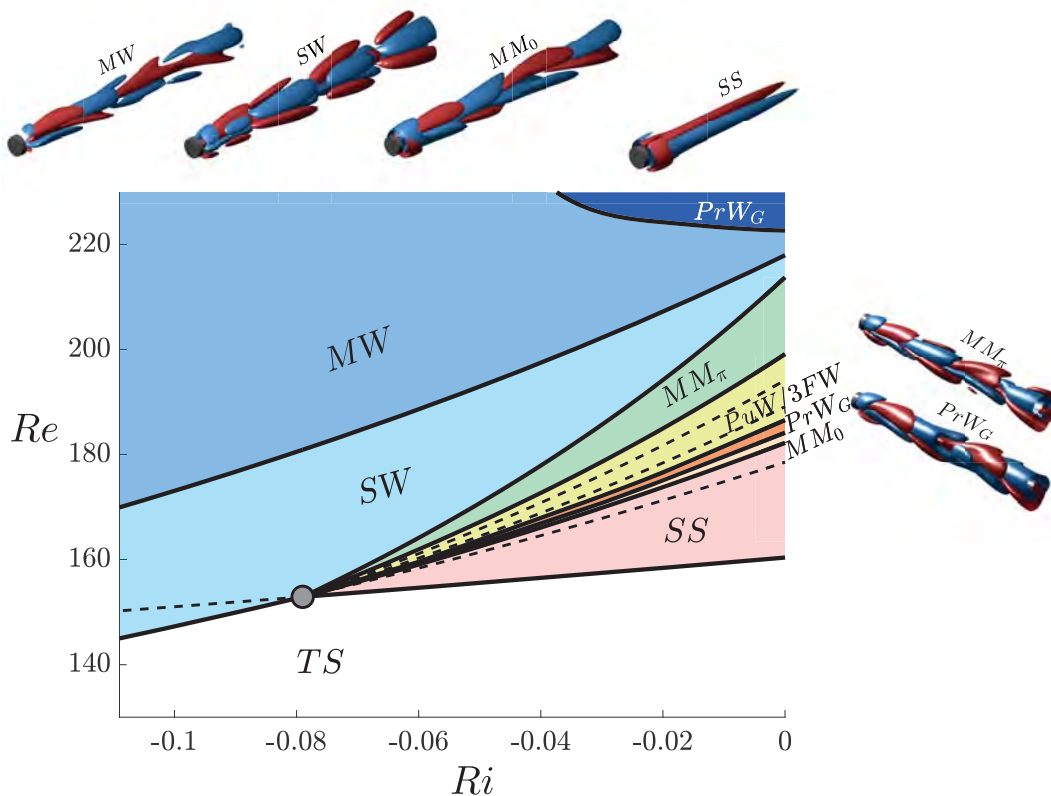


FIG. 26: The predicted patterns in the flow past a disk with $\chi = 3$ under mixed convection (opposing flow) conditions in parameter space. Snapshots of the reconstructed states are included.

For more information, see fig. 26.

Let us return to the discussion of the Knit-Knot region. In our more detailed analysis, this state is actually composed of several simpler states, see fig. 28. The MM_0 bifurcates into a precessing wave PrW_G at $Re \approx 184.5$. This precessing wave is stable up to $Re \approx 186.3$, where a saddle-node bifurcation takes place leading to a $3FW$, denoted as $3FW_A$ in fig. 28. The three-frequency wave is observable only in a small interval, however, and eventually reconnects to a Pulsating Wave via a global homoclinic bifurcation at around $Re \approx 186.9$. This Pulsating Wave is stable up to around $Re \approx 191.9$. At this stage, we can observe two other bifurcations leading to three-frequency waves with $3FW_B$ (unstable) and $3FW_C$ (stable); both of these branches reconnect to the main branch (PuW) following a saddle node bifurcation of limit cycles. The pulsating wave state finally reconnects with the symmetry-breaking mixed mode (MM_π) branch.

IX. DISCUSSION & CONCLUSION

In this article, we have analyzed the properties of the normal form and the bifurcation scenario relevant to the bifurcations observed in axisymmetric wakes described by the Navier–Stokes equation. We have shown that near

the onset of instability, it is possible to reduce the dynamics via center manifold reduction to a normal form, i.e., an ordinary differential equation, whose unfolding fully captures the local behavior of the Navier-Stokes equation. Such normal forms inherit the discrete and continuous symmetries of the system, in the present case $O(2)$ symmetry. We have shown that this approach, carried out in the vicinity of a steady state-Hopf interaction, suffices to predict much of the observed behavior.

Our analysis of the generic steady state-Hopf case relied on a reduction to polar coordinates. The fixed point solutions of the normal form, e.g. the pure modes and the mixed modes, have been observed in a variety of fluid flows, including Taylor-Couette and wake flows. Here, we have attempted to provide a complete description of the fixed point solutions of the normal form, as well as possible bifurcations to periodic solutions of the polar normal form corresponding to two- and three-frequency waves.

Particularly noteworthy is our discovery of robust, potentially attracting, heteroclinic cycles in this mode interaction. In previous studies [57, 58], self-sustained processes have been related to a three-step process involving rolls advecting streamwise velocity, leading to streaks which once unstable lead to wavy perturbations whose nonlinear interaction with itself feeds the rolls. In terms of the mode interaction, the self-sustained cycle described

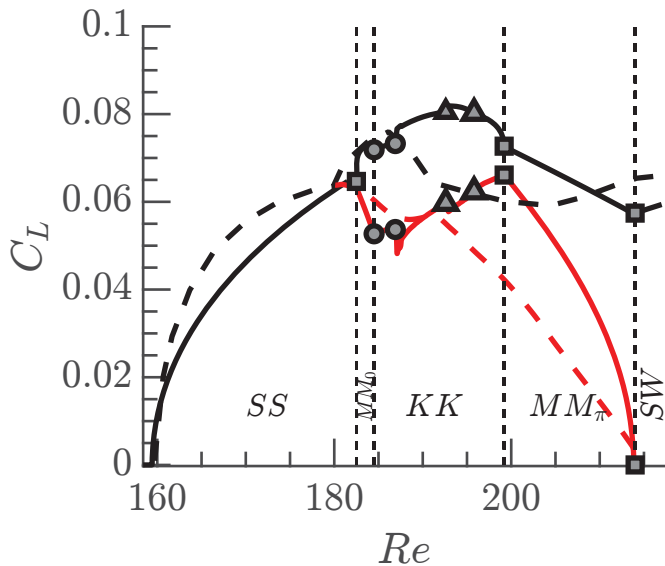


FIG. 27: Bifurcation diagram in terms of the lift coefficient C_L for the WFA problem ($Ri = 0$) with $\chi = 3$. Solid lines were computed from the normal form, dashed lines were extracted from [14]. Black lines denote $C_{L,max}$ and red lines denote the average of C_L . See legend in fig. 28 for a description of the markers.

by Dessup *et al.* [57] corresponds to a Het_{SS-SW} cycle or to an orbit that shadows it. In this sense, one could expect that other, more complex dynamics, for instance a $\text{Het}_{Pr,WA}$ cycle, may also be observed in the bifurcation scenario of real fluid systems. We mention that the indefinite increase in period associated with the approach to an attracting robust heteroclinic cycle cannot in general be seen in numerical integration of the normal form, on account of rounding error. Instead, the solution trajectory settles into a statistical limit cycle with a finite mean period [59]. This is even more so for partial differential equations [60] and in experiments where the presence of noise prevents approach to such a cycle [61]. This fact points to the importance of fluctuations in applications of the theory to fluid dynamics problems, as also emphasized in [47] in connection with the SNIPER bifurcation.

We have applied here the general theory to several distinct fluid flows and used it to explore the bifurcation scenario of wake flows behind a sphere or disk falling through either a constant density fluid or a vertically stratified fluid (problems WFA and WFA-MC, respectively). In particular, in section VII, we determined the normal form coefficients for these problems on the assumption that each object is held fixed, and used these results in section VIII to construct consistent stability diagrams for these flows, comparing the predicted bifurcation scenarios for mixed-convection flow past a fixed axisymmetric object, a disk and a sphere, with the results of direct numerical simulations of these flows. These results enabled us to rationalize the results of previous numerical studies including those in the complicated Knit-Knot region of

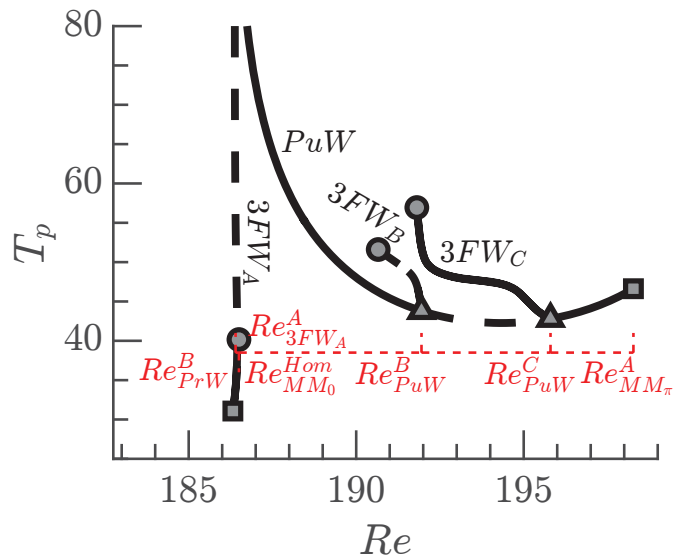


FIG. 28: Bifurcation diagram in the *Knit-Knot* region of fig. 27 in terms of the period T_P of the low frequency modulation. Square markers: Hopf bifurcation. Circles: saddle-node bifurcation. Triangles: Neimark-Sacker bifurcation.

Auguste *et al.* [14] for the WFA problem for a disk with thickness $\chi = 3$ and the WFA-MC problem for a sphere of Kotouč *et al.* [26], states XIII or XIX, thereby demonstrating the utility of our bifurcation-theoretic approach. Unfortunately, neither of these cases predicts the presence of structurally stable heteroclinic cycles, although such states may arise for other parameter values.

Acknowledgement. The work of EK was supported in part by the National Science Foundation under Grant No. DMS-1908891.

Appendix A: Normal form reduction

1. Third order forcing terms

The third order forcing terms are obtained from the substitution of the Ansatz (58) into $\mathbf{F}(\mathbf{q}, \boldsymbol{\eta})$. The general expression of the third order forcing term $\mathbf{F}_{(\varepsilon^3)}$ is as follows:

$$\begin{aligned} \mathbf{F}_{(\varepsilon^3)} \equiv & \sum_{\substack{j=-2 \\ k,\ell=-2}}^2 a_j a_k a_\ell [\mathbf{N}(\hat{\mathbf{q}}_j, \hat{\mathbf{q}}_{k,\ell}) + \mathbf{N}(\hat{\mathbf{q}}_{k,\ell}, \hat{\mathbf{q}}_j)] e^{-im_n \theta} e^{-i\omega_n t} \\ & + \sum_{j=-2, \ell=0}^2 a_j \Delta \eta_\ell [\mathbf{N}(\hat{\mathbf{q}}_j, \mathbf{Q}_0^{(\eta_\ell)}) + \mathbf{N}(\mathbf{Q}_0^{(\eta_\ell)}, \hat{\mathbf{q}}_j)] e^{-im_j \theta} e^{-i\omega_j t} \\ & + \sum_{j=-2, \ell=0}^2 a_j \Delta \eta_\ell \mathbf{G}(\hat{\mathbf{q}}_j, \mathbf{e}_\ell) e^{-im_j \theta} e^{-i\omega_j t}, \end{aligned} \quad (\text{A1})$$

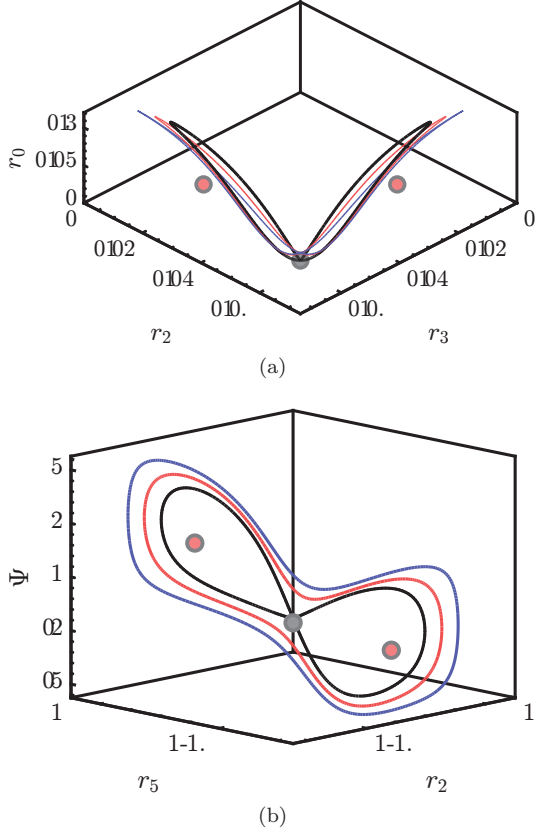


FIG. 29: The ambiclinic orbit $Re_{MM_0}^{\text{Hom}}$ (gray line) at $Re = 186.4$ of fig. 28. The gray dot is the location of MM_0 while the red markers indicate the location of the PrW_G states. The red and blue trajectories represent limit cycles for higher values of Re ; the period T_P of these states diverges logarithmically as $Re \rightarrow 186.4$ from above (not shown).

with a slight abuse of notation such that $\hat{\mathbf{q}}_j = \bar{\mathbf{q}}_{-j}$, $\hat{\mathbf{q}}_{k,j} = \bar{\mathbf{q}}_{-k,-j}$ and $a_j = \bar{a}_{-j}$. Therefore, the azimuthal wavenumber and the frequency associated with a negative index are both considered to be of the opposite sign, i.e., $\omega_{-j} = -\omega_j$ and $m_{-j} = -m_j$. Finally, ω_n and m_n are defined by the relations $\omega_n = \omega_j + \omega_k + \omega_\ell$, $m_n = m_j + m_k + m_\ell$, where $n = j + k + \ell$.

Resonant terms are those for which (ω_n, m_n) is equal to either $(0, m_0)$, (ω_1, m_1) or $(\omega_1, -m_1)$ (plus the complex conjugate pairs). The remaining terms only play a role in higher-order truncations.

Hierarchically, the first class of third-order forcing terms are those that are linear with respect to the amplitudes a_j for $j = 0, 1, 2$,

$$\hat{\mathbf{F}}_{(\varepsilon^3)}^{(a_j)} \equiv \sum_{\ell=0}^2 \Delta\eta_\ell \left([\mathbf{N}(\hat{\mathbf{q}}_j, \mathbf{Q}_0^{(\eta_\ell)}) + \mathbf{N}(\mathbf{Q}_0^{(\eta_\ell)}, \hat{\mathbf{q}}_j)] + \mathbf{G}(\hat{\mathbf{q}}_j, \mathbf{e}_\ell) \right). \quad (\text{A2})$$

The second type of resonant forcing terms are those used to compute the real coefficients l_j for $j = 0, 1, 2, 3$.

They are proportional to the cubic terms in the first equation of the complex normal form (8), and are given by

$$\hat{\mathbf{F}}_{(\varepsilon^3)}^{(a_0|a_0|^2)} \equiv [\mathbf{N}(\hat{\mathbf{q}}_0, \hat{\mathbf{q}}_0, -0) + \mathbf{N}(\hat{\mathbf{q}}_0, -0, \hat{\mathbf{q}}_0)] + [\mathbf{N}(\hat{\mathbf{q}}_{-0}, \hat{\mathbf{q}}_0, 0) + \mathbf{N}(\hat{\mathbf{q}}_0, 0, \hat{\mathbf{q}}_{-0})], \quad (\text{A3})$$

with the notation $\hat{\mathbf{q}}_{-0} = \bar{\mathbf{q}}_0$. Similarly, the terms $\hat{\mathbf{F}}_{(\varepsilon^3)}^{(a_0|a_j|^2)}$ for $j = 1, 2$ are given by

$$\hat{\mathbf{F}}_{(\varepsilon^3)}^{(a_0|a_j|^2)} \equiv [\mathbf{N}(\hat{\mathbf{q}}_0, \hat{\mathbf{q}}_j, -j) + \mathbf{N}(\hat{\mathbf{q}}_j, -j, \hat{\mathbf{q}}_0)] + [\mathbf{N}(\hat{\mathbf{q}}_{-j}, \hat{\mathbf{q}}_0, j) + \mathbf{N}(\hat{\mathbf{q}}_0, j, \hat{\mathbf{q}}_{-j})] + [\mathbf{N}(\hat{\mathbf{q}}_j, \hat{\mathbf{q}}_0, -j) + \mathbf{N}(\hat{\mathbf{q}}_0, -j, \hat{\mathbf{q}}_j)], \quad (\text{A4})$$

while $\hat{\mathbf{F}}_{(\varepsilon^3)}^{(\bar{a}_0 a_1 \bar{a}_2)}$ is expressed as

$$\hat{\mathbf{F}}_{(\varepsilon^3)}^{(\bar{a}_0 a_1 \bar{a}_2)} \equiv [\mathbf{N}(\hat{\mathbf{q}}_{-0}, \hat{\mathbf{q}}_1, -2) + \mathbf{N}(\hat{\mathbf{q}}_1, -2, \hat{\mathbf{q}}_{-0})] + [\mathbf{N}(\hat{\mathbf{q}}_1, \hat{\mathbf{q}}_{-0}, -2) + \mathbf{N}(\hat{\mathbf{q}}_{-0}, -2, \hat{\mathbf{q}}_1)] + [\mathbf{N}(\hat{\mathbf{q}}_{-2}, \hat{\mathbf{q}}_{-0}, 1) + \mathbf{N}(\hat{\mathbf{q}}_{-0}, 1, \hat{\mathbf{q}}_{-2})]. \quad (\text{A5})$$

The third class of forcing terms are those used for the computation of the complex coefficients A, B, C and D . These are $\hat{\mathbf{F}}_{(\varepsilon^3)}^{(a_j|a_j|^2)}$ for $j = 1, 2$:

$$\hat{\mathbf{F}}_{(\varepsilon^3)}^{(a_j|a_j|^2)} \equiv [\mathbf{N}(\hat{\mathbf{q}}_j, \hat{\mathbf{q}}_j, -j) + \mathbf{N}(\hat{\mathbf{q}}_j, -j, \hat{\mathbf{q}}_j)] + [\mathbf{N}(\hat{\mathbf{q}}_{-j}, \hat{\mathbf{q}}_j, j) + \mathbf{N}(\hat{\mathbf{q}}_j, j, \hat{\mathbf{q}}_{-j})], \quad (\text{A6})$$

$\hat{\mathbf{F}}_{(\varepsilon^3)}^{(a_j|a_k|^2)}$ for $j = 1, 2$ and $k = 0, 1, 2$ with $j \neq k$,

$$\hat{\mathbf{F}}_{(\varepsilon^3)}^{(a_j|a_k|^2)} \equiv [\mathbf{N}(\hat{\mathbf{q}}_j, \hat{\mathbf{q}}_k, -k) + \mathbf{N}(\hat{\mathbf{q}}_k, -k, \hat{\mathbf{q}}_j)] + [\mathbf{N}(\hat{\mathbf{q}}_{-k}, \hat{\mathbf{q}}_j, k) + \mathbf{N}(\hat{\mathbf{q}}_j, k, \hat{\mathbf{q}}_{-k})] + [\mathbf{N}(\hat{\mathbf{q}}_k, \hat{\mathbf{q}}_j, -k) + \mathbf{N}(\hat{\mathbf{q}}_j, -k, \hat{\mathbf{q}}_k)]. \quad (\text{A7})$$

Finally, the term $\hat{\mathbf{F}}_{(\varepsilon^3)}^{(a_0 a^2)}$ is expressed as

$$\hat{\mathbf{F}}_{(\varepsilon^3)}^{(a_0 a^2)} \equiv [\mathbf{N}(\hat{\mathbf{q}}_0, \hat{\mathbf{q}}_0, 2) + \mathbf{N}(\hat{\mathbf{q}}_0, 2, \hat{\mathbf{q}}_0)] + [\mathbf{N}(\hat{\mathbf{q}}_2, \hat{\mathbf{q}}_0, 0) + \mathbf{N}(\hat{\mathbf{q}}_0, 0, \hat{\mathbf{q}}_2)]. \quad (\text{A8})$$

Appendix B: Modulated wave mode

The modulated wave mode is a degenerate solution of the normal form (8) truncated at third order. Crawford & Knobloch [32] analyzed the unfolding of the three simplest degeneracy conditions: (i) $A_r + 2B_r = 0$, (ii) $B_r = 0$ and (iii) $A_r = 0$. Hereinafter, we do not aim to provide the complete picture of the unfolding, which was the concern of Crawford & Knobloch [32]. However, we briefly summarize some of their results, and list sufficient conditions for the stability and branching of the modulated wave solution.

The existence of the MW solution is subject to the following conditions

$$\begin{aligned} p^1(0, r_1^2 + r_2^2, (r_2^2 - r_1^2)^2, 0, 0, \lambda) &\equiv 0 \\ p^2(0, r_1^2 + r_2^2, (r_2^2 - r_1^2)^2, 0, 0, \lambda) &\equiv 0. \end{aligned} \quad (\text{B1})$$

Hill and Stewart [62] observed that the condition $p^2 \equiv 0$ is a degeneracy condition if one evaluates the polynomial p^2 at the origin, i.e. $p^2(0,0,0,0,0) \equiv A_r$. Since, to fifth order,

$$\begin{aligned} p^1(0, r_1^2 + r_2^2, (r_2^2 - r_1^2)^2, 0, 0, \lambda) &\equiv \\ \lambda_h + (\frac{1}{2}A_r + B_r)(r_1^2 + r_2^2) & \\ + p_\Delta^1(r_2^2 - r_1^2)^2 + p_N^1(r_1^2 + r_2^2)^2, & \quad (\text{B2}) \\ p^2(0, r_1^2 + r_2^2, (r_2^2 - r_1^2)^2, 0, 0, \lambda) &\equiv \\ \frac{1}{2}A_r + p_N^2(r_1^2 + r_2^2) + p_\Delta^2(r_2^2 - r_1^2)^2, & \end{aligned}$$

the $\{r_1, r_2\}$ evolution is given by

$$\begin{aligned} \dot{r}_1 &= r_1 \left[\lambda_h + B_r r_1^2 + (A_r + B_r) r_2^2 \right. \\ &\quad + (p_\Delta^1 + p_N^1 - p_N^2) r_1^4 + (p_\Delta^1 + p_N^1 + p_N^2) r_2^4 \\ &\quad \left. + 2(p_N^1 - p_\Delta^1) r_2^2 r_1^2 + p_\Delta^2 (r_2^2 - r_1^2)^3 \right], \\ \dot{r}_2 &= \kappa \cdot \dot{r}_1, \end{aligned} \quad (\text{B3})$$

where $\kappa \cdot \dot{r}_1$ stands for the action of the reflection symmetry, defined in eq. (6), and $p_\Delta^2 = 0$ to restrict the equation to fifth order. Inspection of eq. (B3) shows that the fixed points r_a, r_b satisfy

$$\begin{aligned} r_a^2 &= \frac{1}{2} \left[-\frac{A_r}{2p_N^2} - \sqrt{\frac{\chi}{4p_N^2 p_\Delta^1}} \right] \\ r_b^2 &= \frac{1}{2} \left[-\frac{A_r}{2p_N^2} + \sqrt{\frac{\chi}{4p_N^2 p_\Delta^1}} \right], \end{aligned} \quad (\text{B4})$$

where the symbol χ , which is a function of the parameter λ_h , is defined in table VI. Evidently, the MW states exist when $A_r/p_N^2 < 0$ and $0 < \chi/(p_N^2 p_\Delta^1) < A_r^2/(p_N^2)^2$.

The stability within the MW subspace, i.e. with respect to perturbations in $\{r_1, r_2\}$ only, can be analysed in terms of the determinant and trace of the Jacobian stability matrix restricted to this subspace:

$$\det(M^{MW}) = 32p_N^2 p_\Delta^1 r_a^2 r_b^2 (r_a - r_b)^2 (r_a + r_b)^2, \quad (\text{B5a})$$

$$\begin{aligned} \text{tr}(M^{MW}) &= \frac{A_r}{p_N^2} \left[\frac{A_r p_N^1}{p_N^2} - \frac{1}{2}(A_r + 2B_r) \right] \\ &\quad + (r_a^2 - r_b^2)^2 (4p_\Delta^1 - 2p_N^2), \end{aligned} \quad (\text{B5b})$$

In view of eq. (B5a), the determinant vanishes when $r_a r_b = 0$ corresponding to the rotating wave branch and when $r_a = r_b$ corresponding to the standing wave branch. Therefore, the modulated wave branch connects the branches of rotating and standing waves. The standing waves changes stability when $\sigma_{SW} \equiv -2r_{SW}^2(A_r + 4r_{SW}^2 p_N^2)$ changes sign, which can happen if $A_r p_N^2 < 0$. The corresponding standing wave amplitude is given by $r_{SW}^2 = -\frac{A_r}{4p_N^2}$. The standing wave emerges as a stable (resp. unstable) solution within the $\{r_1, r_2\}$ subspace if $A_r > 0$ (resp. $A_r < 0$) and it becomes unstable (resp. stable) when $r_{SW}^2 = -\frac{A_r}{4p_N^2}$. The stability of the rotating wave within the $\{r_1, r_2\}$ subspace is determined by the eigenvalue $\sigma_{RW} \equiv -r_{RW}^2(A_r - 2r_{RW}^2 p_N^2)$ which is stable (resp. unstable) if $A_r < 0$ (resp. $A_r > 0$). The corresponding amplitude is $r_{RW}^2 = -\frac{A_r}{2p_N^2}$.

The conditions on the determinant show that the MW branch does not experience steady bifurcations, except at the two end points. The MW solution is stable if $\det(M^{MW}) > 0$, that is, $p_N^2 p_\Delta^1 > 0$, and the trace is negative. It is sufficient to ensure that the trace is negative at the end points, which is ensured if $A_r > 0$, $p_N^2 < 0$, $p_\Delta^1 < 0$ and $B_r + A_r < 0$. Otherwise, the MW branch may experience a Hopf bifurcation leading to a 3FW.

Let us now focus on the stability of the MW branch with respect to perturbations in the variable r_0 . We see that the MW can bifurcate into a Precessing Wave solution whenever,

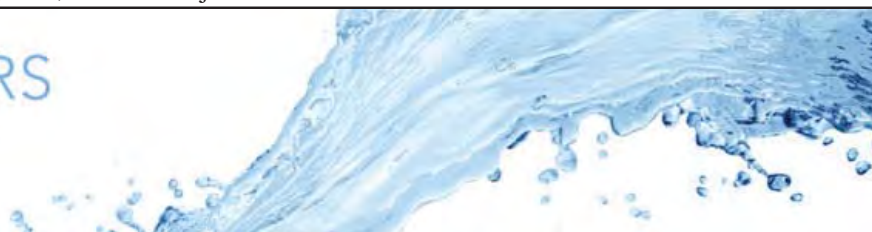
$$\lambda_s - l_1 \frac{A_r}{p_N^2} \geq 0.$$

In the supercritical case, the PrW connects in parameter space a Mixed Mode with a Modulated Wave Mode. Finally, a possible scenario for a bifurcation from a PrW towards a three-frequency wave arises whenever eq. (9d) does not possess a fixed point.

-
- [1] M. Golubitsky and M. Roberts, A classification of degenerate hopf bifurcations with $O(2)$ symmetry, *Journal of Differential Equations* **69**, 216 (1987).
 - [2] J. D. Crawford and E. Knobloch, Symmetry and symmetry-breaking bifurcations in fluid mechanics, *Annual Review of Fluid Mechanics* **23**, 341 (1991).
 - [3] M. Golubitsky and W. Langford, Pattern formation and bistability in flow between counterrotating cylinders, *Physica D: Nonlinear Phenomena* **32**, 362 (1988).
 - [4] P. Chossat and G. Iooss, *The Couette-Taylor Problem*, Vol. 102 (Springer Science & Business Media, 2012).
 - [5] M. Golubitsky, J. Swift, and E. Knobloch, Symmetries and pattern selection in rayleigh-bénard convection, *Physica D: Nonlinear Phenomena* **10**, 249 (1984).
 - [6] J. Sierra, D. Fabre, V. Citro, and F. Giannetti, Bifurcation scenario in the two-dimensional laminar flow past a rotating cylinder, *Journal of Fluid Mechanics* **905**, A2 (2020).
 - [7] D. Ormières and M. Provansal, Transition to turbulence in the wake of a sphere, *Physical Review Letters* **83**, 80 (1999).
 - [8] K. Gumowski, J. Miedzik, S. Goujon-Durand, P. Jenffer, and J. Wesfreid, Transition to a time-dependent state of fluid flow in the wake of a sphere, *Physical Review E* **77**, 055308 (2008).
 - [9] R. Natarajan and A. Acrivos, The instability of the

- steady flow past spheres and disks, *Journal of Fluid Mechanics* **254**, 323 (1993).
- [10] B. Ghidersa and J. Dušek, Breaking of axisymmetry and onset of unsteadiness in the wake of a sphere, *Journal of Fluid Mechanics* **423**, 33 (2000).
- [11] A. G. Tomboulides and S. A. Orszag, Numerical investigation of transitional and weak turbulent flow past a sphere, *Journal of Fluid Mechanics* **416**, 45 (2000).
- [12] J. Sierra-Ausin, M. Lorite-Diez, J. Jimenez-Gonzalez, V. Citro, and D. Fabre, Unveiling the competitive role of global modes in the pattern formation of rotating sphere flows, *Journal of Fluid Mechanics* **942** (2022).
- [13] D. Fabre, F. Auguste, and J. Magnaudet, Bifurcations and symmetry breaking in the wake of axisymmetric bodies, *Physics of Fluids* **20**, 051702 (2008).
- [14] F. Auguste, D. Fabre, and J. Magnaudet, Bifurcations in the wake of a thick circular disk, *Theoretical and Computational Fluid Dynamics* **24**, 305 (2010).
- [15] M. Chrust, G. Bouchet, and J. Dušek, Parametric study of the transition in the wake of oblate spheroids and flat cylinders, *Journal of Fluid Mechanics* **665**, 199 (2010).
- [16] P. Ern, F. Risso, D. Fabre, and J. Magnaudet, Wake-induced oscillatory paths of bodies freely rising or falling in fluids, *Annual Review of Fluid Mechanics* **44**, 97 (2012).
- [17] P. Fernandes, P. Ern, F. Risso, and J. Magnaudet, On the zigzag dynamics of freely moving axisymmetric bodies, *Physics of Fluids* **17**, 098107 (2005).
- [18] P. C. Fernandes, F. Risso, P. Ern, and J. Magnaudet, Oscillatory motion and wake instability of freely rising axisymmetric bodies, *Journal of Fluid Mechanics* **573**, 479 (2007).
- [19] P. C. Fernandes, P. Ern, F. Risso, and J. Magnaudet, Dynamics of axisymmetric bodies rising along a zigzag path, *Journal of Fluid Mechanics* **606**, 209 (2008).
- [20] F. Auguste, J. Magnaudet, and D. Fabre, Falling styles of disks, *Journal of Fluid Mechanics* **719**, 388 (2013).
- [21] M. Chrust, S. Goujon-Durand, and J. E. Wesfreid, Loss of a fixed plane symmetry in the wake of a sphere, *Journal of Fluid Mechanics* **41**, 51 (2013).
- [22] J. Tchoufag, D. Fabre, and J. Magnaudet, Global linear stability analysis of the wake and path of buoyancy-driven disks and thin cylinders, *Journal of Fluid Mechanics* **740**, 278 (2014).
- [23] J. Tchoufag, D. Fabre, and J. Magnaudet, Weakly nonlinear model with exact coefficients for the fluttering and spiraling motion of buoyancy-driven bodies, *Physical Review Letters* **115**, 114501 (2015).
- [24] J. Tchoufag, J. Magnaudet, and D. Fabre, Linear instability of the path of a freely rising spheroidal bubble, *Journal of Fluid Mechanics* **751**, R4 (2014).
- [25] P. Bonnefis, D. Fabre, and J. Magnaudet, When, how, and why the path of an air bubble rising in pure water becomes unstable, *Proceedings of the National Academy of Sciences* **120**, e2300897120 (2023).
- [26] M. Kotouč, G. Bouchet, and J. Dušek, Transition to turbulence in the wake of a fixed sphere in mixed convection, *Journal of Fluid Mechanics* **625**, 205 (2009).
- [27] P. Meliga, J.-M. Chomaz, and D. Sipp, Global mode interaction and pattern selection in the wake of a disk: a weakly nonlinear expansion, *Journal of Fluid Mechanics* **633**, 159 (2009).
- [28] M. Golubitsky, I. Stewart, and D. G. Schaeffer, *Singularities and Groups in Bifurcation Theory: Volume II*, Vol. 69 (Springer Science & Business Media, 2012).
- [29] P. Hirschberg and E. Knobloch, Zigzag and varicose instabilities of a localized stripe, *Chaos: An Interdisciplinary Journal of Nonlinear Science* **3**, 713 (1993).
- [30] P. Hirschberg and E. Knobloch, A robust heteroclinic cycle in an steady-state mode interaction, *Nonlinearity* **11**, 89 (1998).
- [31] G. Mougin and J. Magnaudet, Path instability of a rising bubble, *Physical Review Letters* **88**, 014502 (2001).
- [32] E. Knobloch, On the degenerate hopf bifurcation with $O(2)$ symmetry, *Contemporary Mathematics* **56**, 193 (1986).
- [33] S. A. van Gils and J. Mallet-Paret, Hopf bifurcation and symmetry: travelling and standing waves on the circle, *Proceedings of the Royal Society of Edinburgh, Section A: Mathematics* **104**, 279 (1986).
- [34] A. S. Landsberg and E. Knobloch, Direction-reversing traveling waves, *Physics Letters A* **159**, 17 (1991).
- [35] J. D. Crawford, M. Golubitsky, and W. F. Langford, Modulated rotating waves in $O(2)$ mode interactions, *Dynamics and Stability of Systems* **3**, 159 (1988).
- [36] M. J. Field, Equivariant dynamical systems, *Transactions of the American Mathematical Society* **259**, 185 (1980).
- [37] J. Guckenheimer and P. Holmes, Structurally stable heteroclinic cycles, *Mathematical Proceedings of the Cambridge Philosophical Society* **103**, 189 (1988).
- [38] M. Krupa and I. Melbourne, Asymptotic stability of heteroclinic cycles in systems with symmetry, *Ergodic Theory and Dynamical Systems* **15**, 121 (1995).
- [39] M. Krupa and I. Melbourne, Asymptotic stability of heteroclinic cycles in systems with symmetry II, *Proceedings of the Royal Society of Edinburgh, Section A: Mathematics* **134**, 1177 (2004).
- [40] I. Melbourne, P. Chossat, and M. Golubitsky, Heteroclinic cycles involving periodic solutions in mode interactions with $O(2)$ symmetry, *Proceedings of the Royal Society of Edinburgh, Section A: Mathematics* **113**, 315 (1989).
- [41] E. Knobloch and M. Silber, Oscillatory convection in a rotating layer, *Physica D: Nonlinear Phenomena* **63**, 213 (1993).
- [42] D. A. Weinberg, Canonical forms for symmetric tensors, *Linear algebra and its applications* **57**, 271 (1984).
- [43] J. Porter and E. Knobloch, New type of complex dynamics in the 1:2 spatial resonance, *Physica D: Nonlinear Phenomena* **159**, 125 (2001).
- [44] J. Porter and E. Knobloch, Complex dynamics in the 1:3 spatial resonance, *Physica D: Nonlinear Phenomena* **143**, 138 (2000).
- [45] W. Govaerts, Y. A. Kuznetsov, H. Meijer, B. Al-Hdaibat, V. De Witte, A. Dhooge, W. Mestrom, N. Neirynck, A. Riet, and B. Sautois, *MATCONT: Continuation toolbox for ODEs in Matlab* (2019).
- [46] M. K. S. Yeung and S. H. Strogatz, Nonlinear dynamics of a solid-state laser with injection, *Physical Review E* **58**, 4421 (1998).
- [47] F. Pétrélis, S. Fauve, E. Dormy, and J.-P. Valet, Simple mechanism for reversals of Earth's magnetic field, *Physical Review Letters* **102**, 144503 (2009).
- [48] L. P. Shil'nikov, A case of the existence of a countable number of periodic motions, *Soviet Math. Doklady* **6**, 163 (1965).
- [49] P. Glendinning and C. Sparrow, Local and global behaviour near homoclinic orbits, *Journal of Statistical*

- Physics **35**, 645 (1984).
- [50] L. P. Shilnikov and A. Shilnikov, Shilnikov bifurcation, *Scholarpedia* **2**, 1891 (2007), revision #194931.
- [51] E. Knobloch, D. R. Moore, J. Toomre, and N. O. Weiss, Transitions to chaos in double-diffusive convection, *Journal of Fluid Mechanics* **166**, 409 (1986).
- [52] E. Knobloch and D. R. Moore, Minimal model of binary fluid convection, *Physical Review A* **42**, 4693 (1990).
- [53] H. Gan, J. Chang, J. J. Feng, and H. H. Hu, Direct numerical simulation of the sedimentation of solid particles with thermal convection, *Journal of Fluid Mechanics* **481**, 385 (2003).
- [54] P. Mcleod, D. S. Riley, and R. S. J. Sparks, Melting of a sphere in hot fluid, *Journal of Fluid Mechanics* **327**, 393 (1996).
- [55] S. S. Sadhal, P. S. Ayyaswamy, and J. N. Chung, *Transport phenomena with drops and bubbles* (Springer Science & Business Media, 2012).
- [56] C. H. Chiang and W. A. Sirignano, Interacting, convecting, vaporizing fuel droplets with variable properties, *International Journal of Heat and Mass Transfer* **36**, 875 (1993).
- [57] T. Dessup, L. S. Tuckerman, J. E. Wesfreid, D. Barkley, and A. P. Willis, Self-sustaining process in Taylor-Couette flow, *Physical Review Fluids* **3**, 123902 (2018).
- [58] Y. Bengana and L. S. Tuckerman, Spirals and ribbons in counter-rotating Taylor-Couette flow: Frequencies from mean flows and heteroclinic orbits, *Physical Review Fluids* **4**, 044402 (2019).
- [59] F. H. Busse, Transition to turbulence in Rayleigh-Bénard convection, in *Hydrodynamic Instabilities and the Transition to Turbulence* (Springer-Verlag, Berlin, New York, 1981) pp. 97–137.
- [60] I. Mercader, J. Prat, and E. Knobloch, Robust heteroclinic cycles in two-dimensional Rayleigh-Bénard convection without Boussinesq symmetry, *International Journal of Bifurcation and Chaos* **12**, 2501 (2002).
- [61] E. Stone and P. Holmes, Random perturbations of heteroclinic attractors, *SIAM Journal on Applied Mathematics* **50**, 726 (1990).
- [62] A. Hill and I. Stewart, Hopf-steady-state mode interactions with $O(2)$ symmetry, *Dynamics and Stability of Systems* **6**, 149 (1991).



Unveiling the competitive role of global modes in the pattern formation of rotating sphere flows

J. Sierra-Ausín^{1,2}, M. Lorite-Díez^{2,3}, J.I. Jiménez-González^{4,5,†}, V. Citro¹ and D. Fabre²

¹Dipartimento di Ingegneria Industriale (DIIN), Università degli Studi di Salerno, Fisciano 84084, Italy

²Institut de Mécanique des Fluides de Toulouse (IMFT), Université de Toulouse and CNRS, Toulouse 31400, France

³Departamento de Ingeniería Mecánica, Térmica y de Fluidos, Universidad de Málaga, Málaga 29002, Spain

⁴Departamento de Ingeniería Mecánica y Minera, Universidad de Jaén, Jaén 23071, Spain

⁵Andalusian Institute for Earth System Research, Universidad de Jaén, Jaén 23071, Spain

(Received 11 September 2021; revised 28 February 2022; accepted 25 April 2022)

The wake flow past a streamwise rotating sphere is a canonical model of numerous applications, such as particle-driven flows, sport aerodynamics and freely rising or falling bodies, where the changes in particles' paths are related to the destabilization of complex flow regimes and associated force distributions. Herein, we examine the spatio-temporal pattern formation, previously investigated by Lorite-Díez & Jiménez-González (*J. Fluid Mech.*, vol. 896, 2020, A18) and Pier (*J. Fluids Struct.*, vol. 41, 2013, pp. 43–50), from a dynamical system perspective. A systematic study of the mode competition between rotating waves, which arise from the linearly unstable modes of the steady-state, exhibits their connection to previously observed helical patterns present within the wake. The organizing centre of the dynamics turns out to be a triple Hopf bifurcation associated with three non-axisymmetric, oscillating modes with respective azimuthal wavenumbers $m = -1, -1$ and -2 . The unfolding of the normal form unveils the nonlinear interaction between the rotating waves to engender more complex states. It reveals that for low values of the rotation rate, the flow field exhibits a similar transition to the flow past the static sphere, but accompanied by a rapid variation of the frequencies of the flow with respect to the rotation. The transition from the single helix pattern to the double helix structure within the wake displays several regions with hysteric behaviour. Eventually, the interaction between single and double helix structures within the wake lead towards temporal chaos, which here is attributed to the Ruelle–Takens–Newhouse route. The onset of chaos is detected by the identification of an invariant state of the normal form constituted by three incommensurate frequencies. The evolution of the chaotic attractor is determined using of time-stepping

† Email address for correspondence: jignacio@ujaen.es

© The Author(s), 2022. Published by Cambridge University Press. This is an Open Access article, distributed under the terms of the Creative Commons Attribution-NonCommercial-NoDerivatives licence (<https://creativecommons.org/licenses/by-nc-nd/4.0/>), which permits non-commercial re-use, distribution, and reproduction in any medium, provided the original work is unaltered and is properly cited. The written permission of Cambridge University Press must be obtained for commercial re-use or in order to create a derivative work.

simulations, which were also performed to confirm the existence of bi-stability and to assess the fidelity of the computations performed with the normal form.

Key words: shear-flow instability, wakes

1. Introduction

The flow around a rotating sphere has drawn the attention of many researchers in recent years as it represents a canonical problem with many engineering and physics applications. For instance, such configuration may be found in multiple practical and natural phenomena like particle-driven flows (Shi & Rzehak 2019), fluidized bed combustion (Liu & Prosperetti 2010; Feng & Musong 2014), sports aerodynamics (Passmore *et al.* 2008; Robinson & Robinson 2013), seeds' flight (Barois *et al.* 2019; Rabault, Fauli & Carlson 2019) or free-falling/rising bodies (Ern *et al.* 2012; Auguste & Magnaudet 2018; Mathai *et al.* 2018), among others. In such applications, the instability of paths of the spherical bodies is shown to depend on the forces distributions acting on their surface and, therefore, on the flow regimes that are destabilized for different values of the Reynolds number and rotation rates. Consequently, a profound understanding of the physics of the flow around a rotating sphere and its instability features is required to predict the dynamics of rotating particles and evaluate possibilities of flow and path control.

The unstable flow regimes at the wake past a fixed sphere have been extensively characterized, as it represents a classical example of open flow leading to rich pattern formation and dynamical complexity. As reported by different numerical and stability analyses available in the literature, the flow experiences a complex sequence of laminar bifurcations as the Reynolds number Re increases (see, e.g. Sakamoto & Haniu 1990; Johnson & Patel 1999; Fabre, Auguste & Magnaudet 2008; Fabre *et al.* 2017). For a static (non-rotating) sphere, the flow first experiences a steady bifurcation around $Re_{c1} \simeq 212$, leading to a steady, reflection-symmetric bifid wake (steady-state mode, Fabre *et al.* 2008), followed by a Hopf bifurcation at $Re_{c2} \simeq 272$ (Citro *et al.* 2017), leading to a periodic, vortex-shedding mode which preserves the axial reflection symmetry plane (RSP mode, Fabre *et al.* 2008). This reflection symmetry in the shedding process is lost around $Re_{c3} \simeq 375$, from which the wake starts to oscillate transversely (Chrust, Goujon-Durand & Wesfreid 2013).

When rotation is applied, the bifurcation scenario of the sphere wake is modified, generating even richer dynamics. In particular, as shown by Poon *et al.* (2010), the topology and frequency of the unstable flow regimes depend on the rotation rate Ω and the axis of rotation.

In general, the flow past streamwise rotating spheres has received considerably less attention than transversely rotating spheres (see, e.g. Citro *et al.* 2016), and their dynamics and controllability features are not yet fully understood. However, some numerical and experimental studies have focused on the flow topology and stability modifications produced in the sphere wake as the streamwise rotation speed increases (Kim & Choi 2002; Niazmand & Renksizbulut 2005; Skarysz *et al.* 2018) at low values of Reynolds number. The problem can be also studied under linear stability analysis perspective as in Pier (2013) and Jiménez-González, Manglano-Villamarín & Coenen (2019). Moreover, the influence of streamwise rotation is not only restricted to the sphere, and it has been also studied in wakes behind other axisymmetric geometries which follow a similar series of bifurcations, as in Jiménez-González *et al.* (2013) and Jiménez-González *et al.* (2014) for blunt-based bodies.

The introduction of streamwise rotation introduces unsteadiness and asymmetry in the sphere wake. The steady state is substituted by a frozen rotation with azimuthal wavenumber $m = -1$ symmetry (Kim & Choi 2002; Jiménez-González *et al.* 2019), the negative sign indicating that vortical structures wind in the direction opposite to the swirl motion. When either Re or Ω increase, the periodic behaviour of this low-frequency frozen state diverges to quasiperiodic or even chaotic states. The quasiperiodicity can be caused by the appearance of a medium-frequency component, related to the RSP mode of the non-rotating situation, or to the appearance of a component with $m = -2$ symmetry in the flow, for $Re < 500$ and moderate Ω values (Skarysz *et al.* 2018; Lorite-Díez & Jiménez-González 2020). Moreover, in a more recent study, Lorite-Díez & Jiménez-González (2020) also identified very complex patterns close to chaotic behaviours, by performing direct numerical simulations (DNS). More precisely, with the help of dynamic mode decomposition tools, the nonlinear regimes are reported to be characterized by three fundamental frequency components (related to unstable structures displaying $m = -1$, $m = -1$ and $m = -2$ symmetries, respectively) and their interactions. However, the time-stepping simulations do not provide a clear insight about the origin of instability of these complex regimes and the fundamental nature of the incommensurate or derived frequency components, so that the use of adjoint stability tools seem advisable to isolate fundamental modes and identify mechanisms of receptivity to forcing or control.

Additionally, the time-stepping simulations of such complex dynamical systems are generally demanding in terms of computational cost, especially close to bifurcation thresholds, where long convergence times are usually required to obtain statistically relevant solutions. As a matter of fact, alternative weakly nonlinear approaches, as those based on bifurcation theory (Golubitsky & Langford 1988), may be more efficient to elucidate the pattern of transitions and major features of flow regimes with increasing values of the problem parameters (i.e. Re , Ω), by taking advantage of the symmetry of the base flow and proximity between successive instability thresholds. That said, the transition scenarios of complex systems with underlying symmetries usually lead to a large variety of pattern formations.

Close to the onset of stability, these patterns may be caused by a single instability, or alternatively, the system can display instabilities where several modes are concomitantly accountable for the destabilization of the trivial state. Besides, flow configurations controlled by a diversity of parameters may lose stability in diverse manners. A large diversity of patterns may emerge in the entire parameter space, and, in particular, one can find specific regions displaying mode competition. The combination of symmetry with a parameter space whose dimension is higher than one is a classical scenario where mode interaction occurs. The organizing centre of such cases is denoted as a bifurcation of codimension n , with $n \in \mathbb{N}$. Codimension is herein loosely defined as the number of interacting modes, and also corresponds to the dimension of the low-order dynamical system model called the normal form capturing the essence of the dynamics. The interested reader can find more about pattern formation in symmetric systems in Golubitsky, Stewart & Schaeffer (2012), while the study of the normal form of bifurcations with codimension higher than one may be found in the books of Guckenheimer (2010) or Kuznetsov (2013). The passage from a high-dimensional system to a reduced one with a slow manifold takes advantage of the theoretical framework provided by the singular perturbation theory. For example, the geometric singular perturbation theory, reviewed by Verhulst (2007), is a powerful technique within the singular perturbation theory. In the bifurcation theory of autonomous systems, it is customary to employ centre manifold or normal form reduction. This procedure has been employed for the study of bifurcations from steady

states (Haragus & Iooss 2010), maps (respectively Poincaré maps associated with a limit-cycle solution) (Kuznetsov & Meijer 2005), homoclinic and heteroclinic connections (Homburg & Sandstede 2010). The most commonly used computational procedures to determine the centre manifold are weakly nonlinear analysis, multiple scales expansion or the homological equation. In the past, these approaches have been exploited to study mode interaction in thermally driven convective motions, e.g. the Rayleigh–Bénard (Varé *et al.* 2020) and Langmuir circulation (Allen & Moroz 1997), in the fluid flow between counter-rotating cylinders, e.g. the Taylor–Couette flow (Golubitsky & Langford 1988) and its variants (Renardy *et al.* 1996), in magnetoconvection (Rucklidge *et al.* 2000), in the flow past a rotating cylinder (Sierra *et al.* 2020*b*) and in swirling jets (Meliga, Gallaire & Chomaz 2012).

In light of the aforementioned studies, for the parameters considered herein, one can expect that a linear stability analysis (LSA) discriminates at least three unsteady unstable fundamental modes: two with azimuthal wavenumber $m = -1$ and a third one with $m = -2$; meaning that the organizing centre is a triple-Hopf bifurcation with $SO(2)$ symmetry. Despite the likely existence of three unstable modes, because the dimension of the parameter space is two, the triple-Hopf bifurcation is not expected to occur. Therefore, the approach followed herein for the study of the triple-Hopf bifurcation is based on the extension of the normal form obtained at codimension-two points to the codimension-three manifold. In practical terms, we determine a fifth-order truncation in terms of the expansion parameter of the normal form at codimension-two points, followed by a linear (respectively quadratic for linear coefficients) extension of normal form coefficients to a specific point in the parameter space. Such an approach is detailed in § 4 and it is similar to the centre-unstable manifold reduction, cf. Armbruster, Guckenheimer & Holmes (1989), Podvigina (2006*a*), Podvigina (2006*b*) and Meliga, Chomaz & Sipp (2009*a*). In any case, once the normal form is determined, one can analyse the bifurcation scenario, which displays a rich variety of patterns, among which one can expect: rotating waves, quasiperiodic mixed modes or chaotic solutions displaying multiple frequency components, along with bi-stable states stemming from the coexistence of two stable rotating waves, mixed modes and rotating waves, diverse mixed modes or mixed modes and chaotic attractor.

Some of these transition features and bi-stable dynamics had been confirmed via time-stepping numerical simulations undertaken by Lorite-Díez & Jiménez-González (2020) and Pier (2013) who reported a rich variety of spatio-temporal patterns. However, they did not perform an exhaustive analysis of the nature of the bifurcations between the distinct regimes. Therefore, the objective of the present research is twofold. The first objective is to undertake a global stability analysis to determine the connection between the observed patterns by Lorite-Díez & Jiménez-González (2020) and the linear stability of helical modes. The identification of these fundamental modes allows an identification of the underlying physical mechanisms responsible for the instabilities and the receptivity of the flow to forcing or control possibilities. Secondly, the analysis of the normal form associated with the organizing centre serves to provide a complete phase portrait of the flow attractors before the emergence of temporal chaos and to unravel the transition towards chaotic spatio-temporal dynamics observed by Lorite-Díez & Jiménez-González (2020) and Pier (2013).

The outline of the manuscript is as follows. First, the flow configuration and the numerical approach are presented in § 2. Second, we undergo a LSA in § 3, which identifies the most unstable global modes, their underlying physical mechanisms and sensitivity to forcing. Third, we introduce the methodology for the normal form reduction and we

Triple-Hopf bifurcation in the flow past a rotating sphere

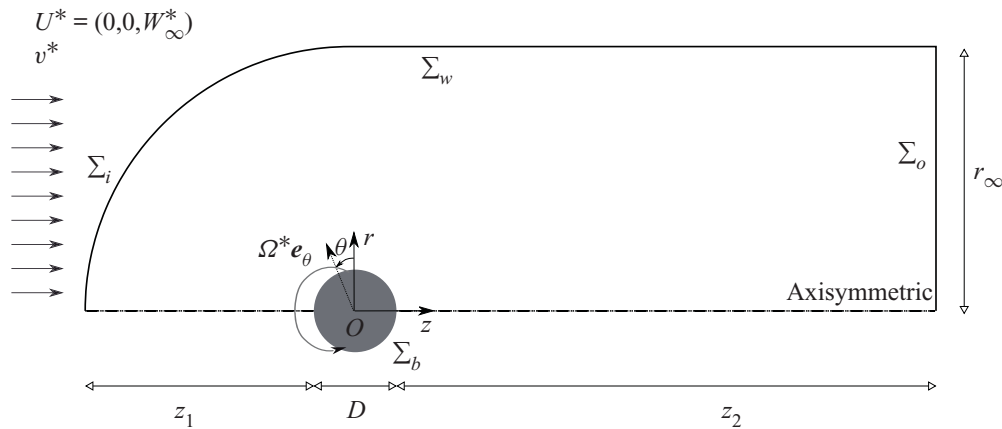


Figure 1. Sketch of the problem and geometric configuration.

illustrate it with a bifurcation diagram at constant rotation rate in § 4. Then, in § 5 we pursue the study by comparing the normal form predictions with DNS results and we provide a complete phase diagram of the stable attractors of the flow in the range $Re \leq 300$ and $\Omega < 4$. Finally, in § 6 we summarise the main findings and we argue of some future applications of the study.

2. Methodology

2.1. Flow configuration – governing equations

The flow past an axisymmetric rotating body is controlled by two parameters: the Reynolds number (Re) and the rotation rate (Ω) which is defined as the ratio of the tangential velocity $\Omega^* D^*/2$ on the sphere surface to the inflow velocity W_∞^* . The fluid motion inside the domain is governed by the incompressible Navier–Stokes equations written in cylindrical coordinates (r, θ, z) ,

$$\frac{\partial \mathbf{U}}{\partial t} + \mathbf{U} \cdot \nabla \mathbf{U} = -\nabla P + \nabla \cdot \boldsymbol{\tau}(\mathbf{U}), \quad \nabla \cdot \mathbf{U} = 0, \quad (2.1a)$$

$$\text{with } \boldsymbol{\tau}(\mathbf{U}) = \frac{1}{Re} (\nabla \mathbf{U} + \nabla \mathbf{U}^T), \quad Re = \frac{W_\infty^* D^*}{\nu^*}, \quad \Omega = \frac{\Omega^* D^*}{2W_\infty^*}, \quad (2.1b)$$

$$\mathbf{x} = \mathbf{x}^* \frac{1}{D^*}, \quad t = t^* \frac{W_\infty^*}{D^*}, \quad \mathbf{U} = \mathbf{U}^* \frac{1}{W_\infty^*}, \quad P = P^* \left(\frac{1}{W_\infty^*} \right)^2. \quad (2.1c)$$

Dimensional quantities are identified with the upperscript symbol $*$. Reference scales are specified in (2.1c). The dimensionless velocity vector $\mathbf{U} = (U, V, W)$ is composed of the radial, azimuthal and axial components, P is the dimensionless reduced pressure and the viscous stress tensor, $\boldsymbol{\tau}(\mathbf{U})$. For representation purposes, it is sometimes necessary to use the Cartesian coordinates (x, y, z) , here z denotes the streamwise direction, y the vertical crosswise direction and x the direction that forms a direct trihedral with z and y . The incompressible Navier–Stokes equations (2.1) are complemented with the following boundary conditions:

$$\mathbf{U} = (0, \Omega, 0) \text{ on } \Sigma_b \quad \mathbf{U} = (0, 0, 1) \text{ on } \Sigma_i. \quad (2.2)$$

No-slip boundary condition is set on the rotating sphere and a uniform boundary condition is set in the inlet, as shown in figure 1.

In the sequel, Navier–Stokes equations (2.1) and the associated boundary conditions will be written symbolically under the form

$$\mathbf{B} \frac{\partial \mathbf{Q}}{\partial t} = \mathbf{F}(\mathbf{Q}, \boldsymbol{\eta}) \equiv \mathbf{L}\mathbf{Q} + \mathbf{N}(\mathbf{Q}, \mathbf{Q}) + \mathbf{G}(\mathbf{Q}, \boldsymbol{\eta}), \quad (2.3)$$

where \mathbf{B} is the projection matrix onto the velocity field with the flow state vector $\mathbf{Q} = [U, P]^T$, and the parameter vector $\boldsymbol{\eta} = [Re^{-1}, \Omega]^T$. Such a form of the governing equations takes into account a linear dependency on the state variable \mathbf{Q} through \mathbf{L} and a quadratic dependency on parameters and the state variable through operators $\mathbf{N}(\cdot, \cdot)$ and $\mathbf{G}(\cdot, \cdot)$, which are detailed in [Appendix A](#).

2.2. Nomenclature

Let us introduce some general concepts that will be employed throughout the study. Steady states, i.e. \mathbf{Q} such that $\mathbf{F}(\mathbf{Q}, \boldsymbol{\eta}) = 0$, periodic orbits, i.e. $\mathbf{Q}(t) = \mathbf{Q}(t + T)$ for every $t \geq 0$, are the simplest invariants of (2.3). In general, an invariant set V of the phase space of (2.3) is a set that is preserved under dynamics, i.e. for every initial solution $\mathbf{Q}(t_0) \in V$, we have $\mathbf{Q}(t) \in V$ for every $t \geq 0$. A T^n -quasiperiodic state, $n > 1$, $n \in \mathbb{N}^*$, is an invariant of the system (2.3) that can be decomposed as a finite sum of n incommensurate frequencies ω_n , i.e.

$$\mathbf{Q} = \mathbf{Q}_0 + \sum_{\ell=1}^n \left(\hat{\mathbf{Q}}_{\ell} e^{i\omega_{\ell} t} + \text{c.c.} \right). \quad (2.4)$$

Incommensurate frequencies are those that are linearly independent, i.e. for $k_{\ell} \in \mathbb{Z}$, we have $\sum_{\ell=1}^n k_{\ell} \omega_{\ell} = 0$ if and only if every $k_{\ell} = 0$. Here, we determine the incommensurate frequencies as those corresponding to the fundamental modes (least stable eigenmodes) identified by LSA.

A second important property is the attractiveness of an invariant set. We denote as basin of attraction the set of initial conditions leading to long-time behaviour that approaches the attractor. The celebrated manuscript of Newhouse, Ruelle & Takens (1978) states that T^n -quasiperiodic states, with $n \geq 3$, are unusual attractors, in the sense that every T^n -quasiperiodic state can be perturbed by an arbitrarily small amount to a new vector field with a chaotic attractor. In other words, for any T^n -quasiperiodic state of (2.3), one may observe a chaotic *Axiom A* attractor by experimental or numerical means. Here, *Axiom A* attractor denotes a class of dynamical systems where the non-wandering set is hyperbolic and the attractor has a dense set of periodic orbits, more details about hyperbolicity may be found, for instance, in the recent article by Ni (2019).

2.3. Direct numerical simulation details

The flow governed by (2.1) is solved by means of DNS, following a time-stepping approach using the finite-volume library OpenFOAM®. The domain shown in [figure 1](#) consists of an upstream hemisphere of radius $r_{\infty} = 15D$ and a downstream tube extending $z_2 = 50D$ downstream of the body.

Regarding boundary conditions at the outlet, Σ_o , we impose an outflow condition that implements a Neumann condition for the velocity, $\mathbf{n} \cdot \nabla U = 0$, where \mathbf{n} is the outward normal, and a Dirichlet condition for the pressure, $P = 0$. The latter may be considered equivalent to setting a stress-free condition at the outlet for small values of the viscosity (as highlighted by Tomboulides & Orszag 2000). Finally, at the outer radial

boundary, Σ_w , we set a slip boundary condition, $\mathbf{n} \cdot \mathbf{U} = 0$. Note that such domain size and boundary conditions have been selected according to previous numerical works on rotating axisymmetric bodies (see, e.g. Jiménez-González *et al.* 2013; Lorite-Díez & Jiménez-González 2020). Additionally, second-order schemes have been employed for spatial and time integration. Nevertheless, for the sake of conciseness, the reader is referred to Appendix A in Lorite-Díez & Jiménez-González (2020) for detailed information about the employed numerical schemes, convergence and validation studies. In the present simulations ~ 2.6 millions of elements mesh, denoted #2 in table 1 (Appendix A) therein, is used.

The three-dimensional time-stepping simulations were computed in parallel. In particular, the DNS are carried out, once converged, for $T \sim 500$ convective units for periodic regimes, and until $T \sim 1000$ convective units for quasiperiodic and most complex regimes. The employed time step is $\Delta t = 0.003$ for all simulations. In terms of computational cost, running on 16 Intel Xeon E5-2665 processors, a simulation lasting $T = 1000$ convective time units corresponds to approximately 10 days.

3. Linear stability analysis

3.1. Methodology

As a first step of the reduction procedure, we identify the base flow solution, which is defined as the steady solution \mathbf{Q}_b of the (axisymmetric) Navier–Stokes equations, namely the solution of $\mathbf{F}(\mathbf{Q}_b) = \mathbf{0}$. We then characterize the dynamics of small-amplitude perturbations around this base flow by expanding them over the basis of linear eigenmodes

$$\mathbf{Q} = \mathbf{Q}_b + \varepsilon \sum_{\ell} \mathbf{q}_{(\varepsilon)}(t, \tau) = \mathbf{Q}_b + \varepsilon \sum_{\ell} \left(z_{\ell}(\tau) \hat{\mathbf{q}}_{(z_{\ell})}(r, z) e^{i(m_{\ell}\theta + \omega_{\ell}t)} + \text{c.c.} \right), \quad \varepsilon \ll 1. \tag{3.1}$$

The eigenpairs $[i\omega_{\ell}, \hat{\mathbf{q}}_{(z_{\ell})}]$ are then determined as the solutions of the eigenvalue problem

$$\mathbf{J}_{(\omega_{\ell}, m_{\ell})} \hat{\mathbf{q}}_{(z_{\ell})} = \left(i\omega_{\ell} \mathbf{B} - \left. \frac{\partial \mathbf{F}}{\partial \mathbf{q}} \right|_{\mathbf{q}=\mathbf{Q}_b, \Delta\boldsymbol{\eta}=\mathbf{0}} \right) \hat{\mathbf{q}}_{(z_{\ell})}, \tag{3.2}$$

where $(\partial \mathbf{F} / \partial \mathbf{q}|_{\mathbf{q}=\mathbf{Q}_b, \Delta\boldsymbol{\eta}=\mathbf{0}}) \hat{\mathbf{q}}_{(z_{\ell})} = \mathbf{L}_{m_{\ell}} \hat{\mathbf{q}}_{(z_{\ell})} + \mathbf{N}_{m_{\ell}}(\mathbf{Q}_b, \hat{\mathbf{q}}_{(z_{\ell})}) + \mathbf{N}_{m_{\ell}}(\hat{\mathbf{q}}_{(z_{\ell})}, \mathbf{Q}_b) + \mathbf{G}(\mathbf{Q}_b, \boldsymbol{\eta}_c)$, with $\boldsymbol{\eta}_c = [Re_c^{-1}, \Omega_c]^T$. The subscript m_{ℓ} indicates the azimuthal wavenumber used for the evaluation of the linearized Navier–Stokes operator $\mathbf{J}_{(\omega_{\ell}, m_{\ell})}$. Please note that here, the term $\Delta\boldsymbol{\eta} = [Re_c^{-1} - Re^{-1}, \Omega_c - \Omega]^T$ denotes the departure from the critical condition attained at $[Re_c^{-1}, \Omega_c]^T$. In the following, we consider that eigenmodes $\hat{\mathbf{q}}_{(z_{\ell})}(r, z)$ have been normalised in such a way that $\langle \hat{\mathbf{q}}_{(z_{\ell})}, \hat{\mathbf{q}}_{(z_{\ell})} \rangle_{\mathbf{B}} = \langle \hat{\mathbf{u}}_{(z_{\ell})}, \hat{\mathbf{u}}_{(z_{\ell})} \rangle = \int_{\Omega} \mathbf{u}(\mathbf{x})^T \mathbf{u}(\mathbf{x}) \, d\mathbf{x} = 1$.

3.1.1. Numerical methodology for stability tools

Results presented herein follow the same numerical approach adopted by Fabre *et al.* (2018), Sierra, Fabre & Citro (2020a) and Sierra *et al.* (2020b). The calculation of the base flow, the eigenvalue problem and the normal form expansion are implemented in the open-source software FreeFem++. Parametric studies and generation of figures are collected by StabFem drivers, an open-source project available at <https://gitlab.com/stabfem/StabFem>. Results shown in §§ 3–5 have been computed with a numerical domain (see figure 1) of size $z_2 = 50D$, $z_1 = 20D$ and $r_{\infty} = 20D$, in the streamwise and crosswise directions, respectively. For steady-state, stability and normal form computations, we set

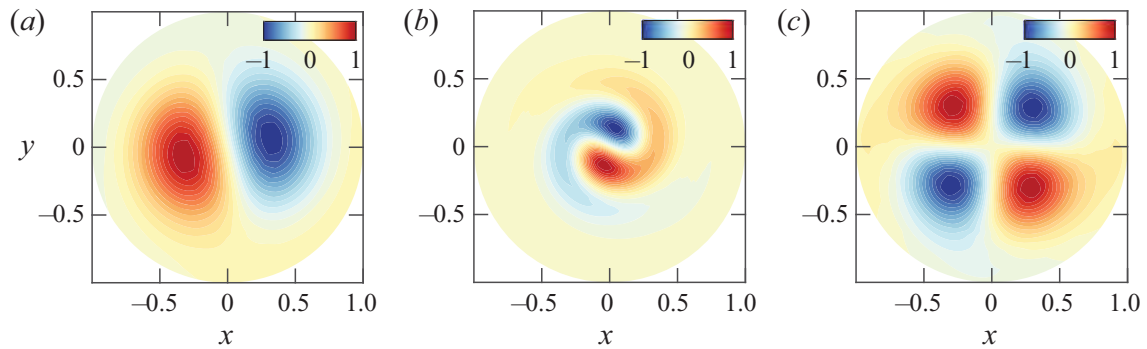


Figure 2. Cross-section view at $z = 3.5$ of the three unstable modes. The streamwise component of the vorticity vector ϖ_z is visualized by colours. Results are shown for (a) RW_1 at point $(Re_A, \Omega_A) = (77, 2.24)$; (b) RW_2 at point $(Re_B, \Omega_B) = (188, 1.01)$; (c) RW_3 at point (Re_A, Ω_A) .

the stress-free boundary condition at the outlet, which is the natural boundary condition in the variational formulation. Numerical convergence issues are discussed in [Appendix D](#). The resolution of the steady nonlinear Navier–Stokes equations is tackled by means of the Newton method. While the generalized eigenvalue problem (3.2) is solved following the Arnoldi method with spectral transformations. The normal form reduction procedure of § 4 only requires us to solve a set of linear systems, which is also carried out within StabFem. On a standard laptop, every computation considered below can be attained within a few hours.

3.2. Neutral curves of stability

In the presence of supercritical self-sustained instabilities, rotating waves are predominant. These patterns prevail in axisymmetric flows, where the reflection symmetry regarding the azimuthal angle is broken. Here, the reflection symmetry is broken because of the rotation of the sphere, which induces a preferential direction of rotation. Consequently, bifurcations that lead to standing waves or to a symmetry breaking steady state do not occur generically. The existence of standing waves or a steady-state mode requires the matching between the phase speed of the helical pattern and the rotation of the body, which is another condition to be met. The global stability analysis of the flow past the sphere confirms that only rotating waves are linearly unstable for the range of Reynolds numbers $Re < 300$ and $\Omega < 4$. The parametric linear stability study of the flow past the rotating sphere shows the existence of three neutral curves, which are associated to the three least stable modes identified by global stability analysis. These correspond to rotating waves, named RW_1 , RW_2 and RW_3 , which are depicted in [figure 2](#). Linear stability results ([figure 3a](#)) reveal that the axisymmetric steady state, referred in the following as a trivial state, is stable in the white shaded region and unstable in the grey shaded region. The neutral curve of stability displays two regions in the parameter space (Re, Ω) for which the first primary bifurcations are rotating waves of low frequency where the wake past the sphere displays a single helix (RW_1), depicted in [figure 2\(a\)](#). In the second region, the flow pattern of the wake displays a double helix (RW_3) with a high frequency, depicted in [figure 2\(c\)](#). The onset of instability of the third branch (RW_2) displaying a flow pattern of the wake with a single helix with a medium frequency, depicted in [figure 2\(b\)](#), turns out to be linearly unstable for $\Omega \leq 4$. Each pair of neutral curves intersects once, leading to three codimension-two points (A, B, C), identified in [table 1](#). Another aspect of importance is the evolution of frequencies of the instability. Frequencies at critical parameters are reported in [figure 3\(b\)](#) as a function of Ω . The frequency evolution is divided into two regions, a

Triple-Hopf bifurcation in the flow past a rotating sphere

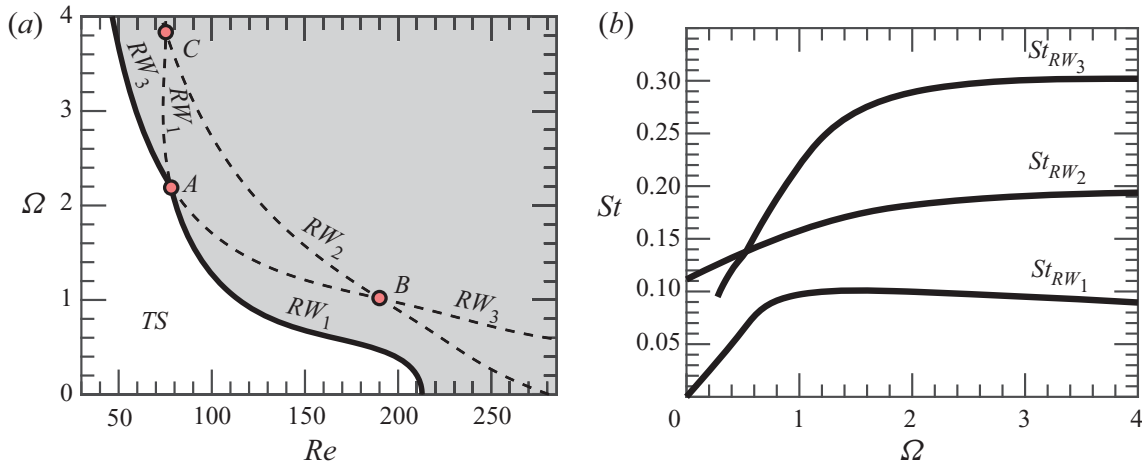


Figure 3. Linear stability properties of the rotating sphere configuration. (a) Neutral curve of stability: the onset of the primary instability is portrayed with a solid black line (—), whereas the continuation of the neutral curves is depicted with dashed black lines (---). (b) Frequency evolution with respect to Ω of linear modes at the critical Reynolds number ($Re_c(\Omega)$).

Name	Re	Ω	Mode inter.	θ_N	γ
Static	212	0	RW_1	4°	0.76
A	77	2.24	(RW_1, RW_3)	$(4.6^\circ, 8.0^\circ)$	(0.89, 0.98)
B	188	1.01	(RW_2, RW_3)	$(0.7^\circ, 2.3^\circ)$	(0.82, 0.80)
C	73	3.95	(RW_1, RW_2)	$(3.8^\circ, 9.9^\circ)$	(0.80, 0.68)

Table 1. Location in the parameter space (Re, Ω) and the pair of modes involved at the codimension-two points. It also lists the main properties of the primary bifurcation of the flow past the static sphere. The last two columns are related to non-normality effects and are defined in § 3.3.

first of rapid evolution for low rotation rates $\Omega < 1$ and a second where the frequency of the three modes hardly depends on the rotation rate.

The neutral curve of stability reveals that the static configuration ($\Omega = 0$) exhibits the largest critical Reynolds number. Then, the critical value of the Reynolds number is hardly modified by weak rotating speeds, in the range $\Omega < 0.3$. However, there is a clear threshold around $\Omega \approx 0.4$ where the critical Reynolds number passes from around $Re_c \approx 200$ to $Re_c \approx 100$ in a narrow interval $\Omega \in [0.4, 1.2]$. The critical Reynolds number remains approximately constant up to the point A, the point which divides the boundary of stability. Below the point A, that is, for $\Omega < \Omega_A$, the steady-state flow transits supercritically to a single helix rotating wave RW_1 ; above the point A, i.e. $\Omega > \Omega_A$, the steady-state flow transits supercritically to the double helix rotating wave, RW_3 . Such a point corresponds to a double-Hopf bifurcation between modes 1 and 3, and its analysis is left to §§ 4 and 5. Other two double-Hopf bifurcation points exist, denoted B and C, which characterize the interaction between modes 2 and 3, and 1 and 2, respectively. Yet, at points B and C the trivial state is already unstable, thus, instabilities associated with these points are not directly observed in experiments or numerical simulations. Instead, these organizing centres play a role in the pattern formation of secondary instabilities, which is left to §§ 4 and 5, where we interpret the subtle implications of these points in dynamics. In addition, authors have looked for the presence of a primary bifurcation that

leads to the RW_2 state. For the studied configuration, there does not exist such a region in the range $0 < \Omega < 6$.

3.3. Properties of the axisymmetric steady state

The analysis presented in this section studies the linear stability of the axisymmetric steady-state solution in the range $Re \leq 250$ and $\Omega \leq 4$. Typical axisymmetric steady-state solutions (TS) at codimension-two points are portrayed in [figure 4](#), which shows the neutrally stable trivial state at $(Re_A, \Omega_A) = (77, 2.24)$ and the two other unstable trivial states at $(Re_B, \Omega_B) = (188, 1.01)$ and $(Re_C, \Omega_C) = (73, 3.95)$, respectively. The flow visualization illustrates the recirculation region behind the sphere, delimited by the separatrix, which divides the recirculation bubble and the unperturbed flow field. Such a line, depicted with a thick solid line in [figure 4](#) connects the separation point on the sphere surface and the stagnation point on the $r = 0$ axis. The development of the recirculation bubble can be measured using the maximum extent of the region

$$L_r = \max \left\{ z - \frac{D}{2} \mid W(r = 0, z) \leq 0 \right\}, \quad (3.3)$$

where D is the diameter of the sphere. [Figure 5\(a\)](#) displays the evolution of the length of the recirculation bubble by varying Ω and Re . The length of the bubble increases monotonically with the angular velocity Ω of the sphere as well as the largest negative values of the streamwise velocity behind the sphere, from around 40 % for $\Omega = 0$ to around 60 % for the largest values of Ω explored. A similar trend was identified by Kim & Choi (2002) at $Re=100$; however, we should consider that the trends observed in [figure 5\(a\)](#) are only valid before bifurcation. After that, L_r does not have to increase with Ω , as seen by Lorite-Díez & Jiménez-González (2020) and Kim & Choi (2002). The results at the onset of stability of the steady state are synthesized in [figure 5\(b\)](#), with a domain of existence of a stable steady state (white shaded) and another of an unstable steady state (grey shaded). In § 3.4 we identify the core of the RW_1 and RW_3 instabilities, which are found within the recirculation region. In particular, a passive control that shortens the recirculation region is an efficient technique to stabilize the flow. Therefore, it is not surprising that the neutrally stable flow is characterized by a shorter recirculation region with respect to the unstable steady state.

Finally, we briefly discuss the influence of non-normality mechanisms, lift-up and convective non-normality as they are partly related to recirculation region length. The main results are included in [table 1](#), where we can see a lower influence of non-normality effects through the obtained values for γ and θ_N , with respect to the static sphere configuration. The estimator θ_N measures the importance of non-normality, the lower θ_N the more important non-normal effects are. On the other hand, the estimator γ characterizes the relative contribution between the lift-up and the convective non-normality mechanisms to the total non-normality effects. A γ value close to 0 indicates the dominance of the lift-up effect. The largest non-normal effects have been measured at point B (lowest values of θ_N), which corresponds to the point with the largest critical Reynolds number among the codimension-two points. The values of θ_N obtained at point B are associated with a larger non-normality than the stationary mode (the case of RW_1 with $O(2)$ symmetry) and RW_2 at the threshold for ($\Omega = 0, Re = 281$), which was found by Meliga, Chomaz & Sipp (2009b) to be 1° . Thus, one may conclude that the rotation of the sphere increases the effect of non-normality, however, it induces an earlier transition with regard to the Reynolds number, which turns out to globally reduce the effect of non-normality. This previous

Triple-Hopf bifurcation in the flow past a rotating sphere

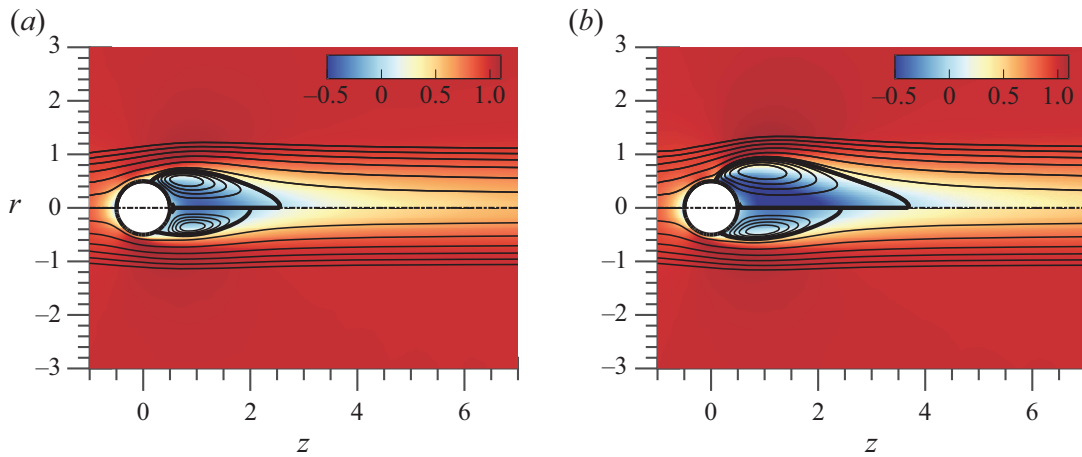


Figure 4. Spatial distribution of the streamwise velocity (contours) at the steady state along with flow streamlines (solid lines) and recirculation region separatrix (thick solid lines). Results are shown for (a) ($Re = 212, \Omega = 0$) in the upper half and (Re_A, Ω_A) in the lower half; (b) (Re_B, Ω_B) in the upper half and (Re_C, Ω_C) in the bottom half. Points A, B and C are defined in table 1.

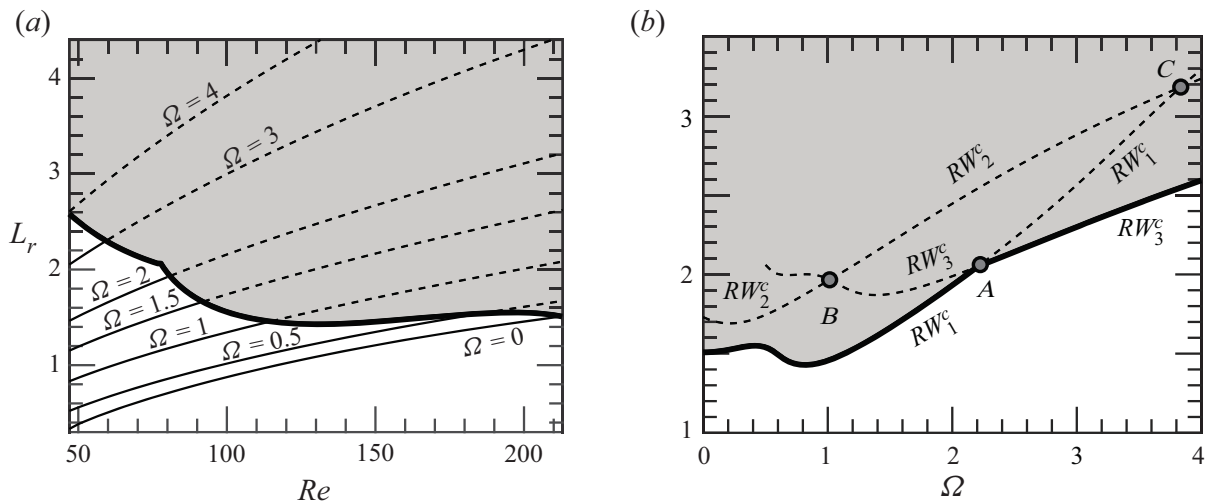


Figure 5. Evolution of the recirculating length L_r in the plane (Re, Ω) . The unstable region is the grey-shaded area, delimited by a thick line. (a) The recirculating length of the stable solution is painted with solid lines, dashed lines are employed for the unstable steady state. (b) Length of the recirculating region at the onset of stability ($Re_c(\Omega)$).

statement can be also indirectly verified from the satisfactory comparison between normal form estimations and DNS results in § 5.1. Furthermore, the analysis of the direct global mode shows a dominant effect of the convective non-normality, which is responsible at most of around 90 % (mode RW_1) and 98 % (mode RW_3) at point A and around 80 % for the remainder modes at points B and C. In comparison, the stationary and oscillating modes of static configuration ($\Omega = 0$) displayed $\gamma = 0.76$ and $\gamma = 0.94$. More details about the non-normality study such as the definition of θ_N and γ can be found in Appendix B.

3.4. Identification of the physical mechanisms from a control perspective

In this section we analyse the physical mechanisms leading to the RW_1 and RW_3 states at the point A. However, we do not discuss the RW_2 state as it will be seen in § 5, this state is not expected to be observed. First, we consider what is the effect of a steady axisymmetric forcing term, which represents the presence of a small obstacle, wall suction/blowing (as

the control applied in Niazmand & Renksizbulut 2005), etc. In this case the governing equations of the resulting flow are the same as (2.3) with the addition of a forcing term $\mathbf{H}_0 \equiv \hat{\mathbf{H}}_0$,

$$\mathbf{B} \frac{\partial \mathbf{Q}}{\partial t} = \mathbf{F}(\mathbf{Q}, \boldsymbol{\eta}) \equiv \mathbf{L}\mathbf{Q} + \mathbf{N}(\mathbf{Q}, \mathbf{Q}) + \mathbf{G}(\mathbf{Q}, \boldsymbol{\eta}) + \hat{\mathbf{H}}_0. \quad (3.4)$$

This case has been treated in the past by Marquet, Sipp & Jacquin (2008) in the case of the flow past a circular cylinder and by Sipp (2012) in the case of the open cavity flow. The introduction of the forcing induces a modification of the eigenvalue $i\omega_\ell \mapsto i\omega_\ell + \Delta i\omega_\ell^0$, where $\Delta i\omega_\ell^0 = \langle \nabla_{\mathbf{H}_0} i\omega_\ell, \hat{\mathbf{H}} \rangle$. Therefore, the control that induces the largest deviation of the growth rate (respectively frequency) of the mode ℓ is in the direction of $\nabla_{\mathbf{H}_0} i\omega_\ell$, which is defined as

$$\nabla_{\mathbf{H}_0} i\omega_\ell = \mathbf{B}^T \mathbf{J}_{(0,0)} \mathbf{B} \nabla_{U_b} i\omega_\ell \quad \text{for } \ell = 1, 2, 3. \quad (3.5)$$

Here $\nabla_{U_b} i\omega_\ell$ is the sensitivity of the eigenvalue of the mode ℓ ($\ell = 1, 2, 3$) with respect to variations in the axisymmetric steady state, cf. (Marquet *et al.* 2008). The sensitivity of the ℓ^{th} eigenvalue $\nabla_{\mathbf{H}_0} \lambda_\ell$ to the introduction of a steady axisymmetric forcing is represented in figure 6 for the two modes present in the codimension point A. The low-frequency mode (RW_1) is most sensitive to a steady axisymmetric forcing at the leftmost end of the recirculation region (see figure 6a,b). This forcing corresponds to one that accelerates the streamwise motion at the end of the recirculation region, thus reducing the counterclockwise motion of the recirculation zone, which would induce an effective decrease of the growth rate (respectively frequency). This is in accordance with the fact that the recirculation motion will be weaker, and the convective motion will be slower (note this is also the case for the sensitivity of the frequency RW_3 to steady forcing figure 6d). On the other hand, the high-frequency mode is most sensitive in a near wake region behind the sphere, close to the recirculation bubble (see figure 6c,d). In this case, a forcing that decelerates the clockwise motion within the recirculation region would cause the largest stabilization effect.

Second, let us consider the receptivity of the flow to the presence of localized feedbacks, as in Giannetti & Luchini (2007). The harmonic forcing $\mathbf{H} \equiv \mathbf{H}_{(z_\ell)} \exp(i(\omega_\ell t + m_\ell \theta))$ is defined as

$$\mathbf{H}_{(z_\ell)} = \delta(\mathbf{x} - \mathbf{x}_0) \mathbf{C}_{(z_\ell)} \cdot \hat{\mathbf{u}}_{(z_\ell)}, \quad \ell = 1, 2, 3, \quad (3.6)$$

where $\mathbf{C}_{(z_\ell)}$ is a generic feedback matrix and $\delta(\mathbf{x} - \mathbf{x}_0)$ is the Dirac distribution centred at the point $\mathbf{x}_0 = (z_0, r_0, \theta_0)$. Thus, the variation of the eigenvalue due to the introduction of the localized feedback is

$$\Delta^u i\omega_\ell = \langle \hat{\mathbf{q}}_{(z_\ell)}^\dagger, \delta \mathbf{H}_{(z_\ell)} \rangle = \mathbf{C}_{(z_\ell)} : \mathbf{s}_s^{(\ell)}(\mathbf{x}_0), \quad \ell \in \text{I} \quad (3.7)$$

The rank two tensor of (3.7) is commonly designated as the structural sensitivity tensor, here denoted as $\mathbf{s}_s^{(\ell)}$,

$$\mathbf{s}_s^{(\ell)} \equiv \hat{\mathbf{u}}_{(z_\ell)}^\dagger \otimes \bar{\hat{\mathbf{u}}}_{(z_\ell)}, \quad \ell = 1, 2, 3. \quad (3.8)$$

The spectral norm of the structural sensitivity tensor for low- and high-frequency modes is depicted in figure 7. Similar to the receptivity to axisymmetric steady forcing, the recirculation bubble (RW_3) and the leftmost end of the recirculation region (RW_1) are the most sensitive regions of the flow.

Triple-Hopf bifurcation in the flow past a rotating sphere

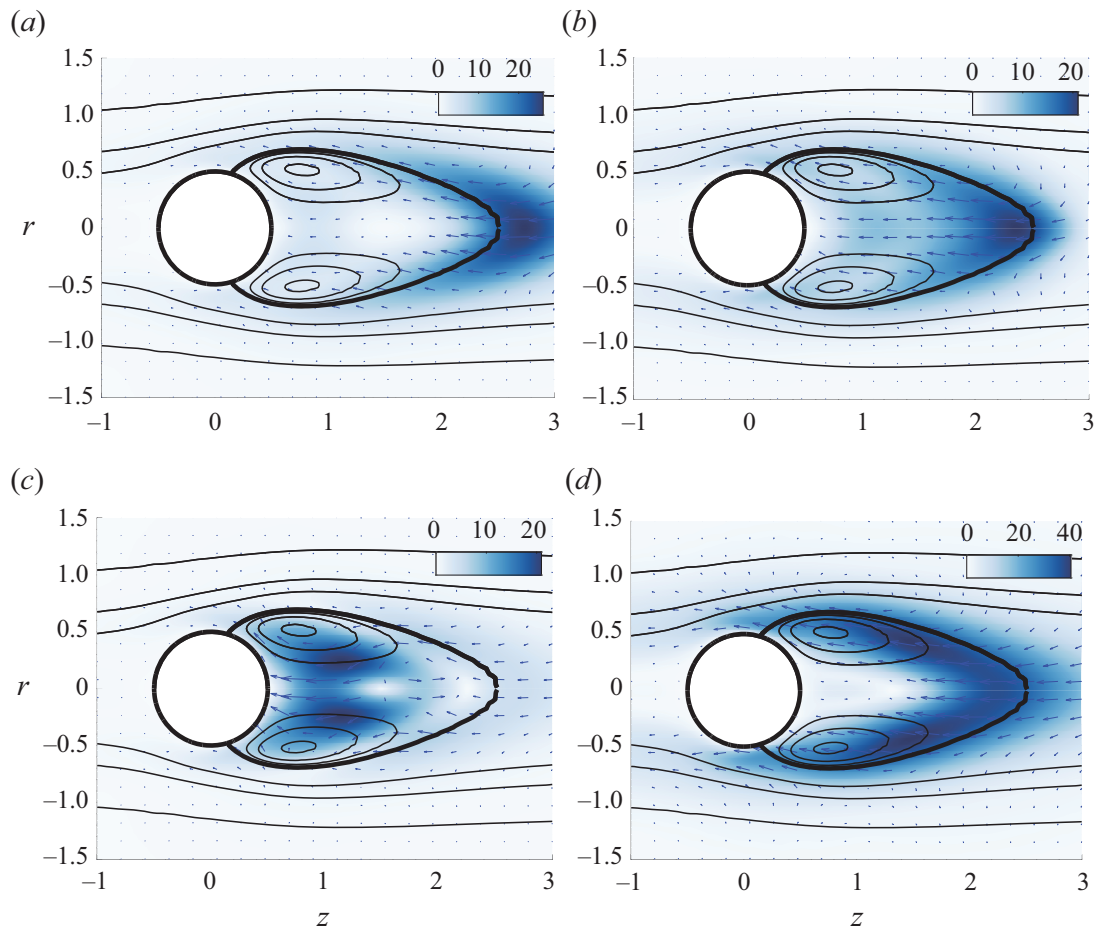


Figure 6. Steady forcing at codimension point A . Sensitivity of amplification rate to the steady axisymmetric forcing $\nabla_{H_0} \lambda_\ell$ for (a) the low-frequency mode, also known as RW_1 , and (c) the high-frequency mode, also known as RW_3 . Sensitivity of the frequency to the steady axisymmetric forcing $\nabla_{H_0} \lambda_\ell$ for (b) the low-frequency mode, RW_1 , and (d) the high-frequency mode, RW_3 . The magnitude of the growth rate and frequency sensitivities is pictured by colours and their orientation by arrows.

4. Normal form reduction

In this study bifurcations involving a steady-state mode uniquely exist for the static configuration ($\Omega = 0$). For such a reason, we will focus our attention on the codimension-two double-Hopf (Chossat, Golubitsky & Lee Keyfitz 1986) and the codimension-three triple-Hopf bifurcations, and we will characterize solutions based on the patterns allowed by these bifurcations. In our problem, the competition between two or more of the several rotating waves occurs in the neighbourhood of the primary bifurcation. For such a reason, the three double-Hopf points (depicted in figure 3a) are of special interest.

These points act as organizing centres of dynamics, and they provide some partial answers about the transition scenario. For instance, around the point A there are regions of bi-stability where either RW_1 and RW_3 coexist. Nevertheless, these codimension-two points do not account for a third interaction. In each of the double-Hopf interactions, the competition with one of the leading modes is omitted. The full instability scenario is accounted by considering the unfolding of the triple-Hopf bifurcation. Yet, such an instability does not show up generally with only two parameters. And the search for a third parameter where such a bifurcation generically occurs is not a trivial task. Not to mention that even in the case one finds such a parameter, the flow configuration may be

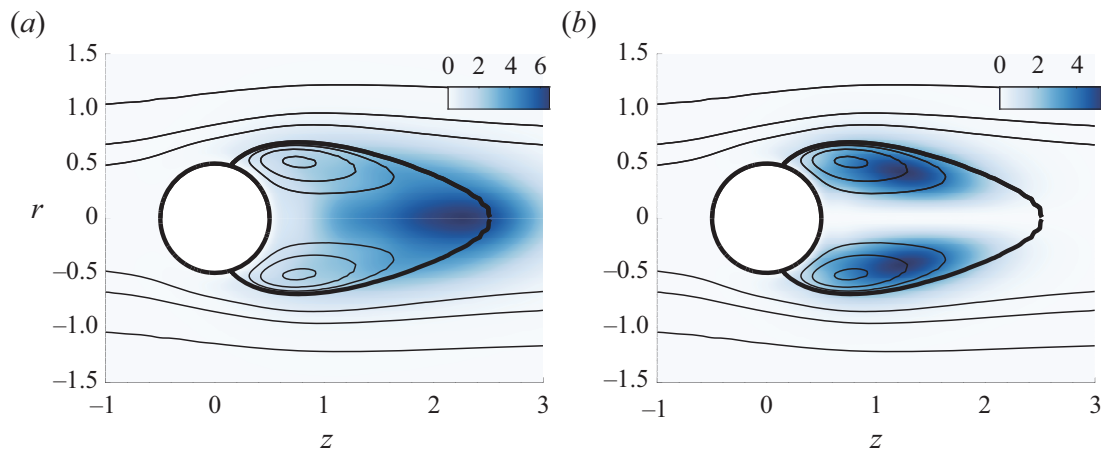


Figure 7. Spectral norm of the structural sensitivity tensor. (a) Low-frequency mode, (b) high-frequency mode.

considerably distinct from the one initially conceived. Therefore, in the current research, we adopt a similar strategy as the one conducted by Meliga *et al.* (2009a) on the wake flow past a disk. However, rather than performing a variation of the centre-unstable manifold reduction, which is an invariant procedure but without the attractiveness property of the centre manifold (Podvigina 2006a,b), we prefer to adopt a higher-order (up to fifth order) multiple scales expansion at each codimension-two point, and then we extend the coefficients to other locations in the parameter space. The chosen approach differentiates from other previous techniques because it allows an exact identification of the polynomial coefficients of the normal form at codimension-two points, where one can employ the Fredholm alternative to determine the normal form coefficients and remove the secular terms of the expansion. Other centre-unstable techniques determine the coefficients of the normal form at non-resonant conditions, which invalidates the use of the Fredholm alternative if one is far from the onset of instability. On the other hand, our technique does not provide an *a priori* knowledge of the error committed in the extension procedure from a codimension-two point to another point in the parameter space. Thus, as with other perturbative techniques, one needs to perform a cross-comparison with DNS in the region of interest of the parameter space, which is performed in § 5.1.

In the following, we briefly outline the main constituents in the study of pattern formation, a comprehensive explanation is left to Appendix A. Pattern formation is studied herein in the framework of bifurcation theory. Near the onset of the bifurcation, dynamics can be reduced to the centre manifold, whose algebraic expression is simplified via a series of topologically equivalent transformations into the normal form. The reduction to the normal form is carried out via a multiple scales expansion of the solution Q of (2.3). The expansion considers a two-scale development of the original time $t \mapsto t + \varepsilon^2 \tau$, here ε is the order of magnitude of the flow disturbances, assumed small $\varepsilon \ll 1$. In this study we carry out a normal form reduction via a weakly nonlinear expansion, where the small parameters are

$$\varepsilon_{\Omega}^2 = (\Omega_c - \Omega) \sim \varepsilon^2 \quad \text{and} \quad \varepsilon_v^2 = (v_c - v) = \left(Re_c^{-1} - Re^{-1} \right) \sim \varepsilon^2. \quad (4.1a,b)$$

The technique decomposes time into a fast time scale t of the phase associated to the self-sustained instabilities and a slow time scale related to the evolution of the amplitudes $z_i(\tau)$, introduced in (4.3), for $i = 1, 2, 3$. The ansatz of the expansion is

$$Q(t, \tau) = Q_b + \varepsilon q_{(\varepsilon)}(t, \tau) + \varepsilon^2 q_{(\varepsilon^2)}(t, \tau) + \varepsilon^3 q_{(\varepsilon^3)}(t, \tau) + \varepsilon^4 q_{(\varepsilon^4)}(t, \tau) + O(\varepsilon^5). \quad (4.2)$$

In the following, we shall consider the normal form equation resulting from the interaction of three rotating wave modes identified by LSA, that is,

$$\begin{aligned} \mathbf{q}_{(\varepsilon)}(t, \tau) = & (z_1(\tau)\hat{\mathbf{q}}_{(z_1)}(r, z) \exp(i(m_1\theta + \omega_1t)) + \text{c.c.}) \\ & + (z_2(\tau)\hat{\mathbf{q}}_{(z_2)}(r, z) \exp(i(m_2\theta + \omega_2t)) + \text{c.c.}) \\ & + (z_3(\tau)\hat{\mathbf{q}}_{(z_3)}(r, z) \exp(i(m_3\theta + \omega_3t)) + \text{c.c.}). \end{aligned} \quad (4.3)$$

Note that the expansion of the left-hand side of (2.3) up to fifth order is

$$\varepsilon \mathbf{B} \frac{\partial \mathbf{q}_{(\varepsilon)}}{\partial t} + \varepsilon^2 \mathbf{B} \frac{\partial \mathbf{q}_{(\varepsilon^2)}}{\partial t} + \varepsilon^3 \left[\mathbf{B} \frac{\partial \mathbf{q}_{(\varepsilon^3)}}{\partial t} + \mathbf{B} \frac{\partial \mathbf{q}_{(\varepsilon)}}{\partial \tau} \right] + \varepsilon^4 \mathbf{B} \frac{\partial \mathbf{q}_{(\varepsilon^4)}}{\partial t} + \varepsilon^5 \left[\mathbf{B} \frac{\partial \mathbf{q}_{(\varepsilon^3)}}{\partial \tau} \right] + O(\varepsilon^5), \quad (4.4)$$

and the right-hand side respectively is

$$\mathbf{F}(\mathbf{q}, \boldsymbol{\eta}) = \mathbf{F}_{(0)} + \varepsilon \mathbf{F}_{(\varepsilon)} + \varepsilon^2 \mathbf{F}_{(\varepsilon^2)} + \varepsilon^3 \mathbf{F}_{(\varepsilon^3)} + \varepsilon^4 \mathbf{F}_{(\varepsilon^4)} + \varepsilon^5 \mathbf{F}_{(\varepsilon^5)} + O(\varepsilon^6). \quad (4.5)$$

Then, the problem truncated at order three is reduced to a low-dimensional system governing the complex amplitudes $z_j(t)$,

$$\left. \begin{aligned} \dot{z}_1 &= z_1 \left[\lambda_1 + \nu_{11}|z_1|^2 + \nu_{12}|z_2|^2 + \nu_{13}|z_3|^2 \right], \\ \dot{z}_2 &= z_2 \left[\lambda_2 + \nu_{21}|z_1|^2 + \nu_{22}|z_2|^2 + \nu_{23}|z_3|^2 \right], \\ \dot{z}_3 &= z_3 \left[\lambda_3 + \nu_{31}|z_1|^2 + \nu_{32}|z_2|^2 + \nu_{33}|z_3|^2 \right], \end{aligned} \right\} \quad (4.6)$$

where $\nu_{k\ell}, \lambda_k \in \mathbb{C}$ for $k, \ell = 1, 2, 3$. The real part of the linear terms, named λ_k , correspond to the growth rate of the k^{th} mode. Respectively, the imaginary part of λ_k is associated to the frequency variation of the k^{th} mode with respect to the frequency of the neutral mode, i.e. with respect to the frequency ω_k determined from LSA. The terms $\nu_{k\ell}$ are the third-order self ($k = \ell$) and cross-interaction ($k \neq \ell$) coefficients. The coefficients of the normal form are estimated as

$$\left. \begin{aligned} \lambda_\ell &= \varepsilon_v^2 \lambda_\ell^{(\varepsilon_v^2)} + \varepsilon_\Omega^2 \lambda_\ell^{(\varepsilon_\Omega^2)} + \varepsilon_v^4 \lambda_\ell^{(\varepsilon_v^4)} + \varepsilon_\Omega^4 \lambda_\ell^{(\varepsilon_\Omega^4)} + \varepsilon_\Omega^2 \varepsilon_v^2 \lambda_\ell^{(\varepsilon_v^2 \varepsilon_\Omega^2)}, \\ \nu_{k\ell} &= \nu_{k\ell}^{(0)} + \varepsilon_v^2 \nu_{k\ell}^{(\varepsilon_v^2)} + \varepsilon_\Omega^2 \nu_{k\ell}^{(\varepsilon_\Omega^2)}, \end{aligned} \right\} \quad (4.7)$$

where $\nu_{k\ell}^{(0)}, \nu_{k\ell}^{(\varepsilon_v^2)}, \nu_{k\ell}^{(\varepsilon_\Omega^2)}$, and the corresponding linear coefficients, are evaluated at the intersection point between the Hopf curves associated to mode k and ℓ . For instance, the coefficient $\nu_{13}^{(0)}$ is evaluated at point A. The distinct coefficients of (4.7) used for the evaluation of the coefficients of the normal form are listed in tables 4 and 5 (Appendix A).

4.1. Classification of solutions

In the following, the right-hand side of (4.6) is designated $\mathbf{f}(\mathbf{z})$ where $\mathbf{z} = (z_1, z_2, z_3)$. The reduced vector \mathbf{f} is equivariant under the action of the group $\Gamma \equiv SO(2) \times \mathbb{T}^3$, with the

Name	Representative	Isotropy group (complex)	Frequencies
TS (Trivial state)	(0, 0, 0)	$SO(2) \times \mathbb{T}^3$	0
RW (Rotating wave)	$(r_a, 0, 0)$	$S(1, r, 0, 0) \times \mathbb{T}^2$	1
MM (Mixed mode)	$(r_a, r_b, 0)$	$S(1, r, l, 0) \times S^1$	2
IMM (Interacting mixed mode)	(r_a, r_b, r_c)	$\mathbb{1}$	3

Table 2. Nomenclature and symmetry group of fixed-point solutions of the system (4.9).

following action representation:

$$\left. \begin{aligned} \theta \cdot \mathbf{z} &\equiv (z_1 e^{i\theta}, z_2 e^{ir\theta}, z_3 e^{is\theta}), \\ (\psi_1, \psi_2, \psi_3) \cdot \mathbf{z} &\equiv (z_1 e^{i\psi_1}, z_2 e^{i\psi_2}, z_3 e^{i\psi_3}). \end{aligned} \right\} \quad (4.8)$$

Here $l, r, s \in \mathbb{Z}$, $\theta \in [0, 2\pi)$ and $\psi_i \in [0, 2\pi)$ for $i = 1, 2, 3$; (ψ_1, ψ_2, ψ_3) and θ are the representations in \mathbb{C}^3 of the actions of the group Γ , which correspond to the time shift and rotational invariance, respectively. The substitution of the polar decomposition of $\mathbf{z} = r e^{i\Phi}$, with $\mathbf{r} = (r_1, r_2, r_3)$ and $\Phi = (\phi_1, \phi_2, \phi_3)$, into (4.6) yields the following decoupled phase-amplitude system:

$$\left. \begin{aligned} \dot{r}_\ell &= r_\ell \left[\Lambda_\ell^R + \mathcal{V}_{\ell k}^R r_k^2 \right], \quad k, \ell = 1, 2, 3, \\ \dot{\phi}_\ell &= \Lambda_\ell^I + \mathcal{V}_{\ell k}^I r_k^2, \quad k, \ell = 1, 2, 3. \end{aligned} \right\} \quad (4.9)$$

Here $\Lambda = \Lambda^R + \Lambda^I \equiv (\lambda_1, \lambda_2, \lambda_3)^T$ and the matrix $\mathcal{V} = \mathcal{V}^R + i\mathcal{V}^I$ is

$$\mathcal{V} \equiv \begin{pmatrix} \nu_{11} & \nu_{12} & \nu_{13} \\ \nu_{21} & \nu_{22} & \nu_{23} \\ \nu_{31} & \nu_{32} & \nu_{33} \end{pmatrix}. \quad (4.10)$$

To ease the presentation of the fixed-point solutions of (4.9), let us introduce the inverse of the linear operator \mathcal{V} , which can be written as

$$\mathcal{V}^{-1} = \frac{1}{\det \mathcal{V}} \begin{pmatrix} \det \mathcal{V}_{11} & \det \mathcal{V}_{21} & \det \mathcal{V}_{31} \\ \det \mathcal{V}_{12} & \det \mathcal{V}_{22} & \det \mathcal{V}_{32} \\ \det \mathcal{V}_{13} & \det \mathcal{V}_{23} & \det \mathcal{V}_{33} \end{pmatrix}, \quad (4.11)$$

where $\det \mathcal{V}_{k\ell}$ denotes the minor of the matrix \mathcal{V} , obtained by eliminating the line k and the column ℓ .

In the following, the notation $\dot{\mathbf{r}} = \mathbf{f}^R(\mathbf{r})$ will be adopted to denote the amplitude equation of the nonlinear system (4.9). The remainder of this subsection will be devoted to the study of the three fixed-point solutions of (4.9).

The classification of the solutions of the generic triple-Hopf bifurcation interaction with $SO(2)$ symmetry is based on maximal isotropy subgroups of the group Γ . This technique predicts the existence up to tertiary bifurcations of fixed points of the complex normal form (4.6). These isotropy subgroups correspond to the symmetries of the solutions within the fixed-point subspace of each isotropy group (cf. table 2).

Triple-Hopf bifurcation in the flow past a rotating sphere

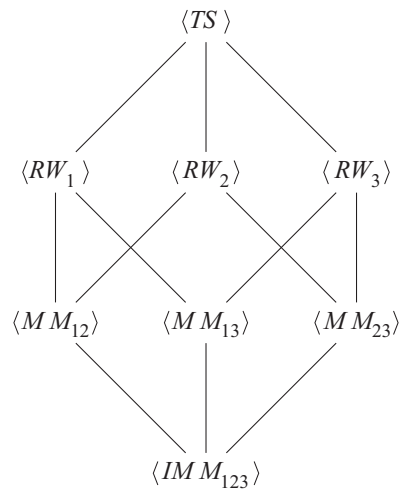


Figure 8. Isotropy lattice of the triple-Hopf bifurcation.

In our discussion, we identify the subgroups of $SO(2) \times \mathbb{T}^3$. Each element in the group has the form

$$(\theta, \psi_1, \psi_2, \psi_3) \in SO(2) \times \mathbb{T}^3. \quad (4.12)$$

Using this notation, the subgroup $S(k, l, r, s)$ of $SO(2) \times \mathbb{T}^3$ is defined as

$$S(k, l, r, s) = \{(k\theta, l\theta, r\theta, s\theta) | \theta \in S^1\}. \quad (4.13)$$

The conjugacy classes of isotropy subgroups of $SO(2) \times \mathbb{T}^3$ are documented with the representative of the fixed-point subspace in polar coordinates and the number of incommensurate frequencies in [table 2](#). Additionally, a graphical representation of the isotropy lattice is displayed in [figure 8](#) in terms of the class representative of the fixed-point subspace.

Rotating waves correspond to the simplest non-trivial fixed point of (4.9), which in the original set of equations is a periodic solution. They arise as the result of a supercritical Hopf bifurcation of the steady state (named trivial state in [table 2](#)) and they may eventually bifurcate into mixed modes; the eigenvalues of rotating waves may be found in the first row of [table 3](#). Mixed modes, defined in [table 3](#), are the result of the interaction between two rotating waves. A mixed mode has a representative in the normal form with two non-zero amplitude terms, thus, they correspond to a T^2 -quasiperiodic state in the original system of equations. These states may experience two kinds of bifurcations. They may lose stability in the transversal direction or within their own subspace, these two conditions are listed in [table 3](#). Eventually, a bifurcation in the transversal direction of a mixed mode may be associated with the appearance of an interacting mixed mode (IMM_{123}) attractor. An interacting mixed mode corresponds to a T^3 -quasiperiodic state in the original system of equations, and it is represented by three non-zero amplitude terms. However, T^3 -quasiperiodic states are hardly observed in numerical simulations of dissipative systems, as it is the case of Navier–Stokes equations (2.1), instead a chaotic attractor is usually detected. A more exhaustive analysis of the unfolding of the triple-Hopf bifurcation is left to [Appendix C](#).

4.2. Illustration of the procedure

Let us detail the procedure followed to compute the bifurcation scenario, a procedure that is also followed in [§ 5](#) for the determination of the parametric portrait. For the sake of

Name of solutions	Definition	Eigenvalues
RW_i (for $i = 1, 2, 3$)	$r_i^{(RW)} = \sqrt{-\frac{\lambda_i^R}{v_{ii}^R}}$	$-\lambda_i^R, \lambda_j^R - v_{ji}^R \frac{\lambda_i^R}{v_{ii}^R}$, for $j \neq i$
MM_{ij} , ($i, j = 1, 2, 3$)	$r_i^{(MM_{ij})} = \sqrt{\frac{\lambda_j^R v_{ij}^R - \lambda_i^R v_{ji}^R}{\det(\mathcal{V}_{kk})}}$	$\frac{v_{ii}^R r_i^2 + v_{jj}^R r_j^2}{2} \pm \sqrt{(v_{ii}^R r_i^2 - v_{jj}^R r_j^2)^2 / 4 + v_{ij}^R v_{ji}^R r_i^2 r_j^2}$
($j \neq i, k \neq i, k \neq j$)	$r_j^{(MM_{ij})} = \sqrt{\frac{\lambda_i^R v_{ji}^R - \lambda_j^R v_{ij}^R}{\det(\mathcal{V}_{kk})}}$	$\frac{1}{\det(\mathcal{V}_{kk}^R)} [\lambda_k^R \det(\mathcal{V}_{kk}^R) + \lambda_i^R \det(\mathcal{V}_{ik}^R) + \lambda_j^R \det(\mathcal{V}_{jk}^R)]$
IMM_{123}	$(r_1^2, r_2^2, r_3^2)^T = -(\mathcal{V}^R)^{-1} \Lambda^R$	Eigs of $D\mathcal{f}^R$

Table 3. Defining equations and eigenvalues of the solutions of the polar third-order normal form (4.9).

simplicity, we first discuss the bifurcation diagram for a constant rotation rate $\Omega = 1.75$ in terms of the amplitudes (r_1, r_2, r_3) . We would like to remind the reader that the amplitudes (r_1, r_2, r_3) are representative of the kinetic energy of the velocity fluctuations, based on the normalization choice of § 3.1. First, we need to determine the coefficients of the normal form, listed in tables 4 and 5, following the procedure of Appendix A. Then, one may evaluate the linear and cubic coefficients of the normal form at $\Omega = 1.75$ for a variable Reynolds number from the evaluation of (4.7). Please note that, for the evaluation of cross-diagonal cubic coefficients, the expansion parameter $\varepsilon_{\Omega}^2 = \Omega_c - \Omega$ depends on the location of the critical rotation rate Ω_c , that is, to evaluate v_{13} one evaluates $\varepsilon_{\Omega, A}^2 = \Omega_A - \Omega$ whereas to evaluate v_{23} one evaluates $\varepsilon_{\Omega, B}^2 = \Omega_B - \Omega$. The diagonal cubic coefficients may be evaluated directly at the bifurcation point for every rotation rate Ω as a function of ε_{Ω}^2 or by considering the cubic coefficient of the nearest codimension-two point. In our procedure, we found good agreement with time-stepping simulations in the range $1 \leq \Omega \leq 3$ if we consider $v_{11} = v_{11}^A$, $v_{22} = v_{22}^B$ and $v_{33} = v_{33}^B$; the consideration of v_{33}^A induces a small deviation in the transition from MM_{23} to IMM_{123} of few units of the Reynolds number. The corresponding coefficients for $\Omega = 1.75$ are listed in table 6 (Appendix A). Please note that the procedure illustrated herein corresponds to a method to determine the coefficients of the normal form; nonetheless, these coefficients can be estimated from numerical simulations as in Fabre *et al.* (2008) or following a data-driven approach, cf. Callaham, Brunton & Loiseau (2022), Loiseau & Brunton (2018) and Loiseau, Noack & Brunton (2018). Bifurcation events are designated by their corresponding value of the Reynolds number $Re_{state_a}^{state_b}$, where $state_a$ stands for the simplest state that exists before the bifurcation and $state_b$ stands for the resulting state after the bifurcation. In addition, the notation $Re_{state_a}^{\sigma_k, s}$ indicates a bifurcation of the $state_a$ where the eigenvalue σ_k ($k = 1, 2, 3$) has changed sign, s indicates stabilization and u indicates the change from stable to unstable of the referring eigenvalue/eigenmode pair. In the following, there is only a bifurcation of this kind, the one associated to the mixed mode MM_{12} that is stabilized/destabilized because of a change of sign of the eigenvalue in the transversal direction (r_3). Thus, we simplify the notation to $Re_{state_a}^s$ or $Re_{state_a}^u$.

Figure 9 displays the bifurcation diagram, with Reynolds number as the control parameter for $\Omega = 1.75$. There exist three primary bifurcations, i.e. bifurcations from the

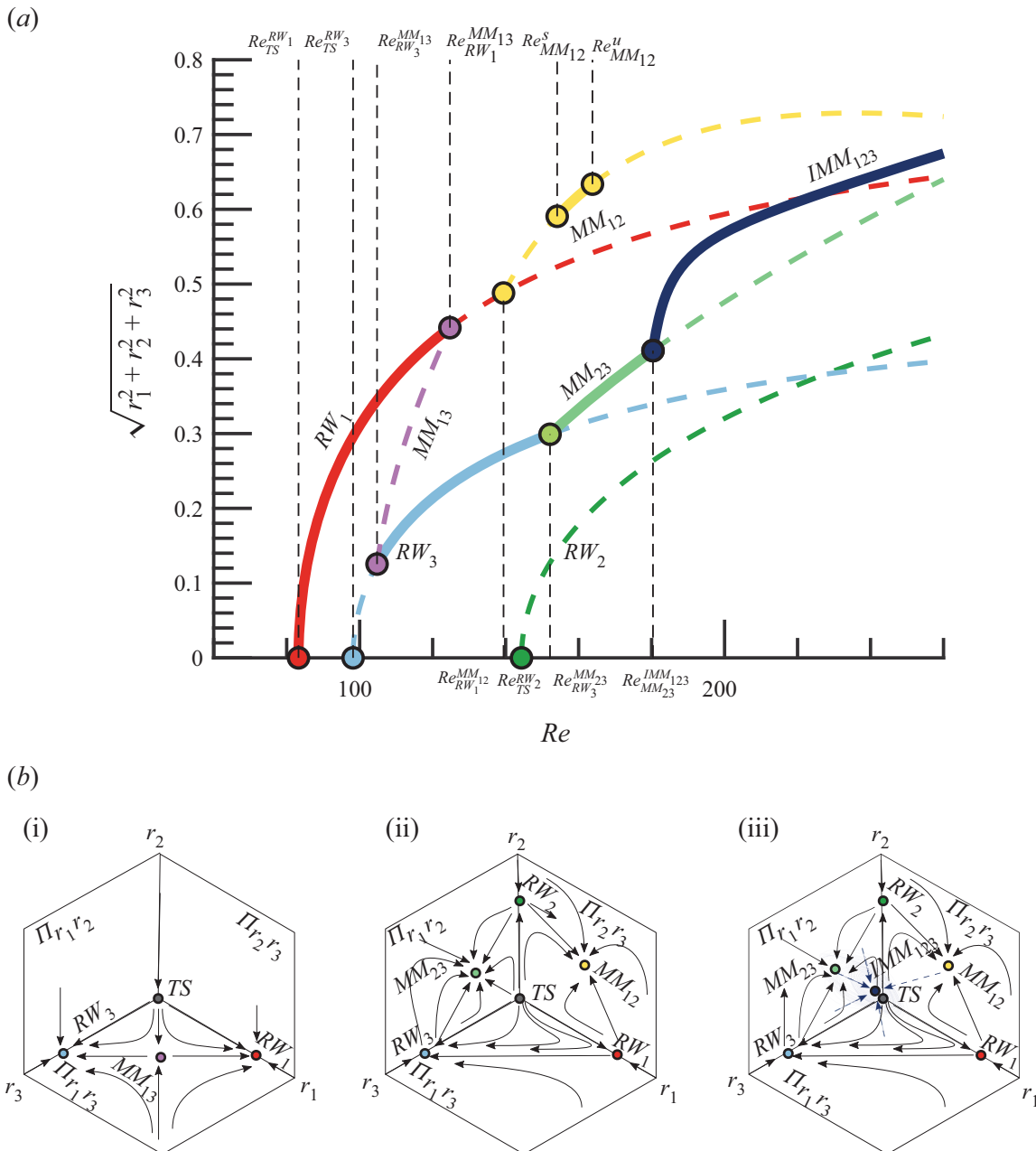


Figure 9. (a) Transition scenario at $\Omega = 1.75$. Attractors are depicted with solid lines, whereas unstable invariant states are represented with dashed lines. (b) Schematic representation of phase portraits. (i) Two stable rotating waves separated by a mixed-mode solution. (ii) Two stable mixed modes. (iii) An interacting mixed-mode attractor, the chaotic attractor that shadows the IMM_{123} is sketched in a lighter blue colour.

axisymmetric steady state, located at $Re_{TS}^{RW_1}$, $Re_{TS}^{RW_2}$ and $Re_{TS}^{RW_3}$, respectively. However, the RW_2 branch remains unstable all along the analysed interval. The first transition to occur is a supercritical Hopf bifurcation leading to the RW_1 solution, which is then followed by another supercritical Hopf bifurcation leading to RW_3 . For the range of Reynolds numbers $Re_{RW_1} < Re < Re_{RW_3}^{MM_{13}}$, there exists a single stable attractor, which corresponds to the limit cycle associated with the solution RW_1 . At $Re_{RW_3}^{MM_{13}}$ the RW_3 branch experiences a Neimark–Sacker bifurcation that results in the appearance of the mixed-mode solution MM_{13} . In the interval $Re_{RW_3}^{MM_{13}} < Re < Re_{RW_1}^{MM_{13}}$ both primary solutions (RW_1 and RW_3) are stable under any arbitrary perturbation and in addition they are connected by the unstable

mixed mode MM_{13} , which is located on the separatrix of the basin of attraction of the two primary solutions, the phase portrait of this scenario is sketched in [figure 9\(bi\)](#). Eventually, the solution branch MM_{13} terminates at $Re = Re_{RW_1}^{MM_{13}}$, which makes RW_3 the single attractor of the system for the interval $Re_{RW_1}^{MM_{13}} < Re < Re_{RW_3}^{MM_{23}}$. The RW_3 branch eventually bifurcates into the mixed-mode branch MM_{23} , which is a stable attractor within the interval $Re_{RW_3}^{MM_{23}} < Re < Re_{MM_{23}}^{IMM_{123}}$. The other primary branch, the unstable RW_1 , undergoes another Neimark–Sacker bifurcation at $Re_{RW_1}^{MM_{12}}$ which results in the existence of the MM_{12} branch, yet unstable for perturbations in the transversal direction of the mixed mode (in the r_3 direction). The MM_{12} mixed-mode branch appears to be stable only within a small interval $Re_{MM_{12}}^s < Re < Re_{MM_{12}}^u$, where two bifurcations, which are associated to an instability in the transversal direction r_3 , occur at the two limit values. We have employed s and u to denote the stable or unstable nature of the MM_{12} regime. Thus, for $Re_{MM_{12}}^s < Re < Re_{MM_{12}}^u$, there is a second region with multiple stable attractors, which is schematically displayed in [figure 9\(b ii\)](#). The last bifurcation accounted by the normal form is the destabilization of the MM_{23} branch at $Re = Re_{MM_{23}}^{IMM_{123}}$ that leads to the appearance of the IMM_{123} branch, whose phase portrait is sketched in [figure 9\(b iii\)](#). Please note that despite the fact that IMM_{123} is a fixed-point solution of the normal form, the Newhouse–Takens–Ruelle theorem indicates that the original system of equations may exhibit a chaotic attractors shadowing the IMM_{123} solution.

5. Bifurcation scenario

5.1. Comparison with DNS

In this section we assess the validity of the normal form to characterize the bifurcation scenario, as well as its capability to predict accurately the frequencies and force coefficients of the flow. The estimations of the normal form are compared with DNS results, which are performed at constant rotation rate $\Omega = 1.75$, the scenario analysed in § 4.2. As a first guess, we show the accurate prediction of the fundamental frequencies of each of the invariant states from normal form analysis in [figure 10\(a\)](#) in comparison with DNS results (markers), which will be discussed below.

Direct numerical simulations have been carried out to confirm the existence of the bi-stability of full governing equations (2.1) at $Re = 110$. In particular, two families of time-stepping simulations have been performed with two distinct initial conditions, in such a way that, after a transient period, each of them converged towards different time-periodic solutions. On the one hand, we have used a static, axisymmetric base flow initially obtained at $Re = 70$, $\Omega = 0$ which is able to develop the RW_1 state (family I, grey markers). On the other hand, we have used the solution obtained by Lorite-Díez & Jiménez-González (2020) at $Re = 250$, $\Omega = 2.2$ as initial seed to find the RW_3 state (family II, blue markers), which in turn confirms the existence of multiple stable attractors at $Re = 110$.

To determine the observed regimes, we have computed the frequency components corresponding to St_{RW_1} and St_{RW_3} , displayed in [figure 10\(b,c\)](#), using fast Fourier transform (FFT) spectra of pointwise streamwise and radial velocities in the near wake. The spectra are calculated using the oscillatory part of the velocity-time evolution, i.e. $U' = U - \bar{U}$ for the radial velocity component, where $\bar{\cdot}$ stands for the temporal averaging operator. The three-dimensional topology of the two rotating wave patterns are displayed by means of iso-surfaces of Q quantity in [figure 11](#), where single and double helices topologies are shown.

Triple-Hopf bifurcation in the flow past a rotating sphere

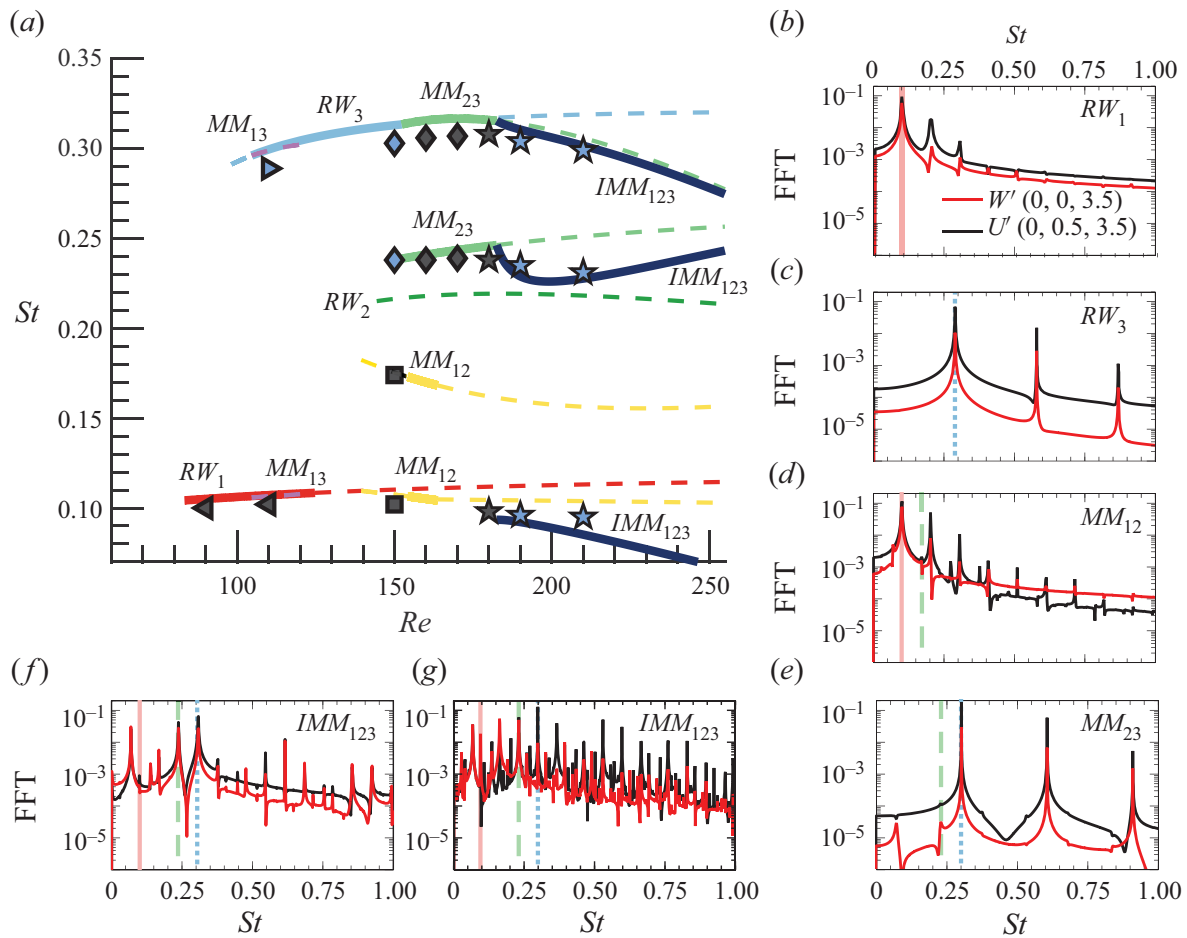


Figure 10. Frequency characterization of the flow at $\Omega = 1.75$. (a) Frequency evolution estimated from the normal form (continuous lines), where attractors are represented with continuous lines, whereas unstable invariant solutions are depicted with dashed lines. The markers of figure (a) denote the resulting pattern obtained from a time-stepping simulation; axisymmetric steady state \circ , RW_1 \triangleleft , RW_3 \triangleright , MM_{12} \square , MM_{23} \diamond , IMM_{123} \star , the family of initial conditions is visualized by colours (family I: grey, family II: blue). Figures (b–g) display the FFT fluctuating velocity spectra for the different regimes obtained by means of DNS. Two velocity components: W' (red solid line), U' (black solid line) and locations $(0, 0, 3.5)$ and $(0, 0.5, 3.5)$, respectively, are selected to characterize all the frequencies in the wake. Unstable mode frequencies are included: low frequency (light red solid line), medium frequency (light green dashed line) and high frequency (light blue dotted line). Results are shown for (b) $Re = 110$, (c) $Re = 110$, (d) $Re = 150$, (e) $Re = 150$, (f) $Re = 181$, (g) $Re = 210$.

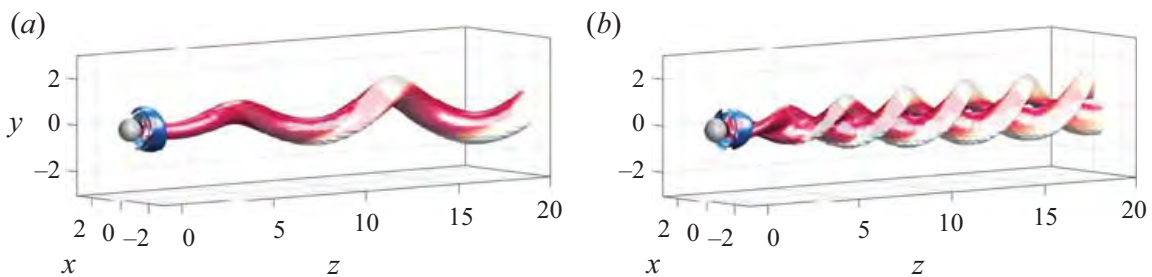


Figure 11. Three-dimensional structures of RW_1 (a) and RW_3 (b) at $Re = 110$ and $\Omega = 1.75$. We have used isosurfaces of Q -criterion, $Q = 0.001$, coloured by streamwise vorticity, $\varpi_z \in [-1, 1]$ (blue to red) to depict the flow structure.

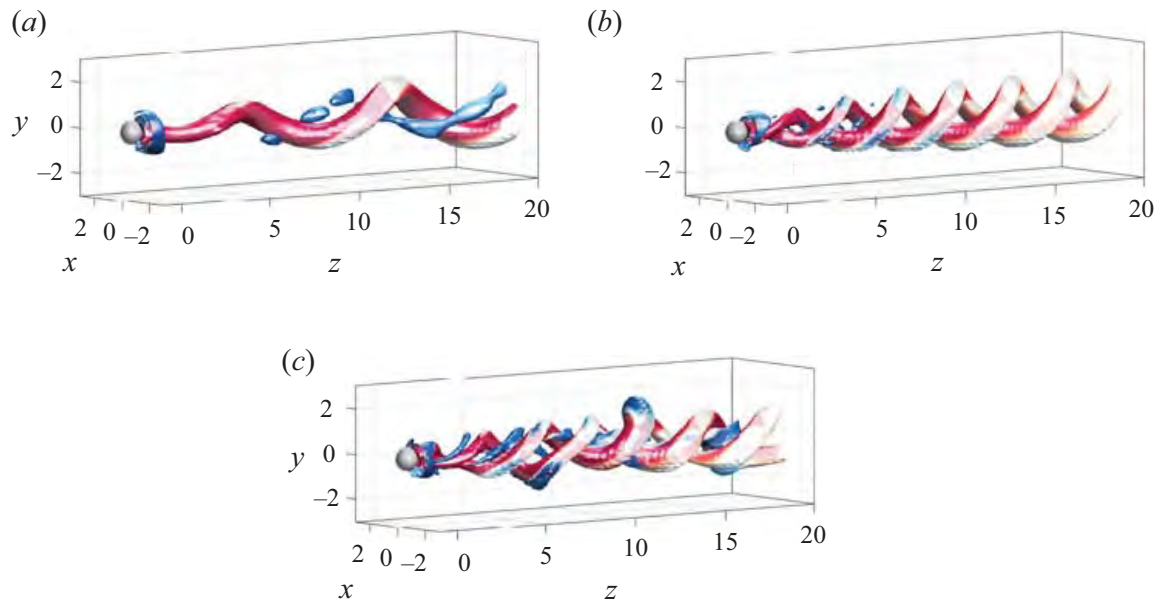


Figure 12. Three-dimensional structure of MM_{12} (a), MM_{23} (b) and IMM_{123} (c) at $Re = 150$ (a,b) and $Re = 210$ (c) and $\Omega = 1.75$. We have used isosurfaces of Q-criterion, $Q = 0.001$, coloured by streamwise vorticity, $\varpi_z \in [-1, 1]$ (blue to red) to depict the flow structure.

Similarly, the existence of two stable mixed-mode attractors (MM_{12} and MM_{23}) is confirmed at $Re = 150$. Two time-stepping simulations of the full governing equations at $Re = 150$ were performed, using RW_1 and RW_3 solutions as initial seeds, the resulting frequency spectra of these patterns are displayed in figure 10(d,e), where the different frequencies associated with MM_{12} and MM_{23} are identified. In particular, we can see that the appearance of the medium-frequency component originates quasiperiodic regimes. The mixed mode MM_{12} has been detected only in a small interval of Reynolds numbers, which is faithfully captured by the normal form; however, the value of $Re_{MM_{12}}^s \approx 154$ slightly differs from the results of the DNS, which show a stable MM_{12} for $Re = 150$. The corresponding patterns are displayed in figure 12(a,b).

The T^3 -quasiperiodic state IMM_{123} has been detected with DNS for Reynolds numbers $Re \approx 181$. Such a state seems to be the single stable attractor in the analysed range $181 < Re < 210$. A series of DNS were carried out with two families of initial conditions: the mixed modes MM_{12} and MM_{23} , both obtained at lower Reynolds numbers. Eventually, every DNS converged to the IMM_{123} state, which seems to confirm the claim that it is the single stable attractor. Their associated spectra is depicted in figure 10(f,g) and its complex topology can be seen in figure 12(c). The identification of the three main frequencies (low, medium and high) in the spectra, figure 10(f), along with the multiple nonlinear interactions between them is possible for Reynolds number values near the bifurcation value $Re_{IMM_{123}}^{IMM_{123}} \simeq 181$. However, it rapidly departs from the T^3 -quasiperiodic state towards a more irregular state ($Re = 210$) with a nearly continuous velocity spectrum, depicted in figure 10(g).

Globally, the good agreement between normal form analysis and DNS frequencies shows the predictive capability of the normal form within the range of Reynolds numbers studied (see figure 10a).

A further investigation of the dynamics of this attractor has been carried out by means of the 0 – 1 test. Such a test was introduced by Gottwald & Melbourne (2004, 2009) to distinguish between regular and chaotic dynamics. More precisely, it corresponds to a dichotomy test where an estimate K , associated to an asymptotic growth of the dynamics,

Triple-Hopf bifurcation in the flow past a rotating sphere

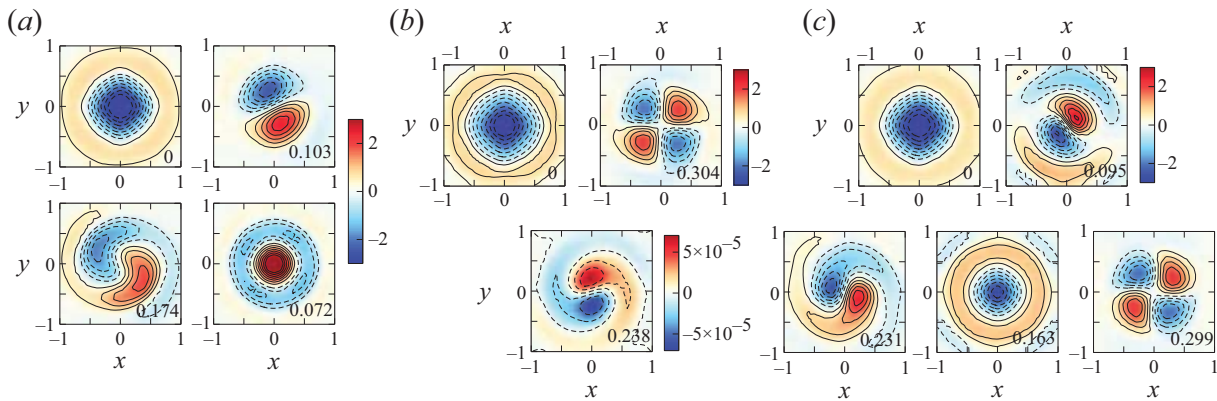


Figure 13. Nonlinear patterns identified through HODMD analysis. The patterns are depicted using streamwise vorticity contours, ϖ_z . Results are shown for (a) MM_{12} , (b) MM_{23} and (c) IMM_{123} regimes. Tags values inside the contours refer to the corresponding frequency of each mode, St_i .

takes discrete values $[0, 1]$ which are associated with non-chaotic (0) and chaotic (1). Further details are given in [Appendix F](#). The results corresponding to the application of the test to the local radial velocity $U'(0, 0.5, 3.5)$, obtained for the two families of computations, indicate a rapid departure towards chaotic dynamics, displayed in the [Appendix \(figure 16\)](#). These results confirm that the transition scenario is eventually ended by the Newhouse–Takens–Ruelle route to chaos.

Furthermore, DNS results can be used to illustrate the spatial pattern associated with each fundamental frequency (low, medium, high). To that aim, a high-order dynamic mode decomposition (HODMD) technique (see [Vega & Le Clainche 2020](#), and references therein) has been applied to instantaneous fields of streamwise vorticity ϖ_z located at $z = 2.5$ to isolate the spatial distributions of the main frequency components. More details about the HODMD technique and its application to present data can be found in [Appendix E](#). In particular, the application of the technique to flow patterns MM_{12} , MM_{23} and IMM_{123} allowed the spatial characterization of the fundamental frequencies and their interactions. Apart from these frequencies, the methodology also provides the approximate contribution of each fundamental mode in the nonlinear state. The spatial patterns identified by HODMD are depicted using contours of spanwise vorticity without normalization. Thus, for the MM_{12} state, the HODMD decomposition identifies four energetic modal contributions, corresponding to frequencies $St = 0, 0.103, 0.174$ and 0.072 , which are depicted in [figure 13\(a\)](#). The use of instantaneous snapshots of ϖ_z allows identifying mean flow ($St = 0$) given by the constant streamwise rotation. Likewise, the low-frequency component ($St = 0.103$) displays a dipole $m = -1$ topology. Similarly, the medium-frequency component ($St = 0.174$), also features a $m = -1$ structure, although their topology resembles the Yin–Yang mode ([Auguste, Fabre & Magnaudet 2010](#)). Finally, an axisymmetric $m = 0$ topology is identified at $St = 0.072$, as the product of the interaction between low-frequency (LF) and medium-frequency (MF) modes, $St_{m_0} \simeq St_{MF} - St_{LF}$. Such a mode is specially energetic close to the longitudinal axis and even dominant in some locations. In [Lorite-Díez & Jiménez-González \(2020\)](#) the authors identified such a mode as a fundamental frequency of the flow, named f_b therein. However, given the results from linear stability and normal form analysis, we have now identified this mode as a subproduct.

The same analysis for the MM_{23} regime allows the identification of three main frequency components, depicted in [figure 13\(b\)](#). Apart from the mean flow ($St = 0$), the flow decomposition pinpoints a mode with high frequency (HF) $St_{HF} = 0.304$, that displays

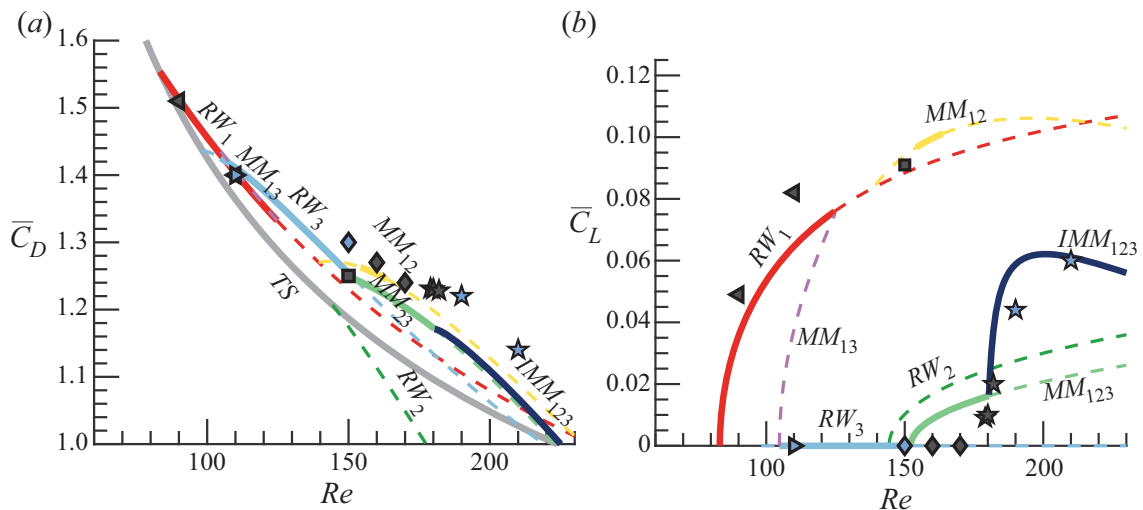


Figure 14. Evolution of the time-averaged forces with respect to Reynolds number for a constant rotation rate $\Omega = 1.75$. The force coefficients determined from the normal form analysis are represented by continuous lines. The force coefficients determined from DNS are depicted with markers. Same legend as in figure 10.

a $m = -2$ structure. In addition, the Yin-Yang mode is also retrieved but now with a frequency, $St_{MF} = 0.238$. Note that, the amplitude associated with this medium-frequency component is very small. The weak energy associated with such a medium-frequency mode in the MM_{23} regime is also observable in the corresponding spectra in figure 10(e).

Furthermore, the HODMD analysis of the complex regime IMM_{123} , present at $Re = 210$ and $\Omega = 1.75$, is depicted in figure 13(c). The decomposition identifies the axisymmetric mean flow, the three fundamental frequencies and many interactions between them, although only five energetic components have been selected for depiction. For instance, the low-frequency and medium-frequency modes display $m = -1$ symmetries and respective frequencies $St_{LF} = 0.095$ and $St_{MF} = 0.231$, which are similar to those corresponding to the MM_{12} and MM_{23} regimes. Similarly, the frequency value of the high-frequency mode ($m = -2$) remains nearly constant with respect to previous regimes, $St_{HF} = 0.299$, indicating that the dependence of frequencies with Re is small (as in figure 3b). Among the main subproducts, the axisymmetric pattern ($m = 0$) produced by the interaction of fundamental frequencies $St_{m0} \simeq St_{LF} + St_{HF} - St_{MF} = 0.163$ stands out. It should be noted that there is a small mismatch between the identified peaks in FFT and the frequencies obtained by HODMD that is produced by the different sampling period and the corresponding recording frequency during the simulation.

To complement the previous analysis, we next focus on the effect of the different flow states, shown in figure 11 and figure 12, on the sphere's aerodynamic forces. Thus, we present in figure 14(a) the evolution with respect to Reynolds number at $\Omega = 1.75$ of the time-averaged drag coefficient, $\overline{C_D} = \overline{C_z}$, and on figure 14(b) the total transverse force coefficient $\overline{C_L} = \sqrt{C_x^2 + C_y^2}$ for normal form analysis and DNS.

The comparison between force coefficients obtained by means of normal form and DNS approaches is indeed fairly satisfactory. The method captures the main trends in the forces and, for most of the states, the prediction is reasonably similar, as it was with the different fundamental frequencies. More precisely, for simpler regimes, such as rotating waves, the normal form analysis and DNS provide the same results. At $Re = 150$, for mixed modes, both methods display a small discrepancy (below five percent). This seems to be related to a small nonlinear contribution of the medium-frequency mode identified by the DNS,

as it can be seen in the corresponding FFT spectra (see [figure 10d,e](#)). That said, the general trend of the mean drag $\overline{C_D}$ displays a general reduction with Re , which may be partly due to a smaller viscous drag contribution. Besides, the pressure drag component is likely to decrease as well, since L_r is shown to increase with Re (see [figure 5b](#)) for a given rotation rate, Ω . In particular, as discussed by Roshko (1993) for three-dimensional bluff body wakes, an increase of the recirculating length leads to a decrease in the drag values on account of a pressure recovery associated to changes in the curvature of the separatrix line. Additionally, major changes in the trends are reported between different flow regimes, as expected from strong modifications in the near wake topology and flow separation (Lorite-Díez & Jiménez-González 2020).

Similarly, the agreement is also good for the mean total transverse coefficient, $\overline{C_L}$, although it displays small deviations for states RW_1 and MM_{23} (see [figure 14b](#)). The value of $\overline{C_L}$ is strongly affected by the wake regime and the corresponding azimuthal symmetry. Therefore, the two families of simulations display quite a different evolution. Moreover, it should be noted that the high-frequency mode does not create a net component of transverse force due their symmetric wake topology, as it is seen for RW_3 and MM_{23} regimes, where this mode is dominant, causing $\overline{C_L} \simeq 0$. In those cases, the wake structures net eccentricity is small, inducing a negligible transverse force. In view of such results, such regimes should be favoured in case of control if a stabilization of the trajectory is wished, e.g. for freely rising or falling rotating spheres, as the transverse displacement of the body might be limited. Conversely, RW_1 , MM_{12} and IMM_{123} are likely to cause lateral shift and destabilization of the trajectory for freely moving bodies due to their greater mean lateral force and their corresponding eccentric wake structures.

5.2. Parametric exploration

Let us discuss the influence of the rotation rate in the dynamics of the flow past the rotating sphere. For that purpose, we determine the stable attractors of the normal form in the range $Re < 300$ and $\Omega < 4$. The cubic normal form coefficients are determined following the same procedure as in § 4.2. However, for low rotation rates ($\Omega < 0.8$), we found that the linear coefficients of the normal form were not correctly estimated. So, for these values of the rotation rate, the linear coefficients are determined exactly at the threshold of instability of each codimension-one bifurcation.

The flow past the static sphere ($\Omega = 0$), analysed by Fabre *et al.* (2008), experiences a symmetry breaking bifurcation that leads to the reflection-symmetric bifid wake (steady-state mode) and eventually a Hopf bifurcation that leads to the RSP. The phase diagram depicted in [figure 15](#) shows that both the rotating wave RW_1 and the mixed mode MM_{12} are the continuation in the parameter space of the steady-state and RSP mode, respectively. Thus, dynamics for low values of the rotation rate ($\Omega < 1$) are qualitatively similar to the flow past the static sphere. However, for rotation rate values slightly larger than Ω_B , one starts detecting a wake with a double helix. This fact has been evidenced by the numerical simulations of Lorite-Díez & Jiménez-González (2020), Pier (2013) and the experimental work of Skarysz *et al.* (2018) who reported that at around $\Omega \approx 1.5$ for large Reynolds numbers ($Re > 250$) the quasiperiodic motion of the wake changes from a single to double helix pattern, which is consistent with the phase diagram in [figure 15](#). However, if we look in detail at how the flow transits from a single helix to the double helix wake in terms of the rotation of the sphere, one can observe three bi-stable regions, between RW_1 and RW_3 , between RW_3 and MM_{12} , and between MM_{12} and MM_{23} . These bi-stable sections connect two regions of the parameter space with distinct attractors, the rotating waves RW_1 and RW_3 and the mixed modes MM_{12} and MM_{23} . It is of interest that the formation of

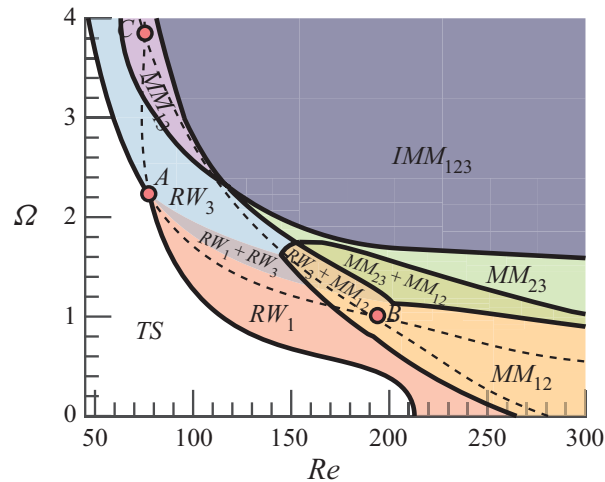


Figure 15. Phase diagram of the nonlinear patterns in the range $\Omega < 4$ and $Re < 300$, as predicted by the normal form (4.9). The axisymmetric state (TS) persists in the white region. Shaded regions indicate the existence of a stable pattern (respectively, stable patterns). Dashed lines illustrate unstable rotating waves neutral curves obtained by LSA.

these new states occurs near the codimension-two point B , which exhibits the importance of this bifurcation as an organizing centre, even though it occurs as a bifurcation for an already unstable trivial state. Furthermore, the importance of the codimension point A is clearly evidenced by figure 15, which also acts as an organizing centre of dynamics. Around point A , one finds four distinct regions with inequivalent dynamics. If we move counterclockwise from point A , we have the left region where the trivial axisymmetric state is stable, the lower region where the RW_1 state is the single attractor, a region with two stable attractors (RW_1 and RW_3) and the upper region where the RW_3 is the single stable state. Finally, the significance of the other codimension-two bifurcation, the point C , is rather more subtle. This point is located in the only region where one can observe the mixed mode MM_{13} , which is only observed for very large rotation rates, and it connects the RW_3 state and the T^3 -quasiperiodic state IMM_{123} .

Therefore, one may conclude that the rotation of the sphere has a mild effect on the bifurcation scenario for low rotation rates ($\Omega < 1$). Rotation rates between $1 < \Omega < 2$ favourise the appearance of a double helix wake and hysteresic behaviour, whereas large rotation rates ($\Omega > 2$) have a destabilizing effect which rapidly triggers the emergence of chaotic dynamics via a Ruelle–Takens–Newhouse route.

6. Conclusion

The present study conducts a complete study of the transition scenario of the flow past a rotating sphere, which is a canonical model of many industrial and natural phenomena like particle-driven flows, sport aerodynamics, bubble motion, plant seeds, etc. In such applications the changes in the paths of the particles are related to the destabilization of complex flow regimes and associated force distributions. To gain a deeper understanding of the underlying physics and evaluate possibilities of flow and path control, we have studied the mode competition involved in the formation of patterns in the flow past a rotating sphere, associated sensitivity to forcing and the effect of flow regimes on the force coefficients. This research aimed to structurally study the pattern formation previously examined by Lorite-Díez & Jiménez-González (2020), Pier (2013) and to determine from a dynamical perspective the fundamental building blocks of dynamics before and up to

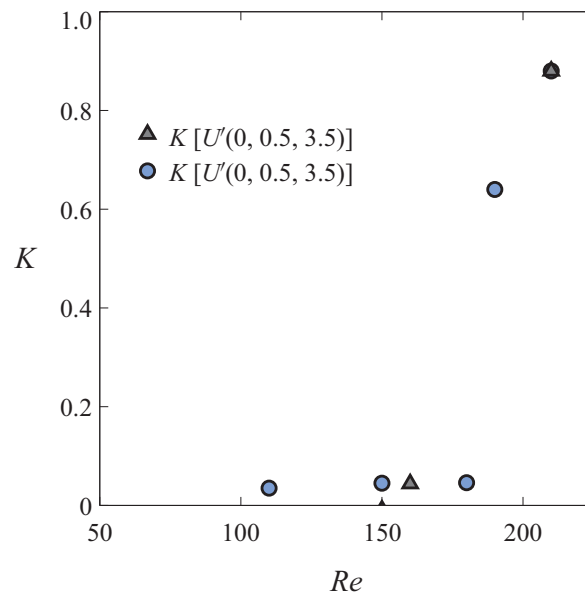


Figure 16. Asymptotic growth K associated with the local radial velocity $U'(0, 0.5, 3.5)$ (same as in figure 10). Results are shown for the different initial seeds: RW_1 (grey triangles) and RW_3 (blue circles).

temporal chaos. In order to do that, we have employed LSA, normal form analysis and DNS.

Rotation of the sphere breaks the reflectional symmetry, thus inducing a preferential direction. This turns out to favourise the presence of rotating wave instabilities, instead of a steady symmetry breaking bifurcation, as it is the case for the flow past the static sphere. These instabilities exhibit a localized wavemaker within the recirculation zone, which is evidenced by the sensitivity maps. In addition, non-normality effects are weaker than in the flow past the static sphere, mainly because the primary bifurcation occurs at lower Reynolds number values. This might be an indication of a weaker transient growth of asymptotically stable perturbations for the rotating sphere wake flow (Chomaz 2005).

The bifurcation scenario is qualitatively distinct and it greatly varies with the rotation rate, as it has been discussed in § 5.2. The flow field displays a large variety of attractors from rotating waves, quasiperiodic mixed modes to T^3 -quasiperiodic structures. In addition, one may find multiple attractors, which is associated to hysteresis, and it seems to be a common feature of many supercritical and subcritical flows, cf. (Subramanian, Sujith & Wahi 2013; Guo *et al.* 2018; Ren *et al.* 2021; Huang *et al.* 2018; Suckale *et al.* 2018). Eventually, for sufficiently large Reynolds numbers, Lorite-Díez & Jiménez-González (2020) and Pier (2013) identified irregular regimes for most rotation rates, which are associated to a T^3 -quasiperiodic attractor. Nonetheless, such a state is just observed by means of DNS near its onset of existence. For larger Reynolds number values, the attractor is no longer quasiperiodic, but it is characterized by a continuous frequency spectra, that turns out to be chaotic. Indeed, such a chaotic attractor shadows the three frequency quasiperiodic state predicted by the normal form, which is evidenced by physical global features of the flow, e.g. the force acting on the surface of the sphere.

The analysis performed in this paper is able to accurately predict the fundamental modes of the wake flow, the bifurcation scenario and the forces acting on the sphere without the need of performing a fully nonlinear DNS. The results are compared against DNS computations at $\Omega = 1.75$ with an excellent agreement in regime zones, mode frequencies and force coefficients. Then, our procedure has been validated without

including non-normal and resonance effects in our analysis. In any case, their impact has been proven to be very reduced in this problem.

In the classification of the observed regimes, one may question which is the path or bifurcation scenario and how are they constituted, i.e. if it is possible to reconstitute the strange attractor with a sparse approximation. The identification of a T^3 -quasiperiodic state, complemented with DNS results, allows the justification that the route to chaos is indeed the Ruelle–Takens–Newhouse. This has several consequences for further studies of this or similar flows. First, we have been able to identify the route to chaos and the fundamental building blocks, which are the three rotating waves. One could attempt to obtain further insight into the chaotic attractor and to investigate physically interesting properties such as mixing or the forces on the sphere from the information extracted from the three unstable periodic orbits associated with the fundamental rotating waves. In this case, it seems reasonable to construct a symbolic alphabet with the main fundamental modes being the rotating waves. Then, one may approximate average quantities or the eigenvalues of the Perron–Frobenius operator by cycle expansions, cf. (Cvitanovic *et al.* 2005), as it has been recently done by Yalnız & Budanur (2020); Yalnız, Hof & Budanur (2021) using algebraic topology techniques.

In addition, if one attempts to design a control procedure to the quasiperiodic state or to prevent the presence of chaotic dynamics, the use of harmonic forcing, as in Sipp (2012), seems a promising option, and the implementation is straightforward from the information provided in §§ 4 and 5. Additionally, the sensitivity to base flow modifications and structural sensitivity have been presented for the low-frequency and high-frequency modes in § 3.4 to analyse harmonic and steady control possibilities. It has been shown that the low-frequency mode displays a strong sensitivity inside the recirculating region, suggesting a higher receptivity to control through surface rear blowing, in line with the results presented in Niazmand & Renksizbulut (2005). In principle, the attenuation of the amplitude of such a mode would imply a decrease in the mean drag and total lift coefficients (see figure 14), which could presumably prevent the path's instability in the case of freely rising bodies, as those analysed by Mathai *et al.* (2018). Therein, the tuning of rotational inertia is proposed to modify the wake and path's instabilities. The effect of changes in the moment of inertia may imply variations of the rotation rate, and consequently, changes in the regimes and associated forces. At that point, the force diagrams presented in figure 14 could be useful to guide such a tuning procedure and selectively set the regime of interest.

Acknowledgements. The authors are grateful to A. Chatterjee for useful discussions and the critical reading of the manuscript.

Funding. This work has been partially financed by the Junta de Andalucía, Universidad de Jaén, and European Funds under Project FEDER-UJA 1262764.

Declaration of interests. The authors report no conflict of interest.

Author ORCIDs.

- 📍 J. Sierra-Ausín <https://orcid.org/0000-0001-6036-5093>;
- 📍 M. Lorite-Díez <https://orcid.org/0000-0002-7392-8622>;
- 📍 J.I. Jiménez-González <https://orcid.org/0000-0001-6669-9000>;
- 📍 V. Citro <https://orcid.org/0000-0003-2923-9157>;
- 📍 D. Fabre <https://orcid.org/0000-0003-1875-6386>.

Coef.	$\lambda_\ell^{(\varepsilon_v^2)}$	$\lambda_\ell^{(\varepsilon_\Omega^2)}$	$\lambda_\ell^{(\varepsilon_v^4)}$	$\lambda_\ell^{(\varepsilon_\Omega^2 \varepsilon_v^2)}$	$\lambda_\ell^{(\varepsilon_\Omega^4)}$
λ_1^A	15 - 0.60i	$(-1.8 + 8.2i) \times 10^{-2}$	$(-1.5 - 2.9i) \times 10^2$	9.6 - 1.5i	$(-38 - 2.9i) \times 10^{-3}$
λ_3^A	43 - 5.5i	$(-22 + 5.8i) \times 10^{-2}$	$(-2.3 - 10i)10^2$	11 - 0.18i	$(-1.6 - 1.6i)10^{-1}$
λ_2^B	$(11 - 3.2i) \times 10^1$	$(-2.6 + 1.64i) \times 10^{-1}$	$(-1.1 + 6.9i) \times 10^2$	5.4 + 5.2i	$(-3.4 - 18i) \times 10^{-2}$
λ_3^B	54 - 50i	0.36 - 0.58i	$(4.2 - 6.9i) \times 10^3$	64 - 22i	$(-1.9 - 4.4i) \times 10^{-1}$
λ_1^C	9.1 - 3.7i	$(1.1 + 11i) \times 10^{-2}$	$(-1.1 - 7.4i) \times 10^2$	-0.80 + 3.8i	$(18 - 4.4i) \times 10^{-2}$
λ_2^C	46 - 18i	$(-1.2 + 1.7) \times 10^{-2}$	$(-2.7 - 18i) \times 10^2$	16 + 10i	$(-4.4 - 3.6i) \times 10^{-2}$

Table 4. Linear coefficients of the normal form (4.9) evaluated at codimension-two points.

Appendix A. Normal form reduction procedure for the triple-Hopf interaction

Before we detail the procedure for the reduction of the governing equations to the normal form (4.6), let us detail the terms that composed the compact notation of the governing equations (2.3), which is reminded here for the sake of conciseness,

$$B \frac{\partial \mathbf{Q}}{\partial t} = F(\mathbf{Q}, \eta) \equiv L\mathbf{Q} + N(\mathbf{Q}, \mathbf{Q}) + G(\mathbf{Q}, \eta). \tag{A1}$$

The operator $G(\mathbf{Q}, \eta) = G(\mathbf{Q}, [\eta_1, 0]^T) + G(\mathbf{Q}, [0, \eta_2]^T)$, where $G(\mathbf{Q}, [\eta_1, 0]^T) = \eta_1 \nabla \cdot (\nabla U + \nabla U^T)$ and $G(\mathbf{Q}, [0, \eta_2]^T)$ expresses the imposition of the boundary condition $U = (0, \eta_2, 0)$ on Σ_b . The nonlinear operator $N(\mathbf{Q}_1, \mathbf{Q}_2) = U_1 \cdot \nabla U_2$, and the linear operator accounts for the remaining terms that are linear on the state variable \mathbf{Q} , i.e. $L\mathbf{Q} = [\nabla P, \nabla \cdot U]^T$. In addition, we consider the following splitting of the parameters $\eta = \eta_c + \Delta\eta$, where η_c denotes the critical parameters $\eta_c \equiv [Re_c^{-1}, \Omega_c]^T$ attained when the spectra of the Jacobian operator of the steady state posses at least an eigenvalue whose real part is zero, and $\Delta\eta = [Re_c^{-1} - Re^{-1}, \Omega_c - \Omega]^T$ the departure from the critical condition.

The procedure followed in this manuscript consists of the determination of a fifth-order Taylor expansion of the centre manifold, also known as the normal form, of the three codimension-two-Hopf points (A, B, C), which enables a linear approximation of the cubic coefficients $v_{k\ell}$ and a quadratic approximation of the linear coefficients λ_ℓ . The ultimate goal of this approach is the determination of the coefficients listed in tables 4–6. That is, to determine the cubic coefficient $v_{k\ell}$ values as

$$v_{k\ell} = v_{k\ell}^{(0)} + \varepsilon_v^2 v_{k\ell}^{(\varepsilon_v^2)} + \varepsilon_\Omega^2 v_{k\ell}^{(\varepsilon_\Omega^2)}, \tag{A2}$$

where $v_{k\ell}^{(0)}$, $v_{k\ell}^{(\varepsilon_v^2)}$ and $v_{k\ell}^{(\varepsilon_\Omega^2)}$ are determined at the two-Hopf point between mode k and ℓ . Similarly, the estimation of the linear coefficient is

$$\lambda_\ell = \varepsilon_v^2 \lambda_\ell^{(\varepsilon_v^2)} + \varepsilon_\Omega^2 \lambda_\ell^{(\varepsilon_\Omega^2)} + \varepsilon_v^4 \lambda_\ell^{(\varepsilon_v^4)} + \varepsilon_\Omega^4 \lambda_\ell^{(\varepsilon_\Omega^4)} + \varepsilon_\Omega^2 \varepsilon_v^2 \lambda_\ell^{(\varepsilon_v^2 \varepsilon_\Omega^2)}. \tag{A3}$$

The reduction to the normal form is carried out via a multiple scales expansion of the solution \mathbf{Q} of (2.3). The expansion considers a two-scale expansion of the original time, a fast time scale t of the self-sustained instability and a slow time scale of the evolution of

Coef.	$v_{kl}^{(0)}$	$v_{kl}^{(\varepsilon_v^2)}$	$v_{kl}^{(\varepsilon_\Omega^2)}$
v_{11}^A	$-0.46 + 0.16i$	$6.3 + 10.1i$	$(4.4 - 1.1i) \times 10^{-2}$
v_{13}^A	$-3.0 + 0.73i$	$(4.6 - 2.3i) \times 10^2$	$-3.6 - 5.2i$
v_{31}^A	$-0.73 + 1.07i$	$(2.2 - 8.6i) \times 10^1$	$(2.2 - 2.4i) \times 10^{-1}$
v_{33}^A	$-1.5 + 2.1i$	$(-1.1 - 11i) \times 10^1$	$-0.56 - 0.30i$
v_{22}^B	$-1.8 + 0.22i$	$(2.2 - 34i) \times 10^1$	$0.46 - 1.0i$
v_{23}^B	$-1.9 - 0.2i$	$(2.9 - 1.4i) \times 10^2$	$2.6 + 2.4i$
v_{32}^B	$(-34 - 3.1i) \times 10^{-2}$	$(3.0 - 10i) \times 10^2$	$-0.22 + 2.2i$
v_{33}^B	$-1.7 + 0.9i$	$(1.0 - 11i) \times 10^2$	$0.30 - 1.54i$
v_{11}^C	$-0.25 + 0.15i$	$34 - 2.1i$	$(5.2 - 10i) \times 10^{-2}$
v_{12}^C	$0.58 - 0.58i$	$(-2.4 + 3.0i) \times 10^2$	$0.74 - 0.28i$
v_{21}^C	$(4.6 - 26i) \times 10^{-2}$	$2.3 - 71i$	$(2.4 - 30i) \times 10^{-2}$
v_{22}^C	$-1.9 + 3.1i$	$(4.7 - 10i) \times 10^2$	$-2.4 + 5.2$

Table 5. Cubic coefficients of the normal form (4.9) evaluated at codimension-two points.

Coef.	Value				
λ_1	$(-0.019 + 0.038i)$	+	$(20.2 - 1.60i)\varepsilon_v^2$	+	$(-1.5 - 2.9i) \times 10^2 \varepsilon_v^4$
λ_2	$(0.1805 + 0.1107i)$	+	$(11 - 2.8i) \times 10^1 \varepsilon_v^2$	+	$(-1.1 + 6.9i) \times 10^2 \varepsilon_v^4$
λ_3	$(-0.13 + 0.003i)$	+	$(49 - 6.3i)\varepsilon_v^2$	+	$(-2.3 - 10i)10^2 \varepsilon_v^4$
v_{11}	$(-0.44 + 0.15i)$	+	$(6.3 - 10i)\varepsilon_v^2$		
v_{12}	$(2.2 - 1.2i)$	+	$(-2.4 + 3.0i) \times 10^2 \varepsilon_v^2$		
v_{13}	$(-4.7 + 1.9i)$	+	$(4.6 - 2.3i) \times 10^2 \varepsilon_v^2$		
v_{21}	$(0.10 + 0.43i)$	+	$(2.3 - 71i)\varepsilon_v^2$		
v_{22}	$(-2.2 + 0.94i)$	+	$(2.2 - 34i) \times 10^1 \varepsilon_v^2$		
v_{23}	$(-0.08 - 1.6i)$	+	$(2.9 - 1.4i) \times 10^2 \varepsilon_v^2$		
v_{31}	$(-0.63 + 0.95i)$	+	$(2.2 - 8.6i) \times 10^1 \varepsilon_v^2$		
v_{32}	$(-0.19 - 0.06i)$	+	$(3.0 - 10i) \times 10^2 \varepsilon_v^2$		
v_{33}	$(-1.9 + 2.0i)$	+	$(1.0 - 11i) \times 10^1 \varepsilon_v^2$		

Table 6. Cubic coefficients of the normal form (4.9) evaluated at $\Omega = 1.75$.

the amplitudes

$$t \mapsto t + \varepsilon^2 \tau, \quad \varepsilon \ll 1, \tag{A4}$$

here ε is the order of magnitude of the flow disturbances. The small parameters are

$$\varepsilon_\Omega^2 = (\Omega_c - \Omega) \sim \varepsilon^2 \quad \text{and} \quad \varepsilon_v^2 = (v_c - v) = (Re_c^{-1} - Re^{-1}) \sim \varepsilon^2. \tag{A5a,b}$$

The ansatz of the expansion is

$$\mathbf{Q}(t, \tau) = \mathbf{Q}_b + \varepsilon \mathbf{q}_{(\varepsilon)}(t, \tau) + \varepsilon^2 \mathbf{q}_{(\varepsilon^2)}(t, \tau) + \varepsilon^3 \mathbf{q}_{(\varepsilon^3)}(t, \tau) + \varepsilon^4 \mathbf{q}_{(\varepsilon^4)}(t, \tau) + O(\varepsilon^5). \tag{A6}$$

Note that the expansion of the left-hand side of (2.3) up to fifth order is

$$\begin{aligned} & \varepsilon \mathbf{B} \frac{\partial \mathbf{q}_{(\varepsilon)}}{\partial t} + \varepsilon^2 \mathbf{B} \frac{\partial \mathbf{q}_{(\varepsilon^2)}}{\partial t} + \varepsilon^3 \left[\mathbf{B} \frac{\partial \mathbf{q}_{(\varepsilon^3)}}{\partial t} + \mathbf{B} \frac{\partial \mathbf{q}_{(\varepsilon)}}{\partial \tau} \right] \\ & + \varepsilon^4 \left[\mathbf{B} \frac{\partial \mathbf{q}_{(\varepsilon^4)}}{\partial t} + \mathbf{B} \frac{\partial \mathbf{q}_{(\varepsilon^2)}}{\partial \tau} \right] + \varepsilon^5 \left[\mathbf{B} \frac{\partial \mathbf{q}_{(\varepsilon^5)}}{\partial t} + \mathbf{B} \frac{\partial \mathbf{q}_{(\varepsilon^3)}}{\partial \tau} \right], \end{aligned} \tag{A7}$$

respectively the right-hand side is

$$F(\mathbf{q}, \eta) = F_{(0)} + \varepsilon F_{(\varepsilon)} + \varepsilon^2 F_{(\varepsilon^2)} + \varepsilon^3 F_{(\varepsilon^3)} + \varepsilon^4 F_{(\varepsilon^4)} + \varepsilon^5 F_{(\varepsilon^5)}. \quad (\text{A8})$$

Then we are left with the determination of the forcing terms of (A8).

The reduction detailed in this appendix considers the interaction between two rotating wave solutions at a codimension-two point. In the following, we adopt the notation for the solutions z_1 and z_2 , which correspond to point C. In order to proceed for the other two points, replace z_1 by z_3 or z_2 by z_3 .

A.1. Notation

Since the number of terms grows quickly with the order, in order to enhance readability, we define the set of vectors of linear, quadratic, cubic and fourth-order interactions as

$$\begin{aligned} \mathbf{Z} &\equiv \{z_1, z_2\}, \quad \bar{\mathbf{Z}} = \{\bar{z}_1, \bar{z}_2\}, \\ \mathbf{Z}^2 &\equiv \mathbf{Z} \otimes \mathbf{Z} \oplus \mathbf{Z} \otimes \bar{\mathbf{Z}} = \{z_1^2, z_1 z_2, z_2^2, |z_1|^2, z_1 \bar{z}_2, |z_2|^2\}, \\ \mathbf{Z}^3 &\equiv \mathbf{Z} \otimes \mathbf{Z}^2 \oplus \mathbf{Z}^2 \otimes \bar{\mathbf{Z}} \\ &= \{z_1^3, z_1^2 z_2, z_1 z_2^2, z_2^3, z_1 |z_1|^2, z_2 |z_1|^2, z_2^2 \bar{z}_1, \bar{z}_2 z_1^2, z_1 |z_2|^2, z_2 |z_2|^2\}, \\ \mathbf{Z}^4 &\equiv \mathbf{Z}^2 \otimes \mathbf{Z}^2 \oplus \mathbf{Z} \otimes \bar{\mathbf{Z}}^3 \\ &= \{z_1^4, z_1^3 z_2, z_1^2 z_2^2, z_1 z_2^3, z_2^4, z_1^2 |z_1|^2, z_1 z_2 |z_1|^2, z_2^2 |z_1|^2, z_1^2 |z_2|^2, \\ &\quad z_1 z_2 |z_2|^2, z_2^2 |z_2|^2, z_1 \bar{z}_2 |z_1|^2, z_1 \bar{z}_2 |z_2|^2, z_1^3 \bar{z}_2, \bar{z}_1 z_2^3\}, \end{aligned} \quad (\text{A9})$$

where only unique elements are kept. We denote by z_α^n any element of the family \mathbf{Z}^n , with $n \in \mathbb{N}^*$. In addition to these sets, we shall define the set of resonant terms

$$\mathbf{Z}_R \equiv \{z_1, z_2, z_1 |z_1|^2, z_1 |z_2|^2\}. \quad (\text{A10})$$

A.2. Zeroth order

The zeroth order corresponds to the steady-state problem of the governing equations evaluated at the threshold of instability, i.e. $\Delta\eta = \mathbf{0}$,

$$\mathbf{0} = F(\mathbf{Q}_b, \mathbf{0}), \quad (\text{A11})$$

whose solution is the steady state \mathbf{Q}_b .

A.3. First order

The first order corresponds to the resolution of a homogeneous linear system, i.e. the generalized eigenvalue problem evaluated at the threshold of instability, i.e. $\Delta\eta = \mathbf{0}$. In such a case, the vector is expanded as

$$\mathbf{q}_{(\varepsilon)} = z_1 \hat{\mathbf{q}}_{(z_1)} \exp(-i(m_1\theta + \omega_1 t)) + z_2 \hat{\mathbf{q}}_{(z_2)} \exp(-i(m_2\theta + \omega_2 t)) + \text{c.c.} \quad (\text{A12})$$

Then, the eigenpairs $[i\omega_\ell, \hat{\mathbf{q}}_{(z_\ell)}]$ are determined as the solutions of the following eigenvalue problem:

$$\mathbf{J}_{(\omega_\ell, m_\ell)} \hat{\mathbf{q}}_{(z_\ell)} = \left(i\omega_\ell \mathbf{B} - \frac{\partial F}{\partial \mathbf{q}} \Big|_{\mathbf{q}=\mathbf{Q}_b, \Delta\eta=\mathbf{0}} \right) \hat{\mathbf{q}}_{(z_\ell)}. \quad (\text{A13})$$

The eigenmode $\hat{\mathbf{q}}_{(z_\ell)}(r, z)$ is then normalised in such a way that $\langle \hat{\mathbf{u}}_{(z_\ell)}, \hat{\mathbf{u}}_{(z_\ell)} \rangle_{L^2} = 1$.

A.4. Second order

The second-order expansion term $\mathbf{q}_{(\varepsilon^2)}(t, \tau)$ is determined by the resolution of a set of linear systems, where the forcing terms are evaluated from first- and zeroth-order terms. The expansion in terms of amplitudes $z_\ell(\tau)$ of $\mathbf{q}_{(\varepsilon^2)}(t, \tau)$ is assessed by collecting the second-order forcing terms. Nonlinear second-order terms in ε are

$$\begin{aligned} F_{(\varepsilon^2)} \equiv & \sum_{j,k=1}^2 \left(z_j z_k N(\hat{\mathbf{q}}_{(z_j)}, \hat{\mathbf{q}}_{(z_k)}) \exp(-i(m_j + m_k)\theta) \exp(-i(\omega_j + \omega_k)t) + \text{c.c.} \right) \\ & + \sum_{j,k=1}^2 \left(z_j \bar{z}_k N(\hat{\mathbf{q}}_{(z_j)}, \hat{\mathbf{q}}_{(\bar{z}_k)}) \exp(-i(m_j - m_k)\theta) \exp(-i(\omega_j - \omega_k)t) + \text{c.c.} \right) \\ & + \sum_{\ell=1}^2 \eta_\ell G(\mathbf{Q}_b, \mathbf{e}_\ell), \end{aligned} \tag{A14}$$

where \mathbf{e}_ℓ is an element of the orthonormal basis of \mathbb{R}^2 . Then the second-order expansion of the flow variable is carried out so it matches the terms of the forcing (A14),

$$\mathbf{q}_{(\varepsilon^2)} \equiv \sum_{z_\alpha^2 \in \mathcal{Z}} \left(z_\alpha^2 \hat{\mathbf{q}}_{(z_\alpha^2)} \exp(-i(m_\alpha \theta + \omega_\alpha t)) + \text{c.c.} \right) + \sum_{\ell=1}^2 \eta_\ell \mathbf{Q}_b^{(\eta_\ell)}. \tag{A15}$$

Terms $\hat{\mathbf{q}}_{(z_j^2)}$ are harmonics of the flow, $\hat{\mathbf{q}}_{(z_j z_k)}$ with $j \neq k$ are coupling terms, $\hat{\mathbf{q}}_{(|z_j|^2)}$ are harmonic base flow modification terms and $\mathbf{Q}_b^{(\eta_\ell)}$ are base flow corrections due to a modification of the parameter η_ℓ from the critical point. Then the second-order terms are determined from the resolution of the following systems of equations:

$$\mathbf{J}_{(\omega_j + \omega_k, m_j + m_k)} \hat{\mathbf{q}}_{(z_j z_k)} = \hat{\mathbf{F}}_{(z_j z_k)}. \tag{A16}$$

Here $\hat{\mathbf{F}}_{(z_j z_k)} \equiv N(\hat{\mathbf{q}}_{(z_j)}, \hat{\mathbf{q}}_{(z_k)}) + N(\hat{\mathbf{q}}_{(z_k)}, \hat{\mathbf{q}}_{(z_j)})$ and

$$\mathbf{J}_{(0,0)} \mathbf{Q}_b^{(\eta_\ell)} = G(\mathbf{Q}_b, \mathbf{e}_\ell). \tag{A17}$$

A.5. Third order

At third order, we proceed as for previous orders, first the forcing term is expanded as

$$\begin{aligned} F_{(\varepsilon^3)} \equiv & \sum_{z_\alpha \in \mathcal{Z}, z_\beta^2 \in \mathcal{Z}^2} z_\alpha \cdot z_\beta^2 \left[N(\hat{\mathbf{q}}_{(z_\beta^2)}, \hat{\mathbf{q}}_{(z_\alpha)}) + N(\hat{\mathbf{q}}_{(z_\alpha)}, \hat{\mathbf{q}}_{(z_\beta^2)}) \right] \exp(i(m_\alpha + m_\beta)\theta + i(\omega_\alpha + \omega_\beta)t) \\ & + \sum_{j=1}^2 \sum_{\ell=1}^2 \left[z_j \eta_\ell \left[N(\hat{\mathbf{q}}_{(z_j)}, \mathbf{Q}_b^{(\eta_\ell)}) + N(\mathbf{Q}_b^{(\eta_\ell)}, \hat{\mathbf{q}}_{(z_j)}) \right] \exp(-im_j \theta) \exp(-i\omega_j t) + \text{c.c.} \right] \\ & + \sum_{j=1}^2 \sum_{\ell=1}^2 \left[z_j \eta_\ell G(\hat{\mathbf{q}}_{(z_j)}, \mathbf{e}_\ell) \exp(-im_j \theta) \exp(-i\omega_j t) + \text{c.c.} \right], \end{aligned} \tag{A18}$$

Triple-Hopf bifurcation in the flow past a rotating sphere

where ω_n and m_n are defined as $\omega_n = \omega_j + \omega_k + \omega_\ell$, $m_n = m_j + m_k + m_\ell$ with $n = j + k + \ell$. Followed by the expansion of the state variable $\mathbf{q}_{(\varepsilon^3)}(t, \tau)$,

$$\begin{aligned} \mathbf{q}_{(\varepsilon^3)}(t, \tau) \equiv & \sum_{z_\alpha^3 \in \mathcal{Z}} \left[z_\alpha^3 \hat{\mathbf{q}}_{(z_\alpha^3)} \exp(-i(m_\alpha \theta + \omega_\alpha t)) + \text{c.c.} \right] \\ & + \sum_{j=1}^2 \sum_{\ell=1}^2 \left[z_j \eta_\ell \mathcal{Q}_{(z_j)}^{(\eta_\ell)} \exp(-im_j \theta) \exp(-i\omega_j t) + \text{c.c.} \right]. \end{aligned} \quad (\text{A19})$$

At this order there exist resonance terms, which are associated with the singular Jacobian $\mathbf{J}_{(\omega_k, m_k)}$ for $k = 1, 2, 3$. To ensure the solvability of these terms, we must enforce compatibility conditions, i.e. the Fredholm alternative. The resonant terms are then determined from the resolution of the following set of bordered systems:

$$\begin{pmatrix} \mathbf{J}_{(\omega_k, m_k)} & \hat{\mathbf{q}}_{(z_k)} \\ \hat{\mathbf{q}}_{(z_k)} & 0 \end{pmatrix} \begin{pmatrix} \hat{\mathbf{q}}_{(z_\alpha^{(R)})} \\ s \end{pmatrix} = \begin{pmatrix} \hat{\mathbf{F}}_{(z_\alpha^{(R)})} \\ 0 \end{pmatrix}, \quad z_\alpha^{(R)} \in \mathcal{Z}_R. \quad (\text{A20})$$

Here $s = \lambda_k^{(\varepsilon_v^2)}$ (respectively $s = \lambda_k^{(\varepsilon_\Omega^2)}$) for $z_\alpha^{(R)} = z_k$ and $s = \nu_{kl}^{(0)}$ for $z_\alpha^{(R)} = z_k |z_\ell|^2$. The non-resonant terms are then determined as at second order from the resolution of forced linear systems.

A.6. Fourth order

At fourth order we proceed as at second order, we expand the forcing term $\mathbf{F}_{(\varepsilon^4)}$ as

$$\begin{aligned} \mathbf{F}_{(\varepsilon^4)} \equiv & \sum_{z_\alpha \in \mathcal{Z}, z_\beta^3 \in \mathcal{Z}^3} z_\alpha \cdot z_\beta^3 \left[N(\hat{\mathbf{q}}_{(z_\beta^3)}, \hat{\mathbf{q}}_{(z_\alpha)}) + N(\hat{\mathbf{q}}_{(z_\alpha)}, \hat{\mathbf{q}}_{(z_\beta^3)}) \right] \exp(i(m_\alpha + m_\beta)\theta + i(\omega_\alpha + \omega_\beta)t) \\ & + \sum_{z_\alpha^2 \in \mathcal{Z}^2, z_\beta^2 \in \mathcal{Z}^2} z_\alpha^2 \cdot z_\beta^2 \left[N(\hat{\mathbf{q}}_{(z_\alpha^2)}, \hat{\mathbf{q}}_{(z_\beta^2)}) \right] \exp(i(m_\alpha + m_\beta)\theta + i(\omega_\alpha + \omega_\beta)t) \\ & + \sum_{\ell=1}^2 \eta_\ell \sum_{z_\alpha^2 \in \mathcal{Z}^2} z_\alpha^2 \mathbf{G}(\hat{\mathbf{q}}_{(z_\alpha^2)}, \mathbf{e}_\ell) \exp(-i(m_\alpha \theta + \omega_\alpha t)) \\ & + \sum_{\ell, k=1}^2 \eta_\ell \eta_k \left[N(\mathcal{Q}_b^{(\eta_k)}, \mathcal{Q}_b^{(\eta_\ell)}) \right] \\ & + \sum_{\ell=1}^2 \eta_\ell \sum_{z_\alpha \in \mathcal{Z}, z_\beta \in \mathcal{Z}} z_\alpha \cdot z_\beta \left[N(\mathcal{Q}_{(z_\alpha)}^{(\eta_\ell)}, \hat{\mathbf{q}}_{(z_\beta)}) \right. \\ & \left. + N(\hat{\mathbf{q}}_{(z_\beta)}, \mathcal{Q}_{(z_\alpha)}^{(\eta_\ell)}) \right] \exp(i(m_\alpha + m_\beta)\theta + i(\omega_\alpha + \omega_\beta)t), \end{aligned} \quad (\text{A21})$$

and the state variable $\mathbf{q}_{(\varepsilon^4)}$ as

$$\begin{aligned} \mathbf{q}_{(\varepsilon^4)} \equiv & \sum_{z_\alpha^4 \in \mathbf{Z}^4} \left(z_\alpha^4 \hat{\mathbf{q}}_{(z_\alpha^4)} \exp(-i(m_\alpha \theta + \omega_\alpha t)) + \text{c.c.} \right) \\ & + \sum_{\ell=1}^2 \eta_\ell \sum_{z_\beta^2 \in \mathbf{Z}^2} z_\beta^2 \mathbf{Q}_{(z_\beta^2)}^{(\eta_\ell)} \exp(-i(m_\beta \theta + \omega_\beta t)) + \sum_{\ell,k=1}^2 \eta_k \eta_\ell \mathbf{Q}_b^{(\eta_\ell \eta_k)}, \end{aligned} \quad (\text{A22})$$

which are determined from the resolution of a forced linear system.

A.7. Fifth order

At fifth order, we uniquely consider the resonant terms. These are the coefficients of members of \mathbf{Z}_R . The resonant forcing terms are

$$\begin{aligned} \hat{\mathbf{F}}_{z_\ell}^{(\eta_j \eta_k)} &= N(\hat{\mathbf{q}}_{(z_\ell)}, \mathbf{Q}_b^{(\eta_j \eta_k)}) + N(\mathbf{Q}_b^{(\eta_j \eta_k)}, \hat{\mathbf{q}}_{(z_\ell)}) \\ &+ \left(\mathbf{G}(\mathbf{Q}_{(z_\ell)}^{(\eta_k)}, \mathbf{e}_j) + \mathbf{G}(\mathbf{Q}_{(z_\ell)}^{(\eta_j)}, \mathbf{e}_k) - \lambda_\ell^{(\eta_j)} \mathbf{B} \mathbf{Q}_{(z_\ell)}^{(\eta_k)} - \lambda_\ell^{(\eta_k)} \mathbf{B} \mathbf{Q}_{(z_\ell)}^{(\eta_j)} \right) \left(1 - \frac{1}{2} \delta_{jk} \right), \\ \hat{\mathbf{F}}_{z_j |z_k|^2}^{(\eta_\ell)} &= N(\hat{\mathbf{q}}_{(z_j)}, \mathbf{Q}_{(|z_k|^2)}^{(\eta_\ell)}) + N(\mathbf{Q}_{(|z_k|^2)}^{(\eta_\ell)}, \hat{\mathbf{q}}_{(z_j)}) \\ &+ N(\hat{\mathbf{q}}_{(\bar{z}_k)}, \mathbf{Q}_{(z_j z_k)}^{(\eta_\ell)}) + N(\mathbf{Q}_{(z_j z_k)}^{(\eta_\ell)}, \hat{\mathbf{q}}_{(\bar{z}_k)}) \\ &+ N(\hat{\mathbf{q}}_{(z_j |z_k|^2)}, \mathbf{Q}_b^{(\eta_\ell)}) + N(\mathbf{Q}_b^{(\eta_\ell)}, \hat{\mathbf{q}}_{(z_j |z_k|^2)}) \\ &+ N(\hat{\mathbf{q}}_{(|z_k|^2)}, \mathbf{Q}_{(z_j)}^{(\eta_\ell)}) + N(\mathbf{Q}_{(z_j)}^{(\eta_\ell)}, \hat{\mathbf{q}}_{(|z_k|^2)}) \\ &+ N(\hat{\mathbf{q}}_{(z_j z_k)}, \mathbf{Q}_{(\bar{z}_k)}^{(\eta_\ell)}) + N(\mathbf{Q}_{(\bar{z}_k)}^{(\eta_\ell)}, \hat{\mathbf{q}}_{(z_j z_k)}) \\ &+ \left(N(\hat{\mathbf{q}}_{(z_j \bar{z}_k)}, \mathbf{Q}_{(z_k)}^{(\eta_\ell)}) + N(\mathbf{Q}_{(z_k)}^{(\eta_\ell)}, \hat{\mathbf{q}}_{(z_j \bar{z}_k)}) \right) (1 - \delta_{jk}) \\ &+ \left(N(\hat{\mathbf{q}}_{(z_k)}, \mathbf{Q}_{(z_j \bar{z}_k)}^{(\eta_\ell)}) + N(\mathbf{Q}_{(z_j \bar{z}_k)}^{(\eta_\ell)}, \hat{\mathbf{q}}_{(z_k)}) \right) (1 - \delta_{jk}) \\ &- \left(\lambda_j^{(\eta_\ell)} + \lambda_k^{(\eta_\ell)} + \bar{\lambda}_j^{(\eta_\ell)} \right) \mathbf{B} \hat{\mathbf{q}}_{(z_j |z_k|^2)} - v_{jk}^{(0)} \mathbf{B} \mathbf{Q}_{(z_j)}^{(\eta_\ell)}, \end{aligned} \quad (\text{A23})$$

with $j, k, \ell = 1, 2$ and δ_{jk} is the Kronecker symbol. Finally, the coefficients of the normal form are obtained as

$$\left. \begin{aligned} \lambda_\ell^{(\eta_j \eta_k)} &= \frac{\langle \hat{\mathbf{q}}_{(z_\ell)}^\dagger, \hat{\mathbf{F}}_{z_\ell}^{(\eta_j \eta_k)} \rangle}{\langle \hat{\mathbf{q}}_{(z_\ell)}^\dagger, \mathbf{B} \hat{\mathbf{q}}_{(z_\ell)} \rangle}, \\ v_{jk}^{(\eta_\ell)} &= \frac{\langle \hat{\mathbf{q}}_{(z_\ell)}^\dagger, \hat{\mathbf{F}}_{z_j |z_k|^2}^{(\eta_\ell)} \rangle}{\langle \hat{\mathbf{q}}_{(z_\ell)}^\dagger, \mathbf{B} \hat{\mathbf{q}}_{(z_\ell)} \rangle} \end{aligned} \right\} \quad (\text{A24})$$

for $j, k, \ell = 1, 2$.

Appendix B. Non-normality (lift-up and convective mechanisms)

In this section we explore the effect of the non-normal mechanisms on the instability. Two non-normal mechanisms were identified in the flow configuration of the static sphere

($\Omega = 0$), cf. Meliga *et al.* (2009b), the lift-up and convective non-normality mechanisms. The lift-up mechanism is associated with the transport of the steady-state solution by the perturbation, that is, to the component $\hat{\mathbf{u}} \cdot \nabla U_b$ of (3.2), cf. Marquet *et al.* (2009). On the other hand, the convective non-normality is due to the advection of disturbances by the steady state, that is, the term $U_b \cdot \nabla_m \hat{\mathbf{u}}$ of (3.2) and $-U_b \cdot \nabla_m \hat{\mathbf{u}}^\dagger$ for the adjoint operator. In physical terms, it corresponds to the convection of disturbances in opposite directions. In terms of direct $\hat{\mathbf{q}}$ and adjoint $\hat{\mathbf{q}}^\dagger$ global modes, the lift-up non-normality is characterized by the near orthogonality of the direct and adjoint components of velocity because they tend to concentrate in different components of velocity, even if both direct and adjoint modes are active in the same region of space. Instead, the convective non-normality is associated with direct and adjoint modes that tend to be orthogonal because they are localized in different regions of the space. The non-normality may be measured by the angle θ_N (Meliga *et al.* 2009b) defined as

$$\cos\left(\frac{\pi}{2} - \theta_N\right) = \frac{\langle \hat{\mathbf{q}}_{(z_\ell)}^\dagger, \mathbf{B}\hat{\mathbf{q}}_{(z_\ell)} \rangle}{\left(\langle \hat{\mathbf{q}}_{(z_\ell)}^\dagger, \mathbf{B}\hat{\mathbf{q}}_{(z_\ell)}^\dagger \rangle\right)^{1/2} \left(\langle \hat{\mathbf{q}}_{(z_\ell)}, \mathbf{B}\hat{\mathbf{q}}_{(z_\ell)} \rangle\right)^{1/2}}, \quad (\text{B1})$$

where the direct and adjoint modes are normalised such that $\langle \hat{\mathbf{q}}_{(z_\ell)}^\dagger, \mathbf{B}\hat{\mathbf{q}}_{(z_\ell)} \rangle = 1$ and $\langle \hat{\mathbf{q}}_{(z_\ell)}, \mathbf{B}\hat{\mathbf{q}}_{(z_\ell)}^\dagger \rangle = 1$. It thus measures the departure of θ_N from $\pi/2$ of the angle between direct and adjoint global modes, that is, the smaller the departure the larger the non-normality. However, such a quantity does not suffice to estimate the global effect of each non-normal mechanism, lift-up and convective non-normality. To overcome such an issue, Meliga *et al.* (2009b) proposed to introduce the estimator γ defined as

$$\gamma = 1 - \frac{\langle |\hat{\mathbf{q}}_{(z_\ell)}^\dagger|, \mathbf{B}|\hat{\mathbf{q}}_{(z_\ell)} \rangle}{\left(\langle \hat{\mathbf{q}}_{(z_\ell)}^\dagger, \mathbf{B}\hat{\mathbf{q}}_{(z_\ell)}^\dagger \rangle\right)^{1/2} \left(\langle \hat{\mathbf{q}}_{(z_\ell)}, \mathbf{B}\hat{\mathbf{q}}_{(z_\ell)} \rangle\right)^{1/2}}, \quad (\text{B2})$$

where $|\hat{\mathbf{q}}_{(z_\ell)}|^2 = |\hat{\mathbf{u}}_{(z_\ell)}|^2 + |\hat{\mathbf{p}}_{(z_\ell)}|^2 = |\hat{u}_{(z_\ell)}|^2 + |\hat{v}_{(z_\ell)}|^2 + |\hat{w}_{(z_\ell)}|^2 + |\hat{p}_{(z_\ell)}|^2$ stands for the Euclidean pointwise norm. Such an estimator is used to determine whether the non-normality is due to the lift-up effect or the convective non-normality and it is bounded $0 \leq \gamma \leq 1$. In the case of dominance of the lift-up effect γ is close to 0, i.e. a similar spatial distribution of direct and adjoint modes. On the other hand, a value of γ close to unity implies separation in the support of the adjoint and direct global modes.

Appendix C. Unfolding of the triple-Hopf bifurcation

C.1. Classification of solutions

The trivial axisymmetric steady-state solution transits into a rotating wave

$$RW_i = \{z_j = 0 \mid \forall j \neq i, \quad i, j = 1, 2, 3\} \quad (\text{C1})$$

via Hopf-bifurcation. Each of the three types of rotating waves are potential candidates for a primary bifurcation, and they appear in distinct regions of the parameter space (Re, Ω).

In addition, in the vicinity of the organizing centre of the type (Hopf-Hopf) one can predict the type of secondary bifurcation from each of the rotating waves. Secondary bifurcations of rotating axisymmetric bodies are of mixed-mode type MM_{ij} , $i, j = 1, 2, 3$,

$$MM_{ij} = \{z_\ell = 0 \mid \forall \ell \neq i, \ell \neq j, \quad i, j, \ell = 1, 2, 3\}. \quad (\text{C2})$$

Mixed-mode solutions are quasiperiodic solutions with possibly different azimuthal patterns. The transition to a mixed-mode solution MM_{12} is possible either from RW_1

or RW_2 but not from RW_3 . Finally, near a triple-Hopf bifurcation point there may exist a mixed mode composed of three (incommensurate) frequencies, here denoted IMM_{123} . This branch can bifurcate from any of the two-frequency component mixed modes MM_{ij} , for distinct $i, j = 1, 2, 3$.

C.2. Unfolding amplitude equations – types of solutions

C.2.1. Rotating waves – RW

Rotating waves RW_i are fixed points of (4.9), where two modes are null, i.e. they satisfy

$$r_i^{(RW)} = \sqrt{-\frac{\lambda_i^R}{v_{ii}^R}}, \quad \text{for } i = 1, 2, 3. \tag{C3}$$

Rotating wave solutions are stable if

$$\lambda_i^R > 0, \quad \lambda_j^R - v_{ji}^R \frac{\lambda_i^R}{v_{ii}^R} < 0, \quad \text{for } j \neq i, \quad \text{for } i, j = 1, 2, 3. \tag{C4}$$

C.2.2. Mixed modes – MM_{ij}

Mixed-mode solutions MM_{12} (respectively MM_{13} or MM_{23}) are two-component solutions of (4.9) where $r_3 = 0$ (respectively $r_2 = 0$ or $r_1 = 0$) and the other two components are non-null. Amplitudes r_i, r_j depend on parameters as follows:

$$r_i^{(MM_{ij})} = \sqrt{\frac{\lambda_j^R v_{ij}^R - \lambda_i^R v_{jj}^R}{\det(\mathcal{V}_{kk}^R)}}, \quad r_j^{(MM_{ij})} = \sqrt{\frac{\lambda_i^R v_{ji}^R - \lambda_j^R v_{ii}^R}{\det(\mathcal{V}_{kk}^R)}}. \tag{C5a,b}$$

Here $i, j, k = 1, 2, 3$ with $i \neq j, k \neq i$ and $k \neq j$.

The Jacobian matrix Df^R can be written in block-diagonal form, which simplifies the stability computations. It is composed of a 2×2 and a 1×1 block. The eigenvalue associated with the 1×1 block is stable if

$$\sigma_k \equiv \frac{1}{\det(\mathcal{V}_{kk}^R)} \left[\lambda_k^R \det(\mathcal{V}_{kk}^R) + \lambda_i^R \det(\mathcal{V}_{ik}^R) + \lambda_j^R \det(\mathcal{V}_{jk}^R) \right] < 0. \tag{C6}$$

The 2×2 block is

$$Df_{ij}^R = 2 \begin{pmatrix} v_{ii}^R (r_i^{(MM_{ij})})^2 & v_{ij}^R r_i^{(MM_{ij})} r_j^{(MM_{ij})} \\ v_{ji}^R r_i^{(MM_{ij})} r_j^{(MM_{ij})} & v_{jj}^R (r_j^{(MM_{ij})})^2 \end{pmatrix}, \tag{C7}$$

with $r_i^{(MM_{ij})} r_j^{(MM_{ij})} = \sqrt{\lambda_i^R \lambda_j^R [v_{ij}^R v_{ji}^R + v_{jj}^R v_{ii}^R] - [(\lambda_i^R)^2 v_{jj}^R v_{ji}^R + (\lambda_j^R)^2 v_{ii}^R v_{ij}^R]} / \det(\mathcal{V}_{kk}^R)$.

Triple-Hopf bifurcation in the flow past a rotating sphere

The eigenvalues that govern the stability of the mixed-mode solutions of kind MM_{ij} are the roots of the characteristic polynomial

$$\sigma^2 - \text{tr} \left(Df_{ij}^R \right) \sigma + \det \left(Df_{ij}^R \right) = 0, \quad (\text{C8})$$

where

$$\text{tr} \left(Df_{ij}^R \right) = v_{ii}^R \left(r_i^{(MM_{ij})} \right)^2 + v_{jj}^R \left(r_j^{(MM_{ij})} \right)^2 \quad (\text{C9})$$

and

$$\det \left(Df_{ij}^R \right) = \left(r_i^{(MM_{ij})} \right)^2 \left(r_j^{(MM_{ij})} \right)^2 \det \left(\mathcal{V}_{kk}^R \right). \quad (\text{C10})$$

Therefore, one can express the pair of eigenvalues as

$$\sigma_{ij}^{\pm} \equiv \frac{v_{ii}^R r_i^2 + v_{jj}^R r_j^2}{2} \pm \sqrt{\left(v_{ii}^R r_i^2 - v_{jj}^R r_j^2 \right)^2 / 4 + v_{ij}^R v_{ji}^R r_i^2 r_j^2}, \quad (\text{C11})$$

where, for ease of notation, the uperscript MM_{ij} has been removed. A necessary condition for the Hopf bifurcation of the mixed-mode solutions to occur is that $v_{ii}^R v_{jj}^R < 0$ and $v_{ij}^R v_{ji}^R < 0$. In other words, a Hopf bifurcation from the mixed mode may occur if one of the rotating waves comprised in the mixed mode arises from a supercritical bifurcation whereas the other arises as a result of a subcritical bifurcation from the axisymmetric steady state. This case is discussed in detail in Kuznetsov (2013, § 8.6) and is denoted as the difficult case. The case where $v_{ii}^R v_{jj}^R > 0$ is denoted as the simple case, in such a case the mixed-mode solution is a sink or a source located in the separatrix of the basin of attraction of rotating waves.

C.3. Interacting mixed mode – IMM_{123}

The IMM_{123} mode is a 3-tori solution (phases ϕ_i are non-resonant) with their amplitudes determined as the solution of the following linear system:

$$r^2 \equiv (r_1^2, r_2^2, r_3^2)^T = - \left(\mathcal{V}^R \right)^{-1} \Lambda^R = \frac{-1}{\det \mathcal{V}^R} \begin{pmatrix} \det \mathcal{V}_{11}^R \lambda_1^R + \det \mathcal{V}_{21}^R \lambda_2^R + \det \mathcal{V}_{31}^R \lambda_3^R \\ \det \mathcal{V}_{12}^R \lambda_1^R + \det \mathcal{V}_{22}^R \lambda_2^R + \det \mathcal{V}_{32}^R \lambda_3^R \\ \det \mathcal{V}_{13}^R \lambda_1^R + \det \mathcal{V}_{23}^R \lambda_2^R + \det \mathcal{V}_{33}^R \lambda_3^R \end{pmatrix}. \quad (\text{C12})$$

The stability of the interacting mixed-mode solution is determined by the eigenvalues of the Jacobian Df^R ,

$$Df^R \equiv 2 \begin{pmatrix} v_{11}^R r_1^2 & v_{12}^R r_1 r_2 & v_{13}^R r_1 r_3 \\ v_{21}^R r_1 r_2 & v_{22}^R r_2^2 & v_{23}^R r_3 r_2 \\ v_{31}^R r_1 r_3 & v_{32}^R r_3 r_2 & v_{33}^R r_3^2 \end{pmatrix}. \quad (\text{C13})$$

The eigenvalues of Df^R are roots of its characteristic polynomial denoted as $p(Df^R)$,

$$\left. \begin{aligned} p(Df^R) &\equiv \sigma^3 - \mathbb{I}_1 \sigma^2 + \mathbb{I}_2 \sigma - \mathbb{I}_3 = 0, \\ \mathbb{I}_1 &= \text{tr} \left(Df^R \right), \quad \mathbb{I}_2 = \frac{1}{2} \left[\left(\text{tr} \left(Df^R \right) \right)^2 - \text{tr} \left([Df^R]^2 \right) \right], \quad \mathbb{I}_3 = \det \left(Df^R \right). \end{aligned} \right\} \quad (\text{C14})$$

The trace of the Jacobian can be expressed as a function of the square of the amplitudes r_1^2 , r_2^2 and r_3^2 and the real part of the matrix of coefficients \mathcal{V} ,

$$\text{tr} \left(Df^R \right) \equiv 2 \left(v_{11}^R r_1^2 + v_{22}^R r_2^2 + v_{33}^R r_3^2 \right), \tag{C15}$$

similarly the second invariant of the Jacobian

$$\frac{1}{2} \left[\left(\text{tr} \left(Df^R \right) \right)^2 - \text{tr} \left([Df^R]^2 \right) \right] \equiv 4 \left(r_1^2 r_2^2 \det \mathcal{V}_{33}^R + r_1^2 r_3^2 \det \mathcal{V}_{22}^R + r_2^2 r_3^2 \det \mathcal{V}_{11}^R \right), \tag{C16}$$

and the determinant

$$\det \left(Df^R \right) = 8 r_1^2 r_2^2 r_3^2 \det \mathcal{V}^R. \tag{C17}$$

The characteristic polynomial (C14) is a cubic polynomial with real coefficients. Thus, the eigenvalues σ of the Jacobian Df^R are either all real or one of them is real and the other two are complex conjugate. The nature of the eigenvalues depends on the discriminant of the cubic equation. A stationary bifurcation occurs when $\det(Df^R) = 0$, which under the generic condition $\det \mathcal{V}^R \neq 0$ only occurs at the origin of the IMM_{123} .

A Hopf bifurcation arises when the following conditions are satisfied:

$$\left. \begin{aligned} & \text{tr} \left(Df^R \right) < 0, \quad \left[\left(\text{tr} \left(Df^R \right) \right)^2 - \text{tr} \left([Df^R]^2 \right) \right] > 0 \\ \text{and} \quad & \left[\left(\text{tr} \left(Df^R \right) \right)^3 - \text{tr} \left(Df^R \right) \text{tr} \left([Df^R]^2 \right) \right] = \det \left(Df^R \right). \end{aligned} \right\} \tag{C18}$$

The condition $\text{tr} \left(Df^R \right) < 0$ ensures that Hopf bifurcation is the primary bifurcation of the IMM_{123} solution, i.e. the real eigenvalue is negative. Such a condition holds true in the supercritical case, when $v_{ii} < 0$, for $i = 1, 2, 3$. Additionally, there is a change in the nature of the solution IMM_{123} whenever the discriminant changes sign, it changes from sink to stable foci, from source to unstable foci, from saddle to saddle foci or vice versa. Even though these local changes in the nature of the fixed-point solution IMM_{123} cannot be considered as a local bifurcation, they could be linked to global changes in dynamics, e.g. the appearance of a heteroclinic cycle as in the difficult case of a Hopf-Hopf bifurcation (Kuznetsov 2013, Ch. 8.7.). Finally, a necessary and sufficient condition for the stability of the asymptotic stability of the IMM_{123} solution can be expressed in terms of the invariants of the Jacobian matrix

$$\mathbb{I}_1 < 0, \quad \mathbb{I}_2 > 0, \quad \mathbb{I}_3 < 0, \quad \mathbb{I}_1 \mathbb{I}_2 > \mathbb{I}_3. \tag{C19}$$

Inspection of (C19) shows that the condition for the Hopf bifurcation indeed corresponds to the limit case of the condition $\mathbb{I}_1 \mathbb{I}_2 \geq \mathbb{I}_3$.

Appendix D. Mesh convergence

Mesh independent solutions have been verified systematically. First, we have considered a given mesh refinement, and we have varied the physical size of the domain. We have observed that, for a domain length of 50 diameters downstream of the sphere centre, 20 diameters upstream of the cylinder centre and 20 in the cross-stream direction, the effects of the boundary condition do not have an effect on the solution. Secondly, we

	M_1	M_2	M_3	M_4
Num. tri.	5.6×10^3	2.4×10^4	3.9×10^4	8.1×10^4
h_{max}	$3D$	$2D$	$1D$	$0.25D$
h_{aniso}	5	2	1	1
Adaptation	Steady state	Steady state and modes	Same as M_2	Same as M_2

Table 7. Properties of the meshes used in the study of mesh convergence.

Coef.	M_1	M_2	M_3	M_4
v_{22}^B	$-1.8 + 0.23i$	$-1.8 + 0.22i$	$-1.8 + 0.22i$	$-1.8 + 0.22i$
v_{23}^B	$-2.1 - 0.26i$	$-2.0 - 0.27i$	$-1.9 - 0.21i$	$-1.9 - 0.22i$
v_{32}^B	$-0.32 - 0.042i$	$-0.35 - 0.027i$	$-0.34 - 0.027i$	$-0.34 - 0.031i$
v_{33}^B	$-1.6 + 0.91i$	$-1.6 + 0.87i$	$-1.7 + 0.89i$	$-1.7 + 0.89i$

Table 8. Cubic coefficients of the normal form (4.9) evaluated at the codimension-two point A .

have looked at the effect of mesh refinement on the properties of the solution. For that purpose, we performed a parametric study of eigenvalues, normal form coefficients of the codimension-two point B (table 8). Every mesh is initially computed by Delauny triangulation, and subsequently adapted to either base flow, eigenmode or both, following the methodology described in Fabre *et al.* (2018); and their properties are summarised in table 7.

Appendix E. Higher-order dynamic mode decomposition

This analysis allows us to gain valuable insight on the dominant modes and associated spatio-temporal flow structures which govern the wake for the different regimes encountered in our transition scenario (figure 9). As detailed by Le Clainche & Vega (2017a), Vega & Le Clainche (2020), HODMD is an extension of the standard dynamic mode decomposition (DMD) technique (Schmid 2010), which has been proven useful to study flow structures associated with quasiperiodic (featuring a large number of frequencies) or transitional regimes (Le Clainche & Vega 2017b), where the classical DMD approach may fail, being therefore applicable to complex spectral and spatial cases, as the problem investigated herein. The number of modes identified by HODMD is determined by M , whose value is related to the spatial resolution of the input data, and N , determined by the temporal resolution.

Thus, the present HODMD tool has been applied to resolve the spatial structure related to dominant frequencies characterizing the different flow regimes identified from the DNS results. Typically, the input data consists of a set of $N = 2000$ streamwise vorticity, ϖ_z , snapshots interpolated in a 80×80 ($M = 6400$) rectangular grid whose domain is $(x, y) \in [-1, 1]$ located at $z = 2.5$. Moreover, it should be noted that the vorticity snapshots are equally spaced in time with a $\Delta t = 0.15$. Such temporal parameters allow us to resolve frequencies between $St_{min} = 0.003$ and $St_{max} = 3.33$, according to the Nyquist criterion. Given such input data, which satisfies the condition $N < M$, the values of the main HODMD parameters, i.e. order, d , and tolerance, ϵ , have been calibrated and fixed at $d = 50$ and $\epsilon = 1e - 6$ to capture a great number of modes.

Appendix F. The 0-1 test

The quantitative 0-1 method (Gottwald & Melbourne 2004) is used to evaluate the dynamic complexity and likely chaotic nature of the flow regimes. The method is directly applied to time series of any scalar, as the pointwise fluctuating radial velocity U' . In particular, given a set of data from velocity of N samples, $U'(j)$ with $j = 1, \dots, N$, a translation variable is defined as $p(m) = \sum_{j=1}^{m_s} U'(j) \cos(js)$, for $m = 1, \dots, m_s$ and $s \in (0, \pi/5)$. The mean square displacement is defined as $M_c(m) = \lim_{N \rightarrow \infty} (1/N) \sum_{j=1}^N [p_c(j+m) - p(j)]^2$, which requires that $m_s \leq N$ (as in Gottwald & Melbourne (2004), we use $m_s = N/10$). Thus, the variable $M_c(m)$ is bounded when $p(j)$ is also bounded which is the case for regular dynamics. However, if the translation variable $p(m)$ is chaotic, $M_c(m)$ grows linearly with m , so that an asymptotic growth K can be defined as

$$K = \lim_{m \rightarrow \infty} \frac{\log(M_c(m))}{\log(m)}, \quad (\text{F1})$$

which will take the value of 1 for chaotic dynamics and 0 for regular dynamics. Further information and validation of the use of this estimate to evaluate the dynamic nature of complex flow regimes can be found in Lorite-Díez & Jiménez-González (2020).

REFERENCES

- ALLEN, T. & MOROZ, I.M. 1997 Hopf-Hopf and Hopf-steady mode interactions with O(2) symmetry in Langmuir circulations. *Geophys. Astrophys. Fluid Dyn.* **85** (3–4), 243–278.
- ARMBRUSTER, D., GUCKENHEIMER, J. & HOLMES, P. 1989 Kuramoto–Sivashinsky dynamics on the center–unstable manifold. *SIAM J. Appl. Maths* **49** (3), 676–691.
- AUGUSTE, F., FABRE, D. & MAGNAUDET, J. 2010 Bifurcations in the wake of a thick circular disk. *Theor. Comput. Fluid Dyn.* **24**, 305–313.
- AUGUSTE, F. & MAGNAUDET, J. 2018 Path oscillations and enhanced drag of light rising spheres. *J. Fluid Mech.* **841**, 228–266.
- BAROIS, T., HUCK, P.D., PALEO, C., BOURGOIN, M. & VOLK, R. 2019 Probing fluid torque with a hydrodynamical trap: rotation of chiral particles levitating in a turbulent jet. *Phys. Fluids* **31** (12), 125116.
- CALLAHAM, J.L., BRUNTON, S.L. & LOISEAU, J.-C. 2022 On the role of nonlinear correlations in reduced-order modelling. *J. Fluid Mech.* **938**, A1.
- CHOMAZ, J.-M. 2005 Global instabilities in spatially developing flows: non-normality and nonlinearity. *Annu. Rev. Fluid Mech.* **37** (1), 357–392.
- CHOSSAT, P., GOLUBITSKY, M. & LEE KEYFITZ, B. 1986 Hopf-Hopf mode interactions with O(2) symmetry. *Dyn. Stab. Syst.* **1** (4), 255–292.
- CHRUST, M., GOUJON-DURAND, S. & WESFREID, J.E. 2013 Loss of a fixed plane symmetry in the wake of a sphere. *J. Fluid Mech.* **41**, 51–56.
- CITRO, V., SICONOLFI, L., FABRE, D., GIANNETTI, F. & LUCHINI, P. 2017 Stability and sensitivity analysis of the secondary instability in the sphere wake. *AIAA J.* **55**, 3661–3668.
- CITRO, V., TCHOUFAG, J., FABRE, D., GIANNETTI, F. & LUCHINI, P. 2016 Linear stability and weakly nonlinear analysis of the flow past rotating spheres. *J. Fluid Mech.* **807**, 62–86.
- CVITANOVIC, P., ARTUSO, R., MAINIERI, R., TANNER, G., VATTAY, G., WHELAN, N. & WIRZBA, A. 2005 Chaos: classical and quantum. *ChaosBook.org (Niels Bohr Institute, Copenhagen 2005)* **69**, 25.
- ERN, P., RISSO, F., FABRE, D. & MAGNAUDET, J. 2012 Wake-induced oscillatory paths of bodies freely rising or falling in fluids. *Annu. Rev. Fluid Mech.* **44** (1), 97–121.
- FABRE, D., AUGUSTE, F. & MAGNAUDET, J. 2008 Bifurcations and symmetry breaking in the wake of axisymmetric bodies. *Phys. Fluids* **20**, 051702.
- FABRE, D., CITRO, V., FERREIRA SABINO, D., BONNEFIS, P., SIERRA, J., GIANNETTI, F. & PIGOU, M. 2018 A practical review on linear and nonlinear global approaches to flow instabilities. *Appl. Mech. Rev.* **70** (6), 060802.
- FABRE, D., TCHOUFAG, J., CITRO, V., GIANNETTI, F. & LUCHINI, P. 2017 The flow past a freely rotating sphere. *Theor. Comput. Fluid Dyn.* **31**, 475–482.
- FENG, Z.-G. & MUSONG, S.G. 2014 Direct numerical simulation of heat and mass transfer of spheres in a fluidized bed. *Powder Technol.* **262**, 62–70.

Triple-Hopf bifurcation in the flow past a rotating sphere

- GIANNETTI, F. & LUCHINI, P. 2007 Structural sensitivity of the first instability of the cylinder wake. *J. Fluid Mech.* **581** (1), 167–197.
- GOLUBITSKY, M. & LANGFORD, W.F. 1988 Pattern formation and bistability in flow between counterrotating cylinders. *Physica D* **32** (3), 362–392.
- GOLUBITSKY, M., STEWART, I. & SCHAEFFER, D.G. 2012 *Singularities and Groups in Bifurcation Theory: Volume II*, vol. 69. Springer Science & Business Media.
- GOTTWALD, G.A. & MELBOURNE, I. 2004 Proceedings of the Royal Society of London. Series A: mathematical and physical sciences. *Proc. R. Soc. Lond. A* **460** (2042), 603–611.
- GOTTWALD, G.A. & MELBOURNE, I. 2009 Higher order dynamic mode decomposition and its applications. *SIAM J. Appl. Dyn. Syst.* **8** (1), 129–145.
- GUCKENHEIMER, J. 2010 Bifurcations of dynamical systems. In *Dynamical Systems* (ed. C. Marchioro), pp. 5–123. Springer.
- GUO, H., FAUCI, L., SHELLEY, M. & KANSO, E. 2018 Bistability in the synchronization of actuated microfilaments. *J. Fluid Mech.* **836**, 304–323.
- HARAGUS, M. & IOOSS, G. 2010 *Local Bifurcations, Center Manifolds, and Normal Forms in Infinite-Dimensional Dynamical Systems*. Springer Science & Business Media.
- HOMBURG, A.J. & SANDSTEDE, B. 2010 Homoclinic and heteroclinic bifurcations in vector fields. *Handb. Dyn. Syst.* **3**, 379–524.
- HUANG, Y., RISTROPH, L., LUHAR, M. & KANSO, E. 2018 Bistability in the rotational motion of rigid and flexible flyers. *J. Fluid Mech.* **849**, 1043–1067.
- JIMÉNEZ-GONZÁLEZ, J.I., SANMIGUEL-ROJAS, E., SEVILLA, A. & MARTÍNEZ-BAZÁN, C. 2013 Laminar flow past a spinning bullet-shaped body at moderate angular velocities. *J. Fluid Mech.* **43**, 200–219.
- JIMÉNEZ-GONZÁLEZ, J.I., SEVILLA, A., SANMIGUEL-ROJAS, E. & MARTÍNEZ-BAZÁN, C. 2014 Global stability analysis of the axisymmetric wake past a spinning bullet-shaped body. *Intl J. Fluid Mech. Res.* **748**, 302–327.
- JIMÉNEZ-GONZÁLEZ, J.I., MANGLANO-VILLAMARÍN, C. & COENEN, W. 2019 The role of geometry on the global instability of wakes behind streamwise rotating axisymmetric bodies. *Eur. J. Mech. B/Fluids* **76**, 205–222.
- JOHNSON, T.A. & PATEL, V.C. 1999 Flow past a sphere up to Reynolds number of 300. *J. Fluid Mech.* **378**, 19–70.
- KIM, D. & CHOI, H. 2002 Laminar flow past a sphere rotating in the streamwise direction. *J. Fluid Mech.* **461**, 365–386.
- KUZNETSOV, Y.A. 2013 *Elements of Applied Bifurcation Theory*, vol. 112. Springer Science & Business Media.
- KUZNETSOV, Y.A. & MEIJER, H.G.E. 2005 Numerical normal forms for codim 2 bifurcations of fixed points with at most two critical eigenvalues. *SIAM J. Sci. Comput.* **26** (6), 1932–1954.
- LE CLAINCHE, S. & VEGA, J. 2017a Higher order dynamic mode decomposition. *SIAM J. Appl. Dyn. Syst.* **16** (2), 882–925.
- LE CLAINCHE, S. & VEGA, J.M. 2017b Higher order dynamic mode decomposition to identify and extrapolate flow patterns. *Phys. Fluids* **29** (8), 084102.
- LIU, Q. & PROSPERETTI, A. 2010 Wall effects on a rotating sphere. *J. Fluid Mech.* **657**, 1–21.
- LOISEAU, J.-C. & BRUNTON, S.L. 2018 Constrained sparse galerkin regression. *J. Fluid Mech.* **838**, 42–67.
- LOISEAU, J.-C., NOACK, B.R. & BRUNTON, S.L. 2018 Sparse reduced-order modelling: sensor-based dynamics to full-state estimation. *J. Fluid Mech.* **844**, 459–490.
- LORITE-DÍEZ, M. & JIMÉNEZ-GONZÁLEZ, J.I. 2020 Description of the transitional wake behind a strongly streamwise rotating sphere. *J. Fluid Mech.* **896**, A18.
- MARQUET, O., LOMBARDI, M., CHOMAZ, J.-M., SIPP, D. & JACQUIN, L. 2009 Direct and adjoint global modes of a recirculation bubble: lift-up and convective non-normalities. *J. Fluid Mech.* **622**, 1–21.
- MARQUET, O., SIPP, D. & JACQUIN, L. 2008 Sensitivity analysis and passive control of cylinder flow. *J. Fluid Mech.* **615**, 221–252.
- MATHAI, V., ZHU, X., SUN, C. & LOHSE, D. 2018 Flutter to tumble transition of buoyant spheres triggered by rotational inertia changes. *Nat. Commun.* **9**, 1792.
- MELIGA, P., CHOMAZ, J.-M. & SIPP, D. 2009a Global mode interaction and pattern selection in the wake of a disk: a weakly nonlinear expansion. *J. Fluid Mech.* **633**, 159–189.
- MELIGA, P., CHOMAZ, J.-M. & SIPP, D. 2009b Unsteadiness in the wake of disks and spheres: instability, receptivity and control using direct and adjoint global stability analyses. *J. Fluids Struct.* **25** (4), 601–616.
- MELIGA, P., GALLAIRE, F. & CHOMAZ, J.-M. 2012 A weakly nonlinear mechanism for mode selection in swirling jets. *J. Fluid Mech.* **699**, 216–262.

- NEWHOUSE, S., RUELLE, D. & TAKENS, F. 1978 Occurrence of strange attractors near quasi periodic flows on t^m , $m \geq 3$. *Commun. Math. Phys.* **64** (1), 35–40.
- NI, A. 2019 Hyperbolicity, shadowing directions and sensitivity analysis of a turbulent three-dimensional flow. *J. Fluid Mech.* **863**, 644–669.
- NIAZMAND, H. & RENKSIZBULUT, M. 2005 Flow past a spinning sphere with surface blowing and heat transfer. *Trans. ASME J. Fluids Engng* **127** (1), 163–171.
- PASSMORE, M.A., TUPLIN, S., SPENCER, A. & JONES, R. 2008 Experimental studies of the aerodynamics of spinning and stationary footballs. *Proc. Inst. Mech. Engrs C* **222** (2), 195–205.
- PIER, B. 2013 Periodic and quasiperiodic vortex shedding in the wake of a rotating sphere. *J. Fluids Struct.* **41**, 43–50.
- PODVIKINA, O.M. 2006a The center manifold theorem for center eigenvalues with non-zero real parts. [arXiv:physics/0601074](https://arxiv.org/abs/physics/0601074).
- PODVIKINA, O.M. 2006b Investigation of the abc flow instability with application of centre manifold reduction. *Dyn. Syst.* **21** (2), 191–208.
- POON, E.K.W., OOI, A.S.H., GIACOBELLO, M. & COHEN, R.C.Z. 2010 Laminar flow structures from a rotating sphere: effect of rotating axis angle. *Intl J. Heat Fluid Flow* **31** (5), 961–972, 6th International Symposium on Turbulence, Heat and Mass Transfer, Rome, Italy, 14–18 September 2009.
- RABAULT, J., FAULI, R.A. & CARLSON, A. 2019 Curving to fly: synthetic adaptation unveils optimal flight performance of whirling fruits. *Phys. Rev. Lett.* **122**, 024501.
- REN, C., CHENG, L., XIONG, C., TONG, F. & CHEN, T. 2021 Bistabilities in two parallel kármán wakes. *J. Fluid Mech.* **929**, A5.
- RENARDY, M., RENARDY, Y., SURESHKUMAR, R. & BERIS, A.N. 1996 Hopf-Hopf and steady-Hopf mode interactions in Taylor–Couette flow of an upper convected Maxwell liquid. *J. Non-Newtonian Fluid Mech.* **63** (1), 1–31.
- ROBINSON, G. & ROBINSON, I. 2013 The motion of an arbitrarily rotating spherical projectile and its application to ball games. *Phys. Scr.* **88** (1), 018101.
- ROSHKO, A. 1993 Perspectives on bluff body aerodynamics. *J. Wind Engng Ind. Aerodyn.* **49** (1), 79–100.
- RUCKLIDGE, A.M., WEISS, N.O., BROWNJOHN, D.P., MATTHEWS, P.C. & PROCTOR, M.R.E. 2000 Compressible magnetoconvection in three dimensions: pattern formation in a strongly stratified layer. *J. Fluid Mech.* **419**, 283–323.
- SAKAMOTO, H. & HANIU, H. 1990 A study on vortex shedding from spheres in a uniform flow. *Trans. ASME J. Fluids Engng* **112** (4), 386–392.
- SCHMID, P.J. 2010 Dynamic mode decomposition of numerical and experimental data. *J. Fluid Mech.* **656**, 5–28.
- SHI, P. & RZEHA, R. 2019 Lift forces on solid spherical particles in unbounded flows. *Chem. Engng Sci.* **208**, 115145.
- SIERRA, J., FABRE, D. & CITRO, V. 2020a Efficient stability analysis of fluid flows using complex mapping techniques. *Comput. Phys. Commun.* **251**, 107100.
- SIERRA, J., FABRE, D., CITRO, V. & GIANNETTI, F. 2020b Bifurcation scenario in the two-dimensional laminar flow past a rotating cylinder. *J. Fluid Mech.* **905**, A2.
- SIPP, D. 2012 Open-loop control of cavity oscillations with harmonic forcings. *J. Fluid Mech.* **708**, 439–468.
- SKARYSZ, M., ROKICKI, J., GOUJON-DURAND, S. & WESFREID, J.E. 2018 Experimental investigation of the wake behind a rotating sphere. *Phys. Rev. Fluids* **3**, 013905.
- SUBRAMANIAN, P., SUJITH, R.I. & WAHI, P. 2013 Subcritical bifurcation and bistability in thermoacoustic systems. *J. Fluid Mech.* **715**, 210–238.
- SUCKALE, J., QIN, Z., PICCHI, D., KELLER, T. & BATTIATO, I. 2018 Bistability of buoyancy-driven exchange flows in vertical tubes. *J. Fluid Mech.* **850**, 525–550.
- TOMBOULIDES, A.G. & ORSZAG, S.A. 2000 Numerical investigation of transitional and weak turbulent flow past a sphere. *J. Fluid Mech.* **416**, 45–73.
- VARÉ, T., NOUAR, C., MÉTIVIER, C. & BOUTERAA, M. 2020 Stability of hexagonal pattern in Rayleigh–Bénard convection for thermodependent shear-thinning fluids. *J. Fluid Mech.* **905**, A33.
- VEGA, J.M. & LE CLAINCHE, S. 2020 *Higher Order Dynamic Mode Decomposition and Its Applications*. Academic Press.
- VERHULST, F. 2007 Singular perturbation methods for slow–fast dynamics. *Nonlinear Dyn.* **50** (4), 747–753.
- YALNIZ, G. & BUDANUR, N.B. 2020 Inferring symbolic dynamics of chaotic flows from persistence. *Chaos* **30** (3), 033109.
- YALNIZ, G., HOF, B. & BUDANUR, N.B. 2021 Coarse graining the state space of a turbulent flow using periodic orbits. *Phys. Rev. Lett.* **126** (24), 244502.

Dynamics of a rounded laminar compressible impinging jet

J. Sierra-Ausin^{1,2}†, F. Giannetti¹ and D. Fabre²

¹Institut de Mécanique des fluides de Toulouse (IMFT), Toulouse 31400, France

²Dipartimento di Ingegneria (DIIN), Università degli Studi di Salerno, Fisciano 84084, Italy

(Received xx; revised xx; accepted xx)

We study the dynamics of a rounded subsonic impinging jet. We investigate this problem by solving the compressible linearised Navier–Stokes equations around a laminar baseflow, with a normal form issued from a weakly-nonlinear approach and by means of axisymmetric time-stepping simulations. The linear stability analysis shows the existence of a family of global modes for every Mach number, which are supported by a non-local feedback loop. In order to get an insight to the core of the instability mechanisms, we propose a non-local decomposition of the structural sensitivity and the endogeneity concepts. The use of these sensitivity maps allows us to differentiate two distinct instability mechanisms. The instability is always initiated by a shear layer instability. Nonetheless, the closure of the feedback differs. At large Mach number, the production of divergence lies inside the jet, and it is responsible for the backward propagation of the guided jet mode. On the other hand, at low Mach number, the wavemaker of the instability is along the region where the module of the linearised Lamb vector is largest. Therefore, indicating that the closure mechanism is a pressure wave issued from a vortical source. We also provide a qualitative description of the tonal and broadband noise by means of the normal form of the bifurcation. Based on a phenomenological reasoning, we also suggest a stochastic model which accounts for the low coherence of the sources of sound at low Mach number. Such a model reproduces reasonably well the sound pressure level measured from time-stepping simulations.

1. Introduction – Aim of the study

It has been established that intense acoustic tonal sound is generated by the impingement of a high subsonic or supersonic jet onto a wall. Early experimental studies carried out by many researchers, including Powell (1953, 1961), Wagner (1971), Neuwerth (1974), Preisser (1979), Ho & Nosseir (1981); Nosseir & Ho (1982) observed that the frequency varies with the distance to the solid boundary, and it is organised in stages. Furthermore, the dynamics of the jet, for instance pressure in the near-field and in the far-field, were found to peak at particular frequency for high subsonic Mach numbers and to be broadband for low Mach numbers (Nosseir & Ho 1982). The staging phenomenon led Powell (1953) to conjecture that the self-sustained mechanism was a two-stage process, which involves the vortical structures convected downstream and the acoustic waves propagating upstream from the solid boundary to the nozzle. Similar feedback loops have been also observed in supersonic impinging jets. The establishment of the feedback loop has been studied experimentally by Norum (1991) and numerically by Gojon *et al.* (2016); Bogey & Gojon (2017) for ideally expanded supersonic jets. Similarly, for underexpanded jets, there is experimental evidence of the existence of the loops by Risborg & Soria

† Email address for correspondence: javier.sierra@imft.fr

(2009); Buchmann *et al.* (2011); Mitchell *et al.* (2012) and numerical by Dauphain *et al.* (2012); Gojon & Bogey (2017*a*). Ho & Nosseir (1981) proposed a simplified frequency selection criterion, assuming the wave propagating upstream to be a free-stream acoustic wave propagating outside the jet. Nevertheless, later studies established that the feedback loop is closed by a guided jet wave propagating mostly inside the jet (Tam & Ahuja 1990). Tam & Ahuja (1990) proposed a theoretical model for the frequency selection. The model considers a Kelvin-Helmholtz mode with a constant frequency and guided jet waves classified by their radial and azimuthal structure with different dispersion relations. The authors conjectured that the loop is closed by the Kelvin-Helmholtz mode and the least-dispersive guided wave. Following this reasoning, they concluded that tonal noise does not exist below a cut-off Mach number because the frequency of the guided waves does not match the frequency of the Kelvin-Helmholtz mode. Particularly, the properties of the guided waves, allow us to explain the frequencies and the axisymmetric or helical nature of the acoustic tones (Gojon *et al.* 2016; Bogey & Gojon 2017; Jaunet *et al.* 2019; Varé & Bogey 2022*a,b*). These guided waves are involved in other resonance phenomena, for examples in screech generation mechanism, as studied by Gojon & Bogey (2017*b*); Edgington-Mitchell *et al.* (2018); Mancinelli *et al.* (2019); Edgington-Mitchell (2019) or in jet-plate interactions, as recently investigated by Jordan *et al.* (2018); Tam & Chandramouli (2020); Varé & Bogey (2022*a*). They also play a role in the generation of acoustic tones near the nozzle (Towne *et al.* 2017; Brès *et al.* 2018; Bogey 2021) and in the upstream acoustic far field of free jets (Bogey 2022).

The paper aims to rationalize previous experimental results on the sound emission from a jet impinging on a perpendicular flat surface at large subsonic Mach numbers. We have several objectives. First, we analyse the properties of the feedback loop, by means of a Helmholtz-Hodge decomposition that allows a global decomposition of the flow perturbations and a local decomposition into the underpinned waves of the baseflow, i.e., we measure the relative magnitude of the acoustic and hydrodynamic components of the global mode. It results that for a sufficiently large Reynolds number, there is always a global unstable mode. However, at low and large Mach numbers of the jet, the mechanisms responsible for the closure of the feedback mechanism are distinct. In particular, that connects with the cut-off criterion of Tam & Ahuja (1990) for the existence of tonal or broadband noise. Tam & Ahuja (1990) conjectured that below the cut-off $M_c \approx 0.6$ high acoustic sound emissions are not possible because the Strouhal of the first guided wave does not match the Strouhal of the Kelvin-Helmholtz instability. Such a conclusion has been widely used in literature to justify the existence of broadband noise emissions below the cut-off Mach number. However, we will show that the feedback mechanism responsible for high acoustic tonal emissions at high subsonic Mach numbers, also exist at low Mach numbers, even at the incompressible limit for the laminar jet, nonetheless distinct closure mechanisms cause the instability. This is shown following a three-step approach:

(i) Determine the linear global mode associated to the feedback mechanism at every Mach number.

(ii) Determine the nature of the feedback-loop at low and high Mach numbers. We introduce a novel decomposition of the structural sensitivity map.

(iii) Perform a wave decomposition of the feedback global mode into Kelvin-Helmholtz and guided waves.

Such a process allows us to unveil the instability core of the feedback-loop and to analyse the physical mechanisms supporting the instability. In addition, the wave decomposition allows us to determine the local characteristics in terms of waves of the loop, e.g., the reflection coefficient at neutrality.

Furthermore, we analyse the nonlinear dynamics of the impinging jet flow configuration. Specifically, we will show that the frequencies involved in the feedback process are mostly determined by geometrical features and the velocity of propagation in the medium, i.e. Mach number and convective velocity. The eigenvalues associated to the global modes are found to form a discrete arc, with a nearly constant frequency distance $\Delta\omega$. Furthermore, performing the expansion of the flow into base flow and harmonic contributions,

$$\mathbf{q}(\mathbf{x}, t) = \mathbf{q}_0(\mathbf{x}) + \sum_{k=1}^N [A_k \mathbf{q}_{A_k} e^{i\omega_k t} + \text{c.c.}] + \dots \quad (1.1)$$

where the higher harmonics and the zeroth-harmonic modification of the meanflow have been omitted. With such an ansatz, we have carried out a normal form reduction approach (Sierra-Ausín *et al.* 2022; Sierra *et al.* 2020b) to determine the reduced-order equation that governs the dynamics of the feedback mechanism, the normal form in polar coordinates $A_k = r_k e^{i\phi_k}$ is as follows

$$\begin{aligned} \dot{r}_j &= r_j (\lambda_j + \sum_k^N \nu_{jk} r_k^2) + F_{\text{res}}(\mathbf{r}, \Psi) \\ \dot{\psi}_j &= F_{\psi_j}(\mathbf{r}, \Psi). \end{aligned} \quad (1.2)$$

The vector $\mathbf{r} = [r_1, \dots, r_{N-1}]^T$ with r_j for $j = 1, \dots, N$ is the vector of (real) amplitudes proportional to each normalized global mode that characterizes the amplitude of the limit cycle, and $\Psi = [\psi_1, \dots, \psi_N]^T$ is the vector of resonant phases, where each resonant phase is a function of an imperfect quantisation of the feedback modes $\Psi_j = \Delta\phi_j - \Delta\phi_{j-1} = (\phi_{j+1} - \phi_j) - (\phi_j - \phi_{j-1})$. Herein, we treat the case with $N = 3$, and the vector fields F_{ψ_j} and F_{res} will be specified later on for this case. In the case of a perfect equi-distribution of feedback modes ($\omega_k = k\Delta\omega$), the limit cycles would be in a perfect resonance. However, nonlinear modulations of the frequency, which could be accounted by the disparity in the amplitude of local sources of divergence of the velocity field perturbations or vortex-sound responsible for the closure of the feedback-loop.

In addition, in order to model the broadband behaviour characteristic of low Mach number flows, we propose a stochastic model which is based on a phenomenological reasoning. It accounts for the low temporal coherence of the sources of sound at low Mach number, which in turn induce a frequency mismatch in the frequency selection criterion. The model is able to capture the qualitative features of low and large Mach number flows.

The outline of the manuscript is as follows. First, the flow configuration and the numerical approach are presented in section 2. Second, in section 3 we describe some basic properties of the baseflow, and we show the main results of the linear stability study, highlighting two mechanisms of closure of the feedback-mechanism. Third, in section 4 we carry out a Helmholtz-Hodge decomposition in order to get a further insight into the hydrodynamic-acoustic feedback loop by means of a novel non-local structural sensitivity decomposition. Therein, we also perform a weakly non-parallel decomposition of the global mode into the waves supported by the baseflow with the aim of determining the reflection coefficient. Then, in section 5 we analyse the interaction between limit cycles by means of axisymmetric time-stepping simulations and the normal form. Finally, in section 6 we summarise the main findings of the study.

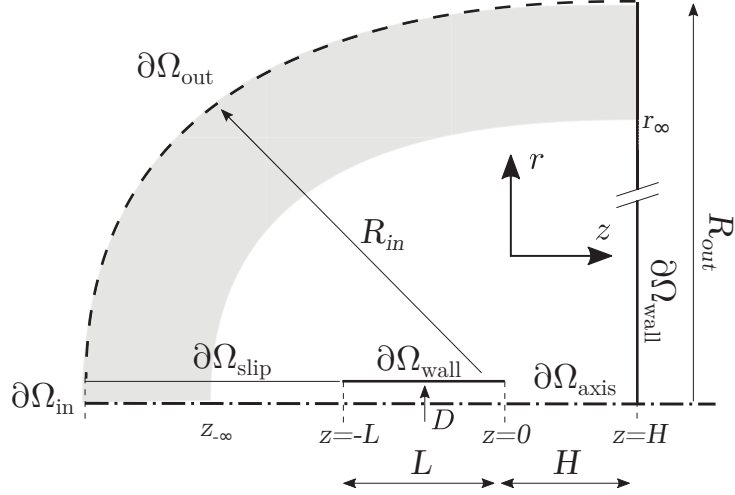


Figure 1: Diagram of the domain. The physical domain, represented as a white area, is complemented with a radial buffer layer, shown as a light grey shaded zone.

2. Numerical approach

2.1. Governing equations

Let us introduce the compressible Navier–Stokes equations as the governing equations of motion of a perfect gas described in primitive variables $\mathbf{q} = [\rho, u_r, u_\theta, u_z, p, T]^T$, and the set of control parameters $\boldsymbol{\eta} = [Re, M_\infty]^T$. These are formally expressed as

$$\mathbf{B} \frac{\partial \mathbf{q}}{\partial t} = \mathbf{F}(\mathbf{q}, \boldsymbol{\eta}) \quad \text{with } \mathbf{B} = \text{diag}(1, \rho \mathbf{I}, \rho, 0), \quad (2.1)$$

$$\mathbf{F}(\mathbf{q}, \boldsymbol{\eta}) = - \begin{pmatrix} \mathbf{u} \cdot \nabla \rho + \rho \nabla \cdot \mathbf{u} \\ \rho \mathbf{u} \cdot \nabla \mathbf{u} - \nabla p + \nabla \cdot \frac{1}{Re} \boldsymbol{\tau}(\mathbf{u}) \\ (\gamma - 1) \left[\rho T \nabla \cdot \mathbf{u} - \gamma \frac{M_\infty^2}{Re} \boldsymbol{\tau}(\mathbf{u}) : \mathbf{D}(\mathbf{u}) \right] - \rho \mathbf{u} \cdot \nabla T + \frac{\gamma}{Pr Re} \nabla^2 T \\ -\rho T + 1 + \gamma M_\infty^2 p \end{pmatrix}, \quad (2.2)$$

The geometric configuration used in the analysis of the acoustic radiation of a rounded impinging jet is sketched in fig. 1. It consists of a pipe that is subdivided into two zones, a first pipe with slip adiabatic walls and a second pipe of length L with no-slip adiabatic walls. The physical domain, depicted as a white region in fig. 1 is complemented with an absorbing boundary layer in the far-field, which is either a complex mapping region (Sierra *et al.* 2020a) for the linear computations of section 2.2 or a sponge region (Fani *et al.* 2018) for the nonlinear computations of section 2.3. In our formulation, the primitive variables have been made dimensionless to

$$\begin{aligned} \mathbf{x} &= \frac{\tilde{\mathbf{x}}}{D}, \quad t = \frac{\tilde{t} \tilde{u}_z|_{z=0}}{D}, \quad \rho = \frac{\tilde{\rho}}{\tilde{\rho}|_{fs}}, \quad \mathbf{u} = \frac{\tilde{\mathbf{u}}}{\tilde{u}_z|_{z=0}}, \quad T = \frac{\tilde{T}}{\tilde{T}|_{fs}}, \\ p &= \frac{\tilde{p} - \tilde{p}|_{fs}}{\tilde{\rho}|_{fs} \tilde{u}_z|_{z=0}^2}, \quad M_\infty = \frac{\tilde{u}_z|_{z=0}}{(\gamma R_g \tilde{T}|_{fs})^{1/2}}, \quad Re = \frac{\tilde{\rho}|_{fs} \tilde{u}_z|_{z=0} D}{\mu(\tilde{T}|_{fs})} \end{aligned} \quad (2.3)$$

where R_g is the ideal gas constant, $\tilde{u}_z|_{z=0}$ denote the average value of the axial velocity at the cross-section $z = 0$, and $\tilde{\rho}|_{fs}$, $\tilde{p}|_{fs}$, $\tilde{T}|_{fs}$ denote the values on the far-field or free-stream. The Navier–Stokes equations eq. (2.1) are complemented with the following

boundary conditions,

$$\begin{aligned}
u_z = 1, & & u_r = 0, & & T = (1 - \frac{\gamma-1}{2}M_\infty^2) & & \text{on } \partial\Omega_{in} \\
u_z = 0, & & u_r = 0, & & \nabla T \cdot \mathbf{n} = 0 & & \text{on } \partial\Omega_{wall} \\
u_r = 0, & & \nabla T \cdot \mathbf{n} = 0 & & & & \text{on } \partial\Omega_{slip} \\
\rho = 1, & & p = 0, & & T = 1 & & \text{on } \partial\Omega_{out}.
\end{aligned} \tag{2.4}$$

The inlet boundary condition models the inflow from a reservoir with a constant total temperature equal to unity. In such a way, the energy of the system is kept constant for every Mach number M_∞ . The length of the pipe is a constant of the problem that determines the height of the boundary layer, here we have chosen $L = 2.5D$. The flow in the slip region is nearly constant, thus the length of this region is not an important parameter of the problem. The location of the start of the absorbing layer is chosen to be $z_{-\infty} = r_\infty = 15D$. Finally, the distance between the nozzle end location ($z = 0$) and the impinging wall is H , which is kept constant $H = 5D$.

2.2. Linear Navier–Stokes equations

The asymptotic linear stability of a steady-state \mathbf{q}_0 is examined from the temporal evolution of an infinitesimal perturbation, i.e. by performing the following expansion $\mathbf{q} = \mathbf{q}_0 + \varepsilon(\hat{\mathbf{q}}e^{-i\omega t} + \text{c.c.})$ where $\varepsilon \ll 1$. The steady-state \mathbf{q}_0 is said to be asymptotically linearly stable if there is not an eigenvalue with a positive growth rate, in other words for every eigenvalue $\omega_i < 0$, otherwise it is said to be linearly unstable. The perturbation $\hat{\mathbf{q}}$ and its eigenvalue $i\omega$ are determined by solving the following eigenvalue problem

$$-i\omega\mathbf{B}|_{\mathbf{q}_0}\hat{\mathbf{q}} + \mathbf{DF}|_{\mathbf{q}_0}(\hat{\mathbf{q}}, \boldsymbol{\eta}) = 0, \tag{2.5}$$

The linear Navier–Stokes equations eq. (2.5) are complemented with the following homogeneous boundary conditions,

$$\begin{aligned}
\hat{u}_z = 0, & & \hat{u}_r = 0, & & \hat{T} = 0 & & \text{on } \partial\Omega_{in} \\
\hat{u}_z = 0, & & \hat{u}_r = 0, & & \nabla\hat{T} \cdot \mathbf{n} = 0 & & \text{on } \partial\Omega_{wall} \\
\hat{u}_r = 0, & & \nabla\hat{T} \cdot \mathbf{n} = 0 & & & & \text{on } \partial\Omega_{slip} \\
\hat{\rho} = 0, & & \hat{p} = 0, & & \hat{T} = 0 & & \text{on } \partial\Omega_{out}.
\end{aligned} \tag{2.6}$$

In the following, we will also consider the adjoint eigenmode $\hat{\mathbf{q}}^\dagger$, which is a solution of the adjoint eigenvalue problem

$$i\bar{\omega}\mathbf{B}|_{\mathbf{q}_0}\hat{\mathbf{q}}^\dagger + \mathbf{DF}^\dagger|_{\mathbf{q}_0}(\hat{\mathbf{q}}^\dagger, \boldsymbol{\eta}) = 0. \tag{2.7}$$

where $\bar{\cdot}$ is employed for the complex conjugation. The boundary conditions of the adjoint problem are the same as the direct, eq. (2.6). The adjoint modes are normalised by the B -inner product, that is $\langle \hat{\mathbf{q}}^\dagger, \hat{\mathbf{q}} \rangle_{\mathbf{B}} = 1$.

2.3. Time-stepping approach

The Navier–Stokes equations (eq. (2.1)) are evolved in time with a fully implicit time integrator. We use a third order BDF scheme to integrate in time the state variable \mathbf{q} . The semi-discrete in time equations are as follows,

$$\mathbf{B} \left[\frac{11}{6}\mathbf{q}(t_{n+1}) - 3\mathbf{q}(t_n) + \frac{3}{2}\mathbf{q}(t_{n-1}) - \frac{1}{3}\mathbf{q}(t_{n-2}) \right] = -\Delta t \mathbf{F}(\mathbf{q}(t_{n+1}), \boldsymbol{\eta}) \tag{2.8}$$

Each time-step, the nonlinear problem eq. (2.8) is solved with a Newton method,

$$\begin{aligned} \left[\frac{11}{6} \mathbf{B} + \Delta t D\mathbf{F}|_{\mathbf{q}^\ell(t_{n+1})} \right] \delta \mathbf{q} &= \mathbf{B} \left[3\mathbf{q}(t_n) - \frac{3}{2}\mathbf{q}(t_{n-1}) + \frac{1}{3}\mathbf{q}(t_{n-2}) \right] - \Delta t \mathbf{F}(\mathbf{q}^\ell(t_{n+1}), \boldsymbol{\eta}) \\ \mathbf{q}^{\ell+1}(t_{n+1}) &= \mathbf{q}^\ell(t_{n+1}) + \delta \mathbf{q}. \end{aligned} \quad (2.9)$$

The assembling of the jacobian matrix $D\mathbf{F}|_{\mathbf{q}^\ell(t_{n+1})}$ is the most expensive step, and as it is conventional, a frozen jacobian matrix is adopted all along the Newton method, that is, $D\mathbf{F}|_{\mathbf{q}^\ell(t_{n+1})} = D\mathbf{F}|_{\mathbf{q}(t_n)}$. Furthermore, provided that the time-step is not too large, the jacobian matrix is kept constant for few time-steps, as long as the number of iterations to convergence of the Newton method do not drastically grow.

2.4. Normal form reduction

In the following, we summarize the normal form reduction procedure, which is carried out to study the interaction between distinct periodic orbits resulting from global instabilities associated to the main feedback mechanism. A comprehensive explanation is left to appendix B.

Near the onset of the bifurcation, dynamics can be reduced to the normal form. The coefficients of the normal form are computed following a multiple scales expansion of the solution \mathbf{q} of eq. (2.1). The expansion considers a two scale development of the original time $t \mapsto t + \varepsilon^2 \tau$, here ε is the order of magnitude of the flow disturbances, assumed small $\varepsilon \ll 1$. Herein, we consider the small parameters ε_{M^2} and ε_ν , which are a function of the Mach number and Reynolds numbers at the far-field,

$$\varepsilon_{M^2}^2 = (M_{\infty,c}^2 - M_\infty^2) \sim \varepsilon^2 \text{ and } \varepsilon_\nu^2 = (\nu_c - \nu) = (Re_c^{-1} - Re^{-1}) \sim \varepsilon^2.$$

The technique decomposes time into a fast timescale t of the phase associated to the self-sustained instabilities and a slow timescale related to the evolution of the amplitudes $z_i(\tau)$, introduced in eq. (2.11), for $i = 1, 2, 3$. The ansatz of the expansion is as follows

$$\mathbf{q}(t, \tau) = \mathbf{q}_b + \varepsilon \mathbf{q}_{(\varepsilon)}(t, \tau) + \varepsilon^2 \mathbf{q}_{(\varepsilon^2)}(t, \tau) + \varepsilon^3 \mathbf{q}_{(\varepsilon^3)}(t, \tau) + O(\varepsilon^4) \quad (2.10)$$

In the following, we shall consider the normal form equation resulting from the interaction of three modes identified by linear stability, that is,

$$\mathbf{q}_{(\varepsilon)}(t, \tau) = \sum_{k=1}^N (z_k(\tau) \hat{\mathbf{q}}_{(z_k)}(r, z) e^{i\omega_k t} + \text{c.c.}) \quad (2.11)$$

Note that the expansion of the LHS of eq. (2.1) up to third order is as follows

$$\varepsilon \mathbf{B} \frac{\partial \mathbf{q}_{(\varepsilon)}}{\partial t} + \varepsilon^2 \mathbf{B} \frac{\partial \mathbf{q}_{(\varepsilon^2)}}{\partial t} + \varepsilon^3 \left[\mathbf{B} \frac{\partial \mathbf{q}_{(\varepsilon^3)}}{\partial t} + \mathbf{B} \frac{\partial \mathbf{q}_{(\varepsilon)}}{\partial \tau} \right] + O(\varepsilon^4), \quad (2.12)$$

and the RHS respectively,

$$\mathbf{F}(\mathbf{q}, \boldsymbol{\eta}) = \mathbf{F}_{(0)} + \varepsilon \mathbf{F}_{(\varepsilon)} + \varepsilon^2 \mathbf{F}_{(\varepsilon^2)} + \varepsilon^3 \mathbf{F}_{(\varepsilon^3)} + O(\varepsilon^4). \quad (2.13)$$

Then, the problem truncated at order three is reduced to a low-dimensional system governing the complex amplitudes $z_j(t)$. Herein we consider the case of $N = 3$, the general case is briefly discussed in appendix B.5. The normal form is as follows,

$$\begin{aligned} \dot{z}_1 &= z_1 \left(\lambda_1 + \nu_{11} |z_1|^2 + \nu_{12} |z_2|^2 + \nu_{13} |z_3|^2 \right) + \chi_1 z_2^2 \bar{z}_3 \\ \dot{z}_2 &= z_2 \left(\lambda_2 + \nu_{21} |z_1|^2 + \nu_{22} |z_2|^2 + \nu_{23} |z_3|^2 \right) + \chi_2 z_1 \bar{z}_2 z_3 \\ \dot{z}_3 &= z_3 \left(\lambda_3 + \nu_{31} |z_1|^2 + \nu_{32} |z_2|^2 + \nu_{33} |z_3|^2 \right) + \chi_3 z_2^2 \bar{z}_1 \end{aligned} \quad (2.14)$$

where $\nu_{k\ell}, \lambda_k, \chi_k \in \mathbb{C}$ for $k, \ell = 1, 2, 3$. The real part of the linear terms, named λ_k , correspond to the growth rate of the k^{th} mode. Respectively, the imaginary part of λ_k is associated to the frequency variation of the k^{th} mode with respect to the frequency

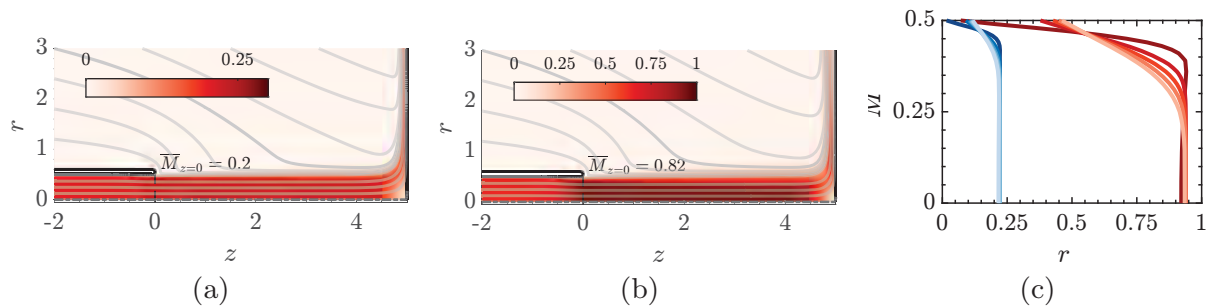


Figure 2: Spatial distribution of the Mach number for a baseflow at (a) $Re = 2200$ and $M_\infty = 0.2$, (b) $M_\infty = 0.6$ and $Re = 800$. (c) Radial evolution of the Mach number (blue for the profiles of (a) and red for (b)) from the nozzle exit ($z = 0$, represented with the darkest colour) to $z = 4D$ (light colour), with an equidistant step of a diameter.

of the neutral mode, i.e., with respect to the frequency ω_k determined from linear stability analysis. The terms $\nu_{k\ell}$ are the third order self ($k = \ell$) and cross interaction ($k \neq \ell$) coefficients. The resonant coefficients χ_k arise because of the quantization of the eigenvalues in the spectrum at a nearly constant distance $\Delta\omega$, i.e. frequency gaps $\Delta\omega_i = (\omega_{i+1} - \omega_i)$ are nearly constant, see fig. 15 (a) in appendix B.5. In the analysis, we consider that the imperfections in the frequency difference between two modes is small, that is, $(\Delta\omega_{i+1} - \Delta\omega_i) \sim \varepsilon^2$. In this way, the term $z_2^2 \bar{z}_3$ is nearly resonant with z_1 , or in other terms $\omega_2 - \Delta\omega_2 \approx \omega_1$.

3. Linear global stability procedure – Parametric analysis

3.1. Baseflow properties

We define the baseflow as the steady-state solution of the Navier–Stokes equations satisfying the boundary conditions listed in eq. (2.4). The baseflow is determined by two dimensionless parameters, the Reynolds number (Re) based on the averaged velocity at the nozzle exit and the Mach number (M_∞) based on the averaged velocity at the nozzle exit and the speed of sound at the far-field. Given this definition of the Mach number based on the speed of sound at the far field (M_∞), the actual Mach number of the flow can be considerably larger, specially for $M_\infty \in [0.5, 0.6]$, where compressibility effects are significant. Figure 2 reports the spatial distribution of the Mach number in the region between the nozzle and the impinging wall. Figure 2 (c) shows the radial evolution of the velocity profile. Since we consider a laminar baseflow the boundary layer thickness at the nozzle exit (darker velocity profile in the figure) is considerably larger than for a turbulent mean flow profile, and it is around a tenth of the diameter.

3.2. Linear stability – Compressibility effects

We analyse the effects of the Mach number on the feedback mechanism. First, we determine the dominant global linear modes for every subsonic Mach number, which corresponds to $M_\infty \in [0, 0.6]$. Figure 3 shows the neutral curves of linear stability of the steady-state. We follow the evolution of the leading five modes, which are characterised by a slow frequency evolution with respect to the Mach number and a nearly constant frequency $\Delta\omega$ distance between modes. At a given Mach number, the modes are characterised by their axial wavenumber; the dominant modes at $M_\infty = 0.6$, displayed in fig. 3 (g-i), are characterised by seven, six and eight half-wavelengths, respectively. Nonetheless, such a characterisation is not constant with varying Mach number, the number of axial wavelengths can vary up to a unit. The change of the axial wavenumber is a continuous

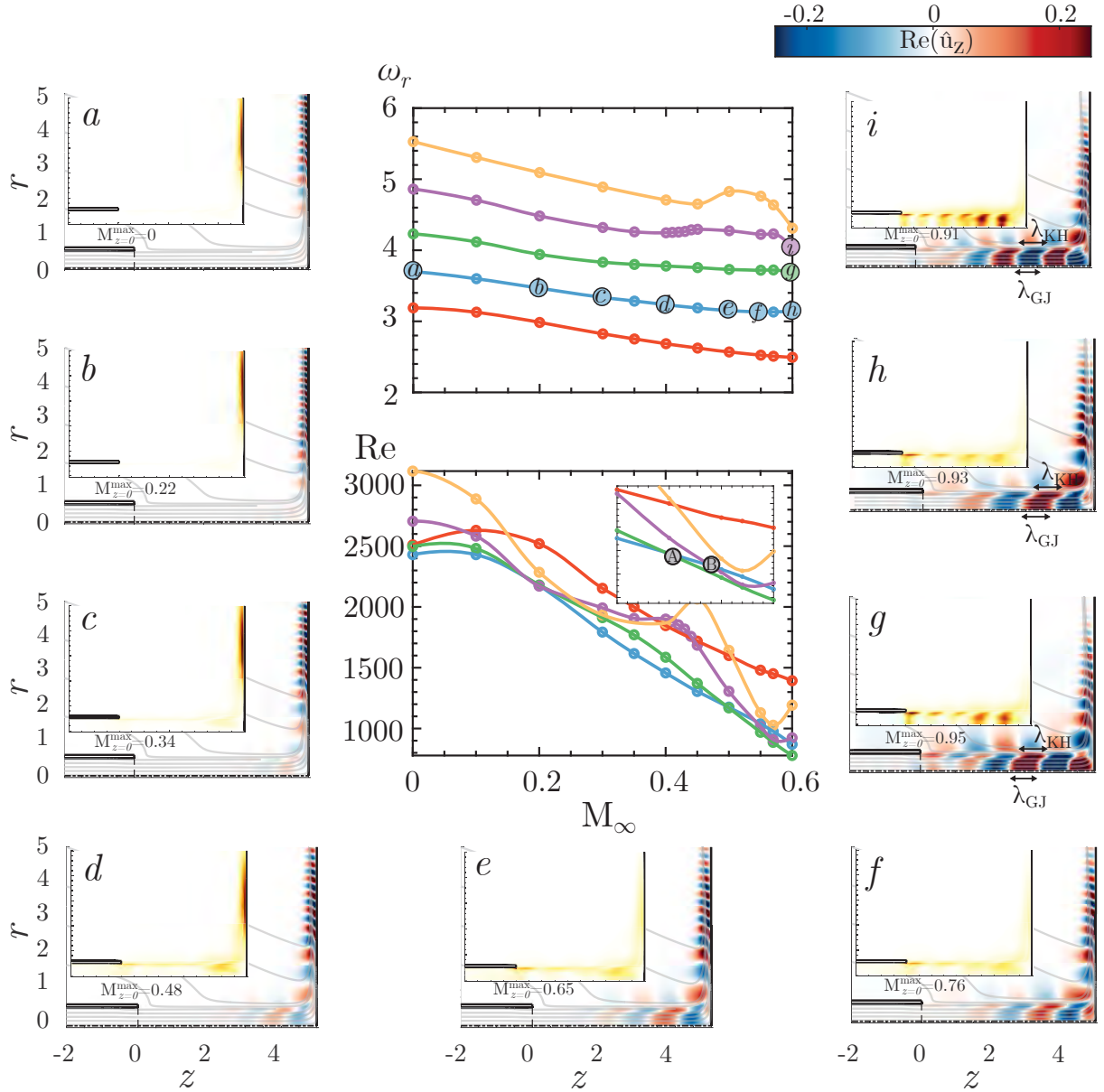


Figure 3: Bifurcation diagram showing the neutral curves of stability and evolution of the critical pulsation ω_r of the axisymmetric steady-state flow for a nozzle to wall distance $H/D = 5$. Visualization of the critical eigenmode (real part of the axial velocity) with overlaid steady-flow streamlines. Each visualization contains a superposed image of the structural sensitivity map.

process and occurs within the interacting region between the axial and radial shear layers, i.e. $4.5D < z < H$.

The primary instability corresponds to a Hopf bifurcation, leading to a periodic solution with $\omega \approx 3.7$ (blue line in fig. 3) for $M_\infty < 0.49$ and to frequency $\omega \approx 4$ (green line in the figure) for $M_\infty > 0.49$. The mode switching happens in a codimension Hopf-Hopf two point, which it has also been experimentally observed in Nosseir & Ho (1982), where they also detected hysteresis-like behaviour between two modes.

The non-local feedback mechanism selects the frequency of the global mode for every Mach number, however the strength of the feedback loop rapidly decreases with the Mach number. This feature may be observed directly from the global modes by comparing the ones obtained at large subsonic Mach number ($M_\infty = 0.6$, $M_J \approx 0.9$) represented by

subfigures (g-i) and the ones for lower Mach numbers, see subfigures (a-f). Please note that the amplitude of the modes is normalised in such a way that the perturbation energy (Chu 1965) is unitary.

Figure 3 also displays, in an inset located at the upper left location of each subfigure, the structural sensitivity, introduced by Giannetti & Luchini (2007) and defined herein in section 4.1. The structural sensitivity highlights the spatial location where a generic modification of the instability core produces the largest drift in the growth rate or frequency of the mode. Therefore, it is hereafter considered as the core of the instability. For large subsonic Mach numbers ($0.5 < M_\infty < 0.6$) the structural sensitivity has an extended compact support within the axial shear layer and the jet region. It is intermittent, located at the axial position of the pulses in the axial shear layer of the direct mode, excluding the region near the wall ($H - D < z < H$). Thus, suggesting that the region near the wall does not play a dominant effect to the instability at large Mach number. Tentatively, one can argue the following about the two types of peaks of the structural sensitivity. The dominant peaks of the structural sensitivity at the shear-layer correspond to the energy transfers between the baseflow shear and the perturbation. And the large amplitude peaks within the jet may be the region where the vortical fluctuations are transformed into acoustics via a coupling mechanism. It may be observed from fig. 4 (a) that the region of largest divergence of the mode matches with the spatial location highlighted by the structural sensitivity. One can determine the production of fluctuating divergence from the divergence of the linearised momentum equation, that is,

$$\begin{aligned}
 -i\omega \nabla \cdot \hat{\mathbf{u}} + \mathbf{u}_0 \cdot \nabla (\nabla \cdot \hat{\mathbf{u}}) + \nabla \cdot \left(\frac{\hat{\rho}}{\rho_0} \mathbf{u}_0 \cdot \nabla \mathbf{u}_0 \right) &= - \overbrace{\hat{\mathbf{u}} \cdot \nabla (\nabla \cdot \mathbf{u}_0)}^{C_A^{\text{div}}} - \overbrace{\frac{\Delta \hat{p}}{\rho_0} + \frac{\nabla \hat{p} \cdot \nabla \rho_0}{\rho_0^2}}^{C_{P,b}^{\text{div}}} - \overbrace{\frac{\nabla \hat{p} \cdot \nabla \rho_0}{\rho_0^2}}^{P_a^{\text{div}}} \\
 &\quad - \underbrace{\left((\nabla \hat{\mathbf{u}})^T : \nabla \mathbf{u}_0 + (\nabla \mathbf{u}_0)^T : \nabla \hat{\mathbf{u}} \right)}_{C_{P,a}^{\text{div}}} \\
 &\quad + \underbrace{\frac{1}{\text{Re}} \nabla \cdot (\nabla \cdot \tau(\hat{\mathbf{u}}))}_{P_b^{\text{div}}} \quad (3.1a)
 \end{aligned}$$

Note that, eq. (3.1) can be written entirely in terms of velocity and density fluctuations, if we assume that the pressure fluctuations are isentropic, i.e., $M_\infty^2 \hat{p} = \hat{\rho} T_0$. The module of the convection term, hereafter referred to as C_A^{div} corresponds to the convection of the divergence and density fluctuations by the baseflow. This term is displayed in fig. 4 (b). The spatial support of C_A^{div} lies within the jet region and the radial shear layer. Nonetheless, despite the fact that it is supported at the location of the maximum fluctuating divergence, one cannot associate this term as a source of divergence production. It merely advects fluctuating divergence and density, that has been already produced within the flow. The spatial support of term $C_{P,a}^{\text{div}}$, displayed in fig. 4 (d), mostly lies within the shear layer and in regions with non-zero divergence of the baseflow (not shown). P_a^{div} is the pressure source term whose spatial support lies in the shear layer, in a region within the jet near the wall ($H - D < z < H$) and the region near the nozzle exit. The largest local contribution to the fluctuating divergence is due to this term. The other two production terms ($C_{P,b}^{\text{div}}$ and P_b^{div}) are of small magnitude, and their spatial support is not found within the region of the maximum of the divergence. However, we have previously argued that the pressure, if we assume an isentropic process at the perturbation level, plays a similar role to the one of the density. Tentatively, one

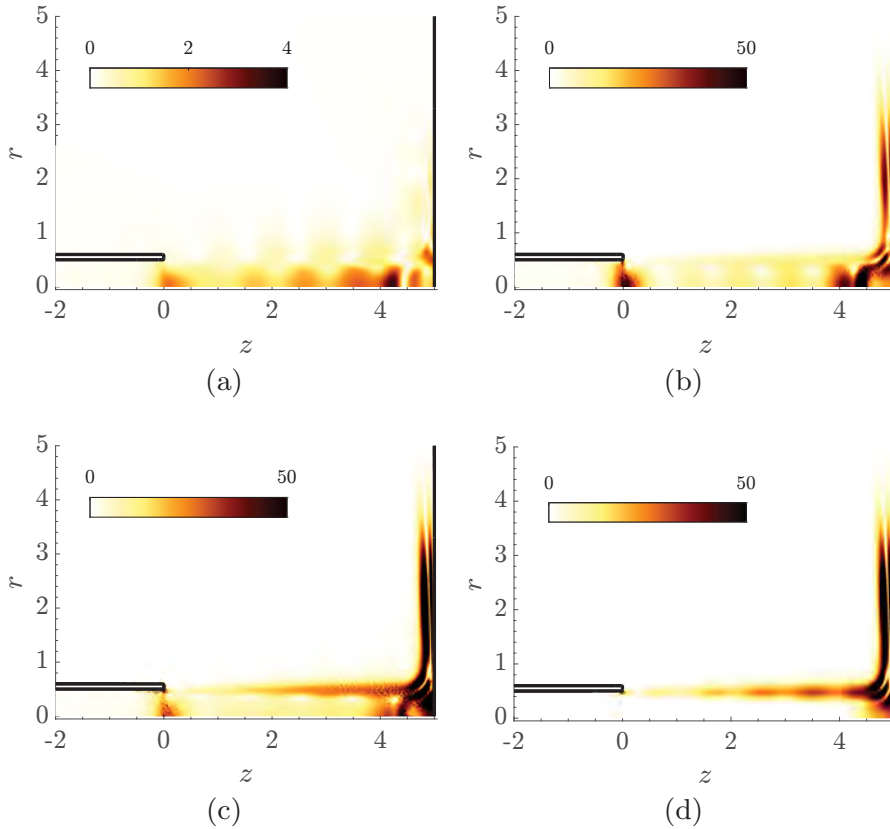


Figure 4: Module of the (a) divergence of the mode; (b) module of the term C_A^{div} in eq. (3.1a); (c) module of the term P_a^{div} in eq. (3.1a); (d) module of the term $C_{P,a}^{\text{div}}$ in eq. (3.1a).

may argue that the pressure serves to enforce the continuity condition, thereby inducing a modification of the volume flux. In a similar way, by taking the material derivative of the linearised continuity equation, it is possible to derive a generalised wave equation, where the dominant source term is a term proportional to the fluctuating divergence (not shown here). Then, we could say that in a second step, the divergence of the mode induces an acoustic pulse that is propagated as a longitudinal density wave, and therefore providing the closure of the feedback-loop.

On the other hand, for low subsonic Mach numbers ($M_\infty < 0.4$), the structural sensitivity has an extended support within the radial shear layer ($2.5D < r < 5D$). In this case, the structural sensitivity has a thin continuous structure. To understand the nature of the wavemaker at low Mach numbers, we write the linearised momentum equation in the Crocco's form (Rienstra & Hirschberg 2004),

$$-i\omega\hat{\mathbf{u}} + \nabla \cdot \left((\mathbf{u}_0 \cdot \hat{\mathbf{u}} + \frac{\hat{p}}{\rho_0})\mathbf{I} - \tau(\hat{\mathbf{u}}) \right) = \mathbf{u}_0 \times \hat{\omega} + \hat{\mathbf{u}} \times \omega_0, \quad (3.2)$$

where we have neglected the term $-\frac{\nabla \rho_0 \hat{p}}{\rho_0^2}$, which is of small magnitude at low Mach number. We can readily observe that the linearised Lamb vector $\mathbf{u}_0 \times \hat{\omega} + \hat{\mathbf{u}} \times \omega_0$ acts a source term, and one could argue that it corresponds first to the region driving the hydrodynamic instability, and second to a source of sound, which is in turn, responsible for the production of the backward propagating acoustic pressure that closes the feedback-loop (Powell 1990; Howe 1975). Figure 5 displays the linearised Lamb vector, which is localised within the radial shear layer and at the same spatial location as the structural sensitivity

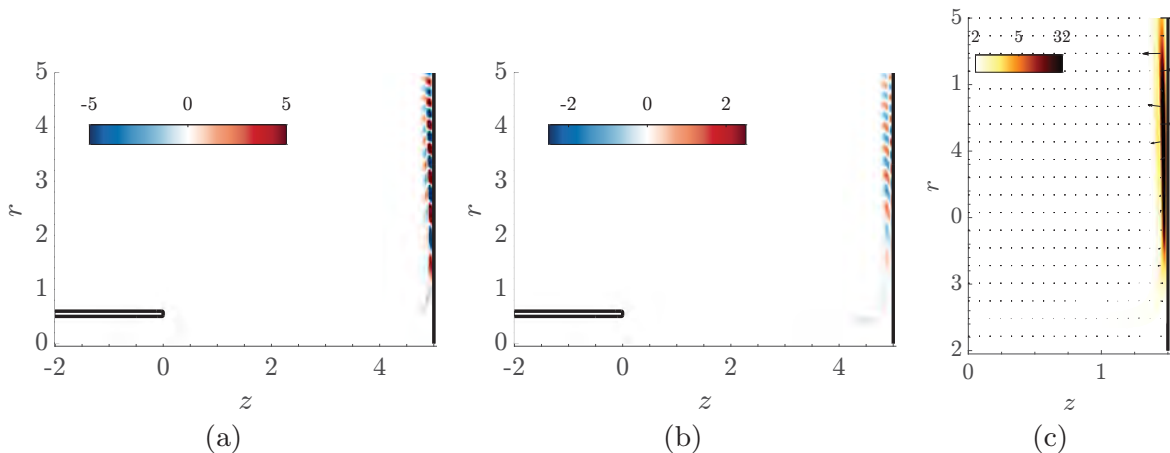


Figure 5: (a-b) Axial and radial components, respectively, of the real part of the linearised Lamb vector $\mathbf{u}_0 \times \hat{\omega} + \hat{\mathbf{u}} \times \omega_0$ at $M_\infty = 0.2$ and $Re = 2200$. (c) Module of the Lamb vector, the arrows indicate the direction.

at low Mach numbers. Thus, providing a rationalisation to the nature of the wavemaker, which in this situation is located along the vortex sheet near the impinging wall. For the sake of consistency, please note that the Lamb vector at large Mach numbers also possess a similar structure, that is, it is a thin-elongated structure along the vortex sheet (not shown). However, the structural sensitivity does not have this kind of structure, thus suggesting that vortex sound is not the dominant vortical-acoustic coupling.

4. Decomposition of the feedback mechanism

In order to gain a better understanding of the feedback process responsible for the instability, we perform two types of decomposition. First, a Helmholtz-Hodge decomposition of the global linear mode $\hat{\mathbf{q}}$, which allows distinguishing between the acoustic and vortical+entropic components of the flow. Additionally, such a decomposition allows us to formulate a finer *structural sensitivity* concept. This decomposition of the structural sensitivity highlights the space location where a vortical (resp. acoustic) modification in the structure of the problem is able to produce the greatest drift in the eigenvalue of the operator projected onto the acoustic or vortical component. The study is then pursued with the analysis of the feedback-loop with the *endogeneity* map, which provides further access to the relation between the growth rate or frequency of the mode in terms of underlying the physical mechanisms. We finish the section with a decomposition of the global mode in terms of the local waves underpinned by the baseflow, which allows us to determine the reflection coefficient between the shear layer wave and the guided jet wave at neutrality.

4.1. Decomposition of the linear perturbation

The linear perturbation $\hat{\mathbf{q}}$ is herein decomposed into three components: *acoustic*, *hydrodynamic* and *entropic*. There is a large literature in decomposition of acoustic sources (Ewert & Schröder 2003; Spieser 2020) to compute acoustic propagation effects. In our case, we follow the reciprocal reasoning, we adopt a monolithic computation of the compressible flow, i.e. we do not decompose the flow in acoustic sources and acoustic propagation, and we would like to unveil the feedback loop responsible for the instability mechanism and the frequency selection.

For this purpose, we adopt a Helmholtz-Hodge decomposition (Schoder *et al.* 2020) of

the perturbation velocity field into *acoustic* (potential) and *hydrodynamic* (solenoidal)

$$\hat{\mathbf{u}} = \hat{\mathbf{u}}_{\text{ac}} + \hat{\mathbf{u}}_{\text{hyd}} = \nabla\phi_c + \nabla \times \Psi \quad (4.1)$$

applying divergence to eq. (4.1), the potential ϕ_c is determined from the following Poisson equation

$$\begin{aligned} \Delta\phi_c &= \nabla \cdot \hat{\mathbf{u}} & \text{in } \Omega \\ \nabla\phi_c \cdot \mathbf{n} &= \hat{\mathbf{u}} \cdot \mathbf{n} & \text{on } \partial\Omega. \end{aligned} \quad (4.2)$$

The hydrodynamic component of the velocity is subsequently determined by subtracting $\hat{\mathbf{u}}_{\text{hyd}} = \hat{\mathbf{u}} - \hat{\mathbf{u}}_{\text{ac}} = \hat{\mathbf{u}} - \nabla\phi_c$. Note that, the uniqueness of the Helmholtz decomposition is subjected to the L^2 -orthogonality condition, in our case satisfied by the suitable boundary condition of eq. (A 6), and the decay of the velocity field at the far-field (Schoder *et al.* 2020).

The pressure component of the mode $\hat{\mathbf{q}}$ is determined from the momentum equation

$$-\frac{1}{\rho_0}\nabla\hat{p} = i\omega\hat{\mathbf{u}} + \hat{\mathbf{u}} \cdot \nabla\mathbf{u}_0 + \mathbf{u}_0 \cdot \nabla\hat{\mathbf{u}} + \frac{\hat{\rho}}{\rho_0}\mathbf{u}_0 \cdot \nabla\mathbf{u}_0 - \frac{1}{\text{Re}}\nabla \cdot \tau(\hat{\mathbf{u}}), \quad (4.3)$$

from the decomposition $\hat{p} = \hat{p}_{\text{ac}} + \hat{p}_{\text{hyd}} + \hat{p}_{\text{s}}$ and applying the divergence operator to the momentum equation, we obtain the following equations

$$\begin{aligned} -\frac{1}{\rho_0}\Delta\hat{p}_{\text{ac}} + \frac{\nabla\rho_0 \cdot \nabla\hat{p}_{\text{ac}}}{\rho_0^2} - \nabla \cdot \left(\frac{M_\infty^2}{T_0} (\mathbf{u}_0 \cdot \nabla\mathbf{u}_0) \frac{\hat{p}_{\text{ac}}}{\rho_0} \right) &= i\omega\nabla \cdot \hat{\mathbf{u}}_{\text{ac}} + \nabla \cdot (\mathbf{u}_0 \cdot \nabla\hat{\mathbf{u}}_{\text{ac}}) \\ &+ \nabla \cdot (\hat{\mathbf{u}}_{\text{ac}} \cdot \nabla\mathbf{u}_0) \end{aligned} \quad (4.4a)$$

$$\begin{aligned} -\frac{1}{\rho_0}\Delta\hat{p}_{\text{hyd}} + \frac{\nabla\rho_0 \cdot \nabla\hat{p}_{\text{hyd}}}{\rho_0^2} - \nabla \cdot \left(\frac{M_\infty^2}{T_0} (\mathbf{u}_0 \cdot \nabla\mathbf{u}_0) \frac{\hat{p}_{\text{hyd}}}{\rho_0} \right) &= \nabla \cdot (\mathbf{u}_0 \cdot \nabla\hat{\mathbf{u}}_{\text{hyd}}) \\ &+ \nabla \cdot (\hat{\mathbf{u}}_{\text{hyd}} \cdot \nabla\mathbf{u}_0) \end{aligned} \quad (4.4b)$$

with decay at the far-field $r \rightarrow \infty$. Details of the derivation are given in appendix A.1. Finally, the entropic part of the pressure is recovered by subtracting the two other components to the pressure of the mode $\hat{p}_{\text{s}} = \hat{p} - \hat{p}_{\text{ac}} - \hat{p}_{\text{hyd}}$, which accounts for the dissipation effects of the viscous stress-tensor.

The other two components, temperature and density, are determined as follows. The acoustic and hydrodynamic components are considered to evolve isentropically and are directly determined from the pressure,

$$\hat{T}_{\text{ac}} = (\gamma - 1)M_\infty^2\hat{p}_{\text{ac}}, \quad \hat{T}_{\text{hyd}} = (\gamma - 1)M_\infty^2\hat{p}_{\text{hyd}}, \quad \hat{T}_{\text{s}} = \hat{T} - \hat{T}_{\text{ac}} - \hat{T}_{\text{hyd}}, \quad (4.5)$$

$$\hat{\rho}_{\text{ac}} = M_\infty^2 \frac{\rho_0}{T_0} \hat{p}_{\text{ac}}, \quad \hat{\rho}_{\text{hyd}} = M_\infty^2 \frac{\rho_0}{T_0} \hat{p}_{\text{hyd}}, \quad \hat{\rho}_{\text{s}} = \hat{\rho} - \hat{\rho}_{\text{ac}} - \hat{\rho}_{\text{hyd}}. \quad (4.6)$$

Let us illustrate the application of this decomposition to a particular example. For that purpose, we have chosen the global mode (h) of fig. 3. Figure 6 depicts the components of the density fluctuations $\hat{\rho}$. The hydrodynamic density fluctuations $\hat{\rho}_{\text{hyd}}$, being only hydrodynamic, resemble to the hydrodynamic pressure fluctuations, which result from a Kelvin-Helmholtz instability of the shear layer, at low Mach numbers (Sierra-Ausin *et al.* 2022). The entropic component of the density $\hat{\rho}_{\text{s}}$, which is illustrated in (c), is localised within the shear layer. In this component, one can perfectly appreciate the wavelength and the number of nodes of forward wave composing the feedback loop, in this case the forward wave has six nodes. The acoustic component of the density $\hat{\rho}_{\text{ac}}$, depicted in (a), is composed of a radiating part and the guided jet wave, which is localised within the jet region. In this case, the guided jet wave is composed of two waves, i.e. it has four nodes. From this decomposition, we can formulate a criterion for the frequency selection,

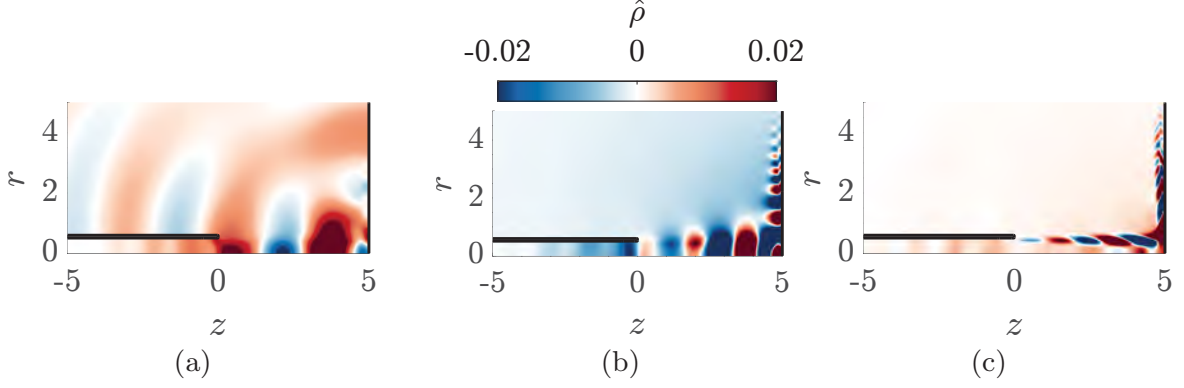


Figure 6: Density decomposition of the global mode with $St \approx 0.5$ at criticality ($Re = 900$) at $M_\infty = 0.6$ (Mode (h) in fig. 3). (a) Acoustic component of density $\hat{\rho}_{ac}$. (b) Hydrodynamic component of density $\hat{\rho}_{hyd}$. (c) Entropic component of density $\hat{\rho}_s$

similar to the Rössiter modes,

$$St^{-1} = \frac{H/D}{U_{c,SL} n_{hyd}} + \frac{H/D}{M_\infty^{-1} n_{ac}}, \text{ with } U_{c,SL} \approx \frac{1}{2} U_{r=0} \quad (4.7)$$

such a criterion considers that the phase velocity of the hydrodynamic forward mode corresponds to the inviscid approximation, that is, $U_{c,SL}$ takes the mean value between the two velocities of the shear layer, and the guided jet wave is propagated back nearly at the speed of sound of the far-field. Such a criterion provides a way to classify the global modes from the number of half-wavelengths of the guided jet wave mode (n_{ac}) and the hydrodynamic mode (n_{hyd}).

4.2. Localization of the non-local structural sensitivity

The global instability is underpinned by a feedback process between two travelling waves, which impedes a direct *local* definition of the *wavemaker* which is identified by the largest values of the *structural sensitivity* map. In other terms, we can still formulate the concept of structural sensitivity, but it is no longer localized in space, i.e., it displays a spatial distribution all along the interacting path between the two travelling waves. We briefly recall the concept of structural sensitivity, before introducing an adequate decomposition of the wavemaker for global instabilities generated by non-local feedback process. The adjoint equations are herein used to evaluate the effect of a linear harmonic forcing $\mathbf{H}(\hat{\mathbf{q}}) \equiv \delta(\mathbf{x} - \mathbf{x}_0) \mathbf{P}_H \mathbf{C}_0 \mathbf{P}_{\hat{\mathbf{q}}} \hat{\mathbf{q}}$,

$$\left(-i\omega \mathbf{B}|_{\mathbf{q}_0} + \mathbf{D}\mathbf{F}|_{\mathbf{q}_0} \right) \hat{\mathbf{q}} = \mathbf{H}(\hat{\mathbf{q}}). \quad (4.8)$$

\mathbf{C}_0 is a generic linear operator acting on $\hat{\mathbf{q}}$, and \mathbf{P}_H a diagonal matrix that selects the type of forcing. In the following, we neglect mass injection to the system, and we simply consider momentum forcing and a source of heat release, that is, $\mathbf{P}_H = \text{diag}(0, \mathbf{I}, 1, 0, 0)$. The projection operator $\mathbf{P}_{\hat{\mathbf{q}}}$ is also a diagonal matrix that selects the dependency of the forcing on the perturbation. The structural sensitivity tensor is therefore defined as

$$i\delta\omega = \langle \mathbf{P}_H \hat{\mathbf{q}}^\dagger, \delta(\mathbf{x} - \mathbf{x}_0) \mathbf{C}_0 \mathbf{P}_{\hat{\mathbf{q}}} \hat{\mathbf{q}} \rangle \leq \| \mathbf{C}_0 \| \| \mathbf{P}_H \hat{\mathbf{q}}^\dagger \|_{L^2} \| \mathbf{P}_{\hat{\mathbf{q}}} \hat{\mathbf{q}} \|_{L^2} = \| \mathbf{C}_0 \| \| \mathbf{S}_s(\mathbf{x}_0) \|_F, \quad (4.9)$$

that is, the structural sensitivity tensor is defined as $\mathbf{S}_s(\mathbf{x}_0) \equiv \mathbf{P}_H \hat{\mathbf{q}}^\dagger \otimes \mathbf{P}_{\hat{\mathbf{q}}} \hat{\mathbf{q}}$, whereas the Frobenius norm of the tensor is referred to as structural sensitivity map, and it is defined as $\| \mathbf{S}_s(\mathbf{x}_0) \|_F \equiv \| \mathbf{P}_H \hat{\mathbf{q}}^\dagger \|_{L^2} \| \mathbf{P}_{\hat{\mathbf{q}}} \hat{\mathbf{q}} \|_{L^2}$. The scalar field $\| \mathbf{S}_s(\mathbf{x}_0) \|_F$ is then an upper bound function for the eigenvalue variation, and it can be employed to determine

locations where the feedback is stronger. Therefore, allowing an identification of the regions where the instability mechanism acts. However, when it is not localized within a small physical region, it does not clearly identify the *wavemaker*, but a possible interacting region between the components of the global mode.

Decomposing the mode $\hat{\mathbf{q}}$ we can rewrite the harmonic forcing as $\mathbf{H}(\hat{\mathbf{q}}) = \mathbf{H}(\hat{\mathbf{q}}_{\text{ac}} + \hat{\mathbf{q}}_{\text{hyd}} + \hat{\mathbf{q}}_{\text{s}})$, which due to linearity of the forcing term on the eigenmode is simply expressed as

$$\mathbf{H}(\hat{\mathbf{q}}) = \mathbf{H}(\hat{\mathbf{q}}_{\text{ac}}) + \mathbf{H}(\hat{\mathbf{q}}_{\text{hyd}}) + \mathbf{H}(\hat{\mathbf{q}}_{\text{s}}). \quad (4.10)$$

Thus, we have a first decomposition of the harmonic forcing $\mathbf{H}(\hat{\mathbf{q}})$ from the splitting of the state variable. However, the term $\mathbf{H}(\hat{\mathbf{q}}_{\text{ac}})$ is not necessarily a forcing term that uniquely induces acoustic perturbations. Assume, for simplicity, that the previous forcing term depends uniquely on the acoustic velocity, $\mathbf{H}(\mathbf{u}_{\text{ac}})$, and it only acts on the momentum equation, that is, we neglect mass or heat injection. The forcing term must be rotational-free, i.e., $\nabla \times \mathbf{H}(\mathbf{u}_{\text{ac}}) = 0$, otherwise it will induce vortical perturbations into the flow. Therefore, $\mathbf{H}(\hat{\mathbf{q}}_{\text{ac}})$ should be interpreted as a generic forcing term that depends on the acoustic perturbation. To determine the effect of the forcing, that is, which kind of response induces, we decompose the forcing operator into $\mathbf{H} = \mathbf{H}_{\text{ac}} + \mathbf{H}_{\text{hyd}} + \mathbf{H}_{\text{s}}$ as in section 4.1. Following, this reasoning, we may decompose eq. (4.8),

$$\begin{aligned} \langle \hat{\mathbf{q}}_{\text{ac}}^\dagger, \left(-i\omega\mathbf{B}|_{\mathbf{q}_0} + \mathbf{DF}|_{\mathbf{q}_0} \right) \hat{\mathbf{q}}_{\text{ac}} \rangle \hat{\mathbf{q}}_{\text{ac}} &= \mathbf{H}_{\text{ac}}(\hat{\mathbf{q}}_{\text{ac}}) + \mathbf{H}_{\text{ac}}(\hat{\mathbf{q}}_{\text{hyd}}) + \mathbf{H}_{\text{ac}}(\hat{\mathbf{q}}_{\text{s}}), \\ \langle \hat{\mathbf{q}}_{\text{hyd}}^\dagger, \left(-i\omega\mathbf{B}|_{\mathbf{q}_0} + \mathbf{DF}|_{\mathbf{q}_0} \right) \hat{\mathbf{q}}_{\text{hyd}} \rangle \hat{\mathbf{q}}_{\text{hyd}} &= \mathbf{H}_{\text{hyd}}(\hat{\mathbf{q}}_{\text{ac}}) + \mathbf{H}_{\text{hyd}}(\hat{\mathbf{q}}_{\text{hyd}}) + \mathbf{H}_{\text{hyd}}(\hat{\mathbf{q}}_{\text{s}}), \\ \langle \hat{\mathbf{q}}_{\text{s}}^\dagger, \left(-i\omega\mathbf{B}|_{\mathbf{q}_0} + \mathbf{DF}|_{\mathbf{q}_0} \right) \hat{\mathbf{q}}_{\text{s}} \rangle \hat{\mathbf{q}}_{\text{s}} &= \mathbf{H}_{\text{s}}(\hat{\mathbf{q}}_{\text{ac}}) + \mathbf{H}_{\text{s}}(\hat{\mathbf{q}}_{\text{hyd}}) + \mathbf{H}_{\text{s}}(\hat{\mathbf{q}}_{\text{s}}), \end{aligned} \quad (4.11)$$

where the sum of the previous three equations is equal to eq. (4.8). Enabling the interpretation of the adjoint $\hat{\mathbf{q}}^\dagger$ as a measure of the receptivity with respect to a harmonic forcing. It thus allows us to decompose the adjoint in a similar manner to the way we decomposed the global mode in section 4.1. In this manner, the adjoint variable serves to project the forcing term onto each of the subspaces, with the following decomposed adjoint $\hat{\mathbf{q}}^\dagger = \hat{\mathbf{q}}_{\text{ac}}^\dagger + \hat{\mathbf{q}}_{\text{hyd}}^\dagger + \hat{\mathbf{q}}_{\text{s}}^\dagger$. That is, $\mathbf{H}_{\text{ac}}(\hat{\mathbf{q}}) = \langle \hat{\mathbf{q}}_{\text{ac}}^\dagger, \mathbf{H}(\hat{\mathbf{q}}) \rangle \hat{\mathbf{q}}_{\text{ac}}$, $\mathbf{H}_{\text{hyd}}(\hat{\mathbf{q}}) = \langle \hat{\mathbf{q}}_{\text{hyd}}^\dagger, \mathbf{H}(\hat{\mathbf{q}}) \rangle \hat{\mathbf{q}}_{\text{hyd}}$ and $\mathbf{H}_{\text{s}}(\hat{\mathbf{q}}) = \langle \hat{\mathbf{q}}_{\text{s}}^\dagger, \mathbf{H}(\hat{\mathbf{q}}) \rangle \hat{\mathbf{q}}_{\text{s}}$. From eq. (4.11), we may conclude that with this decomposition of the adjoint mode, the projected harmonic feedback term, e.g., \mathbf{H}_{ac} , only induces a response in the subspace where the feedback term is projected, following this example $\hat{\mathbf{q}}_{\text{ac}}$. Then, we can rewrite eq. (4.11),

$$\begin{aligned} \left(\langle \hat{\mathbf{q}}_{\text{ac}}^\dagger, \left(-i\omega\mathbf{B}|_{\mathbf{q}_0} + \mathbf{DF}|_{\mathbf{q}_0} \right) \hat{\mathbf{q}}_{\text{ac}} \rangle + \langle \hat{\mathbf{q}}_{\text{ac}}^\dagger, \mathbf{H}(\hat{\mathbf{q}}_{\text{ac}}) \rangle + \langle \hat{\mathbf{q}}_{\text{ac}}^\dagger, \mathbf{H}(\hat{\mathbf{q}}_{\text{hyd}}) \rangle + \langle \hat{\mathbf{q}}_{\text{ac}}^\dagger, \mathbf{H}(\hat{\mathbf{q}}_{\text{s}}) \rangle \right) \hat{\mathbf{q}}_{\text{ac}} &= 0 \\ \left(\langle \hat{\mathbf{q}}_{\text{hyd}}^\dagger, \left(-i\omega\mathbf{B}|_{\mathbf{q}_0} + \mathbf{DF}|_{\mathbf{q}_0} \right) \hat{\mathbf{q}}_{\text{hyd}} \rangle + \langle \hat{\mathbf{q}}_{\text{hyd}}^\dagger, \mathbf{H}(\hat{\mathbf{q}}_{\text{ac}}) \rangle + \langle \hat{\mathbf{q}}_{\text{hyd}}^\dagger, \mathbf{H}(\hat{\mathbf{q}}_{\text{hyd}}) \rangle + \langle \hat{\mathbf{q}}_{\text{hyd}}^\dagger, \mathbf{H}(\hat{\mathbf{q}}_{\text{s}}) \rangle \right) \hat{\mathbf{q}}_{\text{hyd}} &= 0 \\ \left(\langle \hat{\mathbf{q}}_{\text{s}}^\dagger, \left(-i\omega\mathbf{B}|_{\mathbf{q}_0} + \mathbf{DF}|_{\mathbf{q}_0} \right) \hat{\mathbf{q}}_{\text{s}} \rangle + \langle \hat{\mathbf{q}}_{\text{s}}^\dagger, \mathbf{H}(\hat{\mathbf{q}}_{\text{ac}}) \rangle + \langle \hat{\mathbf{q}}_{\text{s}}^\dagger, \mathbf{H}(\hat{\mathbf{q}}_{\text{hyd}}) \rangle + \langle \hat{\mathbf{q}}_{\text{s}}^\dagger, \mathbf{H}(\hat{\mathbf{q}}_{\text{s}}) \rangle \right) \hat{\mathbf{q}}_{\text{s}} &= 0, \end{aligned} \quad (4.12)$$

which exemplifies the role of the decomposed adjoint variable to project the structural forcing perturbation onto the corresponding subspace.

A direct inspection of eq. (4.12) suggests the definition of a *localized structural sensitivity* matrix as

$$\begin{aligned} i\delta\omega_j^k &= \langle \hat{\mathbf{q}}_k^\dagger, \delta(\mathbf{x} - \mathbf{x}_0) \mathbf{C}_0 \hat{\mathbf{q}}_j \rangle \leq \| \mathbf{C}_0 \| \| \hat{\mathbf{q}}_k^\dagger(\mathbf{x}_0) \| \| \hat{\mathbf{q}}_j(\mathbf{x}_0) \| = \| \mathbf{C}_0 \| \| \mathbf{S}^{(j,k)}_s(\mathbf{x}_0) \|_F, \\ \mathbf{S}^{(j,k)}_s(\mathbf{x}_0) &= \mathbf{P}_{\mathbf{H}} \hat{\mathbf{q}}_k^\dagger(\mathbf{x}_0) \otimes \mathbf{P}_{\hat{\mathbf{q}}} \hat{\mathbf{q}}_j(\mathbf{x}_0) \text{ with } j, k = \text{ac, hyd, s}, \\ \| \mathbf{S}^{(j,k)}_s(\mathbf{x}_0) \|_F &= \| \mathbf{P}_{\mathbf{H}} \hat{\mathbf{q}}_k^\dagger(\mathbf{x}_0) \| \| \mathbf{P}_{\hat{\mathbf{q}}} \hat{\mathbf{q}}_j(\mathbf{x}_0) \| \text{ with } j, k = \text{ac, hyd, s}. \end{aligned} \quad (4.13)$$

The new *structural sensitivity* provides information about the cross-interaction between vortical and acoustic components of the flow. In the problem of the impinging jet, the feedback loop is initiated by the hydrodynamic instability of the shear layer, which induces an acoustic response. In turn, when acoustic wave impinges on the nozzle lip promotes back the hydrodynamic instability, continuing the loop. With this novel definition, $\mathbf{S}_s^{(hyd,ac)}$ identifies the most sensitive region of the flow to vortical perturbations, inducing an acoustic response. This first region can be named the wavemaker of the hydrodynamic perturbations exciting an acoustic response, which in the case of the impinging jet is expected to be located near the impinging wall and possibly near sharp corners. The second (and third) wavemaker of interest corresponds to the excitation of a hydrodynamic response from hydrodynamic ($\mathbf{S}_s^{(hyd,hyd)}$) or acoustic perturbations ($\mathbf{S}_s^{(ac,hyd)}$). Physically, $\mathbf{S}_s^{(hyd,hyd)}$ determines the hydrodynamic wavemaker, which in a causal reasoning, could be argued to be the region initiating the feedback process. And $\mathbf{S}_s^{(ac,hyd)}$ determines the most sensitive region of the flow to an acoustic perturbation inducing a hydrodynamic excitation, that is, the retro-action of the acoustic wave into the hydrodynamic instability. Additionally, we introduce a further decomposition of the non-local structural sensitivity map to account only for the forcing of the momentum equation for a forcing term that depends uniquely on the velocity field, that is,

$$\begin{aligned} i\delta\omega_j^k &= \langle \hat{\mathbf{u}}_k^\dagger, \delta(\mathbf{x} - \mathbf{x}_0)\mathbf{C}_0\hat{\mathbf{u}}_j \rangle \leq \|\mathbf{C}_0\| \|\hat{\mathbf{u}}_k^\dagger(\mathbf{x}_0)\| \|\hat{\mathbf{u}}_j(\mathbf{x}_0)\| = \|\mathbf{C}_0\| \|\mathbf{S}_{\mathbf{u},s}^{(j,k)}(\mathbf{x}_0)\|_F, \\ \|\mathbf{S}_{\mathbf{u},s}^{(j,k)}(\mathbf{x}_0)\|_F &= \|\hat{\mathbf{u}}_k^\dagger(\mathbf{x}_0)\| \|\hat{\mathbf{u}}_j(\mathbf{x}_0)\| \text{ with } j, k = ac, hyd, s. \end{aligned} \quad (4.14)$$

We are left with the decomposition of the adjoint eigenmode. Herein, we summarise the decomposition, a detailed derivation is left to appendix A.2. We propose the following decomposition for the adjoint velocity field,

$$\begin{aligned} \hat{\mathbf{u}}^\dagger &= \hat{\mathbf{u}}_{hyd}^\dagger + \hat{\mathbf{u}}_{ac}^\dagger = \nabla\phi_c^\dagger + \nabla \times \Psi^\dagger, \\ \Delta\phi_c^\dagger &= \nabla \cdot \hat{\mathbf{u}}^\dagger \text{ in } \Omega \\ \nabla\phi_c^\dagger \cdot \mathbf{n} &= \hat{\mathbf{u}}^\dagger \cdot \mathbf{n} \text{ on } \partial\Omega. \end{aligned} \quad (4.15)$$

From eq. (4.9), we can interpret the adjoint variable as the sensitivity of the eigenvalue/eigenvector variations with respect to a linear harmonic feedback. In this sense, $\hat{\mathbf{u}}_{ac}^\dagger$ corresponds to the sensitivity to vortical-free eigenvector variations with respect to a generic linear harmonic forcing in the momentum equation. Similarly, $\hat{\mathbf{u}}_{hyd}^\dagger$ should be understood as the sensitivity to the dilation-free eigenvector variations with respect to a generic linear harmonic forcing in the momentum equation.

When considering the adjoint variables, we prefer to consider the evolution equation of the entropy fluctuations \hat{s} instead of the energy equation, see appendix A for the introduction of the linearised governing equations in entropy-form. The inclusion of a source term into the entropy equation, for instance a source of heat release, induces a modification of the entropy evolution. By definition, we defined hydrodynamic and acoustic modes to be isentropic (we neglected the effects of viscous dissipation), thus \hat{s}^\dagger projects sources in the entropy equation to sources of entropic nature, i.e., $\hat{s}^\dagger = \hat{s}_s^\dagger$, a trivial decomposition. Instead, source terms in the energy equation may induce modifications of the acoustic and hydrodynamic components of the flow, and its decomposition is more cumbersome. Finally, the decomposition of the adjoint of the continuity equation, $\hat{\rho}^\dagger$, is determined by substituting the previously decomposed adjoint and entropy adjoint fields into the linearised adjoint equations, which is left to appendix A.2. Overall, the adjoint is decomposed

as follows,

$$\begin{aligned}
\hat{\mathbf{u}}^\dagger &= \hat{\mathbf{u}}_{\text{hyd}}^\dagger + \hat{\mathbf{u}}_{\text{ac}}^\dagger = \nabla\phi_c^\dagger + \nabla \times \Psi^\dagger, \text{ from eq. (4.15)} \\
\hat{s}^\dagger &= \hat{s}_s^\dagger \\
\hat{\rho}^\dagger &= \hat{\rho}_{\text{ac}}^\dagger + \hat{\rho}_{\text{hyd}}^\dagger + \hat{\rho}_s^\dagger, \text{ from eq. (A 14)} \\
\hat{p}^\dagger &= \hat{p}_{\text{ac}}^\dagger = \frac{\nabla \cdot \hat{\mathbf{u}}^\dagger}{\gamma M_\infty^2} \\
\hat{T}^\dagger &= \hat{T}_{\text{ac}}^\dagger + \hat{T}_s^\dagger = -\frac{\nabla \cdot \hat{\mathbf{u}}^\dagger}{\gamma M_\infty^2} + \left(\hat{s}^\dagger \mathbf{u}_0 \cdot \nabla s_0 - \frac{\gamma}{\text{Pr Re}} \frac{1}{\rho_0} \Delta s_0 \right)
\end{aligned} \tag{4.16}$$

An important property of the adjoint-direct mode bases is the bi-orthogonality. The pairs of primitive variables $\{0, \hat{\mathbf{u}}, \hat{s}\}; (0, \hat{\mathbf{u}}^\dagger, \hat{s})$ are bi-orthogonal, but that is no longer true when considering the complete primitive variable $\{(\hat{\rho}, \hat{\mathbf{u}}, \hat{s}); (\hat{\rho}^\dagger, \hat{\mathbf{u}}^\dagger, \hat{s})\}$, that is, when considering the continuity equation or the density variable. The set of bases lacks the bi-orthogonality property when mass is injected to the system, which implies the existence of an intrinsic coupling mechanism between the three components of the mode via the continuity equation. Which, in turn, impedes the decomposition of the sources of mass as acoustic, hydrodynamic or entropic. In the following, we will restrict ourselves to sources in the momentum equation, that is, we use eq. (4.14) to analyse the response of the system to body forces. Figure 7 displays two pairs of structural sensitivity pairs. The first, $\mathbf{S}_{\mathbf{u},s}^{(hyd,ac)}$, is the map measuring the eigenvalue drift due to an acoustic response induced by a hydrodynamic perturbation. At large Mach numbers ($M_J \approx 0.9$), fig. 7 (a) shows that $\mathbf{S}_{\mathbf{u},s}^{(hyd,ac)}$ is localised near the nozzle lip and within the jet at an axial location around $z \approx H - D$. The region within the jet is found at the spatial location with the largest production of divergence of the velocity field (cf section 3.2). An acoustic guided jet mode (cf fig. 6) is then responsible for the closure of the feedback-loop. When the Mach number is decreased, the production of divergence of velocity is less effective and the most effective mechanism to close the feedback loop turns out to be a vortex-sound mechanism, that is, the sensitivity map $\mathbf{S}_{\mathbf{u},s}^{(hyd,ac)}$ highlights the region where the linearised Lamb vector is large (cf section 3.2). The feedback loop in this case can be closed via an acoustic pressure wave released from the region where the Lamb vector is of large magnitude and propagated as a spherical wave towards the nozzle of the lip (fig. 8 (a,c)) or from inside the jet (fig. 8 (b,d)). The spatial location of the source of sound of the latter mechanism is robust with respect to modifications in the Mach or Reynolds number, i.e., the jet has a preferential location where divergence is created, and it corresponds to the region within the jet before the jet impinges the wall, cf fig. 4. On the other hand, the vortical acoustic sources along the region with a large amplitude of the linearised Lamb vector are highly sensitive to non-linear effects and to variations in the Reynolds number. The sensitivity to non-linear effects is due to the roll-up of the vortex sheet and the interaction between vortices emitted at distinct stages of the cycle. This region of the flow is dominated by vortical effects, and it becomes rapidly chaotic. From the acoustic standpoint, there exist several acoustic sources at distinct spatial positions capable to close the loop, which in turn would select a slightly different frequency of the cycle. That is, in some sense, the lack of temporal coherence of the vortical region implies a weaker frequency selection criterion. This aspect will be explored in more detail in section 5.

Figure 7 (c-d) displays the complementary sensitivity map $\mathbf{S}_{\mathbf{u},s}^{(ac,hyd)}$, which measures eigenvalue drift due to a hydrodynamic response induced by an acoustic perturbation. Not surprisingly, the impingement of acoustic perturbations onto the nozzle lip is the

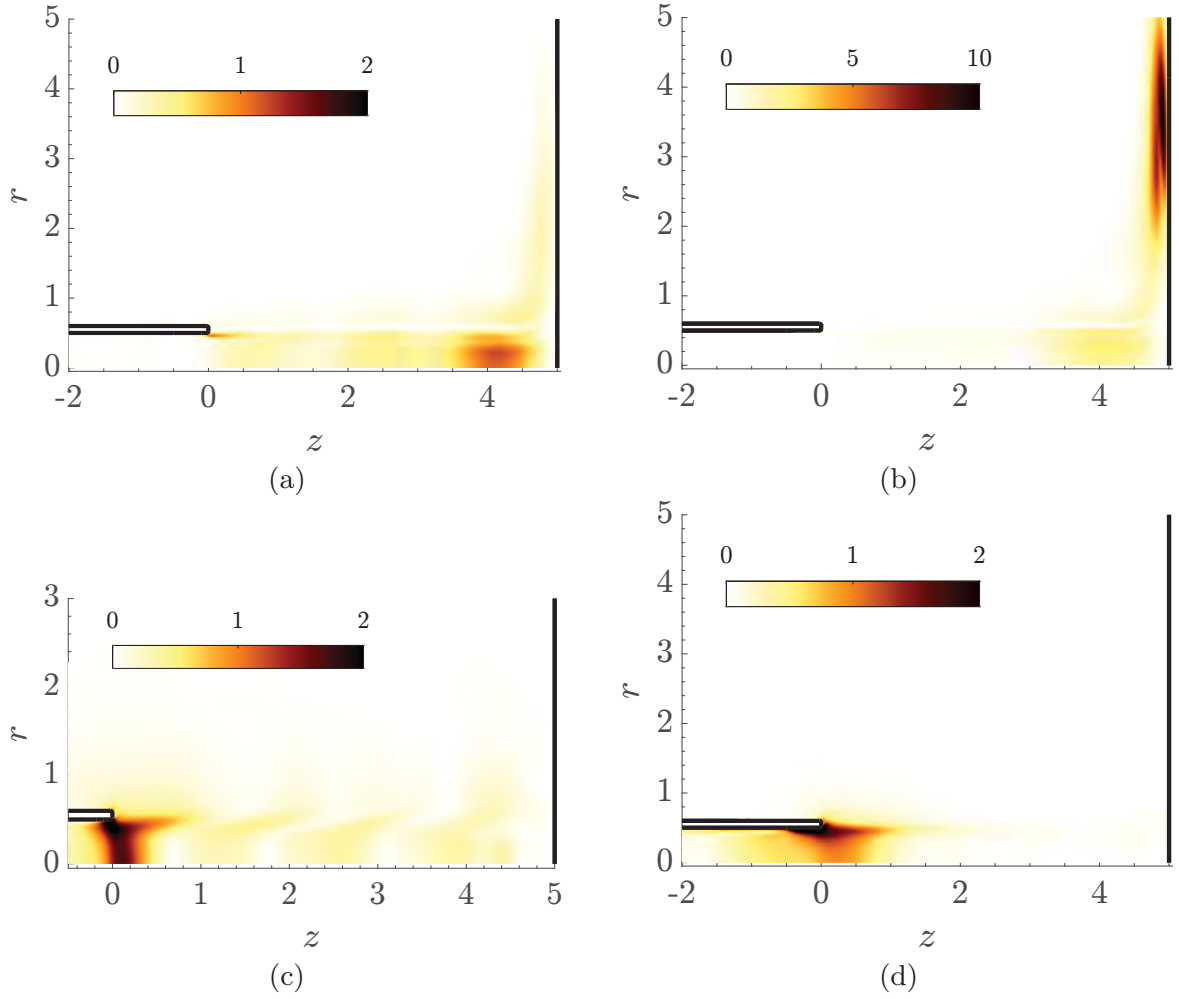


Figure 7: (a-b) Map $\mathbf{S}_{\mathbf{u},s}^{(hyd,ac)}$ for the global mode of points (h) and (e) of fig. 3. (c-d) Map $\mathbf{S}_{\mathbf{u},s}^{(ac,hyd)}$ for the global mode of points (h) and (d) of fig. 3.

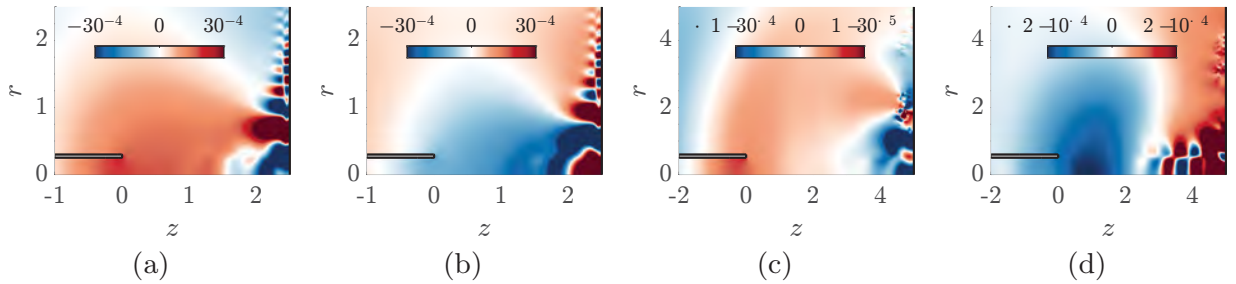


Figure 8: (a,b) Real and imaginary part of the pressure of mode (b) in fig. 3 at $M_\infty = 0.2$. (c,d) Pressure fluctuations issued from an axisymmetric time-stepping simulation at $M_\infty = 0.2$ and $Re = 2200$.

most effect mechanism to trigger the instability of the shear layer, which is mostly of vortical nature. Such a mechanism is largely insensitive to Mach number variations.

4.3. A finer insight to the instability core: An identification of the active flow regions

In previous sections, we have employed the structural sensitivity to identify the most sensitive regions of the flow to cause a drift to the eigenvalue (section 3.2). In addition, our refined *non-local structural sensitivity* allowed us to provide a localised stability core for a non-local instability issued from a feedback loop (section 4.2). In this section, we connect

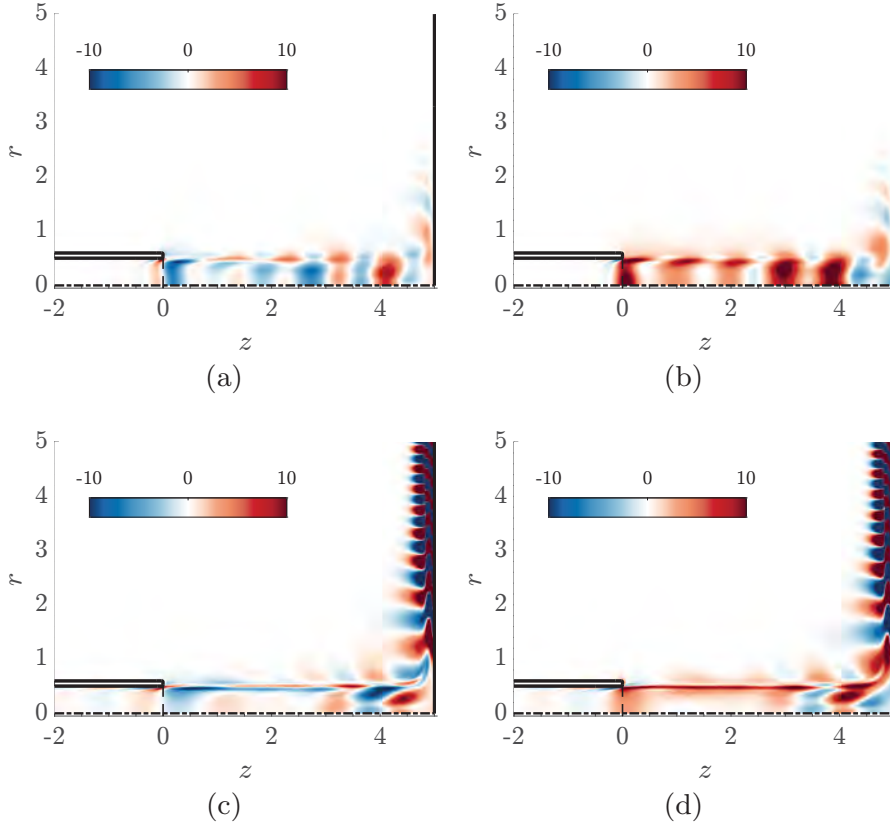


Figure 9: (a-b) Endogeneity field for mode (g) in fig. 3 at $M_\infty = 0.6$; (a) $\text{Re}(E)$, (b) $\text{Im}(E)$. (c-d) Endogeneity field for mode (b) in fig. 3 $M_\infty = 0.2$; (c) $\text{Re}(E)$, (d) $\text{Im}(E)$.

the qualitative description provided in section 3.2 in terms of physical mechanisms with a precise description of the active regions of the flow. For this purpose, we adopt the definition of the *endogeneity* proposed by Marquet & Lesshafft (2015), which yields a direct link between structural modifications in the linearised governing equations and the eigenvalue variations. The endogeneity is introduced as the scalar (complex) field measuring the eigenvalue drift when considering a localised forcing term with the same structure as the Jacobian operator $D\mathbf{F}|_{\mathbf{q}_0}$, that is, $\mathbf{H}(\hat{\mathbf{q}}) = \delta(\mathbf{x} - \mathbf{x}_0)D\mathbf{F}|_{\mathbf{q}_0}\hat{\mathbf{q}}$, which induces the following drift in the eigenvalue,

$$i\delta\omega = \langle \hat{\mathbf{q}}^\dagger, \delta(\mathbf{x} - \mathbf{x}_0)D\mathbf{F}|_{\mathbf{q}_0}\hat{\mathbf{q}} \rangle = \langle \hat{\mathbf{q}}^\dagger(\mathbf{x}_0), D\mathbf{F}|_{\mathbf{q}_0}\hat{\mathbf{q}}(\mathbf{x}_0) \rangle \equiv E(\mathbf{x}_0) \quad (4.17)$$

with the essential property that $\int_\Omega E(\mathbf{x})d\mathbf{x} = -i\omega$. This last property is the most important feature of the endogeneity concept. The scalar field $E(\mathbf{x}_0)$ measures how local variations of the flow alter the global characteristics of the instability, such as growth rate or frequency.

Figure 9 displays the endogeneity fields for the dominant modes at $M_\infty = 0.6$ and $M_\infty = 0.2$, respectively, which corresponds to mode (g) and mode (b) of fig. 3. The imaginary part of the endogeneity for mode (g), displayed in fig. 9 (b), is positive between the nozzle lip and the region where the module of the divergence of velocity of the mode is largest. It also corresponds to the spatial location with the largest positive real part of the endogeneity, shown in fig. 9 (a). Therefore, suggesting that the frequency is selected by the travelling time that the perturbations take to travel back-and-forth. The imaginary part endogeneity of mode (b), shown in fig. 9 (d), is composed of two regions. A region with positive sign along the axial shear layer, and another with larger magnitude and alternating sign along the radial shear layer. It suggests that the frequency is determined

	E_{C_A}	E_{C_P}	E_P
$M_\infty = 0.6$ (g)	$-0.18 + 0.37i$	$0.49 + 1.6i$	$-0.27 + 1.4i$
$M_\infty = 0.2$ (b)	$-1.0 + 2.5i$	$1.17 + 0.79i$	$-0.14 + 0.13i$

Table 1: Decomposition of the integral of the endogeneity field, $\int_\Omega E(\mathbf{x})d\mathbf{x}$, for the dominant mode at $M_\infty = 0.6$ (g) and at $M_\infty = 0.2$ (b) in fig. 3.

by the amount of the time that it takes for the perturbations to be convected downstream towards the wall, but also by the radial position of the acoustical source responsible for the pressure wave closing the feedback-loop. The real part of the endogeneity, shown in fig. 9 (a), has a similar structure to the imaginary part. The axial shear layer plays mostly a passive effect, that is, perturbations are mostly convected downstream towards the impinging wall, which has a net stabilising effect.

The endogeneity provides a further insight into the mechanisms of the instability. Since $\int_\Omega E(\mathbf{x})d\mathbf{x} = -i\omega$, one can decompose the governing equations and analyse the effect that distinct mechanisms have in the instability. For this purpose, we follow a similar decomposition of the linearised compressible Navier–Stokes to the one laid out by Meliga *et al.* (2010) into production (P) and convective terms, where the latter are subdivided into advection-convection (C_A) and production-convection (C_P) terms. The decomposition is as follows,

$$\mathbf{DF}^{(C_A)}|_{\mathbf{q}_0}\hat{\mathbf{q}} \equiv \begin{cases} \mathbf{u}_0 \cdot \nabla \hat{\rho} + \rho_0 \nabla \cdot \hat{\mathbf{u}} \\ \hat{\rho} \mathbf{u}_0 \cdot \nabla \mathbf{u}_0 + \rho_0 \mathbf{u}_0 \cdot \nabla \hat{\mathbf{u}} \\ \rho_0 T_0 \mathbf{u}_0 \cdot \nabla \hat{s} + \hat{\rho} T_0 \mathbf{u}_0 \cdot \nabla s_0 + \rho_0 \hat{T} \mathbf{u}_0 \cdot \nabla s_0 \end{cases} \quad (4.18a)$$

$$\mathbf{DF}^{(C_P)}|_{\mathbf{q}_0}\hat{\mathbf{q}} \equiv \begin{cases} \hat{\rho} \nabla \cdot \mathbf{u}_0 + \hat{\mathbf{u}} \cdot \nabla \rho_0 \\ \rho_0 \hat{\mathbf{u}} \cdot \nabla \mathbf{u}_0 \\ \rho_0 T_0 \hat{\mathbf{u}} \cdot \nabla s_0 \end{cases} \quad (4.18b)$$

$$\mathbf{DF}^{(P)}|_{\mathbf{q}_0}\hat{\mathbf{q}} \equiv \begin{cases} 0 \\ \nabla \hat{p} - \frac{1}{\text{Re}} \nabla \cdot \tau(\hat{\mathbf{u}}) \\ -\gamma(\gamma-1) \frac{M_\infty^2}{\text{Re}} (\tau(\hat{\mathbf{u}}) : \mathbf{D}(\mathbf{u}_0) + \tau(\mathbf{u}_0) : \mathbf{D}(\hat{\mathbf{u}})) - \frac{\gamma}{\text{Pr Re}} \Delta \hat{T} \end{cases} \quad (4.18c)$$

And we define the endogeneity fields for each of the operators,

$$E^{C_A}(\mathbf{x}) \equiv \hat{\mathbf{q}}^\dagger(\mathbf{x}) \cdot \mathbf{DF}^{C_A}|_{\mathbf{q}_0}\hat{\mathbf{q}}(\mathbf{x}) \quad (4.19a)$$

$$E^{C_P}(\mathbf{x}) \equiv \hat{\mathbf{q}}^\dagger(\mathbf{x}) \cdot \mathbf{DF}^{C_P}|_{\mathbf{q}_0}\hat{\mathbf{q}}(\mathbf{x}) \quad (4.19b)$$

$$E^P(\mathbf{x}) \equiv \hat{\mathbf{q}}^\dagger(\mathbf{x}) \cdot \mathbf{DF}^{C_P}|_{\mathbf{q}_0}\hat{\mathbf{q}}(\mathbf{x}) \quad (4.19c)$$

Table 1 reports the global contribution to the instability of the three operators defined in eq. (4.18). For the two modes, the convection-advection and production operators have a global stabilising effect, whereas the convection-production operator plays a global destabilising role. Their spatial distributions (real part) are shown in fig. 10. The convection-production term provides the main root of the growth rate. The largest contribution coming from the base flow shear $\rho_0 \hat{\mathbf{u}} \cdot \nabla \mathbf{u}_0$ term, which is active along the axial shear layer, see fig. 10 (b,e). The convection-advection operator is globally stabilising, however it plays an active role in advecting the perturbation to the instability

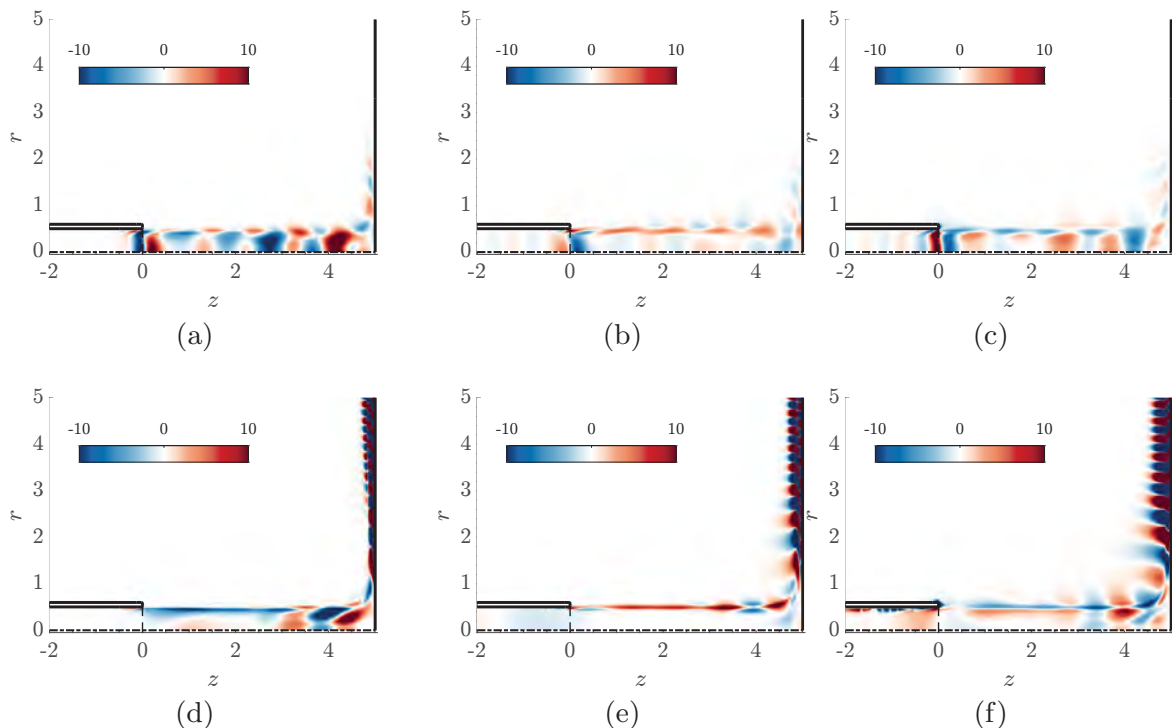


Figure 10: (a-c) Endogeneity field for mode (g) in fig. 3 at $M_\infty = 0.6$; (a) E^{CA} , (b) E^{CP} , (c) E^P . (e-f) Endogeneity field for mode (b) in fig. 3 $M_\infty = 0.2$; (d) E^{CA} , (e) E^{CP} , (f) E^P .

core. Visual inspection of the real part of the E^{CA} field, displayed in fig. 10 (a,d), suggests that at large Mach numbers the acoustic perturbations are propagated along the shear layer to the region of largest divergence of the fluctuating velocity field. On the other hand, at low Mach number, the downstream convection of perturbation counteracts the local growth and makes the instability more convective. Concerning the production terms, at large Mach number, the field, displayed in fig. 10 (c), is positive inside the jet from the nozzle lip to $z \approx H - D$. The effect on the growth rate seems to be associated to the backward propagation of the guided jet mode from the region around $z \approx H - D$ to the nozzle-lip. Instead, at low Mach numbers, the dominant production term is the pressure gradient, which enforces the continuity condition by inducing a perturbation of the volume flux across the shear layer, cf Marquet & Lesshafft (2015). In the region between the nozzle lip and the impinging wall counteracts the effect of the advection operator inside the jet, and it favours the convective effect outside the jet.

Finally, motivated by the significant role played by the divergence of the velocity perturbations in the closure of the feedback-loop at large Mach number, we analyse the effect on the growth rate of local modifications of the divergence of the momentum equation (eq. (3.1)). To do so, we take the inner product of the acoustic velocity adjoint $\hat{\mathbf{u}}_{\text{ac}}^\dagger$ with the momentum equation, which by integration by parts leads to the following definition of E_{div} ,

$$\begin{aligned} i\delta\omega_{\text{div}} &= \langle -\nabla\phi^\dagger, \delta(\mathbf{x} - \mathbf{x}_0)D\mathbf{F}_{(\text{mom})}|_{\mathbf{q}_0}\hat{\mathbf{q}} \rangle \\ &= \langle \phi^\dagger, \delta(\mathbf{x} - \mathbf{x}_0)\nabla \cdot D\mathbf{F}_{(\text{mom})}|_{\mathbf{q}_0}\hat{\mathbf{q}} \rangle + \text{B.T.} \end{aligned} \quad (4.20a)$$

$$E_{\text{div}} \equiv \phi^\dagger(\mathbf{x})(\nabla \cdot D\mathbf{F}_{(\text{mom})}|_{\mathbf{q}_0}\hat{\mathbf{q}})(\mathbf{x}), \quad (4.20b)$$

where it can be shown that the boundary terms (B.T.) are null in the impinging jet

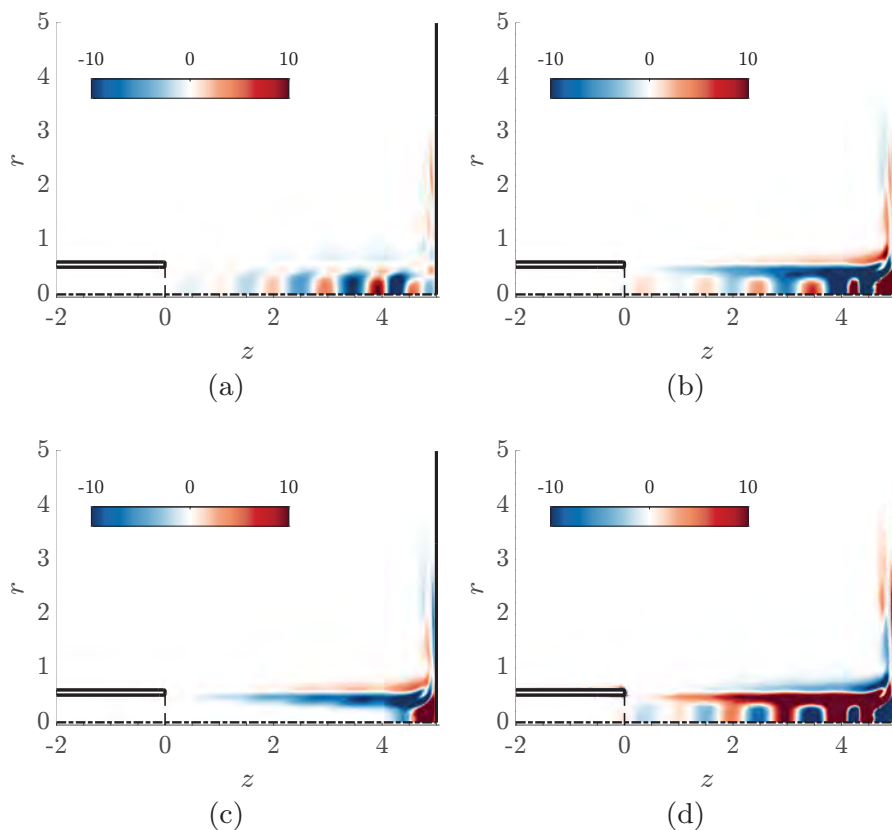


Figure 11: (a) Endogeneity field of the divergence of the momentum equation E_{div} . (b) E_{div}^{CA} . (c) E_{div}^{CP} . (d) E_{div}^P .

configuration. Following the same approach as in eq. (4.19), we can split we split $E_{(\text{div})}$ and analyse the effect of the three aforementioned operators on the growth rate. Such analysis renders possible to study the effect on the growth rate of the physical mechanisms generating and advecting the divergence of the velocity field. Figure 11 (a) displays the real part of the $E_{(\text{div})}$. Not surprisingly, the largest positive contribution comes from the region with the largest divergence of the mode ($z \approx H - D$). The convection production term, displayed in fig. 11 (c), peaks in the region of largest divergence of the baseflow, which suggests a local conversion of divergence from the baseflow to the perturbations. The structure of the convection-advection and production terms is more intriguing. The E_{div}^{CA} and E_{div}^P are almost identical, but of opposite sign, suggesting that the role of the pressure is to counteract the advection of fluctuating divergence. The shear layer, delimits the region inside and outside the jet. Inside the jet, the production of divergence of the fluctuating velocity field has a destabilising effect; instead, the advection of divergence inside the jet renders the instability more convective. The largest growth rate drift by the production of a divergence is observed to happen along thin radial layers inside the jet. The spatial distribution of E_{div}^P composed of cell structures vaguely resembles the shock-cell structure observed in supersonic jets (Edgington-Mitchell *et al.* 2018), where the divergence of the velocity field is produced across the shock cell. Thus, suggesting a connection between the production of divergence and the instability mechanisms between large subsonic and supersonic Mach numbers.

4.4. Wave decomposition of the feedback mechanism

Herein, we perform a weakly non-parallel local decomposition of the different waves supported by the base flow. The configuration under investigation contains in fact

an extended region of quasi-parallel flow, where a simplified analysis can be used to investigate the local stability property of the jet and the supported waves. Specifically, in regions where the flow is almost parallel, we perform a multiple-scale analysis: the disturbance is assumed to have the following asymptotic expansion

$$\mathbf{q}(r, Z) = e^{-i\phi(Z)/\varepsilon} \sum_{n,k} C_k(Z) \mathbf{q}_{n,k}^{(\varepsilon)}(r, Z) \varepsilon^n, \quad (4.21)$$

where the slow variable $Z = \varepsilon z$ is kept $O(1)$ in the limit $\varepsilon \rightarrow 0$. Here the expansion parameter ε is defined as the ratio of the two main length scales occurring in the problem, i.e. $\varepsilon = \frac{\ell_W^*}{\ell_B^*}$ where ℓ_B^* is the characteristic scale over which the base flow experiences an $O(1)$ variation, while ℓ_W^* is the characteristic wavelength of the perturbation. Note that the expansion (4.21) depends on both ε and $\epsilon = 1/Re$ owing to the base flow dependence on the Reynolds number. For our purpose it is not necessary to provide an explicit relation between the two parameters, but it suffices to assume $\varepsilon \sim O(1/Re)$. The validity of the previous assumptions can be verified a posteriori.

In eq. (4.21) we consider the primitive variables $\hat{\mathbf{q}} = [\hat{\rho}, \hat{\mathbf{u}}, \hat{p}, \hat{T}]$, that is, the vector containing the components of the disturbance field. The phase $\phi = -\int(\alpha(Z) + \delta\alpha(Z))dZ$ is a slowly-varying function of Z to be determined during the asymptotic procedure. The slow varying amplitude $C_k(Z)$ should be interpreted as the projection of the global mode onto the local waves supported by the baseflow, and it is also determined using the asymptotic procedure. Introducing eq. (4.21) into the linearised system, up to $O(\varepsilon)$, and collecting different powers of ε , we are left with the following series of problems describing the evolution of the perturbation,

$O(\varepsilon^0)$

$$(-i\omega\mathbf{B}|_{\mathbf{q}_0} + D\mathbf{F}(\alpha)|_{\mathbf{q}_0})\mathbf{q}_{0,k}^{(\varepsilon)}(r, Z) = \mathbf{0} \quad (4.22a)$$

$$u_0, v_0, p_0 \rightarrow 0 \quad \text{as } r \rightarrow \infty \quad (4.22b)$$

$$u_0 = v_0 = 0 \quad \text{at } r = 0 \quad (4.22c)$$

$O(\varepsilon^1)$

$$(-i\omega\mathbf{B} + D\mathbf{F}(\alpha))\mathbf{q}_{1,k}^{(\varepsilon)}(r, Z) = i\frac{d}{d\alpha}(-i\omega\mathbf{B} + D\mathbf{F}(\alpha))\frac{d\mathbf{q}_{0,k}^{(\varepsilon)}}{dZ} \quad (4.23a)$$

$$u_1, v_1, p_1 \rightarrow 0 \quad \text{as } r \rightarrow \infty \quad (4.23b)$$

$$u_1 = v_1 = 0 \quad \text{at } r = 0. \quad (4.23c)$$

At $O(\varepsilon^0)$ the problem is linear, and we determine the pair $(\alpha(Z), \mathbf{q}_{0,k}^{(\varepsilon)}(r, Z))$ from the resolution of the eigenvalue problem eq. (4.22). At the next order, $O(\varepsilon^1)$, the problem has a forcing secular term, which needs to be removed by imposing the solvability condition. The solvability condition provides the weakly-non-parallel correction of the phase, herein named $\delta\alpha(Z)$, and defined as

$$\delta\alpha = \frac{\mathbf{q}_{0,k}^{\dagger,(\varepsilon)} \cdot \left[\frac{d}{d\alpha}(-i\omega\mathbf{B} + D\mathbf{F}(\alpha))\frac{d\mathbf{q}_{0,k}^{(\varepsilon)}}{dZ} \right]}{\mathbf{q}_{0,k}^{\dagger,(\varepsilon)} \cdot \left[\frac{d}{d\alpha}(-i\omega\mathbf{B} + D\mathbf{F}(\alpha))\mathbf{q}_{0,k}^{(\varepsilon)} \right]}. \quad (4.24)$$

In the previous expression, $\mathbf{q}_{0,k}^{\dagger,(\varepsilon)}$ is the adjoint solution of the linear problem eq. (4.22). Finally, we determine the projection of the global mode onto the k^{th} local wave. We use

the local adjoint solution of the k^{th} wave to determine the slowly varying amplitude,

$$C_k(Z) = \mathbf{q}_{0,k}^{\dagger,(\epsilon)} \cdot \left[\frac{d}{d\alpha} (-i\omega \mathbf{B} + D\mathbf{F}(\alpha)) \hat{\mathbf{q}}(r, z) \right] e^{-i \int \alpha_k + \delta \alpha_k dZ}, \quad (4.25)$$

with $\hat{\mathbf{q}}(r, z)$ the global mode.

Figure 12 (a) displays the spectrum of the linear spatial stability problem eq. (4.22) for a baseflow at $Re = 800$ and $M_\infty = 0.6$ (Mode (g) in fig. 3) at the mid-point between the nozzle lip and the impinging wall ($z = 2.5D$). The spectrum displays a set of modes along the axis, which belong to the continuous branches α^+ and α^- of free-stream acoustic modes (Towne *et al.* 2017). Another set of modes emerge from the right end of the spectrum for $\text{Im}(\alpha) > 0$, these modes approximate the entropy continuous branch. There are also four discrete modes. Two duct modes, named D^\pm with the upper script indicating the direction of propagation. The radial support of these two modes lies inside the jet. There is a guided jet mode, which is found at the left of the free-stream continuous branch, that is, it possesses a slower phase speed than the free-stream sound speed. The radial support inside the jet of the pressure component is similar to the duct modes, but it also possesses a radial support outside the jet. There is also a Kelvin-Helmholtz or shear layer mode, with a radial support around the shear layer of the baseflow.

The projection coefficient (C_k) of the global mode onto the duct modes is nearly null. Hereafter, we consider that the global mode is composed only of the shear layer mode (mode 1) and the guided jet wave mode (mode 2), that is, we truncate the sum in eq. (4.21) to just two modes. The global mode and the local waves are normalised with the energy of the fluctuations (Chu 1965). From this assumption, at neutrality, one can recover the reflection coefficient by considering the ratio between the two waves, here we define the reflection coefficient as $r = \frac{C_2(Z_m)}{C_1(Z_m)}$, with $Z_m = H/2$ the mid-point between the impinging wall and the nozzle lip. In the central region, the two slowly varying amplitudes are nearly constant (not shown), which justifies its usage to determine the local properties of the waves. Figure 12 (b) shows the evolution of the two projection coefficients of the local waves onto the global mode. The coefficient of the shear layer mode C_1 is nearly constant and equal to unity. Thus, the evolution of C_2 with respect to the Mach number of the jet provides a direct characterisation of the reflection coefficient. The coefficient of the guided jet mode is $O(10^{-1})$ at large Mach numbers, it evolves roughly as M_J^6 in the interval $(M_{J,c}, 0.9)$, and then it decreases as M_J^2 in the interval $(0, M_{J,c})$, with $M_{J,c} \approx 0.4$. The transition in the reflection coefficient dependency with the Mach number of the jet is another consequence of the modification of the instability mechanism, from the closure of the feedback loop by propagation of the divergence of velocity created within the jet to the closure of the loop by vortical acoustic sources outside the jet near the wall.

5. Nonlinear dynamics of the impinging jet

Herein, we study the dynamics of the normal form involving three global modes, which is the simplest equation displaying tonal dynamics, that is periodic or quasiperiodic resonant solutions, and the decoupling of the resonant mode. We also compare the numerical results obtained from axisymmetric time-stepping simulations at different M_∞ for fixed $Re = 2000$. In addition, we propose a phenomenological model to account for the transition to broadband dynamics using a simple model of additive Gaussian noise on the resonant phase.

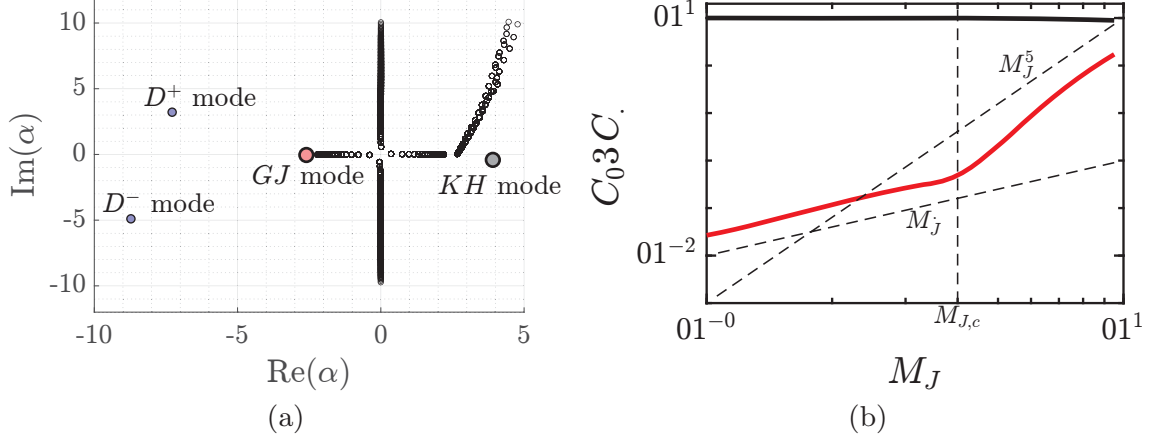


Figure 12: (a) Spectrum of the linear spatial stability problem eq. (4.22) for a baseflow at $Re = 800$ and $M_\infty = 0.6$ (Mode (g) in fig. 3) at the mid-point between the nozzle lip and the impinging wall ($z = 2.5D$). (b) Evolution of the projection coefficients C_1 (Kelvin-Helmholtz mode) and C_2 (Guided-Jet mode) with respect to the Mach number of the jet (M_J).

5.1. Modelling of the non-linear dynamics – Normal form reduction

First, we express eq. (B 20) of section 2.4 in the polar coordinates of the complex amplitudes $z_k(\tau) = r_k(\tau)e^{i\phi_k(\tau)}$. This procedure allow us to reduce the dimension of the normal form from six (three complex amplitudes) to four, three equations for the real amplitudes and an equation for a resonant phase $\psi = (\phi_3 - \phi_2) - (\phi_2 - \phi_1)$,

$$\begin{aligned}
 \dot{r}_1 &= r_1 \left[\lambda_1^R + \nu_{11}^R r_1^2 + \nu_{12}^R r_2^2 + \nu_{13}^R r_3^2 \right] + r_2^2 r_3 \left[\cos(\psi) \chi_1^R + \sin(\psi) \chi_1^I \right] \\
 \dot{r}_2 &= r_2 \left[\lambda_2^R + \nu_{21}^R r_1^2 + \nu_{22}^R r_2^2 + \nu_{23}^R r_3^2 \right] + r_1 r_2 r_3 \left[\cos(\psi) \chi_2^R - \sin(\psi) \chi_2^I \right] \\
 \dot{r}_3 &= r_3 \left[\lambda_3^R + \nu_{31}^R r_1^2 + \nu_{32}^R r_2^2 + \nu_{33}^R r_3^2 \right] + r_2^2 r_1 \left[\cos(\psi) \chi_3^R + \sin(\psi) \chi_3^I \right] \\
 \dot{\psi} &= \delta\omega + \cos(\psi) \left[-\chi_3^I r_1 r_2^2 / r_3 + 2\chi_2^I r_1 r_3 - \chi_1^I r_3 r_2^2 / r_1 \right] \\
 &\quad - \sin(\psi) \left[\chi_3^R r_1 r_2^2 / r_3 + 2\chi_2^R r_1 r_3 + \chi_1^R r_2^2 r_3 / r_1 \right].
 \end{aligned} \tag{5.1}$$

Here, we use the notation $\delta\omega \equiv \delta\omega^L + \delta\omega^{NL}$ with $\delta\omega^L \equiv [\omega_1 + \omega_3 - 2\omega_2]$ the linear frequency mismatch at criticality, and the nonlinear frequency mismatch $\delta\omega^{NL} \equiv \Delta\omega_2^{NL} - \Delta\omega_1^{NL} = [\omega_1^{NL} + \omega_3^{NL} - 2\omega_2^{NL}]$, where $\omega_k^{NL} = \lambda_k^I + \nu_{k1}^I r_1^2 + \nu_{k2}^I r_2^2 + \nu_{k3}^I r_3^2$ for $k = 1, 2, 3$. The upper scripts R and I are used to denote the real and imaginary part of the coefficient.

We analyse the solutions of eq. (5.1) in two steps, first we summarise the results of the non-resonant case ($\chi_1 = \chi_2 = \chi_3 = 0$), which was studied more in detail for the case of the mode interaction in the wake flow behind a rotating sphere (Sierra-Ausin *et al.* 2022). Subsequently, we discuss, in the presence of resonant coupling, the phase-locked transition from a resonant quasiperiodic state to a modulated three frequency state with a small frequency modulation. The new modulating frequency, being proportional to the imperfections in the frequency quantization ($\delta\omega^{NL}$), is expected to induce a transition to a chaotic attractor, following the route to chaos suggested by Ruelle–Takens–Newhouse, when this new frequency is of the order of the frequency difference between two modes, e.g., $\Delta\omega_1^{NL}$.

5.1.1. Stochastic modelling

Ruelle–Takens–Newhouse (Newhouse *et al.* 1978) state that one may obtain a chaotic Axiom A attractor by perturbing a three-tori solution, with a given arbitrarily small

perturbation. However, it fails to provide the precise route to chaos, which may occur following a torus breakdown (Tanaka 2005), which occurs because of the loss of smoothness of the two or three tori attractors (Marques *et al.* 2001). In order to account for the loss of smoothness of the system, we replace

$$\delta\omega^{NL} \mapsto \delta\omega^{NL}(1 + dW),$$

with dW a differential Wiener process and $\delta\omega^{NL}$ determined from the deterministic normal form. This phenomenological modelling is based on the fact that the sources of sound responsible for the closure of the feedback become less coherent with decreasing Mach number (see section 4). Such a modelling is faithful with the deterministic normal form eq. (5.1) in the mean sense, that is, $\mathbb{E}(\delta\omega^{NL}(1 + dW)) = \delta\omega^{NL}$. At low subsonic Mach number, the increase of $\delta\omega^{NL}$ is caused by the elongated nature of the wavemaker, which enables the existence of sources of vortex sound at distinct spatial locations. Each of these sources it is associated with a distinct fundamental frequency $\Delta\omega$, which is inversely proportional to the convective time it takes for the hydrodynamic perturbations to reach the source of vortex sound at the wavemaker and to the acoustic time it takes for the perturbation to reach back to the lip of the nozzle. Therefore, providing a phenomenological interpretation to the increase of the modulation frequency with a decreasing Mach number. Thus, the transition to a broadband spectrum can be interpreted as the consequence of the loss of coherence of the feedback process and the fact that the levels of the sound acoustic pressure decrease with decreasing Mach number. The latter effect is attributed to the fact that with decreasing Mach number, the production of the divergence of velocity field is reduced, which occurs mostly within the jet and near the wall. Additionally, the propagation of the guided jet wave becomes less effective with decreasing Mach number, because of the increase of its wavelength. This phenomenon can be appreciated in fig. 7, where the structural sensitivity to the acoustic response of the system from hydrodynamic perturbations is displaced from a spatial location within the jet to an elongated region near the wall outside the jet.

5.1.2. Properties of the deterministic normal form

In the absence of a coupling between the real amplitudes r_k and the resonant phase ψ , i.e. $\chi_1 = \chi_2 = \chi_3 = 0$, we have that $\psi = (\omega_2^{NL} - \omega_1^{NL})t - (\omega_3^{NL} - \omega_2^{NL})t$, which is generally non-zero. In this case, eq. (5.1) is simplified to

$$\begin{aligned} \dot{r}_\ell &= r_\ell \left[\Lambda_\ell^R + \mathcal{V}_{\ell k}^R r_k^2 \right], & k, \ell = 1, 2, 3, \\ \dot{\phi}_\ell &= \Lambda_\ell^I + \mathcal{V}_{\ell k}^I r_k^2, & k, \ell = 1, 2, 3, \end{aligned} \quad (5.2)$$

where $\Lambda = \Lambda^R + \Lambda^I \equiv (\lambda_1, \lambda_2, \lambda_3)^T$ and the matrix $\mathcal{V} = \mathcal{V}^R + i\mathcal{V}^I$ is

$$\mathcal{V} \equiv \begin{pmatrix} \nu_{11} & \nu_{12} & \nu_{13} \\ \nu_{21} & \nu_{22} & \nu_{23} \\ \nu_{31} & \nu_{32} & \nu_{33} \end{pmatrix} \quad (5.3)$$

To ease the presentation of the fixed point solutions of eq. (5.2), let us introduce the inverse of the linear operator \mathcal{V} , which can be written as

$$\mathcal{V}^{-1} = \frac{1}{\det \mathcal{V}} \begin{pmatrix} \det \mathcal{V}_{11} & \det \mathcal{V}_{21} & \det \mathcal{V}_{31} \\ \det \mathcal{V}_{12} & \det \mathcal{V}_{22} & \det \mathcal{V}_{32} \\ \det \mathcal{V}_{13} & \det \mathcal{V}_{23} & \det \mathcal{V}_{33} \end{pmatrix}, \quad (5.4)$$

where $\det \mathcal{V}_{k\ell}$ denotes the minor of the matrix \mathcal{V} , obtained by eliminating the line k and the column ℓ .

Name	Representative	Frequencies
TS (Trivial state)	(0, 0, 0, n.d.)	0
PW (Periodic Wave mode)	($r_a, 0, 0, \text{n.d.}$)	1
MW (Mixed Wave mode)	($r_a, r_b, 0, \text{n.d.}$)	2
3FW (Three Frequency Wave mode)	($r_a, r_b, r_c, \text{n.d.}$)	3
MrW (Mixed resonant Wave mode)	(r_a, r_b, r_c, ψ_d)	2

Table 2: Nomenclature of fixed point solutions of the system eq. (5.1). The MW and the 3FW correspond to the case of non-resonant coupling $\chi_1 = \chi_2 = \chi_3 = 0$.

Name of solutions	Definition	Eigenvalues
PW_i (for $i = 1, 2, 3$)	$r_i^{(PW)} = \sqrt{-\frac{\lambda_i^R}{\nu_{ii}^R}}$	$-\lambda_i^R,$ $\lambda_j^R - \nu_{ji}^R \frac{\lambda_i^R}{\nu_{ii}^R},$ for $j \neq i$
$MW_{ij}, (i, j = 1, 2, 3)$ $(j \neq i, k \neq i, k \neq j)$	$r_i^{(MW_{ij})} = \sqrt{\frac{\lambda_j^R \nu_{ij}^R - \lambda_i^R \nu_{jj}^R}{\det(\mathcal{V}_{kk}^R)}}$ $r_j^{(MW_{ij})} = \sqrt{\frac{\lambda_i^R \nu_{ji}^R - \lambda_j^R \nu_{ii}^R}{\det(\mathcal{V}_{kk}^R)}}$	$\frac{\nu_{ii}^R r_i^2 + \nu_{jj}^R r_j^2}{2} \pm \sqrt{(\nu_{ii}^R r_i^2 - \nu_{jj}^R r_j^2)^2 / 4 + \nu_{ij}^R \nu_{ji}^R r_i^2 r_j^2}$ $\frac{1}{\det(\mathcal{V}_{kk}^R)} \left[\lambda_k^R \det(\mathcal{V}_{kk}^R) + \lambda_i^R \det(\mathcal{V}_{ik}^R) + \lambda_j^R \det(\mathcal{V}_{jk}^R) \right]$
$3FW_{123}$	$(r_1^2, r_2^2, r_3^2)^T = -(\mathcal{V}^R)^{-1} \Lambda^R$	Eigs of $D\mathbf{f}^R$

Table 3: Defining equations and eigenvalues of the solutions of the polar third order normal form eq. (5.1) in the case of non-resonant coupling $\chi_1 = \chi_2 = \chi_3 = 0$. $D\mathbf{f}^R$ denotes the Jacobian matrix of the polar amplitudes of eq. (5.2).

This equation has four types of solutions, listed in table 2 with their respective nomenclature and number of independent frequencies. The definition of the solutions and their linear stability is enumerated in table 3. The two solutions of interest for us are the PW and the MW, which are representative of *tonal* dynamics.

Now, we turn our attention to the resonant case. In particular, we focus on the dynamics of a resonant MW state, which is a quasiperiodic state and the amplitudes r_1 and r_2 determined as in table 3, with a constant resonant amplitude r_3 and locked phase ψ . This new state, referred to as Mixed resonant Wave (MrW) still possesses two incommensurate frequencies, with the third mode resonant to the other two. A definition of this resonant solution may be found in table 4. The MrW branch may display a Hopf bifurcation, which, in the case of $r_3 \ll r_1, r_2$, can be analysed by simply studying the two-by-two sub-block of the Jacobian matrix of eq. (5.1). The MrW₁₂ branch loses stability in a Hopf bifurcation with a modulation frequency $\omega' \propto \delta\omega^{NL}$, see the last column of table 4. It occurs when the attracting eigenvalue in the r_3 -direction is smaller than $-\sigma_{MW_{12}} \leq \frac{\chi_3^I}{\chi_3^R} \delta\omega$. The right-hand side of the inequality can be interpreted as the effective frequency mismatch $\delta\omega^{\text{eff}} \equiv \frac{\chi_3^I}{\chi_3^R} \delta\omega$ induced by the coupling coefficients. The Modulated Mixed drift Wave (MMdW) is susceptible to be observed as a chaotic attractor when studying the Navier-

Name of solutions	Definition	Stability
MrW ₁₂	$\tan(\psi) = -\frac{\chi_3^R \delta\omega + \sigma_{MW_{12}} \chi_3^I}{\chi_3^I \delta\omega + \sigma_{MW_{12}} \chi_3^R}$ $r_3 = \frac{(\chi_3^R)^2 - (\chi_3^I)^2}{\chi_3^R \delta\omega + \sigma_{MW_{12}} \chi_3^I} r_2^2 r_1 \sin(\psi)$	$\frac{2\chi_3^R (\delta\omega \chi_3^I + \chi_3^R \sigma_{MW_{12}})}{(\chi_3^R)^2 - (\chi_3^I)^2} > 0$ $\omega' = \left \frac{\delta\omega}{\chi_3^R} \left((\chi_3^R)^2 - (\chi_3^I)^2 \right)^{1/2} \right $

Table 4: Defining equations and eigenvalues of the Mixed resonant wave of eq. (5.1) in the case of resonant coupling. The amplitudes r_1 and r_2 are defined in table 3, since they are the same as for the MW_{12} . The eigenvalue $\sigma_{MW_{12}} = \frac{1}{\det(\mathcal{V}_{33}^R)} \left[\lambda_3^R \det(\mathcal{V}_{33}^R) + \lambda_1^R \det(\mathcal{V}_{13}^R) + \lambda_2^R \det(\mathcal{V}_{23}^R) \right]$ is the eigenvalue of the MW in the direction of r_3 . ω' is defined critically, that is, when $\sigma_{MW_{12}} = \frac{\chi_3^I}{\chi_3^R} \delta\omega$.

Stokes equations. However, it is possible to observe this new three-frequency state as a non-chaotic attractor when the modulation frequency is much smaller than the other two frequencies $\omega' \ll \omega_1, \omega_2$, which occurs if $\delta\omega \ll 1$. Similarly, in the actual dynamics of the Navier–Stokes equation, a chaotic attractor is likely to shadow the MMdW state, which is expected to occur when the third amplitude (r_3) is sufficiently large. Therefore, in this sense, we cannot provide a sharp cut-off for the transition of broadband (chaotic) - tonal dynamics, but we provide a qualitative description of the transition in the simplest case with resonance between the modes of the spectrum. In the following sections, we provide a comparison of the deterministic and stochastic normal forms with direct numerical simulations of the axisymmetric impinging jet.

5.2. Normal form – Results

5.2.1. Small subsonic Mach number – An example of broadband noise

At low Mach numbers, a broadband spectrum characterizes the dynamical attractor (obtained from axisymmetric numerical simulations, section 2.3), which is displayed in fig. 13 (b) with red, blue and black solid lines for pressure probes at an axial location $z = 0$ and a radial position $r = 1D$, $r = 2D$ and $r = 4D$, respectively. This type of dynamics is *modelled* by a periodic solution (MMdM) of the normal form eq. (5.1), which is a three-tori solution in the original coordinates of the ansatz eq. (2.11). The MMdM solution emerges almost directly from of the PW₂ branch (fig. 13 (a)), that is, the MrW₁₃ is unstable (not shown). The Modulated Mixed drift Wave possesses a modulation frequency $\omega' \approx \Delta\omega$, that is, the modulation frequency has a similar magnitude to the frequency difference between the other two dominant frequencies. In that scenario, the original dynamics of the Navier–Stokes equations are expected to be chaotic with a broadband spectrum. However, fig. 13 shows a tonal spectrum (yellow line), which has been obtained from the deterministic normal form. Such a feature is characteristic of this particular type of normal form, and it is a pathological property of the truncation. Instead, when considering the stochastic model with $\delta\omega \approx 0.1$, one obtains a spectrum (green line) which offers a considerably better comparison with respect to the data of the axisymmetric simulation. In this case, the spectrum displays a wide peak of small magnitude around f_1 and f_2 , and a broadband spectrum with a similar slope to the numerical results (red line). Though the matching is not perfect, the ratio between the peak and the broadband levels is slightly larger in the deterministic model, which

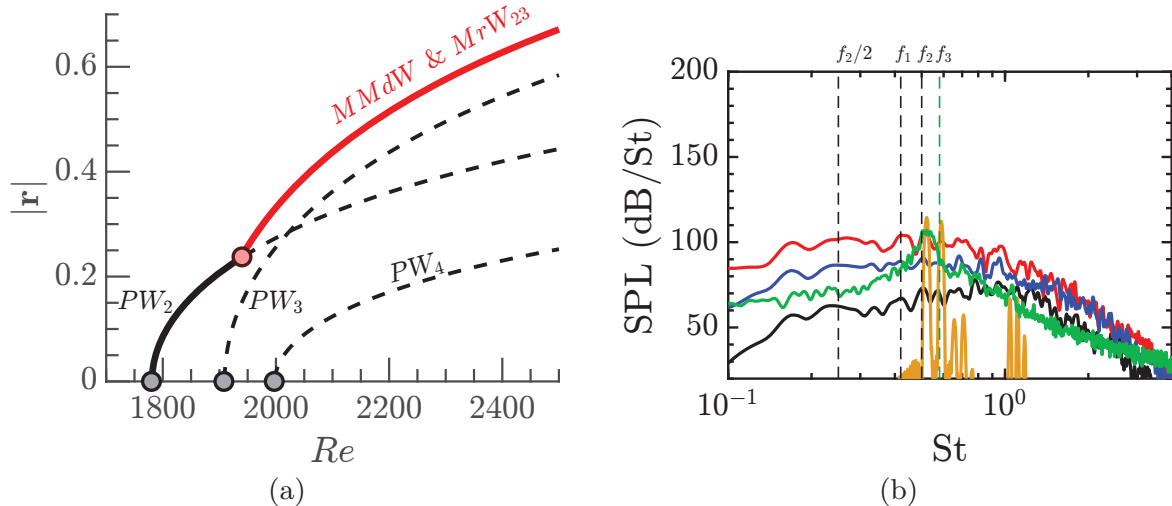


Figure 13: (a) Bifurcation diagram at $M_\infty = 0.3$ with respect to the Reynolds number with $|\mathbf{r}| = \sqrt{r_1^2 + r_2^2 + r_3^2}$. Solid lines indicate stable attractors, dashed lines indicate unstable fixed points of eq. (5.1). (b) Sound pressure levels at $Re = 2000$. Probes of instantaneous pressure fluctuations at the axial location $z = 0$ and radial positions $r = 1D$ (red - axisymmetric time-stepping, yellow - deterministic normal form, green stochastic normal form with $\delta\omega = 0.1$), $r = 2D$ (black - axisymmetric time-stepping) and $r = 4D$ (dark blue - axisymmetric time-stepping). The vertical dashed lines highlight the frequencies of the peaks obtained with the axisymmetric time-stepping simulation.

suggests a higher degree of stochasticity of the axisymmetric numerical simulation. The difference may be explained from the fact that the axisymmetric numerical simulations allow for a vortical feedback, vortices emitted by the roll-up of the radial shear layer near the wall and outside the jet are propagated towards the lip. These vortices are produced aperiodically in a chaotic region of the flow, thus reducing the coherence of the spectrum when they induce a hydrodynamic instability near the lip of the nozzle. Such a feature is strongly nonlinear, and it is not accounted by the normal form. A possible correction to the stochastic model would consist in the inclusion of a diffusion coefficient $\sqrt{D_{\text{eff}}}$ in $\delta\omega(1 + \sqrt{D_{\text{eff}}}dW)$, and thus determine the effective diffusion from the fitting of numerical or experimental data (Callahan *et al.* 2021).

5.2.2. Large subsonic Mach number – An example of weakly resonant tones

At large Mach numbers, the dynamical attractor is characterized by a tonal spectrum with large peaks at discrete frequencies. This type of dynamics is *modelled* by a fixed-point (MrW) or a periodic solution (MMdW) of the normal form eq. (5.1). Figure 14 (a) shows the bifurcation diagram obtained with the deterministic normal form. The mode-switching point reported in section 3 was located at $M_\infty^A \approx 0.49$. For larger values of M_∞ the PW_3 branch emerges from the primary bifurcation as a stable solution, and the PW_2 branch subsequently bifurcates. The PW_2 branch is unstable near the onset of instability, and it is restabilised following a subcritical bifurcation of the MrW_{23} branch. Figure 14 (a) shows the existence of regions with multiple stable attractors (PW_2 and PW_3 , and MW_{13} and $MMdW$), a feature that was also observed in the experimental campaign of Nosseir & Ho (1982) at large Mach numbers of the jet. Specifically, the $MMdW$ coexists with a stable non-resonant quasiperiodic solution (MW_{13}). The MW_{13} state becomes unstable via a symmetry breaking bifurcation to a MrW_{13} . The MrW_{13} branch experiences a saddle-node bifurcation and it folds onto itself to finally reconnect to the MW_{13} branch again. Because of the saddle-node bifurcation in the MrW_{13} branch,

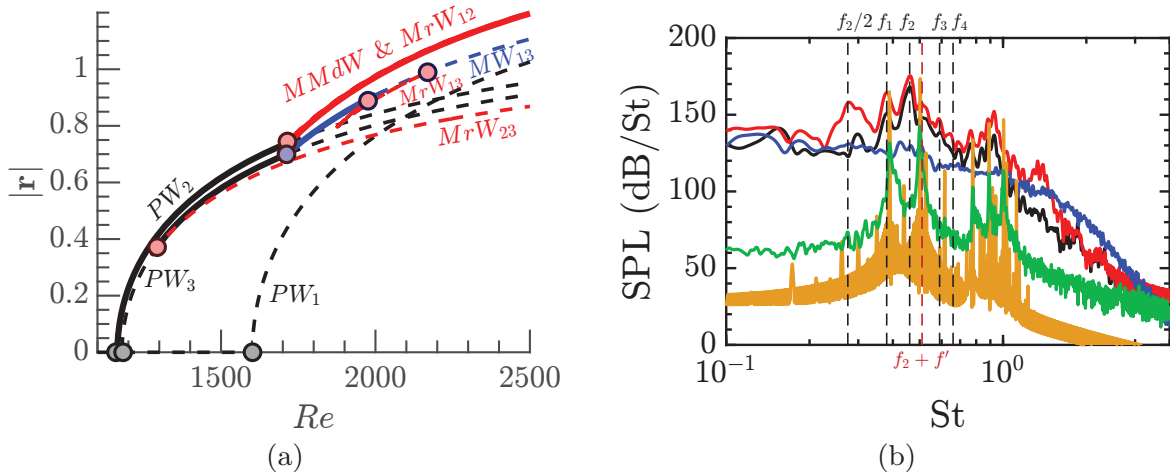


Figure 14: (a) Bifurcation diagram at $M_\infty = 0.5$ with respect to the Reynolds number with $|\mathbf{r}| = \sqrt{r_1^2 + r_2^2 + r_3^2}$. Solid lines indicate stable attractors, dashed lines indicate unstable fixed points of eq. (5.1). (b) Sound pressure levels at $Re = 2000$. Probes of instantaneous pressure fluctuations at the axial location $z = 0$ and radial positions $r = 1D$ (red - axisymmetric time-stepping, yellow - deterministic normal form, green stochastic normal form with $\delta\omega \approx 0.04$), $r = 2D$ (black - axisymmetric time-stepping) and $r = 4D$ (dark blue - axisymmetric time-stepping). The vertical dashed lines highlight the frequencies of the peaks obtained with the axisymmetric time-stepping simulation.

after the second re-connection, the MW_{13} branch continues to be unstable. In addition, even when the MW_{13} branch is stable, its basin of attraction is considerably smaller than the one of the $MMdW$ state, and it shrinks with increasing Reynolds number. That is, in the interval of coexistence of the two branches, most of initial conditions are attracted to the $MMdW$ state. In the following, we simply consider the case at $Re = 2000$ of the $MMdW$ state. In this case, the modulation frequency of the Modulated Mixed resonant Wave is smaller than the frequency difference between the modes ($\omega' \ll \Delta\omega$). In that scenario, the spectrum of the Navier–Stokes equations is expected to be weakly tonal with wide and large magnitude peaks. In this case, the deterministic normal form offers a good qualitative description of the spectrum, it is able to identify the main frequency peaks and the frequency modulation f' . The frequency modulation obtained from numerical simulations is $f'_{DNS} \approx 0.05$, while the frequency modulation from the normal form is $f' \approx 0.04$. Additionally, as in the broadband case, we compare in fig. 14 the results of the axisymmetric numerical simulation (red line) with those of the deterministic normal form (yellow line) and the stochastic model (green line). It shows a reasonable comparison, though the sound pressure levels are underestimated, between the spectrum of the Navier–Stokes equations and the one from the stochastic model. However, since the model is weakly nonlinear, it fails to predict the existence of a peak at $f_2/2$, which occurs because of a secondary instability of the radial shear layer. Inspection of the numerical results suggests that such a frequency peak occurs because of a vortex-pairing instability of the radial shear layer (Shaabani-Ardali *et al.* 2019).

6. Discussion & Conclusion

The dynamics of the hydrodynamic-acoustic feedback instability of a rounded laminar subsonic impinging jet configuration has been analysed. First, it has been shown the existence for every Mach number of a family of unstable modes, which are characterised by their axial wavenumber. It has been discussed the nature of the instability in terms of

the structural sensitivity and later by the complex-valued endogeneity map. It has been argued that the guided jet wave is responsible for the closure of the feedback mechanism initiated by the shear layer instability. The guided jet mode is the consequence of the intense production of divergence of the velocity perturbations at an axial distance around a diameter from the wall, which has been identified using a novel decomposed structural sensitivity, suited to identify these type of non-local acoustic-hydrodynamic feedbacks. Such an instability mechanism is responsible for the strong emission of tonal noise. First it is robust, the mechanism is weakly sensitive to external perturbations, which could be due to inflow perturbations or the interaction with vortices issued from the region near the wall and initiated by the roll-up of the radial vortex sheet. Second, the emission of sound is strong, a feature that is observed when considering the relative amplitude between vortical and acoustic pressure of the linear mode. So, in this sense, linear stability is relevant to determine the possibility of strong sound emissions. On the other hand, at low Mach numbers, the main source of sound comes from *vortex-sound*. The structural sensitivity peaks along the radial vortex-sheet, which is the region with the largest module of the linearised Lamb vector. The difference in the mechanisms have several consequences in the non-linear dynamics. The dynamics of the vorticity field in a region around the radial vortex-sheet becomes rapidly chaotic with small variations of the Reynolds number from the primary Hopf bifurcation. Physically, the low temporal coherence of the vortical sources of sound, which are responsible for the emission of the pressure wave closing the feedback-loop, are at the origin of the measured broadband spectrum of the acoustic pressure field. We provide a reduced model, issued from a weakly non-linear analysis, to account for the qualitative changes in dynamics between low and large subsonic Mach numbers. The deterministic model mimics some features of the actual dynamics, such as the frequency-locking of a third tone with the other two or the appearance of a third slow frequency. Nevertheless, due to the truncation to third order, the model does not display chaotic dynamics. Based on a phenomenological reasoning, we propose a stochastic model which accounts for the low temporal coherence of the sources of sound at low Mach number, which in turn induce a frequency mismatch ($\delta\omega$). Such a model is able to reasonably reproduce the sound pressure level spectrums measured from time-stepping simulations. There exist several appealing perspectives. To mention some, it might be of interest to determine from experimental turbulent rounded impinging jets the coefficients of the normal form with data-assimilation techniques, cf Cenedese *et al.* (2022). In addition, the non-local structural sensitivity map may help to investigate the fine details of the instability mechanism in many other configurations where the instability is issued of a non-local feedback, such as airfoil noise, screech, or cavity flows.

Appendix A. Entropy formulation – Decomposition of the adjoint

In this section, we detail the derivation of the decomposition of the adjoint variable $\hat{\mathbf{q}}^\dagger$ into acoustic, vortical and entropic components. Before, proceeding to the detailed description of the adjoint equations, we introduce the linearised compressible Navier–Stokes equations in the primitive variables $[\hat{\rho}, \hat{\mathbf{u}}, \hat{s}, \hat{T}, \hat{p}]^T$. The motivation to introduce this set of equations is because they have a simpler decomposition. The linearised equations are

$$\left(-i\omega\mathbf{B}|_{\mathbf{q}_0} + \mathbf{DF}|_{\mathbf{q}_0}\right)\hat{\mathbf{q}} = 0, \quad \text{with } \mathbf{B}|_{\mathbf{q}_0} = \text{diag}(1, \rho_0\mathbf{I}, \rho_0T_0, 0, 0), \quad (\text{A } 1)$$

$$\mathbf{DF}|_{\mathbf{q}_0} \hat{\mathbf{q}} = \begin{cases} \mathbf{u}_0 \cdot \nabla \hat{\rho} + \hat{\rho} \nabla \cdot \mathbf{u}_0 + \hat{\mathbf{u}} \cdot \nabla \rho_0 + \rho_0 \nabla \cdot \hat{\mathbf{u}} & (\text{A } 2a) \\ \hat{\rho} \mathbf{u}_0 \cdot \nabla \mathbf{u}_0 + \rho_0 \mathbf{u}_0 \cdot \nabla \hat{\mathbf{u}} + \rho_0 \hat{\mathbf{u}} \cdot \nabla \mathbf{u}_0 + \nabla \hat{p} - \frac{1}{\text{Re}} \nabla \cdot \tau(\hat{\mathbf{u}}) & (\text{A } 2b) \\ -\gamma(\gamma-1) \frac{M_\infty^2}{\text{Re}} (\tau(\hat{\mathbf{u}}) : \mathbf{D}(\mathbf{u}_0) + \tau(\mathbf{u}_0) : \mathbf{D}(\hat{\mathbf{u}})) - \frac{\gamma}{\text{Pr Re}} \Delta \hat{T} & (\text{A } 2c) \\ + \rho_0 T_0 \mathbf{u}_0 \cdot \nabla \hat{s} + \rho_0 T_0 \hat{\mathbf{u}} \cdot \nabla s_0 + \hat{\rho} T_0 \mathbf{u}_0 \cdot \nabla s_0 + \rho_0 \hat{T} \mathbf{u}_0 \cdot \nabla s_0 & (\text{A } 2d) \\ \rho_0 T_0 \hat{s} + (\gamma-1) T_0 \hat{\rho} - \rho_0 \hat{T} & (\text{A } 2d) \\ -\rho_0 \hat{T} - \hat{\rho} T_0 + \gamma M_\infty^2 \hat{p} & (\text{A } 2e) \end{cases}$$

And their adjoint counterpart are

$$\left(i\bar{\omega} \mathbf{B}|_{\mathbf{q}_0} + \mathbf{DF}^\dagger|_{\mathbf{q}_0} \right) \hat{\mathbf{q}}^\dagger = 0, \text{ with } \mathbf{B}|_{\mathbf{q}_0} = \text{diag}(1, \rho_0 \mathbf{I}, \rho_0 T_0, 0, 0), \quad (\text{A } 3)$$

$$\mathbf{DF}^\dagger|_{\mathbf{q}_0} \hat{\mathbf{q}}^\dagger = \begin{cases} -\mathbf{u}_0 \cdot \nabla \hat{\rho}^\dagger + (\mathbf{u}_0 \cdot \nabla \mathbf{u}_0) \cdot \hat{\mathbf{u}}^\dagger & (\text{A } 4a) \\ + (\mathbf{u}_0 \cdot \nabla s_0) \hat{s}^\dagger + T_0 ((\gamma-1) \hat{T}^\dagger - \hat{p}^\dagger) & (\text{A } 4a) \\ -\rho_0 \mathbf{u}_0 \cdot \nabla \hat{\mathbf{u}}^\dagger + \rho_0 \hat{\mathbf{u}}^\dagger \cdot (\nabla \mathbf{u}_0)^T - \frac{1}{\text{Re}} \nabla \cdot \tau(\hat{\mathbf{u}}^\dagger) & (\text{A } 4a) \\ -\rho_0 \nabla \hat{\rho}^\dagger + 2\gamma(\gamma-1) \frac{M_\infty^2}{\text{Re}} \nabla \cdot (\hat{s}^\dagger \tau(\mathbf{u}_0)) + \rho_0 T_0 \hat{s}^\dagger \nabla s_0 & (\text{A } 4b) \\ -\rho_0 T_0 \mathbf{u}_0 \cdot \nabla \hat{s}^\dagger + \rho_0 T_0 \hat{T}^\dagger & (\text{A } 4c) \\ \rho_0 T_0 \hat{s}^\dagger \mathbf{u}_0 \cdot \nabla s_0 - \frac{\gamma}{\text{Pr Re}} \nabla^2 \hat{s}^\dagger - \rho_0 \hat{p}^\dagger - \rho_0 \hat{T}^\dagger & (\text{A } 4d) \\ \gamma M_\infty^2 \hat{p}^\dagger - \nabla \cdot \hat{\mathbf{u}}^\dagger & (\text{A } 4e) \end{cases}$$

A.1. Decomposition of the global mode

We first detail how we decompose the global mode $\hat{\mathbf{q}}$ into: *acoustic*, *hydrodynamic* and *entropic* components.

We adopt a Helmholtz-Hodge decomposition (Schoder *et al.* 2020) of the perturbation velocity field into *acoustic* (potential) and *hydrodynamic* (solenoidal)

$$\hat{\mathbf{u}} = \hat{\mathbf{u}}_{\text{ac}} + \hat{\mathbf{u}}_{\text{hyd}} = \nabla \phi_c + \nabla \times \Psi \quad (\text{A } 5)$$

applying divergence to eq. (4.1), the potential ϕ_c is determined from the following Poisson equation

$$\begin{aligned} \Delta \phi_c &= \nabla \cdot \hat{\mathbf{u}} & \text{in } \Omega \\ \nabla \phi_c \cdot \mathbf{n} &= \hat{\mathbf{u}} \cdot \mathbf{n} & \text{on } \partial\Omega. \end{aligned} \quad (\text{A } 6)$$

The hydrodynamic component of the velocity is subsequently determined by subtracting $\hat{\mathbf{u}}_{\text{hyd}} = \hat{\mathbf{u}} - \hat{\mathbf{u}}_{\text{ac}} = \hat{\mathbf{u}} - \nabla \phi_c$. Note that, the uniqueness of the Helmholtz decomposition is subjected to the L^2 -orthogonality condition, in our case satisfied by the suitable boundary condition of eq. (A 6), and the decay of the velocity field at the far-field (Schoder *et al.* 2020).

The pressure decomposition is derived from the linearised momentum equation. Considering an isentropic relationship between density and pressure fluctuations, i.e, $\hat{\rho} T_0 = M_\infty^2 \hat{p}$, and taking divergence of the linearised momentum equation, we end up with the following

elliptic equation for the pressure,

$$-\frac{1}{\rho_0}\Delta\hat{p} + \frac{\nabla\rho_0 \cdot \nabla\hat{p}}{\rho_0^2} - \nabla \cdot \left(\frac{M_\infty^2}{T_0} (\mathbf{u}_0 \cdot \nabla \mathbf{u}_0) \frac{\hat{p}}{\rho_0} \right) = \nabla \cdot (\mathbf{u}_0 \cdot \nabla \hat{\mathbf{u}}) + \nabla \cdot (\hat{\mathbf{u}} \cdot \nabla \mathbf{u}_0) + i\omega \nabla \cdot \hat{\mathbf{u}} - \frac{1}{\text{Re}} \nabla \cdot (\nabla \cdot \tau(\hat{\mathbf{u}})). \quad (\text{A } 7)$$

Decomposing the velocity field into acoustic and hydrodynamic and leaving the viscous dissipation term to the entropic component, we end up with the following decomposition of the pressure,

$$-\frac{1}{\rho_0}\Delta\hat{p}_{\text{ac}} + \frac{\nabla\rho_0 \cdot \nabla\hat{p}_{\text{ac}}}{\rho_0^2} - \nabla \cdot \left(\frac{M_\infty^2}{T_0} (\mathbf{u}_0 \cdot \nabla \mathbf{u}_0) \frac{\hat{p}_{\text{ac}}}{\rho_0} \right) = i\omega \nabla \cdot \hat{\mathbf{u}}_{\text{ac}} + \nabla \cdot (\mathbf{u}_0 \cdot \nabla \hat{\mathbf{u}}_{\text{ac}}) + \nabla \cdot (\hat{\mathbf{u}}_{\text{ac}} \cdot \nabla \mathbf{u}_0) \quad (\text{A } 8a)$$

$$-\frac{1}{\rho_0}\Delta\hat{p}_{\text{hyd}} + \frac{\nabla\rho_0 \cdot \nabla\hat{p}_{\text{hyd}}}{\rho_0^2} - \nabla \cdot \left(\frac{M_\infty^2}{T_0} (\mathbf{u}_0 \cdot \nabla \mathbf{u}_0) \frac{\hat{p}_{\text{hyd}}}{\rho_0} \right) = \nabla \cdot (\mathbf{u}_0 \cdot \nabla \hat{\mathbf{u}}_{\text{hyd}}) + \nabla \cdot (\hat{\mathbf{u}}_{\text{hyd}} \cdot \nabla \mathbf{u}_0) \quad (\text{A } 8b)$$

$$\hat{p}_s = \hat{p} - \hat{p}_{\text{hyd}} - \hat{p}_{\text{ac}}. \quad (\text{A } 8c)$$

A.2. Decomposition of the adjoint mode

Before introducing the decomposition of the adjoint global mode, we first review the significance of the decomposition in a simpler example, where we only consider the momentum equation. We introduce a harmonic forcing $\mathbf{H}_\mathbf{u}$ to the momentum equation,

$$-i\omega\rho_0\hat{\mathbf{u}} + \hat{\rho}\mathbf{u}_0 \cdot \nabla\mathbf{u}_0 + \rho_0\mathbf{u}_0 \cdot \nabla\hat{\mathbf{u}} + \rho_0\mathbf{u}_0 \cdot \nabla\hat{\mathbf{u}} - \nabla\hat{p} + \frac{1}{\text{Re}}\nabla \cdot \tau(\hat{\mathbf{u}}) = \rho_0\mathbf{H}_\mathbf{u}. \quad (\text{A } 9)$$

The introduction of the forcing term $\mathbf{H}_\mathbf{u}$ induces a response of the velocity field $\hat{\mathbf{u}}$ and the pressure field \hat{p} . In the presence of viscous dissipation, the introduction of the momentum source term always excites an entropic response. However, such a component is expected to become of lesser importance at larger Reynolds numbers and to be localized near wall boundaries and in regions of large magnitudes of the shear tensor. For such a reason, we propose the decomposition of the velocity adjoint into hydrodynamical and acoustic components, but having in mind that this is not a perfect decomposition since they should possess a possibly small entropic part. The excitation of the dilation of velocity is evaluated by taking the divergence of the linearised momentum equation eq. (A 9),

$$-i\omega \nabla \cdot \hat{\mathbf{u}} + \frac{\hat{\rho}}{\rho_0} \nabla \cdot \nabla (\mathbf{u}_0 \mathbf{u}_0) + \nabla \left(\frac{\hat{\rho}}{\rho_0} \right) \cdot \nabla (\mathbf{u}_0 \mathbf{u}_0) + \nabla \cdot \nabla (\mathbf{u}_0 \hat{\mathbf{u}}) - \Delta \left(\frac{\hat{p}}{\rho_0} \right) + \frac{1}{\text{Re}} \nabla \cdot (\nabla \cdot \tau(\hat{\mathbf{u}})) = \nabla \cdot \mathbf{H}_\mathbf{u}. \quad (\text{A } 10)$$

Equation (A 10) implies that divergence free forcing terms, i.e., $\nabla \cdot \mathbf{H}_\mathbf{u} = 0$, do not excite the acoustic component of the global mode. Furthermore, neglecting viscous dissipation effects, this type of forcing term only excites the hydrodynamic component of the global mode. A similar reasoning leads to the conclusion that, when we neglect viscous dissipation effects, a rotational-free forcing, i.e., $\nabla \times \mathbf{H}_\mathbf{u} = 0$, only excites the acoustic component of the perturbation.

Now, interpreting the adjoint global mode as the projector onto the corresponding component of the global mode, we propose a Helmholtz-Hodge decomposition of the

adjoint velocity field,

$$\begin{aligned}\hat{\mathbf{u}}^\dagger &= \hat{\mathbf{u}}_{\text{hyd}}^\dagger + \hat{\mathbf{u}}_{\text{ac}}^\dagger = \nabla\phi_c^\dagger + \nabla \times \Psi^\dagger, \\ \Delta\phi_c^\dagger &= \nabla \cdot \hat{\mathbf{u}}^\dagger \text{ in } \Omega \\ \nabla\phi_c^\dagger \cdot \mathbf{n} &= \hat{\mathbf{u}}^\dagger \cdot \mathbf{n} \text{ on } \partial\Omega.\end{aligned}\tag{A 11}$$

This decomposition is bi-orthogonal when considering only direct and adjoint velocity fields, that is, $\langle \hat{\mathbf{u}}_{\text{hyd}}^\dagger, \rho_0 \hat{\mathbf{u}}_{\text{ac}} \rangle = \langle \hat{\mathbf{u}}_{\text{ac}}^\dagger, \rho_0 \hat{\mathbf{u}}_{\text{hyd}} \rangle = 0$ with $\langle \hat{\mathbf{u}}_{\text{ac}}^\dagger, \rho_0 \hat{\mathbf{u}}_{\text{ac}} \rangle \neq 0$ and $\langle \hat{\mathbf{u}}_{\text{hyd}}^\dagger, \rho_0 \hat{\mathbf{u}}_{\text{hyd}} \rangle \neq 0$. Therefore, the momentum forcing can be expanded as

$$\rho_0 \mathbf{H}_{\mathbf{u}} = \langle \hat{\mathbf{u}}_{\text{hyd}}^\dagger, \rho_0 \mathbf{H}_{\mathbf{u}} \rangle \hat{\mathbf{u}}_{\text{hyd}} + \langle \hat{\mathbf{u}}_{\text{ac}}^\dagger, \rho_0 \mathbf{H}_{\mathbf{u}} \rangle \hat{\mathbf{u}}_{\text{ac}} = \rho_0 \mathbf{H}_{\text{hyd}, \mathbf{u}} + \rho_0 \mathbf{H}_{\text{ac}, \mathbf{u}}.\tag{A 12}$$

The next step in the decomposition consists in the decomposition of the entropy adjoint \hat{s}^\dagger . Here below, we justify that $\hat{s}^\dagger = \hat{s}_s^\dagger$, that is, that a forcing term to the entropy equation only excites the entropy component of the global mode. It derives from the fact that we have defined the acoustic and hydrodynamic components to be entropy-free. Evidently, since $\hat{s}_{\text{hyd}}^\dagger = \hat{s}_{\text{ac}}^\dagger = 0$, the decomposition is bi-orthogonal in the entropy variable.

From these considerations, we can derive the remaining components of adjoint. Substituting the gradient of the density adjoint $\nabla\hat{\rho}^\dagger$ from eq. (A 4a) into eq. (A 4b) we derive an explicit equation for $\hat{\rho}^\dagger$

$$\begin{aligned}-i\bar{\omega}\hat{\rho}^\dagger &= -i\bar{\omega}\mathbf{u}_0 \cdot \hat{\mathbf{u}}^\dagger - \mathbf{u}_0 \cdot (\mathbf{u}_0 \cdot \nabla\hat{\mathbf{u}}^\dagger) + \mathbf{u}_0 \cdot (\hat{\mathbf{u}}^\dagger \cdot (\nabla\mathbf{u}_0)^T) - \hat{\mathbf{u}}^\dagger \cdot (\mathbf{u}_0 \cdot \nabla\mathbf{u}_0) \\ &+ \frac{1}{\text{Re}}\mathbf{u}_0 \cdot \nabla \cdot \tau\hat{\mathbf{u}}^\dagger - 2\gamma(\gamma-1)\frac{M_\infty^2}{\text{Re}}\frac{1}{\rho_0}\mathbf{u}_0 \cdot \nabla \cdot \hat{s}^\dagger\tau(\mathbf{u}_0) \\ &- T_0\hat{s}^\dagger\mathbf{u}_0 \cdot \nabla s_0 + (\gamma-1)T_0\hat{T}^\dagger - T_0\hat{p}^\dagger\end{aligned}\tag{A 13}$$

Substituting $\hat{s}^\dagger = 0$, $\hat{\mathbf{u}}^\dagger = \hat{\mathbf{u}}_{\text{ac}}^\dagger$ (or $\hat{\mathbf{u}}^\dagger = \hat{\mathbf{u}}_{\text{hyd}}^\dagger$), and $\hat{T}^\dagger = -\hat{p}^\dagger$, a relationship that is obtained from eq. (A 4) by considering $\hat{s}^\dagger = 0$, we are led to the following decomposition of $\hat{\rho}^\dagger$

$$\begin{aligned}-i\bar{\omega}\hat{\rho}_{\text{ac}}^\dagger &= -i\bar{\omega}\mathbf{u}_0 \cdot \hat{\mathbf{u}}_{\text{ac}}^\dagger - \mathbf{u}_0 \cdot (\mathbf{u}_0 \cdot \nabla\hat{\mathbf{u}}_{\text{ac}}^\dagger) + \mathbf{u}_0 \cdot (\hat{\mathbf{u}}_{\text{ac}}^\dagger \cdot (\nabla\mathbf{u}_0)^T) \\ &- \hat{\mathbf{u}}_{\text{ac}}^\dagger \cdot (\mathbf{u}_0 \cdot \nabla\mathbf{u}_0) - \gamma T_0\hat{p}^\dagger \\ -i\bar{\omega}\hat{\rho}_{\text{hyd}}^\dagger &= -i\bar{\omega}\mathbf{u}_0 \cdot \hat{\mathbf{u}}_{\text{hyd}}^\dagger - \mathbf{u}_0 \cdot (\mathbf{u}_0 \cdot \nabla\hat{\mathbf{u}}_{\text{hyd}}^\dagger) + \mathbf{u}_0 \cdot (\hat{\mathbf{u}}_{\text{hyd}}^\dagger \cdot (\nabla\mathbf{u}_0)^T)\end{aligned}\tag{A 14}$$

And the entropic component is determined as $\hat{\rho}_s^\dagger = \hat{\rho}^\dagger - \hat{\rho}_{\text{ac}}^\dagger - \hat{\rho}_{\text{hyd}}^\dagger$. The decomposition of $\hat{\rho}^\dagger$ is not generally bi-orthogonal with respect to the density decomposition of the global mode.

However, if at least one of the components of the global mode is small with respect to the other two, it is possible to propose a nearly bi-orthogonal decomposition, while including the adjoint to the continuity equation. In the following, we will assume that $\|\hat{\mathbf{q}}_s\| \ll \|\hat{\mathbf{q}}_{\text{ac}}\|$ and $\|\hat{\mathbf{q}}_s\| \ll \|\hat{\mathbf{q}}_{\text{hyd}}\|$. In this case, the decomposition of the adjoint of the continuity equation is as follows,

$$\begin{aligned}\hat{\rho}_{\text{ac}, \text{bo}}^\dagger &= \hat{\rho}_{\text{ac}}^\dagger - \frac{\langle \hat{\rho}_{\text{ac}}^\dagger, \hat{\rho}_{\text{hyd}} \rangle_{\mathbf{B}}}{\langle \hat{\rho}_{\text{hyd}}^\dagger, \hat{\rho}_{\text{hyd}} \rangle_{\mathbf{B}}} \hat{\rho}_{\text{hyd}}^\dagger \\ \hat{\rho}_{\text{hyd}, \text{bo}}^\dagger &= \hat{\rho}_{\text{hyd}}^\dagger - \frac{\langle \hat{\rho}_{\text{hyd}}^\dagger, \hat{\rho}_{\text{ac}} \rangle_{\mathbf{B}}}{\langle \hat{\rho}_{\text{ac}}^\dagger, \hat{\rho}_{\text{ac}} \rangle_{\mathbf{B}}} \hat{\rho}_{\text{ac}}^\dagger \\ \hat{\rho}_{s, \text{bo}}^\dagger &= \hat{\rho}_s^\dagger + \frac{\langle \hat{\rho}_{\text{hyd}}^\dagger, \hat{\rho}_{\text{ac}} \rangle_{\mathbf{B}}}{\langle \hat{\rho}_{\text{ac}}^\dagger, \hat{\rho}_{\text{ac}} \rangle_{\mathbf{B}}} \hat{\rho}_{\text{ac}}^\dagger + \frac{\langle \hat{\rho}_{\text{ac}}^\dagger, \hat{\rho}_{\text{hyd}} \rangle_{\mathbf{B}}}{\langle \hat{\rho}_{\text{hyd}}^\dagger, \hat{\rho}_{\text{hyd}} \rangle_{\mathbf{B}}} \hat{\rho}_{\text{hyd}}^\dagger\end{aligned}\tag{A 15}$$

From the assumption that the order of magnitude of one of the components of the global mode is smaller than the other two, in our example the entropic component, we can decompose any forcing term in a near orthogonal fashion. That is, assume a generic mass injection H_ρ , we would like to decompose

$$H_\rho = \alpha_{\text{ac}} \hat{\rho}_{\text{ac}} + \alpha_{\text{hyd}} \hat{\rho}_{\text{hyd}} + \alpha_{\text{s}} \hat{\rho}_{\text{s}}. \quad (\text{A } 16)$$

Taking the inner product with the decomposed adjoint of the continuity equation eq. (A15), we can promptly determine the two first Fourier coefficients of eq. (A16), which are as follows,

$$\begin{aligned} \alpha_{\text{ac}} &= \frac{\langle \hat{\rho}_{\text{ac,bo}}^\dagger, H_\rho \rangle_{\mathbf{B}}}{\langle \hat{\rho}_{\text{ac,bo}}^\dagger, \hat{\rho}_{\text{ac}} \rangle_{\mathbf{B}} + \mathcal{O}(\epsilon)} + \mathcal{O}(\epsilon) \approx \frac{\langle \hat{\rho}_{\text{ac,bo}}^\dagger, H_\rho \rangle_{\mathbf{B}}}{\langle \hat{\rho}_{\text{ac,bo}}^\dagger, \hat{\rho}_{\text{ac}} \rangle_{\mathbf{B}}} \\ \alpha_{\text{hyd}} &= \frac{\langle \hat{\rho}_{\text{hyd,bo}}^\dagger, H_\rho \rangle_{\mathbf{B}}}{\langle \hat{\rho}_{\text{hyd,bo}}^\dagger, \hat{\rho}_{\text{hyd}} \rangle_{\mathbf{B}} + \mathcal{O}(\epsilon)} + \mathcal{O}(\epsilon) \approx \frac{\langle \hat{\rho}_{\text{hyd,bo}}^\dagger, H_\rho \rangle_{\mathbf{B}}}{\langle \hat{\rho}_{\text{hyd,bo}}^\dagger, \hat{\rho}_{\text{hyd}} \rangle_{\mathbf{B}}}. \end{aligned} \quad (\text{A } 17)$$

Where the small parameter is defined in such a way that the ratio between the norm of the small component to the other two is small, that is, $\|\hat{\mathbf{q}}_{\text{s}}\|/\|\hat{\mathbf{q}}_{\text{ac}}\| = \mathcal{O}(\epsilon)$. This decomposition, in our example, allows us to measure the receptivity of the acoustic and hydrodynamic components of the global mode with respect to a mass injection. Thus, providing a localised structural sensitivity also in cases where mass is injected to the system, at least for cases where one of the density components is considerably smaller than the other two.

Overall, the adjoint is decomposed as follows,

$$\begin{aligned} \hat{\mathbf{u}}^\dagger &= \hat{\mathbf{u}}_{\text{hyd}}^\dagger + \hat{\mathbf{u}}_{\text{ac}}^\dagger = \nabla \phi_c^\dagger + \nabla \times \Psi^\dagger, \text{ from eq. (A 11)} \\ \hat{s}^\dagger &= \hat{s}_{\text{s}}^\dagger \\ \hat{\rho}^\dagger &= \hat{\rho}_{\text{ac,bo}}^\dagger + \hat{\rho}_{\text{hyd,bo}}^\dagger + \hat{\rho}_{\text{s,bo}}^\dagger \\ \hat{p}^\dagger &= \hat{p}_{\text{ac}}^\dagger = \frac{\nabla \cdot \hat{\mathbf{u}}^\dagger}{\gamma M_\infty^2} \\ \hat{T}^\dagger &= \hat{T}_{\text{ac}}^\dagger + \hat{T}_{\text{s}}^\dagger = -\frac{\nabla \cdot \hat{\mathbf{u}}^\dagger}{\gamma M_\infty^2} + \left(\hat{s}^\dagger \mathbf{u}_0 \cdot \nabla s_0 - \frac{\gamma}{\text{Pr Re } \rho_0} \Delta \hat{s}^\dagger \right) \end{aligned} \quad (\text{A } 18)$$

Appendix B. Normal form reduction

Here, we discuss the computation of the coefficients of the normal form eq. (B20). These are computed following a multiple scales expansion of the solution \mathbf{q} of eq. (2.1). We rewrite the governing equations as follows,

$$\mathbf{B} \frac{\partial \mathbf{q}}{\partial t} = \mathbf{F}(\mathbf{q}, \boldsymbol{\eta}) \equiv -\left(\mathbf{c} + \mathbf{L}\mathbf{q} + \frac{1}{2} \mathbf{N}_2(\mathbf{q}, \mathbf{q}) + \frac{1}{6} \mathbf{N}_3(\mathbf{q}, \mathbf{q}, \mathbf{q}) + \mathbf{G}_1(\mathbf{q}, \boldsymbol{\eta}) + \frac{1}{2} \mathbf{G}_2(\mathbf{q}, \mathbf{q}, \boldsymbol{\eta}) \right), \quad (\text{B } 1)$$

where $\mathbf{c} = [0, \mathbf{0}, 0, 1]^T$, \mathbf{B} is the mass matrix, \mathbf{L} the linear operator on the state variable \mathbf{q} , and \mathbf{G}_1 and \mathbf{G}_2 the linear and quadratic operators in the state variable \mathbf{q} and parameters $\boldsymbol{\eta}$. These operators are defined as

$$\begin{aligned}
\mathbf{B} &= \begin{pmatrix} 1 & 0 & 0 & 0 \\ 0 & \rho \mathbf{I} & 0 & 0 \\ 0 & 0 & \rho & 0 \\ 0 & 0 & 0 & 0 \end{pmatrix}, \quad \mathbf{L} = \begin{pmatrix} 0 & 0 & 0 & 0 \\ 0 & 0 & 0 & \nabla \\ 0 & 0 & 0 & 0 \\ 0 & 0 & 0 & 0 \end{pmatrix}, \\
\mathbf{G}_1(\mathbf{q}, \boldsymbol{\eta}) &= \begin{pmatrix} 0 & 0 & 0 & 0 \\ 0 & -\frac{1}{Re} \nabla \cdot \boldsymbol{\tau}(\cdot) & 0 & 0 \\ 0 & 0 & -\frac{\gamma}{Pr Re} \Delta & 0 \\ 0 & 0 & 0 & \gamma M_\infty^2 \end{pmatrix}, \\
\mathbf{G}_2(\mathbf{q}_1, \mathbf{q}_1, \boldsymbol{\eta}) &= \begin{pmatrix} 0 & 0 & 0 & 0 \\ 0 & \mathbf{0} & 0 & 0 \\ -(\gamma - 1)\gamma M_\infty^2 / Re (\boldsymbol{\tau}(\mathbf{u}_1) : \mathbf{D}(\mathbf{u}_2) + \boldsymbol{\tau}(\mathbf{u}_2) : \mathbf{D}(\mathbf{u}_1)) & 0 & 0 & 0 \end{pmatrix},
\end{aligned} \tag{B 2}$$

while the quadratic nonlinear operator on the state variable is defined as

$$\mathbf{N}_2(\mathbf{q}_1, \mathbf{q}_2) = \begin{pmatrix} \mathbf{u}_1 \cdot \nabla \rho_2 + \mathbf{u}_2 \cdot \nabla \rho_1 + \rho_1 \nabla \cdot \mathbf{u}_2 + \rho_2 \nabla \cdot \mathbf{u}_1 \\ 0 \\ 0 \\ -(\rho_1 T_2 + \rho_2 T_1) \end{pmatrix}, \tag{B 3}$$

and cubic nonlinear operator on the state variable is

$$\mathbf{N}_3(\mathbf{q}_1, \mathbf{q}_2, \mathbf{q}_3) = \begin{pmatrix} 0 \\ \sum_{i,j,k} \rho_i \mathbf{u}_j \cdot \nabla \mathbf{u}_k \\ \sum_{i,j,k} (\gamma - 1) \rho_i T_j \nabla \cdot \mathbf{u}_k + \rho_i \mathbf{u}_j \cdot \nabla T_k \\ 0 \end{pmatrix}, \tag{B 4}$$

The expansion considers a two scale development of the original time $t \mapsto t + \varepsilon^2 \tau$, here ε is the order of magnitude of the flow disturbances, assumed small $\varepsilon \ll 1$. Herein, we consider the small parameters ε_{M^2} and ε_ν , which are a function of the Mach number and Reynolds numbers at the far-field,

$$\varepsilon_{M^2}^2 = (M_{\infty,c}^2 - M_\infty^2) \sim \varepsilon^2 \quad \text{and} \quad \varepsilon_\nu^2 = (\nu_c - \nu) = (Re_c^{-1} - Re^{-1}) \sim \varepsilon^2.$$

With this compact notation we can provide an explicit form of the linearized Navier–Stokes equations with respect to baseflow \mathbf{q}_b ,

$$\mathbf{DF}|_{\mathbf{q}_b}(\mathbf{q}, \boldsymbol{\eta}) \equiv \mathbf{L}\mathbf{q} + \mathbf{N}_2(\mathbf{q}_b, \mathbf{q}) + \frac{1}{2}\mathbf{N}_3(\mathbf{q}_b, \mathbf{q}_b, \mathbf{q}) + \mathbf{G}_1(\mathbf{q}, \boldsymbol{\eta}) + \mathbf{G}_2(\mathbf{q}_b, \mathbf{q}, \boldsymbol{\eta}). \tag{B 5}$$

The technique decomposes time into a fast timescale t of the phase associated to the self-sustained instabilities and a slow timescale related to the evolution of the amplitudes $z_i(\tau)$, introduced in eq. (2.11), for $i = 1, 2, 3$. The ansatz of the expansion is as follows

$$\mathbf{q}(t, \tau) = \mathbf{q}_b + \varepsilon \mathbf{q}_{(\varepsilon)}(t, \tau) + \varepsilon^2 \mathbf{q}_{(\varepsilon^2)}(t, \tau) + \varepsilon^3 \mathbf{q}_{(\varepsilon^3)}(t, \tau) + O(\varepsilon^4) \tag{B 6}$$

In such a case, the vector is expanded as

$$\mathbf{q}_{(\varepsilon)}(t, \tau) = \sum_{k=1}^N (z_k(\tau) \hat{\mathbf{q}}_{(z_k)}(r, z) e^{i\omega_k t} + \text{c.c.}) \tag{B 7}$$

Note that the expansion of the LHS of eq. (2.1) up to third order is as follows

$$\varepsilon \mathbf{B} \frac{\partial \mathbf{q}(\varepsilon)}{\partial t} + \varepsilon^2 \mathbf{B} \frac{\partial \mathbf{q}(\varepsilon^2)}{\partial t} + \varepsilon^3 \left[\mathbf{B} \frac{\partial \mathbf{q}(\varepsilon^3)}{\partial t} + \mathbf{B} \frac{\partial \mathbf{q}(\varepsilon)}{\partial \tau} \right] + O(\varepsilon^4), \quad (\text{B } 8)$$

and the RHS respectively,

$$\mathbf{F}(\mathbf{q}, \boldsymbol{\eta}) = \mathbf{F}_{(0)} + \varepsilon \mathbf{F}_{(\varepsilon)} + \varepsilon^2 \mathbf{F}_{(\varepsilon^2)} + \varepsilon^3 \mathbf{F}_{(\varepsilon^3)} + O(\varepsilon^4). \quad (\text{B } 9)$$

In the following, in order to improve readability, we define the set of vectors of linear, quadratic, and secular interactions.

$$\begin{aligned} \mathbf{Z} &\equiv \{z_1, z_2, z_3\}, & \bar{\mathbf{Z}} &= \{\bar{z}_1, \bar{z}_2, \bar{z}_3\} \\ \mathbf{Z}^2 &\equiv \mathbf{Z} \otimes \mathbf{Z} \oplus \mathbf{Z} \otimes \bar{\mathbf{Z}} = \{z_1^2, z_2^2, z_3^2, z_1 z_2, z_1 z_3, z_2 z_3, |z_1|^2, |z_2|^2, |z_3|^2, \\ & & & z_1 \bar{z}_2, z_1 \bar{z}_3, z_2 \bar{z}_3\} \\ \mathbf{Z}_S &\equiv \{z_1, z_2, z_3, z_1 |z_1|^2, z_1 |z_2|^2, z_1 |z_3|^2, z_2 |z_1|^2, z_2 |z_2|^2, z_2 |z_3|^2, \\ & & & z_3 |z_1|^2, z_3 |z_2|^2, z_3 |z_3|^2, z_1 \bar{z}_2 z_3, z_2^2 \bar{z}_3, z_2^2 \bar{z}_1\} \end{aligned} \quad (\text{B } 10)$$

where only unique elements are kept. We denote by \mathbf{z}_α^n any element of the family \mathbf{Z}^n , with $n \in \mathbb{N}^*$.

B.1. Zeroth order

The zeroth order corresponds to the steady-state problem of the governing equations evaluated at the parameter vector $\boldsymbol{\eta} = (M_\infty, Re)^T$,

$$\mathbf{0} = \mathbf{F}(\mathbf{q}_b, \boldsymbol{\eta}) \quad (\text{B } 11)$$

whose solution is the steady state \mathbf{q}_b .

B.2. First order

The first order corresponds to the resolution of a homogeneous linear system, i.e., a generalized eigenvalue problem evaluated. The eigenpairs $[i\omega_\ell, \hat{\mathbf{q}}_{(z_\ell)}]$ are determined as the solutions of the following *shifted* (Meliga *et al.* 2009) eigenvalue problem

$$\tilde{\mathbf{J}}_{\omega_\ell} \hat{\mathbf{q}}_{(z_\ell)} = \left(i\omega_\ell \mathbf{B} - \varepsilon^2 \mathbf{S} - \mathbf{D}\mathbf{F}|_{\mathbf{q}_b}(\mathbf{q}, \boldsymbol{\eta}) \right) \hat{\mathbf{q}}_{(z_\ell)} \quad (\text{B } 12)$$

where we have introduced the shift operator $\varepsilon^2 \mathbf{S}$, which is defined in such a way that $\tilde{\mathbf{J}}_{\omega_\ell} \hat{\mathbf{q}}_{(z_\ell)} = \mathbf{0}$ at $\boldsymbol{\eta}$ and $\text{Im}(\omega_\ell) = 0$, and $\mathbf{S}\mathbf{q} = \mathbf{0}$ for any other vector field \mathbf{q} distinct to the eigenmodes. The \mathbf{B} -norm of the eigenmodes $\hat{\mathbf{q}}_{(z_\ell)}(r, z)$ is scaled to unity, i.e., $\langle \hat{\mathbf{q}}, \hat{\mathbf{q}} \rangle_{\mathbf{B}} = 1$.

Analogously, the adjoint eigenmodes are determined from the resolution of eq. (2.7) and normalised with respect to the direct mode so the inner product is equal to the unity, i.e., $\langle \hat{\mathbf{q}}^\dagger, \hat{\mathbf{q}} \rangle_{\mathbf{B}} = 1$

B.3. Second order

The second order expansion term $\mathbf{q}_{(\varepsilon^2)}(t, \tau)$ is determined by the resolution of a set of linear systems, where the forcing terms are evaluated from first and zeroth order terms. The expansion in terms of amplitudes $z_\ell(\tau)$ of $\mathbf{q}_{(\varepsilon^2)}(t, \tau)$ is assessed by collecting the

second order forcing terms. Non-linear second order terms in ε are

$$\begin{aligned} \mathbf{F}_{(\varepsilon^2)} &\equiv \sum_{j,k=1}^3 \frac{1}{2} \left(z_j z_k \mathbf{N}_2(\hat{\mathbf{q}}_{(z_j)}, \hat{\mathbf{q}}_{(z_k)}) e^{-i(\omega_j + \omega_k)t} + \text{c.c.} \right) \\ &+ \sum_{j,k=1}^3 \frac{1}{2} \left(z_j \bar{z}_k \mathbf{N}_2(\hat{\mathbf{q}}_{(z_j)}, \hat{\mathbf{q}}_{(\bar{z}_k)}) e^{-i(\omega_j - \omega_k)t} + \text{c.c.} \right) \\ &+ \sum_{\ell=1}^2 \eta_\ell \mathbf{G}_1(\mathbf{q}_b, \mathbf{e}_\ell), \end{aligned} \quad (\text{B } 13)$$

where \mathbf{e}_ℓ is an element of the orthonormal basis of \mathbb{R}^2 . Then the second order expansion of the flow variable is carried out, so it matches the terms of the forcing

$$\mathbf{q}_{(\varepsilon^2)} \equiv \sum_{\mathbf{z}_\alpha^2 \in \mathbf{Z}^2} \left(\mathbf{z}_\alpha^2 \hat{\mathbf{q}}_{(\mathbf{z}_\alpha^2)} e^{-i\omega_\alpha t} + \text{c.c.} \right) + \sum_{\ell=1}^2 \eta_\ell \mathbf{q}_b^{(\eta_\ell)}, \quad (\text{B } 14)$$

The terms $\hat{\mathbf{q}}_{(z_j^2)}$ are harmonics of the flow, $\hat{\mathbf{q}}_{(z_j z_k)}$ with $j \neq k$ are coupling terms, $\hat{\mathbf{q}}_{(|z_j|^2)}$ are harmonic base flow modification terms and $\mathbf{q}_b^{(\eta_\ell)}$ are base flow corrections due to a modification of the parameter η_ℓ from the critical point. Then the second order terms are determined from the resolution of the following (non-singular) systems of equations

$$\mathbf{J}_{(\omega_j + \omega_k)} \hat{\mathbf{q}}_{(z_j z_k)} = \hat{\mathbf{F}}_{(z_j z_k)}, \quad (\text{B } 15)$$

where $\hat{\mathbf{F}}_{(z_j z_k)}$ is the term of eq. (B 13) proportional to $z_j z_k$ and

$$\mathbf{J}_{(0,0)} \mathbf{Q}_b^{(\eta_\ell)} = \mathbf{G}(\mathbf{Q}_b, \mathbf{e}_\ell). \quad (\text{B } 16)$$

B.4. Third order

At third order, we proceed as for previous orders, first the forcing term is expanded

$$\begin{aligned} \mathbf{F}_{(\varepsilon^3)} &= \sum_{\mathbf{z}_\alpha \in \mathbf{Z}, \mathbf{z}_\beta^2 \in \mathbf{Z}^2} \mathbf{z}_\alpha \mathbf{z}_\beta^2 [\mathbf{N}(\hat{\mathbf{q}}_{(\mathbf{z}_\beta^2)}, \hat{\mathbf{q}}_{(\mathbf{z}_\alpha)})] e^{i(\omega_\alpha + \omega_\beta)t} \\ &+ \sum_{\mathbf{z}_\alpha \in \mathbf{Z}, \mathbf{z}_\beta \in \mathbf{Z}, \mathbf{z}_\gamma \in \mathbf{Z}} \mathbf{z}_\alpha \mathbf{z}_\beta \mathbf{z}_\gamma [\mathbf{N}_3(\hat{\mathbf{q}}_{(\mathbf{z}_\gamma)}, \hat{\mathbf{q}}_{(\mathbf{z}_\beta)}, \hat{\mathbf{q}}_{(\mathbf{z}_\alpha)})] e^{i(\omega_\alpha + \omega_\beta + \omega_\gamma)t} \\ &+ \sum_{j=1}^2 \sum_{\ell=1}^2 \left[z_j \eta_\ell [\mathbf{N}_2(\hat{\mathbf{q}}_{(z_j)}, \mathbf{Q}_b^{(\eta_\ell)})] e^{-i\omega_j t} + \text{c.c.} \right] \\ &+ \sum_{j=1}^2 \sum_{\ell=1}^2 \left[z_j \eta_\ell \mathbf{G}_1(\hat{\mathbf{q}}_{(z_j)}, \mathbf{e}_\ell) e^{-i\omega_j t} + \text{c.c.} \right] + \sum_{j=1}^3 z_j \mathbf{S} \hat{\mathbf{q}}_{(z_j)}, \end{aligned} \quad (\text{B } 17)$$

Followed, by the expansion of the third-order secular terms $\mathbf{q}_{(\varepsilon^3)}(t, \tau)$

$$\begin{aligned} \mathbf{q}_{(\varepsilon^3)}(t, \tau) &\equiv \sum_{\substack{\mathbf{z}_\alpha \in \mathbf{Z}_S \\ 2 \quad 2}} \left[\mathbf{z}_\alpha^3 \hat{\mathbf{q}}_{(\mathbf{z}_\alpha)} e^{-i\omega_\alpha t} + \text{c.c.} \right] \\ &+ \sum_{j=1}^2 \sum_{\ell=1}^2 \left[z_j \eta_\ell \mathbf{Q}_{(z_j)}^{(\eta_\ell)} e^{-i\omega_j t} + \text{c.c.} \right] \end{aligned} \quad (\text{B } 18)$$

To ensure the solvability of the resonant terms we must enforce compatibility conditions, i.e. the *Fredholm alternative*. The resonant terms are then determined from the resolution

ν_{11}	ν_{12}	ν_{13}	ν_{21}	ν_{22}	ν_{23}
$-0.57 - 0.28i$	$-0.04 + 0.13i$	$-1.3 - 1.2i$	$-0.1 - 0.23i$	$-0.25 - 0.94i$	$-0.15 - 2.5i$
ν_{31}	ν_{32}	ν_{33}	χ_1	χ_2	χ_3
$-1.6 + 2.3i$	$-1.0 + 0.48i$	$-0.76 + 0.34i$	$1.7 - 1.8i$	$-0.27 - 0.61i$	$-3.0 - 1.7i$

Table 5: $M_\infty = 0.3$.

ν_{11}	ν_{12}	ν_{13}	ν_{21}	ν_{22}	ν_{23}
$-0.068 + 0.032i$	$-0.025 + 0.028i$	$-0.33 + 0.076i$	$-0.10 + 0.090i$	$-0.27 + 0.23i$	$-0.34 + 0.076i$
ν_{31}	ν_{32}	ν_{33}	χ_1	χ_2	χ_3
$-0.15 + 0.022i$	$-0.43 - 0.009i$	$-0.25 - 0.15i$	$-0.015 - 0.047i$	$-0.076 + 0.033i$	$-0.065 - 0.048i$

Table 6: $M_\infty = 0.5$.

of the following set of *bordered systems*

$$\begin{pmatrix} \mathbf{J}(\omega_k, m_k) & \hat{\mathbf{q}}(z_k) \\ \hat{\mathbf{q}}^\dagger(z_k) & 0 \end{pmatrix} \begin{pmatrix} \hat{\mathbf{q}}(z_\alpha^{(S)}) \\ s \end{pmatrix} = \begin{pmatrix} \hat{\mathbf{F}}(z_\alpha^{(S)}) \\ 0 \end{pmatrix}, \quad \mathbf{z}_\alpha^{(S)} \in \mathbf{Z}_S \quad (\text{B } 19)$$

where $s = \lambda_k^{(\varepsilon_v^2)}$ (respectively $s = \lambda_k^{(\varepsilon_{M_\infty^2}^2)}$) for $\mathbf{z}_\alpha^{(S)} = z_k$ and $s = \nu_{kl}^{(0)}$ for $\mathbf{z}_\alpha^{(S)} = z_k |z_\ell|^2$ and $s = \chi_1$ for $\mathbf{z}_\alpha^{(S)} = z_2^2 \bar{z}_3$, $s = \chi_2$ for $\mathbf{z}_\alpha^{(S)} = z_1 \bar{z}_2 z_3$, and $s = \chi_3$ for $\mathbf{z}_\alpha^{(S)} = z_2^2 \bar{z}_1$. Table 5 and table 6 list the cubic coefficients of the normal form for the two considered Mach numbers based on the far-field speed of sound (M_∞).

B.5. Example of a larger number of mode interactions

The general case with arbitrary N limit cycles may be expressed as

$$\dot{z}_j = z_j (\lambda_j + \sum_{k=1}^N \nu_{jk} |z_k|^2) + \text{NL}_{j,\text{res}} \quad \text{for } j = 1, \dots, N \quad (\text{B } 20)$$

where $\text{NL}_{j,\text{res}}$ are the resonant terms at the third order. For $N = 5$, the resonant term is as follows,

$$\text{NL}_{\text{res}} = \begin{bmatrix} \chi_{1,1} z_2^2 \bar{z}_3 + \chi_{1,2} z_2 z_3 \bar{z}_4 + \chi_{1,3} z_2 z_4 \bar{z}_5 + \chi_{1,4} z_3^2 \bar{z}_5 \\ \chi_{2,1} z_1 \bar{z}_2 z_3 + \chi_{2,2} z_1 z_4 \bar{z}_3 \chi_{2,3} z_1 z_5 \bar{z}_4 \chi_{2,4} z_3^2 \bar{z}_4 + \chi_{2,5} z_3 z_4 \bar{z}_5 \\ \chi_{3,1} z_2^2 \bar{z}_1 + \chi_{3,2} z_2 \bar{z}_3 z_4 + \chi_{3,3} z_4^2 \bar{z}_5 \\ \chi_{4,1} z_5 \bar{z}_4 z_3 + \chi_{4,2} z_3^2 \bar{z}_2 + \chi_{4,3} z_3 z_2 \bar{z}_1 \chi_{4,4} z_5 z_2 \bar{z}_3 \chi_{4,5} z_5 z_1 \bar{z}_2 \\ \chi_{5,1} z_4^2 \bar{z}_3 + \chi_{5,2} z_4 z_3 \bar{z}_2 + \chi_{5,3} z_4 z_2 \bar{z}_1 + \chi_{5,4} z_3^2 \bar{z}_1 \end{bmatrix} \quad (\text{B } 21)$$

Figure 15 (b) illustrates the resonant interactions for $N = 5$ for the equation of z_3 , i.e. $\text{NL}_{3,\text{res}} = \chi_{3,1} z_2^2 \bar{z}_1 + \chi_{3,2} z_2 \bar{z}_3 z_4 + \chi_{3,3} z_4^2 \bar{z}_5$.

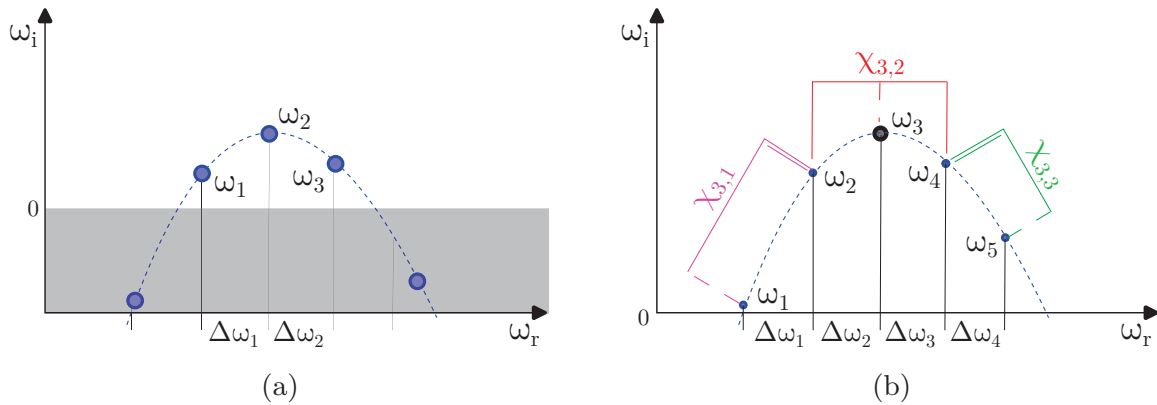


Figure 15: (a) Sketch of the spectrum. (b) Sketch of the spectrum indicating the local contributions to the normal form: (double) solid line indicates the coefficient multiplies the (square) of the mode, dashed line the complex conjugate of the mode.

REFERENCES

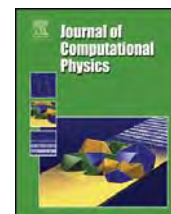
- BOGEY, CHRISTOPHE 2021 Acoustic tones in the near-nozzle region of jets: characteristics and variations between mach numbers 0.5 and 2. *Journal of Fluid Mechanics* **921**.
- BOGEY, CHRISTOPHE 2022 Tones in the acoustic far field of jets in the upstream direction. *AIAA Journal* **60** (4), 2397–2406.
- BOGEY, CHRISTOPHE & GOJON, ROMAIN 2017 Feedback loop and upwind-propagating waves in ideally expanded supersonic impinging round jets. *Journal of Fluid Mechanics* **823**, 562–591.
- BRÈS, GUILLAUME A, JORDAN, PETER, JAUNET, VINCENT, LE RALLIC, MAXIME, CAVALIERI, ANDRÉ VG, TOWNE, AARON, LELE, SANJIVA K, COLONIUS, TIM & SCHMIDT, OLIVER T 2018 Importance of the nozzle-exit boundary-layer state in subsonic turbulent jets. *Journal of Fluid Mechanics* **851**, 83–124.
- BUCHMANN, NA, MITCHELL, DM, INGVOSEN, KRISTIAN MARK, HONNERY, DR & SORIA, J 2011 High spatial resolution imaging of a supersonic underexpanded jet impinging on a flat plate. In *6th Australian Conference on Laser Diagnostics in Fluid Mechanics and Combustion*.
- CALLAHAM, JARED L, LOISEAU, J-C, RIGAS, GEORGIOS & BRUNTON, STEVEN L 2021 Nonlinear stochastic modelling with langevin regression. *Proceedings of the Royal Society A* **477** (2250), 20210092.
- CENEDESE, MATTIA, AXÅS, JOAR, BÄUERLEIN, BASTIAN, AVILA, KERSTIN & HALLER, GEORGE 2022 Data-driven modeling and prediction of non-linearizable dynamics via spectral submanifolds. *Nature communications* **13** (1), 872.
- CHU, BOA-TEH 1965 On the energy transfer to small disturbances in fluid flow (part i). *Acta Mechanica* **1** (3), 215–234.
- DAUPTAIN, A, GICQUEL, LYM & MOREAU, S 2012 Large eddy simulation of supersonic impinging jets. *AIAA journal* **50** (7), 1560–1574.
- EDGINGTON-MITCHELL, DANIEL 2019 Aeroacoustic resonance and self-excitation in screeching and impinging supersonic jets—a review. *International Journal of Aeroacoustics* **18** (2-3), 118–188.
- EDGINGTON-MITCHELL, DANIEL, JAUNET, VINCENT, JORDAN, PETER, TOWNE, AARON, SORIA, JULIO & HONNERY, DAMON 2018 Upstream-travelling acoustic jet modes as a closure mechanism for screech. *Journal of Fluid Mechanics* **855**, R1.
- EWERT, ROLAND & SCHRÖDER, WOLFGANG 2003 Acoustic perturbation equations based on flow decomposition via source filtering. *Journal of Computational Physics* **188** (2), 365–398.
- FANI, ANDREA, CITRO, V, GIANNETTI, F & AUTERI, F 2018 Computation of the bluff-body sound generation by a self-consistent mean flow formulation. *Physics of Fluids* **30** (3), 036102.
- GIANNETTI, FLAVIO & LUCHINI, PAOLO 2007 Structural sensitivity of the first instability of the cylinder wake. *Journal of Fluid Mechanics* **581**, 167–197.

- GOJON, ROMAIN & BOGEY, CHRISTOPHE 2017a Flow structure oscillations and tone production in underexpanded impinging round jets. *Aiaa Journal* **55** (6), 1792–1805.
- GOJON, ROMAIN & BOGEY, CHRISTOPHE 2017b Numerical study of the flow and the near acoustic fields of an underexpanded round free jet generating two screech tones. *International Journal of Aeroacoustics* **16** (7-8), 603–625.
- GOJON, ROMAIN, BOGEY, CHRISTOPHE & MARSDEN, OLIVIER 2016 Investigation of tone generation in ideally expanded supersonic planar impinging jets using large-eddy simulation. *Journal of Fluid Mechanics* **808**, 90–115.
- HO, CHIH-MING & NOSSEIR, NAGY S 1981 Dynamics of an impinging jet. part 1. the feedback phenomenon. *Journal of Fluid Mechanics* **105**, 119–142.
- HOWE, MS 1975 Contributions to the theory of aerodynamic sound, with application to excess jet noise and the theory of the flute. *Journal of fluid mechanics* **71** (4), 625–673.
- JAUNET, VINCENT, MANCINELLI, MATTEO, JORDAN, PETER, TOWNE, AARON, EDGINGTON-MITCHELL, DANIEL M, LEHNASCH, GUILLAUME & GIRARD, STÈVE 2019 Dynamics of round jet impingement. In *25th AIAA/CEAS Aeroacoustics Conference*, p. 2769.
- JORDAN, PETER, JAUNET, VINCENT, TOWNE, AARON, CAVALIERI, ANDRÉ VG, COLONIUS, TIM, SCHMIDT, OLIVER & AGARWAL, ANURAG 2018 Jet–flap interaction tones. *Journal of Fluid Mechanics* **853**, 333–358.
- MANCINELLI, MATTEO, JAUNET, VINCENT, JORDAN, PETER & TOWNE, AARON 2019 Screech-tone prediction using upstream-travelling jet modes. *Experiments in Fluids* **60** (1), 1–9.
- MARQUES, F, LOPEZ, JM & SHEN, J 2001 A periodically forced flow displaying symmetry breaking via a three-tori gluing bifurcation and two-tori resonances. *Physica D: Nonlinear Phenomena* **156** (1-2), 81–97.
- MARQUET, OLIVIER & LESSHAFFT, LUTZ 2015 Identifying the active flow regions that drive linear and nonlinear instabilities. *arXiv preprint arXiv:1508.07620* .
- MELIGA, PHILIPPE, CHOMAZ, JEAN-MARC & SIPP, DENIS 2009 Global mode interaction and pattern selection in the wake of a disk: a weakly nonlinear expansion. *Journal of Fluid Mechanics* **633**, 159–189.
- MELIGA, PHILIPPE, SIPP, D & CHOMAZ, J-M 2010 Effect of compressibility on the global stability of axisymmetric wake flows. *Journal of Fluid Mechanics* **660**, 499–526.
- MITCHELL, DANIEL M, HONNERY, DAMON R & SORIA, JULIO 2012 The visualization of the acoustic feedback loop in impinging underexpanded supersonic jet flows using ultra-high frame rate schlieren. *Journal of visualization* **15** (4), 333–341.
- NEUWERTH, G 1974 Acoustic feedback of a subsonic and supersonic free jet which impinges on an obstacle. *NASA TT F-15719* .
- NEWHOUSE, SHELDON, RUELLE, DAVID & TAKENS, FLORIS 1978 Occurrence of strange axiom a attractors near quasi periodic flows on t m, $m \geq 3$. *Communications in Mathematical Physics* **64**, 35–40.
- NORUM, THOMAS D 1991 Supersonic rectangular jet impingement noise experiments. *AIAA journal* **29** (7), 1051–1057.
- NOSSEIR, NAGY S & HO, CHIH-MING 1982 Dynamics of an impinging jet. part 2. the noise generation. *Journal of fluid mechanics* **116**, 379–391.
- POWELL, ALAN 1953 On edge tones and associated phenomena. *Acta Acustica United with Acustica* **3** (4), 233–243.
- POWELL, ALAN 1961 On the edgetone. *The Journal of the Acoustical Society of America* **33** (4), 395–409.
- POWELL, ALAN 1990 Some aspects of aeroacoustics: From rayleigh until today .
- PREISSER, JOHN S 1979 Fluctuating surface pressure and acoustic radiation for subsonic normal jet impingement. *Tech. Rep.*.
- RIENSTRA, SJOERD W & HIRSCHBERG, AVRAHAM 2004 An introduction to acoustics. *Eindhoven University of Technology* **18**, 19.
- RISBORG, ADAM & SORIA, JULIO 2009 High-speed optical measurements of an underexpanded supersonic jet impinging on an inclined plate. In *28th international congress on high-speed imaging and photonics*, , vol. 7126, pp. 477–487. SPIE.
- SCHODER, STEFAN, ROPPERT, KLAUS & KALTENBACHER, MANFRED 2020 Helmholtz’s decomposition for compressible flows and its application to computational aeroacoustics. *SN Partial Differential Equations and Applications* **1** (6), 1–20.

- SHAABANI-ARDALI, LÉOPOLD, SIPP, DENIS & LESSHAFFT, LUTZ 2019 Vortex pairing in jets as a global floquet instability: modal and transient dynamics. *Journal of Fluid Mechanics* **862**, 951–989.
- SIERRA, JAVIER, FABRE, DAVID & CITRO, VINCENZO 2020a Efficient stability analysis of fluid flows using complex mapping techniques. *Computer Physics Communications* **251**, 107100.
- SIERRA, J, FABRE, DAVID, CITRO, VINCENZO & GIANNETTI, FLAVIO 2020b Bifurcation scenario in the two-dimensional laminar flow past a rotating cylinder. *Journal of Fluid Mechanics* **905**.
- SIERRA-AUSIN, J, FABRE, D, CITRO, V & GIANNETTI, F 2022 Acoustic instability prediction of the flow through a circular aperture in a thick plate via an impedance criterion. *Journal of Fluid Mechanics* **943**, A48.
- SIERRA-AUSÍN, J., LORITE-DÍEZ, M., JIMÉNEZ-GONZÁLEZ, J.I., CITRO, V. & FABRE, D. 2022 Unveiling the competitive role of global modes in the pattern formation of rotating sphere flows. *Journal of Fluid Mechanics* **942**, A54.
- SPIESER, ETIENNE 2020 Modélisation de la propagation du bruit de jet par une méthode adjointe formulée pour l'acoustique potentielle. PhD thesis.
- TAM, CHRISTOPHER KW & AHUJA, KK 1990 Theoretical model of discrete tone generation by impinging jets. *Journal of Fluid Mechanics* **214**, 67–87.
- TAM, CHRISTOPHER KW & CHANDRAMOULI, SATHYANARAYAN 2020 Jet-plate interaction tones relevant to over-the-wing engine mount concept. *Journal of Sound and Vibration* **486**, 115378.
- TANAKA, DAN 2005 Bifurcation scenario to nikolaevskii turbulence in small systems. *Journal of the Physical Society of Japan* **74** (8), 2223–2225.
- TOWNE, AARON, CAVALIERI, ANDRÉ VG, JORDAN, PETER, COLONIUS, TIM, SCHMIDT, OLIVER, JAUNET, VINCENT & BRÈS, GUILLAUME A 2017 Acoustic resonance in the potential core of subsonic jets. *Journal of Fluid Mechanics* **825**, 1113–1152.
- VARÉ, MATHIEU & BOGEY, CHRISTOPHE 2022a Generation of acoustic tones in round jets at a mach number of 0.9 impinging on a plate with and without a hole. *Journal of Fluid Mechanics* **936**.
- VARÉ, MATHIEU & BOGEY, CHRISTOPHE 2022b Mach number dependence of tone generation in impinging round jets. In *28th AIAA/CEAS Aeroacoustics 2022 Conference*, p. 2866.
- WAGNER, FR 1971 *The sound and flow field of an axially symmetric free jet upon impact on a wall*. National Aeronautics and Space Administration.

CHAPTER **VII**

**Articles – A fixed-point
method for limit cycles**



Adjoint-based sensitivity analysis of periodic orbits by the Fourier–Galerkin method



J. Sierra^{a,b}, P. Jolivet^c, F. Giannetti^{b,*}, V. Citro^b

^a Institut de mécanique des fluides de Toulouse (IMFT), Toulouse 31400, France

^b Dipartimento di Ingegneria (DIIN), Università degli Studi di Salerno, Fisciano 84084, Italy

^c CNRS-IRIT, 2 rue Charles Camichel, 31071 Toulouse Cedex 7, France

ARTICLE INFO

Article history:

Available online 13 May 2021

Keywords:

Sensitivity
Fourier–Galerkin method
Floquet stability analysis
Unstable periodic orbits

ABSTRACT

Sensitivity of periodic solutions of time-dependent partial differential equations is commonly computed using time-consuming direct and adjoint time integrations. Particular attention must be provided to the periodicity condition in order to obtain accurate results. Furthermore, stabilization techniques are required if the orbit is unstable. The present article aims to propose an alternative methodology to evaluate the sensitivity of periodic flows via the Fourier–Galerkin method. Unstable periodic orbits are directly computed and continued without any stabilizing technique. The stability of the periodic state is determined via Hill's method: the frequency-domain counterpart of Floquet analysis. Sensitivity maps, used for open-loop control and physical instability identification, are directly evaluated using the adjoint of the projected operator. Furthermore, we propose an efficient and robust iterative algorithm for the resolution of underlying linear systems. First of all, the new approach is applied on the Feigenbaum route to chaos in the Lorenz system. Second, the transition to a three-dimensional state in the periodic vortex-shedding past a circular cylinder is investigated. Such a flow case allows the validation of the sensitivity approach by a systematic comparison with previous results presented in the literature. Finally, the transition to a quasi-periodic state past two side-by-side cylinders is considered. These last two cases also served to test the performance of the proposed iterative algorithm.

© 2021 Elsevier Inc. All rights reserved.

1. Introduction

Steady and periodic states of continuous and discrete dynamical systems are the two simplest cases of invariant sets which are of fundamental importance to characterize dynamics and to design efficient control strategies. Limit cycles may be found in almost every field of physics and applied mathematics. Some complex structures of the phase space, such as invariant tori or some strange attractors, may be preceded by a stable periodic solution. The continuation of these periodic solutions beyond their domain of stability may help unravel some stochastic properties of these complex organizations, i.e., Lyapunov exponents, entropy, natural measure, etc., cf. Cvitanovic [1]. Stability and sensitivity calculations require robust and efficient numerical algorithms for their computation. Concerning uniquely the computation of the periodic orbits there exist two groups of methods: *local methods* which aim to determine a point of the periodic orbit and which is set as the

* Corresponding author.

E-mail address: fgiannetti@unisa.it (F. Giannetti).

initial value for further integration, and *global methods* that aim to reconstruct the whole solution without time integration. Among local methods, one may find the direct integration of the governing equations and the shooting technique. The latter minimizes the distance to the periodic orbit via an iterative procedure, which leads to an improvement on the convergence rate with respect to the simple time integration. These methods, without further modifications, however, fail to compute unstable periodic orbits (UPO) and, in some cases, they are characterized by a low convergence rate. Some of the stabilization techniques applied to UPO are the recursive projection method (RPM) [2] or the residual recombination approach (BoostConv) [3]. Global methods, on the other hand, seek for direct representation of the sought solution on a given basis in a weighted residual approach. In this way, one may distinguish among trigonometric or orthogonal collocation, whose weight basis is composed of Dirac delta functions and its ansatz is either a Fourier or polynomial basis respectively, and Fourier–Galerkin or harmonic balance, whose weight and ansatz basis is composed of Fourier functions. Collocation methods are common in numerical continuation tools, such as AUTO [4] and MatCont [5,6], due to their robustness and generality. They are able to compute not only periodic solutions but also homoclinic or heteroclinic connections. Fourier–Galerkin uses trigonometric base functions as ansatz as well as weight functions. Fourier base functions possess interesting properties: they are by definition periodic, easy to compute, and provide rapid convergence whenever the solution is smooth.

Similarly, the stability of periodic orbits may be carried out in a local or global manner. In the local approach, the computation of Floquet multipliers is realized by a power iteration or Arnoldi algorithm via a matrix-free approach which reconstructs a faithful projection of the monodromy matrix. On the contrary, global methods directly reconstruct the monodromy matrix, either in the time or frequency domain, which generally allows more accurate results with faster convergence. The algorithm for the evaluation of sensitivity quantities is composed of two main building blocks: computation of a periodic solution and resolution of its direct and adjoint linear stability problems. Accordingly, efficient and simpler numerical techniques for the resolution of both problems imply faster and easier evaluations of sensitivity quantities. Such a constraint leads us to discard local methods due to their slow rate of convergence towards the periodic state. Furthermore, given that the nature of the orbit is periodic, every sensitivity equation shall also be. The periodicity requirement is critical in the calculation of accurate sensitivity maps, such as those computed by Giannetti et al. [7]. Therefore, a methodology that respects such a constraint seems a natural choice. The present study presents in a systematic manner the computation of stability and sensitivity of periodic solutions of discretizations of PDEs (resp. solutions to a system of ODE) via the Fourier–Galerkin method where the determination of its stability is carried out by Floquet or Hill’s theory. Authors follow the new framework developed by Giannetti et al. [8] to investigate the sensitivity of periodic orbits. Giannetti et al. [8] studied the sensitivity of the three-dimensional secondary instability of the wake to a structural perturbation of the associated linear equations. The region of maximum coupling between the velocity components was found using the most unstable Floquet mode and its adjoint mode. The authors reported also the variation of this region in time by considering a structural perturbation that is impulsively applied in time at a given phase of the vortex-shedding process. The present approach can be considered an efficient and effective approximation of the framework proposed in Giannetti et al. [8,7].

The text is structured as follows: first, the methodology for the computation of a periodic orbit and the evaluation of its stability is introduced in section 2. The Fourier–Galerkin method is introduced in section 2.1 and section 2.2 is dedicated to the evolution equations with quadratic nonlinearities, e.g., Lorenz-like systems or Navier–Stokes equations. Floquet stability is reviewed in a general context in section 2.3, which is then particularized to the frequency domain in section 2.4. Sensitivity computations are later introduced in section 2.5. Section 2.6 addresses the numerical solution of the large algebraic systems in a parallel context via iterative methods. Finally, the study is concluded by some numerical examples. At first, we show the ability of the present methodology to track the route to chaos via period-doubling in the Lorenz system. Sections 3.2 and 3.3 are then dedicated to two fluid flow cases to discuss the performance of the methodology and to demonstrate the utility of sensitivity maps in the identification of physical instability mechanisms.

2. Methodology

2.1. Periodic boundary value problem

Let us start with a generic autonomous class of evolution equations of the form:

$$\mathbf{B} \frac{\partial \mathbf{q}}{\partial t} = \mathbf{F}(\mathbf{q}, \nu), \quad \mathbf{q}(t + T) = \mathbf{q}(t), \quad (1)$$

where \mathbf{B} is a linear operator, \mathbf{F} is a nonlinear operator on a Hilbert space X with inner product $\langle \cdot, \cdot \rangle$, and $\nu \in \mathbb{R}^p$ the set of parameters. In this way, both differential algebraic problems (DAE) and evolutionary partial differential equations (PDE) are included. Natural Hilbert spaces for the infinite-dimensional case are Sobolev spaces, see Kapitula and Promislow [9], whereas in finite dimensions we will generally consider \mathbb{R}^n . In the following, we assume that the nonlinear operator \mathbf{F} is of quadratic type, i.e., $\mathbf{F}(\mathbf{q}) = \mathbf{L}\mathbf{q} + \mathbf{N}(\mathbf{q}, \mathbf{q})$, where \mathbf{L} and $\mathbf{N}(\cdot, \cdot)$ are linear and quadratic nonlinear operators, respectively. This choice will be clear later in section 2.2, however note that many analytical functions can be recast in this way, see Guillot et al. [10].

2.2. The Fourier–Galerkin method for periodic boundary problems

The solution of eq. (1) is T -periodic. Therefore, it seems a natural choice to parametrize any T -periodic orbit \mathbf{q}^* , in a $t \bmod T$ basis, i.e., a Fourier basis. For that purpose, let us consider the Fourier–Galerkin method, also denoted harmonic balance (HB) in the literature, cf. [11,12]. Fourier–Galerkin can be seen as a weighted residual approach for a periodic ansatz and weight functions. Fourier base functions present the advantage of being easy to compute and provide fast convergence in smooth cases.

We start our analysis by introducing the Fourier–Galerkin projection operator π_N onto the Fourier basis as follows:

$$\begin{aligned} \pi_N : X \times \mathbb{R} &\rightarrow X \times (\mathbb{Z}/(2N+1)\mathbb{Z}) \\ \pi_N(\mathbf{q}) = \mathbf{q}_h(t) &= \mathbf{q}_0 + \sum_{n=1}^N [\mathbf{q}_{c,n} \cos(n\omega t) + \mathbf{q}_{s,n} \sin(n\omega t)] \\ &= \underbrace{[\mathbf{q}_0, \mathbf{q}_{1,c}, \mathbf{q}_{1,s}, \dots, \mathbf{q}_{N,c}, \mathbf{q}_{N,s}]}_{(\mathbf{Q}^{(\tau,N)})^T} \underbrace{[1, \cos(\omega t), \sin(\omega t), \dots, \cos(N\omega t), \sin(N\omega t)]}_{\mathcal{F}_N}, \end{aligned} \quad (2)$$

where $\mathbf{Q}^{(\tau,N)}$ are the $2N+1$ Fourier coefficients of the approximated solution \mathbf{q}_h and \mathcal{F}_N is the Fourier basis in sine/cosine components. The ansatz $\mathbf{q}_h(t)$ and its derivative are smooth T -periodic functions.

The residual is defined as the difference between the nonlinear and the time-derivative term, which is expressed as follows:

$$\begin{aligned} \mathbf{r} : X \times \mathbb{R} &\rightarrow X \times \mathbb{R} \\ \mathbf{r}(\mathbf{q}, \frac{\partial \mathbf{q}}{\partial t}, t) &= \mathbf{B} \frac{\partial \mathbf{q}}{\partial t} - \mathbf{F}(\mathbf{q}). \end{aligned} \quad (3)$$

Following the Fourier–Galerkin or Bubnov–Galerkin method in the Fourier basis, the governing equations of HB are obtained by integrating the truncated residual equations weighted by the Fourier basis over a period $T = \frac{2\pi}{\omega}$. The obtained residual is called the *truncated residual*:

$$\begin{aligned} \hat{\mathbf{r}}_h : X \times (\mathbb{Z}/(2N+1)\mathbb{Z}) &\rightarrow X \times (\mathbb{Z}/(2N+1)\mathbb{Z}) \\ \hat{\mathbf{r}}_h(\mathbf{Q}_N, \omega) &= \int_0^{\frac{2\pi}{\omega}} \mathbf{r}_h(\mathbf{q}_h, \frac{\partial \mathbf{q}_h}{\partial t}, t)^T \mathcal{F}_N dt = \mathbf{0}, \end{aligned} \quad (4)$$

where

$$\mathbf{r}_h(\mathbf{q}_h, \frac{\partial \mathbf{q}_h}{\partial t}, t) = \mathbf{B} \frac{\partial \mathbf{q}_h}{\partial t} - \mathbf{F}(\mathbf{q}_h). \quad (5)$$

Equation (5) provides $2N+1$ equations for $2N+2$ unknowns in the autonomous case. Autonomous systems present a continuous symmetry, i.e., $\mathbf{q}(t + \xi)$ is also a periodic solution with an arbitrary ξ phase. The phase of the limit cycle remains to be fixed. This is usually done by imposing a condition at $t = 0$, i.e., $g(\mathbf{q}, \frac{\partial \mathbf{q}}{\partial t}, 0) = 0$ or an orthogonality condition $\int_0^T \mathbf{F}(\mathbf{q}_h)^T \mathbf{q}_h dt = 0$. Equation (5) corresponds to balancing each harmonic individually, that is to have null Fourier coefficients of the truncated residual.

Fourier–Galerkin equations So far, the procedure to obtain a periodic orbit remains general. Now, without loss of generality, we shall consider the case where the nonlinear flow is of quadratic type. This constraint is far from being restrictive since many evolution problems can be recasted in this form, see Cochelin et al. [13] for the finite-dimensional case. Under these assumptions, eq. (5) takes the form:

$$\begin{aligned} \mathbf{0} &= \mathbf{L}\mathbf{q}_0 + \mathbf{N}_0 \\ n\omega \mathbf{B}\mathbf{q}_{n,s} &= \mathbf{L}\mathbf{q}_{n,c} + \mathbf{N}_{n,c}, \quad n = 1, \dots, N \\ -n\omega \mathbf{B}\mathbf{q}_{n,c} &= \mathbf{L}\mathbf{q}_{n,s} + \mathbf{N}_{n,s}, \quad n = 1, \dots, N \\ g_h(\mathbf{q}_h) &= 0. \end{aligned} \quad (6)$$

For the sake of brevity, Fourier coefficients \mathbf{N}_i are not developed as functions of $\mathbf{Q}^{(\tau,N)}$, see appendix A for an explicit description of these terms. Formally, eq. (6) will be denoted as:

$$\mathbf{0} = -\omega \tilde{\mathbf{B}}\mathbf{Q}^{(\tau,N)} + \tilde{\mathbf{L}}\mathbf{Q}^{(\tau,N)} + \tilde{\mathbf{N}}(\mathbf{Q}^{(\tau,N)}, \mathbf{Q}^{(\tau,N)}) = \tilde{\mathbf{r}}(\mathbf{Q}^{(\tau,N)}), \quad (7)$$

where operators $\tilde{\mathbf{B}}$, $\tilde{\mathbf{L}}$, and $\tilde{\mathbf{N}}(\cdot, \cdot)$ are detailed in appendix A and it is assumed that the phase of the limit cycle has been fixed.

Remark 1. It is here highlighted that if one desires to compute a $2T$ -periodic solution $\tilde{\mathbf{q}}^*$, since a $2T$ -periodic solution is also T -periodic, the current strategy requires some modifications. The methodology is adapted by doubling the number of harmonics to $2N$: the odd harmonics of the initial guess coincide with those of the T -periodic solution, and even modes are initialized to zero or to the Floquet mode associated with a period-doubling bifurcation, see section 2.4.

Finally, we briefly recall that Stokes [14] provided a dedicated theorem about the convergence of eq. (7). In particular, if the exact problem eq. (1) possesses a solution \mathbf{q}^* of period $T = \frac{2\pi}{\omega}$, then the solution $[\mathbf{Q}^{\tau, N}, \omega^{\tau, N}]$ of the system eq. (7), for sufficiently large N , converges to the exact solution \mathbf{q}^* if the monodromy matrix possesses a unique Floquet multiplier of multiplicity one.

Remark 2. In the original work of Stokes [14], where the theorem was originally proved, the main hypothesis was the *non-criticality* of the periodic solution, i.e., the periodic orbit is isolated in the phase space: the neutral Floquet multiplier is of multiplicity one.

2.3. Floquet-time stability theory

In this section, the Floquet theory of finite-dimensional systems in \mathbb{R}^N is addressed. Unfortunately, there does not exist a general theory for time-periodic PDEs but some particular cases have been already tackled, see parabolic and hyperbolic evolution problems in Kuchement [15, Chapter 5] and references therein. For the sake of self-consistency, let us introduce a set of classical definitions in the study of dynamical systems.

For the sake of self-consistency, let us introduce a set of classical definitions in the study of dynamical systems.

Let $t \rightarrow \mathbf{q}^*(t)$ be a T -periodic solution of eq. (1) for a given set of parameters $\nu^* \in \mathbb{R}^p$. The associated flow of eq. (1) is denoted by $\varphi(t; \mathbf{q}_0)$, which solves $\mathbf{B} \frac{\partial \mathbf{q}}{\partial t} = \mathbf{F}(\mathbf{q}, \nu)$ with $\mathbf{q}(0) = \mathbf{q}_0$.

Furthermore, we consider a codimension one hypersurface S , chosen in such a way that every trajectory that crosses S in a neighborhood of the intersection point $\mathbf{o} \in S$ of the periodic orbit with the surface S intersects transversally and in the same direction, see Kuznetsov [16]. Such a section S is denoted as *Poincaré section*. Thanks to the Poincaré section, let us define the *Poincaré map* or *return map* $\mathbf{P}(\mathbf{o})$:

$$\mathbf{P}(\mathbf{o}) := \mathbf{P}_S(\mathbf{o}) = \varphi(T_S(\mathbf{o}); \mathbf{o}), \tag{8}$$

where $T_S(\mathbf{o})$ is the return time and it coincides with the period T of the periodic orbit when \mathbf{o}^* is a fixed point, i.e., $\mathbf{o}^* = \mathbf{P}(\mathbf{o}^*)$:

$$\mathbf{o} \xrightarrow[\mathbf{q} \rightarrow \mathbf{q}^*]{} \mathbf{o}^* \text{ implies } T_S(\mathbf{o}) \rightarrow T.$$

The linear stability of the T -periodic orbit $\mathbf{q}^*(t)$ can be studied by checking the evolution of the perturbed distance $\delta \mathbf{q}(t)$ to the T -periodic orbit \mathbf{q}^* :

$$\delta \mathbf{q}(t) = \varphi(t; \mathbf{q}^* + \delta \mathbf{q}_0) - \varphi(t; \mathbf{q}^*), \quad \text{with } \delta \mathbf{q}(0) = \delta \mathbf{q}_0. \tag{9}$$

Measuring the distance after a period yields:

$$\delta \mathbf{q}(T) = \varphi(T; \mathbf{q}^* + \delta \mathbf{q}_0) - \varphi(T; \mathbf{q}^*) = \frac{\partial \varphi(T; \mathbf{q}^*)}{\partial \mathbf{q}} \delta \mathbf{q}_0 + O(\|\delta \mathbf{q}_0\|^2), \tag{10}$$

where in the last expression appears the *monodromy matrix* $\frac{\partial \varphi(T; \mathbf{q}^*)}{\partial \mathbf{q}}$. To find another representation of the monodromy matrix, consider the following evolution equation:

$$\mathbf{B} \frac{\partial}{\partial t} \frac{\partial \varphi(t; \mathbf{q}^*)}{\partial \mathbf{q}} = \frac{\partial \mathbf{F}(\varphi, \lambda^*)}{\partial \varphi} \frac{\partial \varphi(t; \mathbf{q}^*)}{\partial \mathbf{q}}, \quad \frac{\partial \varphi(0; \mathbf{q}^*)}{\partial \mathbf{q}} = \mathbf{I}. \tag{11}$$

Consequently, the monodromy matrix will be denoted by $\Phi(T) = \frac{\partial \varphi(T; \mathbf{q}^*)}{\partial \mathbf{q}}$, where the *fundamental solution matrix* $\Phi(t) \in \mathcal{M}(\mathbb{R})^{N \times N}$ satisfies the following matrix initial-value problem:

$$\mathbf{B} \frac{\partial \Phi}{\partial t} = \frac{\partial \mathbf{F}}{\partial \mathbf{q}}(\mathbf{q}^*, \lambda^*) \Phi, \quad \Phi(0) = \mathbf{I}. \tag{12}$$

The spectrum of the monodromy matrix is composed of an eigenvalue $\mu = 1$, due to the translation invariance of the periodic orbit and another set of $N - 1$ eigenvalues. Due to the definition of the Poincaré map, it is not difficult to observe that the other $N - 1$ eigenvalues of the Jacobian operator coincide with those of the derivative of the Poincaré map $D\mathbf{P}(\mathbf{o}^*)$, see the book of Seydel [17] and references therein for a proof.

Thanks to Floquet's theorem, the perturbation $\delta\mathbf{q}(t)$ is written as:

$$\delta\mathbf{q}(t) = \sum_{n=1}^N c_n \delta\mathbf{q}_n(t),$$

where *fundamental solutions* $\delta\mathbf{q}_n$ can be rewritten in the Floquet's normal form:

$$\delta\mathbf{q}_n(t) = e^{\lambda_n t} \mathbf{p}_n(t), \tag{13}$$

where \mathbf{p}_n is a T -periodic vector and λ_n are called the *Floquet exponents*. They are related to the eigenvalues μ_n of the monodromy matrix, also called *Floquet multipliers*, by the following relation: $\lambda_n = \frac{\log(\mu_n)}{T} + ik\omega$ for $k \in \mathbb{Z}$. To see this relation, consider linear independence of fundamental solutions and let us substitute the Floquet's normal form into eq. (10). Then, we are left with the following expression:

$$\mu_n \mathbf{p}_n(0) = \frac{\partial \varphi(T; \mathbf{q}^*)}{\partial \mathbf{q}} \mathbf{p}_n(0) \iff \lambda_n \mathbf{B} \mathbf{p}_n = \left[-\mathbf{B} \frac{\partial}{\partial t} + \frac{\partial \mathbf{F}(\mathbf{q}^*, \lambda)}{\partial \mathbf{q}} \right] \mathbf{p}_n. \tag{14}$$

2.4. Hill's method

In section 2.3, we have carried out a brief review of the stability of periodic orbits. Here, we aim to determine an efficient algorithm for the solution of the Floquet stability eq. (14). Prior to the discussion of the algorithm, please note the following analogy between the HBM parametrization of the autonomous problem eq. (1) and the Poincaré map, introduced in eq. (8). Phase condition may be interpreted as the parametrization of a codimension one hypersurface. Then, the T -periodic solution \mathbf{q}_h^* taken at nT instants, $n \in \mathbb{N}$, is a fixed point of the Poincaré map. As discussed in section 2.3, eigenvalues of the derivative of the Poincaré map determine the stability of the periodic orbit, and these arise as a subproduct of the computation of the periodic orbit.

Nevertheless, this procedure to determine the Floquet stability would break the continuous symmetry, i.e., the phase is fixed, then the neutral Floquet multiplier, i.e., $\mu = 1$, would not be in the spectrum set. Therefore, in practice, the phase condition is left in the stability study.

The Fourier–Galerkin form of Floquet stability eq. (14) consists in the projection onto the finite Fourier space $X \times (\mathbb{Z}/(2N+1)\mathbb{Z})$, i.e., on a finite Fourier series.

The Floquet stability problem in the Fourier–Galerkin basis can be formally expressed with the following generalized eigenvalue problem:

$$\begin{aligned} \lambda^{(\tau, N)} \text{diag}(\mathbf{B})_{2N+1} \mathbf{P}^{(\tau, N)} &= D\tilde{\mathbf{r}}(\mathbf{Q}^{(\tau, N)}) \mathbf{P}^{(\tau, N)} \\ \text{where } D\tilde{\mathbf{r}}(\mathbf{Q}^{(\tau, N)}) \mathbf{P}^{(\tau, N)} &= \left[-\omega \tilde{\mathbf{B}} + \tilde{\mathbf{L}} + D\tilde{\mathbf{N}}(\mathbf{Q}^{(\tau, N)}) \right] \mathbf{P}^{(\tau, N)}, \end{aligned} \tag{15}$$

where $\mathbf{P}^{(\tau, N)} = [\mathbf{p}_0, \mathbf{p}_{1,c}, \mathbf{p}_{1,s}, \dots, \mathbf{p}_{N,c}, \mathbf{p}_{N,s}]^T$ is the finite Fourier decomposition of the periodic eigenvector $\mathbf{p}(t)$ and $\lambda^{(\tau, N)}$ is the approximation of the Floquet exponent defined eq. (13).

Please note that the explicit definition of the derivative of the residual operator $D\tilde{\mathbf{r}}(\mathbf{Q}^{(\tau, N)})$ can be found in appendix A.

As depicted in Fig. 1, Floquet exponents are not unique in the complex field \mathbb{C} , nevertheless they are in $\mathbb{C}/i\omega\mathbb{R}$. Let us consider the finite-dimensional case, i.e., $\mathbf{q}^* \in \mathbb{R}^n$. In such a case, the Floquet spectrum is of dimension n , i.e., there are n eigenvalues in $\mathbb{C}/i\omega\mathbb{R}$. Nonetheless, the dimension of the Floquet HBM problem is $(2N+1)n$, there are $2N+1$ in the same conjugacy class, i.e., $\lambda_k^\tau = \lambda_0^\tau + ik\omega$, $k \in \mathbb{Z}$, where λ_0^τ is the eigenvalue closest to the real axis in the complex plane. This remark motivates the definition of the *truncated spectra* Λ_N : this set of converged eigenvalues is a compact set in \mathbb{C} restricted to the strip $C_\omega \equiv \{z \in \mathbb{C} : \omega/2 \leq \text{Im}(z) \leq \omega/2\}$ (Fig. 2).

Notes on the convergence of the truncated spectra Since eq. (15) is a spectral approximation of the continuous problem eq. (10), an important aspect of the methodology is whether or not the eigenvalue λ and the eigenvector \mathbf{P}_N converge to the actual eigenvalue and eigenmode respectively. Zhou et al. [18] have partially answered this query. They proved the convergence of the truncated problem in the strip $C_\omega \equiv \{z \in \mathbb{C} : \omega/2 \leq \text{Im}(z) \leq \omega/2\}$ under the assumption that the nonlinear flow $\mathbf{F}(\mathbf{q}, \nu)$ is piecewise $C^1[0, T]$. Likewise, Deconick et al. [19] proved the convergence of Hill's method in the Floquet–Bloch theory, i.e., periodicity in space, for compact subsets of \mathbb{C} . They proved the absence of spurious eigenvalues, i.e., an eigenvalue λ_n which does not converge to any eigenvalue λ of the problem eq. (14) as the number of harmonics $N \rightarrow \infty$. In the same reference, one may find for self-adjoint operators that for any eigenvalue λ of the monodromy operator, there exists a sequence $\{\lambda_N\}_{N=1}^\infty$ such that $\lim_{N \rightarrow \infty} |\lambda_N - \lambda| \rightarrow 0$ and with a spectral rate of convergence, i.e., $|\lambda_N - \lambda| = O(N^{-p})$ for $p \geq 1$, which has been later extended for a larger family of periodic differential operators by Jonshon et al. [20].

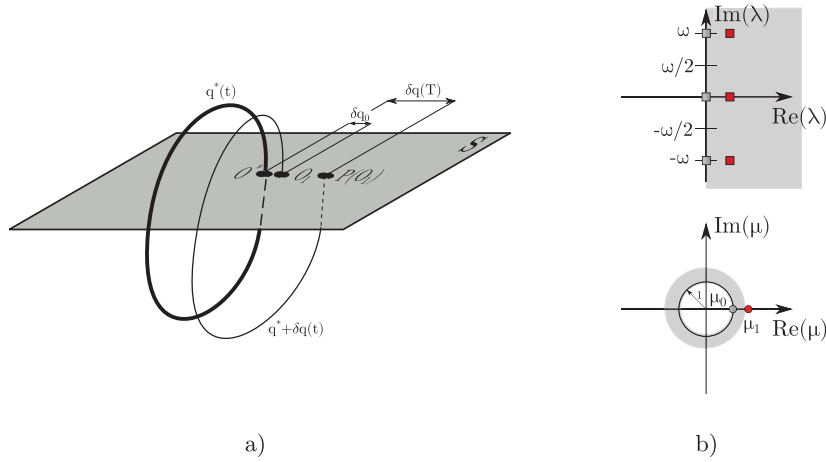


Fig. 1. a) An unstable periodic orbit q^* crossing the Poincaré section at point o^* , and the evolution perturbed orbit $q^* + \delta q(t)$ from the point o_1 . b) Floquet spectrum in terms of Floquet multipliers μ_n (resp. Floquet exponents λ_n on top figure) of an unstable periodic orbit q^* . Red dots (square on the top figure) are associated to the unstable fundamental solution $\delta q_1(t)$ whereas gray markers denote the neutral Floquet eigenvalue. (For interpretation of the colors in the figure(s), the reader is referred to the web version of this article.)

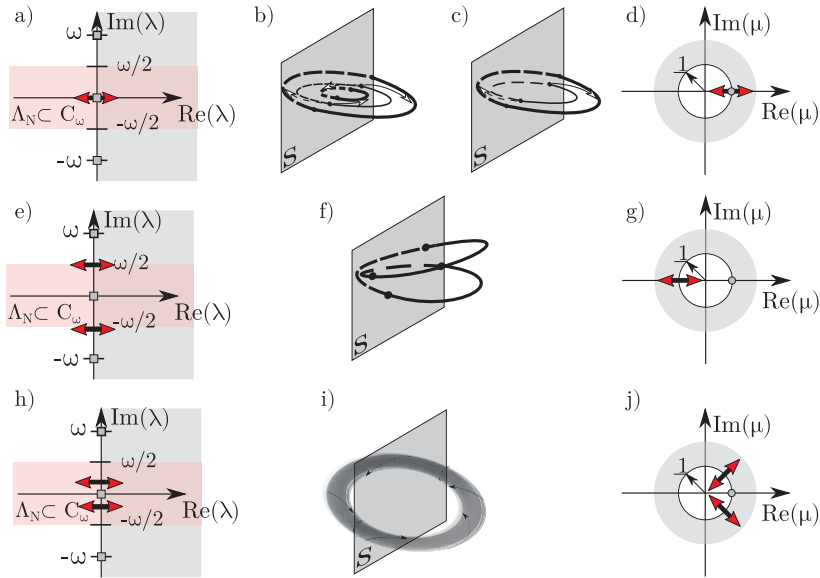


Fig. 2. Local bifurcations of codimension one of periodic orbits. Spectrum in terms of Floquet exponents a), e), and h). Spectrum in terms of Floquet multipliers d), g), and j). Pitchfork bifurcation in a), b), and d). Fold bifurcation in a), c), and d). Period-doubling bifurcation in e), f), and g). Neimark-Sacker in h), i), and j).

Finally, let us contemplate other choices for the selection of the set of converged eigenvalues. Bentvelsen et al. [21] compared different sorting algorithms to determine the set of converged eigenvalues and eigenmodes. They employed a sorting algorithm between elements in the same conjugacy class, i.e., $\lambda_n = \lambda_j + ik\omega$. Numerical experiments reported a faster numerical strategy to produce a set of converged eigenvalues, but such an approach is not yet rigorously justified. Such a sorting algorithm seems to be the preferred strategy for mechanical systems, see Lazarus et al. [22] and Guillot et al. [23].

For convenience, we introduce also the Floquet adjoint stability problem with respect to the natural inner product in the Fourier–Galerkin basis:

$$\bar{\lambda}^{(\tau, N)} \text{diag}(\mathbf{B})_{2N+1} \mathbf{P}^\dagger(\tau, N) = D\tilde{\mathbf{r}}^T(\mathbf{Q}(\tau, N)) \mathbf{P}^\dagger(\tau, N) \tag{16}$$

$$\text{where } D\tilde{\mathbf{r}}^T(\mathbf{Q}(\tau, N)) \mathbf{P}^\dagger(\tau, N) = \left[-\omega \tilde{\mathbf{B}}^T + \tilde{\mathbf{L}}^T + D\tilde{\mathbf{N}}^T(\mathbf{Q}(\tau, N)) \right] \mathbf{P}^\dagger(\tau, N),$$

where $\mathbf{P}^\dagger(\tau, N) = [\mathbf{p}_0, \mathbf{p}_{1,c}^\dagger, \mathbf{p}_{1,s}^\dagger, \dots, \mathbf{p}_{N,c}^\dagger, \mathbf{p}_{N,s}^\dagger]^T$ is the finite Fourier decomposition of the periodic adjoint eigenvector $\mathbf{p}^\dagger(t)$ and the conjugate eigenvalue $\bar{\lambda}^{(\tau, N)}$ is the approximation of the adjoint Floquet exponent.

2.5. Sensitivity analysis for periodic orbits

This section is an introduction to sensitivity computations near a bifurcation point of the periodic solution. Among possible applications to sensitivity theory, one may find passive control or identification of underlying physical mechanisms leading to the instability.

Let us consider the infinitesimal perturbed problem of eq. (1) with respect to the state variable \mathbf{q} :

$$\mathbf{B} \frac{\partial(\mathbf{q}^* + \delta\mathbf{q})}{\partial t} = \mathbf{F}(\mathbf{q}^* + \delta\mathbf{q}, \nu) + \delta\mathbf{H}(\mathbf{q}^* + \delta\mathbf{q}), \quad \mathbf{q}^*(t + T) = \mathbf{q}^*(t). \quad (17)$$

A force-feedback perturbation $\delta\mathbf{H}(\mathbf{q}^* + \delta\mathbf{q})$ leads to changes in dynamics. The original work of Giannetti et al. [8] analyzed the effect of a local force-feedback $\delta\mathbf{H}(\delta\mathbf{q})$. For that purpose, authors introduced the concept of *structural sensitivity* tensor \mathbf{S}_s to the secondary instability, i.e., a bifurcation of the Poincaré map associated with a T -periodic solution, which is the extension of the structural sensitivity tensor of bifurcations from a steady-state solution, introduced by Giannetti et al. [24]. The structural sensitivity measures the variation of a Floquet exponent $\delta\lambda$ with respect to variations of the Floquet mode $\delta\mathbf{p}$. In a second article, the same authors [7] introduced the sensitivity to variations in the periodic orbit \mathbf{q}^* itself. This tensor field is called *sensitivity to baseflow* variations, denoted as \mathbf{S}_b . Analogously to the structural sensitivity, the sensitivity to baseflow variations measures the effect of a localized force-feedback $\delta\mathbf{H}(\mathbf{q}^*)$. This leads to a variation in the Floquet exponent $\delta\lambda$ with respect to variations of the periodic solution $\delta\mathbf{q}^*$. \mathbf{S}_b is evaluated following a similar procedure to \mathbf{S}_s . Nonetheless, one must take special care to ensure the uniqueness of \mathbf{S}_b . Uniqueness is guaranteed by construction and the Fredholm alternative. For the sake of clarity, \mathbf{S}_b will not be rigorously introduced because it would lead to another set of definitions to overcome this technical issue, the interested reader is referred to [7].

Instead, we have decided to introduce another interesting sensitivity map \mathbf{S}_ω , the sensitivity map to frequency variations of the limit cycle, which measures the variation of the frequency (resp. period) of the periodic state with respect to the introduction of a localized feedback. Furthermore, in the present section, authors introduce the novel harmonic sensitivity map \mathbf{S}_s^n (resp. \mathbf{S}_ω^n), which measures the effect of a structural harmonic perturbation. This last set of maps provides new insights into the harmonic nature of the instability. Each sensitivity quantity is directly computed in the frequency domain.

Let us begin with the averaged structural sensitivity tensor $\bar{\mathbf{S}}_s$ of a Floquet exponent λ :

$$\bar{\mathbf{S}}_s(\mathbf{x}) = \frac{\int_t^{T+t} \mathbf{M}\mathbf{p} \otimes \mathbf{M}\mathbf{p}^\dagger dt}{\int_t^{T+t} \int_\Omega \mathbf{M}\mathbf{p} \cdot \mathbf{M}\mathbf{p}^\dagger dxdt}. \quad (18)$$

It is the operator whose contraction with a generic infinitesimal localized feedback operator (in space provides: $\delta\lambda = \mathbf{C}_1 : \bar{\mathbf{S}}_s(\mathbf{x}_0)$), where $\delta\mathbf{H}(\delta\mathbf{q}) = \delta(\mathbf{x} - \mathbf{x}_0)\mathbf{C}_1 \cdot \delta\mathbf{q}$, where $\delta(\mathbf{x} - \mathbf{x}_0)$ is the Dirac distribution at $\mathbf{x} - \mathbf{x}_0$ and \mathbf{C}_1 is a generic constant feedback matrix. In the sensitivity paradigm, it is also helpful to consider phase details of the structural sensitivity which are retrieved by considering impulsive structural perturbations applied in time at a precise phase of the periodic solution, i.e., at $t = t_0$. This consideration leads to the instantaneous structural sensitivity \mathbf{S}_s :

$$\mathbf{S}_s(\mathbf{x}, t) = \frac{\mathbf{M}\mathbf{p} \otimes \mathbf{M}\mathbf{p}^\dagger}{\int_t^{T+t} \int_\Omega \mathbf{M}\mathbf{p} \cdot \mathbf{M}\mathbf{p}^\dagger dxdt}. \quad (19)$$

In such a case, the variation of the Floquet exponent $\delta\lambda = \mathbf{C}_1 : \mathbf{S}_s(\mathbf{x}_0, t_0)$, where $\delta\mathbf{H}(\delta\mathbf{q}) = \delta((t \bmod T) - t_0)\delta(\mathbf{x} - \mathbf{x}_0)\mathbf{C}_1 \cdot \delta\mathbf{q}$, provides access to the phase. However, it fails to determine the harmonic nature of the instability. For such considerations, it is helpful to introduce a novel sensitivity map, the harmonic structural sensitivity \mathbf{S}_s^n , where n indicates the harmonic number. The direct computation of the frequency spectra \mathbf{S}_s^n is in general complex-valued. However, for the sake of self-consistency with the previous methodology, $\mathbf{S}_s^{n,(s/c)}$ is the real harmonic structural sensitivity:

$$\begin{aligned} \mathbf{S}_s^{n,c}(\mathbf{x}) &= \frac{2}{T} \frac{\int_t^{T+t} \mathbf{M}\mathbf{p} \otimes \mathbf{M}\mathbf{p}^\dagger \cos(n\omega t) dt}{\int_t^{T+t} \int_\Omega \mathbf{M}\mathbf{p} \cdot \mathbf{M}\mathbf{p}^\dagger dxdt} \\ \mathbf{S}_s^{n,s}(\mathbf{x}) &= \frac{2}{T} \frac{\int_t^{T+t} \mathbf{M}\mathbf{p} \otimes \mathbf{M}\mathbf{p}^\dagger \sin(n\omega t) dt}{\int_t^{T+t} \int_\Omega \mathbf{M}\mathbf{p} \cdot \mathbf{M}\mathbf{p}^\dagger dxdt}, \end{aligned} \quad (20)$$

where the structural perturbation $\delta\mathbf{H}(\delta\mathbf{q}) = \frac{2}{T} \cos(n\omega t)\delta(\mathbf{x} - \mathbf{x}_0)\mathbf{C}_1 \cdot \delta\mathbf{q}$ (resp. $\sin(n\omega t)$) provides a variation of the Floquet exponent $\delta\lambda = \mathbf{C}_1 : \mathbf{S}_s^{n,c}(\mathbf{x}_0)$ (resp. $\mathbf{S}_s^{n,s}(\mathbf{x}_0)$) due to a harmonic perturbation. The $\frac{2}{T}$ term is simply a normalization factor.

Remark 3. In the original work of Giannetti et al. [8], $\mathbf{M} = \mathbf{B}$. The inclusion of the matrix \mathbf{M} in the definition of the structural sensitivity was done to consider a particular set of variables instead of the whole set of variables. We highlight that definition eqs. (18) to (20) are valid for PDEs. Finite-dimensional systems do not depend on spatial coordinates. Therefore, there is no need to introduce a localized feedback force, i.e., $\delta\mathbf{H}(\delta\mathbf{q}) = \mathbf{C}_1 \cdot \delta\mathbf{q}$.

The averaged structural sensitivity $\bar{S}_s^{(\tau,N)}$ associated to the Floquet exponent $\lambda^{(\tau,N)}$ in the Fourier–Galerkin basis can be expressed as:

$$\bar{S}_s^{(\tau,N)}(\mathbf{x}) = \frac{\mathbf{M}\mathbf{p}_0 \otimes \mathbf{M}\mathbf{p}_0^\dagger + \frac{1}{2} \sum_{n=1}^N \mathbf{M}\mathbf{p}_{n,c} \otimes \mathbf{M}\mathbf{p}_{n,c}^\dagger + \mathbf{M}\mathbf{p}_{n,s} \otimes \mathbf{M}\mathbf{p}_{n,s}^\dagger}{\int_{\Omega} \mathbf{M}\mathbf{p}_0 \cdot \mathbf{M}\mathbf{p}_0^\dagger + \frac{1}{2} \sum_{n=1}^N \mathbf{M}\mathbf{p}_{n,c} \cdot \mathbf{M}\mathbf{p}_{n,c}^\dagger + \mathbf{M}\mathbf{p}_{n,s} \cdot \mathbf{M}\mathbf{p}_{n,s}^\dagger dx} \quad (21)$$

Analogously, harmonic components may be written as:

$$\begin{aligned} S_s^{n,c;(\tau,N)}(\mathbf{x}) &= \frac{2}{T \int_t^{T+t} \int_{\Omega} \mathbf{M}\mathbf{p} \cdot \mathbf{M}\mathbf{p}^\dagger dx dt} \left([\mathbf{M}\mathbf{p}_{i,c} \otimes \mathbf{M}\mathbf{p}_0^\dagger + \mathbf{M}\mathbf{p}_0 \otimes \mathbf{M}\mathbf{p}_{i,c}^\dagger] \right. \\ &\quad + \frac{1}{2} \sum_{j=1}^{i-1} [\mathbf{M}\mathbf{p}_{i,c} \otimes \mathbf{M}\mathbf{p}_{i-j,c}^\dagger - \mathbf{M}\mathbf{p}_{j,s} \otimes \mathbf{M}\mathbf{p}_{i-j,s}^\dagger] \\ &\quad + \frac{1}{2} \sum_{j=i+1}^N [\mathbf{M}\mathbf{p}_{j,c} \otimes \mathbf{M}\mathbf{p}_{j-i,c}^\dagger + \mathbf{M}\mathbf{p}_{j-i,s} \otimes \mathbf{M}\mathbf{p}_{j,s}^\dagger] \\ &\quad \left. + \frac{1}{2} \sum_{j=i+1}^N [\mathbf{M}\mathbf{p}_{j-i,c} \otimes \mathbf{M}\mathbf{p}_{j,c}^\dagger + \mathbf{M}\mathbf{p}_{j,s} \otimes \mathbf{M}\mathbf{p}_{j-i,s}^\dagger] \right) \\ S_s^{n,s;(\tau,N)}(\mathbf{x}) &= \frac{2}{T \int_t^{T+t} \int_{\Omega} \mathbf{M}\mathbf{p} \cdot \mathbf{M}\mathbf{p}^\dagger dx dt} \left([\mathbf{M}\mathbf{p}_{i,s} \otimes \mathbf{M}\mathbf{p}_0^\dagger + \mathbf{M}\mathbf{p}_0 \otimes \mathbf{M}\mathbf{p}_{i,s}^\dagger] \right. \\ &\quad + \frac{1}{2} \sum_{j=1}^{i-1} [\mathbf{M}\mathbf{p}_{i,c} \otimes \mathbf{M}\mathbf{p}_{i-j,s}^\dagger + \mathbf{M}\mathbf{p}_{j,s} \otimes \mathbf{M}\mathbf{p}_{i-j,c}^\dagger] \\ &\quad - \frac{1}{2} \sum_{j=i+1}^N [\mathbf{M}\mathbf{p}_{j,c} \otimes \mathbf{M}\mathbf{p}_{j-i,s}^\dagger + \mathbf{M}\mathbf{p}_{j-i,s} \otimes \mathbf{M}\mathbf{p}_{j,c}^\dagger] \\ &\quad \left. + \frac{1}{2} \sum_{j=i+1}^N [\mathbf{M}\mathbf{p}_{j-i,c} \otimes \mathbf{M}\mathbf{p}_{j,s}^\dagger + \mathbf{M}\mathbf{p}_{j,s} \otimes \mathbf{M}\mathbf{p}_{j-i,c}^\dagger] \right). \end{aligned} \quad (22)$$

In a similar fashion, let us introduce the sensitivity tensor of frequency variations ω , here denoted as \bar{S}_ω :

$$\bar{S}_\omega(\mathbf{x}) = \frac{\int_0^T \mathbf{M}\mathbf{q}^* \otimes \mathbf{M}\mathbf{p}_h^\dagger dt}{\int_0^T \int_{\Omega} \mathbf{M} \frac{\partial \mathbf{q}^*}{\partial t} \cdot \mathbf{M}\mathbf{p}_h^\dagger dx dt}, \quad (23)$$

where \mathbf{p}_h^\dagger is the adjoint Floquet mode associated to the neutral Floquet exponent $\lambda = 0$. \bar{S}_ω is the operator whose contraction with a generic infinitesimal localized feedback operator in space provides the variation of the frequency $\delta\omega = \mathbf{C}_2 : S_\omega$, where $\delta\mathbf{H}(\mathbf{q}^*) = \delta(\mathbf{x} - \mathbf{x}_0) \mathbf{C}_2 \cdot \mathbf{q}^*$.

The instantaneous sensitivity tensor to frequency variations S_ω is defined as:

$$S_\omega(\mathbf{x}) = \frac{\mathbf{M}\mathbf{q}^* \otimes \mathbf{M}\mathbf{p}_h^\dagger dt}{\int_0^T \int_{\Omega} \mathbf{M} \frac{\partial \mathbf{q}^*}{\partial t} \cdot \mathbf{M}\mathbf{p}_h^\dagger dx dt}, \quad (24)$$

where $\delta\omega = \mathbf{C}_2 : S_\omega(\mathbf{x}_0, t_0)$ and $\delta\mathbf{H}(\delta\mathbf{q}) = \delta((t \bmod T) - t_0) \delta(\mathbf{x} - \mathbf{x}_0) \mathbf{C}_2 \cdot \mathbf{q}^*$

Finally, let us introduce harmonic sensitivity to frequency variations maps $S_\omega^{n,c}$ and $S_\omega^{n,s}$. They provide further information for the open-loop control of the periodic solution with harmonic forcing. These quantities are a generalization of the weakly nonlinear expansion introduced by Sipp [25] to perform harmonic control near the onset of unsteadiness. These sensitivity maps are introduced as weighted products with the Fourier basis:

$$\begin{aligned} S_\omega^{n,c}(\mathbf{x}) &= \frac{2 \int_0^T \mathbf{M}\mathbf{q}^* \otimes \mathbf{M}\mathbf{p}_h^\dagger \cos(n\omega t) dt}{T \int_0^T \int_{\Omega} \mathbf{M} \frac{\partial \mathbf{q}^*}{\partial t} \cdot \mathbf{M}\mathbf{p}_h^\dagger dx dt} \\ S_\omega^{n,s}(\mathbf{x}) &= \frac{2 \int_0^T \mathbf{M}\mathbf{q}^* \otimes \mathbf{M}\mathbf{p}_h^\dagger \sin(n\omega t) dt}{T \int_0^T \int_{\Omega} \mathbf{M} \frac{\partial \mathbf{q}^*}{\partial t} \cdot \mathbf{M}\mathbf{p}_h^\dagger dx dt}, \end{aligned} \quad (25)$$

where the structural perturbation $\delta\mathbf{H}(\delta\mathbf{q}) = \frac{2}{T} \cos(n\omega t) \delta(\mathbf{x} - \mathbf{x}_0) \mathbf{C}_2 \cdot \mathbf{q}^*$, resp. $\sin(n\omega t)$, provides a variation of oscillating frequency $\delta\omega = \mathbf{C}_2 : S_\omega^{n,c}(\mathbf{x}_0)$, resp. $S_\omega^{n,s}(\mathbf{x}_0)$, due to an harmonic perturbation. Eventually, the sensitivity of the frequency $\bar{S}_\omega^{(\tau,N)}$ in the Fourier–Galerkin basis is computed as:

$$\bar{S}_\omega^{(\tau,N)}(\mathbf{x}) = \frac{\mathbf{M}\mathbf{q}_0^* \otimes \mathbf{M}\mathbf{p}_{h;0}^\dagger + \frac{1}{2} \sum_{n=1}^N \mathbf{M}\mathbf{q}_{n,c}^* \otimes \mathbf{M}\mathbf{p}_{h;n,c}^\dagger + \mathbf{M}\mathbf{q}_{n,s}^* \otimes \mathbf{M}\mathbf{p}_{h;n,s}^\dagger}{\frac{\omega}{2} \int_{\Omega} \sum_{n=1}^N n [\mathbf{M}\mathbf{q}_{n,s}^* \cdot \mathbf{M}\mathbf{p}_{n,c}^\dagger - \mathbf{M}\mathbf{q}_{n,c}^* \cdot \mathbf{M}\mathbf{p}_{n,s}^\dagger] dx}, \quad (26)$$

and harmonic sensitivity tensors $S_\omega^{n,c;(\tau,N)}$ and $S_\omega^{n,s;(\tau,N)}$ in the Fourier–Galerkin basis:

$$\begin{aligned}
\mathbf{S}_s^{n,c;(\tau,N)}(\mathbf{x}) &= \frac{2}{T \int_t^{T+t} \int_\Omega \mathbf{Mq}^* \cdot \mathbf{Mp}_h^\dagger dxdt} \left([\mathbf{Mq}_{i,c}^* \otimes \mathbf{Mp}_{h;0}^\dagger + \mathbf{Mq}_0^* \otimes \mathbf{Mp}_{h;i,c}^\dagger] \right. \\
&\quad + \frac{1}{2} \sum_{j=1}^{i-1} [\mathbf{Mq}_{i,c}^* \otimes \mathbf{Mp}_{h;i-j,c}^\dagger - \mathbf{Mq}_{j,s}^* \otimes \mathbf{Mp}_{h;i-j,s}^\dagger] \\
&\quad + \frac{1}{2} \sum_{j=i+1}^N [\mathbf{Mq}_{j,c}^* \otimes \mathbf{Mp}_{h;j-i,c}^\dagger + \mathbf{Mq}_{j-i,s}^* \otimes \mathbf{Mp}_{h;j,s}^\dagger] \\
&\quad \left. + \frac{1}{2} \sum_{j=i+1}^N [\mathbf{Mq}_{j-i,c}^* \otimes \mathbf{Mp}_{h;j,c}^\dagger + \mathbf{Mq}_{j,s}^* \otimes \mathbf{Mp}_{h;j-i,s}^\dagger] \right) \\
\mathbf{S}_s^{n,s;(\tau,N)}(\mathbf{x}) &= \frac{2}{T \int_t^{T+t} \int_\Omega \mathbf{Mq}^* \cdot \mathbf{Mp}_h^\dagger dxdt} \left([\mathbf{Mq}_{i,s}^* \otimes \mathbf{Mp}_{h;0}^\dagger + \mathbf{Mq}_0^* \otimes \mathbf{Mp}_{h;i,s}^\dagger] \right. \\
&\quad + \frac{1}{2} \sum_{j=1}^{i-1} [\mathbf{Mq}_{i,c}^* \otimes \mathbf{Mp}_{h;i-j,s}^\dagger + \mathbf{Mq}_{j,s}^* \otimes \mathbf{Mp}_{h;i-j,c}^\dagger] \\
&\quad - \frac{1}{2} \sum_{j=i+1}^N [\mathbf{Mq}_{j,c}^* \otimes \mathbf{Mp}_{h;j-i,s}^\dagger + \mathbf{Mq}_{j-i,s}^* \otimes \mathbf{Mp}_{h;j,c}^\dagger] \\
&\quad \left. + \frac{1}{2} \sum_{j=i+1}^N [\mathbf{Mq}_{j-i,c}^* \otimes \mathbf{Mp}_{h;j,s}^\dagger + \mathbf{Mq}_{j,s}^* \otimes \mathbf{Mp}_{h;j-i,c}^\dagger] \right).
\end{aligned} \tag{27}$$

2.6. Numerical methods

This section presents strategies for the resolution of eqs. (7) and (15). Efficient numerical techniques are required for the solution of linear systems composed of a large number of degrees of freedom. In particular, direct factorization becomes rapidly unfeasible due to the large memory requirements. Iterative methods with inner-outer preconditioning are proposed. Outer preconditioning improves the convergence of the Krylov method and inner preconditioning increases the efficiency of computation on blocks.

Nonlinear problem eq. (7) The solution of eq. (7) is performed via a Newton-like method:

$$D\tilde{\mathbf{r}}(\mathbf{Q}_{(n)}^{(\tau,N)})\delta\mathbf{Q}_{(n+1)}^{(\tau,N)} = -\tilde{\mathbf{r}}(\mathbf{Q}_{(n)}^{(\tau,N)}). \tag{28}$$

A Newton–Krylov strategy is chosen in the case $\tilde{\mathbf{r}}$ arises from semi-discretization in space of a PDE or via a Newton method if $\tilde{\mathbf{r}}$ is the vector field that stems from a differential system with a small number of degrees of freedom. The latter is common in the literature of mechanical systems and it is solved with dense matrices and direct linear solvers, for more information, the interested reader is referred to Krack et al. [12, Chapter 4].

Eigenvalue problem Arnoldi or shift-and-invert iteration are the chosen candidates for efficient extraction of leading Floquet exponents in eqs. (15) and (16).

Linear systems Preconditioning strategies are needed for an efficient resolution of linear systems from Newton iterations eq. (28) or Arnoldi iterations applied to eqs. (15) and (16). In the present study, we have considered three strategies for the outer preconditioning: block Jacobi, upper and lower triangular Gauss–Seidel. Solutions of inner systems, i.e., involving diagonal blocks of $D\tilde{\mathbf{r}}(\mathbf{Q}_{(n)}^{(\tau,N)})$, are computed using exact *LU* factorizations or iterative solvers, e.g., additive Schwarz method (ASM). For other choices of inner block-factorization, the interested reader may consider, for example, the modified augmented Lagrangian method [26] as implemented by Moulin et al. [27]. The preconditioning step is coupled with an iterative Krylov method: the flexible GMRES [28].

3. Results

Numerical results presented in this section have been obtained with in-house codes. Results presented in section 3.1 have been calculated with a MATLAB code developed by the authors for the computation of limit cycles and the evaluation of their stability with the methodology shown in section 2. Numerical examples of sections 3.2 and 3.3 have been computed with FreeFEM, a finite element code for the resolution of PDEs in the variational form, cf. [29]. Navier–Stokes equations written in the weak formulation are discretized by projecting the flow field (u, v, p) upon a basis of Taylor–Hood finite elements with piecewise quadratic velocities and piecewise linear pressure. The number of triangles of the discretized domain considered in sections 3.2 and 3.3 varies in a range of $\mathcal{O}(10^4) - \mathcal{O}(10^5)$ which results in around $\mathcal{O}(10^5) - \mathcal{O}(10^6)$ degrees of freedom per mode, that is $\mathcal{O}(n \cdot 10^5) - \mathcal{O}(n \cdot 10^6)$ with $n = 2N + 1$ the number of modes retained in the Fourier basis. Linear systems and eigenvalue problems are solved by PETSc [30] and SLEPc [31]. For more information, the interested reader is referred to the recent review article in linear and nonlinear stability in fluid flows by Fabre et al. [32] and the StabFem project hosted at <https://stabfem.gitlab.io/StabFem/>. Results presented in section 3.1 provide numerical evidence of the capability of the Fourier–Galerkin methodology to continue stable and unstable branches of periodic solutions past period-doubling bifurcations and to accurately evaluate the stability of a periodic orbit. Evaluation of the performance of numerical techniques described in section 2.6 and an assessment of the accuracy of sensitivity quantities

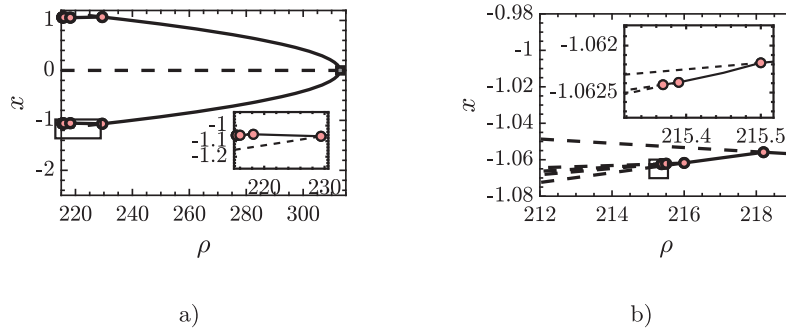


Fig. 3. a) Bifurcation diagram of the Lorenz system. b) Zoom into the interval of period-doubling bifurcations. Solid (resp. dashed) lines denote stable (resp. unstable) solutions. Red (resp. gray) markers denote a period-doubling bifurcation (resp. symmetry breaking).

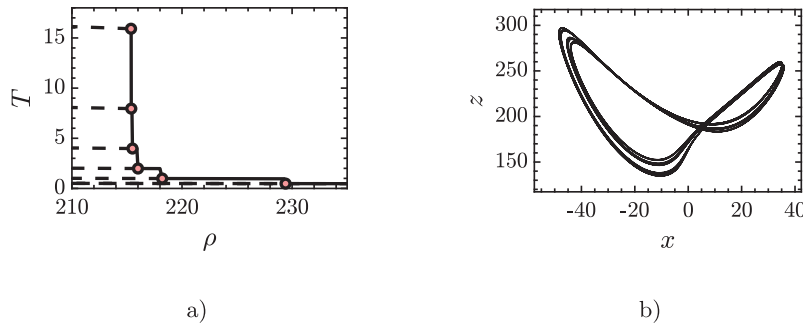


Fig. 4. a) Evolution of the period. b) $x - z$ slice of the stable solution at $\rho = 215.38$, before the sixth period-doubling bifurcation. Same legend as in Fig. 3.

detailed in section 2.5 is carried out in sections 3.2 and 3.3. The authors would like to compare the present methodology with respect to classical time-stepping techniques for the computation of sensitivity maps as in Giannetti et al. [7]. For that purpose, we consider an IMEX time-integration technique, e.g., explicit Runge–Kutta integration for the nonlinear terms and implicit Crank–Nicolson for the linear terms. The computation of the converged periodic solution, the direct and adjoint modes with time-stepping techniques require the solution of around $\mathcal{O}(MT)$ time units, with M the number of periods required for convergence, which is usually of the order of few hundreds for the periodic solution and of thousands for the evaluation of the direct and adjoints modes to obtain accurate results, and T the fundamental period. The evaluation of a period usually requires a number of time steps of the order of $N = \mathcal{O}(T/\Delta t)$, which is $N = \mathcal{O}(10^2)$ in the case of the wake flow past a cylinder, see [3, Sec. 7]. That results in a much larger total computation time than the one required for the evaluation of sensitivity maps with the current methodology. For instance, if we consider a coarse numerical domain, the mesh \mathcal{M}_1 of Table 1, the serial evaluation of Fourier–Galerkin methodology for the periodic solution, direct and adjoint eigenmodes are of the order of few minutes whereas the time-stepping methodology takes several hours, which is highly dependent on the time step which at the same time depends on the level of refinement. During the elaboration of this manuscript authors have compared the sensitivity maps computed with time-stepping techniques and Fourier–Galerkin method. Even if it is difficult to compare results that are coming from different numerical discretizations and different grids, [8] employed finite differences with a staggered grid, comparing the results we found that the sensitivity maps agree very well and the relative error is of few percents depending on the mesh and the physical parameters.

3.1. Lorenz system: the case of Feigenbaum route to chaos

Routes to chaos are of fundamental interest in the study of nonlinear dynamics. Most common routes to chaos are intermittency, crisis, quasiperiodicity, and period-doubling. The current section focuses on the latter. Period-doubling route is also denoted as *Feigenbaum* route to chaos and is characterized by an infinite number of period-doubling bifurcations in a finite interval of the parameter set. In particular, Feigenbaum noted that under mild assumptions of the nonlinear operator, the distance between consecutive bifurcations shrinks in a universal manner, see Collet et al. [33]:

$$\lim_{n \rightarrow \infty} \frac{\nu_{n+1} - \nu_n}{\nu_n - \nu_{n-1}} = \delta,$$

where $\delta \approx 4.6692016\dots$ is the Feigenbaum constant for dissipative dynamical systems and it can be numerically evaluated from Figs. 3 and 4. Period-doubling arises as a pitchfork bifurcation of a fixed point of the associated Poincaré return map.

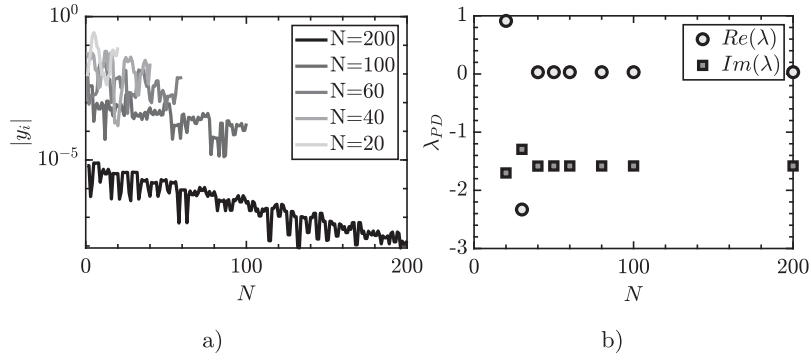


Fig. 5. a) Decay of Fourier modes of y component for a periodic solution near the fourth period-doubling bifurcation. b) Evolution of the eigenvalue associated to the period-doubling mode.

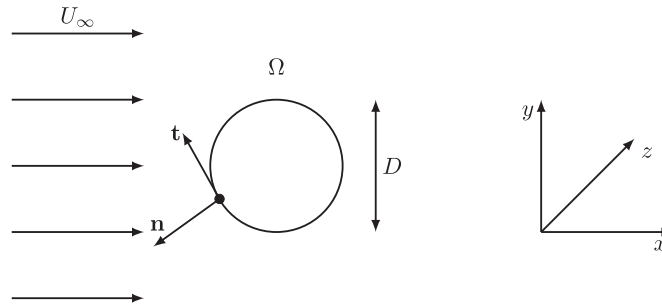


Fig. 6. Sketch of a cylinder immersed in a uniform flow.

In particular, here the Lorenz system illustrates the capability of the Fourier–Galerkin method to track period-doubling bifurcations and compute periodic solutions in a substantially nonlinear system. Let us first introduce Lorenz equations:

$$\begin{aligned}
 \dot{x} &= \sigma(y - x) \\
 \dot{y} &= \rho x - y - xz \\
 \dot{z} &= xy - bz,
 \end{aligned}
 \tag{29}$$

with parameters $b = \frac{8}{3}$, $\sigma = 10$, and $\rho \in (210, 320]$. In this range of parameters, there is a first bifurcation around $\rho \approx 312.9$, where the stable solution ceases to be symmetric via a pitchfork bifurcation due to the reflectional symmetry ($x \rightarrow -x$, $y \rightarrow -y$) of the system. These two branches remain stable up to $\rho \approx 229.4$, where a first period-doubling bifurcation occurs. It is then followed by an infinite number of them, of which the first six have been computed, see Fig. 3. The stable periodic orbit before the sixth period-doubling bifurcation is reported in Fig. 4 b). Fig. 4 a) illustrates the geometric growth of the period past successive period-doubling bifurcations. As pointed out in Remark 1, successive period-doubling solutions have been computed by doubling the number of harmonics of the truncated Fourier series.

The convergence of a periodic solution is evaluated a posteriori by the decay of Fourier modes and by the evolution of the leading eigenvalue. Fig. 5 shows, for a periodic solution at the onset of the fourth period-doubling bifurcation, the irregular decay of Fourier harmonics due to the strong nonlinearities. In addition, Fig. 5 shows that the methodology is able to accurately predict some parts of the spectrum even if the decay of Fourier modes is not smooth. Particularly, prior to the fourth period-doubling bifurcation Fig. 5, a minimum of around $N = 40$ is required for a correct evaluation of the leading Floquet exponent.

Finally, let us conclude this section with a remark concerning the number of Fourier modes retained for the reconstruction of a periodic solution past a period-doubling bifurcation. As stated in Remark 1, a periodic solution whose period is $2^m T$, i.e., the system has experienced m period-doubling bifurcations, is also $2^{m-1} T$ -periodic. The computation of a $2^m T$ -periodic solution requires $2^m \tilde{N}$ Fourier modes, where \tilde{N} is the length of the Fourier basis used for the computation of a T -periodic solution. As a consequence, the number of harmonics for a single T -period is $\tilde{N} = \frac{N}{2^m}$, which, for instance for $N = 40$ and $m = 3$, gives $\tilde{N} = 5$.

3.2. Flow past a two-dimensional circular cylinder

Let us consider a fluid mechanics example: a canonical case of the flow past a bluff body, i.e., the flow past a two-dimensional cylinder sketched in Fig. 6. Dynamics and the first two bifurcations are well known, see Williamson [34].

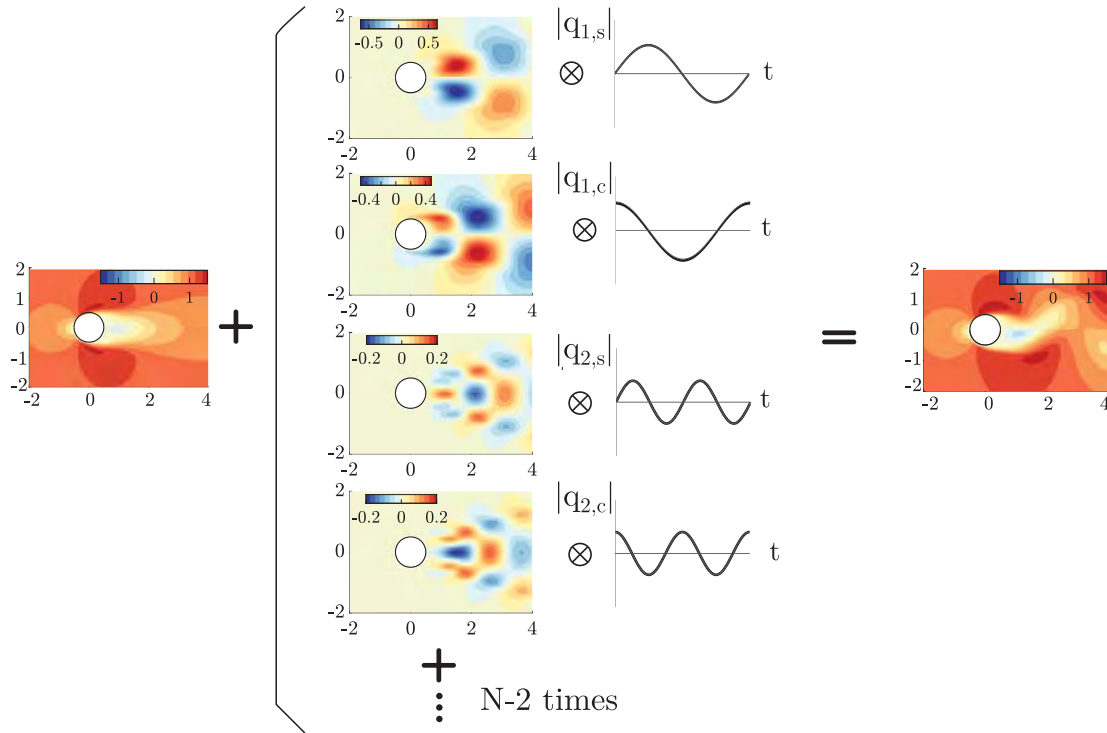


Fig. 7. Reconstruction of the streamwise velocity U_x of the periodic oscillating vortex solution at $Re = 190$. The flow is reconstructed at $t = 0$ for $N = 6$.

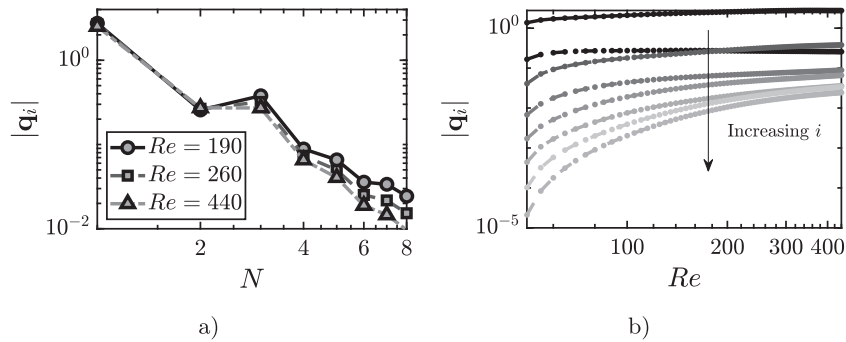


Fig. 8. a) Decay of Fourier spectrum for $Re = 190$, $Re = 260$, and $Re = 440$ b) Evolution of the amplitude of Fourier modes.

The governing equations are the incompressible Navier–Stokes equations which are of quadratic type, see appendix B, therefore they fit into the developed strategy.

3.2.1. Computation of the baseflow

The Fourier–Galerkin strategy reconstructs the periodic solution of the flow past a cylinder, as reported in Fig. 7. The approach is initialized with the unstable eigenmode at the threshold, $Re \approx 47$, and it is continued up to $Re = 450$, with at most $N = 10$ modes. In order to estimate the precision of the results obtained by the numerical procedure, two Reynolds numbers are selected, $Re = 190$ and $Re = 260$, and we run cross-comparison of the estimated Strouhal with the data available in the literature. At $Re = 190$ (resp. $Re = 260$), by retaining $N = 5$ harmonics, a Strouhal number $St = 0.1938$ (resp. $St = 0.2058$) has been obtained, a result in good agreement with the value $St = 0.1950$ (resp. $St = 0.2071$) reported by Barkley et al. [35]. These accurate results with a reduced Fourier basis are due to the rapid decay of the Fourier spectrum, which is displayed in Fig. 8 a). The Fourier spectrum displays a quadratic decay, with small dependence on the Reynolds number if sufficient modes are retained. To determine whether or not the number of retained modes is sufficient, one could evaluate a posteriori the evolution of the amplitude of each mode with respect to the parameter, i.e., Re . The amplitude of each Fourier mode grows exponentially until saturation, see Fig. 8 b). Therefore, an appropriate selection of N could be to retain at least a mode that is not saturated or select the basis length N so that the amplitude of the last mode is below a certain threshold.

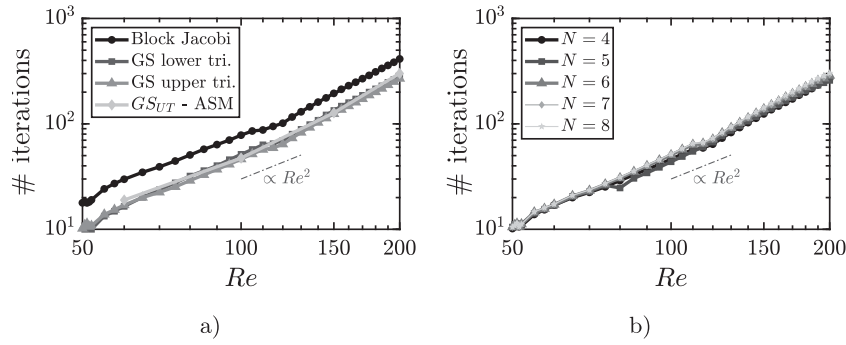


Fig. 9. Effect of Reynolds number, preconditioning technique and number of Fourier modes. a) Compares preconditioning techniques and b) the number of Fourier modes for a Gauss–Seidel upper triangular preconditioner.

Table 1

Average number of GMRES iterations per Newton iteration for three numerical domains \mathcal{M}_1 , \mathcal{M}_2 and \mathcal{M}_3 at $Re = 100$ with upper triangular Gauss–Seidel. The tolerance of the Newton method is set to 10^{-8} .

Mesh ID	# elements	# GMRES iterations		
		$N = 1$	$N = 2$	$N = 3$
\mathcal{M}_1	$1.4 \cdot 10^4$	33	36	38
\mathcal{M}_2	$4.5 \cdot 10^4$	32	37	39
\mathcal{M}_3	$1.85 \cdot 10^5$	33	38	38

Table 2

Total number of GMRES iterations for the resolution of the nonlinear problem eq. (7) at $Re = 100$, $N = 4$ with the numerical domain \mathcal{M}_1 , the upper triangular Gauss–Seidel as the outer preconditioning technique and inexact factorization with the ASM method for inner blocks. Variation of inner iterations and total GMRES iterations with respect to the relative tolerance in the inexact factorization of inner blocks. The tolerance of the Newton method is set to 10^{-8} .

ASM tolerance	10^{-8}	10^{-7}	10^{-6}	10^{-5}	10^{-4}	10^{-3}	LU
# total iterations	344	310	278	246	267	369	238
Average # inner iterations	52	44	35	25	18	16	—

3.2.2. Performance evaluation of iterative methods

Another important aspect to be addressed is the performance of methods used for numerical resolution. In particular, for the present case, authors have evaluated the dependency of the chosen iterative strategy, a flexible restarted GMRES, for the solution of linear systems such as eq. (28) on a set of parameters: Reynolds number, number of elements in the numerical domain, preconditioning techniques and number of modes of the Fourier basis.

Independently of the chosen preconditioning technique, the number of GMRES iterations for the resolution of the linear system eq. (28) increases quadratically with respect to the Reynolds number, see Fig. 9 a). As expected, triangular Gauss–Seidel preconditioning speeds up computations with respect to block Jacobi. However, the gain between choosing an upper or a lower triangular preconditioner is marginal. The second aspect that was studied is the influence of the number of iterations required to solve the linear system under a change of the total number of elements. Table 1 reports the average number of GMRES iterations, for three numerical domains \mathcal{M}_i , $i = 1, 2, 3$. It results that the number of GMRES iterations does scale with the total number of elements in the numerical domain. In addition, authors have studied the effect of an inexact factorization of the inner diagonal blocks. ASM is used to precondition the inner blocks with upper triangular GS as outer preconditioner. It is compared with exact LU factorization for the diagonal blocks. Table 2 reports the variation of the total number of GMRES iterations required to solve the nonlinear problem eq. (7) and the averaged number of inner iterations for each inner diagonal block. It is concluded that inexact factorization of inner blocks hardly changes the number of GMRES iterations, as long as the relative tolerance is correctly tuned. The effect of the number of modes in the truncated Fourier basis is reported in Fig. 9 b). Similar conclusions can be drawn with respect to other preconditioners, the number of modes in the Fourier basis does not affect the iterative strategy, as long as N is sufficient for convergence.

Finally, the performance of the parallel implementation is considered. For that purpose a strong scalability test has been carried out with a fine numerical domain composed of $1.85 \cdot 10^5$ elements. The number of modes is fixed to $N = 4$ and the preconditioning technique is the upper triangular Gauss–Seidel. Fig. 10 a) reports the evolution of the averaged time per Newton iteration with respect to the number of processes. The actual scaling time is degraded by around 35% with respect to perfect linear scaling, that is the average time per Newton iteration approximately evolves as # of processes^{-0.65}.

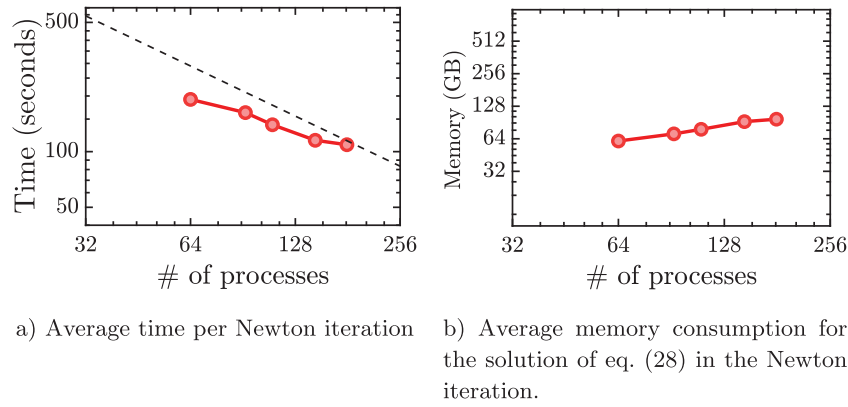


Fig. 10. Performance of the linear solver with upper triangular Gauss–Seidel with a discretized domain composed of $1.85 \cdot 10^5$ elements and $N = 4$.

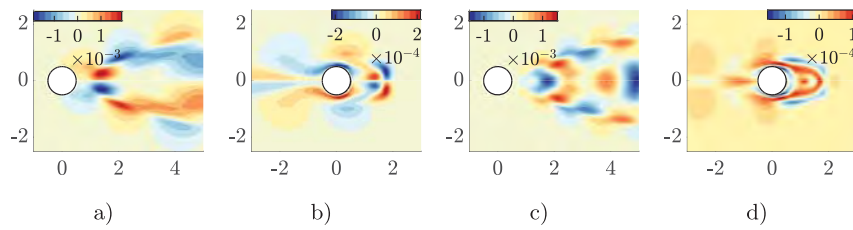


Fig. 11. Spanwise velocity component U_z of mode A at $Re = 190$. a) and c), resp. b) and d), first and second sinus components of direct, resp. adjoint, Floquet modes.

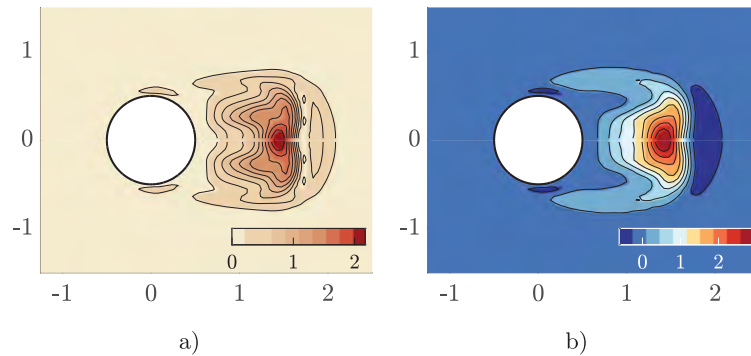


Fig. 12. Averaged structural sensitivity $\bar{S}_s^{(\tau, N)}$ of mode A at $Re = 190$, $k_z = 1.585$, and $N = 4$. a) Spectral norm. b) Trace.

Similarly, Fig. 10 b) reports the total memory consumption for the solution of the linear system eq. (28). It displays an increase of memory of around 20% each time the number of processes doubles.

In conclusion, GMRES iterations depend quadratically on Reynolds number and they are independent on the total number of mesh elements, the dimension of the Fourier basis as long as N is sufficient to characterize the periodic solution. In a future study, authors will study other preconditioning techniques to attempt to reduce the dependency on Re .

3.2.3. Stability & sensitivity analysis

Beyond the threshold of the first instability, which is found at around $Re \approx 47$, a stable two-dimensional T -periodic solution exists up to $Re \approx 190$ where the stable solution ceases to be two-dimensional via a steady symmetry-breaking bifurcation of the spanwise homogeneous direction. The Floquet mode associated to this second instability, reported in Fig. 11, is commonly denoted as *mode A* whose wavenumber is $k_z = 1.585$, see Giannetti et al. [8].

Prior to the discussion of sensitivity quantities, let us point out their validity. The reported sensitivity maps in Figs. 12 and 13 are in perfect agreement with those presented in literature, cf. [7]. A common query in physics is: which are the underlying physical mechanisms responsible for the instability? Structural sensitivity allows to localize the core of the vortex-shedding instability, that is the sensitivity of the Floquet exponent to a generic structural perturbation of the linearized equations. Fig. 12 displays the compact support structure of the sensitivity for mode A, which translates to a localized instability in the near wake. Similarly, if one desires to shift the harmonic frequency ω , the most efficient way is to act on the near wake in accordance with the map S_ω , see Fig. 13.

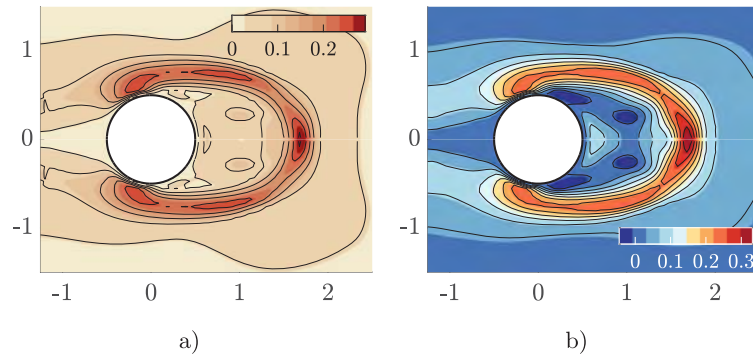


Fig. 13. Averaged sensitivity to frequency variations $\bar{S}_\omega^{(\tau, N)}$ of mode A at $Re = 190$, $k_z = 1.585$, and $N = 4$. a) Spectral norm. b) Trace.

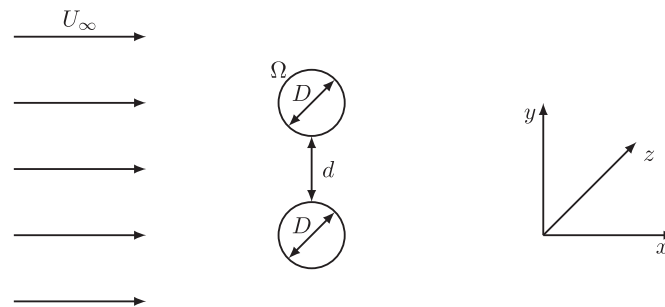


Fig. 14. Sketch of the two circular cylinders in a side-by-side arrangement immersed in a uniform flow.

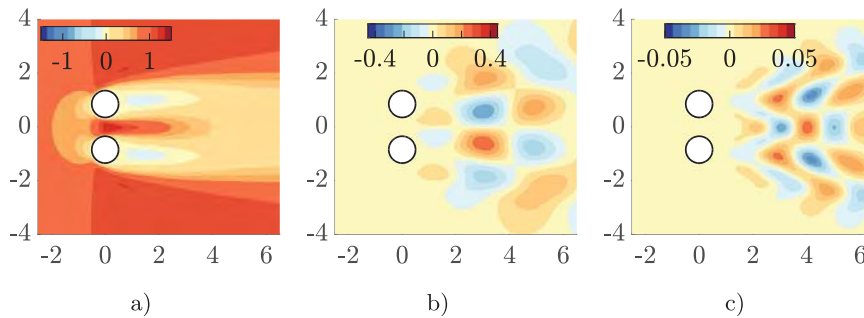


Fig. 15. Streamwise component U_x of the periodic baseflow solution at $Re = 62$. a) Meanflow component. b) First cosine component. c) Second cosine component.

3.3. Flow past two cylinders in tandem

Let us explore a second fluid mechanics example: the flow past two side-by-side circular cylinders. The flow configuration, reported in Fig. 14, is governed by two dimensionless parameters, Reynolds number (Re) and the ratio of the distance between cylinders and their diameter ($g = \frac{d}{D}$). For some ranges of parameters, reported by Carini et al. [36], the two-dimensional flow pattern is characterized by an asymmetric unsteady wake with respect to the horizontal axis. Such a phenomenon, which has been denominated *flip-flop*, develops at low Reynolds numbers, $50 < Re < 90$, through a Neimark–Sacker bifurcation. In the following, the dimensionless distance between cylinders is fixed, $g = 0.7$, such that *flip-flop* instability appears.

3.3.1. Computation of the baseflow

The periodic solution past two side-by-side cylinders is reconstructed by Fourier–Galerkin with $N = 4$ (Fig. 15). The method is initialized with the unstable in-phase eigenmode associated with the first supercritical Hopf bifurcation of the steady state, see section 3.2.3. The accuracy of baseflow computations were compared with reported results in the literature. At $Re = 62$, a $St \approx 0.111$ matches the one computed by Carini et al. [36].

3.3.2. Memory requirements of linear solvers

Section 3.2.2 focuses on the performance of iterative methods by considering the influence of some parameters on the number of iterations required by the linear solver to solve eq. (28) with a relative tolerance of 10^{-5} . Another important facet of linear solvers is their memory consumption. Particularly, the total memory consumption is expected to increase with

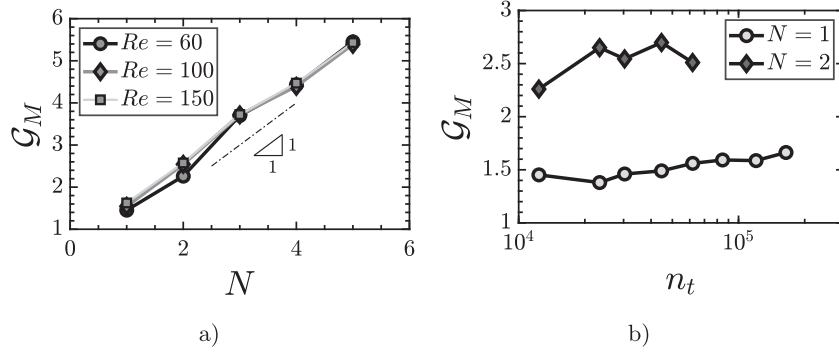


Fig. 16. a) Memory gain evolution w.r.t. number of Fourier modes (for a coarse mesh $n_t = 12354$ triangles) for three Reynolds numbers. b) Memory gain w.r.t. number of mesh triangles.

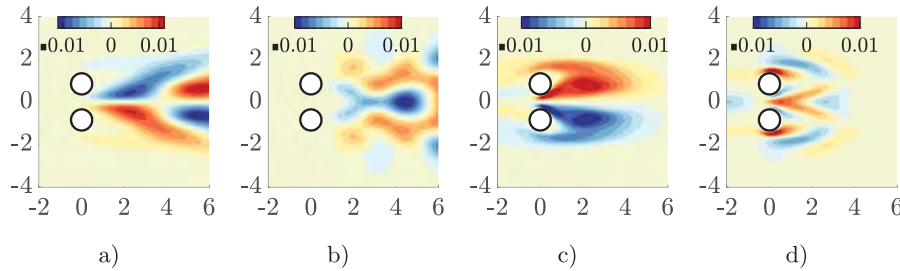


Fig. 17. Mode IP at $Re = 62$. a) and c), resp. b) and d), meanflow and first cosine components of direct, resp. adjoint, Floquet modes.

the number of modes of the truncated Fourier basis and mesh refinement. We define the *memory gain*, $G_M = \frac{\text{memory LU}}{\text{memory GMRES}}$, as the ratio of memory consumed by LU w.r.t. GMRES to solve a linear system whose linear operator is the Jacobian matrix defined in appendix A.3.

Tests have been run on an Intel cluster with 64 Intel(R) Xeon(R) CPU E5-4610 processors and 256 GB of memory. For a fixed mesh with $n_t = 12,354$ triangles, inner iterations of the Newton method are solved with varying N , with the upper triangular Gauss–Seidel preconditioner and LU factorization. They have confirmed the linear memory gain, independently of Re , with respect to the number of elements kept in the Fourier basis, as reported in Fig. 16 a). Analogously, the effect of mesh size on memory storage is also studied. The memory gain is reported in Fig. 16 b) as a function of the number of triangles. Curves correspond to different lengths of the truncated Fourier basis. Clearly, memory gain is independent of the mesh size, regardless of N .

3.3.3. Stability & sensitivity analysis

The stability of the steady state has been studied by Mizushima et al. [37]. They reported three types of instabilities, a symmetry breaking of the steady state via a pitchfork bifurcation, an oscillatory in-phase via a Hopf bifurcation, and a third oscillatory instability far from the near wake. For the chosen configuration ($g = 0.7$) the primary instability is a supercritical Hopf bifurcation at $Re \approx 57.5$ whose most unstable eigenmode is the in-phase oscillatory, *mode IP* partially reported in Fig. 17. The Floquet analysis reveals a pair of complex-conjugate multipliers on the in-phase synchronized vortex shedding periodic solution between the two cylinders. Neimark–Sacker appears at $Re_c = 61.7$, which is in good agreement with the result $Re_c = 61.8$ reported by Carini et al. [36].

Structural sensitivity, reported in Fig. 18, shows a symmetric averaged core of the instability in the near wake that is larger than the sensitive instability core of the single cylinder reported in Fig. 12. In addition, amplitudes of harmonic sensitivity are displayed in the frequency ω -axis. They provide further information about the origin of the flip-flop instability. Sensitive regions to harmonic structural perturbation are found for the first harmonic where it is possible to observe two sensitive regions around $y = \pm 2$ and a single one around $y = 0$ in the near wake for the second harmonic component. Remarkably, in this case, the instability is more sensitive to the second harmonic than the first one. The other sensitivity map, \bar{S}_ω reported in Fig. 19, is particularly concentrated in the zone between cylinders. Not surprisingly, previous results in the literature indicate large variations of baseflow frequency as the gap ratio g is varied.

4. Conclusion

The computation of stability and sensitivity of periodic solutions provides access to inherent mechanisms leading to changes in dynamics. Efficient computational methods are essential for the computation of large-scale systems such as those arising from the semi-discretization of the governing equations. The spectral Fourier–Galerkin method is proposed for the efficient computation and continuation of autonomous problems. The methodology, though general, has been presented

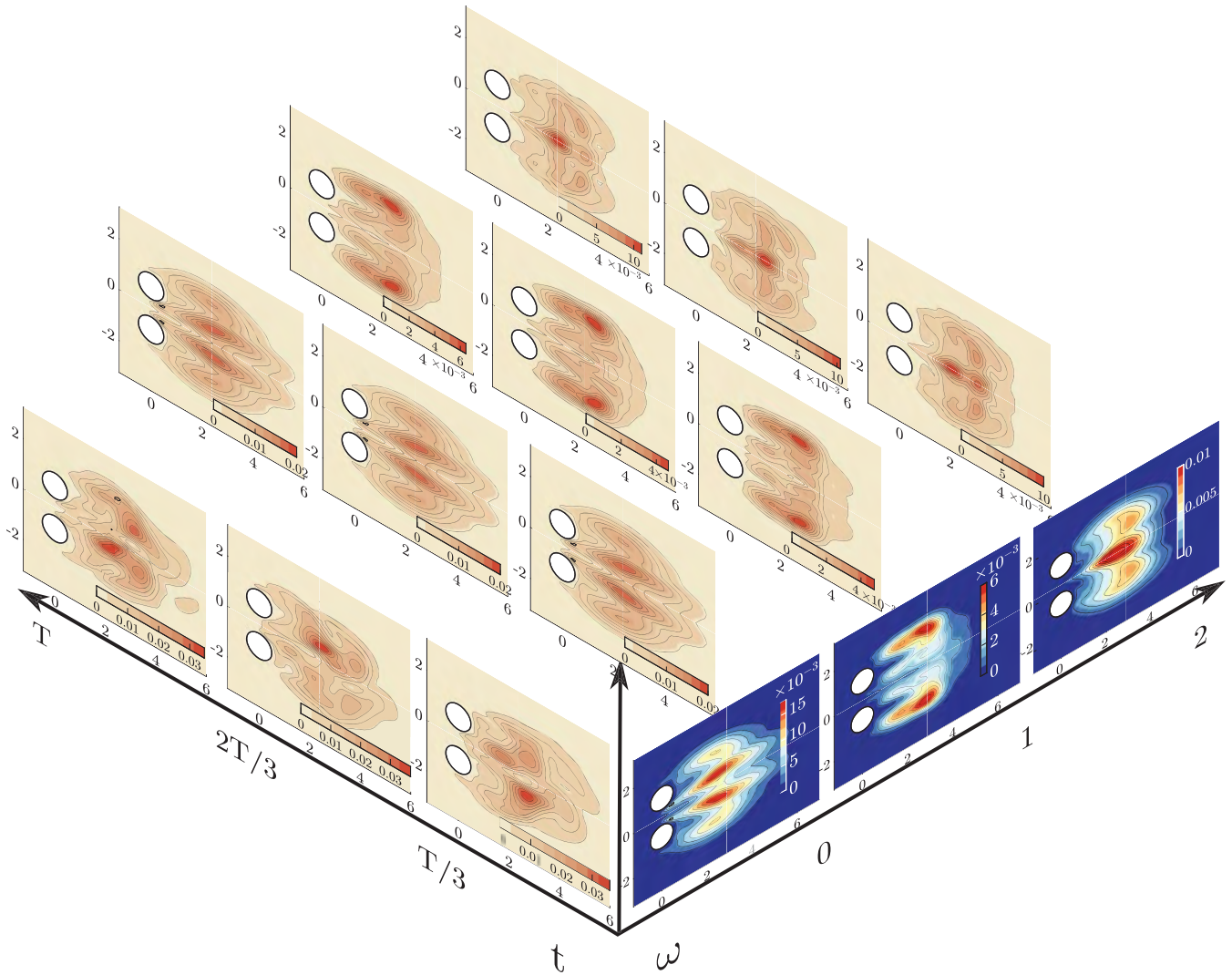


Fig. 18. Structural sensitivity $S_s^{(\tau, N)}$ for $Re = 62$ with $N = 2$. t -axis: reconstruction of the spectral norm of the instantaneous structural sensitivity $S_s^{(\tau, N)}(\mathbf{x}, t)$ at discrete instants $t = \{\frac{T}{3}, \frac{2T}{3}, T\}$. ω -axis: spectral norm of the modulus of harmonic sensitivity $|S_s^{n;(\tau, N)}| = \sqrt{S_s^{n,c;(\tau, N)2} + S_s^{n,s;(\tau, N)2}$ for harmonic components $n = \{0, 1, 2\}$. The spectral norm of the modulus of the harmonic sensitivity $|S_s^{n;(\tau, N)}|$ is reconstructed in time at discrete instants.

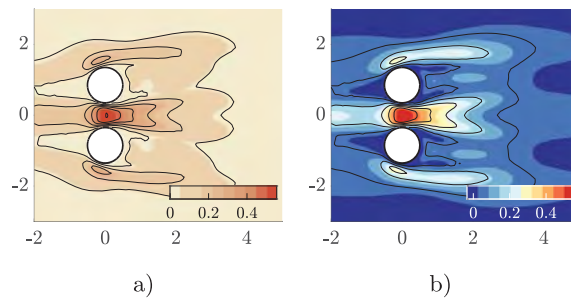


Fig. 19. Averaged sensitivity to frequency variations $\bar{S}_\omega^{(\tau, N)}$ of mode A at $Re = 190$, $k_z = 1.585$, and $N = 4$. a) Spectral norm. b) Trace.

for quadratic nonlinearities, where the frequency transform has a simple form, see appendix A.1. In the case of finite systems with few degrees of freedom, quadratic recasting is an option ([10,13]). However, such a recast increases the computational burden. It multiplies the number of degrees of freedom by a factor, which is not acceptable in large-scale systems. In those cases, an exact Fourier transform of nonlinear terms is required, see for instance the cubic nonlinearity of the compressible Navier–Stokes equations in Sierra et al. [38].

The present methodology is used to analyze three different scenarios. First, a toy model: Lorenz equations are used to display some of the properties of the methodology. Fourier–Galerkin strategy is employed for the continuation of unstable periodic orbits through a series of period-doubling bifurcations in the Feigenbaum route to chaos. Such a situation, usually studied by collocation or shooting methods, proves to be one of the worst-case scenarios for this kind of spectral method

due to the lack of smoothness of the system of equations, see Moore [39]. Regardless, the approach proves to be capable to compute partially and accurately this route to chaos at least in small systems, the continuation of the period-doubling cascade in large systems is still an open challenge for future studies.

Two fluid mechanics cases, archetypal of bluff body flows, are studied with the presented machinery. The vortex-shedding periodic flow past a circular cylinder and the flip-flop instability of two circular cylinders side-by-side have been accurately reconstructed with a finite number of harmonics. Such a set of examples have been employed to test the performance of the numerical resolution. The number of GMRES iterations is independent of the number of harmonics and it depends quadratically on the Reynolds number. Similarly, the memory gain of iterative methods with respect to a direct factorization increases linearly with the length of the truncated basis and it is independent of the mesh size. Two kinds of instabilities are analyzed, the transition of a two-dimensional periodic solution towards a three-dimensional periodic state and the flip-flop instability through a Neimark–Sacker bifurcation. Both instabilities mechanisms have been examined with the aid of sensitivity maps developed in section 2.5. Structural sensitivity of the periodic solution allows the identification of physical mechanisms causing self-sustained instabilities. Two types of instabilities have been reported in section 3: the spatio-temporal symmetry breaking in the case of two circular cylinders in tandem configuration, or the transition to a three-dimensional flow in the single circular cylinder configuration. In addition, sensitivity to frequency variations identifies those regions of the space where open-loop control will be most effective to cause a change in frequency. To conclude, the authors would like to remark that these sensitivity maps are easily computed under this framework, which is also more computationally efficient than direct time-integration in the studied configurations.

CRedit authorship contribution statement

The authors contributed equally to the submitted manuscript.

Declaration of competing interest

The authors declare that they have no known competing financial interests or personal relationships that could have appeared to influence the work reported in this paper.

Appendix A. Fourier–Galerkin equations

A.1. Nonlinear operator

Fourier–Galerkin equations (6) are derived by averaging truncated residual equations over a period T . Given the orthogonality of the Fourier basis, linear terms depend only on a harmonic whereas Fourier coefficients of the quadratic term \mathbf{N}_i may depend on several of them. Here a detailed description of the quadratic terms is given:

$$\begin{aligned} \mathbf{N}_0 &= \mathbf{N}(\mathbf{q}_0, \mathbf{q}_0) + \frac{1}{2} \sum_{i=1}^N \mathbf{N}(\mathbf{q}_{i,s}, \mathbf{q}_{i,s}) + \mathbf{N}(\mathbf{q}_{i,c}, \mathbf{q}_{i,c}) \\ \mathbf{N}_{i,c} &= [\mathbf{N}(\mathbf{q}_{i,c}, \mathbf{q}_0) + \mathbf{N}(\mathbf{q}_0, \mathbf{q}_{i,c})] \\ &\quad + \frac{1}{2} \sum_{j=1}^{i-1} [\mathbf{N}(\mathbf{q}_{j,c}, \mathbf{q}_{i-j,c}) - \mathbf{N}(\mathbf{q}_{j,s}, \mathbf{q}_{i-j,s})] \\ &\quad + \frac{1}{2} \sum_{j=i+1}^N [\mathbf{N}(\mathbf{q}_{j,c}, \mathbf{q}_{j-i,c}) + \mathbf{N}(\mathbf{q}_{j-i,s}, \mathbf{q}_{j,s})] \\ &\quad + \frac{1}{2} \sum_{j=i+1}^N [\mathbf{N}(\mathbf{q}_{j-i,c}, \mathbf{q}_{j,c}) + \mathbf{N}(\mathbf{q}_{j,s}, \mathbf{q}_{j-i,s})] \\ \mathbf{N}_{i,s} &= [\mathbf{N}(\mathbf{q}_{i,s}, \mathbf{q}_0) + \mathbf{N}(\mathbf{q}_0, \mathbf{q}_{i,s})] \\ &\quad + \frac{1}{2} \sum_{j=1}^{i-1} [\mathbf{N}(\mathbf{q}_{j,c}, \mathbf{q}_{i-j,s}) + \mathbf{N}(\mathbf{q}_{j,s}, \mathbf{q}_{i-j,c})] \\ &\quad - \frac{1}{2} \sum_{j=i+1}^N [\mathbf{N}(\mathbf{q}_{j,c}, \mathbf{q}_{j-i,s}) + \mathbf{N}(\mathbf{q}_{j-i,s}, \mathbf{q}_{j,c})] \\ &\quad + \frac{1}{2} \sum_{j=i+1}^N [\mathbf{N}(\mathbf{q}_{j-i,c}, \mathbf{q}_{j,s}) + \mathbf{N}(\mathbf{q}_{j,s}, \mathbf{q}_{j-i,c})]. \end{aligned}$$

A.2. Residual notation

For the sake of a simpler presentation eq. (7) presents a series of operators, i.e., $\tilde{\mathbf{B}}, \tilde{\mathbf{L}}, \tilde{\mathbf{N}}$. Their definition is as follows:

Time derivative matrix $\tilde{\mathbf{B}}$

$$\tilde{\mathbf{B}}\mathbf{Q}_N = \begin{bmatrix} \mathbf{0} & & & \\ & \mathbf{B}_1 & & \\ & & \ddots & \\ & & & \mathbf{B}_N \end{bmatrix} \begin{bmatrix} \mathbf{q}_0 \\ \mathbf{q}_1 \\ \vdots \\ \mathbf{q}_N \end{bmatrix} \text{ with } \mathbf{B}_n = \begin{bmatrix} \mathbf{0} & n\mathbf{B} \\ -n\mathbf{B} & \mathbf{0} \end{bmatrix} \text{ for } n = 1, \dots, N. \quad (\text{A.1})$$

Linear operator $\tilde{\mathbf{L}}$

$$\tilde{\mathbf{L}}\mathbf{Q}_N = \begin{bmatrix} \mathbf{L} & & & \\ & \mathbf{L} & & \\ & & \ddots & \\ & & & \mathbf{L} \end{bmatrix} \begin{bmatrix} \mathbf{q}_0 \\ \mathbf{q}_1 \\ \vdots \\ \mathbf{q}_N \end{bmatrix} \text{ with } \mathbf{q}_n = \begin{bmatrix} \mathbf{q}_{n,c} \\ \mathbf{q}_{n,s} \end{bmatrix} \text{ for } n = 1, \dots, N. \quad (\text{A.2})$$

Nonlinear operator $\tilde{\mathbf{N}}$

$$\tilde{\mathbf{N}}(\mathbf{Q}_N, \mathbf{Q}_N) = \begin{bmatrix} \mathbf{N}_0 \\ \mathbf{N}_1 \\ \vdots \\ \mathbf{N}_N \end{bmatrix} \text{ with } \mathbf{N}_n = \begin{bmatrix} \mathbf{N}_{n,c} \\ \mathbf{N}_{n,s} \end{bmatrix} \text{ for } n = 1, \dots, N. \quad (\text{A.3})$$

A.3. Jacobian operator

Consider a small perturbation of $[\mathbf{Q}^{(\tau,N)}, \omega]^T$, here denoted as $[\delta\mathbf{Q}^{(\tau,N)}, \delta\omega]^T$, the linearized HBM equation is as follows:

$$\begin{aligned} \mathbf{0} &= -\delta\omega\tilde{\mathbf{B}}\mathbf{Q}_N - \omega\tilde{\mathbf{B}}\delta\mathbf{Q}^{(\tau,N)} + \tilde{\mathbf{L}}\delta\mathbf{Q}^{(\tau,N)} + D\tilde{\mathbf{N}}(\mathbf{Q}^{(\tau,N)})\delta\mathbf{Q}^{(\tau,N)} \\ &= -\delta\omega\tilde{\mathbf{B}}\mathbf{Q}^{(\tau,N)} + D\tilde{\mathbf{r}}(\mathbf{Q}^{(\tau,N)})\delta\mathbf{Q}^{(\tau,N)}, \end{aligned} \quad (\text{A.4})$$

where the derivative of the quadratic operator is a dense block-symmetric matrix as follows:

$$D\tilde{\mathbf{N}}(\mathbf{Q}^{(\tau,N)}) = \begin{bmatrix} D\mathbf{N}^{(0)} & \dots & D\mathbf{N}^{(0,i)} & \dots & D\mathbf{N}^{(0,N)} \\ \vdots & \ddots & \vdots & \ddots & \vdots \\ D\mathbf{N}^{(i,0)} & \dots & D\mathbf{N}^{(i)} & \dots & D\mathbf{N}^{(i,N)} \\ \vdots & \ddots & \vdots & \ddots & \vdots \\ D\mathbf{N}^{(N,0)} & \dots & D\mathbf{N}^{(N,i)} & \dots & D\mathbf{N}^{(N)} \end{bmatrix}. \quad (\text{A.5})$$

Let us consider the detailed description of each block. In the following, let us denote $D\mathbf{N}^{(\mathbf{q})} = \mathbf{N}(\cdot, \mathbf{q}) + \mathbf{N}(\mathbf{q}, \cdot)$, the linear operator of the derivative evaluated at \mathbf{q} .

Diagonal blocks $D\mathbf{N}^{(i)}$

$$D\mathbf{N}^{(0)} = D\mathbf{N}^{(\mathbf{q}_0)} \quad (\text{A.6})$$

$$D\mathbf{N}^{(i)} = \begin{bmatrix} D\mathbf{N}^{(\mathbf{q}_0)} + \frac{1}{2}D\mathbf{N}^{(\mathbf{q}_{2i,c})} & \frac{1}{2}D\mathbf{N}^{(\mathbf{q}_{2i,s})} \\ \frac{1}{2}D\mathbf{N}^{(\mathbf{q}_{2i,s})} & D\mathbf{N}^{(\mathbf{q}_0)} - \frac{1}{2}D\mathbf{N}^{(\mathbf{q}_{2i,c})} \end{bmatrix} \text{ if } 0 < i \leq \frac{N}{2} \quad (\text{A.7})$$

$$D\mathbf{N}^{(i)} = \begin{bmatrix} D\mathbf{N}^{(\mathbf{q}_0)} & \mathbf{0} \\ \mathbf{0} & D\mathbf{N}^{(\mathbf{q}_0)} \end{bmatrix} \text{ if } i > \frac{N}{2}. \quad (\text{A.8})$$

Off diagonal-blocks $D\mathbf{N}^{(i,j)}$

$$D\mathbf{N}^{(0,j)} = \begin{bmatrix} \frac{1}{2}D\mathbf{N}^{(\mathbf{q}_{j,c})} & \frac{1}{2}D\mathbf{N}^{(\mathbf{q}_{j,s})} \end{bmatrix} \text{ if } j \neq 0, \quad (\text{A.9})$$

$$D\mathbf{N}^{(i,0)} = \begin{bmatrix} \frac{1}{2}D\mathbf{N}^{(\mathbf{q}_{i,c})} \\ \frac{1}{2}D\mathbf{N}^{(\mathbf{q}_{i,s})} \end{bmatrix} \text{ if } i > 0. \quad (\text{A.10})$$

If $i \neq j, j \neq 0, j < i, j + i \leq N$:

$$D\mathbf{N}^{(i,j)} = \begin{bmatrix} \frac{1}{2}D\mathbf{N}^{(\mathbf{q}_{i-j,c})} + \frac{1}{2}D\mathbf{N}^{(\mathbf{q}_{j+i,c})} & -\frac{1}{2}D\mathbf{N}^{(\mathbf{q}_{i-j,s})} - \frac{1}{2}D\mathbf{N}^{(\mathbf{q}_{j+i,s})} \\ \frac{1}{2}D\mathbf{N}^{(\mathbf{q}_{i-j,s})} + \frac{1}{2}D\mathbf{N}^{(\mathbf{q}_{j+i,s})} & \frac{1}{2}D\mathbf{N}^{(\mathbf{q}_{i-j,c})} + \frac{1}{2}D\mathbf{N}^{(\mathbf{q}_{j+i,c})} \end{bmatrix}. \quad (\text{A.11})$$

If $i \neq j, j \neq 0, j < i, j + i > N$:

$$D\mathbf{N}^{(i,j)} = \begin{bmatrix} \frac{1}{2}D\mathbf{N}^{(\mathbf{q}_{i-j,c})} & -\frac{1}{2}D\mathbf{N}^{(\mathbf{q}_{i-j,s})} \\ \frac{1}{2}D\mathbf{N}^{(\mathbf{q}_{i-j,s})} & \frac{1}{2}D\mathbf{N}^{(\mathbf{q}_{i-j,c})} \end{bmatrix} \text{ if } i \neq j, j \neq 0, j < i, \quad (\text{A.12})$$

otherwise $D\mathbf{N}^{(j,i)} = (D\mathbf{N}^{(i,j)})^T$.

Appendix B. Navier–Stokes operators

In the studied configurations, the flow is controlled by the Reynolds number $Re = \frac{U_\infty D}{\nu}$, U_∞ is the free stream velocity, D the diameter of the cylinder and ν the dynamic viscosity of the fluid. The fluid motion inside the domain is governed by the two-dimensional incompressible Navier–Stokes equations,

$$\frac{\partial \mathbf{U}}{\partial t} + \mathbf{U} \cdot \nabla \mathbf{U} = -\nabla P + \nabla \cdot \boldsymbol{\tau}(\mathbf{U}) \quad (\text{B.1a})$$

$$\nabla \cdot \mathbf{U} = 0, \quad (\text{B.1b})$$

where $\mathbf{q} = [\mathbf{U}, P]$, \mathbf{U} is the velocity vector whose components are (U, V) , P is the reduced pressure and the viscous stress tensor $\boldsymbol{\tau}(\mathbf{u})$ can be expressed as $\nu(\nabla \mathbf{U} + \nabla \mathbf{U}^T)$. The incompressible Navier–Stokes equations (B.1) are complemented with the following boundary conditions: on the cylinder surface, no-slip boundary conditions, uniform boundary conditions are set $U \rightarrow (U_\infty, 0)$ and stress-free at the outlet.

In the main text, Navier–Stokes equations (B.1) and the associated boundary conditions are written under the form $\mathbf{B} \frac{\partial \mathbf{q}}{\partial t} = \mathbf{L}\mathbf{q} + \mathbf{N}(\mathbf{q}, \mathbf{q})$, where $\mathbf{N}(\mathbf{q}, \mathbf{q}) = \mathbf{U} \cdot \nabla \mathbf{U}$ is the convective term.

References

- [1] P. Cvitanović, Invariant measurement of strange sets in terms of cycles, *Phys. Rev. Lett.* 61 (24) (1988) 2729.
- [2] G.M. Shroff, H.B. Keller, Stabilization of unstable procedures: the recursive projection method, *SIAM J. Numer. Anal.* 30 (4) (1993) 1099–1120.
- [3] V. Citro, P. Luchini, F. Giannetti, F. Auteri, Efficient stabilization and acceleration of numerical simulation of fluid flows by residual recombination, *J. Comput. Phys.* 344 (2017) 234–246.
- [4] E.J. Doedel, B. Oldeman, *Auto-07p: Continuation and Bifurcation Software*, 1998.
- [5] A. Dhooge, W. Govaerts, Y.A. Kuznetsov, MATCONT: a MATLAB package for numerical bifurcation analysis of ODEs, *ACM Trans. Math. Softw.* 29 (2) (2003) 141–164.
- [6] W. Govaerts, Y.A. Kuznetsov, V. De Witte, A. Dhooge, H. Meijer, W. Mestrom, A. Riet, B. Sautois, MATCONT and CL MATCONT: Continuation Toolboxes in Matlab, Gent University and Utrecht University, 2011.
- [7] F. Giannetti, S. Camarri, V. Citro, Sensitivity analysis and passive control of the secondary instability in the wake of a cylinder, *J. Fluid Mech.* 864 (2019) 45–72.
- [8] F. Giannetti, S. Camarri, P. Luchini, Structural sensitivity of the secondary instability in the wake of a circular cylinder, *J. Fluid Mech.* 651 (2010) 319–337.
- [9] T. Kapitula, K. Promislow, *Spectral and Dynamical Stability of Nonlinear Waves*, vol. 185, Springer, 2013.
- [10] L. Guillot, B. Cochelin, C. Vergez, A generic and efficient Taylor series-based continuation method using a quadratic recast of smooth nonlinear systems, *Int. J. Numer. Methods Eng.* 119 (4) (2019) 261–280.
- [11] M. Urabe, Galerkin's procedure for nonlinear periodic systems, *Arch. Ration. Mech. Anal.* 20 (1965) 120–152.
- [12] M. Krack, J. Gross, *Harmonic Balance for Nonlinear Vibration Problems*, Springer, 2019.
- [13] B. Cochelin, C. Vergez, A high order purely frequency-based harmonic balance formulation for continuation of periodic solutions, *J. Sound Vib.* 324 (1–2) (2009) 243–262.
- [14] A. Stokes, On the approximation of nonlinear oscillations, *J. Differ. Equ.* 12 (1972) 535–558.
- [15] P. Kuchment, Floquet theory for hypoelliptic equations and systems in the whole space, in: *Floquet Theory for Partial Differential Equations*, Springer, 1993, pp. 103–123.
- [16] Y.A. Kuznetsov, *Elements of Applied Bifurcation Theory*, vol. 112, Springer Science & Business Media, 2013.
- [17] R. Seydel, *Practical Bifurcation and Stability Analysis*, vol. 5, Springer Science & Business Media, 2009.
- [18] J. Zhou, T. Hagiwara, M. Araki, Spectral characteristics and eigenvalues computation of the harmonic state operators in continuous-time periodic systems, *Syst. Control Lett.* 53 (2) (2004) 141–155.
- [19] C. Curtis, B. Deconinck, On the convergence of Hill's method, *Math. Comput.* 79 (269) (2010) 169–187.
- [20] M.A. Johnson, K. Zumbrun, Convergence of Hill's method for non-self-adjoint operators, *SIAM J. Numer. Anal.* 50 (1) (2012) 64–78.
- [21] B. Bentvelsen, A. Lazarus, Modal and stability analysis of structures in periodic elastic states: application to the Ziegler column, *Nonlinear Dyn.* 91 (2) (2018) 1349–1370.
- [22] A. Lazarus, O. Thomas, A harmonic-based method for computing the stability of periodic solutions of dynamical systems, *C. R., Méc.* 338 (9) (2010) 510–517.
- [23] L. Guillot, A. Lazarus, O. Thomas, C. Vergez, B. Cochelin, A purely frequency based Floquet–Hill formulation for the efficient stability computation of periodic solutions of ordinary differential systems, *J. Comput. Phys.* 416 (2020) 109477.
- [24] F. Giannetti, P. Luchini, Structural sensitivity of the first instability of the cylinder wake, *J. Fluid Mech.* 581 (2007) 167–197.
- [25] D. Sipp, Open-loop control of cavity oscillations with harmonic forcings, *J. Fluid Mech.* 708 (2012) 439.
- [26] M. Benzi, M.A. Olshanskii, Z. Wang, Modified augmented Lagrangian preconditioners for the incompressible Navier–Stokes equations, *Int. J. Numer. Methods Fluids* 66 (4) (2011) 486–508.
- [27] J. Moulin, P. Jolivet, O. Marquet, Augmented Lagrangian preconditioner for large-scale hydrodynamic stability analysis, *Comput. Methods Appl. Mech. Eng.* 351 (2019) 718–743.
- [28] Y. Saad, *Iterative Methods for Sparse Linear Systems*, vol. 82, SIAM, 2003.
- [29] F. Hecht, New development in FreeFem++, *J. Numer. Math.* 20 (3–4) (2012) 251–266.
- [30] S. Balay, S. Abhyankar, M. Adams, J. Brown, P. Brune, K. Buschelman, L. Dalcin, A. Dener, V. Eijkhout, W. Gropp, et al., *PETSc Users Manual*, 2019.
- [31] V. Hernandez, J.E. Roman, V. Vidal, SLEPc: a scalable and flexible toolkit for the solution of eigenvalue problems, *ACM Trans. Math. Softw.* 31 (3) (2005) 351–362.
- [32] D. Fabre, V. Citro, D. Ferreira Sabino, P. Bonnefis, J. Sierra, F. Giannetti, M. Pigou, A practical review on linear and nonlinear global approaches to flow instabilities, *Appl. Mech. Rev.* 70 (6) (2018).
- [33] P. Collet, J.-P. Eckmann, O. Lanford, Universal properties of maps on an interval, *Commun. Math. Phys.* 76 (3) (1980) 211–254.
- [34] C.H.K. Williamson, Vortex dynamics in the cylinder wake, *Annu. Rev. Fluid Mech.* 28 (1) (1996) 477–539.
- [35] D. Barkley, R.D. Henderson, Three-dimensional Floquet stability analysis of the wake of a circular cylinder, *J. Fluid Mech.* 322 (1996) 215–241.
- [36] M. Carini, F. Giannetti, F. Auteri, On the origin of the flip-flop instability of two side-by-side cylinder wakes, *J. Fluid Mech.* 742 (2014) 552–576.

- [37] J. Mizushima, Y. Ino, Stability of flows past a pair of circular cylinders in a side-by-side arrangement, *J. Fluid Mech.* 595 (2008) 491–507.
- [38] J. Sierra, V. Citro, F. Giannetti, D. Fabre, Efficient computation of periodic compressible flows with spectral techniques, 2020, Manuscript submitted for publication.
- [39] G. Moore, Floquet theory as a computational tool, *SIAM J. Numer. Anal.* 42 (6) (2005) 2522–2568.



Efficient computation of time-periodic compressible flows with spectral techniques

Javier Sierra-Ausin^{a,b}, Vincenzo Citro^{a,*}, Flavio Giannetti^a, David Fabre^b

^a *DIIN, Via Giovanni Paolo II, 132, 84084 Fisciano SA, Italy*

^b *IMFT, 2 Allé du Professeur Camille Soula, 31400 Toulouse, France*

Received 3 May 2021; received in revised form 17 September 2021; accepted 5 February 2022

Available online 24 February 2022

Abstract

A systematic approach to parametrically analyze compressible time-periodic flows is proposed. Instead of time-stepping simulations, a Fourier–Galerkin strategy is adopted, which consists of the projection of the periodic solution onto a truncated Fourier series. Starting from the compressible Navier–Stokes equations, a truncated nonlinear problem coupling the $2N + 1$ fields, representing the Fourier discretization, is derived. This nonlinear problem is solved by Newton iteration and a set of efficient algorithms for the resolution of the arising inner linear systems is proposed. Compared to alternative methods, the formulation is free of any numerical constraint affecting performance, e.g. a CFL-like condition. It is also free of aliasing effects arising in other spectral techniques. The efficiency of the method is illustrated for two configurations where sound is radiated due to a flow instability, namely the flow around a circular cylinder and the flow through two successive apertures, i.e. the hole-tone configuration.

© 2022 Elsevier B.V. All rights reserved.

Keywords: Spectral method; Acoustics; Compressible flows; Nonlinear dynamics; Limit cycle

1. Introduction

Many fluid dynamics problems are characterized by the spontaneous emergence of time-periodic solutions. The classical approach in the studying of periodic states is to perform time integration of the governing equations up to convergence to a stable (unstable) limit cycle. However, this approach can become rapidly very expensive in some circumstances. For instance, it is notably inefficient near bifurcations leading to unsteadiness where transients can be lengthy. It is also unsuited to cases where the underlying physics imposes tiny time steps. This situation is met for example with compressible, low-Mach-number limit flows involving acoustic radiation, where a severe time-step restriction is imposed by the large separation in convective and acoustic velocity scales.

Several ideas have been proposed to speed-up the convergence of time-stepping towards a limit cycle, for instance, using time filters [1] or considering symmetries [2]. However, the efficiency of such approaches remains case-dependent. An alternative idea is to take advantage of the time periodicity of the expected solution by applying

* Corresponding author.

E-mail address: vcitro@unisa.it (V. Citro).

spectral techniques to the time discretization and directly solving for the entire cycle. The problem may be worked out either in spectral or time domain, leading to two distinct classes of methods.

In the first case, formulating the problem in the spectral domain leads to the Harmonic Balance (or Fourier–Galerkin) formulation, a representation of the cycle by a truncated Fourier series up to N th order. The Navier–Stokes equations are then written in spectral space, leading to a system coupling the $2N + 1$ Fourier components. This last system can be solved globally using, for instance, a Newton iteration. This method is useful for the study of low-dimensional systems of equations modeling mechanical problems [3]. Recently, an alternative formulation of the Harmonic-Balance called *self-consistent method* has been introduced for order $N = 1$ [4,5] and subsequently adapted to order $N = 2$ [6]. Self-consistent method has gained some popularity in the fluid instability community (see [7] for a discussion on the link between harmonic-balance and self-consistent method). Besides a description of the limit cycle, the *self-consistent method* yields an amplitude equation describing the transient dynamics towards it. A generalization of the method to compressible flows was proposed by [8] for the wake of a cylinder. However, the accuracy of the truncation to order $N = 1$ remains case-dependent. A general implementation of the Harmonic Balance method in frequency domain for compressible flows up to arbitrary order N is still missing.

Alternatively, the problem may be formulated in time, leading to the so called time-spectral method. In this case, the $2N + 1$ Fourier components are replaced by $2N + 1$ “snapshots” representing the cycle. The equations are evaluated in the time domain, but the time-derivative is computed in the frequency domain, thus requiring direct and inverse discrete Fourier transforms to pull back this term into the time domain. Time Spectral Method has been successfully used for the characterization of high Reynolds flows in the field of turbomachinery, e.g. Hall et al. [9] and Mavriplis et al. [10], where it is considered as a closure model of averaged equations, or an alternative to Unsteady Reynolds Averaged Navier–Stokes equations (URANS) (see Ekici et al. [11], Sicot et al. [12] and references therein). Recently, it has been extended for the treatment of free-surface flows and fluid structure interaction problems (see Gatin et al. [13] and Yao et al. [14]).

Despite their limited usage in the literature, the Fourier–Galerkin formulation presents a series of advantages regarding other approaches requiring the action of the discrete Fourier transform cf. [15]. First, the approach is free of aliasing errors because the projection onto the Fourier basis is analytical, i.e. it evaluates the analytical Fourier coefficients of the residual. On the contrary, Time-Spectral-Method (TSM) and other similar methodologies rely on sampling a series of time-instants and on the use of successive discrete Fourier transforms, which if in one hand may permit faster evaluations of the residual in case of strong nonlinearity on the other it will inherently add aliasing errors. Under the sampling theorem, higher harmonics of nonlinear terms cannot be resolved with the same number of samples used for linear terms. As a result, methods relying on the discrete Fourier transform must increase the number of degrees of freedom, e.g. the 3/2-rule of Orszag for quadratic nonlinearity [16].

Furthermore, the solution of the TSM formulation may be solved by a fixed-point algorithm, e.g. Newton method or by a pseudo-time marching strategy. In fluid mechanics, in particular for turbomachinery applications, a pseudo-time marching is the preferred strategy to compute the final periodic solution. This strategy is effective at moderate Mach numbers. Nonetheless, at low-Mach-number, where there is a large scale difference between the convective and the acoustic scale, the pseudo-time step must be considerably constrained.

An upper bound for the pseudo-time step is determined from quantities in the acoustic scale either because of CFL or accuracy condition. Regarding the linear stability condition efforts have been paid to enlarge the stability limit: optimal explicit Runge Kutta (ERK) schemes have been determined for several spatial discretization. Examples can be found in the works by Parsani et al. [17] for spectral differences, Citro et al. for classical finite element [18] and Kubatko et al. [19] for discontinuous Galerkin. Nevertheless, the integration of Navier–Stokes equations, even with optimal ERK schemes, requires a significant number of iterations, which makes a full parametric study of low Mach number flows an impractical task.

The aim of the present study is to propose a numerical resolution algorithm for the Fourier–Galerkin method considering an arbitrary truncation order N , allowing an efficient reconstruction of periodic solutions of the compressible Navier–Stokes equations. Governing equations and linear stability are introduced in Section 2. Fourier–Galerkin approach is introduced in Section 3, where particular emphasis is placed on the derivation of nonlinear terms of the Fourier–Galerkin residual (a detailed derivation can be found in [Appendix](#)). The resulting nonlinear problem is solved via a Newton–Krylov approach with an efficient preconditioning strategy in a parallel context. Finally, in Section 4 and Section 5 the presented approach is applied to two numerical examples: the flow past a circular cylinder and the sound generation in a hole tone configuration, both in the low-Mach-number limit. In Section 5.1.2 a comparison of the performance of the current implementation of Fourier–Galerkin with TSM is reported for the cylinder case at several Mach numbers.

2. Theoretical formulation

Let us consider the description of nonlinear saturated states of compressible flows. The exposition is sufficiently general to be extended for the study of other type of flows. Nevertheless, attention will be paid to the Fourier–Galerkin representation of the quadratic and cubic nonlinearity.

2.1. Governing equations

Let us consider a compressible fluid motion of a perfect gas (characterized by its specific constant R_g and adiabatic index γ) with constant dynamic viscosity μ and heat conductivity κ . The flow is described by the fluid density $\tilde{\rho}$, the velocity vector field $\tilde{\mathbf{u}} = (\tilde{u}, \tilde{v}, \tilde{w})$, the pressure \tilde{p} , and temperature \tilde{T} . These dimensional primitive variables are made dimensionless as follows:

$$\mathbf{x} = \frac{\tilde{\mathbf{x}}}{\bar{\ell}}, \quad t = \frac{\tilde{t}\bar{u}}{\bar{\ell}}, \quad \rho = \frac{\tilde{\rho}}{\bar{\rho}}, \quad \mathbf{u} = \frac{\tilde{\mathbf{u}}}{\bar{u}}, \quad T = \frac{\tilde{T}}{\bar{T}}, \quad p = \frac{\tilde{p}}{\bar{\rho}\bar{R}_g\bar{T}}, \quad (1)$$

where reference values are designated by an upper bar $\bar{\cdot}$.

After a convenient choice of the reference length $\bar{\ell}$ and velocity \bar{u} , one can classically define three nondimensional numbers (Reynolds, Mach and Prandtl) as follows:

$$Re = \frac{\bar{\rho}\bar{u}\bar{\ell}}{\bar{\mu}}, \quad M = \frac{\bar{u}}{\sqrt{\bar{\rho}\bar{R}_g\bar{T}}}, \quad Pr = \frac{\bar{\mu}}{\bar{\rho}\bar{\kappa}}. \quad (2)$$

Introducing these notations into the compressible Navier–Stokes equations leads to a set of equations governing the evolution of the nondimensional state vector $\mathbf{q} = [\rho, \mathbf{u}, T, p]$. To facilitate the analysis and enlighten the nature of the nonlinearities, it is convenient to write these equations as follows:

$$\mathcal{NS}(\mathbf{q}) \equiv \mathbf{M}\left(\frac{\partial \mathbf{q}}{\partial t}\right) + \mathbf{L}(\mathbf{q}) + \mathbf{F}_2(\mathbf{q}, \mathbf{q}) + \mathbf{F}_3(\mathbf{q}, \mathbf{q}, \mathbf{q}) = \mathbf{0}. \quad (3)$$

In Eq. (3), the “mass” matrix \mathbf{M} multiplying the time-derivative and the linear operator \mathbf{L} are defined as:

$$\mathbf{M} = \begin{pmatrix} 1 & 0 & 0 & 0 \\ 0 & \rho \mathbf{I} & 0 & 0 \\ 0 & 0 & \rho & 0 \\ 0 & 0 & 0 & 0 \end{pmatrix}, \quad \mathbf{L} = \begin{pmatrix} 0 & 0 & 0 & 0 \\ 0 & -\nabla \cdot \boldsymbol{\tau}(\cdot) & 0 & \frac{1}{\gamma M^2} \nabla \\ 0 & 0 & -\frac{\gamma}{Pr} \nabla^2 & 0 \\ 0 & 0 & 0 & 1 \end{pmatrix} \quad (4)$$

The nonlinear terms involve a quadratic operator \mathbf{F}_2 and a cubic operator \mathbf{F}_3 defined as:

$$\mathbf{F}_2(\mathbf{q}_i, \mathbf{q}_j) = \begin{pmatrix} \mathbf{u}_i \cdot \nabla \rho_j + \rho_i \nabla \cdot \mathbf{u}_j \\ \mathbf{0} \\ (\gamma - 1) [p_i \nabla \cdot \mathbf{u}_j - \gamma M^2 \boldsymbol{\tau}(\mathbf{u}_i) : \mathbf{D}(\mathbf{u}_j)] \\ -\rho_i T_j \end{pmatrix} \quad (5)$$

$$\mathbf{F}_3(\mathbf{q}_i, \mathbf{q}_j, \mathbf{q}_\ell) = \begin{pmatrix} 0 \\ \rho_i \mathbf{u}_j \cdot \nabla \mathbf{u}_\ell \\ \rho_i \mathbf{u}_j \cdot \nabla T_\ell \\ 0 \end{pmatrix} \quad (6)$$

In these expressions, \mathbf{I} denotes the identity operator, whose dimension is determined by the number of velocity components; $\boldsymbol{\tau}(\mathbf{u})$ is the shear stress tensor $\boldsymbol{\tau}(\mathbf{u}) = \frac{1}{Re} [2\mathbf{D}(\mathbf{u}) - \frac{2}{3}(\nabla \cdot \mathbf{u})\mathbf{I}]$ and $\mathbf{D}(\mathbf{u}) = \frac{1}{2} [\nabla \mathbf{u} + \nabla \mathbf{u}^T]$ is the strain tensor. Additionally a set of boundary conditions are needed to close the problem. Specific boundary conditions are case dependent and they are not here specified.

It is important to remark that, unlike incompressible flows where only quadratic nonlinearities are present, compressible Navier–Stokes equations contain both quadratic and cubic nonlinearities. In particular, the term $\rho \mathbf{u} \cdot \nabla \mathbf{u}$, which for incompressible equations is the only nonlinearity and a quadratic one, becomes a cubic nonlinearity in the compressible case. This point explains why a derivation of equations in Fourier–Galerkin method is much more intricate.

To facilitate derivations in following sections, it is convenient to define symmetric nonlinear operators:

$$\mathbf{F}_2^{(sym)}(\mathbf{q}_i, \mathbf{q}_j) = \left[\mathbf{F}_2(\mathbf{q}_i, \mathbf{q}_j) + \mathbf{F}_2(\mathbf{q}_j, \mathbf{q}_i) \right], \quad (7)$$

$$\begin{aligned} \mathbf{F}_3^{(sym)}(\mathbf{q}_i, \mathbf{q}_j, \mathbf{q}_\ell) = & \left[\mathbf{F}_3(\mathbf{q}_i, \mathbf{q}_j, \mathbf{q}_\ell) + \mathbf{F}_3(\mathbf{q}_i, \mathbf{q}_\ell, \mathbf{q}_j) \right. \\ & + \mathbf{F}_3(\mathbf{q}_j, \mathbf{q}_i, \mathbf{q}_\ell) + \mathbf{F}_3(\mathbf{q}_\ell, \mathbf{q}_i, \mathbf{q}_j) \\ & \left. + \mathbf{F}_3(\mathbf{q}_j, \mathbf{q}_\ell, \mathbf{q}_i) + \mathbf{F}_3(\mathbf{q}_\ell, \mathbf{q}_j, \mathbf{q}_i) \right] \end{aligned} \quad (8a)$$

With the aim of a simpler description of Fourier–Galerkin formalism, please note that dyadic interactions (interactions between two modes) are also possible whenever the tryadic nonlinear term $\mathbf{F}_3^{(sym)}$ contains the mean flow and other two harmonics, introduced in Section 3. So, in general dyadic interactions arise in the nonlinear term,

$$\mathbf{F}_2^{(dya)}(\mathbf{q}_i, \mathbf{q}_j) = \mathbf{F}_2^{(sym)}(\mathbf{q}_i, \mathbf{q}_j) + \mathbf{F}_3^{(sym)}(\mathbf{q}_i, \mathbf{q}_j, \mathbf{q}_0). \quad (9)$$

2.2. Linear stability

Before presenting the methodology used to compute a periodic cycle in the nonlinear regime, we recall the principle of Linear Stability Analysis (LSA) [20], which is the favored tool to detect the onset of such cycles from a previous steady state. Accordingly, LSA will be used in Section 5.1.1 to detect the critical Reynolds numbers associated with unsteadiness. Presentation of the LSA formalism also allows to introduce some notations which are used in the sequel.

The linear stability of compressible flows can be studied with a classical normal-mode analysis: the velocity and pressure fields are decomposed into a time-independent base flow, i.e. a steady-state, $\mathbf{q}_0 = [\rho, \mathbf{u}_0, T_0, p_0]$, and a generic three-dimensional small disturbance $\mathbf{q}' = [\rho', \mathbf{u}', T', p']$. After introducing this decomposition into Eq. (3) and linearizing, it is found that the base flow is governed by the steady version of the Navier–Stokes equations, whereas the perturbation field is described by the linearized unsteady Navier–Stokes equations (LNSE) written as follows:

$$\mathbf{M}_{|\mathbf{q}_0} \frac{\partial \mathbf{q}'}{\partial t} + \mathbf{L}\mathbf{q}' + \mathbf{F}_2^{(sym)}(\mathbf{q}_0, \mathbf{q}') + \frac{1}{2}\mathbf{F}_3^{(sym)}(\mathbf{q}_0, \mathbf{q}_0, \mathbf{q}') = \mathbf{0}, \quad (10)$$

where $\mathbf{M}_{|\mathbf{q}_0} = \text{diag}(1, \rho_0\mathbf{I}, \rho_0, 0)$ denotes the mass matrix evaluated at the steady state.

Global modes are modal non-trivial solutions of Eq. (10), which are expressed as follows:

$$\mathbf{q}' = \hat{\mathbf{q}}_\ell e^{\lambda_\ell t} + \text{c.c.}, \quad (11)$$

where λ_ℓ corresponds to the complex eigenvalue ($\sigma_\ell + \mathbf{i}\omega_\ell$) and c.c. stands for complex conjugate and $\hat{\mathbf{q}}_\ell$ is the associated eigenmode. The real part of λ_ℓ represents the growth rate of the perturbation and the imaginary part ω_ℓ its circular frequency. For $\sigma_\ell > 0$, the flow is unstable whereas for $\sigma_\ell < 0$ it is stable. Introducing the ansatz Eq. (11) in the LNSE Eq. (10), we obtain the following generalized eigenvalue problem:

$$\mathbf{0} = \lambda_\ell \mathbf{M}_{|\mathbf{q}_0} \hat{\mathbf{q}}_\ell + L\mathcal{N}\mathcal{S}_{|\mathbf{q}_0}(\hat{\mathbf{q}}_\ell) \quad (12)$$

with

$$\begin{aligned} L\mathcal{N}\mathcal{S}_{|\mathbf{q}_0}(\hat{\mathbf{q}}_\ell) \equiv & \mathbf{L}\hat{\mathbf{q}}_\ell + \mathbf{F}_2^{(sym)}(\mathbf{q}_0, \hat{\mathbf{q}}_\ell) \\ & + \mathbf{F}_3^{(sym)}(\mathbf{q}_0, \mathbf{q}_0, \hat{\mathbf{q}}_\ell) \end{aligned} \quad (13)$$

3. Fourier–Galerkin method for Navier–Stokes equations

3.1. Fourier–Galerkin residual equation

Fourier–Galerkin method employs a truncated Fourier basis \mathcal{F}_N , which is inherently periodic, thus perfectly suitable for the reconstruction of the periodic flow state:

$$\begin{aligned} \pi_N(\mathbf{q}) &\equiv \check{\mathbf{q}}_{(0)} + \sum_{n=1}^N [\check{\mathbf{q}}_{((n,c))} \cos(n\omega t) + \check{\mathbf{q}}_{((n,s))} \sin(n\omega t)] \\ &\equiv \check{\mathbf{Q}}^T \mathcal{F}_N \\ \text{with } \mathcal{F}_N &= [1, \cos(\omega t), \sin(\omega t), \dots, \cos(N\omega t), \sin(N\omega t)]^T \\ \text{and } \check{\mathbf{Q}} &= [\check{\mathbf{q}}_{(0)}, \check{\mathbf{q}}_{((1,c))}, \check{\mathbf{q}}_{((1,s))}, \dots, \check{\mathbf{q}}_{((N,c))}, \check{\mathbf{q}}_{((N,s))}]^T, \end{aligned} \tag{14}$$

where π_N is the projector operator onto the Fourier basis \mathcal{F}_N ; $\check{\mathbf{q}}_{((n,c))}(\mathbf{x})$ and $\check{\mathbf{q}}_{((n,s))}(\mathbf{x})$ are the coefficients of the Fourier series, in other words, they are two real n th-order harmonics describing the nonlinear perturbation at two instants separated by a quarter-period of oscillation. The projection π_N onto a finite Fourier basis \mathcal{F}_N introduces an error, nonetheless for smooth functions ($C^\infty(0, T)$) such an error decreases with an exponential rate, i.e. $\propto e^{-CN}$, $C > 0$ with the number of harmonics N retained in the basis [21, Lemma 2.2].

The first step to obtain Fourier–Galerkin equations consists on the injection of the ansatz (14) into the unsteady Navier–Stokes equations (3). A Galerkin procedure is thus employed, i.e. the previously obtained equation is weighted with each term of the Fourier basis and then integrated over a period. Such a process is summarized below:

$$\mathcal{NS}(\mathbf{q}) \xrightarrow[\text{projection}]{\text{Fourier}} \mathcal{NS}(\pi_N(\mathbf{q})) \xrightarrow[\text{residual}]{\text{Weighted}} \begin{cases} \check{\mathbf{r}}^{(0)} = \frac{1}{T} \int_0^T \mathcal{NS}(\pi_N(\mathbf{q})) dt \\ \check{\mathbf{r}}^{(n,c)} = \frac{2}{T} \int_0^T \mathcal{NS}(\pi_N(\mathbf{q})) \cos(n\omega t) dt \\ \check{\mathbf{r}}^{(n,s)} = \frac{2}{T} \int_0^T \mathcal{NS}(\pi_N(\mathbf{q})) \sin(n\omega t) dt \end{cases}$$

Finally, the residual vector $\check{\mathbf{R}} = [\check{\mathbf{r}}^{(0)}, \check{\mathbf{r}}^{(1,c)}, \check{\mathbf{r}}^{(1,s)}, \dots, \check{\mathbf{r}}^{(N,c)}, \check{\mathbf{r}}^{(N,s)}]^T$ is equated to zero, i.e. $\check{\mathbf{R}} = \mathbf{0}$. In particular, the Fourier–Galerkin residual of the compressible Navier–Stokes equations written in primitive variables is expressed in compact operator notation as follows:

$$\check{\mathbf{r}}^{(0)} = L\mathcal{NS}_{|\check{\mathbf{q}}_{(0)}}(\check{\mathbf{q}}_{(0)}) + \check{\mathbf{F}}_2^{(0)}(\check{\mathbf{Q}}) + \check{\mathbf{F}}_3^{(0)}(\check{\mathbf{Q}}) \tag{15a}$$

$$\check{\mathbf{r}}^{(k,c)} = k\omega \mathbf{M}_{|\check{\mathbf{q}}_{(0)}} \check{\mathbf{q}}_{(k,s)} + L\mathcal{NS}_{|\check{\mathbf{q}}_{(0)}}(\check{\mathbf{q}}_{(k,c)}) + \check{\mathbf{F}}_2^{(k,c)}(\check{\mathbf{Q}}) + \check{\mathbf{F}}_3^{(k,c)}(\check{\mathbf{Q}}) \tag{15b}$$

$$\check{\mathbf{r}}^{(k,s)} = -k\omega \mathbf{M}_{|\check{\mathbf{q}}_{(0)}} \check{\mathbf{q}}_{(k,c)} + L\mathcal{NS}_{|\check{\mathbf{q}}_{(0)}}(\check{\mathbf{q}}_{(k,s)}) + \check{\mathbf{F}}_2^{(k,s)}(\check{\mathbf{Q}}) + \check{\mathbf{F}}_3^{(k,s)}(\check{\mathbf{Q}}) \tag{15c}$$

Linear terms contained in the operator $L\mathcal{NS}$ uniquely consist of interactions among harmonics of the same order and the mean flow. Dyadic and triadic interactions among harmonics are encoded in the nonlinear operators $\check{\mathbf{F}}_2^{(k)}$ and $\check{\mathbf{F}}_3^{(k)}$. For instance, $\check{\mathbf{F}}_2^{(0)}$ and $\check{\mathbf{F}}_3^{(0)}$, are the feedback terms among harmonic interactions and the mean flow. Similarly $\check{\mathbf{F}}_2^{(k,c)}$ and $\check{\mathbf{F}}_3^{(k,c)}$ (resp. $\check{\mathbf{F}}_2^{(k,s)}$ and $\check{\mathbf{F}}_3^{(k,s)}$) are the forcing terms of the k th cosine (resp. sinus) harmonic component. Interactions among different harmonics greatly increase with the degree of non linearity of the nonlinear operator. A detailed description of nonlinear terms may be found in Appendix. Eq. (15a) corresponds to the evolution of the mean flow component $\check{\mathbf{q}}_{(0)}$.

In addition to the $2N + 1$ unknown fields constituting the Fourier expansion, the problem admits one extra scalar unknown, namely the frequency ω . The determination of the frequency it is equivalent to the determination of the period $T = \frac{2\pi}{\omega}$, which is measured as the distance in time between two solution points satisfying $\pi_N(\mathbf{q})(t + T) = \pi_N(\mathbf{q})(t)$. In addition, the problem is autonomous, which implies that for every phase shift ξ , $\pi_N(\mathbf{q})(t + \xi)$ is a solution of the system whenever $\pi_N(\mathbf{q})(t)$ is a solution. Therefore one can start measuring the period T at any solution point $\mathbf{q}(t + \xi)$ along the periodic orbit; in other words, the *phase-condition* that fixes the phase-shift ξ , it is an implicit equation of ω that serves to determine the unknown frequency. Any condition of the form $g(\check{\mathbf{Q}}) = 0$ where g is a linear function of the unknown fields can be used for this purpose. In practice, one can define the function g so as to coincide with a physically relevant integral quantity of the oscillating field at instant $t = 0$. For instance, for wake instability problems (Section 5.1.1) one can use the lift force exerted on the body, or for

oscillating jet problems (Section 5.2), one can use the oscillating flow rate across the aperture. At this stage we keep $g(\check{\mathbf{Q}}) = 0$ as an arbitrary linear function of the oscillating part of the flow. This function can always be decomposed formally as follows:

$$g(\check{\mathbf{Q}}) = \sum_{n=1}^N [g_{(n,c)}(\check{\mathbf{q}}_{(n,c)}) + g_{(n,s)}(\check{\mathbf{q}}_{(n,s)})], \tag{16}$$

where $g_{(n,c)}$, $g_{(n,s)}$ are scalar-valued linear functions of the Fourier components.

3.2. Newton iteration method

Newton iteration is the chosen approach to solve the nonlinear Fourier–Galerkin system. At each step of the procedure, starting from an estimate $[\check{\mathbf{Q}}_n, \omega_n]^T$ of the solution, we look for an improved estimate defined as:

$$\check{\mathbf{Q}}_{n+1} = \check{\mathbf{Q}}_n + \delta\check{\mathbf{Q}}, \quad \omega_{n+1} = \omega_n + \delta\omega. \tag{17}$$

Introducing Eq. (17) into the governing equations and linearizing with respect to perturbations $[\delta\check{\mathbf{Q}}, \delta\omega]$ leads to a linear system which has to be solved at each step of the procedure:

$$D\check{\mathbf{R}} [\delta\check{\mathbf{Q}}, \delta\omega]^T = - [\check{\mathbf{R}}(\check{\mathbf{Q}}_n), g(\check{\mathbf{Q}}_n)]^T, \tag{18a}$$

here $D\check{\mathbf{R}}$ denotes the Jacobian operator, written in block–matrix form as follows:

$$D\check{\mathbf{R}} = \begin{pmatrix} D\check{\mathbf{r}}^{(0;0)} & \dots & D\check{\mathbf{r}}^{(0;k,c)} & D\check{\mathbf{r}}^{(0;k,s)} & \dots & D_{\omega}\check{\mathbf{r}}^{(0)} \\ \vdots & \ddots & \vdots & \vdots & \ddots & \ddots \\ D\check{\mathbf{r}}^{(k,c;0)} & \dots & D\check{\mathbf{r}}^{(k,c;k,c)} & D\check{\mathbf{r}}^{(k,c;k,s)} & \dots & D_{\omega}\check{\mathbf{r}}^{(k,c)} \\ D\check{\mathbf{r}}^{(k,s;0)} & \dots & D\check{\mathbf{r}}^{(k,s;k,c)} & D\check{\mathbf{r}}^{(k,s;k,s)} & \dots & D_{\omega}\check{\mathbf{r}}^{(k,s)} \\ \vdots & \dots & \vdots & \vdots & \ddots & \ddots \\ 0 & \dots & g^{(k,c)} & g^{(k,s)} & \dots & 0 \end{pmatrix} \tag{19}$$

and $D\check{\mathbf{r}}^{(k,c;j,s)}$ denotes the derivative of the residual term $\check{\mathbf{r}}^{(k,c)}$ with respect to the sinus component of the j th harmonic. Those block operators are defined as follows:

$$D\check{\mathbf{r}}^{(0)}\delta\check{\mathbf{Q}} = LN\mathcal{S}|_{\check{\mathbf{q}}_{(0)}}(\delta\check{\mathbf{q}}_{(0)}) + [D\check{\mathbf{F}}_{2|\check{\mathbf{Q}}}^{(0)} + D\check{\mathbf{F}}_{3|\check{\mathbf{Q}}}^{(0)}]\delta\check{\mathbf{Q}} \tag{20a}$$

$$D\check{\mathbf{r}}^{(k,c)}\delta\check{\mathbf{Q}} = k\omega\mathbf{M}|_{\delta\check{\mathbf{q}}_{(0)}}\check{\mathbf{q}}_{(k,s)} + k\omega\mathbf{M}|_{\check{\mathbf{q}}_{(0)}}\delta\check{\mathbf{q}}_{(k,s)} + LN\mathcal{S}|_{\check{\mathbf{q}}_{(0)}}(\delta\check{\mathbf{q}}_{(k,c)}) + [D\check{\mathbf{F}}_{2|\check{\mathbf{Q}}}^{(k,c)} + D\check{\mathbf{F}}_{3|\check{\mathbf{Q}}}^{(k,c)}]\delta\check{\mathbf{Q}} \tag{20b}$$

$$D\check{\mathbf{r}}^{(k,s)}\delta\check{\mathbf{Q}} = -k\omega\mathbf{M}|_{\delta\check{\mathbf{q}}_{(0)}}\check{\mathbf{q}}_{(k,c)} - k\omega\mathbf{M}|_{\check{\mathbf{q}}_{(0)}}\delta\check{\mathbf{q}}_{(k,c)} + LN\mathcal{S}|_{\check{\mathbf{q}}_{(0)}}(\delta\check{\mathbf{q}}_{(k,s)}) + [D\check{\mathbf{F}}_{2|\check{\mathbf{Q}}}^{(k,s)} + D\check{\mathbf{F}}_{3|\check{\mathbf{Q}}}^{(k,s)}]\delta\check{\mathbf{Q}} \tag{20c}$$

$$D_{\omega}\check{\mathbf{r}}^{(0)}\delta\omega = D_{\omega}\check{\mathbf{F}}_{2|\check{\mathbf{Q}}}^{(0)}\delta\omega \tag{21a}$$

$$D_{\omega}\check{\mathbf{r}}^{(k,c)}\delta\omega = \delta\omega(k\mathbf{M}|_{\check{\mathbf{q}}_{(0)}}\check{\mathbf{q}}_{(k,s)}) + D_{\omega}\check{\mathbf{F}}_{2|\check{\mathbf{Q}}}^{(k,c)}\delta\omega \tag{21b}$$

$$D_{\omega}\check{\mathbf{r}}^{(k,s)}\delta\omega = \delta\omega(-k\mathbf{M}|_{\check{\mathbf{q}}_{(0)}}\check{\mathbf{q}}_{(k,c)}) + D_{\omega}\check{\mathbf{F}}_{2|\check{\mathbf{Q}}}^{(k,s)}\delta\omega. \tag{21c}$$

With these notations, the action of each of the linear operators defined in Eq. (20) may be understood as the action of a row vector:

$$D\check{\mathbf{r}}^{(k,c)} = [D\check{\mathbf{r}}^{(k,c;0)}, D\check{\mathbf{r}}^{(k,c;1,c)}, D\check{\mathbf{r}}^{(k,c;1,s)}, \dots, D\check{\mathbf{r}}^{(k,c;N,c)}, D\check{\mathbf{r}}^{(k,c;N,s)}]$$

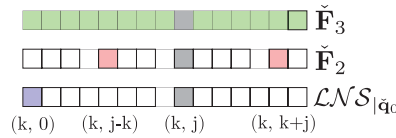


Fig. 1. Dependency pattern in the evaluation of the entry (k, j) in the derivative of each operator.

eventually leading to the block definition of the matrix defined in (19). Because the Fourier components with $k \neq 0$ involve both a cosine and a sine, a given entry (k, j) of the Jacobian operator $D\check{\mathbf{R}}$ is a 2×2 block if $k \neq 0$ and $j \neq 0$, a 2×1 block if $k \neq 0$ and $j = 0$, a 1×2 block if $k = 0$ and $j \neq 0$ or 1×1 block if $k = j = 0$. Each block is computed with respect to a set of harmonics and the mean component. The dependency pattern of each entry greatly depends on the nonlinearity of the operator: Fig. 1 schematizes the dependency stencil. Evaluation of the linear operator $LN\mathcal{S}|_{\check{q}_0}$ depends uniquely on the mode k and on the mean component. Quadratic nonlinearities include interactions with modes $|k - j|$ and $j + k$. Whereas the evaluation of the nonlinear term $\check{\mathbf{F}}_3^{(k,s)}$ may depend on the full set of harmonics. For more details consider the detailed description provided in Appendix.

3.3. Resolution of the linear system of equations

The critical part in the algorithm is the resolution of the linear system (18a). Here, the GMRES method is used for the factorization of the full Jacobian $D\check{\mathbf{R}}$. Nonetheless, such an approach requires efficient preconditioning techniques to speed up convergence. In such a way the linear system Eq. (18a) is transformed into:

$$\mathbf{P}^{-1} D\check{\mathbf{R}} \left[\delta\check{\mathbf{Q}}_{n+1}, \delta\omega_{n+1} \right]^T = -\mathbf{P}^{-1} \left[\check{\mathbf{R}}(\check{\mathbf{Q}}_n), g(\check{\mathbf{Q}}_n, t = 0) \right]^T. \tag{22}$$

Three outer preconditioning techniques have been considered in this study: *Block Jacobi* and *Block Gauss Seidel* (upper and lower triangular). Let us detail these preconditioning techniques. In the following only the Fourier–Galerkin residual is considered. The line in the Jacobian operator that corresponds to the phase condition is included in the set of degrees of freedom of a $D\check{\mathbf{r}}^{(i)}$ block. In such a way the block composed of $D\check{\mathbf{r}}^{(i)}$ and the phase condition is not singular and the following preconditioning techniques are applicable.

Block-Jacobi preconditioning considers only blocks that are found on the diagonal, i.e. it does not take into account interactions with other Fourier components.

$$\mathbf{P}_{BJ}(\check{\mathbf{Q}}_n, \omega_n) = \begin{bmatrix} D\check{\mathbf{r}}^{(0)} & \dots & \mathbf{0} & \dots & \mathbf{0} \\ \vdots & \ddots & & & \vdots \\ \mathbf{0} & \dots & D\check{\mathbf{r}}^{(i)} & \dots & \mathbf{0} \\ \vdots & & & \ddots & \vdots \\ \mathbf{0} & \dots & \mathbf{0} & \dots & D\check{\mathbf{r}}^{(N)} \end{bmatrix} \tag{23}$$

Another possibility consists in the use of a Gauss–Seidel preconditioner. Upper triangular GS solves for each component by considering interactions with only higher harmonics.

$$\mathbf{P}_{GSU}(\check{\mathbf{Q}}_n, \omega_n) = \begin{bmatrix} D\check{\mathbf{r}}^{(0)} & \dots & D\check{\mathbf{r}}^{(0,i)} & \dots & D\check{\mathbf{r}}^{(0,N)} \\ \vdots & \ddots & & & \vdots \\ \mathbf{0} & \dots & D\check{\mathbf{r}}^{(i,i)} & \dots & D\check{\mathbf{r}}^{(i,N)} \\ \vdots & & & \ddots & \vdots \\ \mathbf{0} & \dots & \mathbf{0} & \dots & D\check{\mathbf{r}}^{(N)} \end{bmatrix} \tag{24}$$

Analogously, lower triangular block GS solves for every component by considering interactions uniquely with lower harmonics.

$$\mathbf{P}_{GSL}(\check{\mathbf{Q}}_n, \omega_n) = \begin{bmatrix} D\check{\mathbf{r}}^{(0)} & \dots & \mathbf{0} & \dots & \mathbf{0} \\ \vdots & \ddots & & & \vdots \\ D\check{\mathbf{r}}^{((i,0))} & \dots & D\check{\mathbf{r}}^{(i)} & \dots & \mathbf{0} \\ \vdots & & & \ddots & \vdots \\ D\check{\mathbf{r}}^{((N,0))} & \dots & D\check{\mathbf{r}}^{((N,i))} & \dots & D\check{\mathbf{r}}^{(N)} \end{bmatrix} \quad (25)$$

The preconditioned linear operator $\mathbf{P}^{-1}D\check{\mathbf{R}}$ of Eq. (22) in the case of BJ is composed of identity blocks in the diagonal and non-null blocks off-diagonal. Such a procedure is effective when the matrix is diagonally dominant, e.g. when harmonic components are of small amplitude. Let us consider the expression of $\mathbf{P}^{-1}D\check{\mathbf{R}}$, particularized for the above considered preconditioners:

$$\mathbf{P}_{BJ}^{-1}D\check{\mathbf{R}} = \mathbf{P}_{BJ}^{-1}\mathbf{P}_{GSL} + \mathbf{P}_{BJ}^{-1}\mathbf{P}_{GSU} - \mathbf{I} \quad (26a)$$

$$\mathbf{P}_{GSU}^{-1}D\check{\mathbf{R}} = \mathbf{P}_{GSU}^{-1}\mathbf{P}_{GSL} - \mathbf{P}_{GSU}^{-1} + \mathbf{I} \quad (26b)$$

$$\mathbf{P}_{GSL}^{-1}D\check{\mathbf{R}} = \mathbf{P}_{GSL}^{-1}\mathbf{P}_{GSU} - \mathbf{P}_{GSL}^{-1} + \mathbf{I}, \quad (26c)$$

in the above expressions the decomposition $D\check{\mathbf{R}} = [\mathbf{P}_{GSU} + \mathbf{P}_{GSL} - \mathbf{P}_{BJ}]$ is assumed. Preconditioners \mathbf{P} require the factorization of diagonal blocks $D\check{\mathbf{r}}^{(i)}$. Two methods have been considered, exact factorization (LU) and Additive-Schwarz Method (ASM) with LU as sub-preconditioner.

3.4. Initial condition

When using a Newton method, an essential point for convergence is to start the process from an initial “guess” as close as possible to the expected solution. In parametric studies, continuation methods are commonly employed; namely, we select as initial condition a solution previously computed for close values of the parameters and repeat the procedure. The question remains on how to obtain a very first solution to initiate the continuation. One may start the process for parameter values just above the threshold for the onset of the cycle, where Linear Stability Analysis (LSA) gives a good clue of the solution. The simplest idea is to take the order-zero component as the mean flow of the LSA, namely $\check{\mathbf{Q}}_0 = \mathbf{q}_0$, set the order-one components to coincide with the linear eigenmode with some fitted amplitude ζ , namely $\check{\mathbf{Q}}_{1,c} = \zeta Re(\hat{\mathbf{q}})$, $\check{\mathbf{Q}}_{1,s} = -\zeta Im(\hat{\mathbf{q}})$, and initialize all higher-order components to zero. This method may need some fine hand-tuning of the amplitude ζ . A second, more elaborate method is to use *Weakly Nonlinear Analysis* (WNL), which provides an approximation of the solution close to the threshold up to order $N = 2$. This method is not detailed here; see [7] for a demonstration of this procedure in the incompressible case.

3.5. Summary

To summarize this section, a concise presentation of the whole procedure used to numerically solve the problem is given in algorithm 1.

4. Numerical approach

The FreeFEM software based on a finite element method is used to solve the problem numerically. An initial mesh is generated by decomposing the computational domain in triangles via a Delaunay–Voronoi algorithm. A variational formulation of the problem is then built using \mathbb{P}_2 (quadratic) elements for each component of the velocity and \mathbb{P}_1 (linear) elements for the pressure, temperature and density. Linear systems are solved with the PETSc library in a parallel context. The parallelization is carried out following a memory distributed paradigm. The system is decomposed in space into n_{cores} partitions, where n_{cores} is the number of cores. The $2N + 1$ Fourier components associated with the generic partition i are available for the processor i . Sponge regions are used to damp acoustic waves far from the domain of interest to prevent their reflection. The definition of the sponge region is the same as in Fani et al. [8].

Algorithm 1 Fourier-Galerkin for compressible Navier Stokes

```

Require: Initial guess  $(\check{\mathbf{Q}}_0, \omega_0)$ . Parameters  $M, Re$ .
1: function FOURIER-GALERKIN( $M, Re, \check{\mathbf{Q}}_0, \omega_0$ )
2:    $n = 0$ 
3:   while  $\| [\check{\mathbf{R}}(\check{\mathbf{Q}}_n, \omega_n), g(\check{\mathbf{Q}}_n)]^T \|_2 < \text{tol}$  do
4:     Evaluate  $[\check{\mathbf{R}}(\check{\mathbf{Q}}_n, \omega_n), g(\check{\mathbf{Q}}_n)]$ 
5:     Evaluate  $D\check{\mathbf{R}}(\check{\mathbf{Q}}_n, \omega_n)$  ▷ Full or matrix-vector function
6:      $j = 0$ 
7:     for  $j < m$  do
8:       Assemble preconditioner  $\mathbf{P}$  ▷ e.g. Block Jacobi
9:        $\mathbf{P}^{-1} D\check{\mathbf{R}}_{n,j} [\delta\check{\mathbf{Q}}_{n,j+1}, \delta\omega_{n,j+1}]^T = -\mathbf{P}^{-1} \check{\mathbf{R}}_{n,j}$  ▷ GMRES
10:       $(\check{\mathbf{Q}}_{n,j+1}, \omega_{n,j+1}) = (\check{\mathbf{Q}}_{n,j} + \delta\check{\mathbf{Q}}_{n,j+1}, \omega_{n,j} + \delta\omega_{n,j+1})$ 
11:       $j = j + 1$ 
12:    end for
13:     $(\check{\mathbf{Q}}_{n+1}, \omega_{n+1}) = (\check{\mathbf{Q}}_n + \delta\check{\mathbf{Q}}_{n+1}, \omega_n + \delta\omega_{n+1})$ 
14:     $n = n + 1$ 
15:  end while
16:  return  $(\check{\mathbf{Q}}_{n+1}, \omega_{n+1})$ 
17: end function

```

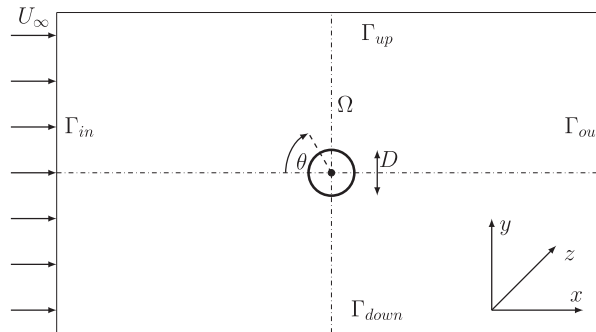


Fig. 2. Sketch of the computational domain Ω of the uniform flow past a circular cylinder.

Parametric studies and generation of figures are performed using Octave/Matlab with the aid of the generic drivers of the StabFem project (see a presentation of these functionalities in [7]). According to the philosophy of this project, a number of example codes generating sample results from the present paper are available online (<https://gitlab.com/stabfem/StabFem>).

Note that in the numerical implementation, we make an extensive use of mesh adaptation to ensure that spatial convergence is reached. The mesh is adapted either to a base flow and a linear eigenmode following the procedure explained in [7], or to the whole set of fields constituting the Fourier coefficients of the flow. Such adaptations are repeated several times during the parametric studies, and each time, the solution is projected onto the new mesh and used as starting point to relaunch the Newton iteration.

5. Results

5.1. Flow past a cylinder

5.1.1. Definition of the problem

The first example is the flow past a circular cylinder, a canonical configuration extensively studied in the literature in the incompressible [7,22] and compressible [8,23] setting. Cross-validations with literature are carried out to

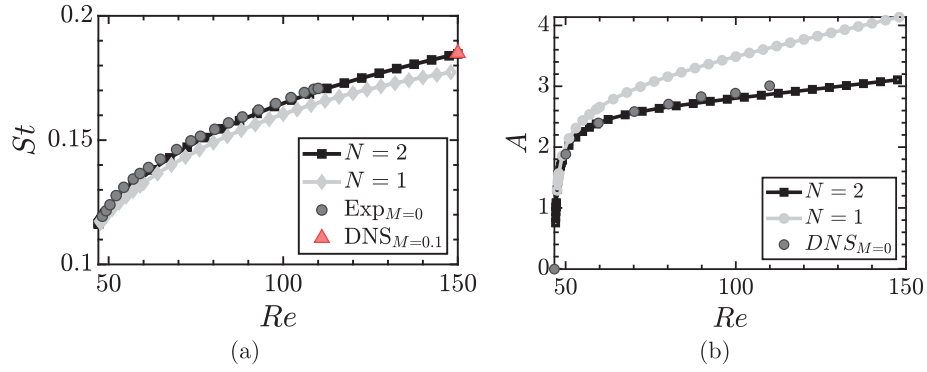


Fig. 3. (a) Evolution of the Strouhal fundamental frequency with Re . Experimental reference was taken from Carte et al. [24] and DNS data from Inoue et al. [25]. (b) Amplitude of the limit cycle. DNS reference data was reported by Mantic et al. [4].

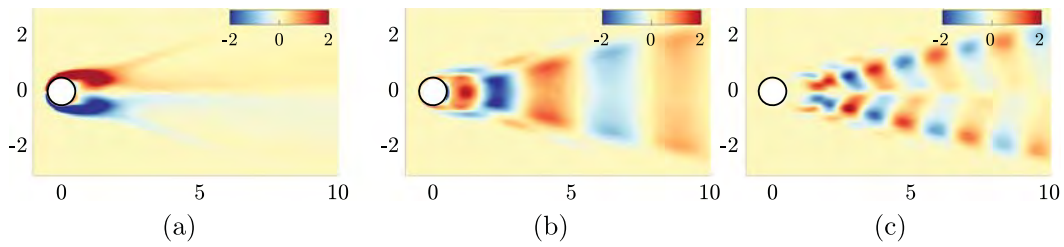


Fig. 4. Vorticity field at $Re = 150$ and $M = 10^{-1}$. (a) Mean component. (b) $\check{q}_{(1,c)}$ component. (c) $\check{q}_{(2,c)}$ component.

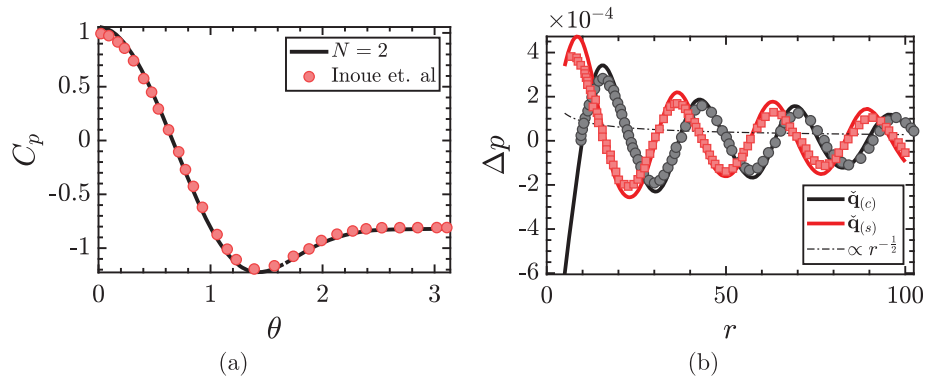


Fig. 5. $Re = 150$ and $M = 0.2$. (a) Pressure distribution around the cylinder. (b) Decay of pressure distribution at $\theta = \frac{\pi}{2}$. Markers report reference data from [25].

assess the precision of the method. In addition the numerical performance of linear solvers is evaluated in this case study.

A schematic representation of the computational domain Ω is shown in Fig. 2. Governing equations are complemented with the following boundary conditions: uniform velocity U_∞ , density ρ_∞ and temperature T_∞ at boundaries Γ_{in} , Γ_{up} , Γ_{down} , Γ_{out} and no-slip adiabatic wall at the cylinder surface. The computational domain is a square of size $(300D \times 300D)$ which is immersed into a sponge domain of $(1000D \times 1000D)$. The chosen sponge size, which is around six wavelengths of the acoustic disturbance at $M = 10^{-2}$ in each direction, is sufficient to prevent any acoustic reflection from the boundaries of the domain Ω . The auxiliary function $g(\check{\mathbf{Q}})$ needed to fix the phase of the cycle was defined as $g(\check{\mathbf{Q}}) = F_y(t = 0) \equiv \int_{\Gamma_w} \left[-pI + \tau(\mathbf{u}) \right]_{t=0} \cdot \mathbf{n} \cdot \mathbf{e}_y d\ell$, where Γ_w is the cylinder wall, so that the instant $t = 0$ corresponds to a zero of the oscillating lift exerted on the cylinder.

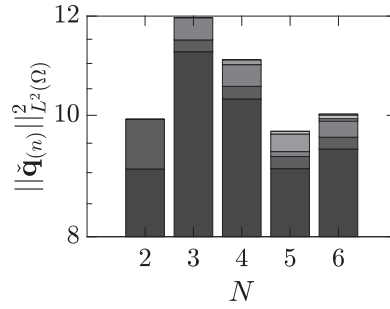


Fig. 6. Spectral reconstruction of the solution at $Re = 150$ and $M = 10^{-1}$. Gray-scale to distinguish the amplitude of each harmonic, lighter grays are used for higher harmonics.

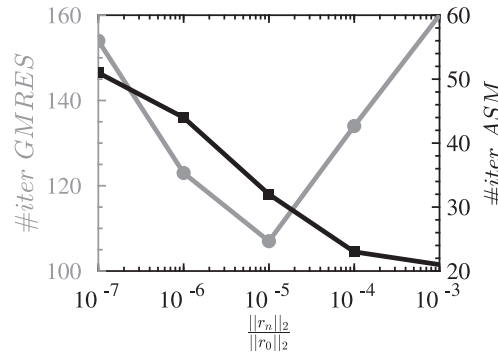


Fig. 7. Evolution of the total number of iterations of the inexact factorization with the ASM method of inner blocks with respect to the tolerance of the ASM procedure. Likewise, total number of GMRES iterations for the resolution of the nonlinear problem with respect to the ASM tolerance. Parameters $Re = 150$, $M = 0.1$, $N = 2$ with a numerical domain composed of $1.3 \cdot 10^5$ elements and the lower triangular Gauss Seidel as the outer preconditioner.

A comparison with other results reported in the literature is shown in Fig. 3. As can be seen (Fig. 3a), the frequency of the limit cycle is reliably evaluated even with a truncation to a single harmonic ($N = 1$). However, it fails to faithfully estimate its amplitude $A = \left(\sum_{n=1}^N \|\check{\mathbf{q}}^{(n)}\|_{L^2(\Omega)}^2 \right)^{\frac{1}{2}}$. By contrast, a truncated Fourier basis with order $N = 2$ is sufficient to correctly predict the amplitude in the studied interval, namely $Re \in [Re_c, 100]$. For higher Reynolds numbers, e.g. $Re = 150$, a larger number of harmonics ($N > 2$) still modifies the spectral reconstruction, see Fig. 6. Such a figure displays the spectral content of the solution at $Re = 150$ and $M = 10^{-1}$. A high-fidelity reconstruction of the periodic solution can be obtained with $N \geq 4$, where the last mode displays a much smaller amplitude than the others.

Fig. 4 portrays the structure of the Fourier components reconstructing the vortex shedding cycle for $Re = 150$ and $M = 10^{-1}$. The structure of the mean flow and first harmonic are in good accordance with [8], but the second harmonic was not computed by these authors. Moreover, to assess the capability of the methodology to correctly reconstruct the solution both in the near field (governed by hydrodynamics) and in the far field (governed by acoustics), Fig. 5 represents the structure of the pressure field for the parameter values $M = 2 \cdot 10^{-1}$ and $Re = 150$, with a truncation $N = 2$. The comparison with reference data from the Direct Numerical Simulations (DNS) of Inoue et al. [25] is excellent, both for pressure along the cylinder wall (Fig. 5a), and along the vertical line defined by $x = 0$ (Fig. 5b).

5.1.2. Performance evaluation

Let us now use this test case to assess the performance of numerical algorithms to efficiently solve linear systems such as Eq. (18a). The tolerance to achieve the convergence of the Newton method corresponds to the L^2 norm of the Newton update of Eq. (18a), i.e. $\|\delta \mathbf{x}\|_{L^2} = \sqrt{\|\delta \check{\mathbf{Q}}\|_{L^2}^2 + |\delta \omega|^2}$, lower than 10^{-8} . Likewise, the relative tolerance of the GMRES procedure (the ratio of the L^2 norm of the residual at the 1st iteration with respect to the i th iteration) for convergence is set to 10^{-5} . The resolution of the linear problems whose associated matrix is an inner

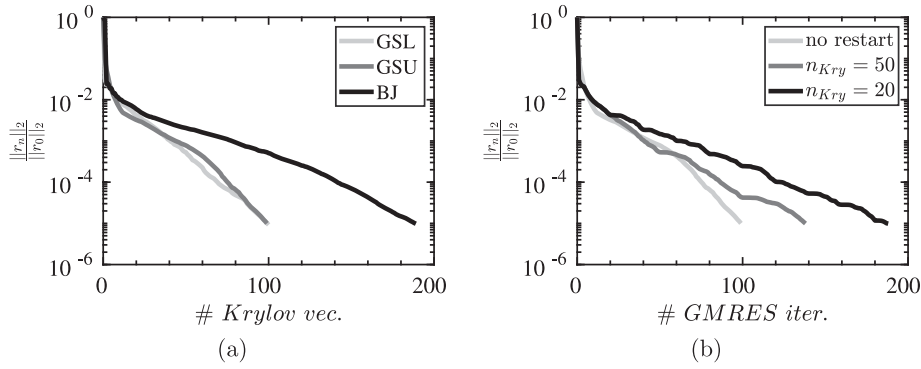


Fig. 8. Same parameters and mesh refinement as Fig. 7. (a) Evolution of relative residual versus cumulative Krylov vectors for the three preconditioners. (b) Evolution of the relative residual versus number of GMRES iterations for several restart configurations (outer preconditioner GSU).

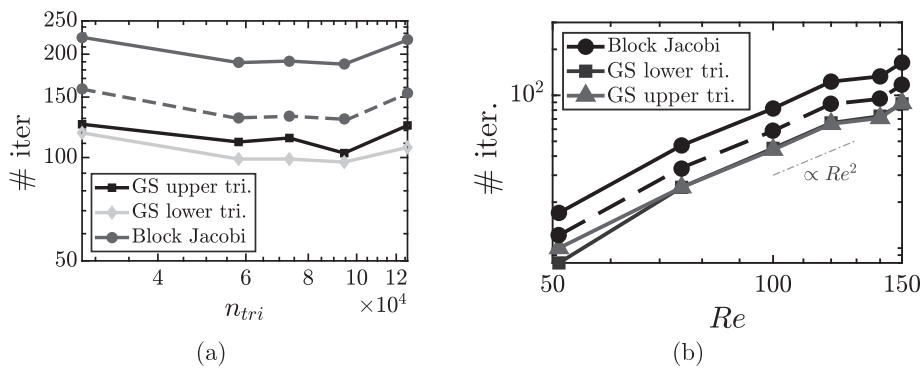


Fig. 9. (a) Dependency of GMRES iteration number with respect to the level of refinement of the computational domain at $Re = 150$ and $M = 0.1$ with $N = 2$. (b) Number of GMRES iterations as a function of Reynolds number and outer preconditioner with $N = 2$. Dashed line denotes the corrected number of GMRES iterations with the Block–Jacobi preconditioning.

block diagonal $D\tilde{r}^{(i)}$, described in Section 3.3, is carried out with two approaches. If memory is not an issue, each block in the diagonal (of the Block–Jacobi or Gauss–Seidel preconditioners) is LU factorized. Otherwise an ASM preconditioner is used to solve the linear problems associated with inner blocks and the tolerance is varied from 10^{-3} to 10^{-7} (cf. Fig. 7). The GMRES approach takes 103 iterations with LU factorization of inner blocks; the number of GMRES iterations (107) reaches a minimum for a relative tolerance of the ASM approach of 10^{-5} (cf. Fig. 7), which shows weak independence of the GMRES procedure on the method used for the resolution of the inner diagonal blocks. On each GMRES iteration a Krylov vector is used (no restart). So the total number of Krylov vectors is equal to the number of GMRES iterations. Fig. 8a reports the evolution of the relative residual versus the cumulative number of Krylov vectors. In addition, on the same problem we tested the effect of n_{Kry} , the number of Krylov vectors retained in the basis (restarted GMRES). As expected the convergence rate deteriorates, but convergence is still reached in a reasonable number of iterations.

As reported in Fig. 9b, the number of GMRES iterations per Newton iteration increases quadratically with Reynolds number. In terms of GMRES iterations, the block diagonal preconditioning is less efficient than the other two but they follow the same trend as Re increases. Nonetheless, the GS preconditioning performs an additional number of $N(2N + 1)$ matrix–vector products, which is around 50% more block matrix–vector operations than BJ; therefore, one should correct the number of GMRES iterations by a factor 1.5, which is displayed in Fig. 9 with a dashed line. The methodology is also independent, as long as it is sufficient to reconstruct the solution from the number of harmonics and grid refinement, the latter reported in Fig. 9a. Finally a linear memory gain relative to an increasing length of the Fourier basis has been reported by Sierra et al. [26] with respect to the direct factorization of the full Jacobian operator.

Table 1

Wall-clock time required for convergence with eight processors for $Re = 150$ and numerical domain composed of $1.4 \cdot 10^4$ elements.

N/Method	Fourier–Galerkin	Explicit TSM	Implicit TSM
$M = 3 \cdot 10^{-1}$			
$N = 4$	2344 s	2451 s	8345 s
$N = 5$	2645 s	2992 s	9745 s
$N = 6$	3049 s	3250 s	11 121 s
$M = 10^{-1}$			
$N = 4$	2357 s	7745 s	22 355 s
$N = 5$	2591 s	8454 s	26 341 s
$N = 6$	3063 s	9721 s	31 545 s
$M = 10^{-2}$			
$N = 4$	2297 s	73 320 s	92 673 s
$N = 5$	2618 s	83 450 s	103 673 s
$N = 6$	3104 s	91 680 s	1 209 452 s

For the sake of comparison with other similar methodologies, authors have considered the Time spectral method (TSM), which solves the following nonlinear problem

$$\mathbf{M}^{\tau,K} \mathbf{D}_{FT} \check{\Omega}^{\tau,K} \mathbf{D}_{FT}^{-1} \mathbf{Q} + \mathbf{L}(\mathbf{Q}) + \mathbf{F}_2(\mathbf{Q}, \mathbf{Q}) + \mathbf{F}_3(\mathbf{Q}, \mathbf{Q}, \mathbf{Q}) = \mathbf{0}, \tag{27}$$

where $\check{\Omega}_k^{\tau,K} = \begin{bmatrix} 0 & k\omega \\ -k\omega & 0 \end{bmatrix}$, $\check{\Omega}_0^{\tau,K} = 0$, \mathbf{D}_{FT} denotes the discrete Fourier Transform operator (resp. \mathbf{D}_{FT}^{-1} corresponds to the inverse Fourier transform operator) and $\mathbf{M}^{\tau,K}$ is the mass matrix \mathbf{M} evaluated at each sampled instance. TSM requires the invertibility of forward and inverse discrete Fourier transforms. Therefore, the number of samples K must be fixed to $K = 2N + 1$. TSM is commonly adapted from an already existing code via a *pseudo-time integration* approach (see e.g. [27]): an extra pseudo-time derivative $\mathbf{M} \frac{\partial \mathbf{Q}}{\partial t_{ps}}$ is added as a source term to Eq. (27). The resulting equations are solved in a pseudo-time direction until the stationary solution of the TSM formulation is reached. Note that the stationary solution of the TSM formulation is a spectral reconstruction of a periodic solution of the original system of equations. Such a technique is relative easy to implement as it only requires to add the TSM time-derivative on an already existing code. However, the pseudo-time marching approach is not able to directly compute an unstable periodic solution without stabilization procedures, see for instance BoostConv [28]. Furthermore, the efficiency of the approach depends on the CFL parameter of the pseudo-time step Δt_{ps} which is constrained as

$$\Delta t_{ps} = \frac{\text{CFL}}{\frac{U_\infty}{h} (1 + \frac{1}{M}) + \omega N} \tag{28}$$

where h is a measure of the size of the grid spacing and an extra term ωN is added due to the extra pseudo-time derivative. In acoustic applications, i.e. when $\frac{1}{M} \gg 1$ the CFL condition is roughly simplified to $\Delta t_{ps} \approx \frac{\text{CFL } hM}{U_\infty}$; from a practical point of view, $O(\frac{1}{M})$ additional iterations are required with respect to the integration of the classical Navier–Stokes equations.

We carried out an accurate comparison at $Re = 150$ for three Mach numbers ($M = 3 \cdot 10^{-1}$, $M = 10^{-1}$ and $M = 10^{-2}$), with $N = 4, 5, 6$. The TSM data are computed by using the OpenSource SU2 code [29], where a finite volume implementation of the TSM method is available. The dual-time integration is realized with either the classical fourth-order Runge–Kutta method or with an implicit Euler iteration at the largest CFL allowed by stability constraints.

Regarding the initial condition, the Fourier–Galerkin–Newton–Krylov approach is initialized with a previous frequency reconstruction at another Mach or Reynolds number (either with the same or less number of harmonics N). Whereas, for the TSM, the initial solution consists of a snapshot of a DNS with the same set of parameters (Re, M). Such a choice was verified a posteriori to be faster than to initialize the TSM computation with a series of snapshots for another parameter configuration as it is done for FG. Additionally, TSM requires ω and T as an

Table 2

Average memory consumption for the resolution of the linear system Eq. (22) in a Newton iteration of the Fourier–Galerkin approach with $n_{cores} = 8$ with a numerical mesh of $7 \cdot 10^4$ elements for $Re = 150$, $M = 10^{-1}$.

	$N = 1$	$N = 2$	$N = 3$	$N = 4$	$N = 5$	$N = 6$
Mem.(Gb)	13.5 Gb	24.5 Gb	34.1 Gb	41.1 Gb	53.6 Gb	64.2 Gb

Table 3

Average memory consumption for the resolution of the linear system Eq. (22) in a Newton iteration of the Fourier–Galerkin approach with $N = 4$ and a mesh of $1.4 \cdot 10^5$ elements for $Re = 150$, $M = 10^{-1}$.

	$n_{cores} = 8$	$n_{cores} = 16$	$n_{cores} = 32$	$n_{cores} = 64$
Mem.(Gb)	75 Gb	93 Gb	129 Gb	171 Gb

input to evaluate the time derivative term. For our test, we have chosen a pair (ω, T) previously computed by a DNS. Sensitivity issues to an incorrect selection of the pair (ω, T) are discussed in Nimmagadda et al. [29]. Both approaches are computed with distinct codes and two different meshes has been used. In order to have a fair comparison, both numerical domains are composed of approximately $1.4 \cdot 10^4$ elements (triangles for FG and quads for TSM).

In reference to the numerical performance, let us first remark the similarity in terms of wall-clock time and memory requirements of the implicit integration of a dual time-step and a GMRES iteration of the Newton–Krylov–Fourier–Galerkin approach cf. [29,30]. However, a formal correspondence between explicit TSM and FG in terms of residual evaluations or matrix–vector products does not seem evident. Therefore, a numerical comparison of both approaches has been carried out in a eight cores Intel i7-9700 architecture. Table 1 reports the wall-clock time required for convergence (norm of the residual below 10^{-6}). Fourier–Galerkin and explicit TSM record a similar wall-clock time for $M = 3 \cdot 10^{-1}$, however TSM suffers a linear increase in the wall-clock time with the $\frac{1}{M}$ factor. Therefore, as the Mach number decreases FG rapidly outperforms TSM in wall-clock time due to the CFL constraint on the pseudo time.

Finally, let us discuss the memory requirements of the Newton–Krylov methodology on two meshes with two different levels of refinement. \mathcal{M}_1 is composed of around $1.4 \cdot 10^5$ elements and \mathcal{M}_2 has around $7 \cdot 10^4$ elements. Tests on memory requirements have been carried out on a cluster node equipped with 64 Intel(R) Xeon(R) CPU E5-4610 processors and 256 GB of RAM memory. The first test, carried out on mesh \mathcal{M}_2 , assess the average memory consumption for the resolution of the linear system associated with each Newton iteration (Eq. (22)). These were performed with eighth processors for parameters $Re = 150$ and $M = 10^{-1}$ and upper Gauss–Seidel as preconditioning. Table 2 reports a sub-linear memory increasing with a empirical factor $N^{0.8}$. Such a factor is mainly due to the direct factorization of each block diagonal of the Jacobian Eq. (19). Similar results have been reported for the implicit TSM cf. [31,32]. The second performance test evaluates the memory scalability with respect to the number of processors; the results are reported in Table 3. A 30% increase of memory consumption is observed each time the number of processors is doubled. More studies regarding the scalability of the methodology have been previously carried out [26].

Finally, we highlight that the TSM wall-clock time reported in Table 1 requires the exact knowledge of the frequency ω . As a consequence, the total time required to get a given solution should take into account also the need to compute such a frequency. Our approach, on the other hand, directly characterizes the frequency within the global solution.

5.2. Whistling jet

The second test case is the flow passing through two circular holes in a plate (known as the hole-tone configuration). Such a flow configuration is encountered in many practical applications, including human whistling, wind instruments, whistling of a tea kettle [33], or birdcalls (devices used by hunters to imitate bird singing) [34,35].

In this study Fourier–Galerkin formalism is adopted with $N = 2, 3$ to study the self-sustained hydrodynamic instability and the radiation of sound past the unsteady onset. The physical domain and mesh structure are the same as in [35]. The numerical domain Ω is axisymmetric, as depicted in Fig. 10, with size $(800R_{h,1} \times 400R_{h,1}) (z \times r)$.

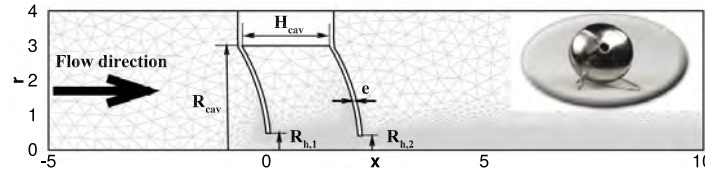


Fig. 10. Sketch of the hole-tone configuration, frame of reference and definition of geometrical parameters. An example of computational mesh is also reported in light gray. An actual birdcall is depicted in the upper right corner. For details about the used geometry see [35].

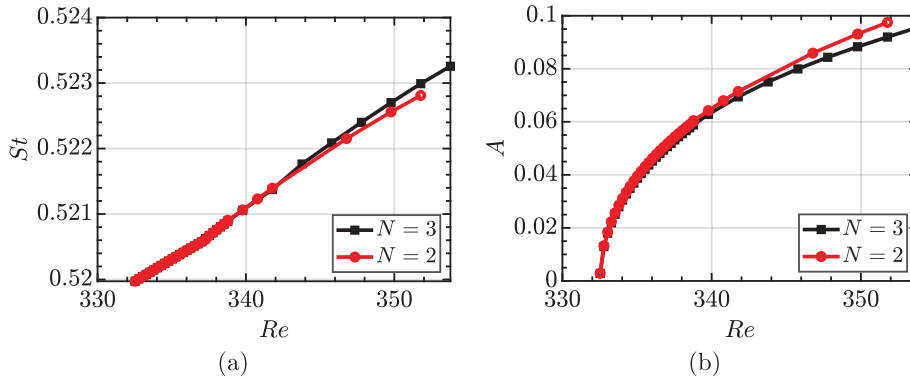


Fig. 11. (a) Evolution of the Strouhal fundamental frequency with Re . (b) Amplitude of the limit cycle.

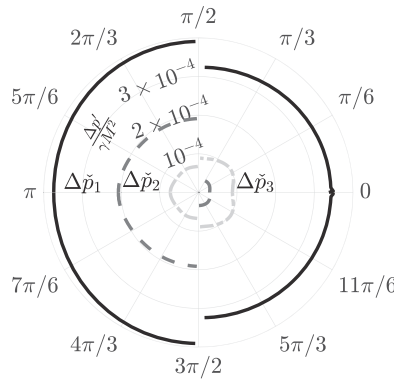


Fig. 12. Sound directivity at $Re = 350$ and $M = 0.02$ at a distance $r = 35$. Pressure variation $\Delta p'$ is scaled by γM^2 .

The problem is complemented with appropriate boundary conditions: adiabatic no-slip walls, inlet mass flux such as the flow rate across the first hole is equal to unity and sponge layers of the order of three to four acoustic wavelengths at the far field. The sponge definition is the same as in [8]. The auxiliary function $g(\mathbf{Q})$ needed to fix the phase of the cycle was defined as $g(\mathbf{Q}) = \int_{\Gamma_{h1}} [(\mathbf{u}(t = 0) - \mathbf{u}_0) \cdot \mathbf{n}] dS$, where Γ_{h1} is the cross section of the first hole, so that the instant $t = 0$ corresponds to a zero of the oscillating volume flow across the hole.

Fig. 11 shows the frequency and amplitude of the cycle as a function of Re , computed with respectively $N = 2$ and $N = 3$ truncations. In the current configuration, a truncated Fourier basis with order two seems sufficient since the results for $N = 2$ and $N = 3$ only differ by a few percents. Note that the flow is steady until the threshold of the first unsteadiness, which is located at $Re_c \approx 332.5$. This threshold value was first determined by linear stability analysis. The initial guess for the Fourier–Galerkin method with $Re > Re_c$ was obtained with a weakly nonlinear expansion and continuation was used afterwards while increasing Re .

The current approach provides direct access to the harmonic decomposition of sound directivity, reported in Fig. 12. The interaction between the jet and the two holes acts as a monopole aerodynamic source with different intensities upstream and downstream the cavity. The total sound radiation is of higher intensity upstream than downstream the obstacle, nonetheless the first harmonic behaves nearly as an isotropic monopole and the third harmonic radiates with higher intensity in the positive z direction.

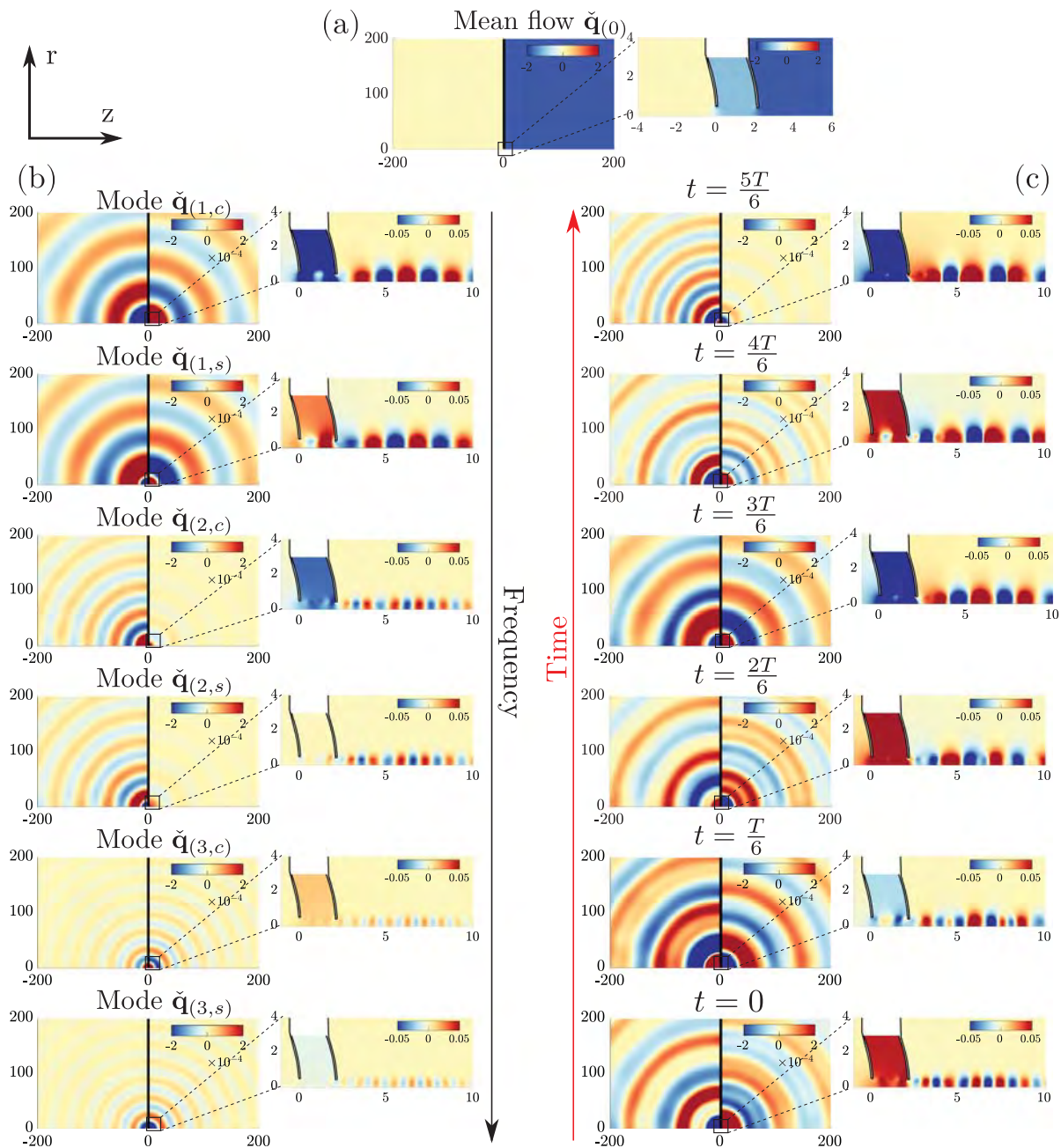


Fig. 13. Pressure component of acoustic and hydrodynamic perturbations at $Re = 350$ and $M = 0.02$ with $N = 3$. Pressure variation $\Delta p'$ is scaled by γM^2 .

The whistling jet test case is a perfect example of what is called in the theory of numerical analysis a stiff problem. Namely, the ratio between the two velocity scales (acoustic and hydrodynamic) of the flow is large, therefore the time step is greatly constrained with respect to an application where the fast velocity scale is not of interest. A reconstruction of a time series of the periodic flow separating both hydrodynamic and acoustic scales is displayed in Fig. 13. Time integration with common numerical schemes, e.g. Runge–Kutta method, of a single point (fixed Re and M) of Fig. 11 requires the integration of several flow time scales, $T = \frac{1}{Sr}$. Moreover, the maximum time step of an explicit time integrator is governed by the fast time scale which is of the order $\Delta t \approx O(M)$. This implies that the simulation of the compressible Navier–Stokes equations at low-Mach-number would take approximately an $O(M^{-1})$ the amount of time necessary for a incompressible simulation. The analysis of acoustic radiation at

the low-Mach-number limit usually becomes prohibitively expensive and it requires the use of low-Mach-number limit approximations, where different scales are solved sequentially with a one-way feedback, see Nana et al. [36]. Fourier–Galerkin approach applied to compressible flows is intended to open new possibilities in the study of flows of acoustic and aeroacoustic interest at low-Mach-number since the CFL constraint does not hold. Additionally, the approach could be adapted to track quasiperiodic solutions by the consideration of two incommensurate frequencies and their interactions.

6. Conclusion

An efficient methodology for the computation of periodic flow solutions has been presented. The approach is based on the orthogonal projection of the sought solution on a truncated Fourier basis. The parametrized limit cycle is then directly accessible by solving a fixed point problem without the requirement of solving for transients. Krylov–Newton method has been selected for the resolution of the nonlinear residual problem Eq. (15). That sort of approach necessitates efficient preconditioning techniques, in the current study two layers of preconditioners are proposed and their performance has been tested in the flow past the circular cylinder in Section 5.1.1. Assembling of the Jacobian and residual operators, as well as the solution of the nonlinear problem is effectuated in a parallel framework. A comparison with similar spectral techniques has been demonstrated in Section 5.1.2, where it is shown the absence of a CFL-like condition for the Fourier–Galerkin approach. The latter property is significant for the reconstruction of solutions of stiff problems. Finally, the hole-tone configuration serves as a test case to demonstrate the ability of the technique to accurately reconstruct the two flow scales.

To conclude, we stress again that in addition to being efficient for computation of a cycle for a single set of parameters, our implementation is designed to perform parametric studies using a *continuation method*. Namely, once we have computed a cycle, taking it as an initial condition to relaunch the Newton iteration for nearby values of the parameter generally converges in only a few iterations. This procedure still needs an initial guess. In the present paper, the latter is constructed for parameters just above the instability onset using a weakly nonlinear expansion. Another possibility is to initialize the approach with a previous solution of a time-stepping simulation. This procedure has not been demonstrated here but might be simpler as any available software performing DNS may be used. Another advantage of the methodology is the ability to track unstable periodic cycles. Such solutions are not accessible with usual time-stepping DNS, but they are important when characterizing the dynamics from a dynamical system perspective, as their knowledge allows to understand more complex dynamics involving, for instance quasi-periodic orbits or chaotic attractors [37,38].

Declaration of competing interest

The authors declare that they have no known competing financial interests or personal relationships that could have appeared to influence the work reported in this paper.

Appendix. Fourier Galerkin equations

Let us detail the derivation of Fourier–Galerkin equations Eq. (15). For the sake of self-consistency let us first summarize the Fourier–Galerkin equations:

$$\check{\mathbf{r}}^{(0)} = L\mathcal{N}\mathcal{S}_{|\check{\mathbf{q}}_{(0)}}(\check{\mathbf{q}}_{(0)}) + \check{\mathbf{F}}_2^{(0)}(\check{\mathbf{Q}}) + \check{\mathbf{F}}_3^{(0)}(\check{\mathbf{Q}}) \tag{A.1a}$$

$$\check{\mathbf{r}}^{(k,c)} = k\omega\mathbf{M}_{|\mathbf{q}_0}\check{\mathbf{q}}_{(k,s)} + L\mathcal{N}\mathcal{S}_{|\check{\mathbf{q}}_{(0)}}(\check{\mathbf{q}}_{(k,c)}) + \check{\mathbf{F}}_2^{(k,c)}(\check{\mathbf{Q}}) + \check{\mathbf{F}}_3^{(k,c)}(\check{\mathbf{Q}}) \tag{A.1b}$$

$$\check{\mathbf{r}}^{(k,s)} = -k\omega\mathbf{M}_{|\mathbf{q}_0}\check{\mathbf{q}}_{(k,c)} + L\mathcal{N}\mathcal{S}_{|\check{\mathbf{q}}_{(0)}}(\check{\mathbf{q}}_{(k,s)}) + \check{\mathbf{F}}_2^{(k,s)}(\check{\mathbf{Q}}) + \check{\mathbf{F}}_3^{(k,s)}(\check{\mathbf{Q}}) \tag{A.1c}$$

where nonlinear operators in the Fourier basis $\check{\mathbf{F}}^{(i)}(\check{\mathbf{Q}})$ have been explicitly written using their quadratic and cubic contributions. The first step in an explicit derivation of Eq. (A.1) consists on the injection of the Fourier

Table A.4

Summary of trigonometric identities. c and s denote cosinus and sinus functions. Each term of the right (sum) is multiplied by a factor of $\frac{1}{4}$.

Product			Sum			
m	n	ℓ	$n + m + \ell$	$n + m - \ell$	$n + \ell - m$	$m + \ell - n$
c	c	c	c	c	c	c
c	c	s	s	$-s$	s	s
c	s	c	s	s	s	$-s$
c	s	s	$-c$	c	$-c$	c
s	c	c	s	s	$-s$	s
s	c	s	$-c$	c	c	$-c$
s	s	c	$-c$	$-c$	c	c
s	s	s	$-s$	s	s	s

representation of the sought solution Eq. (14) into the governing equations:

$$\begin{aligned}
 & \sum_{n=1}^N L\mathcal{N}\mathcal{S}_{|\check{\mathbf{q}}(0)}(\check{\mathbf{q}}(0)) + \left[-k\omega\mathbf{M}_{|\mathbf{q}_0}\check{\mathbf{q}}(k,c) + L\mathcal{N}\mathcal{S}_{|\check{\mathbf{q}}(0)}(\check{\mathbf{q}}(n,s)) \right] \sin(n\omega t) \\
 & + \left[k\omega\mathbf{M}_{|\mathbf{q}_0}\check{\mathbf{q}}(k,s) + L\mathcal{N}\mathcal{S}_{|\check{\mathbf{q}}(0)}(\check{\mathbf{q}}(n,c)) \right] \cos(n\omega t) \\
 & + \sum_{n=1}^N \sum_{m=1}^N \left[\mathbf{F}_2(\check{\mathbf{q}}(n,s), \check{\mathbf{q}}(m,s)) \sin(n\omega t) \sin(m\omega t) \right. \\
 & + \mathbf{F}_2(\check{\mathbf{q}}(n,s), \check{\mathbf{q}}(m,c)) \sin(n\omega t) \cos(m\omega t) \\
 & + \mathbf{F}_2(\check{\mathbf{q}}(n,c), \check{\mathbf{q}}(m,s)) \cos(n\omega t) \sin(m\omega t) \\
 & \left. + \mathbf{F}_2(\check{\mathbf{q}}(n,c), \check{\mathbf{q}}(m,c)) \cos(n\omega t) \cos(m\omega t) \right] \\
 & + \sum_{n=1}^N \sum_{m=1}^N n\omega \left[-\mathbf{M}_{|\check{\mathbf{q}}(m,s)} \check{\mathbf{q}}(n,c) \sin(n\omega t) \sin(m\omega t) \right. \\
 & - \mathbf{M}_{|\check{\mathbf{q}}(m,c)} \check{\mathbf{q}}(n,c) \sin(n\omega t) \cos(m\omega t) \\
 & + \mathbf{M}_{|\check{\mathbf{q}}(m,s)} \check{\mathbf{q}}(n,s) \cos(n\omega t) \sin(m\omega t) + \mathbf{M}_{|\check{\mathbf{q}}(m,c)} \check{\mathbf{q}}(n,s) \cos(n\omega t) \cos(m\omega t) \left. \right] \\
 & + \sum_{\ell=1}^N \sum_{n=1}^N \sum_{m=1}^N \left[\mathbf{F}_3(\check{\mathbf{q}}(\ell,s), \check{\mathbf{q}}(n,s), \check{\mathbf{q}}(m,s)) \sin(\ell\omega t) \sin(n\omega t) \sin(m\omega t) \right. \\
 & + \mathbf{F}_3(\check{\mathbf{q}}(\ell,c), \check{\mathbf{q}}(n,s), \check{\mathbf{q}}(m,s)) \cos(\ell\omega t) \sin(n\omega t) \sin(m\omega t) \\
 & + \mathbf{F}_3(\check{\mathbf{q}}(\ell,s), \check{\mathbf{q}}(n,s), \check{\mathbf{q}}(m,c)) \sin(\ell\omega t) \sin(n\omega t) \cos(m\omega t) \\
 & + \mathbf{F}_3(\check{\mathbf{q}}(\ell,c), \check{\mathbf{q}}(n,s), \check{\mathbf{q}}(m,c)) \cos(\ell\omega t) \sin(n\omega t) \cos(m\omega t) \\
 & + \mathbf{F}_3(\check{\mathbf{q}}(\ell,s), \check{\mathbf{q}}(n,c), \check{\mathbf{q}}(m,s)) \sin(\ell\omega t) \cos(n\omega t) \sin(m\omega t) \\
 & + \mathbf{F}_3(\check{\mathbf{q}}(\ell,c), \check{\mathbf{q}}(n,c), \check{\mathbf{q}}(m,s)) \cos(\ell\omega t) \cos(n\omega t) \sin(m\omega t) \\
 & + \mathbf{F}_3(\check{\mathbf{q}}(\ell,s), \check{\mathbf{q}}(n,c), \check{\mathbf{q}}(m,c)) \sin(\ell\omega t) \cos(n\omega t) \cos(m\omega t) \\
 & \left. + \mathbf{F}_3(\check{\mathbf{q}}(\ell,c), \check{\mathbf{q}}(n,c), \check{\mathbf{q}}(m,c)) \cos(\ell\omega t) \cos(n\omega t) \cos(m\omega t) \right] = \mathbf{0}
 \end{aligned} \tag{A.2}$$

Prior to the weighted residual step, it is convenient to work out trigonometric products of A.2 to $\cos(k\omega t)$ (resp. $\sin(k\omega t)$) where $0 \leq k \leq N$.

Table A.4 summarizes the set of identities to rearrange products of trigonometric terms into sum of terms of the Fourier basis. In the following, instead of working with non-symmetric operators as \mathbf{F}_3 , let us use symmetric operators as $\mathbf{F}_3^{(sym)}$. Symmetric operators simplify the derivation of Fourier–Galerkin nonlinear terms $\check{\mathbf{F}}^{(i,c)}$ (resp. $\check{\mathbf{F}}^{(i,s)}$). Such a choice allows to uniquely consider a set of terms with argument $(n + m + \ell)\omega t$ and $(n + m - \ell)\omega t$ because the symmetric operator intrinsically considers the other set of terms whose arguments are $(n - m + \ell)\omega t$ and $(-n + m + \ell)\omega t$. Nonetheless, special care must be paid to consider unique terms, which is effectuated by the coefficient multiplying each term. In addition, the permutation of (m, n) by (n, m) does not change terms whose argument is $(n + m - \ell)\omega t$, which implies that only six terms of this kind are possible for each (m, n) $m + n \leq N + k$, listed in Table A.5. Analogously, for terms whose arguments are of the kind $(n + m + \ell)\omega t$ only four terms are possible, reported in Table A.6 with their corresponding coefficients.

Table A.5

Coefficients of terms whose argument is of the kind $(n + m - \ell)\omega t$. Element pairs $(m, n) = (n, m)$ are considered the same.

Index (m, n)	ℓ	Coefficient $n + m - \ell = k$
(c, c)	c	$\frac{1}{8}c$
(c, s)	s	$\frac{1}{4}c$
(s, s)	c	$-\frac{1}{8}c$
(c, s)	c	$\frac{1}{4}s$
(c, c)	s	$-\frac{1}{8}s$
(s, s)	s	$\frac{1}{8}s$

Table A.6

Coefficients of terms whose argument is of the kind $(n + m + \ell)\omega t$. Same legend as in Table A.5.

Index (m, n, ℓ)	Coefficient $n + m + \ell = k$
(c, c, c)	$\frac{1}{24}c$
(c, s, s)	$-\frac{1}{8}c$
(c, c, s)	$\frac{1}{8}s$
(s, s, s)	$-\frac{1}{24}s$

A.1. Fourier–Galerkin nonlinear terms of third degree

Once the nonlinear terms of the third degree are written as coefficients of elements of the Fourier basis, the derivation of the Fourier–Galerkin expression of $\check{\mathbf{F}}_3^{(i)}(\check{\mathbf{Q}})$ is immediate:

$$\check{\mathbf{F}}_3^{(0)}(\check{\mathbf{Q}}) = \frac{1}{8} \sum_{\substack{m=1, n=1 \\ m+n \leq N}}^{N-1} \left[2\mathbf{F}_3^{(sym)}(\check{\mathbf{q}}_{(n,s)}, \check{\mathbf{q}}_{(m,c)}, \check{\mathbf{q}}_{(n+m,s)}) - \mathbf{F}_3^{(sym)}(\check{\mathbf{q}}_{(n,s)}, \check{\mathbf{q}}_{(m,s)}, \check{\mathbf{q}}_{(n+m,c)}) + \mathbf{F}_3^{(sym)}(\check{\mathbf{q}}_{(n,c)}, \check{\mathbf{q}}_{(m,c)}, \check{\mathbf{q}}_{(n+m,c)}) \right] \tag{A.3a}$$

$$\begin{aligned} \check{\mathbf{F}}_3^{(k,c)}(\check{\mathbf{Q}}) &= \frac{1}{8} \sum_{\substack{m=1, n=1 \\ m+n \leq N+k}}^N \left[2\mathbf{F}_3^{(sym)}(\check{\mathbf{q}}_{(n,s)}, \check{\mathbf{q}}_{(m,c)}, \check{\mathbf{q}}_{(n+m-k,s)}) - \mathbf{F}_3^{(sym)}(\check{\mathbf{q}}_{(n,s)}, \check{\mathbf{q}}_{(m,s)}, \check{\mathbf{q}}_{(n+m-k,c)}) + \mathbf{F}_3^{(sym)}(\check{\mathbf{q}}_{(n,c)}, \check{\mathbf{q}}_{(m,c)}, \check{\mathbf{q}}_{(n+m-k,c)}) \right] \\ &+ \frac{1}{24} \sum_{\substack{m=1, n=1 \\ m+n \leq k-1}}^{k-2} \left[\mathbf{F}_3^{(sym)}(\check{\mathbf{q}}_{(n,c)}, \check{\mathbf{q}}_{(m,c)}, \check{\mathbf{q}}_{(k-n-m,c)}) - 3\mathbf{F}_3^{(sym)}(\check{\mathbf{q}}_{(n,c)}, \check{\mathbf{q}}_{(m,s)}, \check{\mathbf{q}}_{(k-n-m,s)}) \right] \end{aligned} \tag{A.3b}$$

$$\check{\mathbf{F}}_3^{(k,s)}(\check{\mathbf{Q}}) = \frac{1}{8} \sum_{\substack{m=1, n=1 \\ m+n \leq N+k}}^N \left[2\mathbf{F}_3^{(sym)}(\check{\mathbf{q}}_{(n,c)}, \check{\mathbf{q}}_{(m,s)}, \check{\mathbf{q}}_{(n+m-k,c)}) - \mathbf{F}_3^{(sym)}(\check{\mathbf{q}}_{(n,c)}, \check{\mathbf{q}}_{(m,c)}, \check{\mathbf{q}}_{(n+m-k,s)}) \right]$$

$$\begin{aligned}
 & + \mathbf{F}_3^{(sym)}(\check{\mathbf{q}}_{(n,s)}, \check{\mathbf{q}}_{(m,s)}, \check{\mathbf{q}}_{(n+m-k,s)}) \\
 & + \frac{1}{24} \sum_{\substack{m=1, n=1 \\ m+n \leq k-1}}^{k-2} \left[-\mathbf{F}_3^{(sym)}(\check{\mathbf{q}}_{(n,s)}, \check{\mathbf{q}}_{(m,s)}, \check{\mathbf{q}}_{(k-n-m,s)}) \right. \\
 & \left. + 3\mathbf{F}_3^{(sym)}(\check{\mathbf{q}}_{(n,c)}, \check{\mathbf{q}}_{(m,c)}, \check{\mathbf{q}}_{(k-n-m,s)}) \right]
 \end{aligned} \tag{A.3c}$$

A.2. Fourier-Galerkin nonlinear terms of second degree

Analogously, the quadratic operator $\check{\mathbf{F}}_2^{(i)}(\check{\mathbf{Q}})$ is written as:

$$\begin{aligned}
 \check{\mathbf{F}}_2^{(0)}(\check{\mathbf{Q}}) = \frac{1}{4} \sum_{n=1}^N & \left[2\mathbf{F}_{2,(n\omega, n\omega)}^{\mathbf{M}}(\check{\mathbf{q}}_{(n,s)}, \check{\mathbf{q}}_{(n,c)}) \right. \\
 & + \mathbf{F}_2^{(dya)}(\check{\mathbf{q}}_{(n,c)}, \check{\mathbf{q}}_{(n,c)}) \\
 & \left. + \mathbf{F}_2^{(dya)}(\check{\mathbf{q}}_{(n,s)}, \check{\mathbf{q}}_{(n,s)}) \right]
 \end{aligned} \tag{A.4a}$$

$$\begin{aligned}
 \check{\mathbf{F}}_2^{(k,c)}(\check{\mathbf{Q}}) = \frac{1}{2} \sum_{n=k+1}^N & \left[\mathbf{F}_{2,((k-n)\omega, n\omega)}^{\mathbf{M}}(\check{\mathbf{q}}_{(n,s)}, \check{\mathbf{q}}_{(n-k,c)}) \right. \\
 & + \mathbf{F}_{2,(-n\omega, (n-k)\omega)}^{\mathbf{M}}(\check{\mathbf{q}}_{(n-k,s)}, \check{\mathbf{q}}_{(n,c)}) \\
 & + \mathbf{F}_2^{(dya)}(\check{\mathbf{q}}_{(n,c)}, \check{\mathbf{q}}_{(n-k,c)}) \\
 & \left. + \mathbf{F}_2^{(dya)}(\check{\mathbf{q}}_{(n,s)}, \check{\mathbf{q}}_{(n-k,s)}) \right] \\
 & + \frac{1}{4} \sum_{n=1}^{k-1} \left[\mathbf{F}_{2,(k\omega, k\omega)}^{\mathbf{M}}(\check{\mathbf{q}}_{(n,s)}, \check{\mathbf{q}}_{(k-n,c)}) \right. \\
 & + \mathbf{F}_2^{(dya)}(\check{\mathbf{q}}_{(n,c)}, \check{\mathbf{q}}_{(k-n,c)}) \\
 & \left. - \mathbf{F}_2^{(dya)}(\check{\mathbf{q}}_{(n,s)}, \check{\mathbf{q}}_{(k-n,s)}) \right]
 \end{aligned} \tag{A.4b}$$

$$\begin{aligned}
 \check{\mathbf{F}}_2^{(k,s)}(\check{\mathbf{Q}}) = \frac{1}{2} \sum_{n=k+1}^N & \left[\mathbf{F}_{2,((n-k)\omega, -n\omega)}^{\mathbf{M}}(\check{\mathbf{q}}_{(n,c)}, \check{\mathbf{q}}_{(n-k,c)}) \right. \\
 & + \mathbf{F}_{2,(-n\omega, (n-k)\omega)}^{\mathbf{M}}(\check{\mathbf{q}}_{(n-k,s)}, \check{\mathbf{q}}_{(n,s)}) \\
 & + \mathbf{F}_2^{(dya)}(\check{\mathbf{q}}_{(n,s)}, \check{\mathbf{q}}_{(n-k,c)}) \\
 & \left. - \mathbf{F}_2^{(dya)}(\check{\mathbf{q}}_{(n,c)}, \check{\mathbf{q}}_{(n-k,s)}) \right] \\
 & + \frac{1}{4} \sum_{n=1}^{k-1} \left[\mathbf{F}_{2,((k-n)\omega, n\omega)}^{\mathbf{M}}(\check{\mathbf{q}}_{(n,s)}, \check{\mathbf{q}}_{(k-n,s)}) \right. \\
 & + \mathbf{F}_{2,(-n\omega, (n-k)\omega)}^{\mathbf{M}}(\check{\mathbf{q}}_{(k-n,c)}, \check{\mathbf{q}}_{(n,c)}) \\
 & \left. + 2\mathbf{F}_2^{(dya)}(\check{\mathbf{q}}_{(k-n,c)}, \check{\mathbf{q}}_{(n,s)}) \right]
 \end{aligned} \tag{A.4c}$$

Please also note the definition of the new dyadic operator $\mathbf{F}_{2,(a,b)}^{\mathbf{M}}$:

$$\mathbf{F}_{2,(a,b)}^{\mathbf{M}}(\hat{\mathbf{q}}_i, \hat{\mathbf{q}}_j) \equiv a\mathbf{M}|_{\hat{\mathbf{q}}_i} \hat{\mathbf{q}}_j + b\mathbf{M}|_{\hat{\mathbf{q}}_j} \hat{\mathbf{q}}_i \tag{A.5}$$

where $\mathbf{M}|_{\hat{\mathbf{q}}_j} = \text{diag}(1, \hat{\rho}_j \mathbf{I}, \hat{\rho}_j, 0)$.

A.3. Jacobian operator

Let us consider the Jacobian operator of the Fourier–Galerkin residual Eq. (A.1):

$$D\check{\mathbf{r}}^{(0)}\delta\check{\mathbf{Q}} = LN\mathcal{S}|_{\check{\mathbf{q}}_{(0)}}(\delta\check{\mathbf{q}}_{(0)}) + \left[D\check{\mathbf{F}}_{2|\check{\mathbf{Q}}}^{(0)} + D\check{\mathbf{F}}_{3|\check{\mathbf{Q}}}^{(0)} \right] \delta\check{\mathbf{Q}} \quad (\text{A.6a})$$

$$D\check{\mathbf{r}}^{(k,c)}\delta\check{\mathbf{Q}} = k\omega\mathbf{M}|_{\delta\check{\mathbf{q}}_{(0)}}\check{\mathbf{q}}_{(k,s)} + k\omega\mathbf{M}|_{\check{\mathbf{q}}_{(0)}}\delta\check{\mathbf{q}}_{(k,s)} + LN\mathcal{S}|_{\check{\mathbf{q}}_{(0)}}(\delta\check{\mathbf{q}}_{(k,c)}) + \left[D\check{\mathbf{F}}_{2|\check{\mathbf{Q}}}^{(k,c)} + D\check{\mathbf{F}}_{3|\check{\mathbf{Q}}}^{(k,c)} \right] \delta\check{\mathbf{Q}} \quad (\text{A.6b})$$

$$D\check{\mathbf{r}}^{(k,s)}\delta\check{\mathbf{Q}} = -k\omega\mathbf{M}|_{\delta\check{\mathbf{q}}_{(0)}}\check{\mathbf{q}}_{(k,c)} - k\omega\mathbf{M}|_{\check{\mathbf{q}}_{(0)}}\delta\check{\mathbf{q}}_{(k,c)} + LN\mathcal{S}|_{\check{\mathbf{q}}_{(0)}}(\delta\check{\mathbf{q}}_{(k,s)}) + \left[D\check{\mathbf{F}}_{2|\check{\mathbf{Q}}}^{(k,s)} + D\check{\mathbf{F}}_{3|\check{\mathbf{Q}}}^{(k,s)} \right] \delta\check{\mathbf{Q}} \quad (\text{A.6c})$$

where $LN\mathcal{S}|_{\check{\mathbf{q}}_{(0)}}^{(-k\omega)}(\check{\mathbf{q}}_{(k,c)})$ and $\mathbf{M}|_{\delta\check{\mathbf{q}}_{(0)}}$ are linear operators. So, it is left to compute the derivative of nonlinear terms with respect to $\check{\mathbf{Q}}$, noted $D\check{\mathbf{F}}_{2|\check{\mathbf{Q}}}^{(k,s)}$ and $D\check{\mathbf{F}}_{3|\check{\mathbf{Q}}}^{(k,s)}$, along with the derivative with respect to ω :

$$D_{\omega}\check{\mathbf{r}}^{(0)}\delta\omega = D_{\omega}\check{\mathbf{F}}_{2|\check{\mathbf{Q}}}^{(0)}\delta\omega \quad (\text{A.7a})$$

$$D_{\omega}\check{\mathbf{r}}^{(k,c)}\delta\omega = \delta\omega(k\mathbf{M}|_{\check{\mathbf{q}}_{(0)}}\check{\mathbf{q}}_{(k,s)}) + D_{\omega}\check{\mathbf{F}}_{2|\check{\mathbf{Q}}}^{(k,c)}\delta\omega \quad (\text{A.7b})$$

$$D_{\omega}\check{\mathbf{r}}^{(k,s)}\delta\omega = \delta\omega(-k\mathbf{M}|_{\check{\mathbf{q}}_{(0)}}\check{\mathbf{q}}_{(k,c)}) + D_{\omega}\check{\mathbf{F}}_{2|\check{\mathbf{Q}}}^{(k,s)}\delta\omega \quad (\text{A.7c})$$

Terms $D_{\omega}\check{\mathbf{F}}_{2|\check{\mathbf{Q}}}^{(0)}$, $D_{\omega}\check{\mathbf{F}}_{2|\check{\mathbf{Q}}}^{(k,s)}$ and $D_{\omega}\check{\mathbf{F}}_{2|\check{\mathbf{Q}}}^{(k,c)}$ will be detailed in the following section.

A.4. Jacobian operator of Fourier–Galerkin nonlinear terms of third degree

The Jacobian operator of Eq. (A.3) is a linear operator composed of 2×2 blocks for each harmonic component, except the mean flow component. Jacobian operators of high degree of nonlinearity lead to dense representations of derivative operators in the frequency domain, that is, the interactions between harmonics greatly depend on the degree of nonlinearity. The blocks of the Jacobian corresponding to the mean flow component are expressed as:

$$D\check{\mathbf{F}}_3^{(0;j,s)}\delta\check{\mathbf{q}}_{(j,s)} = \frac{1}{4} \sum_{m=1}^{\min(N-j,1)} \mathbf{F}_3^{(sym)}(\delta\check{\mathbf{q}}_{(j,s)}, \check{\mathbf{q}}_{(m,c)}, \check{\mathbf{q}}_{(j+m,s)}) + \frac{1}{4} \sum_{m=1}^{\min(j-1,1)} \mathbf{F}_3^{(sym)}(\check{\mathbf{q}}_{(j-m,s)}, \check{\mathbf{q}}_{(m,c)}, \delta\check{\mathbf{q}}_{(j,s)}) - \frac{1}{4} \sum_{m=1}^{\min(N-j,1)} \mathbf{F}_3^{(sym)}(\delta\check{\mathbf{q}}_{(j,s)}, \check{\mathbf{q}}_{(m,s)}, \check{\mathbf{q}}_{(j+m,c)}) \quad (\text{A.8a})$$

$$D\check{\mathbf{F}}_3^{(0;j,c)}\delta\check{\mathbf{q}}_{(j,c)} = \frac{1}{4} \sum_{m=1}^{\min(N-j,1)} \mathbf{F}_3^{(sym)}(\check{\mathbf{q}}_{(m,s)}, \delta\check{\mathbf{q}}_{(j,c)}, \check{\mathbf{q}}_{(j+m,s)}) - \frac{1}{8} \sum_{m=1}^{\min(j-1,1)} \mathbf{F}_3^{(sym)}(\check{\mathbf{q}}_{(j-m,s)}, \check{\mathbf{q}}_{(m,s)}, \delta\check{\mathbf{q}}_{(j,c)}) + \frac{1}{4} \sum_{m=1}^{\min(N-j,1)} \mathbf{F}_3^{(sym)}(\check{\mathbf{q}}_{(m,c)}, \delta\check{\mathbf{q}}_{(j,c)}, \check{\mathbf{q}}_{(j+m,c)}) + \frac{1}{8} \sum_{m=1}^{\min(j-1,1)} \mathbf{F}_3^{(sym)}(\check{\mathbf{q}}_{(j-m,c)}, \check{\mathbf{q}}_{(m,c)}, \delta\check{\mathbf{q}}_{(j,c)}) \quad (\text{A.8b})$$

Similarly, the cosinus lines of the Jacobian are expressed as:

$$\begin{aligned}
 D\check{\mathbf{F}}_3^{(k,c;j,s)} \delta\check{\mathbf{q}}_{(j,s)} &= \frac{1}{4} \sum_{m=\max(k-j+1,1)}^{\min(N+k-j,N)} \mathbf{F}_3^{(sym)}(\delta\check{\mathbf{q}}_{(j,s)}, \check{\mathbf{q}}_{(m,c)}, \check{\mathbf{q}}_{(j+m-k,s)}) \\
 &+ \frac{1}{4} \sum_{m=1}^{\min(j+k-1,N)} \mathbf{F}_3^{(sym)}(\check{\mathbf{q}}_{(j+k-m,s)}, \check{\mathbf{q}}_{(m,c)}, \delta\check{\mathbf{q}}_{(j,s)}) \\
 &- \frac{1}{4} \sum_{m=\max(k-j+1,1)}^{\min(N+k-j,N)} \mathbf{F}_3^{(sym)}(\delta\check{\mathbf{q}}_{(j,s)}, \check{\mathbf{q}}_{(m,s)}, \check{\mathbf{q}}_{(j+m-k,c)}) \\
 &- \frac{1}{4} \sum_{m=1}^{\min(k-j-1,1)} \mathbf{F}_3^{(sym)}(\delta\check{\mathbf{q}}_{(j,s)}, \check{\mathbf{q}}_{(m,c)}, \check{\mathbf{q}}_{(k-j-m,s)})
 \end{aligned} \tag{A.9a}$$

$$\begin{aligned}
 D\check{\mathbf{F}}_3^{(k,c;j,c)} \delta\check{\mathbf{q}}_{(j,c)} &= \frac{1}{4} \sum_{m=\max(k-j+1,1)}^{\min(N+k-j,N)} \mathbf{F}_3^{(sym)}(\check{\mathbf{q}}_{(m,s)}, \delta\check{\mathbf{q}}_{(j,c)}, \check{\mathbf{q}}_{(j+m-k,s)}) \\
 &- \frac{1}{8} \sum_{m=1}^{\min(j+k-1,N)} \mathbf{F}_3^{(sym)}(\check{\mathbf{q}}_{(m,s)}, \check{\mathbf{q}}_{(j+k-m,s)}, \delta\check{\mathbf{q}}_{(j,c)}) \\
 &+ \frac{1}{4} \sum_{m=\max(k-j+1,1)}^{\min(N+k-j,N)} \mathbf{F}_3^{(sym)}(\check{\mathbf{q}}_{(m,c)}, \delta\check{\mathbf{q}}_{(j,c)}, \check{\mathbf{q}}_{(j+m-k,c)}) \\
 &+ \frac{1}{8} \sum_{m=1}^{\min(j+k-1,N)} \mathbf{F}_3^{(sym)}(\check{\mathbf{q}}_{(m,c)}, \check{\mathbf{q}}_{(j+k-m,c)}, \delta\check{\mathbf{q}}_{(j,c)}) \\
 &+ \frac{1}{8} \sum_{m=1}^{\min(k-j-1,1)} \mathbf{F}_3^{(sym)}(\check{\mathbf{q}}_{(m,c)}, \check{\mathbf{q}}_{(k-m-j,c)}, \delta\check{\mathbf{q}}_{(j,c)}) \\
 &- \frac{1}{8} \sum_{m=1}^{\min(k-j-1,1)} \mathbf{F}_3^{(sym)}(\delta\check{\mathbf{q}}_{(j,c)}, \check{\mathbf{q}}_{(m,s)}, \check{\mathbf{q}}_{(k-m-j,s)})
 \end{aligned} \tag{A.9b}$$

and finally the derivative of sinus components:

$$\begin{aligned}
 D\check{\mathbf{F}}_3^{(k,s;j,s)} \delta\check{\mathbf{q}}_{(j,s)} &= \frac{1}{4} \sum_{m=\max(k-j+1,1)}^{\min(N+k-j,N)} \mathbf{F}_3^{(sym)}(\delta\check{\mathbf{q}}_{(j,s)}, \check{\mathbf{q}}_{(m,c)}, \check{\mathbf{q}}_{(j+m-k,c)}) \\
 &- \frac{1}{8} \sum_{m=1}^{\min(j+k-1,N)} \mathbf{F}_3^{(sym)}(\check{\mathbf{q}}_{(j+k-m,c)}, \check{\mathbf{q}}_{(m,c)}, \delta\check{\mathbf{q}}_{(j,s)}) \\
 &+ \frac{1}{4} \sum_{m=\max(k-j+1,1)}^{\min(N+k-j,N)} \mathbf{F}_3^{(sym)}(\delta\check{\mathbf{q}}_{(j,s)}, \check{\mathbf{q}}_{(m,s)}, \check{\mathbf{q}}_{(j+m-k,s)}) \\
 &+ \frac{1}{8} \sum_{m=1}^{\min(j+k-1,N)} \mathbf{F}_3^{(sym)}(\check{\mathbf{q}}_{(j+k-m,s)}, \check{\mathbf{q}}_{(m,s)}, \delta\check{\mathbf{q}}_{(j,s)}) \\
 &- \frac{1}{8} \sum_{m=1}^{\min(k-j-1,1)} \mathbf{F}_3^{(sym)}(\delta\check{\mathbf{q}}_{(j,s)}, \check{\mathbf{q}}_{(m,s)}, \check{\mathbf{q}}_{(k-j-m,s)}) \\
 &+ \frac{1}{8} \sum_{m=1}^{\min(k-j-1,1)} \mathbf{F}_3^{(sym)}(\check{\mathbf{q}}_{(k-j-m,c)}, \check{\mathbf{q}}_{(m,c)}, \delta\check{\mathbf{q}}_{(j,s)})
 \end{aligned} \tag{A.10a}$$

$$\begin{aligned}
 D\check{\mathbf{F}}_3^{(k,s;j,c)} \delta\check{\mathbf{q}}_{(j,c)} &= \frac{1}{4} \sum_{m=\max(k-j+1,1)}^{\min(N+k-j,N)} \mathbf{F}_3^{(sym)}(\check{\mathbf{q}}_{(m,s)}, \delta\check{\mathbf{q}}_{(j,s)}, \check{\mathbf{q}}_{(j+m-k,s)}) \\
 &+ \frac{1}{4} \sum_{m=1}^{\min(j+k-1,N)} \mathbf{F}_3^{(sym)}(\check{\mathbf{q}}_{(m,c)}, \check{\mathbf{q}}_{(j+k-m,s)}, \delta\check{\mathbf{q}}_{(j,c)}) \\
 &- \frac{1}{4} \sum_{m=\max(k-j+1,1)}^{\min(N+k-j,N)} \mathbf{F}_3^{(sym)}(\check{\mathbf{q}}_{(m,c)}, \delta\check{\mathbf{q}}_{(j,c)}, \check{\mathbf{q}}_{(j+m-k,s)}) \\
 &+ \frac{1}{4} \sum_{m=1}^{\min(k-j-1,1)} \mathbf{F}_3^{(sym)}(\delta\check{\mathbf{q}}_{(j,c)}, \check{\mathbf{q}}_{(m,c)}, \check{\mathbf{q}}_{(k-m-j,s)})
 \end{aligned} \tag{A.10b}$$

A.5. Jacobian operator of Fourier–Galerkin nonlinear terms of second degree

Let us now detail the expressions of quadratic nonlinear terms. Please note that some of the terms do not appear because their index is higher than N or lower than one. In the following, those terms whose index is equal to $k - j$ may uniquely be present if $j \leq k + 1$. Similarly those terms whose index is $k + j$ should respect $k + j \leq N$. Terms which do not satisfy the previous relations are implicitly suppressed.

$$D\check{\mathbf{F}}^{(0)} \delta\check{\mathbf{q}}_{(j,c)} = \frac{1}{2} \mathbf{F}_{2,(-j\omega,j\omega)}^{\mathbf{M}}(\check{\mathbf{q}}_{(j,s)}, \delta\check{\mathbf{q}}_{(j,c)}) + \frac{1}{2} \mathbf{F}_2^{(dya)}(\check{\mathbf{q}}_{(j,c)}, \delta\check{\mathbf{q}}_{(j,c)}) \tag{A.11a}$$

$$D\check{\mathbf{F}}^{(0)} \delta\check{\mathbf{q}}_{(j,s)} = \frac{1}{2} \mathbf{F}_{2,(-j\omega,j\omega)}^{\mathbf{M}}(\delta\check{\mathbf{q}}_{(j,s)}, \check{\mathbf{q}}_{(j,c)}) + \frac{1}{2} \mathbf{F}_2^{(dya)}(\check{\mathbf{q}}_{(n,s)}, \delta\check{\mathbf{q}}_{(n,s)}) \tag{A.11b}$$

$$\begin{aligned}
 D\check{\mathbf{F}}_2^{(k,c;j,s)} \delta\check{\mathbf{q}}_{(j,s)} &= \frac{1}{2} \left[\mathbf{F}_{2,((k-j)\omega,j\omega)}^{\mathbf{M}}(\delta\check{\mathbf{q}}_{(j,s)}, \check{\mathbf{q}}_{(j-k,c)}) \right. \\
 &+ \mathbf{F}_{2,(-(j+k)\omega,j\omega)}^{\mathbf{M}}(\delta\check{\mathbf{q}}_{(j,s)}, \check{\mathbf{q}}_{(j+k,c)}) \\
 &+ \mathbf{F}_2^{(dya)}(\delta\check{\mathbf{q}}_{(j,s)}, \check{\mathbf{q}}_{(j-k,s)}) + \mathbf{F}_2^{(dya)}(\check{\mathbf{q}}_{(j+k,s)}, \delta\check{\mathbf{q}}_{(j,s)}) \left. \right] \\
 &+ \frac{1}{4} \left[\mathbf{F}_{2,(k\omega,k\omega)}^{\mathbf{M}}(\delta\check{\mathbf{q}}_{(j,s)}, \check{\mathbf{q}}_{(k-j,c)}) \right. \\
 &- \left. 2\mathbf{F}_2^{(dya)}(\delta\check{\mathbf{q}}_{(j,s)}, \check{\mathbf{q}}_{(k-j,s)}) \right]
 \end{aligned} \tag{A.11c}$$

$$\begin{aligned}
 D\check{\mathbf{F}}_2^{(k,c;j,c)} \delta\check{\mathbf{q}}_{(j,c)} &= \frac{1}{2} \left[\mathbf{F}_{2,((j+k)\omega,-j\omega)}^{\mathbf{M}}(\delta\check{\mathbf{q}}_{(j,c)}, \check{\mathbf{q}}_{(j+k,s)}) \right. \\
 &+ \mathbf{F}_{2,((j-k)\omega,-j\omega)}^{\mathbf{M}}(\delta\check{\mathbf{q}}_{(j,c)}, \check{\mathbf{q}}_{(j-k,s)}) \\
 &+ \mathbf{F}_2^{(dya)}(\check{\mathbf{q}}_{(j+k,c)}, \delta\check{\mathbf{q}}_{(j,c)}) + \mathbf{F}_2^{(dya)}(\delta\check{\mathbf{q}}_{(j,c)}, \check{\mathbf{q}}_{(j-k,c)}) \left. \right] \\
 &+ \frac{1}{4} \left[\mathbf{F}_{2,(k\omega,k\omega)}^{\mathbf{M}}(\check{\mathbf{q}}_{(j,s)}, \delta\check{\mathbf{q}}_{(k-j,c)}) \right. \\
 &+ \left. 2\mathbf{F}_2^{(dya)}(\delta\check{\mathbf{q}}_{(j,c)}, \check{\mathbf{q}}_{(k-j,c)}) \right]
 \end{aligned} \tag{A.11d}$$

$$\begin{aligned}
 D\check{\mathbf{F}}_2^{(k,s;j,c)} \delta\check{\mathbf{q}}_{(j,c)} &= \frac{1}{2} \left[\mathbf{F}_{2,(j\omega,-(j+k)\omega)}^{\mathbf{M}}(\check{\mathbf{q}}_{(j+k,c)}, \delta\check{\mathbf{q}}_{(j,c)}) \right. \\
 &+ \mathbf{F}_{2,((j-k)\omega,-j\omega)}^{\mathbf{M}}(\delta\check{\mathbf{q}}_{(j,c)}, \check{\mathbf{q}}_{(j-k,c)}) \\
 &+ \mathbf{F}_2^{(dya)}(\check{\mathbf{q}}_{(j+k,s)}, \delta\check{\mathbf{q}}_{(j,c)}) \\
 &- \mathbf{F}_2^{(dya)}(\delta\check{\mathbf{q}}_{(j,c)}, \check{\mathbf{q}}_{(j-k,s)}) \\
 &+ \mathbf{F}_{2,(-j\omega,(j-k)\omega)}^{\mathbf{M}}(\check{\mathbf{q}}_{(j-k,c)}, \delta\check{\mathbf{q}}_{(j,c)}) \\
 &+ \left. \mathbf{F}_2^{(dya)}(\delta\check{\mathbf{q}}_{(j,c)}, \check{\mathbf{q}}_{(j-k,s)}) \right]
 \end{aligned} \tag{A.11e}$$

$$D\check{\mathbf{F}}_2^{(k,s;j,s)} \delta\check{\mathbf{q}}_{(j,s)} = \frac{1}{2} \left[\mathbf{F}_{2,(-(j+k)\omega,j\omega)}^{\mathbf{M}}(\delta\check{\mathbf{q}}_{(j,s)}, \check{\mathbf{q}}_{(j+k,s)}) \right]$$

$$\begin{aligned}
 & + \mathbf{F}_{2,(-j\omega,(j-k)\omega)}^{\mathbf{M}}(\check{\mathbf{q}}_{(j-k,s)}, \delta\check{\mathbf{q}}_{(j,s)}) \\
 & + \mathbf{F}_2^{(dya)}(\delta\check{\mathbf{q}}_{(j,s)}, \check{\mathbf{q}}_{(j-k,c)}) \\
 & - \mathbf{F}_2^{(dya)}(\check{\mathbf{q}}_{(j+k,c)}, \delta\check{\mathbf{q}}_{(j,s)}) \\
 & + \mathbf{F}_{2,((k-j)\omega,j\omega)}^{\mathbf{M}}(\delta\check{\mathbf{q}}_{(j,s)}, \check{\mathbf{q}}_{(k-j,s)}) \\
 & + \mathbf{F}_2^{(dya)}(\check{\mathbf{q}}_{(k-j,c)}, \delta\check{\mathbf{q}}_{(j,s)}) \quad] \tag{A.11f}
 \end{aligned}$$

Prior to the introduction of the derivative of the quadratic nonlinear term with respect to ω , let us define the derivative with respect to ω of the generic operator $\mathbf{F}_{2,(j\omega,k\omega)}^{\mathbf{M}}(\check{\mathbf{q}}_{(a)}, \check{\mathbf{q}}_{(b)})$:

$$D_\omega \mathbf{F}_{2,(j\omega,k\omega)}^{\mathbf{M}}(\check{\mathbf{q}}_{(a)}, \check{\mathbf{q}}_{(b)}) = (j\mathbf{M}|_{\check{\mathbf{q}}_{(a)}} \check{\mathbf{q}}_{(b)} + k\mathbf{M}|_{\check{\mathbf{q}}_{(b)}} \check{\mathbf{q}}_{(a)}) \tag{A.12}$$

Then the definition of $D_\omega \check{\mathbf{F}}_{2|\check{\mathbf{Q}}}^{(0)}$, $D_\omega \check{\mathbf{F}}_{2|\check{\mathbf{Q}}}^{(k,s)}$ and $D_\omega \check{\mathbf{F}}_{2|\check{\mathbf{Q}}}^{(k,c)}$ is as follows,

$$D_\omega \check{\mathbf{F}}_{2|\check{\mathbf{Q}}}^{(0)} \delta\omega = \frac{1}{2} \delta\omega \sum_{j=1}^N D_\omega \mathbf{F}_{2,(-j,j)}^{\mathbf{M}}(\check{\mathbf{q}}_{(j,s)}, \check{\mathbf{q}}_{(j,c)}) \tag{A.13a}$$

$$\begin{aligned}
 D_\omega \check{\mathbf{F}}_{2|\check{\mathbf{Q}}}^{(k,c)} \delta\omega = & \delta\omega \left[\frac{1}{4} \sum_{j=1}^{k-1} D_\omega \mathbf{F}_{2,(k,k)}^{\mathbf{M}}(\check{\mathbf{q}}_{(j,c)}, \check{\mathbf{q}}_{(k-j,s)}) \right. \\
 & + \frac{1}{2} \sum_{j=i+1}^N D_\omega \mathbf{F}_{2,(k-j,-j)}^{\mathbf{M}}(\check{\mathbf{q}}_{(j,c)}, \check{\mathbf{q}}_{(k-j,s)}) \\
 & \left. + \frac{1}{2} \sum_{j=i+1}^N D_\omega \mathbf{F}_{2,(k-j,j)}^{\mathbf{M}}(\check{\mathbf{q}}_{(j,s)}, \check{\mathbf{q}}_{(k-j,c)}) \right] \tag{A.13b}
 \end{aligned}$$

$$\begin{aligned}
 D_\omega \check{\mathbf{F}}_{2|\check{\mathbf{Q}}}^{(k,s)} \delta\omega = & \delta\omega \left[\frac{1}{4} \sum_{j=1}^{k-1} D_\omega \mathbf{F}_{2,(k-j,j)}^{\mathbf{M}}(\check{\mathbf{q}}_{(j,s)}, \check{\mathbf{q}}_{(k-j,s)}) \right. \\
 & \left. + \frac{1}{4} \sum_{j=1}^{k-1} D_\omega \mathbf{F}_{2,(k-j,-j)}^{\mathbf{M}}(\check{\mathbf{q}}_{(j,c)}, \check{\mathbf{q}}_{(k-j,c)}) \right] \tag{A.13c}
 \end{aligned}$$

$$\begin{aligned}
 & + \frac{1}{2} \sum_{j=i+1}^N D_\omega \mathbf{F}_{2,(j-k,-j)}^{\mathbf{M}}(\check{\mathbf{q}}_{(j,s)}, \check{\mathbf{q}}_{(k-j,s)}) \\
 & + \frac{1}{2} \sum_{j=i+1}^N D_\omega \mathbf{F}_{2,(j-k,j)}^{\mathbf{M}}(\check{\mathbf{q}}_{(j,c)}, \check{\mathbf{q}}_{(k-j,c)}) \tag{A.13d}
 \end{aligned}$$

References

- [1] L. Shaabani-Ardali, D. Sipp, L. Lesshafft, Time-delayed feedback technique for suppressing instabilities in time-periodic flow, *Phys. Rev. Fluids* 2 (11) (2017) 113904.
- [2] D. Jallas, O. Marquet, D. Fabre, Linear and nonlinear perturbation analysis of the symmetry breaking in time-periodic propulsive wakes, *Phys. Rev. E* 95 (6) (2017) 063111.
- [3] M. Krack, J. Gross, *Harmonic Balance for Nonlinear Vibration Problems*, Springer, 2019.
- [4] V. Mantič-Lugo, C. Arratia, F. Gallaire, Self-consistent mean flow description of the nonlinear saturation of the vortex shedding in the cylinder wake, *Phys. Rev. Lett.* 113 (8) (2014) 084501.
- [5] V. Mantič-Lugo, C. Arratia, F. Gallaire, A self-consistent model for the saturation dynamics of the vortex shedding around the mean flow in the unstable cylinder wake, *Phys. Fluids* 27 (2015) 074103.
- [6] P. Meliga, Harmonics generation and the mechanics of saturation in flow over an open cavity: a second-order self-consistent description, *J. Fluid Mech.* 826 (2017) 503–521.
- [7] D. Fabre, V. Citro, D.F. Sabino, P. Bonnefis, J. Sierra, F. Giannetti, M. Pigou, A practical review on linear and nonlinear global approaches to flow instabilities, *Appl. Mech. Rev.* 70 (6) (2019) 060802.
- [8] A. Fani, V. Citro, F. Giannetti, F. Auteri, Computation of the bluff-body sound generation by a self-consistent mean flow formulation, *Phys. Fluids* 30 (2018) 036102.

- [9] K.C. Hall, J.P. Thomas, W.S. Clark, Computation of unsteady nonlinear flows in cascades using a harmonic balance technique, *AIAA J.* 40 (5) (2002) 879–886.
- [10] D.J. Mavriplis, Z. Yang, Time spectral method for periodic and quasi-periodic unsteady computations on unstructured meshes, *Math. Model. Natl. Phenom.* 6 (3) (2011) 213–236.
- [11] K. Ekici, K.C. Hall, Nonlinear analysis of unsteady flows in multistage turbomachines using harmonic balance, *AIAA J.* 45 (5) (2007) 1047–1057.
- [12] F. Sicot, G. Dufour, N. Gourdain, A time-domain harmonic balance method for rotor/stator interactions, *J. Turbomach.* 134 (1) (2012).
- [13] I. Gatin, G. Cvijetić, V. Vukčević, H. Jasak, Š. Malenica, Harmonic balance method for nonlinear and viscous free surface flows, *Ocean Eng.* 157 (2018) 164–179.
- [14] W. Yao, S. Marques, A harmonic balance method for nonlinear fluid structure interaction problems, *Comput. Struct.* 201 (2018) 26–36.
- [15] D. Ramezani, D. Mavriplis, B.R. Ahrabi, An order $n \log n$ parallel solver for time-spectral problems, *J. Comput. Phys.* 411 (2020) 109319.
- [16] S.A. Orszag, On the elimination of aliasing in finite-difference schemes by filtering high-wavenumber components, *J. Atmos. Sci.* 28 (6) (1971) 1074.
- [17] M. Parsani, D.I. Ketcheson, W. Deconinck, Optimized explicit runge–kutta schemes for the spectral difference method applied to wave propagation problems, *SIAM J. Sci. Comput.* 35 (2) (2013) A957–A986.
- [18] V. Citro, F. Giannetti, J. Sierra, Optimal explicit runge–kutta methods for compressible navier–stokes equations, *Appl. Numer. Math.* (2019).
- [19] E.J. Kubatko, B.A. Yeager, D.I. Ketcheson, Optimal strong–stability–preserving runge–kutta time discretizations for discontinuous galerkin methods, *J. Sci. Comput.* 60 (2) (2014) 313–344.
- [20] D. Fabre, V. Citro, D. Ferreira Sabino, P. Bonnefis, J. Sierra, F. Giannetti, M. Pigou, A practical review on linear and nonlinear global approaches to flow instabilities, *Appl. Mech. Rev.* 70 (6) (2018).
- [21] E. Tadmor, The exponential accuracy of Fourier and Chebyshev differencing methods, *SIAM J. Numer. Anal.* 23 (1) (1986) 1–10.
- [22] D. Sipp, A. Lebedev, Global stability of base and mean flows: a general approach and its applications to cylinder and open cavity flows, *J. Fluid Mech.* 593 (2007) 333–358.
- [23] D. Canuto, K. Taira, Two-dimensional compressible viscous flow around a circular cylinder, *J. Fluid Mech.* 785 (2015) 349–371.
- [24] G. Carte, J. Dušek, P. Fraunić, Numerical simulation of the mechanisms governing the onset of the Bénard–von Kármán instability, *Int. J. Numer. Methods Fluids* 23 (8) (1996) 753–785.
- [25] O. Inoue, N. Hatakeyama, Sound generation by a two-dimensional circular cylinder in a uniform flow, *J. Fluid Mech.* 471 (2002) 285.
- [26] J. Sierra, P. Jolivet, F. Giannetti, V. Citro, Adjoint-based sensitivity analysis of periodic orbits by fourier–galerkin method, 440, 2021, p. 110403.
- [27] F. Sicot, G. Puigt, M. Montagnac, Block-jacobi implicit algorithms for the time spectral method, *AIAA J.* 46 (12) (2008) 3080–3089.
- [28] V. Citro, P. Luchini, F. Giannetti, F. Auteri, Efficient stabilization and acceleration of numerical simulation of fluid flows by residual recombination, *J. Comput. Phys.* 344 (2017) 234–246.
- [29] S. Nimmagadda, T.D. Economou, J.J. Alonso, C.R. Ilario da Silva, Robust uniform time sampling approach for the harmonic balance method, in: 46th AIAA Fluid Dynamics Conference, 2016, p. 3966.
- [30] N.L. Mundis, D.J. Mavriplis, Toward an optimal solver for time-spectral fluid-dynamic and aeroelastic solutions on unstructured meshes, *J. Comput. Phys.* 345 (2017) 132–161.
- [31] S. Antheaume, C. Corre, Implicit time spectral method for periodic incompressible flows, *AIAA J.* 49 (4) (2011) 791–805.
- [32] J. Moulin, On the Flutter Bifurcation in Laminar Flows: Linear and Nonlinear Modal Methods (Ph.D. thesis), Institut polytechnique de Paris, 2020.
- [33] R. Henrywood, A. Agarwal, The aeroacoustics of a steam kettle, *Phys. Fluids* 25 (10) (2013) 107101.
- [34] D. Fabre, P. Bonnefis, F. Charru, S. Russo, V. Citro, F. Giannetti, P. Luchini, Application of global stability approaches to whistling jets and wind instruments, in: International Symposium on Musical Acoustics (ISMA), Le Mans, France, 2014, pp. 7–12.
- [35] R. Longobardi, D. Fabre, P. Bonnefis, V. Citro, F. Giannetti, P. Luchini, Studying sound production in the hole-tone configuration using compressible and incompressible global stability analyses, in: IUTAM Symposium on Critical Flow Dynamics Involving Moving/Deformable Structures with Design Applications, 2018, pp. 18–22.
- [36] C. Nana, D. Marx, C. Prax, V. Fortuné, The perturbed low Mach number approximation for the aeroacoustic computation of anisothermal flows, in: Proceedings of the Acoustics 2012 Nantes Conference, 2012, pp. 1285–1290.
- [37] P. Cvitanović, Invariant measurement of strange sets in terms of cycles, *Phys. Rev. Lett.* 61 (24) (1988) 2729.
- [38] P. Cvitanovic, R. Artuso, R. Mainieri, G. Tanner, G. Vattay, N. Whelan, A. Wirzba, *Chaos: Classical and Quantum*, Vol. 69, Niels Bohr Institute, Copenhagen 2005, 2005, ChaosBook.Org.

CHAPTER **VIII**

Articles – The whistling of a
jet past a hole

Acoustic instability prediction of the flow through a circular aperture in a thick plate via an impedance criterion

J. Sierra-Ausin^{1,2}, D. Fabre¹, V. Citro² and F. Giannetti^{2,†}

¹Institut de Mécanique des Fluides de Toulouse (IMFT), Université de Toulouse, CNRS, Toulouse 31400, France

²Dipartimento di Ingegneria (DIIN), Università degli Studi di Salerno, Fisciano 84084, Italy

(Received 20 August 2021; revised 20 April 2022; accepted 25 April 2022)

We investigate the mechanisms leading to acoustic whistling for a jet passing through a circular hole in a thick plate connecting two domains. Two generic situations are considered. In the first one, the upstream domain is a closed cavity while the downstream domain is open, leading to a class of conditionally unstable modes. In this case, the instability source lies in the recirculation region within the thickness of the plate, but coupling with a conveniently tuned resonator is needed to select the conditional instability range. In the second situation, the two regions, upstream and downstream of the hole, are considered as open, leading to a class of hydrodynamic modes where instability of the recirculation region is sufficient to generate self-oscillations without the need of any resonator. A matched asymptotic model, valid in the low Mach limit, is used to derive a global impedance of the system, combining the impedance of the hole and the modelled impedances of the upstream and downstream domains. It is shown that the knowledge of this global impedance along the real ω -axis provides an instability criterion and a prediction of the eigenvalues of the full system. Validations against the solutions of the eigenvalue problem obtained from the linearized fully compressible formulation confirm the accuracy of the approach. Then, it is subsequently used to characterise the range of existence of instabilities as a function of the Reynolds number, the Mach number, the aspect ratio of the hole and (for the cavity configuration) the dimensionless volume of the cavity.

Key words: jet noise, shear-flow instability

1. Introduction

Plates with orifices are very common elements adopted in numerous industrial applications, like, for example, silencers, fuel injectors or wind instruments.

† Email address for correspondence: fgiannetti@unisa.it

Under the effect of a harmonic incident acoustic wave, the vortex sheet formed at the lip of the aperture becomes periodically modulated and acts as an amplifier due to a Kelvin–Helmholtz instability, reorganising the jet into an arrangement of vortex rings. The generation of vorticity is an efficient mechanism to dissipate acoustic energy, as a consequence, the use of multiple perforated plates traversed by a mean flow is widely employed as a sound attenuator device for industrial applications, such as gas turbine combustion systems. These systems may suffer from thermoacoustic instabilities because of the potential for unsteady heat release, which can damage the combustion system itself. The flow through a perforated liner with bias flow has been studied experimentally by Heuwinkel, Enghardt & Rohle (2007) while Hughes & Dowling (1990), Eldredge & Dowling (2003) and Rupp, Carrotte & Macquisten (2012) have conducted both experimental and theoretical investigations. There are, however, situations where the flow through a hole can lead to the opposite effect, namely spontaneous self-oscillations and sound emissions. A particularly favourable situation with respect to sound emission is the flow through two successive holes, as encountered, for instance, in bird calls and tea kettle whistles (Henrywood & Agarwal 2013; Longobardi *et al.* 2021). Although less common, the flow through a single hole can also lead to powerful sound emissions. As in other related examples of aeroacoustic resonators, (including, for instance, the ‘edge tone’ encountered in the mouthpiece of a recorder or organ pipe), two situations may occur. In the first one, the frequency of the whistling may be directly selected by that of an acoustic resonator located in the vicinity of the hole. This is, for instance, the case for the so-called ‘pipe tone’ (or pfeifenton), corresponding to a long cylindrical pipe terminated by an aperture of smaller section. In this configuration, which was intensively investigated experimentally by Anderson (1954), the frequency of the whistling directly corresponds to one of the resonance frequencies of the pipe. In the second one, the frequency may be selected by the flow itself regardless of the existence of any acoustic resonator. This situation was noted by Bouasse (1929), who observed that the flow through a hole in a thick plate separating two large chambers leads to a whistling with a frequency proportional to the thickness of the hole. This observation was rediscovered by Jing & Sun (2000) and Su *et al.* (2015) who, in an effort to improve the performance of perforated plates as sound dampers, reported that, in some circumstances, these devices could lead to self-sustained whistling. In music acoustics one observes the interaction between the two type of mechanisms, cf. Coltman (1976). In the case of the flue instrument, the so-called edge-tone oscillation can coexist with the pipe tone and under some specific circumstances, as, for example, during the attack transients, it may be dominant, cf. Castellengo (1999). Verge, Hirschberg & Causse (1997) proposed a lumped model for flue instruments where these two feedback loops can coexist and interfere: a hydrodynamic loop responsible for the edge tone and a cavity loop responsible for the pipe tone. On the contrary, in the case of the flow past an aperture both mechanisms are associated with the same feedback loop, which is modified by placing a cavity upstream of the perforation. These two situations respectively correspond to the so-called class III and class II categories of aeroacoustic resonators, following the classification of Chanaud (1970).

Recently, Fabre *et al.* (2019) used the linearized Navier–Stokes equations (LNSE) approach to investigate the unsteady flow through a circular aperture in a thin plate subjected to harmonic forcing. A novel non-reflecting boundary condition called the complex mapping method (Sierra, Fabre & Citro 2020) was introduced to overcome the numerical difficulties created by the strong spatial amplification of the fluctuations. The approach allows computing in a rigorous way the impedance of the hole, namely the ratio between unsteady pressure difference across the orifice and unsteady volume

flow rate through the orifice, a quantity which can be directly introduced in more elaborate acoustical models. In that study, the authors confirmed that the LNSE can be effectively adopted to predict the impedance even in cases where the spatial evolution of the perturbations is rapidly dominated by nonlinear effects. The same approach was subsequently used by Fabre *et al.* (2020) for the case of a hole through a thick plate. An important result is that, for sufficiently thick holes, the impedance can acquire a negative real part in some ranges of forcing frequencies, indicating that energy can be extracted from the flow, thus providing a source for self-oscillations. Investigation of the structural sensitivity also allowed the authors to demonstrate that the hydrodynamic instability of the shear layer separating the jet from the recirculation bubble is the driving motor for the observed phenomenon. This corresponds to the same instability as in the jet of a flue instrument or the shear layer for a grazing flow along a cavity, cf. Dai & Aurégan (2016, 2018). In this flow configuration, the sharpness of the aperture corner creates a recirculation bubble that enhances the instability mechanism.

The response of a system to a harmonic forcing is naturally studied via a transfer function: here it corresponds to the concept of impedance, which can also be used to obtain important information regarding the stability properties of a system. First, plotting the impedance in the form of Nyquist diagrams (namely a parametric representation of $Z(\omega)$ in the complex plane for real values of ω) provides a direct way to determine the number of unstable modes of the system, as a function of the number of times the Nyquist contour encircles the origin. Secondly, when the system has a complex eigenvalue located close to the real ω -axis, an approximation of the eigenvalue can be obtained from a Taylor expansion of the impedance function around the real axis. Such methods are widely used in several fields such as in automatics or electronics, but remain underemployed in the flow instability community where eigenvalue computation remains the preferred approach. Note, however, that the second idea was recently applied successfully by Ferreira Sabino *et al.* (2020) for the problem of vortex-induced vibrations for a spring-mounted cylinder.

The links between impedance and stability properties were explored by Fabre *et al.* (2020) for the jet flow through a hole. The discussion revealed the existence of two different instability mechanisms leading to sound production: a purely hydrodynamic instability characterised by spontaneous self-oscillations existing in the absence of any incoming acoustic wave, and a conditional instability due to an over-reflection of acoustic waves. Simple criteria formulated in terms of the impedance were given for both kinds of instabilities, allowing us to determine their range of existences as a function of the hole aspect ratio and the Reynolds number. Among the studies considering a multiply perforated plate, Jing & Sun (2000) and Su *et al.* (2015) measured experimentally the impedances for several configurations with variable hole thickness parameter values, which are in good accordance with the first branch of conditional unstable modes, cf. Fabre *et al.* (2020, § 8). Moussou *et al.* (2007) studied experimentally a long pipe with a constriction for a number of values of the constriction ratio and the thickness ratio. In this study, they identified both the first and second branch of conditionally unstable modes.

In the approach of Fabre *et al.* (2020), the flow was assumed as locally incompressible, a hypothesis which is expected to be valid for small values of the square of the Helmholtz number ($He^2 = \omega^2 M^2$), and which does not directly allow predicting the acoustic field. Nevertheless, they suggested that the locally incompressible solution could be matched to outer solutions incorporating compressibility effects, leading to more elaborate models applicable in situations incorporating, for instance, acoustic resonators and radiation in an open domain.

The object of the present paper is precisely to show how the impedance computations of Fabre *et al.* (2020) based on a locally incompressible solution can be used to build a model applicable for a realistic situation involving compressibility. In addition, acoustic pressure fields, obtained from full compressible LNSE computations complement the study. Two generic situations are considered. In the first situation referred to as cavity/open configuration, the domain located upstream of the hole is considered as a closed cavity of finite volume, while the downstream domain is considered as open. We then show that the presence of the upstream resonator can effectively lead to instabilities, as predicted by the conditional instability criterion. The second situation, referred to as open/open configuration, corresponds to the case where the two regions, upstream and downstream of the hole, are considered as open domains of large dimension. We show, in this case, that an instability of purely a hydrodynamic type can arise.

The paper is organized as follows. In § 2 the two generic situations are introduced, and the parameters are outlined. In § 3 we introduce an asymptotically matched or lumped model which allows defining a global impedance for the selected configuration by combining the hole impedance as computed by Fabre *et al.* (2020) and the impedances of the upstream and downstream domains. We also show that a Taylor expansion of this impedance around the real ω -axis can be used to obtain an instability criterion and an estimation of the eigenvalue of the unstable modes in the fully compressible case. In § 4 we introduce a numerical resolution method for the eigenvalue problem in a fully compressible set-up. In § 5 we present results for the cavity/open configuration. We compare both approaches, demonstrating that the asymptotic model is effectively accurate for low Mach numbers. We then provide a parametric study for both problems, thanks to the asymptotic model. Section 6 presents results for the open/open configuration. We particularly investigate the effect of compressibility on the purely hydrodynamic instability mechanism identified by Fabre *et al.* (2020), and also consider the acoustic directivity of far-field sound emission.

2. Problem definition

2.1. Fluid parameters

The fluid is considered as a perfect gas with specific constant R_g and adiabatic index $\gamma = 1.4$. We denote with ρ_0 the reference density and with T_0 the reference temperature (both corresponding to the values in the upstream domain). The fluid is assumed to have constant dynamic viscosity μ and heat conductivity α . The mass flow rate at the inlet of the domain is denoted with \dot{m}_0 , while the mean velocity across the hole is $U_M = \dot{m}_0 / (\rho_0 \pi R_h^2)$. Based on this velocity scale and the hole diameter $D_h = 2R_h$, the Reynolds and Mach numbers of the flow are then defined as

$$Re = \frac{\rho_0 D_h U_M}{\mu} \equiv \frac{2\dot{m}_0}{\pi R_h \mu}; \quad M = \frac{U_M}{c_0} \quad \text{with } c_0 = \sqrt{\gamma R_g T_0}. \quad (2.1a,b)$$

The fluid is also characterised by a Prandtl number $Pr = \rho_0 \alpha / \mu$ which is here assumed to be $Pr = 0.7$.

2.2. Open/open configuration

In the first configuration, termed open/open configuration and sketched in figure 1, we consider that a plate separates two semi-infinite ‘open domains’ of large dimensions. By ‘open domain’ we mean that acoustic waves generated at either side of the hole

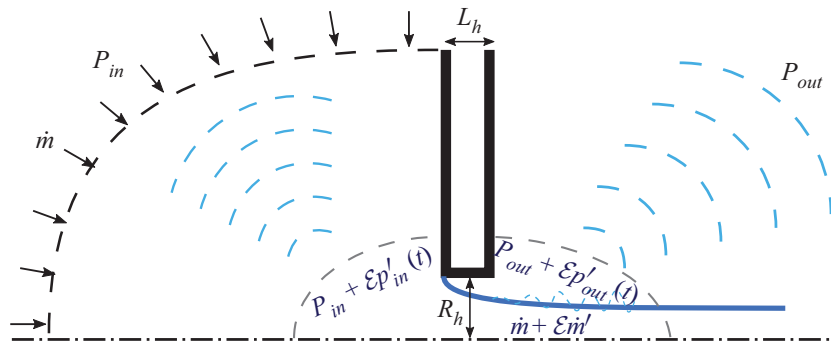


Figure 1. Sketch of the open/open configuration.

propagate towards infinity without reflection. Denoting with L_h the thickness of the plate, the geometry is thus completely defined by a single dimensionless parameter, the aspect ratio of the hole, defined as

$$\beta = \frac{L_h}{2R_h} = \frac{L_h}{D_h}. \quad (2.2)$$

In the fully compressible simulations, boundary conditions have to be applied at the boundary of the domain. For simplicity, a half-spherical boundary is considered upstream, and a uniform radial velocity is imposed, as sketched in the figure. Non-reflective boundary conditions used for the compressible computations are introduced and explained in details in § 4.

2.3. Cavity/open configuration

The second considered configuration, termed cavity/open configuration, is sketched in figure 2. This configuration is selected here to study, in the simplest possible setting, the coupling of the hole with a cavity acting as a resonator. The upper domain is considered as a cavity of dimensions L_{in}, R_{in} which acts as a Helmholtz resonator. Therefore, only its volume is relevant, not the exact dimensions L_{in}, R_{in} or the particular geometry. Thus, in addition to the aspect ratio β defined above, a second geometrical parameter enters the problem, namely the dimensionless volume defined as

$$V_{in} = \frac{L_{in}\pi R_{in}^2}{R_h^3}. \quad (2.3)$$

The inlet condition is imposed at the leftmost boundary where, for simplicity, a constant velocity profile is enforced, as sketched in the figure.

3. Matched asymptotic model

Before considering the resolution of the problem in a fully compressible setting, we detail here a matched asymptotic model which allows us to compute a total impedance characterising the behaviour of linear perturbations of the full system. We first explain how the different regions of the flow domain can be described to obtain the model, and then discuss how the derived total impedance can be used to predict the onset of instabilities.

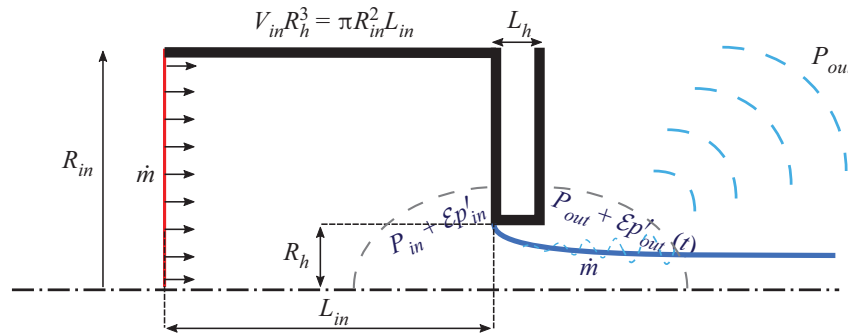


Figure 2. Sketch of the cavity/open configuration.

3.1. Matching principle

Under the hypothesis that the Mach number is small and that acoustic wavelengths are much larger than the dimensions of the hole (acoustic compactness hypothesis), it is possible to assume that the flow in the vicinity of the hole is locally incompressible, while compressibility is only relevant in the upstream and downstream domains. This hypothesis is at the origin of the asymptotically matched or lumped model. The ingredients required for matching are the pressure $p_{in}(t)$ just upstream of the hole, the pressure $p_{out}(t)$ just downstream of the hole, and the volume flow rate $q(t)$ across the hole. Working in the frequency domain, all these quantities are expanded as a constant value associated with the base flow, plus a perturbation with harmonic dependency $e^{-i\tilde{\omega}t}$, where $\tilde{\omega}$ is a (possibly complex) dimensional frequency,

$$\left. \begin{aligned} p_{in}(t) &= P_{in} + p'_{in} e^{-i\tilde{\omega}t}, & p_{out}(t) &= P_{out} + p'_{out} e^{-i\tilde{\omega}t}, \\ q(t) &= Q_0 + q' e^{-i\tilde{\omega}t}. \end{aligned} \right\} \quad (3.1)$$

It is important to understand that here p'_{out} corresponds to the level of the fluctuating pressure field at distances $\|x\|$ considered large in relation to the hole dimension but small compared with the acoustic wavelength, i.e. $R_h \ll \|x\| \ll \tilde{\lambda}$, with $\tilde{\lambda} = 2\pi c_0/\tilde{\omega}$. Consequently, this pressure level corresponds both to the outer limit for the inner solution, and to the inner limit for the outer solution of the classic matched asymptotic expansion procedure. The same holds for p'_{in} which is also used as a matching limit between inner and outer solutions.

3.2. Impedance modelling

3.2.1. Inner region: hole impedance

The inner region, located in the vicinity of the hole (delimited by dotted lines in figures 1 and 2), is governed by the incompressible LNSE. A resolution method for this problem was introduced and validated in Fabre *et al.* (2020): for the benefit of the reader, this approach is also briefly summarised in § A. The cited method allows us ultimately to deduce the (dimensionless) hole impedance $Z_h(\omega)$ defined as

$$Z_h(\omega) = \left[\frac{R_h^2}{\rho_0 U_M} \right] \frac{p'_{in} - p'_{out}}{q'}. \quad (3.2)$$

Here the factor $R_h^2/(\rho_0 U_M)$ is introduced to turn the impedance into a dimensionless one, since the dimensional impedance $(p'_{in} - p'_{out})/q'$ has physical units $\text{kg s}^{-1} \text{m}^{-4}$ in the international system, and it is a function of the dimensionless frequency $\omega = R_h \tilde{\omega}/U_M$.

Acoustic instability prediction via an impedance criterion

The impedance is ultimately searched as $Z_h = \mathbf{P} \cdot (\mathbf{LNS} + i\omega\mathbf{B})^{-1} \cdot \mathbf{F}$, where \mathbf{F} represents a forcing of the LNSE by an imposed flow rate, $(\mathbf{LNS} + i\omega\mathbf{B})^{-1}$ is the linear resolvent of the incompressible LNSE, and \mathbf{P} is an operator allowing us to extract the overall pressure jump from the linear perturbation. After a convenient discretization, computation of the impedance is thus straightforward and only requires inversion of a single linear problem. More details are given in [Appendix A](#). It is thus much faster in comparison to eigenvalue computation, which, using the shift-and-invert method, typically requires numerous iterative resolutions of such problems. Once $Z_h(\omega)$ is computed and tabulated (Fabre *et al.* 2020) a complete parametric study in terms of Mach number and the cavity volume can be performed as shown below.

3.2.2. Downstream region: radiation impedance

When observed from a large distance, the hole can be seen as a monopolar source, which classically gives rise to spherical diverging waves. This is classically described by a radiation impedance defined as the ratio between pressure p'_{out} and flow rate q' . This impedance can be obtained by asymptotically matching an acoustically compact inner solution with a monopolar acoustic source, cf. Fletcher & Rossing (2012), Pierce (2019) and Rossing (2007). The computation is also reproduced in Fabre *et al.* (2020, Appendix A therein). When expressed in dimensionless variables, the result is a purely real impedance Z_{rad} given by

$$Z_{rad} = \left[\frac{R_h^2}{\rho_0 U_M} \right] \frac{p'_{out}}{q'} = \frac{M\omega^2}{2\pi}. \quad (3.3)$$

3.2.3. Upstream region: case of an open domain

In a similar way, in the case of the ‘open domain’ ([figure 1](#)), one can introduce the impedance of the inlet domain Z_{in} , which is defined as

$$Z_{in} = \left[\frac{R_h^2}{\rho_0 U_M} \right] \frac{p'_{in}}{q'} = -\frac{M\omega^2}{2\pi} = -Z_{rad}. \quad (3.4)$$

3.2.4. Upstream region: case of a cavity

In the case where the upstream domain is considered as a closed cavity ([figure 2](#)), we assume that this cavity acts as a Helmholtz resonator, namely the pressure $p' = p'_{in}$, and the density $\rho' = \rho'_{in}$ are uniform. Then a mass budget leads to

$$V_{in} c_0^2 \frac{d\rho'_{in}}{dt} = V_{in} \frac{dp'_{in}}{dt} = \rho_0 q', \quad (3.5)$$

which allows the introduction of the impedance of the cavity Z_{cav} ,

$$Z_{cav} = \left[\frac{R_h^2}{\rho_0 U_M} \right] \frac{p'_{in}}{q'} = \frac{i}{\omega M^2 V_{in}} = \frac{i}{\omega \chi}, \quad \chi = M^2 V_{in}. \quad (3.6)$$

Note that this expression indicates that the cavity acts as a capacitor for an electrical circuit or as a spring in a mechanical system. Moreover, its characteristics only depend upon the quantity $\chi = M^2 V_{in}$ which combines the Mach number and the dimensionless volume of the cavity. Such a model could be complemented with the addition of two other terms

that have been neglected. In particular, one could include on the left-hand side of the mass balance the deviation from isentropic pressure fluctuations due to, for instance, the effects of the thermal boundary layer and on the right-hand side, the convective term involving density fluctuations. These terms have been neglected based on the fact that velocity and temperature gradients within the cavity are small as long as the ratio between the height of the cavity and the radius of the hole is large. In our study, this corresponds to $L_{in} = R_{in} = (V_{in}/\pi)^{1/3} \gg R_h$, which holds for the cavities analysed in this study.

3.2.5. Summary: total impedance of the problem

Regrouping all the regions, we are now able to obtain a single constitutive equation for the total impedance of the system, denoted either as Z_a or Z_b for the two investigated configurations, which allows us to determine the eigenfrequencies of the complete problem.

(a) For the open/open configuration, $Z_h = -2Z_{rad}$, or equivalently,

$$Z_a(\omega) = Z_h(\omega) + \frac{M\omega^2}{\pi} = 0. \quad (3.7)$$

(b) For the cavity/open configuration, $Z_h = -Z_{cav} - Z_{rad}$, or equivalently,

$$Z_b(\omega) = Z_h(\omega) + \frac{M\omega^2}{2\pi} + \frac{i}{M^2V_{in}\omega} = 0. \quad (3.8)$$

We emphasize that the total impedance defined here is designed mainly to be used to detect eigenvalues, hence, only the condition $Z(\omega) = 0$ is significant. The complex zeros $\omega = \omega_R + i\omega_I$ of Z then correspond to the eigenmodes of the system, and the system is therefore unstable if there exists such a zero with $\omega_I > 0$. When not zero, there is no direct physical interpretation to the value $Z(\omega)$ associated with a given ω . Schematically, $1/Z$ can be conceived of as a measure of the response of the system to an imposed forcing, so that $Z = 0$ means that the response is infinite, or in other words that a solution without forcing is possible. For instance, Fabre *et al.* (2020, Appendix A therein) considered the case where the forcing corresponds to a spherically converging wave coming from downstream; in this case the reflection coefficient is effectively proportional to Z^{-1} (see equation (A12) in this reference). Other kinds of forcing could be considered, leading to the same conclusion. In the present paper we remain to an intuitive interpretation of Z^{-1} and do not elaborate on the link between the impedance and any specific forcing.

3.3. Predicting instability from a Taylor expansion of the impedance

As stated in the introduction, knowledge of the impedance function $Z(\omega)$ along the real ω -axis allows obtaining important information regarding instability properties of the system in two ways. First, Cauchy's argument principle (see Appendix C) can be used as a graphical method to determine whether or not an instability exists. This argument is developed in § C. Second, eigenvalues located close to the real axis may be expected to be accurately predicted from a Taylor expansion of the impedance around the real axis. This argument is presented here.

3.3.1. Asymptotic prediction of eigenvalue for the cavity/open configuration

Following an idea previously used in Ferreira Sabino *et al.* (2020) for the problem of vortex-induced vibrations of a spring-mounted cylinder, we assume here that the

impedance of the full system is mostly reactive. In the present case, this means that the impedance is dominated by its imaginary part, while the real parts (i.e. $\text{Re}(Z_h)$ and the radiation impedance) correspond to lower-order terms. Such a hypothesis, together with the fact that the flow is acoustically compact within the region of the hole, allow the use of an asymptotic expansion truncated at first order to determine the zeros of the impedance. We first elaborate this idea for the cavity/open configuration. The hypotheses are as follows:

- (i) $|\text{Re}(Z_h)| \ll |\text{Im}(Z_h)|$, i.e. $|\text{Re}(Z_h)| \sim \varepsilon |\text{Im}(Z_h)|$;
- (ii) $M\omega^2/2\pi \ll |\text{Im}(Z_h)|$, i.e. $M\omega^2/2\pi \sim \varepsilon |\text{Im}(Z_h)|$.

Here the real parameter $0 < \varepsilon \ll 1$. Note that hypothesis (i) is not justified for every value of ω_0 since from the results of Fabre *et al.* (2020) the real and imaginary parts of Z_h are generally of comparable order of magnitudes. However, this hypothesis can be expected to be valid in the vicinity of the threshold of the instability. Hypothesis (ii) is needed for the acoustic compactness and, therefore, directly satisfied.

Consider the frequency expansion

$$\omega = \omega_0 + \varepsilon\omega_1, \quad \omega_0 \in \mathbb{R}, \quad \omega_1 \in \mathbb{C}, \quad \varepsilon \in \mathbb{R}, \tag{3.9}$$

and let us substitute ω in (3.8) by (3.9) and by performing a Taylor expansion in terms of the assumed small quantities leads to

$$\begin{aligned} Z_b(\omega) = & i \left[\text{Im}(Z_h(\omega_0)) + \frac{1}{M^2 V_{in} \omega_0} \right] \\ & \varepsilon \left[\text{Re}(Z_h(\omega_0)) + \frac{M\omega_0^2}{2\pi} + \left(\left(\frac{\partial Z_h}{\partial \omega} \right)_{\omega=\omega_0} - \frac{i}{M^2 V_{in} \omega_0^2} \right) \omega_1 \right] \\ & + O(\varepsilon^2), \end{aligned} \tag{3.10}$$

where $O(\varepsilon^2)$ denotes higher-order terms as a function of the assumed small parameter. The condition $Z_b = 0$ then leads to the following results.

- (i) The zeroth-order terms lead to the condition

$$-\omega_0 \text{Im}(Z_h(\omega_0)) = \frac{1}{M^2 V_{in}} = \frac{1}{\chi}. \tag{3.11}$$

- (ii) The first-order term leads to

$$\begin{aligned} \text{Im}(\omega_1) = & \frac{\left[\text{Re}(Z_h(\omega_0)) + \frac{M\omega_0^2}{2\pi} \right] \left(\left(\frac{\partial \text{Im}(Z_h(\omega))}{\partial \omega_R} \right)_{\omega=\omega_0} - \frac{1}{\chi \omega_0^2} \right)}{\left(\left(\frac{\partial \text{Re}(Z_h(\omega))}{\partial \omega_R} \right)_{\omega=\omega_0} \right)^2 + \left(\left(\frac{\partial \text{Im}(Z_h(\omega))}{\partial \omega_R} \right)_{\omega=\omega_0} - \frac{1}{\chi \omega_0^2} \right)^2}, \\ \text{Re}(\omega_1) = & \frac{- \left[\text{Re}(Z_h(\omega_0)) + \frac{M\omega_0^2}{2\pi} \right] \left(\frac{\partial \text{Re}(Z_h)}{\partial \omega_R} \right)_{\omega=\omega_0}}{\left(\left(\frac{\partial \text{Re}(Z_h(\omega))}{\partial \omega_R} \right)_{\omega=\omega_0} \right)^2 + \left(\left(\frac{\partial \text{Im}(Z_h(\omega))}{\partial \omega_R} \right)_{\omega=\omega_0} - \frac{1}{\chi \omega_0^2} \right)^2} \end{aligned} \tag{3.12}$$

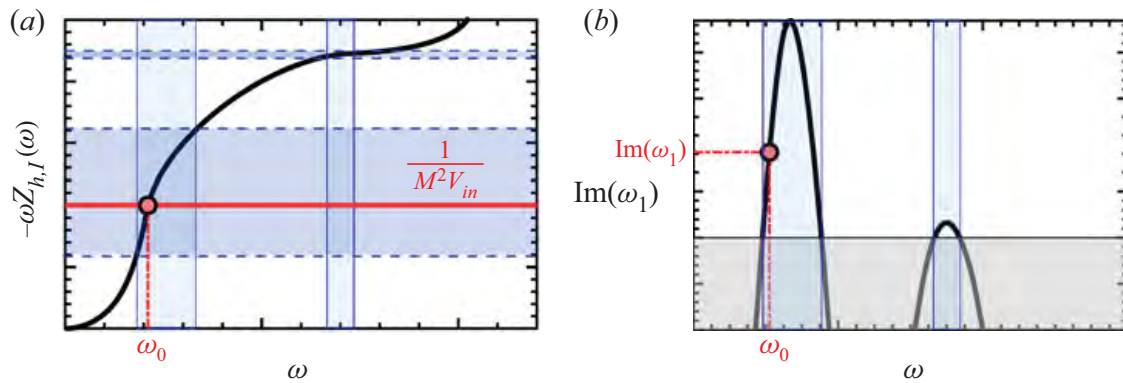


Figure 3. Linear scale representation of the zero computation of (3.9) with the (a) zeroth-order (3.11) and (b) first-order (3.12) approximations.

The imaginary part of the first-order correction directly provides a criterion of stability. Provided that the imaginary part of $\partial Z_h/\partial\omega$ is negative (a condition which is found to hold in all cases where the starting hypotheses are verified), then it is possible to conclude that an instability is possible as soon as

$$\text{Re}(Z_h(\omega_0)) < -\frac{M\omega_0^2}{2\pi}. \tag{3.13}$$

We recognize here an improved version of the conditional instability criterion of Fabre *et al.* (2020). Physically, this condition means that the energy extracted from the base flow $-\text{Re}(Z_h(\omega_0))|q'|^2/2$ must be larger than the energy radiated $Z_{rad}|q'|^2/2$.

Fabre *et al.* (2020) have documented the function $Z_h(\omega)$ for real values of ω over a wide range of parameters. Once the hole impedance function $Z_h(\omega)$ is determined, these results can be used to solve the coupled conditions (3.11), (3.12) and ultimately to obtain an instability criterion and an estimate for the growth rate. Figure 3 explains graphically these conditions. The resolution can be done in two ways. Via a direct method, that is, given the parameters M and V_{in} , one first solves for (3.11), which is an implicit equation in ω_0 as a function of the parameter χ (as sketched in figure 3a). Then one may deduce $\text{Im}(\omega_1)$ which is an explicit function of ω_0 and M (as sketched in figure 3b) and it ultimately provides a criterion of instability.

An alternative is to follow an inverse method. Given M , we first consider $\text{Im}(\omega_1)$ as a function of ω_0 and deduce the ranges of ω_0 where this function is positive (as indicated in blue on figure 3b). Once these unstable ranges are known, we deduce the corresponding ranges for $1/(M^2 V_{in})$ by using (3.11) (as indicated by blue ranges in figure 3a). The approach thus indicates the ranges of V_{in} where, for the given M , the jet is unstable. The great advantage of this inverse method is that the equation (3.11) is explicit when solving for V_{in} in terms of ω_0 .

The inverse method is a very efficient way to obtain an estimation of the eigenvalue of the full problem $\omega = \omega(\text{Re}, \beta, M, V_{in})$ provided one disposes of a tabulation of the function $Z_h(\omega; \text{Re}, \beta)$ for real values of ω . It must be emphasised that the number of parameters has been reduced from four to only two, as V_{in} and M only occur through the modelled impedance of the upstream and downstream domains. However, the reduction relies on a series of strong hypotheses: first $M \ll 1$ and $|\omega| \ll 1/M$ for the matched asymptotic model to hold, and second the assumptions used to treat $\text{Re}(Z_h)$ as a correction. The validity of the approach, therefore, has to be assessed by comparing the results with

those obtained using a fully compressible model in order to clarify the range of validity of the used approximations, as detailed in § 5.1.

3.3.2. Asymptotic prediction of eigenvalue for the open/open configuration

Let us now follow a similar route to achieve an estimation of the eigenvalue ω for the open/open configuration. In this case, the zeroth-order and first-order corrections simplify to

$$-\omega_0 \text{Im}(Z_h)(\omega_0) = 0, \tag{3.14}$$

$$\left. \begin{aligned} \text{Im}(\omega_1) &= \frac{\left[\text{Re}(Z_h(\omega_0)) + \frac{M\omega_0^2}{\pi} \right] \left(\frac{\partial \text{Im}(Z_h)}{\partial \omega_R} \right)_{\omega=\omega_0}}{\left| \left(\frac{\partial Z_h}{\partial \omega} \right)_{\omega=\omega_0} \right|^2}, \\ \text{Re}(\omega_1) &= \frac{- \left[\text{Re}(Z_h(\omega_0)) + \frac{M\omega_0^2}{\pi} \right] \left(\frac{\partial \text{Re}(Z_h)}{\partial \omega_R} \right)_{\omega=\omega_0}}{\left| \left(\frac{\partial Z_h}{\partial \omega} \right)_{\omega=\omega_0} \right|^2}, \end{aligned} \right\} \tag{3.15}$$

where the non-zero ω_0 are the zeros of the imaginary part of the hole impedance function $\text{Im}(Z_h)$ and the growth rate is estimated by (3.15).

Note that this expression is identical to the one obtained for the cavity/open configuration when $V_{in} \rightarrow \infty$, except for the radiation term, which is twice the value in the previous case. This accounts for the fact that radiation occurs on both sides, so that total radiation losses are twice larger.

4. Full compressible formulation

After detailing the matched asymptotic model, we now introduce in this section a numerical method to resolve directly the eigenvalue problem in a fully compressible setting.

4.1. Compressible Navier–Stokes equations

Let us consider a compressible fluid motion of a perfect gas described in primitive variables by $\mathbf{q} = [\rho, \mathbf{u}, T, p]^T$, where the velocity vector field is $\mathbf{u} = (u, v, w)$, pressure p , temperature T and fluid density ρ . Dimensional primitive variables have been made dimensionless, as follows:

$$\mathbf{x} = \frac{\mathbf{x}}{D_h}, \quad t = \frac{\tilde{t}U_M}{D_h}, \quad \rho = \frac{\tilde{\rho}}{\rho_{ref}}, \quad \mathbf{u} = \frac{\tilde{\mathbf{u}}}{U_M}, \quad T = \frac{\tilde{T}}{T_{ref}}, \quad p = \frac{\tilde{p} - p_{ref}}{\rho_{ref}U_M^2}. \tag{4.1a-f}$$

Here dimensional values are designated by an upper tilde $\tilde{\cdot}$, and reference values are indicated with the \cdot_{ref} . Dynamics is governed by the compressible Navier–Stokes equations, which are here written in terms of primitive dimensionless variables in the

compact vector notation

$$\mathbf{M} \left(\frac{\partial \mathbf{q}}{\partial t} \right) = \mathcal{NS}(\mathbf{q}) = \mathbf{L}(\mathbf{q}) + \mathbf{N}(\mathbf{q}) + \mathbf{C} = \mathbf{0}, \quad (4.2)$$

where $\mathbf{C} = [0, \mathbf{0}, 0, 1]^T$, the mass matrix \mathbf{M} and the linear operator \mathbf{L} are defined as

$$\mathbf{M} = \begin{pmatrix} 1 & 0 & 0 & 0 \\ 0 & \rho \mathbf{I} & 0 & 0 \\ 0 & 0 & \rho & 0 \\ 0 & 0 & 0 & 0 \end{pmatrix}, \quad \mathbf{L} = \begin{pmatrix} 0 & 0 & 0 & 0 \\ 0 & -\nabla \cdot \boldsymbol{\tau}(\cdot) & 0 & \nabla \\ 0 & 0 & -\frac{\gamma}{Pr Re} \Delta & 0 \\ 0 & 0 & 0 & \gamma M^2 \end{pmatrix}, \quad (4.3a,b)$$

while the nonlinear operator is written as

$$\mathbf{N}(\mathbf{q}) = \begin{pmatrix} \mathbf{u} \cdot \nabla \rho + \rho \nabla \cdot \mathbf{u} \\ \rho \mathbf{u} \cdot \nabla \mathbf{u} \\ (\gamma - 1) [\rho T \nabla \cdot \mathbf{u} - \gamma M^2 \boldsymbol{\tau}(\mathbf{u}) : \mathbf{D}(\mathbf{u})] + \rho \mathbf{u} \cdot \nabla T \\ -\rho T \end{pmatrix}. \quad (4.4)$$

Here $\mathbf{D} = 1/2(\nabla \mathbf{u} + \nabla \mathbf{u}^T)$ is the rate of strain tensor and $\boldsymbol{\tau}$ is the viscous stress tensor defined as $\boldsymbol{\tau} = 2\mu \mathbf{D} - 2\mu/3 \nabla \cdot \mathbf{u} \mathbf{I}$.

4.2. Compressible Navier–Stokes – base flow equations

The stability of a steady-state solution to infinitesimal perturbations can be analysed using the classical approach based on linearization of the governing equations: the total flow field is expanded into the sum of a steady-state term plus an infinitesimally small unsteady harmonic perturbation as

$$\mathbf{q}(t) = \mathbf{q}_0 + \varepsilon \left(\hat{\mathbf{q}} e^{-i\omega t} + \text{c.c.} \right), \quad (4.5)$$

where $\varepsilon \ll 1$. Inserting (4.5) in the governing equations (4.2) and neglecting quadratic terms leads to two problems, one for the base flow and one for the perturbation. In particular, at leading order, only steady terms are kept, which leads to the steady Navier–Stokes equations

$$\mathcal{NS}(\mathbf{q}_0) = \mathbf{L}(\mathbf{q}_0) + \mathbf{N}(\mathbf{q}_0) + \mathbf{C} = \mathbf{0}, \quad (4.6)$$

complemented with appropriate boundary conditions. No-slip adiabatic boundary conditions are used at the walls (4.7c). At the axis of revolution, the radial component v_0 is set equal to zero, and the radial derivative of the remaining terms is null (4.7d). At the outlet we set stress-free and isothermal boundary conditions (4.7b); in this way the pressure at the outlet is equal to the thermodynamic pressure, i.e. $p_0 = 1$. Finally, at the inlet boundary $\Gamma_{in} = \Gamma_{in,0} \cup \Gamma_{in,1}$, a constant mass flow is enforced on the $\Gamma_{in,0}$ boundary, slip condition, constant density and zero thermal flux are imposed on the $\Gamma_{in,1}$ (4.7a). Summarising,

$$\rho_0|_{\Gamma_{in}} = 1, \quad \int_{\Gamma_{in,0}} \rho_0 \mathbf{u}_0 \cdot \mathbf{n} \, dS = \frac{\pi}{4}, \quad (\mathbf{u}_0 \cdot \mathbf{n})|_{\Gamma_{in,1}} = 0, \quad (\nabla T_0 \cdot \mathbf{n})|_{\Gamma_{in}} = 0, \quad (4.7a)$$

$$T_0|_{\Gamma_{out}} = 1, \quad (-p_0 \mathbf{I} + \boldsymbol{\tau}(\mathbf{u}_0)) \cdot \mathbf{n}|_{\Gamma_{out}} = 0, \quad (4.7b)$$

$$\mathbf{u}_0|_{\Gamma_w} = (0, 0, 0)^T, \quad (\nabla T_0 \cdot \mathbf{n})|_{\Gamma_w} = 0, \quad (4.7c)$$

$$v_0|_{\Gamma_w} = 0, \quad \frac{\partial u_0}{\partial r} = \frac{\partial w_0}{\partial r} = \frac{\partial \rho_0}{\partial r} = \frac{\partial T_0}{\partial r} = \frac{\partial p_0}{\partial r} = 0 \quad \text{on } \Gamma_{axis}. \quad (4.7d)$$

Acoustic instability prediction via an impedance criterion

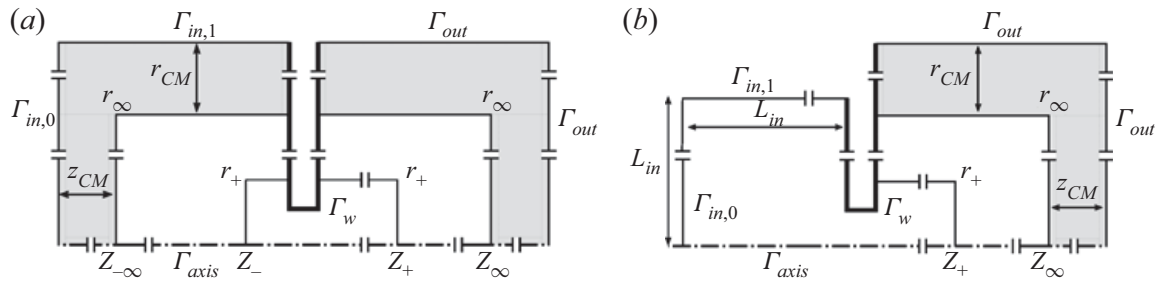


Figure 4. Schematic representation of the computational mesh for both configurations, (a) open/open case, (b) closed/open case: $z_{-\infty}$, z_{∞} , r_{∞} are, respectively, the location of the physical inlet, outlet and lateral boundaries. The physical domain is padded into a complex mapping layer with a radial extension r_{CM} (respectively axial z_{CM} extension). The inner domain corresponds to an inner region with the highest vertex density: z_{-} , z_{+} , r_{+} are, respectively, the location of the left, right and lateral boundaries of this inner domain; in the closed/open case the inner domain includes the cavity located upstream of the hole.

4.3. Linearized compressible Navier–Stokes equations – homogeneous problem

The linearized compressible Navier–Stokes equations govern the evolution of the perturbation \hat{q} ,

$$-i\omega \mathbf{M}\hat{q} = \mathbf{LNS}_0(\hat{q}) = [\mathbf{L} + DN|_{q_0}] \hat{q}, \quad (4.8)$$

where $DN|_{q_0}$ is the Jacobian matrix of the nonlinear operator evaluated at the steady state q_0 .

With the purpose of modelling a large container upstream of the hole, for the open/open case, we have designed a computational domain, [figure 4\(a\)](#), composed of three regions: an inner domain with the highest vertex density, the physical domain and an absorbing layer to eliminate the appearance of spurious eigenvalues. The absorbing layer corresponds to the complex mapping technique, cf. [Sierra et al. \(2020\)](#). The boundary conditions of the linearized full compressible formulation for the open/open case are as follows:

$$\hat{\rho}|_{\Gamma_{in}} = 0, \quad (-\hat{p}\mathbf{I} + \tau(\hat{\mathbf{u}})) \cdot \mathbf{n}_{\Gamma_{out}} = 0, \quad (\nabla \hat{T} \cdot \mathbf{n})|_{\Gamma_{in}} = 0, \quad (4.9a)$$

$$\hat{\rho}|_{\Gamma_{out}} = 0, \quad (-\hat{p}\mathbf{I} + \tau(\hat{\mathbf{u}})) \cdot \mathbf{n}_{\Gamma_{out}} = 0, \quad (\nabla \hat{T} \cdot \mathbf{n})|_{\Gamma_{out}} = 0, \quad (4.9b)$$

$$\hat{\mathbf{u}}|_{\Gamma_w} = (0, 0, 0)^T, \quad (\nabla \hat{T} \cdot \mathbf{n})|_{\Gamma_w} = 0, \quad (4.9c)$$

$$\hat{v}|_{\Gamma_w} = 0, \quad \frac{\partial \hat{u}}{\partial r} = \frac{\partial \hat{w}}{\partial r} = \frac{\partial \hat{\rho}}{\partial r} = \frac{\partial \hat{T}}{\partial r} = \frac{\partial \hat{p}}{\partial r} = 0 \quad \text{on } \Gamma_{axis}. \quad (4.9d)$$

In particular, in the far field (inlet and outlet) we impose null density variations, a stress-free boundary condition and vanishing thermal flux [\(4.9a\)](#) and [\(4.9b\)](#); doing so the mass flux, $\rho_0 \hat{\mathbf{u}} \cdot \mathbf{n}$, is allowed to vary. A no-slip adiabatic boundary condition is used at the walls [\(4.9c\)](#), while at the axis the radial component of the velocity \hat{v} is set to zero, together with a null radial derivative of the remaining terms [\(4.9d\)](#).

For the purpose of modelling a closed cavity that acts as an acoustic resonator, we have a computational domain, which is sketched in [figure 4\(b\)](#), where the complex mapping layer is only present in the region placed downstream of the hole. The set of boundary

conditions are as follows:

$$\hat{\rho}|_{\Gamma_{in}} = 0, \quad \hat{\mathbf{u}}|_{\Gamma_{in}} = (0, 0, 0)^T, \quad (\nabla \hat{T} \cdot \mathbf{n})|_{\Gamma_{in}} = 0, \quad (4.10a)$$

$$\hat{\rho}|_{\Gamma_{out}} = 0, \quad (-\hat{p}\mathbf{I} + \tau(\hat{\mathbf{u}})) \cdot \mathbf{n}|_{\Gamma_{out}} = 0, \quad (\nabla \hat{T} \cdot \mathbf{n})|_{\Gamma_{out}} = 0, \quad (4.10b)$$

$$\hat{\mathbf{u}}|_{\Gamma_w} = (0, 0, 0)^T, \quad (\nabla \hat{T} \cdot \mathbf{n})|_{\Gamma_w} = 0, \quad (4.10c)$$

$$\hat{v}|_{\Gamma_w} = 0, \quad \frac{\partial \hat{\mathbf{u}}}{\partial r} = \frac{\partial \hat{w}}{\partial r} = \frac{\partial \hat{\rho}}{\partial r} = \frac{\partial \hat{T}}{\partial r} = \frac{\partial \hat{p}}{\partial r} = 0 \quad \text{on } \Gamma_{axis}. \quad (4.10d)$$

i.e. null density and velocity variations (4.10a) at the inlet, a stress-free condition, null density variation and vanishing thermal flux (4.10b) at the outlet; no-slip and adiabatic walls (4.10c); null radial velocity component and null radial derivative of the remaining terms (4.10d).

4.4. Numerical implementation

Following a usual route in global stability analysis, the nonlinear problem (4.6) for the base flow is solved using a Newton iteration method and the eigenvalue problem (4.8) is solved using a shift-invert Arnoldi method. Spatial discretization is done using a finite-element method, using P2-elements for velocity components u_x, u_r and P1-elements for thermodynamic variables P, ρ, T . Mesh generation and assembly of matrix operators is performed using the FreeFem++ software (Hecht 2012). Resolution is achieved using PETSc/SLEPc libraries, which are directly implemented in FreeFem++. Monitoring of computation, loop over the parameters and post-processing are handled in Matlab thanks to the StabFem suite (Fabre *et al.* 2018). Note that during the process, mesh adaptation is used in a way similar to as described in Fabre *et al.* (2018), to ensure that the resolution is sufficient to ensure grid independence when computing the base flow and the eigenmodes. Examples of codes reproducing sample results are shared on the website of the StabFem project. Some details about the computed base flows are given in Appendix B. Details about grid convergence are given in Appendix E.

5. Results – cavity/open configuration

5.1. Validation of the asymptotic model – comparison with compressible LNSE

In § 3.3.1 we introduced an asymptotic method which is able to predict the eigenvalues $\omega = \omega(Re, \beta, M, V_{in})$ from a simple tabulation/computation of the function $Z_h(\omega; Re, \beta)$ for real values of ω , hence reducing the number of parameters from four to two only. Before conducting a full parametric study of the instability with the proposed matched asymptotic method, we have to assess its validity by comparing the predictions with resolution of the full eigenvalue problem. This is done in figure 5 which compares the amplification rates (*a,c,e,g*) and frequencies (*b,d,f,h*) obtained with the two approaches for values of M, Re and V_{in} spanning a large range of parameter values, considering a hole with aspect ratio $\beta = 0.3$.

Consider, first, the predictions of the asymptotic model represented by coloured lines in the figures. Thanks to the inverse method explained in § 3.3.1, the asymptotic prediction allows us to plot ω as a continuous function of V_{in} . We use solid lines for the segments of the curves corresponding to unstable modes and dotted lines for those corresponding to stable modes. As identified by Fabre *et al.* (2020), for $\beta = 0.3$, several modes of

Acoustic instability prediction via an impedance criterion

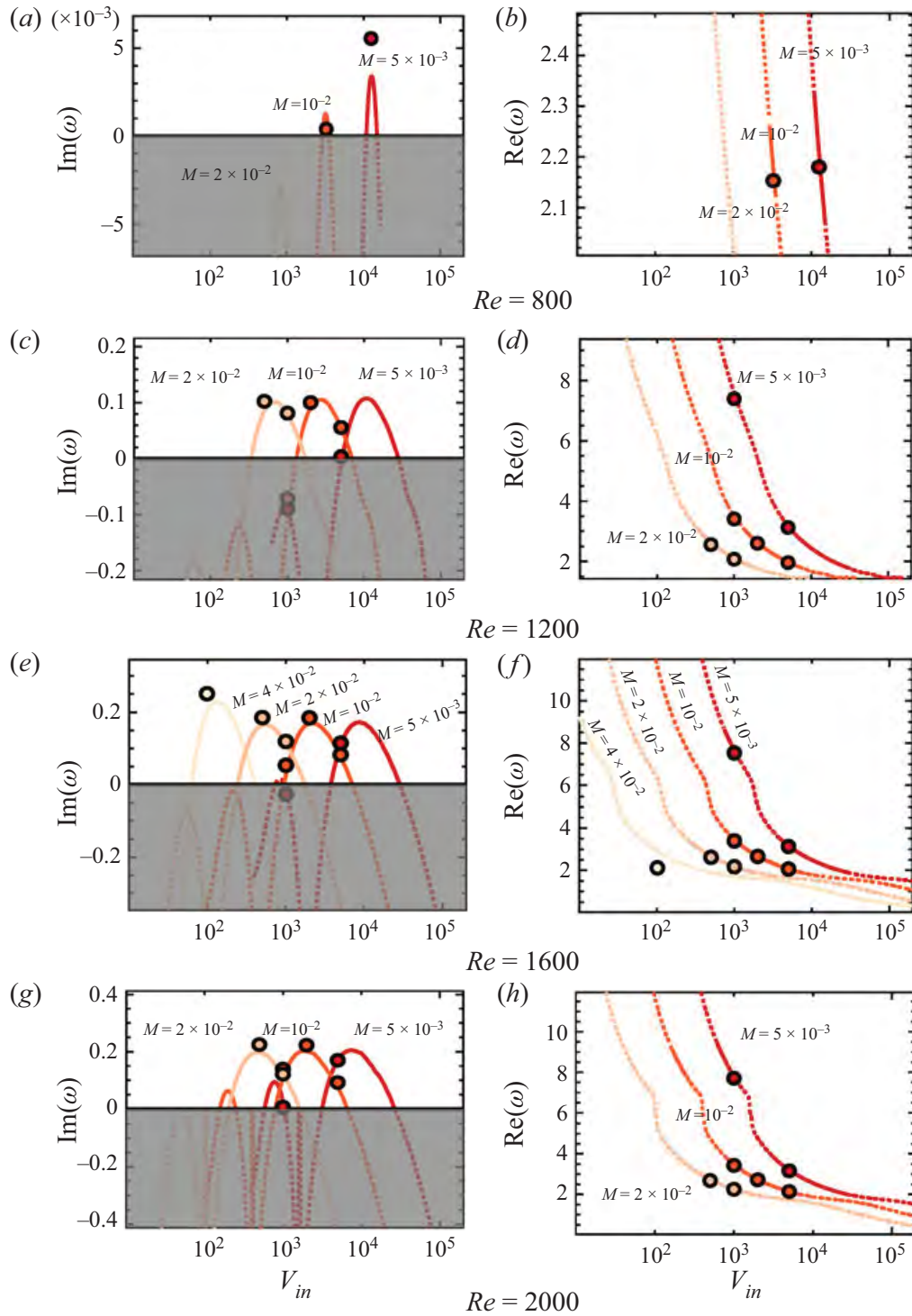


Figure 5. Growth rate (a,c,e,g) and frequency (b,d,f,h) of eigenmodes as a function of V_{in} , M and Re for $\beta = 0.3$. Lines were obtained from the matched asymptotic model and points with the compressible LNSE. Solid lines denote unstable regions, dashed lines are used for stable zones.

conditional instability, termed C_1 , C_2 , etc. . . are expected to arise as the Reynolds number is increased. The corresponding frequencies are quantized, and an argument to explain this quantification was proposed in terms of the dynamics of the shear layer. An alternative argument, in terms of a forward shear wave and a backward acoustic wave, is proposed in [Appendix D](#).

From the results of Fabre *et al.* (2020), for $\beta = 0.3$ (see also [figure 18](#) reproduced in [Appendix D](#)), the first mode C_1 arises just below $Re = 800$ and the second mode C_2 arises

for $Re \approx 1500$. This is in good agreement with the observed results of the asymptotic model, which effectively predicts two ranges of instability for $Re = 1600$ and $Re = 2000$, at least, for the smallest considered values of M . The figure also shows that increasing M results in a shifting of the instability ranges towards smaller values of V_{in} .

Consider now, the eigenvalue calculations, represented by circles in the figures. Results have been computed for a limited set of values of V_{in} where unstable modes were expected. Recall that in the eigenvalue study, V_{in} is linked to the size of the numerical domain, so that the whole process (mesh generation, base flow computation, resolution of eigenvalue problem) has to be restarted for each new value of V_{in} . An excellent matching between the two estimates may be appreciated even for large growth rates, the relative error being less than 3% in most cases. Comparison seems poorer, at first sight, for the case of $Re = 800$ reported in figure 5(a) but it must be remembered that the case is very close to the threshold and amplification rates are very small, so that the absolute error is actually of comparable order to the other cases. Note that an excellent agreement is still found in cases where the amplification rate is not small, a range where the impedance criterion should be *a priori* slightly less reliable due to its perturbative nature. The agreement also remains excellent when the Mach number is raised to $M = 2 \times 10^{-2}$. Note that, for eigenvalue computations, it has been only considered configurations with $V_{in} > 10^2$, since for smaller values, the cavity becomes very small and the modelling as a Helmholtz resonator becomes questionable. This is why we did not attempt to draw any comparisons for $M > 2 \times 10^{-2}$, with the exception of a case with $M = 4 \times 10^{-2}$ represented in plot (e).

5.2. Structure of some eigenmodes

Let us now illustrate the structure of a few eigenmodes computed with the full compressible LNSE. Figure 6 displays the eigenmode computed for $M = 5 \times 10^{-3}$ and $V_{in} = 10^4$ for $Re = 1200$. This mode is correctly predicted by the asymptotic model, and recognized to correspond to the branch C_1 of conditional instability modes, as defined by Fabre *et al.* (2020). As observed, the pressure level inside the cavity is uniform, confirming that the cavity effectively acts as a Helmholtz resonator for this mode so that the modelling hypotheses are correctly verified. Downstream of the hole, the mode is characterised by an alternance of structures of opposite sign, localized along the shear layer. This structure is characteristic of regions associated with a negative real part of impedance, as identified by Fabre *et al.* (2020). Note that very far away in the downstream domain, the structure is expected to match with a spherical diverging wave of the dimensionless wavelength $\lambda = 2\pi/(M\omega_R)$. Here λ is of order 70, so this structure is not visible on the figure. A characterisation of the far-field acoustic radiation is described in § 6.3; see figure 13.

In addition to eigenmodes of the kind presented in figure 6 which are well predicted by our asymptotic approach, one typically observes the existence of other families of eigenmodes with a more complex structure. Figure 7(b) displays a family of such modes, computed for the set of parameters $M = 2 \times 10^{-1}$, $V_{in} = 10^4$ for $Re = 1200$. One clearly observes that the pressure inside the cavity is no longer uniform, but characterised by nodal lines in the radial and axial distributions. These modes are recognised as cavity modes. They arise as soon as the acoustic compactness hypothesis fails, i.e. when the acoustic wavelength is smaller than the characteristic length ($L_{in} = (V_{in}/\pi)^{1/3}$) of the cavity.

5.3. Parametric study

In our previous work, the ranges of parameters corresponding to a conditional instability (requiring the presence of a correctly tuned resonator) were mapped in the $Re-\beta$ plane;

Acoustic instability prediction via an impedance criterion

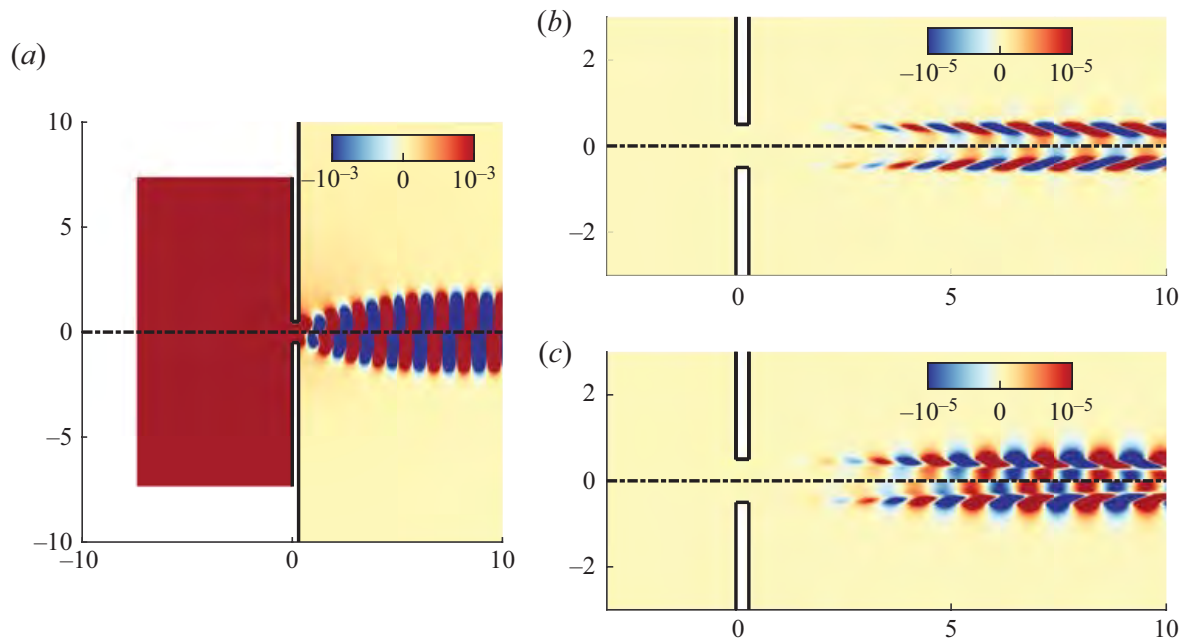


Figure 6. Plot of the C_1 eigenmode for $Re = 1200$ (real part in upper region and imaginary part in the lower region) at $M = 5 \times 10^{-3}$. (a) Pressure, (b) temperature and (c) density.

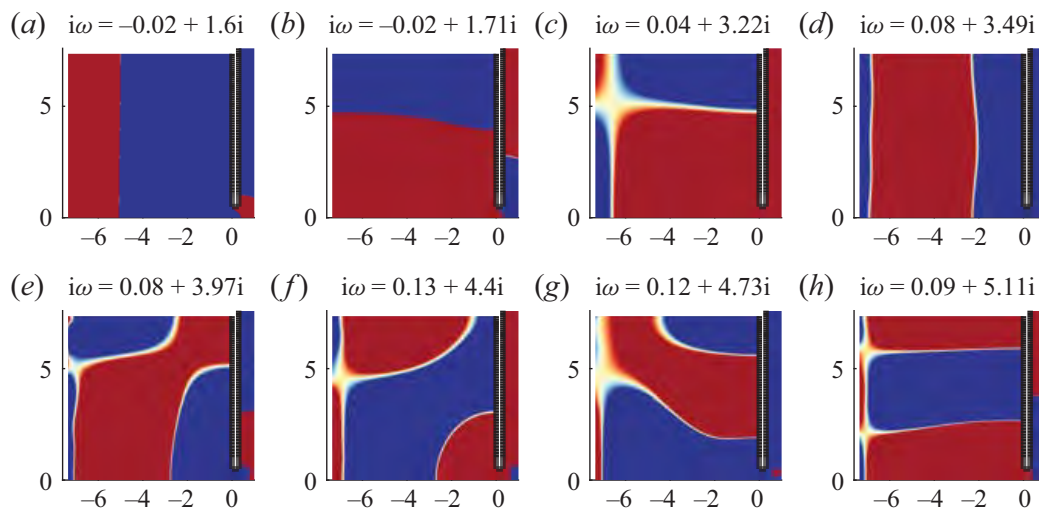


Figure 7. Real part of the pressure component of higher-order cavity modes for $M = 2 \times 10^{-1}$ and a cavity of $V_{in} = 10^4$.

see Fabre *et al.* (2020, figure 13), also reproduced in Appendix D (see figure 18). We are now able to build upon these results a parametric study of the situation where the resonator corresponds to the upstream cavity, as a function of the four parameters (Re , β , M , V_{in}). Figures 8 and 9 display the dependence of the neutral curves on the Mach number and V_{in} for several Reynolds numbers and values $\beta = 0.3$ and $\beta = 1$, respectively. Let us first explore the value $\beta = 0.3$ displayed in figure 8; there exist only two unstable modes, C_1 and C_2 . The cavity is correctly tuned to trigger the instability inside each of the bounded coloured regions of the (V_{in}, M) plane. For the configuration corresponding to $\beta = 1$, there exist four modes of conditional instability. As reported in Fabre *et al.* (2020), C_1 and C_4 instabilities only exist if the cavity connected upstream of the aperture is correctly tuned, that occurs inside each of the bounded coloured regions of the (V_{in}, M) plane of

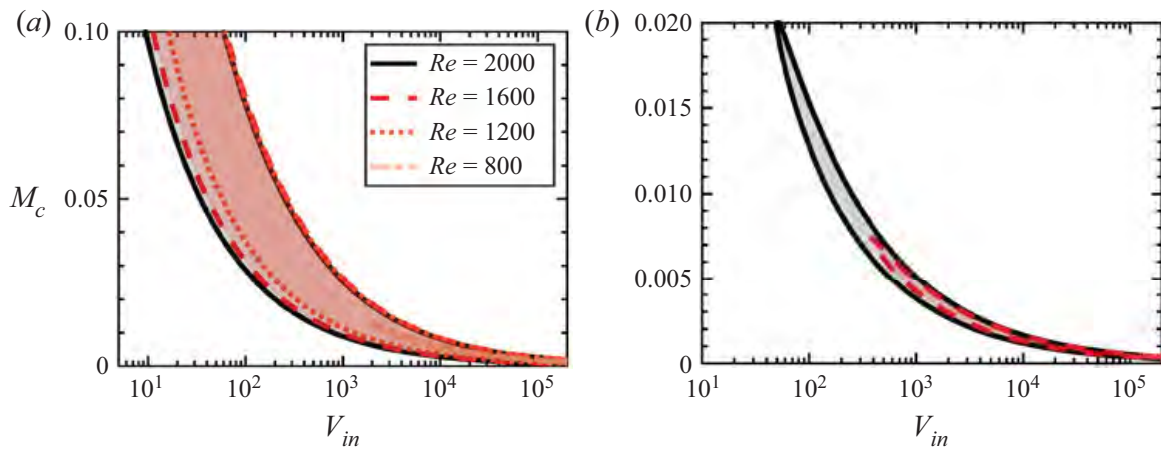


Figure 8. Regions of conditional stability in the (V_{in}, M) plane for $\beta = 0.3$; (a) C_1 , (b) C_2 .

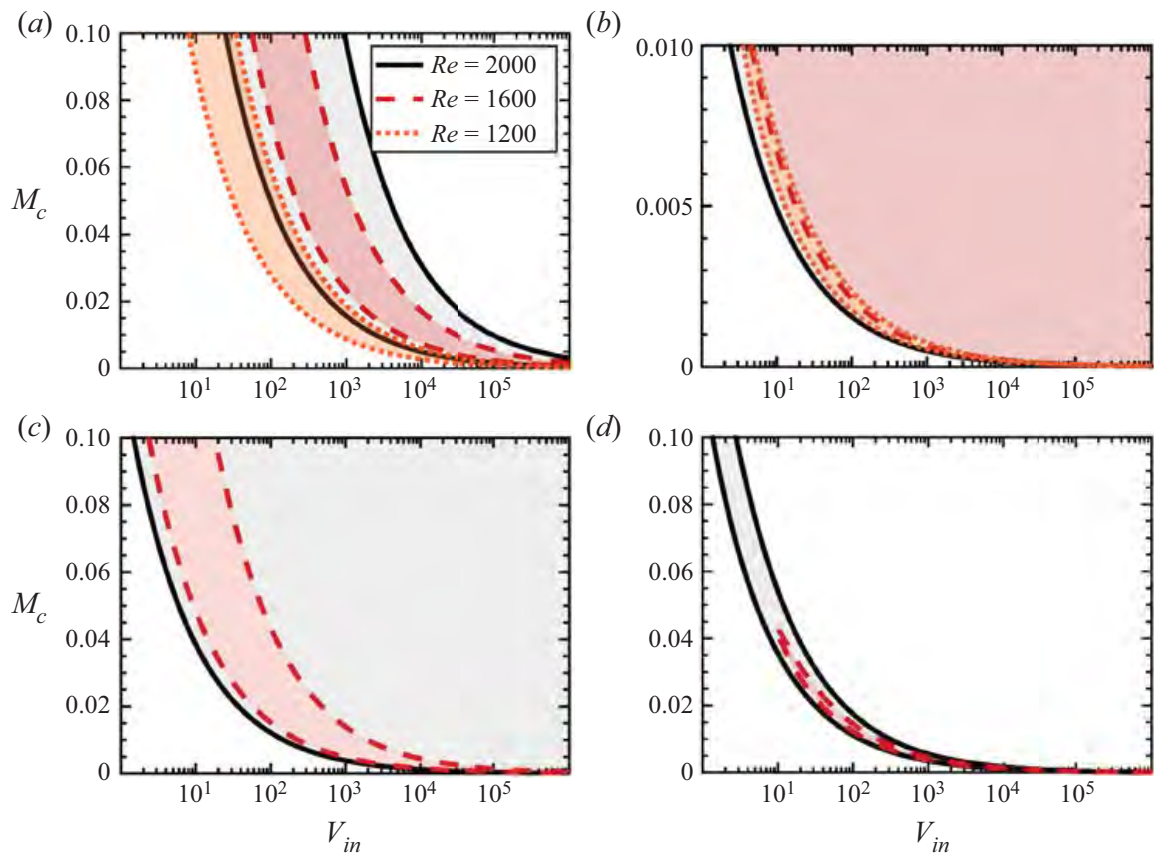


Figure 9. Regions of conditional stability in the (V_{in}, M) plane for $\beta = 1$; (a) C_1 , (b) C_2 , (c) C_3 , (d) C_4 .

figure 9(a,d). These regions of instability grow with the Reynolds number, and they shrink with V_{in} . Contrary to instabilities C_1 and C_4 , for a given value of V_{in} , instabilities C_2 and C_3 may exist for every M ; for this reason, these instabilities may be conceived as a degenerate situation of pure hydrodynamic instabilities H_2 and H_3 , which are discussed in § 6.

Finally, the dependence of this type of instability on the acoustic resonator is better appreciated if we consider the effect of V_{in} and M together with the $\chi = V_{in}M^2$ parameter. This allows us to display neutral curves of stability in the (χ, Re) plane, which is shown in figure 10 for several values of β and M , where the explicit dependence on the Mach

Acoustic instability prediction via an impedance criterion

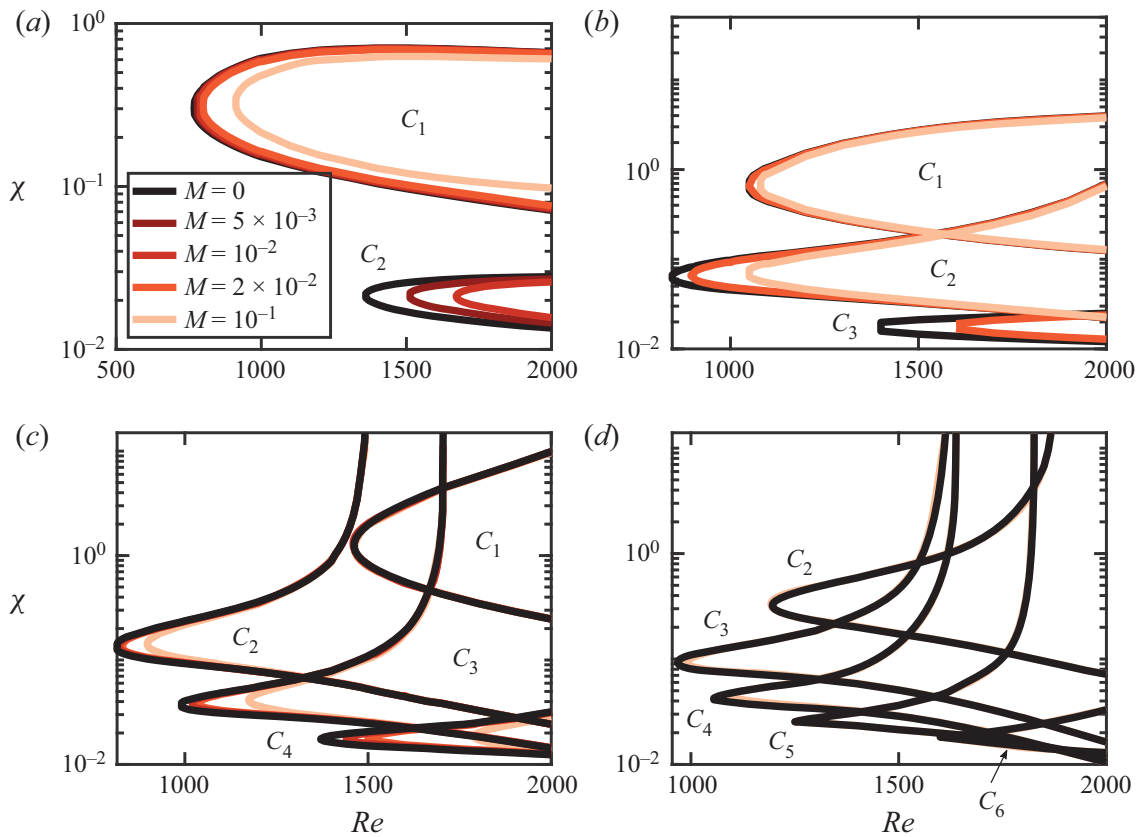


Figure 10. Regions of conditional instability in the (χ, Re) plane; (a) $\beta = 0.3$, (b) $\beta = 0.6$, (c) $\beta = 1$, (d) $\beta = 2$.

number originates from the radiation term of (3.8). Each bounded region corresponds to a conditional instability C_i ; neutral curves display the shape of a ‘tongue’ with the tip located at the lowest Reynolds number of the instability region and a vertical asymptote located at the Reynolds number of the threshold of the H_i instability (if it exists). From figure 10 we can appreciate how C_i conditional instabilities are a generalization of the pure hydrodynamic instabilities H_i . Nevertheless, a connection between hydrodynamic and conditional instabilities for limit values of χ is outside the range of validity of the methodology used for the closed/open case. In fact, one may relate the characteristic cavity length (L_{in}) and the acoustic wavelength (λ_{ac}) in terms of the Strouhal number and the parameter χ ,

$$\left(\frac{L_{in}^{3/2}}{\lambda_{ac}}\right)^2 = St^2 \frac{\chi}{\pi}, \quad (5.1)$$

which implies that, for cavities characterised by $\chi \gg 1$, one cannot rule out the existence of higher cavity modes. Such a finding is only relevant for regions near the vertical asymptotes of figure 9. The methodology remains valid for the C_1 mode, where the product $St^2(\chi/\pi) < 1$, even in the region of $\chi > 1$ for $\beta = 1$, because the Strouhal number of the C_1 mode is approximately one-fourth, cf. Appendix D.

6. Results – open/open configuration

6.1. Parametric study

A purely hydrodynamic instability exists in the present configuration for sufficiently large values of the hole aspect ratios β . In this section we check that such instabilities are

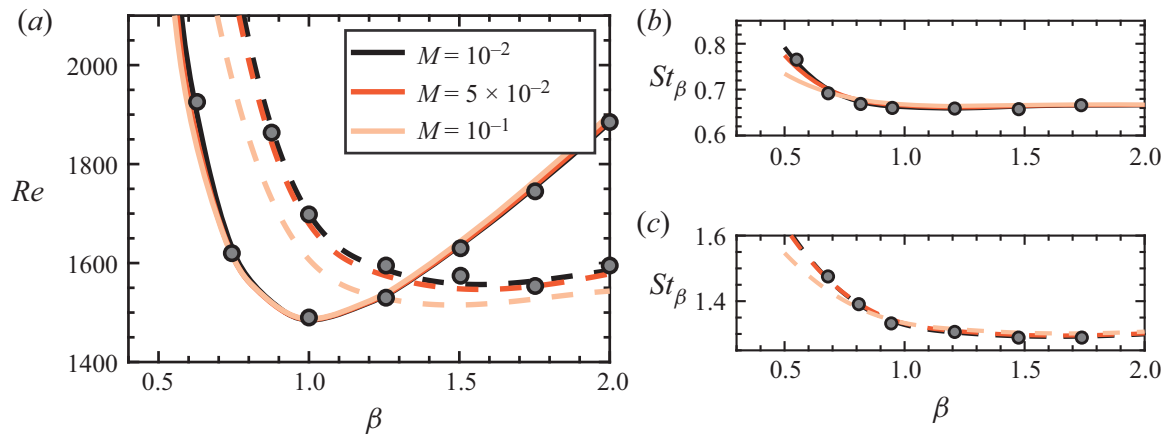


Figure 11. (a) Neutral curves of instability of hydrodynamic modes H_2 (solid lines) and H_3 (dashed lines) for $M = 10^{-2}$, 5×10^{-2} and $M = 10^{-1}$. (b) Strouhal evolution of the H_2 modes with β at the threshold of the instability. (c) The same as (b) for the H_3 modes. Dots correspond to incompressible results of Fabre *et al.* (2020), also reported in Appendix D.

effectively encountered in the open/open configuration and provide a parametric study of their range of existence as a function of the parameters Re , β , M .

Figure 11(a) displays the range of existence of instabilities as a function of Re and β for three values of M . Two different modes, corresponding to the purely hydrodynamic modes H_2 and H_3 as identified by Fabre *et al.* (2020), are documented. Note that higher instability modes, called H_i with $i = 4, 5, 6 \dots$, exist in the studied interval of the parameter β ; however, they arise at larger values of Re and are not considered. The curves displayed in the figure for the smallest value of M , namely 10^{-2} , are very close to the predictions obtained by Fabre *et al.* (2020, figure 15), which is represented by dots in figure 11. One can see that compressibility has almost no effect on the instability threshold of mode H_2 . On the other hand, it has a destabilizing effect on mode H_3 . Figure 11(b) investigates the effect of compressibility on the oscillation frequency, here represented as a Strouhal number $St_\beta = \omega_R \beta / 2\pi$. One can see that compressibility decreases the frequency for the shortest holes and has almost no effect on frequency for longer ones. This behaviour is associated with the significant modification of the threshold of instability (Re) for short holes (left asymptote of either H_2 or H_3 in figure 11), which does not occur for holes with a larger β value. A substantial variation in the critical Reynolds number induces a modification of the vena contracta coefficient α_{vena} (see, e.g. figure 16), which in turn may be linked to the frequency of the instability; see the discussion in Appendix D.

6.2. Effect of Mach number – sensitivity analysis

In order to explain these observed trends, we consider the sensitivity $d\omega/dM$ of the complex frequency ω with respect to M . This quantity may be split into two terms, corresponding respectively to the sensitivity to base flow modifications and to the sensitivity to a Mach number variation of the linearized equations,

$$\left. \frac{d\omega}{dM} \right|_M = \left. \frac{\partial \omega}{\partial M} \right|_{q_0} + \left. \frac{\partial \omega}{\partial q_0} \right|_M \frac{\partial q_0}{\partial M}. \quad (6.1)$$

We have employed two techniques, a continuous adjoint technique described in Meliga, Sipp & Chomaz (2010) and a forward evaluation of the sensitivity. Provided the Mach number is close to the incompressible limit, the continuous adjoint technique provides

less accurate results; for this reason, we have decided to perform a forward evaluation. The first term $\partial\omega/\partial M$ is evaluated using a first-order finite difference, which requires the resolution of two eigenvalue problems (4.8) with the steady state frozen at the Mach number M , and with a Mach number perturbation of a small magnitude $\Delta M \ll M$ in the linearized Navier–Stokes operator of the eigenvalue problem. The second term is also evaluated by finite difference using two different steady states computed at M and $M + \Delta M$ where the Jacobian operator is evaluated at M . Figure 12 displays the sensitivity computed in such a way for a value of Re corresponding to the thresholds of the instability for modes H_2 (with $\beta = 0.8$) and H_3 (with $\beta = 2$). The figure also displays the value of $\partial\omega_1/\partial M$ obtained from the asymptotic model (3.12), which is a constant. Figure 12(a) reports a linear variation of the two terms of the sensitivity with respect to Mach number. A Mach number variation in the base flow has a stabilizing effect, whereas the instability is triggered by small variations of the Mach number of the linearized operator. The most dominant term for this kind of acoustically compact solutions seems to be the base flow effect, which has a small stabilizing effect. In particular, it explains the almost insignificant variation of the H_2 neutral curves in figure 11. Concerning the frequency, both terms have an almost opposite effect, which implies an almost null variation of the instability frequency for the H_2 mode. The impedance criterion in this case predicts a stabilizing effect with a small frequency increase, which holds relatively well for $M < 0.02$. On the other hand, the variation with respect to the Mach number of the growth rate and the frequency of instability of a configuration that is no longer acoustically compact for Mach numbers of the order of $M \sim 10^{-2}$ such as the H_3 mode at threshold for $\beta = 0.8$ greatly differs with the estimations made with the impedance criterion. Figure 12(b) reports a similar stabilizing effect of the base flow to the one of the H_2 mode. However, in this case variations of the Mach number in the linearized operator greatly destabilize the steady state, which causes the large variations in the neutral curves displayed in figure 11. In terms of frequency variations, it is possible to observe much larger excursions, which are negative and constant for $M < 0.07$ and increase linearly for $M > 0.07$. So we may conclude that the impedance criterion holds relatively well for large β and instability modes with low frequency, which are in turn the most acoustically compact, but it fails to predict accurate trends even for low Mach numbers for modes with higher frequencies and small length to thickness ratios.

6.3. Directivity of acoustic emission

Finally, we address the influence of parameters (β, M) on the directivity pattern of instabilities of type H_2 and H_3 . For that purpose, we evaluate the set of neutral eigenmodes for each pair (β, M) . Note that the amplitude of the eigenmodes are arbitrary, the pressure levels displayed in figure 14 have been normalized with respect to the monopole radiation (based on the oscillating volume flux through the perforation). Three values of the Mach number $M = \{10^{-2}, 2 \times 10^{-2}, 5 \times 10^{-2}\}$ and two of the dimensionless parameter $\beta = \{1, 2\}$ are selected for this study. The configuration $\beta = 1$ corresponds to a configuration less acoustically compact than $\beta = 2$ and it seems *a priori* more likely that the radiation differs from the single monopole pattern. Figure 13 displays the acoustic pressure levels of the real part of the neutral eigenmodes, H_2 in the upper part and H_3 in the lower part, for $M = 5 \times 10^{-2}$ and $\beta = 1$ (a) and $\beta = 2$ (b). Figure 13(a) displays the pressure levels in logarithmic scale for $\beta = 1$. In that figure one can appreciate a monopolar-like radiation for H_3 ; however, at $M = 5 \times 10^{-2}$ the H_2 mode displays a radiation pattern with a preferential direction aligned with the streamwise coordinate. In such a configuration,

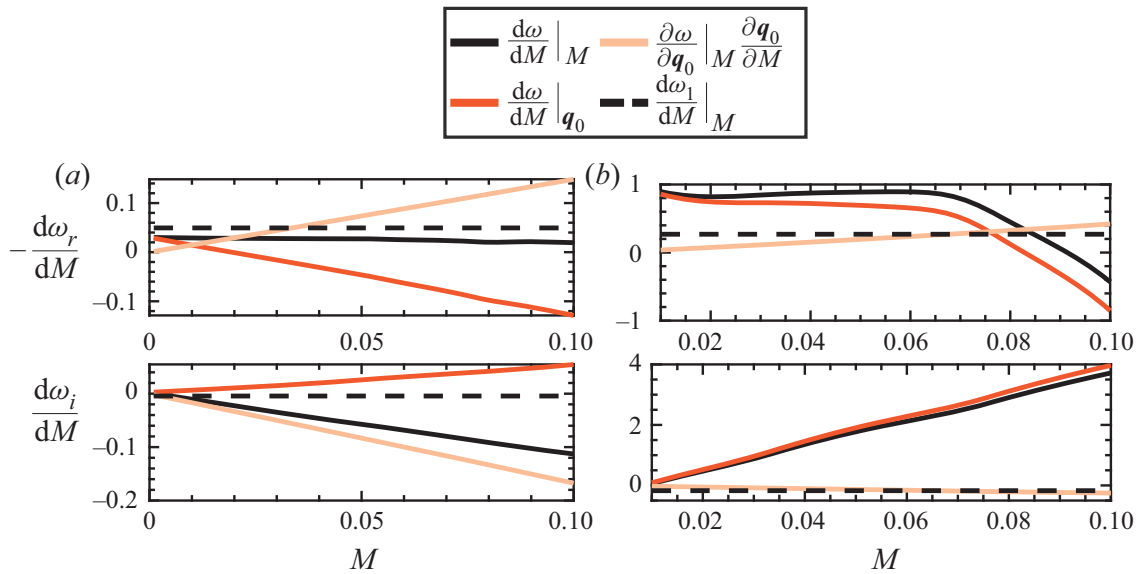


Figure 12. Sensitivity to Mach number variations of the complex frequency ω at the threshold of instability. Dashed line denotes the impedance estimation. (a) Mode H_2 for $\beta = 2$. (b) Mode H_3 for $\beta = 0.8$.

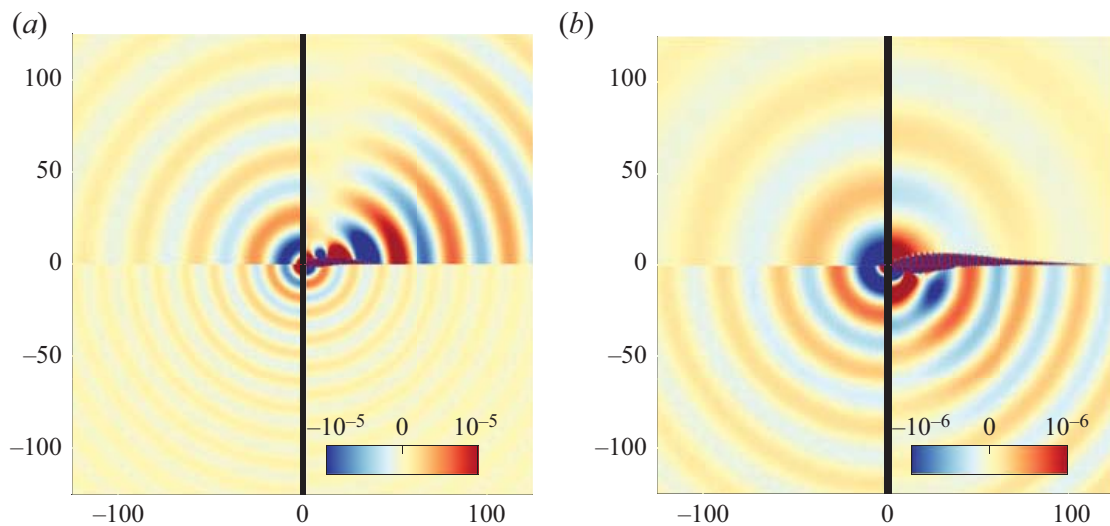


Figure 13. Real part of the pressure component of neutral eigenvalues H_2 (upper part) and H_3 (lower part) at $M = 5 \times 10^{-2}$; (a) $\beta = 1$ and (b) $\beta = 2$.

either the hole and the jet emit sound, which produces an uneven radiation of sound downstream and upstream of the hole. These observations can be better appreciated in [figure 14\(a\)](#), where the departures from an isotropic radiation for $M = 10^{-2}$ and the sound emission for $M = 5 \times 10^{-2}$ are clearly seen. For $\beta = 2$ ([figures 13\(b\)](#) and [14\(c\)](#)), the neutral eigenmodes display a fairly monopolar-like radiation; for the H_3 mode ([figure 14\(d\)](#)), higher pressure levels are measured downstream of the hole for directions forming an angle less than 45 degrees with the axis of symmetry.

7. Conclusion

The objective of the present paper was to investigate how the instability potential of a single jet passing through a hole in a thick plate, recently identified by Fabre *et al.* (2020) using LNSE in a strictly incompressible setting, manifests in a more realistic configuration involving compressibility. For this sake, we considered two generic situations. In the first

Acoustic instability prediction via an impedance criterion

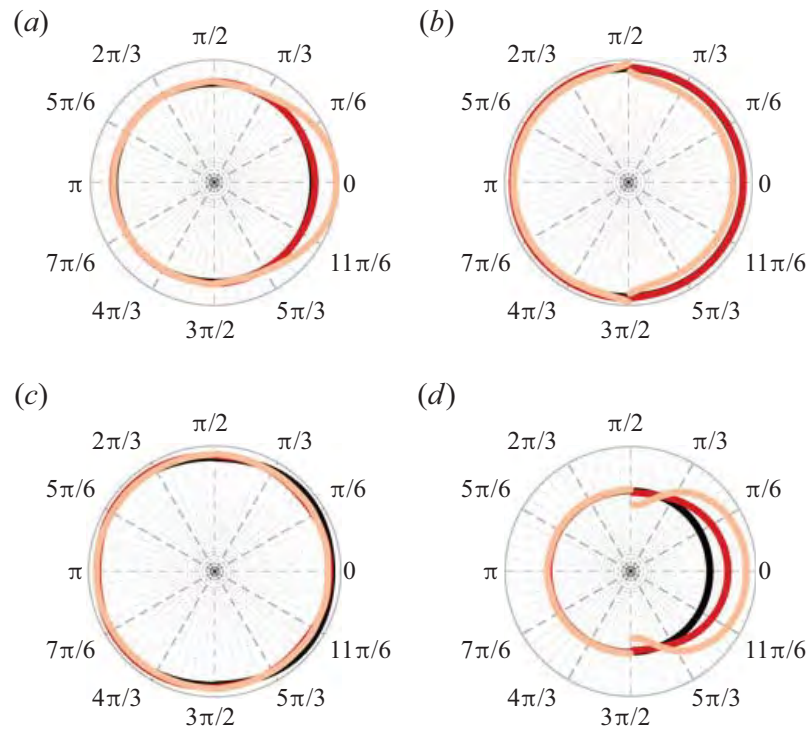


Figure 14. Directivity patterns, in logarithmic scale, measured at $r_x = \sqrt{r^2 + x^2} = 150$. Results are shown for (a) H_2 and $\beta = 1$; (b) H_3 and $\beta = 1$; (c) H_2 and $\beta = 2$; (d) H_3 and $\beta = 2$. Colour legend: (—, black) $M = 10^{-2}$, (—, red) $M = 2 \times 10^{-2}$ and (—, yellow) $M = 5 \times 10^{-2}$.

situation, the upstream domain is a closed cavity and the downstream domain is an open space. This situation was chosen to check the conditional instability mechanism, requiring the existence of a conveniently tuned resonator. In the second situation, the two regions, upstream and downstream of the hole, are considered as open. This situation was chosen to check the purely hydrodynamical instability which is expected to exist even in the absence of a resonator.

The two cases have been analysed with an asymptotic method, which provides an instability criterion and an estimate for the amplification rate. The method consists, in a first step, in writing an impedance of the global system incorporating the hole impedance as computed by Fabre *et al.* (2020) and modelling the impedance of the upstream and downstream regions, and in a second step, in performing a Taylor expansion of this impedance around the real ω -axis to identify its zeros. The great advantage of the method is that the Mach number M and the cavity volume V_{in} appear as parameters in the model, so that a parametric study of the problem can be done entirely in terms of the Reynolds number and aspect ratio, therefore reducing the number of computational parameters from four to two.

The potential to accurately predict the instability properties via the asymptotic model is put into test in §§ 5.3 and 6 for the conditional and pure hydrodynamic cases, respectively. A cross-comparison with the results carried out with the compressible Navier–Stokes equations shows a good match between the two approaches. The impedance criterion has been employed to identify the regions of existence in the (Re, χ) plane of a series of C_i , $i = 1, 2, 3, 4, \dots$ modes. In addition to these acoustically compact modes, at larger Reynolds numbers, there exist unstable modes associated with higher-order modes of the cavity connected upstream (see figure 7 for an example of that phenomenon). The use of the impedance criterion for the characterisation of the compressibility effect in the pure hydrodynamical case is less accurate. We have observed that the estimations of

the growth rate are relatively acceptable for the H_2 mode, but they are faulty for the H_3 mode, in particular for small length to diameter ratios. The inadequacy of the criteria to characterise this case can be attributed to the lack in the asymptotic model of the effect of the backward-travelling acoustic wave. These results suggest that a better modelling of the hydrodynamic-acoustic interaction is required to gain in accuracy. Finally, in § 6 we have examined the influence of the Mach number on the directivity pattern of the family of the pure hydrodynamical modes.

Declaration of interests. The authors report no conflict of interest.

Author ORCIDs.

- J. Sierra-Ausin <https://orcid.org/0000-0001-6036-5093>;
- D. Fabre <https://orcid.org/0000-0003-1875-6386>;
- V. Citro <https://orcid.org/0000-0003-2923-9157>;
- F. Giannetti <https://orcid.org/0000-0002-3744-3978>.

Appendix A. Computation of the hole impedance thanks to incompressible LNSE

A.1. Incompressible Navier–Stokes equations

Under the hypothesis of acoustic compactness, discussed in § 2.3, the flow is assumed to be locally incompressible in the region of the hole, where the fluid motion is governed by the incompressible Navier–Stokes equations

$$\frac{\partial}{\partial t} \begin{bmatrix} \mathbf{u} \\ 0 \end{bmatrix} = \mathcal{NS} \left(\begin{bmatrix} \mathbf{u} \\ p \end{bmatrix} \right) = \begin{bmatrix} -\mathbf{u} \cdot \nabla \mathbf{u} - \nabla p + Re^{-1} \nabla^2 \mathbf{u} \\ \nabla \cdot \mathbf{u} \end{bmatrix}. \quad (\text{A1})$$

The stability of the steady state $[\mathbf{u}_0, p_0]$ is investigated by using the linearized approach, in which the total flow field is decomposed into the sum of a steady base flow and a small time-harmonic perturbation as

$$\begin{bmatrix} \mathbf{u} \\ p \end{bmatrix} = \begin{bmatrix} \mathbf{u}_0 \\ p_0 \end{bmatrix} + \varepsilon \left(\begin{bmatrix} \hat{\mathbf{u}} \\ \hat{p} \end{bmatrix} e^{-i\omega t} + c.c. \right). \quad (\text{A2})$$

A.2. Incompressible Navier–Stokes equations – base-flow equations

The base flow is the solution of the steady version of the Navier–Stokes equations

$$\mathcal{NS}[\mathbf{u}_0; p_0] = 0, \quad (\text{A3})$$

with the following set of boundary conditions:

$$\int_{\Gamma_{in}} \mathbf{u}_0 \cdot \mathbf{n} \, dS = Q_0, \quad (\text{A4a})$$

$$p_0 = 0 \quad \text{on } \Gamma_{out}. \quad (\text{A4b})$$

This problem is solved using a classical Newton iteration.

A.3. Linearized incompressible Navier–Stokes equations – forced problem

The linear perturbation is governed by the equations

$$-i\omega \mathbf{B}[\hat{\mathbf{u}}, \hat{p}]^T = \mathbf{LNS}_0([\hat{\mathbf{u}}, \hat{p}]^T), \tag{A5}$$

where \mathbf{LNS}_0 is the linearized Navier–Stokes operator around the base flow and \mathbf{B} is a weight operator defined as

$$\mathbf{LNS}_0 \begin{bmatrix} \hat{\mathbf{u}} \\ \hat{p} \end{bmatrix} = \begin{bmatrix} -(\mathbf{u}_0 \cdot \nabla \hat{\mathbf{u}} + \hat{\mathbf{u}} \cdot \nabla \mathbf{u}_0) - \nabla \hat{p} + Re^{-1} \nabla^2 \hat{\mathbf{u}} \\ \nabla \cdot \hat{\mathbf{u}} \end{bmatrix}; \quad \mathbf{B} = \begin{bmatrix} 1 & 0 \\ 0 & 0 \end{bmatrix}. \tag{A6a,b}$$

Equation (A6a,b) is complemented with the following boundary conditions:

$$\int_{\Gamma_{in}} \hat{\mathbf{u}} \cdot \mathbf{n} \, dS = q', \tag{A7}$$

$$\hat{p}(x, r) = 0 \quad \text{on } \Gamma_{out}. \tag{A8}$$

A non-zero perturbation of the flow rate q' is imposed, fixed arbitrarily, to $q' = 1$. Equation (A7) thus leads to a non-homogeneous Dirichlet boundary condition at the inlet plane, treated by imposing a constant axial velocity \hat{u}_x . The problem can be symbolically written as

$$[\mathbf{LNS} + i\omega \mathbf{B}][\hat{\mathbf{u}}; \hat{p}] = \mathbf{F}, \tag{A9}$$

where \mathbf{LNS} is the linearized Navier–Stokes operator (implicitly containing the homogeneous boundary condition at the outlet), and \mathbf{F} represents symbolically the non-homogeneous boundary condition at the inlet. This problem is non-singular and readily solved. Since \hat{p} has been set to zero (without loss of generality) along the outlet boundary, the pressure drop $p'_{in} - p'_{out}$ can be extracted from $[\hat{\mathbf{u}}; \hat{p}]$ by retrieving the mean value of the \hat{p} component along the inlet boundary Γ_{in} of the computational domain; such an operation can be written formally as $p'_{in} = \mathbf{P}[\hat{\mathbf{u}}, \hat{p}]$, where \mathbf{P} is a linear operator. The impedance is then ultimately deduced as $Z_h = \mathbf{P} \cdot (\mathbf{LNS} + i\omega \mathbf{B})^{-1} \cdot \mathbf{F}$.

Appendix B. Properties of the compressible steady state

As illustrated in figure 15, the base flow is characterised by a recirculation region originating from the upper corner of the hole. The pressure jump due to this recirculation can be represented by the so-called discharge coefficient (also called the vena contracta coefficient) $\alpha_{vena} = R_h^2/R_J^2$, where R_J is the effective radius of the jet. This function has been tabulated by Fabre *et al.* (2020) as a function of Re and β in the incompressible case. When taking into account the compressibility effects, the discharge coefficient (Bragg 1960) can be written in term of the dimensionless variables introduced in § 4.1 as

$$\alpha_{vena} = \frac{\dot{m}_0}{\pi R_h^2 \frac{1 + \gamma M^2 P_{in}}{\sqrt{T_{in}}} \frac{1}{M} \sqrt{\frac{2}{\gamma - 1} \left[\left(\frac{1 + \gamma M^2 P_{in}}{1 + \gamma M^2 P_{out}} \right)^{-2/\gamma} - \left(\frac{1 + \gamma M^2 P_{in}}{1 + \gamma M^2 P_{out}} \right)^{-(\gamma+1)/\gamma} \right]}}, \tag{B1}$$

which in the low Mach number limit can be approximated as

$$\alpha_{vena} = \frac{\dot{m}_0}{\pi R_h^2 \sqrt{\rho_{in} (2(P_{in} - P_{out}) - 3M^2 (P_{in} - P_{out})^2)}}, \tag{B2}$$

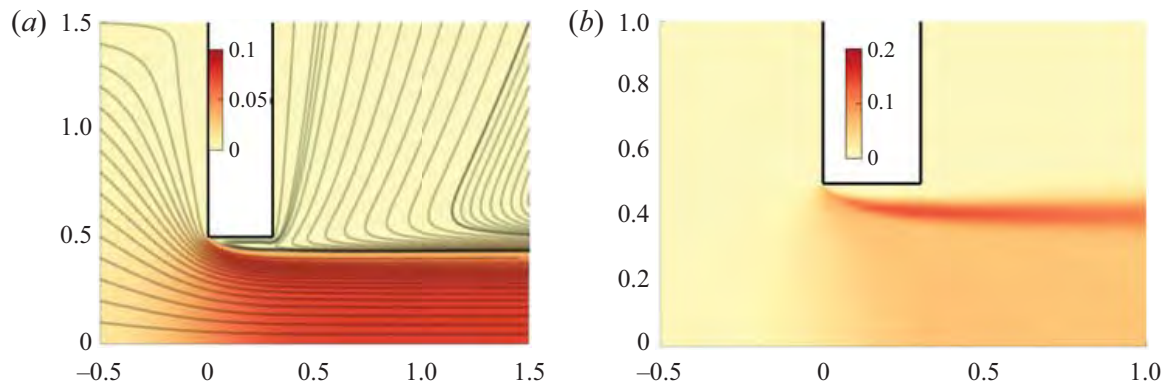


Figure 15. Contour plot of the base flow q_0 for $\beta = 0.3$, $Re = 1400$ and $M = 5 \times 10^{-2}$. (a) Spatial evolution of the Mach number. (b) Spatial evolution of the sensitivity of the axial velocity with respect to the Mach number $\nabla_M \omega_0$.

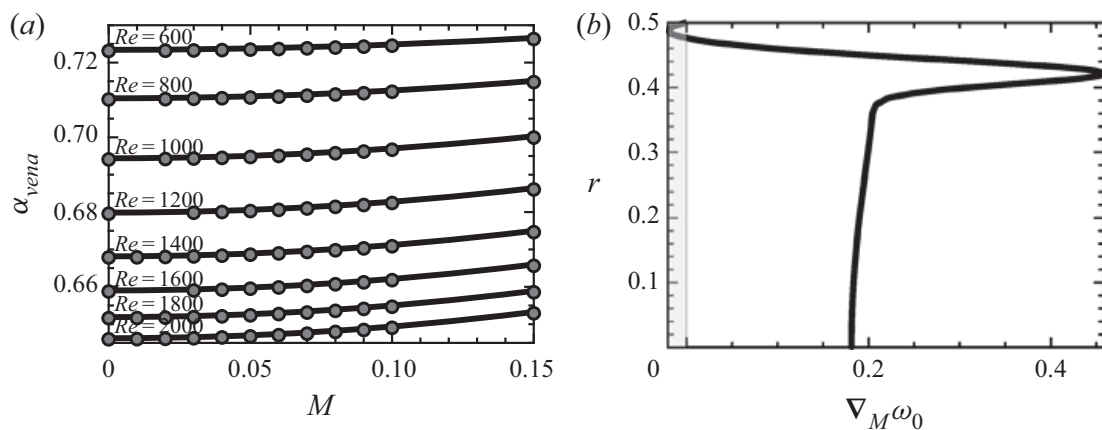


Figure 16. Discharge coefficient as a function of Mach number for several Re for $\beta = 0.3$. Dots correspond to computed values of α_{vena} , lines correspond to the theoretical estimation, cf. Bragg (1960). (b) Axial velocity profile of the sensitivity with respect to Mach number for $\beta = 0.3$, $Re = 1600$, $M = 10^{-1}$ at $z = 0.2$.

and it coincides with the one employed by Fabre *et al.* (2020) at the incompressible limit. Note that at large Reynolds numbers other simpler estimates exist, for instance, see the discussion by Gilbarg (1960) for the compressible Borda tube, which has been revisited by Durrieu *et al.* (2001) and compared against experimental evidence. Figure 16(a) displays the effect of the Mach number on the discharge coefficient. It shows a good quantitative agreement with the theoretical estimation, and it weakly increases with the Mach number. Compressibility effects accelerate the bulk flow within the jet core, whereas the flow within the recirculation region hardly changes (see the evolution of the sensitivity with respect to the Mach number of the streamwise velocity in figures 16(b) and 15(b)). In addition, it has been observed that the shear layer thickness remains unchanged with a weak Mach number increase ($M < 0.2$). In § 6 it is shown that an increase of the Mach number in the steady-state solution has a stabilizing effect, which can be attributed to an attenuated recirculation region.

Appendix C. Nyquist curve – Cauchy’s argument principle

Let us review the use of the Nyquist criterion together with the drawing of Nyquist curves. In the absence of poles in the real axis, the Nyquist plot is drawn along the real axis. However, in the presence of a pole of the impedance in the real axis, one

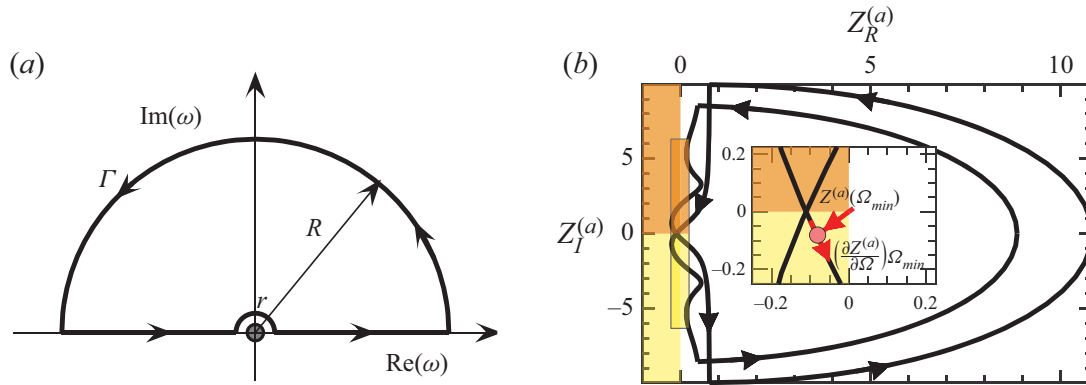


Figure 17. (a) The complex contour Γ of integration enclosing the unstable complex plane, where Cauchy's argument principle is applied. (b) Nyquist curve for the augmented system impedance along Γ .

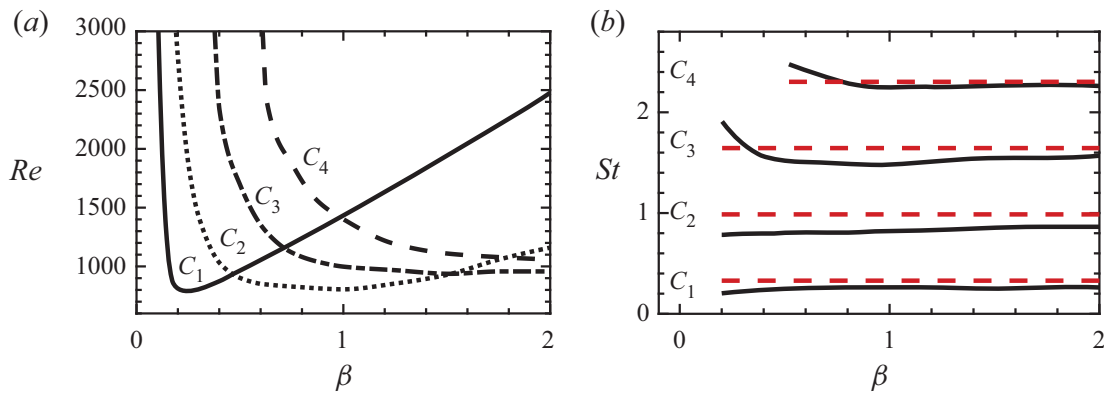


Figure 18. (a) Thresholds of the conditional instabilities C_1 , C_2 , C_3 and C_4 as a function of β and Re . (b) Strouhal evolution with β . Solid lines are the boundaries of the conditional stability computed with incompressible LNSE and dashed lines are the estimation with $\alpha_{vena} = 0.76$.

must take a contour that does not encircle the pole. In particular, the augmented system impedance possess a pole at $\omega = 0$, therefore, a complex contour that does not encircle zero is employed as the one depicted in figure 17(a). In the evaluation of the impedance, let us consider here without loss of generality the augmented system impedance $Z^{(a)}$ (either $Z^{(a)} = Z_a$ or $Z^{(a)} = Z_b$) along the contour Γ , i.e. $Z^{(a)}(\Gamma)$, which provides a direct evaluation of the stability of the system. Provided that the contour of integration does not encircle any pole of the system, which is satisfied by construction, the number of times that the curve $Z^{(a)}(\Gamma)$ encircles the origin in the counterclockwise direction determines the number of zeros in the area surrounded by the contour Γ . In the condition that the contour of integration Γ encloses the unstable complex plane, then any encirclement of the origin implies that the system is unstable. To illustrate this, let us consider the Nyquist curve represented in figure 17(b), where the curve $Z^{(a)}(\Gamma)$ is oriented counterclockwise, and it encircles twice the origin: this implies that the system has two unstable zeros. A more careful evaluation reveals that this corresponds to a pair of conjugated complex zeros.

Additionally, impedance values for real ω can also provide an estimation of the complex zeros whenever $\text{Im}(\omega)$ is of small magnitude. Here, let us detail the procedure followed in § 3.3.1. We consider the case where the Nyquist curve is found near the origin. The first scenario corresponds to a complex frequency $\omega = \omega_R + i\omega_I = \omega_0 + \varepsilon\omega_1$, where ω_0 , ω_R , ω_I are real values, ω_1 is considered to be complex and a small real parameter $\varepsilon \ll 1$.

Provided the impedance $Z^{(a)}(\omega) = \text{Re}(Z^{(a)}(\omega)) + i\text{Im}(Z^{(a)}(\omega)) = Z_R^{(a)}(\omega) + iZ_I^{(a)}(\omega)$ is analytic, the first-order Taylor expansion at ω_0 provides

$$0 = Z^{(a)}(\omega) = Z^{(a)}(\omega_0) + \left(\frac{dZ^{(a)}}{d\omega} \right)_{\omega=\omega_0} (\omega - \omega_0) + R_1(\omega), \tag{C1}$$

where $R_1(\omega)$ is the remainder of the Taylor expansion. The remainder of the expansion can be shown to be bounded, for instance, using Cauchy’s integral formula and the maximum principle (see, for instance, Rudin 1987) yields

$$|R_1(\omega)| \leq M_r \frac{|\omega - \omega_0|^2}{r(r - |\omega - \omega_0|)} \leq M_r \frac{\eta^2}{1 - \eta}, \quad \text{with } M_r \equiv \max_{|\omega - \omega_0|=r} |Z^{(a)}(\omega)| \tag{C2}$$

for $|\omega - \omega_0| < r$ and $|\omega - \omega_0|/r \leq \eta < 1$, where we have assumed that the impedance function is holomorphic in a closed disk of radius r of the complex plane. Therefore, the function $R_1(\omega)/(\omega - \omega_0)$ is also analytic within the disk. In such a way we can approximate the value of zero ω as

$$\begin{aligned} \omega - \omega_0 &= \frac{Z^{(a)}(\omega_0)}{\left(\frac{dZ^{(a)}}{d\omega} \right)_{\omega=\omega_0} + \frac{R_1(\omega)}{\omega - \omega_0}} \approx \frac{Z^{(a)}(\omega_0)}{\left(\frac{dZ^{(a)}}{d\omega} \right)_{\omega=\omega_0}} \\ &= \frac{Z_R^{(a)}(\omega_0) + iZ_I^{(a)}(\omega_0)}{\left(\frac{\partial Z_R^{(a)}(\omega)}{\partial \omega_R} \right)_{\omega=\omega_0} + i \left(\frac{\partial Z_I^{(a)}(\omega)}{\partial \omega_R} \right)_{\omega=\omega_0}}, \end{aligned} \tag{C3}$$

where the error of the approximation is

$$\epsilon \leq \left| \frac{Z(\omega_0)}{\left(\frac{dZ}{d\omega} \right)_{\omega=\omega_0}} \right| \frac{\eta'}{1 - \eta'}, \tag{C4}$$

with $\eta' = |R_1(\omega)|/|\omega - \omega_0|/|(dZ/d\omega)_{\omega=\omega_0}|$, because the radius of convergence of the rational complex function $1/((dZ/d\omega)_{\omega=\omega_0} + z)$ is equal to $|(dZ/d\omega)_{\omega=\omega_0}|$. Thus, the approximation (C3) converges uniformly far from the critical points of the impedance. Furthermore, it provides good estimates whenever $|Z(\omega_0)| \sim \varepsilon \ll 1$ and $|\omega - \omega_0| \sim \varepsilon \ll 1$, which is the motivation to the condition (i) and the expansion in frequency in § 3.3.1. Finally, note that (C3) could be used as a step in a Newton iteration, whenever the initial guess ω_0 is far from the zero of the impedance.

Multiplication by the complex conjugate of the denominator in (C3) leads to

$$\varepsilon \omega_1 \approx \frac{(Z_R^{(a)}(\omega_0) + iZ_I^{(a)}(\omega_0)) \left(\left(\frac{\partial Z_R^{(a)}(\omega)}{\partial \omega_R} \right)_{\omega=\omega_0} - i \left(\frac{\partial Z_I^{(a)}(\omega)}{\partial \omega_R} \right)_{\omega=\omega_0} \right)}{\left(\left(\frac{\partial Z_R^{(a)}(\omega)}{\partial \omega_R} \right)_{\omega=\omega_0} \right)^2 + \left(\left(\frac{\partial Z_I^{(a)}(\omega)}{\partial \omega_R} \right)_{\omega=\omega_0} \right)^2}. \tag{C5}$$

Finally, one could split (C5) in real and imaginary parts, this yields the expression for ω_R ,

$$\varepsilon \operatorname{Re}(\omega_1) = \omega_R - \omega_0 \approx \frac{\left(Z_R^{(a)}(\omega_0) \left(\frac{\partial Z_R^{(a)}(\omega)}{\partial \omega_R} \right)_{\omega=\omega_0} + Z_I^{(a)}(\omega_0) \left(\frac{\partial Z_I^{(a)}(\omega)}{\partial \omega_R} \right)_{\omega=\omega_0} \right)}{\left(\left(\frac{\partial Z_R^{(a)}(\omega)}{\partial \omega_R} \right)_{\omega=\omega_0} \right)^2 + \left(\left(\frac{\partial Z_I^{(a)}(\omega)}{\partial \omega_R} \right)_{\omega=\omega_0} \right)^2}, \quad (\text{C6})$$

and for ω_I ,

$$\varepsilon \operatorname{Im}(\omega_1) = \omega_I \approx \frac{\left(Z_I^{(a)}(\omega_0) \left(\frac{\partial Z_R^{(a)}(\omega)}{\partial \omega_R} \right)_{\omega=\omega_0} - Z_R^{(a)}(\omega_0) \left(\frac{\partial Z_I^{(a)}(\omega)}{\partial \omega_R} \right)_{\omega=\omega_0} \right)}{\left(\left(\frac{\partial Z_R^{(a)}(\omega)}{\partial \omega_R} \right)_{\omega=\omega_0} \right)^2 + \left(\left(\frac{\partial Z_I^{(a)}(\omega)}{\partial \omega_R} \right)_{\omega=\omega_0} \right)^2}. \quad (\text{C7})$$

Appendix D. Frequency selection argument

This appendix provides an argument explaining the quantification of the eigenvalues observed for the cavity/open configuration.

The frequency of the sound generated is selected by considering the two elements that compose the feedback loop of a class III aerodynamic whistle: the hydrodynamic-acoustic wave interaction and the acoustic resonator. In this kind of mechanism, we can distinguish two feedback loops, a first loop composed of the interaction of a hydrodynamic instability with an acoustic wave and a second one which accounts for the interaction of the first feedback loop with the acoustic resonator. A hydrodynamic-acoustic wave interaction develops whenever the shear layer of the jet is unstable and the jet acts as a source of energy, which occurs when the resistance of the hole is negative. The shear layer instability is triggered at the leftmost corner of the hole, disturbances grow along the hole; however, in the case when the shear layer is not sufficiently unstable (so self-sustained oscillations arise by pure hydrodynamical arguments) it requires an acoustic wave to close the loop, which is an instantaneous process in the low Mach number limit. For acoustically compact source regions, the frequency selection of this mechanism is dominated by the hydrodynamic instability, because the travel time of the acoustic wave is of lower order of magnitude. Secondly, the cavity acts a resonator, selecting a set of discrete frequencies among those associated with a negative resistance.

In the present configuration, there exist four branches of instability, each of them denoted as C_n for $n = 1, 2, 3, 4$, which are characterised by a nearly constant Strouhal number

$$St_\beta^{(n)} = \frac{\omega^{(n)} \beta}{2\pi} \quad (\text{D1})$$

as β is varied. The characteristic frequency of C_n branches is related by a frequency shift $St_\beta^{(n)} = St_\beta^{(n-1)} + \Delta St_\beta$, where $\Delta St_\beta \approx [0.6, 0.7]$. This frequency shift may be estimated if one realizes that the global instability is the result of the constructive interaction

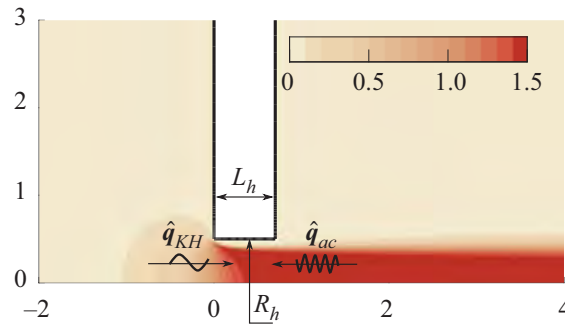


Figure 19. Diagram of the non-local interaction leading to global instability.

between two travelling waves: a downstream-travelling wave, which is excited about the hole lip and propagates around the jet core position, and an upstream-travelling wave that propagates backwards. The non-local constructive interaction of such waves gives rise to a self-sustained global in time instability, which, in some circumstances, is able to radiate an intense acoustic field.

In the following analysis we reconsider the discharge coefficient $\alpha_{vena} = \sqrt{\rho U_M^2 / 2(P_{in} - P_{out})}$, which can be thought of as a measure of the vena contracta phenomenon, assuming that the jet contracts to a top-hat jet with constant velocity U_J and radius R_J . Then applying Bernoulli law, one obtains $\alpha_{vena} = U_M / U_J = \pi R_J^2 / \pi R_h^2$ that was introduced in Fabre *et al.* (2019) in the discussion of the work of Howe (1979), which is classically associated with the pressure loss across the aperture, and it relates the mean velocity U_M with the jet velocity U_J . In Fabre *et al.* (2019, § 2.5 and Appendix A) the importance of the vena contracta coefficient α_{vena} and the actual value of the phase velocity of the Kelvin–Helmholtz instability, where the phase velocity depends on the frequency ω but which is around $U_c = U_J/2$ for sufficiently high ω . The value of the discharge coefficient tends asymptotically to $\alpha_{vena} \rightarrow 0.61$ for large Re ; however, in the range of Reynolds numbers where transition occurs α_{vena} is maximal and takes values $\alpha_{vena} \in [0.7, 0.76]$. In the following, we consider a constant discharge coefficient $\alpha_{vena} = 0.76$, which was the value reported in Fabre *et al.* (2020, figure 5) for most of β in the range of Reynolds numbers where the transition occurs.

In order to estimate the frequency shift ΔSt_β let us consider the travel time of each travelling wave past the hole. The hydrodynamic travelling wave takes $\Delta\tau_{KH} = L_h / U_c = 2\alpha_{vena} L_h / U_M$ and the acoustic wave $\Delta\tau_{ac} = M L_h / U_M$; therefore, the total travelling time

$$\Delta\tau = \Delta\tau_{KH} + \Delta\tau_{ac} = \frac{L_h(2\alpha_{vena} + M)}{U_M} \approx 2\alpha_{vena} \frac{L_h}{U_M}, \quad f^{(n)} = \frac{2n - 1}{2\Delta\tau}, \quad \Delta f = \frac{1}{\Delta\tau}, \quad (D2a-c)$$

where it is considered that $M \ll 1$ and the convective velocity of the hydrodynamic perturbation is $\frac{2\alpha_{vena}}{U_M}$ as it is displayed in figure 19. Thus, the associated Strouhal shift

$$\Delta St_\beta = \frac{\Delta f L_h}{U_M} \approx \frac{1}{2\alpha_{vena}}. \quad (D3)$$

Similarly, the Strouhal frequency of each C_n branch is estimated as

$$St_\beta^{(n)} = \frac{2n - 1}{4\alpha_{vena}}, \quad n = 1, 2, 3, \dots \quad (D4)$$

In the previous reasoning, it has been implicitly assumed that only odd mode structures as those depicted in Fabre *et al.* (2020, figure 9) lead to a conditional instability.

The superposition of the base flow with odd modes (respectively even) at the instant of the cycle where the flow rate through the hole is maximum results in an upward (respectively downward) displacement of the shear layer, thus, pressure is increased (respectively decreased) in the presence of odd modes (respectively *even*). This implies that the hole impedance is negative, which is the criterion of existence of conditional stability.

Finally, let us discuss the influence of compressibility regarding modifications in frequency at the threshold of instability for each of the unstable modes. Compressibility induces a weak variation in the vena contracta coefficient, see figure 16(a), while the threshold of instability is significantly modified for a given value of β near the left asymptote for conditional instabilities (figure 18a) and hydrodynamic instabilities (figure 11a). Thus, for short holes β (here short refers to a value of β near a vertical asymptote of the corresponding instability), the critical Reynolds number is considerably modified by compressible effects, which in turn induces a change in the vena contracta coefficient (more important than the variation of the vena contracta by compressibility at constant Reynolds number). For those cases, one could evaluate the shift in frequency $\delta|_M \Delta St_\beta = \Delta St_\beta(M + \Delta M) - \Delta St_\beta(M)$ as

$$\delta|_M \Delta St_\beta = -\frac{2(\alpha_{vena}(Re_c(M + \Delta M), M + \Delta M) - \alpha_{vena}(Re_c(M), M)) + \Delta M}{(2\alpha_{vena}(Re_c(M), M) + M)^2}, \quad (D5)$$

where the first term, the variation in the vena contracta due to a variation in Mach number, is negligible with respect to the variation in Mach number for long holes, and thus, the variation of frequency for those instabilities is of lesser importance.

Appendix E. Computational domains and absorbing boundary layer

This section discusses the design of computational domains used for the computation of steady states and eigenmodes with the full compressible formulation, and steady states and the forced harmonic response with the incompressible formulation. The computational strategy must be designed in such a way as to avoid the presence of spurious eigenvalues/eigenmodes. The creation of meshes for the full compressible formulation follows a block-structured strategy, similar to the one sketched in figure 4. The domain is divided into three regions: an inner region with the highest vertex density, a mid region with intermediate vertex density and a coarser region for the absorbing layer. Meshes employed for the incompressible case are composed of two regions, a physical domain with the highest vertex density and a coarser region for the absorbing layer. Table 1 lists a number of computational meshes employed in this study ($\mathbb{M}_2, \mathbb{M}_3, \mathbb{M}_4$ and \mathbb{M}_5 for the full compressible case, and \mathbb{M}_1 for the incompressible case). However, such a list is not exhaustive because in addition to the block-strategy refinement, the computational domain has been locally refined following an adaptive local refinement procedure, where the metric for the refinement is based on the steady state and on the eigenmodes (respectively steady state and forced harmonic response in the incompressible case), cf. Hecht (2012) and Fabre *et al.* (2018).

The absorbing boundary layer corresponds to the complex mapping technique (Sierra *et al.* 2020) where a coordinate transformation \mathcal{G} is defined as follows:

$$\left. \begin{aligned} \mathcal{G}_z : \mathbb{R} &\rightarrow \mathbb{C} \quad \text{such that } z = \mathcal{G}_z(Z) = [1 + i\gamma_{z,c}g_z(Z)]Z, \\ \mathcal{G}_r : \mathbb{R} &\rightarrow \mathbb{C} \quad \text{such that } r = \mathcal{G}_r(R) = [1 + i\gamma_{r,c}g_r(R)]R. \end{aligned} \right\} \quad (E1)$$

Here $g_z(Z)$ (respectively $g_r(R)$) has to be chosen as a smooth function such as $g_z(Z) = 0$ for $Z < Z_0$ and $g_z(Z) \approx 1$ for $Z > Z_0 + L_c$ up to Z_{max} . The complex mapping acts on

	Z_{max}	R_{max}	Z_0	L_c	$\gamma_{z,c}$	R_0	R_c	$\gamma_{r,c}$	n_{tri}
M_1	50	50	10	2.5	0.3	5	2.5	0.3	42 460 tri.
M_2	300	300	10	5	0.3	10	2.5	0.3	165 841 tri.
M_3	600	600	10	5	0.3	10	2.5	0.3	235 874 tri.
M_4	600	600	170	5	0.3	170	5	0.3	314 525 tri.
M_5	1500	1500	10	5	0.3	10	2.5	0.3	413 356 tri.

Table 1. Meshes used for cases where the complex mapping technique is adopted. Note: the smooth transition functions are defined as $g_z(Z) = \tanh([(Z - Z_0)/L_c]^2)$ and $g_r(R) = \tanh([(R - R_0)/R_c]^2)$. In the following, $L_{max} = z_{-\infty} + z_{CM} = z_{\infty} + z_{CM}$ and $R_{max} = r_{\infty} + r_{CM}$ (figure 4).

a finite region of length $z_{CM} = Z_{max} - (Z_0 + L_c)$. The function g_z is defined as $g_z(Z) = \tanh([(Z - Z_0)/L_c]^2)$. The application of this map to the linearized Navier–Stokes requires that each spatial derivative, within the complex mapped region, is modified as

$$\frac{\partial}{\partial z} \equiv \mathcal{H}_z \frac{\partial}{\partial Z} \quad \text{with } \mathcal{H}_z(Z) = \left(\frac{\partial \mathcal{G}_z}{\partial Z} \right)^{-1}. \quad (\text{E2})$$

An example of parameters for the usage of the complex mapping layer for the incompressible case is listed in table 1 (M_1). In the full compressible formulation, one must pay particular attention to the extension of the complex mapping region, which here is selected to cover at least two acoustic wavelengths, i.e. $z_{CM} = r_{CM} > 1/StM$. For instance, the largest acoustic wavelength in this study corresponds to the validation case in § 5.1, where $\lambda_{ac} \approx 600$ ($St \approx 1/3$ and $M = 5 \times 10^{-3}$), for which M_5 is an appropriate choice.

REFERENCES

- ANDERSON, A.B.C. 1954 A jet-tone orifice number for orifices of small thickness-diameter ratio. *J. Acoust. Soc. Am.* **26** (1), 21–25.
- BOUASSE, H. 1929 *Instruments à vent*. Impr. Delagrave.
- BRAGG, S.L. 1960 Effect of compressibility on the discharge coefficient of orifices and convergent nozzles. *J. Mech. Engng Sci.* **2** (1), 35–44.
- CASTELLENGO, M. 1999 Acoustical analysis of initial transients in flute like instruments. *Acta Acust. United Acust.* **85** (3), 387–400.
- CHANAUD, R.C. 1970 Aerodynamic whistles. *Sci. Am.* **222** (1), 40–47.
- COLTMAN, J.W. 1976 Jet drive mechanisms in edge tones and organ pipes. *J. Acoust. Soc. Am.* **60** (3), 725–733.
- DAI, X. & AURÉGAN, Y. 2016 Acoustic of a perforated liner with grazing flow: Floquet-Bloch periodical approach versus impedance continuous approach. *J. Acoust. Soc. Am.* **140** (3), 2047–2055.
- DAI, X. & AURÉGAN, Y. 2018 A cavity-by-cavity description of the aeroacoustic instability over a liner with a grazing flow. *J. Fluid Mech.* **852**, 126–145.
- DURRIEU, P.P.J.M., HOFMANS, G., AJELLO, G., BOOT, R., AURÉGAN, Y., HIRSCHBERG, A. & PETERS, M.C.A.M. 2001 Quasisteady aero-acoustic response of orifices. *J. Acoust. Soc. Am.* **110** (4), 1859–1872.
- ELDRIDGE, J.D. & DOWLING, A.P. 2003 The absorption of axial acoustic waves by a perforated liner with bias flow. *J. Fluid Mech.* **485**, 307–335.
- FABRE, D., CITRO, V., FERREIRA, D., BONNEFIS, P., SIERRA, J., GIANNETTI, F. & PIGOU, M. 2018 A practical review on linear and nonlinear global approaches to flow instabilities. *Appl. Mech. Rev.* **70** (6), 060802.
- FABRE, D., LONGOBARDI, R., BONNEFIS, P. & LUCHINI, P. 2019 The acoustic impedance of a laminar viscous jet through a thin circular aperture. *J. Fluid Mech.* **864**, 5–44.
- FABRE, D., LONGOBARDI, R., CITRO, V. & LUCHINI, P. 2020 Acoustic impedance and hydrodynamic instability of the flow through a circular aperture in a thick plate. *J. Fluid Mech.* **885**, A11.
- FERREIRA SABINO, D., FABRE, D., LEONTINI, J. & LO JACONO, D. 2020 Vortex-induced vibration prediction via an impedance criterion. *J. Fluid Mech.* **890**, A4.

Acoustic instability prediction via an impedance criterion

- FLETCHER, N.H. & ROSSING, T.D. 2012 *The Physics of Musical Instruments*. Springer Science & Business Media.
- GILBARG, D. 1960 Jets and cavities. In *Fluid Dynamics/Strömungsmechanik* (ed. S. Flügge), pp. 311–445. Springer.
- HECHT, F. 2012 New development in freefem++. *J. Numer. Maths* **20** (3–4), 251–266.
- HENRYWOOD, R.H. & AGARWAL, A. 2013 The aeroacoustics of a steam kettle. *Phys. Fluids* **25** (10), 107101.
- HEUWINKEL, C., ENGHARDT, L. & ROHLE, I. 2007 Experimental investigation of the acoustic damping of perforated liners with bias flow. In *13th AIAA/CEAS Aeroacoustics Conference (28th AIAA Aeroacoustics Conference)*, AIAA Paper 2007-3525.
- HOWE, M.S. 1979 On the theory of unsteady high Reynolds number flow through a circular aperture. *Proc. R. Soc. Lond. A* **366** (1725), 205–223.
- HUGHES, I.J. & DOWLING, A.P. 1990 The absorption of sound by perforated linings. *J. Fluid Mech.* **218**, 299–335.
- JING, X. & SUN, X. 2000 Effect of plate thickness on impedance of perforated plates with bias flow. *AIAA J.* **38** (9), 1573–1578.
- LONGOBARDI, R., FABRE, D., BONNEFIS, P., CITRO, V., GIANNETTI, F. & LUCHINI, P. 2021 Studying sound production in the hole-tone configuration using compressible and incompressible global stability analyses. In *Advances in Critical Flow Dynamics Involving Moving/Deformable Structures with Design Applications: Proceedings of the IUTAM Symposium on Critical Flow Dynamics involving Moving/Deformable Structures with Design applications* (ed. M. Braza, K. Hourigan & M. Triantafyllou), pp. 251–263. Springer.
- MELIGA, P., SIPP, D. & CHOMAZ, J.-M. 2010 Effect of compressibility on the global stability of axisymmetric wake flows. *J. Fluid Mech.* **660**, 499–526.
- MOUSSOU, P., TESTUD, P., AUREGAN, Y. & HIRSCHBERG, A. 2007 An acoustic criterion for the whistling of orifices in pipes. In *ASME Pressure Vessels and Piping Conference*, vol. 42827, pp. 345–353.
- PIERCE, A.D. 2019 *Acoustics: An Introduction to its Physical Principles and Applications*. Springer.
- ROSSING, T.D. 2007 *Springer Handbook of Acoustics*, vol. 1. Springer.
- RUDIN, W. 1987 *Complex and real Analysis*. McGraw Hill Book Co.
- RUPP, J., CARROTTE, J. & MACQUISTEN, M. 2012 The use of perforated damping liners in aero gas turbine combustion systems. *Trans. ASME J. Engng Gas Turbines Power* **134** (7), 071502.
- SIERRA, J., FABRE, D. & CITRO, V. 2020 Efficient stability analysis of fluid flows using complex mapping techniques. *Comput. Phys. Commun.* **251**, 107100.
- SU, J., RUPP, J., GARMORY, A. & CARROTTE, J.F. 2015 Measurements and computational fluid dynamics predictions of the acoustic impedance of orifices. *J. Sound Vib.* **352**, 174–191.
- VERGE, M.-P., HIRSCHBERG, A. & CAUSSE, R. 1997 Sound production in recorderlike instruments. II. A simulation model. *J. Acoust. Soc. Am.* **101** (5), 2925–2939.

Linear Theory and Experiments for Laminar Bias Flow Impedance: Orifice Shape Effect

L. Hirschberg*

Imperial College London, London SW7 1AY, UK

J. Guzman-Iñigo †

Imperial College London, London SW7 1AY, UK

A. Aulitto‡

Eindhoven University of Technology, 5600 MB Eindhoven, Netherlands

J. Sierra§

IMFT, 31400 Toulouse, France & UNISA, Fisciano, Italy

D. Fabre¶

IMFT, 31400 Toulouse, France

A. Morgans||

Imperial College London, London SW7 1AY, UK

A. Hirschberg**

Eindhoven University of Technology, 5600 MB Eindhoven, Netherlands

Axisymmetric orifices with neck diameter equal to the plate thickness have been investigated. The influence of orifice geometry on the transfer impedance in presence of bias flow was predicted for laminar-flow conditions by means of a compressible Linearized-Navier-Stokes-Equations model. The results are compared to those for an incompressible-flow model and to measurements of the transfer impedance. The effect of confinement on the transfer impedance appears to be negligible for the resistance. The effect of confinement on the inertance (or reactance) can be estimated by means of Fok's classical result for thin orifices. The experimental results agree qualitatively with the predicted impedances. The Strouhal numbers for minima of the resistance are slightly higher than predicted. Negative minima indicating a whistling potentiality correspond to hydrodynamic modes of the orifice. The predicted inertance is at higher Strouhal numbers significantly larger than the measured one. The results indicate how whistling potentiality of a certain hydrodynamic mode can be promoted. The amplitude of the acoustical forcing was varied permitting to delimit the conditions under which the orifice response is linear. As the acoustic velocity amplitude approaches the steady flow velocity, the whistling potentiality of the orifices disappears.

Nomenclature

*Research Associate, Imperial College London, Department of Mechanical Engineering, South Kensington Campus, London SW7 2AZ, UK, AIAA Member.

†Research Associate, Imperial College London, Department of Mechanical Engineering, South Kensington Campus, London SW7 2AZ, UK.

‡PhD student, Department of Mechanical Engineering, Eindhoven University of Technology, P.O. Box 513, 5600 MB Eindhoven, Netherlands.

§PhD Student, Institut de Mécanique des Fluides de Toulouse, IMFT, Université de Toulouse, CNRS; Allée Camille Soula, 31400 Toulouse, France & DIIN, Università degli Studi di Salerno, Via Giovanni Paolo II, 84084 Fisciano (SA), Italy.

¶Lecturer, Institut de Mécanique des Fluides de Toulouse, IMFT, Université de Toulouse, CNRS; Allée Camille Soula, 31400 Toulouse, France.

||Professor of Thermofluids, Imperial College London, Department of Mechanical Engineering, South Kensington Campus, London SW7 2AZ, UK.

**Professor emeritus, Department of Applied Physics, Fluids and Flows, Eindhoven University of Technology, P.O. Box 513, 5600 MB Eindhoven, Netherlands

c	=	Sound speed, $\text{m} \cdot \text{s}^{-1}$
He	=	Helmholtz number
i	=	imaginary unit, $i^2 \equiv -1$
$\text{Im}\{\dots\}$	=	Imaginary part
L	=	Length, m
M	=	Mach number
p	=	Pressure, Pa
q	=	Unsteady volumetric flow, $\text{m}^3 \cdot \text{s}^{-1}$
Q	=	Steady volumetric flow, $\text{m}^3 \cdot \text{s}^{-1}$
r	=	reflection coefficient
R	=	Radius, m
Re	=	Reynolds number
$\text{Re}\{\dots\}$	=	real part
\mathbf{u}	=	velocity, $\text{m} \cdot \text{s}^{-1}$
u	=	axial velocity component, $\text{m} \cdot \text{s}^{-1}$
U	=	Speed, $\text{m} \cdot \text{s}^{-1}$
Z	=	Impedance, $\text{m} \cdot \text{s}^{-1}$
α	=	Factor
δ	=	thickness, m
Δ	=	Difference
θ	=	Angle, rad
ν	=	Kinematic viscosity of air, $1.5 \times 10^{-5} \text{m}^2 \text{s}^{-1}$
ρ	=	Density, $\text{kg} \cdot \text{m}^{-3}$
∇	=	Gradient operator, m^{-1}
Φ	=	porosity
ω	=	Angular frequency, $\text{rad} \cdot \text{s}^{-1}$

Subscripts

0	=	Steady value
1	=	Displacement
2	=	Momentum
cal	=	Calibration
cor	=	Correction
dif	=	Diffuser
dst	=	Downstream
frc	=	Forcing
hfl	=	High-frequency limit
I	=	Imaginary part
inl	=	Inlet
max	=	Maximum
mic	=	Microphone
min	=	Minimum
msr	=	Measurement
lfl	=	Low-frequency limit
o	=	Open
orf	=	Orifice
oul	=	Outlet
r	=	Radial component
R	=	Real part
s	=	Sample
set	=	User set

tws = Thwaites
ust = Upstream
x = Axial component

Superscript

' = Indicates fluctuation
- = Dimensionless quantity

I. Introduction

In many real-world applications—including aeroengines and power gas turbine combustors—one encounters a flow passing through orifices in plates [1–5]. Under unfavorable conditions these orifices produce sound; i.e., they whistle.

Whistling of sharp edged circular orifices in finite-thickness plates was first experimentally observed by Sondhauss [6] and reported by Rayleigh [7]. Experimental investigations by Anderson [8–12] and later by Jing and Sun [13], Karthik et al. [14], Testud et al. [15], Lacombe et al. [16], Zhou and Bodén [17], Su et al. [18], Moers et al. [19] and Wu et al. [20] provided more insight into the controlling parameters. Nair and Sujith [21] studied the chaotic behavior around the onset of whistling. Lacombe et al. [16], Moussou [22] and Fabre et al. [4] used the Nyquist criterion [23] to obtain a prediction of the sharp-edged orifice's whistling based on its acoustic transfer impedance. Jing and Sun [13] used a discrete-vortex model to predict the acoustical response of orifices. Ji and Zhao [24] used a Lattice Boltzmann model to predict the acoustic impedance of orifices. Su et al. [18] and Chen et al. [25] used Unsteady Reynolds Averaged Navier Stokes (URANS) simulations to predict the transfer impedance of thick sharp edged orifices. Alenius et al. [26, 27] and Sorvadi et al. [28] used compressible Large Eddy Simulations (LES) to study sound production by a sharp-edged thick-plate orifice. Kiergegaard et al. [29, 30] and later Fabre et al. [4] used Linearized Navier Stokes Equation (LNSE) models to study the whistling conditions of an orifice in a thick plate.

In particular, Fabre et al. [3] reported a numerical simulation based study of acoustic response of a single sharp-edged circular-shaped perforation in an infinitely-thin plate. In a subsequent publication—Fabre et al. [4] reported a numerical simulation based investigation of whistling by a single sharp-edged cylindrical perforation in a plate of finite thickness. In both studies a laminar steady base flow was established in the direction of the perforation's axis of rotational symmetry. The laminar base flow was then used as the initial condition, for simulations employing a Linearized Navier-Stokes Equations (LNSE) code. These LNSE simulations consisted of acoustically perturbing the base flow at a fixed frequency. The acoustic impedance of the circular perforation was determined for the set frequency. This was repeated for an ensemble of frequencies.

We note that for bias flow through slit-shaped orifices, the influence of the geometry of the edges was investigated experimentally by Tonon et al. [31] and Moers et al. [19]. Moreover, in the absence of flow the influence of a cylindrical orifice's shape on its transfer impedance was investigated by Temiz et al. [32]. The focus of investigation of the presently reported study was on cylindrical orifices of various shapes subject to bias flow.

A sharp-edged orifice subject to a bias flow and upstream acoustic forcing, displays local minima in the real part of the transfer impedance. If, this local minimum is negative it is said that there is whistling potentiality. The Strouhal numbers at which these minima occur correspond to the convection time close to an integer number of shear perturbations from the orifice's inlet to its outlet. The first local minimum corresponds to the presence within the orifice of one perturbation, the second to two, etc. Ergo, in this text these local minima of the real part of the transfer impedance will be referred to as the first, second, etc. hydrodynamic modes.

Guzman-Iñigo et al. [5], made a first step to investigate —by means of numerical simulations and the use of an semi-analytical model (based on Howe's analogy [33])—the influence of the shape of a single circular perforation in a plate of finite thickness. Indeed, Guzman-Iñigo et al. [5] reported results for a slightly rounded upstream inlet of the perforation. They reported that very small changes of the perforation's inlet edge can bring about significant modifications in its acoustic response. One notes that Guzman-Iñigo et al. [5] state: “. . . this paper is restricted to small modifications of the edge when compared with the radius of the hole.” Indeed, in Ref. [5] the influence of more significant rounding of the inlet edge was left to the future.

We note that sound production by orifices—in the situation as sketched above—is similar to that in: whistler nozzles, horns, diffusers and shallow cavities [34–36]. A qualitative explanation of this sound production mechanism—in terms of Howe's analogy [33]—was provided by Hirschberg et al. [34].

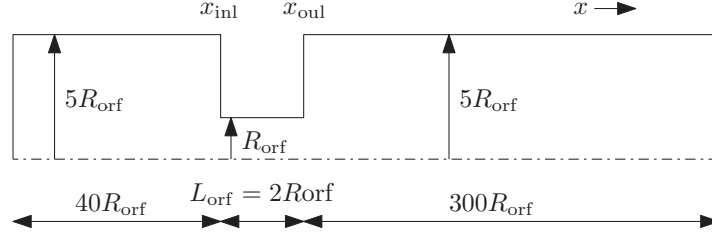


Fig. 1 Sketch of the computational domain.

The present work builds on Fabre’s et al. [3, 4] & Guzman-Iñigo’s et al. [5] work. Indeed, we used a LNSE-simulation approach to investigate the transfer impedance of an orifice in a plate of finite thickness—in the presence of laminar flow through it. In addition, original complementary measurements were carried out using an impedance tube for the four investigated orifice shapes, to wit: a sharp-edged orifice, a rounded-inlet and sharp-outlet orifice, a sharp-inlet and rounded-outlet orifice, a convergent-divergent nozzle orifice (i.e., with a rounded inlet followed by a diffuser section).

We report theoretical results on the influence of significant rounding of the inlet edge. In addition, we present—hitherto unreported—results of a systematic investigation of the effect of a rounded downstream edge. We also numerically and experimentally investigated the acoustic response of a convergent-divergent-nozzle orifice. Moreover, the experiments were used to investigate the influence of the upstream acoustic-forcing amplitude on the results. This was done to probe the limits of the LNSE model’s application regime. In the experiments the orifice is confined within a tube. The influence of this confinement is quantified for the sharp edged orifice.

The compressible numerical-simulation approach—including a description of the computational domain, the equations which are solved and boundary conditions—used to preform the investigation are succinctly described in §II and §II.B.2. In §III, the experimental approach is described. Results are reported in §IV. Two distinct LNSE codes—viz. incompressible and compressible LNSE—are compared in §IV.A. Results of the parameter study performed with the compressible LNSE code are provided in §IV.B. Complementary experimental results are provided and compared to numerical simulation results in §IV.C. Conclusions are drawn in §VI.

II. The numerical simulation approach

In §II.A, a description of the numerical domain is provided. The equations solved for the numerical simulation (mean flow and compressible LNSE) are provided in §II.B. The reader is referred to Guzman-Iñigo et al. [37] for a more expansive discussion of the compressible LNSE model. The boundary conditions used are discussed in §II.C. A description of how the impedance is determined is provided in §II.D.

A. The computational domain

In Fig. 1, a sketch of the computational domain used for the presently-reported investigation is shown. The dashed dotted line is a cylindrical-symmetry axis. The cylindrical symmetric domain had a radius of $5R_{\text{orf}}$ to the left (upstream) and right (downstream) of a constriction with a minimum radius R_{orf} . The length of this constriction

$$L_{\text{orf}} = 2R_{\text{orf}} \quad (1)$$

was fixed for all presently-reported numerical investigations. The lengths of the parts of the domain upstream and downstream from the constriction—henceforth referred to as the orifice—were $40R_{\text{orf}}$ and $300R_{\text{orf}}$, respectively. The axial position of the in- and outlet are—in Fig. 1—indicated with x_{inl} and x_{outl} .

The four orifice shapes considered for our numerical investigation—shown in Fig. 2—were:

- (a) a sharp-edged circular orifice (Fig. 2(a)),
- (b) a rounded upstream edge with a sharp-edged outlet (Fig. 2(b)),
- (c) a sharp-edged inlet with a rounded outlet (Fig. 2(c)),
- (d) a convergent-divergent nozzle geometry (Fig. 2(d)).

The rounded-inlet orifice (Fig. 2(b)) had an upstream-edge radius of curvature, R_{ust} . The rounded-outlet orifice (Fig. 2(c)) had a downstream-edge radius of curvature, R_{dst} . The convergent-divergent nozzle the diffuser angle of the convergent-divergent nozzle orifice (Fig. 2(d)) was

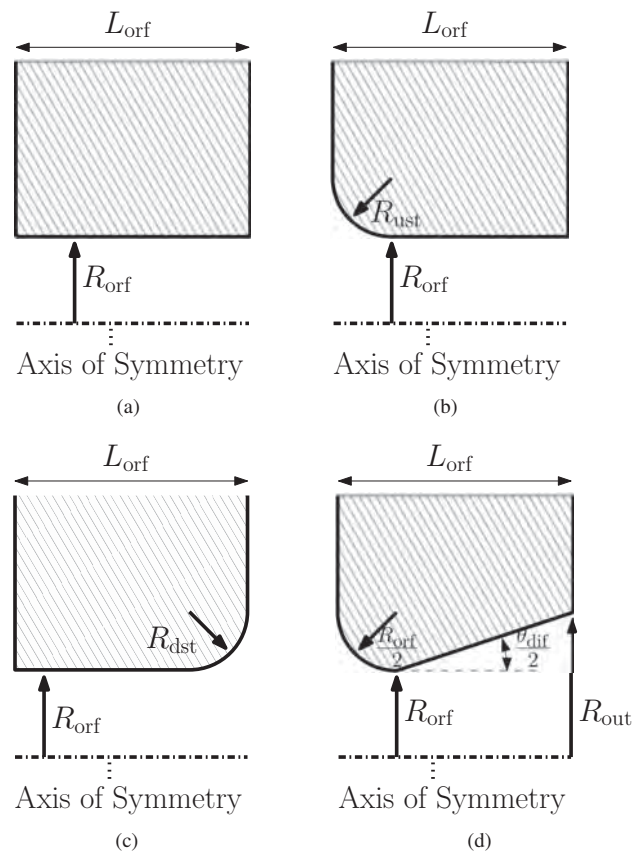


Fig. 2 Orifice shapes considered for the numerical simulation study: (a) sharp-edged orifice (b) rounded upstream edge (c) rounded downstream edge (d) convergent-divergent nozzle.

$$\theta_{\text{dif}} = 2 \arctan \left(\frac{R_{\text{out}} - R_{\text{orf}}}{L_{\text{orf}} - (R_{\text{orf}}/2)} \right) \quad (2)$$

where the neck-cross-section radius R_{orf} and plate thickness L_{orf} were fixed (Eq. (1)) and the radius of the outlet cross section R_{out} (defined in Fig. 2(d)) was varied systematically.

B. The solved equations

The equations solved to establish the mean flow are described in §II.B.1. In §II.B.2 the linearized Navier-Stokes equations (LNSE) are presented.

1. Mean flow

The dimensionless steady incompressible-flow equations (mass and momentum conservation)—which are solved to establish a mean flow—are:

$$\bar{\nabla} \cdot \bar{\mathbf{u}} = 0 \quad (3)$$

$$\bar{\mathbf{u}} \cdot \bar{\nabla} \bar{\mathbf{u}} = -\frac{1}{\bar{\rho}} \bar{\nabla} \bar{p} + \frac{1}{Re_{\text{orf}}} \bar{\nabla}^2 \bar{\mathbf{u}} \quad (4)$$

where

$$Re_{\text{orf}} \equiv \frac{2R_{\text{orf}}U_{\text{orf}}}{\nu} \quad (5)$$

is the Reynolds number based on the orifice diameter $2R_{\text{orf}}$ and U_{orf} the averaged axial flow speed at the orifice's inlet. U_{orf} is defined as follows:

$$U_{\text{orf}} = \frac{Q_{\text{orf}}}{\pi R_{\text{orf}}^2} \quad (6)$$

where Q_{orf} is the volumetric flow rate through the orifice.

These dimensionless equations were discretised using the finite-element method within the FEniCSx computing platform [38] and a first-order accurate Newton integration scheme. A basis of Arnold-Brezzi-Fortin MINI-elements [39], with P_1 elements for the pressure and P_{1b} elements for each velocity component. The discrete non-linear problem was solved using the Newton method.

2. Linearized Navier-Stokes equations

The dimensionless compressible linearized Navier-Stokes equations (LNSE) are:

$$He_{\text{orf}} \frac{\partial \bar{\rho}'}{\partial \bar{t}} = -\bar{\rho}_0 \bar{\nabla} \cdot (\bar{\mathbf{u}}') - \bar{\mathbf{u}}_0 \cdot \bar{\nabla} \bar{\rho}' \quad (7)$$

$$He_{\text{orf}} \frac{\partial \bar{\mathbf{u}}'}{\partial \bar{t}} + \bar{\nabla} \cdot (\bar{\mathbf{u}}' \bar{\mathbf{u}}_0 + \bar{\mathbf{u}}_0 \bar{\mathbf{u}}' + \bar{\rho}' \bar{\mathbf{u}}_0 \bar{\mathbf{u}}_0) = -\bar{\nabla} \bar{p}' + \frac{M_{\text{orf}}}{Re_{\text{orf}}} \bar{\nabla}^2 \bar{\mathbf{u}} \quad (8)$$

where

$$He_{\text{orf}} = \frac{2R_{\text{orf}}\omega}{c_{\text{orf}}} \quad (9)$$

is a Helmholtz number based on the—upstream boundary imposed—forcing frequency, ω , the orifice's diameter, $2R_{\text{orf}}$, and the sound speed, c_{orf} at its inlet; and

$$M_{\text{orf}} = \frac{U_{\text{orf}}}{c_{\text{orf}}} \quad (10)$$

is the Mach number at the orifice's inlet.

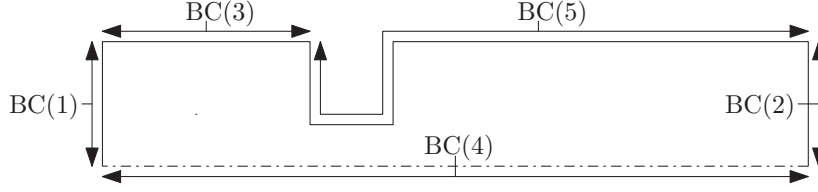


Fig. 3 Sketch of where the boundary conditions (BCs) are applied.

These LNSE simulations—using the previously computed mean flow as a background flow—were performed using the FEniCSx computing platform [38] and a second-order accurate finite-element method. N.b., these equations were solved in the frequency domain.

A detailed description of the numerical model for the incompressible flow simulations are found in Fabre et al. [4].

C. Boundary conditions

In Fig. 3, a sketch of where the boundary conditions (BCs) are applied is shown. The pipe segments, when present upstream or downstream of the orifice have a cross sectional radius of $5R_{\text{orf}}$. Two different sets of boundary conditions are applied to establish the mean flow and to perform the LNSE simulations. These boundary conditions are briefly described in §II.C.1 and §II.C.2, respectively.

1. Mean-flow boundary conditions

The boundary conditions applied to establish the mean flow were:

$$\begin{aligned} \text{BC(1): } u_x &= U_{\text{orf}} R_{\text{orf}}^2 / (5R_{\text{orf}})^2 \\ \text{BC(3): } u_r &= 0 \\ \text{BC(4): } u_r &= 0 \\ \text{BC(5): } u_x &= 0 \text{ and } u_r = 0 \end{aligned}$$

where BC(1) is an inflow boundary condition, BC(3) a slip boundary condition, BC(4) is a symmetry boundary condition and BC(5) is a no-slip boundary condition.

2. LNSE boundary conditions

The boundary conditions used to perform the LNSE simulation were:

$$\begin{aligned} \text{BC(1): } & \text{non-reflective boundary condition} \\ \text{BC(2): } & \text{non-reflective boundary condition} \\ \text{BC(4): } & u_{r,R} = 0 \text{ and } u_{r,I} = 0 \text{ (symmetry boundary condition)} \\ \text{BC(5): } & u_{x,R} = 0 \text{ and } u_{x,I} = 0 \text{ (no-slip boundary condition)} \\ \text{BC(5): } & u_{r,R} = 0 \text{ and } u_{r,I} = 0 \text{ (no-slip boundary condition)} \end{aligned}$$

where BC(4) is a symmetry boundary condition and BC(5) is a no-slip boundary condition. N.b., the subscripts R and I indicate the real and imaginary components, respectively. Moreover, at BC(1) acoustic forcing at a fixed frequency ω was applied.

The boundary conditions for the incompressible flow simulation results are found in Ref. [4]. In the case of the incompressible flow model results, there was a pipe of radius $5R_{\text{orf}}$ upstream of the orifice. The downstream flow emerged into free space, bounded by the downstream side of the orifice plate.

D. Determination of the impedance

The transfer impedance, Z , of the orifice is defined as follows

$$Z = \frac{p'_{\text{ust}} - p'_{\text{dst}}}{q'} = Z_R + iZ_I \quad (11)$$

where q' is the volumetric flow rate fluctuation. p'_{ust} and p'_{dst} are the up- and downstream pressure fluctuation; viz., up- and downstream of the orifice. In dimensionless form the impedance is

$$\bar{Z} = \bar{Z}_R + i\bar{Z}_I = \frac{R_{\text{orf}}^2}{\rho_{\text{orf}}U_{\text{orf}}}Z \quad (12)$$

The impedance is a function of the forcing frequency ω , which in dimensionless form becomes a Strouhal number, to wit:

$$\Omega \equiv \frac{R_{\text{orf}}}{U_{\text{orf}}}\omega \quad (13)$$

The up- and downstream pressure fluctuations are taken to be composed of up- and downstream traveling plane waves in the pipe segments up and downstream of the orifice p_{ust}^{\pm} and p_{dst}^{\pm} , respectively. These wave amplitudes are obtained by wave decomposition of the cross-sectional averaged results of the simulations—the multi-microphone method was used for this. The acoustic field at the axial orifice inlet and outlet positions x_{inl} and x_{oul} (defined in Fig. 1)—is obtained by extrapolation, namely

$$p'_{\text{ust}} = p_{\text{ust}}^+ \exp\left(-i\frac{\omega}{c+u_0}x_{\text{inl}}\right) + p_{\text{ust}}^- \exp\left(i\frac{\omega}{c-u_0}x_{\text{inl}}\right) \quad (14)$$

$$p'_{\text{dst}} = p_{\text{dst}}^+ \exp\left(-i\frac{\omega}{c+u_0}x_{\text{oul}}\right) + p_{\text{dst}}^- \exp\left(i\frac{\omega}{c-u_0}x_{\text{oul}}\right) \quad (15)$$

In terms of velocity fluctuations, one has

$$u'_{\text{ust}} = \frac{p_{\text{ust}}^+}{\rho c} \exp\left(-i\frac{\omega}{c+u_0}x_{\text{inl}}\right) - \frac{p_{\text{ust}}^-}{\rho c} \exp\left(i\frac{\omega}{c-u_0}x_{\text{inl}}\right) \quad (16)$$

$$u'_{\text{dst}} = \frac{p_{\text{dst}}^+}{\rho c} \exp\left(-i\frac{\omega}{c+u_0}x_{\text{oul}}\right) - \frac{p_{\text{dst}}^-}{\rho c} \exp\left(i\frac{\omega}{c-u_0}x_{\text{oul}}\right) \quad (17)$$

The unsteady volumetric flow rate fluctuation is then taken to be

$$q' = 25\pi R_{\text{orf}}^2 u'_{\text{ust}} \quad (18)$$

III. Experimental approach

A succinct description of the experimental setup is provided in §III.A. The experimental method used to determine the transfer impedance is briefly described in §III.C. Appendix A provides a description of the calibration of the flow controller used to set the steady bias flow.

A. Experimental setup

In Fig. 4, a sketch of the experimental setup used to determine the transfer impedance of an orifice subject to a bias flow is shown. A volume-flow rate \dot{Q} is imposed—using a calibrated flow controller—on the upstream side (left-hand side of the orifice in Fig. 4) of the orifice to impose the bias flow.

The radius of the pipe upstream and downstream from the orifice was $R_{\text{pipe}} = 25$ mm. The shapes of the orifices could be varied. Four of the shapes described in Fig. 2 were investigated—viz.: the sharp edge orifice, an orifice with rounded upstream edge $R_{\text{ust}} = 2R_{\text{orf}}$, an orifice with rounded downstream edge $R_{\text{dst}} = 2R_{\text{orf}}$ and a convergent divergent orifice with $R_{\text{out}} = 7R_{\text{orf}}/4$.

Acoustic forcing was done by means of a 25 W loudspeaker fixed flush at the upstream-pipe end. The imposed acoustic-forcing signal was harmonic and its amplitude could be varied. For a fixed forcing amplitude a preset frequency range was scanned. Six pre-polarized 1/4 inch microphones (type BWSA, sensitivity $50 \text{ mV} \cdot \text{Pa}^{-1}$) mounted flush upstream from the orifice under investigation were used to recorded the acoustic response due to forcing.

The samples used were very precise (accuracy of the order of 0.01 mm) reproductions of the geometries depicted in Fig. 2. E.g., the sharp-edge were manufactured such that they were literally razor sharp. This was confirmed by the fact that the transfer impedance measurement results remained identical when the position of the orifice with sharp square edged was inverted with respect to the flow direction.

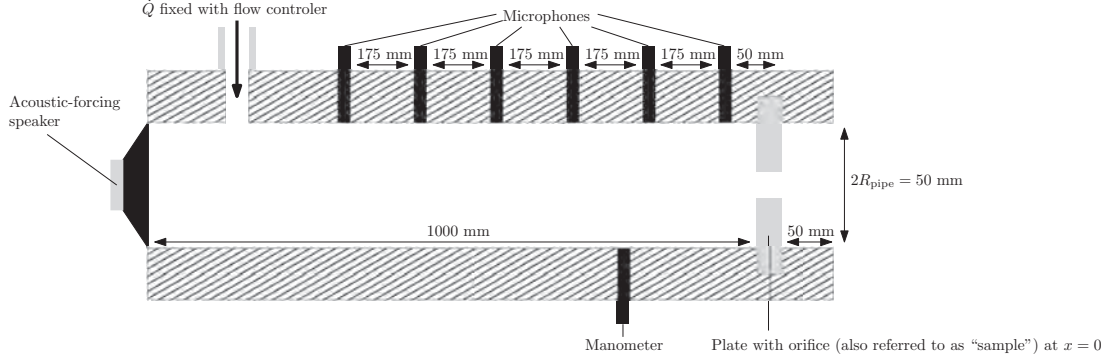


Fig. 4 Sketch of the experimental setup.

B. Acoustic-forcing amplitude

In the experiments, a forcing amplitude was applied using the upstream speaker (as sketch in Fig. 4). This was done by having the user set a forcing voltage V_{frc} target. The actual harmonic pressure fluctuation was measured by means of the calibrated microphone 50 mm upstream of downstream side of the orifice. A feedback system tuned V_{frc} to keep $|p'|$ constant as the frequency was stepwise changed.

The relative velocity-forcing amplitude can be determined, using

$$\frac{|u'_{\text{frc}}|}{U_{\text{orf}}} = \frac{|p'|}{\pi \rho U_{\text{orf}}^2 |\bar{Z}|} \quad (19)$$

One notes that $|\bar{Z}|$ is a function of the forcing frequency (or the Strouhal number Ω). Two order-of-magnitude limits of $|u'_{\text{frc}}|/U_{\text{orf}}$, can be explored: the high-frequency and the low-frequency limits.

Let us start with the high-frequency limit. In this limit \bar{Z} is dominated by the inertia \bar{Z}_I , which in turn is of the order-of-magnitude of Ω . One finds:

$$\lim_{\Omega \rightarrow \infty} \frac{|u'_{\text{frc}}|}{U_{\text{orf}}} = \left(\frac{|u'_{\text{frc}}|}{U_{\text{orf}}} \right)_{\text{hf}} \simeq \frac{1}{\pi \Omega} \frac{|p'|}{\rho U_{\text{orf}}^2} \quad (20)$$

Moving to the low-frequency limit, one applies Bernoulli's quasi-steady equation ($p_{\text{orf}} = \rho U_{\text{orf}}^2/2$), one has

$$U_{\text{orf}} \pm u'_{\text{frc}} = \sqrt{\frac{2(p_{\text{orf}} \pm p')}{\rho}} \simeq U_{\text{orf}} \left(1 \pm \frac{p'}{\rho U_{\text{orf}}^2} \right) \quad (21)$$

one finds

$$\lim_{\Omega \rightarrow 0} \frac{|u'_{\text{frc}}|}{U_{\text{orf}}} = \left(\frac{|u'_{\text{frc}}|}{U_{\text{orf}}} \right)_{\text{lf}} \simeq \frac{|p'|}{\rho U_{\text{orf}}^2} \quad (22)$$

Ergo, going forward $|\bar{p}'| = |p'|/(\rho U_{\text{orf}}^2)$ will be used as an indication for the order-of-magnitude of $|u'|/U_{\text{orf}}$.

C. Experimental determination of the transfer impedance

The transfer impedance was determined using the approach described in more detail by Aulitto et al. [40]. It is based on the measurement of the reflection coefficient with and without the presence of an orifice—also referred to as a “sample”—at $x = 0$. Indeed, the sample could be replaced by a ring to create a smooth open pipe. The reflection coefficient of the open pipe, r_o and the reflection coefficient with the presence of an orifice, r_s were measured using the method described in Jang and Ih [41].

The dimensionless radiation impedance of the open pipe was calculated using

$$\bar{Z}_o = \frac{1 + r_o}{1 - r_o} \quad (23)$$

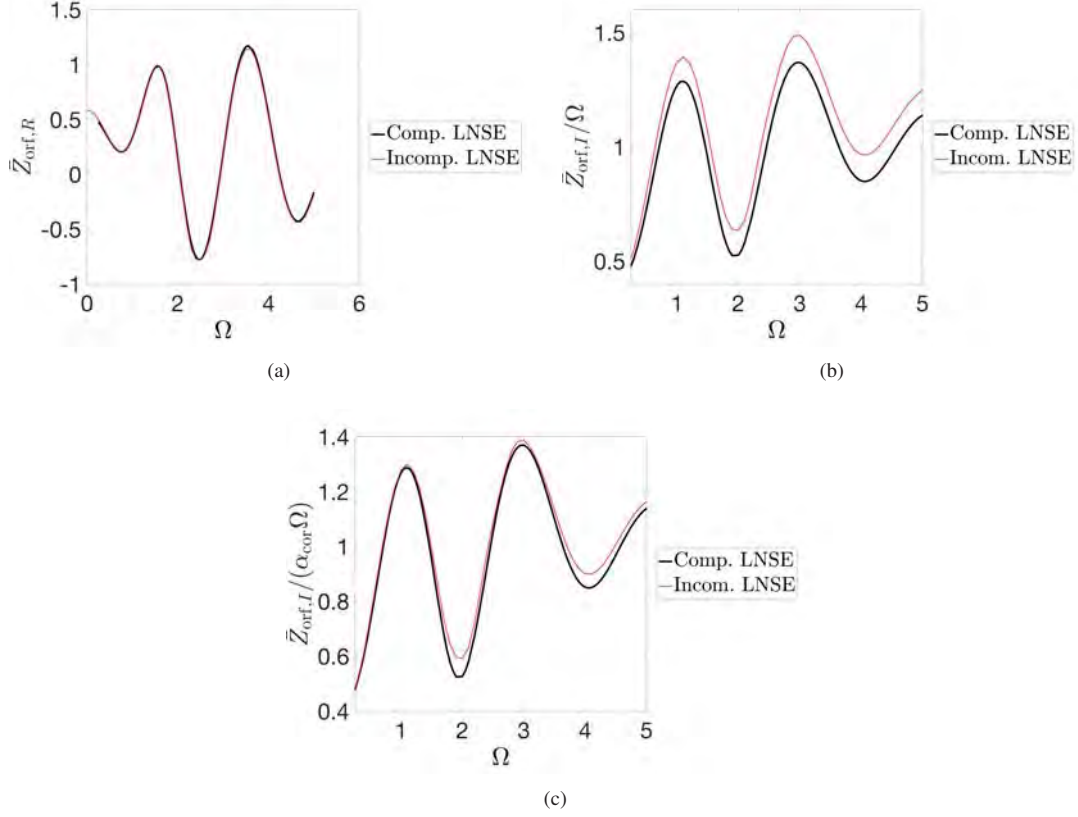


Fig. 5 Sharp-edged orifice compared compressible LNSE simulation compared to Fabre’s et al. incompressible LNSE results for $Re_{\text{orf}} = 1.2 \times 10^3$: (a) \bar{Z}_R vs. Ω (b) \bar{Z}_I/Ω vs. Ω (c) $\bar{Z}_I/(\alpha_{\text{cor}}\Omega)$ vs. Ω .

and the same expression was used to determined the impedance in the presence of a perforated plate

$$\bar{Z}_s = \frac{1 + r_s}{1 - r_s} \quad (24)$$

The transfer impedance was then determined as follows

$$\bar{Z}_{\text{orf}} = \bar{Z}_o - \bar{Z}_s \quad (25)$$

IV. Results

Most of the numerical simulation results presented here, were obtained with the compressible LNSE code described in §II.B.2. However, in §IV.A results for the sharp-edged orifice case are compared to simulations obtained with an incompressible LNSE code described by Fabre et al [3, 4]. In §IV.C, LNSE results are compared to original empirical data obtained using the experimental setup and approach briefly described in §III. All results in this section were obtained with $Re_{\text{orf}} = 1.2 \times 10^3$, the reported measurements were also obtained for this Reynolds number. Under these circumstances the flow within the orifice is expected to be laminar, as assumed in the theoretical model.

A. Comparison of compressible and incompressible LNSE results

In Fig. 5 results for sharp-edged orifice (Fig. 2(a)) obtained with the compressible LNSE code described in §II.B.2 are compared to results obtained with an incompressible LNSE code (the incompressible LNSE code was developed and used for investigations by Fabre et al. [3, 4]). One observes three minima of the real part of the impedance corresponding

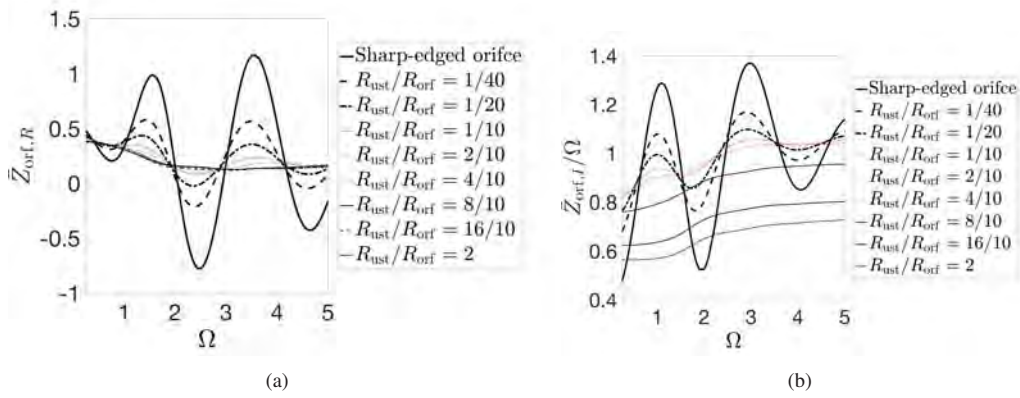


Fig. 6 Rounded-inlet orifice compared to the sharp-edged orifice compressible LNSE simulation results for $Re_{orf} = 1.2 \times 10^3$: (a) \bar{Z}_R vs. Ω (b) \bar{Z}_I/Ω vs. Ω .

to the first three hydrodynamic modes. The first mode (at $\Omega \approx 0.7$) has no whistling potentiality as the minima remains positive. The second ($\Omega \approx 2.5$) and third ($\Omega \approx 4.7$) hydrodynamic mode have a strong whistling potentiality.

One should note that the results produced with the incompressible LNSE code were obtained with a different computational domain and boundary conditions. Indeed, for the incompressible case the boundary condition imposed at BC(5) in Fig. 3, were—excluding the plate and orifice were a no-slip condition was imposed—slip boundary conditions. Moreover, I.e., the results for the incompressible case are a model for a sharp-edged orifice in a plate between an upstream duct of radius $5R_{orf}$ and a downstream unducted space.

In Fig. 5(a), one observes that the results for the real part of the transfer impedance, \bar{Z}_R , overlap within ca. 1%.

In Fig. 5(b) one observes a deviation of not more than 22% in, \bar{Z}_I/Ω , the imaginary part of the transfer impedance divided by the Strouhal number. This deviation is due to a confinement effect on $\bar{Z}_{orf,I}$. Indeed, using Fok's formula [42] the incompressible LNSE result can be corrected for this confinement effect by dividing the imaginary part of the transfer impedance by a correction factor $\alpha_{cor} = 1.073$. The result is shown in Fig. 5(c), one notes that there is overall much better agreement between the results of the two flow simulations. Moreover, the maximum deviation—at the first local minimum or hydrodynamics mode—is reduced to not more than 14% when applying this correction. This significant reduction indicates that the difference in $\bar{Z}_{orf,I}$ is mainly due to confinement effects. We concluded that for the LNSE simulations the fact that the downstream side is ducted or unducted does not play a major role.

The fact that the real part of the impedance is not affected by the confinement indicates that, the dissipation or production of sound occurs locally within the orifice or in a region close to the exit of the orifice. Indeed, the dissipation is related to the modulation of the shear layer at the flow separation point at the orifice inlet. Sound production is related to the exit of the perturbed shear layer from the orifice. The imaginary part of the impedance corresponding to the inertia of the flow is less concentrated and therefore more sensitive to confinement.

B. Parameter variation: compressible LNSE simulation results

In Fig. 6, simulation results are shown for the rounded inlet geometry (2(b)). R_{ust}/R_{orf} was varied from 1/40 to 2. The results are compared with the sharp-edged orifice case (thickest solid black line). One observes in Fig. 6(a) that rounding the even a little bit—e.g. $R_{ust}/R_{orf} = 1/40$ —drastically diminishes, by ca. a factor two, the whistling potentiality of the orifice. Indeed, for $R_{ust}/R_{orf} > 1/20$ $Z_{orf,R} > 0$; i.e. the results for $R_{ust}/R_{orf} > 1/20$ indicate that the whistling potentiality vanishes. This confirms and extends the results obtained by Guzman-Iñigo et al. [5].

Results, for the rounded outlet geometry (Fig. 2(c)) are shown in Fig. 7. R_{dst}/R_{orf} was varied logarithmically from 1/10 to 2. The results are compared to the sharp-edge orifice case (thickest solid black line). One observes, in Fig. 7(a), that as $R_{dst}/R_{orf} > 4/10$ the first hydrodynamic mode (minimum of the real part of the transfer impedance) emerges as the only source of whistling potentiality. Indeed, $R_{dst}/R_{orf} > 4/10$ the second minimum in $\bar{Z}_{orf,R}$ vanishes.

In Fig. 8, results for the convergent-divergent nozzle orifice (Fig. 2(d)) are shown in Fig. 8. θ_{dif} was varied from 0.00 rad to 1.18 rad. One observes as expected an absence of predicted whistling potentiality for $\theta_{dif} = 0$. This corresponds to the configuration in Fig. 2(b). As θ_{dif} is increased, one observes the emergence of a dominant first hydrodynamic mode (minimum in $\bar{Z}_{orf,R}$) (Fig. 8(a)).

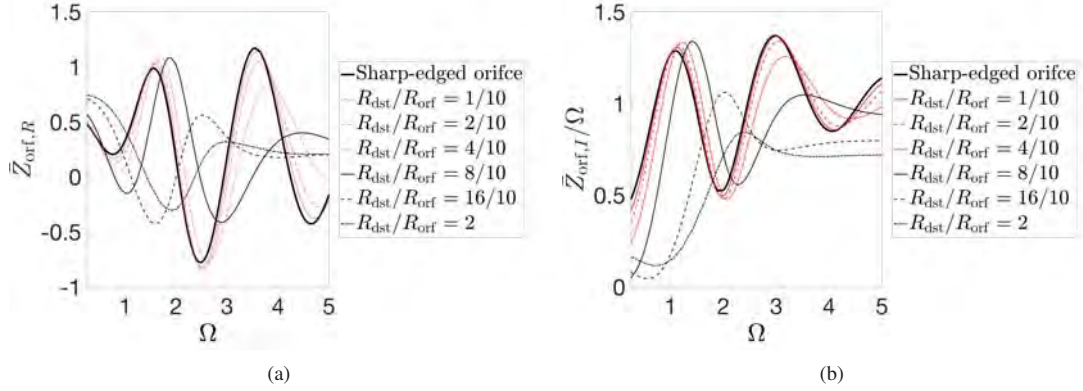


Fig. 7 Rounded-outlet orifice response compared to that of the sharp-edged orifice compressible LNSE simulation results for $Re_{orf} = 1.2 \times 10^3$: (a) \bar{Z}_R vs. Ω (b) \bar{Z}_I/Ω vs. Ω .

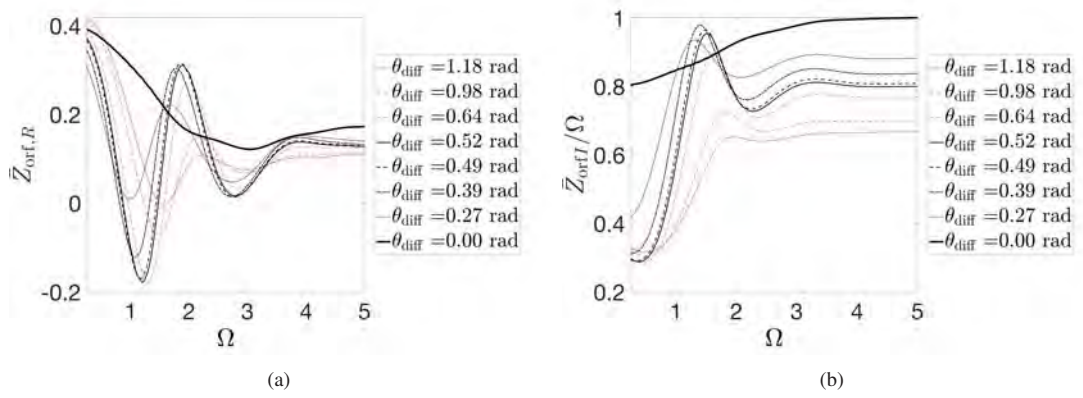


Fig. 8 Transfer impedance for convergent-divergent nozzle geometry compressible LNSE simulation results for $Re_{orf} = 1.2 \times 10^3$ as a function of the Strouhal number Ω : (a) \bar{Z}_R vs. Ω (b) \bar{Z}_I/Ω vs. Ω .

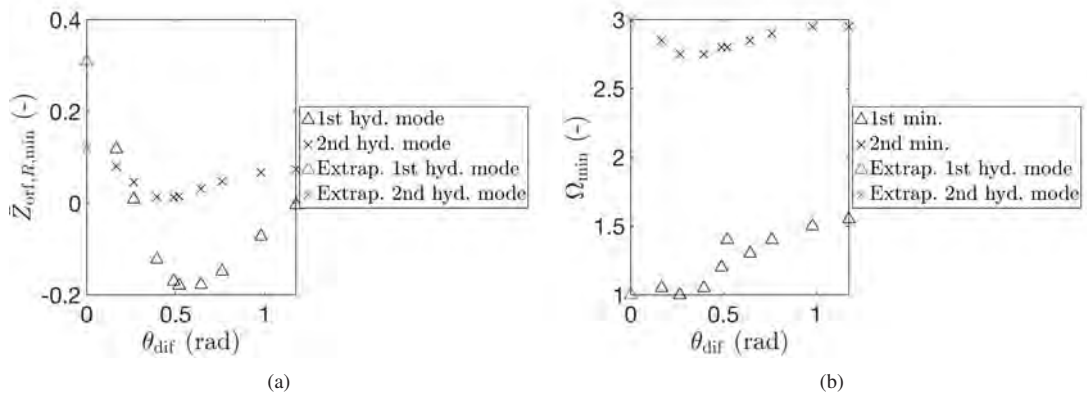


Fig. 9 Convergent-divergent nozzle geometry compressible LNSE simulation hydrodynamic modes for $Re_{orf} = 1200$: (a) $\bar{Z}_{R,min}$ vs. θ_{dif} (b) Ω_{min} vs. θ_{dif}

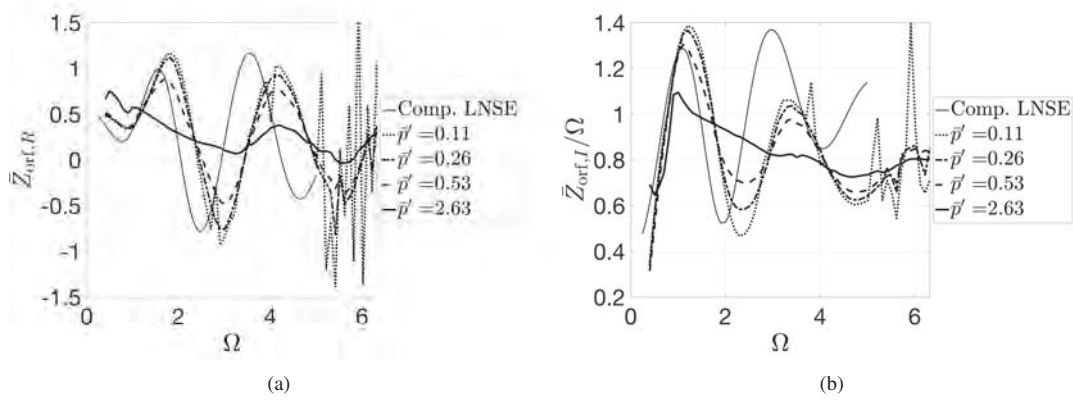


Fig. 10 Sharp-edged orifice measurements compared to compressible LNSE results: (a) \bar{Z}_{R} vs. Ω (b) \bar{Z}_{I}/Ω vs. Ω .

In Fig. 9(a), the first and second minima in $\bar{Z}_{\text{orf},R}$ are shown as a function of θ_{dif} . The Strouhal number at which these minima occur, Ω_{min} , are plotted as a function of θ_{dif} in Fig. 9(b). One notes that the first and second minima occur at $\Omega_{\text{min}} \approx 1.25$ and $\Omega_{\text{min}} \approx 2.9$, respectively. Moreover, one notes that the results predict an optimum in whistling potentiality of the first hydrodynamic mode for $\theta_{\text{dif}} = 0.52$ rad, while the second hydrodynamic mode remains silent for the conditions investigated.

Thus, the shape of an orifice can be changed in order to optimize predicted whistling potentiality. We note that the possibility for a whistling potentiality of the third hydrodynamic mode is obtained for the sharp edged orifice at sufficiently high Reynolds numbers.

C. Comparison of numerical and experimental results

All the experimental and numerical simulation results reported here were obtained with $Re_{\text{orf}} = 1.2 \times 10^3$.

In Fig. 10, experimental results obtained with the sharp-edged orifice are compared to those of the compressible LNSE model. The experimental results were obtained with four dimensionless-forcing amplitudes $\bar{p}' = 0.11$ (thick dotted line), 0.26 (thick dashed-dotted line), 0.53 (thick dashed line) and 2.63 (thick solid line). One notes that the signal is affected by noise for $\bar{p}' = 0.11$ at higher Strouhal numbers, to wit, $\Omega > 5$. However, for $\bar{p}' = 0.11$ and $\Omega < 5$ the signal is quite clean. Moreover, a clear dependence of the experimental results on \bar{p}' is observed. E.g., one notes for $\bar{p}' = 0.11$ and 0.26—although the real part of the transfer impedance is very nearly identical—on the second hydrodynamic mode at $\Omega \approx 2.5$ a significant deviation of ca. 14% in the inertial part $Z_{\text{orf},I}/\Omega$. While for $\bar{p}' = 0.53$ the real and imaginary parts of the transfer impedance follow the global trends of the lower amplitude results, the highest amplitude $\bar{p}' = 2.63$ display drastically different behavior. Moreover, for $\bar{p}' = 2.63$ whistling potentiality is completely suppressed. At these high amplitudes the acoustic velocity amplitude within the orifice becomes comparable to the steady flow velocity. Acoustically induced back flow might occur.

We note that that LNSE model prediction (thin solid line in Fig. 10) deviates structurally from the empirical data. E.g., the Strouhal number prediction for the second hydrodynamic mode deviates by ca. -17% .

The experimental results for a rounded inlet, $R_{\text{ust}}/R_{\text{orf}} = 2$, are compared to the compressible LNSE model predictions (thin solid line) in Fig. 11. The thick dotted, thick dashed-dotted, thick dashed, and thick solid line are for $\bar{p}' = 0.11$, 0.26, 0.53 and 2.63, respectively. One sees that $Z_{\text{orf},R}$ for $\bar{p}' = 0.11$ and $\Omega > 5$ is dominated by noise. It is interesting to note that for $\bar{Z}_{\text{orf},R}$ is basically amplitude independent. A difference in $\bar{Z}_{\text{orf},I}$ for $0.5 < \Omega < 3$ is observed between $\bar{p}' = 2.63$ and the lower forcing amplitudes. One notes, that the LNSE model predictions for $\bar{Z}_{\text{orf},I}/\Omega$ differ wildly from the experimental results. That said, one observes that both the LNSE model and the measurements for all four \bar{p}' show a completely suppressed whistling potentiality for $R_{\text{ust}}/R_{\text{orf}} = 2$.

Experimental results for the rounded-outlet orifice are shown in Fig. 12 for $\bar{p}' = 0.11$ (thick dotted line), 0.26 (dashed dotted line), 0.53 (thick dashed line), 2.63 (thick solid line). The results obtained with $\bar{p}' = 0.11$ for $\Omega > 5$ are dominated by noise. It is interesting to note that the highest forcing amplitude suppresses the orifice's whistling potentiality. Although quantitative agreement between the empirical data and the LNSE model is observed, obvious quantitative differences are discernible in e.g. the prediction of Ω for the first hydrodynamic mode.

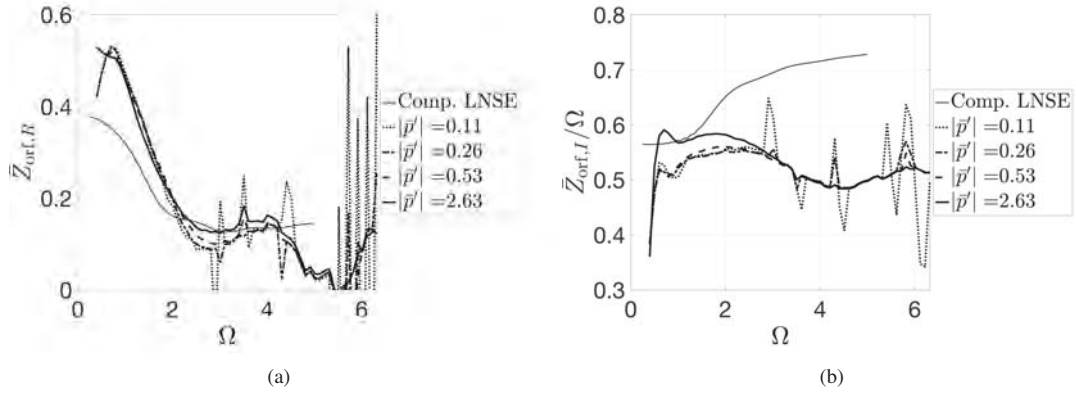


Fig. 11 Rounded-inlet sharp-edged outlet orifice, $R_{\text{ust}}/R_{\text{orf}} = 2$, measurements compared to compressible LNSE results: (a) \bar{Z}_R vs. Ω (b) \bar{Z}_I/Ω vs. Ω .

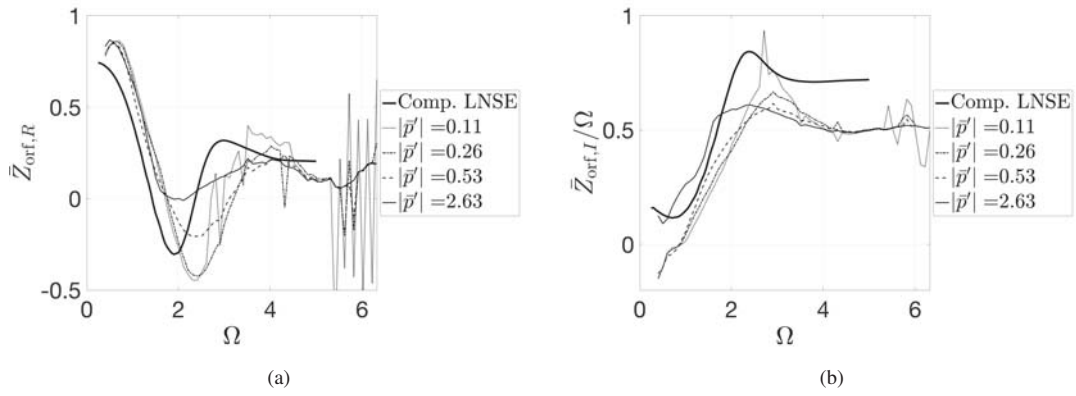


Fig. 12 Sharp-edged inlet rounded-outlet orifice, $R_{\text{dst}}/R_{\text{orf}} = 2$, measurements compared to compressible LNSE results: (a) \bar{Z}_R vs. Ω (b) \bar{Z}_I/Ω vs. Ω .

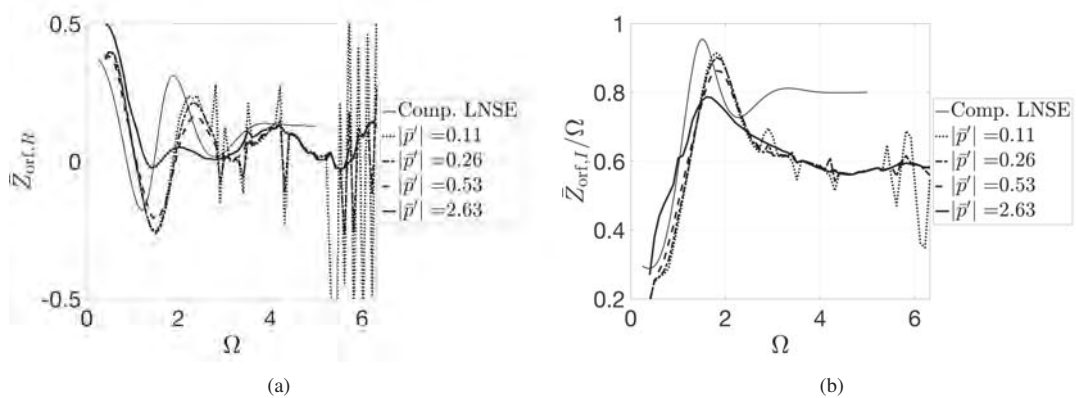


Fig. 13 Convergent-divergent nozzle orifice, $\theta_{\text{dif}} = 0.52$ rad, measurements compared to compressible LNSE results: (a) \bar{Z}_R vs. Ω (b) \bar{Z}_I/Ω vs. Ω .

Experimental and LNSE model results for the convergent-divergent nozzle orifice are shown in Fig. 13. Experimental data for $\bar{p}' = 0.11$ (thick dotted line), 0.26 (thick dashed dotted line), 0.53 (thick dashed line) and 2.63 (thick solid line) are shown. One noted that the signal for $\bar{p}' = 0.11$ with a Strouhal number above 5 is dominated by noise. That said, the experimental results for $\bar{p}' = 0.11$ and 0.26 are discerned to be essentially the same. This indicates that the results are in the linear regime. Notably, the whistling potentiality of the orifice appears to be suppressed for the highest forcing amplitude $\bar{p}' = 2.63$. In spite of the fact that qualitative agreement between the empirical data and the LNSE model is observed, clear quantitative differences are discernible in e.g. the prediction of Ω for the first hydrodynamic mode.

V. Discussion

The influence of an orifice's shape on its transfer impedance and by extension its whistling potentiality, were investigated using a LNSE model and experimentally. Four cylindrical orifice shapes were considered: a sharp-edged (inlet and outlet) orifice, a rounded-inlet sharp-edged outlet orifice, a sharp-edged inlet rounded outlet orifice, and a convergent-divergent nozzle orifice. The thickness of the plate containing the orifice, L_{orf} , was twice the minimum radius, R_{orf} of the orifice; viz., $L_{\text{orf}} = 2R_{\text{orf}}$. The individually probed orifices were subject to a bias flow, which was fixed such that the Reynolds number based on the orifice neck diameter $2R_{\text{orf}}$ was $Re_{\text{orf}} = 1.2 \times 10^3$.

The experimental and simulation results for sharp-edged orifice confirm that the second hydrodynamic mode—viz., the second and most pronounced local minimum in the real part of the transfer impedance of the orifice—has the largest whistling potentiality. This is in agreement with the experimental observations of Testud et al. [15] and Moers et al. [19]. The fact that they have a higher whistling potentiality than the first mode is due to the fact that at low Strouhal numbers the amplification of the perturbations by the shear layer perturbations increases exponentially with the ratio of shear layer length to hydrodynamic wavelength. Hence, the second hydrodynamic mode corresponds to an amplification of perturbations, which is the square of the amplification for the first mode. The fact that the third mode does not have a much larger whistling potentiality is due to the reduction of the amplification at higher Strouhal numbers. As predicted by Michalke [43], there is a critical Strouhal number based on the shear layer thickness above which the shear layer is hydrodynamically stable. This effect is therefore Reynolds dependent, as illustrated by the results presented by Fabre et al. [4] for the same orifice geometry. An interesting result obtained by Fabre et al. [4] is that the Strouhal number of the hydrodynamic modes is only weakly dependent on the Reynolds number and that when the plate thickness is used as reference length instead of R_{orf} the Strouhal number becomes almost independent of the plate thickness. A systematic study of the Reynolds number and plate thickness on the Strouhal number for the first two hydrodynamic modes is provided by Testud et al. [15]

In the case of the rounded-inlet sharp-outlet orifice, the results show that even for minor rounding $R_{\text{ust}}/R_{\text{orf}} = 1/40$ the whistling potentiality —i.e., compared to for $R_{\text{ust}}/R_{\text{orf}} > 1/10$ the whistling potentiality is essentially suppressed. These findings confirm and extend those found by Guzman-Iñigo et al. [5].

Results for the sharp-inlet rounded outlet orifice show that rounding of the outlet affects the whistling potentiality of the orifice significantly. Indeed, for $R_{\text{dst}}/R_{\text{orf}} > 4/10$ the orifice's whistling potentiality is shifted to the first hydrodynamic mode. I.e., rounding the downstream edge, whilst keeping the upstream edge sharp, enhances the whistling potentiality of the first hydrodynamic mode—yet reduces that of higher modes. It is noteworthy that Vortex Sound Theory qualitatively predicts this. Moreover, this confirms that the notion that sound production can only occur through impingement on e.g. a sharp-downstream edge is inadequate.

In the case of the convergent-divergent nozzle geometry, the first hydrodynamic mode was found to dominate its whistling potentiality. Moreover, the diffusor angle, θ_{dif} , was varied systematically whilst keeping all other parameters of the problem fixed. For $\theta_{\text{dif}} = 0.52$ an optimum in whistling potentiality was found. I.e., a orifice's shape can be changed to optimize its whistling potentiality. For diffusers (conical pipe diameter expansion) in gas transport systems, van Lier et al. [35] also found a large whistling potentiality at an angle of this magnitude.

In the experiments, the forcing-amplitude, $|\bar{p}'|$, was varied. Overall, one observes a dependence of the results on the amplitude for $\bar{p}' > 0.26$. I.e., results obtained with $\bar{p}' > 0.26$ are in the nonlinear regime.

Obviously, the nonlinear regime is formally outside of the LNSE model's application regime. That said, generally remarkable qualitative agreement is observed between the LNSE and experimental data. Notably, in some instances this qualitative agreement extends to experimental data in the nonlinear regime.

However, a structural quantitative deviation between the LNSE predictions and experimental data in the linear regime is noted. E.g., in the case of a sharp-edged orifice—even though $\bar{Z}_{\text{orf}, R_{\text{min}}}$ is well predicted for the second hydrodynamic mode, viz., within a few percent—the corresponding Strouhal number deviates by ca. 17%. Moreover, the observed imaginary part was at high Strouhal numbers systematically lower than the predicted values.

Interestingly, the highest forcing amplitude, $\bar{p}' = 2.63$, was observed to suppress whistling potentiality. This can obviously not be predicted with a LNSE model.

VI. Conclusions

The shape of an orifice subject to a bias flow can significantly affect its transfer impedance and ergo its whistling potentiality. Moreover, an orifice's geometric parameters can be manipulated to optimize its whistling potentiality. It was experimentally observed that high forcing amplitudes suppress whistling potentiality. While the real part of the impedance (resistance) is not affected by the confinement of the orifice within a pipe, the imaginary part (inertance) is.

A. Flow controller calibration

The flow controller (Bronkhorst F202Av) used to set the volume flow was calibrated against a static pressure difference measurement at the highest available flow rate for the orifice with upstream rounded edge $R_{ust} = 2R_{orf}$ (without any acoustic forcing). These measurements were corrected for the influence of the displacement thickness of the viscous boundary layers. For moderately high Reynolds numbers $Re_{orf} = 9 \times 10^3$ as used for this calibration the boundary are laminar and rather thin compared to R_{orf} .

Using the method of Thwaites, one can determine the square of the momentum thickness

$$\delta_2^2 = \frac{0.45\nu}{U^6} \int_0^{L_{orf}} U^5 dx \quad (26)$$

where x is the axial coordinate. Moreover, one has that

$$\delta_1 = H_{12}(L_{orf})\delta_2 \quad (27)$$

where $H_{12}(L_{orf}) = 2.61$ for $(dU/dx)_{x=L_{orf}} = 0$, as prevails at the exit of this orifice.

Assuming a quasi-1D flow across the rounded-inlet orifice (Fig. 2(b)) and neglecting the displacement thickness δ_1 , one finds for the axial velocity

$$U = \left(\frac{R_{orf}}{R}\right)^2 U_{orf} \quad (28)$$

where

$$R = R_{orf} + L_{orf} - \sqrt{L_{orf}^2 - (L_{orf} - x)^2} \quad (29)$$

Eq. (26) can now be rewritten to find

$$\delta_2^2 = \frac{0.45\nu}{U_{orf}} R_{orf} \int_0^{L_{orf}/R_{orf}} \left(\frac{R_{orf}}{R}\right)^{10} d\left(\frac{x}{R_{orf}}\right) \quad (30)$$

We defined the integral

$$I \equiv \int_0^{L_{orf}/R_{orf}} \left(\frac{R_{orf}}{R}\right)^{10} d\left(\frac{x}{R_{orf}}\right) \quad (31)$$

which using Mathematica was found to be $I = 0.57$. Using Eq. (27), one finds

$$\frac{\delta_1}{R_{orf}} = H_{12}(L_{orf}) \sqrt{\left(\frac{2 \times 0.45}{Re_{orf}} I\right)} \quad (32)$$

We define

$$\alpha_{tws} = 1 - \frac{2\delta_1}{R_{orf}} \quad (33)$$

and note that

$$U_{\text{orf}} = \alpha_{\text{tws}} U_{\text{max}} \quad (34)$$

where U_{max} is the maximum velocity on the center line at the rounded inlet orifice's outlet. Using Bernoulli one finds

$$U_{\text{max}} = \sqrt{\frac{2\Delta p}{\rho}} \quad (35)$$

The static pressure difference, Δp , measured by means of a TROTEC TA400 manometer (Fig. 4) across the rounded-inlet orifice (Fig. 2(b)) can now be related to the volumetric flow through it:

$$\dot{Q}_{\text{msr}} = \pi R_{\text{orf}}^2 \alpha_{\text{tws}} U_{\text{max}} = \pi R_{\text{orf}}^2 \alpha_{\text{tws}} \sqrt{\frac{2\Delta p}{\rho}} \quad (36)$$

Using the interface with the flow controller a volumetric flow, \dot{Q}_{set} , can be set. $\dot{Q}_{\text{set}} = 1.31 \times 10^{-3} \text{ m}^3 \cdot \text{s}^{-1}$ was set (90% of the highest imposable volumetric-flow rate) and the corresponding $\Delta p = 119 \text{ Pa}$ was determined (uncertainty 1 Pa). One finds $U_{\text{orf}} \approx \alpha_{\text{tws}} U_{\text{max}} = 13.3 \text{ m} \cdot \text{s}^{-1}$, which yields $Re_{\text{orf}} = 2R_{\text{orf}} U_{\text{orf}} / \nu = 8.87 \times 10^3$. Using Eqs. (32) and (36), one can determine $\alpha_{\text{tws}} = 0.960$ and the calibration coefficient:

$$\frac{\dot{Q}_{\text{msr}}}{\dot{Q}_{\text{set}}} = 0.81 \quad (37)$$

Acknowledgements

The authors gratefully acknowledge the European Research Council (ERC)—who supported this work through the Consolidator Grant AFIRMATIVE (2018-2023). Alessia Aulitto received support and training through the Marie Skłodowska-Curie Initial Training Network Pollution Know-How and Abatement (POLKA)—as such, we are thankful for the financial support from the European Commission under call H2020-MSCA-ITN-2018 (project number: 813367). Thanks is due to Ines Lopez Arteaga. Lionel Hirschberg thanks Catherine Lemaitre and Assa Ashuach for their help.

References

- [1] Zhao, D., and Li, X., “A review of acoustic dampers applied to combustion chambers in aerospace industry,” *Progress in Aerospace Sciences*, Vol. 74, 2015, pp. 114–130. doi:<https://doi.org/10.1016/j.paerosci.2014.12.003>.
- [2] Lahiri, C., and Bake, F., “A review of bias flow liners for acoustic damping in gas turbine combustors,” *Journal of Sound and Vibration*, Vol. 400, 2017, pp. 564–605. doi:[10.1016/j.jsv.2017.04.005](https://doi.org/10.1016/j.jsv.2017.04.005).
- [3] Fabre, D., Longobardi, R., Bonnefis, P., and Luchini, P., “The acoustic impedance of a laminar viscous jet through a thin circular aperture,” *Journal of Fluid Mechanics*, Vol. 864, 2019, p. 5–44. doi:[10.1017/jfm.2018.1008](https://doi.org/10.1017/jfm.2018.1008).
- [4] Fabre, D., Longobardi, R., Citro, V., and Luchini, P., “Acoustic impedance and hydrodynamic instability of the flow through a circular aperture in a thick plate,” *Journal of Fluid Mechanics*, Vol. 885, 2020, p. A11. doi:[10.1017/jfm.2019.953](https://doi.org/10.1017/jfm.2019.953).
- [5] Guzmán-Iñigo, J., Yang, D., Johnson, H. G., and Morgans, A. S., “Sensitivity of the Acoustics of Short Circular Holes with Bias Flow to Inlet Edge Geometries,” *AIAA Journal*, Vol. 57, No. 11, 2019, pp. 4835–4844. doi:[10.2514/1.J057996](https://doi.org/10.2514/1.J057996).
- [6] Sondhauss, C. F. J., “Über die Beim Ausströmen der Luft Entstehende Töne,” *Pogg. Ann. Phys. Chem.*, Vol. 91, 1854, pp. 126–147.
- [7] Rayleigh, L., *Theory of Sound*, Vol. 2, Dover Publications, Inc., New York, 1945.
- [8] Anderson, A. B. C., “Dependence of Pfeifenton (Pipe Tone) Frequency on Pipe Length, Orifice Diameter, and Gas Discharge Pressure,” *The Journal of the Acoustical Society of America*, Vol. 24, No. 6, 1952, pp. 675–681. doi:[10.1121/1.1906955](https://doi.org/10.1121/1.1906955).
- [9] Anderson, A. B. C., “A Circular-Orifice Number Describing Dependency of Primary Pfeifenton Frequency on Differential Pressure, Gas Density, and Orifice Geometry,” *The Journal of the Acoustical Society of America*, Vol. 25, No. 4, 1953, pp. 626–631. doi:[10.1121/1.1907154](https://doi.org/10.1121/1.1907154).
- [10] Anderson, A. B. C., “A Jet-Tone Orifice Number for Orifices of Small Thickness-Diameter Ratio,” *The Journal of the Acoustical Society of America*, Vol. 26, No. 1, 1954, pp. 21–25. doi:[10.1121/1.1907284](https://doi.org/10.1121/1.1907284).

- [11] Anderson, A. B. C., “Structure and Velocity of the Periodic Vortex-Ring Flow Pattern of a Primary Pfeifenton (Pipe Tone) Jet,” *The Journal of the Acoustical Society of America*, Vol. 27, No. 6, 1955, pp. 1048–1053. doi:10.1121/1.1908112.
- [12] Anderson, A. B. C., “Vortex-Ring Structure-Transition in a Jet Emitting Discrete Acoustic Frequencies,” *The Journal of the Acoustical Society of America*, Vol. 28, No. 5, 1956, pp. 914–921. doi:10.1121/1.1908516.
- [13] Jing, X., and Sun, X., “Effect of plate thickness on impedance of perforated plates with bias flow,” *AIAA journal*, Vol. 38, 2000, pp. 1573–1578.
- [14] Karthik, B., R., C. S., and I., S. R., “Mechanism of pipe-tone excitation by flow through an orifice in a duct,” *Int. J. Aeroacoustics*, Vol. 7, No. 3-4, 2008, pp. 321–348. doi:10.1260/1475-472X.7.3.321.
- [15] Testud, P., Aurégan, Y., Moussou, P., and Hirschberg, A., “The whistling potentiality of an orifice in a confined flow using an energetic criterion,” *Journal of Sound and Vibration*, Vol. 325, No. 4, 2009, pp. 769–780. doi:https://doi.org/10.1016/j.jsv.2009.03.046.
- [16] Lacombe, R., Moussou, P., and Aurégan, Y., “Whistling of an orifice in a reverberating duct at low Mach number,” *The Journal of the Acoustical Society of America*, Vol. 130, No. 5, 2011, pp. 2662–2672. doi:10.1121/1.3641427.
- [17] Zhou, L., and Bodén, H., “Experimental investigation of an in-duct orifice with bias flow under medium and high level acoustic excitation,” *International Journal of Spray and Combustion Dynamics*, Vol. 6, 2014, pp. 267–292.
- [18] Su, J., Rupp, J., Garmory, A., and Carrotte, J., “Measurements and computational fluid dynamics predictions of the acoustic impedance of orifices,” *Journal of Sound and Vibration*, Vol. 352, 2015, pp. 174–191.
- [19] Moers, E., Tonon, D., and Hirschberg, A., “Strouhal number dependency of the aero-acoustic response of wall perforations under combined grazing-bias flow,” *Journal of Sound and Vibration*, Vol. 389, 2017, pp. 292–308. doi:https://doi.org/10.1016/j.jsv.2016.11.028.
- [20] Wu, G., Guan, Y. H., Ji, C., and Gay, F. Y. X., “Experimental studies on sound absorption coefficients of perforated pipes with bias-grazing flows at low Mach and Strouhal number,” *Aerospace Science and Technology*, Vol. 107, 2020, p. 106255. doi:10.1016/j.ast.2020.106255.
- [21] Nair, V., and Sujith, R., “Precursors to self-sustained oscillations in aeroacoustic systems,” *International Journal of Aeroacoustics*, Vol. 15, No. 3, 2016, pp. 312–323. doi:10.1177/1475472X16630877.
- [22] Moussou, P., “Acoustically Induced Instabilities in Pipes by the Nyquist Criterion,” *Proceedings of ASME 2014 Pressure Vessels & Piping Division Conference, Pressure Vessels and Piping Conference*, Vol. 4: Fluid-Structure Interaction, 2014, pp. 1–9. doi:10.1115/PVP2014-28306.
- [23] Kopitz, J., and Polifke, W., “CFD-based application of the Nyquist criterion to thermo-acoustic instabilities,” *Journal of Computational Physics*, Vol. 227, 2008, p. 6754–6778. doi:10.1016/j.jcp.2008.03.022.
- [24] Ji, C., and Zhao, D., “Lattice Boltzmann investigation of acoustic damping mechanism and performance of an in-duct circular orifice,” *The Journal of the Acoustical Society of America*, Vol. 135, 2014, p. 3243–3251. doi:10.1121/1.4876376.
- [25] Chen, Z., Ji, Z., and Huang, H., “Acoustic impedance of perforated plates in the presence of bias flow,” *Journal of Sound and Vibration*, Vol. 446, 2019, pp. 159–175. doi:10.1016/j.jsv.2019.01.031.
- [26] Alenius, E., Åbom, M., and Fuchs, L., “Large eddy simulations of acoustic-flow interaction at an orifice plate,” *Journal of Sound and Vibration*, Vol. 345, 2015, pp. 162–177. doi:https://doi.org/10.1016/j.jsv.2015.02.012.
- [27] Alenius, E., “Mode switching in a thick orifice jet, an LES and dynamic mode decomposition approach,” *Computers & Fluids*, Vol. 90, 2014, pp. 101–112. doi:https://doi.org/10.1016/j.compfluid.2013.11.022.
- [28] Sovardi, C., Jaensch, S., and Polifke, W., “Concurrent identification of aero-acoustic scattering and noise sources at a flow duct singularity in low Mach number flow,” *Journal of Sound and Vibration*, Vol. 377, 2016, pp. 90–105. doi:https://doi.org/10.1016/j.jsv.2016.05.025.
- [29] Kierkegaard, A., Boij, S., and Efraimsson, G., “A frequency domain linearized Navier–Stokes equations approach to acoustic propagation in flow ducts with sharp edges,” *The Journal of the Acoustical Society of America*, Vol. 127, No. 2, 2010, pp. 710–719. doi:10.1121/1.3273899.

- [30] Kierkegaard, A., Allam, S., Efraimsson, G., and Åbom, M., “Simulations of whistling and the whistling potentiality of an in-duct orifice with linear aeroacoustics,” *Journal of Sound and Vibration*, Vol. 331, No. 5, 2012, pp. 1084–1096. doi:<https://doi.org/10.1016/j.jsv.2011.10.028>.
- [31] Tonon, D., Moers, E., and Hirschberg, A., “Quasi-steady acoustic response of wall perforations subject to a grazing-bias flow combination,” *Journal of Sound and Vibration*, Vol. 332, No. 7, 2013, pp. 1654–1673. doi:<https://doi.org/10.1016/j.jsv.2012.11.024>.
- [32] Temiz, M. A., Lopez Arteaga, I., Efraimsson, G., Åbom, M., and Hirschberg, A., “The influence of edge geometry on end-correction coefficients in micro perforated plates,” *The Journal of the Acoustical Society of America*, Vol. 138, No. 6, 2015, pp. 3668–3677. doi:10.1121/1.4937748.
- [33] Howe, M. S., *Acoustics of fluid-structure interactions*, Cambridge university press, Cambridge, UK, 1998. doi:10.1017/CBO9780511662898.
- [34] Hirschberg, A., Bruggeman, J.C., A., Wijnands, and Smits, N., “The whistler nozzle and horn as aeroacoustics sound source in pipe systems,” *Acta Acustica United with Acoustica*, Vol. 68, No. 2, 1989, p. 157–160.
- [35] van Lier, L., Dequand, S., Hirschberg, A., and Gorter, J., “Aeroacoustics of diffusers: An experimental study of typical industrial diffusers at Reynolds numbers of 10^5 ,” *The Journal of the Acoustical Society of America*, Vol. 109, No. 1, 2001, pp. 108–115. doi:10.1121/1.1329618.
- [36] Nakiboğlu, G., Manders, H. B. M., and Hirschberg, A., “Aeroacoustic power generated by a compact axisymmetric cavity: prediction of self-sustained oscillation and influence of the depth,” *Journal of Fluid Mechanics*, Vol. 703, 2012, p. 163–191. doi:10.1017/jfm.2012.203.
- [37] Guzmán-Iñigo, J., Yang, D., Gaudron, R., and Morgans, A. S., “On the scattering of entropy waves at sudden area expansions,” *Manuscript under review*, 2021. URL <https://arxiv.org/abs/2111.13043>.
- [38] Schaefer, K. L., Jones, T. D., Hill, R., Mella, H., Sim, S. J., and Yamamoto, K., “FEniCsx computing platform,” <https://fenicsproject.org>, 2022.
- [39] Matsumoto, J., and Kawahara, M., “Shape identification for fluid-structure interaction problem using improved bubble element,” *International Journal of Computational Fluid Dynamics*, Vol. 15, No. 1, 2001, pp. 33–45.
- [40] Aulitto, A., Hirschberg, A., Lopez Arteaga, I., and Buijssen, E., “Effect of slit length on linear and non-linear acoustic transfer impedance of a micro-slit plate,” *Acta Acust.*, Vol. 6, No. 6, 2022. doi:10.1051/aacus/2021059.
- [41] Jang, S.-H., and Ih, J.-G., “On the multiple microphone method for measuring in-duct acoustic properties in the presence of mean flow,” *The Journal of the Acoustical Society of America*, Vol. 103, No. 3, 1998, pp. 1520–1526. doi:10.1121/1.421289.
- [42] Naderyan, V., Raspet, R., Hickey, C. J., and Mohammadi, M., “Acoustic end corrections for micro-perforated plates,” *The Journal of the Acoustical Society of America*, Vol. 146, No. 4, 2019, pp. EL399–EL404. doi:10.1121/1.5129560.
- [43] Michalke, A., “On spatially growing disturbances in an inviscid shear layer,” *Journal of Fluid Mechanics*, Vol. 23, No. 3, 1965, p. 521–544. doi:10.1017/S0022112065001520.



Efficient stability analysis of fluid flows using complex mapping techniques[☆]



Javier Sierra^{a,b,*}, David Fabre^a, Vincenzo Citro^b

^a IMFT, UPS, Allée du Professeur Camille Soula, 31400 Toulouse, France

^b DIIN, University of Salerno, 84084 Fisciano, Italy

ARTICLE INFO

Article history:

Received 22 October 2019

Received in revised form 27 November 2019

Accepted 5 December 2019

Available online 16 December 2019

Keywords:

Linear stability analysis

Linear acoustics

Non-reflecting boundary conditions

ABSTRACT

Global linear stability analysis of open flows leads to difficulties associated to boundary conditions, leading to either spurious wave reflections (in compressible cases) or to non-local feedback due to the elliptic nature of the pressure equation (in incompressible cases). A novel approach is introduced to address both these problems. The approach consists of solving the problem using a complex mapping of the spatial coordinates, in a way that can be directly applicable in an existing code without any additional auxiliary variable. The efficiency of the method is first demonstrated for a simple 1D equation modeling incompressible Navier–Stokes, and for a linear acoustics problem. The application to full linearized Navier–Stokes equation is then discussed. A criterion on how to select the parameters of the mapping function is derived by analyzing the effect of the mapping on plane wave solutions. Finally, the method is demonstrated for three application cases, including an incompressible jet, a compressible hole-tone configuration and the flow past an airfoil. The examples allow to show that the method allows to suppress the artificial modes which otherwise dominate the spectrum and can possibly hide the physical modes. Finally, it is shown that the method is still efficient for small truncated domains, even in cases where the computational domain is comparable to the dominant wavelength.

© 2019 Elsevier B.V. All rights reserved.

1. Introduction

Numerical simulations of real flow configurations in open domains require artificial boundary conditions to allow vortical structures to freely escape from the domain and avoid wave reflections. The most common Artificial Boundary Conditions (here denoted as ABC) chosen for compressible fluid flows are the *sponge* regions which imply the introduction of an artificial damping term in an outer ‘sponge layer’ located far away from the interesting regions. The main advantage of this method is its simplicity. However, it generally leads to extremely large meshes characterized by sponge layers much larger than the regions of interest. An alternative method is the Perfectly Matched Layer (PML) treatment of ABCs. First introduced by Berenger [1] for electromagnetic radiation problems and later extended for linear acoustics problems by Bermudez et al. [2], this method has proven its efficiency for studying compressible flows using linearized Navier–Stokes Equations (LNSE) in the frequency domain. However, since the method introduces a spatial attenuation

which depends upon the frequency, it cannot be directly applied to global stability problems where the frequency is unknown. A possible solution is to introduce auxiliary variables in the buffer region leading to a formulation where the dependency with respect to the frequency does not appear anymore, as done for instance by Hu et al. [3] and Whitney [4]. However the introduction of these new variables significantly increases the dimension of the problems under investigation. As well, in the formulation of PML the estimation of a base state is required, which is not generally an easy task for flows with domains whose geometry is convoluted.

ABC are also required for the stability analysis of purely incompressible open configurations such as swirling flows (see [5]). The difficulties are due to the strong convective amplification of vortical perturbations, which may still be active at the outlet boundary, and to the elliptic nature of the pressure equation leading to nonlocal feedback between upstream and downstream boundary conditions. Lesshaft [6] showed that these two problems lead to the existence of two families of artificial eigenmodes which can in some situations dominate the spectrum and hide the physically relevant modes. Fabre et al. [7] observed similar difficulties in studying the response to harmonic forcing of a jet flow through a zero-thickness circular hole. In this work, the authors introduced a method based on the Complex Mapping

[☆] The review of this paper was arranged by Prof. N.S. Scott.

* Corresponding author at: IMFT, UPS, Allée du Professeur Camille Soula, 31400 Toulouse, France.

E-mail address: javier.sierra@imft.fr (J. Sierra).

(CM) of the spatial coordinates. The key idea is to introduce a spatial damping which is independent upon the frequency and thus directly fitted to eigenvalue computations. In a subsequent work Fabre et al. [8], the method was successfully applied to the eigenvalue analysis of the jet through a circular hole of nonzero thickness, allowing to capture unstable global modes arising from the existence of a recirculation region within the thickness of the hole.

The purpose of this work is to explain the principle of the CM technique and to show that is applicable to the linear stability analysis of both compressible and incompressible flows. We demonstrate that (i) it is efficient as a non-reflexion condition for acoustic perturbations and (ii) it is able to provide a sufficient decay for the large convective amplification of vortical perturbations, thus efficiently fixing both problems identified above.

The remainder of the paper is organized as follows: In Section 2 we introduce the complex mapping methodology for a linear PDE problem and we draw some parallels between CM and PML. In Section 3 we apply CM to a canonical scalar PDE problem, the Ginzburg–Landau equation. This toy model serves to demonstrate how CM can be used to reduce non-local effects, i.e. to suppress the (elliptic) feedback pressure mechanism in the incompressible Navier–Stokes equations. In Section 4 we discuss the effect of CM on the spectrum of the Helmholtz equation that governs inviscid linear acoustics, showing that the methods effectively work as a non-reflective boundary condition. Sections 5 and 6 focus on the application of complex mapping to Navier–Stokes equations. We first review the concept of global stability of both incompressible and compressible flows, which motivates the study of the effect of CM in plane acoustic and hydrodynamic waves. Finally, in Section 6 three application cases, where CM is used for stability computations, are presented. First an incompressible jet flow which suffers from non-local feedback due to strong spatial amplification of linear perturbations. ABC are mandatory in this case to correctly characterize the spectrum of the linear problem. Second, we study the effect of CM in a compressible flow, the hole-tone configuration, by looking at the performances of CM with respect to sponge layers. The last numerical case is the weakly compressible flow past a symmetric airfoil at a large angle of attack. In this last test case, it is shown that complex mapping region is still effective even when its length is shorter than the acoustic wavelength. The Navier–Stokes and linear acoustics computations are performed using the FreeFem++ solvers and Octave/Matlab drivers provided by the StabFem suite (see the review paper by Fabre et al. [9] for details). Programs reproducing most of the figures of the paper are available online on the web page of the project (<https://gitlab.com/stabfem/StabFem>).

2. Introduction of the complex mapping technique for eigenvalue problems

2.1. Mathematical framework (1D case)

To introduce the method, let us first consider for simplicity a one dimensional autonomous linear partial differential equation (PDE) with the following form:

$$\frac{\partial \Psi}{\partial t} = \mathcal{L}\Psi \quad (1)$$

where $\Psi(x, t)$ is defined on the domain $x \in \Omega = [0, \infty]$, and \mathcal{L} is a linear operator. The *asymptotic linear stability* of such PDE is driven by modal solutions with the form

$$\Psi(x, t) = \hat{\Psi}(x)e^{-i\omega t} \quad (2)$$

where ω is the *complex* eigenvalue. We are therefore led to a linear eigenvalue problem with the form

$$-i\omega\Psi = \mathcal{L}\Psi. \quad (3)$$

The problem is then said to be linearly unstable if there exists at least one eigenvalue such as $\omega_i > 0$. Note that the modal ansatz (2) is also at the basis of the so-called *frequency-domain* approach to harmonically forced non-homogeneous PDEs (such as wave scattering problems). The difference is that in the frequency-domain approach it is sufficient to consider the solution for *real* values of the frequency ω , while in the linear stability approach ω has generally to be solved as a complex number.

2.2. Motivation of the complex mapping

The difficulty we want to solve is associated to the existence of solutions behaving as $\Psi(x, t) \approx e^{ikx - i\omega t}$ as $x \rightarrow \infty$, which, according to the argument of k , may be oscillating, or even worse, exponentially growing. The idea is to consider an analytical continuation of the solution for *complex* x , and solve in a region of the complex plane where all physically relevant solutions are nicely decaying. To this aim, we will define a mapping from a (real) numerical coordinate X defined in a truncated domain $X \in [0, X_{max}]$ to the physical coordinate x .

2.3. Definition of a smooth mapping

The application of the proposed method to a given problem leads to two separate regions: (i) an unmodified domain for $X < X_0$ and (ii) a mapped region for $X > X_0$, characterized by a parameter γ_c defining the direction in the complex plane. The simplest choice is as follows:

$$x = \mathcal{G}_x(X) = \begin{cases} X & \text{for } X < X_0, \\ [1 + i\gamma_c]X & \text{for } X > X_0, \end{cases} \quad (4)$$

which transforms the x -derivatives as follows:

$$\frac{\partial}{\partial x} = \begin{cases} \frac{\partial}{\partial X} & \text{for } X < X_0, \\ \frac{1}{1 + i\gamma_c} \frac{\partial}{\partial X} & \text{for } X > X_0, \end{cases} \quad (5)$$

In practice it is desirable to design a mapping function which gradually enters into the complex plane with a transition region of characteristic length L_c , in order to avoid possible reflections caused by an abrupt change at $X = X_0$. This can be achieved using a mapping function with the form:

$$\mathcal{G}_x : \mathbb{R} \rightarrow \mathbb{C} \quad \text{such that} \quad x = \mathcal{G}_x(X) = [1 + i\gamma_c g(X)]X \quad (6)$$

where $g(X)$ has to be chosen as a smooth function such as $g(X) = 0$ for $X < X_0$ and $g(X) \approx 1$ for $X > X_0 + L_c$ up to X_{max} for a length $L_{CM} = X_{max} - (X_0 + L_c)$ where complex mapping is activated. We found good performance using $g(X) = \tanh\left(\left[\frac{X-X_0}{L_c}\right]^2\right)$. To apply the method to a linear PDE of the form (3), one has simply to modify the spatial derivatives as follows:

$$\frac{\partial}{\partial x} \equiv \mathcal{H}_x \frac{\partial}{\partial X} \quad \text{with} \quad \mathcal{H}_x(X) = \left(\frac{\partial \mathcal{G}_x}{\partial X}\right)^{-1}. \quad (7)$$

For a given PDE problem, complex mapping function $g \in C^r(\Omega)$, where r is equal to the highest derivative order of the considered PDE problem. This requirement is due to the fact that the derivative should be continuous between the physical and the complex mapping domain to avoid any numerical reflection.

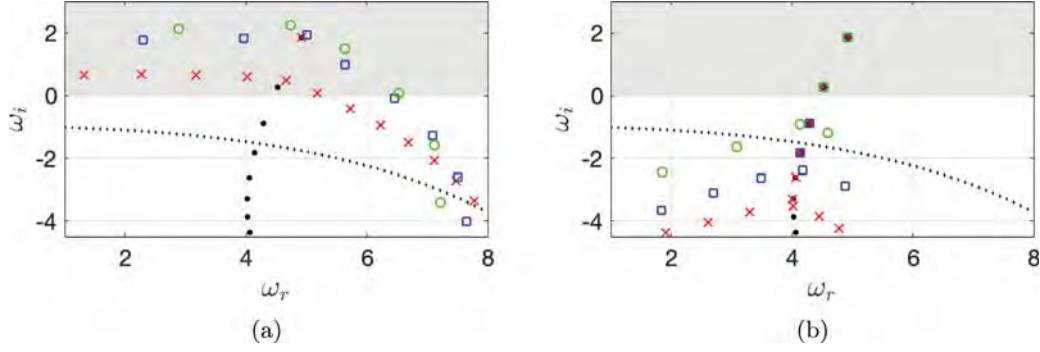


Fig. 1. Numerical spectrum of the Ginzburg Landau equation (a) without and (b) with complex mapping, for domain size $X_{max} = 40$ (red crosses), $X_{max} = 20$ (blue squares) and $X_{max} = 15$ (green circles). The theoretical solution in infinite domain in absence of non-local feedback is displayed by black dots (discrete spectrum) and black dotted line (essential spectrum).

2.4. Comparison with the perfectly matched layer method

The CM method introduced here shares similarities with the PML technique. The PML technique was first introduced by Berenger in the context of electromagnetic waves (Maxwell equations). The initial exposition of the method was formulated in the temporal domain and involved the introduction of auxiliary variables. Soon after, the method was reformulated in the frequency domain (i.e. considering solutions with modal temporal dependence $e^{-i\omega t}$) by Teixeira [10] who showed that it is equivalent to modifying the spatial derivative operators as follows :

$$\frac{\partial}{\partial x} \rightarrow \frac{1}{1 + i\frac{\sigma(x)}{\omega}} \frac{\partial}{\partial x}. \quad (8)$$

Teixeira & Chew [10] also pointed out that this reformulation is equivalent to solving for a complex variable defined as follows:

$$x = \mathcal{G}_{PML}(X) = X + \frac{i}{\omega} \int^X \sigma(X') dX'. \quad (9)$$

Comparing these equations with the ones defining our complex mapping, we immediately see that the two methods are closely related, the difference being that in the PML the coordinate mapping depends upon the frequency ω . Therefore, the method is not directly applicable to eigenvalue problems, where ω is unknown.

3. Application to a 1D model problem

3.1. Description of the model and theoretical solution

In this section we first demonstrate the efficiency of the method for a one dimensional PDE which has often been used as a model for global hydrodynamical instability of open shear flow, namely the linear Ginzburg–Landau equation (see the recent book of Schneider & Uecker [11, Ch. 10] for a rigorous mathematical derivation and analysis of this equation):

$$-i\omega\Psi = -U\frac{\partial\Psi}{\partial x} + \kappa\frac{\partial^2\Psi}{\partial x^2} + \mu(x)\Psi + \mathcal{F}(\psi). \quad (10)$$

In this model, U represents the convective velocity, κ a diffusion coefficient, $\mu(x)$ a local growth rate of the instability, \mathcal{F} a non-local coupling term. We use the following law for the local growth rate:

$$\mu(x) = \mu_\infty + \mu_1 e^{-x/L^*}. \quad (11)$$

where $\mu_\infty, \mu_1, L^* \in \mathbb{R}$ are parameters of the problem. With this choice, the homogeneous problem in a semi-infinite domain (without the term \mathcal{F}) admits a discrete spectrum ω_n with $n =$

$1, 2, \dots$ (where the linear operator is Fredholm and closed, that is the solution belongs to the space, here $H_0^1(\mathbb{R}^+)$). Discrete modes are alike to eigenvalues in finite dimensional problems. The spectrum of Eq. (10) is also composed of a second set, denoted as *essential spectrum* $\omega_{ess}(\ell)$ with $\ell \in \mathbb{R}$ (where the linear operator is no longer Fredholm or closed, for more details on the spectrum of infinite dimensional operators see the book of Kapitula & Promislow [12, Ch. 3]). This set depends uniquely on asymptotic coefficients of Eq. (10). The corresponding solution is given in Appendix A (Eq. (35) and Eq. (37)). Following Lesshaft [6], we introduce a nonlocal feedback term defined as

$$\mathcal{F}(\psi) = \epsilon e^{-\frac{(x-x_A)^2}{b^2}} \Psi(x_S) \quad (12)$$

where ϵ is a coupling parameter, x_S is the location of a “sensor” (located close to the outlet) and x_A the location of an activator (located close to the inlet). Such a feedback exists in real flows through the pressure, either as a result of backward-propagating pressure waves (in compressible flows) or as an instantaneous non-local effect (in incompressible flows). Lesshaft [6] showed that this nonlocal term leads to the appearance of a family of artificial eigenmodes called “arc branch modes” which are clearly dependent on the size of the domain and hence have to be ruled out when one wants to focus on the discrete modes. We will show that the complex mapping technique efficiently reaches this objective.

3.2. Numerical solution and effect of CM

In this section, we assume the following values for the model parameters: $\mu_\infty = -1, \mu_1 = 10, \kappa = 1 - i, U = 6.5$ and $L^* = 10$. With this choice, the problem is absolutely unstable in the range $x \in [0, 4.6]$, convectively unstable in the range $x \in [4.6, 23]$, and locally stable for $x \in [23, \infty]$. Moreover, the analytical solution (see Appendix A) tells us that the two first modes of the discrete spectrum are unstable while the higher-order discrete eigenvalues and the essential spectrum are stable. In the following we will consider the numerical solution of the problem using a feedback term with parameters $x_A = 1, b = 0.2, x_B = X_{max} - 1, \epsilon = 0.1$. The numerical solution is done using a Chebyshev collocation method.

Fig. 1 (a) displays the numerically computed spectra without complex mapping ($x \equiv X$) for three values of the numerical domain size, namely $X_{max} = 15, 20$ and 40 . In all cases, the numerically computed spectra are dominated by the “arc-branch” artificial modes whose location clearly depends upon the size of the domain. Note that with the chosen parameters, the arclength modes are located in the unstable ($\omega_i > 0$) half-plane. For the smallest domains ($X_{max} = 15$ and 20) these modes completely

mask the physically relevant discrete modes. Computing the most unstable mode is only possible with the largest domain ($X_{max} = 20$), and yet some mismatch with the theoretical solution can be observed on the figure. Fig. 1 (b) displays the numerically computed spectra using the complex mapping technique, with the same values of the numerical domain size ($X_{max} = 15, 20$ and 40), and applying the complex mapping starting from $L_0 = X_{max} - 5$. The other parameters affecting the complex mapping are $\gamma_c = 10$ and $L_c = 1$.

As one can observe, the introduction of CM has the effect of completely suppressing the arc-branch of artificial modes, and for all cases the two unstable discrete eigenvalues (plus two stable ones) are correctly recovered. One still observes a branch of artificial eigenvalues, but they are rejected far away from the unstable region, and below the theoretical essential spectrum. It is remarkable that the CM technique allows to correctly compute the unstable discrete modes independently of the size of the domain, even in the two smallest cases ($X_{max} = 15, X_{max} = 20$) where the problem remains convectively unstable at the location of the numerical truncation.

4. Application to linear acoustics

4.1. Physical problem and asymptotic solution

In this section, we demonstrate the efficiency of the complex mapping method for a purely linear acoustic wave problem, corresponding to a cylindrical pipe of radius $\frac{D}{2}$ and length L opening to a semi-infinite domain. This is a classical problem in linear acoustics, the interested reader is referred to the book of Fletcher & Rossing [13, Ch. 8] for a brief review.

In an inviscid framework, it is classical to express the velocity and pressure in terms of the velocity potential Φ , namely $\mathbf{u} = \nabla\Phi$, $p = \rho \frac{\partial\Phi}{\partial t}$. The problem reduces to the Helmholtz equation:

$$\nabla^2\Phi + \left(\frac{\omega}{c_\infty}\right)^2\Phi = 0 \quad \text{in } \Omega \quad (13)$$

where c_∞ is the speed of sound. Eq. (13) is complemented with boundary conditions. At the walls, the bottom and the axis we impose non-penetration conditions:

$$\nabla\Phi \cdot \mathbf{n} = 0 \quad \text{at } \Gamma_{in}, \Gamma_{wall}, \Gamma_a \quad (14)$$

In addition, in an unbounded space, the relevant asymptotic condition is the Sommerfeld condition (see the review of Schot [14]):

$$\frac{\partial\Phi}{\partial r_s} - \left(i\frac{\omega}{c_\infty}\Phi + \frac{\Phi}{r_s}\right) \rightarrow 0 \quad \text{as } r_s = \sqrt{r^2 + z^2} \rightarrow \infty \quad (15)$$

Physically this condition means that away from the outlet, the acoustic field matches with a monopolar source leaving the domain, and there is no wave coming from infinity. In practice, when working with a truncated domain, this asymptotic condition has to be replaced by an artificial boundary condition at the outlet surface Γ_{out} which does not lead to any notable reflection. We will show in the next subsection that the use of CM efficiently fulfills this goal. Note that the physical problem considered here admits an analytical solution in the limit of long pipes ($L/D \gg 1$). This solution is obtained by matching a plane-wave description within the pipe to a monopolar radiation in the outer domain, and details are given in Appendix B. The corresponding result is as follows:

$$\omega \approx (n - 1/2)\pi \frac{c_\infty}{L + \Delta} - \frac{i\pi^2 (2n - 1)^2 c_\infty D^2}{32 (L + \Delta)^3} \quad \text{with } n = 1, 2, \dots \quad (16)$$

where $\Delta = 4D/3\pi$ is the so-called correction length [13]. The first term in this expression means that the acoustical wavelength $\lambda_{ac} = 2\pi c_\infty/\omega_r$ is $4/(2n - 1)$ times the effective length $(L + \Delta)$ of the pipe, which corresponds to the resonance condition of an ideally open pipe. The second term represents the damping rate due to radiation in the semi-infinite space, which is found to be largest for higher-order modes. In addition, the physical problem in infinite domain admits an essential spectrum whose outer boundary, the Fredholm border (FB), is located on the real ω -axis, corresponding to weak solutions of the problem which are not square-integrable and do not satisfy the Sommerfeld condition, and defined as:

$$\omega_{FB} = c_\infty \ell, \quad \text{for } \ell \in \mathbb{R} \quad (17)$$

Physically, these solutions correspond to plane waves coming from infinity and reflecting along the wall (with weak influence of the pipe).

4.2. Numerical results

In this section we present results obtained using the CM method. Technically, the method was used by applying the mapping equation (6) to both r and z coordinates, namely $r = \mathcal{G}(R)$ and $z = \mathcal{G}(Z)$ where R, Z are the numerical coordinates in the truncated domain Ω . Hence, both r and z derivatives appearing in the Laplacian operator are modified using Eq. (7). We apply the mapping outside of the box $(R, Z) = [0, R_0] \times [-H, Z_0]$ (corresponding to the dashed box in Fig. 2).

Fig. 3 displays the computed spectra for a long and a short pipe, respectively $L/D = 10$ and $L/D = 3$. The results of the CM method are compared to a reference solution using a much larger domain ($R_{max} = 50$) and imposing directly the Sommerfeld boundary condition at the outlet (see Appendix C for details about implementation of this case). For the longest pipe, the both the CM method and the reference case allow to compute accurately the discrete spectrum (8 discrete modes can be found in the range displayed in the figure). In the reference case without CM, the numerically computed spectrum also contains a large number of artificial eigenvalues, all located in the stable range ($\omega_i < -0.05$), which correspond to a discretized version of the essential spectrum discussed above.

For the physical modes, the numerical results fit well with the asymptotic formula equation (16) for the lowest modes. For the higher frequency modes the asymptotic formula overpredicts the damping; this is not surprising since the asymptotic theory assumes monopolar radiation while high frequency modes are known to be more directive, hence less energy is radiated.

For the shortest pipe (Fig. 3 (b)), the discrete modes are much more damped. As one can observe, the computation without CM only allows to compute the first mode of the series. All the others are located in the region occupied by the artificial modes, leading to the impossibility to compute them. Note that the agreement with the asymptotic formula equation (16) is less good than for the long pipe because the hypothesis $L/D \gg 1$ does not hold. Considering the second mode, the pressure component along the axis for $L/D = 3$ is reported in Fig. 2 (b). The pressure field in the physical case (without CM) is approximately a standing wave within the pipe (with real and imaginary parts in phase) and an outward propagating wave outside of the pipe (with a $\pi/2$ phase shift). As can be seen, use of the CM leaves the pressure field unaffected within the pipe and up to $z = Z_0$, but the structure is completely damped for farther distances.

As for the artificial eigenvalues, using the CM technique has the effect of 'sweeping' them towards much larger damping rates, and allows to correctly compute the 6 first modes of the series. Moreover, it can be seen that the imposition of the CM method

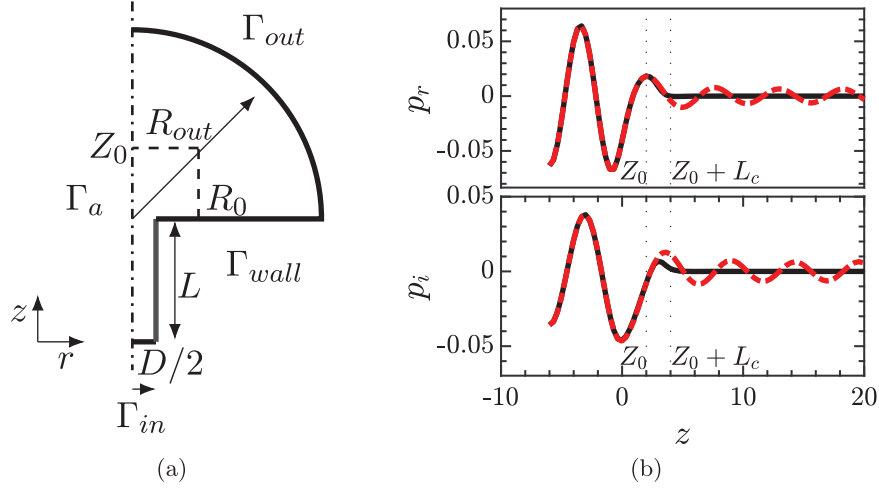


Fig. 2. (a) Sketch of the flow configuration representing the flow through the acoustic circuit. Geometric parameters are displayed. (b) Evolution of acoustic waves along the z -direction at the axis for the short pipe ($L/D = 3$). Real and imaginary parts of the pressure component of the leading mode (see Fig. 3 (b)) are depicted. Solid line corresponds to CM and dashed-dotted (red online) to Sommerfeld boundary condition. (For interpretation of the references to color in this figure legend, the reader is referred to the web version of this article.)

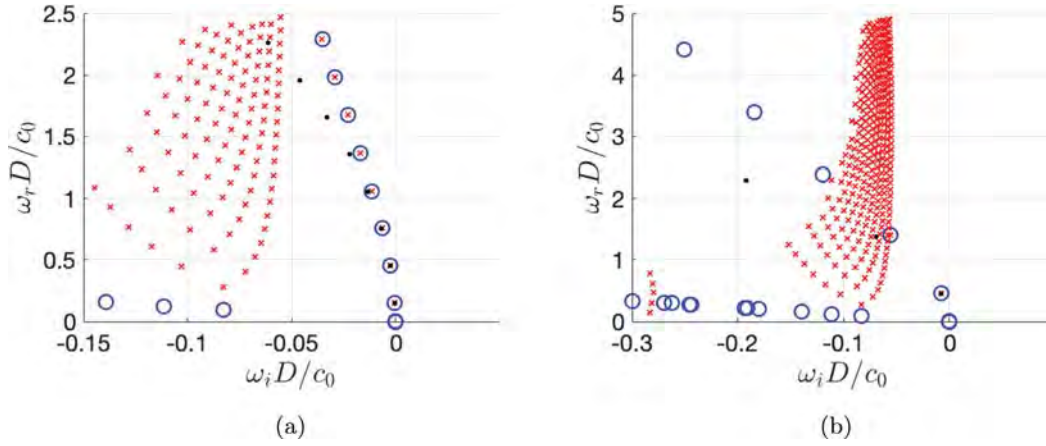


Fig. 3. Acoustic spectrum of the open-pipe configuration for (a) a long pipe ($L/D = 10$) and (b) a short pipe ($L/D = 3$). Blue circles correspond to result using CM (with parameters $X_0 = Z_0 = 2, L_c = 2, \gamma_c = 1$ and domain size $R_{out} = 10$), and red crosses to a reference solution using a much larger domain ($R_{max} = 50$) and Sommerfeld boundary condition at the outlet. Black dots correspond to the asymptotic formula equation (16).

dramatically affects their location in the complex plane. Mathematical analysis of the essential spectrum shows that the effect of CM is to ‘tilt’ it from the real axis (as defined by (17)) to a line in the complex plane defined by

$$\omega_{FB} = c_\infty \ell \frac{1}{1 + i\gamma_c} = i c_\infty \ell e^{-i \arctan(\gamma_c)}, \text{ for } \ell \in \mathbb{R}. \quad (18)$$

The artificial modes obtained with CM are observed to lie approximately along this line.

Note that in addition to being more accurate with shorter domains, the CM is numerically less demanding than the Sommerfeld method. In effect, as the eigenvalue appears only as ω^2 , it is enough to formulate the problem for Φ and solve for ω^2 . On the other hand, using the Sommerfeld method, as the eigenvalue appears as ω^2 in the Helmholtz equation and ω in the boundary condition, it is required to solve for an augmented state vector $[\Phi, \Phi_1]$ with $\Phi_1 = \omega \Phi$. The corresponding formulation is detailed in Appendix C.

To investigate the performance of the CM method, we display in Table 1 the numerical values of the three first eigenvalues of the short pipe (with $L/D = 3$) for various choices of the domain size R_{out} and complex mapping parameters r_0, z_0, L_c and γ_c . We note that the results agree within 1%. Considering that

the acoustic wavelength of the first mode is $\lambda_{ac} \approx 2\pi/\omega_{1,r} \approx 13.7$, it is specially remarkable that the CM method is able to produce accurate results with a domain as short as $R_{out} = 5$, which represents a fraction of this wavelength.

5. Application to global stability analysis

5.1. Governing equations

Let us consider both compressible or incompressible Navier-Stokes equations written in compact operator form as

$$\mathcal{B} \frac{\partial \mathbf{q}(\mathbf{x}; t)}{\partial t} = \mathcal{NS}(\mathbf{q}(\mathbf{x}; t)). \quad (19)$$

Here \mathbf{q} denotes the state vector defined as $\mathbf{q} = [\mathbf{u}; \rho; T; p]$ using non-conservative variables for compressible or $\mathbf{q} = [\mathbf{u}; p]$ for incompressible flows. \mathcal{B} is a linear operator specifying how the time derivative applies to variables. Finally, \mathcal{NS} is the nonlinear Navier-Stokes operator. A detailed form of the compressible operator is given by Fani et al. [15] and the incompressible case is detailed in the review article of Fabre et al. [9]. In the following sections, Reynolds number is defined as $Re = \frac{U_r L_r}{\nu_\infty}$ where L_r, U_r are the characteristic length and velocity scales of the flow

Table 1
Eigenvalues of a short open pipe ($L/D = 3$) for various choices of the complex-mapping parameters.

R_{out}	r_0	z_0	L_c	γ_c	ω_1	ω_2	ω_3
20	2	2	1	1	0.4623−0.0076i	1.4089−0.0560i	2.3894−0.1197i
10	2	2	1	1	0.4624−0.0076i	1.4091−0.0560i	2.3898−0.1200i
5	2	2	1	1	0.4639−0.0061i	1.4085−0.0561i	2.3895−0.1199i
10	2	2	1	0.2	0.4624−0.0076i	1.4091−0.0560i	2.3898−0.1200i
10	5	5	2	1	0.4627−0.0089i	1.4092−0.0562i	2.3897−0.1199i

configuration and ν_∞ is the kinematic viscosity at the far field. For compressible cases, the Mach number is defined as the ratio of the characteristic velocity to the speed of sound at the far field, $M = \frac{U_r}{c_\infty}$.

5.1.1. Base flow solution & linearized Navier–Stokes-modal decomposition

Stability studies rely on the linearization about a base state \mathbf{q}_0 . We define here \mathbf{q}_0 as the *base flow* corresponding to the solution of the steady Navier–Stokes equations :

$$\mathcal{NS}(\mathbf{q}_0(\mathbf{x})) = \mathbf{0} \quad (20)$$

In addition, the base-flow has to fulfill a set of *boundary conditions* which depend on the application case and will be detailed in Section 6.

In the framework of LNSE, we are led to consider small-amplitude perturbations of this base flow:

$$\mathbf{q} = \mathbf{q}_0(\mathbf{x}) + \epsilon \mathbf{q}'(\mathbf{x}, t), \quad (21)$$

where ϵ is a small parameter and the perturbation is expressed as in Eq. (3) under the modal form

$$\mathbf{q}'(\mathbf{x}, t) = \hat{\mathbf{q}} e^{-i\omega t} + c.c. \quad (22)$$

For both the forced and the autonomous problem, injecting the modal ansatz in Navier–Stokes equations (21) leads to a linear problem which can be written as follows:

$$-i\omega \mathcal{B} \hat{\mathbf{q}} = \mathcal{LNS} \hat{\mathbf{q}} \quad (23)$$

Here \mathcal{LNS} is the Linearized Navier–Stokes operator whose definition may be found in the analysis of Fani et al. [15] for the compressible and in see Fabre et al. [9] for the incompressible case. In addition to the case-dependent set of physical boundary conditions, an unbounded problem requires another set of asymptotic conditions. Physically, we can expect the velocity perturbations associated with vortical structures to decay under the effect of viscous diffusion, and the pressure perturbations to behave like a divergent acoustic wave as function of the spherical coordinate $r_s = |\mathbf{x}|$. In the compressible case these conditions are expressed as follows

$$\hat{\mathbf{u}}, \nabla \hat{\mathbf{u}} \approx \mathbf{0} \quad \text{for } r_s = |\mathbf{x}| \rightarrow \infty; \quad (24)$$

$$r_s \left[c_\infty \frac{\partial \hat{p}}{\partial r_s} + \left(U_\infty \frac{\partial}{\partial x} - i\omega + \frac{1}{r_s} \right) \hat{p} \right] \approx 0 \quad \text{for } r_s = |\mathbf{x}| \rightarrow \infty. \quad (25)$$

where the second expression is recognized as the so-called *Sommerfeld condition*, which coincides with Eq. (15) in the case of quiescent ambient flow. In the incompressible setting Eq. (24) is the unique boundary condition, because pressure is automatically set by the velocity–pressure Poisson equation. Note that this way of exposing the boundary conditions is not fully rigorous and involves a number of pedagogical shortcuts. For instance, the assumption that vortical perturbations are eventually damped relies on the effect of viscosity, while the Sommerfeld condition comes from an inspection of the inviscid equations. To express the conditions more rigorously one should also separate the perturbations of the thermodynamical variables into adiabatic (acoustic)

and non-adiabatic (entropy) components. However, this pair of equations contains all problems related to artificial boundary conditions and is well suited to the discussion in the next section.

5.2. Effect of CM in the spatial structure of modes

5.2.1. Study of plane-wave solutions for a parallel flow

The condition that the base-flow is asymptotic to a *uniform* flow $\mathbf{u} \approx U_\infty \mathbf{e}_x$ is generally impossible to reach in a truncated domain with reasonable dimensions. On the other hand, it is generally reasonable to assume that in the vicinity of the truncation plane, the flow approaches a parallel shear flow. We will thus first investigate the behavior of possible solutions of the LNSE under this hypothesis. We thus consider a parallel shear flow defined as $\mathbf{u}_0 = U(y)\mathbf{e}_x$ (or for problems with axial symmetry $\mathbf{u}_0 = U(r)\mathbf{e}_x$) developing in the half-space defined by $x > 0$, here \mathbf{e}_x denotes a unit vector in the x positive direction. We suppose that $U(y)$ tends to U_∞ when y is sufficiently large, and note $U_c = U(0)$ the velocity at the centerline. This situation represents both a wake (with $U_c < U_\infty$) or a jet (with $U_c > U_\infty$) (see Fig. 4). It is also reasonable to assume that U_c and U_∞ are both positive which means that the local velocity profile is *convectively unstable* (see the book of Huerre & Rossi [16]).

Under those hypotheses, the solution of the eigenvalue problem can be expected as a superposition of plane-wave solutions, namely

$$\hat{\mathbf{q}}(x, y) e^{-i\omega t} = \sum_k \hat{\mathbf{q}}(y)_{k,\omega} e^{i(kx - \omega t)} \quad (26)$$

Two kinds of solutions can be expected. The first kind corresponds to *acoustic waves*. Restricting to longitudinal waves (independent of the y -direction) and assuming $U_c \approx U_\infty$ for simplicity, two solutions are defined as

$$\frac{\omega}{k_{ac}^\pm} = \pm c_\infty + U_\infty \quad (27)$$

If the mean flow is subsonic ($U_\infty - c_\infty < 0$), then the solution k_{ac}^- (representing an acoustic wave propagating in the negative direction) does not verify the condition equation (25) and has to be canceled by the ABC. On the other hand, k_{ac}^+ must not be affected by the ABC.

The second kind corresponds to *vorticity waves*. The corresponding values for k can be obtained from the local stability analysis of the considered shear flow. This topic is well known and such solutions can be found in several textbooks (e.g. Huerre & Rossi [16]). The possible solutions are given by a dispersion relation $D(k_H, \omega)$. In the *spatial stability* framework which is relevant here, the solutions $k_H(\omega)$ are of two different types, noted k_H^+ and k_H^- . Only the k_H^+ branches should appear in a solution developing in the positive x -direction, so one should check that the ABC does not result in any problem related to the k_H^- branches. For the present discussion, we will consider the simplest case of a shear layer of zero thickness (see Fig. 1b). The problem corresponds to the classical Kelvin–Helmholtz instability, and the corresponding solutions for k as given by:

$$\begin{aligned} \frac{\omega}{k_{H,s}^+} &= \frac{U_\infty + U_c}{2} - i \frac{|U_\infty - U_c|}{2} \\ \frac{\omega}{k_{H,u}^+} &= \frac{U_\infty + U_c}{2} + i \frac{|U_\infty - U_c|}{2} \end{aligned} \quad (28)$$

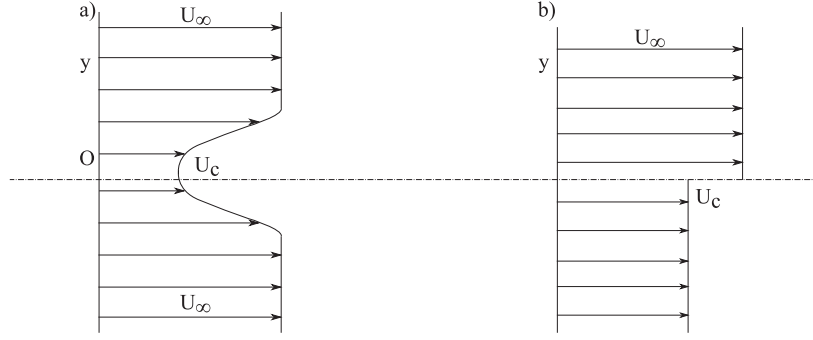


Fig. 4. (a) Basic velocity profile of wake shear flow. (b) Simple velocity profile model of a zero-thickness shear layer.

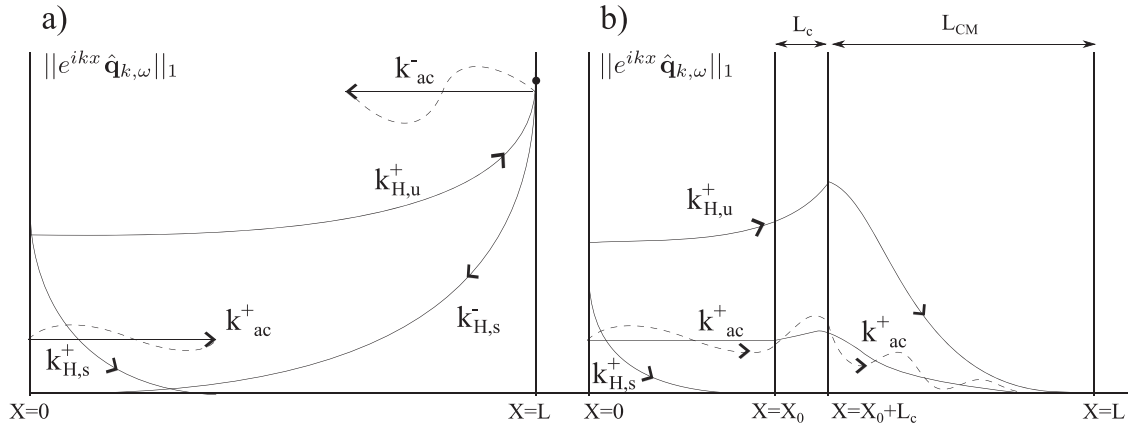


Fig. 5. Sketch of the propagation of hydrodynamic and acoustic waves, where for the sake of illustration L_{CM} and L_c are depicted intentionally large with respect to the physical domain. In ordinate the amplitude of a plane-wave, $\|e^{ikx} \hat{\mathbf{q}}_{k,\omega}\|_1$, is represented. (a) without CM : waves $k_{H,u}^+$ and k_{ac}^+ are present at the outlet, thus leading to reflected waves (only the reflections caused by wave $k_{H,u}^+$ are represented). (b) with CM, and choosing γ_c according to (33): Waves $k_{H,u}^+$ and k_{ac}^+ are damped when reaching the boundary, so no reflection is generated.

Here $k_{H,u}^+$ is the spatially unstable Kelvin–Helmholtz wave and $k_{H,s}^+$ is a spatially stable wave which does not lead to particular problems but has to be retained in the discussion. Note that both solutions belong to the k_H^+ category and should thus be present in the solution of the problem for $x \rightarrow +\infty$. The zero-thickness shear layer does not possess any k_H^- solutions (for reasons discussed in Huerre & Rossi [16]) but continuous $U(y)$ profiles admit such solutions which, except in cases where U_∞ and/or U_c are negative, are always located in the half-plane $Im(k) < 0$ and far away from the $k_{H,s}^+$ solutions.

5.2.2. Effect of CM on plane-waves

For the present discussion we will thus restrict to five solutions. Acoustic waves k_{ac}^\pm , the KH waves $k_{H,s}^+$ and a possible k_H^- solution. The behavior of these solutions as $|x| \rightarrow \infty$ is one of the three following cases:

(i) Dominant if $Im(kx) < 0$, i.e. $arg(kx) \in [-\pi, 0]$ (29)

(ii) Evanescent if $Im(kx) > 0$, i.e. $arg(kx) \in [0, \pi]$ (30)

(iii) Oscillating if $Im(kx) = 0$, i.e. $arg(kx) = 0, \pi$ (31)

We will consider the asymptotic effect of complex mapping equation (4). The situation differs according to the argument of ω . We consider three cases:

Case 1: $arg(\omega) = 0$

The case where ω is real is particularly important as it is relevant to both the forced problem resolved in frequency domain, and to the stability problem at marginal conditions. Fig. 6(a) sketches the location of the five considered plane-wave solutions

in the complex k -plane. The region $Im(k) < 0$ corresponding to dominant solutions in the absence of mapping is indicated by the gray area. Both solutions $k_{H,u}^+$ and k_H^- belong to this region, while $k_{H,s}^+$ is evanescent and k_{ac}^\pm are both oscillating.

As sketched in Fig. 6(b), the effect of the complex mapping Eq. (4) for x is to ‘tilt’ the boundary between dominant and evanescent solutions by an angle $arg(\gamma_c)$. As a result, the choice $\gamma_c > 0$ is sufficient to turn the physically relevant k_{ac}^+ into an evanescent wave and the unwanted k_{ac}^- into a dominant wave, which will thus be damped as it propagates backwards. However, if γ_c is small, the solution will still contain a dominant $k_{H,u}^+$ wave.

This solution corresponds to the spatially growing Kelvin–Helmholtz instability, and is perfectly relevant from a physical point of view. However, if the spatial growth of this wave is larger than the spatial damping of the backward-propagating k_{ac}^- induced by the mapping, the k_{ac}^- solution may still be present in the domain as a reflection of the $k_{H,u}^+$. The remedy to avoid this is to chose γ_c such as $k_{H,u}^+$ becomes evanescent, see Fig. 5 (b). This requirement leads to the following condition:

$$\arctan(\gamma_c) > -arg(k_{H,u}^+), \quad \text{i.e. } \gamma_c > \frac{|U_\infty - U_c|}{U_\infty + U_c} \quad (32)$$

The corresponding situation, where only the k_{ac}^- wave is dominant, is sketched in Fig. 6 (b). CM is also effective in a situation where $k_{H,u}^+$ does not decay enough before reaching the outer boundary, but backward propagating wave does before escaping complex mapping region and reaching the physical domain. It is found that in that case CM is more effective for compressible flows and Eq. (32) turns to be the condition for the low Mach limit, see Appendix D for details.

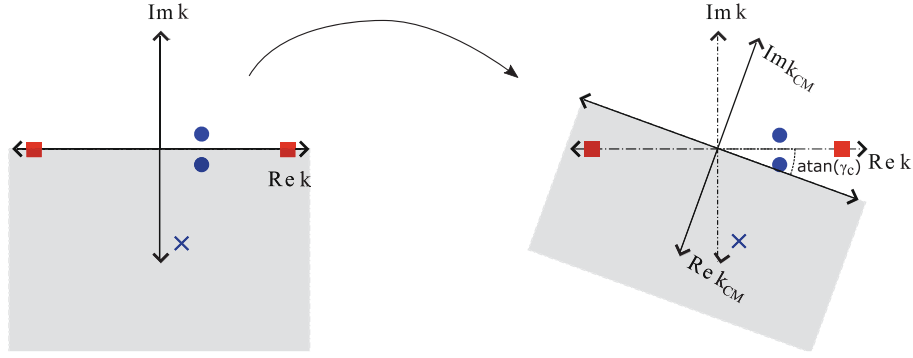


Fig. 6. Diagram displaying a complex mapping $\mathcal{G}_x(X)$ for a real frequency ω , such that $\arg(\omega) = 0$, in the complex plane of the wave-vector k . Red squares represent spatial acoustic modes k_{ac}^{\pm} , whereas blue circles represent hydrodynamic modes $k_{H,u}^{\pm}$ and the blue cross denotes the k_{H}^{-} mode.

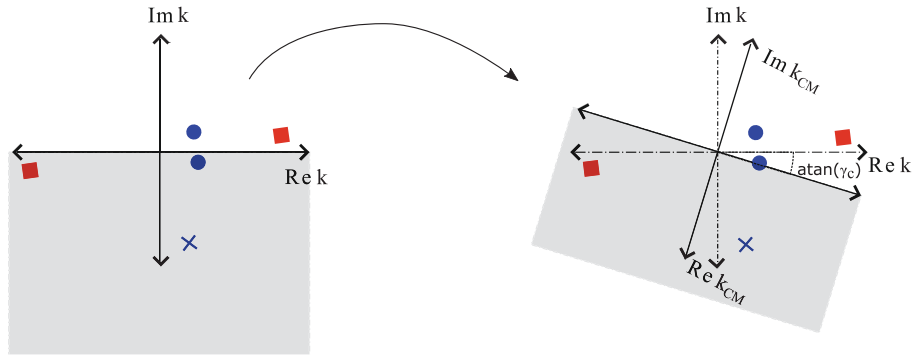


Fig. 7. Diagram displaying a complex mapping $\mathcal{G}_x(X)$ for an unstable frequency ω , in the complex plane of the wave-vector k . Legend of symbols is the same as in Fig. 6.

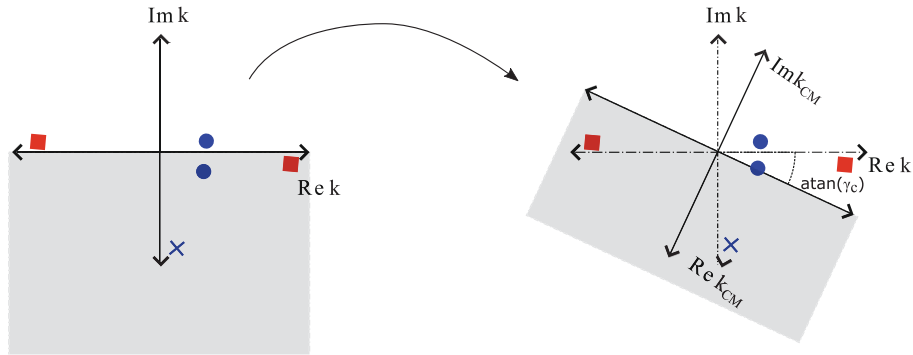


Fig. 8. Diagram displaying a complex mapping $\mathcal{G}_x(X)$ for a stable frequency ω , in the complex plane of the wave-vector k . Legend of symbols is the same as in Fig. 6.

Case 2: $0 < \arg(\omega) \ll \frac{\pi}{2}$

This second case corresponds to the expected behavior of a temporally unstable mode. As seen in Fig. 7, this case is more favorable, as the k_{ac}^{-} wave is already in the dominant region without need of the mapping. If one wants to turn the $k_{H,u}^{+}$ wave into an evanescent as in Fig. 5 (b) one needs to choose γ_c in such a way it possesses a sufficient decay (see Fig. 7):

$$\arctan(\gamma_c) > \arctan\left(\frac{|U_{\infty} - U_c|}{U_{\infty} + U_c}\right) - \arg(\omega) \quad (33)$$

Case 3: $-\frac{\pi}{2} \ll \arg(\omega) < 0$

Now we consider a value ω corresponding to a stable global mode. This case is the less favorable, as without mapping (see Fig. 8 (a)). The k_{ac}^{-} wave is in the dominant region, meaning that it will be amplified as propagating backwards, destroying any chances to correctly compute the mode. The condition to change this mode

into a dominant one and turn the $k_{H,u}^{+}$ into an evanescent one is still given by Eq. (33), but it is more restrictive here than in previous cases since $\arg(\omega) < 0$.

6. Application cases

6.1. Incompressible flow through a single hole

In this section we will discuss the application of the complex mapping methodology to incompressible Navier–Stokes equations. The hole diameter is considered as the reference length, denoted by L_r and the characteristic scale, U_r is the mean velocity across the hole. The application case is the flow past a single hole of finite thickness. This configuration has been recently studied by Fabre et al. see [8, Sec. 3] for the definition of the problem and a discussion about boundary conditions. Severe numerical difficulties arise in the solution of the linearized Navier–Stokes equations

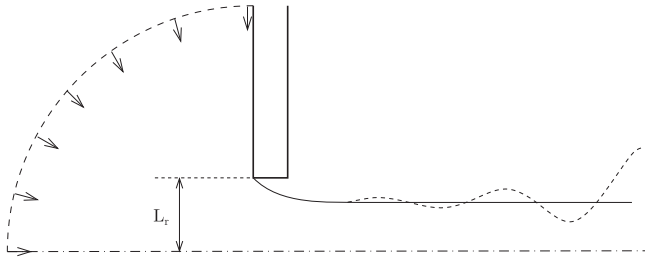


Fig. 9. Sketch of the flow configuration representing the oscillating flow past a circular hole in a thick plate.

Table 2

Description of meshes M_i for $i = 1, 2, 3$. N_v denotes the number of vertices of the mesh. Geometrical parameter L_{out} denotes the axial longitude of the mesh and R_{out} is the radial extension of the numerical domain.

Description of numerical domains $M_1 - M_3$						
Mesh	L_{out}	R_{out}	X_0	L_c	γ_c	N_v
M_1	20	15	5	1	0.5	17915
M_2	30	20	-	-	-	30695
M_3	60	20	-	-	-	78300

due to the strong spatial amplification of linear perturbations, in particular pressure (see Fig. 9).

An artificial boundary treatment is a mandatory technique for this type of study. Large amplifications of linear perturbations lead to physical perturbations far downstream the hole. Ideally, this would require an infinite domain, at least in the streamwise direction. However, numerical computations are realized in truncated domains. If the computational domain is not sufficiently large, that is amplitude of the perturbed field is negligible close to the outer boundary, “spurious eigenvalues” constituting the discretized version of the continuous spectrum may arise. In the case of large perturbations, these “spurious eigenvalues” can be even located in the unstable side of the spectrum and close to discrete physical eigenvalues as Reynolds number increases.

The linear stability study of the flow past a hole in a thick plate shows that dynamics of $Re < 3000$ can be explained by the presence of three discrete physical modes, here denoted by H_1 , H_2 and H_3 . For validation purposes we have designed three computational meshes M_i for $i = 1, 2, 3$, the first one with CM uniquely in the axial direction and the other two without any ABC but with longer axial dimension, denoted L_{out} (see Table 2).

Fig. 11 displays the numerically computed spectra using numerical domains M_1 , M_2 and M_3 for $Re = 1700$, $Re = 2000$. The spectra here displayed presents three discrete eigenvalues H_i for $i = 1, 2, 3$ and a set of “spurious eigenvalues”, named arc-branch by Lesshafft [6], which arise due to non-local feedback mechanism of spurious pressure signals from the truncated boundary

Table 3

Eigenvalue computations for $Re = 1600$.

Mesh	H_1	H_2	H_3
M_1	$-0.1156i + 0.5024$	$0.0854i + 2.0985$	$-0.0926i + 4.1230$
M_2	$-0.1259i + 0.5017$	$0.13916i + 2.1051$	$-0.1051i + 4.1359$
M_3	$-0.1189i + 0.5017$	$0.0826i + 2.107$	$-0.0944i + 4.1240$

Table 4

Eigenvalue computations for $Re = 2000$.

Mesh	H_1	H_2	H_3
M_1	$-0.0435i + 0.5615$	$0.3032i + 2.2436$	$0.2418i + 4.3184$
M_2	$-0.0421i + 0.5645$	$0.3114i + 2.2467$	$0.2287i + 4.3268$
M_3	$-0.0420i + 0.5628$	$0.2965i + 2.2399$	$0.1232i + 4.2807$

and upstream locations. Computations of the spectra without ABC, M_2 and M_3 , lead to the presence of unstable spurious eigenvalues ($\omega_i > 0$). Moreover, as the Reynolds number increases they tend to approach discrete eigenvalues H_i . The use of CM results in a good separation of physical and spurious eigenvalues. However, CM methodology with $\gamma_c > 0$ does not allow to identify the complex conjugate modes of H_i located in $\omega_r < 0$. The exploration of the other side of the spectrum can be determined by choosing $\gamma_c < 0$. In Fig. 10 it is possible to visualize the effect of complex mapping on the structure of the pressure component of the H_2 mode. Indeed, one may observe how CM can efficiently transform a convective dominant wave into evanescent, hence any non-local effect, i.e. arc-branch eigenvalues, is avoided.

Finally, Table 3 and Table 4 display a comparison of the numerical efficiency of numerical methodologies M_i for $i = 1, 2, 3$ for the computation of discrete eigenvalues. Following, similar arguments as in Fabre et al. [8] we conclude that CM methodology allows a precise identification of discrete spectrum with a lower number of vertices with respect to methodologies without ABC.

6.2. Hole-tone configuration

The problem of the flow passing through a circular hole in a plate is encountered in many practical applications and has been widely studied by experimental and numerical investigations. This situation is encountered in various applications, including the whistle of a tea kettle, which has been studied by Henrywood & Agarwal [17] or birdcalls (devices used by hunters to imitate bird singing) analyzed by Fabre et al. [18] (see Fig. 12).

Attempts to characterize the instability mechanism were previously made using incompressible (see Fabre et al. [18]) and compressible (see Longobardi et al. [19]) LNSE. These efforts allowed to identify the difficulties associated to boundary conditions. The diameter of the first hole is taken as the characteristic length scale L_r and the mean velocity along the hole as the reference velocity scale U_r . This test case has been previously used to

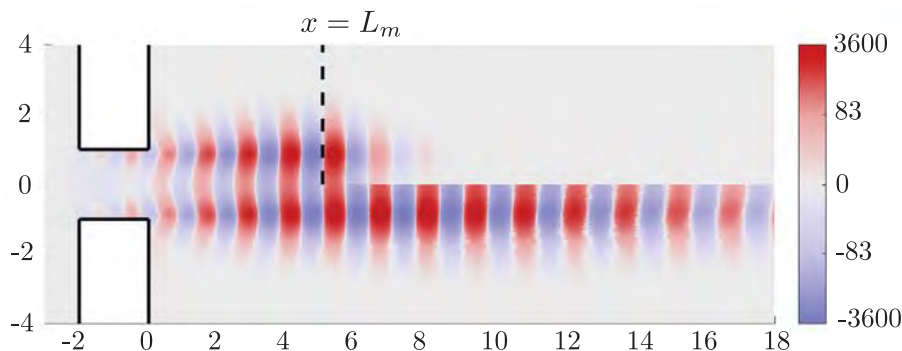


Fig. 10. Pressure component of the eigenmode H_2 with mesh M_1 (upper) and mesh M_3 (lower).

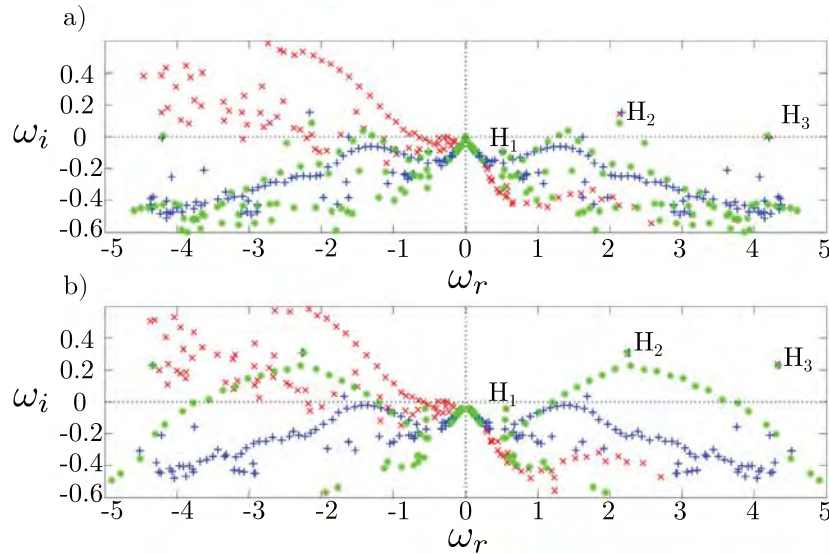


Fig. 11. Spectrum computed with three meshes. \times (red online) denotes eigenvalues computed with \mathbb{M}_1 , $*$ (green online) with \mathbb{M}_2 and $+$ (blue online) with \mathbb{M}_3 for (a) $Re = 1700$ and (b) $Re = 2000$. (For interpretation of the references to color in this figure legend, the reader is referred to the web version of this article.)

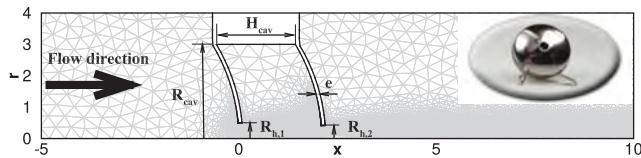


Fig. 12. Sketch of the hole-tone configuration, frame of reference and definition of geometrical parameters. An example of computational mesh is also reported in light gray. An actual birdcall is depicted in the upper right corner. e denotes the thickness of the cavity wall, radius of holes $R_{h,i}$, $i = 1, 2$, radius and length of the cavity are denoted by R_{cav} and H_{cav} respectively. Values of geometrical parameters can be found in Longobardi et al. [19].

show CM efficiency by Sierra et al. [20], where more details about governing equations, i.e. compressible Navier–Stokes, boundary conditions and methodology may be found.

6.2.1. Eigenvalue computations

We study some characteristics of the spectrum of the flow by solving Eq. (19) in the compressible setting. Linear dynamics of the birdcall flow at a sufficiently high Reynolds number is governed by a set of unstable discrete modes, the continuous spectrum remains stable. In the studied range of Re and M_∞ , we have appreciated the presence of four unstable modes up to $Re = 1600$. These modes have been computed with two techniques, sponge as boundary condition at the far field and complex mapping. Artificial boundary conditions are needed to compute physically relevant modes and to avoid the appearance of spurious modes in the spectrum due to boundary conditions.

To identify these modes at threshold we have used complex mapping. Complex mapping technique allows to *tilt the continuous branch of the spectrum* to leave discrete modes isolated and easy to be identified at the threshold. This phenomenon is briefly described in Section 4. At Fig. 13, spectrum is displayed for two Reynolds numbers at $M_\infty = 0.05$. The spectrum corresponding to the simulation with sponge boundary condition at far field at threshold presents some discrete eigenvalues and a continuous branch along the real axis. Let us consider the case $Re = 320$ and $M_\infty = 0.05$. At that configuration Mode 1 is neutrally stable. However, we are not able to identify it by numerical means since it is clustered inside the continuous branch. So, one should increase further the Reynolds number hoping to find the

mode in the unstable zone. With the complex mapping technique continuous branches are rotated from the origin with an angle $\arg \mathbf{x}$ whereas discrete modes remain invariant. This allows to identify modes near and at threshold. These modes are displayed in Fig. 14. In that figure it is possible to appreciate the hydrodynamic instability which is the part of the mode of highest amplitude. It is possible to remark a few properties of these modes. The pressure is fairly constant in the cavity but it is not constant as it has been reported by Longobardi et al. [19]. The spatial structure of pressure mode inside and outside the cavity is proportionally dependent of the temporal frequency ω , which indicates a direct link between the quantization of frequency and pressure oscillations between both holes (see Fig. 14 (a) and (b) for the structure of Mode 1 and 2 at $Re = 1600$ and Fig. 16 (b) for the frequency). Similarly, as ω increases a given mode tends to have its support farther from the cavity. From the vorticity field of Fig. 14 it is possible to observe the antisymmetric pattern of vorticity inside the cavity for mode 1 and mode 2 and the tendency of the shear layer to become symmetric and reduce its thickness as ω increases, this is specially remarkable for mode 4.

Finally in Fig. 15, we depict the imaginary part of the pressure of global modes for $Re = 1600$ and $M_\infty = 0.05$ for Mode 2 and Mode 4. It is possible to observe the radiation of acoustic waves propagating into the far field as spherical waves. Acoustic radiation between Mode 2 and Mode 4 differs in wavelength λ_{ac} and acoustic directivity. Wavelength decreases as ω increases whereas the acoustic directivity seems to change when the acoustic wave is able to penetrate into the cavity as it has been previously observed by Longobardi et al. [19].

For this study we have used four meshes which are shown in Table 5. \mathbb{M}_1 has been used as a reference test case computed with sponge layers. Remaining meshes are used with CM methodology which allows to greatly reduce the size of the domain and the number of points. The size of the domain is denoted by $[X_{min}, X_{max}, R_{max}]$, where X_{min} is the x -coordinate of the inlet, X_{max} is the x -coordinate of the outlet and R_{max} corresponds to the outer radius of the domain. Please note that the minimum size of the sponge section, denoted by $[X_{min}, X_{max}, R_{max}]$ in Table 5, is the minimum domain size to effectively damp acoustic waves. The outer boundary is located at a distance approximately three times the acoustic wavelength of the first bifurcated mode. The reduction in computational time from the use of Sponge or Complex mapping can be also perfectly visualized in Table 5 where it

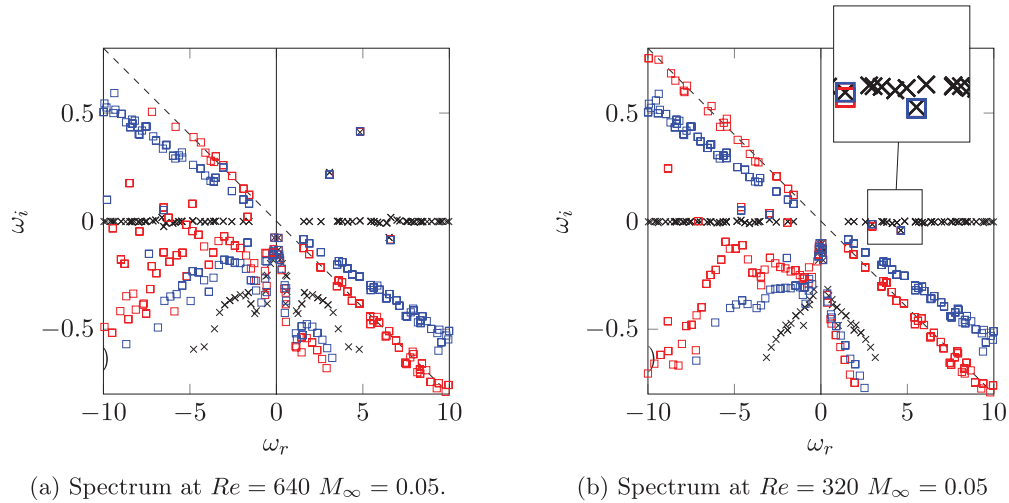


Fig. 13. Spectrum near two bifurcation Re at $M_\infty = 0.05$. Legend : \square are used to denote eigenvalues corresponding to CM. Red is used for $\gamma_c = 0.1$ and blue for $\gamma_c = 0.15$. Black \times denotes those eigenvalues computed without artificial boundary conditions. (For interpretation of the references to color in this figure legend, the reader is referred to the web version of this article.)

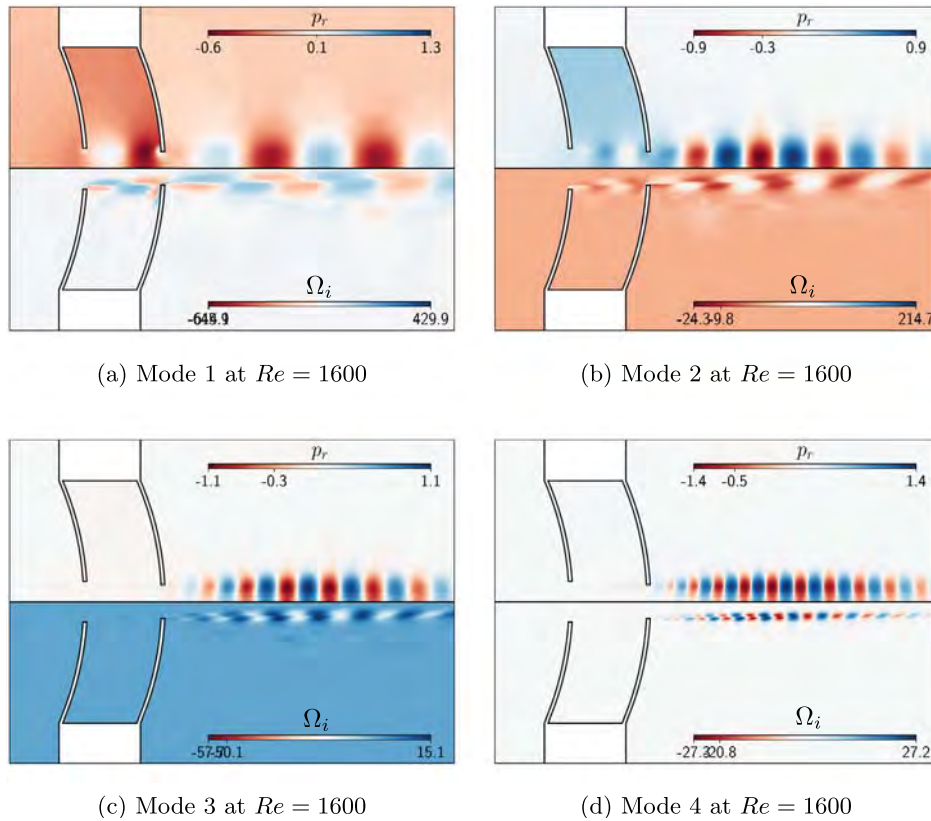


Fig. 14. It displays the four unstable modes at $Re = 1600$ and $M_\infty = 0.05$. The real part of the pressure mode p_r and the imaginary part of the vorticity Ω_i are shown for each mode at the upper and lower sides of each figure respectively.

is displayed the time needed to compute the leading eigenvalue with each of the considered meshes.

Computations with mesh M_1 were carried out in serial with an Intel i7 2.6 GHz whereas numerical tests for M_i for $i = 2, 3, 4$ were computed with an Intel i7 2.2 GHz. Computational time takes into account the computation of the baseflow and the leading eigenvalue at $Re = 400$ and $M_\infty = 0.05$. The gain in computational time between Sponge and CM is around 50 for the finest mesh and 125 for the coarsest. This gain in performance is due to the fact that the domain size of the mesh is greatly

reduced, therefore reducing the number of elements required for the computation.

Concerning precision, a comparison between the four considered meshes is displayed in Fig. 16. In that figure it is possible to observe in (b) linear frequency results are in agreement between the two considered methodologies. Whereas for the linear growth despite the fact the good fit between both methodologies and the four considered meshes there is a slighter disagreement between M_4 and M_1 for the mode with linear frequency around $\omega_r \approx 9$ at high Re . The difference in the growth rate between M_3 and M_1 is

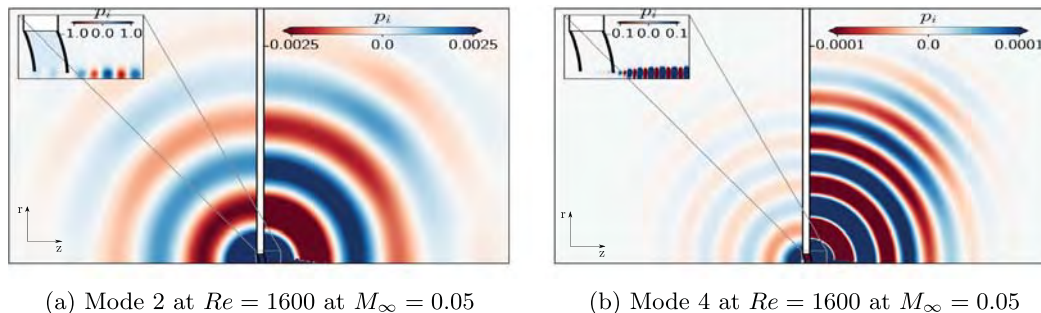


Fig. 15. Imaginary part of the pressure p_i of two direct modes the second mode at the left and the fourth mode at the right. The main figure displays the radiation of the acoustic field whereas the zoomed region shows the spatially localized hydrodynamic mode.

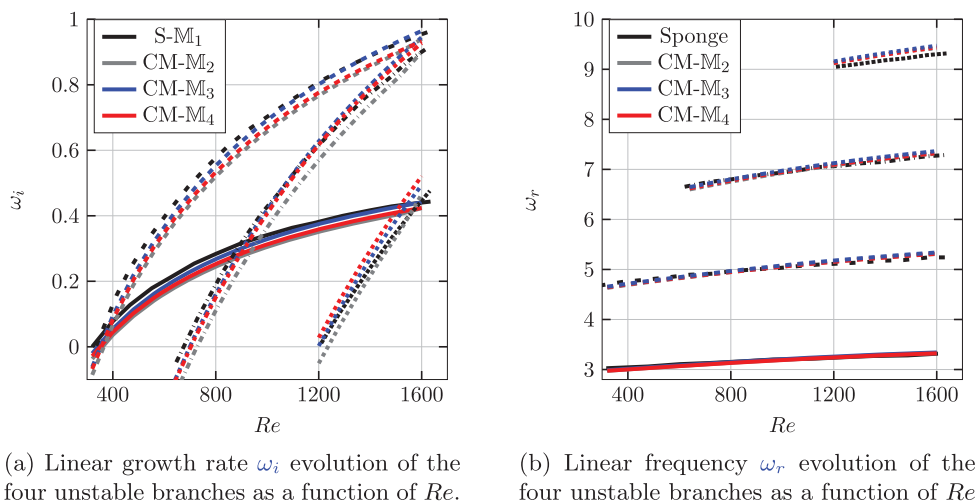


Fig. 16. Comparison of CM with sponge for the four unstable branches. Black lines are used to denote the results computed with the sponge method, whereas gray, blue and red are used for the mesh generated with the mesh adaptation algorithm detailed in the review article of Fabre et al. [9]. Solid lines denote the first mode, loosely dashed lines the second, dash dotted the third and densely dotted the fourth one. (For interpretation of the references to color in this figure legend, the reader is referred to the web version of this article.)

Table 5

Mesh definition and performances. $[X_{min}, X_{max}, R_{max}]$ denotes the size of the computational domain, X_0 the location above which the CM is applied (in both (r, x) directions) and N_v the number of mesh vertices where the boundary conditions are effectively applied. The table also displays the computed eigenvalue ω and the time required for computation $Re = 400$ and $M_\infty = 0.05$. The required time to perform a computation of baseflow and leading eigenvalue with a single processor is displayed.

Mesh	Methodology	N_v	$[X_{min}, X_{max}, R_{max}]$	X_0	γ_c	ω	Time (s)
M_1	Sponge	1211054	$[-120, 120, 130]$	-	-	$4.7574 + 0.0792i$	83944 s
M_2	CM	31986	$[-30, 30, 30]$	10	0.2	$4.6922 + 0.0666i$	1655 s
M_3	CM	40942	$[-80, 80, 80]$	40	0.2	$4.7151 + 0.0945i$	1421 s
M_4	CM	14337	$[-30, 30, 30]$	10	0.15	$4.7051 + 0.0747i$	669 s

lower than 5% in the worst case scenario, which corresponds to the growth rate of Mode 4. In this case the relative error is large because of the small magnitude of the growth rate.

6.3. Flow past an airfoil

Low Reynolds number flow past an airfoil is a flow configuration which has attracted interest from micro-air vehicles or bio inspired air vehicles designers. Airfoils in these types of configurations are usually configured to operate at high angles of attack. Characteristic length and velocity scales are the chord length of the airfoil profile and the far field uniform velocity. Flow unsteadiness is encountered in the separated shear layer due to a Kelvin-Helmholtz instability and in the wake of the airfoil in the form of a Von Karman vortex street. In the past Zhang & Samtaney [21] [22] have carried out the study of a NACA 0012 profile at angle of attack $\alpha = 16^\circ$. In the current section we

reproduce previous results of the NACA 0012 airfoil for a given flow configuration. Effectiveness of the CM methodology will be shown by a parametric study of the length of the CM layer and cross comparison with reference results.

In Table 6, it is displayed the leading eigenvalue for several meshes $M_1 - M_4$ which correspond to different lengths of CM layer. CM is activated outside a rectangle whose upper right corner is $[X_0, Y_0]$ and its lower left corner is $[-X_0, -Y_0]$ with CM parameters $\gamma_c = 0.3$ and $L_c = 5$. R_{out} is the radial extension of the numerical domain and $L_{CM} \approx R_{out} - 10$. Acoustic wavelength, $\lambda_{ac} = \frac{2\pi}{\omega_r} \left(\frac{1}{M_\infty} + 1 \right)$, for $M_\infty = 0.1$ at $Re = 1000$ is around $\lambda_{ac} \approx 28$, where length is non-dimensional with respect to the chord of the airfoil. A length of the CM region, of around $L_{CM} \approx [50, 60]$ is sufficient to capture the leading eigenvalue, which has been also computed with sponge layers, see M_5 . Nevertheless, M_1 whose length of the complex mapping region is $L_{CM} \approx \frac{\lambda_{ac}}{3}$ presents a relative error of around 1%. This is another example of the

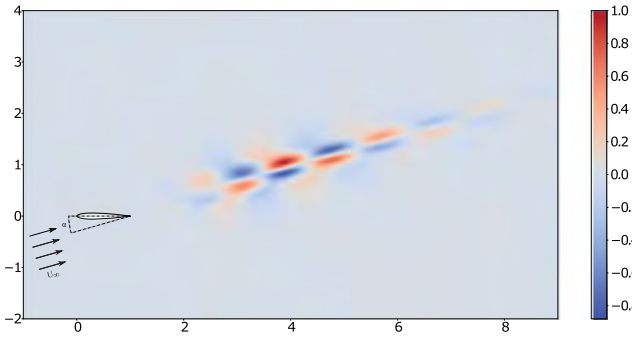


Fig. 17. Streamwise velocity $u_{x,1}$ of the most unstable mode at $Re_\infty = 1000$, $M_\infty = 0.1$ and $\alpha = 16^\circ$.

Table 6

Eigenvalue computation for $Re = 1000$ and $M_\infty = 0.1$ with respect to incompressible DNS results of [22]. CM corresponds to $M_1 - M_6$. M_5 corresponds to a computational domain of size R_{out} and a sponge region activated at $[X_0, Y_0]$.

Re = 1000 and $M_\infty = 0.1$				
Mesh	R_{out}	$[X_0, Y_0]$	ω_i	ω_r
M_1	20	[10, 10]	0.7110	2.6102
M_2	30	[10, 10]	0.7079	2.5954
M_3	40	[10, 10]	0.7071	2.5862
M_4	70	[10, 10]	0.7048	2.5692
M_5	30	[5, 5]	0.7079	2.5954
M_6	30	[2, 2]	0.7067	2.5953
M_5	100	[10, 10]	0.7036	2.5660
Ref. [22]	—	—	0.716	2.5095

strength of CM with respect to sponges which require several acoustic wavelengths to avoid any reflection. In Table 6 it is also displayed a parametric comparison of $[X_0, Y_0]$, the size of the physical domain, we find that the activation of CM close to the body $X_0 = Y_0 = 2$ does not affect much the leading eigenvalue, the relative error of the growth rate is less than 0.3% and the frequency varies less 0.1%. This result is not surprising due to the fact that eigenvalue sensitivity tensor has its support close to the trailing edge of the body, then in the physical domain even for small values of $[X_0, Y_0]$ (see Fig. 17).

7. Conclusion

A novel non-reflecting boundary condition for *linear stability computations*, i.e. modal stability, has been introduced. Complex mapping arises as a spectral transformation of the PDE problem to easily identify the onset of unsteady modes near the threshold by the rotation of the continuous spectrum, see Section 6.2. It is also an artificial boundary treatment that preserves the number of degree of freedoms and it is easy to implement in any numerical code. In the present study, we have discussed the effect of CM in the spectrum of PDE problem, see Section 3. As well, a guideline for the choice of the direction and length of the complex mapping has been introduced in the framework of hydrodynamic and acoustic flow instabilities. Complex mapping avoids the increase of the number of degrees of freedom imposed by buffer layers or Perfectly Matched Layer methods, whereas precision is similar to those as it has been shown in the four numerical cases. Opposed to sponge regions which require enormous domain sizes at low Mach numbers to damp acoustic wave reflections, complex mapping has proved to be much more efficient at this regime. In the hole tone configuration at $M_\infty = 0.05$ the number of degrees of freedom was reduced by at least 50 which demonstrates the usefulness of the methodology, see Section 6.2. It has been also shown in the flow past a NACA 0012 airfoil, Section 6.3, or in

the acoustic circuit of cylindrical pipe, Section 4, the application of a complex mapping layer with a length of fraction around a fourth or a third of the acoustic wavelength is sufficient for the computation of the quantity of interest, i.e. leading eigenvalue, within 1% of error. Moreover, the application of complex mapping to incompressible flows with large amplifications due to convective instabilities allows to mitigate the non local feedback effect between downstream and upstream boundaries due to the elliptic nature of Navier–Stokes equations, see Section 6.1. In those cases, the complex transformation is able to provide sufficient decay to vortical perturbations to alleviate non-local interactions with the outer boundary. The current discussion of the methodology is mainly focused on the study of fluid mechanics instabilities nevertheless, the proposed approach can be used to simulate other wave supporting problems. Here we cite some other physical phenomena, for instance those described by Maxwell’s, Helmholtz, elastodynamic or poroelasticity equations.

Declaration of competing interest

The authors declare that they have no known competing financial interests or personal relationships that could have appeared to influence the work reported in this paper.

Appendix A. Analytical solution of the Ginzburg–Landau model

In this appendix we derive the analytical solution of the Ginzburg–Landau equation:

$$-i\omega\Psi = -U\frac{\partial\Psi}{\partial x} + \kappa\frac{\partial^2\Psi}{\partial x^2} + \mu(x)\Psi \quad (34)$$

with homogeneous boundary conditions: $\psi(0, t) = 0$; $\psi(\infty, t) = 0$, and with a local growth rate defined as $\mu(x) = \mu_\infty + \mu_1 e^{-x/L^*}$, where $\mu_\infty, \mu_1, L^* \in \mathbb{R}$ are parameters of the problem. The local stability of the Ginzburg–Landau equation depends on the local growth rate $\mu(x)$ (see Huerre & Rossi [16, Ch. 3] for more details). The theoretical solution in the physical domain $x \in [0, \infty]$ consists of two kinds of modes:

- First, a *discrete spectrum* corresponding to square-integrable solutions. With our choice for $\mu(x)$, the corresponding modes can be searched in analytical form as

$$\Psi(x) = e^{\frac{Ux}{2\kappa}} \left[A J_s(ae^{-\frac{Ux}{2\kappa}}) + B Y_s(ae^{-\frac{Ux}{2\kappa}}) \right]. \quad (35)$$

where J_s and Y_s are Bessel functions of first and second kinds, $s = 2L^* \sqrt{\frac{U^2}{4\kappa} - \frac{1}{\kappa}(\mu_\infty + i\omega)}$ and $a = 2L^* \sqrt{\frac{\mu_1}{\kappa}}$. The condition that $\Psi(x, \omega)$ should decay at $x \rightarrow \infty$ leads to $B = 0$, and application of the homogeneous Dirichlet boundary condition at $X = 0$ leads to the transcendental equation

$$J_s(a) = 0 \quad (36)$$

which admits discrete solutions corresponding to frequencies ω_n ($n = 1, 2, \dots$) of the discrete modes.

- Secondly, the fact that $\mu(x)$ asymptotes to a constant value μ_∞ for large x leads to the existence of an *essential spectrum*, corresponding to solutions which are not square-integrable but oscillating, with asymptotic form $\psi(x) \approx e^{i\ell x}$ with $\ell \in \mathbb{R}$. Injecting this form in the equation with $\mu(x) \approx \mu_\infty$ leads to the following definition of the essential spectrum:

$$\omega_{ess} = i(\mu_\infty - \kappa\ell^2) + U\ell; \quad \ell \in \mathbb{R}. \quad (37)$$

Convergence of the finite difference discretization. In order to guarantee that the centered second order finite difference discretization does not introduce a systematic error a convergence test is carried out, see Fig. 18. Eigenvalues corresponding to analytical solution are compared with numerical results. The expected second order of convergence is recovered whenever the cell size Δx is sufficiently small.

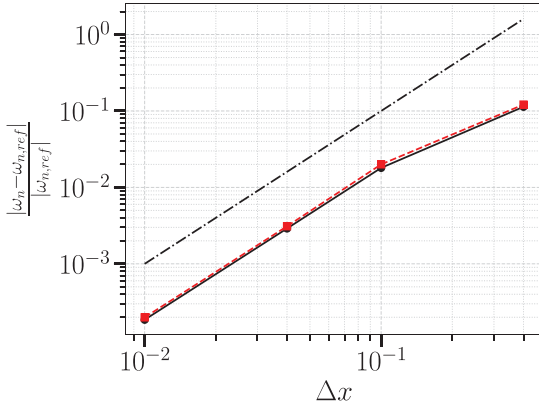


Fig. 18. Convergence test of the centered second order finite difference method for the GL problem. ω_n denotes the n th eigenvalue where $n = 1, 2$ and $\omega_{n,ref}$ are analytical eigenvalues. Solid line (resp. dashed line) corresponds to first (resp. second) eigenvalue. Dashed-dotted line is used to display the asymptotic second order of convergence.

Appendix B. Asymptotic solution for a finite-length acoustic pipe opening to an infinite domain

In this appendix, we derive an asymptotic solution for eigenvalues of the acoustic problem of Section 4 valid for long pipes, namely $L/D \gg 1$. For this sake, we first consider a forced problem, assuming that the pipe is driven at its bottom by a harmonic forcing with frequency $u'_{x,in} = e^{-i\omega t}$. Under this framework, the forced response of the pipe to acoustic forcing can be fully characterized by the inlet impedance

$$\hat{Z}_{in}(\omega) = \frac{p_{in}}{Q_{in}} \quad (38)$$

where $q' = Q_{in}e^{-i\omega t}$ and $p' = p_{in}e^{-i\omega t}$. Moreover, the eigenmodes of the autonomous problem for a pipe closed at the bottom can be tracked as zeros of the impedance. Following the book of Fletcher & Rossing [13], the inlet impedance of the pipe can be expressed in terms of the characteristic impedance $Z_0 = \frac{\rho_\infty c_\infty}{S_{in}}$ and the outlet impedance Z_L :

$$Z_{in} = Z_0 \frac{Z_L \cot(\frac{\omega}{c_\infty} L) + iZ_0}{[iZ_L + Z_0 \cot(\frac{\omega}{c_\infty} L)]} \quad (39)$$

In the asymptotic limit $\lambda/D \gg 1$ where λ is the asymptotic wavelength, the outlet impedance of a circular in a semi-infinite domain has the following expression:

$$Z_L = Z_0 \left[\frac{1}{2} \left(\frac{\omega D}{2c_\infty} \right)^2 + \Delta i\omega/c_\infty \right] \quad (40)$$

where Δ is the so-called correction length given by $\Delta = \frac{8D}{6\pi} \approx 0.425D$.

Therefore, substituting Eq. (40) into Eq. (39):

$$Z_{in} = Z_0 \frac{\frac{1}{2} \left(\frac{\omega D}{2c_\infty} \right)^2 \cot(\frac{\omega}{c_\infty} (L + \Delta)) + i}{\left[\frac{i}{2} \left(\frac{\omega D}{2c_\infty} \right)^2 + \cot(\frac{\omega}{c_\infty} (L + \Delta)) \right]} \quad (41)$$

The eigenvalues of the autonomous problem for a pipe closed at the bottom can be tracked as poles of the impedance (or zeros of the admittance $Y_{in} = Z_{in}^{-1}$). At leading order (neglecting the radiation term) these correspond to $\cot[\frac{\omega}{c_\infty} (L + \Delta)] = 0$, hence

$$\omega^{(0)} = (2n - 1)\pi \frac{c_\infty}{2(L + \Delta)}.$$

A first-order approximation can be obtained by setting $\omega = \omega^{(0)} + \omega^{(1)}$ assuming $|\omega^{(1)}| \ll |\omega^{(0)}|$, and injecting into Y_{in} . This leads to

$\omega^{(1)} = -\frac{Y_{in}(\omega^{(0)})}{[\partial Y_{in}/\partial \omega]_{\omega^{(0)}}}$ which eventually leads to

$$\omega^{(1)} = -\frac{i\pi^2 (2n - 1)^2 c_\infty D^2}{32 (L + \Delta)^3}$$

Appendix C. Acoustic problem

In this section we detail the formulation of the free acoustic problem with Sommerfeld boundary condition at the outer boundary. The linear dependency of Sommerfeld equation (15) on ω forces to add an extra field $\Phi_1 = \frac{\omega}{c_\infty} \Phi$. The subsequent eigenvalue problem reads

$$\nabla^2 \Phi + \frac{\omega}{c_\infty} \Phi_1 = 0 \quad (42a)$$

$$\Phi_1 - \frac{\omega}{c_\infty} \Phi = 0 \quad (42b)$$

$$\text{Sommerfeld: } \frac{\partial \Phi}{\partial r_s} - \left(i\Phi_1 + \frac{\Phi}{r_s} \right) = 0$$

$$\text{where } r_s = \sqrt{r^2 + z^2} \quad \text{at } \Gamma_{out} \quad (42c)$$

Appendix D. Effect of CM on plane-waves

In this section we study how CM affects plane waves. Consider the situation of a wave whose amplitude is A_0 at $X = X_0 + L_c$ and the complex parameter $\gamma_c > 0$ is not sufficiently large to sufficiently decay $k_{H,u}^-$ before the end of the domain. Backward-propagating waves occur, among which k_{ac}^- possess the largest spatial growth rate. In this simplified analysis we take the hypothesis, $k_{i,ac}^- \gg k_{i,H,s}^-$, which is usually the case in shear flows because acoustic waves are oscillating and backward propagating hydrodynamic modes are dominant, thus $k_{i,H,s}^- < 0$. In the following the amplitude of backward propagating wave at $X = X_0 + L_c$ is A_0^{CM} .

$$A_0 e^{-k_{i,H,u}^+ L_{CM} - \gamma_c L_{CM} (k_{r,H,u}^+ - k_{r,ac}^-)} = A_0^{CM} \quad (43)$$

From dispersion relations equation (27) and equation (28) we obtain that γ_c needs to be chosen

$$\gamma_c = \frac{|U_\infty - U_c| (1 - M_\infty)}{(U_\infty + U_c) - M_c (U_\infty - U_c)} - \frac{\ln(\frac{A_0}{A_0^{CM}})}{2\omega L_{CM}} \frac{(1 - M_\infty)(U_\infty^2 + U_c^2)}{(U_\infty + U_c) - M_c (U_\infty - U_c)} \quad (44)$$

where $M_\infty = \frac{U_\infty}{c_\infty}$, $M_c = \frac{U_c}{c_\infty}$. We note that the second term is positive and its absolute value is controlled by the complex mapping length, L_{CM} . We consider the case $M_c \ll 1$, which is equivalent to suppose that the speed of sound is much larger than the velocity difference in the shear layer $c_\infty \gg U_c$. Then the final expression is as follows

$$\gamma_c > (1 - M_\infty) \frac{|U_\infty - U_c|}{(U_\infty + U_c)} \quad (45)$$

Note that in the low Mach limit $M_\infty \rightarrow 0$, Eq. (32) is recovered.

References

- [1] J.-P. Berenger, J. Comput. Phys. 114 (2) (1994) 185–200, <http://dx.doi.org/10.1006/jcph.1994.1159>.
- [2] A. Bermúdez, L. Hervella-Nieto, A. Prieto, R. Rodríguez, J. Comput. Phys. 223 (2) (2007) 469–488, <http://dx.doi.org/10.1016/j.jcp.2006.09.018>.
- [3] F.Q. Hu, X. Li, D. Lin, J. Comput. Phys. 227 (9) (2008) 4398–4424.
- [4] J.P. Whitney, (Ph.D. thesis), Massachusetts Institute of Technology, 2006.
- [5] P. Meliga, F. Gallaire, J.-M. Chomaz, J. Fluid Mech. 699 (2012) 216–262.

- [6] L. Lesshaft, *Theor. Comput. Fluid Dyn.* 32 (3) (2018) 245–262.
- [7] D. Fabre, R. Longobardi, P. Bonnefis, P. Luchini, *J. Fluid Mech.* 864 (2019) 5–44.
- [8] D. Fabre, R. Longobardi, V. Citro, P. Luchini, *J. Fluid Mech.* (2019).
- [9] D. Fabre, V. Citro, D.F. Sabino, P. Bonnefis, J. Sierra, F. Giannetti, M. Pigou, *Appl. Mech. Rev.* 70 (6) (2019) 060802, <http://dx.doi.org/10.1115/1.4042737>.
- [10] F. Teixeira, W.C. Chew, *IEEE Microw. Guid. Wave Lett.* 7 (11) (1997) 371–373.
- [11] G. Schneider, H. Uecker, American Mathematical Soc., vol. 182, 2017.
- [12] T. Kapitula, K. Promislow, vol. 457, Springer, 2013.
- [13] N.H. Fletcher, T.D. Rossing, Springer Science & Business Media, 2012.
- [14] S.H. Schot, *Hist. Math.* 19 (4) (1992) 385–401.
- [15] A. Fani, V. Citro, F. Giannetti, F. Auteri, *Phys. Fluids* 30 (3) (2018) 036102.
- [16] P. Huerre, M. Rossi, *Collection Alea Saclay Monographs and Texts in Statistical Physics*, vol. 1(3), 1998, pp. 81–294.
- [17] R. Henrywood, A. Agarwal, *Phys. Fluids* 25 (10) (2013) 107101.
- [18] D. Fabre, P. Bonnefis, F. Charru, S. Russo, V. Citro, F. Giannetti, P. Luchini, International Symposium on Musical Acoustics (ISMA), Le Mans, France, July, 2014, pp. 7–12.
- [19] R. Longobardi, D. Fabre, P. Bonnefis, V. Citro, F. Giannetti, P. Luchini, IU-TAM Symposium on Critical Flow Dynamics Involving Moving/deformable Structures With Design Applications, 2018.
- [20] J. Sierra, D. Fabre, V. Citro, International Symposium on Fluid-Structure-Sound Interactions and Control (FSSIC), Crete, Greece, August, 2019.
- [21] W. Zhang, R. Samtaney, *Phys. Fluids* 27 (5) (2015) 055101.
- [22] W. Zhang, R. Samtaney, *Phys. Fluids* 28 (4) (2016) 044105.

CHAPTER **IX**

**Articles – Linear stability
with moving interfaces**



Contents lists available at ScienceDirect

Journal of Fluids and Structures

journal homepage: www.elsevier.com/locate/jfs

Linear stability analysis of fluid–structure interaction problems with an immersed boundary method



Antonia Tirri^a, Alessandro Nitti^a, Javier Sierra-Ausin^{b,c}, Flavio Giannetti^b, Marco D. de Tullio^{a,*}

^a Department of Mechanics Mathematics and Management, Polytechnic University of Bari, Via Re David 200, Bari, 70125, Italy

^b Department of Industrial Engineering, University of Salerno, Via Giovanni Paolo II 132, Fisciano, 84084, Italy

^c Institut de Mécanique des Fluides de Toulouse - IMFT, 2 allée du Pr. Camille Soula, Toulouse, 31400, France

ARTICLE INFO

Article history:

Received 24 June 2022

Received in revised form 4 December 2022

Accepted 23 December 2022

Available online xxx

Keywords:

Linear stability analysis

Immersed-boundary method

Fluid–structure interaction

Jacobian-free methods

ABSTRACT

In this work, we present a novel approach to perform the linear stability analysis of fluid–structure interaction problems. The underlying idea is the combination of a validated immersed boundary solver for the nonlinear coupled dynamics with Krylov-based techniques to obtain a robust and accurate global stability solver for elastic structures interacting with incompressible viscous flows. The computation of the leading eigenvalues of the linearized system is carried out in a matrix-free framework by adopting a classical Krylov subspace method. The proposed algorithm avoids the complex analytical linearization of the equations while retaining all the relevant aspects of the fully-coupled fluid–structure system.

The methodology has been tested for several cases involving two-dimensional incompressible flows around elastically mounted circular cylinders. The obtained results show a good quantitative agreement with those available in the literature. Finally, the method was applied to investigate the linear stability of the laminar flow past two elastically mounted cylinders in tandem configuration at $Re = 100$, revealing the existence of two complex dominant modes. For low values of the reduced velocity U^* , only one mode is found to be unstable and related to the stationary wake mode. The loss of stability of the second mode at $U^* = 4$ marks the beginning of the lock-in region. We also show that for $U^* = 5$ the modes interact, giving rise to the beating phenomenon observable in the nonlinear time evolution of the system. For larger values of the reduced velocity, the linear dynamics is governed by one dominant mode characterized by wider oscillations of the rear cylinder, matching the results of the nonlinear simulations.

© 2022 Elsevier Ltd. All rights reserved.

1. Introduction

The interaction of elastic bodies with incompressible flows has attracted the interest of many researchers since the pioneering studies on aeroelasticity (Theodorsen, 1934; Kornecki et al., 1976). These configurations are encountered in a large variety of engineering applications, spanning from biomedical devices (de Tullio et al., 2009; Borazjani, 2013) to energy harvesting systems (Doaré and Michelin, 2011; Grouthier et al., 2014; Nitti et al., 2022) and unmanned underwater vehicles (Tangorra et al., 2007; Mansoorzadeh and Javanmard, 2014). Such systems are prone to several types of instability

* Corresponding author.

E-mail address: marcodonato.detullio@poliba.it (M.D. de Tullio).

and, despite their complex nonlinear behavior, the early stages of the transition between two distinct dynamical states can often be explained in terms of the excitation of a linearly unstable mode. While being a well-established technique for investigating fluid flows (Theofilis, 2011), linear stability analysis (LSA) has been adopted quite recently for cases involving fully coupled fluid–structure interactions (FSI), mainly to provide insights into the physical mechanisms associated with the emergence of flow-induced oscillations and to design control strategies able to suppress them.

The first examples of linear stability analyses over FSI configurations date back to the pivotal studies of Theodorsen (1934) on the flutter instability of an aerodynamic section. Theodorsen formulation was based on the potential flow and slender body assumptions. While the adoption of these simplified flow models is legitimate in the field of classical aeronautics, applications involving low to medium Reynolds numbers or flow separation require the simultaneous solution of the linearized Navier–Stokes equations coupled with the linearized equation of motion of the elastic solid.

Cossu and Morino (2000) were the first to perform a linear stability analysis of a two-dimensional low Reynolds number flow interacting with an elastically-mounted bluff body. They investigated the primary instability of a circular cylinder, which was free to oscillate in the cross-flow direction by solving the linearized flow equations in a moving reference frame. Navrose and Mittal (2016) adopted the same approach with a non-inertial frame of reference to conduct a parametric study of the lock-in phenomenon exhibited by elastically-mounted circular cylinders in the laminar flow regime. Cossu and Morino (2000) reported a critical Reynolds number half the value obtained for the fixed cylinder case with low solid-to-fluid density ratios. Meliga and Chomaz (2011) extended the stability analyses to smaller mass ratios ($\mathcal{O}(10^{-4})$). The numerical technique employed therein consisted in a multiple-time-scale expansion to decouple fluid and solid dynamics at the leading order of the perturbation.

More recently, Pfister et al. (2019) adopted a Lagrangian-based approach to derive a linearization of the equations of motion for a coupled fluid–structure problem written in an Arbitrary-Lagrangian–Eulerian (ALE) framework. This formulation becomes cumbersome when it is based on the Lagrangian motion of the structure, requiring important modifications in the residual of the Navier–Stokes equations to take into account the motion of the mesh. Fernández and Le Tallec (2002) proposed, instead, an Eulerian-based formulation in an attempt to overcome the difficulties arising from a moving grid. In their formulation, obtained starting from the weak form of the ALE equations, the coupling between the flow and the solid is made via a transpiration technique. Although reducing considerably the complexity of the problem, this method produces additional stress contributions at the interface, termed *added stiffness*, that depend on higher-order derivatives of the flow variables. Negi et al. (2020) followed the same methodology but performed the linearization of the equations of motion in their integral form.

Moulin et al. (2017) suggested the use of non-conforming methods to investigate the stability of strongly coupled FSI systems, discussing, in particular, the adoption of a fictitious domain formulation to handle the coupling between the fluid and the solid. Goza et al. (2018), who also proposed a non-conforming approach, conducted a global stability analysis of inverted flags submerged in uniform flows using an Immersed Boundary (IB) method. They resorted to the numerical derivation of the Jacobian matrix linearizing the discretized operators around the steady state via a first-order finite difference scheme. The memory requirements with matrix-forming strategies become rapidly unfeasible when dealing with a large number of degrees of freedom, e.g., three-dimensional FSI configurations. This aspect is even more relevant in the computation of neutral curves since the Jacobian matrix must be re-evaluated for each base flow.

In this work, we propose an alternative procedure to study the linear stability characteristics of FSI systems by adopting a Jacobian-free approach (Mettot et al., 2014). Matrix-free strategies lead to significant memory savings at the cost of longer integration times. In contrast, they provide access to only a subset of the spectrum associated with the eigenvalue problem (EVP) that originates from the classic normal-mode approach. Nonetheless, the accessible portion of the spectrum is generally the most relevant, consisting of the most unstable eigenvalues.

In the present article, we adopt a time-stepping methodology that makes use of high-fidelity nonlinear simulations obtained with a direct-forcing IB method, based on a moving-least-square (MLS) approach. One of the main advantages of the IB formulation resides in the fact that it can handle multi-body configurations with no additional complexity. In addition, the fluid equations are resolved on a staggered Cartesian grid, which makes the method prone to a simple parallel implementation for three-dimensional computations.

The choice of the specific IB forcing technique is crucial for the success of the computation. It has been noted that the use of a sharp forcing field usually leads to the appearance of unphysical fluctuations of the hydro-dynamical force acting on the solid body (Uhlmann, 2003). Seo and Mittal (2011) attribute the emergence of pressure oscillations to an unintended *transpiration* effect at the immersed boundary, due to the fact that the role of the Eulerian nodes close to the interface can change from a time-step to the next as the body moves. These spurious oscillations can be suppressed by spreading the forcing term over a wider stencil through the use of a smoother Lagrangian–Eulerian transfer function (Yang et al., 2009). In view of these considerations, and after a few trials, we adopted an MLS forcing procedure that provides a good trade-off between accuracy and robustness. Details on the IB treatment are provided in the next section.

The proposed strategy involves the adoption of the matrix exponential, first introduced by Eriksson and Rizzi (1985) in the context of global stability analysis. In their paper, the authors proposed to approximate the action of the Jacobian matrix via finite differences to investigate the instability of the transonic flow over an airfoil, a phenomenon modeled by the two-dimensional Euler equations. They also highlighted the need for a matrix transformation to retrieve the least stable portion of the spectrum of the discrete operator. The same approach was later extended to the full Navier–Stokes equations by Chiba (1998), who performed a linear stability analysis of the two-dimensional square lid-driven cavity flow,

and by Tezuka and Suzuki (2006), who carried out a TriGlobal stability analysis (Theofilis and Colonius, 2011) of the flow around various spheroids.

Gómez et al. (2011) incorporated the approach of Tezuka and Suzuki (2006) into publicly-available computational fluid dynamics (CFD) solvers, highlighting the flexibility of the method that looks at the CFD solver as a black-box source. In a successive paper (Gómez et al., 2015), Gomez et al. extended that work by inserting a shift-invert strategy to grant access to specific portions of the spectrum. Our contribution builds on the above-mentioned series of papers and provides an extension of Chiba's approach to FSI problems.

This paper is organized as follows. First, in Section 2, we introduce the problem of linear stability in the context of fluid–structure interaction and derive the theoretical foundations of the methodology. Numerical validation of the solver is presented in Section 3, together with the results obtained by applying the presented strategy to the problem of flow-induced vibrations of two cylinders in tandem. In Section 4, the main results and conclusions are summarized.

2. Methodology

In this work, the discussion is restricted to the motion of elastically-mounted rigid bodies immersed in a two-dimensional incompressible viscous flow, although the derived method remains completely general.

2.1. Governing equations

The governing equations of the flow dynamics are the incompressible Navier–Stokes equations, written in the dimensionless form:

$$\begin{aligned} \frac{\partial \mathbf{u}}{\partial t} + \mathbf{u} \cdot \nabla \mathbf{u} &= -\nabla p + \frac{1}{Re} \nabla^2 \mathbf{u} + \mathbf{f}, \\ \nabla \cdot \mathbf{u} &= 0, \end{aligned} \quad (1)$$

where \mathbf{u} and p denote the fluid velocity and pressure, respectively. The body force term \mathbf{f} , in the absence of other external fields, corresponds to the IB body-force field. Eq. (1) is closed by appropriate boundary conditions related to the specific considered configuration. Flow variables have been made dimensionless by considering a reference length L_r and velocity scale U_r ; the Reynolds number is defined as $Re = (U_r L_r)/\nu$, with ν the kinematic viscosity of the fluid.

The structure is modeled as a rigid body with the elastic center coincident with the center of mass. Its motion is governed by Newton's second law for the i th degree of freedom:

$$\ddot{x}_i + \frac{\sigma_i}{A_i^* \rho^*} \dot{x}_i + \frac{k_i}{A_i^* \rho^*} (x_i - x_i^{eq}) = C_i, \quad i = 1, \dots, n_{DOF} \quad (2)$$

where the variables have been made dimensionless by means of the bulk parameters of the flow field.

The system of equations given by (2) represents a spring–mass–damper system where σ_i and k_i are, respectively, the non-dimensional linear damping and stiffness coefficients of the i th degree of freedom (DOF), x_i^{eq} is the equilibrium position of the i th spring and n_{DOF} gives the total number of degrees of freedom. For instance, $n_{DOF} = 3$ in two-dimensional problems, comprising the two components of the displacement and the rigid rotation around the center of mass. The term $A_i^* \rho^*$ represents the non-dimensional mass coefficient. In two dimensions, for the translational DOFs, A_i^* corresponds to A^* , which is the ratio of the cross-sectional area of the body to the square of the reference length, L_r . For the rotational DOF, $A_i^* = I^*$, which is the second moment of area with respect to the centroidal axis divided by the fourth power of L_r . The coefficient C_i represents the non-dimensional force (or torque) acting upon the i th DOF.

In the examples illustrated throughout this work, the effect of gravity has been neglected and the only contribution to the forcing term in the body equations comes from the interaction with the flow. That being the case, the behavior of a rigid body with only one degree of freedom is governed by two dimensionless parameters: the density ratio $\rho^* = \rho_s/\rho_f$, which is the ratio of solid to fluid density, and the reduced velocity $U^* = \sqrt{(A_1^* \rho^* 4\pi^2)/k_1}$, representing the ratio of two characteristic time scales of the problem, *i.e.*, the period of the natural mode of the body and that of the convective motions of the flow.

2.2. Time stepping - Pressure-segregation algorithm

The Navier–Stokes equations (1) are integrated in time through a semi-implicit procedure (Nitti et al., 2020), where the convective and viscous terms are discretized by a third-order Runge–Kutta (RK) and a Crank–Nicolson scheme, respectively. Each substep is resolved by means of a classical fractional-step method,

$$\begin{aligned} \hat{\mathbf{u}} &= \hat{\varphi}_{\Delta t}^{[1]} \mathbf{u}^k, \\ \tilde{\mathbf{u}} &= \varphi_{\Delta t}^{[1]} \mathbf{u}^k, \\ \mathbf{u}^{k+1} &= \varphi_{\Delta t}^{[2]} \tilde{\mathbf{u}} = \left(\varphi_{\Delta t}^{[2]} \circ \varphi_{\Delta t}^{[1]} \right) \mathbf{u}^k, \end{aligned} \quad (3)$$

where \mathbf{u}^k is the velocity field at the k th RK substep, $\hat{\mathbf{u}}$ is an intermediate velocity field that does not satisfy the interface conditions, $\tilde{\mathbf{u}}$ is a provisional field that is globally divergence-free, but not locally, and \mathbf{u}^{k+1} is the updated velocity field at the $(k + 1)$ th substep. The preliminary velocity $\hat{\mathbf{u}}$ is computed explicitly via the discrete flow $\hat{\varphi}_{\Delta t}^{[1]}$,

$$\hat{\varphi}_{\Delta t}^{[1]}\mathbf{u}^k \equiv \mathbf{u}^k + \Delta t \left[-\alpha^k \nabla p^k + \frac{\alpha^k}{Re} \nabla^2 \mathbf{u}^k + \beta^k H^k + \gamma^k H^{k-1} \right], \quad (4)$$

where H represents the nonlinear terms $\mathbf{u} \cdot \nabla \mathbf{u}$ and α^k , β^k and γ^k are the coefficients of the time scheme (see Nitti et al. (2020) for details). The computed field is next used to evaluate the IB forcing \mathbf{f} , whose detailed description is left to Section 2.2.1. Then, the provisional velocity field $\tilde{\mathbf{u}}$ is computed by solving the Helmholtz equation

$$\left(1 - \frac{\alpha^k \Delta t}{2Re} \nabla^2 \right) \Delta \tilde{\mathbf{u}} = \hat{\mathbf{u}} - \mathbf{u}^k + \Delta t \mathbf{f}(\hat{\mathbf{u}}), \quad (5)$$

where $\Delta \tilde{\mathbf{u}} = \tilde{\mathbf{u}} - \mathbf{u}^k$. The discrete flow $\varphi_{\Delta t}^{[1]}$ is defined as

$$\varphi_{\Delta t}^{[1]}\mathbf{u}^k = \mathbf{u}^k + \left(1 - \frac{\alpha^k \Delta t}{2Re} \nabla^2 \right)^{-1} (\hat{\mathbf{u}} - \mathbf{u}^k + \Delta t \mathbf{f}(\hat{\mathbf{u}})) \quad (6)$$

Finally, the pressure is updated according to

$$p^{k+1} = p^k + \left(1 - \frac{\alpha^k \Delta t}{2Re} \nabla^2 \right) p^*, \quad (7)$$

with the scalar quantity p^* resulting from the solution of the Poisson equation,

$$\nabla^2 p^* = \frac{\nabla \cdot \tilde{\mathbf{u}}}{\alpha^k \Delta t}. \quad (8)$$

The RHS of Eq. (8) enforces the continuity of the final velocity field \mathbf{u}^{k+1} , given by the discrete flow $\varphi_{\Delta t}^{[2]}$,

$$\mathbf{u}^{k+1} = \varphi_{\Delta t}^{[2]}\tilde{\mathbf{u}} \equiv \tilde{\mathbf{u}} - \alpha^k \Delta t \nabla p^*. \quad (9)$$

A second-order-accurate spatial discretization is achieved using centered finite differences in a non-uniform staggered Cartesian grid.

Given the time-splitting nature of the fractional-step approach, the boundary conditions at the fluid–structure interface are enforced on an intermediate non-solenoidal velocity field. This imposition is subsequently spoiled in the corrector step to enforce local continuity (Fadlun et al., 2000); however, the modification of the interface velocity caused by the correction step can be minimized through a repetition of the forcing procedure after the solution of the Helmholtz equation (5). Observations have shown that the discrepancy between the interpolated final fluid velocity and the local body velocity is effectively reduced with three to five iterations of the forcing procedure (Breugem, 2012), up to a root-mean-square error equal to $\sim \mathcal{O}(10^{-5})$.

Within the present method, the local difference between the interpolated fluid velocity and the solid velocity employed in the forcing stage is measured downstream of the time-scheme, and its Root Mean Square (RMS) is evaluated over the set of Lagrangian markers (see Section 2.2.1). In presence of moving surfaces, the RMS error is found to be $\sim \mathcal{O}(10^{-4})$ of the freestream velocity (see fig. 11 of Nitti et al. (2020)).

The equations of motion for the rigid body are integrated in time by means of a Crank–Nicolson scheme. Within this staggered approach, at each sub-step, the fluid, and structural systems are solved in a sequential fashion: first, a low-order extrapolation for the fluid–solid interface position and velocity is employed in the IB procedure to advance the flow field in time; then the coupling between fluid and rigid-body dynamics is accomplished using the Eulerian load distribution \mathbf{f} coming from the IB procedure to obtain the total force and moment integrals (Lācis et al., 2016; chih Lai and Peskin, 2000) in the RHS of Newton's equations (2). This procedure avoids the integration of pressure and viscous stresses on the contour of the body, circumventing the need for a reconstruction procedure. When the density ratio ρ^* is close to unity, a strong coupling of the fluid and solid solutions may be needed (Förster et al., 2007). For the majority of the examples presented, a weak coupling between the fluid and structural systems was able to capture the dynamics with sufficient accuracy. A strong iterative coupling was employed for the tandem cylinders case presented in Section 3.3, for which $\rho^* = 2.546$. Within this simple iterative approach, we measure the L^∞ norm of the relative difference in the body displacement between two successive iterations and iterate until its value is below the convergence tolerance $tol = 10^{-8}$. The method usually converges within two to six iterations. For the investigated cases, though, the loosely and strongly coupled algorithms yield negligible differences, as shown in fig. 9 of Borazjani and Sotiropoulos (2009) within a similar IB-FSI framework.

The simulations employed for the stability calculations were performed with a fixed time-step taken small enough to keep the CFL condition around the value of 0.2, in order to capture the FSI dynamics with sufficient accuracy for all explored configurations. The average spacing between adjacent Lagrangian markers was set equal to $0.5 \Delta x_{loc}$, where Δx_{loc} is the local Eulerian cell dimension. Further details on the method can be found in Nitti et al. (2020).

2.2.1. Immersed boundary procedure

The boundary conditions at the fluid–structure interface are imposed on the provisional velocity field using a direct-forcing immersed boundary technique. Following Uhlmann (2005), body-force terms are computed over a set of suitably spaced Lagrangian markers laying on the immersed surface. Each velocity component is interpolated at the Lagrangian markers via an MLS approximation (Vanella and Balaras, 2009),

$$\hat{V}_i(\mathbf{x}^l) = \Psi^T(\mathbf{x}^l)\hat{\mathbf{u}}_i, \tag{10}$$

where $\hat{\mathbf{u}}_i$ is the array that collects the i th velocity component at the face centers within the support domain (see Fig. 1) of each Lagrangian marker and \hat{V}_i is the i th velocity component at the Lagrangian position \mathbf{x}^l . In two dimensions, the minimum number of grid cells n_e contained in the support domain is equal to 9. The linear operator $\Psi^T(\mathbf{x}^l)$ is defined as

$$\Psi^T(\mathbf{x}^l) \equiv \mathbf{p}^T(\mathbf{x}^l)(\mathbf{A}(\mathbf{x}^l))^{-1}\mathbf{B}(\mathbf{x}^l), \tag{11}$$

where

$$\begin{aligned} \mathbf{p}^T(\mathbf{x}^l) &= [1, x^l, y^l], \\ \mathbf{A}(\mathbf{x}^l) &= \sum_{k=1}^{n_e} W(\mathbf{x}^l - \mathbf{x}^k) \mathbf{p}(\mathbf{x}^k) \mathbf{p}^T(\mathbf{x}^k), \\ \mathbf{B}(\mathbf{x}^l) &= [W(\mathbf{x}^l - \mathbf{x}^1)\mathbf{p}(\mathbf{x}^1) \dots W(\mathbf{x}^l - \mathbf{x}^{n_e})\mathbf{p}(\mathbf{x}^{n_e})]. \end{aligned} \tag{12}$$

The weight function $W(\mathbf{x}^l - \mathbf{x}^k)$ plays the role of a convolution kernel. Throughout this work, the exponential function is used,

$$W(\mathbf{x}^l - \mathbf{x}^k) = \begin{cases} e^{-(r_k/\epsilon)^2} & \text{for } r_k \leq 1 \\ 0 & \text{for } r_k > 1 \end{cases} \tag{13}$$

where $r_k = |\mathbf{x}^l - \mathbf{x}^k|/r_i$, with r_i the size of the support domain in the i th direction and $\epsilon = 0.3$. A volume force component is then computed for each Lagrangian marker l ,

$$F_i^l = \frac{V_i^l - \hat{V}_i(\mathbf{x}^l)}{\Delta t}, \tag{14}$$

where V_i^l is the i th component of velocity to be imposed at the interface and Δt is the time-step of the numerical scheme. Finally, the forcing term to be added to the RHS of the Navier–Stokes equations (1) is computed at each Eulerian grid point using again the shape functions of the interpolation procedure

$$f_i^k = \sum_{l=1}^{n_l} c_l \Psi_k^l F_i^l, \tag{15}$$

where f_i^k is the i th component of the forcing for the k th Eulerian grid point, n_l is the number of Lagrangian markers whose support domain contains the selected Eulerian point and c_l is a scaling coefficient (see Nitti et al. (2020) for details).

2.3. Linear stability

In this section, we focus on the linear stability of the coupled system. After spatial discretization, fluid and solid variables are collected into the state vector \mathbf{q} , and the problem is reformulated as

$$\frac{d\mathbf{q}}{dt} = \mathbf{R}(\mathbf{q}), \tag{16}$$

where \mathbf{R} is the nonlinear evolution operator of the system. The linear stability of a steady-state \mathbf{q}_b of the system ($\mathbf{R}(\mathbf{q}_b) = \mathbf{0}$) can be studied by observing the evolution in time of a small-amplitude perturbation, $\epsilon \mathbf{q}'$, superimposed on the base state ($\mathbf{q}(t) = \mathbf{q}_b + \epsilon \mathbf{q}'(t)$). By injecting this decomposition into (16) and retaining only the first-order terms, the evolution of \mathbf{q}' is governed by

$$\frac{d\mathbf{q}'}{dt} = \left. \frac{\partial \mathbf{R}}{\partial \mathbf{q}} \right|_{\mathbf{q}_b} \mathbf{q}' = \mathbf{J}(\mathbf{q}_b)\mathbf{q}', \tag{17}$$

where $\mathbf{J}(\mathbf{q}_b)$ is the linear Jacobian operator evaluated with respect to the steady-state \mathbf{q}_b . Following the traditional normal-mode approach, the stability characteristics of the system are deduced from the spectrum of the Jacobian operator,

$$\mathbf{q}'(t) = \hat{\mathbf{q}} e^{\omega t} + \text{c.c.} \tag{18}$$

$$(\mathbf{J}(\mathbf{q}_b) - \mathbf{I}\lambda) \hat{\mathbf{q}} = 0 \tag{19}$$

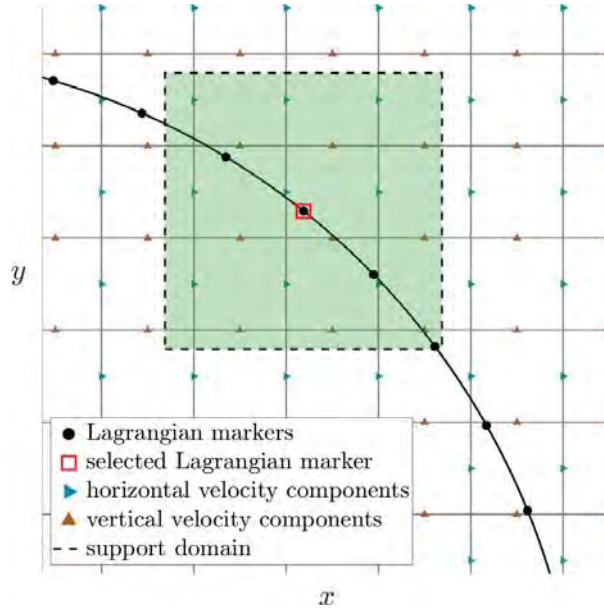


Fig. 1. Scheme of the IB forcing. The Eulerian nodes contained in the support domain of the selected marker are involved in the forcing procedure.

where ω is a complex eigenvalue, $\hat{\mathbf{q}}$ is the spatial structure of the related eigenmode and *c.c.* indicates the complex conjugate. For an autonomous system, the exact solution of the linear initial value problem expressed by Eq. (17) is given by

$$\mathbf{q}'(t_0 + T) = e^{\mathbf{J}(\mathbf{q}_b)^T T} \mathbf{q}'(t_0) = \Phi(T) \mathbf{q}'(t_0), \quad (20)$$

where the operator Φ is known as the *exponential propagator* of the system. Injecting into Eq. (20) the modal decomposition, we get the following eigenvalue problem

$$\mu \hat{\mathbf{q}} = \Phi(T) \hat{\mathbf{q}}. \quad (21)$$

The eigenvalues of the two problems are related through the exponential transformation $\mu = e^{\omega T}$, while the eigenvectors remain unchanged. The asymptotic linear stability properties of the system are dictated by the module of the eigenvalues μ . If all eigenvalues have $|\mu| < 1$, the system is linearly stable, while it is unstable if at least one eigenvalue has $|\mu| > 1$. For $|\mu| = 1$, the system is neutrally stable. The exponential transformation alters the spectrum in such a way that the *dominant* eigenvalues, *i.e.* the eigenvalues of largest modulus, correspond to the leading ones in the original eigenvalue problem, where with the term *leading*, we refer to the eigenvalues with the largest real parts.

2.3.1. Numerical strategy

The problem of linear stability is now reduced to finding the eigenvalues of an $N \times N$ matrix Φ , where the dimension N is given by the number of cells or nodes of the discretized domain times the number of flow variables, plus the degrees of freedom of the body. For real-world systems, the explicit calculation (and storage) of the matrix exponential often carries a prohibitive computational load and one must resort to iterative algorithms, such as those belonging to the class of Krylov-subspace projection methods. In these algorithms, an M -dimensional Hessenberg matrix \mathbf{H} (with $M \ll N$) approximates the matrix exponential in a low-dimensional Krylov subspace, which is constructed via the repeated action of operator Φ on a given starting vector. The eigenvalues of the Hessenberg matrix, the so-called *Ritz values*, constitute an approximation of the eigenvalues of the exponential matrix.

Given the matrix-free framework of this method, we aim at the approximation of the action of Φ on a perturbation vector. In doing so, we introduce the propagator $\mathbf{F}(\mathbf{q})$ of the complete solution,

$$\mathbf{q}(t_0 + T) = \mathbf{F}(\mathbf{q}_0, T), \quad (22)$$

where $\mathbf{q}_0 = \mathbf{q}(t = t_0)$ is the value assumed by the state vector \mathbf{q} at a given time $t = t_0$ and $\mathbf{q}(t_0 + T)$ represents its evolution after a time T . The solution at time $t = t_0$ can be expressed as the superposition of the previously defined steady-state \mathbf{q}_b and a small amplitude deviation for this base state $\epsilon \mathbf{q}'(t_0)$. A Taylor expansion of operator \mathbf{F} around the base state \mathbf{q}_b yields

$$\mathbf{F}(\mathbf{q}_b + \epsilon \mathbf{q}'(t_0), T) = \mathbf{F}(\mathbf{q}_b, T) + \left. \frac{\partial \mathbf{F}(\mathbf{q}, T)}{\partial \mathbf{q}} \right|_{\mathbf{q}_b} \epsilon \mathbf{q}'(t_0) + O(\epsilon^2), \quad (23)$$

where $\epsilon \mathbf{q}'(t_0)$ represents a small deviation from the base state.

It can be shown that the second term on the RHS is, up to the scalar ϵ , an approximation of $(\mathbf{q}'(t_0 + T) - \mathbf{q}'(t_0))$ for small values of T . The details of this derivation are provided in [Appendix A](#).

Substituting the derivative of $\mathbf{F}(\mathbf{q}, T)$ into the RHS of (23) and neglecting higher order terms in ϵ , we get an expression for evaluating the advancement in time of the perturbation based only on the propagator of the complete solution,

$$\mathbf{q}'(t_0 + T) \approx \frac{\mathbf{F}(\mathbf{q}_b + \epsilon \mathbf{q}'(t_0), T) - \mathbf{F}(\mathbf{q}_b, T)}{\epsilon}. \quad (24)$$

Taking the limit of Eq. (24) as $\epsilon \rightarrow 0$, the RHS gives a Gateaux derivative of \mathbf{F} at \mathbf{q}_b ,

$$\lim_{\epsilon \rightarrow 0} \frac{\mathbf{F}(\mathbf{q}_b + \epsilon \mathbf{q}'(t_0), T) - \mathbf{F}(\mathbf{q}_b, T)}{\epsilon}. \quad (25)$$

In a discrete context, the action of the time-marching matrix of the perturbation can be recovered through a finite difference that only involves calls to the time-stepping scheme described in Section 2.2 (here we have adopted the same nomenclature to refer to both discrete and time-continuous operators). Selecting a small but non-zero value of ϵ , the derivative given by (25) can be approximated by

$$\frac{\mathbf{F}(\mathbf{q}_b + \epsilon \mathbf{q}_p(t_0), n\Delta t) - \mathbf{F}(\mathbf{q}_b, n\Delta t)}{\epsilon}, \quad (26)$$

where \mathbf{q}_p represents the perturbation vector in the discrete system. For ease of notation, we employ the same notation \mathbf{q}_b to refer to both the continuous and discrete base state. The parameter n is the number of time-steps by which the solution is advanced in time and Δt is simply the time-step of the scheme, chosen according to the desired CFL condition.

A better approximation of (25) can be built via higher-order finite differences. In the present work, we employ a second-order finite difference to approximate the evolution of a given perturbation $\mathbf{q}_p(t_0)$:

$$\mathbf{q}_p(t_0 + n\Delta t) = \frac{\mathbf{q}_+ - \mathbf{q}_-}{2\epsilon}, \quad (27)$$

where \mathbf{q}_+ and \mathbf{q}_- are the results of two separate calls to the FSI solver, advancing in time the base state after the addition and subtraction, respectively, of the same small perturbation:

$$\mathbf{q}_+ = \mathbf{F}(\mathbf{q}_b + \epsilon \mathbf{q}_p(t_0), n\Delta t), \quad (28)$$

$$\mathbf{q}_- = \mathbf{F}(\mathbf{q}_b - \epsilon \mathbf{q}_p(t_0), n\Delta t). \quad (29)$$

Although such an approach presents the disadvantage of requiring two calls to the time-stepper, it reduces the number of required iterations by providing a more accurate estimate for the matrix–vector product ([Knoll and Keyes, 2004](#)).

We can compute a set of the least stable eigenvalues via a Krylov projection method. In this work, approximations to the leading eigenvalues of the system are computed using the *implicitly restarted Arnoldi method* (IRAM) ([Sorensen, 1992](#)) as implemented in the ARPACK open source package ([Lehoucq et al., 1998](#)).

The base states here considered are equilibrium solutions of the fully coupled nonlinear system, therefore their evaluation requires the solution of a nonlinear algebraic system.

For large-scale problems, a pure Newton–Raphson method is prohibitive because of the size of the systems, hence the most common approach to overcome this difficulty is the use of a Newton–Krylov technique. In this work, the base state for each test case was computed using *BoostConv* ([Citro et al., 2017](#)), an iterative residual recombination procedure belonging to the class of Krylov methods.

The choice of such an algorithm fits perfectly into our matrix-free approach since *BoostConv* can be easily applied as a black-box procedure requiring only several calls to a pre-existing time-marching algorithm, without any modification.

The outline of the algorithm is shown below:

1. The base flow is computed via *BoostConv* ([Citro et al., 2017](#))
2. Arnoldi iterations are performed until the desired convergence is reached: ($k = 1, 2, \dots$)
 - (a) Vector \mathbf{q}_p^k is generated
 - (b) Reverse communication ([Lehoucq et al., 1998](#)) with the flow solver provides $\mathbf{q}_p^k = \frac{\mathbf{q}_+ - \mathbf{q}_-}{2\epsilon}$
 - (c) Convergence of the desired Ritz pairs is checked
3. A logarithmic transformation is performed to recover the original eigenvalues: $\lambda = (\log |\mu| + i \arg(\mu)) (n\Delta t)^{-1}$.

For all cases shown in this article, a non-zero pseudo-random perturbation has been employed as a starting vector for the Arnoldi iterations, respecting the divergence constraint on the velocity. It is worth pointing out that the present approach circumvents the need to select appropriate boundary conditions for the perturbation field, while the boundary conditions of the nonlinear evolution problem are included in the discrete operator \mathbf{F} .

Some remarks on the effect of the IB interface on the linear results. With the IB approach, the solid–fluid interface is enforced by a time-varying distribution of forcing terms that mimics the effect of the body on the flow. Since, in general, the interface does not coincide with the grid lines, the need for an interpolation procedure arises. The way this transfer of information is done defines the specific variant of the IB method.

In the presence of a moving interface, the choice of the interpolation scheme is even more important. It has been noted, for instance, that non-physical force oscillations arise, in this case, with some variants of the IB method (Yang et al., 2009), like the discrete Delta function formulation. Complications emerge also with the Cartesian grid (or cut-cell) approach, in which the fluid–solid interface is sharply tracked, in view of the fact that the role of the grid points near the interface can change from time-step to time-step (Yang and Balaras, 2006) (*i.e.* a grid point that belongs to the portion of the domain occupied by the solid at a given time-step can drop out of the body contour at the next time-step and viceversa). While the role of the node changes, it still carries the physical information about its previous phase, consequently, the local pressure field is strongly perturbed.

The choice of the above-described MLS technique, among the diverse options belonging to the class of non-conforming methods, is motivated by the need for a smooth transfer between Lagrangian and Eulerian nodes (Vanella and Balaras, 2009; Uhlmann, 2003). Indeed, the emergence of non-physical pressure oscillations in the nonlinear solution would have a detrimental impact on the accuracy of Eq. (27), involved in the computation of the linear modes with respect to the steady-state. The present method shows reduced spurious oscillations in the vicinity of the interface due to the fact that the IB forcing field is slightly smeared within the compact support of the MLS interpolation.

One issue of interest is to what extent the smeared representation of the interface affects the accuracy of the computation for higher Reynolds number flows. The wall-resolved computation of the viscous shear layer in presence of moving immersed boundaries is still an open research area. One way to improve the local accuracy with reasonable computational expense within an IB framework is to employ a locally refined semi-structured grid (Durbin and Iaccarino, 2002; de Tullio et al., 2007) in order to increase the grid resolution near the body. It is worth recalling that the present method relies on the linearization of the system around steady solutions of the Navier–Stokes equations, which usually exist for sufficiently low Reynolds numbers.

Another point to be considered is the effect of the IB treatment on the evaluation of the finite difference in Eq. (27) itself. When the position of a given Lagrangian marker falls into a certain grid cell in the solution \mathbf{q}_+ and into an adjacent cell in \mathbf{q}_- , the subtraction $(\mathbf{q}_+ - \mathbf{q}_-)$ involves grid points that are included in the support domain of the marker in one case and left out in the other. To avoid this problem, the support domain of each marker is kept fixed during the evaluation of \mathbf{q}_+ and \mathbf{q}_- , such that the forced fluid cells are the same in the two solutions. The corresponding marker is prevented from falling outside of the fixed support owing to the short integration time T and the small scaling factor ϵ employed in the linearization procedure. In this way, the procedure provides an accurate and robust computation of leading modes with a finite difference approach.

2.3.2. Selection of the linearization parameters

One critical aspect of the presented procedure is the selection of the linearization parameters, *i.e.*, the integration period $T = n\Delta t$ and the perturbation scaling factor ϵ .

The choice of the integration time is somewhat problem dependent. As reported by Goldhirsch et al. (1987), for a given number of requested eigenvalues k , the order of the error related to the model reduction is given by $|e^{(\lambda_k - \lambda_M)T}|$. This means that the accuracy can be improved either by increasing the number of integration time steps n , or by augmenting the dimension of the basis M . Eriksson and Rizzi (1985) refer to n as a *selectivity* parameter, in the sense that, as it increases, the separation among the least damped eigenvalues is magnified. Both options can provide sufficient separation between the desired eigenvalues and the remaining part of the spectrum.

In spite of that, it is worth noting that this methodology is based on an approximation of the evolved perturbation, given by Eq. (24), which is valid for short integration periods. For this reason, it is legitimate to keep T small while increasing the value of M for particularly clustered eigenvalues.

One issue to be considered when dealing with iterative methods is the need for convergence acceleration that arises for high-resolution simulations. The rate of convergence of an iterative method decreases with the condition number of the Jacobian matrix, which in turn increases as the grid is refined. To address this issue and improve the performance of the method, adequate preconditioning is usually required. Building a preconditioner in a matrix-free context is not a trivial task because the matrix is never formed and standard preconditioning techniques cannot be directly applied.

To preserve the flexibility of the time-stepping global stability solver, the technique employed to control the convergence must be iterative and matrix-free. As an example, Mack and Schmid (2010) proposed a Jacobian-free DNS-based global stability solver for compressible flows with the addition of a preconditioning matrix in explicit form. Instead, Asgharzadeh and Borazjani (2017) addressed this issue through the use of an analytical Jacobian as a preconditioner in a Newton–Krylov method for the implicit solution of the Navier–Stokes equations. Some other options for matrix-free preconditioning are discussed in Knoll and Keyes (2004).

The remaining parameter that must be selected by the user is the linearization coefficient ϵ , *i.e.* the amplitude of the discrete perturbation. Its value should result from a trade-off between the truncation error of the finite difference and round-off errors related to the finite precision arithmetic.



Fig. 2. Spatial distribution of the vorticity for the real (a) and imaginary (b) parts of the unstable eigenmode of the flow past a fixed circular cylinder at $Re = 50$.

Table 1

Unstable eigenvalue for the flow past a fixed circular cylinder at $Re = 50$. Present results show good agreement with values present in the literature, as indicated by the relative error reported on the right.

Reference	ω	(%)
Siconolfi et al. (2017)	$0.0160 + 0.759i$	2.85
Negi et al. (2020)	$0.0133 + 0.742i$	0.61
Present	$0.0154 + 0.738i$	–

Literature provides some guidelines for the appropriate choice of ϵ , the interested reader is referred to the works of Eriksson and Rizzi (1985), Knoll and Keyes (2004), Schulze et al. (2009) and Mack and Schmid (2010). In this work, we follow a commonly used approach that selects the scaling factor of the perturbation at each time-stepper call via

$$\epsilon = \epsilon_0 \frac{\|\mathbf{q}_b\| + \|\mathbf{q}_p\|}{\|\mathbf{q}_p\|}, \quad (30)$$

where $\|\mathbf{q}\|$ is the L_2 norm of vector \mathbf{q} and ϵ_0 is a user-defined parameter related to the truncation error (An et al., 2011) of the FSI time-stepping scheme.

The choice of ϵ_0 has a great influence on the success of this time-stepping approach, and the user should keep in mind that this task is somewhat solver-dependent. Following the example of Mack and Schmid (2010), we report in Appendix C a parametric study that illustrates the influence of the parameter ϵ_0 on the accuracy of the results obtained for a given configuration.

3. Validation and results

In this section, to validate the algorithm derived above, we present the results of several numerical tests involving the vortex-induced vibration (VIV) of elastically mounted circular cylinders in a cross-flow. After the validation, a multi-body configuration is finally explored, consisting of the VIV of two identical spring-mounted cylinders in tandem configuration.

3.1. Flow past a fixed circular cylinder

The proposed methodology has been first validated with respect to the two-dimensional flow past a fixed circular cylinder, which is the subject of abundant literature in the field of hydrodynamic instability as it is considered the prototype flow around bluff bodies.

For this case, the flow quantities are made dimensionless by taking the diameter of the cylinder D and the incoming flow velocity U_∞ as reference variables. The reported results are obtained over a rectangular domain with size $[-28D : 52D] \times [-28D : 28D]$, with the origin placed on the cylinder axis. A uniform streamwise velocity is imposed at the inlet boundary along with a zero cross-sectional velocity ($u = 1, v = 0$), while free-shear boundary conditions are enforced on the lateral boundaries. At the outlet, a convective boundary condition allows the outgoing waves to exit the computational domain with minimal reflections while preserving local continuity. No-slip conditions are applied to the velocity at the surface of the cylinder via the IB procedure described in the previous section. Fig. 3 illustrates an example of the stretched Cartesian grid used for the computations. To obtain the results here presented, a grid containing 900×570 cells was employed, with a minimum grid spacing of $0.022D$ attained over a uniformly spaced rectangular region around the cylinder measuring $10D$ in the streamwise direction and $4D$ in the cross-stream direction.

An estimate for the globally unstable eigenvalue ω at $Re = 50$ is reported in Table 1 along with results from Refs. Siconolfi et al. (2017) and Negi et al. (2020), while Fig. 2 shows the vorticity field of the real and imaginary parts of the related unstable eigenmode.

3.2. VIV of an isolated cylinder

As a second validation case, we report the results of the linear stability analysis of the VIV of an isolated elastically mounted circular cylinder, to test the ability of our IB solver to accurately capture the dynamics of a small perturbation of the fluid–structure system.

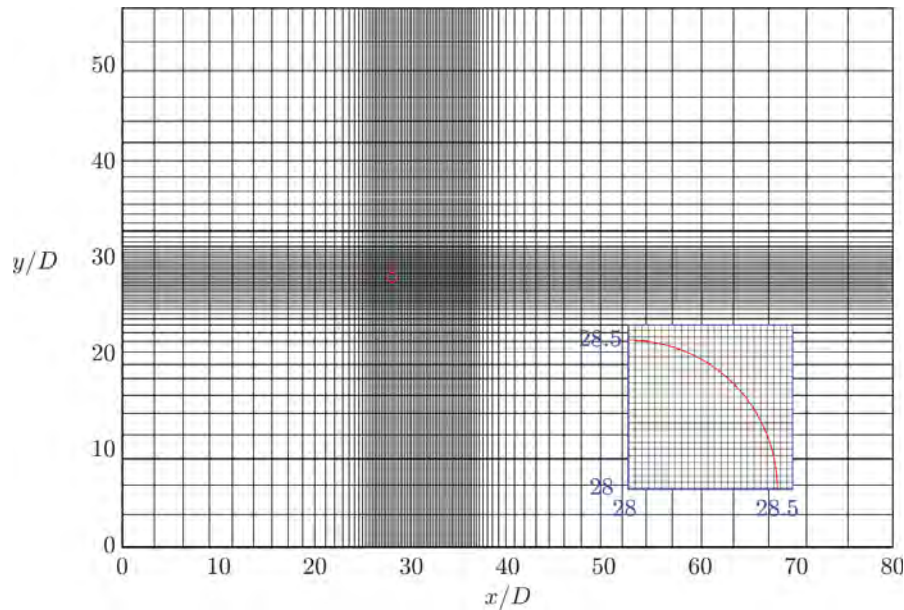


Fig. 3. Example of a grid used for the linear stability analysis of the flow past a circular cylinder (for both the fixed and oscillating cases). To make the graph more readable, every tenth grid point in each direction is displayed. The inset shows a close-up of the cylinder region for the actual grid employed in the calculations.

The size of the domain and the distance of the center of mass of the cylinder from its boundaries are the same as in the case of the fixed cylinder, as well as the boundary conditions. For all cases investigated, the Reynolds number based on the cylinder diameter is kept fixed at $Re = 60$, the cylinder being free to oscillate only in the cross-stream direction with no structural damping.

For the computations, the same grid used for the case of the fixed cylinder was employed after a grid convergence study. Results and details of the grid refinement study are reported in [Appendix B](#) together with an investigation of the influence of the domain size on the accuracy of the results.

In [Fig. 4](#), we report the variation of the non-dimensional frequency and growth rate of the two least stable eigenvalues with the reduced velocity U^* , for two distinct values of the relative density, namely, $\rho^* = 20$ and $\rho^* = 5$. For the largest density ratio, the two leading modes exhibit a clear distinction for each value of the reduced velocity U^* . Following [Navrose and Mittal \(2016\)](#), we denote them as the *fluid mode* (FM), due to the high affinity that it shows with the wake mode of the fixed cylinder (see [Fig. 5](#)), and the *elastic mode* (EM). This classification is further confirmed by noticing how the frequency of the FM remains close to that of the unstable mode for the flow around a fixed cylinder at the same Reynolds number (see [Table 1](#)) for all values of U^* , while the frequency of the EM, on the other hand, decreases following the variation of the natural frequency of the cylinder, given by $1/U^*$.

For $\rho^* = 5$, the two modes lose their distinction for intermediate values of U^* , therefore, following [Navrose and Mittal \(2016\)](#), we refer to them as the coupled fluid–elastic modes (FEM) I and II. For low values of U^* , modes *FEMI* and *FEMII* resemble the stationary wake mode (*i.e.* the mode associated with the vortex-shedding in the wake of the fixed cylinder) and the elastic mode, respectively; however, as U^* increases, the two eigenmodes become coupled and exchange their characteristics (see [Fig. 6](#)).

3.3. Flow-induced vibrations of two cylinders in tandem

The case considered in this section is the configuration proposed by [Borazjani and Sotiropoulos \(2009\)](#), with two identical elastically mounted cylinders in tandem arrangement placed in a free-stream flow. A parametric exploration of the dynamics of the system is beyond the scope of the current work, so we restricted our analysis to the 1-DOF case in which the cylinders are free to oscillate only in the cross-stream direction. The streamwise distance between their centers is equal to 1.5 diameters, while the cross-stream offset is zero. No structural damping is considered and the solid-to-fluid density ratio is kept constant at $\rho^* = 2.546$ for all simulations. Given the low value of the density ratio and the close proximity of the cylinders, the problem under investigation represents a challenging test case that can prove the flexibility of the method.

We first present the nonlinear response of the cylinders at the diameter-based Reynolds number $Re = 200$, for values of the reduced velocity spanning the range $1.5 \leq U^* \leq 14$. A sketch of the computational domain along with the boundary conditions employed is shown in [Fig. 7](#). The inlet is located at a distance $L_{in} = 15D$ from the midpoint between the centers of the cylinders, with the total length of the domain being equal to $L_{in} + L_{out} = 55D$, while the lateral boundaries are placed

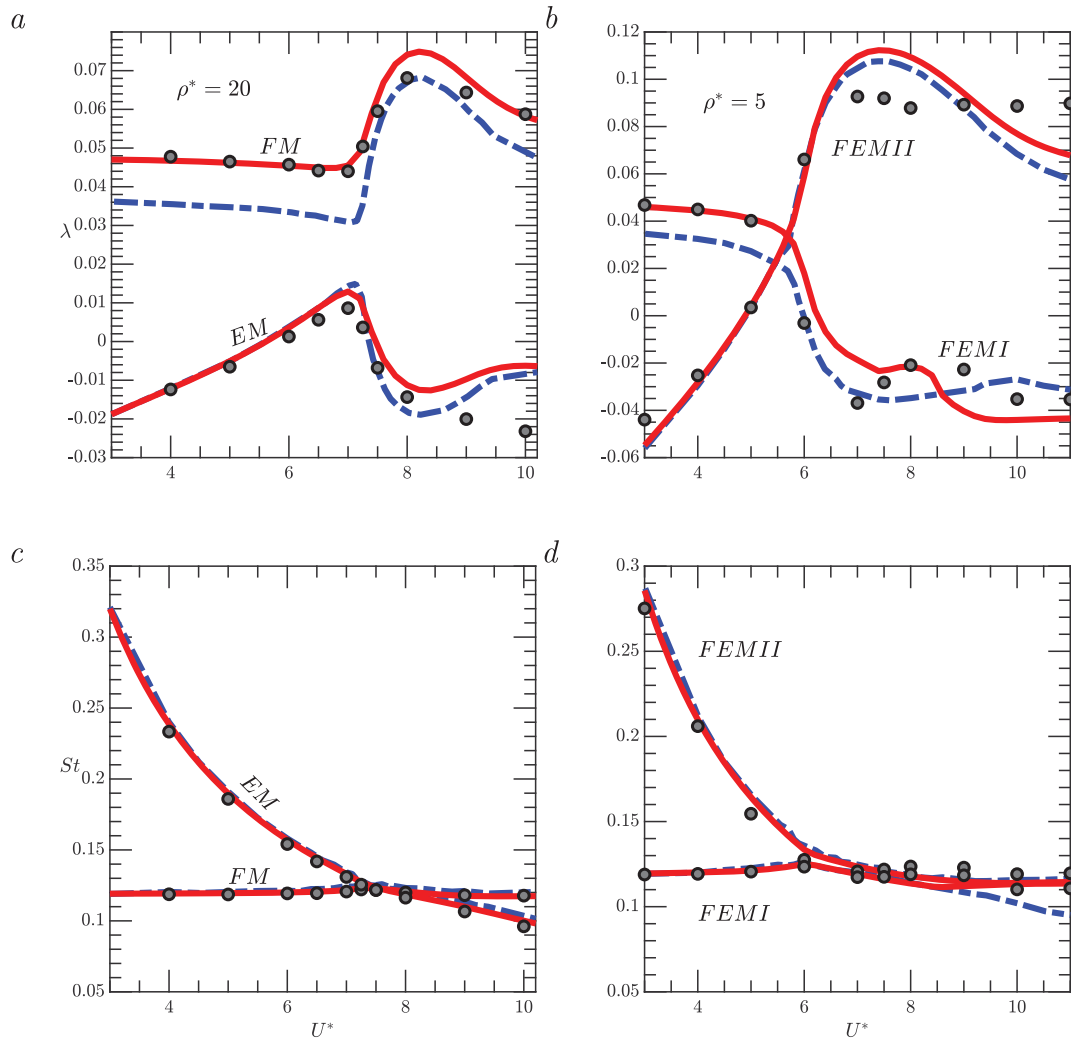


Fig. 4. Linear stability results: change of the growth rate λ and the Strouhal number, $St = (fD)/U_\infty$, of the two least stable modes with U^* for $\rho^* = 20$ (a, c) and $\rho^* = 5$ (b, d) at $Re = 60$. Continuous red line: results from Sabino et al. (2020); dashed blue line: results from Navrose and Mittal (2016); gray circles: present results. The red curves were reproduced using the open-source Matlab drivers of the StabFem project (<https://gitlab.com/stabfem/StabFem>). (For interpretation of the references to color in this figure legend, the reader is referred to the web version of this article.)

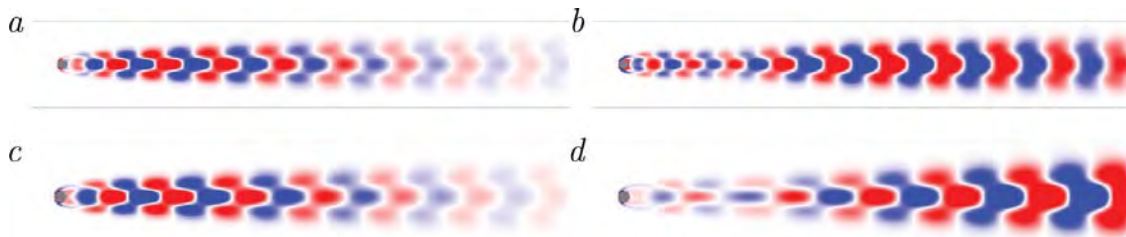


Fig. 5. Spanwise vorticity field of the real part of FM (a, c) and EM (b, d) for ($Re = 60, \rho^* = 20$) at $U^* = 7$ (a, b) and $U^* = 9$ (c, d). The fluid flows from left to right. Note how the fluid mode resembles the unstable mode for a fixed cylinder reported in Fig. 2.

at a distance $L_{lat} = 15D$ from the centers. A uniform Dirichlet boundary condition is given at the inlet and on the lateral boundaries, while a convective condition is assigned at the outlet with a convective velocity $c = 0.8$. The computations were performed over a stretched Cartesian grid containing 900×520 cells, with a minimum grid spacing of $0.0154D$ in the regularly spaced box region around the origin, measuring $4D$ in each direction.

All simulations were initialized with the steady base flow computed via *BoostConv* (Citro et al., 2017) by keeping the cylinders fixed at their initial positions. No starting perturbation was superposed to the stabilized solution; thus, the initial departure from the base flow was triggered only by round-off errors. Fig. 8 shows the temporal evolution of the

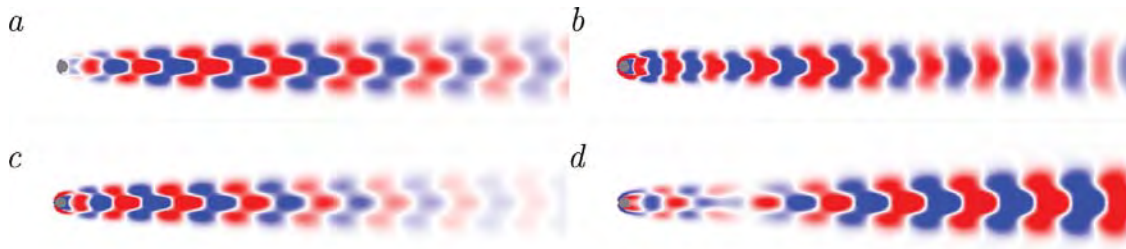


Fig. 6. Spanwise vorticity field of the real part of FEMI (a, c) and FEMII (b, d) for ($Re = 60, \rho^* = 5$) at $U^* = 5$ (a, b) and $U^* = 6$ (c, d). The fluid flows from left to right.

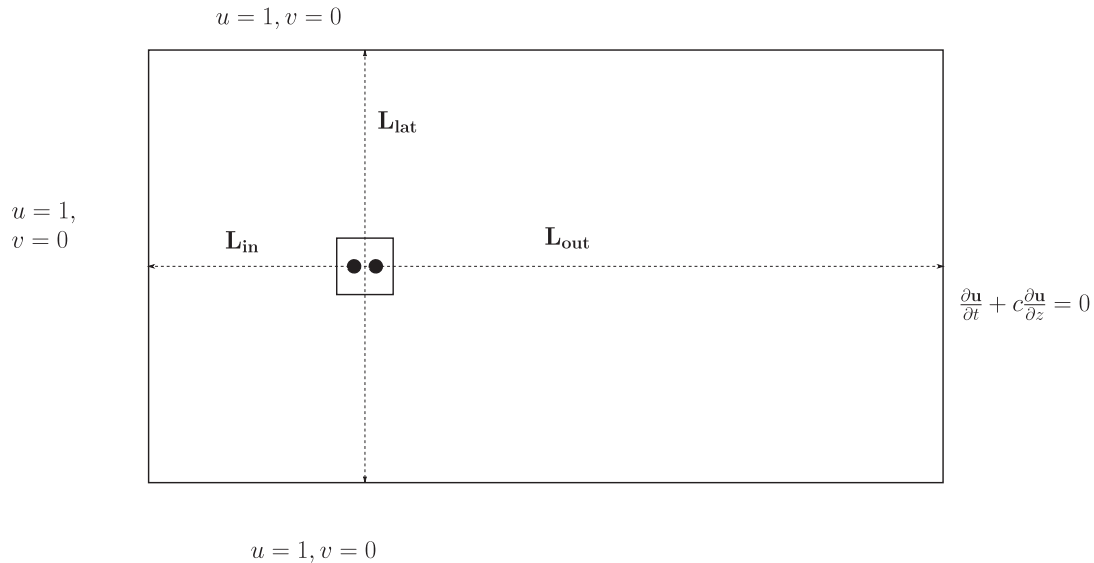


Fig. 7. Sketch of the computational domain employed for the direct numerical simulations of the flow interacting with two circular cylinders in tandem arrangement at $Re = 200$.

position of the centers of mass of the two cylinders for different values of U^* , each one being representative of a distinct behavior of the system. For $U^* = 3$ (see Fig. 8(a)) the cylinders experience a longer transient phase characterized by low-amplitude vibrations before reaching a periodic regime where the two cylinders oscillate out-of-phase with the front one exhibiting higher amplitude than the rear. Borazjani and Sotiropoulos (2009) classified this behavior as state 1 of the system and referred to the vibration state where the rear cylinder achieves a larger oscillation amplitude as state 2. When the reduced velocity is increased to $U^* = 4$, the dynamic response of the fluid–structure system changes noticeably as the two cylinders exhibit a quasi-periodic behavior distinguished by larger amplitudes of vibration that undergo a low-frequency modulation in time. As can be seen from the close-up region in Fig. 8(b), such modulations come with a change in the phase difference between the two oscillatory motions, as the phase angles are generally out of phase, but match periodically.

As the reduced velocity is further increased to $U^* = 5$, a shift from state 1 to state 2 is observed and the two cylinders oscillate in phase opposition, with the rear one exhibiting greater amplitude than the front one. For higher values of the reduced velocity, there is no qualitative change in the dynamical response of the system. The trailing cylinder continues to oscillate at a higher amplitude and out-of-phase with respect to the front one. Fig. 9(a) shows the variation of the maximum displacement A_{MAX}^* with the reduced velocity for each cylinder; the A_{MAX}^* value was measured disregarding the early transient phase. Results from Borazjani and Sotiropoulos (2009) and Griffith et al. (2017) are also included for comparison, showing a good overall agreement with the present outcome. The main discrepancy observed for the higher values of U^* can be ascribed to the different initial conditions. To verify this assumption, we repeated the computations for $11 \leq U^* \leq 14$ starting from a snapshot of the unsteady solution at $U^* = 10$; the results, represented in Fig. 9(a) by dashed lines, are markedly closer to the data present in the literature. These findings could indicate the existence of a hysteresis effect, already observed for the case of two stationary cylinders in tandem (Papaioannou et al., 2006) and for the VIV of a single cylinder (Prasanth and Mittal, 2009; Singh and Mittal, 2005). However, a detailed characterization of the system dynamics is beyond the scope of this article. Results obtained by running simulations of the same configuration at $Re = 100$ are presented in Fig. 9(b); the behavior of the system is found to depend strongly on the reduced velocity with a good qualitative agreement with the $Re = 200$ case. Time traces of the displacements of the two cylinders are reported in Fig. 10 for four different values of the reduced velocity, along with the spectral content of the time history of

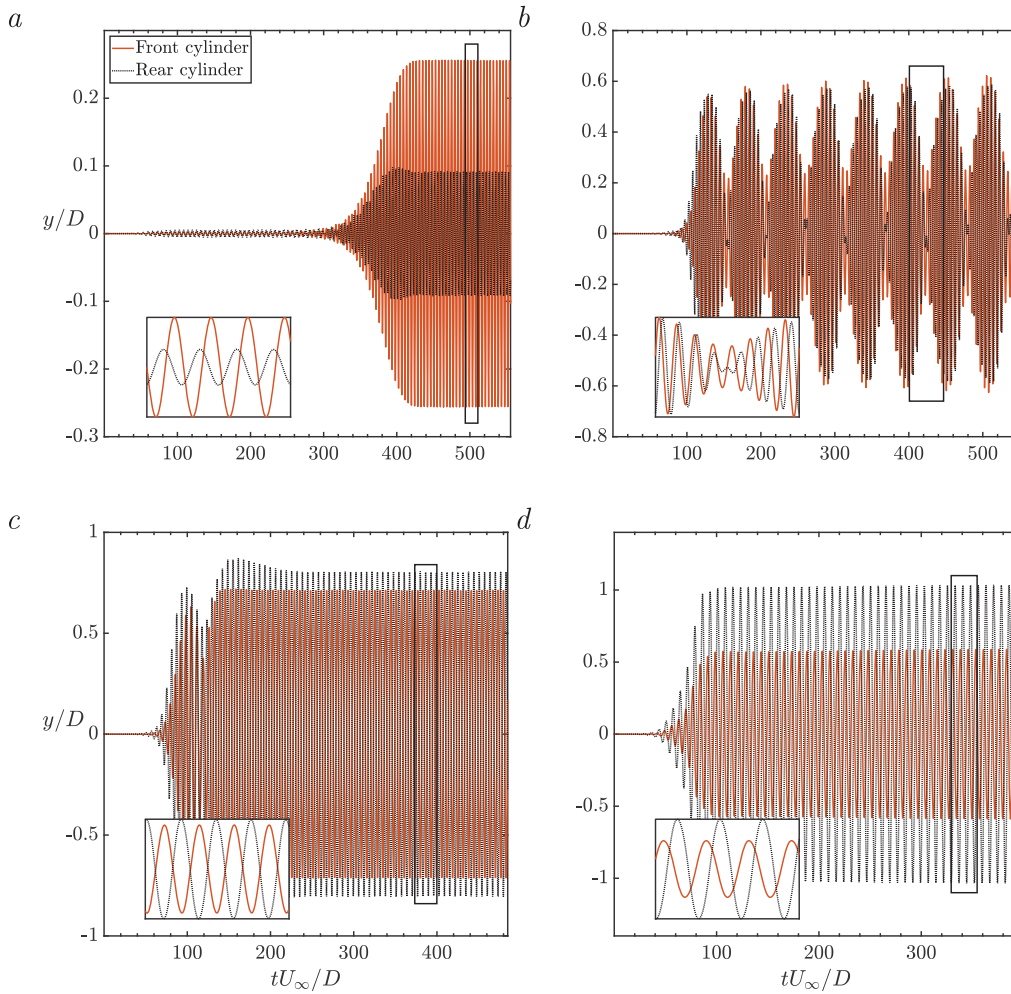


Fig. 8. Flow past two freely vibrating cylinders in tandem at $(Re, \rho^*) = (200, 2.546)$: time evolution of the vertical displacement of the cylinders for different values of U^* ; a: $U^* = 3$; b: $U^* = 4$; c: $U^* = 5$; d: $U^* = 7$. The inset in the lower-left corner of each figure provides a zoom-in of the region delimited by the black rectangle.

the vertical separation Δy between the centers of the two cylinders. For low values of the reduced velocity, the cylinders are found to oscillate in phase with small amplitudes, indicating that we are still outside the lock-in regime. For $U^* = 3$ (see Fig. 10a), the phase difference between the front and rear cylinders is small, with the rear one exhibiting somewhat larger displacements. When the reduced velocity is increased to $U^* = 4$, the dynamic response of the system changes considerably as the cylinders enter the lock-in regime, oscillating out-of-phase at a higher frequency and with the front cylinder now exhibiting wider oscillations. As the velocity is further increased to $U^* = 5$, a change in the behavior of the system is observed again since the rear cylinder now oscillates with larger relative amplitude, while the vertical separation between the cylinders undergoes oscillations with a periodic amplitude modulation that closely resembles a beating motion. This observation is confirmed by looking at the frequency content in Fig. 10c, which shows two main peaks having similar frequencies. In a linear system, the superposition of these two harmonics would result in a beating frequency, given by $f_b = |f_2 - f_1|$, and a corresponding period of about 97 time units, which is very close to the characterizing period of the oscillations of both cylinders. This beating phenomenon disappears by further increasing the reduced velocity as the frequency of vibration diminishes. It is interesting to notice that Borazjani & Sotiropoulos identified $U^* = 5$ as the critical state of the system at $Re = 200$, delimiting the transition from state 1 to state 2.

3.3.1. Global stability

In this section, we investigate the interaction between the fluid and the two elastically mounted cylinders in tandem through a global linear stability analysis, to further ascertain the validity and robustness of the proposed methodology.

The computations were performed on the same grid used to conduct the flow analysis presented in the previous section. Given the low value of the density ratio ρ^* , the results of the nonlinear simulations obtained with a weak coupling of the fluid and solid dynamics were compared with those obtained via a strong coupling. Even though the two procedures exhibited very similar results, the iterative procedure provided more accurate results with a reduced number of Arnoldi

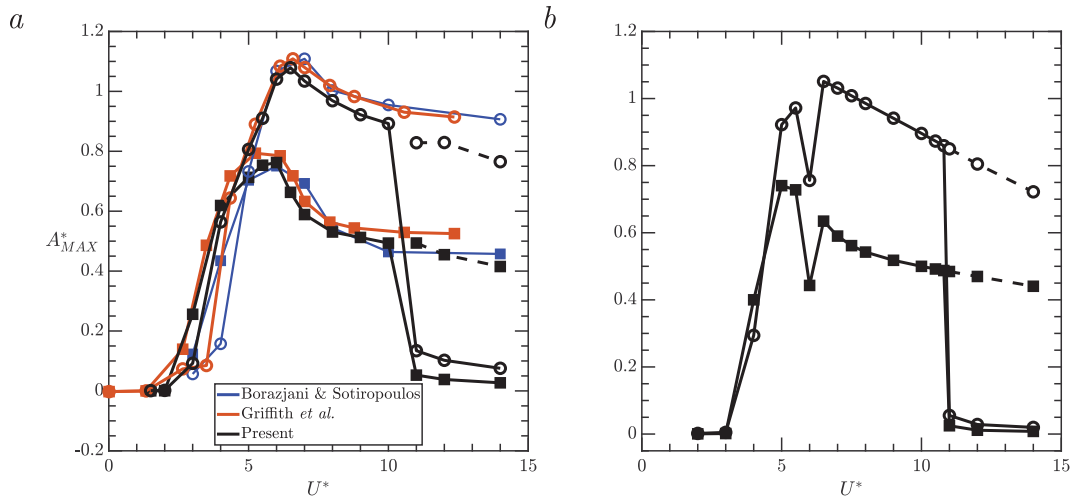


Fig. 9. Variation with the reduced velocity U^* of the maximum non-dimensional displacement A_{MAX}^* of two identical cylinders in tandem ($L = 1.5$) at $Re = 200$ (a) and $Re = 100$ (b). Squares: front cylinder; circles: rear cylinder. The present results for $Re = 200$ are compared with the ones from Borazjani and Sotiropoulos (2009) and Griffith et al. (2017). Dotted line: the simulations were initialized from an instantaneous snapshot of the solution for a smaller value of U^* .

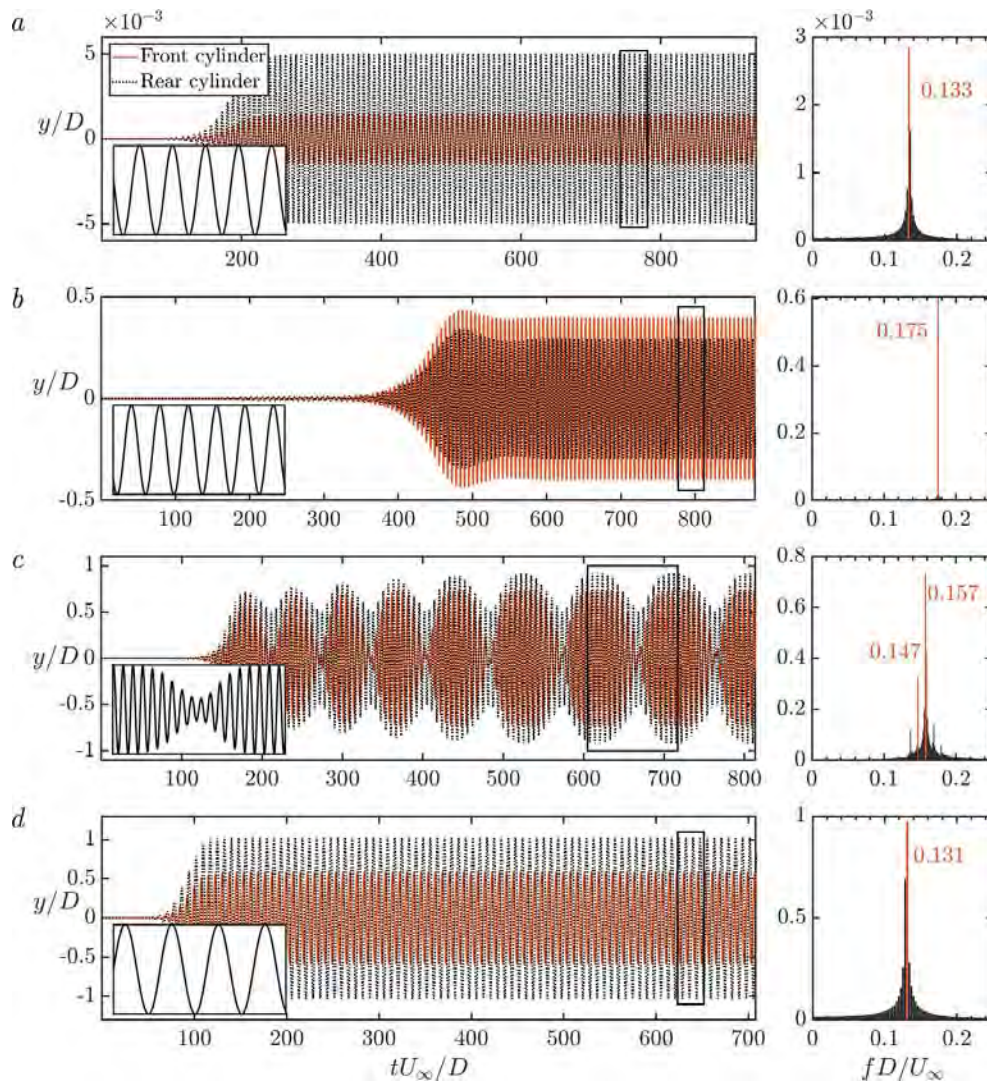


Fig. 10. Flow past two freely vibrating cylinders in tandem arrangement at $(Re, \rho^*) = (100, 2.546)$: time evolution of the vertical displacement of the cylinders for different values of U^* ; a: $U^* = 3$; b: $U^* = 4$; c: $U^* = 5$; d: $U^* = 7$. The inset in the lower-left corner of each figure shows the time history of the vertical distance Δy between the cylinders for the time interval marked by the black rectangle. On the right, it is reported the single-sided amplitude spectrum of Δy .

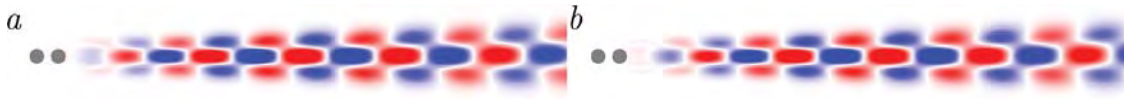


Fig. 11. Spatial distribution of the vorticity for the real (a) and imaginary (b) parts of the unstable eigenmode for the flow past two fixed cylinders in tandem arrangement at $Re = 100$.

iterations for the stability calculations. The fixed time-step size was chosen in order to keep the CFL number under the 0.4 value.

As in the case of the single cylinder, the linear stability analysis of the fluid alone predicts the existence of an unstable eigenvalue $\omega_s = 0.0404 + 0.7907i$ associated with the vortex shedding in the wake of the two cylinders. In the following, we refer to this eigenvalue as the *stationary wake mode*. The corresponding eigenmode (see Fig. 11) closely resembles the unstable eigenmode of the single cylinder case. This observation is consistent with results from literature asserting that, for small streamwise spacings, the two cylinders shed like a single body (Papaioannou et al., 2006).

When the cylinders are free to move in the cross-stream direction, the LSA identifies the presence of an additional eigenmode for the range of parameters considered. In Fig. 12, the two least stable eigenvalues are tracked over a wide range of reduced velocities, in an attempt to identify the mechanisms responsible for the lock-in regime and for the change of behavior that occurs around $U^* = 5$. It is observed that, for the lower values of U^* , the two leading modes are quite distinct, with the frequency of the first mode (represented by blue dots in Figs. 12(b) and 12(d)) being close to the frequency of the stationary wake mode, $f_s D/U_\infty = 0.1258$. Conversely, the frequency associated with the second mode (red dots in Figs. 12(b) and 12(d)) is slightly smaller than the natural frequency of the cylinders for values of the reduced velocity up to $U^* = 7$, where the frequencies of the two modes are almost coincident and remarkably close to that of the limit cycle shown in Fig. 10(d). Therefore, for the lower values of U^* , we associate the first mode with the wake instability and the second one with the structural mode. For $U^* = 5$ the two modes show comparable growth rates and close frequencies, flagging an interaction that is visible in the nonlinear evolution as well. The peak frequencies revealed by the amplitude spectrum on the right side of Fig. 10(c) are, indeed, quite close to the frequencies of the leading modes at $U^* = 5$ reported in Fig. 12(d). After the crossing of the two modes, both frequencies remain close to that of the stationary wake mode for all U^* , and a classification of the modes as fluid mode and structural mode is not possible.

For values of the reduced velocity lower than $U^* = 4$, the mode associated with the structure is still stable. This finding is coherent with the small amplitude of oscillation observed in the calculations. Then, at the critical value $U^* = 5$, the growth rate of mode 2 surpasses that of mode 1, possibly explaining the transition from state 1 to state 2 and the greater amplitudes of vibration observed in the nonlinear simulations. In an attempt to shed further light on this phenomenon, we report in Figs. 12(a) and 12(c) the growth rate and the frequency, respectively, of the two least stable modes for the same tandem arrangement when only the rear cylinder is free to move. For this configuration, we find that the growth rate of the unstable mode increases considerably for $U^* \geq 5$, while the growth rate of the stable mode attains its maximum value.

These results indicate that the mechanism responsible for the large amplitude oscillations is already present in this fixed-free case. The temporal evolution of the flow starting from the base state shows that, for all the values of the reduced velocity, a regular vortex street excites the oscillation of both cylinders, with the rear one undergoing larger vibrations. This is due to the fact that vortices are initially shed only from the rear cylinder, which thus experiences a greater pressure difference. The outcome is coherent with the observations of Borazjani and Sotiropoulos (2009), who suggest that it is the vortex-shedding in the wake that initiates the excitation of the system and subsequently generates a vertical separation between the cylinders. When this separation becomes large enough, other interaction mechanisms come into play and give rise to different dynamical states.

There is, however, another point to address which is the passage from state 2 to state 1 that is observed when changing the value of U^* from $U^* = 3$ to $U^* = 4$ and the switch from state 1 to state 2 that occurs at $U^* = 5$. To investigate this phenomenon, we have reported in Fig. 13a the early transient of the time history of the vertical displacement of the cylinders for $U^* = 4$. It is clearly visible that the cylinders oscillate almost in phase, with a low amplitude of vibration as in the case $U^* = 3$ (Fig. 13b) and the rear cylinder exhibits larger oscillations, following the characteristics of the first mode. The temporal evolution shows that the growth of the first mode saturates as the oscillations approach a limit cycle with small amplitude. Later, the cylinders lose their synchronization owing to the emergence of the second mode. The greater amplitude of vibration of the front cylinder, however, cannot be explained with linear arguments. For $U^* > 5$, the dynamics of the linearized system is governed by the second mode, characterized by the counter-phase oscillation of the cylinders, with the rear one undergoing larger vibrations.

Fig. 14 shows the vorticity fields of the two unstable eigenmodes related to the eigenvalues reported in Fig. 12, for three different values of the reduced velocity. Again, for $U^* = 4$, mode 1 resembles the stationary wake mode of Fig. 11 but departs from it for the higher values of U^* . On the other hand, the shape of mode 2 also changes when the reduced velocity is increased from $U^* = 4$ to $U^* = 5$, while a further increase in the value of U^* produces a shift upstream of the high vorticity region.

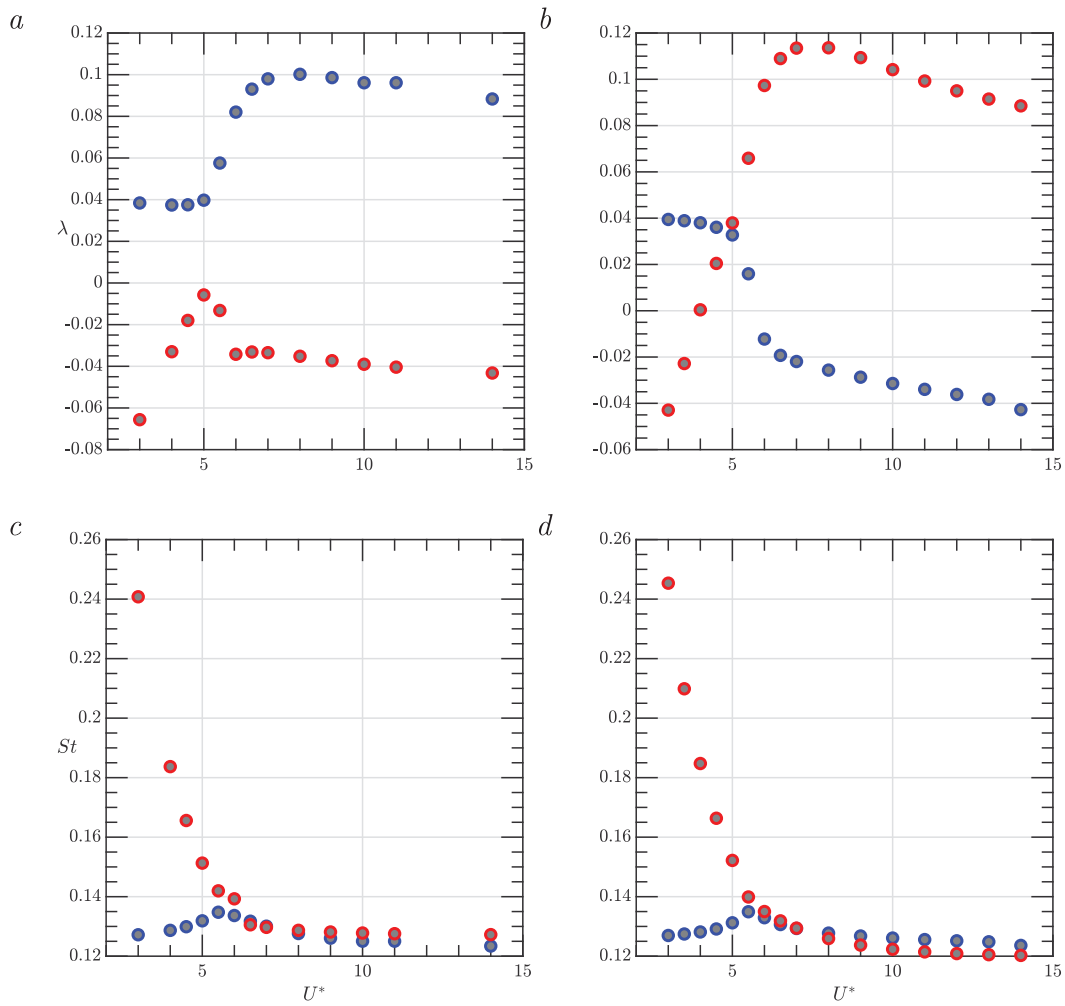


Fig. 12. Results of the LSA for the flow around two elastically-mounted cylinders in tandem at $Re = 100$. Evolution with U^* of the growth rate λ and the Strouhal number St of the two least stable modes. Fig. (a, c): only the rear cylinder is free to oscillate; fig. (b, d): both cylinders are free to move. (For interpretation of the references to color in this figure legend, the reader is referred to the web version of this article.)

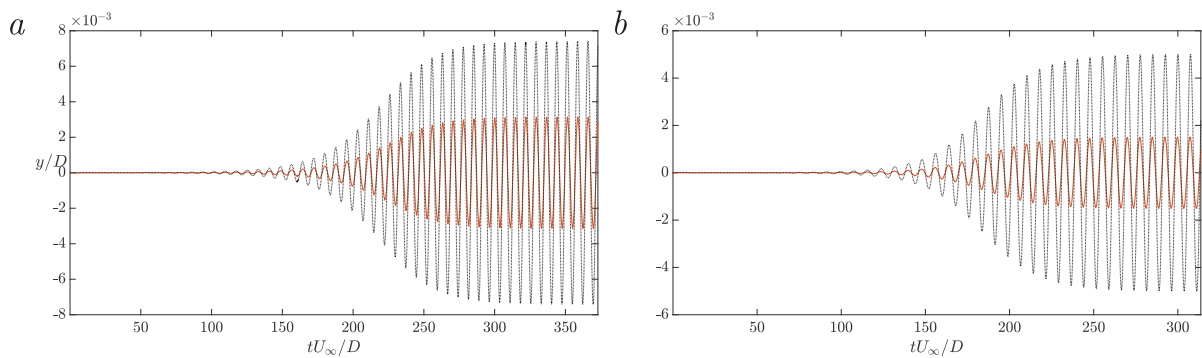


Fig. 13. Time evolution of the vertical displacement of two freely vibrating cylinders in tandem arrangement at $(Re, \rho^*) = (100, 2.546)$ for $U^* = 4$ (a) and $U^* = 3$ (b).

4. Summary and conclusions

The role played by linear effects in the loss of stability of a fluid–structure system has motivated researchers to develop new techniques to perform linear stability analyses of coupled FSI problems.

In this paper, we propose a method that extends Chiba’s approach (Chiba, 1998) to study the coupled dynamics of flow–structure systems. A time-stepping iterative procedure, based on the exponential transformation of the Jacobian matrix, was derived in a general setting. This was implemented within an existing immersed boundary solver and

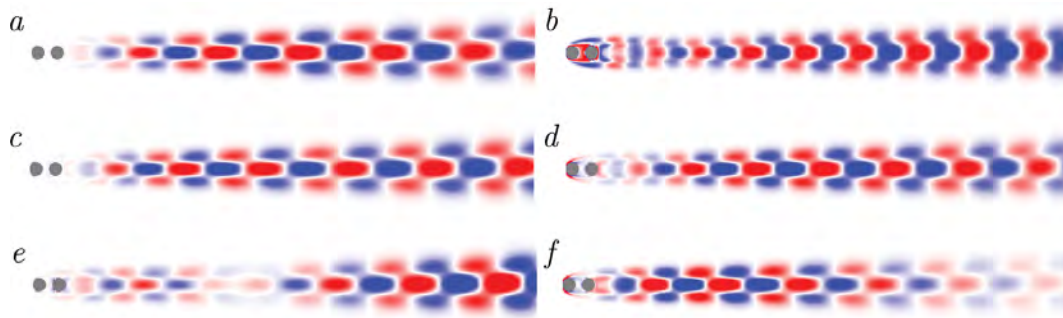


Fig. 14. Flow past two spring-mounted circular cylinders in tandem arrangement at $Re = 100$. Spatial distribution of the vorticity of the real part of mode 1 (a, c, e) and mode 2 (b, d, f) for $U^* = 4$ (a, b), $U^* = 5$ (c, d) and $U^* = 6$ (e, f).

validated against well-documented cases of flow-induced vibrations of rigid bodies. The outcomes of the linear stability analysis showed a good overall agreement with the results from the literature, obtained using mesh-conforming methods. Future developments of the method could include a local grid refinement to achieve a higher resolution near the immersed surface at a lower cost (Vanella et al., 2010). The validation tests were limited to the case of rigid-body motion, nevertheless, it is straightforward to extend the range of applicability of the method to deformable structures.

The matrix-free nature of the algorithm makes it particularly convenient for the analysis of three-dimensional flows around structures with complex geometries, where an analytical linearization of the coupled systems of equations would be impracticable. Moreover, the Cartesian grid employed within the IB framework facilitates the parallelization of the numerical scheme, which is an essential feature for solving three-dimensional problems within a reasonable time.

In Section 3.3, the method was tested on the case of two oscillating cylinders in tandem; the results of the stability analysis matched reasonably well with the nonlinear simulations, providing further confidence in the robustness of the method and opening the way to the instability analysis of multi-body configurations. Two dominant modes were identified across the range $3 \leq U^* \leq 14$. For values of the reduced velocity $U^* < 4$, only one mode is unstable and the cylinders oscillate out of lock-in. At $U^* = 4$ the second mode loses its stability and the cylinders enter the lock-in zone, then for $U^* = 5$ the modes cross and their interaction gives rise to the beating phenomenon observed in the nonlinear simulations. For $U^* > 5$ the growth rate of the dominant mode is significantly greater than that of the other one, justifying the higher amplitude of vibration observed in the calculations. The comparison with the linear stability of the fixed-free configuration shows that the mechanism giving rise to large amplitude oscillations is already present in the latter case, as the growth rate of the unstable mode grows in a similar fashion for $U^* > 5$, while its frequency is always close to that of the stationary wake mode. This observation implies that the vortex-shedding plays a major role in triggering the vibrations and that interference effects between the cylinders come into play only when the vertical separation between the two cylinders is large enough, as suggested by Borazjani and Sotiropoulos (2009).

One major advantage of the methodology consists of the generality of the formulation, which does not depend on the specific time-stepping scheme chosen for integrating the governing equations. Without the pretense of being exhaustive, in Section 2.3.2, some guidelines were provided for the selection of the linearization parameters, with the purpose to furnish the reader with the necessary tools to implement the strategy within existing CFD codes.

CRediT authorship contribution statement

Antonia Tirri: Conceptualization, Methodology, Software development, Computations, Validation, Writing – original draft, Reviewing and editing. **Alessandro Nitti:** Conceptualization, Software development, Writing – review & editing. **Javier Sierra-Ausin:** Conceptualization, Software development, Writing – review & editing. **Flavio Giannetti:** Conceptualization, Supervision, Writing – review & editing. **Marco D. de Tullio:** Conceptualization, Supervision, Software development, Writing – review & editing.

Declaration of competing interest

The authors declare that they have no known competing financial interests or personal relationships that could have appeared to influence the work reported in this paper.

Data availability

Data will be made available on request.

Acknowledgments

This work was supported by the Italian Ministry of Education, University and Research (MIUR) via PRIN2017 XFAST-SIMS (Grant No. 20173C478N). The simulations were carried out on the computational facilities provided by the Department of Mechanics Mathematics and Management, Polytechnic University of Bari (Italy).

Appendix A. Derivation of the Gateaux derivative

In this section, we report further details of the derivation of Eq. (24) presented in Section 2.3.1. Combining the definitions of \mathbf{F} and $\mathbf{R}(\mathbf{q})$ given in Section 2, we get

$$\mathbf{F}(\mathbf{q}(t_0), T) = \int_{t_0}^{t_0+T} \mathbf{R}(\mathbf{q}(t))dt + \mathbf{q}(t_0). \quad (\text{A.1})$$

We now consider the second term on the right-hand side of Eq. (23). Substituting the expression above, it reads

$$\left. \frac{\partial \mathbf{F}(\mathbf{q}, T)}{\partial \mathbf{q}} \right|_{\mathbf{q}_b} \mathbf{q}'(t_0) = \left. \frac{\partial}{\partial \mathbf{q}} \right|_{\mathbf{q}_b} \left[\int_{t_0}^{t_0+T} \mathbf{R}(\mathbf{q})dt \right] \mathbf{q}'(t_0) + \mathbf{q}'(t_0). \quad (\text{A.2})$$

Recognizing that the extremes of integration do not depend on \mathbf{q} and that $\mathbf{q}'(t_0)$ does not depend on time, we can interchange integration and differentiation and bring $\mathbf{q}'(t_0)$ inside the integral,

$$\left. \frac{\partial \mathbf{F}(\mathbf{q}, T)}{\partial \mathbf{q}} \right|_{\mathbf{q}_b} \mathbf{q}'(t_0) = \int_{t_0}^{t_0+T} \left. \frac{\partial \mathbf{R}(\mathbf{q})}{\partial \mathbf{q}} \right|_{\mathbf{q}_b} \mathbf{q}'(t_0)dt + \mathbf{q}'(t_0). \quad (\text{A.3})$$

Supposing then a little variation of $\mathbf{q}'(t)$ in the interval $[t_0, t_0 + T]$, which is true for small values of T , we have replaced $\mathbf{q}'(t_0)$ into the integral with $\mathbf{q}'(t)$.

$$\int_{t_0}^{t_0+T} \left. \frac{\partial \mathbf{R}(\mathbf{q})}{\partial \mathbf{q}} \right|_{\mathbf{q}_b} \mathbf{q}'(t_0)dt \approx \int_{t_0}^{t_0+T} \mathbf{J}(\mathbf{q}_b) \mathbf{q}'(t)dt. \quad (\text{A.4})$$

Finally, we recognize that (A.4) is simply the integration of the initial value problem given by Eq. (17), and therefore

$$\left. \frac{\partial \mathbf{F}(\mathbf{q}, T)}{\partial \mathbf{q}} \right|_{\mathbf{q}_b} \mathbf{q}'(t_0) \approx \mathbf{q}'(t_0 + T) - \mathbf{q}'(t_0). \quad (\text{A.5})$$

Appendix B. Grid convergence tests

To assess the grid and domain convergence of the stability results, eigenvalue computations were performed on different grids for the VIV case presented in Section 3.2, with $(\rho^*, U^*) = (20, 7)$.

Table B.2 reports the growth rate λ and the Strouhal number St of the least stable eigenvalue for four different discretizations of the same domain of size $[-28D : 52D] \times [-28D : 28D]$, with the origin placed on the cylinder axis. On the rightmost column, it is reported the percentage error $e_{\%j}$ made in computing the eigenvalue ω_j , as the finest grid is taken as reference,

$$e_{\%j} = \frac{|\omega_j - \omega_{ref}|}{|\omega_{ref}|} \times 100. \quad (\text{B.1})$$

Table B.3 reports the growth rate and the non-dimensional frequency of both the fluid and elastic modes for three distinct domains. The corresponding grids are coincident in the uniformly spaced rectangular zone around the cylinder, the minimum spacing being equal to $\Delta x_{min} = 0.022$. In particular, the grid used for the medium domain $D2$ corresponds to grid 2 in Table B.2. The analysis shows a minor difference between the medium and big domains, thus motivating the choice of $D2$ as the computational domain for the cases presented in Section 3.2. The blockage ratio reported in Table B.3 is defined as the ratio of the cylinder diameter to the cross-stream dimension of the computational domain.

Appendix C. Effect of the linearization parameter ϵ_0

To evaluate the influence of the user-defined linearization parameter ϵ_0 on the accuracy of the results, we report in Fig. C.1 the variation of the relative error e_r and the residual $\|\mathbf{r}\|$ of the least stable Ritz pair against ϵ_0 . The former is given by

$$e_r = \frac{|\omega - \omega_{ref}|}{|\omega_{ref}|}, \quad (\text{C.1})$$

where ω is the least stable eigenvalue computed for a given value of ϵ_0 on the chosen grid and ω_{ref} is a reference value. In the absence of an exact solution of the EVP, the selected ω_{ref} is the least stable eigenvalue computed on a reference grid with the parameter ϵ_0 chosen so as to minimize the residual $\|\mathbf{r}\|$. The results displayed in Fig. C.1 refer to the VIV case introduced in Section 3.2 with $(Re, \rho^*, U^*) = (60, 20, 7)$.

Table B.2

Convergence study with respect to grid resolution. For each of the four grids, the total number of cells N_c and the minimum cell dimension Δx_{min} are reported, together with the growth rate λ and the Strouhal number St of the least stable mode for $(Re, \rho^*, U^*) = (60, 20, 7)$. Grid 2 was used to obtain the results presented throughout the manuscript, while the relative error $e_{\%}$ is computed with respect to the values obtained with grid 4.

Grid	N_c	Δx_{min}	λ	St	$e_{\%}$
1	310 800	0.0286	0.0427	0.1205	0.662
2	513 000	0.0220	0.0447	0.1210	0.221
3	765 600	0.0182	0.0448	0.1211	0.106
4	1 068 600	0.0154	0.0447	0.1213	–

Table B.3

Sensitivity of the rightmost eigenvalues to the size of the computational domain for $(Re, \rho^*, U^*) = (60, 20, 7)$. D1: $[-35 : 65] \times [-35 : 35]$, D2: $[-28 : 52] \times [-28 : 28]$, D3: $[-21 : 39] \times [-21 : 21]$. All the grids used for the analysis have the same minimum cell dimension Δx_{min} . The percentage blockage ratio is reported for each domain size.

	D1 1.43%		D2 1.78%		D3 2.38%	
	λ_r	St	λ_r	St	λ_r	St
FM	0.0440	0.1206	0.0447	0.1210	0.0461	0.1219
EM	0.0086	0.1309	0.0085	0.1309	0.0080	0.1308

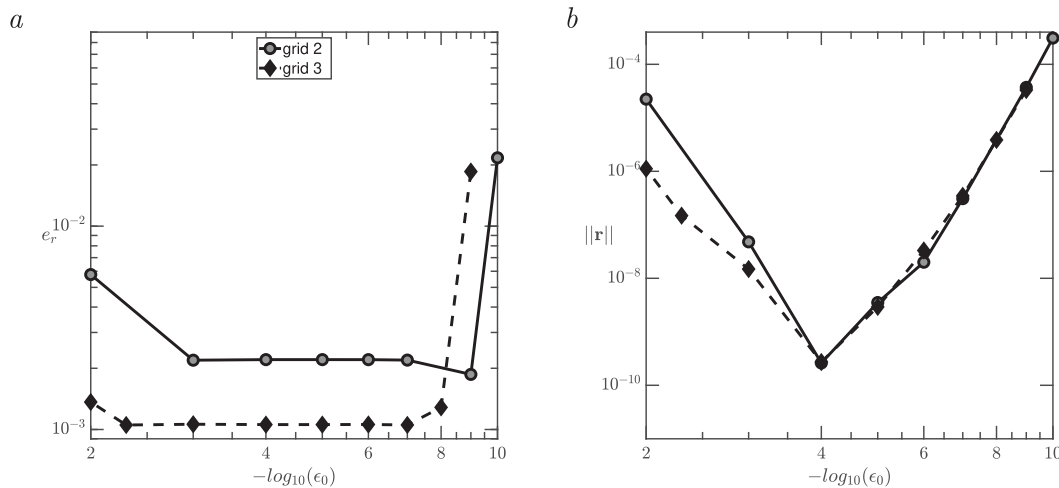


Fig. C.1. Effect of the input parameter ϵ_0 on the relative error (a) and direct residual (b) for the VIV case reported in Section 3.2 with the following set of parameters ($\rho^* = 20$, $Re = 60$, $U^* = 7$). Results are reported for two different grids (see Table B.2 for details), the relative error is computed with respect to the finest grid in Table B.2.





References

- An, H.-B., Wen, J., Feng, T., 2011. On finite difference approximation of a matrix-vector product in the Jacobian-free Newton–Krylov method. *J. Comput. Appl. Math.* 236 (6), 1399–1409. <http://dx.doi.org/10.1016/j.cam.2011.09.003>.
- Asgharzadeh, H., Borazjani, I., 2017. A Newton–Krylov method with an approximate analytical Jacobian for implicit solution of Navier–Stokes equations on staggered overset-curvilinear grids with immersed boundaries. *J. Comput. Phys.* 331, 227–256. <http://dx.doi.org/10.1016/j.jcp.2016.11.033>.
- Borazjani, I., 2013. Fluid–structure interaction, immersed boundary-finite element method simulations of bio-prosthetic heart valves. *Comput. Methods Appl. Mech. Engrg.* 257, 103–116. <http://dx.doi.org/10.1016/j.cma.2013.01.010>.
- Borazjani, I., Sotiropoulos, F., 2009. Vortex-induced vibrations of two cylinders in tandem arrangement in the proximity–wake interference region. *J. Fluid Mech.* 621, 321–364. <http://dx.doi.org/10.1017/S0022112008004850>.
- Breugem, W.-P., 2012. A second-order accurate immersed boundary method for fully resolved simulations of particle-laden flows. *J. Comput. Phys.* 231, 4469–4498. <http://dx.doi.org/10.1016/j.jcp.2012.02.026>.
- Chiba, S., 1998. Global stability analysis of incompressible viscous flow. *J. Jpn. Soc. Comput. Fluid Dyn.* 7, 20–48, (In Japanese).
- Citro, V., Luchini, P., Giannetti, F., Auteri, F., 2017. Efficient stabilization and acceleration of numerical simulation of fluid flows by residual recombination. *J. Comput. Phys.* 344, 234–246. <http://dx.doi.org/10.1016/j.jcp.2017.04.081>.
- Cossu, C., Morino, L., 2000. On the instability of a spring-mounted circular cylinder in a viscous flow at low Reynolds numbers. *J. Fluids Struct.* 14 (2), 183–196. <http://dx.doi.org/10.1006/jfls.1999.0261>.
- de Tullio, M., De Palma, P., Iaccarino, G., Pascazio, G., Napolitano, M., 2007. An immersed boundary method for compressible flows using local grid refinement. *J. Comput. Phys.* 225 (2), 2098–2117. <http://dx.doi.org/10.1016/j.jcp.2007.03.008>, URL <https://www.sciencedirect.com/science/article/pii/S0021999107001222>.
- Doaré, O., Michelin, S., 2011. Piezoelectric coupling in energy-harvesting fluttering flexible plates: linear stability analysis and conversion efficiency. *J. Fluids Struct.* 27 (8), 1357–1375. <http://dx.doi.org/10.1016/j.jfluidstructs.2011.04.008>.

- Durbin, P., Iaccarino, G., 2002. An approach to local refinement of structured grids. *J. Comput. Phys.* 181 (2), 639–653. <http://dx.doi.org/10.1006/jcph.2002.7147>, URL <https://www.sciencedirect.com/science/article/pii/S0021999102971470>.
- Eriksson, L.E., Rizzi, A., 1985. Computer-aided analysis of the convergence to steady state of discrete approximations to the euler equations. *J. Comput. Phys.* 57 (1), 90–128. [http://dx.doi.org/10.1016/0021-9991\(85\)90054-3](http://dx.doi.org/10.1016/0021-9991(85)90054-3).
- Fadlun, E., Orlandi, P., Mohd-Yusof, J., 2000. Combined immersed-boundary finite-difference methods for three-dimensional complex flow simulations. *J. Comput. Phys.* 161, 35–60. <http://dx.doi.org/10.1006/jcph.2000.6484>.
- Fernández, M.A., Le Tallec, P., 2002. Linear stability analysis in fluid-structure interaction with transpiration. Part I: formulation and mathematical analysis. Research Report RR-4570, INRIA.
- Förster, C., Wall, W., Ramm, E., 2007. Artificial added mass instabilities in sequential staggered coupling of nonlinear structures and incompressible viscous flows. *Comput. Methods Appl. Mech. Engrg.* 196, 1278–1293. <http://dx.doi.org/10.1016/j.cma.2006.09.002>.
- Goldhirsch, L., Orszag, S., Maulik, B., 1987. An efficient method for computing leading eigenvalues and eigenvectors of large asymmetric matrices. *J. Sci. Comput.* 2 (1), 33–58. <http://dx.doi.org/10.1007/BF01061511>.
- Gómez, F., Gomez, R., Theofilis, V., 2011. Coupling time-stepping numerical methods and standard aerodynamics codes for instability analysis of flows in complex geometries. In: 6th AIAA Theoretical Fluid Mechanics Conference. <http://dx.doi.org/10.2514/6.2011-3753>.
- Gómez, F., Pérez, J.M., Blackburn, H.M., Theofilis, V., 2015. On the use of matrix-free shift-invert strategies for global flow instability analysis. *Aerosp. Sci. Technol.* 44, 69–76. <http://dx.doi.org/10.1016/j.ast.2014.11.003>, Instability and Control of Massively Separated Flows.
- Goza, A., Colonius, T., Sader, J.E., 2018. Global modes and nonlinear analysis of inverted-flag flapping. *J. Fluid Mech.* 857, 312–344. <http://dx.doi.org/10.1017/jfm.2018.728>.
- Griffith, M.D., Lo Jacono, D., Sheridan, J., Leontini, J.S., 2017. Flow-induced vibration of two cylinders in tandem and staggered arrangements. *J. Fluid Mech.* 833, 98–130. <http://dx.doi.org/10.1017/jfm.2017.673>.
- Grouthier, C., Michelin, S., Bourguet, R., Modarres-Sadeghi, Y., de Langre, E., 2014. On the efficiency of energy harvesting using vortex-induced vibrations of cables. *J. Fluids Struct.* 49, <http://dx.doi.org/10.1016/j.jfluidstructs.2014.05.004>.
- Knoll, D., Keyes, D., 2004. Jacobian-free Newton–Krylov methods: a survey of approaches and applications. *J. Comput. Phys.* 193 (2), 357–397. <http://dx.doi.org/10.1016/j.jcp.2003.08.010>.
- Kornecki, A., Dowell, E., O'Brien, J., 1976. On the aeroelastic instability of two-dimensional panels in uniform incompressible flow. *J. Sound Vib.* 47 (2), 163–178. [http://dx.doi.org/10.1016/0022-460X\(76\)90715-X](http://dx.doi.org/10.1016/0022-460X(76)90715-X).
- Lács, U., Taira, K., Bagheri, S., 2016. A stable fluid–structure–interaction solver for low-density rigid bodies using the immersed boundary projection method. *J. Comput. Phys.* 305, 300–318. <http://dx.doi.org/10.1016/j.jcp.2015.10.041>.
- Chih Lai, M., Peskin, C.S., 2000. An immersed boundary method with formal second-order accuracy and reduced numerical viscosity. *J. Comput. Phys.* 705–719.
- Lehoucq, R.B., Sorensen, D.C., Yang, C., 1998. ARPACK Users' Guide. Society for Industrial and Applied Mathematics, <http://dx.doi.org/10.1137/1.9780898719628>, arXiv:<https://epubs.siam.org/doi/pdf/10.1137/1.9780898719628>.
- Mack, C.J., Schmid, P.J., 2010. A preconditioned krylov technique for global hydrodynamic stability analysis of large-scale compressible flows. *J. Comput. Phys.* 229 (3), 541–560. <http://dx.doi.org/10.1016/j.jcp.2009.09.019>.
- Mansoorzadeh, S., Javanmard, E., 2014. An investigation of free surface effects on drag and lift coefficients of an autonomous underwater vehicle (AUV) using computational and experimental fluid dynamics methods. *J. Fluids Struct.* 51, <http://dx.doi.org/10.1016/j.jfluidstructs.2014.09.001>.
- Meliga, P., Chomaz, J.-M., 2011. An asymptotic expansion for the vortex-induced vibrations of a circular cylinder. *J. Fluid Mech.* 671, 137–167. <http://dx.doi.org/10.1017/S0022112010005550>.
- Mettot, C., Renac, F., Sipp, D., 2014. Computation of eigenvalue sensitivity to base flow modifications in a discrete framework: Application to open-loop control. *J. Comput. Phys.* 269, 234–258. <http://dx.doi.org/10.1016/j.jcp.2014.03.022>.
- Moulin, J., Bonnet, P., Pfister, J.-L., Carini, M., Marquet, O., 2017. A distributed Lagrangian multiplier/fictitious domain approach for coupled fluid/structure stability analysis. In: 12th ERCOFTAC SIG 33 Workshop, Progress in Flow Instability, Transition and Control (Certosa Di Pontignano, Italy).
- Navrose, Mittal, S., 2016. Lock-in in vortex-induced vibration. *J. Fluid Mech.* 794, 565–594. <http://dx.doi.org/10.1017/jfm.2016.157>.
- Negi, P.S., Hanifi, A., Henningson, D.S., 2020. On the linear global stability analysis of rigid-body motion fluid–structure–interaction problems. *J. Fluid Mech.* 903, A35. <http://dx.doi.org/10.1017/jfm.2020.685>.
- Nitti, A., De Cillis, G., de Tullio, M., 2022. Cross-flow oscillations of a circular cylinder with mechanically coupled rotation. *J. Fluid Mech.* 943, A30. <http://dx.doi.org/10.1017/jfm.2022.442>.
- Nitti, A., Kiendl, J., Reali, A., de Tullio, M., 2020. An immersed-boundary/isogeometric method for fluid–structure interaction involving thin shells. *Comput. Methods Appl. Mech. Engrg.* 364, 112977. <http://dx.doi.org/10.1016/j.cma.2020.112977>.
- Papaioannou, G.V., Yue, D.K.P., Triantafyllou, M.S., Karniadakis, G.E., 2006. Three-dimensionality effects in flow around two tandem cylinders. *J. Fluid Mech.* 558, 387–413. <http://dx.doi.org/10.1017/S0022112006000139>.
- Pfister, J.-L., Marquet, O., Carini, M., 2019. Linear stability analysis of strongly coupled fluid–structure problems with the arbitrary-Lagrangian–Eulerian method. *Comput. Methods Appl. Mech. Engrg.* 355, 663–689. <http://dx.doi.org/10.1016/j.cma.2019.06.024>.
- Prasanth, T., Mittal, S., 2009. Vortex-induced vibration of two circular cylinders at low Reynolds number. *J. Fluids Struct.* 25, 731–741. <http://dx.doi.org/10.1016/j.jfluidstructs.2008.12.002>.
- Sabino, D., Fabre, D., Leontini, J.S., Jacono, D.L., 2020. Vortex-induced vibration prediction via an impedance criterion. *J. Fluid Mech.* 890, <http://dx.doi.org/10.1017/jfm.2020.104>.
- Schulze, J.C., Schmid, P.J., Sesterhenn, J.L., 2009. Exponential time integration using Krylov subspaces. *Internat. J. Numer. Methods Fluids* 60 (6), 591–609. <http://dx.doi.org/10.1002/flid.1902>, arXiv:<https://onlinelibrary.wiley.com/doi/pdf/10.1002/flid.1902>.
- Seo, J.H., Mittal, R., 2011. A sharp-interface immersed boundary method with improved mass conservation and reduced spurious pressure oscillations. *J. Comput. Phys.* 230, 7347–7363. <http://dx.doi.org/10.1016/j.jcp.2011.06.003>.
- Siconolfi, L., Citro, V., Giannetti, F., Camarri, S., Luchini, P., 2017. Towards a quantitative comparison between global and local stability analysis. *J. Fluid Mech.* 819, 147–164. <http://dx.doi.org/10.1017/jfm.2017.167>.
- Singh, S., Mittal, S., 2005. Vortex-induced oscillations at low Reynolds numbers: Hysteresis and vortex-shedding modes. *J. Fluids Struct.* 20, 1085–1104. <http://dx.doi.org/10.1016/j.jfluidstructs.2005.05.011>.
- Sorensen, D.C., 1992. Implicit application of polynomial filters in a k-step Arnoldi method. *SIAM J. Matrix Anal. Appl.* 13, 357–385.
- Tangorra, J.L., Davidson, S.N., Hunter, I.W., Madden, P.G.A., Lauder, G.V., Dong, H., Bozkurtas, M., Mittal, R., 2007. The development of a biologically inspired propulsor for unmanned underwater vehicles. *IEEE J. Ocean. Eng.* 32 (3), 533–550. <http://dx.doi.org/10.1109/JOE.2007.903362>.
- Tezuka, A., Suzuki, K., 2006. Three-dimensional global linear stability analysis of flow around a spheroid. *AIAA J.* 44 (8), 1697–1708. <http://dx.doi.org/10.2514/1.16632>, arXiv:<https://doi.org/10.2514/1.16632>.
- Theodorsen, T., 1934. General theory of aerodynamic instability and the mechanism of flutter.
- Theofilis, V., 2011. Global linear instability. *Annu. Rev. Fluid Mech.* 43 (1), 319–352. <http://dx.doi.org/10.1146/annurev-fluid-122109-160705>, arXiv:<https://doi.org/10.1146/annurev-fluid-122109-160705>.

- Theofilis, V., Colonius, T., 2011. Special issue on global flow instability and control. *Theor. Comput. Fluid Dyn.* 25, 1–6. <http://dx.doi.org/10.1007/s00162-010-0217-3>.
- de Tullio, M.D., Cristallo, A., Balaras, E., Verzicco, R., 2009. Direct numerical simulation of the pulsatile flow through an aortic bileaflet mechanical heart valve. *J. Fluid Mech.* 622, 259–290. <http://dx.doi.org/10.1017/S0022112008005156>.
- Uhlmann, M., 2003. First experiments with the simulation of particulate flows.
- Uhlmann, M., 2005. An immersed boundary method with direct forcing for the simulation of particulate flows. *J. Comput. Phys.* 209 (2), 448–476. <http://dx.doi.org/10.1016/j.jcp.2005.03.017>.
- Vanella, M., Balaras, E., 2009. A moving-least-squares reconstruction for embedded-boundary formulations. *J. Comput. Phys. (Print)* 228 (18), 6617–6628.
- Vanella, M., Rabenold, P., Balaras, E., 2010. An embedded-boundary method with adaptive mesh refinement for fluid-structure interactions problems. *J. Comput. Phys.* 229, 6427–6449. <http://dx.doi.org/10.1016/j.jcp.2010.05.003>.
- Yang, J., Balaras, E., 2006. An embedded-boundary formulation for large-eddy simulation of turbulent flows interacting with moving boundaries. *J. Comput. Phys.* 215, 12–40. <http://dx.doi.org/10.1016/j.jcp.2005.10.035>.
- Yang, X., Zhang, X., Li, Z., He, G.-W., 2009. A smoothing technique for discrete delta functions with application to immersed boundary method in moving boundary simulations. *J. Comput. Phys.* 228, 7821–7836. <http://dx.doi.org/10.1016/j.jcp.2009.07.023>.

Dynamics of a gas bubble in a straining flow: Deformation, oscillations, self-propulsion

Javier Sierra-Ausin ^{*}, Paul Bonnefis, Antonia Tirri [†], David Fabre , and Jacques Magnaudet 
*Institut de Mécanique des Fluides de Toulouse (IMFT), Université de Toulouse, CNRS,
31400 Toulouse, France*



(Received 6 July 2022; accepted 4 November 2022; published 28 November 2022)

We revisit from a dynamical point of view the classical problem of the deformation of a gas bubble suspended in an axisymmetric uniaxial straining flow. Thanks to a recently developed Linearized Arbitrary Lagrangian-Eulerian approach, we compute the steady equilibrium states and associated bubble shapes. Considering perturbations that respect the symmetries of the imposed carrying flow, we show that the bifurcation diagram is made of a stable and an unstable branch of steady states separated by a saddle-node bifurcation, the location of which is tracked throughout the parameter space. We characterize the most relevant global mode along each branch, namely, an oscillatory mode that becomes neutrally stable in the inviscid limit along the stable branch, and an unstable nonoscillating mode eventually leading to the breakup of the bubble along the unstable branch. Next, considering perturbations that break the symmetries of the carrying flow, we identify two additional unstable nonoscillating modes associated with the possible drift of the bubble centroid away from the stagnation point of the undisturbed flow. One of them corresponds merely to a translation of the bubble along the elongational direction of the flow. The other is counterintuitive, as it corresponds to a drift of the bubble in the symmetry plane of the undisturbed flow, where this flow is compressional. We confirm the existence and characteristics of this mode by computing analytically the corresponding leading-order disturbance in the inviscid limit, and show that the observed dynamics are made possible by a specific self-propulsion mechanism that we explain qualitatively.

DOI: [10.1103/PhysRevFluids.7.113603](https://doi.org/10.1103/PhysRevFluids.7.113603)

I. INTRODUCTION

The dynamics of a gas bubble (more generally a drop) freely suspended in a viscous fluid undergoing a uniaxial straining flow has received considerable attention since the pioneering work of Taylor [1]. When the fluid inertia cannot be neglected, the bubble shape results from the competition of pressure and viscous stresses that act to increase the interface deformation and the capillary stress that resists it. Under certain conditions, capillary effects are insufficient to keep the deformation finite, leading eventually to the breakup of the bubble. This physical configuration is commonly described in terms of the Weber (We) and Reynolds (Re) numbers which characterize the relative importance of inertial forces with respect to capillary and viscous forces, respectively. At low-but-finite Reynolds number, Acrivos and Lo [2] showed that no steady bubble shape exists beyond a critical Weber number, We_c , increasing as $Re^{3/4}$. The same qualitative conclusion was

^{*} Also at Department of Industrial Engineering (DIIN), University of Salerno UNISA, Fisciano, 84084, Italy; javier.sierra@imft.fr

[†] Also at Department of Mechanics, Mathematics and Management, Polytechnic University of Bari, Bari, 70125, Italy.

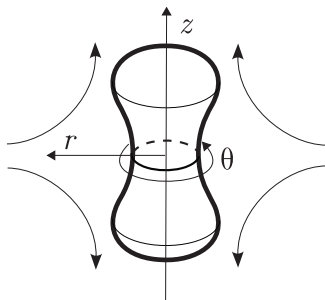


FIG. 1. Sketch of the physical configuration with the symmetry axis $r = 0$ and the symmetry plane $z = 0$ of the undisturbed straining flow, and the corresponding (r, θ, z) coordinate system.

reached in the inviscid limit by Miksis [3] who determined the corresponding $O(1)$ value of We_c . Subsequently, Ryskin and Leal [4] computed the steady bubble shape over a wide range of We and Re by solving the full stationary Navier-Stokes equations on a boundary-fitted grid. They found that We_c increases monotonically with Re and recovered with a good accuracy the predictions of [2] and [3] in the respective limits. These findings were confirmed by Kang and Leal [5] who considered the time-dependent bubble evolution, starting from some arbitrary initial shape. Among other things, they showed that the critical Weber number is highly sensitive to this initial condition, observing that it decreases as the initial elongation of the bubble is increased beyond that of the steady solution. They also considered the case of oscillating bubbles in the inviscid limit and showed that their oscillation frequency decreases as We increases and vanishes for $We = We_c$.

In this study, we revisit this rich phenomenology with the help of a global linear stability approach. Obviously, the chief technical difficulty in this free-boundary problem stands in the fact that the geometry of the flow domain is a priori unknown. This is why up to now it has been tackled numerically either with boundary integral methods in the creeping-flow limit ($Re = 0$) [6,7] or in the potential flow limit [8,9], or with Navier-Stokes solvers making use of time-evolving boundary-fitted grids [4,5]. Here we overcome this difficulty by making use of the recently developed Linearized Arbitrary Lagrangian-Eulerian approach [10], which allows the governing equations and boundary conditions of the problem to be expanded rigorously on an appropriate reference domain. We specify the problem in Sec. II and provide an overview of the Linearized Arbitrary Lagrangian-Eulerian methodology in the Appendix. In Sec. III we take advantage of this approach to determine the complete bifurcation diagram of the system by considering perturbations respecting the symmetries of the imposed straining flow. This diagram is found to comprise a stable and an unstable branch connected through a saddle-node bifurcation. The stable branch corresponds to the previously computed steady states. The unstable branch, which was only reported before under creeping-flow conditions [7], is shown to be associated with the breakup of the bubble under subcritical conditions. In Sec. IV we characterize the dominant linearly unstable or marginally stable mode of the system along each branch. By letting the bubble centroid move freely, we also identify two unstable modes that break the symmetries of the imposed straining flow and, to the best of our knowledge, have not been described up to now. We observe that in one of them the bubble drifts away from the symmetry axis of the straining flow. We show that this surprising dynamics are associated with an original self-propulsion mechanism.

II. STATEMENT OF THE PROBLEM

We consider a gas bubble with negligible viscosity and constant volume \mathcal{V}_b immersed in a Newtonian fluid, with dynamic viscosity μ and density ρ . The surface tension γ acting at the interface is assumed constant and the flow is considered incompressible. The fluid is subject to a uniaxial straining flow which, in the $(\mathbf{e}_r, \mathbf{e}_\theta, \mathbf{e}_z)$ basis sketched in Fig. 1, induces the velocity field $\mathbf{U}_\infty = -\frac{S}{2}r\mathbf{e}_r + Sz\mathbf{e}_z$, where S denotes the uniform strain rate. The bubble centroid stands

initially at the origin $r = z = 0$ which is also the hyperbolic point of the straining flow. The stationary configuration (but not necessarily the eigenmodes to be considered later) is assumed to stay axisymmetric about the z axis ($r = 0$) and to exhibit a mirror symmetry with respect to the midplane $z = 0$ (see Fig. 1). Defining the equilibrium diameter d of the bubble such that $\mathcal{V}_b = \frac{\pi}{6}d^3$, we characterize the bubble deformation in the parameter space (Oh, We). The Ohnesorge number, $\text{Oh} = \frac{\mu}{\sqrt{\rho\gamma d}}$, is defined as the ratio of the viscous force $\mu U_c d$ based on the capillary velocity scale $U_c = [\gamma/(\rho d)]^{1/2}$ and the capillary force γd . Similarly, the Weber number, $\text{We} = \frac{\rho S^2 d^3}{4\gamma}$, is defined as the ratio of the inertial force $\rho U_o^2 d^2$ based on the outer velocity scale $U_o = Sd/2$ and the capillary force. A Reynolds number may also be built by combining these two parameters in the form $\text{Re} = \frac{\sqrt{\text{We}}}{\text{Oh}} = \frac{\rho U_o d}{\mu}$. The bubble elongation may be characterized through the aspect ratio $\chi = \frac{d_z}{d_r}$, with d_z and d_r the major and minor axis lengths, respectively.

Let $\Omega(t)$ and $\Gamma_b(t)$ denote the time-dependent fluid domain and bubble-fluid interface, respectively. The problem is governed by the set of equations

$$\partial_t \Omega \mathbf{u} + \mathbf{u} \cdot \nabla_{\Omega} \mathbf{u} = \rho^{-1} \nabla_{\Omega} \cdot \Sigma_{\Omega} \quad \text{in } \Omega(t), \quad (1)$$

$$\nabla_{\Omega} \cdot \mathbf{u} = 0 \quad \text{in } \Omega(t), \quad (2)$$

$$\partial_t \Omega \eta = \mathbf{u} \cdot \mathbf{n} \quad \text{on } \Gamma_b(t), \quad (3)$$

$$\Sigma_{\Omega} \cdot \mathbf{n} = (-p_b + \gamma \kappa) \mathbf{n} \quad \text{on } \Gamma_b(t), \quad (4)$$

supplemented with appropriate boundary conditions at $r = 0$, $z = 0$ and in the far field. In (1)–(4), the subscript Ω is used to stress the fact that the time and space derivatives are to be evaluated in the time-dependent domain $\Omega(t)$. The no-penetration condition (3) implies that, at any location \mathbf{x} on the interface, the time derivative of the interface position $\eta(\mathbf{x}, t)$ must coincide with the normal component $\mathbf{u} \cdot \mathbf{n}$ of the local fluid velocity $\mathbf{u}(\mathbf{x}, t)$, $\mathbf{n}(\mathbf{x}, t)$ denoting the local unit normal directed into the fluid. The stress tensor in the fluid is $\Sigma_{\Omega}(\mathbf{u}, p) = -p\mathbf{I} + 2\mu\mathbf{D}_{\Omega}(\mathbf{u})$, with p , \mathbf{I} , and $\mathbf{D}_{\Omega}(\mathbf{u})$ the pressure, unit tensor, and strain-rate tensor, respectively. The normal projection of (4) expresses the fact that the normal stress $\mathbf{n} \cdot \Sigma_{\Omega} \cdot \mathbf{n}$ balances the difference between the uniform pressure $p_b(t)$ inside the bubble and the local capillary pressure $\gamma \kappa \mathbf{n}$, with $\kappa(\mathbf{x}, t) = \nabla_{\Omega} \cdot \mathbf{n}(\mathbf{x}, t)$ the local mean curvature of the interface. Last, the tangential projection of (4) yields the shear-free condition $\mathbf{n} \times (\Sigma_{\Omega} \cdot \mathbf{n}) = \mathbf{0}$ which holds if the interface is free of any contamination.

Determining the steady solutions of (1)–(4) and performing subsequently a rigorous global linear stability analysis of the system is made difficult by the deformable nature of the fluid domain. Developing robust and efficient computational strategies to achieve this goal is currently an active research area in the field of fluid-structure interactions; see, e.g., [11,12] and references therein. Here we adopt a Linearized Arbitrary Lagrangian-Eulerian approach, hereinafter referred to as L-ALE, which is a hybrid formulation combining the Eulerian and Lagrangian descriptions of the fluid motion. This approach, initially developed by one of us [10], is well adapted to the treatment of problems involving deformable fluid interfaces subjected to capillary forces. An overview of the L-ALE methodology and of its numerical implementation is given in the Appendix.

An important strength of this approach is that steady-state solutions are computed using the steady form of the governing equations, i.e., the time derivatives in (1) and (3) are dropped. Making use of a Newton algorithm combined with a suitable continuation method (see the Appendix), this allows the determination of both stable and unstable steady states, which would not be possible with a time-marching approach. Once a steady state is reached, its linear stability is assessed by examining the evolution of disturbances with a prescribed eigenmode form. In the present problem, the base configuration exhibits an axial symmetry about the z axis. It is thus relevant to consider disturbances of velocity, pressure, and position in the form $\Psi(r, z)e^{im\theta - i\omega t}$, with θ the polar angle in the cylindrical coordinate system sketched in Fig. 1 and m the corresponding wave number. Unstable

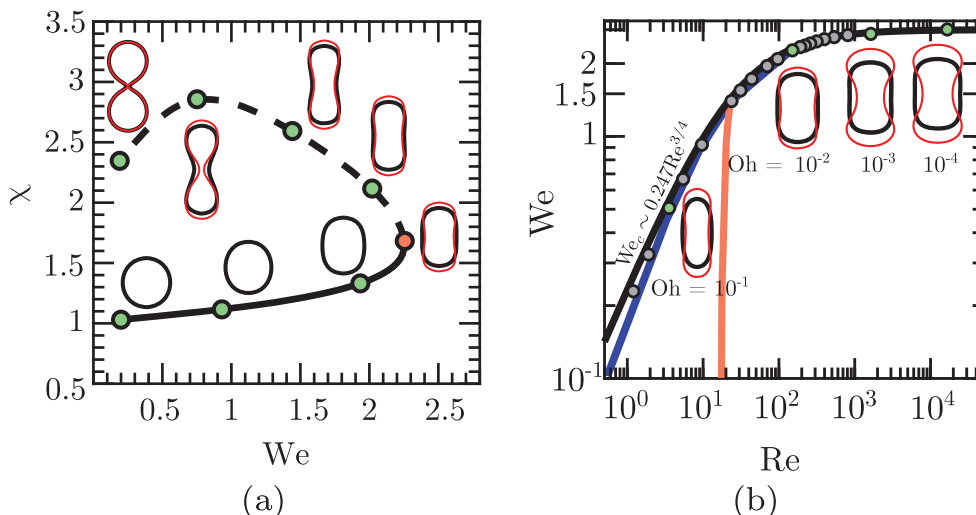


FIG. 2. Bifurcation diagram. (a) Variation of the bubble elongation with the Weber number for a fixed value of the Ohnesorge number, here $Oh = 10^{-2}$; (b) variation of the critical Weber number with the Reynolds number. Bullets: present results obtained with the L-ALE approach [the red bullet in (a) pinpoints the critical Weber number where the saddle-node bifurcation takes place]; solid black line in(a)–(b): empirical correlation proposed in [4]; dashed line in (a): unstable branch determined with the continuation method. In (b) the blue line is the maximum Weber number $We = We_c^*(Re)$ beyond which Mode 0-S (o) stops oscillating; the red line indicates the minimum Reynolds number beyond which Mode 1-S (s) (see Sec. IV B) is unstable. In both panels, bubble shapes are shown for selected values of the parameters corresponding to the green bullets; the black and red contours correspond to the steady state and the unstable Mode 0-S (s), respectively.

eigenmodes satisfying $\text{Im}(\omega) > 0$ can be classified as stationary (s) if $\text{Re}(\omega) = 0$ or oscillating (o) if $\text{Re}(\omega) \neq 0$. They can also be classified as symmetric (S) or antisymmetric (A) with respect to the plane $z = 0$. In what follows, we classify the modes using a nomenclature that summarizes their three characteristic properties, starting with their polar wave number m . For instance a “0-S (s)” mode is axisymmetric ($m = 0$), symmetric with respect to the plane $z = 0$, and stationary.

III. BIFURCATION DIAGRAM

Figure 2(a) displays the bifurcation diagram obtained by setting the Ohnesorge number to the constant value $Oh = 10^{-2}$. This diagram reveals the existence of two branches below a critical Weber number $We_c \approx 2.27$ beyond which no stationary solution exists. Previous studies, for instance [5], showed that the bubble extends indefinitely when $We > We_c$ and eventually breaks up. We tracked the two branches found for $We \leq We_c$ using the pseudo-arc-length continuation method described in the Appendix. Bubbles standing along the lower branch exhibit a convex shape while those along the upper branch are characterized by the presence of a concave neck in the symmetry plane. For a given $We < We_c$, solutions found along the lower branch (corresponding to the bubble with the smaller aspect ratio) are linearly stable in the sense that, following the nomenclature introduced above, all eigenmodes belonging to the 0-S subspace are damped. In contrast, the solutions found along the upper branch are unstable due to the existence of an amplified eigenmode of the 0-S (s) type. In the creeping-flow limit, Gallino *et al.* [7] identified this branch as an edge state of the underlying dynamical system, a qualification that still holds in the presence of finite-Reynolds-number effects. More precisely, if the initial conditions are located in the basin of attraction of this branch, the system first converges toward the corresponding steady state, before the solution becomes unstable at some point and the bubble eventually breaks up. The route to breakup then takes the form of a specific unstable deformation mode, hereinafter referred to as Mode 0-S (s), shown with thin red contours in Fig. 2(a). Compared with the corresponding equilibrium shape, this

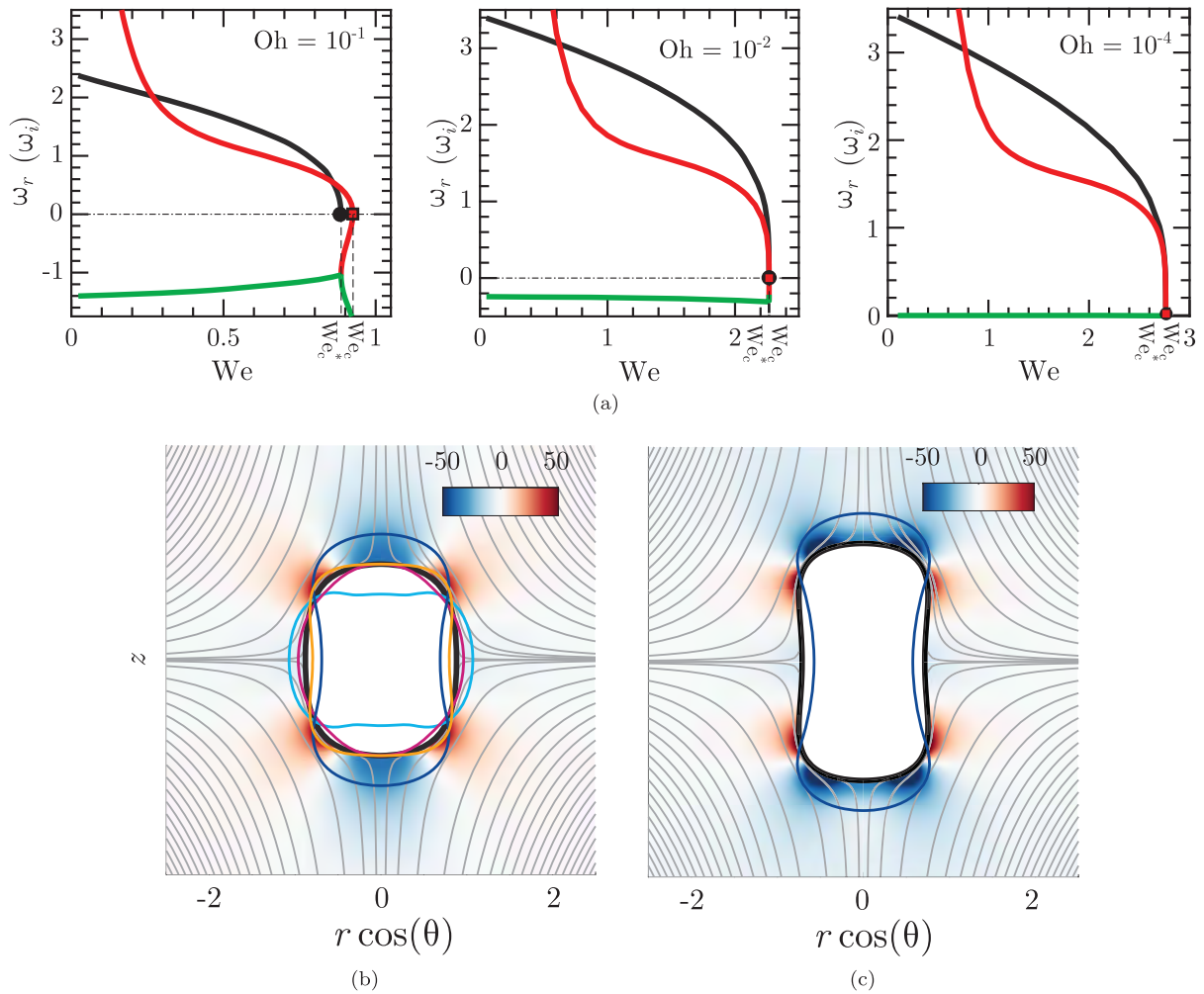


FIG. 3. (a) Variation of the frequency (black lines), growth rate of Mode 0-S (o) (green lines) and of Mode 0-S (s) (red lines) with respect to We , for three values of the Ohnesorge number. The black bullet and red square help to identify the critical Weber numbers We_c^* and We_c , respectively. (b) Pressure disturbance and bubble shape for Mode 0-S (o) (lower branch of the bifurcation diagram), for $We = 2.5$ and $Oh = 1 \times 10^{-4}$. The black contour and gray lines represent the bubble shape and the streamlines in the base state, respectively. The colors show the imaginary part of the pressure disturbance at time $t = T/4$ and the contours display the bubble shape at $t = T/4$ (cyan), $t = T/2$ (orange), $t = 3T/4$ (dark blue), and $t = T$ (magenta), with T the period of oscillation. (c) Same for Mode 0-S (s) (upper branch of the bifurcation diagram), for the same (We, Oh) pair.

mode is characterized by an increase in the bubble elongation and a reduction in the diameter of the neck. The parametric dependence of the critical Weber number with respect to the Reynolds number is reported in Fig. 2(b). Present results are found to agree well with those of [4] (solid black line). In particular, the $Re^{3/4}$ dependence predicted in [2] (after it was reinterpreted in [4]) in the low- Re limit, and the asymptotic value $We_c^\infty \approx 2.77$ determined in [3] in the inviscid limit are recovered. It may be observed that the stationary bubble shape corresponding to critical conditions is convex for intermediate and large Ohnesorge numbers, $Oh \gtrsim O(10^{-2})$, say, but becomes slightly concave in the neighborhood of the symmetry plane at lower Oh .

IV. LINEAR STABILITY

A. Symmetry-preserving unstable or least stable modes

In experiments, the bubble centroid is usually constrained to stay fixed at the stagnation point of the undisturbed flow using computer-controlled devices [13,14]. Under such circumstances, the oscillations (for stable cases) or the deformations leading to breakup (for unstable cases) are expected to respect the polar and mirror symmetries of the base flow. This is why we first consider eigenmodes belonging to the subspace 0-S following the nomenclature introduced above. Two such modes emerge as the most unstable or least stable ones. One is the already mentioned unstable Mode 0-S (s), found along the upper branch of the bifurcation diagram. This mode is stationary, i.e., it is associated with a frequency such that $\text{Re}(\omega) = 0$, and emerges from the saddle-node bifurcation at the critical Weber number We_c . In contrast, the second mode, hereinafter referred to as Mode 0-S (o), is oscillating and stable. Figure 3(a) shows how the frequency of this mode (black line) decreases as We increases and becomes eventually zero at a critical Weber number $We = We_c^*$. At this specific value, the complex eigenvalue associated with Mode 0-S (o) splits into two real eigenvalues. Both are negative, i.e., the corresponding two modes are damped, but they behave in opposite ways as $We - We_c^*$ increases within the interval $[We_c^*, We_c]$. The damping rate of the mode associated with the smallest eigenvalue (in absolute value) decreases continuously and vanishes eventually at $We = We_c$, leading to the amplification of Mode 0-S (s) beyond the saddle-node point [red line in Fig. 3(a)]. In contrast, the damping rate of the original Mode 0-S (o) [green line in Fig. 3(a)] increases continuously from We_c^* to We_c , making this mode aperiodic throughout this interval. The spatial structure of modes 0-S (o) and 0-S (s) at a slightly subcritical Weber number ($We = 2.5$) is illustrated in Figs. 3(b) and 3(c). Mode 0-S (o) is associated with the complex eigenvalue $\omega = 1.3284 - 0.0044i$ and therefore oscillates with a period $T = 2\pi/1.3284 \approx 4.73$. These oscillations result from the competition of inertial and capillary effects. They are characterized by a periodic sequence of compressional ($t = T/4$) and extensional ($t = 3T/4$) displacements of the bubble surface in the z direction. Conversely, Mode 0-S (s) is unstable ($\omega = +0.2797i$) and is characterized by a growing elongation of the bubble along its symmetry axis and a continuous shrinking within its equatorial plane.

Variations of the growth rate of Mode 0-S (s) with respect to $We_c - We$ are displayed in Fig. 4(a). The growth rate exhibits a marked increase with the distance to the threshold, scaling as $(We_c - We)^\alpha$ with $\alpha = 1/4$ and $\alpha = 1/2$ in the high- and low-Reynolds-number limits, respectively. The $(We_c - We)^{1/4}$ -scaling is seen to hold up to $Oh \approx 10^{-3}$, while the $(We_c - We)^{1/2}$ -scaling applies for $Oh \gtrsim 10^{-1}$. Variations of the oscillation frequency (ω_r) of Mode 0-S (o) with respect to $We_c^* - We$ are displayed in Fig. 5. The frequency is also found to grow as $(We_c^* - We)^\alpha$ with $\alpha = 1/4$ and $\alpha = 1/2$ in the high- and low-Reynolds-number limits, respectively. The similarity of the above two scalings, albeit with the role of We_c played by We_c^* in the case of Mode 0-S (o), suggests a close connection between the dynamics of the two modes. As the respective positions of the black bullet and red square in Fig. 3(a) makes clear [see also the blue line in the range $\text{Re} < 10$ in Fig. 2(b)], We_c^* is slightly lower than We_c when viscous effects are large, and coincides with We_c when $Oh \rightarrow 0$. These findings are in line with those reported in [5]. That Mode 0-S (o) exhibits aperiodically damped oscillations within a finite interval $[We_c^*(Oh), We_c(Oh)]$ in the presence of significant viscous effects was also pointed out in [15]. Indeed, assuming the steady bubble shape to be spherical and accounting for viscous effects in the dynamic boundary condition only through the influence of normal stresses (i.e., ignoring the shear-free condition), it was found in [15] that this aperiodically damped regime emerges for $Oh \gtrsim 0.12$. Based on an expansion around $We = 0$, it was predicted that ω_r scales as $(We_{c0} - We)^{1/2}$, with $We_{c0} \approx 3.23$. According to the inset in Fig. 5, this prediction holds for $We_c^* - We \gtrsim 0.3$ but fails to predict the rapid variations of the frequency near the critical Weber number.

The decay rate of Mode 0-S (o) is plotted in Fig. 4(b). This plot confirms the conclusion of Fig. 3(a), showing that this mode is stable throughout its domain of existence. Its decay rate increases linearly with Oh and is virtually independent of We . This mode becomes neutrally stable

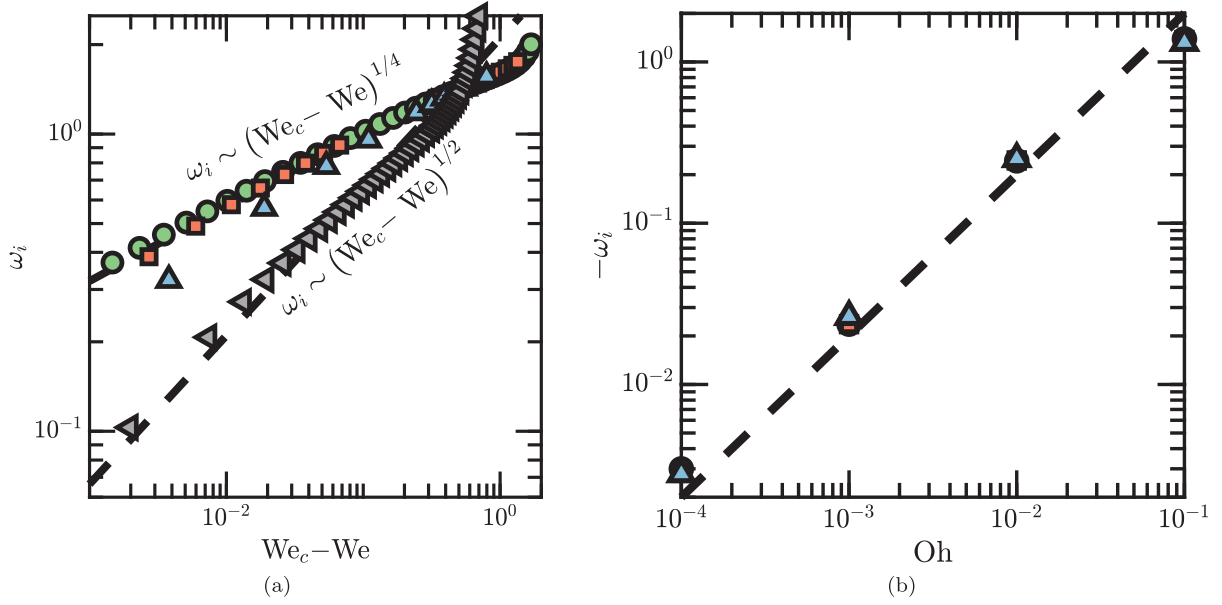


FIG. 4. Variations of the growth rate of modes 0-S (o) and 0-S (s). (a) With respect to $We_c - We$ for Mode 0-S (s) on the unstable branch; (b) with respect to Oh for Mode 0-S (o) on the stable branch. In (a) the green bullets, red squares, blue triangles, and gray triangles refer to $Oh = 10^{-4}, 10^{-3}, 10^{-2},$ and 10^{-1} , respectively; in (b) the green circles, red squares, and blue triangles refer to $We = 0.1, 0.2,$ and 0.4 , respectively. The dashed lines indicate the asymptotic scalings.

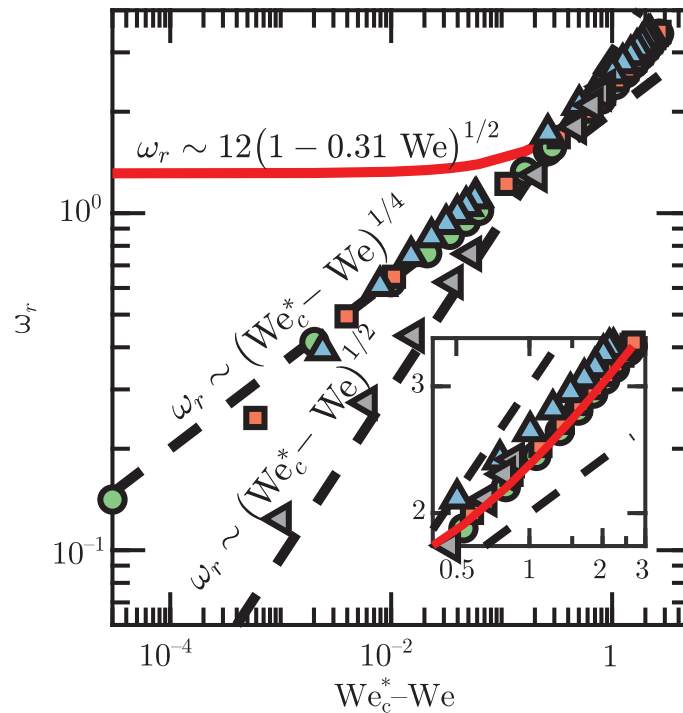


FIG. 5. Variation of the oscillation radian frequency ω_r of Mode 0-S (o) with respect to We . The black dashed lines correspond to the asymptotic scalings suggested by present results. The red line shows the low-We expansion of [15]. The green bullets, red squares, blue triangles, and gray triangles refer to $Oh = 10^{-4}, 10^{-3}, 10^{-2},$ and 10^{-1} , respectively. The inset provides a zoom on the range $0.5 \leq We_c^* - We \leq 3$.

in the inviscid limit $Oh \rightarrow 0$, and We_c^* then coincides with We_c as the right panel in Fig. 3(a) shows. This is no surprise since the problem becomes time-reversible in this limit and the bifurcation becomes a conservative saddle-node one, with two purely complex eigenvalues changing into two purely real ones. That Mode 0-S (o) is stable for finite Reynolds numbers indicates that inertial and capillary effects stay in balance in the corresponding dynamics, with viscous effects providing an additional stabilizing ingredient. This scenario works as long as the elongation of the bubble is small enough for the latter to remain in the basin of attraction of the stable steady state, i.e., close to the lower branch of the bifurcation diagram in Fig. 2(a). Conversely, if the bubble aspect ratio is large enough, breakup occurs through a Mode 0-S (s) deformation after the system has first approached the unstable (upper) branch of the bifurcation diagram and then moved away from it. In this case, the capillary force in the neck region close to the $z = 0$ symmetry plane is weaker than with a Mode 0-S (o) deformation having the same magnitude, owing to the larger concavity of the bubble surface [compare the blue contours in Figs. 3(b) and 3(c)]. This makes the capillary force insufficient to balance the compressional force exerted by the base flow in that region. Beyond the linear stage considered here, this situation leads unavoidably to breakup through the classical end-pinching scenario [16,17].

One can wonder how relevant the dynamics associated with the unstable branch of the bifurcation diagram are from an experimental point of view. In other words, how can this branch be reached in practice, and how Mode 0-S (s) can be triggered. Elements of answer stand in [16] which considered the transient response of a previously elongated drop once the extensional flow is stopped. It was observed that, provided the drop has reached a sufficient elongation prior to the stop, such that it has already taken a waisted shape, it eventually breaks up via an end-pinching instability [17] instead of relaxing towards its initial shape. These observations suggest that the unstable branch may be reached by first elongating the bubble for some time under suitable supercritical conditions, i.e., by imposing a Weber number $We_1 > We_c$, until the bubble attains the desired waisted shape. Then, after having identified the subcritical Weber number $We_2 < We_c$ at which the bubble achieves the same or a very similar stationary shape on the unstable branch, the imposed strain may be suitably reduced to decrease the Weber number $We(t)$ down to the value We_2 . Provided this transient is calibrated in such a way that the disturbance it generates remains small (which may represent a serious experimental challenge), the subsequent dynamics would correspond for some time to those of the linearly unstable Mode 0-S (s) described here.

B. Symmetry-breaking unstable modes

In cases where the bubble centroid is left free, one has to consider eigenmodes breaking either the axial symmetry about the $r = 0$ axis or the mirror symmetry about the $z = 0$ plane. Two new unstable modes are then detected. To the best of our knowledge, these modes have not been characterized so far. One of them, denoted as Mode 0-A (s), is unstable for every (We, Re) . This mode is stationary but antisymmetric with respect to the plane $z = 0$. As Fig. 6 (b) shows, this mode corresponds to a drift of the bubble centroid along the direction of elongation of the undisturbed flow. The existence of this unstable mode is the reason why in experiments a dynamic control such as that described in [14] has to be applied in order to prevent the bubble (or drop) from escaping along the extensional direction of the flow. The second mode, which we refer to as Mode 1-S (s), is also stationary. It is symmetric with respect to the plane $z = 0$ and associated with the wave number $m = 1$ in the polar direction \mathbf{e}_θ . As the red line in Fig. 2(b) indicates, this mode is unstable when the Reynolds number exceeds a value of the order of 20 which only weakly depends on the Weber number. Beyond this threshold, the bubble is found to drift radially in the $z = 0$ plane; the direction of this drift is arbitrary since it is dictated by the definition of the angle θ . What is remarkable is that this drift is performed against the compressional component of the undisturbed flow. Since no external force is applied to the system, this unexpected motion may be thought of as an example of self-propulsion. The possibility for a deformable body immersed in a potential flow to self-propel was examined in several studies, especially [18–20]. It was

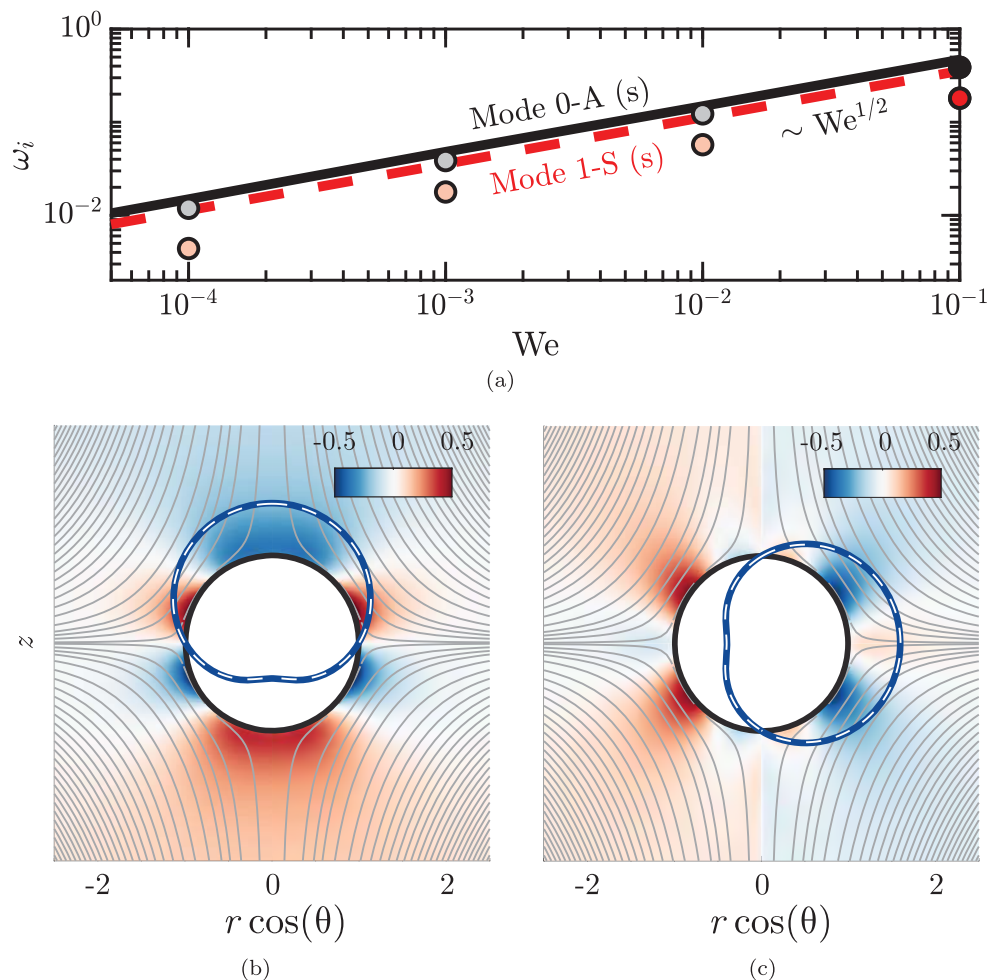


FIG. 6. Modes 0-A (s) and 1-S (s) in a high-Reynolds-number case. (a) Variation of the growth rate of the two modes with respect to We , computed through the truncated potential flow solution of (7) and (8) (lines), and the L-ALE approach in a slightly viscous flow with $Re = 10^3$ (bullets); black/gray: Mode 0-A (s), red/pink: Mode 1-S (s). (b) Pressure disturbance (colours) and bubble shape (contours) for Mode 0-A (s) with $We = 10^{-1}$ and $Re = 10^3$, corresponding to the black bullet in (a). The almost superimposed blue and dashed white contours refer to the results provided by the L-ALE approach and the truncated potential flow solution, respectively. (c) Same with Mode 1-S (s), corresponding to the red bullet in (a). In (b)–(c) the black contour represents the bubble shape in the base state and the gray lines show the corresponding streamlines.

concluded that a deformable body experiencing a net rate of deformation may self-propel provided its time-dependent shape presents some asymmetry. However, these references mostly considered oscillatory deformations of bodies moving in a fluid at rest. In contrast, the mode involved in the present case is stationary in the sense defined in Sec. II and the bubble moves in a straining flow. These two features make the present situation quite different from those envisaged in the aforementioned references.

The above predictions, especially those concerning Mode 1-S (s), need confirmation. For this purpose, following the approach of [15,21], we considered the low-Oh (hence high-Re) regime and determined analytically to first order in We the evolution of a linear perturbation of the bubble shape, assuming that the disturbed flow is strictly irrotational. That is, assuming $\mathbf{u} = \nabla\phi$, we sought the harmonic function ϕ satisfying

$$\partial_t \eta = \nabla\phi \cdot \mathbf{n}, \quad \partial_t \phi + \frac{1}{2}(\nabla\phi \cdot \nabla\phi) + \rho^{-1} p_b = \rho^{-1} \gamma \nabla \cdot \mathbf{n} \quad \text{on } \Gamma_b. \quad (5)$$

For this, assuming that the Weber number is low enough for the undisturbed bubble to be close to a sphere, we expanded the velocity potential and the bubble shape in the form

$$\begin{aligned}
 \phi &= \frac{Sd^2}{4}(\phi_s + \varepsilon\phi_u^m), & \eta &= \frac{d}{2}(\eta_s + \varepsilon\eta_u^m), \\
 \phi_s &= P_2^0(\zeta)\left(\frac{1}{2}r_s^2 + \frac{1}{3}r_s^{-3}\right), & \eta_s &= 1, \\
 \phi_u^m &= \sum_{n=0}^{\infty} \chi_n^m(t)r_s^{-(n+1)}Y_n^m(\Theta, \varphi), & \eta_u^m &= \sum_{n=1}^{\infty} \delta_n^m(t)Y_n^m(\Theta, \varphi),
 \end{aligned} \tag{6}$$

with $Y_n^m(\Theta, \varphi) = P_n^m(\zeta)e^{-im\varphi}$ the spherical harmonics, P_n^m the associated Legendre polynomial, and $\zeta = \cos \Theta$. The corresponding spherical coordinate system is such that $\Theta = 0$ (π) on the positive (negative) half of the z axis defined in Fig. 1, the meridional angle φ is equivalent to the angle θ defined in the same figure, and r_s is the radial position (normalized by $d/2$) measured from the centroid of the undisturbed bubble. Injecting the ansatz (6) in (5), assuming $\varepsilon \ll 1$ and keeping only terms of $O(\varepsilon)$ yields the eigenvalue problem

$$\begin{aligned}
 \dot{\chi}_n^m &= (n-1)(n+2)\delta_n^m \\
 &+ \frac{5}{2}\left(\frac{1}{2}\text{We}\right)^{\frac{1}{2}}\left\{\frac{(n-1-m)(n-m)(n-2)}{(2n-3)(2n-1)}\chi_{n-2}^m - \frac{n(n+1)-3m^2}{(2n-1)(2n+3)}\chi_n^m\right. \\
 &\left.- \frac{(n+3)(n+1+m)(n+2+m)}{(2n+3)(2n+5)}\chi_{n+2}^m\right\},
 \end{aligned} \tag{7}$$

$$\begin{aligned}
 \dot{\delta}_n^m &= -(n+1)\chi_n^m \\
 &+ \frac{5}{2}\left(\frac{1}{2}\text{We}\right)^{\frac{1}{2}}\left\{\frac{(n-1-m)(n-m)(n+1)}{(2n-3)(2n-1)}\delta_{n-2}^m + \frac{n(n+1)-3m^2}{(2n-1)(2n+3)}\delta_n^m\right. \\
 &\left.- \frac{n(n+1+m)(n+2+m)}{(2n+3)(2n+5)}\delta_{n+2}^m\right\},
 \end{aligned} \tag{8}$$

with the dot denoting the time derivative. Solving the problem (7)–(8) for $m = 0$ and $m = 1$ up to $n = N_{\max}$ (with N_{\max} large enough that the eigenvalues no longer vary by further increasing the number of harmonics) reveals that modes 0-A (s) and 1-S (s) are also the most unstable ones in the potential flow limit. Their growth results from imbalances among the terms of the right-hand side of (7)–(8), which involve the velocity $\nabla\phi_s$ of the undisturbed straining flow. In (7) the imbalance is between the variations of the dynamic pressure, $-\nabla\phi_s \cdot \nabla\phi_u$, and those of the capillary pressure, $-\nabla \cdot (\nabla\eta_u)$. In (8) it is between the variations of the normal velocity at the interface induced by the velocity disturbance, $\mathbf{e}_{r_s} \cdot \nabla\phi_u$ (with \mathbf{e}_{r_s} the unit radial vector), and those induced by the disturbance of the interface position, $-\nabla\phi_s \cdot \nabla\eta_u$. Figure 6(a) shows how the growth rate of the two modes varies with We according to the above truncated potential model and to the L-ALE approach. Both solutions indicate that the growth rate increases as $\text{We}^{1/2}$, as may be anticipated from the form of the right-hand sides in (7)–(8). The growth rate of Mode 1-S (s) is slightly smaller than that of Mode 0-A (s). Hence, to observe the former in a laboratory experiment, it is necessary to prevent the bubble from moving along the z axis. As the location of the bullets in the figure shows, the growth rates estimated with the L-ALE approach are lower than those resulting from the truncated potential flow model, especially in the case of Mode 1-S (s). This is due to the fact that finite-We effects affecting the steady state solution are not taken into account in the low-We potential flow expansion, nor are viscous effects arising in the boundary layer that surrounds the bubble. Although these effects are expected to be weak for $\text{Re} = 10^3$, they are likely to be stabilizing, hence to reduce the growth rate. Despite these limitations, the truncated potential flow solution is found to provide a reliable

estimate of the bubble deformation for modes 0-A (s) and 1-S (s) [dashed contour in Figs. 6(b) and 6(c)]. At leading order, this deformation takes the form $\eta_u^0(\Theta, t) \propto \cos \Theta$ for Mode 0-A (s) and $\eta_u^1(\Theta, \phi, t) \propto \sin \Theta \cos \phi$ for Mode 1-S (s). In summary, the above perturbative approach confirms that the presence of the unstable Mode 1-S (s) and its unexpected dynamics are not artifacts of the L-ALE approach. This mode is part of the intrinsic dynamical response of the system when the bubble centroid is not constrained to stay at the stagnation point of the uniaxial flow.

The bubble shapes and the pressure disturbance distribution displayed in Fig. 6(c) help to understand the physical mechanism that makes the self-propulsion associated with Mode 1-S (s) possible. Consider that the bubble is initially spherical and stands at the stagnation point. If a disturbance in the form of Mode 1-S (s) is applied, the geometric centroid of the bubble shifts to a radial position $r_0 \neq 0$. At this position, due to the radial pressure gradient $-\rho \frac{S^2}{4} r_0$ induced by the carrying flow, the disturbance past the bubble is no longer symmetric, even though the latter is still considered spherical. This pressure gradient is responsible for the left/right asymmetry in the pressure distribution of Fig. 6(c). That the pressure disturbance at the bubble surface reaches its extrema approximately midway between the z axis and the symmetry plane $z = 0$ is a classical feature of a nearly inviscid flow past a sphere translating in a straining flow (see, e.g., [22]). These pressure extrema having opposite signs, they result in a net thrust (corresponding to an added-mass force) propelling the bubble in the direction opposite to the pressure gradient, i.e., from left to right in the figure. Moreover, the pressure on the outer side of the interface being equal to that within the bubble minus the capillary pressure, the asymmetric pressure distribution tends to make the bubble shape more asymmetric by decreasing (increasing) the mean curvature of the interface on the high- (low-) pressure side. Again, these deformations change the position of the bubble centroid, and they do it cooperatively with the above added-mass effect, as both mechanisms act to move the bubble to a position $r > r_0$ [i.e., to push it to the right in Fig. 6(c)]. Since the inward velocity of the straining flow increases with r , so does the relative velocity between the carrying flow and the bubble centroid. This in turn enhances the pressure asymmetry at the bubble surface, which reinforces both the added-mass thrust and the asymmetric changes in the interface curvature, and so on. This qualitative scenario confirms that applying an asymmetric perturbation corresponding to the mode $m = 1$ to an initially spherical bubble resting at the stagnation point allows it to move radially thanks to what may be considered as a self-propulsion mechanism assisted by the straining flow. This mechanism grounds on the cooperative effect of capillary and inertial stresses, the latter resulting from the interaction of the carrying flow with the velocity disturbance. Of course this picture only holds as long as viscous effects are weak enough. Indeed, since the bubble leads the fluid, the drag resulting from the corresponding relative velocity resists the bubble drift (whereas the two cooperate in the case of Mode 0-(A) (s) in which the bubble lags the fluid). Therefore, it is only under conditions where this drag is small enough for the inertial forces involved in the above scenario to dominate that the bubble may drift. This is why Mode 1-S (s) only grows when the Reynolds number is large enough, i.e., $\text{Re} \gtrsim 20$ according to the red line in Fig. 2(b). This is also why this intriguing behavior was not observed in the experiments of [13] in which the Reynolds number was kept very low (in the range 10^{-2} – 10^{-4}) by using very viscous oils as suspending fluid.

V. SUMMARY

In this study, we employed the recently developed L-ALE approach to revisit the dynamics of a gas bubble immersed in a uniaxial straining flow. This approach proved to be able to accurately determine the equilibrium shapes of the bubble, as well as the maximum Weber number $We_c(\text{Oh})$ beyond which no equilibrium is possible. As already reported in the literature, the return to equilibrium of a slightly disturbed bubble under subcritical conditions takes place through damped oscillations, except within a small interval $[We_c^*, We_c]$ where an aperiodic damped regime takes place. We analyzed the eigenmode associated with these behaviors in detail. In particular, we characterized the scaling laws governing the variations of the corresponding eigenvalue with Oh and $We_c^* - We$. Thanks to a suitable continuation method, we also found a second branch of solutions

linked to the branch of stable solutions through a saddle-node point. This branch was not identified up to now, except in the creeping-flow limit. Indeed, equilibrium shapes corresponding to this second branch are always unstable, which makes them unreachable with traditional time-marching approaches. The linear stability analysis revealed that the most amplified eigenmode on that branch is stationary and is characterized by the occurrence of a neck on the symmetry plane of the bubble. In the nonlinear stage, this would eventually lead to the breakup of the bubble through the end-pinching mechanism. We sketched how this unstable branch and the above stationary mode may be approached in a laboratory experiment. We also examined the case where the bubble centroid is not constrained to stay at the stagnation point of the undisturbed flow, a situation that was not considered in previous studies. In this case, two other unstable modes arise. The most amplified one corresponds to the drift of the bubble along the elongational axis of the undisturbed flow. Surprisingly, the slightly less amplified second mode leads to a drift of the bubble within the symmetry plane of the undisturbed flow, a region where this flow is directed toward the stagnation point. To check this unexpected prediction, we considered the low-We inviscid limit in which a truncated potential flow model can be established. We solved the corresponding eigenvalue problem and confirmed the predictions of the L-ALE approach in that limit. We also presented a qualitative scenario explaining why, after imposing an asymmetric initial perturbation to the bubble, the pressure and the interface curvature distributions develop growing asymmetric components that cooperate to make the bubble drift against the base flow possible when viscous effects are weak enough.

APPENDIX A: OVERVIEW OF THE L-ALE APPROACH

Free-boundary problems involving a Newtonian fluid contained in a time-dependent fluid domain $\Omega(t)$ bounded by a fixed boundary Γ_s and a free boundary $\Gamma_b(t)$ subjected to capillary effects are governed by (1)–(4) supplemented with appropriate boundary conditions on Γ_s . In the L-ALE approach, we first consider a *reference* domain Ω_0 , which is fixed and allows unknowns to be evaluated in an Eulerian manner, and the *physical* domain $\Omega(t)$, which depends upon time and where Lagrangian quantities are evaluated. Let \mathbf{x}_0 and \mathbf{x} denote the local position (with respect to some fixed origin) of a given geometrical point in Ω_0 and Ω , respectively. Then the two domains are connected through the diffeomorphism $\Phi : \Omega_0 \mapsto \Omega$, with $\Phi(\mathbf{x}_0, t) = \mathbf{x}$. In the L-ALE approach, this diffeomorphism is linearized in the form $\Phi(\mathbf{x}_0, t) = \mathbf{x}_0 + \boldsymbol{\xi}(\mathbf{x}_0)$, where $\boldsymbol{\xi}(\mathbf{x}_0)$ is a displacement field such that $\|\boldsymbol{\xi}(\mathbf{x}_0)\| = \|\mathbf{x} - \mathbf{x}_0\| \sim O(\varepsilon_0 \|\mathbf{x}_0\|)$ with $\varepsilon_0 \ll 1$. The field $\boldsymbol{\xi}(\mathbf{x}_0)$ propagates the Lagrangian displacement of the interface η into the fluid domain. This displacement field is arbitrary since it is not determined by the governing equations (1)–(4), i.e., it is not dictated by the actual motion of the fluid elements, except at the free boundary. It only needs to obey the no-penetration condition (3), plus some mild smoothness properties. Usually the smoothness of $\boldsymbol{\xi}$ is ensured by assuming that its distribution within the fluid domain is governed by an elliptic equation, such as the Laplace equation or the Cauchy equation for an elastic material. An illustration of the L-ALE methodology is depicted in Fig. 7(a). The sketch shows how the free boundary, labeled Γ_b in the physical domain Ω and $\Gamma_{b,0}$ in the reference domain Ω_0 , transforms from one domain to the other. Although the geometric properties of this boundary, especially its unit normal \mathbf{n} and tangent \mathbf{t} , may be evaluated in both domains, we always evaluate them in Ω_0 , after which they may be mapped forward onto the physical domain via Φ if needed.

The L-ALE formalism leads to an approach in which the governing equations and the deformation of the physical domain are solved simultaneously and consistently, which ensures the stability of the algorithms involved. Such an approach, in which the unknown to be determined is the state vector $\mathbf{q} = [\mathbf{u}, p, p_b, \boldsymbol{\xi}, \eta]^T$ (the superscript T denoting the transpose), is sometimes referred to as “monolithic.” To obtain the steady-state solution of (1)–(4), we solve the corresponding *steady* nonlinear problem using a Newton method, following the methodology introduced in [10].

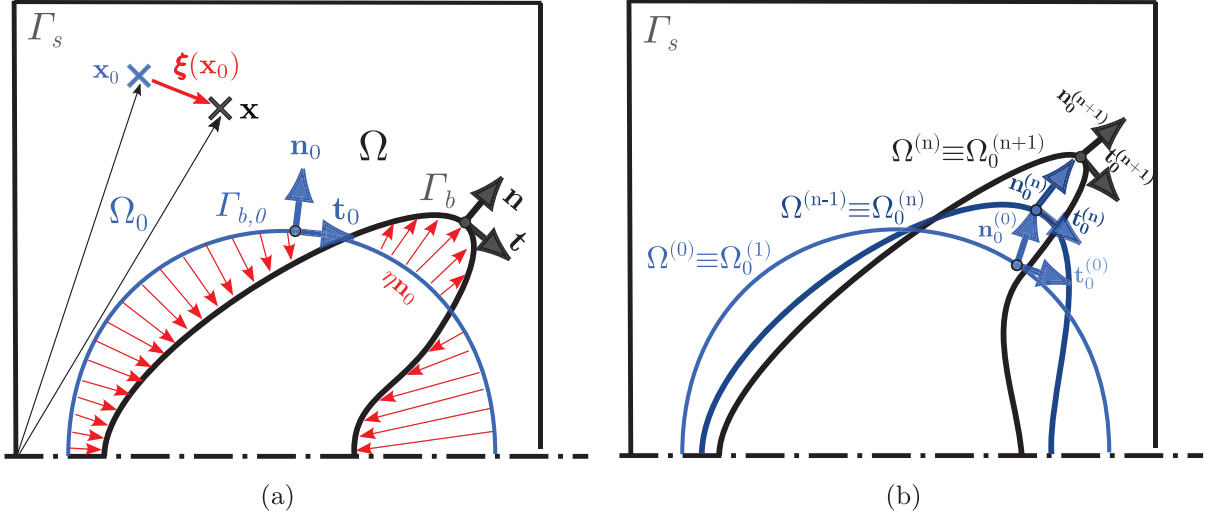


FIG. 7. Sketch of the geometrical transformations involved in the L-ALE approach. (a) General framework, showing in particular the current physical domain Ω and free boundary Γ_b (black), and the reference domain Ω_0 and free boundary $\Gamma_{b,0}$ (blue); (b) successive updates of the reference domain during the iterations of the Newton method.

That is, the steady-state solution, $\mathbf{q}_0 = [\mathbf{u}_0, p_0, p_{b,0}, \mathbf{0}, 0]^T$, is determined iteratively by solving the system of equations governing the increment $\mathbf{q}' = [\mathbf{u}', p', p'_b, \xi, \eta]^T$:

$$\begin{aligned}
 \mathbf{L}_{NS}[\mathbf{q}'] &\equiv \mathbf{u}' \cdot \nabla_{\Omega_0} \mathbf{u}_0 + \mathbf{u}_0 \cdot \nabla_{\Omega_0} \mathbf{u}' - \rho^{-1} \nabla_{\Omega_0} \cdot \Sigma_{\Omega_0}(\mathbf{u}', p') + \mathbf{Q}_{\Omega_0}(\xi) &= -\mathbf{u}_0 \cdot \nabla_{\Omega_0} \mathbf{u}_0 + \rho^{-1} \nabla_{\Omega_0} \cdot \Sigma_{\Omega_0} && \text{in } \Omega_0, \\
 \mathbf{L}_{\text{div}}[\mathbf{q}'] &\equiv \nabla_{\Omega_0} \cdot \mathbf{u}' - \nabla_{\Omega_0} \mathbf{u}_0 : \nabla_{\Omega_0}^T \xi &= -\nabla_{\Omega_0} \cdot \mathbf{u}_0 && \text{in } \Omega_0, \\
 \mathbf{L}_{\text{kin}}[\mathbf{q}'] &\equiv \mathbf{u}' \cdot \mathbf{n}_0 + \mathbf{u}_0 \cdot \mathbf{n}' &= -\mathbf{u}_0 \cdot \mathbf{n}_0 && \text{on } \Gamma_{b,0}, \\
 \mathbf{L}_{\text{dyn}}[\mathbf{q}'] &\equiv (p'_b - p' - \gamma \kappa') \mathbf{n}_0 + 2\mu \mathbf{D}_{\Omega_0}(\mathbf{u}') \cdot \mathbf{n}_0 &= (p_0 - p_{b,0} + \gamma \kappa_0) \mathbf{n}_0 && \text{on } \Gamma_{b,0}, \\
 &\quad + (p_{b,0} - p_0 - \gamma \kappa_0) \mathbf{n}' + 2\mu \mathbf{D}_{\Omega_0}(\mathbf{u}_0) \cdot \mathbf{n}' &= -2\mu \mathbf{D}_{\Omega_0}(\mathbf{u}_0) \cdot \mathbf{n}_0 && \\
 \mathbf{L}_{\text{com}}[\mathbf{q}'] &\equiv \xi - \eta \mathbf{n}_0 &= \mathbf{0} && \text{on } \Gamma_{b,0}, \\
 \mathbf{L}_E[\xi] &\equiv \nabla_{\Omega_0} \cdot \mathbf{E}(\xi) &= \mathbf{0} && \text{in } \Omega_0,
 \end{aligned} \tag{A1}$$

where $\mathbf{n}' = -(\mathbf{t}_0 \cdot \nabla_{\Gamma_{b,0}} \eta) \mathbf{t}_0$, $\kappa' = \nabla_{\Omega_0} \cdot \mathbf{n}'$, and the Ω_0 and $\Gamma_{b,0}$ subscripts indicate that the corresponding spatial derivative is evaluated in the reference domain Ω_0 bounded (partly) by the free boundary $\Gamma_{b,0}$. In (A1) the first four equations correspond to the linearized form of the governing equations (1)–(4). The deformation of the domain induces several extra terms in these linearized equations, especially an extra momentum source term $\mathbf{Q}_{\Omega_0}(\xi) = -\mathbf{u}_0 \cdot \nabla_{\Omega_0} \mathbf{u}_0 \cdot \nabla_{\Omega_0} \xi + \rho^{-1} (\nabla_{\Omega_0} \cdot \Sigma_{\Omega_0}) \cdot \nabla_{\Omega_0}^T \xi + \rho^{-1} \mu \nabla_{\Omega_0} \cdot \{ \nabla_{\Omega_0} \mathbf{u}_0 \cdot \nabla_{\Omega_0} \xi + (\nabla_{\Omega_0} \mathbf{u}_0 \cdot \nabla_{\Omega_0} \xi)^T \}$ in the momentum equation. The last two equations determine the displacement field ξ throughout the domain. The elliptic operator \mathbf{E} controls the spatial distribution of this arbitrary displacement within Ω_0 , subject to the compatibility condition $\xi = \eta \mathbf{n}_0$ on $\Gamma_{b,0}$. Here, following [12], we assume that this distribution obeys a linear elastic response, i.e., we set $\mathbf{E}(\xi) = 2\mu_e \mathbf{D}_{\Omega_0}(\xi) + \lambda_e (\nabla_{\Omega_0} \cdot \xi) \mathbf{I}$. With this choice, the last equation in (A1) may be interpreted as the Cauchy equation of elasticity, the coefficients λ_e and μ_e being Lamé pseudocoefficients which we both set to unity.

At each iteration n , the pseudo-steady-state solution is updated in the form $\mathbf{q}_0^{(n)} = \mathbf{q}_0^{(n-1)} + \mathbf{q}' = [\mathbf{u}_0 + \mathbf{u}', p_0 + p', p_{b,0} + p'_b, \xi, \eta]^T$. The reference domain Ω_0 is also updated, based on conditions $\mathbf{x}_{\Omega_0^{(n)}} = \mathbf{x}_{\Omega_0^{(n-1)}} + \xi$ and $\mathbf{x}_{\Gamma_0^{(n)}} = \mathbf{x}_{\Gamma_0^{(n-1)}} + \eta \mathbf{n}_0^{(n-1)}$ linking the position of a given point standing in the fluid domain or on the free boundary in two successive reference configurations, as sketched in Fig. 7(b). In other words, the steady-state solution is obtained by considering the governing equations (A1) on a succession of physical domains such that the n th of them only differs slightly from the $(n-1)$ th one, the latter being considered as the new reference domain during the n th iteration.

In cases where the free boundary is a closed surface (such as for a bubble), the enclosed volume must stay equal to its initial value, \mathcal{V}_b , provided effects of compressibility are negligible in the corresponding medium. This implies

$$\mathbf{L}_{\text{vol}}[\mathbf{q}'] \equiv \int_{\Gamma_{b,0}} \eta d\mathcal{S}_0 = \int_{\Omega_{b,0}} (1 + \nabla_{\Omega_0} \cdot \boldsymbol{\xi}) d\mathcal{V}_0 - \mathcal{V}_b \quad \text{on } \Gamma_{b,0}. \quad (\text{A2})$$

The various matrices involved in the problem (A1)–(A2) are built and inverted within the finite-element software FreeFem++. The volume fields (\mathbf{u} , p) are discretized following a Taylor-Hood scheme, i.e., the mixed finite-element Lagrange basis (P_2 , P_1). The volume displacement field $\boldsymbol{\xi}$ is discretized within the P_2 finite-element space. The free-boundary displacement field η is discretized within the Galerkin-Fourier space. This displacement is orthogonally projected onto the local Fourier basis ϕ_k in the form $\eta(s_0) = \sum_{k=0}^{N_b} \phi_k(s_0) X_\eta(k)$, with $X_\eta(k)$ the coefficients of η in that basis, N_b the number of Fourier elements and s_0 the arc length coordinate.

In the vicinity of a saddle-node bifurcation, the Jacobian matrix of (A1) is ill-conditioned. In particular it is singular at the bifurcation point. In such situations, instead of the usual continuation procedure performed on some control parameter, for instance, We , we continue the solution on a suitable arc length with a pseudo-arc-length continuation method. This technique consists in replacing the Jacobian matrix with a bordered matrix, i.e., a matrix with an additional column and an additional row. The practical application of this technique, i.e., the definition of the arc length, depends on the parameters of the problem under consideration. In the context of this paper, we build the arc length on the pressure within the bubble, p_b , and the strain rate of the base flow, S , so that the infinitesimal arc length is $(ds)^2 = (dp_b)^2 + (dS)^2$. If (A1) [or (A1)–(A2)] is written symbolically in the form $\mathbf{L}|_{\mathbf{q}_0}[\mathbf{q}'] = -\mathbf{F}(\mathbf{q}_0)$, the bordered system then takes the form

$$\begin{pmatrix} \mathbf{L}|_{\mathbf{q}_0^{(n-1)}} & \mathbf{D}_{bc} \\ \frac{dp_b}{ds} & \frac{dS}{ds} \end{pmatrix} \begin{pmatrix} \mathbf{q}' \\ S' \end{pmatrix} = \begin{pmatrix} -\mathbf{F}(\mathbf{q}_0^{(n-1)}) - \mathbf{D}_{bc}(S_0^{(n-1)}) \\ -\frac{dp_b}{ds}(p_{b,0}^{(n-1)} - p_{b,0}^{(0)}) - \frac{dS}{ds}(S_0^{(n-1)} - S_0^{(0)}) + \Delta s \end{pmatrix}, \quad (\text{A3})$$

where the state vector \mathbf{q}' is augmented with the update of the strain rate, S' , and Δs denotes the arc length step. The operator \mathbf{D}_{bc} , which takes the form of a column vector in the bordered matrix, serves to impose the boundary conditions on the velocity field and only depends on S . The derivative $\frac{dp_b}{ds}$ acts on the pressure within the bubble only, while $\frac{dS}{ds}$ only acts on the strain rate. These derivatives are determined at the initial step of the Newton method by inverting the matrix operator $\mathbf{L}|_{\mathbf{q}_0^{(0)}}$ and computing the derivative of \mathbf{q} with respect to S as $\frac{d\mathbf{q}}{dS}|_{\mathbf{q}_0^{(0)}} = -\mathbf{L}^{-1}|_{\mathbf{q}_0^{(0)}} \cdot \frac{d\mathbf{F}}{dS}(\mathbf{q}_0^{(0)})$. Then, selecting the component $\frac{dp_b}{ds}|_{\mathbf{q}_0^{(0)}}$ in the vector field $\frac{d\mathbf{q}}{dS}|_{\mathbf{q}_0^{(0)}}$ and making use of the definition $(ds)^2 = (dp_b)^2 + (dS)^2$, the extra derivatives involved in (A3) are computed as $\frac{dp_b}{ds} = \frac{dp_b}{ds}|_{\mathbf{q}_0^{(0)}} \{ (\frac{dp_b}{ds}|_{\mathbf{q}_0^{(0)}})^2 + 1 \}^{-1/2}$ and $\frac{dS}{ds} = \{ (\frac{dp_b}{ds}|_{\mathbf{q}_0^{(0)}})^2 + 1 \}^{-1/2}$.

Once the steady state is reached, the linear stability of the corresponding solution is determined by examining the fate of disturbances with the eigenmode form $\mathbf{q}' = [\hat{\mathbf{u}}, \hat{p}, \hat{p}_b, \hat{\boldsymbol{\xi}}, \hat{\eta}]^T e^{-i\omega t}$, the hatted complex amplitudes depending on \mathbf{x}_0 . In cases where the base configuration is axisymmetric, as in the physical problem considered in this paper, we rather consider disturbances of the form $\mathbf{q}' = [\hat{\mathbf{u}}, \hat{p}, \hat{p}_b, \hat{\boldsymbol{\xi}}, \hat{\eta}]^T e^{im\theta - i\omega t}$, with θ the polar angle of the (r, θ, z) cylindrical coordinate system and m the corresponding wave number, the hatted amplitudes depending now only on r and z . Such solutions are obtained by solving the eigenvalue problem

$$\begin{aligned} -i\omega(\hat{\mathbf{u}} - \hat{\boldsymbol{\xi}} \cdot \nabla_{\Omega_0} \mathbf{u}_0) + \mathbf{L}_{\text{NS}}[\hat{\mathbf{q}}] &= \mathbf{0} && \text{in } \Omega_0, \\ \mathbf{L}_{\text{div}}[\hat{\mathbf{q}}] &= 0 && \text{in } \Omega_0, \\ -i\omega\hat{\eta} + \mathbf{L}_{\text{kin}}[\hat{\mathbf{q}}] &= 0 && \text{on } \Gamma_{b,0}, \\ \mathbf{L}_{\text{dyn}}[\hat{\mathbf{q}}] &= \mathbf{0} && \text{on } \Gamma_{b,0}, \\ \mathbf{L}_{\text{com}}[\hat{\mathbf{q}}] &= \mathbf{0} && \text{on } \Gamma_{b,0}, \\ \mathbf{L}_E[\hat{\boldsymbol{\xi}}] &= \mathbf{0} && \text{in } \Omega_0, \end{aligned} \quad (\text{A4})$$

supplemented with

$$\mathbf{L}_{\text{vol}}[\hat{\mathbf{q}}] = 0 \quad \text{on } \Gamma_{b,0} \quad (\text{A5})$$

if the constraint (A2) holds for the steady state and the perturbation. In (A4) the term $i\omega\hat{\boldsymbol{\xi}} \cdot \nabla_{\Omega_0}\mathbf{u}_0$ arising in the linearized momentum equation is the acceleration of the moving domain, which must be subtracted to obtain the actual fluid acceleration in Ω_0 . Here the reference domain is that corresponding to the steady-state solution of (A1), i.e., $\Omega_0 \equiv \Omega_0^{(N)}$, with N the number of iterations carried out to reach the steady solution through the Newton method, as depicted in Fig. 7(b). The eigenpairs of (A4)–(A5) are obtained using the SLEPc library.

-
- [1] G. I. Taylor, The formation of emulsions in definable fields of flow, *Proc. R. Soc. Lond. A* **146**, 501 (1934).
 - [2] A. Acrivos and T. S. Lo, Deformation and breakup of a single slender drop in an extensional flow, *J. Fluid Mech.* **86**, 641 (1978).
 - [3] M. J. Miksis, A bubble in an axially symmetric shear flow, *Phys. Fluids* **24**, 1229 (1981).
 - [4] G. Ryskin and L. G. Leal, Numerical solution of free-boundary problems in fluid mechanics. Part 3. Bubble deformation in an axisymmetric straining flow, *J. Fluid Mech.* **148**, 37 (1984).
 - [5] I. S. Kang and L. G. Leal, Numerical solution of axisymmetric, unsteady free-boundary problems at finite Reynolds number. I. Finite-difference scheme and its application to the deformation of a bubble in a uniaxial straining flow, *Phys. Fluids* **30**, 1929 (1987).
 - [6] G. K. Youngren and A. Acrivos, On the shape of a gas bubble in a viscous extensional flow, *J. Fluid Mech.* **76**, 433 (1976).
 - [7] G. Gallino, T. M. Schneider, and F. Gallaire, Edge states control droplet breakup in subcritical extensional flows, *Phys. Rev. Fluids* **3**, 073603 (2018).
 - [8] J. Rodríguez-Rodríguez, J. M. Gordillo, and C. Martínez-Bazan, Breakup time and morphology of drops and bubbles in a high-Reynolds-number flow, *J. Fluid Mech.* **548**, 69 (2006).
 - [9] J. C. Padrino and D. D. Joseph, Viscous irrotational analysis of the deformation and break-up time of a bubble or drop in uniaxial straining flow, *J. Fluid Mech.* **688**, 390 (2011).
 - [10] P. Bonnefis, Etude des instabilités de sillage, de forme et de trajectoire de bulles par une approche de stabilité linéaire globale, Ph.D. thesis, Institut National Polytechnique de Toulouse, Toulouse, France (2019), <http://www.theses.fr/2019INPT0070>.
 - [11] M. Heil, A. L. Hazel, and J. Boyle, Solvers for large-displacement fluid-structure interaction problems: Segregated versus monolithic approaches, *Comput. Mech.* **43**, 91 (2008).
 - [12] J. L. Pfister, O. Marquet, and M. Carini, Linear stability analysis of strongly coupled fluid–structure problems with the Arbitrary Lagrangian–Eulerian method, *Comput. Methods Appl. Mech. Eng.* **355**, 663 (2019).
 - [13] B. J. Bentley and L. G. Leal, An experimental investigation of drop deformation and breakup in steady, two-dimensional linear flows, *J. Fluid Mech.* **167**, 241 (1986).
 - [14] B. J. Bentley and L. G. Leal, A computer-controlled four-roll mill for investigations of particle and drop dynamics in two-dimensional linear shear flows, *J. Fluid Mech.* **167**, 219 (1986).
 - [15] I. S. Kang and L. G. Leal, Small-amplitude perturbations of shape for a nearly spherical bubble in an inviscid straining flow (steady shapes and oscillatory motion), *J. Fluid Mech.* **187**, 231 (1988).
 - [16] H. A. Stone, B. J. Bentley, and L. G. Leal, An experimental study of transient effects in the breakup of viscous drops, *J. Fluid Mech.* **173**, 131 (1986).
 - [17] H. A. Stone and L. G. Leal, Relaxation and breakup of an initially extended drop in an otherwise quiescent fluid, *J. Fluid Mech.* **198**, 399 (1989).
 - [18] P. G. Saffman, The self-propulsion of a deformable body in a perfect fluid, *J. Fluid Mech.* **28**, 385 (1967).
 - [19] T. B. Benjamin and A. T. Ellis, Self-propulsion of asymmetrically vibrating bubbles, *J. Fluid Mech.* **212**, 65 (1990).

- [20] T. Miloh and A. Galper, Self-propulsion of general deformable shapes in a perfect fluid, *Proc. R. Soc. London A Math. Phys. Eng. Sci.* **442**, 273 (1993).
- [21] S. M. Yang, Z. C. Feng, and L. G. Leal, Nonlinear effects in the dynamics of shape and volume oscillations for a gas bubble in an external flow, *J. Fluid Mech.* **247**, 417 (1993).
- [22] J. Magnaudet, M. Rivero, and J. Fabre, Accelerated flows past a rigid sphere or a spherical bubble. Part 1. Steady straining flow, *J. Fluid Mech.* **284**, 97 (1995).

Bibliography

- Poincaré, Henri (1890). “Sur le problème des trois corps et les équations de la dynamique”. In: *Acta mathematica* 13.1, A3–A270.
- Lorenz, Edward N (1963). “Deterministic nonperiodic flow”. In: *Journal of atmospheric sciences* 20.2, pp. 130–141.
- Briggs, Richard J et al. (1964). *Electron-stream interaction with plasmas*. Vol. 187. MIT press Cambridge, MA.
- Urabe, M. (1965). “Galerkin’s procedure for nonlinear periodic systems”. In: *Arch. Rational Mech. Anal.* 20, pp. 120–152.
- Crow, S Cj and FH Champagne (1971). “Orderly structure in jet turbulence”. In: *Journal of fluid mechanics* 48.3, pp. 547–591.
- Ruelle, David and Floris Takens (1971). “On the nature of turbulence”. In: *Les rencontres physiciens-mathématiciens de Strasbourg-RCP25* 12, pp. 1–44.
- Stokes, A. (1972). “On the approximation of nonlinear oscillations”. In: *J. Differential Equations* 12, pp. 535–558.
- Bers, Abraham (1975). “Linear waves and instabilities”. In: *Plasma physics–les houches 1972*.
- Hénon, Michel (1976). “A two-dimensional mapping with a strange attractor”. In: *The theory of chaotic attractors*. Springer, pp. 94–102.
- Newhouse, Sheldon, David Ruelle, and Floris Takens (1978). “Occurrence of strange Axiom A attractors near quasi periodic flows on T^m , $m \geq 3$ ”. In: *Communications in Mathematical Physics* 64.1, pp. 35–40.
- Chirikov, Boris V (1979). “A universal instability of many-dimensional oscillator systems”. In: *Physics reports* 52.5, pp. 263–379.
- Penrose, Oliver (1979). “Foundations of statistical mechanics”. In: *Reports on Progress in Physics* 42.12, p. 1937.
- Hughes, Thomas JR, Wing Kam Liu, and Thomas K Zimmermann (1981). “Lagrangian-Eulerian finite element formulation for incompressible viscous flows”. In: *Computer methods in applied mechanics and engineering* 29.3, pp. 329–349.

- Van Dyke, M and S Widnall (1983). “An album of fluid motion”. In: *Journal of Applied Mechanics* 50.2, p. 475.
- Dangelmayr, Gerhard (1986). “Steady-state mode interactions in the presence of 0 (2)-symmetry”. In: *Dynamics and Stability of Systems* 1.2, pp. 159–185.
- Knobloch, E (1986). “On the degenerate Hopf bifurcation with O(2) symmetry”. In: *Contemporary Mathematics* 56, pp. 193–201.
- Dumortier, F, R Roussarie, and J Sotomayor (1987). “Generic 3-parameter families of vector fields on the plane, unfolding a singularity with nilpotent linear part. The cusp case of codimension 3”. In: *Ergodic theory and dynamical systems* 7.3, pp. 375–413.
- Jones, CA and MRE Proctor (1987). “Strong spatial resonance and travelling waves in Bénard convection”. In: *Physics Letters A* 121.5, pp. 224–228.
- Armbruster, Dieter, John Guckenheimer, and Philip Holmes (1988). “Heteroclinic cycles and modulated travelling waves in systems with O (2) symmetry”. In: *Physica D: Nonlinear Phenomena* 29.3, pp. 257–282.
- Huerre, Patrick and Peter A Monkewitz (1990). “Local and global instabilities in spatially developing flows”. In: *Annual review of fluid mechanics* 22.1, pp. 473–537.
- Monkewitz, PA (1990). “The role of absolute and convective instability in predicting the behavior of fluid systems”. In: *European Journal of Mechanics B Fluids* 9.5, pp. 395–413.
- Chiang, C H and W A Sirignano (1993). “Interacting, convecting, vaporizing fuel droplets with variable properties”. In: *International Journal of Heat and Mass Transfer* 36.4, pp. 875–886.
- Cross, Mark C and Pierre C Hohenberg (1993). “Pattern formation outside of equilibrium”. In: *Reviews of modern physics* 65.3, p. 851.
- Kuchment, Peter (1993). “Floquet Theory for Hypoelliptic Equations and Systems in the Whole Space”. In: *Floquet Theory for Partial Differential Equations*. Springer, pp. 103–123.
- Edwards, W Stuart and S Fauve (1994). “Patterns and quasi-patterns in the Faraday experiment”. In: *Journal of Fluid Mechanics* 278, pp. 123–148.
- Barkley, Dwight and Ronald D Henderson (1996). “Three-dimensional Floquet stability analysis of the wake of a circular cylinder”. In: *Journal of Fluid Mechanics* 322, pp. 215–241.
- Mcleod, Paul, David S Riley, and R Stephen J Sparks (1996). “Melting of a sphere in hot fluid”. In: *Journal of Fluid Mechanics* 327, pp. 393–409.
- Palacios, Antonio et al. (1997). “Cellular pattern formation in circular domains”. In: *Chaos: An Interdisciplinary Journal of Nonlinear Science* 7.3, pp. 463–475.
- Trefethen, Lloyd N (1999). *Spectra and Pseudospectra: The Behaviour of Non-normal Matrices and Operators*. Springer.

- Porter, J and E Knobloch (2000). “Complex dynamics in the 1:3 spatial resonance”. In: *Physica D: Nonlinear Phenomena* 143.1-4, pp. 138–168.
- Marques, F, JM Lopez, and J Shen (2001). “A periodically forced flow displaying symmetry breaking via a three-tori gluing bifurcation and two-tori resonances”. In: *Physica D: Nonlinear Phenomena* 156.1-2, pp. 81–97.
- Mougin, Guillaume and Jacques Magnaudet (2001). “Path instability of a rising bubble”. In: *Physical Review Letters* 88.1, p. 014502.
- Porter, J and E Knobloch (2001). “New type of complex dynamics in the 1:2 spatial resonance”. In: *Physica D: Nonlinear Phenomena* 159.3-4, pp. 125–154.
- Mercader, Isabel, Joana Prat, and Edgar Knobloch (2002). “Robust heteroclinic cycles in two-dimensional Rayleigh–Bénard convection without Boussinesq symmetry”. In: *International Journal of Bifurcation and Chaos* 12.11, pp. 2501–2522.
- Ewert, Roland and Wolfgang Schröder (2003). “Acoustic perturbation equations based on flow decomposition via source filtering”. In: *Journal of Computational Physics* 188.2, pp. 365–398.
- Fernández, Miguel Angel and Patrick Le Tallec (2003a). “Linear stability analysis in fluid–structure interaction with transpiration. Part I: Formulation and mathematical analysis”. In: *Computer methods in applied mechanics and engineering* 192.43, pp. 4805–4835.
- (2003b). “Linear stability analysis in fluid–structure interaction with transpiration. Part II: Numerical analysis and applications”. In: *Computer methods in applied mechanics and engineering* 192.43, pp. 4837–4873.
- Gan, Hui et al. (2003). “Direct numerical simulation of the sedimentation of solid particles with thermal convection”. In: *Journal of Fluid Mechanics* 481, pp. 385–411.
- Nore, Caroline, Laurette S Tuckerman, et al. (2003). “The 1 [ratio] 2 mode interaction in exactly counter-rotating von Kármán swirling flow”. In: *Journal of Fluid Mechanics* 477, pp. 51–88.
- Drazin, Philip G and William Hill Reid (2004). *Hydrodynamic stability*. Cambridge university press.
- Vandenbergh, Nicolas, Jun Zhang, and Stephen Childress (2004). “Symmetry breaking leads to forward flapping flight”. In: *Journal of Fluid Mechanics* 506, pp. 147–155.
- Wedin, Hakan and Rich R Kerswell (2004). “Exact coherent structures in pipe flow: travelling wave solutions”. In: *Journal of Fluid Mechanics* 508, pp. 333–371.
- Cvitanovic, Predrag et al. (2005). “Chaos: classical and quantum”. In: *ChaosBook.org (Niels Bohr Institute, Copenhagen 2005)* 69, p. 25.

-
- Gasull, Armengol, Viéctor Mañosa, and Jordi Villadelprat (2005). “On the period of the limit cycles appearing in one-parameter bifurcations”. In: *Journal of Differential Equations* 213.2, pp. 255–288.
- Mariano, Paolo Maria and Furio Lorenzo Stazi (2005). “Computational aspects of the mechanics of complex materials”. In: *Archives of Computational Methods in Engineering* 12.4, pp. 391–478.
- Nore, C, F Moisy, and L Quartier (2005). “Experimental observation of near-heteroclinic cycles in the von Kármán swirling flow”. In: *Physics of Fluids* 17.6, p. 064103.
- Porter, J and E Knobloch (2005). “Dynamics in the 1: 2 spatial resonance with broken reflection symmetry”. In: *Physica D: Nonlinear Phenomena* 201.3-4, pp. 318–344.
- Tanaka, Dan (2005). “Bifurcation scenario to Nikolaevskii turbulence in small systems”. In: *Journal of the Physical Society of Japan* 74.8, pp. 2223–2225.
- Dumortier, Freddy, Robert Roussarie, Jorge Sotomayor, and Henryk Zoladek (2006). *Bifurcations of planar vector fields: Nilpotent Singularities and Abelian Integrals*. Springer.
- Hoyle, Rebecca and Rebecca B Hoyle (2006). *Pattern formation: an introduction to methods*. Cambridge University Press.
- Brøns, M. (2007). “Streamline topology: Patterns in fluid flows and their bifurcations”. In: *Advances in applied mechanics* 41, pp. 1–42.
- Fernandes, Pedro C et al. (2007). “Oscillatory motion and wake instability of freely rising axisymmetric bodies”. In: *Journal of Fluid Mechanics* 573, pp. 479–502.
- Giannetti, Flavio and Paolo Luchini (2007). “Structural sensitivity of the first instability of the cylinder wake”. In: *Journal of Fluid Mechanics* 581, pp. 167–197.
- Schmid, Peter J (2007). “Nonmodal stability theory”. In: *Annual review of fluid mechanics* 39.1, pp. 129–162.
- Sipp, D. and A. Lebedev (2007). “Global stability of base and mean flows: a general approach and its applications to cylinder and open cavity flows”. In: *J. Fluid Mech.* 593, pp. 333–358.
- Fabre, David, Franck Auguste, and Jacques Magnaudet (2008). “Bifurcations and symmetry breaking in the wake of axisymmetric bodies”. In: *Physics of Fluids* 20.5, p. 051702.
- Gibson, John F, Jonathan Halcrow, and Predrag Cvitanović (2008). “Visualizing the geometry of state space in plane Couette flow”. In: *Journal of Fluid Mechanics* 611, pp. 107–130.
- Marquet, Olivier, Denis Sipp, and Laurent Jacquin (2008). “Sensitivity analysis and passive control of cylinder flow”. In: *Journal of Fluid Mechanics* 615, pp. 221–252.

- Veldhuis, Christian, Arie Biesheuvel, and Leen Van Wijngaarden (2008). “Shape oscillations on bubbles rising in clean and in tap water”. In: *Physics of fluids* 20.4, p. 040705.
- Coudene, Yves (2009). “A short proof of the unique ergodicity of horocyclic flows”. In: *Ergodic theory* 485, pp. 85–89.
- Gibson, John F, Jonathan Halcrow, and Predrag Cvitanović (2009). “Equilibrium and travelling-wave solutions of plane Couette flow”. In: *Journal of Fluid Mechanics* 638, pp. 243–266.
- Kotouč, Miroslav, Gilles Bouchet, and Jan Dušek (2009). “Transition to turbulence in the wake of a fixed sphere in mixed convection”. In: *Journal of Fluid Mechanics* 625, pp. 205–248.
- Meliga, Philippe, Jean-Marc Chomaz, and Denis Sipp (2009). “Global mode interaction and pattern selection in the wake of a disk: a weakly nonlinear expansion”. In: *Journal of Fluid Mechanics* 633, pp. 159–189.
- Seydel, Rudiger (2009). *Practical bifurcation and stability analysis*. Vol. 5. Springer Science & Business Media.
- Auguste, Franck, David Fabre, and Jacques Magnaudet (2010). “Bifurcations in the wake of a thick circular disk”. In: *Theoretical and Computational Fluid Dynamics* 24.1, pp. 305–313.
- Chrust, Marcin, Gilles Bouchet, and Jan Dušek (2010). “Parametric study of the transition in the wake of oblate spheroids and flat cylinders”. In: *Journal of Fluid Mechanics* 665, pp. 199–208.
- Giannetti, Flavio, Simone Camarri, and Paolo Luchini (2010). “Structural sensitivity of the secondary instability in the wake of a circular cylinder”. In: *Journal of Fluid Mechanics* 651, pp. 319–337.
- Pralits, Jan O, Luca Brandt, and Flavio Giannetti (2010). “Instability and sensitivity of the flow around a rotating circular cylinder”. In: *Journal of Fluid Mechanics* 650, pp. 513–536.
- Charru, François (2011). *Hydrodynamic instabilities*. Vol. 37. Cambridge University Press.
- Chossat, Pascal and Gérard Iooss (2012). *The Couette-Taylor Problem*. Vol. 102. Springer Science & Business Media.
- Golubitsky, Martin, Ian Stewart, and David G Schaeffer (2012). *Singularities and Groups in Bifurcation Theory: Volume II*. Vol. 69. Springer Science & Business Media.
- Meliga, Philippe, François Gallaire, and Jean-Marc Chomaz (2012). “A weakly nonlinear mechanism for mode selection in swirling jets”. In: *Journal of Fluid Mechanics* 699, pp. 216–262.
- Sadhal, Satwindar S, Portonovo S Ayyaswamy, and Jacob N Chung (2012). *Transport phenomena with drops and bubbles*. Springer Science & Business Media.

- Sipp, Denis (2012). “Open-loop control of cavity oscillations with harmonic forcings”. In: *Journal of Fluid Mechanics* 708, p. 439.
- Garnaud, X et al. (2013). “Modal and transient dynamics of jet flows”. In: *PHYSICS OF FLUIDS* 25, p. 044103.
- Kapitula, Todd and Keith Promislow (2013). *Spectral and dynamical stability of nonlinear waves*. Vol. 457. Springer.
- Kuznetsov, Yuri A (2013). *Elements of applied bifurcation theory*. Vol. 112. Springer Science & Business Media.
- Schmuck, M et al. (2013). “New stochastic mode reduction strategy for dissipative systems”. In: *Physical Review Letters* 110.24, p. 244101.
- Tchoufag, Joël (2013). “Étude de la trajectoire d’objets en chute ou en ascension dans un fluide visqueux: une approche de stabilité globale”. PhD thesis. Université de Toulouse, Université Toulouse III-Paul Sabatier.
- Luchini, Paolo and Alessandro Bottaro (2014). “Adjoint equations in stability analysis”. In: *Annual Review of fluid mechanics* 46, pp. 493–517.
- Thompson, MC et al. (2014). “The Existence of Multiple Solutions for Rotating Cylinder Flows”. In.
- Marquet, Olivier and Lutz Lesshafft (2015). “Identifying the active flow regions that drive linear and nonlinear instabilities”. In: *arXiv preprint arXiv:1508.07620*.
- Tchoufag, Joël, David Fabre, and Jacques Magnaudet (2015). “Weakly nonlinear model with exact coefficients for the fluttering and spiraling motion of buoyancy-driven bodies”. In: *Physical Review Letters* 115.11, p. 114501.
- Citro, Vincenzo, Joël Tchoufag, et al. (2016). “Linear stability and weakly nonlinear analysis of the flow past rotating spheres”. In: *Journal of Fluid Mechanics* 807, pp. 62–86.
- Gallaire, Francois et al. (2016). “Pushing amplitude equations far from threshold: application to the supercritical Hopf bifurcation in the cylinder wake”. In: *Fluid Dynamics Research* 48.6, p. 061401.
- Canton, J., F. Auteri, and M. Carini (2017). “Linear global stability of two incompressible coaxial jets”. In: *J. Fluid Mech.* 824, pp. 886–911.
- Heil, M. et al. (2017). “Topological fluid mechanics of the formation of the Kármán-vortex street”. In: *Journal of Fluid Mechanics* 812, pp. 199–221.
- Olvera, D and RR Kerswell (2017). “Exact coherent structures in stably stratified plane Couette flow”. In: *Journal of Fluid Mechanics* 826, pp. 583–614.
- Taira, Kunihiko et al. (2017). “Modal analysis of fluid flows: An overview”. In: *Aiaa Journal* 55.12, pp. 4013–4041.
- Wouters, J and GA Gottwald (2017). “Edgeworth expansions for slow-fast systems and their application to model reduction for finite time scale separation”. In: *arXiv preprint arXiv:1708.06984* 10.
- Chakravarthy, RVK, Lutz Lesshafft, and P Huerre (2018). “Global stability of buoyant jets and plumes”. In: *Journal of Fluid Mechanics* 835, pp. 654–673.

- Fabre, David, Vincenzo Citro, et al. (2018). “A practical review on linear and nonlinear global approaches to flow instabilities”. In: *Applied Mechanics Reviews* 70.6.
- Lesshafft, Lutz (2018). “Instability dynamics in jets and plumes”. PhD thesis. Université Paris-Sud Orsay.
- Allen, Liz, Alison O’Connell, and Veronique Kiermer (2019). “How can we ensure visibility and diversity in research contributions? How the Contributor Role Taxonomy (CRediT) is helping the shift from authorship to contributorship”. In: *Learned Publishing* 32.1, pp. 71–74.
- Bonnefis, Paul (2019). “Etude des instabilités de sillage, de forme et de trajectoire de bulles par une approche de stabilité linéaire globale”. PhD thesis.
- Fabre, David, Raffaele Longobardi, Paul Bonnefis, et al. (2019). “The acoustic impedance of a laminar viscous jet through a thin circular aperture”. In: *Journal of Fluid Mechanics* 864, pp. 5–44.
- Giannetti, F, S Camarri, and V Citro (2019). “Sensitivity analysis and passive control of the secondary instability in the wake of a cylinder”. In: *Journal of Fluid Mechanics* 864, pp. 45–72.
- Jaunet, Vincent et al. (2019). “Dynamics of round jet impingement”. In: *25th AIAA/CEAS Aeroacoustics Conference*, p. 2769.
- Krack, Malte and Johann Gross (2019). *Harmonic balance for nonlinear vibration problems*. Springer.
- Moulin, Johann, Pierre Jolivet, and Olivier Marquet (2019). “Augmented Lagrangian preconditioner for large-scale hydrodynamic stability analysis”. In: *Computer Methods in Applied Mechanics and Engineering* 351, pp. 718–743.
- Pfister, Jean-Lou (2019). “Instabilities and optimization of elastic structures interacting with laminar flows”. PhD thesis. UNIVERSITE PARIS-SACLAY.
- Shaabani-Ardali, Léopold, Denis Sipp, and Lutz Lesshafft (2019). “Vortex pairing in jets as a global Floquet instability: modal and transient dynamics”. In: *Journal of Fluid Mechanics* 862, pp. 951–989.
- Sierra-Ausin, Javier, Vincenzo Citro, and David Fabre (2019). “On boundary conditions for compressible flow simulations”. In: pp. 335–340.
- Citro, V, F Giannetti, and J. Sierra-Ausin (2020). “Optimal explicit Runge-Kutta methods for compressible Navier-Stokes equations”. In: *Applied Numerical Mathematics* 152, pp. 511–526.
- Fabre, D, R Longobardi, V Citro, et al. (2020). “Acoustic impedance and hydrodynamic instability of the flow through a circular aperture in a thick plate”. In: *Journal of Fluid Mechanics* 885.
- Nitti, Alessandro et al. (June 2020). “An immersed-boundary/isogeometric method for fluid–structure interaction involving thin shells”. In: *Computer Methods in Applied Mechanics and Engineering* 364, p. 112977. DOI: 10.1016/j.cma.2020.112977.

- Sabino, Diogo et al. (2020). “Vortex-induced vibration prediction via an impedance criterion”. In: *Journal of Fluid Mechanics* 890, A4.
- Schoder, Stefan, Klaus Roppert, and Manfred Kaltenbacher (2020). “Helmholtz’s decomposition for compressible flows and its application to computational aeroacoustics”. In: *SN Partial Differential Equations and Applications* 1.6, pp. 1–20.
- Sierra-Ausin, Javier, David Fabre, and Vincenzo Citro (2020). “Efficient stability analysis of fluid flows using complex mapping techniques”. In: *Computer Physics Communications* 251, p. 107100.
- Sierra-Ausin, Javier, David Fabre, Vincenzo Citro, and Flavio Giannetti (2020). “Bifurcation scenario in the two-dimensional laminar flow past a rotating cylinder”. In: *Journal of Fluid Mechanics* 905.
- Spieser, Etienne (2020). “Modélisation de la propagation du bruit de jet par une méthode adjointe formulée pour l’acoustique potentielle”. PhD thesis.
- Callahan, Jared L et al. (2021). “Nonlinear stochastic modelling with Langevin regression”. In: *Proceedings of the Royal Society A* 477.2250, p. 20210092.
- Sierra-Ausin, Javier, Pierre Jolivet, et al. (2021). “Adjoint-based sensitivity analysis of periodic orbits by the Fourier–Galerkin method”. In: *Journal of Computational Physics* 440, p. 110403.
- Cenedese, Mattia et al. (2022). “Data-driven modeling and prediction of non-linearizable dynamics via spectral submanifolds”. In: *Nature communications* 13.1, p. 872.
- Hirschberg, Lionel et al. (2022). “Linear Theory and Experiments for Laminar Bias Flow Impedance: Orifice Shape Effect”. In: p. 2887.
- Sáez-Mischlich, Gonzalo, Sierra-Ausin, Javier, and Jérémie Gressier (2022). “The Spectral Difference Raviart–Thomas Method for Two and Three-Dimensional Elements and Its Connection with the Flux Reconstruction Formulation”. In: *Journal of Scientific Computing* 93.2, pp. 1–54.
- Sáez-Mischlich, Gonzalo, Sierra-Ausin, Javier, Gilles Grondin, et al. (2022). “On the properties of high-order least-squares finite-volume schemes”. In: *Journal of Computational Physics* 457, p. 111043.
- Sierra-Ausin, J, M Lorite-Diez, et al. (2022). “Unveiling the competitive role of global modes in the pattern formation of rotating sphere flows”. In: *Journal of Fluid Mechanics* 942.
- Sierra-Ausin, J., D Fabre, V Citro, et al. (2022). “Acoustic instability prediction of the flow through a circular aperture in a thick plate via an impedance criterion”. In: *Journal of Fluid Mechanics* 943.
- Sierra-Ausin, Javier, Paul Bonnefis, et al. (2022). “Dynamics of a gas bubble in a straining flow: Deformation, oscillations, self-propulsion”. In: *Physical Review Fluids* 7.11, p. 113603.

- Sierra-Ausin, Javier, Vincenzo Citro, Flavio Giannetti, et al. (2022). “Efficient computation of time-periodic compressible flows with spectral techniques”. In: *Computer Methods in Applied Mechanics and Engineering* 393, p. 114736.
- Corrochano, A. et al. (2023). “Mode selection in concentric jets with resonance 1:2”. In: *Journal of Fluid Mechanics (accepted)*.
- Hirschberg, Lionel et al. (2023). “Linear Theory and Experiments for Laminar Bias Flow Impedance”. In: *AIAA (to be submitted)*.
- Sierra-Ausin, J., D. Fabre, and E. Knobloch (2023). “Wake dynamics in buoyancy-driven flows: steady state–Hopf mode interaction with $O(2)$ symmetry revisited”. In: *Phys. Rev. E (submitted)*.
- Sierra-Ausin, J. and F. Giannetti (2023). “On the linear and nonlinear mechanisms for the tonal and broadband noise of subsonic rounded impinging jets”. In: *Journal of Fluid Mechanics (to be submitted)*.
- Tirri, Antonia et al. (2023). “Linear stability analysis of fluid–structure interaction problems with an immersed boundary method”. In: *Journal of Fluids and Structures* 117, p. 103830.